

Zengqi Sun
Zhidong Deng
Editors

Proceedings of 2013 Chinese Intelligent Automation Conference

Intelligent Automation

Lecture Notes in Electrical Engineering

Volume 254

For further volumes:
<http://www.springer.com/series/7818>

Zengqi Sun · Zhidong Deng
Editors

Proceedings of 2013 Chinese Intelligent Automation Conference

Intelligent Automation

 Springer

Editors
Zengqi Sun
Zhidong Deng
Department of Computer Science
Tsinghua University
Beijing
People's Republic of China

ISSN 1876-1100 ISSN 1876-1119 (electronic)
ISBN 978-3-642-38523-0 ISBN 978-3-642-38524-7 (eBook)
DOI 10.1007/978-3-642-38524-7
Springer Heidelberg New York Dordrecht London

Library of Congress Control Number: 2013939563

© Springer-Verlag Berlin Heidelberg 2013

This work is subject to copyright. All rights are reserved by the Publisher, whether the whole or part of the material is concerned, specifically the rights of translation, reprinting, reuse of illustrations, recitation, broadcasting, reproduction on microfilms or in any other physical way, and transmission or information storage and retrieval, electronic adaptation, computer software, or by similar or dissimilar methodology now known or hereafter developed. Exempted from this legal reservation are brief excerpts in connection with reviews or scholarly analysis or material supplied specifically for the purpose of being entered and executed on a computer system, for exclusive use by the purchaser of the work. Duplication of this publication or parts thereof is permitted only under the provisions of the Copyright Law of the Publisher's location, in its current version, and permission for use must always be obtained from Springer. Permissions for use may be obtained through RightsLink at the Copyright Clearance Center. Violations are liable to prosecution under the respective Copyright Law. The use of general descriptive names, registered names, trademarks, service marks, etc. in this publication does not imply, even in the absence of a specific statement, that such names are exempt from the relevant protective laws and regulations and therefore free for general use.

While the advice and information in this book are believed to be true and accurate at the date of publication, neither the authors nor the editors nor the publisher can accept any legal responsibility for any errors or omissions that may be made. The publisher makes no warranty, express or implied, with respect to the material contained herein.

Printed on acid-free paper

Springer is part of Springer Science+Business Media (www.springer.com)

Preface

The 2013 Chinese Intelligent Automation Conference (CIAC2013) was Sponsored by Intelligent Automation Committee, Chinese Association of Automation and organized by Yangzhou University in Yangzhou, Jiangsu Province, China; 23–25, August, 2013. The objective of CIAC2013 was to provide a platform for researchers, engineers, academicians as well as industrial professionals from all over the world to present their research results and development activities in Intelligent Control, Intelligent Information Processing and Intelligent Technology and Systems. This conference provided opportunities for the delegates to exchange new ideas and application experiences face-to-face, to establish research or business relations and to find partners for future collaboration.

We have received more than 800 papers. The topics include adaptive control, fuzzy control, neural network-based control, knowledge-based control, hybrid intelligent control, learning control, evolutionary mechanism-based control, multi-sensor integration, failure diagnosis, and reconfigurable control, etc. Engineers and researchers from academia, industry, and government can gain an inside view of new solutions combining ideas from multiple disciplines in the field of Intelligent Automation. All submitted papers have been subject to a strict peer-review process; 285 of them were selected for presentation at the conference and included in the CIAC2013 proceedings. We believe the proceedings can provide the readers a broad overview of the latest advances in the fields of Intelligent Automation.

CIAC2013 has been supported by many professors (see the name list of the committees); we would like to take this opportunity to express our sincere gratitude and highest respect to them. At the same time, we also express our sincere thanks for the support of every delegate.

Zengqi Sun
Chair of CIAC2013

Committees

Honorary Chairs

Yanda Li, Tsinghua University, China

Bo Zhang, Tsinghua University, China

General Chair

Zengqi Sun, Tsinghua University, China

General Co-Chairs

Hongxin Wu, Beijing Institute of Control Engineering

Qidi Wu, Tongji University

Jue Wang, Institute of Automation, Chinese Academy of Science

Wenli Xu, Tsinghua University

Xingyu Wang, East China University of Science and Technology

Yixin Yin, University of Science and Technology, Beijing

Zushu Li, Chongqing University

Limin Jia, Beijing Jiaotong University

Zhidong Deng, Tsinghua University

Junping Du, Beijing University of Posts and Telecommunications

Technical Program Committee Co-Chairs

Zhidong Deng, Tsinghua University

Yixin Yin, University of Science and Technology, Beijing

Limin Jia, Beijing Jiaotong University

Junping Du, Beijing University of Posts and Telecommunications

Tianping Zhang, Yangzhou University

Organizing Committee Co-Chairs

Bin Li, Yangzhou University
Tianping Zhang, Yangzhou University
Yun Li, Yangzhou University
Yuequan Yang, Yangzhou University
Hua Ye, Southeast University

Contents

1	Formation Control of Autonomous Underwater Vehicles Based on Finite-Time Consensus Algorithms	1
	Jian Yuan, Zhong-Hai Zhou, Hua Mu, Yu-Ting Sun and Lei Li	
2	The Research on Fault Diagnosis of Building Electrical System Based on RBF Neural Network	9
	Qian Wu, Yahui Wang, Long Zhang and Li Shen	
3	Adaptive Dynamic Surface Control of Stochastic Strict Feedback Nonlinear Systems	21
	Xiaocheng Shi, Tianping Zhang, Huating Gao and Fei Wang	
4	Three-Dimensional Path Planning for AUV Based on Fuzzy Control	31
	Lisha Jiang and Daqi Zhu	
5	Consensus Analysis of Multi-Agent System with Impulsive Effects and Time-Varying Delays	41
	Dandan Li, Mei Sun, Dun Han and Anna Gao	
6	One Method of Judging Spatial Topological Relations in N-Dimensional Space and Its Application in Interpolation	49
	Binhui Chen, Bofeng Wu and Jiaxiang Lin	
7	Modified Ant Colony Optimization Algorithm for the Multi-Sensor Dynamic Scheduling	65
	Hai Huang, Jing Zhang, Xiaomin Ran and Wengao Lv	
8	Experimental Study on Improved Differential Evolution for System Identification of Hammerstein Model and Wiener Model	75
	Weili Xiong, Minfang Chen, Le Yao and Baoguo Xu	

9	The Coverage Optimization for Wireless Sensor Networks Based on Quantum-Inspired Cultural Algorithm	87
	Yi-nan Guo, Dandan Liu, Yun Liu and Meirong Chen	
10	Sensor Failure Detection and Diagnosis via Polynomial Chaos Theory–Part I: Theoretical Background	97
	Weilin Li, Xiaobin Zhang, Wenli Yao and Huimin Li	
11	Adaptive Tracking Control of Nonlinear Systems with Unmodeled Dynamics and Unknown Gain Sign	107
	Zhiyuan Gao, Tianping Zhang and Yuequan Yang	
12	Generalized Projective Synchronization of Takagi–Sugeno Fuzzy Drive-Response Dynamical Networks with Time Delay . . .	119
	Yongai Zheng and Lei Shang	
13	Immune Mobile Agent and Its Application in IDS	127
	Tao Ji, Yongzhong Li and Jing Xu	
14	The Improved Discernibility Matrix Based on Decision Vector. . .	137
	Jingfu Li and Denghui Bu	
15	Backward Circular Motion Control for Mobile Robot with Two Trailers.	145
	Jin Cheng, Yong Zhang, Zhonghua Wang and Li Gong	
16	Instruments Fault Detection in Process Industry with Independent Component Analysis	153
	Jichen Hu and Guoyong Huang	
17	Nonlinear Process Fault Detection Based on Multi-Scale Sparse Kernel Classifier	161
	Xiaogang Deng and Xuemin Tian	
18	Backstepping Based Type-2 Adaptive Fuzzy Control for a Generic Hypersonic Flight Vehicle	169
	Fang Yang, Ruyi Yuan, Jianqiang Yi, Guoliang Fan and Xiangmin Tan	
19	Ahead of the End Dynamic Time Warping Distance Algorithm Application in Iterative Learning Control	179
	Qun Gu and Xiaohong Hao	

20 Application of Discrete Particle Swarm Optimization Algorithm to Aviation Rescue Base Location 187
 Xiuyu Wu, Guoping Xing, Yongren Chen and Lijie Wu

21 Intelligent Control Based on ADRC for Large Container Ship Course Keeping 195
 Yang Liu, Chen Guo and Zhengling Lei

22 Course Keeping Control of Underactuated Surface Vessels Based on Improved PSO Algorithm 207
 Guangyu Li, Chen Guo and Yanxin Li

23 On-line Optimization of Fuzzy-Immune PID for PEMFC Temperature Control Based on RBF Neural Network 215
 Dazi Li, Yadi Yu and Qibing Jin

24 Adaptive Fuzzy Controller Design for Strict-Feedback Nonlinear System Using Command Filtering 223
 Junsheng Ren

25 Consensus Problem of Second-Order Multi-Agent Systems with Communication Delay and Input Delay 233
 Pingping Dai, Chenglin Liu and Fei Liu

26 An Image-Based Visual Servo Control of Robots with Omni-Directional Camera 245
 Haiyong Chen, Guansheng Xing, Zihan Ma, Jinsuo Wang and Peng Yang

27 Simulation and Forecast About Vegetable Prices Based on PSO-RBFNN Model. 255
 Qigang Xu and Mingjun Liu

28 A Belief-Rule-Based Inference Method for Carrier Battle Group Recognition 261
 Lianmeng Jiao, Quan Pan, Xiaoxue Feng and Feng Yang

29 Multi-Robot Cooperation Handling Based on Immune Algorithm in the Known Environment 273
 Mingxin Yuan, Zhaoli Ye, Shuai Cheng and Yafeng Jiang

30 Global Exponential Synchronization Between Two Different Complex Networks with Time Vary Delays 281
Guoliang Cai, Yihong Du and Xianbin Wu

31 Pattern Recognition of the Thigh Amputee Motion Based on Genetic Algorithm and BP 291
Lei Liu, Peng Yang, Zuojun Liu, Lingling Chen and Yanli Geng

32 R-Fuzzy Subsemigroups 299
Xiao-ying Zhu, Zu-hua Liao and Cui-yun Hao

33 A New Constant Gain Kalman Filter Based on TP Model Transformation 305
Fan Yang, Zhen Chen, Xiangdong Liu and Bing Liu

34 Spacecraft Attitude Control via New Non-Singular Fast Terminal Sliding Mode Control 313
Xin Lv, Zhen Chen, Xiangdong Liu, Binglong Cong and Liang Wang

35 Time-Variant Gait Planning for Under-Actuated Biped Robot via Optimization. 323
Xiaowei OuYang, Gang Pan and Ling Yu

36 Immune Network Risk Evaluation Model Based on the Spreading of Infectious Diseases 333
Jin Yang, Tang Liu and Lingxi Peng

37 Recurrent Neural Network for Human Activity Recognition in Smart Home. 341
Hongqing Fang, Hao Si and Long Chen

38 Optimization of an Advanced Guidance Scheme for Long-Range AAMs Based on SPSO 349
Xilian Li, Shutang Fu and Huitao Fan

39 Research on High-Accuracy Data Association of Space-Borne SAR and AIS 359
Zhi Zhao, Kefeng Ji, Xiangwei Xing and Huanxin Zou

40 A Control Method of Inclined Inverted Pendulum on a Mobile Foundation with Disturbances 369
Cheng Guo, Xiaoyu Han and Yingmin Jia

41 TiltRotor Aircraft Flight Control Study Based on Fuzzy Logic Control via Genetic Algorithm 377
 Heng Chen, Xu Wang and Tengfei Lei

42 Hybrid Projective Synchronization of a New Hyperchaotic System 385
 Jinchen Yu and Caiyan Zhang

43 Fuzzy Observer-Based Robust H_∞ Guaranteed Cost Fault-Tolerant Design for Nonlinear NCS 393
 Jun Wang, Wei Li and Zhanming Li

44 Study on Adaptive Parameters for GDFNN via Genetic Algorithms. 403
 Jin Chen, Shaojian Song and Xiaofeng Lin

45 A Decreased Extreme Learning Machine with Ridge Parameter for Online Identification of Nonlinear Systems. 413
 Mingtao Zhang, Yi Liu and Zengliang Gao

46 Security Region Estimation of the Peak of Track Irregularity Based on Dangerous Points Distribution Ratio and SVM. 421
 Yong Qin, Shan Yu, Yuan Zhang, Limin Jia and Zongyi Xing

47 On the Symmetry of Interval Type-2 Fuzzy Logic Controllers Using Different Type-Reduction Methods 429
 Chengdong Li, Guiqing Zhang, Jianqiang Yi and Ming Wang

48 Development of Database System for Overhead Power Transmission Line Inspection Robot 439
 Dezheng Zhao, En Li, Guodong Yang and Zize Liang

49 Two Methods for Solving the Parameters of Weibull Distribution of Wind Velocity 449
 Baoqing Xu, Rui Tian and Guolin Yang

50 A Direct Robust Predictive Control Algorithm for Multi-Rate Systems. 457
 Xiaohua Liu and Rong Gao

51 Nonlinear Adaptive Control of Magnetic Levitation System with Uncertain Parameters and Unknown Disturbances. 467
 Baobin Liu

52	Mass Metrology Based on Robotic Mass Measurement System	477
	Xiaoping Ren, Changqing Cai, Yi Li, Aibin Chen and Qingxiong Ren	
53	A Reconfigurable Intelligent Gateway for Heterogeneous Networks	485
	Tiantian Guo, Ming'an Zhou and Qing Shen	
54	Robust Stability of a Class of Uncertain Discrete-Time Stochastic Systems	495
	Fengwei Yang, Yali Dong and Yangang Wang	
55	H_2 Controller Design for Markov Jump Systems with Polytopic-Type Uncertainty and Partly Known Transition Probabilities	503
	Quanyong Fan, Xinglei Gao and Dan Ye	
56	A New Control Method in pH Neutralization Process	511
	Juan Chen, Zhanfu Liu, Yawei Peng and Qing Guo	
57	Control Technology Research of the Underground Hydraulic Support Motion Simulation	521
	Guoying Zhang, Jiangwei You, Liang Xu and Yiyu Cheng	
58	Research on Chilled Water Pressure Difference of the Model Reference Adaptive Control	531
	Hongmei Jiang, Dongdong Cai, Yugui Nian and Qingchang Ren	
59	Research on Greenhouse Climate Control Based on RBF Neural Networks	541
	Baicheng Liu, Yifei Chen, Kai Qi and Shangfeng Du	
60	Research on Neural Network Model for Greenhouse Temperature Predictive Control	551
	Kai Qi, Yifei Chen, Baicheng Liu and Shangfeng Du	
61	The Research on Fault Diagnosis Method of the Coal Mill Based on Information Fusion	559
	Zheng Zhao and Xueyan Lu	
62	Higher Sliding Mode Tracking Control for Underactuated Surface Vessel	569
	Zhuang Lin, Benjie Dong and Zhiqun Guo	

63 Modeling and Simulation of Biomimetic Motion Dynamics for Dextrous Hand 579
 Mingkun Zhang, Yizhi Shi, Jun Shen and Yao Li

64 Nonlinear Integrator Sliding Mode Control for Brushless Double-Fed Wind Power Generation System 591
 Zongkai Shao, Jichen Hu and Guoyong Huang

65 Time-Varying Constant Identification Based on PSO and Dynamic Compensation of Temperature Sensors. 601
 Chao Wang, Yakun Zhao and Hongbing Ding

66 Path Tracking Control of Underactuated AUVs Based on ADRC 609
 Yushan Sun, Yinghao Zhang, Guocheng Zhang and Yueming Li

67 Fuzzy Method for Sub-Communities Identification in Complex Networks 617
 Danling Wang and Yanfei Wang

68 Modeling for the Clarifying Process of Sugar Mills with ESN 625
 Xiao-feng Lin and Yun-peng Liu

69 A Method of Metro Vehicle Auxiliary Inverter Fault Diagnosis Based on Weighted Fuzzy Clustering Algorithm 633
 Zengtao Ma, Junwei Gao, Bin Zhang, Dechen Yao and Yong Qin

70 The Inverted Pendulum Control System Based on Two Degree of Freedom Model Driven PID 641
 Lixiang Zhang and Haiyan Zhang

71 Delay-Dependent Robust Stabilization for Singular Nonlinear System with Markovian Jumping Parameters 649
 Chunmei Duan and Hongqian Lu

72 A Free-Weighting Matrices Technique for Stochastic Stability Analysis of Uncertain Singular Hybrid System 657
 Hongqian Lu, Wuneng Zhou and Xingping Liu

73 Application of EKF Training RBFNN in Fault Diagnosis of Subway Auxiliary Inverter 667
 Junwei Gao, Ziwen Leng, Yong Qin, Xiaofeng Li and Dechen Yao

74 Fuzzy Combination Rule of Multiple Classifiers System Based on Yager Triangular Norm	675
Pengtao Jia, Shuhui Liang and Jun Deng	
75 Application of Swarm Intelligence Optimization in EEG Analysis	683
Lu Huang and Hong Wang	
76 Blind Detection of BPSK Signals Using Hysteretic Hopfield Neural Network	693
Shu-Juan Yu, Di Feng and Yun Zhang	
77 Design of Sewage Treatment Using Iron Nanoparticles Based on Fuzzy Logic Control	703
Miaomiao Tan, Yinan Li and Hui Jiao	
78 The Application of Fuzzy PI and RBF Neural Network Tuning PID in Servo System	711
Guozhi Li, Xiaohong Ren, Bing Ren and Ling Qiu	
79 Navigation Control of Humanoid Robot Based on Motor Imaginary	721
Fei Wang, Chucheng Zhou, Guangda Yang, Xiang Hao and Song Wang	
80 Stabilizability of a Class of Singularly Perturbed Systems via Switched Output Feedback	729
Hongwang Yu and Baoshan Zhang	
81 Design and Stability Analysis of the RRD Fuzzy Controller with D-Stability Constraint	735
Wenying Zhang, Xiuyan Peng, Zhonghui Hu and Yan Chang	
82 Short-Term Forecasting of Traffic Flow Based on Genetic Algorithm and BP Neural Network	745
Junwei Gao, Ziwen Leng, Bin Zhang, Guoqiang Cai and Xin Liu	
83 Joint State and Parameter Estimation for a Robot Hydraulic Actuator	753
Guangbin Sun and Hong Wang	

84 Delay-Dependent Robust Control for Output PDFs of Discrete-Time Non-Gaussian Stochastic Processes 761
 Yao An, Yang Yi, Weixing Zheng and Tianping Zhang

85 Review and Perspective of Theories and Methods About Emergency Evacuation Plans for UMT Station 771
 Yashu Kang, Jie Xu, Limin Jia, Jianyuan Guo and Xin Zhang

86 The Allocation of Berth and Quay Crane by Using a Particle Swarm Optimization Technique 779
 Chutian Yang, Su Wang and Jun Zheng

87 Optimal Trajectory Planning of Gaze Shifts Based on Modified Simulated Annealing Algorithm 789
 Ming Zeng, Zhanxie Wu, Haiyan Jia, Qinghao Meng and Hao Yang

88 Robust Dissipative Filter for Time-Varying and Time-Delay T-S Fuzzy Descriptor Systems with Parameter Uncertainties 799
 Yuechao Ma and Huijie Yan

89 The Realization of Fuzzy Control in Fire-Proof Material Batching System 807
 Xue Jun He and Jun Zhang

90 An Intuitionistic Fuzzy Neural Network with Triangular Membership Function 813
 Xiaoguang Zhou, Renhou Zhao and Lili Zhang

91 Covariance Intersection Fusion Robust Steady-State Kalman Predictor for Two-Sensor Systems with Unknown Noise Variances 821
 Wenjuan Qi, Peng Zhang and Zili Deng

92 Weighted Measurement Fusion Steady-State Robust Kalman Filter 829
 Peng Zhang, Wenjuan Qi and Zili Deng

93 Research on Evaluation of Cabin Design in Naval Ship Based on the Method of Intuitionistic Fuzzy Multiple Attribute Group Decision-Making 837
 Xiaowen Li, P. Li, Z. Lin, Z. Guo and D. Yang

94 Studying the Effect of the Group-Size on the Search Computing Cost of MEC for Function Optimization 845
Liai Wang and Chengyi Sun

95 Covariance Intersection Fusion Robust Steady-State Kalman Filter for Multi-Sensor Systems with Unknown Noise Variances 853
Wenjuan Qi, Peng Zhang, Wenqing Feng and Zili Deng

96 Study on Online ϵ NN Q-Learning for Multi-Robot System Based on Community Perception Network. 861
Lu Jin, Yuequan Yang, Chunbo Ni, Yifei Kong and Zhiqiang Cao

Chapter 1

Formation Control of Autonomous Underwater Vehicles Based on Finite-Time Consensus Algorithms

Jian Yuan, Zhong-Hai Zhou, Hua Mu, Yu-Ting Sun and Lei Li

Abstract Formation control of autonomous underwater vehicles is investigated. A finite-time consensus algorithm for second-order system is proposed, the consensus on velocities of AUV (linear velocity and angular velocity) and positions (displacement and attitude) are carried out with the finite-time consensus. Because of the limited communication range, the communication ranges of AUVs are predefined, so the AUVs system is modeled as a networked system with variable communication topologies. We demonstrate the formation control of multiple AUVs with different communication ranges, which show that the finite-time consensus on positions and velocities is obtained. Finally, we demonstrate the formation control of multiple AUVs with constraints on maximum velocity. Simulation results verify the effectiveness of the proposed control algorithms.

Keywords Autonomous underwater vehicle · Formation control · Finite-time consensus

1.1 Introduction

Cooperative control of multiple autonomous underwater vehicles (AUV) plays an important role on marine scientific investigation and marine development. The formation of multi-AUV can significantly enhance applications on the marine sampling, imaging, surveillance and communications. Compared to the formation

J. Yuan (✉) · Z.-H. Zhou · H. Mu · Y.-T. Sun · L. Li
Institute of Oceanographic Instrumentation of Shandong Academy of Sciences,
Qingdao, China
e-mail: jyuanjian801209@163.com

J. Yuan · Z.-H. Zhou · H. Mu · Y.-T. Sun · L. Li
Shandong Provincial Key Laboratory of Ocean Environment Monitoring Technology,
Shandong, China

control of multi-robot, the formation control of multi-AUV is particularly difficult, especially on controlling attitude and direction of AUV; what is more, the communication method among AUVs is acoustic. When communication distance increases, the communication qualities deteriorate quickly; this mainly makes time-delay, signal attenuation and distortion. Although formation control of multiple AUVs obtains a wide range of attention in recent years, the fruits on formation control problem are less than ones on land multi-robot problems. For example, Fiorelli conducted a collaborative and adaptive sampling research of multi-AUV at the Monterey Bay [1]; Yu and Ura carried out the cable-based modular fast-moving and obstacle-avoidance experiments, and presented an interconnected multi-AUV system with three-dimension sensors. On the aspect of formation control framework [2–4] proposed a four-layer cooperative control strategy based on hierarchical structure; Ref. [5] proposed a hierarchical control framework based on hybrid model. In addition, Yang converted a nonholonomic system to a chain one and designed a controller to implement a leader-follower formation for multiple AUVs in [6]. Formation control of land multi-robot has appeared more sophisticated control methods. Kalantar and Zimmer [7] studied the distributed formation control. References [8, 9] adopted the centralized formation control based on virtual structure; Refs. [10–13] used a distributed formation framework based on virtual structure to realize the formation control. Do studied the control of robot formation with limited communications [14], Dong and Farrell [15] studied collaboration control of robots with nonholonomic constraints, Kumar et al. [16] studied the cooperative control of robots with nonholonomic constraints based on omni-direction vision and designed distributed controllers and estimators. The authors proposed synchronization methods for two categories of complex networks: linearly and nonlinearly time-delay coupled networks with multiple agents in [17]. Convergence analysis of decentralized slot time synchronization algorithms for wireless Ad Hoc networks is shown with multiple-agent technologies in [18]. The formation control for multiple autonomous underwater vehicles is rather different than the control methods for other vehicles, because the formation control for AUVs is of its characteristics, such as the large-scale distribution in space. The finite-time consensus controller designing based on finite-time control and consensus problem has important theoretical and practical significance. Wang and Xiao [19] proposed a finite-time formation control framework for the large-scale multiple agents. The formation information is divided into the global information and local information, the former decides the formation shape of the whole formation, and only the leader can obtain such whole information but followers can only obtain the local information. This framework can greatly reduce the amount of communication between the agents. And then they designed a nonlinear consensus algorithm to time-varying, time invariant formation and trajectory tracking control. Wang and Hong [20] proposed a few kinds of algorithms for agents' network with a dynamic coupled topology. And then they designed a finite-time consensus protocol with Lyapunov function and graph theory and proposed a time invariant nonsmooth controller.

The decentralized controller methods for the autonomous underwater vehicle are applied more and more, but they ignore the coupling relationship between them. Another method is that an AUV is modeling as an agent, but this method ignores attitude characteristics of AUV's (pitch, roll and yaw). In this paper, we consider the cooperative control problem in three dimensional spaces. The proposed algorithm is based on finite-time consensus algorithms to realize the formation control for underwater vehicles. Finally, the simulation results show the effectiveness of the control strategy.

1.2 A Modeling of AUV in Three-Dimension Space

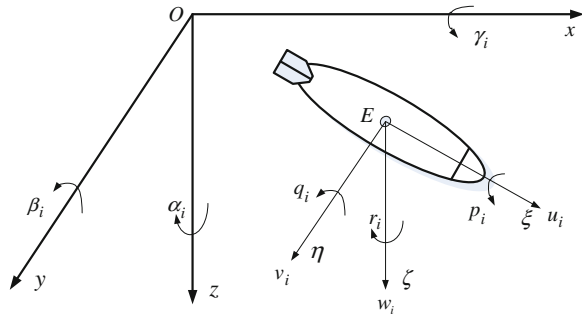
Firstly, we establish two coordinate frames: the geocentric inertial coordinate frame $O-xyz$ and the body-fixed coordinate frame $E-xhz$. The origin O in inertial coordinate frame is defined in some point at sea level, the $O-x$ and $O-y$ are in horizontal level, and $O-x$ is parallel with the longitude and points northwardly, $O-y$ is parallel with the latitude and points eastwardly, and $O-z$ is perpendicular to horizontal level and points to the earth's core. The three axes form the right-hand screw relation. The origin O in body-fixed coordinate frame is defined in some point at the AUV's canceoids. $E-x$ is defined in longitudinal section plane and points to the orientation of linear velocity, $E-h$ is perpendicular to the portrait section plane and points to the right-hand orientation, and $E-z$ is in the longitudinal section plane and points to the down orientation. Also the three axes form the right-hand screw relation. $E-x$, $E-h$ and $E-z$ are inertia principal axis of an AUV. The coordinates of AUV i in inertial coordinate frame are shown in Fig. 1.1.

The transformation matrix from the inertial coordinate frame to the body-fixed coordinate frame is

$$T_i = \begin{bmatrix} T_{vi} & 0 \\ 0 & T_{wi} \end{bmatrix}$$

where

Fig. 1.1 The coordinates of AUV i in coordinate frame



$$T_{vi} = \begin{bmatrix} \cos \beta_i \cos \alpha_i & -\sin \beta_i \cos \gamma_i + \cos \beta_i \sin \gamma_i \sin \alpha_i & \sin \beta_i \sin \gamma_i + \cos \beta_i \cos \gamma_i \sin \alpha_i \\ \sin \beta_i \cos \alpha_i & \cos \beta_i \cos \gamma_i + \sin \beta_i \sin \gamma_i \sin \alpha_i & -\cos \beta_i \sin \gamma_i + \sin \beta_i \cos \gamma_i \sin \alpha_i \\ -\sin \alpha_i & \sin \gamma_i \cos \alpha_i & \cos \gamma_i \cos \alpha_i \end{bmatrix}$$

$$T_{wi} = \begin{bmatrix} 1 & \tan \beta_i \sin \gamma_i & \tan \beta_i \cos \gamma_i \\ 0 & \cos \gamma_i & -\sin \gamma_i \\ 0 & \sin \gamma_i / \cos \beta_i & \cos \gamma_i / \cos \beta_i \end{bmatrix}$$

where a_i is the roll angle of AUV i , b_i is the pitch angle of AUV i and g_i is the yaw angle of AUV i . We define $\mathbf{X}_i = [x_{si} \ y_{si} \ z_{si} \ f_i \ q_i \ j_i]^T$, which denotes the positions and attitudes, and $\mathbf{v}_i = [u_i \ v_i \ w_i \ p_i \ q_i \ r_i]^T$ which denotes the linear velocity and the angular velocity in body-fixed coordinate frame. So $\dot{\mathbf{X}}_i = T_i^{-1} \cdot \mathbf{v}_i = \mathbf{V}_i$. Then we define $\mathbf{U}_i = \dot{\mathbf{V}}$ as acceleration in the inertial coordinate frame. So the dynamics equation is modeled as the following second-order system

$$\begin{aligned} \dot{\mathbf{X}}_i &= \mathbf{V}_i \\ \dot{\mathbf{V}}_i &= \mathbf{U}_i \end{aligned} \quad (1.1)$$

1.3 Finite-Time Second-Order Consensus Control Algorithm Based on Positions of Virtual Leader

The proposed formation control scheme is only based on the position information of the virtual leader, which makes a consensus on the distance \mathbf{H}_i with its position vector minus the range from its position to the virtual leader. That means the position vector of the virtual leader belonging to every AUV \mathbf{X}_{vl}^i ($\mathbf{X}_{vl}^i = \mathbf{X}_i(1:3) - \mathbf{H}_i$) will reach a consensus: $\mathbf{X}_{vl}^i \rightarrow \mathbf{X}_{vl}^j$, $i \neq j$. So AUVs form a fixed shape shown in Fig. 1.3. The proposed control algorithm still require linear velocity vector, angular velocity vector and angular position vector in inertial coordinate frame to reach a consensus in finite time and obtain a consensus on position vectors of the virtual leader for every AUVs. So there is a time t_s when $t \geq t_s$, the following equations hold

$$\begin{cases} \|\mathbf{X}_{vl}^i - \mathbf{X}_{vl}^j\| = 0 \\ \|\mathbf{X}_i(4:6) - \mathbf{X}_j(4:6)\| = 0 \\ \|\mathbf{V}_j - \mathbf{V}_i\| = 0, i \neq j, j \in N_j \end{cases}$$

where N_j denotes the set of all neighbor AUVs, $\|\cdot\|$ denotes the vector norm and \mathbf{H}_i denotes the distance vector from AUV i to the virtual leader. The expression of \mathbf{H}_i with seven AUVs is as follows

$$\mathbf{H}_i = \begin{cases} \sin(3\pi/4)[r(i-4) & 0.5r & r(4-i)]^T, & i = 1, 2, 3, 4 \\ \cos(3\pi/4)[r(4-i) & 0.5r & r(4-i)]^T, & i = 5, 6, 7 \end{cases}$$

where r denotes the predefined unit distance.

For the second-order system in Eq. (1.1), we propose a following consensus protocol with the second-order dynamic equation

$$\mathbf{U}_i = \sum_{j \in N_j} (a \mathbf{sgn}(\mathbf{X}_{vl}^j - \mathbf{X}_{vl}^i) |(\mathbf{X}_{vl}^j - \mathbf{X}_{vl}^i)|^\chi + b \mathbf{sgn}(\mathbf{V}_j - \mathbf{V}_i) |\mathbf{V}_j - \mathbf{V}_i|^\chi) \quad (1.2)$$

where $0 < a, b \leq 1$ and $0 < \chi < 1$ are the convergence coefficients, $|\cdot|$ denotes the absolute value of every element, and $\mathbf{sgn}(\cdot)$ denotes the vector sign function with the expression $\mathbf{sgn}(\boldsymbol{\sigma}) = [\text{sign}(\sigma_1) \cdots \text{sign}(\sigma_i) \cdots \text{sign}(\sigma_n)]^T$ where $\boldsymbol{\sigma} = [\sigma_1 \cdots \sigma_i \cdots \sigma_n \in \mathbf{R}^n]$ denotes a vector with

$$\text{sign}(\sigma_i) = \begin{cases} 1, & \sigma_i > 0 \\ 0, & \sigma_i = 0 \\ -1, & \sigma_i < 0 \end{cases}$$

We define $\mathbf{sig}(\boldsymbol{\sigma})^\rho = \mathbf{sgn}(\boldsymbol{\sigma})|\boldsymbol{\sigma}|^\rho = [\text{sign}(\sigma_1)|\sigma_1|^\rho \cdots \text{sign}(\sigma_i)|\sigma_i|^\rho \cdots \text{sign}(\sigma_n)|\sigma_n|^\rho]^T$.

So Eq. (1.2) can be written as

$$\mathbf{U}_i = \sum_{j \in N_j} (a \mathbf{sig}(\mathbf{X}_{vl}^j - \mathbf{X}_{vl}^i)^\chi + b \mathbf{sig}(\mathbf{V}_j - \mathbf{V}_i)^\chi).$$

In the following section the boundedness of the closed loop system is verified with consensus protocol in (1.2).

Proof (The $\text{sign} \cdot$ denotes the product of corresponding elements of a vector)

We define a vector Lyapunov function

$$V = \sum_{i=1}^n \sum_{j=1}^n \int_0^{X_{vl}^j - X_{vl}^i} a \mathbf{sig}(\mathbf{s})^\chi \cdot d\mathbf{s} + \sum_{i=1}^n V_i \cdot \dot{V}_i / 2.$$

Solve the differential coefficients along the closed loop system trajectory, and we notice that $\mathbf{sig}(\mathbf{X}_{vl}^j - \mathbf{X}_{vl}^i)^\chi$ is odd function, we obtain

$$\begin{aligned}
\dot{V} &= \sum_{i=1}^n V_i \cdot \dot{V}_i + \sum_{i=1}^n \sum_{j=1}^n a \mathbf{sig}(X_{vl}^i - X_{vl}^j)^\chi \cdot ds \\
&= \sum_{i=1}^n V_i \cdot \sum_{i=1}^n (a \mathbf{sig}(X_{vl}^j - X_{vl}^i)^\chi + b \mathbf{sig}(V_j - V_i)^\chi) - \sum_{i=1}^n \sum_{j=1}^n a \mathbf{sig}(X_{vl}^j - X_{vl}^i)^\chi \cdot V_i \\
&= \sum_{i=1}^n \sum_{j=1}^n b V_i \cdot \mathbf{sig}(V_j - V_i)^\chi \\
&= \frac{1}{2} \sum_{i=1}^n \sum_{j=1}^n (b + b) V_i \cdot \mathbf{sig}(V_j - V_i)^\chi
\end{aligned}$$

Notice that $(V_i - V_j) \cdot \mathbf{sig}(V_j - V_i)^\chi = |V_i - V_j|^{1+\chi}$, so

$$\dot{V} = \frac{1}{2} \sum_{i=1}^n \sum_{j=1}^n b (V_i - V_j) \cdot \mathbf{sig}(V_j - V_i)^\chi \leq \mathbf{0}.$$

Because of the limited communication range of every AUV, which means the AUV communicate only with the AUVs in communication range (noted as *SetDis*). In the formation shaping procedure the communication topology is dynamic which means the matrix $A(t)$ is time variant.

1.4 Numerical Simulations

We simulate some squares in space as AUVs with velocity and attitude. The effectiveness of the control scheme is shown with two simulation results. Choose $a = 1$, $b = 1$, $\chi = 0.3$ and $SetDis = 30(\text{m})$. Simulation results is shown in

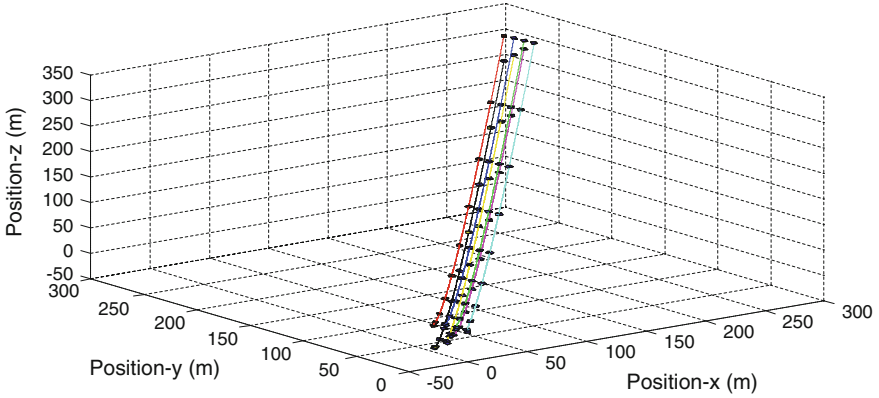


Fig. 1.2 Formation control with 7 AUVs

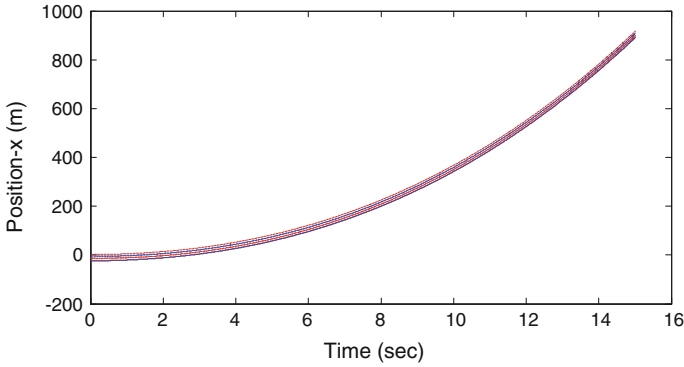


Fig. 1.3 Consensus on position x

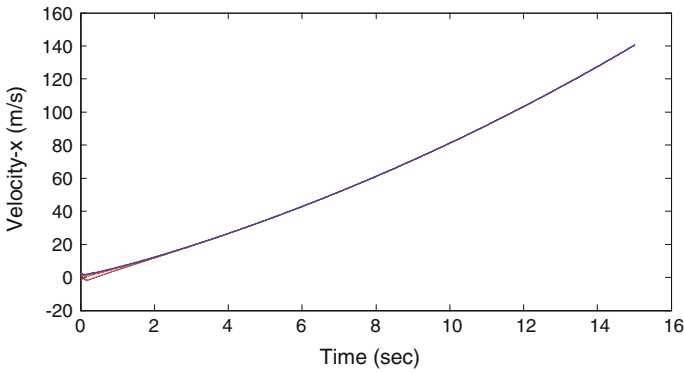


Fig. 1.4 Consensus on linear velocity x

Figs. 1.2, 1.3 and 1.4. From the simulation results, we notice that the AUVs form the desired shape in the finite time and the attitudes of all AUVs reach a consensus in finite time.

1.5 Conclusions

The formation control problem based the proposed consensus algorithm in two cases is investigated. The effectiveness of the proposed finite-time consensus is verified. Typically the velocity of AUV can not instantaneously increase to infinity; it will definitely lengthen the synchronization time or lead the formation can not achieve the desired formation shape in the presence of maximum speed constraint. So the formation fault diagnosis and formation reconfiguration problem is the next focus of our research.

Acknowledgments This work is supported by the Natural Science Foundation of Shandong Province with grant number ZR2012FL18, the International Science and Technology Cooperation Project with grant number 2011DFR60810 and the Science and Technology Development Foundation of Shandong Academy of Sciences.

References

1. Fiorelli E (2006) Multi-AUV control and adaptive sampling in Monterey bay. *IEEE J Oceanic Eng* 31(4):935–948
2. Yu SC, Ura T (2004) A system of multi-AUV interlinked with a smart cable for autonomous inspection of underwater structures. *Int J Offshore Polar Eng* 14(4):264–272
3. Yu SC, Ura T (2004) Experiments on a system of multi-AUV interlinked with a smart cable for autonomous inspection of underwater structures. *Int J Offshore Polar Eng* 14(4):273–283
4. Xiang XB (2007) Coordinated control for multi-AUV systems based on hybrid automata. In: *Proceedings of IEEE international conference on robotics and biomimetics*, pp 2121–2126
5. Tangirala S, Kumar R, Bhattacharyya S et al (2005) Hybrid-model based hierarchical mission control architecture for autonomous underwater vehicles, *American control conference*, vol 1. Portland, pp 668–673
6. Yang EF, Gu DB (2007) Nonlinear formation-keeping and mooring control of multiple autonomous underwater vehicles. *IEEE/ASME Trans Mechatron* 2(2):164–178
7. Kalantar S, Zimmer UR (2007) Distributed shape control of homogeneous swarms of autonomous underwater vehicles. *Auton Robots* 22(1):37–53
8. Lewis MA, Tan KH (1997) High precision formation control of mobile robots using virtual structure approach. *Auton Robots* 4:387–403
9. Lawton AR, Young BJ, Beard RW (2000) A decentralized approach to elementary formation maneuvers, *IEEE international conference on robotics and automation*, vol 3. San Francisco, pp 2728–2733
10. Leonard NE, Fiorelli E (2001) Virtual leader, artificial potentials and coordinated control of groups, *IEEE conference on decision and control*, vol 3. Orlando, pp 2968–2973
11. Lawton JR, Beard RW, Young BJ (2003) A decentralized approach to formation maneuvers. *IEEE Trans Robot Autom* 19(6):933–941
12. Ren W, Sorensen N (2008) Distributed coordination architecture for multi-robot formation control. *Robot Auton Syst* 56(4):324–333
13. Ren W, Beard RW (2004) Decentralized scheme for spacecraft formation flying via the virtual structure approach. *J Guidance Control Dyn* 27(1):73–82
14. Do KD (2008) Formation tracking control of unicycle-type mobile robots with limited sensing ranges. *IEEE Trans Control Syst Technol* 16(3):527–538
15. Dong WJ, Farrell JA (2009) Decentralized cooperative control of multiple nonholonomic dynamic systems with uncertainty. *Automatica* 45:706–710
16. Das K, Fierro R, Kuma V et al (2002) A vision-based formation control framework. *IEEE Trans Robot Autom* 18(5):813–825
17. Wu XF, Xu C (2011) Mean synchronization of pinning complex networks with linearly and nonlinearly time-delay coupling. *Int J Digit Content Technol Appl*. 5(3):33–46
18. Yang Q, Shi J, Tang B (2010) Convergence analysis of decentralized slot synchronization algorithm for wireless ad hoc networks. *J Convergence Inf Technol* 5(10):223–232
19. Xiao F, Wang L, Chen J, Gao Y (2009) Finite-time formation control for multi-agent systems. *Automatica* 45(11):2605–2611
20. Wang X, Hong Y (2010) Distributed finite-time χ -consensus algorithms for multi-agent systems with variable coupling topology. *J Syst Sci Complexity* 23(2):209–218

Chapter 2

The Research on Fault Diagnosis of Building Electrical System Based on RBF Neural Network

Qian Wu, Yahui Wang, Long Zhang and Li Shen

Abstract Building electrical system fault diagnosis is the blank in the fault diagnosis field at home and abroad. The main reason is that the building electrical systems have many complex and huge subsystems; meanwhile, it is very hard to establish the mathematical model of system. By using the neural networks which is not depending on the model and using its advantage of convergence speed, the difficulties of building electrical system fault diagnosis can be well solved. This paper puts forward a method of fault diagnosis based on radial basis function neural network (hereinafter referred to as the RBF network) and applied it to building electrical system fault diagnosis. Beijing institute of civil engineering and architecture building intelligent experiment center provides building electrical test platform which can collect actual fault samples for RBF network training. After experiments and verification, RBF network's accuracy and speed on fault diagnosis of building electrical system is significantly better than BP network. The effective RBF network in building electric system fault diagnosis field will have good engineering application prospect in the future.

Keywords Fault diagnosis · Building electrical system · RBF neural network

Q. Wu (✉) · Y. Wang · L. Shen
Department of Electrical and Information Engineering, Beijing University
of Civil Engineering and Architecture, 100044 Xi Cheng District, Beijing, China
e-mail: wq05dianzi@126.com

Y. Wang
e-mail: yahui-wang@vip.sina.com

L. Shen
e-mail: Shenligood1988@sina.com

L. Zhang
Department of Electrical and Information Engineering, Beijing Forestry University,
Hai Dian District, Beijing, China
e-mail: long1988iacf@yahoo.com.cn

2.1 Introduction

With the acceleration of urbanization, the number of high-rise and super high-rise buildings is increasing; meanwhile, there is a growing pursuit of building functionality and comfort in the residence and office. Due to the rapid development of electronic communication and network technology, building electrical system is moving in the development of large-scale, complex structure, including lighting, power, and control in one large intelligent system, so that building electrical system failure will bring great inconvenience to people's work and lives. Even some serious accident of electricity would threaten property and personal safety, therefore security and reliability have become a major issue in the current building electrical.

Building electrical system failure can be divided into two categories: electrical equipment faults and the line faults. Traditional building electrical system failures were most manually detected by the electrician to identify the location of the faults, and then replace the line or components. Manual detection often rely on personal experience of maintenance electrician, but for the increasingly complex coupling relationship exists between the various subsystems, modern building electrical system need to put forward a new intelligent fault diagnosis method.

The neural network is an important way to solve the fault diagnosis problem, through the effective training of the neural network can remember the process of knowledge, learn directly from the historical data, and make it suitable for online detection and fault diagnosis. It has the ability to distinguish the cause of the malfunction and the type of fault. In fact, the neural network technology has become a valid means of fault diagnosis. Radial basis function neural network (RBFNN) which rely on its simple network structure and fast training procedure, received extensive attention in many areas. This paper presents a fault diagnosis method for complex building electrical system based on RBF network. This method can quickly identify and determine the type of failure, and can diagnose the same category of the new faults. From engineering point of view, it has a good practical application value and bright prospect.

2.2 Basic Principles of RBF Neural Network Algorithm

2.2.1 The Basic Concepts of the RBF Network

Radial Basis Function (RBF) is a kind of neural network function whose independent variables are the distance to a fixed point. In the two-dimensional Euclidean space, the distance is:

$$r_k = r_k(x, y, x^{(k)}, y^{(k)}) = \sqrt{(x - x^{(k)})^2 + (y - y^{(k)})^2} \quad (2.1)$$

r_k is the independent variable of radial basis function, denoted $\phi^{(k)}(r_k)$, (x, y) is arbitrary coordinates of the Euclidean space, $(x^{(k)}, y^{(k)})$ is the coordinates of the fixing points k , known as the center of the radial basis function, radial basis function $\phi(r)$ is generally divided into two categories: local and overall. If $\lim_{r \rightarrow \infty} \phi(r)$ is zero, called a local radial basis function, otherwise it is called the overall radial basis function. Local radial basis function interpolate in the center of the input data area, while the overall radial basis function can interpolate globally.

2.2.2 Principle of RBF Network

RBF network is a three-layer network structure, as shown in Fig. 2.1, the three layers include the input layer, hidden layer and output layer. The input layer to the hidden layer is nonlinear mapping and output layer is linear weight sum of the hidden layer unit, so it is a linear mapping.

The hidden layer of RBF network takes radial basis function as the activation function, and this function is usually Gaussian function, when the input sample is x , the output of the i unit of the hidden layer is as follows:

$$R_i(x) = e^{-\frac{\|x-c_i\|^2}{2\sigma_i^2}} \quad i = 1, 2, \dots, L \tag{2.2}$$

Wherein, c_i is a base function center, σ_i is the width of the Gaussian function in hidden layer unit i , the output of the corresponding output node is:

$$Y = \sum_{i=1}^L W_i R_i(x) \tag{2.3}$$

W_i represent hidden layer i to the output layer weights. When the input sample is at the farther distance from the center, the lower degree of neurons is activating,

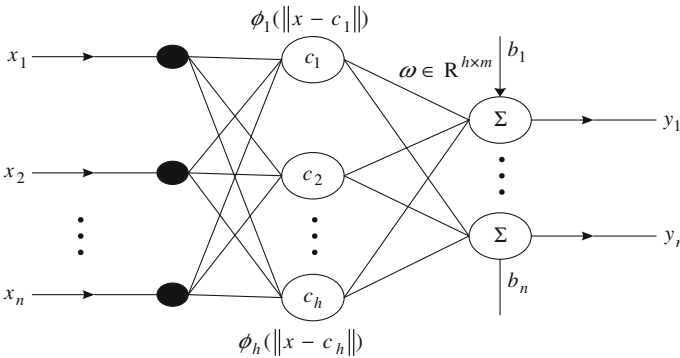


Fig. 2.1 RBF neural network diagram

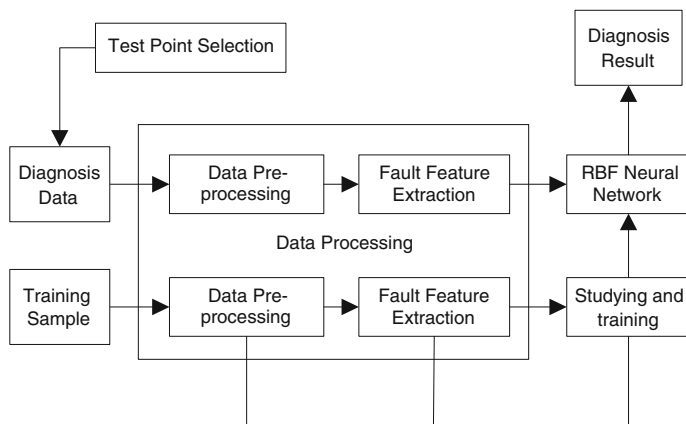


Fig. 2.2 Standard model of fault diagnosis system

and when it more than a certain distance, the neurons will not be activated. Therefore, for the RBF neural network, each hidden layer node has a data center.

In the neural network fault diagnosis algorithm, the input general is corresponding to the fault features, and the output node are the causes and reasons of the fault. The fault samples are used to network training, so as to make sure the structure of network, and reference value, such as neuron weights and threshold value. After training, the process of setting nonlinear mapping between fault features and fault set is complete. Standard model of fault diagnosis system is shown as Fig. 2.2. Testing point selection is very important to the fault diagnosis result, especially to large and complex system which includes electric circuit; this topic will be discussed in another paper.

2.3 In the Application of the Building Electrical Fault Diagnosis

2.3.1 Introduction of Building Electrical Test Platform

The METREL Building Electrical Testing Experimental Systems is original made in German. It is actually an integration of constructions electrical elements which are concentrated in a test platform. It has brought great convenience to the construction of electrical test experiment. The physical model of electrical test platform is shown as Fig. 2.3.

In Fig. 2.3, the construction of low-voltage distribution system is composed of a variety of elements, such as circuit breakers, fuses, single-phase sockets and three-phase sockets. Power supply of the electrical test platform is 220 V and 50 Hz mains, and the transformer output 15 V DC to the weak protection part and

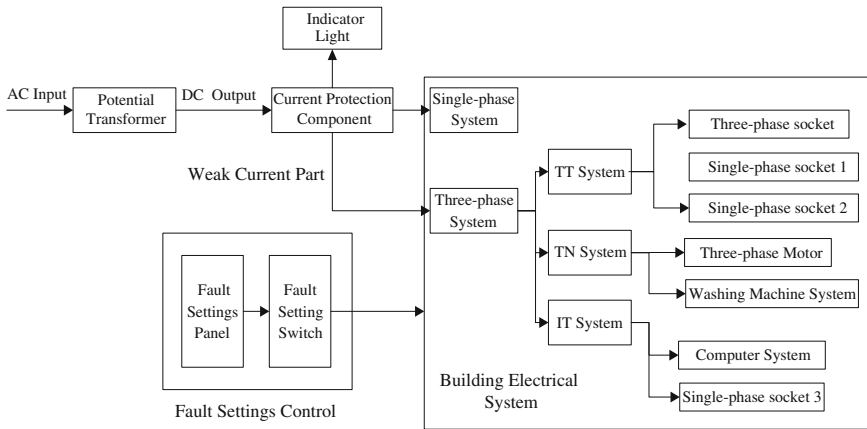


Fig. 2.3 Physical model of electrical test platform

the fault setting control board. The fault setting panel can provide five categories of common household electricity insulation test failures and the 22 faults location button, which completely simulate civilian residential electrical systems and common faults in the real life.

2.3.2 Basic Methods of Diagnosis

The basic idea of fault diagnosis that base on RBF neural network is use fault features as network input and diagnostic result as network output, apply a large amount of historical fault data to network offline training, so that the specific corresponding relationship between the network and the right weight value that remember fault symptoms and corresponding fault type can be set up.

According to the various fault signals collected by the monitoring and data acquisition system, the input layers are fault data, because there are odd data in the collected set, normalization process should be operate according to the formula 3.1 firstly.

$$y = \frac{x - MinValue}{MaxValue - MinValue} \tag{3.1}$$

Fault feature vector is $X = [x_1, x_2, \dots, x_n]$. Intermediate layer input layer get input information and transform into a targeted solution by internal learning to complete the non-linear mapping of input to the output. The output layer is a vector of the failure mode, through comparing with a threshold value; the diagnostic result can be obtained. In this case, the total number of the failed node are 10 and the fault type respectively are the line impedance fault, the continuity fault, the grounding resistance abnormal and ground resistivity insulation resistance is

too small. From the above, five categories failure will occur stochastic at 10 fault location. In every output vector, the judging rule is that number 0 indicating no failure, 1 indicates a failure. So the fault encoding state are Line impedance fault (1,0,0,0,0), Continuity fault (0,1,0,0,0), Grounding resistance anomalies (0,0,1,0,0), Grounding resistivity anomalies (0,0,0,1,0), Insulation resistance too small (0,0,0,0,1).

2.3.3 The RBF Network Design and Training

Firstly, using the algorithm of random selection to select the center of RBF network, and the center of the hidden unit is in the data of the input sample, and fix the center.

There are generally two methods to determine the number of hidden layer neurons of RBF network training, the commonly used method is the input vector elements are equal to the number of neuron, however, when there are more of the input vectors this method will result in excessive number of hidden layer units so that the network structure more complicated. Another method does not need to be determined the number directly, but through the training and optimization to calculate the number of neurons, the way of the second methods is setting the number of nodes of the hidden layer to 0 and then start training by checking the input error, automatically increase the hidden layer neurons. Cumulative iterative loop, so that the network produces the maximum error of the corresponding input vector as a weight vector, resulting in a new hidden layer neuron, then check the error of the new network, repeating this processes until reach the error requirements or maximum hidden layer number of neurons.

The actual collection sample data are 90 groups, also 30 groups of collected data are used to test and there are some excerpts of the collected samples in the Table 2.1. It includes five kinds of failure modes and each sample has 10 position characteristic parameters. So the number of neurons in the input layer is 10, while output neurons number is 5. The number of hidden layer is not fixed, and it will adjust after several constantly training tests. The corresponding network training output and fault diagnosis results is as shown in Table 2.2 (Fig. 2.4).

2.4 Comparison and Analysis of the Experimental Test Result

In order to stress the training effect, using BP network as a comparison objective. The process of set up BP network is little complicated than RBF. In order to make the training get best training effect, the parameters of the BP network should be change continually. The number of neurons in the hidden layer of BP network which selected according to multiple test and experience are 15 Figs. 2.7, 2.8.

Table 2.1 RBF neural network training input samples

Number	Fault samples	Set of characteristic parameters																				
		2000	2004	2002	2000	2003	2001	2000	2005	2000	2000	2000	2000	2000	2000	2000	2000	2000	2001			
1	Line impedance fault	10.77	10.74	10.72	10.79	10.75	10.77	10.71	10.73	10.72	10.73	10.71	10.73	10.72	10.78	10.79	10.77	10.71	10.73	10.72	10.79	10.77
2		10.74	10.71	10.73	10.75	10.74	10.73	10.79	10.74	10.73	10.72	10.73	10.79	10.73	10.72	10.79	10.77	10.73	10.79	10.72	10.79	10.77
3		9.89	9.91	9.86	9.81	9.81	9.83	9.81	9.81	9.83	9.87	9.83	9.81	9.81	9.87	9.89	9.87	9.87	9.81	9.87	9.89	9.87
4	Continuity fault	2000	2004	2002	2000	2003	2001	2000	2003	2001	2001	2000	2000	2005	2000	2000	2001	2000	2000	2005	2000	2000
5		3.68	3.76	3.45	3.56	3.45	3.65	3.64	3.45	3.65	3.61	3.64	3.64	3.61	3.69	3.58	3.61	3.64	3.61	3.61	3.69	3.58
6		2.78	2.71	2.34	2.77	2.21	2.45	2.56	2.21	2.45	2.64	2.56	2.56	2.64	2.57	2.54	2.64	2.56	2.64	2.64	2.57	2.54
7	Grounding resistance Anomaly	3.45	3.65	3.76	3.56	3.54	3.85	3.25	3.54	3.85	3.42	3.25	3.25	3.42	3.62	3.52	3.42	3.25	3.42	3.42	3.62	3.52
8		3.66	3.68	3.67	3.89	3.67	3.45	3.44	3.67	3.45	3.76	3.44	3.44	3.76	3.25	3.78	3.76	3.44	3.76	3.76	3.25	3.78
9		6.01	6.19	6.05	6.07	6.12	6.11	6.09	6.12	6.11	6.03	6.09	6.09	6.03	6.07	6.11	6.03	6.09	6.03	6.03	6.07	6.11
10	Ground resistivity Anomaly	0.32	0.33	0.31	0.36	0.34	0.33	0.36	0.34	0.33	0.33	0.36	0.36	0.35	0.33	0.34	0.33	0.36	0.35	0.35	0.33	0.34
11		9.21	9.32	9.24	9.2	9.27	9.25	9.29	9.27	9.25	9.31	9.29	9.29	9.31	9.34	9.42	9.31	9.29	9.31	9.31	9.34	9.42
12		0.143	0.141	0.139	0.142	0.144	0.147	0.148	0.144	0.147	0.143	0.147	0.148	0.143	0.141	0.145	0.143	0.147	0.148	0.143	0.141	0.145
13	Insulation resistance Too small	0.32	0.33	0.31	0.36	0.34	0.33	0.36	0.34	0.33	0.33	0.36	0.36	0.35	0.33	0.34	0.33	0.36	0.35	0.35	0.33	0.34
14		9.21	9.32	9.24	9.21	9.27	9.25	9.29	9.27	9.25	9.31	9.29	9.29	9.31	9.34	9.42	9.31	9.29	9.31	9.31	9.34	9.42
15		0.143	0.141	0.139	0.142	0.144	0.147	0.148	0.144	0.147	0.143	0.147	0.148	0.143	0.141	0.145	0.143	0.147	0.148	0.143	0.141	0.145
16	Trouble-free	1.21	1.11	1.15	0.23	0.58	0.63	0.25	0.58	0.63	0.27	0.25	0.25	0.27	0.36	0.68	0.27	0.25	0.27	0.27	0.36	0.68
17		1.23	1.13	1.18	0.22	0.49	0.60	0.22	0.49	0.60	0.29	0.22	0.22	0.29	0.33	0.68	0.29	0.22	0.29	0.29	0.33	0.68
18		1.23	1.13	1.18	0.22	0.49	0.60	0.22	0.49	0.60	0.29	0.22	0.22	0.29	0.33	0.68	0.29	0.22	0.29	0.29	0.33	0.68

Table 2.2 RBF actual output of the neural network diagnostic results

Number	Diagnostic results		The type of fault				
	Ideal output	Diagnostic results					
1	1, 0, 0, 0, 0	1.0321	0.0005	0.0000	0.0002	0.0006	0.0006
2	1, 0, 0, 0, 0	1.0331	0.0006	0.0005	0.0007	0.0005	0.0005
3	1, 0, 0, 0, 0	1.0331	0.0005	0.0000	0.0005	0.0004	0.0004
4	0, 1, 0, 0, 0	0.0002	0.9984	0.0002	0.0001	0.0012	0.0012
5	0, 1, 0, 0, 0	0.0001	0.9998	0.0000	0.0004	0.0015	0.0015
6	0, 1, 0, 0, 0	0.0001	1.0005	0.0000	0.0005	0.0004	0.0004
7	0, 0, 1, 0, 0	0.0001	0.0006	1.0012	0.0019	0.0009	0.0009
8	0, 0, 1, 0, 0	0.0001	0.0002	1.0000	0.0000	0.0009	0.0009
9	0, 0, 1, 0, 0	0.0001	0.0002	0.0000	0.0003	0.0005	0.0005
10	0, 0, 0, 1, 0	0.0002	0.0005	0.0001	1.0009	0.0006	0.0006
11	0, 0, 0, 1, 0	0.0001	0.0002	0.0000	1.0000	0.0004	0.0004
12	0, 0, 0, 1, 0	0.0001	0.0000	0.0005	1.0001	0.0009	0.0009
13	0, 0, 0, 0, 1	0.0000	0.0002	0.0004	0.0001	1.0006	1.0006
14	0, 0, 0, 0, 1	0.0001	0.0002	0.0000	0.0008	1.0006	1.0006
15	0, 0, 0, 0, 1	0.0001	0.0000	0.0006	0.0002	1.0004	1.0004

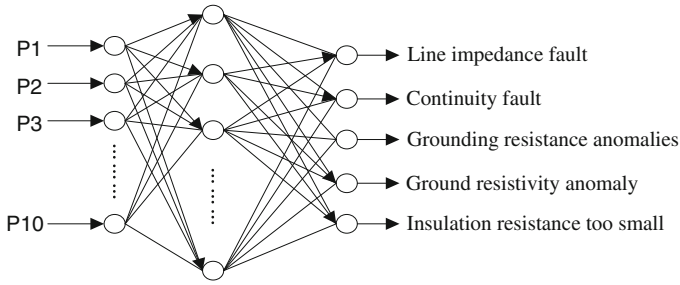


Fig. 2.4 Structure of RBF fault diagnosis model of building electrical system

Fig. 2.5 RBF training result

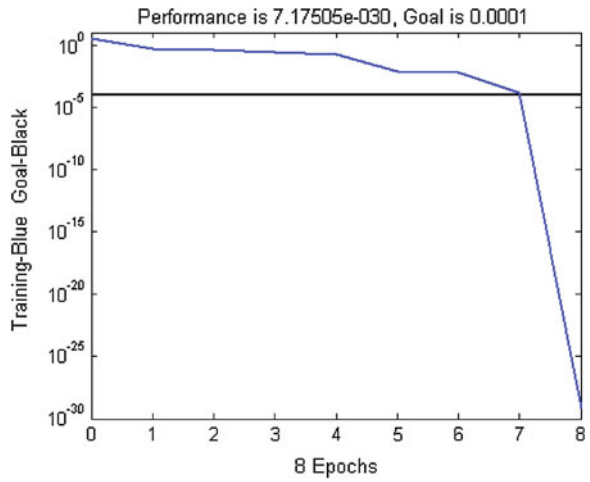


Fig. 2.6 BP training result

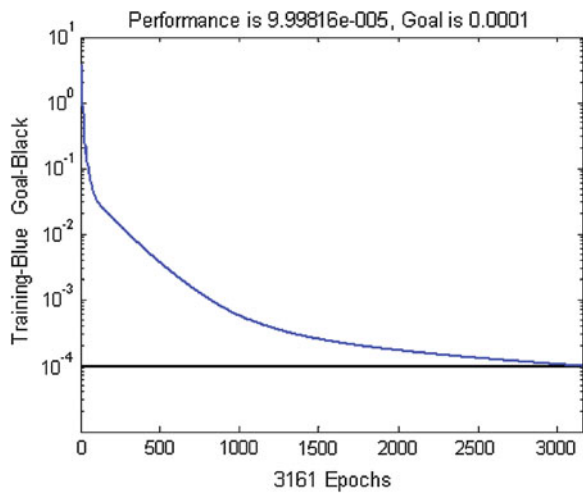


Fig. 2.7 RBF network fault identification

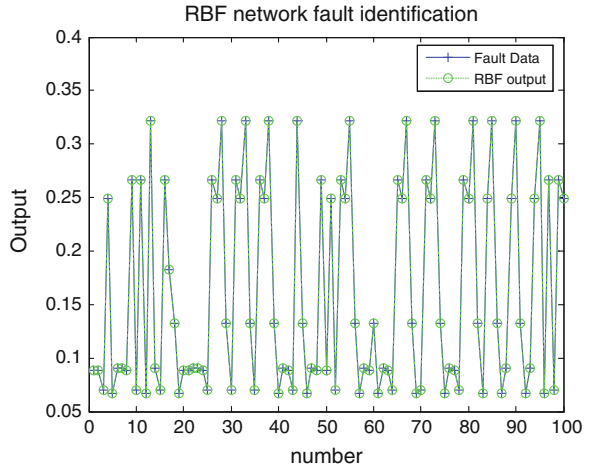
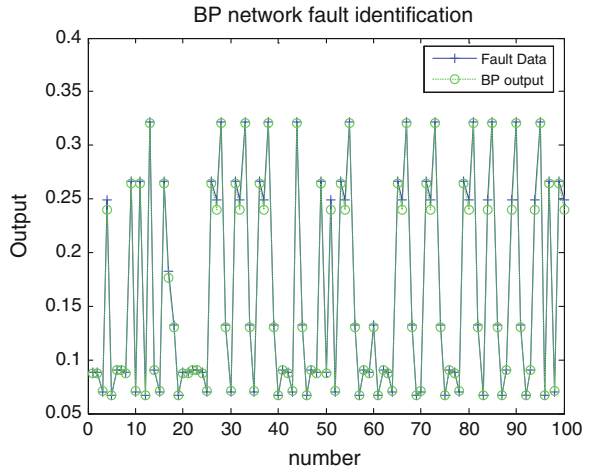


Fig. 2.8 BP network fault identification



The Figs. 2.5 and 2.6 are the training curve of RBF and BP network. In the figures, X axis is training epochs, Y axis is system error. In order to compare effectiveness, set error goal is $10e-4$. According to the simulation results shown in Figs. 2.5 and 2.6, it can be seen that when the error of BP network is $10e-4$, training epochs are 3,161, while RBF network just takes 8 epochs. During the training, even if the entire parameters of BP network have been determined, every training result is different, while the result of RBF network is more stable and not easy to fall into local minimum, when all the parameters are determined.

In addition, RBF network compared with BP network, the output layer is linear weight sum of hidden units and its learning speed is faster than the BP network, however, due to its generally radial basis function using a Gaussian function as the

activation function, the input space area is small, so it need set more radial basis neurons. On the whole, RBF network structure is easier to build, and training speed is fast and stable. In the case of building electrical system fault diagnosis, the RBF neural network is superior to BP neural network.

2.5 Conclusion and Outlook

The application of artificial neural network in building electrical system fault diagnosis, the RBF neural network is able to determine the fault type accurately and quickly. This approach verified by building electrical data acquisition and test platform which was research and development by Electrical and intelligent Experimental Center of Beijing University of Civil Engineering and Architecture. Especially, this equipment cooperate the method of RBF fault diagnosis can monitor the real-time status of critical node. Believe in the near future, this method's advantages, such as early detection and troubleshooting can play a good role, and it will have broad application prospects.

Chapter 3

Adaptive Dynamic Surface Control of Stochastic Strict Feedback Nonlinear Systems

Xiaocheng Shi, Tianping Zhang, Huating Gao and Fei Wang

Abstract Based on the integral-type Lyapunov function and the approximation capability of neural networks, an adaptive dynamic surface control scheme is proposed for a class of stochastic strict-feedback nonlinear systems in this paper. The design makes the approach of dynamic surface control be extended to the stochastic nonlinear systems, and relaxes the extent of application of the dynamic surface control approach. By introducing the first order filter, the explosion of complexity caused by the repeated differentiations of certain nonlinear functions such as virtual controls in traditional backstepping design is avoided. Compared with the existing literature, the proposed approach reduces the number of adjustable parameters effectively. By theoretical analysis, it is shown that all signals in the closed-loop system are bounded in probability.

Keywords Stochastic strict-feedback nonlinear systems · Adaptive control · Neural networks · Dynamic surface control · Integral-type Lyapunov function

3.1 Introduction

As the development of the backstepping technique, this technique has been relatively mature, and successfully applied to the controller design of the stochastic systems [1–14]. Pan and Basar [1, 2] first derived a backstepping design approach for stochastic nonlinear systems. Deng and Krstic [4–6] solved the stabilization problem of stochastic nonlinear systems, by using the quartic Lyapunov function instead of the classical quadratic one. Chen [10, 11] studied the problem of

X. Shi · T. Zhang (✉) · H. Gao · F. Wang
Department of Automation, College of Information Engineering, Yangzhou University,
Yangzhou 225127, China
e-mail: tpzhang@yzu.edu.cn

adaptive neural network output feedback control for a class of stochastic strict-feedback nonlinear systems. Yu and Du [12] discussed the problem of bounded adaptive stabilization for uncertain stochastic nonlinear systems with time-delay. Psillakis and Alexandridis [13] considered the tracking control problem for a class of uncertain nonlinear systems disturbed by unknown covariance noise. Wang and Zhang [14] proposed a fuzzy adaptive control of stochastic nonlinear systems with unknown virtual control gain function. However, these results still inherit the open problem of ‘explosion of complexity’ in the backstepping design, which is even more serious than that in deterministic systems owing to the appearance of Hessian term in the infinitesimal generator. This drawback makes it difficult to carry out the designed backstepping control scheme. In fact, for deterministic systems, the above problem has been solved well by the dynamic surface control approach. Swaroop [15] first proposed dynamic surface control approach to solve the problem. Zhang [16, 17] proposed an adaptive neural network control by using dynamic surface control approach for the deterministic systems. The dynamic surface control approach is to avoid differentiating the virtual control variables by introducing a first-order filter in each step of the backstepping design procedure, which overcomes the drawback of traditional backstepping design. Unfortunately, to the authors’ knowledge, few papers have been reported to extend the dynamic surface control approach to the stochastic nonlinear systems. Chen [18] first introduced the dynamic surface control approach to solve the stabilization problem of stochastic nonlinear systems with the output feedback form.

In this paper, a novel adaptive neural network dynamic surface control is developed for a class of stochastic strict-feedback nonlinear systems with unknown virtual control gain functions. The design makes the dynamic surface control approach be extended to stochastic nonlinear systems, and relaxes the extent of application of the approach of dynamic surface control. The estimation of the Euclidean normal square of weight vectors is taken as the estimation for the parameters, which reduces the number of adjustable parameters. By theoretical analysis, it is shown that all signals in the closed-loop system are bounded in probability, and the tracking error converges to a small neighborhood of the origin in probability.

3.2 Problem Statement and Basic Assumptions

Throughout this paper, the following notations will be used. R^+ denotes the set of all non-negative real numbers, R^n denotes the real n -dimensional space. For a given vector or matrix X , X^T denotes its transpose, tr denotes its trace when X is square and $\|X\|$ denotes the Euclidean norm of a vector X . $E[Y]$ denotes the expectation of stochastic variable Y . C^i denotes the set of functions with continuous i th partial derivatives; and $C^{1,2}$ denotes the family of all functions, which are C^1 in the first argument and C^2 in the second argument. κ denotes the set of all

functions: $R^+ \rightarrow R^+$, which are continuous, strictly increasing and vanishing at zero; κ_∞ denotes the set of all functions which are of class κ and unbounded.

Consider a class of stochastic strict feedback nonlinear systems in the following form

$$\begin{cases} dx_i = (f_i(\bar{x}_i) + g_i(\bar{x}_i)x_{i+1})dt + h_i^T(\bar{x}_i)dw, & i = 1, \dots, n-1 \\ dx_n = (f_n(\bar{x}_n) + g_n(\bar{x}_n)u)dt + h_n^T(\bar{x}_n)dw \\ y = x_1 \end{cases} \quad (3.1)$$

where $x_i \in R$ ($i = 1, \dots, n$) are the states, $\bar{x}_i = (x_1, \dots, x_i)$, $u \in R$ is the input, y is the output, $f_1(\bar{x}_1), \dots, f_n(\bar{x}_n), g_1(\bar{x}_1), \dots, g_n(\bar{x}_n), h_1(\bar{x}_1), \dots, h_n(\bar{x}_n)$ are the unknown continuous functions, w is an r -dimensional standard Brownian motion defined on the complete probability space (Ω, F, P) , with Ω being a sample space, F being a σ field, and P being a probability measure. The control objective is to design adaptive control u for system (3.1) such that the output y follows the specified desired trajectory y_d .

Consider the following stochastic nonlinear system

$$dx = f(t, x)dt + h^T(t, x)dw \quad (3.2)$$

where $x \in R^n$ is the system state, w is an r -dimensional standard Brownian motion, $f : R^n \times R^+ \rightarrow R^n$, $h^T : R^n \times R^+ \rightarrow R^{n \times r}$ are locally Lipschitz and $f(t, 0), h(t, 0)$ are uniformly ultimately bounded. For any given $V(t, x(t)) \in C^{1,2}$, associated with the stochastic system (3.2), the infinitesimal generator L is defined as follows

$$LV(t, x(t)) = \frac{\partial V(t, x(t))}{\partial t} + \frac{\partial V(t, x(t))}{\partial x^T} f + \frac{1}{2} tr \left\{ h \frac{\partial^2 V(t, x(t))}{\partial x^T \partial x} h^T \right\} \quad (3.3)$$

Definition 1 The stochastic process $\{x(t)\}$ is said to be bounded in probability, if $\lim_{c \rightarrow \infty} \sup_{0 \leq t < \infty} P\{\|x(t)\| > c\} = 0$

Lemma 1 For any stochastic process $\{\xi(t)\}$, if there exists integer p and a positive constant C_0 such that $E|\xi(t)|^p \leq C_0, \forall t \geq 0$, then $\{\xi(t)\}$ is bounded in probability.

Lemma 2 [7] Consider system (3.2) and suppose there exists a C^2 function $V(t, x(t)) : R^n \times R \rightarrow R^+$, two constants $c_1 > 0, c_2 \geq 0$, class κ_∞ functions μ_1, μ_2 such that $\mu_1(\|x\|) \leq V(t, x) \leq \mu_2(\|x\|)$ and $LV \leq -c_1 V + c_2$ for all $x \in R^n$ and $t > t_0$. Then, (1) for any initial state $x_0 \in R^n$, there exists a unique strong solution $x(t)$ for system (3.2); (2) the solution $x(t)$ of system (3.2) is bounded in probability; (3) $E[V(t_0, x)] \leq EV(x_0, t_0)e^{-c_1 t} + c_1^{-1}c_2, \forall t \geq t_0$.

Assumption 1 The signs of $g_i(\bar{x}_i) \in C^2$ are known, and there exist constants g_{i0} and g_{i1} , such that $0 < g_{i0} \leq |g_i(\bar{x}_i)| \leq g_{i1}, \forall \bar{x}_i \in R^i, i = 1, \dots, n$. Without loss of generality, we shall assume that $0 < g_{i0} \leq g_i(\bar{x}_i) \leq g_{i1}, \forall \bar{x}_i \in R^i, i = 1, \dots, n$.

Assumption 2 The desired trajectory vectors are continuous and available, and $x_d = [y_d, \dot{y}_d, \ddot{y}_d]^T \in \Omega_d$ with known compact set $\Omega_d = \{x_d : y_d^2 + \dot{y}_d^2 + \ddot{y}_d^2 \leq B_0\} \in \mathbb{R}^3$, whose size B_0 is a known positive constant.

In this paper, unknown continuous function $\psi_i(Z_i) : \mathbb{R}^{i+2} \rightarrow \mathbb{R}$ will be approximated on a compact set Ω_{Z_i} by the following radial basis function neural networks

$$\psi_i(Z_i) = W_i^T \varphi_i(Z_i) + \varepsilon_i(Z_i), \forall Z_i \in \Omega_{Z_i} \quad (3.4)$$

where Z_i , $\psi_i(Z_i)$ will be given later, $\varepsilon_i(Z_i)$ is an approximation error, $\varphi_i(Z_i) = [\varphi_{i1}(Z_i), \dots, \varphi_{il_i}(Z_i)]^T : \Omega_{Z_i} \rightarrow \mathbb{R}^{l_i}$ is a known smooth vector function with the neural networks node number $l_i > 1$, the basis function $\varphi_{ik}(Z_i)$, $1 \leq k \leq l_i$ is chosen as the commonly used Gaussian function with the form

$$\varphi_{ik}(Z_i) = \exp(-\eta_i^{-1} \|Z_i - \mu_{ik}\|^2), k = 1, \dots, l_i \quad (3.5)$$

where μ_{ik}, η_i are the center and the width of the basis function $\varphi_{ik}(Z_i)$ respectively. The optimal weight vector $W_i = (w_{i1}, \dots, w_{il_i})^T$ is defined as

$$W_i = \arg \min_{\hat{W}_i \in \mathbb{R}^{l_i}} \left\{ \sup_{Z_i \in \Omega_{Z_i}} |\psi_i(Z_i) - \hat{W}_i^T \varphi_i(Z_i)| \right\}$$

3.3 Adaptive Controller Design

For the sake of clarity and convenience, let $\theta_i = \|W_i\|^2$, $i = 1 \dots n$, then they are unknown constants. Their adaptive laws are employed as follows:

$$\dot{\hat{\theta}}_i = \gamma_i (0.5b_i^{-2} z_i^6 - \sigma_i \hat{\theta}_i) \quad (3.6)$$

where $\gamma_i > 0$, $b_i > 0$ and σ_i are design constants, specified by the designer, $\hat{\theta}_i$ is the estimate of unknown constant θ_i at time t .

Step 1 ($i = 1$) Let $w_1 = y_d$. Then, we have $z_1 = x_1 - w_1$.

Consider the first equation of (3.1), we have

$$dz_1 = (f_1(\bar{x}_1) + g_1(\bar{x}_1)x_2 - \dot{w}_1)dt + h_1^T(\bar{x}_1)dw \quad (3.7)$$

To design adaptive control, define a smooth scalar function as follows:

$$V_{z_1} = \int_0^{z_1} g_1^{-1}(\sigma + w_1) \sigma^3 d\sigma \quad (3.8)$$

By second mean value theorem for integral, V_{z_1} can be rewritten as $V_{z_1} = 0.25g_1^{-1}(\lambda_1 z_1 + w_1)z_1^4$ with $\lambda_1 \in (0, 1)$. Because $0 < g_{10} \leq g_1(\bar{x}_1) \leq g_{11}$, it is shown that V_{z_1} is positive definite with respect to z_1 .

According to (3.3), we obtain

$$\begin{aligned}
 LV_{z_1} = & g_1^{-1}(\bar{x}_1)z_1^3(f_1(\bar{x}_1) + g_1(\bar{x}_1)x_2 - \dot{w}_1) + \dot{w}_1(g_1^{-1}(\bar{x}_1)z_1^3 \\
 & - z_1^3 \int_0^1 3\rho^2 g_1^{-1}(\rho z_1 + w_1) d\rho) + (1.5z_1^2 g_1^{-1}(\bar{x}_1) + 0.5z_1^3 \frac{\partial g_1^{-1}(\bar{x}_1)}{\partial z_1})h_1^T(\bar{x}_1)h_1(\bar{x}_1)
 \end{aligned} \quad (3.9)$$

From Young's inequality, we have

$$\frac{3z_1^2 g_1^{-1}(\bar{x}_1)}{2} h^T(\bar{x}_1)h(\bar{x}_1) \leq \frac{1}{\beta_1} + \frac{9\beta_1}{16g_1^2(\bar{x}_1)} \|h_1(\bar{x}_1)\|^4 z_1^4 \quad (3.10)$$

Substituting (3.10) into (3.9), we have

$$LV_{z_1} \leq z_1^3 x_2 + 0.5a_1^{-2} z_1^6 \theta_1 l_1 + 0.5a_1^2 + z_1^3 \varepsilon_1(Z_1) + \beta_1^{-1} \quad (3.11)$$

where $a_1 > 0$ is a positive constant, $Z_1 = [x_1, y_d, \dot{y}_d]^T \in R^3$,

$$\begin{aligned}
 \psi_1(Z_1) = & \frac{f_1(\bar{x}_1)}{g_1(\bar{x}_1)} - \dot{w}_1 \int_0^1 \frac{3\rho^2}{g_1(\rho z_1 + w_1)} d\rho + \frac{9\beta_1}{16g_1^2(\bar{x}_1)} \|h_1(\bar{x}_1)\|^4 z_1 \\
 & + \frac{1}{2} \frac{\partial g_1^{-1}(\bar{x}_1)}{\partial z_1} \|h_1(\bar{x}_1)\|^2
 \end{aligned}$$

Choose virtual control α_1 as follows:

$$\alpha_1 = -k_1 z_1 - 0.5b_1^{-2} z_1^3 \hat{\theta}_1 \quad (3.12)$$

where $\hat{\theta}_1$ is determined by (3.6) corresponding to $i = 1$, $a_1 = b_1 \sqrt{l_1}$.

Define w_2 in such a way that

$$\tau_2 \dot{w}_2 + w_2 = \alpha_1, \quad w_2(0) = \alpha_1(0) \quad (3.13)$$

where τ_2 is a design constant that we will choose later.

From (3.13), let $y_2 = w_2 - \alpha_1$, we have $\dot{w}_2 = -\tau_2^{-1} y_2$.

$$x_2 = z_2 + y_2 + \alpha_1 = z_2 + y_2 - k_1 z_1 - 0.5a_1^{-2} z_1^3 \hat{\theta}_1 l_1 \quad (3.14)$$

Using (3.11) and Young's inequality, we obtain

$$\begin{aligned}
 LV_{z_1} \leq & (-k_1 + 2.25)z_1^4 + 0.25z_2^4 + 0.25y_2^4 \\
 & - 0.5a_1^{-2} z_1^6 \tilde{\theta}_1 l_1 + 0.5a_1^2 + \beta_1^{-1} + 0.25\eta_1^4(Z_1)
 \end{aligned} \quad (3.15)$$

where continuous function $\eta_1(Z_1)$ satisfies $|\varepsilon_1(Z_1)| \leq \eta_1(Z_1)$.

$$\begin{aligned}
 L\alpha_1 = & -k_1(f_1(\bar{x}_1) + g_1(\bar{x}_1)x_2 - \dot{w}_1) - 0.5a_1^{-2} l_1 [3z_1^2 \hat{\theta}_1 (f_1(\bar{x}_1) \\
 & + g_1(\bar{x}_1)x_2 - \dot{w}_1) + z_1^3 \dot{\hat{\theta}}_1 + 3z_1 \hat{\theta}_1 h_1^T(\bar{x}_1)h_1(\bar{x}_1)] \\
 d\alpha_1 = & L\alpha_1 dt - (k_1 + 1.5a_1^{-2} l_1 z_1^2 \hat{\theta}_1) h_1^T(\bar{x}_1) dw
 \end{aligned} \quad (3.16)$$

$$\begin{aligned}
Ly_2 &= -\tau_2^{-1}y_2 + k_1(f_1(\bar{x}_1) + g_1(\bar{x}_1)x_2 - \dot{w}_1) + 0.5a_1^{-2}l_1[3z_1^2\hat{\theta}_1(f_1(\bar{x}_1) \\
&\quad + g_1(\bar{x}_1)x_2 - \dot{w}_1) + z_1^3\hat{\theta}_1 + 3z_1\hat{\theta}_1h_1^T(\bar{x}_1)h_1(\bar{x}_1)] \\
dy_2 &= Ly_2dt + (k_1 + 1.5l_1a_1^{-2}z_1^2\hat{\theta}_1)h_1^T(\bar{x}_1)dw
\end{aligned} \tag{3.17}$$

$$0.25Ly_2^4 \leq -\tau_2^{-1}y_2^4 + 0.75y_2^4 + 0.25z_2^4 + p_2^{-1} \tag{3.18}$$

Step i ($2 \leq i \leq n-1$) Let $z_i = x_i - w_i$.

Consider the i th equation of (3.1), we have

$$dz_i = (f_i(\bar{x}_i) + g_i(\bar{x}_i)x_{i+1} - \dot{w}_i)dt + h_i^T(\bar{x}_i)dw \tag{3.19}$$

Define a smooth scalar function as follows:

$$V_{z_i} = \int_0^{z_i} \sigma^3 g_i^{-1}(\bar{x}_{i-1}, \sigma + w_i) d\sigma \tag{3.20}$$

Similar to Step 1, it is easily shown that V_{z_i} is positive definite with respect to z_i . From (3.3), we obtain

$$\begin{aligned}
LV_{z_i} &= z_i^3 g_i^{-1}(\bar{x}_i)(f_i(\bar{x}_i) + g_i(\bar{x}_i)x_{i+1} - \dot{w}_i) \\
&\quad + \int_0^{z_i} \sum_{j=1}^{i-1} \sigma^3 \frac{\partial g_i^{-1}(\bar{x}_{i-1}, \sigma + w_i)}{\partial x_j} (f_j(\bar{x}_j) + g_j(\bar{x}_j)x_{j+1}) d\sigma \\
&\quad + \left(\frac{z_i^3}{g_i(\bar{x}_i)} - \int_0^{z_i} \frac{3\sigma^2}{g_i(\bar{x}_{i-1}, \sigma + w_i)} d\sigma \right) \dot{w}_i + (1.5z_i^2 g_i^{-1}(\bar{x}_i) \\
&\quad + 0.5z_i^3 \frac{\partial g_i^{-1}(\bar{x}_i)}{\partial z_i}) h_i^T(\bar{x}_i) h_i(\bar{x}_i) + z_i^3 \sum_{p=1}^{i-1} \frac{\partial g_i^{-1}(\bar{x}_i)}{\partial x_p} h_i^T(\bar{x}_i) h_p(\bar{x}_p) \\
&\quad + \frac{1}{2} \int_0^{z_i} \sum_{p,q=1}^{i-1} \sigma^3 \frac{\partial^2 g_i^{-1}(\bar{x}_{i-1}, \sigma + w_i)}{\partial x_p \partial x_q} d\sigma h_p^T(\bar{x}_p) h_q(\bar{x}_q)
\end{aligned} \tag{3.21}$$

Using Young's inequality, we obtain

$$1.5z_i^2 g_i^{-1}(\bar{x}_i) h_i^T(\bar{x}_i) h_i(\bar{x}_i) \leq \beta_i^{-1} + \frac{9\beta_i}{16g_i^2(\bar{x}_i)} \|h_i(\bar{x}_i)\|_{z_i}^4 \tag{3.22}$$

Substituting (3.23) into (3.22) yields

$$\begin{aligned}
LV_{z_i} &\leq z_i^3(x_{i+1} + \psi_i(Z_i)) + \beta_i^{-1} \\
&\leq z_i^3 x_{i+1} + 0.5a_i^{-2} z_i^6 \theta_i l_i + 0.5a_i^2 + z_i^3 \varepsilon_i(Z_i) + \beta_i^{-1}
\end{aligned} \tag{3.23}$$

where $a_i > 0$ is a positive constant, $Z_i = [\bar{x}_i^T, z_i, \dot{w}_i]^T \in R^{i+2}$,

$$\begin{aligned}
 \psi_i(Z_i) &= f_i(\bar{x}_i)g_i^{-1}(\bar{x}_i) - \dot{w}_i \int_0^1 3\rho^2 g_i^{-1}(\bar{x}_{i-1}, \rho x_i + w_i) d\rho \\
 &+ \int_0^1 \sum_{j=1}^{i-1} z_i \frac{\partial g_i^{-1}(\bar{x}_{i-1}, \rho x_i + w_i)}{\partial x_j} (f_j(\bar{x}_j) + g_j(\bar{x}_j)x_{j+1}) d\rho \\
 &+ \frac{9\beta_i}{16g_i^2(\bar{x}_i)} \|h_i(\bar{x}_i)\|^4 z_i + \frac{1}{2} \frac{\partial g_i^{-1}(\bar{x}_i)}{\partial z_i} \|h_i(\bar{x}_i)\|^2 + \sum_{p=1}^{i-1} \frac{\partial g_i^{-1}(\bar{x}_i)}{\partial x_p} h_i^T(\bar{x}_i) h_p(\bar{x}_p) \\
 &+ \frac{1}{2} \int_0^1 \sum_{p,q=1}^{i-1} z_i \frac{\partial^2 g_i^{-1}(\bar{x}_{i-1}, \rho x_i + w_i)}{\partial x_p \partial x_q} d\rho h_p^T(\bar{x}_p) h_q(\bar{x}_q)
 \end{aligned}$$

Choose virtual control α_i as follows:

$$\alpha_i = -k_i z_i - 0.5b_i^{-2} z_i^3 \hat{\theta}_i \quad (3.24)$$

where $\hat{\theta}_i$ is determined by (3.6), $a_i = b_i \sqrt{l_i}$.

Define w_{i+1} in such a way that

$$\tau_{i+1} \dot{w}_{i+1} + w_{i+1} = \alpha_i, \quad w_{i+1}(0) = \alpha_{i+1}(0) \quad (3.25)$$

where τ_{i+1} is a design constant that we will choose later.

From (3.25), let $y_{i+1} = w_{i+1} - \alpha_i$, we have $\dot{w}_{i+1} = -\tau_{i+1}^{-1} y_{i+1}$.

$$x_{i+1} = z_{i+1} + y_{i+1} + \alpha_i = z_{i+1} + y_{i+1} - k_i z_i - 0.5a_i^{-2} z_i^3 \hat{\theta}_i l_i \quad (3.26)$$

Using (3.23) and Young's inequality, we obtain

$$\begin{aligned}
 LV_{z_i} &\leq (-k_i + 2.25)z_i^4 + 0.25z_{i+1}^4 + 0.25y_{i+1}^4 - 0.5a_i^{-2} z_i^6 \hat{\theta}_i l_i \\
 &+ 0.5a_i^2 + \beta_i^{-1} + 0.25\eta_i^4(Z_i)
 \end{aligned} \quad (3.27)$$

where continuous function $\eta_i(Z_i)$ satisfies $|\varepsilon_i(Z_i)| \leq \eta_i(Z_i)$.

$$\begin{aligned}
 L\alpha_i &= -k_i(f_i(\bar{x}_i) + g_i(\bar{x}_i)x_{i+1} - \dot{w}_i) - 0.5a_i^{-2} l_i [3z_i^2 \hat{\theta}_i (f_i(\bar{x}_i) \\
 &+ g_i(\bar{x}_i)x_{i+1} - \dot{w}_i) + z_i^3 \dot{\hat{\theta}}_i + 3z_i \hat{\theta}_i h_i^T(\bar{x}_i) h_i(\bar{x}_i)] \\
 d\alpha_i &= L\alpha_i dt - (k_i + 1.5a_i^{-2} l_i z_i^2 \hat{\theta}_i) h_i^T(\bar{x}_i) dw
 \end{aligned} \quad (3.28)$$

$$\begin{aligned}
 Ly_{i+1} &= -\tau_{i+1}^{-1} y_{i+1} + k_i(f_i(\bar{x}_i) + g_i(\bar{x}_i)x_{i+1} - \dot{w}_i) \\
 &+ 0.5a_i^{-2} l_i [3z_i^2 \hat{\theta}_i (f_i(\bar{x}_i) + g_i(\bar{x}_i)x_{i+1} - \dot{w}_i) + z_i^3 \dot{\hat{\theta}}_i + 3z_i \hat{\theta}_i h_i^T(\bar{x}_i) h_i(\bar{x}_i)] \\
 dy_{i+1} &= Ly_{i+1} dt + (k_i + \frac{3l_i}{2a_i^2} z_i^2 \hat{\theta}_i) h_i^T(\bar{x}_i) dw
 \end{aligned} \quad (3.29)$$

$$0.25Ly_{i+1}^4 \leq -\tau_{i+1}^{-1} y_{i+1}^4 + 0.75y_{i+1}^4 + 0.25z_{i+1}^4 + p_{i+1}^{-1} \quad (3.30)$$

Step n ($i = n$): Let $z_n = x_n - w_n$. Consider the n -th Equation of (3.1), we have $dz_n = (f_n(\bar{x}_n) + g_n(\bar{x}_n)u - \dot{w}_n)dt + h_n^T(\bar{x}_n)dw$.

Choose control law u as follows:

$$u = -k_n z_n - 0.5b_n^{-2}z_n^3\hat{\theta}_n \quad (3.31)$$

where $\hat{\theta}_n$ is determined by (3.6) corresponding to $i = n$, $a_n = b_n\sqrt{I_n}$.

Similar to the discussion at the i -th step, we have

$$LV_{z_n} \leq (-k_n + 0.75)z_n^4 - 0.5a_n^{-2}z_n^6\tilde{\theta}_n l_n + 0.5a_n^2 + 0.25\eta_n^4(Z_n) + \beta_n^{-1} \quad (3.32)$$

where continuous function $\eta_n(Z_n)$ satisfies $|\varepsilon_n(Z_n)| \leq \eta_n(Z_n)$. Let

$$V_1 = V_{z_1} + 0.5\gamma_1^{-1}\tilde{\theta}_1^2, \quad V_i = \sum_{j=1}^i (V_{z_j} + 0.5\gamma_j^{-1}\tilde{\theta}_j^2) + 0.25 \sum_{j=1}^{i-1} y_{j+1}^4, \quad i = 2, \dots, n$$

Theorem 1 Consider the closed-loop system consisting of the plant (3.1) under Assumptions 1 and 2, the controller (3.31), and adaptation law (3.6). For bounded initial conditions, there exist constants $k_i > 0$, $\tau_{i+1} > 0$, $\gamma_i > 0$, $\sigma_i > 0$ such that all of the signals in the closed-loop system are bounded in probability, and z_1, \dots, z_n , y_2, \dots, y_n are SGUUB in four-moment, $\tilde{\theta}_1, \dots, \tilde{\theta}_n$ are SGUUB in mean square, and k_i and τ_{i+1} satisfy

$$\begin{cases} k_i \geq 2.5 + 0.25\alpha_0 g_{i0}^{-1}, & i = 1, \dots, n \\ \tau_{i+1}^{-1} \geq 1 + \alpha_0, & i = 1, \dots, n-1 \\ \alpha_0 \leq \min\{\gamma_1\sigma_1, \dots, \gamma_n\sigma_n\} \end{cases} \quad (3.33)$$

Proof Consider the Lyapunov function candidate

$$V = \sum_{i=1}^n (V_{z_i} + 0.5\gamma_i^{-1}\tilde{\theta}_i^2) + 0.25 \sum_{i=1}^{n-1} y_{i+1}^4 \quad (3.34)$$

We obtain

$$LV = \sum_{i=1}^n (LV_{z_i} + \gamma_i^{-1}\tilde{\theta}_i\dot{\tilde{\theta}}_i) + 0.25 \sum_{i=1}^{n-1} Ly_{i+1}^4 \quad (3.35)$$

Substituting (3.6), (3.15), (3.18), (3.27) and (3.32) into (3.35), it follows that

$$\begin{aligned} LV \leq & \sum_{i=1}^n (-k_i + 2.5)z_i^4 + \sum_{i=1}^n (0.5a_i^2 + 0.25\eta_i^4(Z_i) + \beta_i^{-1}) \\ & + \sum_{i=1}^{n-1} (-\tau_{i+1}^{-1}y_{i+1}^4 + y_{i+1}^4 + 0.25\xi_{i+1}^4 + p_{i+1}^{-1}) + \sum_{i=1}^n (-\sigma_i\tilde{\theta}_i\hat{\theta}_i) \end{aligned} \quad (3.36)$$

By completion of squares, the following inequality holds

$$-\sigma_i \tilde{\theta}_i \hat{\theta}_i = -\sigma_i \tilde{\theta}_i (\tilde{\theta}_i + \theta_i) \leq \sigma_i (-0.5 \tilde{\theta}_i^2 + 0.5 \theta_i^2) \quad (3.37)$$

If $EV \leq p$, then we obtain $\tilde{\theta}_1, \dots, \tilde{\theta}_n, z_1, \dots, z_n, y_2, \dots, y_n$ are bounded in probability by Chebyshev's inequality or Lemma 1. Therefore, there exists a positive constant $\varepsilon(p)$ such that

$$\sum_{i=1}^n 0.25 \eta_i^4 (Z_i) + \sum_{i=1}^{n-1} 0.25 \zeta_{i+1}^4 \leq \varepsilon(p) \quad (3.38)$$

holds in probability. Let

$$\mu = \sum_{i=1}^n (0.5 \sigma_i \theta_i^2 + 0.5 a_i^2 + \beta_i^{-1}) + 0.25 \sum_{i=1}^{n-1} p_{i+1}^{-1} + \varepsilon(p) \quad (3.39)$$

Substituting (3.33) into (3.36), we obtain

$$LV \leq -\alpha_0 V + \mu \quad (3.40)$$

From (3.40), we obtain $\frac{d(E[V])}{dt} = E[LV] \leq -\alpha_0 E[V] + \mu$. From (3.33) and (3.39), we know that μ does not depend on the design parameters $\gamma_1, \dots, \gamma_n$. If $EV(t) = p$ and $\alpha_0 \geq \mu/p$, then $d(E[V])/dt < 0$. It implies that $EV(t) \leq p, \forall t \geq 0$ for $EV(0) \leq p$. According to Lemma 2, (3.40) further implies that $0 \leq E[V(t)] \leq V(0)e^{-\alpha_0 t} + \mu/\alpha_0, t \geq 0$. Thus, $\tilde{\theta}_1, \dots, \tilde{\theta}_n$ are SGUUB in mean square, $z_1, \dots, z_n, y_2, \dots, y_n$ are SGUUB in four-moment. According to Lemma 1, we have that all signals in the closed-loop system are bounded in probability.

To save space, simulation results are omitted.

3.4 Conclusions

Based on the integral-type Lyapunov function, and using the radial basis function neural networks and Young's inequality, a novel adaptive dynamic surface control scheme has been presented for a class of stochastic strict-feedback nonlinear systems. The explosion of complexity in traditional backstepping design is avoided by utilizing dynamic surface control. It is shown that all signals in the closed-loop system are bounded in probability by theoretical analysis. Simulation results are given to illustrate the effectiveness of the proposed control scheme.

Acknowledgments This work was partially supported by the National Natural Science Foundation of China (61174046 & 61175111).

References

1. Pan ZG, Basar T (1997) Backstepping controller design for nonlinear stochastic systems under a risk-sensitive cost criterion. In: Proceedings of the American control conference, Albuquerque, New Mexico, pp 1278–1282
2. Pan ZG, Basar T (1998) Adaptive controller design for tracking and disturbance attenuation in parametric strict-feedback nonlinear systems. *IEEE Trans Autom Control* 43(8):1066–1083
3. Liu YG, Shi SJ, Pan ZG (2001) Backstepping robust adaptive feedback control design for stochastic nonlinear systems. *Acta Automatica Sinica* 27(5):613–620 (in Chinese)
4. Deng H, Krstic M (1997) Stochastic nonlinear stabilization-PART I: a backstepping design. *Syst Control Lett* 32(3):143–150
5. Deng H, Krstic M (1997) Stochastic nonlinear stabilization-PART II: inverse optimality. *Syst Control Lett* 32(3):151–159
6. Deng H, Krstic M (1999) Output-feedback stochastic nonlinear stabilization. *IEEE Trans Autom Control* 44(2):328–333
7. Deng H, Krstic M, Williams RJ (2001) Stabilization of stochastic nonlinear systems driven by noise of unknown covariance. *IEEE Trans Autom Control* 46(8):1237–1253
8. Liu SJ, Zhang JF (2008) Output-feedback control of a class of stochastic nonlinear systems with linearly bounded unmeasurable states. *Int J Robust Nonlinear Control* 18(6):665–687
9. Liu SJ, Zhang JF (2008) Adaptive output-feedback control for a class of uncertain stochastic non-linear systems with time delays. *Int J Control* 81(8):1210–1220
10. Chen WS, Jiao LC, Li J et al (2010) Adaptive NN backstepping output-feedback control for stochastic nonlinear strict-feedback systems with time-varying delays. *IEEE Trans Syst Man Cybern B Cybern* 40(3):939–950
11. Li J, Li JM, Chen WS (2010) Adaptive neural network output-feedback stabilization for a class of stochastic nonlinear strict-feedback systems. *Acta Automatica Sinica* 36(3):450–453 (in Chinese)
12. Yu ZX, Du HB (2010) Neural-network-based bounded adaptive stabilization for uncertain stochastic nonlinear systems with time-delay. *Control Theor Appl* 27(7):855–860 (in Chinese)
13. Psillakis HE, Alexandridis AT (2007) NN-based adaptive tracking control of uncertain nonlinear systems disturbed by unknown covariance noise. *IEEE Trans Neural Networks* 18(6):1830–1835
14. Wang YC, Zhang HG, Wang YZ (2006) Fuzzy adaptive control of stochastic nonlinear systems with unknown virtual control gain function. *Acta Automatica Sinica* 32(2):170–178 (in Chinese)
15. Swaroop D, Hedrick JK, Yip PP et al (2000) Dynamic surface control for a class of nonlinear systems. *IEEE Trans Autom Control* 45(10):1893–1899
16. Zhang TP, Ge SS (2007) Direct adaptive NN control of nonlinear systems in strict-feedback form using dynamic surface control. *IEEE Int Symp Intell Control*, Singapore, pp 315–320
17. Zhang TP, Zhu QQ, Zhu Q (2010) Adaptive NN dynamic surface control of strict-feedback nonlinear systems. In: Proceedings of the 8th world congress on intelligent control and automation, Jinan, China, pp 2124–2129
18. Chen WS, Jiao LC, Du ZM (2010) Output-feedback adaptive dynamic surface control of stochastic non-linear systems using neural network. *IET Control Theor Appl* 4(12):3012–3021

Chapter 4

Three-Dimensional Path Planning for AUV Based on Fuzzy Control

Lisha Jiang and Daqi Zhu

Abstract A novel fuzzy control method is presented for AUV (Autonomous underwater vehicles) path planning in three-dimensional environment. On the basis of the forward looking sonar model, the virtual acceleration of AUV in both horizontal and vertical plane can be gotten through the fuzzy system. Surge and heave velocity of AUV are calculated respectively and the synthetic velocity is obtained. Finally, simulation results illustrate the effectiveness and feasibility of the proposed approach.

Keywords AUV · Fuzzy controller · Three-dimensional path planning

4.1 Introduction

Now numerous path planning algorithms have been developed [1, 2], such as template matching approach [3], map building [4] and artificial intelligence approach [5], etc. Each method mentioned above has its own advantages as well as disadvantages.

As the better performance of fuzzy logic in uncertain information processing, it has many applications in mobile robot path planning. For example, Perez et al. [6] proposed the fuzzy logic path planning for autonomous navigation under velocity field control. Zun et al. and Shen et al. [7, 8] proposed UAV path planning and obstacle avoidance based on fuzzy data fusion. Recently, Leblanc and Saffiotti [9]

L. Jiang · D. Zhu (✉)

Laboratory of Underwater Vehicles and Intelligent Systems, Shanghai Maritime University,
Haigang Avenue 1550, Shanghai 201306, China
e-mail: zdq367@yahoo.com.cn

further studied the fuzzy fusion algorithm of multi-robot target location. These correlation algorithms can not only improve sensor test precision, but also reduce the uncertainty of the environment. Yang and Zhu [10] proposed a solution of AUV's local path planning based on fuzzy logic. The result of planning is based on the environment which includes information of relationship between obstacles and the vehicle.

However, the proposed method mentioned above only discusses static path planning in horizontal plan for AUV, there is no research concerning three-dimension environment. In addition, it's difficult to acquire prior knowledge and predefine all of the fuzzy rules in these fuzzy methods. Therefore, a novel fuzzy inference controller is proposed for AUV navigation with undefined and incomplete environmental factors, which enables AUV to automatically avoid static obstacles and generate a satisfying path.

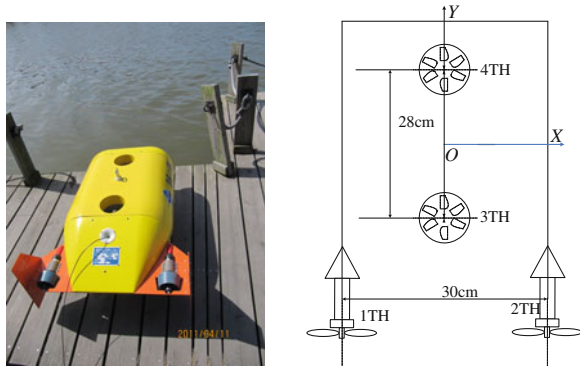
This paper is organized as follows: Second section describes AUV architecture; Third section discusses static path planning both in horizontal and vertical plane, then the synthetic path planning is given. Simulation results are presented in fourth section. Finally, conclusions are drawn and recommendations for future work are presented in section fifth.

4.2 AUV Structure and Sensor Model

4.2.1 Structure of AUV

AUV (from Lab. of Underwater Vehicles and Intelligent Systems, Shanghai Maritime University) has four thrusters shown in Fig. 4.1. Two of them in the horizontal plane are installed symmetrically on the robot tail, which control the surge and yaw velocity of AUV. The other two thrusters in the vertical plane are installed on the robot center of gravity, which control the heave and pitch velocity of AUV.

Fig. 4.1 Thruster arrangement of AUV



4.2.2 Forward Looking Sonar Model of AUV

Figure 4.2 shows that two sonars are mounted on AUV to gather its surrounding information of horizontal plane. In order to utilize the sonars efficiently, the range of these two sonars sensed are divided into three groups: right group; front group; left group and each group covers 60 degrees. The sonar arrangement is the same in vertical plane, just as Fig. 4.3 shows, the range are also divided into three groups: up group, ahead group and down group. Then compare all the measured data and choose the minimum values which can represent the distances between AUV and obstacles in six directions. It is efficient and sufficient for obstacle avoidance here.

Fig. 4.2 Sensors arrangement of AUV in horizontal plane

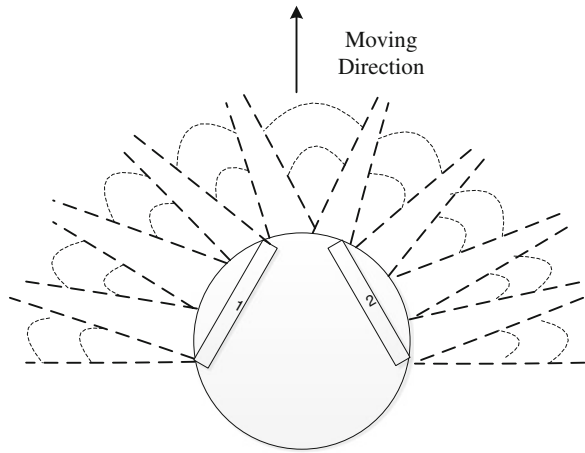
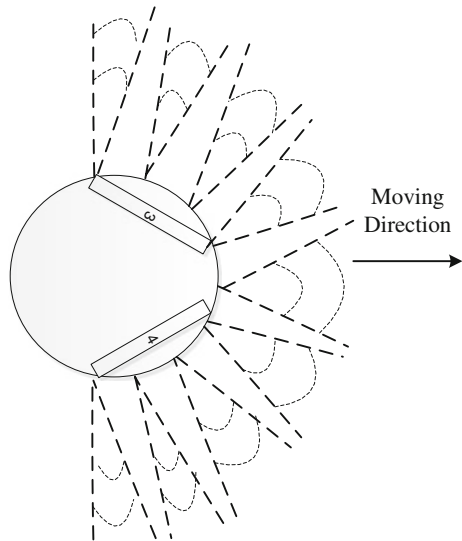


Fig. 4.3 Sensors arrangement of AUV in vertical plane



4.3 Fuzzy Control Design for AUV with Static Obstacles

4.3.1 Fuzzy Algorithm

A fuzzy controller block diagram is illustrated in Fig. 4.4. The concept of fuzzy logic was first articulated by Zadeh in 1965 [11], who described the basic concepts of fuzzy system and the continuous membership function. Its foundations and applications have grown wider over years. Here, Mamdani Controllers [12] are adopted to acquire the fuzzy matrix.

4.3.2 Three-Dimensional Path Planning with Static Obstacles

During the navigation of AUV, three-dimensional path planning with obstacle avoidance turns out to be a key task. In this section, static obstacle avoidance is discussed. Here three-dimensional path planning is divided into two parts: horizontal path planning and vertical path planning, then synthetic path is given.

4.3.2.1 Horizontal Path Planning

Using the same input and output assignments proposed by Tan and Yang [13], there are five signals that represent the inputs to the fuzzy controller in the horizontal plane: the distance from AUV to obstacles in left, front and right directions d_l , d_f , d_r ; AUV surge velocity u' and the target direction $\psi(t)$. There are two representations of outputs from the fuzzy controller: a'_l and a'_r , which represent the accelerations of the left and right wheels respectively.

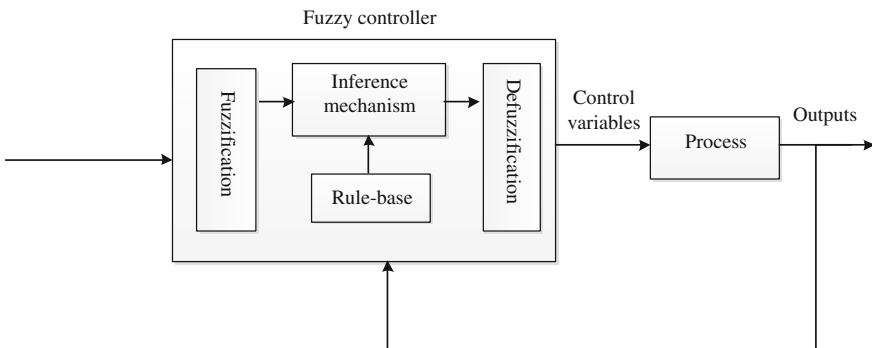


Fig. 4.4 Fuzzy controller architecture

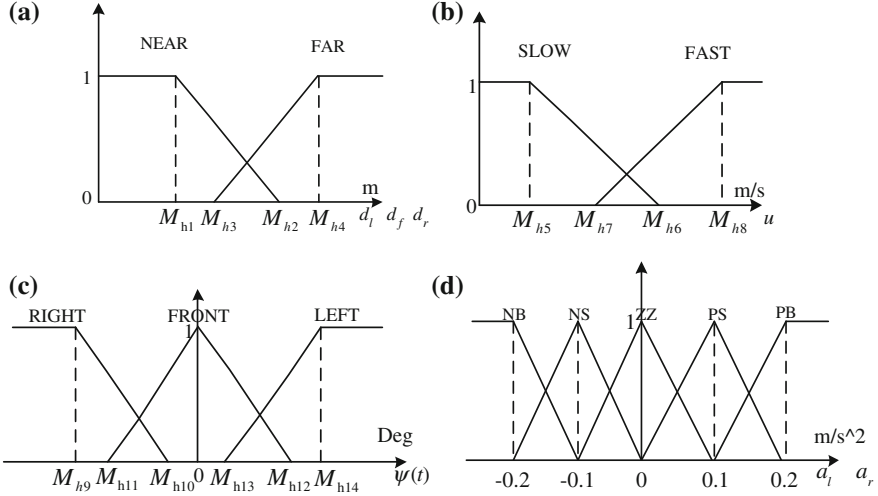


Fig. 4.5 Membership function for input and output variables in horizontal plane. **a** Distance. **b** Velocity. **c** Angle. **d** Acceleration

The variables are translated into linguistic values according to the membership functions which show in Fig. 4.5. $M = [M_{h1} \dots M_{h7} \dots M_{h14}]$ is seen as 14 boundary parameters of the three input membership functions which is acquired mainly by the substantial experience.

In this fuzzy controller, there are five inputs, four of them contain two fuzzy grades respectively and the other one contains three, so forty-eight rules in total are set in Table 4.1.

Table 4.1 Fuzzy rules in horizontal plane

Rule order	Input(5)					Output(2)	
	d_i	d_j	d_r	$\psi(t)$	u'	a'_i	a'_r
1	FAR	FAR	FAR	LEFT	SLOW	PS	PB
2	FAR	FAR	FAR	LEFT	FAST	NS	PS
...
6	NEAR	FAR	NEAR	RIGHT	FAST	PS	NS
7	FAR	FAR	NEAR	LEFT	SLOW	ZZ	PS
...
21	FAR	NEAR	NEAR	FROT	SLOW	ZZ	PS
22	FAR	NEAR	NEAR	FRON	FAST	NS	ZZ
...
47	NEAR	NEAR	NEAR	RIGHT	SLOW	PS	ZZ
48	NEAR	NEAR	NEAR	RIGHT	FAST	NS	NB

After getting the left and right acceleration a'_i, a'_r , the surge velocity u'_i, u'_r can be obtained through the integral of them, just as Eq. (4.1) shows. Then the synthetic surge velocity u' and the yaw velocity r' can be gotten by Eq. (4.2), here L is the distance between left and right thrusters.

$$u'_l = \int a'_l dt, \quad u'_r = \int a'_r dt \quad (4.1)$$

$$u' = \frac{1}{2}(u'_l + u'_r), \quad r' = \frac{1}{2L}(u'_r - u'_l) \quad (4.2)$$

4.3.2.2 Vertical Path Planning

Vertical path planning is just similar to horizontal path planning, as Eq. (4.3–4.4) shows.

$$w'_1 = \int a'_{h1} dt, \quad w'_2 = \int a'_{h2} dt \quad (4.3)$$

$$w' = \frac{1}{2}(w'_1 + w'_2), \quad q' = \frac{1}{2M}(w'_1 - w'_2) \quad (4.4)$$

where w'_1, w'_2 is the heave velocity and a'_{h1}, a'_{h2} is the acceleration.

4.3.2.3 Synthetic Path Planning

Now four virtual control variables u', w', r' and q' are obtained, to control AUV in three-dimensional space, they should be converted into the body-fixed frame, which can really control the movement of AUV in three-dimensional environment, the conversion equations are shows below and the real control variables u, w, r and q are obtained:

$$u = w' \sin \theta + u' \cos \theta \quad (4.5)$$

$$w = w' \cos \theta - u' \sin \theta \quad (4.6)$$

$$r = r' \cos \theta \quad (4.7)$$

$$q = q' \quad (4.8)$$

4.4 Simulation Results

According to the proposed algorithm for AUV path planning, the simulation experiment is conducted on the Matlab platform. Firstly, the underwater environment is set as follows: the workspace for static environment is 12 m*12 m*12 m; The starting and target points are randomly distributed, here set (0,0,0) and (10,10,10) respectively.

To be simplified, the shapes and locations of each static obstacle are already known. S_1 – S_6 are the static obstacles, of which S_1 and S_5 are the cubes with side length of 1 m, S_3 and S_4 are the 2 m*1 m*1 m cuboids, S_2 and S_6 are the triangular pyramid. Parameters are set as follows: the sensing range of the ultrasonic sensors is from 0 m to 2 m; L is the distance between left and right thrusters, $L = 0.25$ m; M is the distance between front and rear thrusters, $M = 0.25$ m.

4.4.1 Simulation Results in Horizontal Plane

Figure 4.6 shows the static obstacle avoidance in horizontal plane. When the obstacle is far from AUV, it will move along its target direction; When AUV detects a static obstacle, it will slow down a little bit. When the obstacle is close enough, AUV will choose the best way to avoid it according to the fuzzy controller. As shown in Fig. 4.6, when AUV moves to the point &1, it detects a static obstacle, with left sensory value $d_l = 0.5685$ (NEAR), front sensory value $d_f = 0.9235$ (FAR) and right sensory value $d_r = 1.3163$ (FAR), $\psi(t) = -44.68^\circ$ (RIGHT) and the surge velocity $u' = 0.2$ m/s (FAST), by means of fuzzy inference, the acceleration of left and right thrusters can be gotten, namely $a'_l = 0.0929$ m/s² (PB), $a'_r = 0.0151$ m/s² (PS), which can result a right turn for AUV to avoid obstacle S_{h2} , at the same time, keep far away from obstacle S_{h1} . With the same method, AUV can finally generate a secure and collision-free path, just as the red path in Fig. 4.6.

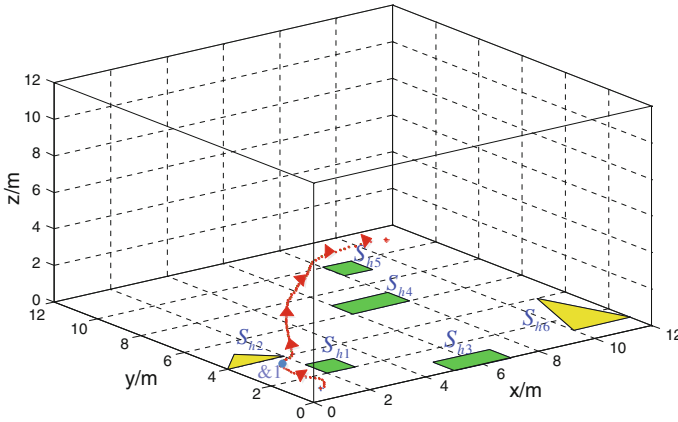


Fig. 4.6 Static path planning for AUV in horizontal plane

4.4.2 Simulation Results in Vertical Plane

Figure 4.7 shows the static obstacle avoidance in vertical plane. The condition is the same as 4.1, and AUV can generate a secure and collision-free path shown in Fig. 4.7.

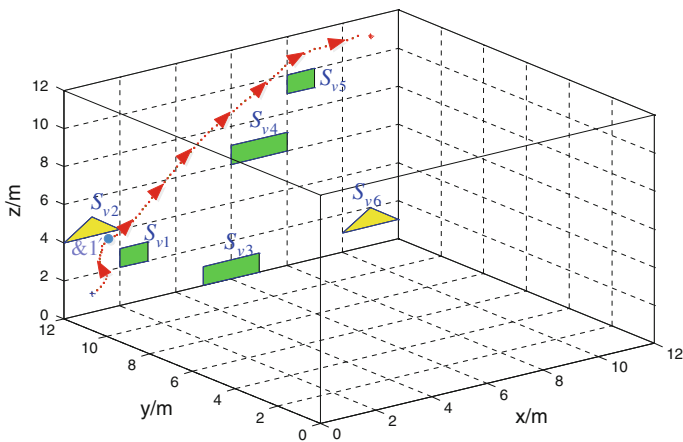


Fig. 4.7 Static path planning for AUV in vertical plane

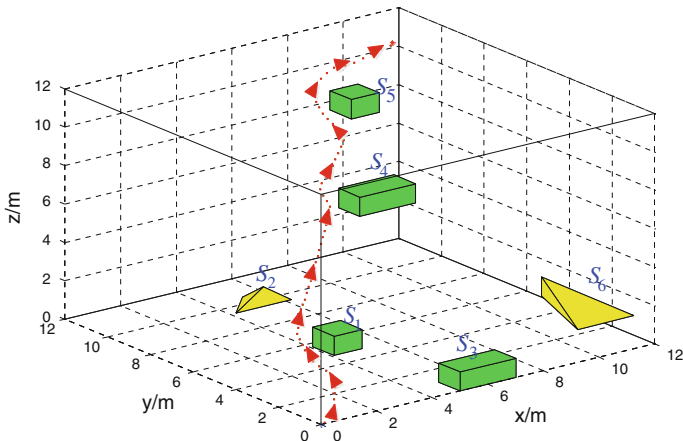


Fig. 4.8 Three-dimensional static path planning for AUV

4.4.3 Simulation Results of Synthetic Path Planning in Static Environment

Through the process above, the acceleration of right, left, front and rear thrusters a_r, a_l, a_{h1}, a_{h2} can be gotten. Then the final surge velocity u and heave velocity w are calculated respectively and the synthetic velocity v_s is obtained. Subsequently three-dimensional synthesis path in static environment is shown in Fig. 4.8.

4.5 Conclusion

In this paper, the architecture of autonomous underwater vehicle in three-dimensional environment is established firstly. Then the path planning with static obstacles is presented by using Fuzzy-Control method, here according to different situations, specific fuzzy memberships are assigned. From the simulation results, it is clear to see that the designed control system can accomplish the three-dimensional path planning successfully and effectively.

Acknowledgments This project is supported by the National Natural Science Foundation of China (51075257), Research Fund of Ministry Transport of China (2011-329-810-440) and the Project of Excellent Academic Leaders of Shanghai (11XD1402500).

References

1. Yang YY, Zhu DQ (2011) Research on dynamic path planning of AUV based on forward looking sonar and fuzzy control. Control and decision conference, China, pp 2425–2430
2. Huang H, Zhu DQ (2012) Dynamic task assignment and path planning for multi-AUV system in 2D variable ocean current environment, Control and decision conference (CCDC), China, pp 3660–3664
3. Vasudevan C, Ganesan K (1994) Case-based path planning for autonomous underwater vehicles. In: IEEE international symposium on intelligent control, Columbus, Ohio, USA, pp 160–165
4. Dissanayake MWMG, Newman P, Clark S, Durrany-Whyte HF, Csorba M (2001) A solution to the simultaneous localization and map building (SLAM) problem. IEEE Trans Robot Autom 17(3):229–241
5. Cheng CT, Fallahi K, Leung H (2012) A genetic algorithm-inspired UUV path planner based on dynamic programming. IEEE Trans Syst Man Cybern Part C Appl Rev 42(6):1128–1134
6. Perez DA, Melendez WM, Guzman J, Fermin L, Lopez GF (2009) Fuzzy logic based speed planning for autonomous navigation under velocity field control, IEEE international conference on mechatronics, Malaga, Spain pp 14–17
7. Zun AD, Kato N, Nomura Y, Matsui H (2006) Path planning based on geographical features information for an autonomous mobile robot. Artificial Life Robot 10(2):149–156
8. Shen D, Chen GS, Cruz JJ, Blasch E (2008) A game theoretic data fusion aided path planning approach for cooperative UAV ISR, IEEE international conference on aerospace, Montana, USA pp 1–9

9. Leblanc K, Saffiotti A (2009) Multirobot object localization: a fuzzy fusion approach. *IEEE Trans Syst Man Cybern B Cybern* 39(5):1259–1276
10. Yang XS, Zhu A (2012) A bioinspired neurodynamics based approach to tracking control of mobile robots. *IEEE Trans Industr Electron* 59(8):3211–3220
11. Zadeh LA (1998) Fuzzy Logic. *Computer* 21:483–493
12. Wen S, Zhu Q, Zhang X (2005) Simulation of the path planning of mobile robot based on the fuzzy controller. *Appli Sci Technol* 32(4):32–33
13. Tan S, Yang SX (2008) A fuzzy inference controller with accelerate/break module for mobile robots, *IEEE international conference on automation and logistics*, Qingdao, China, pp 810–815

Chapter 5

Consensus Analysis of Multi-Agent System with Impulsive Effects and Time-Varying Delays

Dandan Li, Mei Sun, Dun Han and Anna Gao

Abstract Based on the stability analysis of the impulsive functional differential equation, the consensus of the multi-agent systems with impulsive effects and communication delays is investigated in this paper. Moreover, impulsive effects are considered in the process of communication between the leader and the follower agents which directly exchange information with the leader. Some new criteria are derived for the follower agents converging to the leader. Finally, the numerical simulation is presented to demonstrate the effectiveness of our theories.

Keywords Multi-agent · Consensus · Impulsive effects · Time-varying delays

5.1 Introduction

In the research of multi-agent systems, leader-following consensus problem were widely investigated [1–4]. In [1], the researchers studied the leader-following consensus problem for the multi-agent system with a varying-velocity leader and time-varying delays. In [2], the leader-following consensus problem of second-order multi-agent systems with non-uniform time-varying delays was studied. In [3], based on graph, matrix theory, and LaSalle's invariance principle a pinning control algorithm is proposed to achieve leader-following consensus in a network of agents with nonlinear second-order dynamics. In [4], the adaptive control method is employed to achieve leader-following consensus for third-order nonlinear multi-agent systems.

Impulsive widely exist in many realistic systems such as signal processing systems, automatic control systems, flying object motions and telecommunications,

D. Li · M. Sun (✉) · D. Han · A. Gao
Nonlinear Scientific Research Center, Jiangsu University 301 Xuefu Road,
Zhenjiang, 212013 Jiangsu, People's Republic of China
e-mail: sunm@ujs.edu.cn

impulsive effects is common phenomena characterized by abrupt changes at certain moments due to instantaneous perturbations [5–7]. Furthermore, in practical networked multi-agent systems, time-delays are unavoidable in information transmission which should be taken into consideration [8–10]. Therefore, the study of multi-agent systems associated with impulsive and time delays is important for understanding the consensus problem of the most real-world multi-agent systems.

In this paper, we consider the patterns of information exchange between leader and follower agents are different, the follower agents are classified into two types: directly and indirectly exchange information with leader agent. Then, impulsive effects are considered in the process of communication between the leader agent and the former class of follower agents, which is more challenging than previous works.

The organization of this paper is as follows, in Sect. 5.2, we formulate the leader agent system and the follower agent systems with impulsive effects. In Sect. 5.3, the consensus analysis of leader-following multi-agent systems with time-varying delays is discussed. In Sect. 5.4, numerical simulations are given to demonstrate the theoretical analysis. Conclusions are finally drawn.

5.2 Problem Formulation

Here, we describe the multi-agent dynamical system, which is composed of one leader system and N follower systems with impulsive effects.

The leader agent is an isolated agent, whose dynamic is described by:

$$\begin{cases} \dot{x}_0(t) = v_0(t), \\ \dot{v}_0(t) = f_0(t, x_0(t), v_0(t)) \end{cases} \quad (5.1)$$

where $x_0(t)$ and $v_0(t)$ are the position and velocity of the leader at time t , respectively. $f_0(t, x_0(t), v_0(t))$ is a vector-valued continuous nonlinear function to describe the intrinsic dynamics of agent.

The dynamics of each follower agent with impulsive effects is described by:

$$\begin{cases} \dot{x}_i(t) = v_i(t) + u_{i1}(t), & t \neq t_k, \\ \Delta x_i(t_k) = x_i(t_k^+) - x_i(t_k^-) = d_{i1}^k [b_i(x_i(t_k) - x_0(t_k))], & t = t_k \\ \dot{v}_i(t) = f_i(t, x_i(t), v_i(t)) + u_{i2}(t), & t \neq t_k, \\ \Delta v_i(t_k) = v_i(t_k^+) - v_i(t_k^-) = d_{i2}^k [b_i(v_i(t_k) - v_0(t_k))], & t = t_k. \end{cases} \quad (5.2)$$

where d_{i1}^k, d_{i2}^k are the impulsive gains. If the follower agent i is a neighbor of leader, then $b_i = 1$, otherwise, $b_i = 0$. The impulsive sequence $\{t_k\}_{k=1}^{\infty}$ satisfies $0 = t_0 < t_1 < t_2 < \dots < t_k < \dots$, $\lim_{k \rightarrow \infty} t_k = \infty$, and $x_i(t_k^+) = \lim_{h \rightarrow 0^+} (x_i(t_k + h))$, $x_i(t_k^-) = \lim_{h \rightarrow 0^-} (x_i(t_k + h))$. $u_{i1}(t), u_{i2}(t)$ are the controller in the following form:

$$\begin{cases} u_{i1}(t) = c \left[\sum_{j \in N_i} a_{ij} (x_i(t - \tau(t)) - x_j(t - \tau(t))) \right. \\ \quad \left. + b_i (x_i(t - \tau(t)) - x_0(t - \tau(t))) \right], t \neq t_k, \\ u_{i2}(t) = c \left[\sum_{j \in N_i} a_{ij} (v_i(t - \tau(t)) - v_j(t - \tau(t))) \right. \\ \quad \left. + b_i (v_i(t - \tau(t)) - v_0(t - \tau(t))) \right], t \neq t_k. \end{cases} \quad i = 1, 2, \dots, N. \quad (5.3)$$

If agent j is a neighbor of agent i , which means information is flowing from agent i to agent j , then $a_{ij} = 1$, otherwise $a_{ij} = 0$. c is a constant.

Let $e_{i1}(t) = x_i(t) - x_0(t)$, $e_{i2}(t) = v_i(t) - v_0(t)$ be the synchronization errors, then the error systems between system (1) and (2) as follows:

$$\begin{cases} \dot{e}_i(t) = C e_i(t) + B_i e_i(t - \tau(t)) + F_i(t) + H_i(t), & t \neq t_k, \\ \Delta e_i(t_k) = D_i^k e_i(t_k), & t = t_k, \quad i = 1, 2, \dots, N, \quad k = 1, 2, \dots \end{cases} \quad (5.4)$$

where

$$\begin{aligned} C &= \begin{bmatrix} 0 & 1 \\ 0 & 0 \end{bmatrix}, B_i = \begin{bmatrix} c b_i & 0 \\ 0 & c b_i \end{bmatrix}, D_i^k = \begin{bmatrix} d_{i1}^k b_i & 0 \\ 0 & d_{i2}^k b_i \end{bmatrix}, \\ e_i(t) &= [e_{i1}(t), e_{i2}(t)]^T, F_i(t) = [0, f_i(t, x_i, v_i) - f_0(t, x_0, v_0)]^T, \\ H_i(t) &= \left[c \sum_{j \in N_i} a_{ij} (e_{i1}(t - \tau(t)) - e_{j1}(t - \tau(t))), c \sum_{j \in N_i} a_{ij} (e_{i2}(t - \tau(t)) - e_{j2}(t - \tau(t))) \right]^T. \end{aligned}$$

Furthermore, we introduce the following notation:

$$\hat{e}_1(t) = [e_{11}(t), e_{21}(t), \dots, e_{N1}(t)]^T, \quad \hat{e}_2(t) = [e_{12}(t), e_{22}(t), \dots, e_{N2}(t)]^T.$$

Definition 1 The leader follower consensus of multi-agent system (1) and (2) is said to be achieved, if its solution satisfies

$$\lim_{t \rightarrow \infty} e_{i1}(t) = \lim_{t \rightarrow \infty} \|x_i(t) - x_0(t)\| = 0, \quad \lim_{t \rightarrow \infty} e_{i2}(t) = \lim_{t \rightarrow \infty} \|v_i(t) - v_0(t)\| = 0, \\ i = 1, 2, \dots, N,$$

Lemma 1 For all $x, y \in R$, $\sigma > 0$ and $\varepsilon \in (0, 1)$, the following inequality holds:

$$2\sigma|xy| \leq \sigma^{2\varepsilon} x^2 + \sigma^{2(1-\varepsilon)} y^2.$$

Lemma 2 [11] Let $r, s \geq 0$, $\tau > 0$ and $d_k > 0$, $k = 1, 2, \dots$, be constants, and assume that $x(t)$ is piecewise continuous nonnegative function satisfying:

$$\begin{cases} D^+ x(t) \leq r x(t) + s \bar{x}(t), & t \geq t_0, t \neq t_k, \\ x(t_k^+) \leq d_k(x(t_k)), & k = 1, 2, \dots, \\ x(t) = \varphi(t), & t \in [t_0 - \tau, t_0]. \end{cases}$$

If there exists β such that for $k = 1, 2, \dots$, $\frac{\ln d_k}{t_k - t_{k-1}} \leq \beta$ and $r + ds + \beta < 0$, then $x(t) \leq d \left(\sup_{t_0 - \tau \leq t \leq t_0} |\varphi(t)| \right) \exp\{-\lambda(t - t_0)\}$, where $d = \sup_{1 \leq k < +\infty} \{\exp(\beta(t_k - t_{k-1}))\}$, $\bar{x}(t) = \sup_{t - \tau \leq \sigma \leq t} x(\sigma)$, and λ is a unique positive solution of $\lambda + r + ds \exp(\lambda\tau) + \beta = 0$.

5.3 Main Results

In this section, we discuss the consensus problem of leader–follower multi-agent systems with impulsive effect and time-varying delays.

Assumption 1 For the nonlinear functions f_i , there exist nonnegative constants θ_{i1}, θ_{i2} , such that $|f_i(t, x_1, x_2) - f_0(t, y_1, y_2)| \leq \theta_{i1}|x_1 - y_1| + \theta_{i2}|x_2 - y_2|$, $i = 1, 2, \dots, N$.

Theorem 1 Assume that assumption 1 holds, and there exists a constant β such that for any $k = 1, 2, \dots$ satisfy

$$\ln \mu_k - \beta(t_k - t_{k-1}) \leq 0 \text{ and } \omega + d\eta + \beta < 0,$$

where

$$\begin{aligned} \mu_k &= \max_{1 \leq i \leq N} \left\{ (1 + d_{i1}^k b_i)^2, (1 + d_{i2}^k b_i)^2 \right\}, \\ \omega &= \max_{1 \leq i \leq N} \lambda_{\max} \begin{bmatrix} \theta_{i1} + |c|^{2\varepsilon_1} + \frac{c}{p} & 1 \\ 1 & \theta_{i1} + 2\theta_{i2} + |c|^{2\varepsilon_2} + \frac{c}{q} \end{bmatrix}, \\ \eta &= \max_{1 \leq i \leq N} \lambda_{\max} \begin{bmatrix} |c|^{2(1-\varepsilon_1)} + cp\lambda_N^2 & 0 \\ 0 & |c|^{2(1-\varepsilon_2)} + cq\lambda_N^2 \end{bmatrix}, \\ \lambda_N &= \lambda_{\max}(L), \quad d = \sup_{1 \leq k < +\infty} \left\{ \exp(\beta(t_k - t_{k-1})), \frac{1}{\exp(\beta(t_k - t_{k-1}))} \right\}, \end{aligned}$$

L is Laplacian matrix, $0 < \tau(t) \leq \tau$, for some $p, q > 0$, $\varepsilon_1, \varepsilon_2 \in (0, 1)$, then the error system (4) is globally exponentially stable. That is, the leader system (1) and the follower systems (2) achieve consensus.

Proof Consider the following Lyapunov function candidate

$$V(t) = \sum_{i=1}^N e_i^T(t) e_i(t).$$

For $t \in (t_{k-1}, t_k]$, $k = 1, 2, \dots$, taking the upper Dini derivative of $V(t)$ along the trajectory of the error system (4), we have

$$D^+V(t) = \sum_{i=1}^N [e_i^T(t)(C + C^T)e_i(t) + (e_i^T(t)B_i e_i(t - \tau(t)) + e_i^T(t - \tau(t))B_i^T e_i(t)) \\ + (e_i^T(t)F_i(t) + F_i^T(t)e_i(t)) + (e_i^T(t)H_i(t) + H_i^T(t)e_i(t))]. \quad (5.5)$$

$$e_i^T(t)B_i e_i(t - \tau(t)) = e_i^T(t - \tau(t))B_i^T e_i(t) \\ = cb_i(e_{i1}(t)e_{i1}(t - \tau(t)) + e_{i2}(t)e_{i2}(t - \tau(t))) \\ \leq |c|(|e_{i1}(t)e_{i1}(t - \tau(t))| + |e_{i2}(t)e_{i2}(t - \tau(t))|) \\ \leq \frac{1}{2}|c|^{2\epsilon_1}e_{i1}^2(t) + \frac{1}{2}|c|^{2(1-\epsilon_1)}e_{i1}^2(t - \tau(t)) + \frac{1}{2}|c|^{2\epsilon_2}e_{i2}^2(t) \\ + \frac{1}{2}|c|^{2(1-\epsilon_2)}e_{i2}^2(t - \tau(t)) \\ = e_i^T(t) \begin{bmatrix} \frac{1}{2}|c|^{2\epsilon_1} & 0 \\ 0 & \frac{1}{2}|c|^{2\epsilon_2} \end{bmatrix} e_i(t) \\ + e_i^T(t - \tau(t)) \begin{bmatrix} \frac{1}{2}|c|^{2(1-\epsilon_1)} & 0 \\ 0 & \frac{1}{2}|c|^{2(1-\epsilon_2)} \end{bmatrix} e_i(t - \tau(t)). \quad (5.6)$$

$$e_i^T(t)F_i(t) = F_i^T(t)e_i(t) = e_{i2}(t)[f_i(t, x_i, v_i) - f_0(t, x_0, v_0)] \\ \leq |e_{i2}(t)|(|\theta_{i1}|e_{i1}(t) + \theta_{i2}|e_{i2}(t)|) \leq \frac{1}{2}\theta_{i1}[e_{i1}^2(t) + e_{i2}^2(t)] + \theta_{i2}e_{i2}^2(t) \\ = e_i^T(t) \begin{bmatrix} \frac{1}{2}\theta_{i1} & 0 \\ 0 & \frac{1}{2}\theta_{i1} + \theta_{i2} \end{bmatrix} e_i(t). \quad (5.7)$$

$$\sum_{i=1}^N e_i^T(t)H_i(t) = \sum_{i=1}^N H_i^T(t)e_i(t) \\ = c \sum_{i=1}^N e_{i1}(t) \sum_{j \in N_i} a_{ij}(e_{i1}(t - \tau(t)) - e_{j1}(t - \tau(t))) \\ + c \sum_{i=1}^N e_{i2}(t) \sum_{j \in N_i} a_{ij}(e_{i2}(t - \tau(t)) - e_{j2}(t - \tau(t))) \\ = c[\hat{e}_1^T(t)L\hat{e}_1(t - \tau(t)) + \hat{e}_2^T(t)L\hat{e}_2(t - \tau(t))] \\ \leq c[\frac{1}{2p}\hat{e}_1^T(t)\hat{e}_1(t) + \frac{q}{2}\hat{e}_1^T(t - \tau(t))L^T L\hat{e}_1(t - \tau(t)) \\ + \frac{1}{2q}\hat{e}_2^T(t)\hat{e}_2(t) + \frac{q}{2}\hat{e}_2^T(t - \tau(t))L^T L\hat{e}_2(t - \tau(t))] \\ = \sum_{i=1}^N e_i^T(t) \begin{bmatrix} \frac{c}{2p} & 0 \\ 0 & \frac{c}{2q} \end{bmatrix} e_i(t) + \sum_{i=1}^N e_i^T(t - \tau(t)) \begin{bmatrix} \frac{cq}{2}\lambda_N^2 & 0 \\ 0 & \frac{cq}{2}\lambda_N^2 \end{bmatrix} e_i(t - \tau(t)) \quad (5.8)$$

Combine (5.5)–(5.8), one obtains

$$\begin{aligned} D^+V(t) &\leq \sum_{i=1}^N e_i^T(t) \begin{bmatrix} \theta_{i1} + |c|^{2\varepsilon_1} + \frac{\varepsilon}{p} & & 1 \\ & 1 & \\ & & \theta_{i1} + 2\theta_{i2} + |c|^{2\varepsilon_2} + \frac{\varepsilon}{q} \end{bmatrix} e_i(t) \\ &\quad + \sum_{i=1}^N e_i^T(t - \tau(t)) \begin{bmatrix} |c|^{2(1-\varepsilon_1)} + cp\lambda_N^2 & & 0 \\ & 0 & \\ & & |c|^{2(1-\varepsilon_2)} + cq\lambda_N^2 \end{bmatrix} e_i(t - \tau(t)) \\ &\leq \omega V(t) + \eta V(t - \tau(t)) \leq \omega V(t) + \eta \bar{V}(t). \end{aligned}$$

Where $\bar{V}(t) = \sup_{-\tau \leq \sigma \leq 0} V(t + \sigma)$.

On the other hand, from (5.4) we have

$$\begin{aligned} V(t_k^+) &= \sum_{i=1}^N e_i^T(t_k^+) e_i(t_k^+) = \sum_{i=1}^N e_i^T(t_k) (I_2 + D_i^k)^T (I_2 + D_i^k) e_i(t_k) \\ &\leq \mu_k \sum_{i=1}^N e_i^T(t_k) e_i(t_k) = \mu_k V(t_k), \end{aligned}$$

Therefore, it follows Lemma 2 and conditions of this theorem that

$$V(t) \leq d \left(\sup_{t_0 - \tau \leq t \leq t_0} |V(t)| \right) \exp\{-\lambda(t - t_0)\}$$

where d and λ is the unique positive solution of $\lambda + \omega + d\eta \exp(\lambda\tau) + \beta = 0$.

Therefore,

$$e_i^2(t) \leq d \left(\sup_{t_0 - \tau \leq t \leq t_0} |V(t)| \right) \exp\{-\lambda(t - t_0)\}, \quad i = 1, 2, \dots, N.$$

Hence, the origin of error system (4) is globally exponentially stable. The leader and follower agents achieve globally exponentially consensus.

5.4 Numerical Simulations

In this section, an example is given to illustrate the previous theories.

Example Consider a multi-agent system with one leader agent and five follower agents. The adjacency matrix, the diagonal matrix of graph and intrinsic dynamics are as follows:

$$A = (a_{ij})_{5 \times 5} = \begin{pmatrix} 0 & 0 & 0 & 0 & 0 \\ 0 & 0 & 0 & 1 & 0 \\ 0 & 0 & 0 & 0 & 1 \\ 0 & 0 & 0 & 0 & 0 \\ 0 & 0 & 0 & 0 & 0 \end{pmatrix}, \quad B = (b_{ij})_{5 \times 5} = \text{diag}\{1, 1, 1, 0, 0\}, \quad f_i = \sin(x_i(t)).$$

Fig. 5.1 Position errors

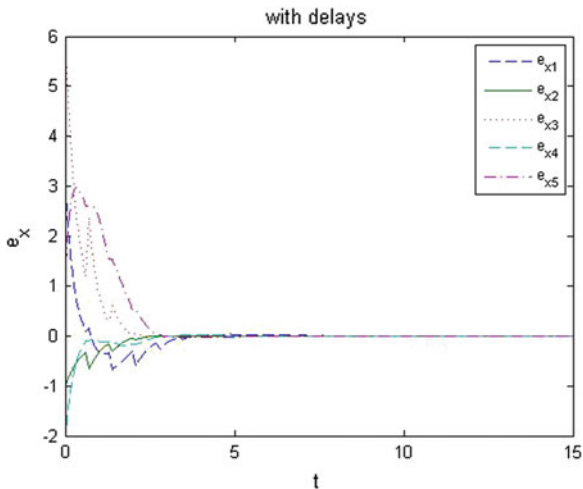
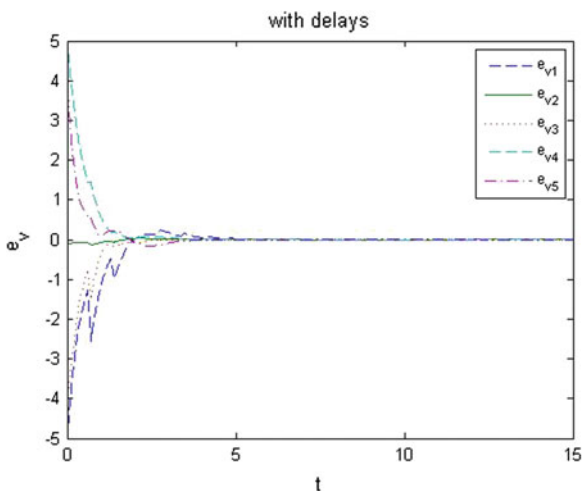


Fig. 5.2 Velocity errors



Let $c = -2$, $d_{i1}^k = d_{i2}^k = 1$, $p = q = 2$, $\varepsilon_1 = \varepsilon_2 = \frac{1}{2}$, $t_k - t_{k-1} = \ln(2)$, $\beta = 2$, $\tau(t) = 0.2 \times |\sin(t)|$, then we can get $\lambda_N = 1$, $\mu_k = 4$, $d = 4$, $\tilde{\omega} = 3$, $\eta = -2$, and $\ln \mu_k - \beta(t_k - t_{k-1}) \leq 0$, $\omega + d\eta + \beta < 0$. Then all conditions in Theorem 1 can be satisfied. The trajectories of position errors and velocity errors are shown in Figs. 5.1, 5.2, respectively.

5.5 Conclusions

This paper investigates the consensus problem of the multi-agent system with impulsive effects and time-varying delays. We give the criteria to make the origin of error system achieve globally exponentially stable. That is, the leader system and the follower systems achieve consensus. The examples are formulated to illustrate the theoretical analysis.

Acknowledgments This research is funded by the National Nature Science Foundation of China (No. 71073071;71273119), Key Program of Social Science Foundation of Jiangsu Provincial Department of Education (No. 2010-2-10) and the Priority Academic Program Development of Jiangsu Higher Education Institutions.

References

1. Peng K, Yang YP (2009) Leader-following consensus problem with a varying-velocity leader and time-varying delays. *Phys A* 388:193–208
2. Zhu W, Cheng DZ (2010) Leader-following consensus of second-order agents with multiple time-varying delays. *Automatica* 46:1994–1999
3. Song Q, Cao JD, Yu WW (2010) Second-order leader-following consensus of nonlinear multi-agent systems via pinning control. *Syst Control Lett* 59:553–562
4. Sun M, Chen Y, Cao L, Wang XF (2012) Adaptive third-order leader-following consensus of nonlinear multi-agent systems with perturbations. *Chin Phys Lett* 29(2):020503
5. Yang YQ, Cao JD (2007) Exponential lag synchronization of a class of chaotic delayed neural networks with impulsive effects. *Phys A* 386:492–502
6. Yang YQ, Cao JD (2010) Exponential synchronization of the complex dynamical networks with a coupling delay and impulsive effects. *Nonlinear Anal Real World Appl* 11:1650–1659
7. Zhou J, Xiang L, Liu ZR (2007) Synchronization in complex delayed dynamical networks with impulsive effects. *Phys A* 384:684–692
8. Lu XQ, Austin F, Chen SH (2011) Flocking in multi-agent systems with active virtual leader and time-varying delays coupling. *Commun Nonlinear Sci Numer Simulat* 16:1014–1026
9. Zhu W, Cheng DZ (2010) Leader-following consensus of second-order agents with multiple time-varying delays. *Automatica* 6:1994–1999
10. Qin JH, Gao HJ, Zheng WX (2011) Second-order consensus for multi-agent systems with switching topology and communication delay. *Syst Control Lett* 60:390–397
11. Pan LJ, Cao JD (2011) Anti-periodic solution for delayed cellular neural networks with impulsive effects. *Nonlinear Anal Real World Appl* 12(6):3014–3027

Chapter 6

One Method of Judging Spatial Topological Relations in N-Dimensional Space and Its Application in Interpolation

Binhui Chen, Bofeng Wu and Jiayang Lin

Abstract Recently, the methods of judging spatial topological relations mainly concentrate in the fields of plane and three-dimensional space. To overcome this shortage, a method of judging topological relationships between a point and a polyhedron was proposed by studying the definite proportion and division point formula of line segments. The method improves the performance of spatial interpolation progress by its application.

Keywords Definite proportion and division point formula · GIS · Spatial interpolation · Topological relation · Data mining

6.1 Introduction

Judgment of spatial topological relations is an important factor in GIS. The conventional method of judging is: Firstly, find the intersection of two objects (including the internal part, external part and border), then determine the spatial topological relation by the intersection. This method need comparing the positional relationship of various elements repeatedly which is too computationally. Recently, research of topological relations in plane and three-dimensional space is mature, while the research in higher dimensional space is not satisfactory [1, 2]. As the development of GIS and data mining the research on spatial data mining and application become a hot spot, and the interpolation in spatial data is an important field. For various reasons the data we got would be irregular which make the data processing and mining work be harder. Therefore, interpolation is valuable. The

B. Chen (✉) · B. Wu · J. Lin
Department of Computer Teaching and Research, Zhicheng College of Fuzhou University,
No.523 Gongye Road, Fuzhou, Fujian, China
e-mail: cbh@fzu.edu.cn

aims of interpolation including: estimating the missing data, gridding data, interpolating contour for data and predicting data of new area [3, 4].

The positional relationship of interpolation points and interpolation region would affect the performance of interpolation algorithm. Take the interpolation in plane as a example, it is assumed that a finite number N of triplets (x_i, y_i, z_i) are given, where x_i and y_i are the coordinates of the point D_i , and z_i is the corresponding data value. Data point locations may not be coincident. An interpolation function $z = f(x, y)$ to assign a value to any location $P(x, y)$ in the plane is sought. Data interpolation is based on such a assumption: the interpolation points would be similar to the nearby points more than the distant points. There are many algorithms based on this assumption, such as the nearest interpolation method, Thiessen polygon method and Kriging interpolation. In accordance with the accuracy, the methods can be divided into cubic polynomial, quartic polynomial and quintic polynomial interpolation methods [4, 5]. By the above assumption, the contribution of the sampling points on the interpolation point will be different due to the different topological relationship of interpolation point and sampling area. The contribution will be positive when the interpolation point in the sampling area internal. The contribution will be negative when the interpolation point in the sampling area external. In practical applications the negative contribution is meaningless and harmful which should be avoided. Thus, a fast and efficient method of judging the spatial topological relations of point and interpolation area would improve the performance of interpolation greatly.

By study the definite proportion and division point formula of line segments and generalize the formula to N -dimensional space, a method of judging topological relationships between a point and a polyhedron was proposed. The method is applied on a real geographic information dataset, and the result shows the effectiveness of it.

6.2 Method of Judging Spatial Topological Relations in N-Dimensional Space

6.2.1 The Definite Proportion and Division Point Formula of Line Segments

Let A and B be two points in a line, and third point C . Define $\lambda = \frac{\overrightarrow{AC}}{\overrightarrow{CB}}$, where λ is called the definite proportion and division value of C in line AB . The formula (6.1) can be deduced easily.

$$x_C = \frac{x_A + \lambda \cdot x_B}{1 + \lambda} = \frac{x_A + \frac{\overrightarrow{AC}}{\overrightarrow{CB}} \cdot x_B}{1 + \frac{\overrightarrow{AC}}{\overrightarrow{CB}}} = \frac{\overrightarrow{CB}}{\overrightarrow{AB}} \cdot x_A + \frac{\overrightarrow{AC}}{\overrightarrow{AB}} \cdot x_B \quad (6.1)$$

In elementary geometry, the positional relationship between point and line segment can be determined by λ . (1) While $\lambda \geq 0$, C located in line segment AB (includes the beginning point A , and does not include the end point B). (2) While $\lambda < -1$, C located in the extension cord of line segment AB . (3) While $-1 < \lambda < 0$, C located in the reverse extension cord of line segment AB . (4) If C located in B which is the end point of line segment AB , λ can not be defined. It is assumed two random points A and B , define $d(A, B) = \begin{vmatrix} x_A & x_B \\ 1 & 1 \end{vmatrix}$. The formula (6.1) can be deduced into formula (6.2).

$$x_C = \frac{d(C, B)}{d(A, B)} \cdot x_A + \frac{d(A, C)}{d(A, B)} \cdot x_B \quad (6.2)$$

When point C located in point B λ can not be defined, however formula (6.2) still makes sense.

Recent methods of studying the topological relation by vector product and definite proportion and division formula focus on one-dimensional and two-dimensional field. The work on three-dimensional and higher dimensional field, about the spatial positional relation between a point and a polyhedron specially, is still inadequate [1, 2].

6.2.2 The Definite Proportion and Division Point Formula of Plane

Let A, B, C be three points which are not in one straight line on the plane XOY . Define fourth point $D(x, y)$, the follow conclusion can be drawn.

Conclusion 1: It is assumed that $A(x_1, y_1), B(x_2, y_2), C(x_3, y_3)$ are the coordinate of three ordered points. Define $S(A, B, C) = \begin{vmatrix} x_1 & x_2 & x_3 \\ y_1 & y_2 & y_3 \\ 1 & 1 & 1 \end{vmatrix}$, the area of the triangle ABC is given by $|S(A, B, C)|/2$. Now define:

$$S(A, B, C) = S(D, B, C) + S(A, D, C) + S(A, B, D) \quad (6.3)$$

$$z = \frac{S(D, B, C)}{S(A, B, C)} \cdot A + \frac{S(A, D, C)}{S(A, B, C)} \cdot B + \frac{S(A, B, D)}{S(A, B, C)} \cdot C \quad (6.4)$$

The formula (6.3) and (6.4) can be proved. The prove process is as follow:

Let $F(z) = S(z, B, C) + S(A, z, C) + S(A, B, z) - S(A, B, C)$, $G(z) = S(z, B, C) \cdot A + S(A, z, C) \cdot B + S(A, B, z) \cdot C - S(A, B, C) \cdot z$. Proving formula (6.3) and (6.4) can be converted to proving $F(z) \equiv 0, G(z) \equiv 0$. Firstly, solving the x component of $G(z)$:

$$\begin{aligned}
 G(z)_x &= S(z, B, C) \cdot A_x + S(A, z, C) \cdot B_x + S(A, B, z) \cdot C_x - S(A, B, C) \cdot z_x \\
 &= \begin{vmatrix} x & x_2 & x_3 \\ y & y_2 & y_3 \\ 1 & 1 & 1 \end{vmatrix} \cdot x_1 + \begin{vmatrix} x_1 & x & x_3 \\ y_1 & y & y_3 \\ 1 & 1 & 1 \end{vmatrix} \cdot x_2 + \begin{vmatrix} x_1 & x_2 & x \\ y_1 & y_2 & y \\ 1 & 1 & 1 \end{vmatrix} \cdot x_3 - \begin{vmatrix} x_1 & x_2 & x_3 \\ y_1 & y_2 & y_3 \\ 1 & 1 & 1 \end{vmatrix} \cdot x \\
 &= \begin{vmatrix} x_2 & x_3 & x \\ y_2 & y_3 & y \\ 1 & 1 & 1 \end{vmatrix} \cdot x_1 - \begin{vmatrix} x_1 & x_3 & x \\ y_1 & y_3 & y \\ 1 & 1 & 1 \end{vmatrix} \cdot x_2 + \begin{vmatrix} x_1 & x_2 & x \\ y_1 & y_2 & y \\ 1 & 1 & 1 \end{vmatrix} \cdot x_3 - \begin{vmatrix} x_1 & x_2 & x_3 \\ y_1 & y_2 & y_3 \\ 1 & 1 & 1 \end{vmatrix} \cdot x \\
 &= \begin{vmatrix} x_1 & x_2 & x_3 & x \\ x_1 & x_2 & x_3 & x \\ y_1 & y_2 & y_3 & y \\ 1 & 1 & 1 & 1 \end{vmatrix} = 0 \text{ (the first line is same to the second line.)} \\
 \text{Similarly, } G(z)_y &= \begin{vmatrix} y_1 & y_2 & y_3 & y \\ x_1 & x_2 & x_3 & x \\ y_1 & y_2 & y_3 & y \\ 1 & 1 & 1 & 1 \end{vmatrix} = 0, F(z) = \begin{vmatrix} 1 & 1 & 1 & 1 \\ x_1 & x_2 & x_3 & x \\ y_1 & y_2 & y_3 & y \\ 1 & 1 & 1 & 1 \end{vmatrix} = 0.
 \end{aligned}$$

Thus, for random point z on plane XOY , $F(z) \equiv 0, G(z) \equiv 0$. Formula (6.3) and (6.4) are proved. The formula (6.4) is called the definite proportion and division point formula of plane.

6.2.3 The Definite Proportion and Division Point Formula of Three-Dimensional and Higher-Dimensional Space

6.2.3.1 The Definite Proportion and Division Point Formula of Three-Dimensional Space

Let A, B, C, D be four points which are not in one plane on the space $OXYZ$. Define fifth point $P(x, y)$, the follow conclusion can be drawn.

Conclusion 2: It is assumed that $A(x_1, y_1, z_1), B(x_2, y_2, z_2), C(x_3, y_3, z_3), D(x_4, y_4, z_4)$ are four non-coplanar points. Define

$$V(A, B, C, D) = \begin{vmatrix} x_1 & x_2 & x_3 & x_4 \\ y_1 & y_2 & y_3 & y_4 \\ z_1 & z_2 & z_3 & z_4 \\ 1 & 1 & 1 & 1 \end{vmatrix}, \text{ the volume of the tetrahedron } ABCD \text{ is given}$$

by $|V(A, B, C, D)|/6$. The follow formula (6.5) and formula (6.6) can be proved.

$$V(A, B, C, D) = V(P, B, C, D) + V(A, P, C, D) + V(A, B, P, D) + V(A, B, C, P) \tag{6.5}$$

$$P = \frac{V(P, B, C, D)}{V(A, B, C, D)} \cdot A + \frac{V(A, P, C, D)}{V(A, B, C, D)} \cdot B + \frac{V(A, B, P, D)}{V(A, B, C, D)} \cdot C + \frac{V(A, B, C, P)}{V(A, B, C, D)} \cdot D \tag{6.6}$$

The proof of formula (6.5) and (6.6) is same to the proof of formula (6.3) and (6.4). The formula (6.6) is called the definite proportion and division point formula of three-dimensional space, whose form is same to formula (6.4).

6.2.3.2 The Definite Proportion and Division Point Formula of High-Dimensional Space

Let $z_1, z_2, z_3, \dots, z_{n+1}$ be $n + 1$ points which are on the N -dimensional space Ω_n , where $z_i = (x_{i1}, x_{i2}, \dots, x_{in})^T \quad i = 1, 2, \dots, n + 1$. Define $V_n(z_1, z_2, z_3, \dots, z_{n+1}) = \begin{vmatrix} z_1 & z_2 & z_3 & \dots & z_{n+1} \\ 1 & 1 & 1 & 1 & 1 \end{vmatrix}$, the follow conclusion 3 can be drawn by the proof aforementioned.

Conclusion 3: It is assumed that $z_1, z_2, z_3, \dots, z_{n+1}$ are $n + 1$ points on the N -dimensional space Ω_n , and corresponding vectors $\overrightarrow{z_1 z_2}, \overrightarrow{z_1 z_3}, \dots, \overrightarrow{z_1 z_{n+1}}$ are nonlinear. Then the $n + 1$ points can define the N -dimensional space Ω_n , which are called the base of Ω_n . Given a random point z on Ω_n , formula (6.7) and formula (6.8) can be proved.

$$V(z_1, z_2, z_3, \dots, z_{n+1}) = V_n(z, z_2, z_3, \dots, z_{n+1}) + V_n(z_1, z, z_3, \dots, z_{n+1}) + V_n(z_1, z_2, z, \dots, z_{n+1}) + \dots + V_n(z_1, z_2, z_3, \dots, z_n, z) \tag{6.7}$$

$$z = \frac{V_n(z, z_2, z_3, \dots, z_{n+1})}{V_n(z_1, z_2, z_3, \dots, z_{n+1})} \cdot z_1 + \frac{V_n(z_1, z, z_3, \dots, z_{n+1})}{V_n(z_1, z_2, z_3, \dots, z_{n+1})} \cdot z_2 + \dots + \frac{V_n(z_1, z_2, z_3, \dots, z)}{V_n(z_1, z_2, z_3, \dots, z_{n+1})} \cdot z_{n+1} \tag{6.8}$$

The formula (6.8) is called the definite proportion and division point formula of N -dimensional space.

6.3 Judgment and Interpolation of Topological Relationships Between A Point and A Polyhedron

The ordinary topology and Geographic Information Science have defined the concepts of objects, internal, border and external, which formed a method of describing spatial topological relationship [6, 7]. Most recent research focus on the spatial topological relationship of a point with plane, 2.5-dimensional and 3-dimensional object, and the research about spatial topological relationship in high-dimensional space is still less [2, 8].

Let $f(z)$ be a attribute of point z which is in the n -dimensional space, and the value of definite proportion and division be the contribution to point z given by base point. The value of $f(z)$ can be thus given by contribution $f(z_i)$ of related base points, calculated with formula (6.8) as follow:

$$f(z) = \sum_{i=0}^n c_i \cdot f(z_i), \quad \text{s.t.} \quad c_i = \frac{V_n(z_1, \dots, z_{i-1}, z, z_{i+1}, \dots, z_{n+1})}{V_n(z_1, z_2, z_3, \dots, z_{n+1})}, \quad i = 1, 2, \dots, n \quad (6.9)$$

In one sense, this interpolation is quasi-point interpolation which is continuous, smooth and uniform. Therefore, in some certain applications, the definite proportion and division formula of N -dimensional space can be used in interpolation while the function $f(x)$ is hard to calculate and only the base points are given. It can be given by formula (6.7):

$$\begin{aligned} |V(z_1, z_2, z_3, \dots, z_{n+1})| &= |V_n(z, z_2, z_3, \dots, z_{n+1}) + V_n(z_1, z, z_3, \dots, z_{n+1}) \\ &\quad + V_n(z_1, z_2, z, \dots, z_{n+1}) + \dots + V_n(z_1, z_2, z_3, \dots, z_n, z)| \\ &\leq |V_n(z, z_2, z_3, \dots, z_{n+1})| + |V_n(z_1, z, z_3, \dots, z_{n+1})| \\ &\quad + |V_n(z_1, z_2, z, \dots, z_{n+1})| + \dots + |V_n(z_1, z_2, z_3, \dots, z_n, z)| \end{aligned} \quad (6.10)$$

It can be derived that the necessary and sufficient condition of above formula be equal is point z is not external of polyhedron $z_1, z_2, z_3, \dots, z_{n+1}$. Thus a method of judging spatial topological relations between a point and a polyhedron is found. For example, while judging the topological relation between a point and a triangle $z_1 z_2 z_3$ in two-dimensional space, the conclusion can be given by follow formula:

$$|S(z_1, z_2, z_3)| = |S(z, z_2, z_3)| + |S(z_1, z, z_3)| + |S(z_1, z_2, z)| \quad (6.11)$$

If formula (6.11) is not satisfied, point z is external of triangle. Otherwise, point z is internal or on the border of triangle. Similarly, while judging the topological relations between a point and tetrahedron $z_1 z_2 z_3 z_4$, determine the value of follow formula firstly:

$$\begin{aligned} |V(z_1, z_2, z_3, z_4)| &= |V(z, z_2, z_3, z_4)| + |V(z_1, z, z_3, z_4)| + |V(z_1, z_2, z, z_4)| \\ &\quad + |V(z_1, z_2, z_3, z)| \end{aligned} \quad (6.12)$$

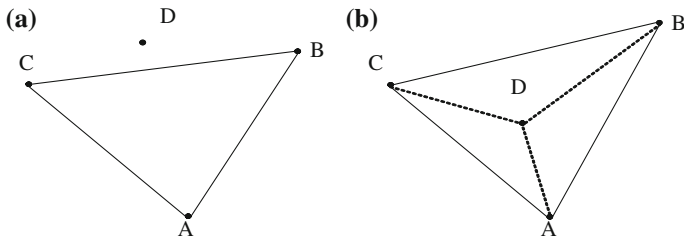


Fig. 6.1 Two kinds of typical relationship between point and triangle. **a** When the equation does not hold, point D is external. **b** When the equation holds, point D is internal

If formula (6.12) is not satisfied, point z is external of tetrahedron. Otherwise, it is internal or on the border of tetrahedron. A polyhedron in three-dimensional space can be divided into a finite number of tetrahedrons, therefore, the topological relation between a point and a polyhedron could be determined. The topological relation between a point and a polyhedron in N-dimensional space can be determined by the same way.

Two usual interpolation methods are: method based on triangle and method based on radial basis function. The method based on triangle is easy to adjust and its geometric meaning is obvious, thus is more popular [9, 10]. Triangular Irregular Network (TIN) is an important application technology in geosciences analysis, computer vision, object surface reconstruction, finite element analysis, road CAD technology and other fields. Delaunay network is a kind of special triangulation network, which can be constructed with many methods such as incremental insertion and divide and conquer insertion [11]. While interpolate a point into a triangle, judging the topological relation between a point and the triangle is an important job. The usual judging method is: firstly record the three edges of triangle in counterclockwise order, then judge whether the interpolation point is on the left side of three edges. If it is, it is internal of triangle. Otherwise, it is external of triangle [5, 12]. Obviously this method is computationally intensive. If judging with the method proposed in this paper, the topological relation can be determined by only once calculation. As Fig. 6.1 shown, while judging the relation between point D and triangle ΔABC , if $|S(A, B, C)| = |S(D, B, C)| + |S(A, D, C)| + |S(A, B, D)|$ does not hold point D is external, otherwise point D is internal (including the border).

6.4 Experiment

Soil protection is important for environmental protection, and the content of heavy metals in soils is one of the evaluation criteria to measure the extent of soil contamination which is important to research soil environment. The experiment data is from “Coastal Economic Zone In Fujian Province Ecological Geochemical

Survey Project” hold by China geological survey bureau. The data is mainly sampling from Fuzhou and Quanzhou area, and the time of sampling is around 2003 to 2004.

6.4.1 Data Preprocessing

The content of 8 kinds of heavy metal element (Cd, Hg, As, Cu, Pb, Zn, Cr, Ni) were selected from 52 kinds of chemical element for interpolation experiment. The data points are selected in Fuzhou administrative region regularly (As Fig. 6.2 shown, select one point per 2000 m).

As any three sample points could build a region, we select the nearest three points to build the interpolation area. Because geographic data’s shape often is irregular and geographical features are complex, the interpolation performance would be bad if selected unsuitable sample points. For example, if selected three points which are in the straight line, the two-dimensional interpolation would degenerate into linear interpolation. Another example, if selected the points in coastal area, the interpolation area would be ocean which is meaningless in reality. In order to solve the above problems we preprocess the data with Delaunay triangulation, the result of pretreatment is as Fig. 6.3 shown.

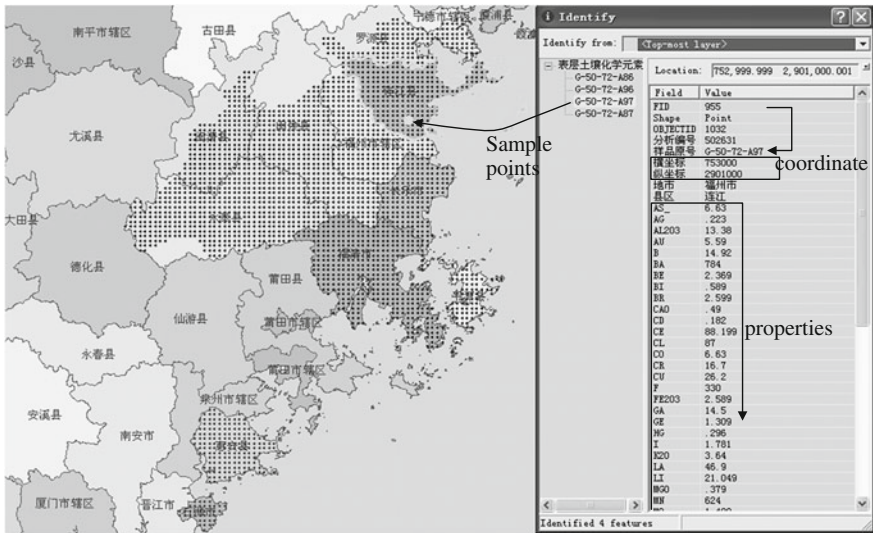


Fig. 6.2 Data sample of surface soil chemical element in Fujian coastal area

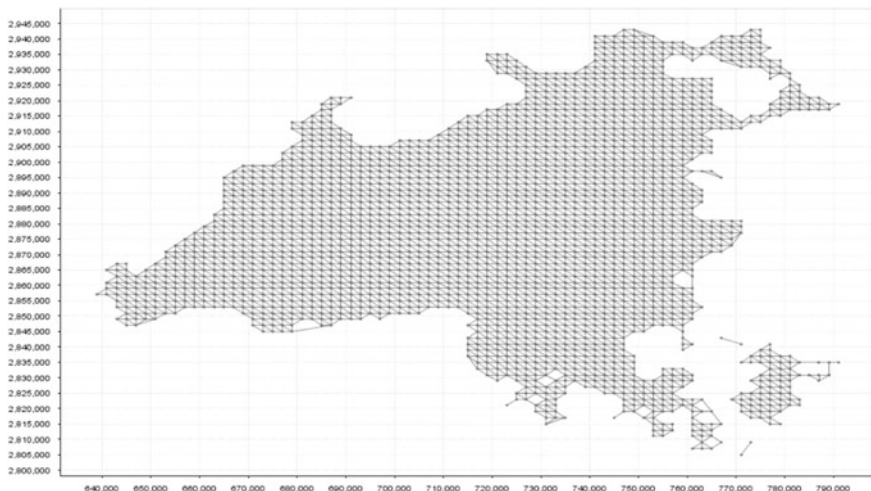


Fig. 6.3 Delaunay triangulation of soil dataset

6.4.2 Interpolation

As the sample points were set per 2000 m, setting an interpolation per 200 m in both longitude and latitude direction. Given three base points $A(x_1, y_1)$, $B(x_2, y_2)$, $C(x_3, y_3)$ which are not in one straight line in the plane, and set their related

property are $f(A)$, $f(B)$, $f(C)$. Let $S(A, B, C) = \begin{vmatrix} x_1 & x_2 & x_3 \\ y_1 & y_2 & y_3 \\ 1 & 1 & 1 \end{vmatrix}$, then in terms of

interpolation point $D(x, y)$, $\lambda_1 = \frac{S(D, B, C)}{S(A, B, C)}$, $\lambda_2 = \frac{S(A, D, C)}{S(A, B, C)}$, $\lambda_3 = \frac{S(A, B, D)}{S(A, B, C)}$ are the distance proportion of point D and base points A , B and C . Taking the distance proportion as the contribution of point A , B and C to point D , the property value of point D can be given as follow, which is the interpolation formula of this experiment.

$$\begin{aligned}
 f(D) &= \frac{S(D, B, C)}{S(A, B, C)} \cdot f(A) + \frac{S(A, D, C)}{S(A, B, C)} \cdot f(B) + \frac{S(A, B, D)}{S(A, B, C)} \cdot f(C) \\
 &= \lambda_1 \cdot f(A) + \lambda_2 \cdot f(B) + \lambda_3 \cdot f(C)
 \end{aligned}
 \tag{6.13}$$

6.4.3 Result of Experiment and Analysis

The interpolation value of 8 attributions is as Fig. 6.4 shown.

Overlapping the interpolation data and original data, and visualizing the result data with ArcMap to build “map of heavy metal element distributed” as Figs. 6.5, 6.6, 6.7, 6.8, 6.9, 6.10, 6.11 and 6.12 shown. The color of map is decided by the

	A	B	C	D	E	F	G	H	I	J
1	abscissa	ordinate	AS	CD	CR	CU	HG	NI	PB	ZN
2	651000	2859200	29.8801	0.0758	13.13	6.6599	0.0745	5.3299	32.98	50.099
3	667400	2885200	12.309	0.135	26.1298	14.9799	0.1118	11.4799	51.9693	70.0098
4	721800	2838600	7.523	0.058	27.3396	8.5198	0.0802	11.8798	32.0598	69.679
5	696600	2863800	4.2998	0.211	19.2394	10.4396	0.0938	8.1992	96.2198	87.3792
6	748200	2932000	3.2046	0.0878	24.3094	13.51	0.0844	11.05	33.8695	55.4995
7	730400	2920200	7.3853	0.0862	14.7997	6.33	0.0658	5.5896	52.8397	66.45
8	712400	2898200	3.8157	0.1864	22.3396	25	0.1058	11.3093	79.9094	96.9193
9	651000	2859800	21.6634	0.0782	12.02	5.6396	0.07	5.1196	31.72	44.099
10	667400	2885000	12.756	0.1386	26.4398	15.5	0.1106	11.76	53.8592	72.5198
11	737600	2874400	7.6903	0.3721	47.12	27.6093	0.5214	20.79	76.669	140.4597
12	753400	2861000	4.8532	0.0704	26.2592	8.5	0.1934	11.18	41.9198	72.62
13	664600	2865600	3.6788	0.0705	11.7199	5.4099	0.0671	5.5498	33.7	44.7991
14	683200	2887600	3.3317	0.0759	11.5794	7.9493	0.0551	5.7296	37.7194	52.9893
15	728800	2851800	5.2161	0.1288	25.4497	12.59	0.0748	10.2294	40.0196	70.2191
16	659000	2863200	3.227	0.0783	13.269	5.99	0.07	4.9391	33.7891	48.3
17	720200	2902200	2.3176	0.2998	11.96	11.4796	0.0952	5.8196	110.6198	158.52
18	755800	2895200	4.3165	0.1242	26.3394	16.4899	0.4487	10.9395	54.8099	84.6299
19	696800	2875000	2.3631	0.1432	17.9199	9.5399	0.0616	8.4	48.6691	67.2591
20	737800	2866400	5.5631	0.1836	33.2891	26.7799	1.8064	14.8996	66.2796	99.9193
21	658800	2871600	8.4242	0.076	16.62	8.3399	0.1181	5.7897	32.72	46.8392
22	712200	2907600	3.028	0.1286	19.4599	7.93	0.0764	8.9594	52.3697	62.5699
23	744600	2870800	3.2241	0.1066	16.96	11.3097	0.3122	6.4391	52.3999	79.8292
24	705800	2877800	3.9556	0.1116	23.32	6.559	0.0908	11.02	41.2196	84.6996
25	690400	2875000	2.993	0.1121	15.35	8.3093	0.0963	8.66	55.6697	68.9697
26	697000	2850800	5.5859	0.2073	33.4891	13.4399	0.1121	16.52	43.4391	115.4791
27	676400	2899200	2.8766	0.0958	12.6294	4.9194	0.0669	5.4894	40.8193	54.5994
28	728600	2876600	6.5972	0.2636	37.6392	27.5592	0.2076	16.4192	62.42	110.2392
29	748200	2932400	2.9906	0.0846	23.4894	13.81	0.0792	10.59	34.8893	54.8197
30	769400	2880400	5.4531	0.1221	13.3393	15.249	0.0206	5.3	32.1292	49.999

Fig. 6.4 Part of interpolation results screenshot

Fig. 6.5 Eco earth soil chemical element As

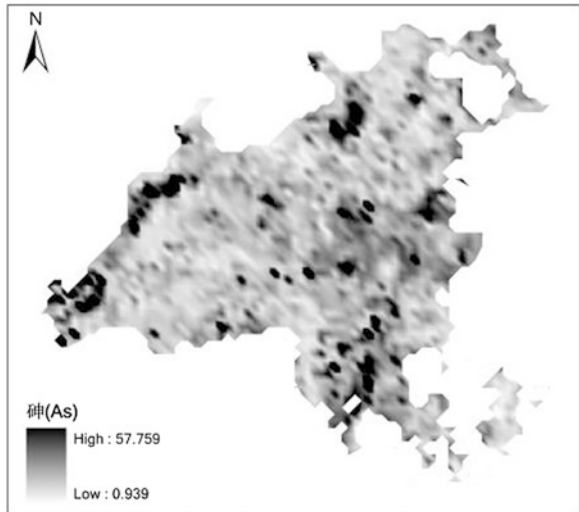


Fig. 6.6 Eco earth soil chemical element Cd

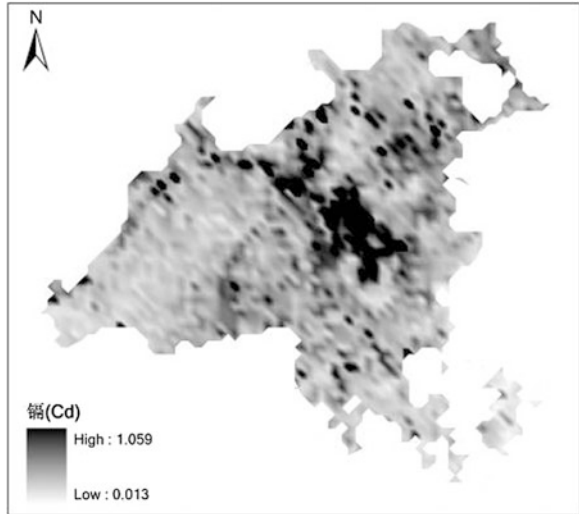
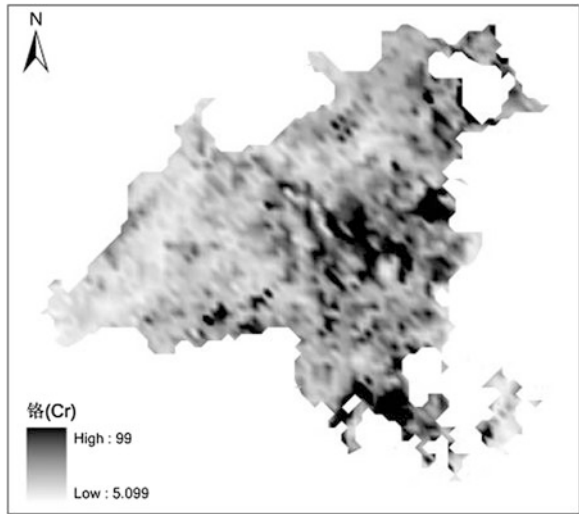


Fig. 6.7 Eco earth soil chemical element Cr



heavy metal content. If the content is higher the color would be deeper, otherwise the color would be lighter.

According to Figs. 6.5, 6.6, 6.7, 6.8, 6.9, 6.10, 6.11 and 6.12 it can be concluded that the interpolation result is accurate, distribution is reasonable and the performance of interpolation is great. By simplifying the judgment of topological relation, the time complexity and space complexity of interpolation procedure have been reduced.

Fig. 6.8 Eco earth soil
chemical element Cu

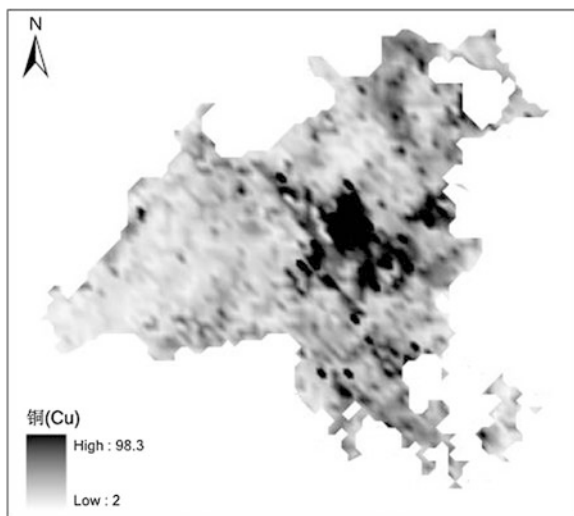


Fig. 6.9 Eco earth soil
chemical element Hg

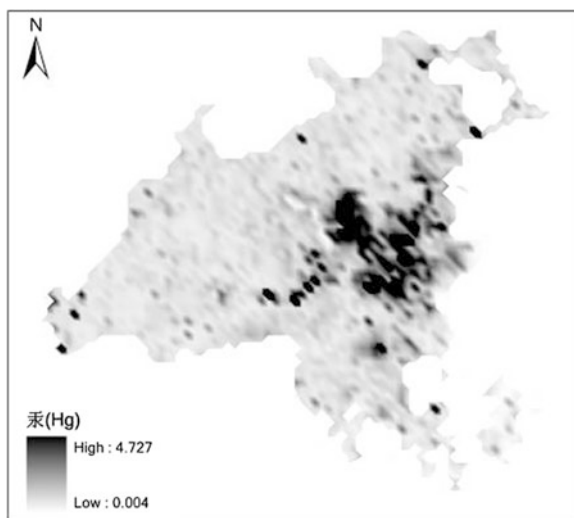


Fig. 6.10 Eco earth soil chemical element Ni

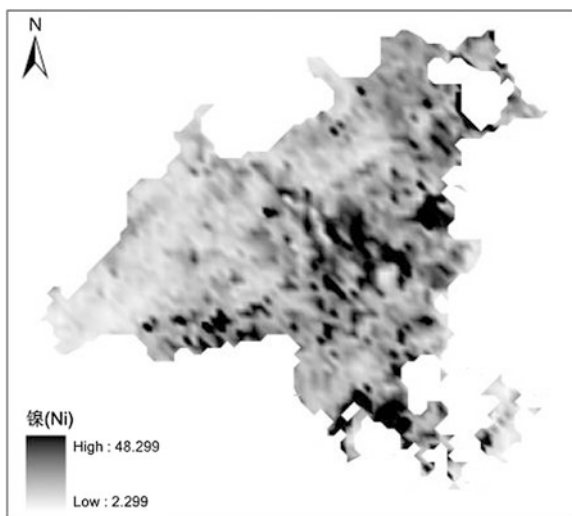


Fig. 6.11 Eco earth soil chemical element Pb

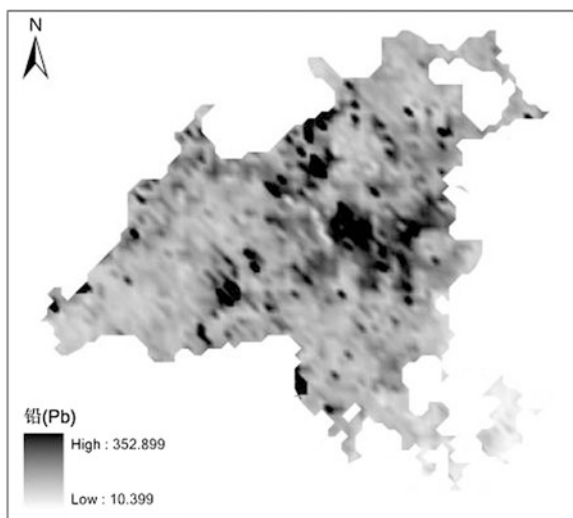
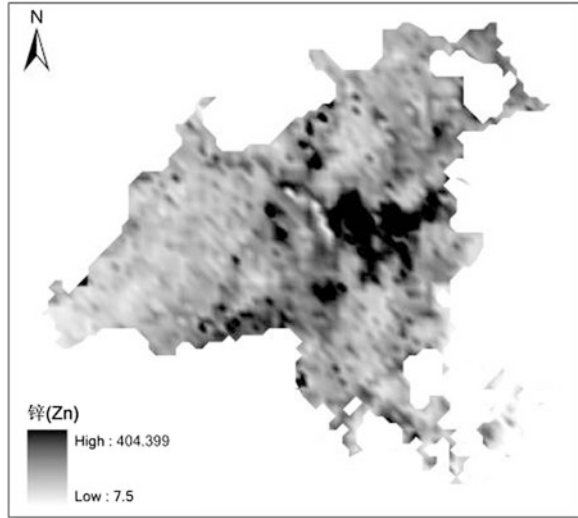


Fig. 6.12 Eco earth soil chemical element Zn



6.5 Conclusion

By studying the definite proportion and division point formula of line segments and extending it to N-dimensional space, a method of judging topological relationships between a point and a polyhedron in N-dimensional space was proposed. The method could not only be used in 1-dimensional, 2-dimensional, 2.5-dimensional and 3-dimensional space, and also could be used in the higher N-dimensional space. It provides a choice and tool for spatial data mining and its application area is wide. By every component of base points multiplying by the property value, the formula can be transformed into interpolation formula. In order to solve the problem of how to divide the polyhedron in N-dimensional space during the interpolation process, the further research is needed.

Acknowledgments The work was supported by the Department of Education of Fujian Province under grant JA11292 and JB12375. We would like to thank the anonymous reviewers for their comments and suggestions.

References

1. Li C, Chen J (1997) The nine intersection model for describing spatial relation. *J Wuhan Tech Univ Surveying Mapp* 22(03):207–211 (in Chinese)
2. Frenkel G, Blumenfeld R, King PR et al (2009) Topological analysis of foams and tetrahedral structures. *Adv Eng Mater* 11(3):169–176
3. Zhu Q, Zhang WC, Yu JH (2004) The spatial interpolations in GIS. *J Jiangxi Norm Univ* 28(2):183–188 (in Chinese)

4. Donald S (1968) A two-dimensional interpolation function for irregularly-spaced data. In: Proceedings of the 1968 23rd ACM national conference, pp 517–524
5. Xu L (2007) Infinite interpolation on triangles. *J Soft* 18(2):430–441 (in Chinese)
6. Zhang H, Wen YN, Liu AL (2007) Geographic information system algorithm. Science Press, Beijing (in Chinese)
7. Zhou R, Zhang L, Pang X et al (2001) Smooth piecewise spline surfaces over arbitrary control polyhedron. *Chin J Aeronaut* 14(1):57–64
8. Szilvasi-Nagy M (1991) Flexible rounding operation for polyhedra. *CAD Comput Aided Design* 23(9):629–633
9. Zhou XY, Zhu XX (1993) A survey of triangulation methods for scattered data points. *J Eng Graphic* 1:48–54 (in Chinese)
10. Wang JB, Pan M, Zhang XD (1999) The Kriging interpolation method for scattered data points. *J Comput-Aided Design-Comput Graph* 11(6):525–529 (in Chinese)
11. Wu XB, Wang SX, Xiao CS (1999) A new study of delaunay triangulation creation. *Acta Geodaetica Et Cartographic Sinica* 28(1):28–35 (in Chinese)
12. Wu BF, Lin JX, Wang W (2010) The research on judging topological relationships between a point and a polyhedron. *J Fuzhou Univ* 38(5):634–643 (in Chinese)

Chapter 7

Modified Ant Colony Optimization Algorithm for the Multi-Sensor Dynamic Scheduling

Hai Huang, Jing Zhang, Xiaomin Ran and Wengao Lv

Abstract Sensor is a sort of important monitoring resources and plays an irreplaceable role in the modern battlefield. Multi-sensor scheduling optimization is a problem of theoretical and practical significance. In order to monitor the multi-target with time windows effectively, this paper presents a multi-sensor dynamic scheduling model and demonstrates its reasonableness. Based on the model, we adopt a modified Ant Colony Optimization (ACO) algorithm with local optimization method to find optimal solutions, and conduct several experiments under different scenarios. The results show that more targets are monitored effectively in each solution, therefore the modified ACO algorithm has better performance than basic ACO algorithm in scheduling optimization.

Keywords Ant colony optimization (ACO) · Multi-sensor · Dynamic scheduling · Time window · Local optimization

7.1 Introduction

With the development of network and information technology, a variety of sensors is widely used on the battlefield, multi-sensor scheduling subsequently becomes an important problem. Multi-sensor scheduling try to fulfill a series of monitoring tasks using a given set of sensors. The number of sensor and target creates a huge number of combinations to be searched for producing a scheduling solution that optimizes appraisal indices such as monitoring quality and sensor utilization. In essence, it is a combinatorial optimization problem that has been proven to be a NP-hard problem. Exact optimization algorithms cannot produce an acceptable

H. Huang (✉) · J. Zhang · X. Ran · W. Lv
Zhengzhou Information Science and Technology Institute, Zhengzhou, Henan, China
e-mail: huanghai1111@sina.com

solution in the available time. It is also awkward to deal with some necessary constraints or objective function characteristics in the algebraic form required by classical optimization methods. Therefore, the algorithm cannot meet the requirements of practical application. Moreover, when the targets with feature of time window, static scheduling cannot make full use of sensor resources and a large number of missions cannot be completed.

In the field of research on sensor dynamic scheduling, Liu [1] proposed a sensor management method based on utility function. It obtains the optimal solution by establishing a linear programming objective function that relates to effective matching function and target priority. Although this method is simple and feasible, the amount of computing is too large to achieve large-scale scheduling. Xiao and Xiao [2, 3] proposed an incremental sensor selection heuristic algorithm and introduced the Monte Carlo operator to calculate the detection probability of target and schedule the sensors under the condition that the sensor must meet the effective detection probability demand. However, this method only refers to a single target tracking tasks. Considering the characteristics of multi-sensor multi-target assignment, Zhang et al. [4] presented a sensor scheduling method amid at Joint Information incremental performance. The method is combined with Genetic Algorithm. However, this method only focuses on the overall incremental information. Besides, all the methods mentioned above are not involved in the target problem of time window.

In this paper, we present a sensor dynamic scheduling model that adapted to the scheduling environments of multi-sensor and multi-target with time window. It takes global coverage of targets as the optimization objective. Then we introduce an approach to scheduling that relies on a biologically-inspired optimization algorithm known as Ant Colony Optimization (ACO). Moreover, the algorithm has been modified. The simulation results show that the improved ACO is more effective than basic ACO. The results are simply intended to be a proof that ACO can successfully deal with the challenge we describe.

7.2 Models and Problem Statement

$U = \{u_1, u_2, \dots, u_M\}$ denotes a monitoring system with M sensors. The target set $T = \{t_1, t_2, \dots, t_N\}$ is composed of N targets. A real-time task to monitor t_i is represented by the tuple (tb_i, te_i) , where tb_i is the task start time and te_i is the task end time. v_{ij} denotes the monitoring ability when t_j is monitored by u_i . d_{ij} denotes the distance between u_i and t_j . e_i denotes the probability that t_i can be detected. It is related to the size, shape and velocity of target. Therefore, the monitoring ability v_{ij} is almost linearly related to the product of e_i and $1/d_{ij}^2$: $v_{ij} \propto e_i \times 1/d_{ij}^2$. g_i denotes the threshold which is the lowest value when u_i can monitor target effectively. It is determined by the sensitivity of sensor.

In order to utilize resource fully and monitor as more targets as possible, we take global coverage of targets as the optimization objective, rather than the usual total monitoring quality. So this problem can be described as a mathematical programming model as shown below:

$$\max f(X) = \sum_{i=1}^M \sum_{j=1}^N x_{ij} / N \quad (7.1)$$

s.t.

$$\sum_{i=1}^M x_{ij} \leq 1, \quad j = 1, 2, \dots, N \quad (7.2)$$

$$x_{ij} = 1, u_i \in U, t_i \in T \Rightarrow v_{ij} \geq g_i \quad (7.3)$$

$$\forall i, j, t_i \in T, t_j \in T, u_k \in U, \text{ if } x_{ki} = x_{kj} = 1 \Rightarrow tb_i \geq te_j \text{ or } tb_j \geq te_i \quad (7.4)$$

Where $X = (x_{ij})_{M \times N}$ is the decision matrix and the x_{ij} is as follows:

$$x_{ij} = \begin{cases} 1, & \text{if sensor } i \text{ is to target } j \\ 0, & \text{otherwise} \end{cases} \quad (7.5)$$

As stated in constraint given in Eq. 7.2, the target cannot be monitored by multiple sensors. It means that some targets can be abandoned for the global optimization. Eq. 7.3 explains the requirement of the effective monitoring: the monitoring quality v_{ij} must be greater than or equal to the ability threshold of u_i when t_j is assigned to u_i . Meanwhile, Eq. 7.4 means that one sensor can monitor only one target simultaneously, but can monitor other target at non-intersecting time window. The two constraints cannot only avoid invalid monitoring, but also increase resource utilization.

According to the analysis above, the dynamic scheduling problem is abstracted to a combination problem with optimization objectives and complex constraints. Based on the model, we will adopt the method combined with Ant Colony Optimization (ACO) algorithm and local optimization to solve the problem effectively. The details are as follows.

7.3 The Solving Method for Multi-Sensor Dynamic Scheduling

7.3.1 ACO Background

The Ant Colony Optimization was inspired by the behavior of ants. Ants communicate among themselves through pheromone, a substance they deposit on the ground in variable amounts as they move about. It has been observed that the more ants use a particular path, the more pheromone is deposited on that path and the

more it becomes attractive to other ants seeking food. The pheromone on the shorter path will therefore be more strongly reinforced and will eventually become the preferred route for the other ants. The works of Colomi et al. [5] offer detailed information on the workings of the algorithm and the choice of the various parameters. Moreover, the ACO algorithm has been applied to many classical problem such as TSP [6], VRP [7], JSP [8] and so on.

7.3.2 Modified ACO Algorithm for the Problem

We use a digraph based on the ACO algorithm [9, 10] to treat the complex problem that we have described. As shown in Fig. 7.1, each node except starting node represents a target and each path in front of node represents a sensor. Each ant establishes a complete tour in a digraph (a feasible solution) by repeatedly choosing path to next node in probability. The probability is a combination of heuristic and pheromone information. To ensure the production of a feasible solution, paths that ant cannot go through because of constraints on the current tour are excluded from the choice by using a tabu list. After a tour, ant leaves the pheromone on the path. The pheromone trails reinforce successful paths discovered by the ants so that those paths are more likely to be followed in future tours. The algorithm will end and output the best result when it gets max iteration. We will explain the key steps as follow.

7.3.3 Trail Selection Probability

Ant $k = (1, 2, \dots, N_{ants})$ selects moving path according to probability in the process of solution construction. $p_{ij}^k(t)$ is the probability that an ant will assign task j to sensor i ant at time t :

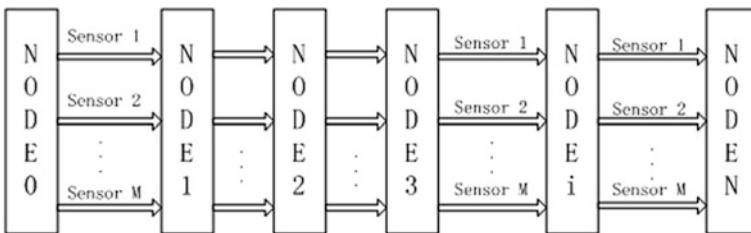


Fig. 7.1 Digraph based on the ACO algorithm

$$p_{ij}^k(t) = \begin{cases} \frac{\tau_{ij}^k(t)^\alpha (\eta_{ij})^\beta}{\sum_{i \notin \text{tabu}_j^k(t)} \tau_{ij}^k(t)^\alpha (\eta_{ij})^\beta}, & i \notin \text{tabu}_j^k(t) \\ 0, & i \in \text{tabu}_j^k(t) \end{cases} \quad (7.6)$$

For the selection of a path, the ant uses heuristic information as well as pheromone information. The heuristic information, denoted by η_{ij} and the pheromone information, denoted by $\tau_{ij}^k(t)$. Initial pheromone in each path is τ_0 , where α , β denote the parameters correlating to the importance of the pheromone and heuristic, respectively. $\text{tabu}_j^k(t)$ is the tabu list of ant k that represents the sensors can not assigned to target j . η_{ij} is shown by Eq. 7.7:

$$\eta_{ij} = \begin{cases} v_{ij}/g_i, & v_{ij} \geq g_i \\ 0, & v_{ij} < g_i \end{cases} \quad (7.7)$$

7.3.4 Pheromone Update

7.3.4.1 Local Update Rule

The pheromones $\tau_{ij}^k(t)$ are updated by the local updating rule after an ant has one solution. The modified ACO adopts the following local updating rule to prevent succeeding ants from searching in the neighborhood of the current schedule of the current ant. The pheromone levels are modified as follows:

$$\tau_{ij}^{k+1}(t) = (1 - \rho)\tau_{ij}^k(t) + \rho\Delta\tau, \text{ if } (i, j) \in \pi_k \quad (7.8)$$

Where $\Delta\tau$ represents local pheromone increment and is constant. ρ is the local evaporation rate of pheromone trails. π_k is the solution of ant k .

7.3.4.2 Global Update Rule

After all ants have built all feasible schedules, the global update rule, Eq. (7.10) is used to increase the pheromone $\tau_{ij}^k(t)$ by applying the best solution in this iteration. For all $\tau_{ij}^k(t)$, the pheromone is increased by the global update and evaporated by global pheromone evaporation rate, as shown in Eq. (7.10).

$$\tau_{ij}(t+1) = (1 - \lambda)\tau_{ij}^{N_{ants}}(t) + \Delta\tau_{ij}^*(t), \lambda \in (0, 1) \quad (7.9)$$

$$\Delta\tau_{ij}^*(t) = \begin{cases} Q \times BestValue, & \text{if } (i,j) \in \pi^*(t) \\ 0, & \text{else} \end{cases} \quad (7.10)$$

Where λ is the global evaporation rate of pheromone trails. $\Delta\tau_{ij}^*(t)$ is the pheromone of best solution in the t th iteration. Q represents local pheromone increment and is constant. N_{ants} is the max number. $BestValue$ is the best solution in t th iteration when the algorithm runs.

This is an elitist strategy that leads ants to search near the best-found solution. Using the best ant for updating makes the search much more aggressive. Best combinations which often occur in good solutions will get a lot of reinforcement. Therefore, the algorithm has some extra features to balance exploration versus exploitation. So we must make choice between using the iteration-best ant and the global-best. Using global-best results in strong exploitation will lead to quick convergence of algorithm, so we will alternate it with the use of iteration-best.

7.3.5 Local Optimization Strategy

It is known that the performance of ACO algorithms can sometimes be greatly improved when coupled to local search algorithms [11]. What normally happens is that a population of solutions is created using ACO, and then these solutions are improved via local search. The improved solutions are then used to update the pheromone trail, so it is in fact a form of Lamarckian search.

In the our version of the ACO algorithm, the best solution is improved through local optimisation phase. In this phase, one of the targets that have been monitored frees its sensor. Then, for every remaining targets that no sensor monitors it, it is investigated whether the sensors can be allocated to it. If it is possible, the algorithm assigns one of the feasible sensors to this targets randomly. The algorithm successively tries to make more other vacant targets get sonor. So, a complete new solution is created. If the result of new solution is better than the best solution before, the complete local search procedure is then repeated with this new solution and updates the pheromone trail globally. This procedure is iterated until no improvement in fitness is detected between the solutions before and after the local search is applied. Hence, the local search is in fact a hill-climbing algorithm which takes the original solution created by the ACO procedure to the nearest local optimum.

7.4 Experimental Simulations

To verify the validity of our proposed methods, we conduct two experiments. After many simulations, we get optimal parameters and set it in the experiments: $\rho = 0.9$, $\alpha = 2$, $\beta = 1$, $\tau_0 = 1$, $\lambda = 0.85$, $Q = 10$, $\Delta\tau = 1.5$, $N_{ants} = 20$, $NC_{max} = 100$.

Table 7.1 The targets' time information of experiment 1

Target	1	2	3	4	5	6	7	8	9	10	11	12
StartTime	41	184	182	135	89	115	122	183	154	173	52	114
EndTime	55	196	198	146	100	127	132	195	169	188	67	124

Experiment 1: We test the improved ACO algorithm with data of small scale. Suppose there are 5 sensors and 12 targets in this numerical example. Table 7.1 shows the time information of the targets. Table 7.2 shows the capacity that every sensor monitors the targets. Table 7.3 shows the scheduling scheme result of modified ACO. The result shows that the algorithm is effective to solve this problem. The scheduling scheme is reasonable and makes full use of multi-sensor. Almost all targets can be monitored effectively and timely.

Experiment 2: The modified ACO algorithm is tested on the different size problem and compared with basic ACO algorithm. We generate four groups of data randomly to test the algorithm we introduce. The capacity v_{ij} is a integer value set to a uniform random number in $[0, 25]$. g_i is a integer value set to a uniform random number in $[15, 20]$. Scheduling time is between 0 and 200. The period of task $te_i - tb_i$ is set to a uniform random number in $[10, 30]$.

Table 7.4 shows the simulation results of modified ACO and basic ACO. Each case was simulated 100 times; each simulation as set to run for 100 iterations. Simulation results indicate that the modified ACO can find optimal solution for the problems of different size. Moreover, when the problem size is small, modified algorithm runs faster to find optimal solution. In the problem of large size, modified ACO can reach better value than basic ACO though needs a little more iterations. Actually, we can accept time consumption the modified ACO makes.

Figure 7.2 shows the global-best value of modified ACO and basic ACO for cases of 35 sensors and 150 targets in best simulation result. It illustrates that basic ACO is trapped in local optimum. However, modified ACO avoid immature convergence and the global search ability of the algorithm is strengthened to escape from local optimum and approach the global optimum.

Table 7.2 The monitoring quality matrix of experiment 1

Target sensor	1	2	3	4	5	6	7	8	9	10	11	12
1	7	5	2	11	8	0	2	4	6	10	3	24
2	17	12	5	13	15	23	20	17	20	21	10	22
3	10	7	8	19	21	6	7	3	3	3	24	18
4	20	13	24	25	24	14	11	13	17	17	19	15
5	8	25	5	18	6	14	18	14	17	20	21	23

Table 7.3 Scheduling result of experiment 1

Target	1	2	3	4	5	6	7	8	9	10	11	12
Sensor	4	5	4	4	3	4	2	-	2	2	4	1

Table 7.4 Comparison of modified ACO with basic ACO in different problem size

Problem size	Modified ACO			Basic ACO		
	Best-value (%)	Best-iteration	Avg-value (%)	Best-value (%)	Best-Iteration	Avg-value (%)
M = 15, N = 50	94	17	90.6	94	19	90.3
M = 15, N = 100	78	26	72.4	72	29	69.2
M = 20, N = 100	84	39	81.1	77	36	75.8
M = 35, N = 150	92.67	50	87.3	90	47	81.7

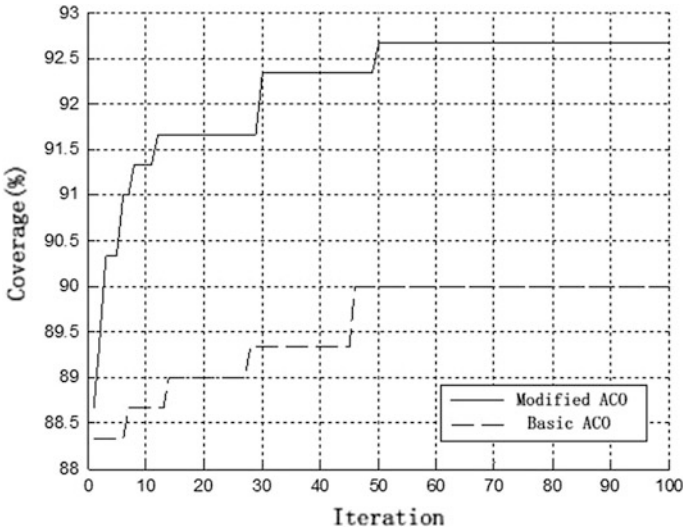


Fig. 7.2 Global-best value for cases of 35 sensors and 150 targets

7.5 Conclusion and Future Work

In this paper, we propose a sensor dynamic scheduling model considering time windows of targets. The global coverage of targets and several constraints are introduced to the model. We also present a hybrid ACO algorithm combined with local optimization method to solve the problem. Preliminary test shows that this approach is appropriate for multi-sensor dynamic scheduling and has better performance than basic ACO algorithm. Experimental results regarding the reduction of energy consumption will be presented in a future paper. We also plan to investigate the impact of heuristic on the performance of our ACO algorithm.

References

1. Liu X (2000) Study on algorithm of sensor management based on functions of efficiency and waste. *Chin J Aeronaut* 13(1):39–44 (in Chinese)
2. Xiao W, Wu J, Xie L et al (2006) Sensor scheduling for target tracking in networks of active sensors. *ACTA Automatica Sinica* 32(6):922–928
3. Xiao W et al (2006) Multi-sensor scheduling for reliable target tracking in wireless sensor networks. In: *International conference on its telecommunications proceedings*, pp 996–1000
4. Zhang G, Wang F, Wei Z (2008) Sensor management algorithm based on genetic algorithm. *Mod Defence Technol* 36(6):91–95
5. Colomi A, Dorigo M, Maniezzo V (1991) Distributed optimization by ant colonies. *Proceedings of the first European conference on artificial life*, Paris, France, pp 134–142
6. You X et al (2009) On multi-behavior based multi-colony ant algorithm for TSP. *Intell Inf Technol Appl*, pp 178–189
7. Huai-long, Hua D (2010) Vehicle routing problem of logistics based on dynamic ant colony algorithm. *Educ Technol Comput Sci (ETCS)* 256–262
8. Cao Y, Song X (2009) A hybrid algorithm of converse ant colony optimization for solving JSP. *Comput Intel Soft Eng* 234–240
9. Haibin D (2005) *The theory and application of ant colony algorithm*. Science Press, Beijing, pp 745–752 (in Chinese)
10. Zong-yong L, Xia P, Zhixue W, Ying L (2007) Scheduling interrelated tasks in grid based on ant algorithm. *J Syst Simul* 6:3196–3199 (in Chinese)
11. Dorigo M, Stützle T (2001) The ant colony optimization metaheuristic: algorithms, applications, and advances. *Handbook of metaheuristics*. In: Glover F, Kochenberger G (eds) pp 733–742

Chapter 8

Experimental Study on Improved Differential Evolution for System Identification of Hammerstein Model and Wiener Model

Weili Xiong, Minfang Chen, Le Yao and Baoguo Xu

Abstract For nonlinear system of the Hammerstein model and Wiener model, a method for nonlinear system identification is proposed based on differential evolution Algorithm (DE). The based idea of the method is that the problem of nonlinear system identification is changed into optimization problems in parameter space. In order to enhance the performance of the DE identification, put forward a kind of adaptive mutation differential evolution algorithm for scaling factor (MDE), and on this basis, we make an improvement on crossover to make a better performance. To make an analysis for particle swarm optimization (PSO), DE and improved DE, the improvement DE has higher accurate and recognition ability, stronger convergence.

Keywords DE · Hammerstein model · Wiener model · Improvement

8.1 Introduction

For the linear system identification, theoretical studies have tended to mature, but in real life, actual system is almost nonlinear system, so the research for nonlinear system is necessary [1]. The Wiener model and Hammerstein model [2] which Narendra and Gallman proposed not only simple but also can effectively describe the nonlinear characteristics of dynamic system. Literature [3] based on PSO has a identification for Hammerstein model, although the algorithm has a good

W. Xiong (✉) · M. Chen · L. Yao · B. Xu
Key Laboratory of Advanced Process Control for Light Industry (Ministry of Education),
Automation Institute of Jiangnan University, Wuxi, Jiangsu, China
e-mail: greenpre@163.com

W. Xiong · M. Chen · L. Yao · B. Xu
Room C421 in School of Internet of Things Engineering, Lihu Campus in Jiangnan
University, Wuxi, Jiangsu Province

robustness, the running speed of the program is relatively slow; Literature [4] based on PSO has a identification for Hammerstein model, QPSO algorithm has more strong nonlinear recognition ability, the program running time is also relatively fast, however, to some extent, identification of the complexity of the operation increased.

Differential evolution (DE) algorithm was first introduced by Storn and Price for global optimization in 1995 [5], as a stochastic global optimizer, DE has appeared as a simple and very efficient optimization technique. The DE's advantages are easy to implement, require a few control parameters turning and exhibit fast convergence. The DE algorithm is a population-based algorithm using the following operators: crossover, mutation and selection. In recent years, DE is widely applied in neural network [6], parameter identification [7], function optimization [8, 9] and constraint optimization problem [10, 11] and other areas. However, it has been observed that the convergence rate of DE do not meet the expectation in cases of highly multimodal problems. Several variants of DE have been proposed to improve its performance.

8.2 Differential Evolution

In this section we will describe briefly the working of basic DE. Compared with other evolutionary algorithms (EA), DE is a simple yet powerful optimizer with fewer parameters [12]. Scale factor (F) and crossover rate (CR) are two very important control parameters of DE. Setting the parameters to inappropriate values may not only deteriorate the search efficiency, but also lead to solutions with poor quality. Differential evolution's basic steps can be described as follows [13]:

Mutation operation: The mutation operation of DE applies the vector differentials between the existing population members for determining both the degree and direction of perturbation applied to the individual subject of the mutation operation. The mutation process at each generation begins by randomly selecting three individuals $X_{r_1,G}$, $X_{r_2,G}$ and $X_{r_3,G}$, in the population set of NP elements. The i th perturbed individual, $V_{i,G+1}$, is generated based on the three chosen individuals as follows:

$$V_{i,G+1} = X_{r_3,G} + F * (X_{r_1,G} - X_{r_2,G}) \quad (8.1)$$

where, $i = 1 \cdots NP$, $r_1, r_2, r_3 \in \{1 \cdots NP\}$ are randomly selected such that $r_1 \neq r_2 \neq r_3 \neq i$, F is the control parameter such that $F \in [0, +1]$.

Crossover operation: once the mutant vector is generated, the perturbed individual, $V_{i,G+1} = (V_{1,i,G+1}, \dots, V_{n,i,G+1})$, and the current population member, $X_{i,G} = (X_{1,i,G}, \dots, X_{n,i,G})$, are then subject to the crossover operation, that finally generates the population of candidates, or "trial" vectors, $U_{i,G+1} = (u_{1,i,G+1}, \dots, u_{n,i,G+1})$, as follows:

$$u_{j,i,G+1} = \begin{cases} v_{j,i,G+1} & \text{if } rand_j \leq C_r \vee j = k \\ x_{j,i,G} & \text{otherwise} \end{cases} \quad (8.2)$$

where, $j = 1 \cdots n$, $k \in \{1 \cdots n\}$ is a random parameter's index, chosen once for each i . The crossover rate, $C_r \in [0, 1]$, is set by the user.

Selection operation: If the new individual is better than the original one then the new individual is to be an offspring in the next generation $G = t + 1$ else the new individual is discarded and the original one is retained in the next generation.

$$X_{i,G+1} = \begin{cases} U_{i,G+1} & \text{if } f(U_{i,G+1}) \leq f(X_{i,G}) \\ X_{i,G} & \text{otherwise} \end{cases} \quad (8.3)$$

where, $f()$ is the fitness function. Each individual of the temporary population is compared with its counterpart in the current population. The one with the lower projective function value will survive generation.

8.2.1 Improvement of DE

To make DE more efficient for different scenarios, efforts are needed to improve its performance and a chaotic algorithm, simulated annealing algorithm or some adaptive methods have been applied in DE.

- A. In the differential evolution algorithm, the constant of differentiation F is a scaling factor of the difference vector. It is an important parameter that controls the evolving rate of the population. One of the most useful differential evolution strategies are described in the following.

It is proposed a adaptive scaling factor formula [14]:

$$M = F_0 * 2^\lambda \quad \lambda = e^{(1 - \frac{T}{T+1-t})} \quad (8.4)$$

where F_0 is the initial scaling factor, T is the number of iterations and t is the current evolution number. Early in the algorithm, $\lambda = 1$, make the $M = 2F_0$, the improvement called MDE.

Early in the algorithm, adaptive mutation operator was $F_0 - 2F_0$, it has great value and makes the individuals diversity in the population at the initial generations to overcome the premature. With the algorithm progress, mutation operator gradually reduced, mutation rates is closed to F_0 later, preserve the excellent individuals, enhance the probability of obtaining the global optimum.

- B. As mentioned in the above subsection, CR is a very important control parameters of DE. At early stage, the diversity of population is large because the population individuals are all different from each other. Small values of CR increase the possibility of stagnation and slow down the search process. On the

other hand, if the CR value is relatively high, this will increase the population diversity and improve the convergence. Therefore, the CR must take a suitable value in order to avoid the premature convergence or slow convergence rate. Based on the analysis above, in order to balance between the diversity and the convergence rate, a dynamic nonlinear increased crossover probability method was proposed, which is called KDE, formula is as follows [15]:

$$CR = CR_{\max} + (CR_{\min} - CR_{\max}) * (1 - count/gen_max)^k \tag{8.5}$$

Which $count$ is the current generation number, gen_max is the maximum number of generations, CR_{\min} and CR_{\max} denote the maximum and minimum value of the CR , and k is a positive number. The optimal setting for these parameters are $CR_{\min} = 0.5$, $CR_{\max} = 0.55$ and $k = 4$.

In this paper, a new method is put forward. Combining the two kinds of methods include KDE and MDE, which have mentioned above, trying to combine MDE and KDE, make use of MDE can increase the global search of the optimal value of the probability and KDE has a good performance in accuracy.

8.2.2 Hammerstein Model and Wiener Model

A. Hammerstein model is a special kind of nonlinear system, the structure series composition by a no memory nonlinear gain link and a dynamic linear link, as Fig 8.1 show.

The difference equation of Hammerstein model expressed as:

$$\begin{cases} A(q^{-1})y(k) = B(q^{-1})x(k) + C(q^{-1})w(k) \\ x(k) = f(u(k)) = u(k) + r_2u^2(k) + \dots + r_pu^p(k) \\ A(q^{-1}) = 1 + a_1q^{-1} + \dots + a_nq^{-n} \\ B(q^{-1}) = b_0 + b_1q^{-1} + \dots + b_lq^{-l} \\ C(q^{-1}) = 1 + c_1q^{-1} + \dots + c_mq^{-m} \end{cases} \tag{8.6}$$

Among them $u(k)$ and $y(k)$ are identification system input and output sequence; $w(k)$ is the Gaussian white noise sequence with zero-mean and variance of σ^2 , $u(k)$ and $w(k)$ independent; $x(k)$ is unmeasured intermediate input signal, it is not only linear dynamic input but also the output of the nonlinear part. q^{-1} for lag

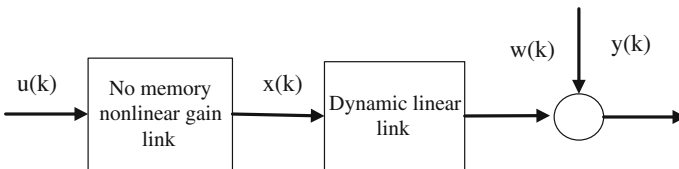


Fig. 8.1 Hammerstein model

operator, $A(q^{-1})B(q^{-1})$ and $C(q^{-1})$ are lagging operator polynomial; $f(\cdot)$ is no memory for the nonlinear gain. Introducing parameter vector for $\theta_1 = [a_1 \ a_2 \ \dots \ a_n \ b_1 \ b_2 \ \dots \ b_t \ c_1 \ c_2 \ \dots \ c_m \ r_1 \ r_2 \ \dots \ r_p]^T$, identify target is based on a given input $u(k)$ and system output $y(k)$ estimate parameter vector θ_1 , set the estimate of parameter vector θ_1 , $\hat{\theta}_1 = [\hat{a}_1 \ \hat{a}_2 \ \dots \ \hat{a}_n \ \hat{b}_1 \ \hat{b}_2 \ \dots \ \hat{b}_t \ \hat{c}_1 \ \hat{c}_2 \ \dots \ \hat{c}_m \ \hat{r}_1 \ \hat{r}_2 \ \dots \ \hat{r}_p]^T$.

B. Wiener model is a special kind of nonlinear system, the structure series composition by a no memory nonlinear gain link and a dynamic linear link, as Fig 8.2 shows.

The difference equation of Wiener model expressed as:

$$\begin{cases} A(q^{-1})z(k) = q^{-d}B(q^{-1})u(k) \\ y(k) = f[z(k)] + e(k) \\ A(q^{-1}) = 1 + a_1q^{-1} + \dots + a_nq^{-n} \\ B(q^{-1}) = b_0 + b_1q^{-1} + \dots + b_tq^{-t} \end{cases} \quad (8.7)$$

Among them $u(k)$ and $y(k)$ are identification system input and output sequence, $e(k)$ is white Gaussian noise, $z(k)$ is the linear part of the output. Definition parameter variables $\theta_2 = [a_1 \ \dots \ a_n \ b_0 \ \dots \ b_t]^T$, identify target is based on a given input $u(k)$ and system output $y(k)$ estimate parameter vector θ_2 , set the estimate of parameter vector θ_2 , $\hat{\theta}_2 = [\hat{a}_1 \ \dots \ \hat{a}_n \ \hat{b}_0 \ \dots \ \hat{b}_t]^T$.

The estimate of the deviation can use the following criterion function to measure.

$$J(k) = \sum_{i=0}^L \left[y(k-i) - \hat{y}(k-i) \right]^2 \quad (8.8)$$

The L for identification window length, $y(k-i)$ $\hat{y}(k-i)$ is $k-i$ ($i=1, \dots, L$) moment output measurement signal and estimate.

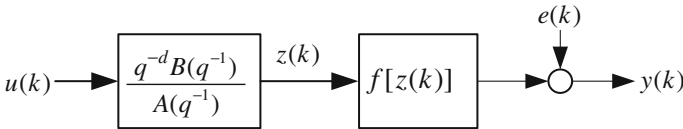


Fig. 8.2 Wiener model

8.3 Experiment Study

8.3.1 Test Function Used in Simulation Studies

In this paper, aim at the problem of Hammerstein model, using PSO, DE and improved DE do some simulation. For PSO, study gene $c_1 = 2, c_2 = 1.6$, inertia weight w linear decreases along with the iteration times 0.4 from 0.9, maximum speed limit in 1; For DE, the scale factor $F = 0.5$ and the crossover probability $CR = 0.3$; for MDE, $F_0 = 0.1$, and $CR = 0.4$; for MKDE, $F_0 = 0.3, CR_{\min} = 0.3, CR_{\max} = 0.55$. population size (NP) between 5D and 10D, D is the number of the goal function decision variables, no less than 4, this lab take $NP = 40$, the maximum iterations are for 1,200. Each differential evolution algorithm based on each improvement is run 20 times, the results are presented in Tables 8.1, 8.2, where various standard statistical measures including mean, minimum and RMSE. The Hammerstein model select is as follows:

$$\begin{cases} A(q^{-1})y(k) = B(q^{-1})x(k) + C(q^{-1})w(k) \\ x(k) = f(u(k)) = u(k) + 0.5u^2(k) + 0.3u^3(k) + 0.1u^4(k) \\ A(q^{-1}) = 1 - 1.5q^{-1} + 0.7q^{-2} \\ B(q^{-1}) = q^{-1} + 0.5q^{-2} \\ C(q^{-1}) = 1 + 1.5q^{-1} \end{cases} \quad (8.9)$$

Wiener model select is as follows:

$$\begin{cases} x(k) = 15x(k-1) - 07x(k-2) + u(k-1) + 0.5u(k-2) \\ y(k) = f[x(k)] + e(k), \\ f[x(k)] = \begin{cases} \sqrt{x(k)/2}, x(k) \geq 0, \\ -\sqrt{-x(k)/2}, x(k) > 0 \end{cases} \end{cases} \quad (8.10)$$

Table 8.1 The numerical comparison of four kinds of algorithm for Hammerstein model

Parameter	Truth-value	Estimate-value			
		PSO	DE	MDE	MKDE
a_1	-1.5	-1.5001	-1.5000	-1.5000	-1.5000
a_2	0.7	0.7000	0.7000	0.7000	0.7000
b_1	1.0	1.0430	1.0000	0.9997	1.0000
b_2	0.5	0.4998	0.5000	0.5000	0.5000
c_1	1.5	1.4566	1.5000	1.5003	1.5000
r_1	0.5	0.4855	0.5000	0.4999	0.5000
r_2	0.3	0.3342	0.3001	0.3021	0.3001
r_3	0.1	0.0483	0.1005	0.1319	0.1005
RMSE		5.3506e-004	3.7822e-004	2.5512e-008	2.5512e-008

Table 8.2 The numerical comparison of four kinds of algorithm for Wiener model

Parameter	Truth-value	Estimate-value			
		PSO	DE	MDE	MKDE
a_1	-1.5	-1.4998	-1.5000	-1.5000	-1.5000
a_2	0.7	0.6998	0.7000	0.7000	0.7000
b_0	1.0	1.0000	1.0000	1.0000	1.0000
b_1	0.5	0.4999	0.5000	0.5000	0.5000
RMSE		2.47e-008	1.32e-010	1.32e-012	4.81e-015

The input signal $u(k)$ is zero-mean, variance is 1 of the Gaussian white noise sequence, $w(k)$ is Gaussian white noise which variance is 0.1, identify window width is 500, to identify the parameters of the true value vector is, $\theta_1 = [-1.5 \ 0.7 \ 1.0 \ 0.5 \ 1.5 \ 0.5 \ 0.3 \ 0.1]^T$, $\theta_2 = [-1.5 \ 0.7 \ 1.0 \ 0.5]^T$. In simulation experiments, define root mean square error (RMSE) to measure precision.

$$RMSE = \sqrt{\frac{\sum_{j=1}^L [y(j) - \hat{y}(j)]^2}{L}} \tag{8.11}$$

8.3.2 Experimental Results

The experiment works on MATLAB7.1 software simulation platform. For Hammerstein model, There are 8 parameters ($a_1 \ a_2 \ b_1 \ b_2 \ c_1 \ r_1 \ r_2 \ r_3$), this paper drawing results put five linear parameters ($a_1 \ a_2 \ b_1 \ b_2 \ c_1$) and three nonlinear parameter ($r_1 \ r_2 \ r_3$) separate display. Figures 8.3, 8.4, 8.5, 8.6 are respectively the parameter identification results of Hammerstein model system with PSO algorithm DE algorithm and improved DE algorithm, Figs. 8.7, 8.8, 8.9, 8.10 are the results of Wiener model.

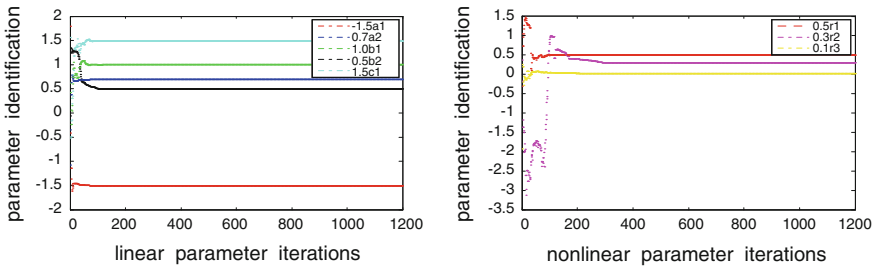


Fig. 8.3 Performance curves of PSO algorithm for Hammerstein model

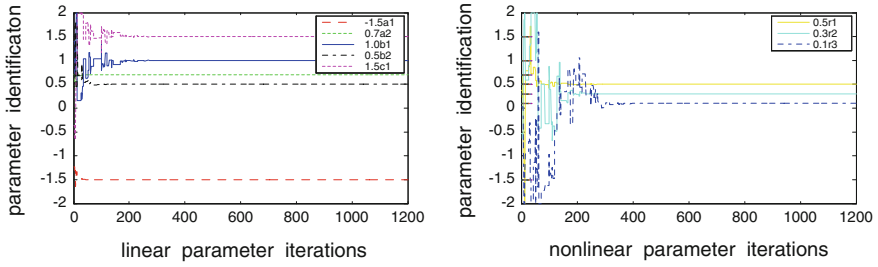


Fig. 8.4 Performance curves of DE algorithm for Hammerstein model

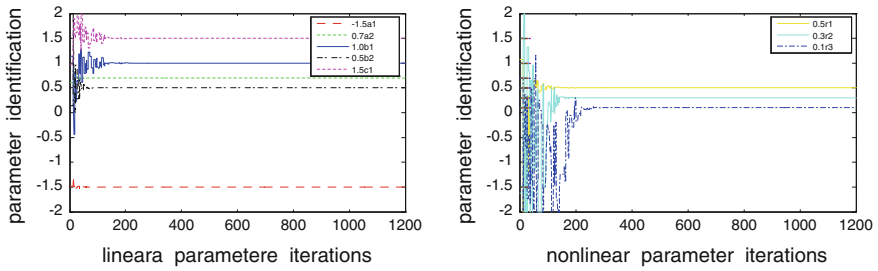


Fig. 8.5 Performance curves of MDE algorithm for Hammerstein model

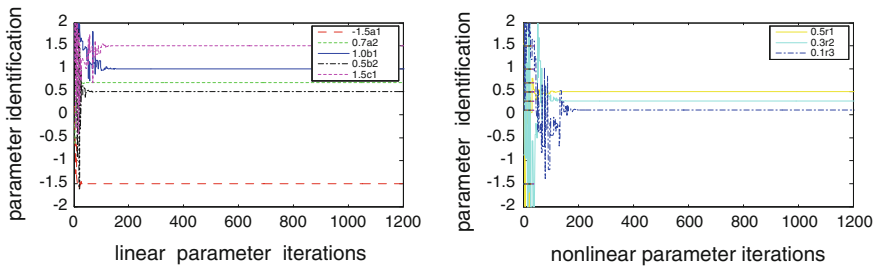


Fig. 8.6 Performance curves of MKDE algorithm for Hammerstein model

Fig. 8.7 Performance curves of PSO algorithm for Wiener model

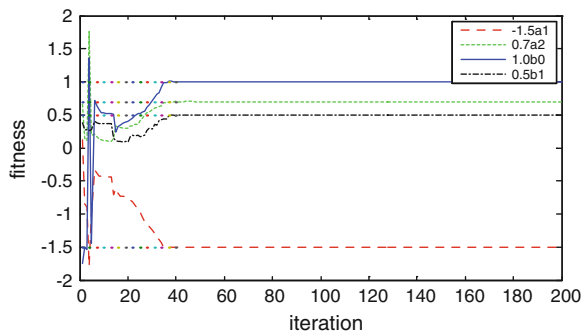


Fig. 8.8 Performance curves of DE algorithm for Wiener model

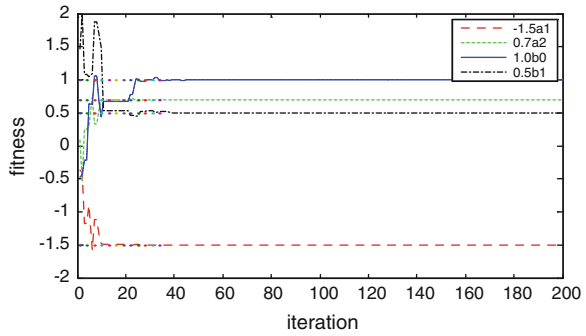


Fig. 8.9 Performance curves of MDE algorithm for Wiener model

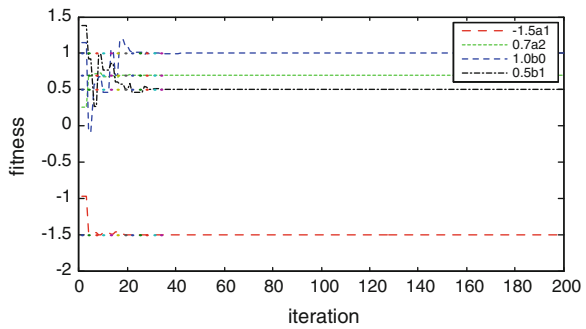


Fig. 8.10 Performance curves of MKDE algorithm for Wiener model

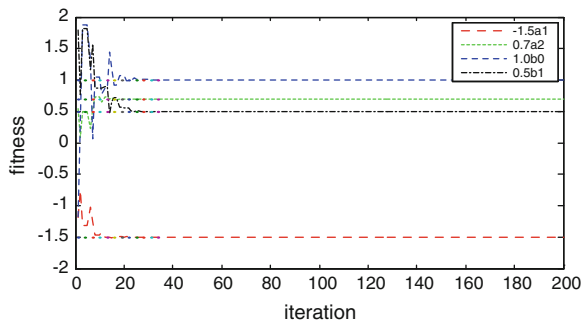


Figure 8.3 shows that PSO algorithm identifies Hammerstein model parameters with less iteration, the whole curve relatively smooth, identify the linear parameter within 100 generation, identify the nonlinear parameter in about 300 generation, but its program running time is many times as other algorithm.

Figure 8.4 shows that DE algorithm identify Hammerstein model parameters a little more iteration than PSO algorithm, identify the linear parameter around 200 generation, also identify the nonlinear parameter in about 340 generation, but its running faster and has more accurate identification parameter results.

We can see from Fig. 8.5 that MDE algorithm not only identify Hammerstein model parameters with less iteration, identify the linear parameter around 150 generation, identify the nonlinear parameter around 250 generation, but also its running faster with the most accurate result, and has the maximum probability of getting the global optimal solution.

It is shown in Fig. 8.6 that MKDE algorithm identifies the linear parameters with only about 100 iterations, identify the nonlinear parameters with about 200 iterations. Compare this method with the methods mentioned above, we know that the convergence rate of the MKDE is much fast than the other algorithms.

From Figs. 8.7, 8.8, 8.9, 8.10, we also can see that it is evident that the convergence of DE algorithm is faster than PSO algorithm. Figure 8.7 shows the identification iterations of PSO is about 36 generations and the oscillating amplitude is big before it achieves stability; Fig. 8.8 illustrates that DE algorithm can identify the parameters of Wiener model with 30 iterations, and the oscillating amplitude is smaller than the PSO algorithm; Fig. 8.9 shows that MDE algorithm identify the parameters of Wiener model in about 25 iterations; Fig. 8.10 shows that MKDE algorithm identify the parameters of Wiener model with only about 20 iterations.

In the same parameter setting conditions, we get the data result when the graph output. Take the average of the 30 group data, the results shown in Tables 8.1 and 8.2.

From Tables 8.1 and 8.2, it can be clearly observed that the DE algorithm and the improved DE algorithms perform more or less in a similar result although MKDE outperforms other algorithms. Although MDE can increase global search ability, and MKDE has a better performance both in accuracy and convergence. From Tables 8.1 and 8.2, we can see that the accuracy of PSO algorithm is smaller than the DE and the improved DE. PSO algorithm identifies the parameters is closed to the truth-value, however, the DE algorithm and improved DE can identify the parameters perfectly with little error, especially the MKDE algorithm.

8.4 Conclusions

In this paper we have investigated the performance of DE and the improved DE, the simulation of results showed that relative to the basic DE algorithm, improved DE algorithm some more advanced, the MKDE not only do better than other algorithms in accuracy, but also performs excellent at convergence speed. It turns out that the performance of DE algorithm is very sensitive to the choice of parameters and is related with the feature of problem. The next work we should do is to improve the stability of the DE algorithm.

Acknowledgments This work was supported by the National Natural Science Foundation of China (21206053,21276111); General Financial Grant from China Postdoctoral Science Foundation (2012M511678); A Project Funded by the Priority Academic Program Development of Jiangsu Higher Education Institutions.

References

1. Fang F, Reed E, Dickason DK, Simien HJ et al (2005) Technology review of multi-agent systems and tools. Bureau of Naval Personnel, Washington
2. Natrnfts K, Gallman P (1996) An iterative method for the identification of nonlinear systems using a Hammerstein model. *IEEE Trans Autom Control* 11(3):546–550
3. Lin X, Zhang H, Liu S et al (2006) The Hammerstein model identification based on PSO. *Chin J Sci Instrum* 27(1):76–79 (in Chinese)
4. Shen J, Sun J, Xu W (2009) System identification based on QPSO algorithm. *Comput Eng Appl* 45(9):67–70
5. Storn R, Price K (1997) Differential evaluation: a simple and efficient adaptive scheme for global optimization over continuous spaces. *Global Optim* 11:341–359
6. Ming Z, Guoxun W, Yipu Y (2010) Application of neural network and differential evolution algorithm in adaptive filterin. *Process Automation Instrum* 31(4):8–11 (in Chinese)
7. Chang W (2006) Parameter identification of Rossler’s chaotic system by an evolutionary algorithm. *Science* 29(5):1047–1053 (in Chinese)
8. Xu Q, Wang L, He B et al (2011) Opposition-based differential evolution using the current optimum for function optimization. *J Appl Sci Electron Inf Eng* 29(3):309–314 (in Chinese)
9. Tang HS, Xue ST, Fan CX (2008) Differential evolution strategy for structural system identification. *Comput Struct* 86(21–22):2004–2012
10. Liu R, Jiao L, Lei Q et al (2011) New differential evolution constrained optimization algorithm. *J Xidian Univ (Nat Sci Ed)* 38(1):47–52 (in Chinese)
11. Qian WY, Ii AJ (2008) Adaptive differential evolution algorithm for multi-objective optimization problems. *Appl Math Comput* 201(1):431–440
12. Zhang D, Liu Y, Huang S (2012) Differential evolution based parameter identification of static and dynamic J-A models and Its application to inrush current study in power converters [J]. *IEEE Trans Magnet* 48(11):3482–3485
13. Yan X, Yu J, Qian F et al (2006) Kinetic parameter estimation of oxidatical water based on modified differential evolution. *J East China Univ Sci Technol (Nat Sci Ed)* 32(1):94–97 (in Chinese)
14. Mohamed AW, Sabry HZ (2012) Constrained optimization based on modified differential evolution algorithm. *Inf Sci* 194:171–208

Chapter 9

The Coverage Optimization for Wireless Sensor Networks Based on Quantum-Inspired Cultural Algorithm

Yi-nan Guo, Dandan Liu, Yun Liu and Meirong Chen

Abstract In order to properly distribute sensor nodes in wireless sensor networks, a coverage model considering maximum coverage ratio and minimum redundancy is given and the optimization strategy based on quantum-inspired cultural algorithm is proposed. In population space, quantum-inspired evolutionary algorithm is used to increase the observed probability. In belief space, the implicit knowledge embodied in the evolution is extracted from the better individuals chosen from the population. It is used to guide the search direction of evolutionary population and influence the update of quantum individuals. Simulation results indicate that the algorithm is superior to other algorithms in coverage optimization and effectively improve the coverage performance of wireless sensor networks.

Keywords Wireless sensor networks · Quantum-inspired algorithm · Cultural algorithm · Coverage optimization

9.1 Introduction

Wireless sensor network (WSN) is composed of a large number of sensor nodes to detect the environment and monitor target in coverage area via a self-organized way. Sensor node scattered in monitored area has the capability of sensing, processing and communicating. The goal of coverage optimization for WSN is to obtain reasonable distribution of sensor nodes so as to maximize the coverage area and delay the network's lifetime. Aiming at different coverage mode including point coverage, area coverage and barrier coverage, many coverage optimization methods are proposed. In the exposed traversing coverage control algorithm [1],

Y. Guo (✉) · D. Liu · Y. Liu · M. Chen
College of Information and Electronic Engineering, China University of Mining and Technology, Xuzhou, 221116 Jiangsu, People's Republic of China
e-mail: nanfly@126.com

different routes with various accuracies are gotten by distributed methods. However, higher exposure accuracy may increase running time. Node self-scheduling coverage control protocol [2] can effectively extend the network lifetime by switching ‘active’ and ‘sleep’ nodes. Jiang [3] designed a centralized approximate algorithm based on Voronoi partition so as to obtain the minimum node set. But the optimal distribution of nodes is not considered. Greedy algorithm [4] was adopted to obtain minimum node set, which usually contains more nodes than actual need. So intelligent optimization algorithms are applied to solve the coverage problems in WSN. Though the optimal distribution of sensor nodes can be found by genetic algorithm [5], it is difficult to meet the real-time requirement of the dynamic nodes. Fu [6] introduced quantum genetic algorithm to improve coverage ratio so as to avoid the shadows and blind spots. Ramalho [7] adopted colony algorithm to solve the set coverage problem. However, when the number of sets and the elements contained in a set is larger, the algorithm’s complexity is increased. This leads to the overburden on the nodes in WSN and results in network bottlenecks. Particle swarm algorithm is applied to realize coverage optimization of WSN [8]. Although these methods can find the satisfied solution, the algorithms’ performance is limited because the knowledge embedded in evolution is not fully used.

So a novel coverage optimization for WSN based on quantum-inspired cultural algorithm is proposed. In quantum-inspired cultural algorithm (QCA), dual evolution structure is introduced. In population space, evolutionary individuals are generated from quantum individuals. In belief space, implicit knowledge extracted from evolutionary individuals is utilized to influence the evolution operators and quantum individuals’ update. We introduce QCA to solve the coverage optimization problem of WSN so as to obtain maximum coverage ratio and minimum redundancy ratio with better solution precision.

9.2 The Coverage Model for WSN

We adopt the lattice model [4] in the paper, in which the monitored area is uniformly partitioned into many sub-areas. The intersections of beelines are pixel points labeled by p_j . Each sub-area has the same acreage and is represented by corresponding pixel point. Once the pixel point is covered, corresponding sub-area is considered to be covered. We assume A is two-dimensional monitored area with $a \times b$ grids. Suppose the number of sensor nodes placed in the monitored area is N and the sensor nodes set is $S = \{s_1, \dots, s_N\}$. We assume each node’s sensing range is a circle. $s_i = \{x_i, y_i, r\}$ denotes i th sensor node, in which (x_i, y_i) and r respectively denote coordinate and sensing radius. Let (\bar{x}_j, \bar{y}_j) be the coordinates of p_j . The Euclidean distance between p_j and s_i is defined as $d(s_i, p_j)$. The coverage probability of p_j covered by s_i is denoted by $P_{\text{cov}}(p_j, s_i)$, which is determined by $d(s_i, p_j)$, the node’s physical characteristic and so on. Let $r_e (0 < r_e < r)$ be the

measuring reliability of sensor nodes. Suppose $\lambda_1 = r_e - r + d(s_i, p_j)$, $\lambda_2 = r_e + r - d(s_i, p_j)$. $\alpha_1, \alpha_2, \beta_1, \beta_2$ are the parameters related to the sensing characteristics of sensor nodes. The sensor nodes' model based on sensing probability [9] is shown as follows.

$$P_{\text{cov}}(p_j, s_i) = \begin{cases} 1 & d(s_i, p_j) \leq r - r_e \\ \exp\left(\frac{-\alpha_1 \lambda_1 \beta_1}{\lambda_2 \beta_2} + \alpha_2\right) & r - r_e < d(s_i, p_j) < r + r_e \\ 0 & \text{other} \end{cases} \quad (9.1)$$

As all sensor nodes contribute to the detection of a pixel point, whether a pixel point can be detected is determined by the joint detected probability [7] defined by $P_{\text{cov}}(p_j) = 1 - \prod_{s_i \in S} (1 - P_{\text{cov}}(p_j, s_i))$. A point can be detected as $\min\{P_{\text{cov}}(p_j)\} \geq C_{th}$ is satisfied. Here, C_{th} is the probability threshold.

The effective coverage ratio (ECR) and redundancy ratio (RR) are adopted to measure the coverage performances. ECR describes the distribution degree of nodes. RR measures average distribution of nodes. Let S_w be the total monitored area. S_{eff} and S_n are the effective coverage area and the coverage area in theory.

$$ECR = \frac{S_{\text{eff}}}{S_w} = \frac{\sum_{j=1}^{a \times b} P_{\text{cov}}(p_j, s_i) \Delta x \Delta y}{a \times b} \quad (9.2)$$

$$RR = \frac{S_n - S_{\text{eff}}}{S_n} = \frac{N\pi r^2 - \sum_{j=1}^{a \times b} P_{\text{cov}}(p_j, s_i) \Delta x \Delta y}{N\pi r^2} \quad (9.3)$$

The coverage optimization problem can be described as how to reasonably place sensor nodes in the monitored area so as to maximize ECR and minimize RR . In the paper, above objective functions are transformed to one weighted objective function. Let ω_1, ω_2 be weights of sub-objective functions.

$$\begin{aligned} F(x) &= \omega_1 ECR + \omega_2 (1 - RR) \\ \text{s.t. } & \omega_1 + \omega_2 = 1 \end{aligned} \quad (9.4)$$

9.3 The Coverage Optimization for Wireless Sensor Networks Based on Quantum-Inspired Cultural Algorithm

9.3.1 The Real-Coded Quantum Individual

In real-coded quantum model, a gene is denoted by a rectangle region, which is determined by its center and width. The relative fitness value of quantum individuals is defined as the rectangle's height [10]. Suppose the quantum population is formed by n quantum individuals. Each quantum individual contains m genes. c_{ij} and w_{ij} are

the rectangle's center and width of j th gene in i th quantum individual. A quantum individual is recorded as $q_i = [(c_{i1}, w_{i1}), (c_{i2}, w_{i2}), \dots, (c_{im}, w_{im})]$ ($i = 1, 2, \dots, n$). In the paper, the coordinates of each sensor node's location are encoded by real-coded quantum individual $q_i = s_i = \{cx_{i1}, wx_{i1}, cy_{i1}, wy_{i1}, \dots, cx_{iN}, wx_{iN}, cy_{iN}, wy_{iN}\}$. The rectangle's height h_i of quantum individual is gotten by quantum individual's relative fitness value.

$$h_i = \frac{f(q_i)}{\sum_{k=1}^n f(q_k)} \quad (9.5)$$

The probability density function expressed by $PDF_j = \sum_{i=1}^n q_{ij}$ and cumulative probability distribution function noted by $CDF_j = \int PDF_j$ are obtained by superposed among the quantum individuals. Corresponding inverse function is used to generate a real number $x_{ij} = CDF_j^{-1}(r)$ by selecting a random number $r \sim U(0, 1)$ so as to form the genes of an evolutionary individual.

9.3.2 Extraction and Utilization of Implicit Knowledge

In belief space, implicit knowledge is extracted from samples and described as knowledge. Now, five kinds of knowledge have been given by researchers. In this paper, normative knowledge and situational knowledge are used.

Normative knowledge memorizes the feasible search space of the optimization problems, expressed by $K_1 = \langle L(t), U(t), F^L(t), F^U(t) \rangle$, $L(t) = \{l_1(t), \dots, l_m(t)\}$, $U(t) = \{u_1(t), \dots, u_m(t)\}$. Here, m is the dimension of variables. u_j and l_j are the upper and lower bounds of j th variable. $F^L(t) = \{f_1^L(t), \dots, f_m^L(t)\}$, $F^U(t) = \{f_1^U(t), \dots, f_m^U(t)\}$. f_j^U and f_j^L denote corresponding fitness values. Let size $(I_j(t)) = u_j - l_j$ is the extent of variable. Along with the evolution, the search space will focus on the dominant area. When the dominant individual is beyond current search space, normative knowledge is updated.

$$l_j(t+1) = \begin{cases} x_{ij}(t) & (x_{ij}(t) < l_j(t)) \text{ or } (f(x_i(t)) < f_j^L(t)) \\ l_j(t) & \text{other} \end{cases} \quad (9.6)$$

$$f_j^L(t+1) = \begin{cases} f(x_i(t)) & (x_{ij}(t) < l_j(t)) \text{ or } (f(x_i(t)) < f_j^L(t)) \\ f_j^L(t) & \text{other} \end{cases} \quad (9.7)$$

$$u_j(t+1) = \begin{cases} x_{ij}(t) & (x_{ij}(t) > u_j(t)) \text{ or } (f(x_i(t)) < f_j^U(t)) \\ u_j(t) & \text{other} \end{cases} \quad (9.8)$$

$$f_j^U(t+1) = \begin{cases} f(x_i(t)) & (x_{ij}(t) > u_j(t)) \text{ or } (f(x_i(t)) < f_j^U(t)) \\ f_j^U(t) & \text{other} \end{cases} \quad (9.9)$$

Situational knowledge labeled by $K_2 = \langle E_1, E_2, \dots, E_s \rangle$ records the dominant individuals in the evolution. s is the capability of this knowledge. $E_i = \{x_i | f(x_i)\}$ is i th dominant individual in sample database. All dominant individuals are sorted in descending order according to their fitness values. Suppose $x^*(t)$ is the best individual in t th generation. Situational knowledge is updated as follows:

$$\langle E_1(t+1), E_2(t+1), \dots, E_l(t+1) \rangle = \begin{cases} \langle x^*(t), E_1(t), \dots, E_l(t) \rangle & \{f(x^*(t)) > f(E_1(t))\} \wedge (l < s) \\ \langle x^*(t), E_1(t), \dots, E_{l-1}(t) \rangle & \{f(x^*(t)) > f(E_1(t))\} \wedge (l = s) \\ \langle E_1(t), \dots, E_l(t) \rangle & \text{other} \end{cases} \quad (9.10)$$

Above knowledge are respectively used to adjust the step size and the direction of variable movement. Suppose $x_{ij}(t)$ and $\bar{x}_{ij}(t)$ are the j th variable of i th evolutionary individuals before and after mutation. Let λ is the constriction factor of step size. $N(0, 1)$ is a random number satisfying uniform distribution. The knowledge-inducing update method is shown as follows.

$$\bar{x}_{ij}(t) = \begin{cases} x_{ij}(t) + |size(I_j)N(0, 1)| & x_{ij}(t) < x_i^*(t) \\ x_{ij}(t) - |size(I_j)N(0, 1)| & x_{ij}(t) > x_i^*(t) \\ x_{ij}(t) + \lambda size(I_j)N(0, 1) & \text{other} \end{cases} \quad (9.11)$$

The dominant individuals recorded by situational knowledge are used to update the rectangle's center and width of quantum individuals [11, 12].

$$c_{ij}(t+1) = x_{ij}^*(t) \quad (9.12)$$

$$w_{ij}(t+1) = \begin{cases} w_{ij}(t) - |size(I_j)N(0, 1)| & \sigma < 1/5 \\ w_{ij}(t) + |size(I_j)N(0, 1)| & \sigma > 1/5 \\ w_{ij}(t) & \sigma = 1/5 \end{cases} \quad (9.13)$$

Here, $\sigma = \sum_{i=1}^n \delta_i / n$ is the threshold reflecting the evolution situation.

$$\delta_i = \begin{cases} 1 & f(x_{ij}(t)) < f(x_{ij}(t-1)) \\ 0 & f(x_{ij}(t)) \geq f(x_{ij}(t-1)) \end{cases} \quad (9.14)$$

9.4 Simulation Results and Their Analysis

In the simulation tests, we assume that A is the monitored area. It is a square with 20×20 and divided into 21×21 pixels. The main parameters of sensor nodes and the algorithms are respectively listed in the following: $N = 5$, $r = 3$, $r_e = 1.5$, $\alpha_1 = 1$, $\alpha_2 = 0$, $\beta_1 = 1$, $\beta_2 = 0$, $C_{th} = 0.5$; $n = 100$, $P_c = 0.9$, $P_m = 0.1$, $T = 1,000$; 20% better individuals in evolutionary population will selected into sample database every 5 generation and no more than 15 samples contained in

Table 9.1 Comparison of the coverage performance with different number of sensor nodes

N	10	15	20	25	30	35	40	45
ECR	45.25	56.58	79.58	95.17	98.25	100	100	100
RR	25.32	29.92	32.19	34.07	39.71	45.25	53.53	58.43
F	39.15	47.83	63.23	74.65	79.12	81.60	85.24	89.08
T	309	312	461	430	269	254	156	125

sample database. The weights of two objectives are $\omega_1 = 0.66$, $\omega_2 = 0.34$. In order to statistically analyze the experiments' results, all experiments run 30 times.

9.4.1 Comparison of Algorithms' Performances with Different Parameters

All sensor nodes with the same setting are randomly deployed in the target area. The coverage performances of WSN with different number of sensor nodes are shown in Table 9.1. F is the weighted objective values. T is the generation.

When the number of sensor nodes is less, ECR and RR are less. Along with the increasing of number, ECR is largely improved till $N = 35$, whereas RR slowly becomes larger. The reason for these is that less sensor nodes cannot satisfy the coverage requirement. On the other hand, although more sensor nodes can satisfy the coverage requirements, they cannot be uniformly distributed. And more sensor nodes are overlapped. So $N = 25$ in this paper.

By adopting different sensing radius, the nodes' distribution and the coverage performance are compared, as shown in Fig. 9.1 and Table 9.2. Here, dots represent sensor nodes. The circles indicate the nodes' coverage range.

Smaller sensing radius can lead to less effective coverage ratio and redundancy ratio. Along with the increasing of sensing radius, the convergence speed gets slower and RR is worse. When r is larger than 4, the detected area is completely covered. So $r = 3$ in this paper.

9.4.2 Comparison of Performances among Different Algorithms

In order to validate the rationality of QCA-based coverage optimization for WSN, it is compared with genetic algorithm (GA), quantum evolutionary algorithm (QEA) and cultural algorithm (CA) under the same conditions. The optimal distributions of sensor nodes by different algorithms are respectively shown in Fig. 9.2.

The algorithms' performances are compared in Table 9.3. Compared with GA, QEA and CA, ECR of QCA-based coverage optimization increases 4.92, 2.45 and

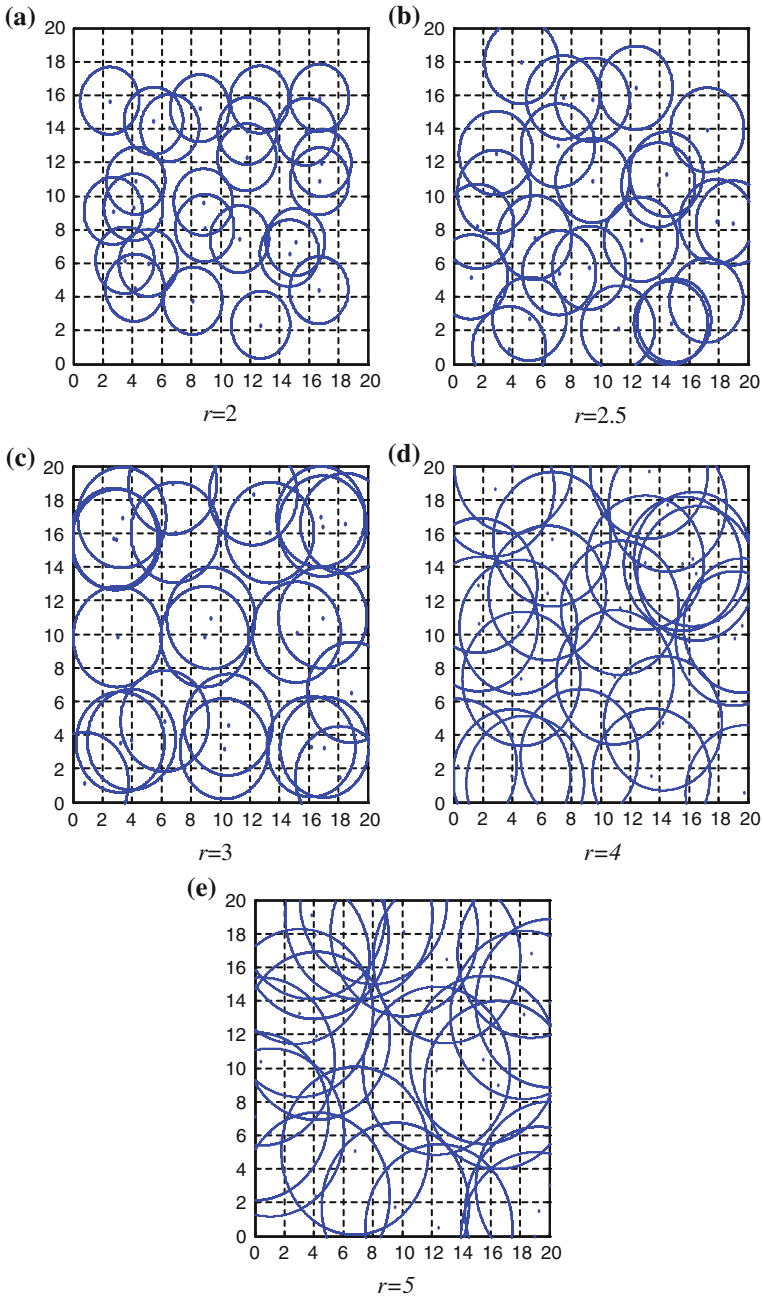


Fig. 9.1 The optimal results of nodes' distribution with different r . **a** $r = 2$, **b** $r = 2.5$, **c** $r = 3$, **d** $r = 4$, **e** $r = 5$

Table 9.2 Comparison of the coverage performance with different sensing radius

r	2	2.5	3	4	5
ECR	45.05	73.00	95.17	100	100
RR	30.59	35.87	34.07	53.13	68.11
F	41.50	60.38	74.65	86.71	93.64
T	684	496	430	302	235

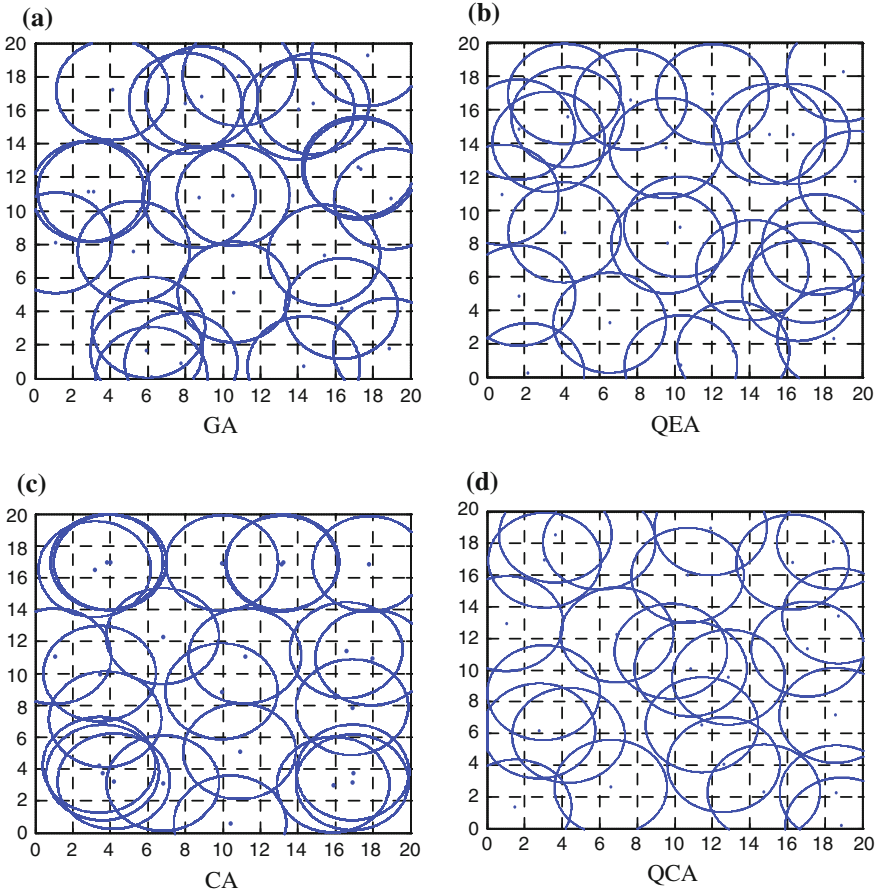


Fig. 9.2 The optimal distribution of sensor nodes by different algorithms. **a** GA, **b** QEA, **c** CA, **d** QCA

1.33 %. *RR* decreases 3.81, 0.07 and 3.95 %. The values of weighted objective function increase 3.03, 2.20 and 0.36 %. Moreover, the convergence speed is also fastest. In a word, quantum-inspired cultural algorithm has better coverage performance in coverage optimization of WSN.

Table 9.3 Comparison of the performances among Different algorithms

Algorithm	ECR	RR	F	T
GA	90.25	37.88	71.62	468
QEA	92.72	34.14	72.45	495
CA	93.84	38.02	74.29	462
QCA	95.17	34.07	74.65	430

9.5 Conclusions

The coverage optimization is one of the most important issues in WSN. The reasonable distribution of sensor nodes can maximize coverage area and delay the network's lifetime. So a coverage optimization method for WSN based on quantum-inspired cultural algorithm is proposed. Dual evolution structure is introduced in the algorithm. In population space, quantum-inspired evolutionary algorithm is adopted to increase the probability of being observed. The dominating individuals are submitted to belief space. Then implicit knowledge embodied in the evolution is extracted in belief space and used to guide the search direction of evolutionary population and influence the update of quantum population. Simulation results indicate that the algorithm has better coverage performance. In the future, multi-objective quantum-inspired cultural algorithm and its application in coverage optimization is our interest.

Acknowledgments This work was supported by Natural Science Foundation of Jiangsu under Grant BK2010183, the Fundamental Research Funds for the Central Universities under Grant 2012LWB76 and Jiangsu Overseas Research & Training Program for University Prominent Young & Middle-aged Teachers and Presidents.

References

1. Meguerdichian S, Koushanfar, Qu G, et al (2001) Exposure in wireless ad-hoc sensor networks. In: The ACM Int'l conference on mobile computing and networking. pp 139–150
2. Tian D, Georganas ND (2003) A node scheduling scheme for energy conservation in large wireless sensor networks. *Wireless Commun Mobile Comput* 3(2):271–290
3. Jiang J, Fang L, Zhang HY et al (2006) An algorithm for minimal connected cover set problem in wireless sensor networks. *J Softw* 17(2):175–184
4. Chen H, Wu H, Zeng T (2004) Grid-based approach for working node selection in wireless sensor networks. In: *IEEE international conference on communications*. pp 3673–3678
5. Jia J, Chen J, Chang G et al (2007) Optimal coverage scheme based on genetic algorithm in wireless sensor networks. *Control Decis* 22(11):1289–1292 (in Chinese)
6. Fu H, Han S (2008) Optimal sensor node distribution based on the new quantum genetic algorithm. *Chin J Sens Actuators* 21(7):1259–1263 (in Chinese)
7. De A Silva RM, Ramalho GL (2001) Ant system for the set covering problem. *IEEE Int Conf Sys Man Cybern* 5:3129–3133
8. Wang X, Wang S (2006) Dynamic development optimization in wireless sensor networks. *Intell Control Autom LNCS* 344:182–187

9. Li S, Xu C, Pan Y. (2005) Sensor deployment optimization for detecting maneuvering targets. In: 7th international conference on information fusion. pp 1629–1635
10. Qin C, Zheng J (2009) Novel quantum-inspired evolutionary algorithm and its application to numerical optimization problems. *J Syst Simul* 21(10):2862–2865 (in Chinese)
11. Guo Y, Liu D-D (2011) A novel real-coded quantum-inspired cultural algorithm. *J Central South Univ (Sci Technol)* 42(9):130–137 (in Chinese)
12. Cruz AVA, Vellasco MBR, Pacheco MAC (2006) Quantum-inspired evolutionary algorithm for numerical optimization. In: IEEE congress on evolutionary computation. pp 19–37

Chapter 10

Sensor Failure Detection and Diagnosis via Polynomial Chaos Theory—Part I: Theoretical Background

Weilin Li, Xiaobin Zhang, Wenli Yao and Huimin Li

Abstract Sensors are widely used in engineering applications to provide measurements to the control and protection centers. In order to achieve higher level reliability of the whole system in engineering applications, polynomial chaos theory (PCT) is applied for sensor failure detection and diagnosis (SFDD) considering parameter uncertainties. The proposed approach allows for independent model development by propagation of uncertainty through systems. First, a review of the SFDD methods both at home and abroad is given. Then, the standard process for PCT expansion, together with the proposed new SFDD algorithm is presented. Simulation verification with a DC/DC boost converter has also been done, and the results show good consistency with the theoretical analysis.

Keywords Sensor failure detection and diagnosis · Polynomial chaos theory · Parameter uncertainty · Data reconstruction

10.1 Introduction

Sensors are widely used in many engineering applications due to their capabilities to provide measurements required to implement control, supervision, coordination and management, and so on. The reliability of measurements is considered as fundamental to improve product quality, plant efficiency, availability and safety, and to enhance the feedback performance. Since most engineering systems are

W. Li (✉) · X. Zhang · W. Yao
Department of Electrical Engineering, Northwestern Polytechnical University,
Xi'an 710072, China
e-mail: li.weilin@hotmail.com

H. Li
EE Department, University of South Carolina, Columbia, SC 90089, USA

always strongly connected, failure of sensors may lead to a waste of the effort in design, optimization, or even damage the whole system.

The efforts related to sensor failure detection and diagnosis (SFDD) go back to 1970s according to the survey reported in 1976 by Willsky in [1]. Generally speaking, four kinds of strategies have been tried for SFDD [2]: physical redundancy, knowledge redundancy, signal processing strategy, and analytical redundancy.

However, some parameter uncertainties in relation to the system itself are always present and may also explicitly affect the sensor response. Uncertainty is attributed to the lack of perfect information concerning the phenomena, process and data involved in problem definition and resolution [3]. For most engineering applications, parameter uncertainties can make the modeling process, especially the determination of a proper threshold or a tolerated residual for sensor validation, very challenging because it is impossible to express the behavior of an uncertain system with a deterministic approach. This situation becomes even more challenging when studying closed-loop control systems because of the uncertainty propagation in the whole system.

By selecting an appropriate uncertainty propagation method, it would be possible to develop approaches to better bounding the sensor behaviors. For the evaluation of uncertainty in simulation, the Monte Carlo method is widely accepted as an “exact method” for determining uncertainty [4]. However, Monte Carlo method does not represent a feasible option for on-line operation. This limitation can be overcome by means of Polynomial Chaos Theory (PCT), a fast stochastic modeling method. Performances of both Monte Carlo and PCT in circuit simulation have been analyzed by the authors in [5].

This paper introduces a new analytical approach for SFDD under uncertainty, based on the mathematics of PCT. The objective is to improve the self-healing abilities of a system, and to achieve a higher level system reliability and safety. The sensor detection and diagnosis solutions are developed using polynomial chaos mathematical procedures to create a general technique for bounding the dynamic behavior of sensors. Bad data are handled with the resulting algorithms to reject them from control unit. The use of PCT marks a migration in the field of sensor failure diagnosis towards online operation by counting for parameter uncertainties. Furthermore, it can be used not only for the purpose of sensor failure detection and diagnosis but also for system monitoring.

10.2 Polynomial Chaos Theory

10.2.1 Overview of PCT

Polynomial chaos is a method that uses a polynomial based stochastic space to represent the evolution of the uncertainty propagation into the system [6]. PCT concept was first introduced by Wiener in 1938 as “Homogeneous Chaos” [7].

The theory evolved into the Wiener–Askey polynomial chaos, which extended the theory to the entire Askey scheme of orthogonal polynomials [8]. The fundamental of PCT can be summarized as approximating a random process by the sums of orthogonal polynomials from Askey scheme.

10.2.2 PCT Expansion

PCT expansion was used for analysis of engineering applications by Xiu et al. in [9]. In general, the PCT expansion of a system is performed based on the system model described by differential equations or state space.

Considering a linear time-invariant dynamic system in state space form:

$$\begin{aligned}\dot{x}(t) &= Ax(t) + Bu(t) \\ y(t) &= Cx(t) + Du(t)\end{aligned}\tag{10.1}$$

where

$x(t) \in R^n$ system state vector; $u(t) \in R^r$ input vector; $y(t) \in R^m$ output vector; A, B, C system metrics with appropriate dimensions.

Polynomial chaos expansion can augment the original model of system in Eq. (10.1) to a new version in which the uncertainty information is embedded in these polynomial chaos coefficients. Furthermore, the PCT coefficients also evolve with time. This expansion could be taken step by step, as portryed in Fig. 10.1.

By choosing corresponding polynomial base ψ , uncertain parameter X can be expanded into PCT domain as shown in Eq. (10.2).

$$X(\theta) = \sum_{n=0}^{\infty} a_n \Psi_n(\xi(\theta))\tag{10.2}$$

where

$X(\theta)$ Radom process or function under analysis in terms of θ , which represents the random event; a_n The coefficients of the expansion; Ψ_n The selected polynomial basis; ξ Radom vector with a probability distribution function (PDF) according to selected Ψ_n .

The spectral representation of an uncertain parameter on this limited space is given by

$$X(\theta) = \sum_{i=0}^P a_i \psi_i(\xi(\theta)).\tag{10.3}$$

Notes on the selection of appropriate parameter P and on the convergence of the PCT approach are reported in detail Ref. [8].

The solution of this new set of state equations provides the coefficients of the polynomial chaos expansion of the state variables. The 0th order of such expansion

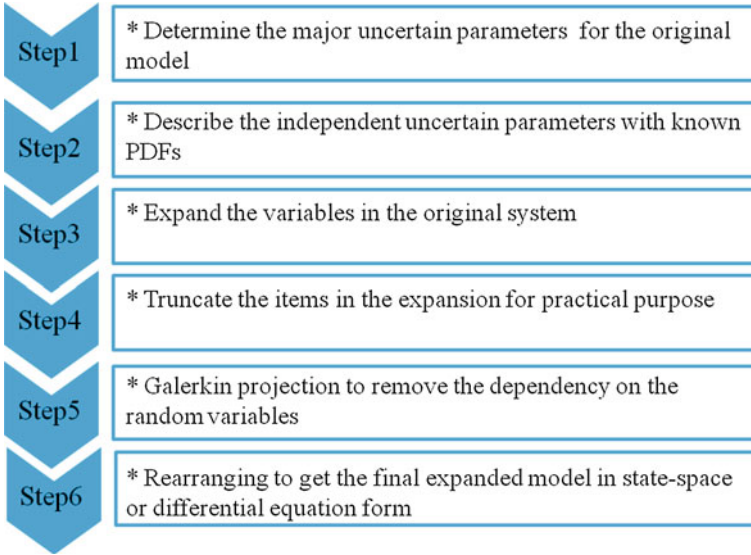


Fig. 10.1 Flow chart of a general PCT expansion

represents the most likely value. The generic form of the system in PCT domain can be presented as in Eq. (10.4).

$$\begin{aligned}\dot{x}_{pct}(t) &= A_{pct}x_{pct}(t) + B_{pct}u_{pct}(t) \\ y_{pct}(t) &= C_{pct}x(t) + D_{pct}u_{pct}(t)\end{aligned}\quad (10.4)$$

where

$x_{pct}(t) \in R^{n_{pct}}$ system state vector; $u_{pct}(t) \in R^{r_{pct}}$ input vector; $y_{pct}(t) \in R^{m_{pct}}$ output vector; A_{pct} , B_{pct} , C_{pct} system metrics with appropriate dimensions.

10.3 PCT Observer

The idea of PCT observer (PCO) is to use the available measured sensor outputs to estimate the uncertain system states. These uncertain states can be elaborated to construct the range for sensor output. This provides a way to bind the sensor behavior. To be more precise, using a PCT-based observer, it is viable not only to get the estimation of a quantity but also to get the uncertainty evolutions of this quantity with a specified confidence level.

If the system is observable, a closed-loop state observer can be designed. Assuming that the set of variables y in (10.4) defines the measurable variables, the observer can be defined as:

$$\hat{x}_{pct}(t) = A_{pct}\hat{x}_{pct}(t) + B_{pct}u_{pct}(t) + K_{pct}(y_{pct}(t) - C_{pct}\hat{x}_{pct}(t)) \quad (10.5)$$

where $\hat{x}_{pct}(t)$ estimated uncertain states in PCT form; Gain K_{pct} is a design parameter, and different strategies for setting this gain matrix can be introduced. Such strategies include pole placement and optimal/suboptimal Kalman filter design.

A PCO allows the introduction and management of uncertainty in a process by utilizing a stochastic model based on the PCT. This newly proposed PCO structure is able to reconstruct the state in the presence of uncertainty. By using higher polynomial order, more complex PDF can be reconstructed.

10.4 PCT Based Sensor Failure Diagnosis

In this part, SFDD consists of measurement failure detection, isolation, and bad-data reconstruction. Because multiple uncertain sources are considered in the system, the mean and the variance of the sensor response could be reconstructed from the uncertain states with circuit laws as [10].

$$E[f_i(x)] = f_i(x_0); V[f_i(x)] = \sum_{n=1}^p f_i^2(x_n) \quad (10.6)$$

The interval z_t representing the possible values of an arbitrary measured variable is defined through its boundaries as:

$$z_t = [z_L, z_U] \quad (10.7)$$

With

$$z_L(t) = f_i(x_0) - \sqrt{\sum_{n=1}^P f_i^2(x_n)}; z_U(t) = f_i(x_0) + \sqrt{\sum_{n=1}^P f_i^2(x_n)}$$

As a result of the PCT approach, a reasonable interval, z_t , can be determined for each measured variable. The diagnosis of the measured data then becomes a decision making process based on the fact that measured value belonging or not to a continuously evolving interval.

The basic operation logic of SFDD could be summarized as follows [11]:

*If measurement is within the uncertain thresholds,
Sensor is healthy;
Else, sensor has failed. Identifying and isolating the failed sensors, Rebuilding the bad data.*

Figure 10.2 illustrates the process of data reconstruction as described above [12].

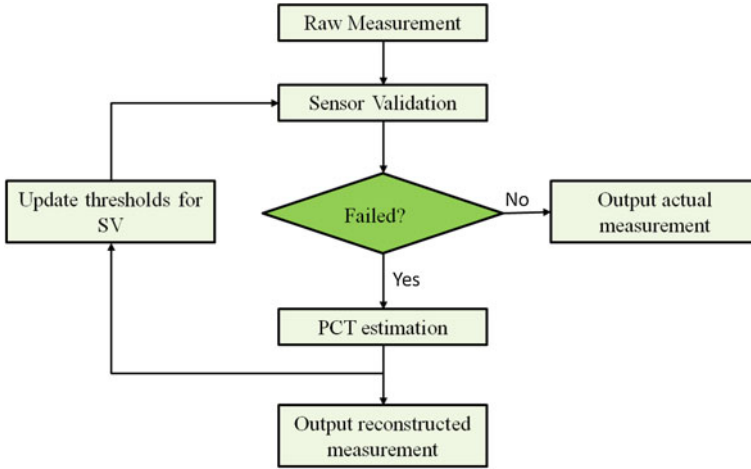


Fig. 10.2 Missing data reconstruction algorithm

10.5 Simulation Verification

The DC/DC Boost converter is adopted as an appropriate case study in this paper. As shown in Fig. 10.3, two control loops are used, the external voltage feedback loop and the internal current feedback loop. The voltage control loop is realized with a proportional integral (PI) controller that provides a feedback control signal which is a reference value for the current control loop. The voltage control loop assures maintenance of the rated voltage in every normal and non-faulty situation. The current control loop is also realized with a PI controller. PCT based SFDD modules are developed and inserted between the controller and the instruments. The purpose is to make the controller capable to survive from malfunction of the measurement devices.

As stated above, SFDD module is developed based on PCT. The linear time-invariant system model of the converter is considered in this paper. For the sake of simplicity, we assume that the resistances that are associated with the inductor and

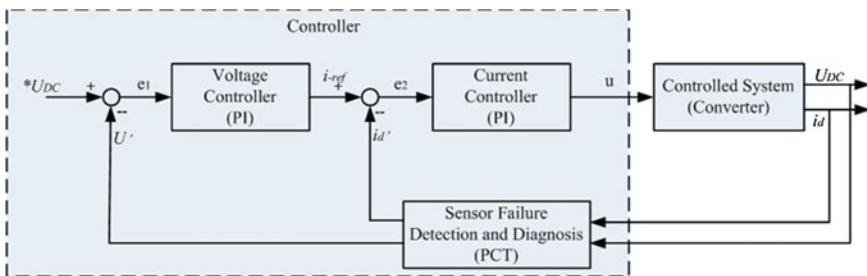


Fig. 10.3 Controller structure of the boost converter with SFDD module

capacitor are null, as in the case of an ideal lossless converter. The average model of the converter can be written as:

$$\begin{aligned}\frac{di(t)}{dt} &= -\frac{v(t)}{L}(1-u) + \frac{v_{cc}}{L} \\ \frac{dv(t)}{dt} &= \frac{i(t)}{C}(1-u) - \frac{GX_2}{C}\end{aligned}\quad (10.8)$$

where $R = 10 \Omega$; $L = 5e - 2H$; $C = 4e - 5F$

Assuming that a single parameter and its PDF is given, the above equation can be expanded using PCT with a convenient polynomial basis that is chosen based on that PDF. In this specific case, uncertainties in the load are taken as the major uncertain sources to expand the deterministic model into PCT domain. The PDF of the load conductance, G , is assumed to be uniform here with an interval of 8 % of the central value. A first-order polynomial ($n_p = 1$) is adopted. The PCT expansion of all the uncertain variables is given as:

$$G = \sum_{a=0}^P G_a \Phi_a(\xi); i(t) = \sum_{b=0}^P i_b(t) \Phi_b(\xi); v(t) = \sum_{c=0}^P v_c(t) \Phi_c(\xi) \quad (10.9)$$

Then the calculation and development of the PCT based SFDD modular will follow the instructions briefly introduced in Fig. 10.1. This simulation results show the consequences that defective current sensors, whose measurements are used by the controller, can cause if no PCT based sensor failure diagnosis action is taken.

Figure 10.4 shows that at 0.6 s a failure of the measurement is detected. Figure 10.5 shows the difference in converter output current in case incorrect measurements are used as they are (left side of Fig. 10.5). Notice that, following a failure of the current sensor, even without resuming to data reconstruction, the DC bus voltage that directly feeds the load may stay rather constant (bottom of the left side Fig. 10.5). However, current tends to increase unlimitedly (top left side Fig. 10.5), since the local controllers take actions based on both voltage and current at the output points of the converter. As a result, the current may keep increasing till the converter is damaged. However, when the incorrect measurements are replaced with reconstructed data, the situation is mitigated (right side of Fig. 10.5). This measurement fault is a potential threat to the converter that

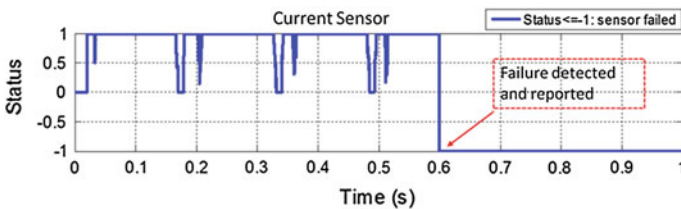


Fig. 10.4 Current sensor status monitoring of the converter

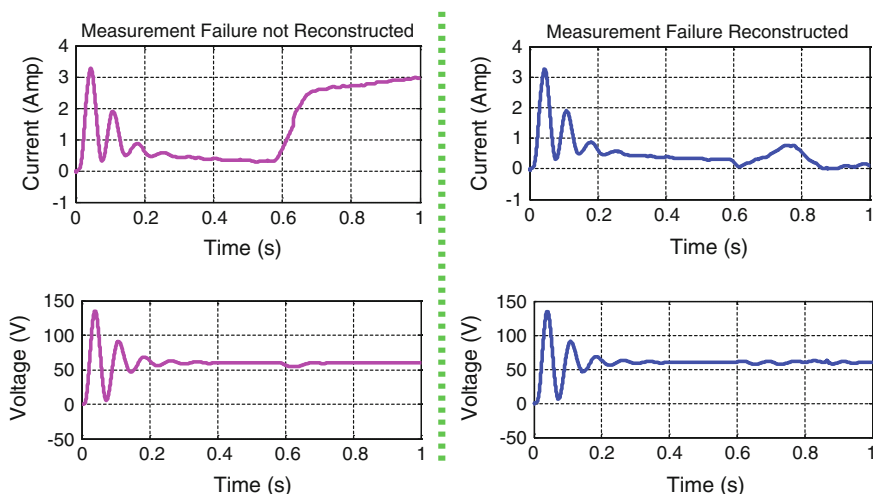


Fig. 10.5 Impact of the measurement failures on the vital load bus

directly feeds the DC bus, and it may also result in unpredictable damage of other components in the power system. On the contrary, the situation is mitigated or even avoided with reconstructed data.

10.6 Conclusion

This paper reviews the methods and algorithms that have been adopted in the field of SFDD. A new SFDD method that considers parameter uncertainties has been proposed based on PCT. The detailed process of the PCT based expansion is provided. And finally, the PCT based SFDD algorithm is presented. A DC/DC boost converter is adopted as an appropriate case study to do simulation verifications of the proposed algorithm. In the following papers, these aspects will be addressed: digital realization of the proposed sensor diagnosis algorithm; the potential applications of the proposed algorithm, for example, in the field of state estimation, controller design, as well as system protection.

References

1. Alan S-W (1967) A survey of design methods for failure detection in dynamic systems. *Automatica* 12(6):601–611
2. Luigi F (2007) *Soft sensors for monitoring and control of industrial processes*. Springer, Berlin
3. Tung Y-K, Yen B-C (2005) *Hydrosystems engineering uncertainty analysis*. McGraw-Hill, New York

4. Balaban P, Golembiski J-J (1975) Statistical analysis for practical circuit design. *IEEE Trans Circ Syst* 22(2):100–108
5. Lovett T-E (2004) A polynomial chaos approach to network simulation under uncertainty. Ph.D. dissertation, University of South Carolina
6. Smith A-H-C (2007) Robust and optimal control using polynomial chaos theory. Ph.D. dissertation, University of South Carolina
7. Wiener N (1938) The homogeneous chaos. *Amer J Math* 60:897–936
8. Xiu D, Karniadakis G-E (2002) The Wiener–Askey polynomial chaos for stochastic differential equations. *SIAM J Sci Comput* 24(2):619–644
9. Xiu D, Lucor D, Su C-H, Karniadakis G-E (2002) Stochastic modeling of flow-structure interactions using generalized polynomial chaos. *J Fluid Eng* 124:51–59
10. Kewlani G, Iagnemma K (2009) A multi-element generalized polynomial chaos approach to analysis of mobile robot dynamics under uncertainty. In: *Proceedings of IEEE/RSJ international conference intelligent robots and systems*. pp 1177–1182
11. Li W, Li H, Ni F, Zhang X, Monti A (2011) Digital automatic voltage regulator for synchronous generator considering sensor failure. *Eur Trans Electr Power* 22(8):1037–1052
12. Li H, Li W, Luo M, Monti A, Ponci F (2011) Design of smart MVDC power grid protection. *IEEE Trans Instrum Meas* 60(9):3035–3046

Chapter 11

Adaptive Tracking Control of Nonlinear Systems with Unmodeled Dynamics and Unknown Gain Sign

Zhiyuan Gao, Tianping Zhang and Yuequan Yang

Abstract Based on backstepping design, a novel adaptive tracking control scheme is proposed for a class of strict feedback nonlinear systems with unmodeled dynamics and completely unknown function control gain in this paper. An available dynamic signal is used to dominate the unmodeled dynamics. The unknown virtual control gain signs are dealt with using the property of Nussbaum function. The controller singularity problem is avoided using integral Lyapunov function. By theoretical analysis, the closed-loop systems is proved to be semi-global uniformly ultimately bounded.

Keywords Strict feedback systems · Adaptive neural control · Dynamic signal · Nussbaum function

11.1 Introduction

In recent years, adaptive control of nonlinear systems with unknown gain sign has received a great deal of attention [1–4]. Nussbaum function was firstly proposed in Ref. [1] for the control problem of a class of linear time-invariant systems with unknown control gain coefficient. Nussbaum function has already been used to cope with the adaptive control problem of nonlinear systems with unknown control gain. The backstepping design was an important method to construct nonlinear adaptive controller recursively, and has solved a lot of problems that appeared in the process of the design of adaptive controllers in the early stage of the research, such as the matching condition, the growth condition. An adaptive control design was investigated in Ref. [2], using a modified Lyapunov function to remove the

Z. Gao · T. Zhang (✉) · Y. Yang
Department of Automation, College of Information Engineering, Yangzhou University,
Yangzhou 225127, China
e-mail: tpzhang@yzu.edu.cn

possible controller singularity problem. Applying the universal approximation properties of fuzzy logic systems (FLS) and the properties of Nussbaum function, an adaptive control scheme was developed for a class of MIMO nonlinear systems with unknown control gain in Ref. [3]. Using the dynamic surface control method and the properties of Nussbaum function, two adaptive neural network control schemes were proposed for a class of nonlinear pure feedback systems with dead-zone in Ref. [4].

The unmodeled dynamics exists widely in the actual systems, which influences the stability of nonlinear systems, and limits the performance of practical systems. Two robust adaptive control schemes were proposed for the existing unmodeled dynamics in Ref. [5, 6]. On the basis of it, using the universal approximation properties of neural networks, a robust adaptive approach was developed for a class of nonlinear pure feedback systems in Ref. [7]. Applying the small-gain approach and the properties of output feedback, [a novel adaptive control design is investigated in [8]. By introducing an available dynamic signal to dominate the unmodeled dynamics, a fuzzy adaptive control approach was developed for a class of nonlinear systems in Ref. [9]. Based on the neural networks universal approximator, adaptive neural dynamic surface control (DSC) was proposed for a class of pure feedback nonlinear systems in Ref. [10]. This scheme relaxed the assumption of the systems, and used the technique of DSC to deal with the control problem of nonlinear systems including the unmodeled dynamics. A new fuzzy adaptive control approach was developed for a class of nonlinear with unknown virtual control gain and the unmodeled dynamics in Ref. [11].

On the basis of Refs. [4, 10, 11], a novel adaptive neural network control scheme is developed for a class of strict feedback nonlinear systems in this paper. The main contributions of this paper are addressed as follows: (1) The discussed plant in Ref. [11] is extended to more general strict-feedback nonlinear systems, and the assumption of the dynamic disturbances is relaxed. Furthermore, tracking performance is carried out by constructing appropriately unknown continuous functions; (2) The completely unknown virtual function control gains are dealt using the property of Nussbaum function while the completely unknown virtual constant control gains are only discussed in Ref. [11]; (3) The other restriction of class k_∞ function $\bar{\gamma}(|x_1|)$ is removed except $\bar{\gamma}(|x_1|) \geq \gamma(|x_1|)$.

11.2 Problem Formulation and Preliminaries

Consider a class of strict-feedback systems with unmodeled dynamics in the following form:

$$\begin{cases} \dot{z} = q(z, x) \\ \dot{x}_i = f_i(\bar{x}_i) + g_i(\bar{x}_i)x_{i+1} + \Delta_i(x, z, t) \\ t\dot{x}_n = f_n(\bar{x}_n) + g_n(\bar{x}_n)u + \Delta_n(x, z, t) \\ y = x_1 \end{cases} \quad (11.1)$$

where $i = 1, 2, \dots, n-1$, $z \in R^{r_0}$ is the unmodeled dynamics, $\bar{x}_i = [x_1, x_2, \dots, x_i]^T \in R^i$, $\bar{x}_n = [x_1, x_2, \dots, x_n]^T \in R^n$ is the state vector, $u \in R$ is the system input, $y \in R$ is the system output, $f_i(\bar{x}_i)$ and $g_i(\bar{x}_i)$ are the unknown continuous functions, $\Delta_i(z, x, t)$, $i = 1, 2, \dots, n$ are the nonlinear dynamic disturbances, and $\Delta_i(z, x, t)$ and $q(z, x)$ are uncertain Lipschitz functions.

The control objective is to design adaptive control u for system (11.1) such that the output y follows the specified desired trajectory y_d .

Assumption 1 The unknown dynamic disturbance $\Delta_i(z, x, t)$, $i = 1, 2, \dots, n$ satisfies:

$$|\Delta_i(z, x, t)| \leq \phi_{i1}(\|\bar{x}_i\|) + \phi_{i2}(\|z\|) \quad (11.2)$$

where $\phi_{i1}(\cdot)$ and $\phi_{i2}(\cdot)$ is an unknown non-negative continuous function, $\phi_{i2}(\cdot)$ is a non-negative non-decreasing function, and $\|\cdot\|$ is the Euclidean norm.

Assumption 2 The unmodeled dynamics are exponentially input-to-state practically Stable (exp-ISpS); that is, the system $\dot{z} = q(z, x)$ has an exp-ISpS Lyapunov function $V(z)$ satisfying:

$$\alpha_1(\|z\|) \leq V(z) \leq \alpha_2(\|z\|) \quad (11.3)$$

$$\frac{\partial V(z)}{\partial z} q(z, x) \leq -cV(z) + \gamma(|x_1|) + d \quad (11.4)$$

where $\alpha_1(\cdot)$, $\alpha_2(\cdot)$ and $\gamma(\cdot)$ are of class of k_∞ functions, c and d are known positive constants. Moreover, $\gamma(\cdot)$ is a known function.

Assumption 3 The desired tracking trajectory \bar{x}_{id} is continuous and available, and $\|\bar{x}_{nd}\| \in L_\infty$, i.e., $\sum_{i=0}^n [y_d^{(i)}]^2 \leq B_0, \forall t > 0$, where $\bar{x}_{id} = [y_d, \dot{y}_d, \dots, y_d^{(i)}]^T$, $i = 1, \dots, n$, B_0 is a positive constant.

Assumption 4 The sign of control gain $g_i(\cdot)$ is unknown. Moreover, there exist positive constants g_{\min} and g_{\max} such that $0 < g_{\min} \leq |g_i(\cdot)| \leq g_{\max}$, $1 \leq i \leq n$.

Lemma 1 [6] *If V is an exp-ISpS Lyapunov function for a control system $\dot{z} = q(z, x)$, i.e. Eqs. (11.3) and (11.4) hold, then for any constants \bar{c} in $(0, c)$, any initial instant $t_0 > 0$, any initial condition $z_0 = z(t_0)$ and $v_0 > 0$, for any function $\bar{\gamma}(\cdot)$ such that $\bar{\gamma}(|x_1|) \geq \gamma(|x_1|)$, there exists a finite $T_0 = V(z_0)v_0^{-1}e^{(c-\bar{c})t_0} \times (c - \bar{c})^{-1} \geq 0$, an available signal $v > 0$, a nonnegative function $D(t_0, t)$ defined for all $t \geq t_0$ with $D(t_0, t) = 0$ and $V(z) \leq v(t) + D(t_0, t)$ when $t \geq t_0 + T_0$, and a signal described by*

$$\dot{v} = -\bar{c}v + \bar{\gamma}(|x_1|) + d, \quad v(t_0) = v_0 \quad (11.5)$$

Without loss of generality, we choose $\bar{\gamma}(|x_1|) = \gamma(|x_1|)$.

Lemma 2 [12] *For any real-valued continuous function $f(x, y)$ where $x \in R^m$ and $y \in R^n$, there are smooth scalar-value functions $\varphi(x) \geq 0$ and $\vartheta(y) \geq 0$, such that $|f(x, y)| \leq \varphi(x) + \vartheta(y)$.*

The Nussbaum gain technique is introduced in this paper, in order to deal with the unknown sign of control gain. A function $N(\zeta)$ is called a Nussbaum-type function if it has the following properties [1]:

$$\limsup_{s \rightarrow \infty} s^{-1} \int_0^s N(\zeta) d\zeta = +\infty \text{ and } \liminf_{s \rightarrow \infty} s^{-1} \int_0^s N(\zeta) d\zeta = -\infty \quad (11.6)$$

Commonly used Nussbaum functions include: $\zeta^2 \cos(\zeta)$, $\zeta^2 \sin(\zeta)$ and $\exp(\zeta^2) \cos((\pi/2)\zeta)$. We assume that $N(\zeta) = e^{\zeta^2} \cos((\pi/2)\zeta)$ is used in throughout this paper.

Lemma 3 [13] *Let $V(\cdot)$ and $\zeta(\cdot)$ both be smooth functions on $[0, t_f)$, with $V(t) \geq 0$ and $\forall t \in [0, t_f)$, $N(\cdot)$ be an even smooth Nussbaum-type function, if the following inequality holds:*

$$V(t) \leq c_0 + e^{-c_1 t} \int_0^t g(x(\tau)) N(\zeta) \dot{\zeta} e^{c_1 \tau} d\tau + e^{-c_1 t} \int_0^t \dot{\zeta} e^{c_1 \tau} d\tau, \forall t \in [0, t_f) \quad (11.7)$$

where c_0 is a suitable constant, c_1 is a positive constant, $g(x(t))$ is a time-varying parameter that takes values in the unknown closed intervals $I := [l^-, l^+]$, with $0 \notin I$, then $V(t)$, $\zeta(t)$ and $\int_0^t g(x(\tau)) N(\zeta) \dot{\zeta} d\tau$ must be bounded on $[0, t_f)$.

Lemma 4 [14] *For any given positive constant $t_f > 0$, if the solution of the resulting closed-loop system is bounded on the interval $t \in [0, t_f)$, then $t_f = \infty$.*

Let $W_i^{*T} \psi_i(\xi_i)$ be the approximation of the radial basis function neural networks on a given compact set $\Omega_{\xi_i} \subset R^q$ to the unknown continuous function $h_i(\xi_i)$, i.e., $h_i(\xi_i) = W_i^{*T} \psi_i(\xi_i) + w_i(\xi_i)$, where $\xi_i \in \Omega_{\xi_i} \subset R^q$ is the input vector of neural networks; $W_i^* \in R^{l_i}$ is the ideal weight vector for sufficient large integer l_i which denotes the neural networks node number satisfying $l_i > 1$; the basis function vector $\psi_i(\xi_i) = [\rho_{i1}(\xi_i), \dots, \rho_{il_i}(\xi_i)]^T \in R^{l_i}$ with $\rho_i(\xi_i)$ being chosen as the commonly used Gaussian functions, which have the form:

$$\rho_{ij}(\xi_i) = \exp[-(\xi_i - \varsigma_{ij})^T (\xi_i - \varsigma_{ij}) \phi_{ij}^{-2}], \quad 1 \leq j \leq l_i, 1 \leq i \leq n \quad (11.8)$$

where, $\varsigma_{ij} = [\varsigma_{ij1}, \varsigma_{ij2}, \dots, \varsigma_{ijq_{ij}}]^T$ is the center of the receptive field and ϕ_{ij} is the width of the Gaussian function. The unknown ideal weight vector is defined as follows:

$$W_i^* = \arg \min_{W_i \in R^{l_i}} [\sup_{\xi_i \in \Omega_{\xi_i}} |W_i^T \psi_i(\xi_i) - f_i(\xi_i)|] \quad (11.9)$$

$|w_i(\xi_i)| \leq \varepsilon_i$, and $\varepsilon_i > 0$ is the unknown constant

11.3 Control System Design and Stability Analysis

Based on backstepping, an adaptive neural control scheme will be proposed in this section. The control procedure consists of n steps, and is based on the following change of coordinates: $s_1 = x_1 - y_d$, $s_2 = x_2 - \alpha_1$, $\dots, s_n = x_n - \alpha_{n-1}$, where $\alpha_i, i = 1, \dots, n-1$ is the virtual control input, and will be obtained in the following design. For convenience, define the Lyapunov function candidates as follows:

$$V_{s_1} = \int_0^{s_1} |g_1^{-1}(\sigma + y_d)| \sigma d\sigma + \lambda^{-1} v \quad (11.10)$$

$$V_{s_j} = \int_0^{s_j} |g_j^{-1}(\bar{x}_{j-1}, \sigma + \alpha_{j-1})| \sigma d\sigma, 2 \leq j \leq n \quad (11.11)$$

$$V_i = V_{s_i} + 0.5\gamma_i^{-1}\tilde{\theta}_i^2 \quad (11.12)$$

where $\tilde{\theta}_i = \hat{\theta}_i - \theta_i$, $\hat{\theta}_i$ is the estimate of θ_i at time t , $\theta_i = \|W_i^*\|$, $\gamma_i > 0$ is a design constant, $i = 1, \dots, n$.

The virtual control laws and the adaptive laws are employed as follows ($i = 1, \dots, n$):

$$\alpha_i = N(\zeta_i)[k_i s_i + 0.5a_i^{-2}s_i\hat{\theta}_i\|\psi_i(\zeta_i)\|^2] \quad (11.13)$$

$$\dot{\zeta}_i = k_i s_i^2 + 0.5a_i^{-2}s_i^2\hat{\theta}_i\|\psi_i(\zeta_i)\|^2 \quad (11.14)$$

$$\dot{\hat{\theta}}_i = \gamma_i[0.5a_i^{-2}s_i^2\|\Psi_i(\zeta_i)\|^2 - \sigma_i\hat{\theta}_i] \quad (11.15)$$

where k_i is a design constant, a_i , γ_i and σ_i are strictly positive constants.

For the sake of clarity and convenience, let

$$B_1 = |g_1(x_1)|, F_1(\sigma, y_d) = |g_1^{-1}(\sigma + y_d)| \quad (11.16)$$

$$B_i = |g_i(\bar{x}_i)|, F_i(\sigma, \alpha_{i-1}) = |g_i^{-1}(\bar{x}_{i-1}, \sigma + \alpha_{i-1})| \quad (11.17)$$

$$G_{i,j}(\sigma, \alpha_{i-1}) = \partial |g_i^{-1}(\bar{x}_{i-1}, \sigma + \alpha_{i-1})| / \partial x_j \quad (11.18)$$

$$K_i(t) = g_i(\bar{x}_i)B_i^{-1} \quad (11.19)$$

where $j = 1, \dots, i-1, i = 2, \dots, n$.

Step 1: According to the second mean value theorem, there exists $\lambda_1 \in (0, 1)$ such that $\int_0^{s_1} F_1(\sigma, y_d)\sigma d\sigma$ can be rewritten as $\int_0^{s_1} F_1(\sigma, y_d)\sigma d\sigma = 0.5s_1^2 F_1(\lambda_1 s_1, y_d)$. Due to $0 < g_{\min} \leq |g_i(\cdot)| \leq g_{\max}$, it is shown that $\int_0^{s_1} F_1(\sigma, y_d)\sigma d\sigma$ is positive definite with respect to s_1 . Differentiating s_1 with respect to t , we obtain

$$\dot{s}_1 = \dot{x}_1 = f_1(\bar{x}_1) + g_1(\bar{x}_1)x_2 + \Delta_1(x, z, t) - \dot{y}_d \quad (11.20)$$

The time derivative of V_{s_1} is:

$$\dot{V}_{s_1} = B_1^{-1}s_1\dot{s}_1 + \dot{y}_d \left[B_1s_1 - \int_0^{s_1} F_1(\sigma, y_d)d\sigma \right] + \lambda_0^{-1}\bar{\gamma}(|x_1|) + d\lambda_0^{-1} - \bar{c}\lambda_0^{-1}v \quad (11.21)$$

According to Assumption 1, using Young's inequality, we obtain

$$|s_1\Delta_1(x, z, t)| \leq |s_1|\phi_{11}(|\bar{x}_1|) + |s_1|\phi_{12}(|z|) \quad (11.22)$$

$$B_1^{-1}|s_1|\phi_{11}(|\bar{x}_1|) \leq s_1^2\phi_{11}^2(|\bar{x}_1|)\varepsilon_1^{-2}B_1^{-2} + 0.25\varepsilon_1^2 \quad (11.23)$$

Because of $\alpha_1(\cdot)$ being class of k_∞ -functions, it's seen that $\alpha_1^{-1}(\cdot)$ is also a single-increasing function. Noting Assumption 2 and Lemma 1, we have

$$\|z\| \leq \alpha_1^{-1}(v(t) + D(t_0, t)) \quad (11.24)$$

$$\phi_{12}(\|z\|) \leq \phi_{12} \circ \alpha_1^{-1}(v(t) + D(t_0, t)) \quad (11.25)$$

where $\phi_{12} \circ \alpha_1^{-1}(\cdot) = \phi_{12}(\alpha_1^{-1}(\cdot))$. Noticing that $\phi_{12} \circ \alpha_1^{-1}(\cdot)$ is a non-negative smooth function, and using Lemma 2, we have

$$|s_1|\phi_{12}(\|z\|) \leq |s_1|\phi_{12} \circ \alpha_1^{-1}(v(t) + D(t_0, t)) \leq |s_1|\varphi_1(v(t)) + |s_1|\vartheta_1(D(t_0, t)) \quad (11.26)$$

Similar to the inequalities (11.23), from Young's inequalities, we obtain

$$B_1^{-1}|s_1|\varphi_1(v(t)) \leq s_1^2\varphi_1^2(v(t))\varepsilon_{\varphi_1}^{-2}B_1^{-2} + 0.25\varepsilon_{\varphi_1}^2 \quad (11.27)$$

$$B_1^{-1}|s_1|\vartheta_1(D(t_0, t)) \leq s_1^2\vartheta_1^2(D(t_0, t)) + 0.25\vartheta_1^2(D(t_0, t)) \quad (11.28)$$

From Lemma 1, it is shown that $D(t_0, t)$ turns to be zero, when $t \geq t_0 + T_0$. We assume that $\vartheta_i^2(D(t_0, t)) \leq \vartheta_i^*$, $i = 1, 2, \dots, n$, due to $D(t_0, t)$ and $\vartheta_i(\cdot)$ being smooth functions to be bounded. From Young's inequality, we obtain

$$K_1(t)s_1s_2 \leq s_1^2 + 0.25s_2^2 \quad (11.29)$$

$$s_1w_1(\xi_1) \leq s_1^2 + 0.25w_1^2(\xi_1) \leq s_1^2 + 0.25w_1^{*2} \quad (11.30)$$

Substituting (11.23) (11.27) and (11.28) into (11.21), we have

$$\begin{aligned} \dot{V}_{s_1} \leq & K_1(t)s_1x_2 + s_1h_1(\xi_1) + \left[1 - s_1^2/\varepsilon_{\bar{\gamma}}^2 \right] \lambda_0^{-1}\bar{\gamma}(|x_1|) \\ & - \bar{c}\lambda_0^{-1}v + d\lambda_0^{-1} + 0.25\varepsilon_1^2 + 0.25\varepsilon_{\varphi_1}^2 + 0.25\vartheta_1^* \end{aligned} \quad (11.31)$$

where $h_1(\xi_1) = B_1^{-1}f_1(\bar{x}_1) + s_1\varphi_1^2(v(t))B_1^{-2}\varepsilon_{\varphi_1}^{-2} + s_1\phi_{11}^2(|\bar{x}_1|)B_1^{-2}\varepsilon_1^{-2} + s_1B_1^{-2}$

$$-\dot{y}_d s_1^{-1} \int_0^{s_1} F_1(\sigma, y_d) d\sigma + \lambda_0^{-1} s_1 \bar{\gamma}(|x_1|) \varepsilon_{\bar{\gamma}}^{-2}.$$

In the above inequalities, $\varepsilon_{\bar{\gamma}}$ is a positive constant. Substituting (11.29) and (11.30) into (11.31), we have:

$$\begin{aligned} \dot{V}_{s_1} \leq & K_1(t) s_1 \alpha_1 + 2s_1^2 + s_1^2 \theta_1 \|W_1(\zeta_1)\|^2 / a_1^2 + 0.25s_2^2 + 0.25w_1^{*2} + 0.25a_1^2 \\ & - \bar{c} \lambda_0^{-1} v + d \lambda_0^{-1} + 0.25\varepsilon_1^2 + 0.25\varepsilon_{\varphi_1}^2 + 0.25\vartheta_1^* + \left[1 - s_1^2 \varepsilon_{\bar{\gamma}}^{-2}\right] \lambda_0^{-1} \bar{\gamma}(|x_1|) \end{aligned} \quad (11.32)$$

Substituting (11.13) and (11.14) into (11.32), we obtain:

$$\begin{aligned} \dot{V}_{s_1} \leq & [K_1(t)N(\zeta_1) + 1] \dot{\zeta}_1 - (k-2)s_1^2 + s_1^2 \tilde{\theta}_1 \|W_1(\zeta_1)\|^2 / 2a_1^2 - \bar{c} \lambda_0^{-1} v + 0.25s_2^2 \\ & + 0.25\varepsilon_1^2 + 0.25\varepsilon_{\varphi_1}^2 + 0.5a_1^2 + 0.25\vartheta_1^* + 0.25w_1^{*2} + d \lambda_0^{-1} + \left[1 - s_1^2 \varepsilon_{\bar{\gamma}}^{-2}\right] \lambda_0^{-1} \bar{\gamma}(|x_1|) \end{aligned} \quad (11.33)$$

Differentiating V_1 with respect to time t , moreover, substituting (11.15) and (11.33) into (11.12), we have

$$\begin{aligned} \dot{V}_1 \leq & [K_1(t)N(\zeta_1) + 1] \dot{\zeta}_1 - (k_1-2)s_1^2 - 0.5\sigma_1 \tilde{\theta}_1^2 + 0.25s_2^2 - \bar{c} \lambda_0^{-1} v + 0.25w_1^{*2} + 0.5a_1^2 \\ & + d \lambda_0^{-1} + 0.25\varepsilon_1^2 + 0.25\varepsilon_{\varphi_1}^2 + 0.25\vartheta_1^* + 0.5\sigma_1 \theta_1^2 + \left[1 - s_1^2 \varepsilon_{\bar{\gamma}}^{-2}\right] \lambda_0^{-1} \bar{\gamma}(|x_1|). \end{aligned} \quad (11.34)$$

Define $c_{11} = \min\{2(k_1-2), \gamma_1 \sigma_1, \bar{c}\}$, $c_{12} = 0.5\sigma_1 \theta_1^2 + 0.25w_1^{*2} + 0.5a_1^2 + d \lambda_0^{-1} + 0.25\varepsilon_1^2 + 0.25\varepsilon_{\varphi_1}^2 + 0.25\vartheta_1^*$. From inequality (11.34), we obtain:

$$\dot{V}_1 \leq [K_1(t)N(\zeta_1) + 1] \dot{\zeta}_1 - c_{11} V_1 + c_{12} + 0.25s_2^2 + \left[1 - s_1^2 \varepsilon_{\bar{\gamma}}^{-2}\right] \lambda_0^{-1} \bar{\gamma}(|x_1|) \quad (11.35)$$

Multiplying (11.35) by $e^{c_{11}t}$, it becomes:

$$\begin{aligned} d(V_1(t)e^{c_{11}t})/dt \leq & c_{12}e^{c_{11}t} + [K_1(t)N(\zeta_1) + 1] \dot{\zeta}_1 e^{c_{11}t} \\ & + 0.25s_2^2 e^{c_{11}t} + \left[1 - s_1^2 \varepsilon_{\bar{\gamma}}^{-2}\right] \lambda_0^{-1} \bar{\gamma}(|x_1|) e^{c_{11}t} \end{aligned} \quad (11.36)$$

Integrating (11.36) over $[0, t]$, we have:

$$\begin{aligned} V_1(t) \leq & c_{13} + V_1(0) + \int_0^t ([K_1(t)N(\zeta_1) + 1] \dot{\zeta}_1 e^{c_{11}(t-\tau)}) d\tau \\ & + 0.25e^{-c_{11}t} \int_0^t s_2^2 e^{c_{11}\tau} d\tau + e^{-c_{11}t} \int_0^t \left[1 - s_1^2 \varepsilon_{\bar{\gamma}}^{-2}\right] \lambda_0^{-1} \bar{\gamma}(|x_1|) e^{c_{11}\tau} d\tau \end{aligned} \quad (11.37)$$

where $c_{13} = c_{11}^{-1}c_{12}$. Note that

$$e^{-c_{11}t} \int_0^t s_2^2 e^{c_{11}\tau} d\tau \leq c_{11}^{-1} \sup_{\tau \in [0,t]} [s_2^2(\tau)] \quad (11.38)$$

Therefore, if s_2^2 can be regulated to be bounded, we easily notice from inequality (11.38) that, the extra term $0.25e^{-c_{11}t} \int_0^t s_2^2 e^{c_{11}\tau} d\tau$ can be bounded. The effect of $0.25e^{-c_{11}t} \int_0^t s_2^2 e^{c_{11}\tau} d\tau$ will be handled with in the following steps. The other extra term will be discussed in the last of the paper.

Step i ($2 \leq i \leq n-1$): The time derivative of s_i is:

$$\dot{s}_i = f_i(\bar{x}_i) + g_i(\bar{x}_i)x_{i+1} + \Delta_i(x, z, t) - \dot{\alpha}_{i-1} \quad (11.39)$$

Because α_{i-1} is a function of $\bar{x}_{i-1}, \zeta_1, \dots, \zeta_{i-1}, \bar{x}_{id}, \hat{\theta}_1, \dots, \hat{\theta}_{i-1}, v, \dot{\alpha}_{i-1}$ can be expressed as $\dot{\alpha}_{i-1} = \sum_{j=1}^{i-1} \frac{\partial \alpha_{i-1}}{\partial x_j} [f_j(\bar{x}_j) + g_j(\bar{x}_j) + \Delta_j(x, z, t)] + \omega_{i-1}(t)$, where

$$\omega_{i-1}(t) = \sum_{j=1}^{i-1} \frac{\partial \alpha_{i-1}}{\partial \zeta_j} \dot{\zeta}_j + \frac{\partial \alpha_{i-1}}{\partial \bar{x}_{(i-1)d}} \dot{\bar{x}}_{(i-1)d} + \sum_{j=1}^{i-1} \frac{\partial \alpha_{i-1}}{\partial \hat{\theta}_j} \dot{\hat{\theta}}_j + \sum_{j=1}^{i-1} \frac{\partial \alpha_{i-1}}{\partial v} \dot{v} \quad (11.40)$$

The time derivative of V_{s_i} is

$$\begin{aligned} \dot{V}_{s_i} &= B_i^{-1} s_i \dot{s}_i + \dot{\alpha}_{i-1} [B_i^{-1} s_i - \int_0^{s_i} F_i(\sigma, \alpha_{i-1}) d\sigma] \\ &\quad + \sum_{j=1}^{i-1} \int_0^{s_i} \sigma G_{i,j}(\sigma, \alpha_{i-1}) (f_j(\bar{x}_j) + g_j(\bar{x}_j)x_{j+1} + \Delta_j(x, z, t)) d\sigma \end{aligned} \quad (11.41)$$

Using Assumption 1, we have:

$$\begin{aligned} &|s_i| \left| \Delta_i(x, z, t) - \sum_{j=1}^{i-1} \frac{\partial \alpha_{i-1}}{\partial x_j} \Delta_j(x, z, t) \right. \\ &\quad \left. + |s_i| \left| \sum_{j=1}^{i-1} \int_0^1 \eta G_{i,j}(\eta s_i, \alpha_{i-1}) \Delta_j(x, z, t) d\eta \right| \leq |s_i| \left[\bar{\phi}_{i1}(|\bar{x}_i|) + \bar{\phi}_{i2}(|z|) \right] \end{aligned} \quad (11.42)$$

where $\bar{\phi}_{i1}(|\bar{x}_i|) \geq \phi_{i1} + \sum_{j=1}^{i-1} \left| \frac{\partial \alpha_{i-1}}{\partial x_j} \right| \phi_{j1}$, $\bar{\phi}_{i2}(|z|) \geq \phi_{i2} + \sum_{j=1}^{i-1} \left| \frac{\partial \alpha_{i-1}}{\partial x_j} \right| \phi_{j2}$.

Similar to step 1, and according to Lemma 2, we have

$$|s_i| \phi_{i2}(|z|) \leq |s_i| \phi_i(v(t)) + |s_i| \vartheta_i(D(t_0, t)) \quad (11.43)$$

Furthermore, applying Young's inequality, we have:

$$B_i^{-1} |s_i| \phi_{i1}(|\bar{x}_i|) \leq B_i^{-2} \varepsilon_i^{-2} s_i^2 \phi_{i1}^2(|\bar{x}_i|) + 0.25 \varepsilon_i^2 \quad (11.44)$$

$$B_i^{-1} |s_i| \varphi_i(v(t)) \leq B_i^{-2} \varepsilon_{\phi_i}^{-2} s_i^2 \varphi_i^2(v(t)) + 0.25 \varepsilon_{\phi_i}^{-2} \quad (11.45)$$

$$B_i^{-1} |s_i| \vartheta_i(D(t_0, t)) \leq B_i^{-2} s_i^2 + 0.25 \vartheta_i^2(D(t_0, t)) \quad (11.46)$$

$$K_i(t) s_i s_{i+1} \leq s_i^2 + 0.25 s_{i+1}^2 \quad (11.47)$$

$$s_i w_i(\xi_i) \leq s_i^2 + 0.25 w_i^2(\xi_i) \leq s_i^2 + 0.25 w_i^{*2} \quad (11.48)$$

where $i = 1, \dots, n$. From Lemma 1, we notice that when $t \geq t_0 + T_0$, $D(t_0, t)$ turns to be zero. $D(t_0, t)$ and $\vartheta_1(\cdot)$ are smooth functions. Thus there exists a unknown positive constant ϑ_i^* such that $\vartheta_i^2(D(t_0, t)) \leq \vartheta_i^*$. Let

$$\begin{aligned} h_i(\xi_i) &= B_i^{-1} f_i(\bar{x}_i) + B_i^{-2} \varepsilon_i^{-2} s_i \phi_{i1}^2(|\bar{x}_i|) + B_i^{-2} s_i \varepsilon_{\phi_i}^{-2} \varphi_i^2(v(t)) + B_i^{-2} s_i \\ &\quad + s_i \sum_{j=1}^{i-1} \int_0^1 \eta G_{i,j}(f_j(\bar{x}_j) + g_j(\bar{x}_j) x_{j+1}) d\eta - s_i^{-1} \dot{\alpha}_{i-1} \int_0^{s_i} F_i(\sigma, \alpha_{i-1}) d\sigma \end{aligned} \quad (11.49)$$

where $\xi_i = [\bar{x}_i^T, \alpha_{i-1}, \frac{\partial \alpha_{i-1}}{\partial x_1}, \frac{\partial \alpha_{i-1}}{\partial x_2}, \dots, \frac{\partial \alpha_{i-1}}{\partial x_{i-1}}, \omega_{i-1}, v]^T \in \Omega_{s_i} \subset R^{2i+2}$. Substituting (11.42)–(11.46) into (11.41), we obtain

$$\dot{V}_i \leq K_i(t) s_i x_{i+1} + s_i h_i(\xi_i) + 0.25 \varepsilon_i^2 + 0.25 \varepsilon_{\phi_i}^2 + 0.25 \vartheta_i^* \quad (11.50)$$

Similar to the discussion in the step 1, substituting (11.47) and (11.48) into (11.50), we have

$$\begin{aligned} \dot{V}_i &\leq [K_i(t) N(\zeta_i) + 1] \dot{\zeta}_i - (k_i - 2) s_i^2 - 0.5 \sigma_i \tilde{\theta}_i^2 + 0.5 \sigma_i \theta_i^2 \\ &\quad + 0.25 s_{i+1}^2 + 0.25 w_i^{*2} + 0.5 a_i^2 + 0.5 \varepsilon_i^2 + 0.25 \varepsilon_{\phi_i}^2 + 0.25 \vartheta_i^* \end{aligned} \quad (11.51)$$

Define $c_{i1} = \min\{2(k_i - 2), \gamma_i \sigma_i\}$, $c_{i2} = 0.5 \sigma_i \theta_i^2 + 0.25 w_i^{*2} + 0.5 a_i^2 + 0.25 \varepsilon_i^2 + 0.25 \varepsilon_{\phi_i}^2 + 0.25 \vartheta_i^*$. From the above inequality, we have

$$\dot{V}_i \leq [K_i(t) N(\zeta_i) + 1] \dot{\zeta}_i - c_{i1} V_i + c_{i2} + 0.25 s_{i+1}^2 \quad (11.52)$$

Multiplying (11.52) by $e^{c_{i1} t}$, we obtain

$$d(V_i(t) e^{c_{i1} t})/dt \leq c_{i2} e^{c_{i1} t} + [K_i(t) N(\zeta_i) + 1] \dot{\zeta}_i e^{c_{i1} t} + 0.25 s_{i+1}^2 e^{c_{i1} t} \quad (11.53)$$

Integrating (11.53) over $[0, t]$, we have

$$V_i(t) \leq c_{i3} + V_i(0) + \int_0^t ([K_i(\tau) N(\zeta_i) + 1] \dot{\zeta}_i e^{c_{i1}(\tau-t)}) d\tau + 0.25 c_{i1}^{-1} \sup_{\tau \in [0, t]} [s_{i+1}^2(\tau)] \quad (11.54)$$

where $c_{i3} = c_{i1}^{-1} c_{i2}$.

Step n : The time derivative of s_n is

$$\dot{s}_n = f_n(\bar{x}_n) + g_n(\bar{x}_n)u + \Delta_n(x, z, t) - \dot{\alpha}_{n-1} \quad (11.55)$$

where α_{n-1} is a function of \bar{x}_{n-1} , $\zeta_1, \dots, \zeta_{n-1}$, \bar{x}_{nd} , $\hat{\theta}_1, \dots, \hat{\theta}_{n-1}$ and v , $\dot{\alpha}_{i-1}$ can be expressed as $\dot{\alpha}_{n-1} = \sum_{j=1}^{n-1} \frac{\partial \alpha_{n-1}}{\partial x_j} [f_j(\bar{x}_j) + g_j(\bar{x}_j) + \Delta_j(x, z, t)] + \omega_{n-1}(t)$, where

$$\omega_{n-1}(t) = \sum_{j=1}^{n-1} \frac{\partial \alpha_{n-1}}{\partial \zeta_j} \dot{\zeta}_j + \frac{\partial \alpha_{n-1}}{\partial \bar{x}_{(n-1)d}} \dot{\bar{x}}_{(n-1)d} + \sum_{j=1}^{n-1} \frac{\partial \alpha_{n-1}}{\partial \hat{\theta}_j} \dot{\hat{\theta}}_j + \sum_{j=1}^{n-1} \frac{\partial \alpha_{n-1}}{\partial v} \dot{v} \quad (11.56)$$

Differentiating V_{s_n} with respect to time t , we obtain

$$\begin{aligned} \dot{V}_{s_n} &= B_n^{-1} s_n \dot{s}_n + \dot{\alpha}_{n-1} \left[B_n^{-1} s_n - \int_0^{s_n} F_n(\sigma, \alpha_{n-1}) d\sigma \right] \\ &\quad + \sum_{j=1}^{n-1} \int_0^{s_n} \sigma G_{i,j}(\sigma, \alpha_{i-1}) (f_j(\bar{x}_j) + g_j(\bar{x}_j) x_{j+1} + \Delta_j(x, z, t)) d\sigma \end{aligned} \quad (11.57)$$

Similar to step i , let

$$\begin{aligned} h_n(\zeta_n) &= B_n^{-1} f_n(\bar{x}_n) + B_n^{-2} \varepsilon_n^{-2} s_n \phi_{n1}^2(|\bar{x}_n|) + B_n^{-2} \varepsilon_{\varphi n}^{-2} s_n \varphi_n^2(v(t)) + B_n^{-2} s_n \\ &\quad + s_n \sum_{j=1}^{n-1} \int_0^1 \eta G_{n,j} (f_j(\bar{x}_j) + g_j(\bar{x}_j) x_{j+1}) d\eta - s_n^{-1} \dot{\alpha}_{n-1} \int_0^{s_n} F_n(\sigma, \alpha_{n-1}) d\sigma \end{aligned} \quad (11.58)$$

where $\zeta_n = [\bar{x}_n^T, \alpha_{n-1}, \frac{\partial \alpha_{n-1}}{\partial x_1}, \frac{\partial \alpha_{n-1}}{\partial x_2}, \dots, \frac{\partial \alpha_{n-1}}{\partial x_{n-1}}, \omega_{n-1}, v]^T \in \Omega_{s_n} \subset R^{2n+2}$.

Substituting (11.42)-(11.46) into (11.57) yields,

$$\dot{V}_{s_n} \leq K_n(t) s_n u + s_n B_n^{-1} h_n(\zeta_n) + \varepsilon_n^2 + 0.25 \varepsilon_{\varphi n}^2 + 0.25 v_n^* \quad (11.59)$$

Similar to the discussion in step i , substituting (11.47) and (11.48) into (11.59), we have

$$\begin{aligned} \dot{V}_n &\leq [K_n(t)N(\zeta_n) + 1] \dot{\zeta}_n - (k_n - 1) s_n^2 - 0.5 \sigma_n \tilde{\theta}_n^2 + 0.5 \sigma_n \theta_n^2 \\ &\quad + 0.25 w_n^{*2} + 0.5 a_n^2 + 0.25 \varepsilon_n^2 + 0.25 \varepsilon_{\varphi n}^2 + 0.25 v_n^* \end{aligned} \quad (11.60)$$

Define $c_{n1} = \min\{2(k_n - 1), \gamma_n \sigma_n\}$, $c_{n2} = 0.5 \sigma_n \theta_n^2 + 0.25 w_n^{*2} + 0.5 a_n^2 + .25 \varepsilon_n^2 + 0.25 \varepsilon_{\varphi n}^2 + 0.25 v_n^*$. The above inequality can be rewritten as

$$\dot{V}_n \leq [K_n(t)N(\zeta_n) + 1] \dot{\zeta}_n - c_{n1} V_n + c_{n2} \quad (11.61)$$

Multiplying (11.61) by $e^{c_{n1}t}$, we obtain

$$d(V_n(t)e^{c_{n1}t})/dt \leq c_{n2}e^{c_{n1}t} + [K_n(t)N(\zeta_n) + 1] \dot{\zeta}_n e^{c_{n1}t} \quad (11.62)$$

Integrating (11.62) over $[0, t]$, we have:

$$V_n(t) \leq c_{n3} + V_n(0) + \int_0^t ([K_n(\tau)N(\zeta_n) + 1] \dot{\zeta}_n e^{c_{n1}(t-\tau)}) d\tau \quad (11.63)$$

where $c_{n3} = c_{n1}^{-1} c_{n2}$.

Theorem 1 Consider the closed-loop system consisting of plant (11.1) under Assumptions 1–4, the control law (11.13) for $i = n$, and the adaptation laws (11.14)–(11.15). Then for the bounded initial conditions, the following properties hold:

- (1) All signals in the closed-loop system are semi-globally uniformly ultimately bounded.
- (2) The vector ξ_i stays in the compact set $\Omega_{\xi_i} \subset R^{2i+1}$, specified as

$$\Omega_{\xi_i} = \left\{ \xi_i | s_j^2 \leq 2g_{\max} \mu_j, \|\tilde{\theta}_j\|^2 \leq 2\gamma_j \mu_j, j = 1, \dots, i, v \leq \lambda_0 \mu_1, s_{i+1}^2 \leq 2g_{\max} \mu_{i+1} \right\}$$

$$\Omega_{\xi_n} = \left\{ \xi_n | s_j^2 \leq 2g_{\max} \mu_j, \|\tilde{\theta}_j\|^2 \leq 2\gamma_j \mu_j, \bar{x}_{jd} \in \Omega_{jd}, j = 1, \dots, n, v \leq \lambda_0 \mu_1 \right\}.$$

Proof Similar to the discussion in Ref. [4], the conclusion is true.

11.4 Conclusion

Based on the backstepping design and the Nussbaum function properties, an adaptive neural control scheme is proposed for a class of strict feedback nonlinear systems including unmodeled dynamics. In this paper, an available dynamic signal is introduced to dominate the unmodeled dynamics. Moreover, the unknown control direction and the unknown function control gain are dealt with using the property of Nussbaum function. The controller singularity problem is avoided using integral Lyapunov function, which may be caused by time-varying gain functions. The processing procedure of unmodeled dynamics is simplified. By theoretical analysis, the developed controller can guarantee that all the signals involved are semi-globally uniformly ultimately bounded.

Acknowledgments This work was partially supported by the National Natural Science Foundation of China (61174046 & 61175111).

References

1. Nussbaum RD (1983) Some remarks on the conjecture in parameter adaptive control. Syst Control Lett 3(3):243–246
2. Zhang T, Ge SS, Hang CC (2000) Stable adaptive control for a class of nonlinear systems using a modified Lyapunov function. IEEE Trans Autom Control 45(1):129–132

3. Zhang TP, Ge SS (2007) Adaptive neural control of MIMO nonlinear state time-varying delay systems with unknown nonlinear dead-zones and gain signs. *Automatica* 43(6):1021–1033
4. Zhang TP, Zhu Q, Yang YQ (2012) Adaptive neural control of non-affine pure-feedback nonlinear systems with input nonlinearity and perturbed uncertainties. *Int J Syst Sci* 43(4):691–706
5. Jiang ZP, Hill DJ (1999) A Robust Adaptive backstepping scheme for nonlinear systems with unmodeled dynamics. *IEEE Trans Autom Control* 44(9):1705–1711
6. Jiang ZP, Praly L (1998) Design of robust adaptive controllers for nonlinear systems with dynamic uncertainties. *Automatica* 34(7):825–840
7. Zhang TP, Lu Y (2012) Adaptive dynamic surface control of nonlinear systems with unmodeled dynamics. *Control Decision* 27(3):335–342
8. Jiang ZP (1999) A combined backstepping and small-gain approach to adaptive output feedback control. *Automatica* 35(6):1131–1139
9. Tong SC, Li YM (2009) Fuzzy adaptive robust control for a class of nonlinear systems with unmodeled dynamics. *Control Decision* 24(3):417–422
10. Zhang XY, Lin Y (2011) Adaptive tracking control for a class of pure-feedback nonlinear systems including actuator hysteresis and dynamic uncertainties. *IET Control Theory Appl* 5(16):1868–1880
11. Tong SC, Li YM (2010) Fuzzy adaptive robust backstepping stabilization for SISO nonlinear systems with unknown virtual control direction. *Inf Sci* 180(23):4619–4640
12. Lin W, Qian CJ (2002) Adaptive control of nonlinearly parameterized systems: a non-smooth feedback framework. *IEEE Trans Autom Control* 47(5):757–774
13. Ge SS, Hong F, Lee TH (2004) Adaptive neural control of nonlinear time-delay system with unknown virtual control coefficients. *IEEE Trans Syst Man Cybernetics Part B Cybernetics* 34(1):499–516
14. Ryan EP (1991) A universal adaptive stabilizer for a class of nonlinear systems. *Syst Control Lett* 16(3):209–218

Chapter 12

Generalized Projective Synchronization of Takagi–Sugeno Fuzzy Drive-Response Dynamical Networks with Time Delay

Yongai Zheng and Lei Shang

Abstract This paper defines the Takagi–Sugeno fuzzy drive-response dynamical networks with time delay (TSFDRDNs) by extending the drive-response dynamical networks. An fuzzy impulsive control scheme is adapted to synchronize the TSFDRDNs to a desired scalar factor. By using the stability theory of the impulsive differential equation, the criteria for the generalized projective synchronization are derived. Moreover, numerical simulations are provided to verify the correctness and effectiveness of the scheme.

Keywords Generalized projective synchronization · Impulsive control · T-S fuzzy model · Delayed network

12.1 Introduction

Since the pioneering work by Pecora and Carroll [1], much attention has been devoted to research on synchronization of chaos. Amongst all kinds of chaos synchronization, projective synchronization (PS) proposed by Mainieri and Rehacek [2] in partially linear systems that the master and slave vectors synchronize up to a constant scaling factor α (α proportional relation), is the most noticeable due to its proportionality between the synchronized dynamical states. In the early study of projective synchronization, the investigated chaotic systems must be the coupled partially linear systems [3]. Later, some researchers extended it to generalized projective synchronization (GPS). However, most existing studies pertaining to PS or GPS have mainly concentrated on two coupled chaotic systems. Recently, the PS of more than two chaotic systems has obtained much more attention. In [4], Hu et al.

Y. Zheng (✉) · L. Shang
College of Information Engineering, Yangzhou University, Yangzhou, China
e-mail: zhengyongai@163.com

studied a drive-response dynamical networks model with $n + 1$ partially linear systems and pinning control techniques are adopted to direct the scaling factor onto the desire value. Zhao and Yang [5] proposed an impulsive control scheme to realize the PS in drive-response dynamical networks of partially linear systems. Using a linear controller and an updated law, Sun et al. [6] realized the PS in drive-response dynamical networks of partially linear systems with time-varying coupling delay.

On the other hand, The well-known Takagi–Sugeno (TS) systems [7] have shown to be a popular and convenient tool to deal with the analysis and synthesis problems for complex nonlinear systems. This class of systems is described as a weighted sum of some simple linear subsystems, and thus is easily analyzed. Based on the TS fuzzy model, some systematic model-based fuzzy control and synchronization methods to chaos systems have been developed. For example, Lian et al. [8] represent many well-know chaotic systems by TS fuzzy models and design the local linear feedback controllers for the control and synchronization of these chaotic fuzzy systems using parallel-distributed compensation scheme. Zheng and Chen [9] present a few fuzzy impulsive control schemes for control of chaotic systems combining TS fuzzy model and impulsive control. Kim et al. [10] propose a fuzzy model-based adaptive approach for synchronization of chaotic systems with unknown parameters.

In this paper, we introduce a kind of novel drive-response dynamical network with time delay, whose nodes are chaotic systems represented by TS fuzzy models, called TS fuzzy drive-response dynamical networks with time coupling delay (TSFDRDNs). We discuss GPS in TSFDRDNs. By using the fuzzy impulsive control technique, TSFDRDNs can be easily synchronized to a given scaling factor in advance. Some criteria for the generalized projective synchronization are derived.

12.2 Model Description and Preliminaries

The TS fuzzy drive-response dynamical network with time coupling delay, whose nodes are chaotic systems represented by TS fuzzy models, are described by the following equations:

Rule i : IF $z_1(t)$ is M_{i1} and...and $z_p(t)$ is M_{ip} , THEN $\dot{x}(t) = A_i x(t)$, $i = 1, 2, \dots, r$,

Rule i : IF $z_1(t)$ is M_{i1} and...and $z_p(t)$ is M_{ip} ,

$$\text{THEN} \begin{cases} \dot{y}_j(t) = A_i y_j(t) + \sum_{l=1}^N c_{jl} \Gamma_l y_l(t - \tau), \quad t \neq t_k \\ \Delta y_j(t_k) = y_j(t_k^+) - y_j(t_k^-) = B_i y_j((t_k^-) - \alpha x(t_k^-)), \\ t = t_k, i = 1, 2, \dots, r, j = 1, 2, \dots, N, k = 1, 2, \dots, \end{cases} \quad (12.1)$$

where the premise variables $z_1(t), \dots, z_p(t)$ are proper state variables, $M_{ij}(j = 1, 2, \dots, p)$ is the fuzzy set and r is the number of IF–THEN rules, $x(t) \in$

R^n and $y_j(t) \in R^n$ are the state vectors, A_i and B_i are system matrices with appropriate dimensions, $\Gamma \in R^{n \times n}$ is inner-coupling matrix and $C = (c_{ij})_{N \times N} \in R^{N \times N}$ is coupling configuration matrix. If there is a connection from node i to node j ($j \neq i$), then $c_{ij} \neq 0$; otherwise $c_{ij} = 0$ ($j \neq i$), and the diagonal elements of matrix C are defined $c_{ij} = -\sum_{j=1, j \neq i}^N c_{ij}$, $i = 1, 2, \dots, N$.

The final output of the fuzzy system (12.1) is inferred as follow:

$$\begin{cases} \dot{x}(t) = \sum_{i=1}^r h_i(z(t))A_i x(t), \\ \dot{y}_j(t) = \sum_{i=1}^r h_i(z(t))A_i y_j(t) + \sum_{l=1}^N c_{jl} \Gamma y_l(t - \tau), t \neq t_k, \\ \Delta y_j(t_k) = y_j(t_k^+) - y_j(t_k^-) = \sum_{i=1}^r h_i(z(t_k))B_i(y_j(t_k^-) - \alpha x(t_k^-)), t = t_k, i = 1, 2, \dots, r, j = 1, 2, \dots, N, k = 1, 2, \dots, \end{cases} \quad (12.2)$$

where $h_i(z(t)) = \omega_i(z(t)) / \sum_{i=1}^r \omega_i(z(t))$, $\omega_i(z(t)) = \prod_{j=1}^p M_{ij}(z_j(t))$, and $\omega_i(z(t)) \geq 0$, $\sum_{i=1}^r \omega_i(z(t)) > 0$, thus $h_i(z(t)) \geq 0$, $\sum_{i=1}^r h_i(z(t)) = 1$.

Define the synchronization errors $e_j(t) = y_j(t) - \alpha x(t)$ (α is a scaling factor), (12.2) can be rewritten as:

$$\begin{cases} \dot{e}_j(t) = \sum_{i=1}^r h_i(z(t))A_i e_j(t) + \sum_{l=1}^N c_{jl} \Gamma e_l(t - \tau), t \neq t_k, \\ \Delta e_j(t_k) = e_j(t_k^+) - e_j(t_k^-) = \sum_{i=1}^r h_i(z(t_k))B_i e_j(t_k^-), t = t_k \\ i = 1, 2, \dots, r, j = 1, 2, \dots, N, k = 1, 2, \dots \end{cases} \quad (12.3)$$

Definition 1 The error system (12.3) is said to realize GPS, if synchronization errors $e_j(t)$ such that $\lim_{t \rightarrow \infty} \|e_j(t)\| = \lim_{t \rightarrow \infty} \|y_j(t) - \alpha x(t)\| = 0$ for any $j(1 \leq j \leq N)$. Let $S_\rho = \{x \in R^n : \|x\| < \rho\}$, $K = \{\varphi \in C(R^+, R^+) : \varphi(t) \text{ is strictly increasing and } \varphi(0) = 0\}$, $K^* = \{\varphi \in K : \varphi(t) < t \text{ for all } t > 0\}$, $\Sigma = \{\varphi \in C(R^+, R^+) : \varphi(0) = 0, \varphi(t) > 0 \text{ for } t > 0\}$, $PC = \{\varphi : [-\tau, 0] \rightarrow R^n, \varphi(t) \text{ is continuous everywhere except at the finite number of points } \bar{\tau}, \text{ at which } \varphi(\bar{\tau}^+) \text{ and } \varphi(\bar{\tau}^-) \text{ exist and } \varphi(\bar{\tau}^+) = \varphi(\bar{\tau}^-)\}$.

System (12.3) can be categorized as a kind of the following impulsive functional differential equation:

$$\begin{cases} \dot{x}(t) = f(t, x_t), t \neq t_k, t \geq t_0, \\ x(t_k^+) = J_k(x(t_k^-)), t = t_k, k = 1, 2, \dots, \\ x(t) = x_0 \in [-\tau, 0], \end{cases} \quad (12.4)$$

where $f : [0, \infty] \times PC \rightarrow R^n$ ensures that (12.4) has a zero solution. $J_k(x) : S_\rho \rightarrow R^n$ with $J_k(0) = 0$. $x_t(s) = x(t + s)$ for $s \in [-\tau, 0]$.

Definition 2 Let $V : [t_0, +\infty] \times S_\rho \rightarrow R^n$. Then, V is said to belong to class V_0 if

1. V is continuous in each of the sets $[t_{k-1}, t_k] \times S_\rho$ and each $x \in S_\rho$,

$$\lim_{(t,y) \rightarrow (\tau_k^-, x(t))} V(t, y) = V(\tau_k^-, x) \quad (12.5)$$

exists for $k = 1, 2, \dots$,

2. V is locally Lipschitzian in $x \in S_\rho$ and for all $t > t_0$, $V(t, 0) = 0$.

Definition 3 For $(t, x) \in (t_{k-1}, t_k] \times R^n$, define

$$D^+V(t, x) = \limsup_{h \rightarrow 0^+} \frac{1}{h} [V \leq (t + h, x(t) + hf(t, x)) - V(t, x)]. \quad (12.6)$$

Lemma 1 (See [11]) Assume that there exist $V \in V_0$, $\omega_1, \omega_2 \in K$, $\varphi \in K^*$ and $H \in \sum$ such that

1. $\omega_1(\|x\|) \leq V(t, x) \leq \omega_2(\|x\|)$ for $(t, x) \in [t_0, \infty] \times S_\rho$,
2. for all $x \in S_\rho$, $0 \leq \rho_1 \leq \rho$, $V(t_k, J_k(x)) \leq \varphi(V(t_k^-, x))$ for all k ,
3. for any solution $x(t)$ of Eq.(12.4), $V(t + s, x(t + s)) \leq \varphi(V(t, x(t)))$, $-\tau \leq s \leq 0$ implies that $D^+(V(t, x(t))) \leq g(t)H(V(t, x(t)))$, where $g : [t_0, \infty]$

$\rightarrow R^+$ is locally integrable, φ^{-1} is the inverse function of φ ,

4. H is nondecreasing and there exist constants $\lambda_2 \geq \lambda_1 \geq 0$ and $A > 0$ such that for any $\mu > 0$, $\lambda_1 \leq t_k - t_{k-1} \leq \lambda_2$ and $\int_{\varphi(\mu)}^\mu \frac{ds}{H(s)} - \int_{t_{k-1}}^{t_k} g(s)ds \geq A$,

then the zero solution of Eq. (12.4) is uniformly asymptotically stable.

Lemma 2 (See [12]) For any vectors $x, y \in R^n$ and positive definite matrix $Q \in R^{n \times n}$, the following matrix inequality holds: $2x^T y \leq x^T Q x + y^T Q^{-1} y$.

12.3 GPS in TSFDRDNs

The aim here is to investigate the generalized projective synchronization of (12.1) or (12.2) by the stability analysis of impulsive functional differential equation.

Theorem 1 Let $I_n \in R^{n \times n}$ and $I_N \in R^{N \times N}$ denote two identity matrixes, \otimes represents the Kronecker product. If there exists a symmetric and positive definite matrix P and a positive constant λ , $0 < \lambda < 1$, such that the following conditions hold:

1. $(I_n + B_i)^T P (I_n + B_i) - \lambda P < 0$,
2. $I_N \otimes (A_i^T P + P A_i) + (C \otimes (P \Gamma))^T (I_N \otimes P)^{-1} (C \otimes (P \Gamma)) + \frac{1}{\lambda} (I_N \otimes P) < \gamma (I_N \otimes P)$,
3. $\ln \lambda + \gamma \sup(t_k - t_{k-1}) < 0$,

then the origin of system (12.3) is asymptotically stable, which means the TSFDRDNs (12.1) or (12.2) can realize GPS for an arbitrary scaling factor α .

Proof Let $e(t) = (e_1^T(t), e_2^T(t), \dots, e_N^T(t))^T \in R^{nN}$ and $e(t - \tau) = (e_1^T(t - \tau), e_2^T(t - \tau), \dots, e_N^T(t - \tau))^T \in R^{nN}$. Considering a Lyapunov-like function:

$$V(t, e(t)) = \sum_{j=1}^N e_j^T(t) P e_j(t) \quad (12.7)$$

It follows from (12.7) that

$$\lambda_{\min}(P) e_j^T(t) e_j(t) \leq V(t, e(t)) \leq \lambda_{\max}(P) e_j^T(t) e_j(t) \quad (12.8)$$

Therefore,

$$\begin{aligned} V(t_k, e(t_k^+)) &= V\left(t_k, e(t_k^-) + \sum_{i=1}^r h_i(z(t)) B_i e(t_k^-)\right) = V\left(t_k, \sum_{i=1}^r h_i(z(t)) (I + B_i) e(t_k^-)\right) \\ &= \sum_{l=1}^N \sum_{i,j=1}^r h_i(z(t)) h_j(z(t)) e_l^T(t_k^-) (I + B_i)^T P (I + B_j) e_l(t_k^-) \\ &\leq \sum_{l=1}^N \sum_{i=1}^r h_i(z(t)) e_l^T(t_k^-) (I + B_i)^T P (I + B_i) e_l(t_k^-) \leq \lambda V(e(t_k^-)) \end{aligned} \quad (12.9)$$

Let $\varphi(s) = \lambda s$, then $\varphi \in K^*$. For any solution of Eq. (12.3), if $V(t + s, e(t + s)) \leq \varphi^{-1} V(t, e(t))$, $s \in [-\tau, 0]$, specially, for $s = -\tau$, we have

$$\sum_{j=1}^N e_j^T(t - \tau) P e_j(t - \tau) \leq \frac{1}{\lambda} \sum_{j=1}^N e_j^T(t) P e_j(t) \quad (12.10)$$

Taking the Dini derivative of $V(t, e(t))$ along the trajectories of Eq. (12.3) and using Kronecker product, (12.10) and Lemma 2, we have

$$\begin{aligned}
 D^+V(t, e(t)) &= 2 \sum_{j=1}^N e_j^T(t) P \dot{e}_j(t) = 2 \sum_{j=1}^N e_j^T(t) P \left[\sum_{i=1}^r h_i(z(t)) A_i e_j(t) + \sum_{l=1}^N c_{jl} \Gamma e_l(t - \tau) \right] \\
 &= \sum_{j=1}^N \sum_{i=1}^r h_i(z(t)) e_j^T(t) (A_i^T P + P A_i) e_j(t) + 2 \sum_{j=1}^N \sum_{l=1}^N c_{jl} e_j^T(t) P \Gamma e_l(t - \tau) \\
 &= \sum_{i=1}^r h_i(z(t)) e^T(t) (I_N \otimes (A_i^T P + P A_i)) e(t) + 2 e^T(t) (C \otimes (P \Gamma)) e(t - \tau) \\
 &\leq \sum_{i=1}^r h_i(z(t)) e^T(t) (I_N \otimes (A_i^T P + P A_i)) e(t) \\
 &\quad + e^T(t) (C \otimes P \Gamma)^T (I_N \otimes P)^{-1} C \otimes (P \Gamma) e(t) + e^T(t - \tau) I_N \otimes P e(t - \tau) \\
 &\leq \sum_{i=1}^r h_i(z(t)) e^T(t) \left[I_N \otimes (A_i^T P + P A_i) + (C \otimes (P \Gamma))^T (I_N \otimes P)^{-1} C \otimes (P \Gamma) + \frac{1}{\lambda} I_N \otimes P \right] e(t) \\
 &\leq \sum_{i=1}^r h_i(z(t)) e^T(t) \gamma (I_N \otimes P) e(t) = \gamma e^T(t) (I_N \otimes P) e(t) = \gamma V(t, e(t))
 \end{aligned} \tag{12.11}$$

Let $g(s) = 1$ and $H(s) = \gamma s$. Then

$$\int_{\varphi(\mu)}^{\mu} \frac{ds}{H(s)} - \int_{t_{k-1}}^{t_k} g(s) ds = -\frac{\ln \lambda}{\gamma} - (t_k - t_{k-1}) > -\frac{\ln \lambda}{\gamma} - \sup\{t_k - t_{k-1}\} > 0 \tag{12.12}$$

Based on Lemma 1, the origin of system (12.3) is asymptotically stable.

Let the impulses be equidistant and separated by interval δ , $P = I, \Gamma = I$ in Theorem 1, the following corollary holds.

Corollary 1 *Let γ_1 be the largest eigenvalue of the matrix $A_i + A_i^T$, γ_2 be the largest eigenvalue of the matrix $C^T C$, and $\lambda(0 < \lambda < 1)$ be the largest eigenvalue of the matrix $(I + B_i)^T (I + B_i)$. Then, the TSFDRDNs (12.1) or (12.2) can realize GPS for an arbitrary scaling factor α if $\ln \lambda + \left(\gamma_1 + \gamma_2 + \frac{1}{\gamma}\right) \delta < 0$.*

12.4 Numerical Simulations

In this section, we place the Rössler systems on TSFDRDNs (12.1) as an example to illustrate the derived results in the previous section and have

Rule i IF $x_1(t)$ is $F_i(x_1(t))$, THEN $\dot{x}(t) = A_i x(t), i = 1, 2$,

Rule i IF $x_1(t)$ is $F_i(x_1(t))$, THEN

$$\begin{cases} \dot{y}_j(t) = A_i y_j(t) + \sum_{l=1}^N c_{jl} \Gamma y_l(t - \tau), t \neq t_k, \\ \Delta y_j(t_k) = y_j(t_k^+) - y_j(t_k^-) = B_i(y_j(t_k^-) - \alpha x(t_k^-)), \\ t = t_k, i = 1, 2, j = 1, 2, \dots, N, k = 1, 2, \dots, \end{cases} \tag{12.13}$$

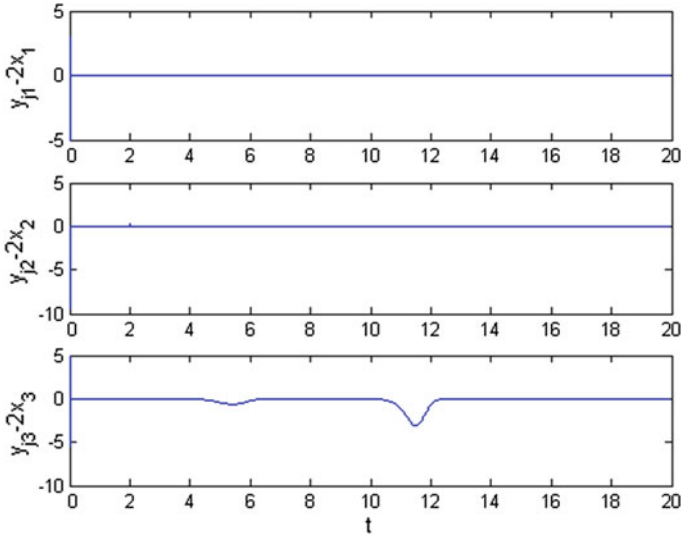


Fig. 12.1 The generalized projective synchronization errors with $\alpha = 2$ and $\tau = 2$

where $x(t) = [x_1(t), x_2(t), x_3(t)]$, $y_j(t) = [y_{j1}(t), y_{j2}(t), y_{j3}(t)]^T$, $a = 0.34$, $b = 0.4$, $c = 4.5$, $d = 10$, $\Gamma = I_3$, and $\tau = 2$,

$$A_1 = \begin{bmatrix} 0 & -1 & -1 \\ 1 & a & 0 \\ b & 0 & -d \end{bmatrix}, \quad A_2 = \begin{bmatrix} 0 & -1 & -1 \\ 1 & a & 0 \\ b & 0 & d \end{bmatrix},$$

$$B_1 = \begin{bmatrix} -0.99 & 0 & 0 \\ 0 & -0.99 & 0 \\ 0 & 0 & -0.99 \end{bmatrix}, \quad B_2 = \begin{bmatrix} -0.8 & 0 & 0 \\ 0 & -0.8 & 0 \\ 0 & 0 & -0.8 \end{bmatrix}$$

and the fuzzy sets are chosen as

$$F_1(x_1(t)) = (1/2)(1 + (c - x_1(t))/d), \quad F_2(x_1(t)) = (1/2) (1 - (c - x_1(t))/d).$$

The coupling configuration matrix

$$C = \begin{bmatrix} -1 & 1 & 2 & 3 & 4 & 5 & -5 & -4 & -3 & -2 \\ 1 & -6 & 2 & -1 & 1 & 0 & 0 & 0 & 0 & 3 \\ 2 & 2 & 0 & 0 & 0 & 0 & 0 & 0 & 0 & -4 \\ 3 & -1 & 0 & 1 & -4 & 1 & 0 & 0 & 0 & 0 \\ 4 & 1 & 0 & -4 & -10 & 2 & 3 & 4 & 0 & 0 \\ 5 & 0 & 0 & 1 & 2 & -1 & -2 & -5 & 0 & 0 \\ -5 & 0 & 0 & 0 & 3 & -2 & 2 & 5 & -3 & 0 \\ -4 & 0 & 0 & 0 & 4 & -5 & 5 & 1 & -1 & 0 \\ -3 & 0 & 0 & 0 & 0 & 0 & -3 & -1 & 8 & -1 \\ -2 & 3 & -4 & 0 & 0 & 0 & 0 & 0 & -1 & 4 \end{bmatrix}$$

For the above parameter set, we can get $0 < \delta < 0.0172$ by Corollary 1. In numerical simulations, the initial values are $(1, 2, 1, 1, 2, -1, 0.2, 2, 3, -2, 0.4, 1.5, 2.6, 4, 0.6, -3, -5, 4, 0.8, 3, 4, 5, 1.0, -3.5, 1.7, 3.2, 1.2, 1.4, 2.6, -2.8, 1.4, -5.5, 7)$ and $\delta = 0.01$. The simulation results are shown in Fig. 12.1. Figure 12.1 displays the time response of the generalized projective synchronization errors $y_{j1} - 2x_1$, $y_{j2} - 2x_2$ and $y_{j3} - 2x_3$ ($j = 1, 2, \dots, 10$), respectively.

12.5 Conclusions

This paper investigates the problem of generalized projective synchronization of Takagi–Sugeno fuzzy drive-response dynamical networks with time delay. By using the stability results for impulsive differential system, the fuzzy impulsive control method is adopted to control the desired scaling factors and some criteria are derived. A numerical simulation is given to show the effectiveness and feasibility of the proposed method.

Acknowledgments The work is supported by the National Natural Science Foundation of China (No.61074129).

References

1. Pecora LM, Carroll TL (1990) Synchronization in chaotic systems. *Phys Rev Lett* 64:821–824
2. Mainieri R, Rehacek J (1999) Projective synchronization in three dimensional chaotic systems. *Phys Rev Lett* 82:3042–3045
3. Xu D, Ong WL, Li Z (2002) Criteria for the occurrence of projective synchronization in chaotic systems of arbitrary dimension. *Phys Lett A* 305:167–172
4. Hu M, Yang Y, Xu Z, Zhang R, Guo L (2007) Projective synchronization in drive-response dynamical networks. *Phys A* 381:457–466
5. Zhao Y, Yang Y (2008) The impulsive control synchronization of the drive-response complex system. *Phys Lett A* 372:7165–7171
6. Sun M, Zeng C, Tian L (2008) Projective synchronization in drive C response dynamical networks of partially linear systems with time-varying coupling delay. *Phys Lett A* 372:6904–6908
7. Takagi T, Sugeno M (1985) Fuzzy identification of systems and its applications to modeling and control. *IEEE Trans Syst Man Cybern* 15:116–132
8. Lian KY, Chiu CS, Chiang TS, Liu P (2001) LMI-based fuzzy chaotic synchronization and communications. *IEEE Trans Fuzzy Syst* 9:539–553
9. Zheng Y, Chen G (2009) Fuzzy impulsive control of chaotic systems based on TS fuzzy model. *Chaos Solitons Fractals* 39:2002–2011
10. Kim JH, Park CW, Kim E, Park M (2005) Fuzzy adaptive synchronization of uncertain chaotic systems. *Phys Lett A* 334:295–305
11. Yan JR, Shen JH (1999) Impulsive stabilization of functional differential equations by Lyapunov C Razumikhin functions. *Nonlinear Anal* 37:245–255
12. Lu J, Cao J (2007) Synchronization-based approach for parameters identification in delayed chaotic neural networks. *Phys A* 382:672–682

Chapter 13

Immune Mobile Agent and Its Application in IDS

Tao Ji, Yongzhong Li and Jing Xu

Abstract In current distributed intrusion detection systems, data is collected mostly using distributed component to send for processing center. Data is analyzed in the processing center. Nevertheless, these models have the following problems: bad real time capability, bottleneck, and single point of failure. In addition, because of the low detecting speed and high false positive rate of traditional intrusion detection system and in order to overcome these shortcomings of current intrusion detection techniques, we have constructed an immune agent by combining immune system with mobile agent. A new distributed intrusion detection model based on mobile agent is proposed in this paper. Intelligent and mobile characteristics of the agent are used to make computing move to data. The system is robust and fault-tolerant. Because mobile agent only can improve the structure of system, dynamic clonal selection algorithm is adopted for reducing false positive rate. The experimental results on KDD99 data set prove that the new model has low false positive rate and high detection rate.

Keywords Mobile agent · Immune agent · Network security · Distributed intrusion detection

T. Ji · Y. Li (✉)
School of Computer Science and Engineering, Jiangsu University of Science
and Technology, Zhenjiang 212003, China
e-mail: liyongzhong61@163.com

J. Xu
College of Information Engineering, Yancheng Institute of Technology,
Yancheng 224051, China

13.1 Introduction

Most traditional intrusion detection systems (IDS) are centralized and based on a monolithic architecture. Data are collected on a single machine by looking at log files or network flow and are analyzed on a single computer, which has some defects both in the structure and in the detection technology. So distributed intrusion detection system (DIDS) appears. It becomes a research focus in the field of intrusion detection. Reference [1] presented a distributed information-gathering step, but centralized on analyzing process. The Graph-based Intrusion Detection System (GrIDS) [2] and Event Monitoring Enabling Responses to Anomalous Live Disturbances (EMERALD) [3] are IDS that use a hierarchical approach in a more sophisticated way. The hierarchical approach seems to show better scalability by allowing local analyses at distributed monitoring areas. However, a monitor operating at the highest level may induce single point of failure. When the topology of current network is changed, it causes a change of network hierarchy, and the whole mechanism for aggregation of local analysis reports must be changed. Autonomous Agent for Intrusion Detection (AAFID) is the first attempt to use autonomous agents for network intrusion detection by Spafford and Crosbie in [4]. In AAFID, nodes of the IDS are arranged in a hierarchical structure in a tree. Agents in AAFID were not mobile. Current DIDS mostly use distributed component to collect data, and then send collected data to processing center. These models solve the problem of distributed data acquisition effectively in wide bandwidth network. However, they have bad real time capability, bottleneck problem, and single point of failure because of the central processing node. The above-mentioned problems can be solved by utilizing the intelligent, mobile, and self-adaptive characteristics of agent and its distributed collaborative calculation capability [5, 6].

False positive rate and false negative rate are other import aspects that IDS must consider. In [7], the authors stated similarities between the defenses of natural immune systems and computer security: both must discriminate self and non-self to protect a complex system from inimical agent. Be inspired of immune system, Kim and Bentley in [8] have proposed dynamic clonal selection algorithm and shown that this algorithm could reduce false positive rate.

In this paper, dynamic clonal selection algorithm is adopted. Detectors are embedded in agents. With their communication mechanism, detection agents can detect cooperatively. Using the mobile characteristic of agent, detection agent can move to local host, and thus it can reduce network load and improve real-time capability. The model is full distributed.

13.2 Immune System and Mobile Agent

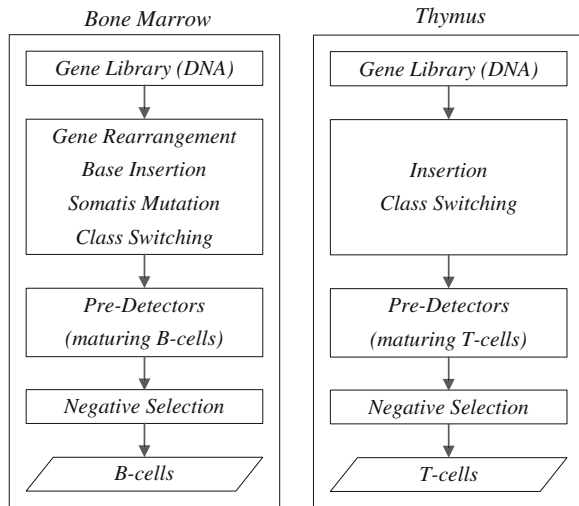
13.2.1 Immune System

The immune system [9–13] is a complex network of organs and cells responsible for the organisms defense against alien particles. Among a large number of different innate and acquired cells, lymphocytes play a central role. Lymphocytes are classified into two main types: B cells and T-cells. B cells are antibody-secreting cells and T-cells kill antigens or help or suppress the development of B cells. Both originate from bone marrow, and they are developed by the bone marrow and the thymus, respectively.

Before leaving the bone marrow and the thymus, maturing B- and T-cells have to pass the last test-negative selection. Mature B- and T-cells that pass the negative selection are released from the bone marrow and thymus, respectively. The development of B cells and T-cells are shown in Fig. 13.1.

The antibodies of B-cells, which recognize harmful antigens by binding to them, are activated directly or indirectly. When B-cell antibody receptors bind to antigen epitopes with strong affinity above a threshold, they are directly activated. When B-cell antibody receptors fasten to antigen epitopes with weak affinity, MHC molecules try to find some hidden antigens inside cells. When MHC molecules find them, they transport them on the surface of B-cells. The receptors of T-cells are genetically structured to recognize the MHC molecule on the B-cell surface. When the T-cell binds to an MHC molecule with strong affinity, it sends a chemical signal to the B-cell, which allows it to activate, grow, and differentiate.

Fig. 13.1 Development of B-cells and T-cells



13.2.2 Mobile Agent

Mobile agent is a type of software agent, with the feature of autonomy, social ability, learning, and most import, mobility [14].

Mobile agent can transport its state from one environment to another with its data intact and still be able to perform appropriately in the new environment. When a mobile agent decides to move, it saves its own state, transports this saved state to the next host and resumes execution from the saved state.

Mobile agent neither brings new method to detect for IDS nor increases detection speed for some kind of attracting. Nevertheless, it improves the design, construct, and execute of IDS obviously.

13.3 Immune Mobile Agent and Its Applications in Intrusion Detection System

13.3.1 System Architecture

Be inspired of immune system, this paper combines immune mechanism with mobile agent, and constructs some immune agents to monitor and detect attraction on the network. Figure 13.2 presents the architecture of intrusion detection based on immune mobile agent. It composes of central control agent (C-agent), detection agent (B-agent), memory agent (M-agent), and response agent (K-agent). C-agent runs in the server and plays a role of manger. B-agent and M-agent travel though the network in order to detect attacking. If any attacking is detected by B-agent or M-agent, K-agent is activated and responds to it immediately.

The function of each component in this model is de-scribed as follows.

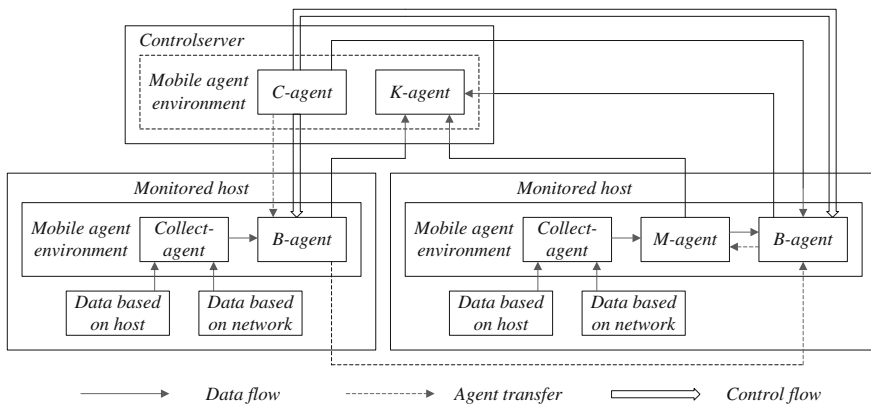


Fig. 13.2 Architecture of immune agent intrusion detection system

C-agent is a kind of agents, which mainly manage, co-ordinate, and control roaming agent on the network. Its function is similar to that of bone marrow and thymus. It can create, dispatch, and recall agent. Once B-agent is created, it can work continually without the connection between server and client. Although we adopt server and client model, it does not induce single point of failure.

Each B-agent contains a set of mature detectors. The function of B-agent is similar to that of B-cells. B-agent strays on the network to monitor intrusion. If antigen comes, B-agent is activated, and it will move to the local host to detect whether intrusion occurs.

Each M-agent contains a set of memory detectors. It imitates the mechanism of secondary response in immune system. If antigen comes and M-agent exists, M-agent is activated, and they will be detected by M-agent firstly. If it does not match these antigens, B-agent will detect continually. It can improve the speed of detecting known intrusion.

The function of K-agent is analogous to that of T-cells. If any intrusion is detected by B-agent or M-agent, K-agent will be activated immediately. It will act in response to it by disconnecting suspicious connection, locking account, or restricting login.

Collect-agent's main job is collecting data, which are foundation of intrusion detection system. It can collect data based on host and based on network. Collect-agent in this paper mainly captures network packet. In order to improve efficiency of detection, collect-agent needs to extract useful property of data packet besides of capturing data packet.

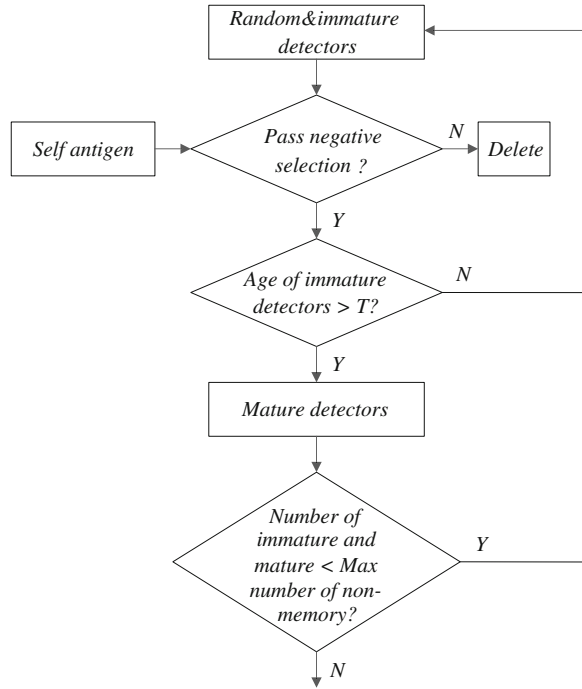
13.3.2 Generation of Detectors

Detectors play an import part in intrusion detection. The more attacking features these detectors have, the higher detection rate the system has. The less normal network features these detectors contain, the less false positive rate the system has. Kim presents dynamic clonal selection algorithm and experiment shows it can reduce false positive rate with high detection rate [8]. When detectors are generated, they are embedded in mobile agent. Suppose that there are N mature detectors in total and each B-agent can carry n detectors, the system will generate N/n B-agents. These agents with detectors roam on the network and realize the distributed computing.

The dynamic selection algorithm is described in detail as follows:

Step 1: the function of it is to generate mature detectors; the progress is shown in Fig. 13.3. The parameter T and number of non-memory detectors is defined before-hand. And the progress is repeated for T generation.

Fig. 13.3 Flow chart of mature detector generation



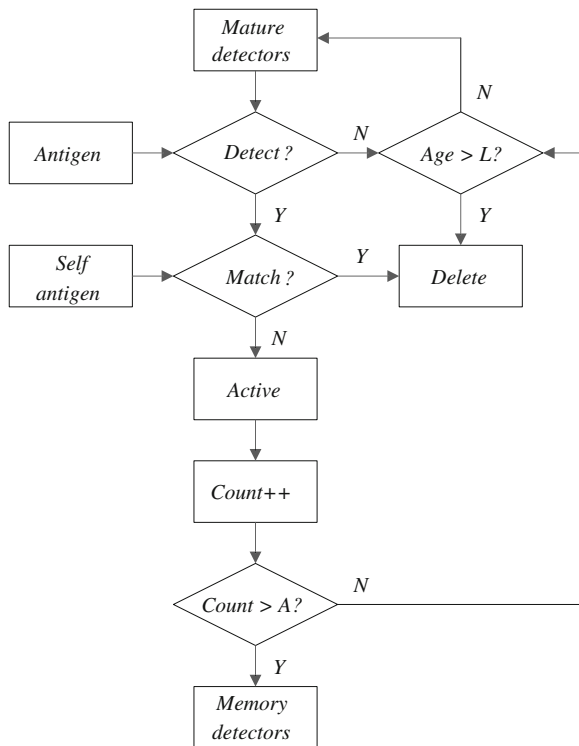
Step 2: at generation $T + 1$, the function is to generate memory detectors. It is the progress of studying attack feature for the sake of detecting more attack. In this progress, dynamic clonal selection algorithm is improved. A step of activating mature detector is increased. When one mature detector detects an attack, it will be activated. Figure 13.4 is the flow chart of memory detector generation.

Step 3: at generation $T + 2$, it is the monitor progress. When memory detectors match any antigen and the detected antigen binds any self-antigen, the memory detector is added to immature detectors. In addition, if the detected antigen does not bind self-detectors, it is removed directly. The remaining antigens are matched by activated mature detectors and the process is the same as the period of $T + 1$.

13.4 Simulations

In order to survey and evaluate research in intrusion detection, KDD99 data set is the data set, which was obtained from the 1998 DARPA. The data set is composed of a big number of connection records. Each connection is labeled as either normal or as an attack with exactly one specific attack type. Attacks in the data set can be

Fig. 13.4 Flow chart of memory detector generation



classified into four main categories namely Denial of service (DOS), Remote to User (R2L), User to Root (U2R) and Probe. In our experiment, we only used 10 percents of the raw training data (kddcup.data_10_percent) for training and the test data set (corrected.gz) for testing. It is important to note that the test data is not from the same probability distribution as the training data, and it includes specific attack types not in the training data. The test data contains of 20 types of training attack and 17 types unknown attacks. 37 types of attacks are classified into four categories as follows:

DOS: {back, land, Neptune, pod, smurf, teardrop, processtable, udpstorm, mail-bomb, apache2}

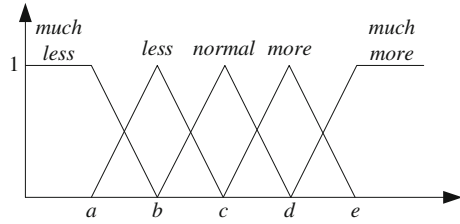
R2L: {ftp_write, guess_passwd, imap, multihop, phf, warezmaster, sendmail, xlock, snmpguess, named, xsnoop, snmpgetattack, worm}

U2R: {buffer_overflow, loadmodule, perl, rootkit, xterm, ps, httptunnel, sqlattack}

Probing: {ipsweep, nmap, portsweep, satan, mscan, saint}

For each connection, there are 41 features. Among them, 32 features are continuous variables and 9 features are discrete variables. Among these features, some are redundant and some contribute little to the intrusion detection process [13–15]. Considering efficiency, we select features 1, 2, 3, 5, 6, 7, 8, 9, 15, 16, 18, 19 and 20 to compose of detector and choose statistical features 20–41 except for 30 to be

Fig. 13.5 Features of detector



collaborative signal. We can use much less, less, normal, more and much more to express bytes from source to destination. Moreover, the value of them is 000, 001, 010, 011, and 100, respectively. Figure 13.4 shows its membership functions.

$$P(|x - \mu| \geq \varepsilon) \leq \frac{\sigma^2}{\varepsilon^2} \tag{13.1}$$

According to Chebyshev’s inequality (13.1) and the proportion of normal and attack data in KDD99, the values of variables in Fig. 13.5 are shown as follows: $a = \mu - 2\sigma$, $b = \mu - \sigma$, $c = \mu$, $e = \mu + \sigma$, $d = \mu + 2\sigma$. For all collaborative signals, we use normal, suspicious and abnormal to express them, and the process is the same as the above. The value of it is 00, 01 and 10 respectively.

This paper implemented on IBM’s aglet toolkit, which is composed of a set of java-based mobile software agents that carry out specific tasks on the network and collaborate on the problem of network intrusion detection. Aglet is installed in three computers. Among them one is as sever, and others are as clients. When detectors are generated, they are embedded in agents. Utilizing aglet, agents can be dispatched, cloned, and recalled.

13.4.1 Simulation Results

Test of Robust and Fault-tolerant of the system: When the system is start-up, B-agent in one host is bro-ken off in order to observe its effect to the system. Experiment shows that system can discover the invalidated agent and then create and dispatch new agent to this host. One node invalidate does not induce disability of the system. This indicates that the system is robust and fault-tolerant.

Detection result: The size of non-memory detectors is defined as 100,000, the training data is divided into self-antigen set and non-self antigen set. In addition, in our experiment, self-antigen set and non-self antigen set are classified into four antigen clusters. Moreover, the iterative generation is set 200.

In Table 13.1, comparing with winning entry of KDD’99 Classifier Learning Contest, the proposed approach has a good performance in detecting DOS, Probe, U2R attack and Normal behavior. Nevertheless, the performance of detecting R2L is poor. This is because the packet of R2L is slightly different from the packet of normal. How to improve the ability of the detecting R2L and U2R is the future work.

Table 1 Comparison with winning entry of KDD' 99 classifier learning contest

	Detection result	
	TP of the winning entry (%)	TP of the proposed approach (%)
Normal(60593)	99.5	98.127
DOS(229853)	97.1	97.565
Probe(4166)	83.3	90.494
U2R(228)	13.2	71.491
R2L(16189)	8.4	0.371

13.5 Conclusion

In this paper, a new distributed intrusion detection model based on immune mobile agent is proposed. Dynamic clonal selection algorithm and mobile agent are described in detail. The simulation results showed that our model is efficiently to classify the anomaly profile from the normal profile. Our model has following advantages. First, the model realized that computing move to data by utilizing mobile agent. Therefore, real time capability is improved and bottleneck problem is overcome. Second, compared with other hierarchical model, it surmounts single point of failure. Dependability of the system is enhanced. In addition, the system is robust and fault-tolerant. Third, false positive rate is low and true positive rate is high by adopting dynamic clonal selection algorithm.

Acknowledgments This paper is supported by Research fund of University of Jiangsu Province and Jiangsu University of Science and Technology's Basic Research Development Program (No. 2005DX006J).

References

1. Huntman W (1997) Automated information system (AIS) alarm system. In: Proceedings of the 20th national information systems security conference, 20th NISSC, 7–10, IEEE Press, Baltimore, pp 394–405
2. Staniford-Chen S, Cheung S, Crawford R, et al (1996) GrIDS-a graph based intrusion detection system for large networks. In: Proceedings of the 19th national information systems security conference, 19th NISSC, 22–25, IEEE Press, Baltimore, pp 361–370
3. Porras PA, Neumann PG (1997) EMERALD: event monitoring enabling response to anomalous live disturbances. In: Proceedings of the 20th national information systems security conference, 20th NISSC, 7–10, IEEE Press, Baltimore, pp 353–365
4. Spafford EH, Zamboni D (2000) Intrusion detection using autonomous agent. *Comput Netw* 3(4):547–570
5. Dasgupta D, Brian H (2001) Mobile security agents for network traffic analysis. Proceedings of the DARPA information survivability conference and exposition II, DISCEX'01, 12–14, IEEE Press, Anaheim, pp 332–340
6. Jansen W, Mell P, Karygiannis T, Marks D (2000) Mobile agents in intrusion detection and response In: Proceedings of the 12th annual Canadian information technology security symposium, 19-23, IEEE Press, Ottawa, pp 12–18

7. Hofmeyr SA, Forrest S, Somayaji A (1998) Intrusion detection using sequences of system calls. *J Comput Sec* 6(3):151–180
8. Kim J, Bentley PJ (2002) Towards an artificial immune system for network intrusion detection: an investigation of dynamic clonal selection. In: *Proceedings of the 2002 congress on evolutionary computation, CEC'02*, 12–17, IEEE Press, Honolulu, pp 1244–1252
9. Li YZ, Wang RS, Xu J (2009) A novel distributed intrusion detection model based on immune mobile agent. *Proceedings of the 2009 international symposium on web information systems and applications, WISA'09*, 22–24, IEEE Press, Nanchang, pp 72–75
10. Kim J, Bentley PJ, Aickelin U et al (2007) Immune system approaches to intrusion detection—a review. *Nat Comput* 6(4):413–466
11. Aickelin U, Greensmith J, Twycross J (2004) Immune system approaches to intrusion detection—a review. In: Nicosia G, Cutello V, Bentley PJ, Timmis J (eds.) *ICARIS 2004*. LNCS, vol 3239, pp 316–329
12. Glickman M, Balthrop J, Forrest S (2005) A machine learning evaluation of an artificial immune system. *Evolutionary Comput* 13(2):179–212
13. Gomez J, Gonzalez F, Dasgupta D (2003) An immuno-fuzzy approach to anomaly detection. In: *Proceedings of the 12th IEEE international conference on fuzzy systems, FUZZ'03*, 25–28, IEEE Press, Missouri, pp 1219–1224
14. Zainal A, Maarof MA, Shamduddin SM (2006) Feature selection using rough set in intrusion detection. In: *Proceedings of 2006 IEEE region 10 conference, IEEE TENCON 2006*, 14–17, IEEE Press, Hongkong, pp 1–4
15. Kim B-j, Kim I-k (2005) Kernel based intrusion detection system. In: *Proceedings of the 4th Annual ACIS international conference on computer and information science, ICIS'05*, 14–16, IEEE Press, Jeju Island, pp 13–18

Chapter 14

The Improved Discernibility Matrix Based on Decision Vector

Jingfu Li and Denghui Bu

Abstract Skowron's discernibility matrix is the evolvement of the attribute reduction models under algebra view. Aiming at the generating process of discernibility matrix, this paper simplifies decision system by introducing decision vector, and designs an improved discernibility matrix, which is capable of suiting inconsistency of decision system, as well as largely reducing comparison times and storage space for constructing discernibility matrix. Finally, an illustrative example is used to show the feasibility and efficiency of this improved discernibility matrix.

Keywords Rough set · Discernibility matrix · Attribute reduction · Decision vector

14.1 Introduction

The theory of rough set, as proposed by Pawlak, is an efficient mathematical theory to deal with uncertainty and vagueness of decision system, and it has many successful applications in the fields of artificial intelligence such as experts system, pattern recognition, machine learning and knowledge discovery [1, 2]. Attribute reduction plays important role in analyzing enormous data, for it provides the equivalent information descriptive ability as the entire set of attributes [3].

Skowron and Rauszer introduced two basic notions in 1991, namely discernibility matrix and discernibility function [4], which provides a canonical and precise mathematical model for finding core and reduction of decision system [5, 6]. However, this method has some disadvantages: generating discernibility

J. Li (✉) · D. Bu
International College, Huanghuai University, 6# Kaiyuan Road,
Zhumadian, Henan, China
e-mail: sysgl007@gmail.com

matrix would consume enormous time and space; and it is difficult to suit inconsistent circumstance of decision system [7, 8].

In this paper, these disadvantages mentioned above are analyzed in detail, and an efficient method of simplifying decision system is proposed to find minimum discernibility set. This method not only considers inconsistent circumstance of decision system sufficiently, but also saves executive time and space greatly. The theoretic analysis and simulation instance shows that this algorithm is feasible and effective in practice.

14.2 Preliminaries

Formally, an decision information system DS is denoted as $DS = \langle U, A, V, f \rangle$, where $U = \{x_1, x_2, \dots, x_n\}$ is a nonempty finite set of objects, U is also called as the universe; $A = C \cup D$ is a nonempty finite set of attributes, C is condition attribute set and D is decision attribute set; $V = \cup_{a \in A} V_a$, V_a is the value domain of the attribute a ; $f : U \times A \rightarrow V$ is a information mapping function such that $f(x_i, a) \in V_a (x_i \in U, a \in A)$.

Definition 1 Given a subset of attributes $R \subseteq A$, an indiscernible relation $IND(R) \subseteq U \times U$ is denoted as: $IND(R) = \{(x_i, x_j) \in U \times U : \forall a \in R, f(x_i, a) = f(x_j, a)\}$. For any object pair $\langle x_i, x_j \rangle$, if $x_i IND(R) x_j$ then x_i and x_j have the same value on the attribute set R , i.e. they are indiscernible on the attribute set R . The partition of the universe induced by C and D is denoted by $U/IND(C)$ and $U/IND(D)$, which are called as condition partition and decision partition respectively.

Definition 2 Given an set of object $X \subseteq U$, the lower and upper approximation of X are defined as below:

$$\begin{aligned} \underline{R}(X) &= \cup \{X_i : X_i \in U/IND(R) \wedge X_i \subseteq X\}, \\ \bar{R}(X) &= \cup \{X_i : X_i \in U/IND(R) \wedge X_i \cap X \neq \emptyset\}. \end{aligned}$$

According to indiscernible relation $IND(R)$ R , the lower approximation $\underline{R}(X)$ is the greatest definable set contained in X , and the upper approximation $\bar{R}(X)$ is the least definable set containing X .

Definition 3 Given decision system $DS = \langle U, A = C \cup D, V, f \rangle$, the positive region is defined by:

$$POS_c(D) = \cup_{X \in U/D} C(X).$$

The positive region is the union of such condition partitions that can be fully contained in the decision partitions.

Definition 4 Given decision system $DS = \langle U, A, V, f \rangle$, considering the characteristic Ψ of DS , an attribute set $B \subseteq A$ is called as a reduction of DS iff:

1. $\Psi(B) = \Psi(A)$;
2. $\forall B' \subset B, \Psi(B') \neq \Psi(B)$.

The intersection of all reductions is called as core. Different characteristic Ψ is corresponding to different function standard of reduction goal, for example keeping condition partition unchanged, keeping relative positive region unchanged, and keeping information entropy unchanged.

As important development of attribute reduction in rough set theory, Skowron and Rauszer introduced the notion of discernibility matrix based on which discernibility function was designed, and proved that the set of prime implicants in minimal disjunctive form of discernibility function is corresponding to all reduction of given information system.

Definition 5 Given decision system $DS = \langle U, A = C \cup D, V, f \rangle$, Discernibility matrix is a $|U| \times |U|$ matrix denoted as M , its element $M(i, j)$ is defined by:

$$M(i, j) = \begin{cases} \{a: a(x_i) \neq a(x_j), (a \in C) \wedge (x_i, x_j \in U)\} & (D(x_i) \neq D(x_j)) \wedge \left(\min \left\{ \left| V_D([x_i]_{IND(C)}) \right|, \left| V_D([x_j]_{IND(C)}) \right| \right\} = 1 \right) \\ \emptyset & \text{otherwise} \end{cases}$$

$M(i, j)$ is an element located on the i th row and the j th column of discernibility matrix M ; $[x_i]_{IND(C)}$ is the equivalence class of x_i with respect to condition attribute set C , i.e. $[x_i]_{IND(C)} \in U/IND(C)$; $V_D([x_i]_{IND(C)})$ denotes the value domain of $[x_i]_{IND(C)}$, $|Y|$ denotes the cardinality of the set Y .

“ $\left(\min \left\{ \left| V_D([x_i]_{IND(C)}) \right|, \left| V_D([x_j]_{IND(C)}) \right| \right\} = 1 \right)$ ” indicates that at least one of the two objects x_i and x_j is contained in the positive region.

It consists of all attributes on which two objects x_i and x_j possess different value, simultaneously at least one of x_i and x_j has only one decision value. Definition 5 assures that discernibility matrix must be capable of discerning the object of positive region from other objects, therefore this discernibility matrix may be considered as discernibility matrix based on changeless positive region.

14.3 Discernibility Matrix Based on Decision Vector

Discernibility matrix is a kind of efficient method to find the reduction. However, generating discernibility matrix would consume enormous time and space, and it is also difficult to suit inconsistent circumstance of decision system. This section would analysis these disadvantages in detail, introduce decision vector to simplify decision system for improving discernibility matrix. This improved matrix is

capable of describe inconsistent objects, and decreasing the comparison times and storage spaces.

Definition 6 Given an decision system $DS = \langle U, A = C \cup D, V, f \rangle$, $U = \{x_1, x_2, \dots, x_n\}$, $U/IND(D) = \{Y_1, Y_2, \dots, Y_{|U/IND(D)|}\}$, then the value domain of system decision can be achieved: $F_D = \{f(Y_1, D), f(Y_2, D), \dots, f(Y_{|U/IND(D)|}, D)\}$. For $\forall x_i \in U$, $B \subseteq C$, the decision of $[x_i]_B$ with respect to D can be denoted as a decision vector: $DV([x_i]_B) = \left(\mu_{DV([x_i]_B)}(f(Y_1, D)), f(Y_1, D), \dots, \left(\mu_{DV([x_i]_B)}(f(Y_{U/IND(D)}, D)), f(Y_{U/IND(D)}, D) \right) \right)$ where $f(Y_j, D)$ is the value domain of decision class $Y_j (1 \leq j \leq |U/IND(D)|)$ over decision attribute D , $\mu_{DV([x_i]_B)}(f(Y_j, D)) = |Y_j \cap [x_i]_B| / |[x_i]_B|$. Obviously, $DV([x_i]_B) = \mu_{DV([x_i]_B)}(f(Y_1, D)), \dots, \mu_{DV([x_i]_B)}(f(Y_{|U/IND(D)|}, D))$ is the probability distribution of the equivalence class $[x_i]_B$ on each decision equivalence class, so $\mu_{DV([x_i]_B)}(f(Y_1, D)) + \dots + \mu_{DV([x_i]_B)}(f(Y_{|U/IND(D)|}, D)) = 1$.

Definition 7 For a decision vector DV , its λ -cut defined for $\lambda \in (0, 1]$ by: $DV_\lambda = \{x : DV(x) \geq \lambda\}$

All elements whose membership are higher than λ constitute the λ -cut of decision vector DV .

Definition 8 For an decision system $DS = \langle U, A = C \cup D, V, f \rangle$, its simplification decision system is defined by: $DS' = \langle U/IND(C), C \cup D', V', f' \rangle$, $V' = \cup_{a \in C \cup D'} V_a$, V_a is the value domain of the attribute a ; $f' : U \times (C \cup D') \rightarrow V'$ is an information mapping function such that

$$f'(X_i, a) \in V'_a (X_i \in U/IND(C), a \in C \cup D'), \text{ here } f'(X_i, D') = \tilde{F}_D(X_i).$$

Based on simplification decision system, we can define discernibility matrix which keeps positive region and information entropy unchanged respectively.

Definition 9 Given decision system $DS = \langle U, A = C \cup D, V, f \rangle$ and its simplification decision system $DS' = \langle U/IND(C), C \cup D', V', f' \rangle$, Discernibility matrix is a $|U/IND(C)| \times |U/IND(C)|$ matrix denoted as M' , its element $M'(i, j)$ is defined by:

$$M_{(i,j)} = \begin{cases} \{a: a(x_i) \neq a(x_j), (a \in C) \wedge (x_i, x_j \in U)\} & |(DV(X_i))_1| = 1 \vee |(DV(X_j))_1| = 1 \\ \emptyset & \text{otherwise} \end{cases}$$

where $(DV(X_i))_1$ is 1-level set (1-cut) of $DV(X_i)$, $|(DV(X_i))_1| = 1$ indicates that X_i is contained in positive region. This discernibility matrix assures that at least one of two compared objects is contained in positive region, so it is capable of keeping positive region unchanged.

Definition 10 Given an decision system $DS = \langle U, A = C \cup D, V, f \rangle$ and its simplification decision system $DS' = \langle U/IND(C), C \cup D', V', f' \rangle$, Discernibility matrix is a $|U/IND(C)| \times |U/IND(C)|$ matrix denoted as M' , its element $M'(i, j)$ is defined by:

$$M'(i, j) = \begin{cases} \{a : a(x_i) \neq a(x_j), (a \in C) \wedge (x_i, x_j \in U)\} & DV(X_i) \neq DV(X_j) \\ \emptyset & \text{otherwise} \end{cases}$$

where $DV(X_i) \neq DV(X_j)$ indicates that the probability distribution of X_i and X_j on decision equivalence class are not equal. Therefore, this discernibility matrix is capable of keeping information entropy unchanged.

The improved discernibility matrix defined as definition 9 and definition 10, considering the equivalence class as elementary comparison unit. There is not more than one time of comparison between two condition equivalence classes, so the improved discernibility matrix is able to save the time and spaces consumed in generating discernibility matrix than before.

Definition 11 For an simplification decision system $DS' = \langle U/IND(C), C \cup D', V', f' \rangle$ and its improved discernibility matrix M' , the discernibility function is a Boolean expression defined as follows:

$$f(M') = \wedge \{ \vee M'(i, j) : 1 < j < i \leq |U/IND(C)|, M'(i, j) \neq \emptyset \}$$

The expression $\vee M'(i, j)$ denotes making disjunction operation among all attributes which belong to nonempty element $M'(i, j)$. The expression $\wedge \{ \vee M'(i, j) \}$ means making conjunction operation among all $\vee M'(i, j)$. The physical meaning of discernibility function consists in the fact that the pair (X_i, Y_j) can be discerned by using any attribute in $M'(i, j)$, so disjunction operations are made among all attributes which belong to $M'(i, j)$; and all discernible pairs of condition equivalence class can be assured to be still discernible, therefore conjunction operations are made among all $\vee M'(i, j)$. Thus, the value of $\wedge \{ \vee M'(i, j) \}$ becomes true by selecting some attributes (if $a \in M'(i, j)$ is selected, then the value of $\vee M'(i, j)$ is true; if the value of all $\vee M'(i, j)$ in $f(M')$ is true, then $f(M')$ is true.)

Based on the discernibility matrix and discernibility function, attribute reduction and core can be considered in association with knowledge reduction. The core attributes are common part of all reduction, and they are indispensable to preserve original knowledge in information system.

Theorem 1 Given an decision system $DS = \langle U, A = C \cup D, V, f \rangle$ and its improved discernibility matrix M' , $R \subseteq C$ is a reduction if and only if R satisfies:

1. $\forall M'(i, j) \neq \emptyset (1 \leq j < i \leq n) \Rightarrow R \cap M'(i, j) \neq \emptyset$;
2. $\forall R' \subset R, \exists M'(i, j) \neq \emptyset$ such that $R' \cap M'(i, j) = \emptyset$.

The condition (1) shows R is jointly sufficient to distinguish all object pairs which are discernible in original information system, and the condition (2) indicates R is minimal subset of attributes satisfying condition (1). These two

conditions ensure that $R \subseteq C$ is a minimal subset of attributes which preserve particular property of given information system, so R is a reduction.

Theorem 2 *Suppose $f'(M)$ is the minimal disjunctive form which is equivalent to $f(M)$, $R \subseteq C$ is a reduction if and only if $\wedge R$ is a prime implicant of $f'(M)$.*

Every disjunctive item of the minimal disjunctive form is called a prime implicant. $\wedge R$ denotes the conjunctive form of all attributes in R . Theorem 2 illuminates that the problem of finding all reduction is equivalent to transforming the conjunctive form $f(M)$ to the minimal disjunctive form $f'(M)$ by applying many times of the absorption or multiplication laws on Boolean expression.

Theorem 3 *For improved discernibility matrix M' , the attribute core is the collection of singleton attribute element in M' , i.e. $Core(M') = \{M'(i, j) : |M'(i, j)| = 1\}$.*

Where $M'(i, j)$ is an element of discernibility matrix M' , and $|M'(i, j)|$ is the cardinality of $M'(i, j)$, namely the number of attributes contained in $M'(i, j)$. $|M'(i, j)| = 1$ denotes $M'(i, j)$ is an element of singleton attribute, then it is necessary for $M'(i, j)$ contained in each prime implicant of the minimal disjunctive form $f'(M')$. So $Core(M')$ is indispensable to all reductions, and be contained in every reduction.

14.4 Analysis of an Instance

In order to illustrate the method mentioned above, we give an example of application. This example is simple, but it illustrates essential characteristics. Given an decision system in Table 14.1, where $U = \{x1, \dots, x8\}$ $C = \{a, b, c, d, e, f\}$.

Its simplification decision system DS' can be computed as Table 14.2.

The improved discernibility matrix based on changeless positive region and information entropy are shown as Tables 14.3 and 14.4 respectively.

Based on Table 14.3, we can get the discernibility function $f'(M) = (a \vee b \vee c) \wedge (c \vee d) \wedge (b \vee c \vee f) = c \vee (b \wedge d) \vee (a \wedge d \wedge f)$, so the reduction

Table 14.1 Decision system

U	a	b	c	d	d	f	D
x1	0	0	0	0	0	0	0
x2	0	0	0	0	0	0	1
x3	1	1	1	0	0	0	1
x4	1	1	0	1	0	0	0
x5	1	1	0	1	0	0	1
x6	1	1	0	1	0	0	1
x7	1	0	0	0	0	1	0
x8	1	0	0	0	0	1	1

Table 14.2 Simplification decision system DS'

U	a	b	c	d	d	f	D'
X1	0	0	0	0	0	0	(1/2, 1/2)
X2	1	1	1	0	0	0	(0, 1)
X3	1	1	0	1	0	0	(1/3, 2/3)
X4	1	0	0	0	0	1	(1/2, 1/2)

Table 14.3 The improved discernibility matrix based on positive region

	X1	X2	X3	X4
X1				
X2	{a, b, c}			
X3	Φ	{c, d}		
X4	Φ	{b, c, f}	Φ	

Table 14.4 The improved discernibility matrix based on information entropy

	X1	X2	X3	X4
X1				
X2	{a, b, c}			
X3	{a, b, d}	{c, d}		
X4	Φ	{b, c, f}	{b, d, f}	

set based positive region is $\{\{c\}, \{b, d\}, \{a, d, f\}\}$. Based on Table 14.4, we can get the discernibility function $f'(M) = (a \vee b \vee c) \wedge (a \vee b \vee d) \wedge (c \vee d) \wedge (b \vee c \vee f) \wedge (b \vee d \vee f)$, so we can compute that the reduction set based information entropy is $\{\{a, d, f\}, \{a, c, f\}, \{b, c\}, \{b, d\}, \{c, d\}\}$.

14.5 Conclusions

Attribute reduction based on discernibility matrix is one of important parts researched in rough set theory. This paper analyses some disadvantages of discernibility matrix before in detail, and proposes an efficient method of simplifying decision system to find minimum discernibility set. By introducing decision vector, this paper designs an improved discernibility matrix that can suit inconsistency of decision system, as well as be capable of reducing comparison times and storage space for building discernibility matrix by the greatest extent. The theoretic analysis and simulation instance shows that this algorithm is feasible and effective in practice.

References

1. Skowron A, Pawlak Z (2007) Rough sets and Boolean reasoning. *Inf Sci* 177:41
2. Thangavel K, Pethalakshmi A (2009) Dimensionality reduction based on rough set theory: a review. *Appl Soft Comput* 9:1
3. Skowron A, Pawlak Z (2007) Rudiments of rough sets. *Inf Sci* 177:3
4. Skowron RC (1992) The discernibility matrices and functions in information systems. *Intelligent decision support, handbook of applications and advances of rough sets theory*. Kluwer, The Netherlands, p 331
5. Zhao Y, Yao Y, Luo F (2007) Data analysis based on discernibility and indiscernibility. *Inf Sci* 177:4959
6. Yao Y, Zhao Y (2009) Discernibility matrix simplification for constructing attribute reducts. *Inf Sci* 179:867
7. Huang Z, Sun W, Wu H (2008) Reduction tree algorithm based on discernibility matrix. *Comput Appl* 28:1457
8. Huang Z, Wang D (2009) Study on data reduction algorithm based on rough set. *Comput Eng Des* 30:4284

Chapter 15

Backward Circular Motion Control for Mobile Robot with Two Trailers

Jin Cheng, Yong Zhang, Zhonghua Wang and Li Gong

Abstract The purpose of the paper is to provide asymptotic stable feedback control laws to reverse the mobile robot with two trailers along curve trace. The paper presents a new approach to stabilizing the system in backward motion by controlling the orientation angles of the two trailers. Nonlinear smooth control laws for orientations of the trailers with asymptotic stability in backward motion are then proposed. The stability of the closed loop feedback system is proved with Lypunov theory about stability. Results of numeric Simulation implemented on the robot with two trailers also illustrate the effectiveness of the proposed control laws.

Keywords Mobile robot with two trailers · Asymptotic stability · Backward circular motion

15.1 Introduction

Mobile robot with trailers which is considered as a nonholonomic system has given rise to plenty of work in recent years [1]. However, the path planning and motion execution for the tractor-trailer mobile robot is much more challenging due to the nonholonomic constraints existing on the motion of transverse direction and additional holonomic constraints introduced by the joint axis [2]. In addition, the subsystems of the trailers are open-loop unstable when the robot moves backward, which results in the so-called jack-knife effects on the relative angle between the tractor and the trailer [3].

Due to the system is more complex than the robot with one trailer, the path planning and control problems of the mobile robot with two trailers are much more

J. Cheng (✉) · Y. Zhang · Z. Wang · L. Gong
School of Electrical Engineering, University of Jinan, No. 106, Road Jiwei,
Jinan 250022, China
e-mail: cse_chengj@ujn.edu.cn

difficult and challenging. Brockett has proven that there exists no continuous state feedback control law for the stabilization problem of such nonholonomic systems [4]. As a direct result of Brockett's condition, discontinuous feedback is usually considered the alternative approach. With high order sliding mode, Zhang proposed a discontinuous feedback control with finite-time convergence for the stabilization problem of a mobile robot with one trailer [5]. M. D. Romano carried out an experimental study to verify the control methods for the stabilization of articulated and non-articulated robot with one trailer [6]. Whereas, related work about motion control of the mobile robot with two trailers is few at present. J. Lee analyzes the mechanical structure and kinematics of three trailer models of indoor service robots with multiple trailers in [7]. Myoungkuk proposed path tracking control method and a backward motion controller for the passive multiple trailer system in [8].

As a core function of the mobile robot, the robot with two trailers is expected to track the reference trajectory generated by the path-planning algorithm, which is usually composed of a sequence of circular and line segments. In this paper, stable control law for the orientation angle when the robot with two trailers moves backward along circular trace are proposed. The robot can be reversed with asymptotic stability at given orientation to track circular trajectory. Stability of the closed system is proved by Lyapunov theory on stabilization.

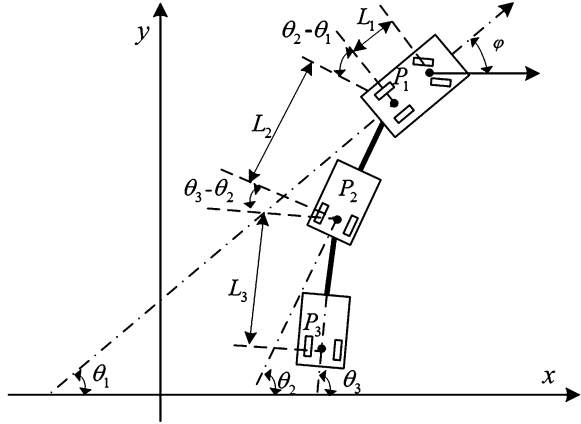
The paper is organized as follows. Model of the system kinematics of the tractor-trailer mobile robot with two trailers is given in Sect. 15.2. The asymptotically stable control law for the tracking of curve trace is proposed and proven in Sect. 15.3. Numeric simulation results are presented to illustrate the effectiveness of proposed control laws in Sect. 15.4. Finally, Sect. 15.5 gives the conclusion.

15.2 Kinematics of Mobile Robot with Two Trailers

The tractor-trailer mobile robot considered in this paper is driven by a car-like tractor towing two passive trailers as shown in Fig. 15.1. The first trailer is hooked up at the middle point of the rear wheels of the tractor and the second trailer is hooked up at the middle point of the rear wheels of the first trailer. The tractor is rear-wheel driven with linear speed v . The configuration of the system can be described by a vector $(x_1, y_1, \theta_1, \theta_2, \theta_3)$, which x_1 and y_1 denote the position coordinates of the tractor's in Cartesian coordinates, θ_1 and θ_2 measure the orientation of the tractor and the trailer with respect to the x axis, φ is the steering angle. L_1, L_2 and L_3 are length parameters of the tractor and trailers. For simplicity, it is assumed that the tractor tracks the reference path with constant velocity, which is set with $v = -1$ (m/s) to drive the robot backward in this paper.

The nonholonomic constraint derives from the fact that the tractor and trailers are rolling without slipping between the wheels and the ground. The kinematics of the mobile robot with two trailers are described by

Fig. 15.1 Geometry of mobile robot with two trailers



$$\begin{aligned}
 \dot{x}_1 &= v \cos \theta_1 \\
 \dot{y}_1 &= v \sin \theta_1 \\
 \dot{\theta}_1 &= \frac{v \tan \varphi}{L_1} \\
 \dot{\theta}_2 &= \frac{v}{L_2} \sin \gamma_1 \\
 \dot{\theta}_3 &= \frac{v}{L_3} \cos \gamma_1 \sin \gamma_2
 \end{aligned} \tag{15.1}$$

where $\gamma_1 = \theta_1 - \theta_2$ and $\gamma_2 = \theta_2 - \theta_3$ are respectively the intersection angles between the two adjacent axis of the tractor and the two trailers.

It can be easily proven that the sub-system of the second trailer is not controllable at $|\gamma_2| = \frac{\pi}{2}$. In many applications, to avoid collision between the bodies, the absolute value of γ_i ($i = 1, 2$) is bounded with $|\gamma_i| < \frac{\pi}{2}$ ($i = 1, 2$).

15.3 Asymptotically Stable Control Law for Backward Circular Motion

The system of the mobile robot with two trailers in backward motion is stable only at two forms. One form is that the robot moves backward along a circle, i.e., $\gamma_1 = \gamma_{1d}$ and $\gamma_2 = \gamma_{2d}$ with control inputs $v = -1$ and $\varphi = \varphi_d$, which $|\gamma_{1d}| < \frac{\pi}{2}$ and $|\gamma_{2d}| < \frac{\pi}{2}$ and $|\varphi_d| < \frac{\pi}{2}$. The other form is that the robot moves backward along a rectilinear line, i.e., $\gamma_1 = \gamma_2 = 0$ with control inputs $v = -1$ and $\varphi = 0$.

For the circular motion it has $\dot{\gamma}_1 = \dot{\gamma}_2 = 0$, which yields that $\dot{\theta}_3 = \dot{\theta}_2 = \dot{\theta}_1$ and

$$\tan \varphi_d = \frac{L_1}{L_2} \sin \gamma_{1d}, \quad \tan \gamma_{1d} = \frac{L_2}{L_3} \sin \gamma_{2d} \tag{15.2}$$

So for any given $|\gamma_{2d}| < \frac{\pi}{2}$, there exists a stable circular trajectory for the mobile robot with two trailers in backward motion. In this section, the feedback control law for the orientation stabilization of the trailers along circular trajectory is firstly proposed.

For the stabilization of the tracking problem of γ_2 with desired reference γ_{2d} , we have the following proposition.

Proposition 1 Consider the system (15.1) with control input $v = -1$. Assume $|\gamma_{2d}| < \frac{\pi}{2}$ and $\dot{\gamma}_{2d} = 0$. There exists a feedback control law for the control input φ for system (15.1), which the intersection angles γ_1 and γ_2 will track the desired γ_{1d} and γ_{2d} with exponential stability.

Proof Define the tracking error with

$$s_1 = \sin \gamma_{2d} - \sin \gamma_2 \quad (15.3)$$

and the Lyapunov function with

$$V_1 = \frac{1}{2} s_1^2 \quad (15.4)$$

Computing the time derivative of V_1 along the trajectories of the system (15.1) yields

$$\dot{V}_1 = -v(\sin \gamma_{2d} - \sin \gamma_2) \cos \gamma_1 \cos \gamma_2 \left(\frac{1}{L_2} \tan \gamma_1 - \frac{1}{L_3} \sin \gamma_2 \right) \quad (15.5)$$

According to back-step technique, define an instrumental variable

$$s_2 = \frac{1}{L_2} \tan \gamma_1 - \frac{1}{L_3} \sin \gamma_2 + k_1 s_1 \quad (15.6)$$

with $k_1 > 0$, and the new Lyapunov function

$$V_2 = V_1 + \frac{1}{2} s_2^2 \quad (15.7)$$

Differentiate V_2 with respect to time along system (15.1), one obtains

$$\dot{V}_2 = kv(\sin \gamma_{2d} - \sin \gamma_2)^2 \cos \gamma_1 \cos \gamma_2 + s_2(\dot{s}_2 - v \cos \gamma_1 \cos \gamma_2(\sin \gamma_{2d} - \sin \gamma_2)) \quad (15.8)$$

Let

$$\dot{s}_2 = v \cos \gamma_1 \cos \gamma_2(\sin \gamma_{2d} - \sin \gamma_2) - k_2 s_2 \quad (15.9)$$

with $k_2 > 0$. The solution of (15.9) is calculated with

$$\varphi = -a \tan\left(\frac{L_1 \cdot \eta(\gamma_1, \gamma_2, \gamma_{2d})}{vL_2L_3^2(1 + \tan^2 \gamma_1)}\right), \quad (15.10)$$

where

$$\begin{aligned} \eta(\gamma_1, \gamma_2, \gamma_{2d}) = & -L_3^2v \sin \gamma_1 - L_3^2v \sin \gamma_1 \tan^2 \gamma_1 - L_2L_3v \sin \gamma_1 \cos \gamma_2 \\ & - L_2L_3^2k_1v \sin \gamma_1 \cos \gamma_2 + L_2^2v \cos \gamma_1 \cos \gamma_2 \sin \gamma_2 \\ & - L_2^2L_3k_1v \cos \gamma_1 \cos \gamma_2 \sin \gamma_2 - L_2^2L_3^2v \cos \gamma_1 \cos \gamma_2 \sin \gamma_{2d} \\ & + L_2^2L_3^2v \cos \gamma_1 \cos \gamma_2 \sin \gamma_2 + k_2L_2L_3^2 \tan \gamma_1 - k_2L_2^2L_3 \sin \gamma_2 \\ & + k_1k_2L_2^2L_3^2 \sin \gamma_{2d} - k_1k_2L_2^2L_3^2 \sin \gamma_2 \end{aligned} \quad (15.11)$$

It yields

$$\dot{V}_2 = v \cos \gamma_1 \cos \gamma_2 k_1 s_1^2 - k_2 s_2^2 \quad (15.12)$$

For $|\gamma_i| < \frac{\pi}{2}$ ($i = 1, 2$) and $v < 0$, one has $\dot{V}_2 \leq 0$.

The stability of the equilibrium $s_1 = 0$ and $s_2 = 0$ for the closed system with control input (15.10) and $v = -1$ that can be proven with Lyapunov theory directly are exponentially stable. From (15.3) and (15.6), when $s_1 \rightarrow 0$ and $s_2 \rightarrow 0$, it has $\gamma_2 \rightarrow \gamma_{2d}$ and $\gamma_1 \rightarrow \gamma_{1d}$. So the intersection angles γ_1 and γ_2 will track the desired γ_{1d} and γ_{2d} with exponentially stability.

15.4 Simulation Result

Numeric simulations were performed to illustrate the effectiveness of the proposed control laws. The parameters of the mobile robot with two trailers are set with $L_1 = 1$, $L_2 = 2$, $L_3 = 2$. The initial configuration of the robot is set with $[x_1, y_1, \theta_1, \theta_2, \theta_3] = [0, 0, \pi, \pi, \pi]$ and the robot moves backward with speed $v = -1$ m/s. For the problem of reversing robot along circular trajectory, the parameters in control law (15.10) are chosen to be $k_1 = k_2 = 1$ and the desired intersection angle is set with $\gamma_{2d} = \frac{\pi}{5} = 0.6283$ (rad). According to (15.2), $\gamma_{1d} = a \tan(L_2 \sin \gamma_{2d} / L_3) = 0.5314$ (rad).

Simulation results are shown in Figs. 15.2, 15.3 and 15.4. Responses of the trace and orientation angles of the tractor and the two trailers are shown in Figs. 15.2 and 15.3, which obviously indicate that the proposed control law successfully reverses the robot along a circular trajectory. The result of intersection angles γ_1 and γ_2 shown in Fig. 15.4 corroborates the effectiveness of the proposed control law. With time t increases, the intersection angles $\gamma_1 \rightarrow 0.5314 = \gamma_{1d}$ and $\gamma_2 \rightarrow 0.6283 = \gamma_{2d}$.

Fig. 15.2 Traces of the tractor and the two trailers

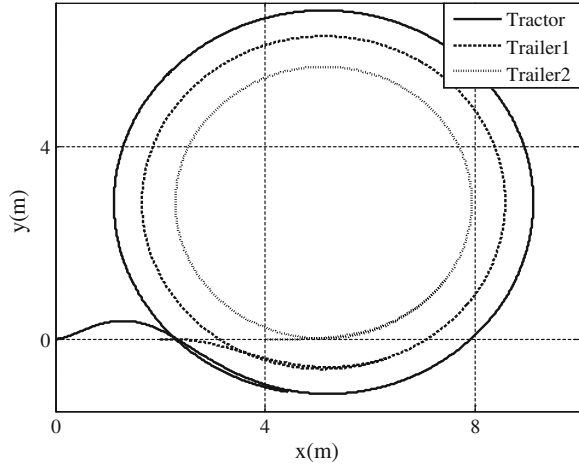


Fig. 15.3 Orientation angles of the tractor and the two trailers

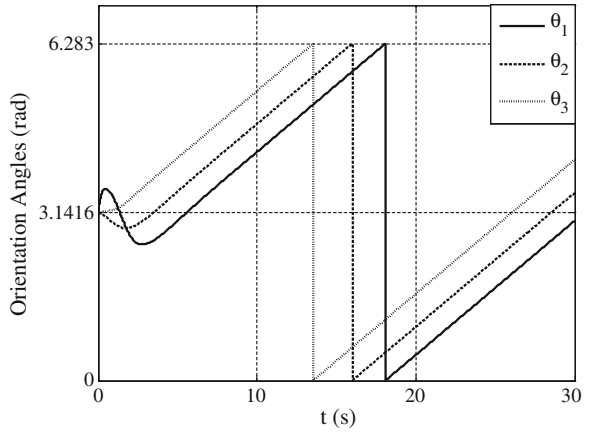
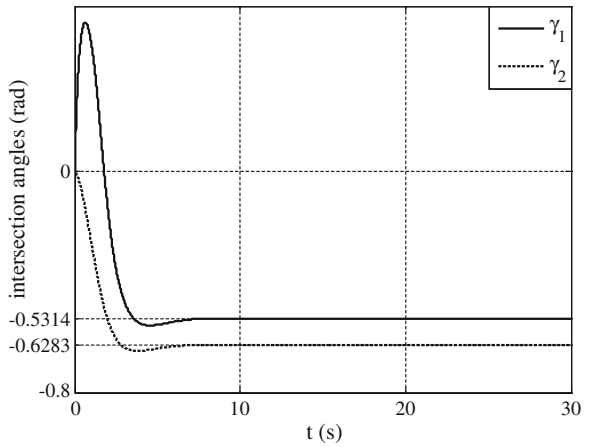


Fig. 15.4 Intersection angles γ_1 and γ_2



15.5 Conclusion

The control problems of reversing the mobile robot with two trailers have been addressed in this paper. With the proposed feedback control laws, the robot with two trailers can be reversed respectively with asymptotic stability on tracking desired intersection angle along a circular trajectory. Stability of the proposed control laws are proved with Lyapunov Theory. Numerical simulation results also verify the effectiveness of the control laws. According to Dubins theorem, an optimal curve with minimal length is composed of circular arcs and/or line segments. The control laws proposed in this paper will contribute to the future work about robot motion planning problem.

Acknowledgments This work was supported by the National Natural Science Foundation of China (No. 61203335) and partly supported by the National Natural Science Foundation of China (No. 61074021).

References

1. Cheng J et al (2010) Stabilization control of a backward tractor-trailer mobile robot. In: Intelligent control and automation in proceeding of 8th world congress in Jinan, China, IEEE, pp 2136–2141
2. Dong Y et al (2005) Kinematics and constraint analysis of tractor-trailer mobile robot. In: Machine learning and cybernetics in 2005 proceedings of international conference in Guangzhou, China, IEEE, pp 1380–1384
3. Martinez JL et al (2008) Steering limitations for a vehicle pulling passive trailers. *IEEE Trans Control Syst Technol* 16(4):809–818
4. Brockett RW (1983) Asymptotic stability and feedback stabilization. In: *Progress in Mathematics of proceeding of conference in Birkhauser, Boston*, vol 27, pp 181–208
5. Zhang Y et al (2008) Point stabilization of a tractor-trailer mobile robot. In: 10th International conference on control, automation, robotics and vision, pp 17–20, 1747–1751
6. Romano MD et al (2002) Experimental stabilization of tractor and tractor-trailer like vehicles. In: *Intelligent control in 2002 proceeding of IEEE international symposium in Vancouver, Canada*, IEEE, pp 188–193
7. Lee J et al (2001) A passive multiple trailer system for indoor service robots. In: *Intelligent robots and systems in 2001 proceeding of IEEE/RSJ international conference in Maui, Societies and Associations, Hawaii, USA*, vol 2, pp 827–832
8. Park M et al (2004) Control of a mobile robot with passive multiple trailers. In: *Robotics and automation in 2004 proceeding of IEEE international conference in New Orleans, Louisiana, USA*, IEEE, vol 5, pp 4369–4374

Chapter 16

Instruments Fault Detection in Process Industry with Independent Component Analysis

Jichen Hu and Guoyong Huang

Abstract In order to solve the problems of difficult and complex instruments fault detection in process industry, an instruments fault detection method based on independent component analysis (ICA) is proposed. The proposed method uses ICA arithmetic to establish the faults detection model with normal data recorded by instruments, and then calculate the statistic variables as on-line fault detecting strategy. An improved algorithm of contribution is proposed to locate the fault instrument. Simulation result with the data from Tennessee Eastman process verifies the effectiveness of proposed faults detection method and the improved contribution algorithm.

Keywords Process industry · Instruments fault detection · Independent component analysis · Contribution

16.1 Introduction

There are three methods of instrument fault detection, such as method based on quantifies models, method based on know-how and method on process data. The method based on process data is the focus of research [1]. However, some proposed instrument fault detection method is established on low derivative and simple statistical of single instrument, such as variance [2]. It can not reflect the relationship between each instrument in process industry.

Multivariate statistical process control (MSPC) is proposed to solve the problem of multivariate statistical. Principal component analysis (PCA) and its extension

J. Hu · G. Huang (✉)

Faculty of Information Engineering and Automation, Kunming University of Science and Technology, Engineering Research Center for Mineral Pipeline Transportation Yunnan, No 727 JingMing South Road, Kunming City, Cheng Gong, China
e-mail: 42427566@qq.com

methods have been widely and successfully used to detect fault in chemical process [3–5]. But it always does not have a good performance because PCA assumes that the variables data have a Gaussian distribution.

Independent component analysis (ICA) is an extension method of PCA on non-Gaussian information, and has been used as fault detection method in chemical process [6–8]. This study proposes that instruments fault detection with ICA and improves the contribution algorithm for isolating the instrument which has a fault. Simulation with TE process data proves the effective of ICA instrument fault detection method and the improved contribution algorithm.

16.2 Independent Component Analysis

ICA algorithm decomposes linearly the observation data of the instrument into multiple independent components [9], it is given as

$$\mathbf{X} = \mathbf{A}\mathbf{S} \quad (16.1)$$

Where $\mathbf{X} = [\mathbf{x}_1, \mathbf{x}_2, \dots, \mathbf{x}_m]^T \in R^{m \times n}$ is the data matrix, contains m observation variables with n measurements of each variable. $\mathbf{A} \in R^{m \times l}$ is the mixing matrix. $\mathbf{S} = [s_1, s_2, \dots, s_l]^T \in R^{l \times n}$ is the independent components matrix, contains l ($l \leq m$) independent components, s_i is called independent component (IC).

The key point is to estimate the unknown mixing matrix \mathbf{A} and get the independent components matrix \mathbf{S} with the only known data matrix \mathbf{X} . ICA algorithm can find a demixing matrix \mathbf{W} to reconstruct independent components matrix as $\hat{\mathbf{S}}$, it is given as follow:

$$\hat{\mathbf{S}} = \mathbf{W} \cdot \mathbf{X} = \mathbf{W} \cdot \mathbf{A} \cdot \mathbf{S} \approx \mathbf{S} \quad (16.2)$$

The demixing matrix \mathbf{W} can be got by fast and robust fix-point algorithm (FastICA) [10]. In FastICA algorithm, the number of IC equals to the number of observation variables. FastICA algorithm is based on the definition of negentropy as follows

$$J(y) = H(y_{guass}) - H(y) \quad (16.3)$$

where $H(y)$ is the definition of entropy, as $H(y) = - \int f(y) \log f(y) dy$. y_{guass} is a Gaussian random variables with the same variance as y . A simpler approximations of negentropy is suggested as follows

$$J(y) \approx k[E\{G(y)\} - E\{G(y_{guass})\}] \quad (16.4)$$

Where y is assumed to be of zero mean and unit variance, k is a constant, and G is any non-quadratic function. G can be chosen with different needs.

16.3 ICA Fault Detection Model

16.3.1 Data Preprocessing

Before applying ICA algorithm, it is very useful to do some preprocessing on data to make the problem of ICA simpler and better conditioned [9].

The first step of preprocessing is normalizing. It means that each variable of data matrix has a zero mean and unit variance.

The second step is whitening the variables. It transforms the variables linearly. One of the widely used whitening methods is eigenvalue decomposition of the covariance $\mathbf{R}_x = E\{\mathbf{X}\mathbf{X}^T\} = \mathbf{U}\mathbf{\Lambda}\mathbf{U}^T$, the whitening transformation is expressed as

$$\mathbf{Z} = \mathbf{Q}\mathbf{X} \quad (16.5)$$

where $\mathbf{Q} = \mathbf{\Lambda}^{-1/2}\mathbf{U}^T$. After transformation, it can be gotten

$$\mathbf{Z} = \mathbf{Q}\mathbf{X} = \mathbf{Q}\mathbf{A}\mathbf{S} = \mathbf{B}\mathbf{S} \quad (16.6)$$

\mathbf{B} is an orthogonal matrix proved by $E\{\mathbf{Z}\mathbf{Z}^T\} = \mathbf{B}E\{\mathbf{X}\mathbf{X}^T\}\mathbf{B}^T = \mathbf{B}\mathbf{B}^T = \mathbf{I}$. From Eqs. (16.2) and (16.6), $\hat{\mathbf{S}}$ is estimated as

$$\hat{\mathbf{S}} = \mathbf{B}^T\mathbf{Z} = \mathbf{B}^T\mathbf{Q}\mathbf{X} \quad (16.7)$$

The relationship between \mathbf{W} and \mathbf{B} is expressed $\mathbf{W} = \mathbf{B}^T\mathbf{Q}$ from Eq. (16.7).

16.3.2 Fault Monitoring Model

An important part of ICA monitoring is selection of an optimal number of dominant components from all ICs. Sorting the row of demixing matrix \mathbf{W} with Euclidean norm (L_2) is a very simple method and has a good result [11]. The data dimension can be reduced by selecting a few rows of \mathbf{W} . These rows have a large percentage of the sum of L_2 of each row.

With the normal instruments observation data \mathbf{X} , \mathbf{W} is obtained from FastICA algorithm as well as \mathbf{S} . Then select d rows of \mathbf{W} according L_2 of each row to constitute a reduced matrix \mathbf{W}_d . \mathbf{W}_d is the dominant part of \mathbf{W} , and the remaining rows of \mathbf{W} constitute \mathbf{W}_e . The matrix \mathbf{B} and \mathbf{Q} are obtained by FastICA algorithm and whiten model, $\mathbf{B}_d = (\mathbf{W}_d\mathbf{Q}^{-1})^T$, $\mathbf{B}_e = (\mathbf{W}_e\mathbf{Q}^{-1})^T$. The dominant and remaining independent components, \mathbf{S}_d and \mathbf{S}_e can be obtained as follows

$$\mathbf{S}_d = \mathbf{W}_d\mathbf{X}, \mathbf{S}_e = \mathbf{W}_e\mathbf{X} \quad (16.8)$$

At sample k of \mathbf{X} , statistical variables of $\mathbf{x}(k)$ are defined as [8]

$$I^2(k) = \mathbf{s}_d(k)^T \cdot \mathbf{s}_d(k) = (\mathbf{W}_d\mathbf{x}(k))^T \cdot \mathbf{W}_d\mathbf{x}(k) \quad (16.9)$$

$$I_e^2(k) = \mathbf{s}_e(k)^T \cdot \mathbf{s}_e(k) = (\mathbf{W}_e \mathbf{x}(k))^T \cdot \mathbf{W}_e \mathbf{x}(k) \quad (16.10)$$

$$SPE = \mathbf{e}(k)^T \cdot \mathbf{e}(k) = (\mathbf{x}(k) - \widehat{\mathbf{x}}(k))^T (\mathbf{x}(k) - \widehat{\mathbf{x}}(k)) \quad (16.11)$$

where $\widehat{\mathbf{x}}(k)$ can be calculated with $\widehat{\mathbf{x}}(k) = \mathbf{Q}^{-1} \mathbf{B}_d \mathbf{s}_d(k) = \mathbf{Q}^{-1} \mathbf{B}_d \mathbf{W}_d \mathbf{x}(k)$. The limits of the statistic variables are defined using kernel density [12].

For a new observation data vectors at sample k , $\mathbf{x}_{new}(k) = [\mathbf{x}_1, \mathbf{x}_2, \dots, \mathbf{x}_m]^T$, use the same normalized method as before. And then calculate the statistic variables I^2 , I_e^2 , and SPE to check whether they exceed the limit. If one of the statistic variables exceeds the limit continually, it means that some of the instruments have a fault.

16.3.3 Locating the Fault Instrument

The fault monitoring model can not locate the fault instrument when it detects a fault. As a simple tool, contribution plots can reveal the contribution of each observation variable. However, all of the instrument observation variables fluctuate differently. In order to eliminate the effects of different deviations of observed variables, multiply the left of the independent component vector by a generalized inverse of the demixing matrix \mathbf{W} . The variable contributions of data vectors at sample k for I^2 and I_e^2 are improved as follow

$$C_{I^2}(k) = \frac{\mathbf{W}_d^{-1} \mathbf{s}(k)}{\|\mathbf{W}_d^{-1} \mathbf{s}(k)\|} \|\mathbf{s}(k)\| \quad (16.12)$$

$$C_{I_e^2}(k) = \frac{\mathbf{W}_e^{-1} \mathbf{s}_e(k)}{\|\mathbf{W}_e^{-1} \mathbf{s}_e(k)\|} \|\mathbf{s}_e(k)\| \quad (16.13)$$

where \mathbf{W}_d^{-1} is the generalized inverse of \mathbf{W}_d and \mathbf{W}_e^{-1} is the generalized inverse of \mathbf{W}_e . Also the variable contributions of data vectors at sample k for SPE is defined as

$$C_{SPE}(k) = \mathbf{x}(k) - \mathbf{W}_d^{-1} \mathbf{W}_d \mathbf{x}(k) \quad (16.14)$$

It is unnecessary to calculate contributions at each sample. When some of the statistic variables exceed the limit continually, calculate the contribution of each observation variable. The variable whose contribution is the largest may be the instrument which has a fault. The steps of the monitoring method are summarized below (step1 to step3 is the offline modeling procedure and step4 to step6 is the online monitoring procedure):

- Step 1: Get the normal instruments data set \mathbf{X} , then normalize and whiten it;
- Step 2: Obtain demixing matrix with FastICA algorithm and extract ICs, select an optimal number of dominant components using Euclidean norm.

- Step 3: Establish fault detection model, calculate statistic variables and decide their limits.
- Step 4: For a new sample data vectors, normalize with the same scaling method as used before.
- Step 5: Calculate statistics variables with fault detection model.
- Step 6: Calculate contributions for each instrument variable when statistic variables exceed the limit continuously at recent several samples.

16.4 Simulation

As a benchmark simulation, the Tennessee Eastman (TE) process has been widely used to test the performance of various monitoring approaches. It has 41 measured variables and 12 manipulated variables. 6 variables (reactor pressure, temperature, product separator temperature, pressure, stripper pressure and temperature) are selected and marked from No. 1 to No. 6. The simulation data selected are separated into two parts, training datasets with 4,000 normal samples and testing datasets with 1,000 samples.

Obtain demixing matrix \mathbf{W} with FastICA algorithm and select dominant ICs with the L_2 of each row of \mathbf{W} . Figure 16.1 shows the percentage of the L_2 norm of each row of \mathbf{W} . The last two ICs are much higher than the rest, so the two ICs are dominant.

The instrument faults usually show as four styles: impulse, step deviation, periodic oscillation and drift fault. Add the analog step deviation fault signal to the No. 1 instrument variable from sample 200. Figure 16.2 shows the fault detection result. The statistical variable I^2 exceeds its limit continually from sample 200.

Fig. 16.1 %Euclidean norm of each row of demixing matrix

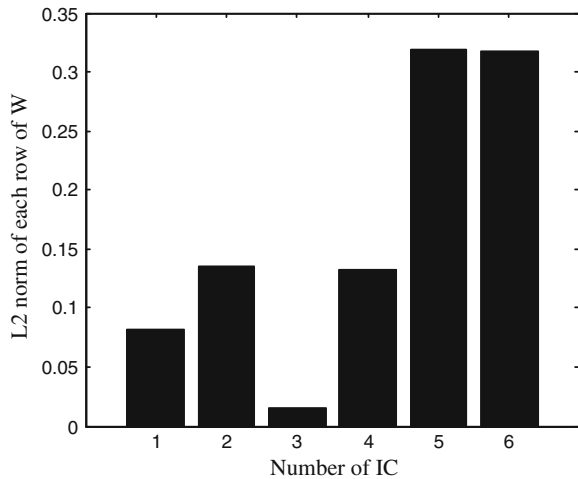
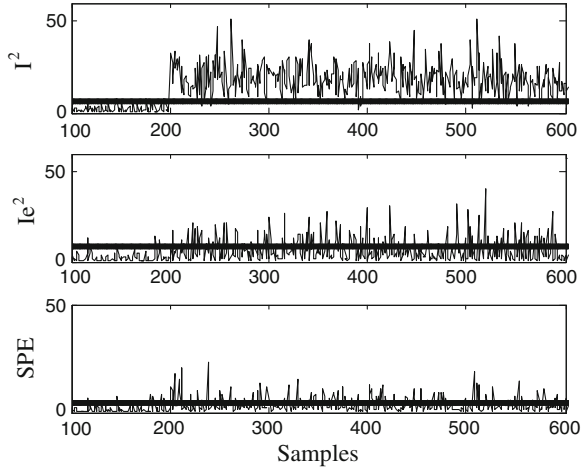


Fig. 16.2 No. 1 instrument faults detection result



The statistical variable I_e^2 and SPE do not exceed their limits continually.

Add the analog periodic oscillation fault signal to the No. 3 instrument variable from sample 200. Figure 16.3 shows the fault detection result. The statistical variable I_e^2 exceeds its limit continually from sample 200. The statistical variable I^2 and SPE do not exceed their limits continually.

Add the analog drift fault signal to the No. 3 instrument variable from sample 150. The drift fault is hard to be detected in time. Figure 16.4 shows the fault detection result. The statistical variable I_e^2 exceeds its limit continually from sample 180 and it is the earliest statistical variable which detects the fault than others.

Fig. 16.3 No. 3 instrument fault detection result

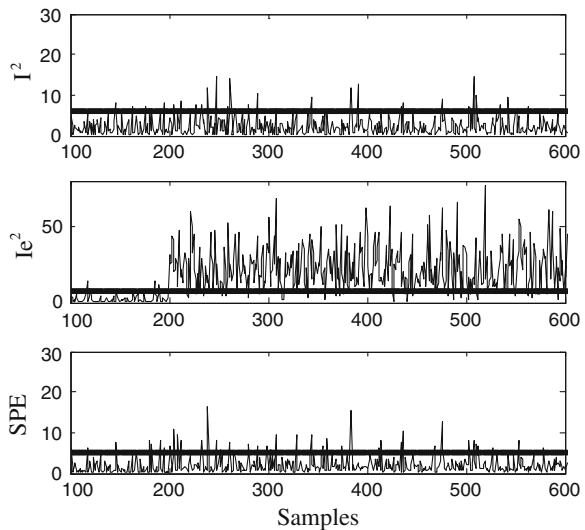
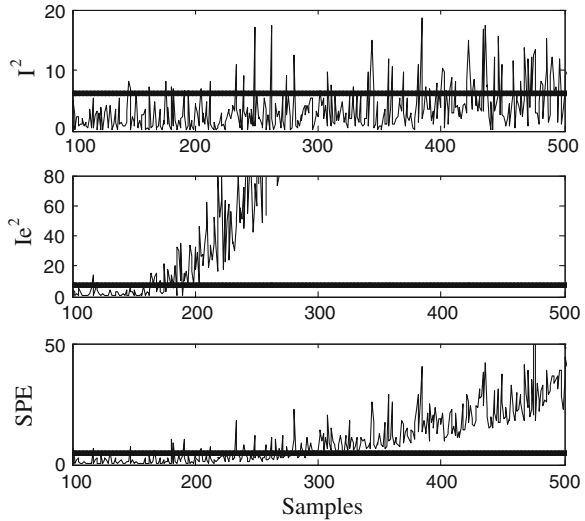


Fig. 16.4 No. 3 instrument fault detection result



When one of the statistic variables exceeds its limit continually, the instrument which has a fault can be found by contribution algorithm. Figure 16.5 shows contribution plots of I^2 . It exceeds its limit caused by that the No. 1 instrument variable was added an analog step deviation fault signal from sample 200.

Figure 16.5a shows the result of improved contribution algorithm. No. 1 instrument variable has the largest contribution; it is consistent with the simulation. Figure 16.5b shows the result of contribution algorithm based on quadratic sum used before, it can not locate fault instrument correctly. It is clearly that the improved contribution algorithm is more effective to locate the fault instrument.

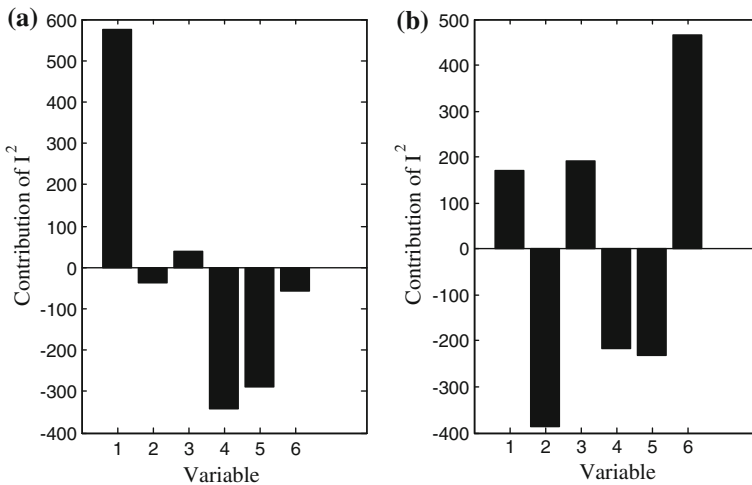


Fig. 16.5 Contribution plots

16.5 Conclusion

In this paper, a fault detection method based on ICA is proposed to solve the problem of instruments fault detection in process industry. Three statistical variables construct a comprehensive fault detection model for different fault. The simulation with the data from TE process shows that the effective of this method and the improved contribution algorithm can locate the fault instrument correctly.

Acknowledgments This work is supported by the National Natural Science Founder of China (No. 51169007), Science and Research Program of Yunnan province (No. 2010DH004 & No. 2011CI017 & No. 2011DA005 & 2011FZ036).

References

1. Venkatasubramanian V, Reccgaswamy R, Yin K et al (2003) Review of process fault detection and diagnosis part I; quantitative model-based methods. *Comput Chem Eng* 27(3):293–311
2. Bai X, Dai L (2008) The rapid instrument fault detection method in process industry. *Control Instrum Chem Ind* 35(1):36–39 (in Chinese)
3. Fan Y, Li P, Song Z (2005) KPCA Based on feature samples for fault detection. *Control Decis* 20(12):1415–1418 (in Chinese)
4. Liu XQ, Xie L, Kruger U et al (2008) Statistical-based monitoring of multivariate non-gaussian systems. *AIChE J* 54(9):2379–2391
5. Deng X, Tian X (2008) Fault diagnosis method based on immune kernel principal component analysis. *J Tsinghua Univ (Sci Technol)* 48(10):1794–1798 (in Chinese)
6. Yang Y, Wu Y, Chen X (2006) Process monitoring based on independent component analysis method. *Control Decis* 21(10):1190–1192 (in Chinese)
7. Bo C, Qiao X, Zhang G (2009) ICA-SVM based fault diagnosis method for complex chemical process. *J Chem Ind Eng* 60(9):2259–2264 (in Chinese)
8. Lee J, Yoo C, Lee I (2004) Statistical process monitoring with independent component analysis. *Process Control* 8:467–485
9. Hyvarinen A, Oja E (2000) Independent component analysis: algorithms and applications. *Neural Works* 13(4):411–430
10. Hyvarinen A (1999) Fast and robust fixed-point algorithms for independent component analysis. *IEEE Trans Neural Networks*. 10:626–634
11. Cardoso JF, Soulomica A (1993) Blind beamforming for non-Gaussian signals. *IEEE Proc Radar Signal Process* 140(6):362–370
12. Qian C, Wynne RJ, Goulding P et al (2000) The application of principal component analysis and kernel density estimation to enhance process monitoring. *Control Eng Practice* 8(5):531–543

Chapter 17

Nonlinear Process Fault Detection Based on Multi-Scale Sparse Kernel Classifier

Xiaogang Deng and Xuemin Tian

Abstract In this paper, a novel nonlinear process fault detection method is proposed based on multi-scale sparse kernel classifier (MSSKC). The proposed method applies ensemble empirical model decomposition (EEMD) to capture multi-scale system dynamics and decompose signals into various time scales. Nonlinear classifiers based on kernel trick are built for process monitoring at different scales. In order to reduce the complexity of kernel model, a forward orthogonal selection procedure is applied to minimize the leave one out error. Lastly monitoring statistic is developed and confidence limit is computed by kernel density estimation. Simulation of a continuous stirred tank reactor system shows that the proposed method has a better performance compared with kernel principal component analysis.

Keywords Nonlinear system · Fault detection · EEMD · Sparse kernel classifier

17.1 Introduction

For the increasing focus on process safety and quality improvement, fault detection has been one of the most fascinating topics in process control field. Because large amounts of data are available in modern large-scale industrial process, data-driven fault detection methods have gained great attentions which include Principal Component Analysis (PCA), Partial Least Square (PLS) and Independent Component Analysis (ICA) [1]. However, these methods are static and linear

X. Deng (✉) · X. Tian

College of Information and Control Engineering, China University of Petroleum,
No. 66 Changjiang West Road, Economic & Technological Development Zone,
Qingdao 266580, China
e-mail: dengxg2002@gmail.com

transformation techniques and sometimes show quite poor monitoring performance for the nonlinear and multi-scale dynamic processes.

To deal with the nonlinear relationship, many modified nonlinear methods have been developed such as principal curve method [2], neural network method [3] and kernel PCA method [4]. Compared to other nonlinear methods, kernel method has gained considerable interest and shown to be a promising nonlinear tool because there is no nonlinear optimization involved and nonlinear transformation is completed implicitly through kernel function. A major disadvantage of kernel method lies in its computation complexity. In the modeling stage of kernel methods, the size of kernel matrix is the square of the sample number. When the sample number becomes large, matrix calculation will be complex and time-consuming.

For extracting dynamic information from multi-scale process data, many approaches based on multi-scale analysis have appeared. In [5], multi-scale principal component analysis (MSPCA) was firstly discussed by introducing wavelet analysis. Multi-scale nonlinear monitoring approaches combining kernel PCA or kernel PLS with wavelet analysis were proposed by [6, 7]. Recently, a new multi-scale analysis technique called Ensemble Empirical Mode Decomposition (EEMD) was proposed by [8]. As a self-adaptive and directly data-driven multi-resolution decomposition tool, EEMD has shown its advantage over wavelet analysis whose performance is influenced by the selection of wavelet function [9].

In this paper, we propose a multi-scale sparse kernel classifier (MSSKC) method to monitor nonlinear multi-scale process. The proposed method uses EEMD to extract multi-scale dynamics and applies kernel classifier to handle the nonlinearities. To reduce computation complexity of kernel modeling, forward orthogonal selection technique is applied to make classifier sparse. The monitoring charts at different scales are constructed to detect faults.

17.2 Multi-Scale Data Analysis Using EEMD

Empirical mode decomposition was first studied for adaptive time–frequency data analysis in [10]. In the EMD approach, the signal $x(t)$ can be decomposed into a sum of elementary, zero-mean, empirical and nearly orthogonal oscillation modes with different time scales called intrinsic mode functions (IMFs) as

$$x(t) = \sum_{i=1}^S c_i(t) + r_S(t) \quad (17.1)$$

where S is the number of IMFs, $r_S(t)$ is the residue after S numbers of IMFs are extracted and represents the mean trend of the signal, $c_i(t)$ is the IMFs $\{c_1(t), c_2(t), \dots, c_S(t)\}$ which include different components ranging from high frequency to low frequency.

EMD has been proved quite useful but its major problem is mode mixing caused by signal intermittency. To solve the problem of mode mixing, ensemble empirical mode decomposition (EEMD) was proposed by [8]. EEMD is a noise-assisted method which reduces the chance of undue mode mixing and preserves the dyadic property of the decomposition for any data. The EEMD algorithm can be given as follows.

- (1) Initialize the number of ensemble M , the amplitude of the added white noise, and $m = 1$.
- (2) Add a white noise series with the given amplitude to the original signal

$$x_m(t) = x(t) + n_m(t) \tag{17.2}$$

where $n_m(t)$ indicates the m -th added noise series, and $x_m(t)$ represents the noise added signal of the m -th trial.

- (3) Decompose the noise-added signal $x_m(t)$ into S IMFs using EMD method and note the decomposition as $\{c_{1,m}(t), c_{2,m}(t), \dots, c_{s,m}(t), r_{s,m}(t)\}$.
- (4) If $m < M$, $m = m + 1$ and go to step (2) for next trial with different noise series.
- (5) Calculate the ensemble mean of the S trials for each IMF as final IMFs.

$$c_i(t) = \frac{1}{M} \sum_{m=1}^M c_{i,m}(t), \quad r_S(t) = \frac{1}{M} \sum_{m=1}^M r_{S,m}(t), \quad i = 1, \dots, S \tag{17.3}$$

By adding finite noise, the EEMD eliminates largely the mode mixing problem and preserves physical uniqueness of decomposition. In this paper we use EEMD for multi-scale analysis of monitored process data.

17.3 Process Monitoring Based on Sparse Kernel Classifier

The objective of process monitoring is to detect whether abnormal process behavior has occurred on-line, which can be considered as two-class classification between normal and fault class. Given modeling data $\mathbf{X} = [\mathbf{x}_1, \dots, \mathbf{x}_n]^T$ and $\mathbf{y} = [y_1, \dots, y_n]^T$, where $\mathbf{X} \in \mathbf{R}^{n \times m}$ stands for normal and fault data set with n samples of process vector \mathbf{x}_i , $\mathbf{y} \in \mathbf{R}^{n \times 1}$ stands for n samples of class variable, $y_i = 1$ for normal class data and $y_i = -1$ for fault class data. The training procedure of a two-class classifier is to find a classification hyper plane $f(\mathbf{x}) = 0$ based on training data set. For nonlinear classification problem, a nonlinear function $\Phi(\cdot) : \mathbf{x} \rightarrow \Phi(\mathbf{x})$ is applied. So the classification hyper plane is formulated as

$$f(\mathbf{x}) = \Phi(\mathbf{x})^T \boldsymbol{\beta} \tag{17.4}$$

where vector $\boldsymbol{\beta}$ determines the position of the separating hyper plane. As decision vector $\boldsymbol{\beta}$ can be spanned by training samples, Eq. (17.5) can be expressed as

$$f(\mathbf{x}) = \Phi(\mathbf{x})^T \sum_{i=1}^n \Phi(\mathbf{x}_i) \theta_i \quad (17.5)$$

where θ_i is projection parameter.

With the application of kernel trick [11], a dot product of the feature space mappings is a kernel calculation of original data points as $K(\mathbf{x}, \mathbf{y}) = \Phi(\mathbf{x})^T \Phi(\mathbf{y})$. So the decision function $f(\mathbf{x})$ will be

$$f(\mathbf{x}) = \sum_{i=1}^n K(\mathbf{x}, \mathbf{x}_i) \theta_i \quad (17.6)$$

According to [12], the classification problem can be solved in the framework of regression modeling with the known class labels used as the desired output. By defining the modeling error $e_j = y_j - f(\mathbf{x}_j)$ for all modeling data, the kernel classifier can be obtained by solving (17.7)

$$\mathbf{y} = f(\mathbf{X}) + \mathbf{e} = \mathbf{K}\boldsymbol{\theta} + \mathbf{e} \quad (17.7)$$

where \mathbf{K} is the kernel matrix, $\mathbf{K}_{ji} = K(\mathbf{x}_j, \mathbf{x}_i)$ and \mathbf{e} is the error vector.

In order to obtain a sparse kernel classifier (SKC), we use the orthogonal least squares regression method based on orthogonal forward selection technique developed by [12, 13]. Firstly, matrix orthogonal decomposition methods are used by $\mathbf{K} = \mathbf{W}\mathbf{A}$. The calculation of matrix \mathbf{W} and \mathbf{A} could be completed through improved Gram-Schmidt method. Therefore, Eq. (17.8) is available as:

$$\mathbf{y} = \mathbf{W}\mathbf{g} + \mathbf{e} \quad (17.8)$$

where $\mathbf{A}\boldsymbol{\theta} = \mathbf{g}$, $\mathbf{g} = [g_1 \ g_2 \ \dots \ g_n]^T$.

In (17.8) \mathbf{W} could be viewed as the model base vectors and \mathbf{g} is the model parameter. Due to existence of correlation in modeling data, only a part of model basis vectors is needed to build sparse model, which means selecting n_s ($n_s \ll n$) uncorrelated model subsets \mathbf{W}_s from \mathbf{W} and determining a sparse parameter vector \mathbf{g}_s through optimization method.

To solve (17.8), the optimization objective function is set as [12]

$$J(\mathbf{g}, \boldsymbol{\Lambda}) = \mathbf{e}^T \mathbf{e} + \mathbf{g}^T \boldsymbol{\Lambda} \mathbf{g} \quad (17.9)$$

where $\boldsymbol{\Lambda} = \text{diag}(\lambda_1 \ \lambda_2 \ \dots \ \lambda_n)$ stands for regularization parameters which represent the prior distribution of \mathbf{g} . For the objective function in (17.9), sparse parameter vector \mathbf{g}_s can be obtained through orthogonal forward selection procedure [13]. To improve generalization capability of model, error calculation methods with good generalization performance should be used, that is the MSE based on leave-one-out method (LOO MSE).

According to above discussions, the subset model selection procedure is carried out and \mathbf{g}_s can be obtained. Then we can get sparse kernel classifier model as

$$f(\mathbf{x}) = \sum_{l=1}^{n_s} K(\mathbf{x}, \mathbf{x}_l) \theta_l \quad (17.10)$$

where $\{\mathbf{x}_l\}$ $\{\theta_l\}$, $l = 1, 2, \dots, n_s$ are model sparse base vector and sparse parameters.

When input data \mathbf{x} is from normal operation condition, classifier output $f(\mathbf{x})$ should range around 1, so $(f(\mathbf{x}) - 1)$ should be a small number. For sparse kernel classifier, we can construct monitoring index

$$F(\mathbf{x}) = (f(\mathbf{x}) - 1)^2 \quad (17.11)$$

Monitoring index F indicates process status by its value. Under normal operation, monitoring index F would be a small positive number, otherwise a large positive number. After monitoring statistic F is obtained, we need to calculate the confidence limit to determine whether process is in control. In this section the confidence limit of F statistic for nominal operating regions is determined by non-parametric empirical density estimation using kernel density estimation [14].

17.4 Process Monitoring Strategy Using MSSKC

The MSSKC monitoring strategy of combining sparse kernel classifier and ensemble empirical mode decomposition is proposed in this section. This strategy is motivated from the idea that SKC can capture nonlinear relationship among variables while EEMD is more effective multi-resolution analysis method. For the measured data matrix \mathbf{X} , EEMD is first used to analyze \mathbf{X} at multiple scales, resulting in new data matrix $\{\mathbf{C}_1, \mathbf{C}_2, \dots, \mathbf{C}_S, \mathbf{R}_S\}$ at different scales. Then SKC is performed for each new data matrix to build nonlinear monitoring statistics for fault detection.

17.5 Simulation Study

The proposed process monitoring strategy is tested with a simulated process, a non-isothermal continuous stirred tank reactor (CSTR) system. A schematic diagram of the CSTR with feedback control system can be seen in [7].

The data of normal operating condition and faulty conditions are generated by simulating the CSTR process. Ten process variables are recorded and Gaussian noise is added to all measurements in simulation procedure. The simulation brings normal operating data and six kinds of fault pattern data. The applied fault pattern can be seen in Table 17.1. These faults contain operation condition change,

Table 17.1 A list of fault patterns

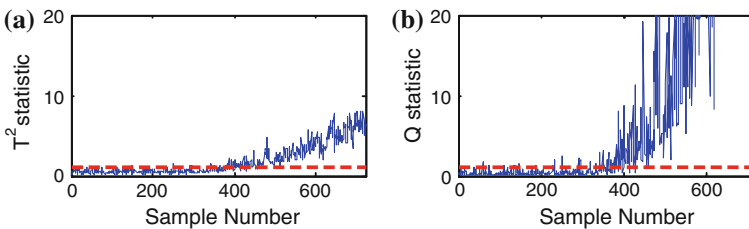
Fault	Description
F1	The coolant feed temperature ramps down
F2	The feed temperature ramps up
F3	Catalyst deactivation
F4	The heat transfer coefficient ramps down
F5	The coolant valve is in malfunction state
F6	The coolant temperature measurement has a bias

process parameter change, and valve malfunction and sensor bias. During process simulation, data are sampled every 10 s and 720 samples are stored. For each fault pattern data, fault is introduced after the 240th sample.

In this section, the monitoring results of KPCA and MSSKC are compared. For KPCA, two statistics T^2 and Q are plotted for process monitoring. The details about KPCA method can be seen in related papers [4, 11]. For MSSKC, number of IMFs is chosen as 2 so we can build three monitoring statistics at different scales $\{C_1, C_2, R_2\}$. For convenience of methods comparison, all monitoring statistics are to divide its confidence limit when the monitoring charts is plotted so that alarm limits in all figures are same as 1.

Firstly we compare the model complexity of KPCA and MSSKC. In the modeling stage, 200 normal samples are collected as modeling data. For KPCA, all samples are used to construct kernel matrix whose size is 200×200 . When new data is sampled online, it has to compute kernel function 200 times. For MSSKC, 8 samples are selected for modeling at each scale. Although MSSKC builds monitoring models for three scales respectively, it computes kernel function totally 24 times for new sample. So MSSKC decreases computation complexity.

The monitoring results of fault F2 are illustrated to show the effectiveness of MSSKC. In all monitoring charts, we think fault is detected if continuous 6 samples exceed confidence limit which is plotted as dashed line. As shown in Fig. 17.1, the T^2 and Q monitoring charts of KPCA method are plotted for fault F2, where the feed temperature ramps up. This fault cannot be detected by T^2 and Q statistic before the 400th and 381th sample respectively. When multi-scale nonlinear method MSSKC is applied, we can see three monitoring charts at different scales in Fig. 17.2. Figure 17.2a, b shows the monitoring results respectively for scale $\{R_2, C_2\}$. The F statistic at the coarsest scale C_2 detects fault F2 at

**Fig. 17.1** KPCA monitoring results for fault F2. **a** KPCA T^2 chart. **b** KPCA Q chart

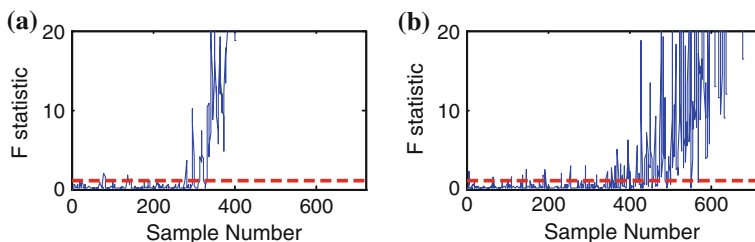


Fig. 17.2 MSSKC monitoring results for fault F2. **a** MSSKC F chart at scale R_2 . **b** MSSKC F chart at scale C_2

the 394th sample successfully for its multi-scale property, much earlier than the KPCA method. F_u , the F statistic at scale R_2 is more sensitive for fault F2 and it detects the fault at the 296th sample. Generally, MSSKC can detect the fault F2 more quickly than KPCA.

17.6 Conclusions

In order to monitor nonlinear multi-scale process, a novel method based on multi-scale sparse kernel classifier has been formulated in this paper. Multi-resolution analysis technique EEMD is applied to decompose the observed signal into IMFs at different scales. Based on multi-scale decomposition, sparse kernel classifier using orthogonal forward selection is constructed to complete nonlinear model. The proposed method is tested by a simulation CSTR system lastly. The application results show that the proposed strategy builds more parsimonious model and behaves more sensitive to fault than KPCA because of application of multi-scale analysis.

Acknowledgments This work is supported by the Natural Science Foundation of Shandong Province of China (ZR2011FM014), the Natural Science Foundation of China (61273160) and the Fundamental Research Funds for the Central Universities (10CX04046A).

References

1. Qin SJ (2012) Survey on data-driven industrial process monitoring and diagnosis. *Annu Rev Control* 36:220–234
2. Dong D, McAvoy TJ (1996) Nonlinear principal component analysis based on principal curves and neural networks. *Comput Chem Eng* 20(1):65–78
3. Geng ZQ, Zhu QX (2005) Multi-scale nonlinear principal component analysis and its application for chemical process monitoring. *Ind Eng Chem Res* 44(10):3585–3593
4. Nguyen VH, Golinval JC (2010) Fault detection based on Kernel principal component analysis. *Eng Struct* 32:3683–3691

5. Bakshi BR (1998) Multi-scale PCA with applications to multivariate statistical process monitoring. *AIChE J* 44(7):1596–1610
6. Zhang Y, Ma C (2011) Fault diagnosis of nonlinear processes using multi-scale KPCA and multi-scale KPLS. *Chem Eng Sci* 66(1):64–72
7. Deng X, Tian X (2006) Multivariate statistical process monitoring using multi-scale kernel principal component analysis. In: *Proceedings of the 6th IFAC symposium on fault detection, supervision and safety of technical processes*, Tsinghua University, Beijing, China, pp 108–112
8. Wu Z, Huang NE (2009) Ensemble empirical mode decomposition: a noise-assisted data analysis method. *Adv Adapt Data Anal* 1(1):1–41
9. Zvokelj M, Zupan S, Prebil I (2011) Non-linear multivariate and multi-scale monitoring and signal denoising strategy using kernel principal component analysis combined with ensemble empirical mode decomposition method. *Mech Syst Signal Process* 25(7):2631–2653
10. Huang NE, Shen Z, Long SR, Wu MC, Shih HH, Zheng Q, et al (1998) The empirical mode decomposition and the Hilbert spectrum for nonlinear and non-stationary time series analysis. *Proc R Soc A: Math Phys Eng Sci* 454:903–995
11. Scholkopf B, Smola AJ, MJuller K (1998) Nonlinear component analysis as a kernel eigenvalue problem. *Neural Comput* 10(5):1299–1319
12. Chen S, Hong X, Luk BL, Harris CJ (2009) Orthogonal least squares regression: a unified approach for data modeling. *Neurocomputing* 72(10–12):2670–2681
13. Hong X, Chen S, Harris CJ (2008) Fast kernel classifier construction using orthogonal forward selection to minimize leave-one-out misclassification rate. *Int J Syst Sci* 39(2): 119–125
14. Lee JM, Yoo CK, Lee IB (2004) Statistical process monitoring with independent component analysis. *J Process Control* 14(5):467–485

Chapter 18

Backstepping Based Type-2 Adaptive Fuzzy Control for a Generic Hypersonic Flight Vehicle

Fang Yang, Ruyi Yuan, Jianqiang Yi, Guoliang Fan
and Xiangmin Tan

Abstract A backstepping controller is designed for the altitude subsystem of a generic hypersonic flight vehicle. The derivatives of the virtual signals in backstepping control design are obtained by command filters with magnitude, bandwidth and rate limit constraints. Dynamic inversion control is used in velocity subsystem design. General uncertainties are estimated online using interval type-2 adaptive fuzzy logic system. Simulation results demonstrate the effectiveness and robustness of the proposed controller and also validate type-2 fuzzy logic is more capable of handling uncertainties than type-1 fuzzy logic.

Keywords Backstepping · Hypersonic flight control · Type-2 fuzzy logic · Adaptive control · Command filter · Dynamic inversion control

18.1 Introduction

Hypersonic flight vehicle (HFV) flies at a speed of more than 5 Mach and through a large altitude range. Although HFV has many application advantages, its flight control law design is highly challenging. There exist complex interactions between the propulsion system, aerodynamics and structural dynamics [1]. Furthermore, flight tests data are lacking and aerodynamic characteristics are difficult to measure and estimate. In summary, uncertainty is a major problem which needs to be dealt with in control design.

Backstepping (BS) control method provides a recursive method for stabilizing the origin of a system in strict-feedback form. [2] combines backstepping method with fuzzy adaptive approximator to track the velocity and altitude command. But

F. Yang · R. Yuan (✉) · J. Yi · G. Fan · X. Tan
Institute of Automation, Chinese Academy of Sciences, 95 Zhongguancun East Road,
Beijing 100190, China
e-mail: ruyi.yuan@ia.ac.cn

the derivative process of the virtual control signal is very complicated and it does not consider the signal constraint. [3] introduces command filter to obtain the derivative of the virtual control signal and also consider its magnitude and rate constraints. But the adaptive law is tightly dependent on the coefficients model and when the uncertainty becomes bigger, the robustness becomes weaker.

Type-2 fuzzy set (T2-FS) is characterized by membership functions (MFs) that are themselves fuzzy while type-1 fuzzy set's (T1-FS) MF is crisp. Figure 18.1 shows the membership function example of T2-FS and the structure of type-2 fuzzy logic system (T2-FLS). Here we use interval T2-FLS (IT2-FLS) whose type reducer just involves computing the lower and upper MFs of the antecedent and consequent sets [4],[5, 6] use an adaptive IT2-FLS to approximate unknown nonlinear system online and it does not need any prior knowledge about the nonlinear terms.

This paper proposes a backstepping based type-2 adaptive fuzzy controller for a generic hypersonic flight vehicle (GHFV). Uncertainties are estimated online by IT2-FLS. The derivatives of signals are obtained by command filters. Simulation results show its effectiveness and robustness under big uncertainties and noises.

18.2 Problem Statement and Preliminaries

The mathematical model of the longitudinal dynamics of the GHFV is given by

$$\begin{aligned} \dot{V} &= \frac{T \cos \alpha - D}{m} - g \sin \gamma, \dot{\gamma} = \frac{L + T \sin \alpha}{mV} - \frac{g \cos \gamma}{V} \\ \dot{h} &= V \sin \gamma, \dot{\alpha} = q - \dot{\gamma}, \dot{q} = M_y/I_y \end{aligned} \tag{18.1}$$

where the forces, the moment and the coefficients are

$$\begin{aligned} L &= \frac{1}{2} \rho V^2 s C_L, D = \frac{1}{2} \rho V^2 s C_D, T = \frac{1}{2} \rho V^2 C_T, M_y = \frac{1}{2} \rho V^2 s \bar{c} C_M \\ C_L &= C_L^\alpha \alpha, C_T = C_T^\phi \phi + C_T^0, C_M = C_M^{\delta_e} \delta_e + C_M^0 \end{aligned} \tag{18.2}$$

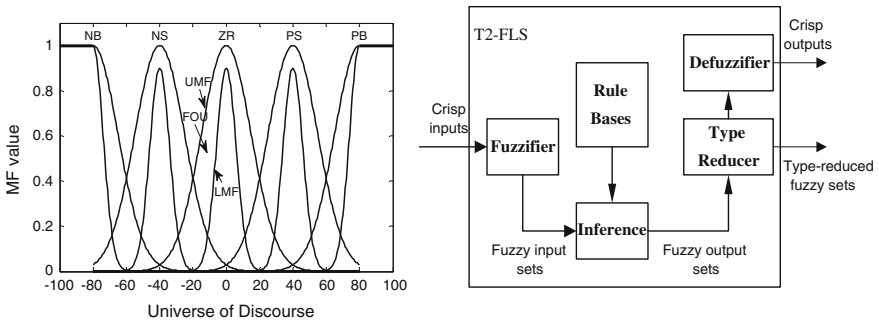


Fig. 18.1 Membership function example of T2-FS (left) and structure of T2-FLS (right)

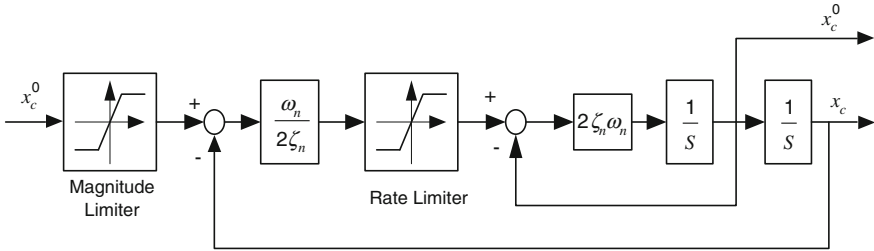


Fig. 18.2 Command filter with magnitude, bandwidth and rate limit constraints

Detailed coefficients can be seen in [7].

In usual backstepping control design, the analytic computation of virtual control signal derivatives is tedious. Here instead, we use command filters to obtain the derivatives of virtual control signals as well as reference command signals. Command filters are also used to filter out high-frequency noise and get the transient process of the reference command signals. As Fig. 18.2 shows, command filter puts magnitude, bandwidth and rate limitations on the signal [8]. ζ_n , ω_n are damping ratio and bandwidth. When command limiting is not in effect, the transfer function from the input to the output is

$$\frac{x_c(s)}{x_c^0(s)} = \frac{\omega_n^2}{s^2 + 2\zeta_n\omega_n s + \omega_n^2} \quad (18.3)$$

18.3 Control Design

18.3.1 Velocity Subsystem Dynamic Inversion Controller Design

The overall control scheme is shown in Fig. 18.3. The model error, parameter variation, external disturbances are all taken as the general uncertainty Δ^* and are estimated online by IT2-FLS. The error dynamics of the velocity subsystem is

$$\dot{\tilde{V}} = \dot{V} - \dot{V}_c = \bar{q}S \cos \alpha C_T^\phi / m * \phi + \bar{q}S(\cos \alpha C_T^0 - C_D) / m - g \sin \gamma - \dot{V}_c \quad (18.4)$$

Denote $f_1 = \bar{q}S \cos \alpha C_T^\phi / m$, $g_1 = \bar{q}S(\cos \alpha C_T^0 - C_D) / m$. When using nominal parameters, f_1, g_1 are nominal values. In practice there exist measurement uncertainties, model uncertainties and external disturbances. We take all of them as ideal general uncertainty Δ_1^* . An IT2-FLS is used to estimate Δ_1^* online and get $\widehat{\Delta}_1$ instead. So (18.4) can be written as

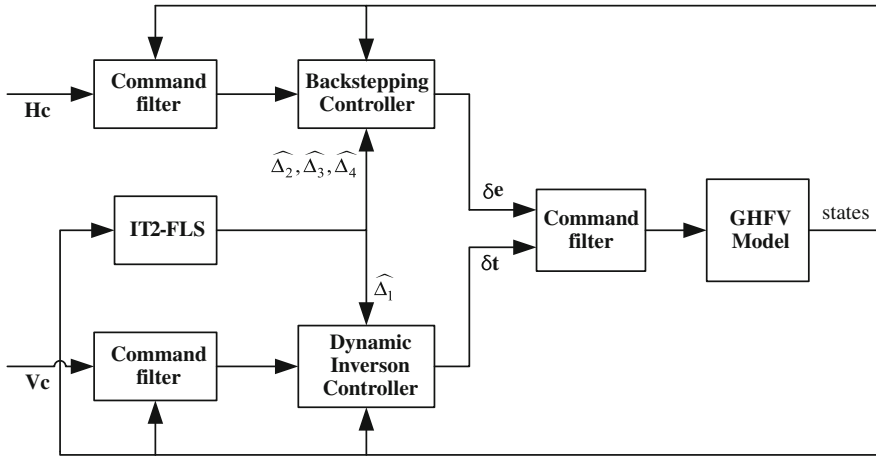


Fig. 18.3 The block diagram of the overall control scheme

$$\dot{\tilde{V}} = f_1 \phi + g_1 - g \sin \gamma - \dot{V}_c - \Delta_1^* \tag{18.5}$$

In order to stabilize the tracking error, by dynamic inversion control, the throttle setting signal is chosen as

$$\phi_c = [-g_1 + g \sin \gamma + \dot{V}_c - k_1 \tilde{V} + \widehat{\Delta}_1] / f_1 \tag{18.6}$$

Where k_1 is a positive constant and (18.5) can be written as

$$\dot{\tilde{V}} = -k_1 \tilde{V} + (\widehat{\Delta}_1 - \Delta_1^*) \tag{18.7}$$

18.3.2 Altitude Subsystem Backstepping Controller Design

The error dynamics of the altitude is

$$\dot{\tilde{h}} = \dot{h} - \dot{h}_c = V \sin \gamma - \dot{h}_c \tag{18.8}$$

In order to stabilize (18.8), the flight path angle command can be chosen as

$$\gamma_c = \sin^{-1} \frac{\dot{h}_c - k_2 \tilde{h}}{V} \tag{18.9}$$

where k_2 is a positive constant and (18.8) can be written as

$$\dot{\tilde{h}} = -k_2 \tilde{h} \tag{18.10}$$

The error dynamics of the flight path angle is

$$\dot{\tilde{\gamma}} = \dot{\gamma} - \dot{\gamma}_c = \bar{q}SC_L^z/mV^*\alpha + \bar{q}S \sin \alpha C_T/mV - g \cos \gamma/V - \dot{\gamma}_c \quad (18.11)$$

Denote $f_2 = \bar{q}SC_L^z/mV$, $g_2 = \bar{q}S \sin \alpha C_T/mV$. As $T \sin \alpha \ll L$, γ is mainly driven by α , so we choose α as the virtual control signal. Similar to the design in velocity subsystem, we consider the general uncertainty Δ_2^* and its estimate $\widehat{\Delta}_2$. Then the virtual control signal is chosen as

$$\alpha_c = [-g_2 + \frac{g \cos \gamma}{V} + \dot{\gamma}_c - k_3\tilde{\gamma} + \widehat{\Delta}_2]/f_2 \quad (18.12)$$

where k_3 is a positive constant and (18.11) can be written as

$$\dot{\tilde{\gamma}} = -k_3\tilde{\gamma} + (\widehat{\Delta}_2 - \Delta_2^*) \quad (18.13)$$

The error dynamics of the angle of attack is

$$\dot{\tilde{\alpha}} = \dot{\alpha} - \dot{\alpha}_c = q - (L + T \sin \alpha)/mV + g \cos \gamma/V - \dot{\alpha}_c \quad (18.14)$$

Denote $g_3 = (L + T \sin \alpha)/mV$ and choose the virtual control signal as

$$q_c = g_3 - g \cos \gamma/V + \dot{\alpha}_c - k_4\tilde{\alpha} + \widehat{\Delta}_3 \quad (18.15)$$

where k_4 is a positive constant and (18.14) can be written as

$$\dot{\tilde{\alpha}} = -k_4\tilde{\alpha} + (\widehat{\Delta}_3 - \Delta_3^*) \quad (18.16)$$

The error dynamics of the pitch rate is

$$\dot{\tilde{q}} = \dot{q} - \dot{q}_c = \bar{q}ScC_M^{\delta_e}/I_y * \delta_e + \bar{q}ScC_M^0/I_y - \dot{q}_c \quad (18.17)$$

Denote $f_3 = \bar{q}ScC_M^{\delta_e}/I_y$, $g_4 = \bar{q}ScC_M^0/I_y$ and choose the elevator deflection signal as

$$\delta_{ec} = [-g_4 + \dot{q}_c - k_5\tilde{q} + \widehat{\Delta}_4]/f_3 \quad (18.18)$$

where k_5 is a positive constant and (18.17) can be written as

$$\dot{\tilde{q}} = -k_5\tilde{q} + (\widehat{\Delta}_4 - \Delta_4^*) \quad (18.19)$$

18.3.3 Interval Type-2 Adaptive Fuzzy Controller Design

In order to obtain the general uncertainty $\widehat{\Delta}_k$ ($k = 1, 2, 3, 4$), we use an interval type-2 adaptive fuzzy controller with pre-determined IT2 antecedent sets and

adaptive T1 consequent sets. The fuzzy rule bases consist of a collection of IF–THEN rules in the following form

$$R^i : \text{ If } \begin{matrix} \widetilde{V} \\ \widetilde{\gamma} \\ \widetilde{\alpha} \\ \widetilde{q} \end{matrix} \text{ is } \begin{matrix} \widetilde{A}_1^i \\ \widetilde{A}_2^i \\ \widetilde{A}_3^i \\ \widetilde{A}_4^i \end{matrix} \text{ and } \begin{matrix} \dot{\widetilde{V}} \\ \dot{\widetilde{\gamma}} \\ \dot{\widetilde{\alpha}} \\ \dot{\widetilde{q}} \end{matrix} \text{ is } \begin{matrix} \widetilde{B}_1^i \\ \widetilde{B}_2^i \\ \widetilde{B}_3^i \\ \widetilde{B}_4^i \end{matrix}, \text{ then } \begin{matrix} \widehat{\Delta}_1 \\ \widehat{\Delta}_2 \\ \widehat{\Delta}_3 \\ \widehat{\Delta}_4 \end{matrix} \text{ is } \begin{matrix} C_1^i \\ C_2^i \\ C_3^i \\ C_4^i \end{matrix} \quad i = 1, 2, \dots, M$$

where M is the number of rules, \widetilde{A}_k^i and \widetilde{B}_k^i are IT2 antecedent sets, C_k^i is T1 consequent sets. \widetilde{A}_k^i and \widetilde{B}_k^i each has 5 IT2-FS like Fig. 18.1, so $M = 5^2 = 25$. By using the singleton fuzzification, product inference, centre-average defuzzification and the center-of-sets type reducer, the type-reduced T1-FS is given by

$$\Delta_{k \cos} = \int_{y_k^1} \dots \int_{y_k^M} \int_{f_k^1} \dots \int_{f_k^M} \prod_{i=1}^M \mu_{C_k^i}(y_k^i) \prod_{i=1}^M \mu_{F_k^i}(f_k^i) \bigg/ \frac{\sum_{i=1}^M f_k^i y_k^i}{\sum_{i=1}^M f_k^i} \quad (18.20)$$

where y_k^i is the centroid of C_k^i and f_k^i is the firing value associated with the i th rule. Here the centroid y_k^i is defined as the point which has the maximum membership value 1. As $\mu_{F_k^i}(f_k^i) = 1, \mu_{C_k^i}(y_k^i) = 1$, so

$$\Delta_{k \cos} = \int_{y_k^1} \dots \int_{y_k^M} \int_{f_k^1} \dots \int_{f_k^M} 1 \bigg/ \frac{\sum_{i=1}^M f_k^i y_k^i}{\sum_{i=1}^M f_k^i} = [\Delta_{kl}, \Delta_{kr}] \quad (18.21)$$

In the adaptive controller, y_k^i is the adaptive parameter and is denoted by new symbol θ_k^i . The fuzzy basis function is

$$\underline{\zeta}_k^i = f_{kl}^i / \sum_{i=1}^M f_{kl}^i, \overline{\zeta}_k^i = f_{kr}^i / \sum_{i=1}^M f_{kr}^i \quad (18.22)$$

f_{kl}^i, f_{kr}^i denote the firing values used to compute the bounds Δ_{kl}, Δ_{kr} which can be obtained using the Karnik–Mendel algorithm [9]. Denote $\underline{\zeta}_k = (\underline{\zeta}_k^1, \underline{\zeta}_k^2, \dots, \underline{\zeta}_k^M)^T, \overline{\zeta}_k = (\overline{\zeta}_k^1, \overline{\zeta}_k^2, \dots, \overline{\zeta}_k^M)^T, \zeta_k = (\underline{\zeta}_k + \overline{\zeta}_k) / 2, \theta_k = (\theta_k^1, \theta_k^2, \dots, \theta_k^M)^T$. The general uncertainty Δ_k can be achieved by

$$\widehat{\Delta}_k = (\Delta_{kl} + \Delta_{kr}) / 2 = \theta_k^T \zeta_k \quad (18.23)$$

18.3.4 Adaptive Law

Denote $e = [\widetilde{V} \widetilde{h} \widetilde{\gamma} \widetilde{\alpha} \widetilde{q}]^T, K = \text{diag}(k_1, k_2, k_3, k_4, k_5), \widetilde{\theta}_k = \widehat{\theta}_k - \theta_k^*, k = 1, 2, 3, 4, P = \text{diag}(p_1, p_2, p_3, p_4, p_5), \widetilde{\Delta} = [\widetilde{\Delta}_1, 0, \widetilde{\Delta}_2, \widetilde{\Delta}_3, \widetilde{\Delta}_4]^T = [\widetilde{\theta}_1^T \zeta_1, 0, \widetilde{\theta}_2^T \zeta_2, \widetilde{\theta}_3^T \zeta_3,$

$\tilde{\theta}_4^T \xi_4]^T$, $\psi = [\psi_1, \psi_2, \psi_3, \psi_4]^T = [p_1 \tilde{V}, p_3 \tilde{\gamma}, p_4 \tilde{\alpha}, p_5 \tilde{q}]^T$. Then the state error dynamics can be written as

$$\dot{e} = -Ke + \tilde{\Delta} \quad (18.24)$$

Consider the following Lyapunov function candidate

$$V_L = \frac{1}{2} e^T P e + \sum_{i=1}^4 \frac{1}{2\eta_i} \tilde{\theta}_i^T \tilde{\theta}_i \quad (18.25)$$

Where P is positive diagonal weight matrix and η_i is positive learning rate. The time derivative of V_L is

$$\dot{V}_L = \dot{e}^T P e + \sum_{i=1}^4 \frac{\dot{\tilde{\theta}}_i^T \tilde{\theta}_i}{\eta_i} = -e^T K P e + \sum_{i=1}^4 \tilde{\theta}_i^T \left(\frac{\dot{\tilde{\theta}}_i}{\eta_i} + \psi_i \xi_i \right) \quad (18.26)$$

So by Lyapunov synthesis approach, the parameter adaptive law can be

$$\dot{\tilde{\theta}}_i = Proj(-\eta_i \psi_i \xi_i), \quad i = 1, 2, 3, 4 \quad (18.27)$$

Where $Proj(\bullet)$ is the projection operator which guarantees all parameters are in their allowed compact sets.

18.4 Simulations

At the trimmed condition $V_0 = 4590.3$ m/s, $h_0 = 33528$ m, $\gamma_0 = 0$ rad, $q_0 = 0$ rad/s, $\alpha_0 = 0.04799$ rad, we choose the reference periodic signal as $600 \sin(0.04\pi t)$ in altitude change. Frequencies of the command filters are $\omega_v = 1$, $\omega_h = 5$, $\omega_\gamma = 20$, $\omega_\alpha = 10$, $\omega_q = 10$, $\omega_e = 40$, $\omega_t = 40$ and all damping ratios equal 1. Weights p_i and learning rates η_i are 1. $k_1 = 38.4096$, $k_2 = 0.4730$, $k_3 = 0.4217$, $k_4 = 0.6768$, $k_5 = 1.1971$. $m = m_0(1 + U + 0.8 * GWN)$, $I_y = I_{y0}(1 + U + 0.8 * GWN)$, $\rho = \rho_0(1 + U + 0.8 * GWN)$, $s = s_0(1 + U + 0.8 * GWN)$, $\bar{c} = \bar{c}_0(1 + U + 0.8 * GWN)$, where $U = -30\%$ is the parameter uncertainty and GWN represents the Gaussian white noise whose power is 0.002.

Simulations are conducted in 3 cases: (a) BS controller; (b) BS + IT2-AFC; (c) BS + T1-AFC. Figure 18.4 shows the results when there is no uncertainty. We see that V and h can track the reference commands very well with or without adaptive fuzzy controllers and that all three controllers have nearly the same control effect.

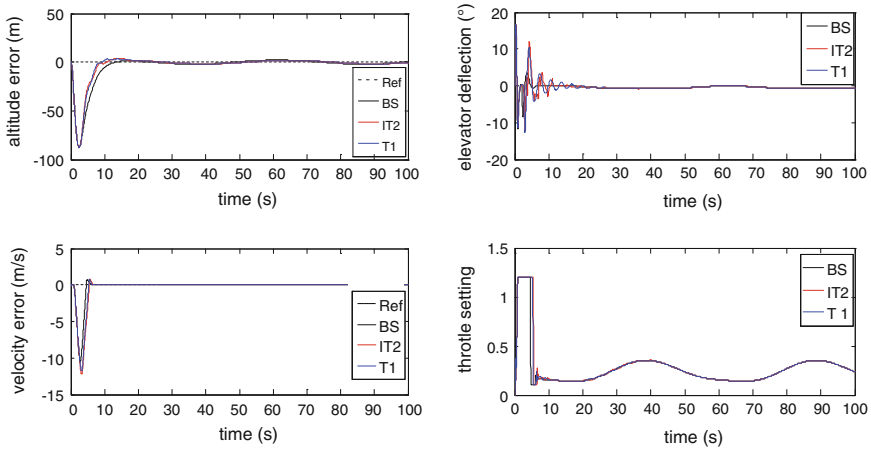


Fig. 18.4 Velocity and altitude tracking error (*left*) and control signals (*right*) without uncertainty

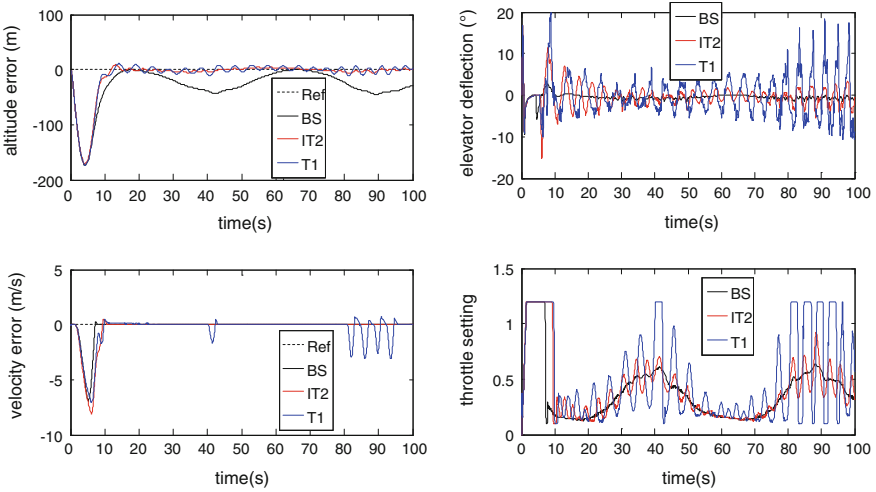


Fig. 18.5 Velocity and altitude tracking error (*left*) and control signals (*right*) with uncertainty

Figure 18.5 shows the results when there exists big uncertainty. The pure backstepping controller has large steady-state altitude tracking error. When we use T1-AFC to compensate the general uncertainty, it has large oscillating tracking errors and large control chattering while the tracking errors and control chattering of IT2-AFC are much smaller.

18.5 Conclusion

In this paper, we designed a backstepping based interval type-2 adaptive fuzzy logic controller for a generic hypersonic flight vehicle. Command filters were used to obtain the derivatives of the wanted signals. Simulation results validated its effectiveness and robustness and also showed that T2-FLS is more capable of handling uncertain problem than T1-FLS.

Acknowledgments This work is supported by National Natural Science Foundation of China (No. 61203003, No. 61273149), Knowledge Innovation Program of the Chinese Academy of Sciences (YYYJ-1122) and Innovation Method Fund of China (No. 2012IM010200).

References

1. Parker JT, Serrani A, Yurkovich S et al (2007) Control-oriented modeling of an air-breathing hypersonic vehicle. *J Guidance Control Dyn* 30(3):856–869
2. Gao D, Sun Z, Luo X et al (2008) Fuzzy adaptive control for hypersonic vehicle via backstepping method. *Control Theory Appl* 25(5):805–810 (in Chinese)
3. Huang X, Wang Q, Dong C (2011) Robust adaptive control of hypersonic vehicles via Backstepping method. *Syst Eng Electron* 33(6):1321–1326 (in Chinese)
4. Mendel JM (2007) Type-2 fuzzy sets and systems: an overview. *IEEE Comput Intell Mag* 2(1):20–29
5. Yang F, Tan X, Yi J (2013) A type-2 adaptive fuzzy logic controller for a generic hypersonic flight vehicle. *ICIC Express Lett* 7(5):1583–1588
6. Ougli AE, Lagrat I, Boumhidi I (2008) A type-2 fuzzy adaptive controller of a class of nonlinear system. *Int J Inf Math Sci* 4(4):282–288
7. Xu H, Mirmirani MD, Ioannou PA (2004) Adaptive sliding mode control design for a hypersonic flight vehicle. *J Guidance Control Dyn* 27(5):829–838
8. Farrell J, Sharma M, Polycarpou M (2005) Backstepping-based flight control with adaptive function approximation. *J Guidance Control Dyn* 28(6):1089–1102
9. Liang Q, Mendel JM (2000) Interval type-2 fuzzy logic systems: theory and design. *IEEE Trans Fuzzy Syst* 8(5):535–550

Chapter 19

Ahead of the End Dynamic Time Warping Distance Algorithm Application in Iterative Learning Control

Qun Gu and Xiaohong Hao

Abstract In this paper, we present a new iterative learning control (ILC) design for a class of linear systems. Ahead of the end dynamic time warping distance (EADTW) algorithm proposed as a method to solve optimization problems in iterative learning control. In the algorithm, after each trail, using EADTW comparative field method for solving optimization problems, the input data and the error data between model output and real output are used to revise plant model, and the new plant model will be used in next trail. The model modifying device is designed for non-linear plant and also can be used in linear plant. The results show that the proposed accelerated algorithms are capable of ensuring monotonic error norm reductions and the convergence speed of the algorithm is increased. Realization of the algorithms is discussed and numerical simulations are provided for comparative purposes and to demonstrate the numerical performance and effectiveness of the proposed methods.

Keywords Iterative learning control · Dynamic time warping · Optimization methods · Constraints · Convergence speed

19.1 Introduction

Iterative learning control (ILC) is a well-known technique to increase the tracking accuracy of a system repeating a given operation, or to suppress a repetitive disturbance acting on system. Significant progress has been made for both

Q. Gu (✉) · X. Hao

School of Electrical and Information Engineering, Lanzhou University of Technology, Lanzhou 730050, China
e-mail: lzgq66@163.com

X. Hao

e-mail: 1119253891@qq.com

technologies and applications of ILC in the past decade for batch processes [1, 2], e.g., chemical batch process.

Recently, a number of references have presented incorporate control methods with ILC. Kira L. Barton, Douglas A. Bristow and Andrew G. Alleyne propose A numerical method for determining monotonicity and convergence rate in iterative learning control [3]. Weisheng Chen, Li Zhang consider adaptive iterative learning control for nonlinearly parameterized systems with unknown time-varying delays [4]. Kira L. Barton, Douglas A. Bristow and Andrew G. Alleyne has presented an alternative method for calculating the ILC norm, which is used as an analysis tool for comparing the convergence rate of different learning algorithms that have been designed elsewhere. And more recently, Dabid H. Owens and Bing Chu has modelled observed behaviour of norm optimal iterative learning control (NOILC) when the plant has one or more non-minimum phase (NMP) zeros [5–7]. Li Heng-jie, Hao Xiao-hong, and Zeng Xian-qiang realize effective tracking of output of nonlinear systems with constraint and model uncertainty in specified time domain, improved clonal selection algorithms are employed to solve optimization problems in iterative learning control. A clonal selection algorithm based nonlinear optimal iterative learning control is proposed. Fang Guo-hua, Zhong Lin-juan, Wu Xue-wen, Tan Wei-xiong Based on the optimal control theory and relevant technology the optimal input-output control model for water resources utilization and water pollution control is established. The method for determining the main parameters of the model were analyzed and investigated, and the model was solved. Then output level of each sector of national economy, speed of development and the corresponding total amount of water resources use and water pollution control from 2006 to 2010 which meet the sustainable utilization of water resources and the requirement of water pollution control of the Jiangsu Province were obtained.

In this article a novel technique for accelerating the predictive Norm-Optimal Iterative Learning Control methodology has been proposed [8]. Ahead of the End Dynamic time warping distance (EADTW) algorithm proposed as a method to solve optimization problems in iterative learning control. The EADTW algorithm is used to solve the optimal solution, the proposed accelerated algorithms are capable of ensuring monotonic error norm reductions and the convergence speed of the algorithm is increased.

19.2 Problem Formulation

19.2.1 Iterative Learning Control Algorithm

Consider the following discrete time, linear time invariant system:

$$\begin{cases} x(t + T_s) = f(x(t), u(t), t) \\ y(t) = g(x(t), u(t), t) \end{cases} \quad (19.1)$$

where $t \in [0, T_s, 2T_s, \dots, T_f]$, $T_f = NT_s$.

The initial condition $x_k(0) = x_0$, denotes $y_d(t)$ as the desired output trajectory.

Ideally, the ILC controller will iteratively generate a command signal, from trial to trial, such that the error $e_k(t)$ converges to zero. This problem is characterized in that whenever the system (19.1) at the end of time $t = T_f$, its status was restored to the original state. In the revised after input, and try again to the desired output approximation. This repetition enables us to a time correction control input, the system output as the final iteration and can well track the desired output. More precisely, the iterative learning control thought is to find optimal control rate:

$$u_{k+1} = f(u_k, u_{k-1}, \dots, u_{k-r}, e_{k+1}, e_k, \dots, e_{k-s}) \quad (19.2)$$

$$\lim_{k \rightarrow \infty} \|e_k\| = 0 \text{ and } \lim_{k \rightarrow \infty} \|u_k - u^*\| = 0$$

where

$$\begin{aligned} y_k &= [y_k(0), y_k(T_s), y_k(2T_s), \dots, y_k(T_f)]^T \\ u_k &= [u_k(0), u_k(T_s), u_k(2T_s), \dots, u_k(T_f)]^T \\ e_k &= [(y_d(0) - y_k(0) | u_0(0), \dots, u_{k-1}(0)), (y_d(T_s) - y_k(T_s) | u_0(T_s), \dots, u_{k-1}(T_s)), \\ &\quad (y_d(2T_s) - y_k(2T_s) | u_0(2T_s), \dots, u_{k-1}(2T_s)), \\ &\quad \dots, (y_d(T_f) - y_k(T_f) | u_0(T_f), \dots, u_{k-1}(T_f))]^T \end{aligned}$$

where u^* to achieve optimal tracking system input. If the system is described for a linear time invariant model

$$\begin{cases} x(t + T_s) = Ax(t) + Bu(t) \\ y(t) = Cx(t) \end{cases} \quad (19.3)$$

So we have $y_k = G_e u_k$.

where

$$G_e = \begin{bmatrix} 0 & 0 & 0 & \dots & 0 \\ CB & 0 & 0 & \dots & 0 \\ CAB & CB & 0 & \dots & 0 \\ \vdots & \vdots & \vdots & \ddots & \vdots \\ CA^{T_l-1}B & CA^{T_l-2}B & \dots & \dots & 0 \end{bmatrix}, \quad T_l = T_f/T_s.$$

This expression can be simplified ILC convergence analysis.

For the linear system optimal iterative learning control algorithms are norm optimal iterative learning control and parameter optimization of two kind of iterative learning control. Norm optimal iterative learning control of the main idea is to solve the optimization problem before each iteration:

$$J_{k+1} = \|u_{k+1} - u_k\|^2 + \|e_{k+1}\|^2 \quad (19.4)$$

where $e_{k+1} = y_{k+1} - y_d$, $y_{k+1}(t) = [G_e u_{k+1}](t)$, G_e as object. The advantage of this method is that as long as the in each iteration for solving the optimization problem (19.4) optimal input u_{k+1} .

If

$$\|e_{k+1}\|^2 \leq J_{k+1}(u_{k+1}) \leq \|e_k\|^2 \tag{19.5}$$

The algorithm can guarantee the output error is monotone convergence. When $y_{k+1}(t) = [G_e u_{k+1}](t)$ of G_e for linear time invariant systems, optimal input can be directly obtained by type:

$$u_{k+1}(t) = u_k(t) + [G_e^* e_{k+1}](t) \tag{19.6}$$

G_e^* is the adjoint operator G_e .

19.2.2 Based on Ahead of the End Dynamic Time Warping Distance (EADTW) comparison method

Definition 1 For the two time series $X = \{x_1, x_2, \dots, x_m\}$, and $Y = \{y_1, y_2, \dots, y_m\}$, DTW distance can be defined recursively as:

$$\begin{cases} D_{DTW}(\langle \rangle, \langle \rangle) = 0, \\ D_{DTW}(X, \langle \rangle) = D_{DTW}(\langle \rangle, X) = \infty, \\ D_{DTW}(X, Y) = d(x_1, y_1) + \begin{cases} D_{DTW}(X, \text{Re st}(Y)) \\ D_{DTW}(\text{Re st}(X), Y) \\ D_{DTW}(\text{Re st}(X), \text{Re st}(Y)) \end{cases}, \\ d(x, y) = \|x - y\|_p \end{cases}$$

where $\text{Re st}(X) = \{x_2, \dots, x_m\}$, $\text{Re st}(Y) = \{Y_2, \dots, Y_m\}$.

Based on DTW distance similarity are essential in the static data, due to its computational complexity is relatively complex, so the flow data on the DTW distance compared with the situation less.

Definition 2 In calculating the distance in the process of, If $D_{DTW}(X, Y) = \sum_{i=1}^m d_i^2 > \varepsilon$, called computational paths to overflow, stop the calculation. Where ε is the error threshold.

For a time series $X = \{x_1, x_2, \dots, x_m\}$ and $Y = \{y_1, y_2, \dots, y_m\}$, Ahead of the End of DTW distance algorithm (EADTW) for process:

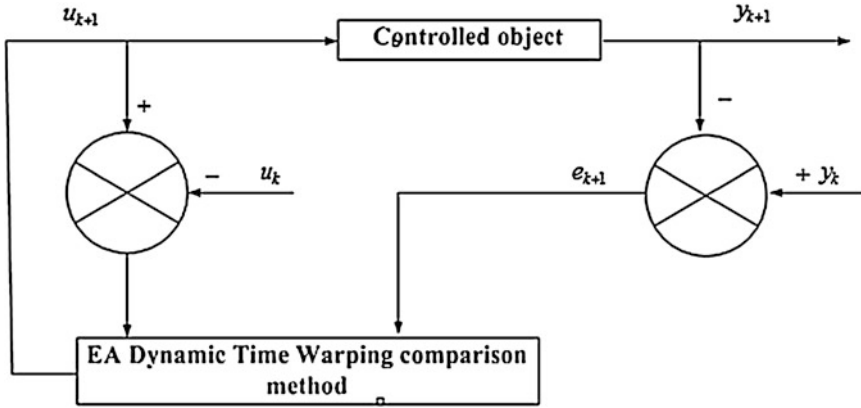


Fig. 19.1 The EADTW-ILC structure

give ε is the error threshold

$sum = 0, overflow = 0$

for $i = 1$ to i $sum = D_{DRW}(X, Y)_i^2$

if $sum > \varepsilon^2$ then $overflow = i$

$$\begin{cases} \text{if } overflow > 0 & \text{There is no overflow} \\ \text{if } overflow < 0 & \text{There is overflow} \end{cases}$$

After each trail, using EADTW comparative field method for solving optimization problems (10), the input data and the error data between model output and real output are used to revise plant model, and the new plant model will be used in next trail. The model modifying device is designed for non-linear plant and also can be used in linear plant (Fig. 19.1).

19.3 Simulation

The mathematics model of the controlled object to

$$\begin{aligned} x_1(i + 1) &= -0.1x_3(i) + u(i) \\ x_2(i + 1) &= x_1(i) \\ x_3(i + 1) &= x_2(i) \end{aligned}$$

where $y = x_1, y_d(i) = 0, i = 1, y_d(i) = \sin(0.05\pi(i - 2)), 2 \leq i \leq 23$.

On the input constraints

$$u_i^{\min} \leq u_i \leq u_i^{\max} \quad i = 1, 2, \dots, 23$$

Fig. 19.2 $\log\|e_k(t)\|$ convergence curve

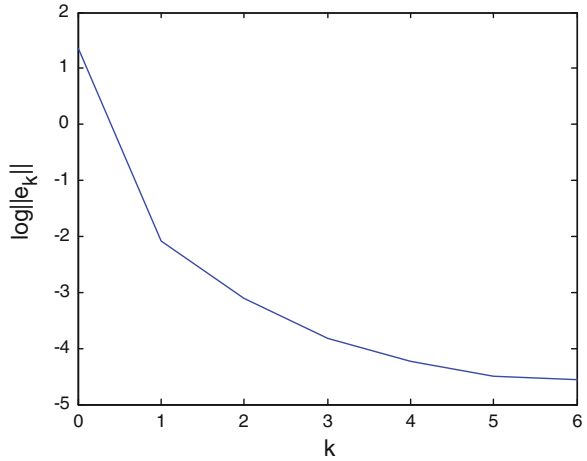
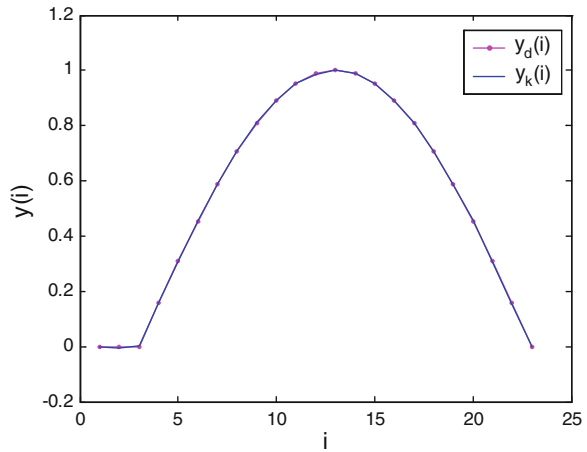


Fig. 19.3 Linear system output tracking curve



EADTW needs to minimize the objective function

$$J_{k+1} = \|u_{k+1} - u_k\|^2 + 0.1\|e_{k+1}\|^2, -1.5 \leq u_i \leq 1.5.$$

The constraint is taken to be $|u_i| \leq 1.5$, Logarithmic error $\log\|e_k(t)\|$ convergence curve with the number of iterations is shown in Fig. 19.2. From the figure, it can be seen that the use of EADTW-ILC control method can achieve this overall output tracking error of the monotone convergence and has a fast convergence rate, which verifies our expectations. Figure 19.3 shows a linear system output tracking curve, when $-1.5 \leq u_i \leq 1.5$.

Acknowledgments This research was supported by The National Nature Science Foundation of China No. 61263008. The natural science foundation of Gansu Province, China No. 1112RJZA023. The natural science foundation of Gansu Province, China No. 1107RJZA150.

References

1. de Castro LN, Timmis J (2002) Artificial immune systems: a new computational intelligence approach. Springer, London
2. de Castro LN, von Zuben FJ (1999) Artificial immune systems Part I-Basic theory and applications. Technical Report RT DCA 01/99, FEEC/UNICAMP, Brazil
3. Barton KL, Bristow DA, Alleyne AG (2010) A numerical method for determining monotonicity and convergence rate in iterative learning control. *J Control* 63:219–226
4. Chen W, Zhang L (2010) Adaptive iterative learning control for nonlinearly parameterized systems with unknown time-varying delays. *Int J Control* 8:177–186
5. Chu B, Owens DH (2010) Iterative learning control for constrained linear systems. *Int J Control* 83(7):1397–1413
6. Hao X, Zhang L, Li H (2008) A new PD type learning control in active control for vibration. In: The 7th World congress on intelligent control and automation (WCICA), Chongqing, China, pp 922–926
7. Hatzikos VE, Owens DH, Hätonen J (2003) An evolutionary based optimization method for nonlinear iterative learning control systems. In: Proceedings of the American control conference, Denver, Colorado, pp 3415–3420
8. Hatzikos V, Hätonen J, Owens DH (2004) Genetic algorithms in norm-optimal linear and non-linear iterative learning control. *Int J Control* 77(2):188–197

Chapter 20

Application of Discrete Particle Swarm Optimization Algorithm to Aviation Rescue Base Location

Xiuyu Wu, Guoping Xing, Yongren Chen and Lijie Wu

Abstract Based on the theoretic study of location of general facilities, this paper makes an attempt to optimize the typical discrete element of the location of aviation rescue base through discrete binary particle swarm (PSO) algorithm in order to find out an optimized location method with more simplified calculation and more optimized result, which will finally provide a solid theoretical foundation for the location of aviation rescue base.

Keywords Aviation rescue base · Location model · Particle swarm optimization algorithm

20.1 Introduction

The scheme for the location of the aviation rescue base determines the structure, mode and scale of the whole rescue network. And its rationality is the basic prerequisite for an effective rescue system. The location of aviation rescue base belongs to that of facilities, which is a matter of non-linear programming with constraint conditions in math. With a few parameters, the discrete particle swarm

X. Wu (✉) · Y. Chen

Department of Aviation Lifesaving, Aviation University of Air Force of PLA,
7855 Renmin Street, Changchun 130022, China
e-mail: wuxiuyu2005@163.com

G. Xing

Aviation University of Air Force of PLA, 2222 Nanhu Road, Changchun 130022, China
e-mail: guopingxing@gmail.com

L. Wu

Department of Foreign Language and Traveling, Chengde Petroleum College,
Chengde 067000, China
e-mail: anyone0212@163.com

optimization (DPSO) is easy to understand and to realize. Thus DPSO algorithm is employed in this paper for the optimization calculation of the aviation rescue base location.

20.2 Discrete Particle Swarm Optimization [1, 2]

Definition 1 (*Discrete solution value set of the DPSO algorithm*) The discrete value set $S = [s_1, s_2, \dots, s_n]$ constituted by any limited discrete values $s_i \in R$ is called the discrete solution value set of the DPSO algorithm.

Definition 2 (*The discrete velocity value set of the DPSO algorithm*) The value of the velocity $v = (i \rightarrow j)$, $i, j \in R$ represents the change of the discrete value from i to j . the velocity value set $V = [v_1, v_2, \dots, v_n]$, which is constituted by any finite velocity values, is called the discrete velocity value set of the DPSO algorithm.

For the above definitions, the basic calculation rule of the discrete solution value set and discrete velocity value set should also be defined, i.e. the subtraction operator between the discrete solution value sets, the addition operator between the discrete velocity value sets, the multiplication operator between the constant and the discrete velocity value set as well as the addition operator between the discrete solution value set and the discrete velocity value set. The basic equation by which the four basic operators constitute the DPSO algorithm is as follows:

$$v_{d+1} = \omega v_d \oplus c_1 \cdot (\text{pBest}_{i_d} \ominus x_d) \oplus c_2 \cdot (\text{gBest}_d \ominus x_d) \quad (20.1)$$

$$x_{d+1} = x_d \otimes v_{d+1} \quad (20.2)$$

The calculation of the four newly defined operators is shown below:

Definition 3 (*The subtraction operator between the discrete solution value sets* \ominus) This operator represents the subtraction operation of the particle between discrete solution values, as is presented in the calculation of $\text{pBest}_{i_d} \ominus x_d$ and $\text{gBest}_d \ominus x_d$ in Eq. (20.1). And the result is the discrete velocity value set of the particle. The result of the discrete value $i \ominus j$ is the velocity of the particle ($j \rightarrow i$), which shows the change of discrete value from j to i .

Definition 4 (*The addition operator between the discrete velocity value sets* \oplus) The operator represents the addition operation of the particle between the discrete velocity value sets, and the result is still the discrete velocity value sets of the particle. In the operation of the velocity values ($j \rightarrow i$) \oplus ($k \rightarrow m$), if $j = k$, then the result will be ($i \rightarrow m$); or the result will be ($i \rightarrow j$).

Definition 5 (*The multiplication operator between the constant and the discrete velocity value sets* \bullet) This operator is the multiplication operation between the constant and the discrete velocity value set. The result is still the discrete velocity

value set of the particle. C is a constant selected from $(0, 1)$, c' is a random number in $(0, 1)$. If $c' \leq c$, then $c \bullet (i \rightarrow j) = (i \rightarrow i)$; if $c' > c$, then $c \bullet (i \rightarrow j) = (i \rightarrow j)$.

Definition 6 (The addition operator between the discrete solution value set and the discrete velocity value set \otimes) This operator is the addition operation between the discrete solution set and the discrete velocity value set, and the result is the discrete solution value of the particle. In the operation $i \otimes (k \rightarrow m)$ of the discrete value, if $i = k$, the result will be m ; or the result will be i .

The operators defined above can meet the need of the DPSO algorithm equation.

20.3 The Application of Discrete Particle Swarm Optimization Algorithm in Aviation Rescue Base Location [3–6]

20.3.1 Model Construction [7]

Assuming that there are i ($i = 1, 2, \dots, t$) medical institutions in the specified region, and there are j ($j = 1, 2, \dots, v$) rescue base candidate points chosen through the collected data, and demand points of the rescue base are divided into k regions ($k = 1, 2, \dots, r$).

20.3.1.1 Selecting Decision Variables

There are three types of variables in the location selection models:

z_j is an integer variable between 0–1, and there is j in total, representing j rescue base candidate points respectively. The selection of the final program is decided by its different values: if the value is 0, z_j represents that the candidate point address is not selected; if the value is 1, z_j represents the selection of the address.

x_{ij} represents the distance (kilometres) between the medical institutions i and the rescue base j , and the unit is hundred kilometres.

x_{jk} represents the distance between the rescue base j and the rescue demand point k , and the unit is hundred kilometers.

20.3.1.2 Determination of the Objective Function

Assuming f is the total efficiency of the rescue base layout program, according to the rescue base location and the purpose of network plan, the efficiency should be maximized, so there is the objective function:

$$\begin{aligned} \max f(x_{ij}, x_{jk}, z_j, U_j) = & \sum_{j=1}^v \sum_{k=1}^r z_j (10^2 \cdot b_{jk} - d_{jk}) x_{jk} - \sum_{j=1}^v z_j v (10^3 \cdot U_j)^\zeta \\ & - \sum_{j=1}^v z_j 10^4 \cdot (f_j + g_j) - \sum_{j=1}^v \sum_{i=1}^t z_j (a_{ij} + c_{ij}) x_{ij} \end{aligned} \quad (20.3)$$

where

- a_{ij} represents the average unit cost of rescuing the wounded from the rescue base j to the medical institution point i , and the unit is yuan/km
- b_{jk} represents the benefit rate the rescue base j can get from the air rescue of the rescue demand point k , and the unit is hundred yuan/km
- c_{ij} represents the average unit freight of rescuing the wound from the rescue base j to medical institution point i , and the unit is yuan/km
- d_{jk} represents the unit depletion fee for the air rescue from the rescue base j to rescue demand point k , and the unit is yuan/km
- $v(10^3 \cdot U_j)^\zeta$ represents the equipment maintenance cost of the rescue base, which is the coverage concave function of rescue base. According to experience, the value ζ is usually set as 0.5
- f_j represents the initial investment cost of the rescue base, and the unit is ten thousand RMB
- g_j is the daily operating cost of the rescue base j , and the unit is ten thousand RMB
- U_j is the coverage of the j th rescue base, and the unit is thousand kilometers

s.t. Constraints

$$\sum_{j=1}^t z_{ij} \leq G, \quad j = 1, 2, \dots, v \quad (20.4)$$

$$\sum_{i=1}^t x_{ij} + \sum_{k=1}^r x_{jk} = 10^3 \cdot z_j U_j, \quad j = 1, 2, \dots, v \quad (20.5)$$

$$z_j \in \{0, 1\}, \quad x_{ij}, x_{jk} \geq 0, \quad U_j \geq 0 \quad (20.6)$$

$$\sum_{j=1}^v x_{jk} \leq D_k, \quad i = 1, 2, \dots, r \quad (20.7)$$

$$z_j U_j \geq z_j S_j \quad (20.8)$$

$$\sum_{j=1}^v z_j f_j \leq W, \quad j = 1, 2, \dots, v \quad (20.9)$$

$$\sum_{j=1}^v x_{ij} \leq M_i, \quad i = 1, 2, \dots, t \quad (20.10)$$

$$\sum_{i=1}^t x_{ij} = h \sum_{k=1}^r x_{jk}, \quad j = 1, 2, \dots, v \quad (20.11)$$

where

- G represents the maximum number of the rescue bases that can be built
- D_k represents the maximum rescue distance of the rescue-demand point k, and the unit is kilometre
- S_j represents the maximum coverage of the jth rescue base, and the unit is thousand kilometres
- W represents the quota of the total investment in the rescue base, and the unit is 10 thousand RMB
- M_i represents the acceptable capacity of the medical institutions, and the unit is person

Since this model consists of concave functions, it is a Mixed Integer Linear Programming model. Through the analysis of the model above, it consists of three types of variables, that is, $v \times (t + r)$ x variables, v U variables, and v z variables, and $t + r + 7v + (t + r) \times v$ constraints. With the increase of the number of the medical institutions, alternate rescue bases, and rescue-demand points, the complexity of the solving procedure grows exponentially, which makes it difficult to solve through the conventional algorithm. As a result, PSO optimizing algorithm is proposed in this thesis.

20.3.2 The Rrealization of the Model Optimizing of DPSO Algorithm [8, 9]

The site selection is a typical non-linear programming issue with constraints. The variables of the model are in discrete distribution, so the thesis proposes discrete PSO algorithm to solve the model. Before solving, according to the special characteristics of site selection for a rescue base, the thesis puts forward several solution projects as follows:

1. According to the mathematical Eq. (20.1) of the discrete PSO algorithm, the feasible expression of the site-selection model can be determined. And the solution in the location model is in accordance with the location of the particle in Eq. (20.1). The by searching the optimal position of the particle swarm, the feasible solution is found.
2. The selection of inertia weight ω

The value of ω should abide by some rules as follows: the value maintains the maximum at first, then it is set smaller and smaller, and at last, it maintains the minimum (close to zero).

3. The selection of the acceleration coefficients c_1, c_2

To improve the effect of searching optimization through the algorithm, it is generally hoped that c_1 gradually decreases while c_2 gradually increases. The function model of c_1 and c_2 are as follows:

$$c_1 = (c_{1\max} - c_{1\min}) \left(\frac{t}{T_{\max}} \right)^2 + (c_{1\min} - c_{1\max}) \left(\frac{t}{T_{\max}} \right) + c_{1\max} \quad (20.12)$$

$$c_2 = (c_{2\min} - c_{2\max}) \left(\frac{t}{T_{\max}} \right)^2 + (c_{2\max} - c_{2\min}) \left(\frac{t}{T_{\max}} \right) + c_{2\min} \quad (20.13)$$

4. The establishment of the fitness function

Make a loose treatment of the constraints of the site-selection model by formula (20.14), based on which a fitness function is built accordingly [10].

$$\text{Fitness}(\vec{x}) = \begin{cases} f(\vec{x}), & g_j(\vec{x}) \leq \varepsilon \quad \forall j=1,2,\dots,m \\ f_{\max} + \sum_{j=1}^m g_j(\vec{x}), & \text{其他} \end{cases} \quad (20.14)$$

20.3.3 Diffset

According to the basic requirements for the location of the aviation rescue base, the author makes a location optimization calculation with the test data of six preliminarily selected aviation rescue bases through C++ programming, just as the method abovementioned.

The parameters involved in the algorithm are as follows:

1. Inertia weight [3-5] $\omega = \frac{1}{1 + e^{0.02 \times (t - \frac{T_{\max}}{3})}}$.

2. Acceleration coefficient

$$c_1 = (c_{1\max} - c_{1\min}) \left(\frac{t}{T_{\max}} \right)^2 + (c_{1\min} - c_{1\max}) \left(\frac{t}{T_{\max}} \right) + c_{1\max}$$

$$c_2 = (c_{2\min} - c_{2\max}) \left(\frac{t}{T_{\max}} \right)^2 + (c_{2\max} - c_{2\min}) \left(\frac{t}{T_{\max}} \right) + c_{2\min}$$

where set $c_{1\max} = c_{2\max} = 2.5$, $c_{1\min} = c_{2\min} = 1$, t is the current number of iterations.

3. The scale of the particle swarm $N = 150$
4. The maximal number of the iterations $T_{\max} = 1,000$

With the development of Visual Studio software, the DPSO algorithm of the location of the aviation rescue base is realized through VC programming.

After the operation of these procedures, the data that meet the conditions for the establishment of the base are selected as the optimal result, while the other four alternative schemes are deleted.

20.4 Conclusions

In this paper, the location of the aviation rescue base is selected as the subject and the particle swarm algorithm as the research method. The PSO algorithm is applied to the military issue of aviation rescue base location. Based on the sample analysis of the DPSO-based model with the solution optimization method through related data, as well as the diffset, the effectiveness and the feasibility of the DPSO algorithm in the aviation rescue base location is well tested and verified.

References

1. Clerc M (1999) The swarm and the queen: towards a deterministic and adaptive particle swarm optimization. In: Proceedings of CEC, pp 1951–1957
2. Kennedy J, Eberhart RC (1997) Discrete binary version of the particle swarm algorithm. In: Proceedings of the IEEE international conference on systems, pp 4104–4108
3. Zhang PL, Wei QY (2003) Model of the location of the logistics voyage repair factory and its heuristic algorithm. *J Transport* 7:65–68 (in Chinese)
4. Cao ZY, Zhou GG, Xu Q (2007) The issue of the location of the maintenance center. *J Oper Res* 11:275–277 (in Chinese)
5. Liu F, Sun M, Li N (2004) The Particle Swarm Algorithm and its Application in layout optimization. *Comput Eng Appl* 40:12 (in Chinese)
6. Yang FM, Hua G, Wi, Deng M (2005) The progress of the location issue. *Oper Res Manage Sci* 14(6):1–7 (in Chinese)
7. Hu S (2009) Research on aviation overhaul depot base on particle swarm optimization. Master's Dissertation of Aviation University of the Air Force (in Chinese)
8. Zhang LP, Yu HJ, Chen DZ, Hu SX (2004) An analysis and improvement of the particle swarm optimization algorithm. *Inf Control* 33(5):513–517 (in Chinese)
9. Angeline PJ (1998) Using selection to improve particle swarm optimization. In: IEEE international conference on evolutionary computation, Anchorage, Alaska, USA, pp 84–89
10. Deb K (2000) Efficient constraint handling method for genetic algorithms. *Comput Methods Appl Mech Eng* 186(2):311–338

Chapter 21

Intelligent Control Based on ADRC for Large Container Ship Course Keeping

Yang Liu, Chen Guo and Zhengling Lei

Abstract In this paper, the course keeping control problem of a 5446TEU container ship is considered, a ship mathematical model is set up based on MMG modeling theory, the model's validity is verified through a comparison study of turning simulation. A LADRC method is applied to the ship motion model, the simulation results illustrate the effectiveness of the control method.

Keywords Course keeping · Container ship · MMG model · LADRC method

21.1 Introduction

Large container ships are characteristic of large-scale and high-speed. Usually the LOA is over 250 m, with displacement more than 80,000 DWT and a full speed of 25–32 Knots. Moreover, the large container ships also have their inherent characteristics, such as large inertia, area by wind, draft, side area below the waterline, and the influence of current on the ship maneuvering, together with poor course keeping ability, Yaw checking ability, steerage and stopping ability. These features make the manipulation of large container ships different from the others, therefore, great emphasis should be attached to the course keeping control. With regard to its large inertia [1], long time delay and non-linear characteristics, the course keeping control is in essence a complex multi-input and multi-output dynamic system, run in uncertain circumstances.

Currently, the course keeping control methods of large container ships mainly include PID control [2], adaptive control [3] and robust control [4], etc. Taking account of the engineering practice, the complexity and the stability of the

Y. Liu (✉) · C. Guo · Z. Lei
Department of Seamanship, Navigation College, Dalian Maritime University,
Dalian 116026, Liaoning, China
e-mail: liuyang0880@126.com

system [5], the control methods begin to involve many linear and non-linear combination or a variety of non-linear combinations. For example, Fuzzy Controller with PID Structure for Ship Course [6] is based on conventional fuzzy controller, multiplies the integral term, constructs a new ship course keeping PID fuzzy controller by attaching the PD-type fuzzy controllers to PI-type fuzzy controllers. Additionally, Controller Design Based on Adaptive Fuzzy Sliding Mode Control for Ship Course [7] uses a fuzzy logic system to approximate the system unknown function, combining the sliding mode control with adaptive fuzzy control.

Active Disturbance Rejection Control (ADRC) is to control the object as a simple integral tandem-shaped, namely the standard. It regards those dynamically different parts against the standard as a ‘total disturbance’ to deal with, and promptly estimates and eliminate it through the means of extended state observer, forcing the controlled object full of disturbance, uncertainty and nonlinear into the standard integral tandem-shaped [8]. Contrast to Robust control and adaptive control, ADRC makes the object adjust to the controller and converts the complicated nonlinear, time-varying and uncertain control problem to a simple linear, time-invariant, and constant one. In view of this, this paper introduces Linear Active Disturbance Rejection Control (LADRC) into large container ship course keeping control.

21.2 Ship Motion Model

According to separate modeling theory [9], a ship motion simulation model is established with a 5446TEU container ship data in this paper. In this section, the idea how to build the ship model is illustrated in details as the follows.

$$\left. \begin{aligned} m(\dot{u} - vr) &= X_{H_0} + X_P + X_R + X_{disturbance} \\ m(\dot{v} + ur) &= Y_{H_0} + Y_P + Y_R + Y_{disturbance} \\ I_{zz}\dot{r} &= N_{H_0} + N_P + N_R + N_{disturbance} \end{aligned} \right\} \quad (21.1)$$

where the subscript m denotes ship quality, I_{zz} is the moment of quality inertia for hull around the vertical axis which through the gravity center, H_0 denotes the ship hull, P describes the propeller, R denotes rudders while disturbance describes the environmental disturbances from wind, waves and currents.

In the above equations, Ship motion parameters as well as the hydrodynamic derivative are dimensionless, in order to facilitate the application of the boat model test data into a real ship, those data need to be nondimensionalized according to prime system.

21.2.1 The Fluid Forces and Moments Acting on the Hull

Fluid force and torque can be divided into the inertia class and viscous class according to the nature of the produce. It can be depicted in the following equations:

$$\left. \begin{aligned} X_{H_0} &= X_I + X_H \\ Y_{H_0} &= Y_I + Y_H \\ N_{H_0} &= N_I + N_H \end{aligned} \right\} \quad (21.2)$$

where subscript I denotes fluid force and torque of the inertia class while H is viscous class. The effect of fluid force and torque of the inertia class acting on the hull can be expressed as the form of added mass m_x , m_y and additional moment of inertia J_{zz} . The ship motion model considering the effect of fluid force and torque of the inertia class can be described as:

$$\left. \begin{aligned} (m + m_x)\dot{u} - (m + m_y)vr &= X_H + X_P + X_R + X_{disturbance} \\ (m + m_y)(\dot{v} + ur) &= Y_H + Y_P + Y_R + Y_{disturbance} \\ (I_{zz} + J_{zz})\dot{r} &= N_H + N_P + N_R + N_{disturbance} \end{aligned} \right\} \quad (21.3)$$

The calculation detailed methods of m_x , m_y and J_{zz} can be reached in the book [9].

When the ship operates at a normal speed in the fluid, the size of the drift angle produce a great impact on the size of the viscous forces and moments. In this paper, ‘Kijima’ model [10] is adopted when the drift angle $\beta \leq 20^\circ$ while ‘Yasuo Yoshimura’ model [11] when $\beta > 30^\circ$, and the interpolation between the two models is used when $20^\circ < \beta \leq 30^\circ$.

The estimation formula of Kijima viscous hydrodynamic forces [10] and torque can be expressed as:

$$\left. \begin{aligned} X_H &= X_{(u)} + X_{vv}v^2 + X_{vr}vr + X_{rr}r^2 \\ Y_H &= Y_{v}v + Y_{r}r + Y_{|v|v}|v|v + Y_{|r|r}|r|r + Y_{vvr}v^2r + Y_{vrr}vr^2 \\ N_H &= N_{v}v + N_{r}r + N_{|v|v}|v|v + N_{|r|r}|r|r + N_{vvr}v^2r + N_{vrr}vr^2 \end{aligned} \right\} \quad (21.4)$$

where $X_{(u)}$ denotes direct resistance, $X_{vv}v^2$, $X_{vr}vr$, $X_{rr}r^2$ describe viscous resistance caused by ship movement, $Y_{v}v$, $Y_{r}r$, $N_{v}v$, $N_{r}r$ are linear lateral hydrodynamic forces and torque, and $Y_{|r|r}|r|r$, $Y_{|v|v}|v|v$, $Y_{vvr}v^2r$, $Y_{vrr}vr^2$, $N_{|v|v}|v|v$, $N_{|r|r}|r|r$, $N_{vvr}v^2r$, $N_{vrr}vr^2$ denote nonlinear lateral hydrodynamic forces and torque.

The estimation formula of Yasuo Yoshimura viscous hydrodynamic forces [11] and torque can be expressed as:

$$\left. \begin{aligned} X_H &= X_H(r=0) + X_{vr}vr + X_{rr}r^2 \\ Y_H &= Y_H(r=0) + Y_r|u|r + 1/2\rho d C_d \left\{ Lv|v| - \int_{-L/2}^{L/2} (v + C_{ry}xr)|v + C_{ry}xr|dx \right\} \\ N_H &= N_H(r=0) + N_r|u|r - 1/2\rho d C_d \int_{-L/2}^{L/2} (v + C_{m}xr)|v + C_{m}xr|xdx \end{aligned} \right\} \quad (21.5)$$

where $X_H(r=0)$, $Y_H(r=0)$, $N_H(r=0)$ describe the hydrodynamic forces and torque of the low-speed domain when the turn angular velocity is 0.

The calculation details of viscous hydrodynamic forces and torque can be referred in paper [12].

21.2.2 The Fluid Forces and Moments Acting on the Propeller

Compared with the hull transverse force and transverse torque, propeller transverse force and transverse torque are a small amount when propeller is running ahead. It has been taken into the bare hull hydrodynamic calculation model. Propeller force calculation model is expressed as:

$$\left. \begin{aligned} X_p &= (1 - t_p)\rho n^2 D_p^4 K_T(J_p) \\ Y_p &= 0 \quad N_p = 0 \end{aligned} \right\} \quad (21.6)$$

where t_p denotes thrust deduction factor, D_p records propeller diameter, n denotes main engine rate of revolution, K_T marks thrust coefficient, and J_p describe the propeller advance coefficient. The calculation details can be referred in book [9].

21.2.3 The Fluid Forces and Moments Acting on the Rudder

The calculation model of the rudder used in this paper can be expressed as follows:

$$\left. \begin{aligned} X_R &= (1 - t_R)F_N \sin \delta \\ Y_R &= (1 + a_H)F_N \cos \delta \\ N_R &= (x_R + a_H x_H)F_N \cos \delta \end{aligned} \right\} \quad (21.7)$$

where x_R denotes the vertical coordinates of the point of the transverse force acting on the rudder, and a_H , x_H , t_R marks the influence coefficient between hull and rudder.

21.3 Shanghai Turning Test Simulation

Based on the real ship data of 5446TEU container ship named Shanghai, MMG model of the ship is established, and turning test simulation is made to verify the credibility of the ship mathematical model in this section. Basal parameters of Shanghai are shown in [12].

The ship sailing test status: Forward and after draft is $d_f = 4.97$ m, $d_a = 9.34$ m respectively. Displacement $\Delta = 39,893$ t, area of rudder $A_R = 43.14$ m², block coefficient $C_b = 0.626$. High-speed right-hand and left-hand turning simulations are conducted in this section.

21.3.1 High-Speed Right-Hand Turning Simulation

Set the simulation environment as: Initial speed $V_0 = 27.4$ kn, main engine revolution $n = 86$ r/min, wind velocity $V_{wind} = 8.8$ m/s, angle between wind direction and initial heading $\alpha = 21^\circ$ steer the rudders right to 35° , assume the ship's initial speed as 27.4 kn. Record the time the bow first turns to 360° . The simulation results are given in Figs. 21.1 and 21.2.

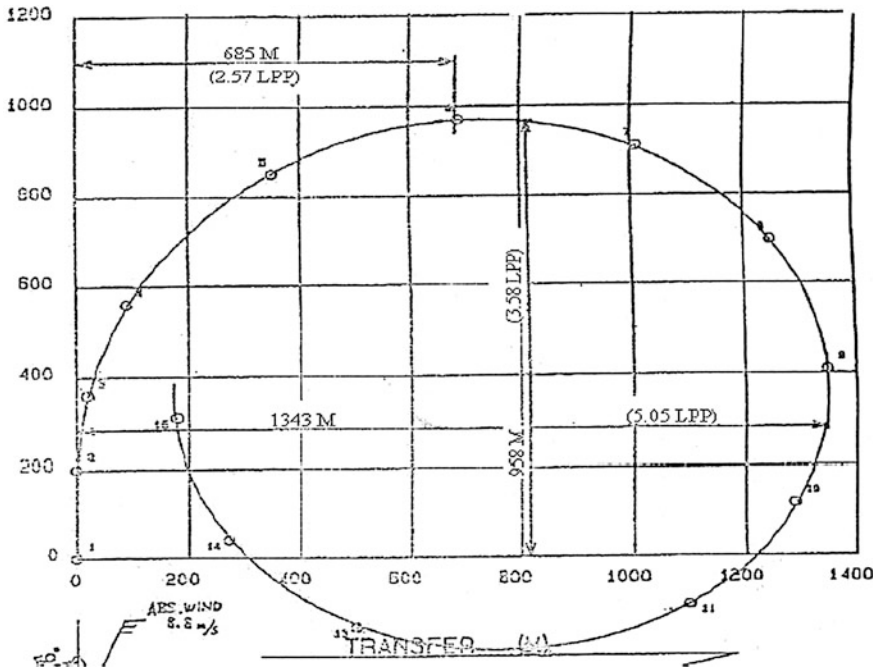


Fig. 21.1 Track of right-hand turning of real test

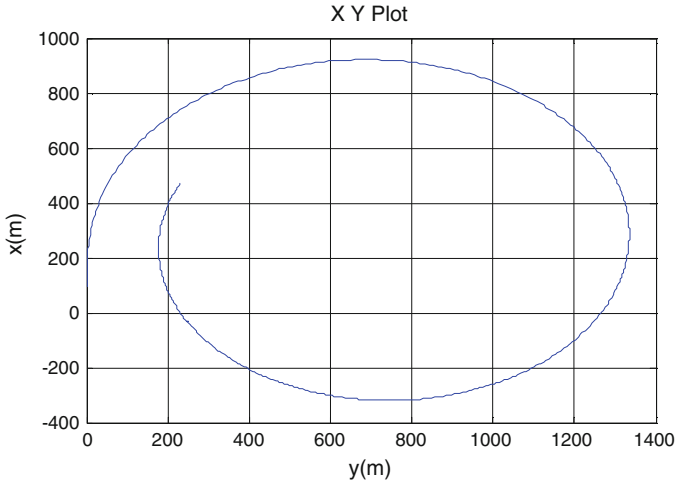


Fig. 21.2 Track of right-hand turning of simulation

21.3.2 High-Speed Life-Hand Turning Simulation

Set the simulation environment the same as the high-speed right-hand turning simulation, steer the rudders left to 35°, the simulation result is depicted in Figs. 21.3 and 21.4.

Analysis and comparison of the Figs. 21.1–21.4, the error between the real ship’s tactical diameter and the simulation’s is less than 0.11L_{PP}; and the error between the real ship’s advance and the simulation’s is less than 0.22L_{PP}, the errors are both less than 20 %. In a word, we take the ship mathematical model as credible.

21.4 LADRC and its Application in Course Keeping Control

LADRC has been widely used in different application researches due to the simple parameters tuning methods proposed by Dr. Gao [13]. We apply the very method to the large container ship’s course keeping control, and test its anti-interference capacity in this section.

As for this MMG ship model, the Linear Extended State Observer (LESO) is designed as follows:

$$\dot{z} = \begin{bmatrix} -3\omega_o & 1 & 0 \\ -3\omega_o^2 & 0 & 1 \\ -\omega_o^3 & 0 & 0 \end{bmatrix} z + \begin{bmatrix} 0 & 3\omega_o \\ b_o & 3\omega_o^2 \\ 0 & \omega_o^3 \end{bmatrix} \begin{bmatrix} \delta \\ \psi \end{bmatrix} \quad (21.8)$$

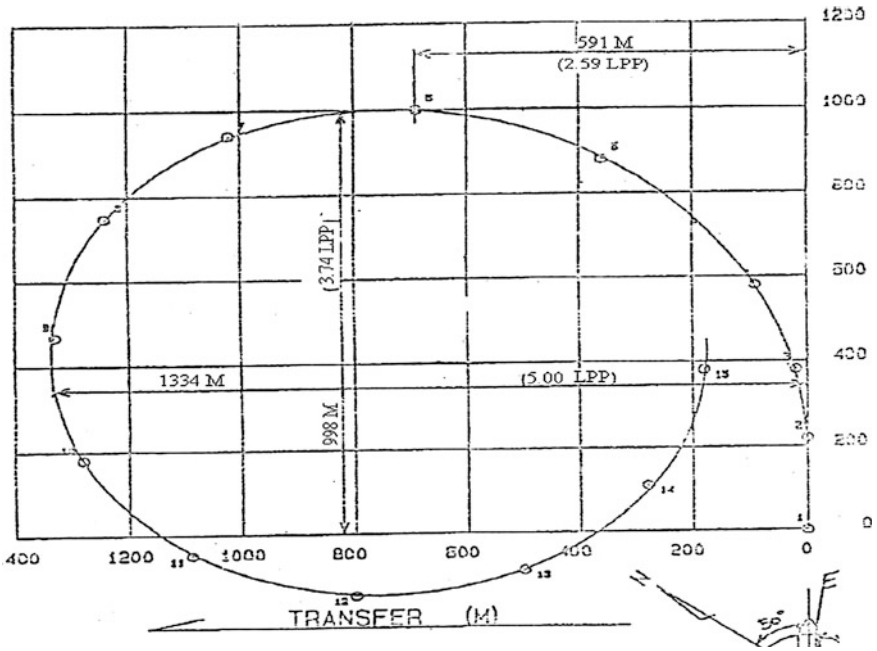


Fig. 21.3 Track of right-hand turning of real test

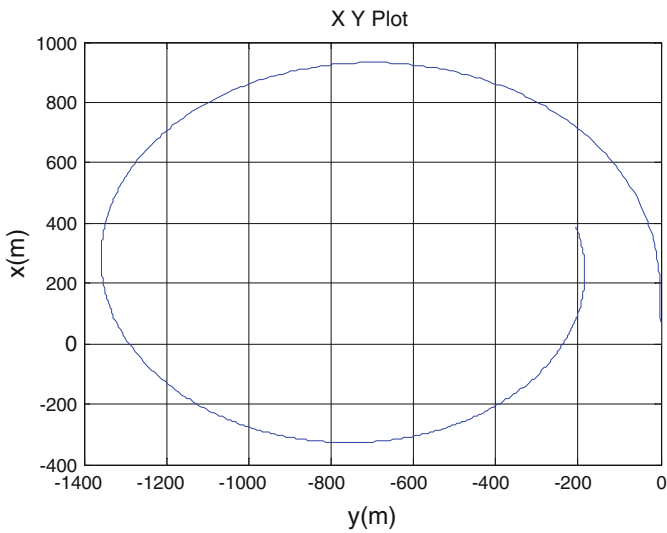


Fig. 21.4 Track of right-hand turning of simulation

And for appropriate values of ω_o and b_o , z_1 can approach ψ , z_2 approaches $\dot{\psi} = r$, and z_3 approaches the uncertainties.

The controller is defined as:

$$u = \frac{u_o - z_3}{b_o} \text{ and } u_o = k_p(r - z_1) - k_d z_2, k_p = \omega_c^2, k_d = 2\zeta\omega_c \text{ and } \zeta = 1$$

Thus there're three parameters ω_c, ω_o, b_o to be tuned to keep the ship's heading on the desired direction.

21.4.1 Comparison Simulation for Systems of LADRC and PID

Assume ship speed is 27.1 kn, the ship's start heading direction is 0, and the target heading is 10°. In the case of not considering the effects of wind, wave and current, the desired direction will be reached if the parameters of LADRC are tuned as follows: $\omega_c = 0.1, \omega_o = 9, b_o = 0.05$.

The heading curve is depicted in Fig. 21.5.

As for the same ship mathematical model, the desired heading also can be targeted if the parameters are tuned as $k_p = 1.3, k_I = 0.01, k_d = 50$ for a PID controller. The heading curve is shown in Fig. 21.6.

It can be read from the above curves that both the LADRC and PID can achieve the control goal within 100 s. However, it also can be noticed that LADRC system responds faster than PID system under the condition that both the two controllers are well tuned.

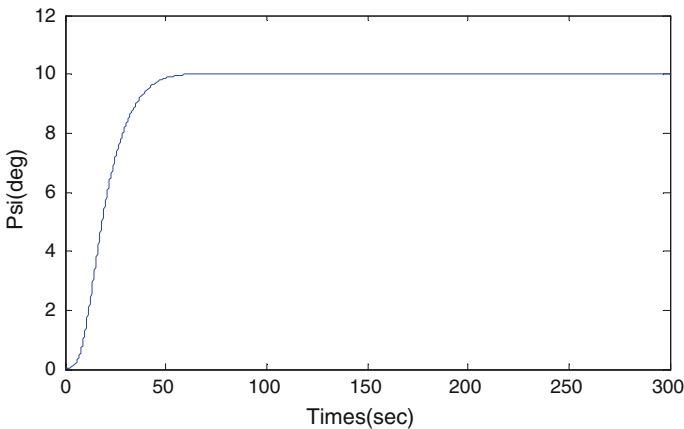


Fig. 21.5 Heading curve of LADRC

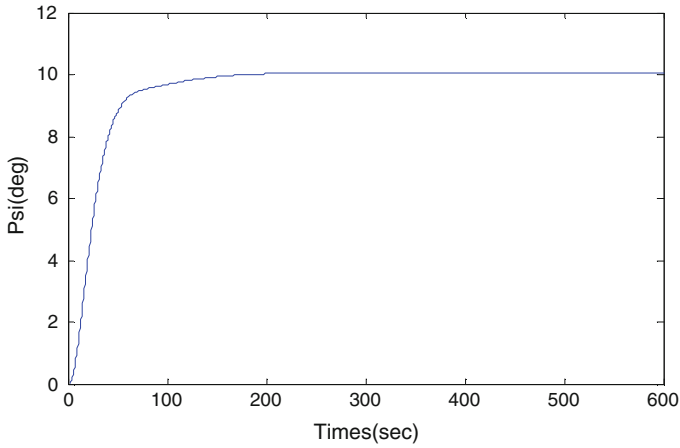


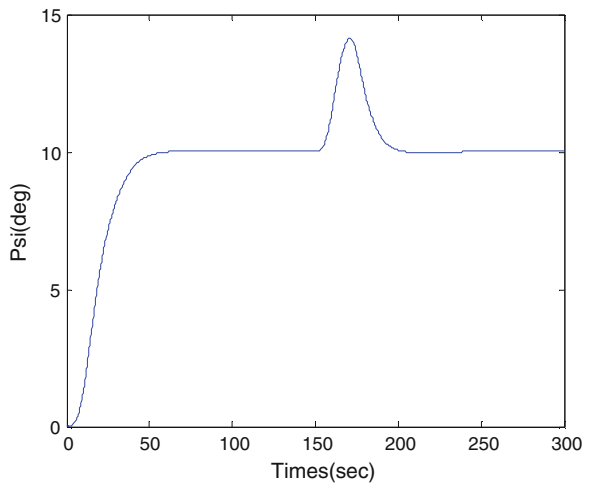
Fig. 21.6 Heading curve of PID

21.4.2 Anti-Interference Performance Test

In order to verify the anti-interference capacity of LADRC, a pulse interference about 5° is added to the controller output at 150 s since started. This interference is produced by pulse generator in simulink, the source block parameters are set as: amplitude is 5 and pulse width is 1 s.

Maintain both the two controller's parameters unchanged, the heading curve of LADRC is depicted in Fig. 21.7. The error curve and output of the LADR controller is given in Fig. 21.8, and the uncertainties estimated by the LESO is shown in Fig. 21.9.

Fig. 21.7 Heading curve



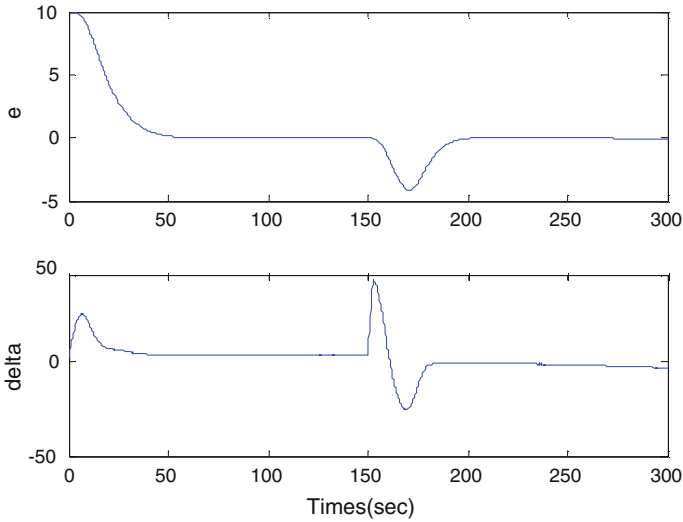
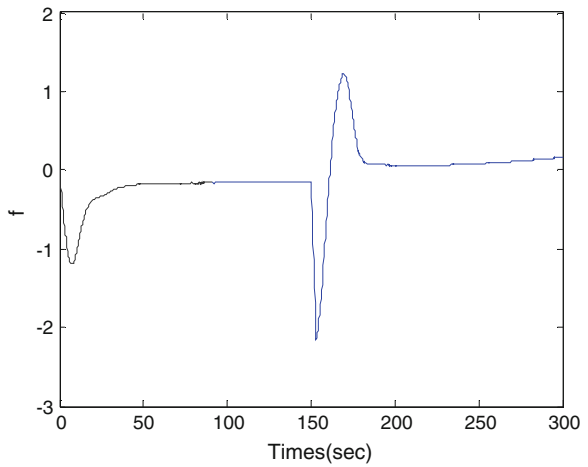


Fig. 21.8 Error and controller output

Fig. 21.9 Uncertainties estimated by LESO



Under the same impact of pulse interference, the simulation results of PID system demonstrated a different case. The heading curve is shown in Fig. 21.10. The error curve and output of the controller is given in Fig. 21.11.

It is clear from the above curves that the PID control system cannot recover the ship heading to the reference direction after the interference disappears while the LADRC system can target the desired heading exactly again, which demonstrates that the LADRC system possesses a stronger robustness than PID control system.

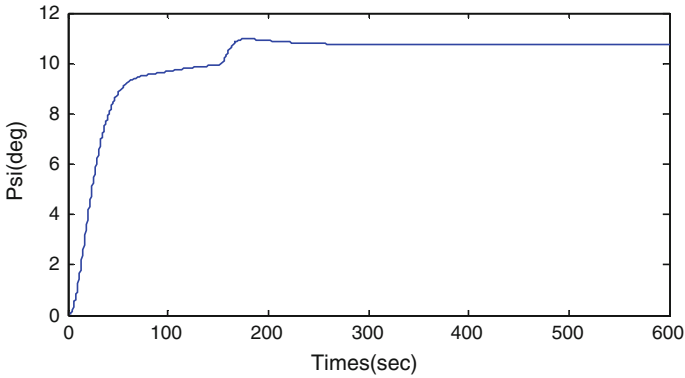


Fig. 21.10 Heading curve of PID

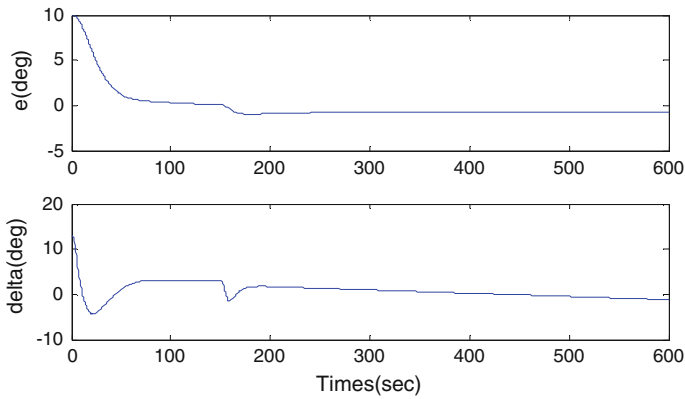


Fig. 21.11 Curves of error and controller output

21.5 Conclusions

The course keeping problem of a 5446TEU container ship has been investigated. A linear ESO is used to estimate the uncertainties, and a PD controller based on the LESO is designed to force the system output to keep on a desired ship heading. The simulation results demonstrate that the LADRC shows a strong robustness against pulse interference.

Acknowledgments This work was supported by the National Nature Science Foundation of China (No. 61074053) and the Applied Basic Research Program of Ministry of Transport of China (No. 2011-329-225-390).

References

1. Jia XL, Zhang XK (2002) Ship motion intelligent control and H_∞ robust control. Dalian Maritime University Press, Dalian (in chinese)
2. Han CS, Liu J, Ru FX, Xu JA (2012) Track keeping control for a ship with PID algorithm. *Tech Autom Appl* 31(4):9–12 (in chinese)
3. Wu Y, Wu HS, Yuan L (2012) Adaptive fuzzy sliding mode controller for ship's track-keeping systems based on input-output linearization. *Comput Technol Autom* 31(3):5–9 (in chinese)
4. Wang ZY, Wu HS, Wu Y (2012) Straight-line tracking control of ships based on input-state linearization. *Mar Electr Electron Eng* 32(8):47–53 (in chinese)
5. Liu WJ (2012) Nonlinear robust control study on course and track for underactuated marine surface vessels. Graduate School of Dalian Maritime University, Dalian (in chinese)
6. Zhang WM, Guo C (2012) Investigation on fuzzy controller with PID structure for ship course. *Shipbuilding China* 53(1):45–52 (in chinese)
7. Liu WJ, Sui QM, Zhou FY, Xiao HR (2012) Controller design based on adaptive fuzzy sliding mode control for ship course. *Inf Control* 41(2):136–141 (in chinese)
8. Han JQ (2009) Active disturbance rejection control technique—the technique for estimating and compensating the uncertainties. National Defense Industry Press, Beijing
9. Jia XL, Yang YS (1999) Ship motion mathematical model: mechanism modeling and identification model. Dalian Maritime University Press, Dalian (in chinese)
10. Yang YS (1996) Study on ship manoeuvring mathematical model in shiphandling simulator. In: *Proceedings of the international conference Marsim' vol 96*, pp 607–615
11. Yoshimura Y, Kensaku N (1978) The processing of ship maneuvering motion in accordance with speed increase or decrease. *J Soc Naval Architects Japan* 144:57–69
12. Liu T (2010) Study on modeling and simulation of manoeuvring and control for large container ship. Graduate School of Dalian Maritime University, Dalian (in chinese)
13. Gao ZQ (2003) Scaling and bandwidth-parameterization based controller tuning. *Am Control Conf* 6:4989–4996

Chapter 22

Course Keeping Control of Underactuated Surface Vessels Based on Improved PSO Algorithm

Guangyu Li, Chen Guo and Yanxin Li

Abstract Based on the relationship between parameter speed v_{\max} and inertia factor ω in the particle swarm optimization (PSO) algorithm, the improved PSO algorithm that is time-varying nonlinear trigonometric function to control PSO algorithm parameters is proposed to prevent the particles fall into local optimum, and the improved PSO algorithm is used to optimize parameters of PID controller which is used in course control for underactuated surface vessels (USV). Two different PSO algorithms for optimizing parameters of PID controller are compared in this paper, and the results of simulation experiments show that, according to dynamic characteristics changes of USV, the controller which used improved PSO algorithm can optimize the adaptive parameters well and automatically, and has a high tracking speed, small overshoot and strong immunity etc.

Keywords Underactuated surface vessels · Improved particle swarm optimization algorithm · PID controller · Course keeping control · Automatic rudder

22.1 Introduction

In recent years, maneuvering of underactuated surface vessels has become the focus. The underactuated system is defined as a system that the spatial dimension of control input is less than spatial dimension of configuration, which is the

G. Li (✉) · C. Guo
Navigation College of Dalian Maritime University, No.1 Lingshui Road,
Dalian, China
e-mail: ligyu@163.com

C. Guo
e-mail: guoc@dlnu.edu.cn

G. Li · Y. Li
Software Institute of Dalian Jiaotong University, No.216 XingFa Road,
Dalian, China
e-mail: lyx7977@163.com

number of control system input less than the freedom degrees of system [1, 2]. In the study of maneuvering of USV, ship course control is an important standard for the evaluation of ship maneuvering performance. When the ship is sailing on the sea, the disturbance of it is very complicated, so the stability of ship course cannot be guaranteed [3, 4]. Course control device for traditional USV is digital PID automatic rudder, but it is sensitive to the high-frequency disturbances which lead to frequent steer. The particle swarm optimization algorithm which used to optimize parameters of PID controller is introduced; it can effectively improve the control precision of ship course.

The key parameter of PSO algorithm is inertia factor ω , when ω is larger, the global search ability of algorithm is strong; when ω is smaller, the local search ability of algorithm is strong [5]. In order to improve the fast and robust of ship course control based on the relationship between parameter speed v_{max} and inertia factor ω in PSO algorithm, the improved PSO algorithm which is time-varying nonlinear trigonometric function to control PSO algorithm parameters is proposed to prevent the particles fall into local optimum in this paper.

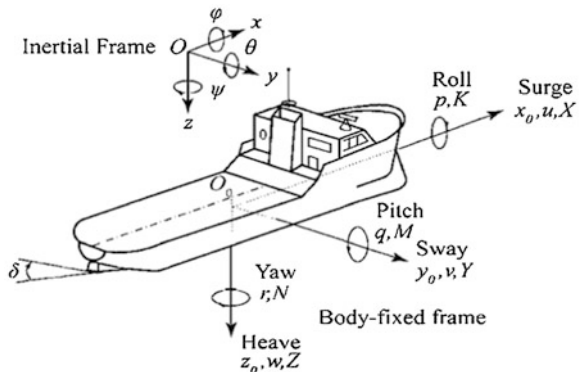
22.2 Model of Underactuated Surface Vessels

22.2.1 Maneuvering Mathematical Model

For an ocean vessel moving in 6 DOF, the 6 different motion components are conveniently denoted as surge, sway, heave, roll, pitch, and yaw, see Fig. 22.1.

Considering the course control problem of an underactuated surface vessel, the vessel is moving in the horizontal plane, and the heave, roll, and pitch are usually neglected. The mathematical model of an underactuated surface vessel can be written as below

Fig. 22.1 Reference frames and variables for ship motion description



$$\begin{cases} \dot{x} = u \cos \psi - v \sin \psi \\ \dot{y} = u \sin \psi + v \cos \psi \\ \dot{\psi} = r \\ \dot{u} = \frac{m_{22}}{m_{11}} vr - \frac{d_{11}}{m_{11}} u + \frac{1}{m_{11}} \tau_u \\ \dot{v} = -\frac{m_{11}}{m_{22}} ur - \frac{d_{22}}{m_{22}} v \\ \dot{r} = \frac{m_{11}-m_{22}}{m_{33}} uv - \frac{d_{33}}{m_{33}} r + \frac{1}{m_{33}} \tau_r \end{cases} \quad (22.1)$$

Where x , y and ψ denote the surge displacement, sway displacement, and yaw angle in the earth fixed frame; u , v and r are the surge, sway and yaw velocities, respectively; m_{11} , m_{22} and m_{33} denote the inherent mass and additional mass of ship, which are model uncertainties; d_{11} , d_{22} and d_{33} denote the hydrodynamic damping of the surge displacement, sway displacement, and yaw angle, which are model uncertainties; τ_u and τ_r denote longitudinal force and torque of turning ship.

22.2.2 Norrbin Nonlinear Model for Course Control

The USV usually looks as a dynamic system in the design of ship course controller. The system input is rudder angle δ , output is yaw angle. In the case of steering is not very frequent, the Norrbin nonlinear model of course control for USV is deduced from the maneuvering mathematical model of USV.

$$\ddot{\psi} = -a_1 \dot{\psi} - a_2 \psi^3 + b \delta \quad (22.2)$$

In which, $a_1 = \alpha b$, $a_2 = \beta b$, $b = K/T$ are all model parameters, K and T are ship indexes; α and β are nonlinear coefficient. K , T , α and β are relevant to the speed and structure of ship.

22.3 The Design of Course controller

22.3.1 Improved Particle Swarm Optimization Algorithm

The particle swarm optimization algorithm originates in the research of prey behavior of birds. It is essentially belongs to the iterative random search algorithm, has a parallel processing feature, and good robustness, easy to implement. In principle, it can be used on the larger probability to find the global optimal solution of the optimal problem, and has high calculation efficiency [6]. Through the information sharing between groups and the individual experience, the individual action strategy can be corrected; the optimization problem results can be obtained finally. However, the convergence speed of PSO algorithm is becoming slowly in the later evolution, easy to fall into local optimum and optimization accuracy is

poor. To enhance the performance of the algorithm, it is very important the inertia factor ω of PSO algorithm control parameters, which can effectively regulate the global searching ability of the algorithm and local exploitation ability. In the chapter, based on the relationship between parameter speed v_{\max} and inertia factor ω in PSO algorithm, the improved PSO algorithm that is time-varying nonlinear trigonometric function to control PSO algorithm parameters is proposed to prevent the particles fall into local optimum. Because the parameter speed v_{\max} of PSO algorithm determines the regional resolution between the current location and the best position, and the large inertia factor ω can make the algorithm not easy to fall into local optimal; to the later period of the algorithm, small inertia factor ω can make the convergence rate be accelerated and not occur oscillation. When the parameter speed v_{\max} became larger, reducing inertia factor ω can prevent particles fly out of the search area; and when the parameter speed v_{\max} became smaller, increasing inertia factor ω can prevent the particles wandering in the local optimal point which causes local optimum. According to the relationship of the parameter speed v_{\max} and inertia factor ω , because the decline characteristic of concave function is better than the linear decline characteristics, and the linear function decline characteristic is better than the decline characteristic of convex function [7, 8]. Therefore, in order to improve the convergence of particle swarm algorithm and avoid falling into local optimal algorithm, this chapter uses the time varying nonlinear trigonometric function method to control the parameters of PSO algorithm for the improved algorithm. The following equation is

$$\omega^k = \omega \sin(v^k \theta), \theta \in (-\pi, \pi) \quad (22.3)$$

In the improved PSO algorithm, supposes the total number of particles for N , each particle has a position x_i in space, this particle flight forward from x_i by the speed v_i , the optimal position which each particle search in the space is p_i , the optimal position which the particle swarm search in the space is p_g , the second iteration correction of x_i is $v_i^k = [v_{i1}^k, v_{i2}^k, \dots, v_{in}^k]$, then

$$\begin{aligned} v_i^k &= \omega v_i^{k-1} + c_1 \text{rand}_1 (p_i - x_i^{k-1}) + c_2 \text{rand}_2 (p_g - x_i^{k-1}); x_i^k = x_i^{k-1} + v_i^{k-1}, i \\ &= 1, 2, \dots, N \end{aligned} \quad (22.4)$$

In the formula (22.4), k is the number of iterations; c_1 and c_2 are acceleration factor, which keep the motion inertial of particles and have the ability of extending search space trend; rand_1 and rand_2 are random number between 0 and 1; ω is inertia factor, the search ability can be changed by adjust inertia factor. The termination condition of the improved PSO algorithm is that the largest iterations number or the fitness value of the optimal position which particle swarm searches so far meets the predetermined minimum fitness threshold value.

22.3.2 The Parameter Optimization Process of PID Controller

PID control is a regulator which is a linear combination of proportional, integral and differential. The Mathematical formula is as follows:

$$u(t) = K_p(e(t) + \frac{1}{T_i} \int_0^t e(t)d\tau + T_d \frac{de(t)}{dt}) \tag{22.5}$$

In which, K_p , $K_i = K_p/T_i$ and $K_d = K_p T_d$ is respectively proportional, integral and differential; $e(t)$ is feedback bias; $u(t)$ is output volume of controller. The aim of improved PSO-PID parameter optimization is to obtain the optimal control effect by selecting the proper parameters of proportion, integral and differential.

To optimize parameters of PID controller by the improved PSO algorithm, its process is shown in Fig. 22.2.

In which, the particles as PID controller parameters, and the particles corresponding to the adaptive value as control system performance index are the connecting bridge between particle swarm algorithm and Simulink model. The optimization process is as follows, PSO generates particle swarm which can be initialized or be updated, the particles of particle swarm are assigned to the PID controller parameters which are K_p , K_i , K_d , then run the Simulink model of control system, and obtain the performance index of the corresponding parameters, the

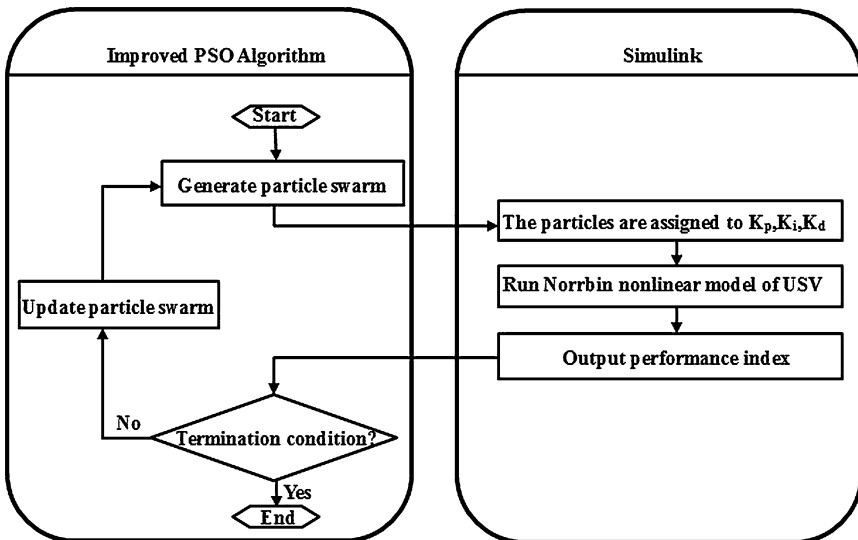


Fig. 22.2 Process flow of improved PSO algorithm

performance index is transferred to the PSO as the particle’s fitness value. Finally, determine whether the algorithm can be ended.

22.4 Numerical Simulations

The simulation experiment uses the data of 5446TEU container ship of COSCO Group, supposes the rated speed of this ship is $V = 24.51knots$, and the parameters are shown in Table 22.1.

According to Table 22.1, the parameters can be calculated $K = 0.2419$, $T = 2067958$, $\alpha = 11.6049$ and $\beta = 10.1966$ in the rated speed. The maximum rudder angle limits at $-35^\circ \sim +35^\circ$, in $0 \sim 1000$ s the expected course angle takes 20° and in $1001 \sim 2000$ s the expected course angle takes 30° , conventional PSO-PID control and improved PSO-PID control are used to control ship course respectively, and the simulation results are shown in Figs. 22.3 and 22.4. Using the improved PSO-PID controller, steering is less frequent than the conventional PSO-PID controller, rudder angle is smaller than the conventional PSO-PID controller, and the overshoot is much smaller much smaller than conventional PSO-PID

Table 22.1 Parameters of 5445TEU container ship

Parameter	Value	Parameter	Value
Ship length LOA	280 M	Two column length L	267 M
Ship width B	39.8 M	Gravity center distance X_c	2.64 M
Rudder area A_δ	61.0 M ²	Square coefficient C_b	0.67
No load mass m	3.5453 Million tons	Fully load mass m	6.5531 Million tons
Design draft T	12.532 M	Fully load draft	14.023 M

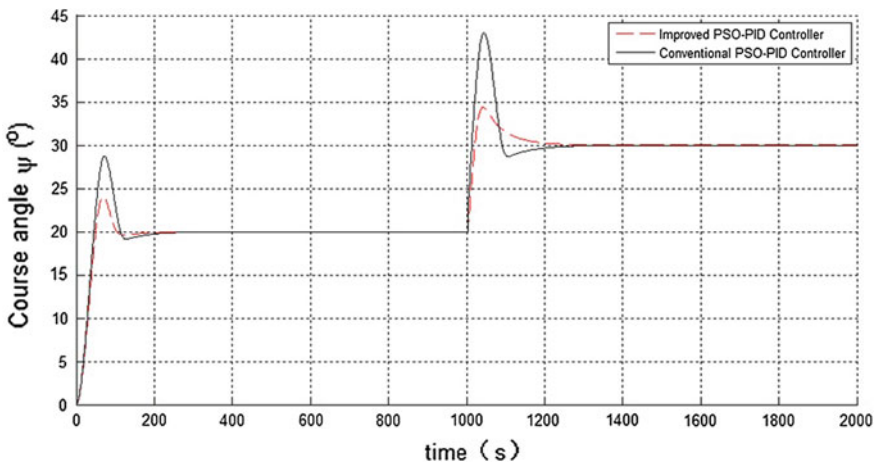


Fig. 22.3 Control tracking curve comparison of course angle in 20 and 30°

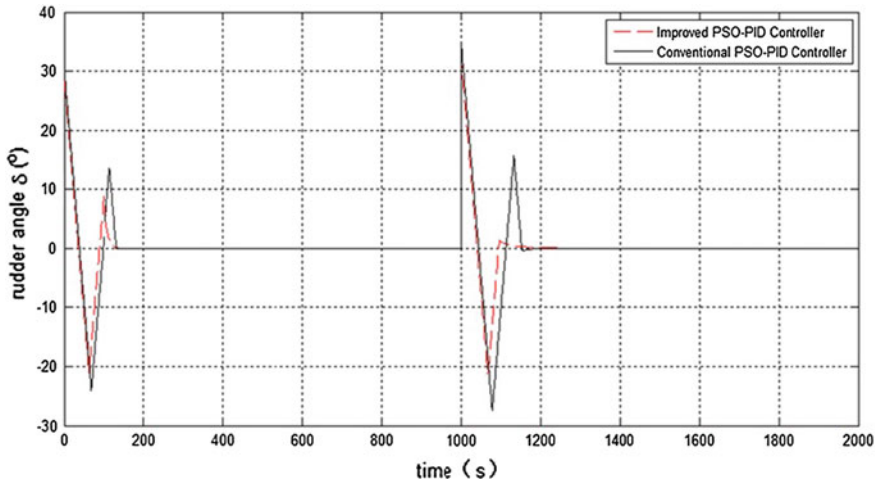


Fig. 22.4 Rudder angle comparison of different course angle

controller at the same time. In the same interference conditions, the controller used improved PSO is superior to the conventional PSO-PID controller in the immunity ability and the adaptive ability.

22.5 Conclusion

In this study the improved particle swarm optimization algorithm that is time-varying nonlinear trigonometric function to control PSO algorithm parameters was discussed. Numerical simulations were conducted and the results show that the performance of improved PSO-PID controller is better than the conventional PSO-PID controller. The controller which used improved PSO can optimize the adaptive parameters well, and has a high robustness, small overshoot and strong immunity. It has high spreading value.

Acknowledgments Foundation item: Supported by the National Natural Science Foundation of China (Grant No. 61074053) and the Applied Basic Research Program of Ministry of Transport of China (Grant No. 2011-329-225-390).

References

1. Kolmanovsky I, McClamroch NH (1995) Developments in nonholonomic control problems. IEEE Control Syst Mag 15:20–36
2. Meng W, Guo C, Liu Y (2012) Robust adaptive path following for underactuated surface vessels with uncertain dynamics. J Mar Sci Appl 11:244–250

3. Du JL, Guo C, Zhao YS et al (2007) Adaptive robust nonlinear design of course keeping ship steering autopilot. 8th International Conference on Control, Automation, Robotics, and Vision, Kunming, China, pp 13–18
4. Liu S, Fang L, Li J (2007) Application of H control in rudder/flap vector robust control for ship course. International conference on mechatronics and automation, ICMA2007, pp 774–778 (in Chinese)
5. Zhang CL, Jiang JL (2010) A PID controller parameter tuning method based on improved PSO algorithm. *J Control Instrum Chem Ind* 37(12):15–18 (in Chinese)
6. Del Valle Y, Venayagamoorthy GK (2008) Particle swarm optimization: basic concepts, variants and applications in power systems. *IEEE Trans Evol Comput* 12(2):171–195
7. Hou YH, Huang S (2011) Regression analysis of ship principal dimensions based on improved PSO-BP algorithm. *J Adv Mater Res* 308–310:1029–1032
8. Liu G, Lao SY (2012) OACRR-PSO algorithm for anti-ship missile path planning. *J Acta Automatica Sinica* 38(9):1528–1537

Chapter 23

On-line Optimization of Fuzzy-Immune PID for PEMFC Temperature Control Based on RBF Neural Network

Dazi Li, Yadi Yu and Qibing Jin

Abstract Proton Exchange Membrane Fuel Cell (PEMFC) temperature exists complex nonlinearity and is deeply disturbed by load change. Considering the characteristics of PEMFC temperature control, an improved fuzzy-immune PID algorithm is derived based on the immune feedback regulating law. Compared with general fuzzy-immune PID algorithm, radial basis function (RBF) neural network is introduced to the on-line optimization work of fuzzy-immune PID parameters, which optimizes the PID parameters on-line. Simulation results show that the proposed method in this study achieves good performance in temperature control and is useful for wide application of PEMFC.

Keywords PEMFC · Fuzzy-immune PID · RBF neural network · Temperature control

23.1 Introduction

PEMFC is one of the most compromising new power sources because of its being environmentally clean, quick start-up, light weight and so on [1, 2]. An effective temperature-control method is one of the key issues to the efficient and safe operation of PEMFC, because electrical characteristics are very sensitive to temperature change [3]. As the temperature goes higher than 90 °C, the efficiency of PEMFC will be reduced because of the increasing vapor pressure and losing water from membrane. On the contrary, low operating temperature will decrease

D. Li (✉) · Y. Yu · Q. Jin
Institute of automation, College of Information Science and Technology, Beijing University of Chemical Technology, No.15 North East Road of Sanhuan, Chaoyang District, Beijing 10029, China
e-mail: lidz@mail.buct.edu.cn

the electrochemical reaction rate and increase the ohmic resistance. Generally, the operating temperature range is 60–90 and 70 °C is treated as the ideal point [4].

For getting better performance of PEMFC, it is necessary to develop a suitable control algorithm to operate PEMFC at a reasonable temperature range. Some efforts have been made to control PEMFC temperature in recent years. Lee et al. [5] applied PID algorithm to control PEMFC temperature, but the accuracy is low. A fuzzy logic controller is designed for PEMFC temperature control and achieves good performance in disturbance rejection [4]. A non-linear predictive controller is designed to optimize the thermal management of PEMFC [6]. For PEMFC system, the main disturbance to temperature control is load change, so disturbance rejection, error eliminating and response are key factors to evaluating the performance of temperature controller. However, the mentioned key factors have not received enough attention in control strategy design. It is very important to integrate the mentioned factors above and design safe, practical control strategy for PEMFCs operation.

Fuzzy-immune PID has good performance in anti-disturbance and error eliminating, which simulates the natural immune mechanism and absorbs the characteristics of PID controller [7]. However, the optimization of PID parameters becomes more complex due to the nonlinearity in proportional term of PID. RBF neural network is adopted to tune the PID parameters adaptively due to its good performance in solving optimization problems. The advantages of artificial immune algorithm meet the requirement of temperature control of PEMFC nicely. In order to achieve satisfactory results, it is necessary to attach enough importance to artificial immune algorithm.

In this paper, an improved fuzzy-immune PID algorithm is applied to temperature control of PEMFC. Compared with general fuzzy PID controller, the PID parameters are optimized by RBF neural network and the proposed strategy has advantages of fast set-point tracking, small overshoot, and strong anti-disturbance capability and robustness etc. It can improve the control performance of PEMFC temperature and popularize the artificial immune algorithm.

23.2 Dynamic Modeling of PEMFC Temperature

The dynamic temperature model of PEMFC is presented and calculated along the channel. This model accounts for energy conversation and thermal transfer of the stack.

23.2.1 Electrical Power Model

The output voltage of the fuel cell is given as follows:

$$V_{\text{cell}} = V_{\text{oc}} + \eta_{\text{act}} + \eta_{\text{ohm}} \quad (23.1)$$

where V_{oc} is open circuit output voltage, η_{act} is voltage loss due to activation, η_{ohm} is ohmic voltage, the three terms are calculated as below:

23.2.2 Dynamic Temperature Model

The solid temperature of the PEMFC is affected by various mechanisms such as (a) heat transfer by conduction; (b) heat transfer to the fuel and oxidant flows and coolant channels; (c) heat generation by reaction; (d) heat of evaporation/condensation. The energy balance is given by

$$mc_{ps} \frac{dT_s}{dt} = Q_r + Q_{in} - P_{st} - Q_{out} - Q_{cool} - Q_{amb} \quad (23.2)$$

where m denotes the mass of the stack, c_{ps} denotes the average thermal transmission coefficient of the stack, Q_r denotes the heat produced by reaction Q_{in} denotes the heat brought in by input gas, P_{st} denotes the power produced by the stack, Q_{out} denotes the heat brought out by exhaust gas, Q_{cool} denotes the heat brought out by cooling water, Q_{amb} denotes the conversation between the stack and environment.

23.3 Improved Fuzzy-immune PID Algorithm

Artificial immune system is the collective name for all kinds of information computing and processing technology which is developed from principles and mechanisms of biological immune system [7, 8]. Artificial immune algorithm has attached much attention in control field, which makes the controller get immunity to multi-disturbance.

23.3.1 Design of Fuzzy-Immune PID

According to inspiration and the simulation of biological immune system, the artificial immune system has a strong adaptive ability for anti-antigens, although it is very complex [7, 9]. Because of the invasion of antigens, B cell accepts the activation of T_H -cell and inhibition of T_S -cells. Assume that the output of helper B-cells is $T_H(k)$ and amount of suppressor T-cells is $T_S(k)$. Therefore, the total B-cells at k-generation can be expressed as follows:

$$s(k) = T_H(k) - T_S(k) = k_1 \varepsilon(k) - k_2 f(\Delta(\Delta s(k))) (k) \quad (23.3)$$

where, $\varepsilon(k)$ is the number of k-generation antigens, k_1 is the promoting factor, k_2 is the inhibiting factor. $f(\cdot)$ is a selected nonlinear function, which denotes the immune effects of interacting between antibody and antigen.

The output of fuzzy-immune PID is given as follows:

$$u(k) = u(K-1) + k'_p(e(k) - e(k - 1)) + k_i(k)e(k) + k_d(k)(e(k) - 2e(k - 1) + e(k - 2)) \tag{23.4}$$

where, $k'(p) = k_p(k)(1 - \alpha f(u(k), \Delta u(k)))$.

Taking advantage of the good performance of fuzzy controller in approximation, a two-dimensional fuzzy controller (FC) is introduced to resolve the difficulty of choosing non-linear function $f(\cdot)$. Inputs of FC are a fuzzy data set of output $u(k)$ and its change rate $\Delta u(k)$. Each input variable has been made fuzzy by two sets: positive (P) and negative (N). Each output variable is classified by three sets: positive (P), zero (Z), negative (N). According to the principles of “the more stimulation cells, the less inhibiting ability” and “the smaller stimulation cells, the greater inhibiting ability”, the membership functions are shown in Fig. 23.1 and the fuzzy rules are introduced as follows:

- (1) If u is PB and du is PB then f is N(1);
- (2) If u is PB and du is NB then f is Z(1);
- (3) If u is NB and du is PB then f is Z(1);
- (4) If u is NB and du is NB then f is P(1);

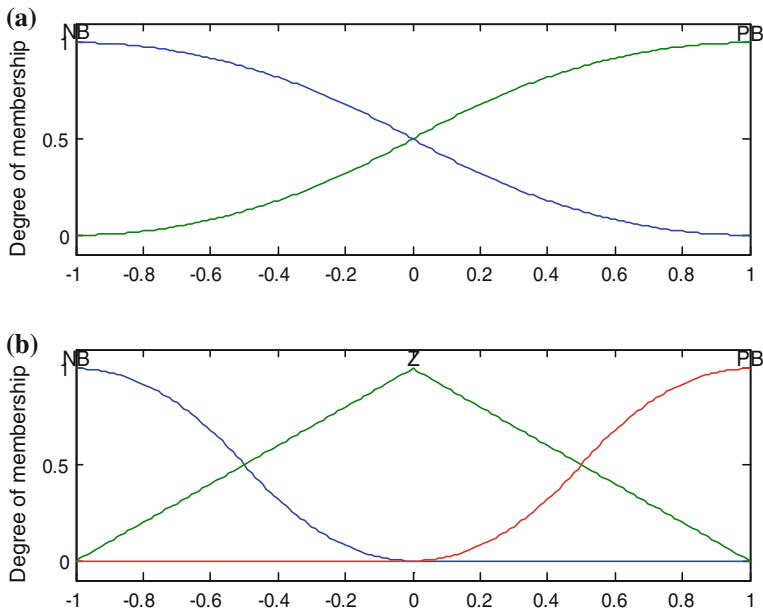


Fig. 23.1 Membership functions of input and output variables

23.3.2 On-line Optimization Based on RBF Neural Network

As a result of the nonlinearity of the fuzzy-immune controller, the parameters in PID are difficult to be optimized on-line by traditional means. With the advantages of simple calculation, fast learning rate, effective escape of local minima, RBF neural network is widely used to solve optimization problem in the area of process control [10]. Concerning the complexity of PEMFC system and necessity of optimizing PID parameters, RBF neural network is adopted to solve the optimizing problem on-line in this study. The structure of RBF neural network is shown in Fig. 23.2, which includes input layer, hidden and output layer.

In RBF neural network, $\mathbf{X} = [x_1, x_2, \dots, x_n]^T$ is input vector, $\mathbf{H} = [h_1, h_2, \dots, h_i, \dots, h_m]^T$ is radial direction base vector, in which h_i is the Gauss function:

$$h_i = \exp\left(-\frac{\|\mathbf{X} - \mathbf{C}_i\|^2}{2b_i^2}\right) \quad i = (1, 2, \dots, m) \tag{23.5}$$

where, \mathbf{C}_i is hidden units center and its width is b_i .

The objective function of RBF neural network is minimizing the mean square deviation between plant output $y(k)$ and model output $y_m(k)$:

$$J = \frac{1}{2}(y(k) - y_m(k))^2 \tag{23.6}$$

According to the gradient descent method, the iterative algorithm of output weights, node center and width can be stated as follows:

$$w_j(k) = w_j(k - 1) + \eta(y(k) - y_m(k))h_j + \alpha(w_j(k - 1) - w_j(k - 2)) \tag{23.7}$$

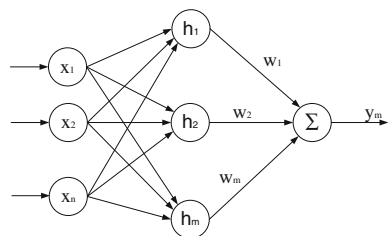
$$\Delta b_j = (y(k) - y_m(k))w_j h_j \left(-\frac{\|\mathbf{X} - \mathbf{C}_j\|^2}{b_j^3}\right) \tag{23.8}$$

$$b_j(k) = b_j(k - 1) + \eta \Delta b_j + \alpha(b_j(k - 1) - b_j(k - 2)) \tag{23.9}$$

$$\Delta c_{ji} = (y(k) - y_m(k))w_j \frac{x_j - c_{ji}}{b_j^2} \tag{23.10}$$

$$c_{ji} = c_{ji}(k - 1) + \eta \Delta c_{ji} + \alpha(c_{ji}(k - 1) - c_{ji}(k - 2)) \tag{23.11}$$

Fig. 23.2 The structure of RBF neural network



where, η is learning rate, α is momentum factor, c_{ji} is the i th center node of the j th module, w_j is the weight of output layer. The Jacobian value of PID controller is given by:

$$\frac{\partial y(k)}{\partial \Delta u(k)} \approx \frac{\partial y_m(k)}{\partial \Delta u(k)} = \sum_{j=1}^m w_j h_j \frac{c_{ji} - \Delta u(k)}{b_j^2} \quad (23.12)$$

Control error $e(k) = rin(k) - y(k)$, $rin(k)$ is the set-point, controller performance index function is given by:

$$E(k) = \frac{1}{2} e(k)^2 \quad (23.13)$$

Based on gradient descent algorithm, optimization of PID parameters can be carried out as follows:

$$\begin{aligned} \Delta k_p &= -\eta \frac{\partial E}{\partial k_p} = -\eta \frac{\partial E}{\partial k_p} \frac{\partial \Delta y}{\partial \Delta u} \frac{\partial \Delta u}{\partial \Delta k_p} = \eta e(k) \frac{\partial y(k)}{\partial u(k)} (e(k) - e(k-1)) \\ &\approx \eta e(k) \frac{\partial y_m(k)}{\partial \Delta u(k)} (e(k) - e(k-1)) \end{aligned} \quad (23.14)$$

$$\Delta k_i = -\eta \frac{\partial E}{\partial k_i} = -\eta \frac{\partial E}{\partial k_i} \frac{\partial y}{\partial \Delta u} \frac{\partial \Delta u}{\partial k_i} = \eta e(k) \frac{\partial y(k)}{\partial \Delta u(k)} e(k) \approx \eta e^2(k) \frac{\partial y_m(k)}{\partial \Delta u(k)} \quad (23.15)$$

$$\begin{aligned} \Delta k_d &= -\eta \frac{\partial E}{\partial k_d} = -\eta \frac{\partial E}{\partial k_d} \frac{\partial y}{\partial \Delta u} \frac{\partial \Delta u}{\partial k_d} = \eta e(k) \frac{\partial y(k)}{\partial \Delta u(k)} (e(k) - 2e(k-1) + e(k-2)) \\ &\approx \eta e(k) \frac{\partial y_m(k)}{\partial \Delta u(k)} (e(k) - 2e(k-1) + e(k-2)) \end{aligned} \quad (23.16)$$

Consequently, the PID parameters are given by the following formulations:

$$\begin{cases} k_p(k+1) = k_p(k) + \Delta k_p \\ k_i(k+1) = k_i(k) + \Delta k_i \\ k_d(k+1) = k_d(k) + \Delta k_d \end{cases} \quad (23.17)$$

23.4 Simulation and Analysis

In this study an improved fuzzy-immune PID controller is carried out and compared with general fuzzy adaptive PID controller as which is widely used in PID parameters adjustment. In order to test the controller's performance of disturbance rejection, the output voltage is changed from 40 to 45 V at the 150th second,

Fig. 23.3 Controlled temperature curves under different control strategies

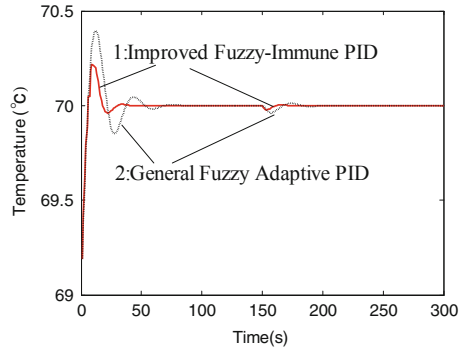
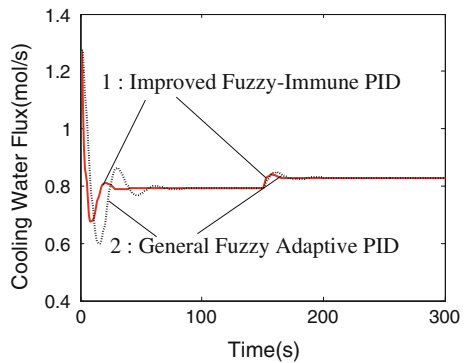


Fig. 23.4 Change of cooling water flux during the process



which simulates the load change in practical application. The set-point of PEMFC stack here is taken as a constant 70 °C (343 K) the temperature of circulated cooling water is taken as environmental temperature which is a constant.

The temperature change is shown in Fig. 23.3, which shows that the improved fuzzy-immune PID controller achieves not only lower overshoot, but also faster response speed than general fuzzy adaptive PID. This performance shows the RBF neural network receives better effect in optimization work than fuzzy logic adjustment. After the load change at 150th second, the proposed method in this study obtain smaller temperature fluctuation, because fuzzy immune set plays an important role in disturbance rejection. The result shows that the improved fuzzy-immune PID controller is more suitable for PEMFC temperature control.

Control action is another important index to evaluate the performance of controller. The temperature of PEMFC is controlled by cooling water, so the cooling water flux is shown in Fig. 23.4. The result shows that whether in set-point tracking or anti-disturbance phase, the improved fuzzy-immune PID controller pays less control cost. This performance confirms that the controller has got better self-adjusting ability and immunity to disturbance by adopting the proposed algorithm. Hence, the proposed method above can prolong the service life of control equipment and protect the PEMFC system.

23.5 Conclusion

In this paper, dynamic temperature model is adopted to simulate PEMFC system, which is calculated along the channel. In order to achieve better temperature control performance such as fast response, disturbance rejection, low overshoot, an improved fuzzy-immune PID control algorithm based on RBF neural network is presented for the PEMFC operating temperature control. Simulation results demonstrate the effectiveness and advantage of this approach in disturbance rejection, set-point tracking and control cost reducing. The proposed method is suitable for PEMFC temperature control and popularizes artificial immune algorithm. In the future, PEMFC system will be used in various environments, the fuzzy-immune control strategy can be optimized based on specific requirements.

Acknowledgments This research was supported by the National Natural Science Foundation (Grant No. 61273132) and the Beijing City talent training project (Grant No. 2009D013000000003).

References

1. Methekar RN, Patwardhan SC, Rengaswamy R (2010) Control of proton exchange membrane fuel cells using data driven state space models. *Chem Eng Res Des* 88:861
2. Yilanci A, Dincer I, Ozturk HK (2008) Performance analysis of a PEM fuel cell unit in a solar-hydrogen system. *Int J Hydrogen Energy* 33:7538
3. Golbert J, Lewin DR (2004) Model-based control of fuel cells: (1) regulatory control. *J Power Sour* 135:135
4. Hu P, Cao GY, Zhu XJ (2011) Temperature model and fuzzy control for the proton-exchange-membrane fuel cell. *Control Theor Appl* 28(10):1371 (in Chinese)
5. Lee HI, Lee CH, Oh TY (2002) Development of 1 kW class proton exchange membrane fuel cell power generation system. *J Power Sour* 107:110
6. Li X, Cao GY, Zhu XJ (2005) Non-linear predictive control for PEMFC stack operation temperature. *J Shanghai Jiao tong Univ (Science)* 10(2):157
7. Wei W, Zhang GH (2002) Artificial immune system and its applications in control system. *Control Theor Appl* 19(2):157 (in Chinese)
8. Wen DD (2008) Adaptive Fuzzy Immune-PID Control of Resistance-Heated Furnace Temperature Control System. *Instrum Tech Sens* 7:22
9. Ren XY, DU FS et al (2011) Application of improved fuzzy immune PID controller to bending control system. *J Iron Steel Res* 18(3):28
10. Chen YF, XU S, Cao R, Zhou T (2011) The study and simulation of PID control based on RBF neural network. *International conference on electronic & mechanical engineering and information technology*, pp 3453

Chapter 24

Adaptive Fuzzy Controller Design for Strict-Feedback Nonlinear System Using Command Filtering

Junsheng Ren

Abstract An adaptive tracking control architecture is proposed and evaluated for a class of continuous-time nonlinear dynamic systems for which an explicit expression of the dynamics is either unknown or impossible. The architecture employs fuzzy logic system to approximate the plant nonlinearities. Under mild assumptions about the uncertainties, the algorithm is proven to be ultimately uniformly bounded, with tracking errors converging to a neighborhood of zero. A constructive procedure is detailed. Command filtering technique ensures no need of the repeated differential of virtual control law. The performance of the resulting controller is illustrated through simulations.

Keywords Nonlinear system · Adaptive control · Fuzzy control · Command filtering

24.1 Introduction

Recently, “integrator backstepping” methodology has attracted much interest in the field of robust nonlinear control [1–5]. The book [1] develops the backstepping approach to the point of step by step design procedure. Backstepping is a technique to control the nonlinear systems with parameter uncertainty, particularly those systems in the form of strict-feedback form. However, we note that, although the backstepping approach is a powerful and elegant design methodology, the integrator approach suffers from the problem of “explosion of terms” in [6, 7], which caused by the repeated differentiations of virtual input.

J. Ren (✉)

Laboratory of Marine Simulation and Control, Navigation College, Dalian Maritime University, No.1, Linghai Road, Dalian, Liaoning 116026, People’s Republic of China
e-mail: jsren@dlnu.edu.cn

Furthermore, conventional adaptive control methodology can only deal with the systems with known dynamic structure, but unknown (constant or slowly-varying) parameters. Recently, fuzzy logic systems (FLS) [8–10] have been added to the list of techniques to tackle the uncertainties in a dynamical system due to the simplicity in design and implementation. FLS possesses the inherent capability to handle the uncertainties in dynamic systems and incorporate easily experiences into the controller design. Especially, FLS can be used to be applied to control those systems which are ill-defined or too complex to have a mathematical model.

In this paper, an adaptive fuzzy tracking controller strategy is proposed for a class of nonlinear system in strict-feedback form. The system dynamics are completely unknown. We use fuzzy logic system to approximate the unknown system functions. By using command filtering technique, the proposed design avoids the repeated differential of virtual control law completely. Therefore, the controller structure is quite simple and easy to implement in engineering.

24.2 Problem Statement

Consider a class of n th order single-input–single-output nonlinear system in strict-feedback form as follows

$$\begin{cases} \dot{x}_1 = x_2 + f(x_1) + d_1, \\ \dot{x}_2 = x_3 + f(x_1, x_2) + d_2, \\ \dots \\ \dot{x}_{n-1} = x_n + f_{n-1}(x_1, \dots, x_{n-1}) + d_{n-1}, \\ \dot{x}_n = u + f_n(x_1, \dots, x_n) + d_n, 1 \leq i \leq n, \end{cases} \quad (24.1)$$

where $x = [x_1, \dots, x_n] \in \mathfrak{R}^n$ is the state vector with initial condition $x(0) = x_0$, the first state x_1 is considered as the scalar output, and u is the scalar control signal. The functions $f_i(x_1, \dots, x_i) : \mathfrak{R}^i \rightarrow \mathfrak{R}$ are assumed to be unknown and satisfy the following assumption. External disturbances d_i are unknown smooth functions that satisfy the following conditions. Namely, there exist parameter values $\psi_i^* \geq 0$ and smooth functions $p_i(x_1, \dots, x_i)$, such that $|d_i(x, t)| \leq \phi_i^* p_i(x_1, \dots, x_i)$, $1 \leq i \leq n - 1$. The objective of the control design are to specify a control signal $u(t)$ to steer $x(t)$ from any initial conditions to track the reference input $x_{1c}(t)$, to achieve ultimate uniform boundedness (UUB) of all signals and states defined in the control law from $i = 2, \dots, n$.

Takagi–Sugeno (T-S) fuzzy model is a successful approach that deals with nonlinear system identification [8–10]. Hence, we introduce the structure of the Takagi–Sugeno (T-S) fuzzy model. T-S fuzzy rules are a set of linguistic statements as follows

$$\begin{aligned} R_j: & \text{ IF } x_1 \text{ is } F_1^j \text{ and } x_2 \text{ is } F_2^j \text{ and } \dots \text{ and } x_n \text{ is } F_n^j, \\ & \text{ THEN } y_j = a_0^j + a_1^j x_1 + \dots + a_n^j x_n, j = 1, 2, \dots, K, \end{aligned}$$

where $a_i^j, i = 0, 1, \dots, n$ are the unknown constants to be adapted, y_j is the output variable of the fuzzy system. In this paper, it's assumed that singleton fuzzifier and center-average defuzzifier are chosen. Then, $f(x)$ can be expressed as the following

$$f(x) = \sum_{j=1}^K y_j \left[\prod_{i=1}^n \mu_{F_i}^j(x_i) \right] / \sum_{j=1}^K \left[\prod_{i=1}^n \mu_{F_i}^j(x_i) \right] = \zeta(x)A_z^0 + \zeta(x)A_z^1x + \delta, \quad (24.2)$$

$$\text{where } \zeta(x) = [\zeta_1(x), \zeta_2(x), \dots, \zeta_K(x)], \zeta_j(x) = \frac{\prod_{i=1}^n \mu_{F_i}^j(x_i)}{\sum_{j=1}^K \left[\prod_{i=1}^n \mu_{F_i}^j(x_i) \right]}$$

$$X = [x_1, x_2, \dots, x_n]^T, A_z^0 = [a_0^1, a_0^2, \dots, a_0^K]^T, A_z^1 = \begin{bmatrix} a_1^1 & a_2^1 & \cdots & a_n^1 \\ a_1^2 & a_2^2 & \cdots & a_n^2 \\ \vdots & \vdots & \ddots & \vdots \\ a_1^K & a_2^K & \cdots & a_n^K \end{bmatrix}.$$

24.3 Adaptive Controller Design

The backstepping design contains n steps, where n is the order of the nonlinear system (1). At each step, an intermediate stabilizing function shall be developed using an appropriate Lyapunov function. The procedures of the backstepping approach are presented as follows.

Step 1: Firstly, we define two tracking errors for the state x_1 as follows.

$$\tilde{x}_1 = x_1 - x_{1c}, \bar{x}_1 = \tilde{x}_1 - \zeta_1 \quad (24.3)$$

where x_{1c} is the desired trajectory, \tilde{x}_1 is tracking error, and \bar{x}_1 is compensated tracking error. We will construct T-S fuzzy system $\hat{f}_1(x_1, A_1)$ with input vector x_1 to approximate the system function $f_1(x_1)$. Then, according to Sect. 24.2, $f_1(x_1)$ can be expressed as

$$f_1(x_1) = \zeta_1(x_1)A_{z1} + \delta_1 = \zeta_1(x_1)A_{z1}^1\bar{x}_1 + \zeta_1(x_1)(A_{z1}^0 + A_{z1}^1x_{1c}) + \zeta_1(x_1)A_{z1}^1\xi_1 + \delta_1 \quad (24.4)$$

where $A_{z1}, A_{z1}^0, A_{z1}^1$ are matrices with unknown elements, ξ_1 will be defined later. Then, we obtain

$$\dot{\tilde{x}}_1 = x_2 + \zeta_1(x_1)A_{z1}^1\bar{x}_1 + \Upsilon_1 \quad (24.5)$$

where Υ_1 is an introduced variable for simplicity and discussed as follows

$$\begin{aligned}
\Upsilon_1 &= \zeta_1(x_1)(A_{z_1}^0 + A_{z_1}^1 x_{1c}) + \zeta_1(x_1)A_{z_1}^1 \zeta_1 + \delta_1 + p_1^* \phi_1(x_1) - \dot{x}_{1c} \\
&\leq \|\zeta_1(x_1)\| \|A_{z_1}^0 + A_{z_1}^1 x_{1c}\| + \|\zeta_1(x_1)\| \|A_{z_1}^1\| \|\zeta_1\| + \|\delta_1\| \\
&\quad + \|p_1^*\| \|\psi_1(x_1)\| + \|\dot{x}_{1c}\| \leq \chi_1 \psi_1
\end{aligned} \tag{24.6}$$

Where

$$\begin{aligned}
\chi_1 &= \max\{\|A_{z_1}^0\| + |c_{\theta 1}| \cdot |x_{1c}|, |c_{\theta 1}|, |\delta_1^*| + |\dot{x}_{1c}|, \|p_1^*\|\}, \\
\psi_1(x_1) &= 1 + \|\zeta_1(x_1)\| + \|\phi_1(x_1)\| + \|\zeta_1(x_1)\| \cdot \|\zeta_1\|.
\end{aligned} \tag{24.7}$$

where $c_{\theta 1}$ is a constant only for analytic purpose, the accurate value of which is not necessarily known, δ_1^* is the bound of approximation error, and $\|\bullet\|$ stands for Euclidean norm of vectors and induced norm of matrices. Next, we define

$$\dot{\zeta}_1 = -k_1 \zeta_1 + (x_{2c} - x_{2c}^0), \quad x_{2c}^0 = \alpha_1 - \zeta_2, \tag{24.8}$$

where ζ_2 will be define in Step i , the signal x_{2c}^0 is filtered produce the command signal x_{2c} and its derivative \dot{x}_{2c} , α_1 is virtual control input which will be discussed later, k_1 is positive constant and chosen by designer. By use of Eq. (24.8), the dynamics of the compensated tracking errors are described by

$$\dot{\bar{x}}_1 = \dot{\hat{x}}_1 - \dot{\zeta}_1 = \zeta_1(x_1)A_1^1 \bar{x}_1 + v_1 + \bar{x}_2 + \alpha_1 + k_1 \zeta_1. \tag{24.9}$$

Choose Lyapunov candidate function as follows

$$V_1 = \frac{1}{2} \bar{x}_1^2 + \frac{1}{2} \Gamma_1^{-1} \tilde{\vartheta}_1^2, \tag{24.10}$$

where $\tilde{\vartheta}_1 = \vartheta_1^* - \hat{\vartheta}_1$, Γ_1 is positive constant, which will be chosen by designer. Then, the derivative of the Lyapunov candidate is given as follows.

$$\dot{V}_1 = \bar{x}_1 \zeta_1(x_1) A_1^1 \bar{x}_1 + \bar{x}_1 \Upsilon_1 + \bar{x}_1 \bar{x}_2 + \bar{x}_1 \alpha_1 + \bar{x}_1 k_1 \zeta_1 + \Gamma_1^{-1} \tilde{\vartheta}_1 \dot{\tilde{\vartheta}}_1. \tag{24.11}$$

Next, we will discuss some items in (11). From Young's inequality, we have

$$\begin{aligned}
&\bar{x}_1 \zeta_1(x_1) A_1^1 \bar{x}_1 + \bar{x}_1 \Upsilon_1 \\
&\leq \frac{c_{\theta 1}^2}{2w_1} \bar{x}_1^2 \zeta_1(x_1) \zeta_1^T(x_1) + \frac{w_1}{2} \|A_1^m\|^2 \bar{x}_1^T \bar{x}_1 + \chi_1^* |\bar{x}_1| \|\psi_1(x)\| \\
&\leq \vartheta_1^* \frac{1}{2w_1} \bar{x}_1^2 \zeta_1(x_1) \zeta_1^T(x_1) + \vartheta_1^* |\bar{x}_1| \|\psi_1(x_1)\| + \frac{w_1}{2} \bar{x}_2^T \bar{x}_2 \\
&\leq \hat{\vartheta}_1 \frac{1}{2w_1} \bar{x}_1^2 \zeta_1(x_1) \zeta_1^T(x_1) + \hat{\vartheta}_1 |\bar{x}_1| \|\psi_1(x_1)\| + \frac{w_1}{2} \bar{x}_1^T \bar{x}_1 \\
&\quad + \tilde{\vartheta}_1 \frac{1}{2w_1} \bar{x}_1^2 \zeta_1(x) \zeta_1^T(x_1) + \tilde{\vartheta}_1 |\bar{x}_1| \|\psi_1(x)\|.
\end{aligned} \tag{24.12}$$

We use the following virtual control law

$$\alpha_1 = -k_1 \tilde{x}_1 - \frac{1}{2w_1} \hat{\vartheta}_1 \bar{x}_1 \zeta_1(x_1) \zeta_1^T(x_1) - \frac{\bar{x}_1 \hat{\vartheta}_1^2 \psi_1^2(x_1)}{|\bar{x}_1| \hat{\vartheta}_1 \psi_1(x_1) + \varepsilon_1}, \quad (24.13)$$

with adaptive law

$$\dot{\hat{\vartheta}}_1 = \Gamma_1 \left[\frac{1}{2w_1} \bar{x}_1^2 \zeta_1(x_1) \zeta_1^T(x_1) + |\bar{x}_1| \psi_1(x_1) - \sigma_1 (\hat{\vartheta}_1 - \vartheta_1^0) \right], \quad (24.14)$$

where Γ_1 , σ_1 and $\vartheta_1^0 \geq 0$ are design constants. Furthermore, by completion of squares, there exist the following inequalities

$$\tilde{\vartheta}_1 (\hat{\vartheta}_1 - \vartheta_1^0) \leq -\frac{1}{2} \tilde{\vartheta}_1^2 - \frac{1}{2} (\hat{\vartheta}_1 - \vartheta_1^0)^2 + \frac{1}{2} (\vartheta_1^* - \vartheta_1^0)^2. \quad (24.15)$$

Then, substituting (24.13)–(24.15) into (24.11) yields

$$\dot{V}_1 \leq -k_1 \bar{x}_1^2 + \frac{w_1}{2} \bar{x}_1^2 - \frac{\sigma_{12}}{2} \tilde{\vartheta}_1^2 + \varepsilon_1 + \frac{\sigma_1}{2} (\vartheta_1^* - \vartheta_1^0) + \bar{x}_1 \bar{x}_2. \quad (24.16)$$

We introduce

$$c_1 := \min\{2k_1 - w_1, \sigma_1 \Gamma_1\}, \varpi_1 := \frac{\sigma_{12}}{2} (\vartheta_1^* - \vartheta_1^0)^2 + \varepsilon_1,$$

then \dot{V} can be further written as follows

$$\dot{V}_1 \leq -c_1 V_1 (\bar{x}_1, \hat{\vartheta}_1) + \varpi_1 + \bar{x}_1 \bar{x}_2 \quad (24.17)$$

Since step i ($2 \leq i \leq n-1$) is quite similar to Step 1, we omit the discussions of Step i herein.

Step n : We define two tracking errors for the state x_n respectively as follows

$$\tilde{x}_n = x_n - x_{nc}, \bar{x}_n = \tilde{x}_n - \zeta_n, \quad (24.18)$$

Similar to Step i , we obtain

$$\dot{\tilde{x}} = u + \zeta_n(x_n) c_{0n} A_n^m \tilde{x}_n + \Upsilon_n. \quad (24.19)$$

Next, we define

$$\bar{x}_n = \tilde{x}_n - \zeta_n, \dot{\zeta}_n = -k_n \zeta_n + (u_c - u_c^0). \quad (24.20)$$

Furthermore, note that $u_c = u_c^0 = u$. Then, we obtain

$$\dot{\bar{x}} = u + \zeta_n c_{0n} A_n^m \bar{x}_n + \Upsilon_n + k_n \zeta_n. \quad (24.21)$$

Choose Lyapunov candidate function

$$V_n = V_{n-1} + \frac{1}{2} \bar{x}_n^2 + \frac{1}{2} \Gamma_n^{-1} \tilde{\vartheta}_n^2. \quad (24.22)$$

where $\tilde{\vartheta}_n = \vartheta_n^* - \hat{\vartheta}_n$, Γ_n is positive constant and chosen by designer. The derivative of V_n is given as follows

$$\dot{V}_n = \dot{V}_{n-1} + \bar{x}_n \zeta_n c_{\vartheta n} A_n^m \bar{x}_n + \bar{x}_n \Upsilon_n + \bar{x}_n u + \bar{x}_n k_n \xi_n + \Gamma_n^{-1} \tilde{\vartheta}_n \dot{\hat{\vartheta}}_n. \quad (24.23)$$

We use the following control law

$$u = -k_n \tilde{x}_n - \frac{1}{2w_n} \hat{\vartheta}_n \bar{x}_n \zeta_n(x_n) \zeta_n^T(x_n) - \bar{x}_{n-1} - \frac{\bar{x}_n \hat{\vartheta}_n^2 \psi_n^2(x_n)}{|\bar{x}_n| \hat{\vartheta}_n \psi_n(x_n) + \varepsilon_n}, \quad (24.24)$$

Where

$$\psi_n(x_n) = 1 + \|\zeta_n(x_n)\| + \|\phi_n(x_n)\| + \|\zeta_n(x_n)\| \cdot |\xi_n|, \quad (24.25)$$

$$\dot{\hat{\vartheta}}_n = \Gamma_n \left[|x_n| \psi_n(x_n) + \frac{1}{2w_n} \bar{x}_n^2 \zeta_n(x_n) \zeta_n^T(x_n) - \sigma_n (\hat{\vartheta}_n - \vartheta_n^0) \right]. \quad (24.26)$$

We introduce

$$C := \min\{2k_n - w_n, \sigma_n \Gamma_n, 2c_{n-1}\}, M := \sum_{i=1}^{n-1} \varpi_i + \frac{\sigma_n}{2} (\vartheta_n^* - \vartheta_n^0)^2 + \varepsilon_n,$$

then, \dot{V}_n will be rewritten into

$$\dot{V}_n \leq -CV_n(\bar{x}_n, \tilde{\vartheta}_n) + M. \quad (24.27)$$

The Eq. (24.27) implies that

$$V_n(t) \leq V_n(t_0) \exp[-C(t - t_0)] + \frac{C}{M} \leq V_n(t_0) + \frac{C}{M}, \quad \forall t \geq t_0. \quad (24.28)$$

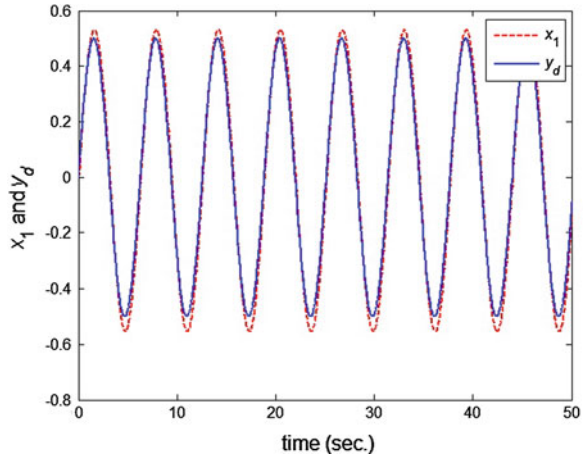
As a result, all \bar{x}_i and $\tilde{\vartheta}_i$ belong to compact set $\{(\bar{x}_i, \tilde{\vartheta}_i) | V \leq V(t_0) + \frac{M}{C}\}$. Namely, all the signals, i.e. \bar{x}_i and $\tilde{\vartheta}_i$ in the closed-loop system are bounded. From (8), it is concluded that $x_{(i+1)c} - x_{(i+1)c}^0$ can be made arbitrarily small by well-defined command filter. Then, ξ_i is bounded. Tracking errors \tilde{x}_i is also bounded, since \bar{x}_i is bounded. Namely, tracking errors \tilde{x}_i are UUB.

24.4 Simulation Example

To illustrate the previous results, we consider the following second-order nonlinear system

$$\begin{cases} \dot{x}_1(t) = x_2(t) + x_1 e^{-0.5x_1} = x_2(t) + f_1(x_1), \\ \dot{x}_2(t) = u(t) + x_1 \sin(x_2^2) = u(t) + f_1(x_1, x_2), \end{cases} \quad (24.29)$$

Fig. 24.1 Trajectories of x_1 and y_d



where we suppose that $f_1(x_1)$ and $f_1(x_1, x_2)$ are unknown nonlinear functions. The control objective is to steer the output to track the reference signal $y_d = \sin(t)/2$.

Choose the membership functions of $x_1(t)$ and $x_2(t)$ as follows

$$\mu_{F_1^l}(x_1) = \exp \left[-\frac{(x_1 - 3 + l)^2}{16} \right], l = 1, 2, \dots, 5 \tag{24.30}$$

$$\mu_{F_2^l}(x_2) = \exp \left[-\frac{(x_2 - 3 + l)^2}{16} \right], l = 1, 2, \dots, 5 \tag{24.31}$$

where the membership functions of $x_1(t)$ and $x_2(t)$ are of the same structures, l denotes the number of membership functions. In this example, we use totally 5

Fig. 24.2 Control input

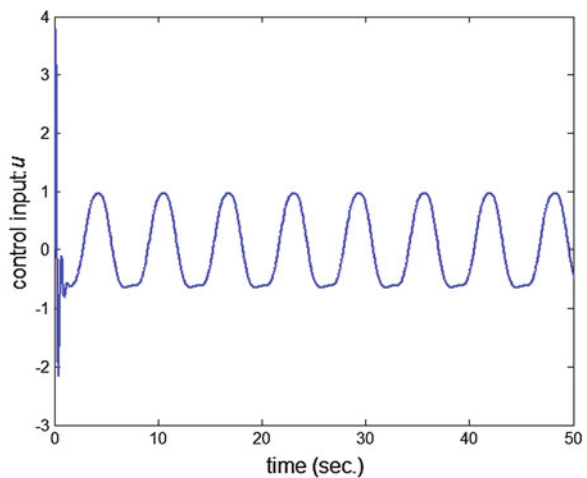


Fig. 24.3 Adaptive law: $\hat{\vartheta}_1$

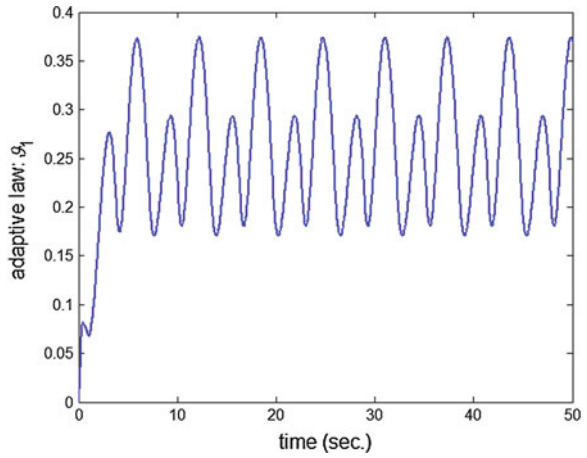
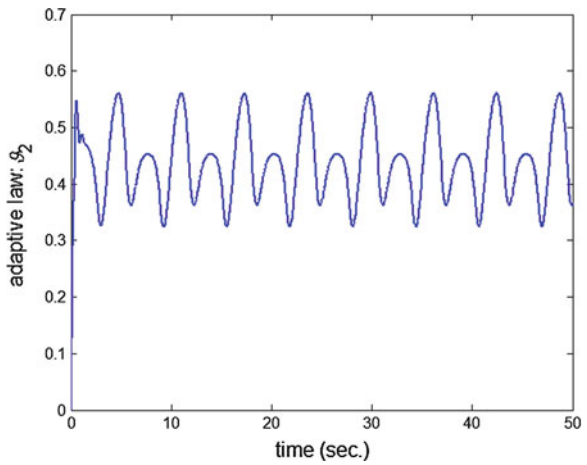


Fig. 24.4 Adaptive law: $\hat{\vartheta}_2$



rules to construct T-S fuzzy system for the unknown parts, namely, $f_1(x_1)$ and $f_1(x_1, x_2)$.

Simulation results in Figs. 24.1, 24.2, 24.3, 24.4 show the effectiveness of the proposed adaptive control design. Figure 24.1 shows that the tracking error converges to a small neighborhood around zero. Figure 24.2 shows that the boundness of control input. Figs. 24.3, 24.4 show the time histories of learning parameters $\hat{\vartheta}_1, \hat{\vartheta}_2$, which also are bounded.

24.5 Conclusion

In this paper, adaptive tracking fuzzy control scheme is proposed for a class of nonlinear system in strict-feedback form. T-S fuzzy system is employed to approximate the system function. The proposed algorithm can guarantee the boundedness of all the signals in the closed-loop system. Furthermore, the iterative differential of virtual control input is bypassed. Numerical example is used to demonstrate the effectiveness of the control scheme.

Acknowledgments This work is supported by National Natural Science Foundation of China under Grant No. 51109020, National 973 Projects of China under Grant No. 2009CB320800 and the Fundamental Research Funds for the Central Universities No. 2011JC022.

References

1. Krstić M, Kanellakopoulos I, Kokotović P (1995) Nonlinear and adaptive control design. Wiley, New York
2. Mayhew CG, Sanfelice RG, Andrew RT (2011) Further results on synergistic Lyapunov functions and hybrid feedback design through backstepping. IEEE conference on decision and control and european control conference, Orlando, pp 7428–7433
3. Li P, Yang GH (2009) Adaptive fuzzy dead-zone control for unknown nonlinear systems. American control conference, St. Louis, pp 5671–5676
4. Li C, Tong S, Li Y et al (2009) Fuzzy adaptive observer and filter backstepping control for nonlinear systems. American control conference, St. Louis, pp 4290–4295
5. Zhang TP, Wen H, Zhu Q (2010) Adaptive fuzzy control of nonlinear systems in pure feedback form based on input-to-state stability. IEEE Trans Fuzzy Sys 18:80–93
6. Farrell JA, Polycarpou MM (2006) Adaptive approximation based control: unifying neural, fuzzy, and traditional adaptive approximation approaches. Wiley, NJ
7. Dong W, Farrell JA, Polycarpou MM et al (2012) Command filtered adaptive backstepping. IEEE Trans Control Sys Tech 20:566–580
8. Chen SH, Ho WH, Chou JH (2009) Robust controllability of T-S fuzzy-model-based control systems with parametric uncertainties. IEEE Trans Fuzzy Sys 17:1324–1335
9. Xi Z, Feng G, Hesketh T (2011) Piecewise integral sliding-mode control for T-S fuzzy systems. IEEE Trans Fuzzy Sys 19:707–716
10. Zou AM, Hou ZG, Tan M (2008) Adaptive control of a class of nonlinear pure-feedback system using fuzzy backstepping approach. IEEE Trans Fuzzy Sys 16:886–897

Chapter 25

Consensus Problem of Second-Order Multi-Agent Systems with Communication Delay and Input Delay

Pingping Dai, Chenglin Liu and Fei Liu

Abstract In this paper, asynchronously-coupled algorithm is used to solve the consensus problem of second-order multi-agent systems with both communication delay and input delay. By constructing Lyapunov–Krasovskii functional, sufficient consensus conditions are obtained for second-order systems under invariant input delays accompanied with time-invariant and time-varying communication delays respectively. The conditions are all in the forms of linear matrix inequality (LMI). Simulation illustrates the correctness of the results.

Keywords Consensus problem · Second-order multi-agent systems · Communication delay · Input delay · Linear matrix inequality

25.1 Introduction

With rapid development of computer technology, communication technology and control technology, coordination control of multi-agent systems has been studied extensively in last decade for its broad engineering application, including automated highway system, wireless sensor network, satellite position coordinate control, robot cooperative control [1]. Consensus problem, which is one of the most important and fundamental problems of multi-agent systems, means that system requires the agents through the mutual information transmission finally to reach a common value.

In consensus coordination control of multi-agent systems, there exist communication delays between neighboring agents when the agents exchange information, and each agent needs certain input delay for itself due to accepting and

P. Dai · C. Liu (✉) · F. Liu

Key Laboratory of Advanced Process Control for Light Industry (Ministry of Education),
Institute of Automation, Jiangnan University, Jiangsu, Wuxi, China
e-mail: liucl@jiangnan.edu.cn

processing information. According to different analysis methods, consensus problem of first-order multi-agent systems with communication delay and input delay has gained extensively attention [2–9]. However, consensus of second-order multi-agent systems with communication delay and input delay is difficult to analyze, and relative results are not too many. By using frequency-domain analysis, Liu and Liu [10] analyzed the consensus convergence problem of second order multi-agent system with constant communication and input delays under directed topology, and obtained the sufficient consensus conditions depending on communication and input delays. Yu et al. [11] got sufficient and necessary condition, which can be used to get the maximum allowable delay, for second-order multi-agent systems with identical communication delay. Decentralized consensus conditions have been obtained for second order multi-agent systems with different communication delays and input delays [12]. By constructing Lyapunov functional, references [13] and [14] investigated the consensus problem of second order multi-agent systems with time varying communication delay under switching topology, and got sufficient consensus conditions. Reference [15] studied consensus problem of second order multi-agent systems with different communication delay. Sun and Wang [16] analyzed the feasibility of the consensus condition for second-order multi-agent systems with asymmetric delay constraints exist. Gao et al. [17] analyzed consensus problem of discrete-time second order multi-agent systems with time-varying delay and switching topology.

This paper studies the consensus problem of second order multi-agent systems with both communication delay and input delays. According to Lyapunov stability theory, firstly, consensus condition, which is expressed by linear matrix inequality (LMI), is obtained for second order systems with constant communication delay and invariant input delay through constructing Lyapunov–Krasovskii functional. Secondly, delay-dependent consensus condition is obtained for second order multi-agent systems with time invariant input delay and time-varying communication delay, and is also expressed by LMI. By using LMI toolbox in Matlab software, delay upper bound can be determined based on LMI.

25.2 Graph Theory

The information flow in multi-agent systems can be regarded as topology, which is divided into to directed topology and undirected topology. In this paper, a multi-agent system is described as general directed topology.

A weighted digraph $G = (V, E, A)$ of order n is composed of a set of vertices $V = \{1, \dots, n\}$, a set of edges $E \subseteq V \times V$ and a weighted adjacency matrix $A = [a_{ij}] \in R^{n \times n}$ with $a_{ij} \geq 0$. The node indexes belong to a finite index set $\Gamma = \{1, \dots, n\}$. A directed edge from the node i to the node j of the digraph G is denoted by $e_{ij} = (i, j) \in E$. We assume that the adjacency elements associated with the edges of the digraph are positive, i.e., $a_{ij} > 0 \Leftrightarrow e_{ij} \in E$. Moreover, we assume

$a_{ii} \geq 0$ for all $i \in L$. The set of neighbors of node i is denoted by $N_i = \{j \in V, (i, j) \in E\}$. The Laplacian matrix of the weighted digraph G is defined as $L = D - A = [l_{ij}] \in R^{n \times n}$, where $D = \text{diag}\{\sum_{j=1}^n a_{ij}, i \in \mathcal{I}\}$ is the degree matrix of G .

In the digraph, if there is a path from one node i to another node j , then j is said to be reachable from i . If not, then j is said to be not reachable from i . If a node is reachable from every other node in the digraph, then we say it globally reachable.

25.3 Problem Description

Second-order multi-agent systems with n nodes are given by

$$\begin{cases} \dot{x}_i(t) = v_i(t), \\ \dot{v}_i(t) = u_i(t), i=1, 2, \dots, n, \end{cases} \quad (25.1)$$

where $x_i \in R$, $v_i \in R$, and $u_i \in R$ are the position, velocity and acceleration, respectively, of the agent i . This paper considers agents with constant input delay $\tau > 0$ and time-varying communication delay $\eta(t) > 0$ between each other.

With communication delay, the asynchronous-coupled consensus algorithm is given as follows:

$$u_i(t) = -k_2 v_i(t - \tau) + \frac{k_1}{d_i} \sum_{j=1}^n a_{ij} (x_j(t - \eta(t) - \tau) - x_i(t - \tau)) \quad (25.2)$$

where $k_1 > 0, k_2 > 0$ are the control parameters, $a_{ij} > 0, j \in N_i$ is the adjacency neighbors element of neighbors matrix A , $d_i = \text{deg}_{\text{out}}(i) \neq 0, i \in \Gamma$, means that each agent can receive information from other agents. Control algorithm (25.2) requires that the number of each agent's neighboring agents is at least one.

Under the control algorithm (25.2), the closed-loop form for second-order multi-agent systems (25.1) is given by

$$\begin{cases} \dot{x}_i(t) = v_i(t), \\ \dot{v}_i(t) = -k_2 v_i(t - \tau) + \frac{k_1}{d_i} \sum_{j=1}^n a_{ij} (x_j(t - \eta(t) - \tau) - x_i(t - \tau)), i = 1, 2, \dots, n, \end{cases} \quad (25.3)$$

The closed-loop system (25.3) can be rewritten as

$$\begin{cases} \dot{x}(t) = v(t) \\ \dot{v}(t) = -k_2 v(t - \tau) + k_1 D^{-1} [Ax(t - \eta(t) - \tau) - Dx(t - \tau)] \end{cases}$$

where $x(t) = [x_1(t), x_2(t), \dots, x_n(t)]^T$, $v(t) = [v_1(t), v_2(t), \dots, v_n(t)]^T$, A and D are connection matrix and degree matrix of digraph G .

Define $\bar{x}_i = x_i - x_1$, $\bar{v}_i = v_i - v_1$, $i = 2, 3 \dots, n$, and we get

$$\begin{cases} \dot{\bar{x}}(t) = EF\bar{v}(t) \\ \dot{\bar{v}}(t) = -k_2EF\bar{v}(t - \tau) + k_1ED^{-1}AF\bar{x}(t - \eta(t) - \tau) - k_1EF\bar{x}(t - \tau) \end{cases} \quad (25.4)$$

where, $\bar{x}(t) = [\bar{x}_2, \bar{x}_3, \dots, \bar{x}_n]^T$, $\bar{v}(t) = [\bar{v}_2, \bar{v}_3, \dots, \bar{v}_n]^T$, $E = [-1_{n-1}I_{n-1}]$, $F = \begin{bmatrix} 0_{n-1}^T \\ I_{n-1} \end{bmatrix}$, $-1_{n-1} = [-1, -1, \dots, -1]^T \in \mathbb{R}^{n-1}$, $0_{n-1} = [0, 0, \dots, 0]^T \in \mathbb{R}^{n-1}$, and $I_{n-1} \in \mathbb{R}^{(n-1) \times (n-1)}$ is an unit matrix. System (25.4) can be rewritten as

$$\dot{y}(t) = H_1y(t) + H_2y(t - \tau) + H_3y(t - \eta(t) - \tau) \quad (25.5)$$

where, $y^T(t) = [\bar{x}(t) \quad \bar{v}(t)]^T$, $H_1 = \begin{bmatrix} 0 & I_{n-1} \\ 0 & 0 \end{bmatrix}$, $H_2 = \begin{bmatrix} 0 & 0 \\ -k_1I_{n-1} & -k_2I_{n-1} \end{bmatrix}$, and $H_3 = \begin{bmatrix} 0 & 0 \\ k_1ED^{-1}A & 0 \end{bmatrix}$.

Therefore, the consensus convergence problem of multi-agent system (25.3) is equivalent to the asymptotic stability of system (25.6).

25.4 Consensus Protocol

25.4.1 Constant Communication Delay

This section investigates the system (25.5) with time-invariant communication delay as

$$\dot{y}(t) = H_1y(t) + H_2y(t - \tau) + H_3y(t - \eta - \tau) \quad (25.6)$$

Assumption 1 $0 \leq \eta \leq h, h > 0, \tau > 0, t \geq 0$.

Theorem 1 *The interconnection topology G of multi-agent systems (25.6) has globally reachable node, and the output degree of each node is greater than zero. Then, multi-agent systems (25.6) achieve an asymptotic consensus with appropriate $h > 0, \tau > 0$, and the allowed upper bound of delay τ can be obtained by solving the following LMI:*

$$M = \begin{bmatrix} M_{11} & 0 & M_{13} & M_{14} \\ * & M_{22} & 0 & M_{24} \\ * & * & M_{33} & M_{34} \\ * & * & * & M_{44} \end{bmatrix} < 0 \quad (25.7)$$

$$\begin{aligned}
M_{11} &= PH_1 + H_1^T P + Q_1 + Q_4 + \tau H_1^T (R_1 + R_3) H_1 + \eta H_1^T R_2 H_1 - \tau^{-1} R_1 \\
M_{13} &= PH_2 + \tau H_1^T R_1 H_2 + \eta H_1^T R_2 H_2 + {}_1^T R_3 H_3 + \tau^{-1} R_1 \\
M_{14} &= PH_3 + \tau H_1^T R_1 H_3 + \eta H_1^T R_2 H_3 + \tau H_1^T R_3 H_3 \\
M_{22} &= Q_2 - \tau^{-1} R_3, \quad M_{24} = \tau^{-1} R_3 \\
M_{33} &= -Q_1 + Q_3 + \tau H_2^T R_1 H_2 + h H_2^T R_2 H_2 + \tau H_2^T R_3 H_2 - \tau^{-1} R_1 - \eta^{-1} R_2 \\
M_{34} &= \tau H_2^T R_1 H_3 + \eta H_2^T R_2 H_3 + {}_2^T R_3 H_3 + \eta^{-1} R_2 \\
M_{44} &= -Q_2 - Q_3 - Q_4 + \tau H_3^T R_1 H_3 + \eta H_3^T R_2 H_3 + {}_3^T R_3 H_3 - \eta^{-1} R_2 - \tau^{-1} R_3
\end{aligned}$$

where the positive definite matrixes $P, Q_j, j = 1, 2, 3, 4, R_j, j = 1, 2, 3$ are of appropriate dimension. Before prove theorem 1, we firstly give the following lemma [9, 18]:

Lemma 1 Assume that $0 \leq \eta(t) \leq h, h > 0$ is piecewise continuous functions. For arbitrary differentiable vector function $x(t) : [-h, \infty) \rightarrow R^n$ and arbitrary positive definite matrix $M \in R^{n \times n}$, the following inequality is established:

$$\left(\int_{t-\eta(t)}^t \dot{x}^T(s) ds \right) M \left(\int_{t-\eta(t)}^t \dot{x}(s) ds \right) \leq h \int_{t-h}^t \dot{x}^T(s) M \dot{x}(s) ds, t \geq 0$$

Now, we give the proof of theorem 1.

Proof Construct Lyapunov–Krasovskii functional for the system (25.6) as follows:

$$V(t) = V_1(t) + V_2(t) + V_3(t)$$

$$V_1(t) = y^T(t) P y(t),$$

$$\begin{aligned}
V_2(t) &= \int_{t-\tau}^t y^T(s) Q_1 y(s) ds + \int_{t-\eta-\tau}^{t-\eta} y^T(s) Q_2 y(s) ds \\
&\quad + \int_{t-\eta-\tau}^{t-\tau} y^T(s) Q_3 y(s) ds + \int_{t-\eta-\tau}^t y^T(s) Q_4 y(s) ds,
\end{aligned}$$

$$\begin{aligned}
V_3(t) &= \int_{-\tau}^0 \int_{t+\theta}^t \dot{y}^T(s) R_1 \dot{y}(s) ds d\theta + \int_{-\eta-\tau}^{-\tau} \int_{t+\theta}^t \dot{y}^T(s) R_2 \dot{y}(s) ds d\theta \\
&\quad + \int_{-\eta-\tau}^{-\eta} \int_{t+\theta}^t \dot{y}^T(s) R_3 \dot{y}(s) ds d\theta
\end{aligned}$$

Calculating the derivative of $V(t)$ yields

$$\begin{aligned} \dot{V}(t) \leq & \dot{y}^T(t)Py(t) + y^T(t)P\dot{y}(t) + y^T(t)(Q_1 + Q_4)y(t) + y^T(t - \eta)Q_2y(t - \eta) \\ & - y^T(t - \tau)(Q_1 - Q_3)y(t - \tau) - y^T(t - \eta - \tau)(Q_2 + Q_3 + Q_4)y(t - \eta - \tau) \\ & + \tau\dot{y}^T(t)R_1\dot{y}(t) - \int_{t-\tau}^t \dot{y}^T(s)R_1\dot{y}(s)ds + h\dot{y}^T(t)R_2\dot{y}(t) - \int_{t-\eta-\tau}^{t-\tau} \dot{y}^T(s)R_2\dot{y}(s)ds \\ & + \tau\dot{y}^T(t)R_3\dot{y}(t) - \int_{t-\eta-\tau}^{t-\eta} \dot{y}^T(s)R_3\dot{y}(s)ds \end{aligned}$$

From Lemma 1, we get

$$\begin{aligned} \dot{V}(t) \leq & \dot{y}^T(t)Py(t) + y^T(t)P\dot{y}(t) + y^T(t)(Q_1 + Q_4)y(t) + y^T(t - \eta)Q_2y(t - \eta) \\ & - T(t - \tau)(Q_1 - Q_3)y(t - \tau) - y^T(t - \eta - \tau)(Q_2 + Q_3 + Q_4)y(t - \eta - \tau) \\ & + \tau\dot{y}^T(t)R_1\dot{y}(t) - (y^T(t) - y^T(t - \tau))R_1(y(t) - y(t - \tau)) + h\dot{y}^T(t)R_2\dot{y}(t) \\ & - (y^T(t - \tau) - y^T(t - \eta - \tau))R_2(y(t - \tau) - y(t - \eta - \tau)) + \tau\dot{y}^T(t)R_3\dot{y}(t) \\ & - (y^T(t - \eta) - y^T(t - \eta - \tau))R_3(y(t - \eta) - y(t - \eta - \tau)) \end{aligned}$$

Define $\varphi^T(t) = [y^T(t), y^T(t - \eta), y^T(t - \tau), y^T(t - \eta - \tau)]$, and we obtain

$$\dot{V}(t) \leq \varphi^T(t)M\varphi(t)$$

where M is defined as (25.7). Therefore, if (25.7) established, the system (25.6) is asymptotically stable, i.e., the agents in system (25.3) achieve an asymptotic consensus.

25.4.2 Time-Varying Communication Delay

This section investigates the system (25.5) with time-varying communication delay.

Assumption 2 $0 \leq \eta(t) \leq h, 0 \leq \dot{\eta}(t) \leq d < 1, h > 0, \tau > 0, t \geq 0$.

Theorem 2 *If $\eta(t)$ and τ satisfy Assumption 2, the interconnection topology G of multi-agent systems (25.3) has global accessible node, and the output degree of each node are greater than zero. Then, multi-agent systems (25.3) achieve an asymptotic consensus with appropriate $h > 0, \tau > 0$, and the allowed upper bound of delay τ can be obtained by solving the following LMI:*

$$M = \begin{bmatrix} M_{11} & M_{12} & M_{13} & M_{14} \\ * & M_{22} & 0 & M_{24} \\ * & * & M_{33} & M_{34} \\ * & * & * & M_{44} \end{bmatrix} < 0 \quad (25.8)$$

$$\begin{aligned}
M_{11} &= PH_1 + H_1^T P + Q_1 + Q_3 + \tau H_1^T (R_1 + R_3) H_1 + h H_1^T (R_2 + R_4) H_1 - \tau^{-1} R_1 - h^{-1} R_4 \\
M_{12} &= h^{-1} R_4, \quad M_{13} = PH_2 + \tau H_1^T (R_1 + R_3) H_2 + h H_1^T (R_2 + R_4) H_2 + \tau^{-1} R_1 \\
M_{14} &= PH_3 + \tau H_1^T (R_1 + R_3) H_3 + h H_1^T (R_2 + R_4) H_3 \\
M_{22} &= -\tau^{-1} R_3 - h^{-1} R_4, \quad M_{24} = \tau^{-1} R_3 \\
M_{33} &= -Q_1 + Q_2 + \tau H_2^T (R_1 + R_3) H_2 + h H_2^T (R_2 + R_4) H_2 - \tau^{-1} R_1 - h^{-1} R_2 \\
M_{34} &= \tau H_2^T (R_1 + R_3) H_3 + h H_2^T (R_2 + R_4) H_3 + h^{-1} R_2 \\
M_{44} &= (d-1)(Q_2 + Q_3) + \tau H_3^T (R_1 + R_3) H_3 + h H_3^T (R_2 + R_4) H_3 - h^{-1} R_2 - \tau^{-1} R_3
\end{aligned}$$

where, the positive definite matrixes $P, Q_1, Q_2, Q_3, R_j, j = 1, 2, 3, 4$ are of appropriate dimension.

Proof Construct Lyapunov–Krasovskii functional of the system as:

$$V(t) = V_1(t) + V_2(t) + V_3(t)$$

$$V_1(t) = y^T(t) P y(t)$$

$$\begin{aligned}
V_2(t) &= \int_{t-\tau}^t y^T(s) Q_1 y(s) ds + \int_{t-\eta(t)-\tau}^{t-\tau} y^T(s) Q_2 y(s) ds \\
&\quad + \int_{t-\eta(t)-\tau}^t y^T(s) Q_3 y(s) ds
\end{aligned}$$

$$\begin{aligned}
V_3(t) &= \int_{-\tau}^0 \int_{t+\theta}^t \dot{y}^T(s) R_1 \dot{y}(s) ds d\theta + \int_{-h-\tau}^{-\tau} \int_{t+\theta}^t \dot{y}^T(s) R_2 \dot{y}(s) ds d\theta \\
&\quad + \int_{-h-\tau}^{-h} \int_{t+\theta}^t \dot{y}^T(s) R_3 \dot{y}(s) ds d\theta + \int_{-h}^0 \int_{t+\theta}^t \dot{y}^T(s) R_4 \dot{y}(s) ds d\theta
\end{aligned}$$

The derivative of Lyapunov–Krasovskii functional is given by:

$$\begin{aligned}
\dot{V}(t) &\leq \dot{y}^T(t) P y(t) + y^T(t) P \dot{y}(t) + y^T(t) Q_1 y(t) \\
&\quad - y^T(t-\tau)(Q_2 - Q_1)y(t-\tau) + (d-1)y^T y(t-\eta(t)-\tau)(Q_2 + Q_3)y(t-\eta(t)-\tau) \\
&\quad + \tau \dot{y}^T(t) R_1 \dot{y}(t) - \int_{t-\tau}^t \dot{y}^T(s) R_1 \dot{y}(s) ds + h \dot{y}^T(t) R_2 \dot{y}(t) - \int_{t-\eta(t)-\tau}^{t-\tau} \dot{y}^T(s) R_2 \dot{y}(s) ds \\
&\quad + \tau \dot{y}^T(t) R_3 \dot{y}(t) - \int_{t-\eta(t)-\tau}^{t-\eta(t)} \dot{y}^T(s) R_3 \dot{y}(s) ds + h \dot{y}^T(t) R_4 \dot{y}(t) - \int_{t-\eta(t)}^t \dot{y}^T(s) R_4 \dot{y}(s) ds
\end{aligned}$$

From Lemma 1, we get

$$\begin{aligned} \dot{V}(t) \leq & \dot{y}^T(t)Py(t) + y^T(t)P\dot{y}(t) + y^T(t)Q_1y(t) \\ & - y^T(t-\tau)(Q_2 - Q_1)y(t-\tau) + (d-1)y^T(t-\eta(t)-\tau)(Q_2 + Q_3)y(t-\eta(t)-\tau) \\ & + \tau\dot{y}^T(t)R_1\dot{y}(t) - (y^T(t) - y^T(t-\tau))R_1(y(t) - y(t-\tau)) + h\dot{y}^T(t)R_2\dot{y}(t) \\ & - (y^T(t-\tau) - y^T(t-\eta(t)-\tau))R_2(y(t-\tau) - y(t-\eta(t)-\tau)) + \tau\dot{y}^T(t)R_3\dot{y}(t) \\ & - (y^T(t-\eta(t)) - y^T(t-\eta(t)-\tau))R_3(y(t-\eta(t)) - y(t-\eta(t)-\tau)) + h\dot{y}^T(t)R_4\dot{y}(t) \\ & - (y^T(t) - y^T(t-\eta(t)))R_4(y(t) - y(t-\eta(t))) \end{aligned}$$

Define $\varphi^T(t) = [y^T(t), y^T(t-\eta(t)), y^T(t-\tau), y^T(t-\eta(t)-\tau)]$, we obtain $\dot{V}(t) \leq \varphi^T(t)M\varphi(t)$ where M is defined as (25.8). Therefore, if (25.8) established, the system (25.5) is asymptotically stable, and the multi-agent systems (25.3) the asymptotic convergence consistent proof.

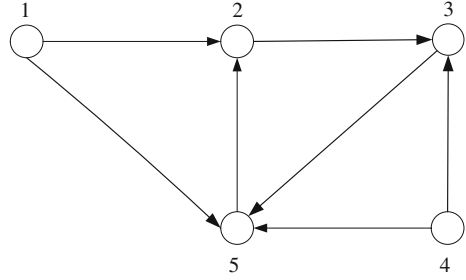
Corollary 1. *Communication delay $\eta(t)$ and input delay τ satisfy: $0 \leq \eta(t) \leq h, h > 0, \tau > 0, t \geq 0$, i.e., $d \geq 1$ or unknown. Then, construct Lyapunov-Krasovskii function as follows:*

$$\begin{aligned} IV(t) = & y^T(t)Py(t) + \int_{-\tau}^0 \int_{t+\theta}^t \dot{y}^T(s)R_1\dot{y}(s)dsd\theta + \int_{-h-\tau}^{-\tau} \int_{t+\theta}^t \dot{y}^T(s)R_2\dot{y}(s)dsd\theta \\ & + \int_{-h-\tau}^{-h} \int_{t+\theta}^t \dot{y}^T(s)R_3\dot{y}(s)dsd\theta + \int_{-h-\tau}^0 \int_{t+\theta}^t \dot{y}^T(s)R_4\dot{y}(s)dsd\theta \end{aligned}$$

Since the interconnection topology G of multi-agent systems (25.6) has global accessible nodes, and each node of the output degree are greater than zero. Then, multi-agent systems (25.3) achieve an asymptotic convergence consensus with appropriate $h > 0, \tau > 0$, and the allowed upper bound of delay τ can be obtained by solving the following LMI:

$$M = \begin{bmatrix} M_{11} & 0 & M_{13} & M_{14} \\ * & M_{22} & 0 & M_{24} \\ * & * & M_{33} & M_{34} \\ * & * & * & M_{44} \end{bmatrix} < 0 \quad (25.9)$$

Fig. 25.1 Interconnection topology G of second order agents systems



$$\begin{aligned}
 M_{11} &= PH_1 + H_1^T P + \tau^{-1} (R_1 + R_3 + R_4)H_1 + hH_1^T (R_2 + R_4)H_1 - \tau^{-1}R_1 - (h + \tau)^{-1}R_4 \\
 M_{13} &= PH_2 + \tau H_1^T (R_1 + R_3 + R_4)H_2 + hH_1^T (R_2 + R_4)H_2 + \tau^{-1}R_1 \\
 M_{14} &= PH_3 + \tau H_1^T (R_1 + R_3 + R_4)H_3 + hH_1^T (R_2 + R_4)H_3 + (h + \tau)^{-1}R_4 \\
 M_{22} &= -\tau^{-1}R_3, \quad M_{24} = \tau^{-1}R_3 \\
 M_{33} &= \tau H_2^T (R_1 + R_3 + R_4)H_2 + hH_2^T (R_2 + R_4)H_2 - \tau^{-1}R - h^{-1}R_2 \\
 M_{34} &= \tau H_2^T (R_1 + R_3 + R_4)H_3 + hH_2^T (R_2 + R_4)H_3 + h^{-1}R_2 \\
 M_{44} &= \tau H_3^T (R_1 + R_3 + R_4)H_3 + hH_3^T (R_2 + R_4)H_3 - h^{-1}R_2 - \tau^{-1}R_3 - (h + \tau)^{-1}R_4
 \end{aligned}$$

where, the positive definite matrixes $P, R_j, j = 1, 2, 3, 4$ are of appropriate dimension.

25.4.3 Numerical Simulation

Assume that the multi-agent systems have five nodes, and the interconnection topology is shown in Fig. 25.1. The weights of edges are: $a_{12} = 0.05, a_{15} =$

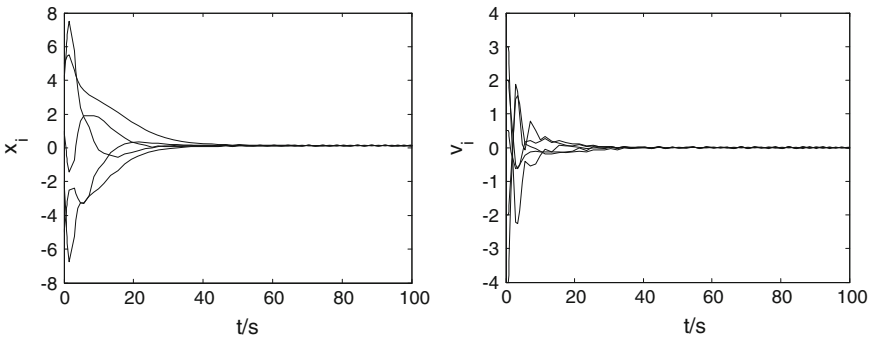


Fig. 25.2 Positions and speed of agents when is η constant

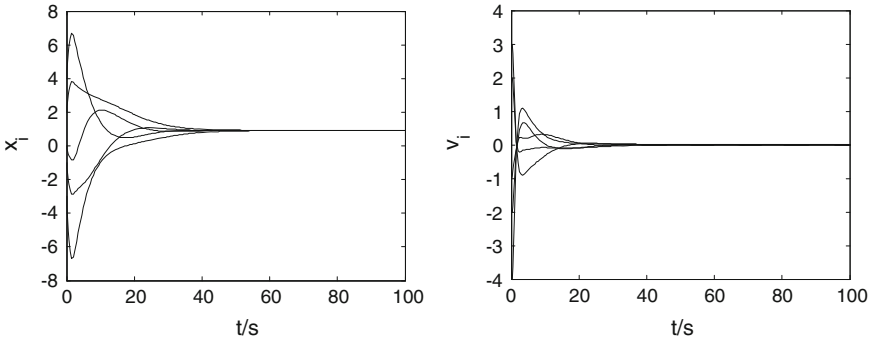


Fig. 25.3 Positions and speed of agents when $d < 1$

0.15, $a_{23} = 0.2$, $a_{35} = 0.2$, $a_{43} = 0.08$, $a_{45} = 0.12$, $a_{52} = 0.2$. Obviously, the out-degrees of each node are greater than zero, and globally reachable nodes are $\{2, 3, 5\}$. The control gains are chosen as $k_1 = 0.1$ and $k_2 = 1$, and the initial position and velocity of each node are generated as random initial states.

1. When the communication delay is time-invariant, e.g., $\eta = 10$. Using the Matlab linear matrix inequality toolbox, we can get upper bound of input delay $\tau < 0.8131$ from condition (25.7), and we choose $\tau = 0.8$. Then, the closed-loop system (25.3) converges to a consensus asymptotically, i.e., $\lim_{t \rightarrow \infty} x_i(t) = 0.133$, $\lim_{t \rightarrow \infty} v_i(t) = 0$, $i = \{1, 2, 3, 4, 5\}$, and simulation results are shown in Fig. 25.2.
2. When the communication delay is time-varying, we choosed $d < 1$ and $\eta(t) = 10|\sin(0.05t)|$. From condition (25.8), we can get $\tau < 0.8131$. Choose $\tau = 0.4$, and the closed-loop system (25.3) achieve an asymptotic consensus, i.e., $\lim_{t \rightarrow \infty} x_i(t) = 0.913$, $\lim_{t \rightarrow \infty} v_i(t) = 0$, $i = \{1, 2, 3, 4, 5\}$. The simulation results are shown in Fig. 25.3.

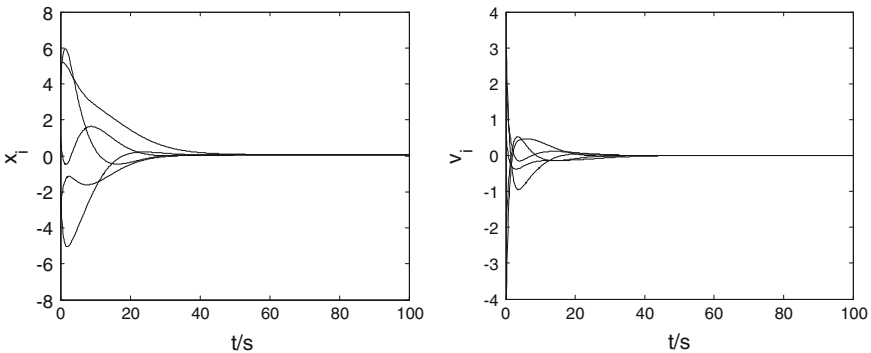


Fig. 25.4 Positions and speed of agents when $d \geq 1$

3. When $d \geq 1$, we take the time-varying communication delay $\eta(t) = 6|\sin(2t)|$. From condition (25.9), we can get $\tau \leq 0.4915$. Choose $\tau = 0.2$, and the closed-loop system (25.3) converges to a consensus asymptotically, i.e., $\lim_{t \rightarrow \infty} x_i(t) = 0.05$, $\lim_{t \rightarrow \infty} v_i(t) = 0$, $i = \{1, 2, 3, 4, 5\}$. The simulation results are shown in Fig. 25.4.

25.5 Conclusion

This paper considers the consensus problem of second-order multi-agent systems with communication delay and input delay under fixed topology. By constructing Lyapunov–Krasovskii functional, consensus condition is provided for second order multi-agent systems under time-invariant communication and input delays. For second-order multi-agent systems under time-invariant input delay and time-varying communication delay, furthermore, consensus conditions are obtained under the derivative of communication delay less than 1 and unknown or greater than 1 respectively. Consensus conditions in this paper are dependent on input delay and communication delay, and formulated in the form of linear matrix inequalities (LMI).

Acknowledgments This work was supported by the National Natural Science Foundation of China (Grant No. 61104092).

References

1. Fax JA, Murray RM, Olfati-Saber R (2007) Consensus and cooperation in networked multi-agent systems. *Proc IEEE* 95(1):215–233
2. Murray RM, Olfati-Saber R (2004) Consensus problems in networks of agents switching topology and time-delays. *IEEE Trans Autom Control* 9(49):1520–1533
3. Liu CL, Tian YP (2008) Consensus of multi-agent systems with diverse input and communication delays. *IEEE Trans Autom Control* 53(9):2122–2128
4. Liang Y, Liu C, Liu F (2012) Consensus problem of first-order multi-agent systems with communication delay and input delay. *Inf Control* 41(1):14–21 (in Chinese)
5. Lin P, Qin K, Zhao H et al (2012) A new approach to average consensus problems with multiple time-delay and jointly-connected topologies. *J Franklin Inst* 349:293–304
6. Huang QZ (2012) Consensus analysis of multi-agent discrete-time systems. *Acta Automatica Sinica* 38(7):1127–1133
7. Sun YG (2012) Average consensus in networks of dynamic agents with uncertain topologies and time-varying delays. *J Franklin Inst* 349(3):1061–1073
8. Sun YG, Wang L (2009) Consensus of multi-agent systems in directed networks with nonuniform time-varying delays. *IEEE Trans Autom Control* 54(7):1607–1613
9. Sun YG, Wang L, Xie GM (2008) Average consensus in networks of dynamic agents with switching topologies and multiple time-varying delays. *Sys Control Lett* 57(1):175–183

10. Liu CL, Liu F (2011) Consensus problem of second-order multi-agent systems with input delay and communication delay. In: Proceedings of the 30th Chinese control conference, pp 4747–4752
11. Cao M, Chen GR, Yu WW (2010) Some necessary and sufficient conditions for second-order consensus in multi-agent dynamical systems. *Automatica* 46(6):1089–1095
12. Liu CL, Liu F (2010) Consensus problem of second-order dynamic agents with heterogeneous input and communication delays. *Int J Comput Commun Control* 5(3):325–335
13. Liu CL, Liu F (2011) Consensus problem of second-order multi-agent systems with time-varying communication delay and switching topology. *J Syst Eng Electron* 22(4):672–678
14. Ting ZH, Jia YM, Lin P, Ting ZH et al (2008) Distributed control of multi-agent systems with second-order agent dynamics and delay-dependent communications. *Asian J Control* 10(2):254–259
15. Jin LS, Ting ZH, Zhao JT (2012) Consensus of second-order multi-agent systems with nonuniform time-varying delays. *Neurocomputing* 97:410–414
16. Sun Y, Wang L (2012) H_∞ consensus of second-order multi-agent systems with asymmetric delays. *Syst Control Lett* 61(8):857–862
17. Gao Y, Ma J, Zuo M (2012) Consensus of discrete-time second-order agents with time-varying topology and time-varying delays. *J Franklin Inst* 349(8):2598–2608
18. Gu K (2000) An integral inequality in the stability problem of time-delay systems. In: Proceedings of 39th IEEE conference on decision and control, pp 2805–2810

Chapter 26

An Image-Based Visual Servo Control of Robots with Omni-Directional Camera

Haiyong Chen, Guansheng Xing, Zihan Ma, Jinsuo Wang
and Peng Yang

Abstract An image-based visual servo with omni-directional camera is proposed to reach the desired distance and bearing between leaders' robot and followers' robot. First, the model of the omni-directional vision system is given. Then the improved vision model is presented and used during the following controller design. Furthermore, a nonlinear feedback control method is proposed for stabilizing the desired distance and bearing between the two robots. And the control algorithm utilizes estimations of the external input term which is only relative to the leader's translational and angular accelerations. Finally, some experimental results show that the proposed model and control approach can effectively realize the formation by using only omni-directional vision system.

Keywords Vision servo · Mobile robot · Formation control · Nonlinear control

26.1 Introduction

The visual servo control is a flexible and efficient strategy to control robot motion. In the past several years, the image-based visual servo (IBVS) has been increasingly an interesting research topic [1–3]. Vision seems to be a critical component in animals' abilities to respond to their neighbors' motions, which also can be applied

H. Chen · G. Xing · Z. Ma · P. Yang (✉)
School of Control Science and Engineering, Hebei University of Technology,
Tianjin 300130, China
e-mail: yphebut@yahoo.com.cn

H. Chen
e-mail: haiyong@hebut.edu.cn

J. Wang
School of Automation Science and Electrical Engineering, Beijing University of
Aeronautics and Astronautics, Beijing 100191, China

to track a predefined geometric of robots. It is noticed that an omni-directional camera is a camera with a 360° field of view in the horizontal plane, which is important in areas where large visual field coverage is needed, such as robotics. Thus the study will focus on how the robot is controlled to some position under the condition of not depending on the global communication but omni-directional vision.

An image-based visual servo control of robot with omni-directional camera omits the pose estimation step, and uses the image features directly in the vision frame. The control is performed in image coordinate frame. The desired robotic pose with respect to the other robot is defined implicitly by the image feature values at the goal pose [4–10].

An image-based visual formation control is presented by Hyeun [5]. Hyeun employs a single common monocular camera, instead of omni-directional camera, to capture the robotic teammate image in the formation. Then the multi-robot formation shape is controlled by using a geometric based visual tracking method in the image frame. However, the formation control can only deal with small number of robot formation due to the limit of the field of view of the common camera. Nicolás et al. propose a homography-based framework relying on the homography induced by the multi-robot system, and give a desired homography to be used to define the reference target. And an image-based control law is presented, which can drive the robots to the desired configuration by imposing a planar motion considering nonholonomic constraints [6]. Shakernia et al. design formation control algorithms based on omni-directional visual servoing and motion segmentation [7–10]. However, the model used also shows its non-singularity in some direction that can be shown in its simulation results, and no experiments result with real robot is given. The above problems motivate the contribution of this paper.

In this work, a novel model and control of the robot in the image frame will be proposed. This paper is organized as follows. Section 26.2 gives the model of omni-directional camera and vision servo of robot. Section 26.3 presents the new formation control method along with an analysis of its stability. Some examples of simulation results with real robots will be shown in Sect. 26.4.

26.2 Model of the Parabolic Catadioptric Camera

The model should indeed take into account the reflection operated by the mirror in the case of a catadioptric camera. Thus the omni-directional camera in the work is composed of the parabolic mirror and camera with an orthographic lens, which is shown by Fig. 26.1.

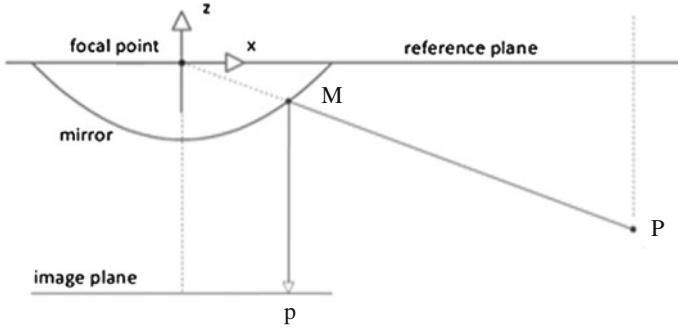


Fig. 26.1 The point P in camera frame is reflected and refracted to the point p

26.2.1 Model Representation

In this typical configuration of the catadioptric camera, the parabolic mirror is placed in front of the camera with an orthographic projecting lens whose focus is at infinity, which leads that the line MP is parallel to the z-axis [11]. The point P(X, Y, Z) in the camera frame is reflected and refracted by through the parabolic mirror and orthographic lens, respectively, to the point p(x, y) in the image frame. O_i -uv is the image plane frame whose z axis coincides with the one of the camera frame, which is shown in Fig. 26.1.

The project process can be separated into two steps. First, point P is projected to point M(x, y, z) on the surface of the parabolic mirror, and the parabola can be given by

$$z = \frac{1}{4q}(x^2 + y^2) - q \tag{26.1}$$

Second, it is assumed that the camera is attached to a mobile robot moving on the ground with the optical axis parallel to the Z axis, then the angular velocity is $\Omega = (0, 0, \Omega_z)^T$ and the linear velocity is $V = (V_x, V_y, 0)^T$. Thus the optical flow equation considering the focus length of the parabola can be given by

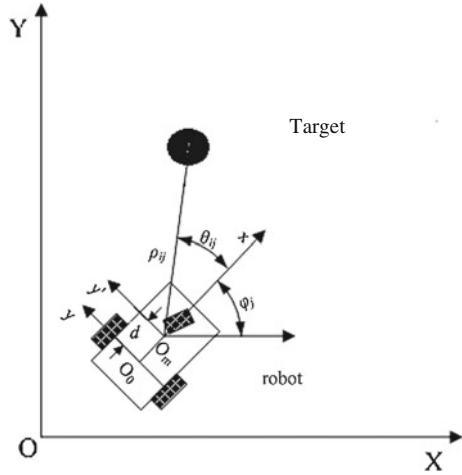
$$\begin{bmatrix} \dot{x} \\ \dot{y} \end{bmatrix} = \begin{bmatrix} -y \\ x \end{bmatrix} \omega + \frac{2q}{\lambda} \begin{bmatrix} \frac{1+z-x^2}{1+z} & \frac{-xy}{1+z} \\ \frac{-xy}{1+z} & \frac{1+z-y^2}{1+z} \end{bmatrix} v \tag{26.2}$$

where, $\lambda = -Z + \sqrt{X^2 + Y^2 + Z^2}$, $z = (x^2 + y^2)/4q - q$, $\Omega_z = \omega$, $v = [V_x \ V_y]^T$.

26.2.2 Robots' Motion Model

In the Fig. 26.2, the XOY is the world frame, O_m is the mass point of the robot, $xO_{m'y'}$ is the reference frame of robot. The point, O_0 , is the inter-point of the

Fig. 26.2 Two-wheel driven mobile robot



wheels' axis and reference frame of the robot. The xO_0y is the image plane. ρ_{ij} , θ_{ij} , is the distance and direction between target i , and robot j , respectively, in the reference frame $xO_m y$ of the robot. ϕ_j is the angle of the robot with respect to the X-axis in world frame.

The kinematics of robot can be abstracted as a unicycle model

$$\dot{X}_j = v_j \cos \theta_j; \quad \dot{Y}_j = v_j \sin \theta_j; \quad \dot{\theta}_j = \omega_j \tag{26.3}$$

where, $(X_j, Y_j$ and $\theta_j)$ are the position and orientation of the robot, v_j and ω_j are the linear and angular velocities, respectively, (X_j, Y_j) are the position of the target. Let $(X_{ij}, Y_{ij}) = ((X_i - X_j), (Y_i - Y_j))$ is the relative coordinates of target respect to robot, where the angular in the Cartesian frame is given by

$$\theta_{ij} + \phi_j = \arctan \frac{Y_{ij}}{X_{ij}} \tag{26.4}$$

Next, we can project (X_{ij}, Y_{ij}) into (x_{ij}, y_{ij}) on image plane. Without loss of generality, it is assumed that the focus of the parabolic mirror equals one, e.g. $q = 1$. In order to improve the closed-loop performance of system, these robots' center of mass is considered by adding a compensation d that is the distance between y' axis in reference frame and y axis in image frame, which is shown by Fig. 26.2. The model of system in the image frame is given by

$$\begin{aligned} \begin{bmatrix} \dot{x}_{ij} \\ \dot{y}_{ij} \end{bmatrix} = & - \begin{bmatrix} \left(\frac{1-\rho x_{ij}^2}{\lambda}\right) & -y_{ij} \\ \left(\frac{-\rho x_{ij} y_{ij}}{\lambda}\right) & x_{ij} \end{bmatrix} \begin{bmatrix} v_i \\ \omega_i \end{bmatrix} + \begin{bmatrix} \left(\frac{1-\rho x_{ij}^2}{\lambda}\right) & \left(\frac{-\rho x_{ij} y_{ij}}{\lambda}\right) & -y_{ij} \\ \left(\frac{-\rho x_{ij} y_{ij}}{\lambda}\right) & \frac{1-\rho y_{ij}^2}{\lambda} & x_{ij} \end{bmatrix} \begin{bmatrix} F_{ij} \\ \omega_i \end{bmatrix} \\ & + \begin{bmatrix} \left(\frac{-\rho(2x_{ij}d+d^2)}{\lambda}\right) & 0 \\ \left(\frac{-\rho dy_{ij}}{\lambda}\right) & d \end{bmatrix} \begin{bmatrix} v_i \\ \omega_i \end{bmatrix} + \begin{bmatrix} \left(\frac{-\rho(2x_{ij}d+d^2)}{\lambda}\right) & \left(\frac{-\rho dy_{ij}}{\lambda}\right) & 0 \\ \left(\frac{-\rho dy_{ij}}{\lambda}\right) & 0 & d \end{bmatrix} \begin{bmatrix} F_{ij} \\ \omega_i \end{bmatrix} \end{aligned} \tag{26.5}$$

Thus, we rewrite the robot dynamics in polar coordinates in the image frame so as to more easily realize the distance and direction control. Assumed that a desired pixel location (x_d, y_d) for target is given, where $(x_d, y_d) = (r_d \cos(a_d), r_d \sin(a_d))$. Then the control model in polar coordinates is given by

$$\begin{bmatrix} \dot{r}^{ij} \\ \dot{\alpha}^{ij} \end{bmatrix} = -H^{ij}(r^{ij}, \alpha^{ij}) \begin{bmatrix} v_j \\ w_j \end{bmatrix} + d^{ij} \quad (26.6)$$

where, d^{ij} , H^{ij} represents system matrix that robot to toward target, and can be described by $h_{11}^{ij}, h_{12}^{ij}, h_{21}^{ij}, h_{22}^{ij}$. r^{ij} , α^{ij} are distance, direction between i^{th} robot and j^{th} robot, respectively. It is noticed that we can get better trajectory tracking performance by using robot's center of mass as origin of the reference coordinates, which makes the system matrix in model Eq. (26.6) to become non-singular matrix.

$$\begin{aligned} h_{11}^{ij} &= \frac{\cos \alpha^{ij} (1 - \rho(r^{ij})^2)}{\lambda} + \frac{-\rho(dr^{ij} \cos^2 \alpha^{ij} + dr^{ij} + d^2 \cos \alpha^{ij})}{\lambda} \\ h_{12}^{ij} &= d \sin \alpha^{ij}; h_{22}^{ij} = 1 + \frac{d \cos \alpha^{ij}}{r^{ij}} \\ h_{21}^{ij} &= \frac{-\sin \alpha^{ij}}{\lambda r^{ij}} + \frac{\rho(dr^{ij} \cos \alpha^{ij} \sin \alpha^{ij} + d^2 \sin \alpha^{ij})}{\lambda r^{ij}} \end{aligned} \quad (26.7)$$

The elements of matrix $G^{ij}(r^{ij}, \alpha^{ij})$ are represented as

$$\begin{aligned} g_{11}^{ij} &= \frac{\cos \alpha^{ij} (1 - \rho(r^{ij})^2)}{\lambda} + \frac{-\rho(dr^{ij} \cos^2 \alpha^{ij} + dr^{ij} + d^2 \cos \alpha^{ij})}{\lambda} \\ g_{12}^{ij} &= \frac{\sin \alpha^{ij} (1 - \rho(r^{ij})^2)}{\lambda} - \frac{\rho dr^{ij} \sin \alpha^{ij} \cos \alpha^{ij}}{\lambda} \\ g_{13}^{ij} &= d \sin \alpha^{ij}; g_{23}^{ij} = 1 + \frac{d \cos \alpha^{ij}}{r^{ij}} \\ g_{21}^{ij} &= \frac{-\sin \alpha^{ij}}{\lambda r^{ij}} + \frac{\rho(dr^{ij} \cos \alpha^{ij} \sin \alpha^{ij} + d^2 \sin \alpha^{ij})}{\lambda r^{ij}} \\ g_{22}^{ij} &= \frac{\cos \alpha^{ij}}{\lambda r^{ij}} + \frac{\rho dr^{ij} \sin^2 \alpha^{ij}}{\lambda r^{ij}} \end{aligned} \quad (26.8)$$

26.3 Controller Design

We start with a simple configuration that is composed of one robot and a target object, which is shown in Fig. 26.2. In this configuration, the robot j moves to the target i with a desired distance and relative bearing. The system is transformed into a new image plane where the state of the target is treated as an exogenous input. Thus, the kinematics equation is given by Eq. (26.6).

By applying input–output feedback linearization, the control velocities for the robot is given by

$$u_j = (H^{ij})^{-1} \left(\begin{bmatrix} k_1(r^{ij} - r_d^{ij}) \\ k_2(\alpha^{ij} - \alpha_d^{ij}) \end{bmatrix} + d^{ij} \right) \quad (26.9)$$

where, r_d^{ij}, α_d^{ij} is the desired distance and direction between them, respectively. The external input term d^{ij} need be estimated by using following equation

$$d^{ij} = \begin{bmatrix} \dot{x}_i \\ \dot{y}_i \end{bmatrix} - H(x_i, y_i)H(x_i, y_i)^{-1} \begin{bmatrix} \dot{x}_w \\ \dot{y}_w \end{bmatrix} \quad (26.10)$$

where, (x_w, y_w) is a still point in the world frame. With the controller, the closed-loop dynamics of the tracking error $e_r = r^{ij} - r_d^{ij}$ and $e_\alpha = \alpha^{ij} - \alpha_d^{ij}$ is given by

$$\begin{bmatrix} \dot{e}_r \\ \dot{e}_\alpha \end{bmatrix} = \begin{bmatrix} k_1 & \\ & k_2 \end{bmatrix} \begin{bmatrix} e_r \\ e_\alpha \end{bmatrix} \quad (26.11)$$

It is apparent that the controller can lead to a locally exponentially stable system around $(r_d^{ij}, \alpha_d^{ij})$ whenever $k_1 > 0$ and $k_2 > 0$.

26.4 Experimental Results

The experimental robot system includes two robots. One is the yellow leader, the other is the black follow robot with an omni-directional visual system, an embedded computer with operator system, e.g. Windows 2000 and a DSP motion controller of the motor. The yellow leader robot can be recognized by employing image processing algorithm that run in the computer of the follower. The image capture rate is 30 frames per second.

We present the results of two experiments that the robot is driven to keep the desired and direction to the still one. The initial distance and angle is (950 mm, 45°) in world frame, (0.65, -45°) in image frame. The output of controller and final state are shown in Figs. 26.3 and 26.4. The final poses are (0.45 mm, 0°) in image frame, thus the desired results are obtained.

In the Figs. 26.5 and 26.6, the desired poses are (0.45 mm, 45°) in image frame. And the practical experimental result is in the Fig. 26.3. Figure 26.4 is the final status of the robot and also verified that desired distance and bearing in the image plane is 0.45 mm and 45° is reached.

From Figs. 26.3 to 26.6, it can be shown that the desired distance and bearing in the image plane can be reached by using the proposed method in the study. And the different desired pose control of target with respect to a still robot can also be reached accurately.

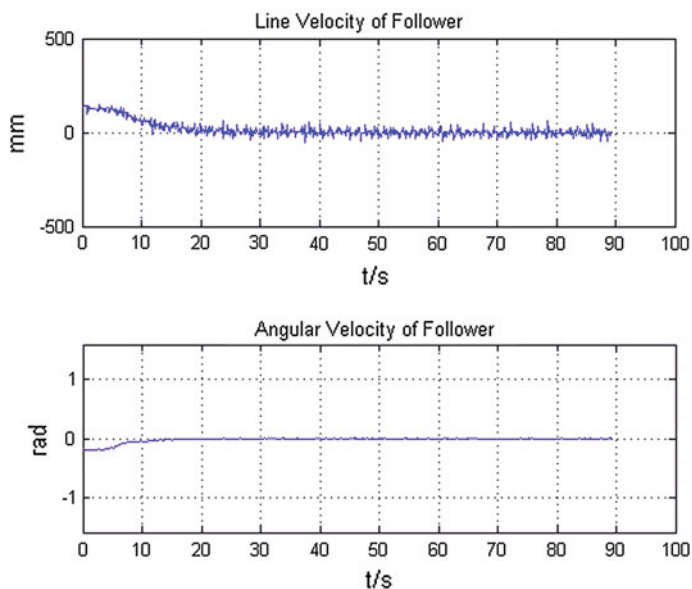


Fig. 26.3 Control curve for first group pose

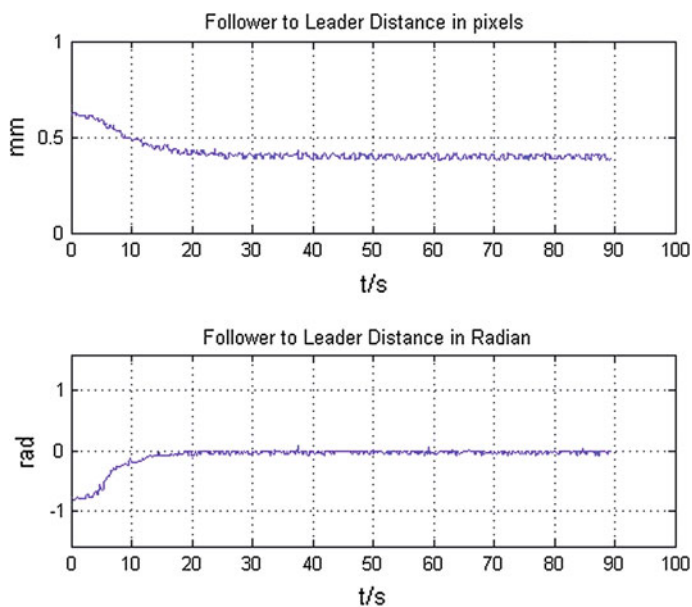


Fig. 26.4 Output curve for first group pose

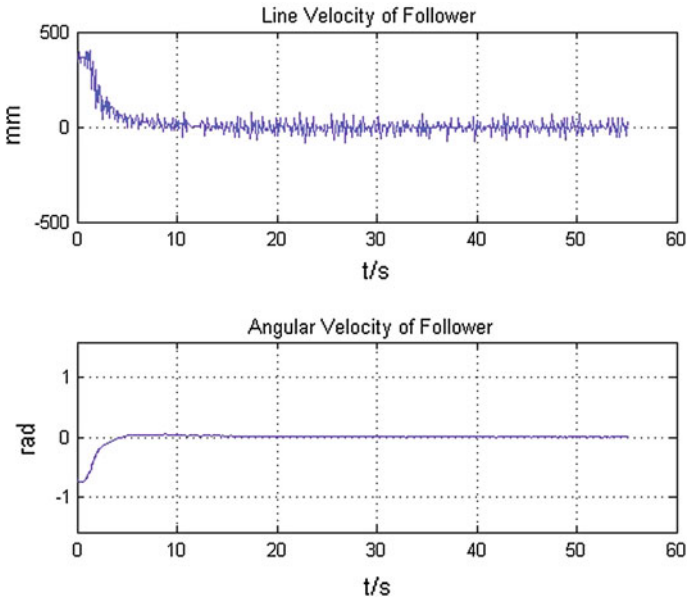


Fig. 26.5 Control curve for second group pose

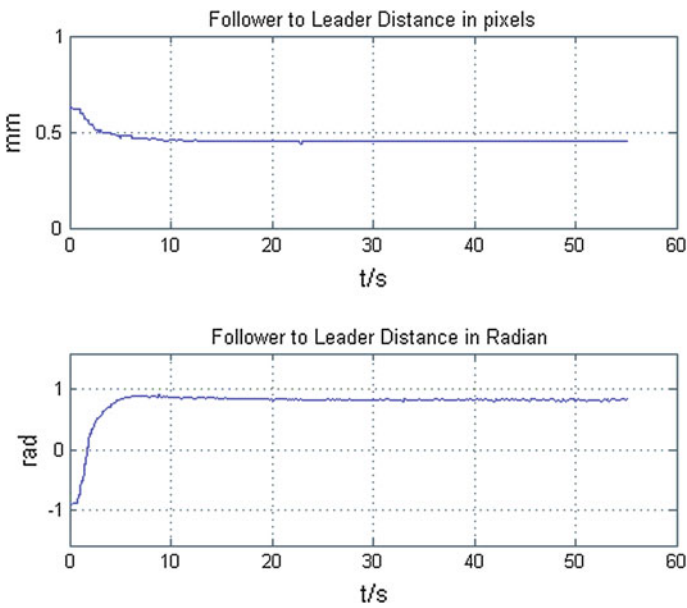


Fig. 26.6 Output curve for second group pose

Acknowledgments This work was supported by the National Natural Science Foundation of China under grant 61203275 and the Tianjin Research Program of Application Foundation and Advanced Technology (11JCYBJC06500).

References

1. Hutchinson S, Hager G, Corke P (1996) A tutorial on visual servo control. *IEEE Trans Robot Automat* 12(5):651–670
2. Dani AP, Gans N et al (2009) Position-based visual servo control of leader-follower formation using image-based relative pose and relative velocity estimation. *Am Contr Conf* 1(9):5271–5527
3. Carvalho E, Silva MP et al. (2009) Decentralized formation control of autonomous mobile robots, *IECON 2009—35th annual conference of IEEE industrial electronics*, pp 1504–1509
4. Espiau B, Chaumette F, Rives P (1992) A new approach to visual servoing in robotics. *IEEE Trans Robot Automat* 8(3):313–326
5. Hyeun JM, Nikolaos P (2012) Robot formations using a single camera and entropy-based segmentation. *J Intell Rob Syst* 68(1):21–41
6. López NG, Aranda M, Mezouar Y, Sagüés C (2012) Visual control for multirobot organized rendezvous. Part B: Cybern *IEEE Trans Sys Man Cybern* 42(4):1155–1168
7. Omid S, Yi M, John TK, Shankar S (1999) Landing an unmanned air vehicle vision based motion estimation and nonlinear control. *Asian J Contr* 1(3):128–145
8. Vidal R, Shakernia O et al (2003) Following the flock: distributed formation control with omnidirectional vision-based motion segmentation and visual servoing. *IEEE Robot Autom Mag* 11(4):14–20
9. Vidal R, Shakernia O, Kim HJ et al (2002) Probabilistic pursuit-evasion games: theory, implementation, and experimental evaluation. *IEEE Trans Robot Autom* 18(5):662–669
10. Cowan N, Shakernia O et al (2003) Vision-based follow-the-leader. 2003 *IEEE/RSJ international conference on intelligent robots and systems*, vol 2, pp 1796–1801
11. Maynard P (2007) *Drawing distinctions: the varieties of graphic expression*. Cornell University Press, NY

Chapter 27

Simulation and Forecast About Vegetable Prices Based on PSO-RBFNN Model

Qigang Xu and Mingjun Liu

Abstract RBF neural network is a kind of forward neural network model with good perform, it has the best approximation performance. Using improved PSO algorithm which is proposed in this paper, the neural network parameters are optimized, the training method is quick and easy operation. Taking the Chinese cabbage price change trend of Qingdao south village wholesale market in Shandong province as example, and discuss the way to solve the problem by adopting RBF neural network. Constructing time interval unified time series data and normalized processing. Through the training network model to realized the simulation and forecast of price trend. The experimental results show that the model has fast calculation speed and the forecast precision is high.

Keywords RBF neural network · PSO algorithm · Time series

27.1 Introduction

Agricultural product's price fluctuation is influenced by many factors, such as the season, weather, grew, production, circulation and so on. So directly discuss the problem from the influence factors of agricultural product prices is a complicated subject. However, study of the agricultural product price change trend has a very realistic significance.

RBFNN (Radial Basis Function Neural Network) is a kind of forward neural network model with good perform, it has the best approximation performance. Its biggest advantage is that it can eliminate the influence of the external factors, can through to the data information from organizational learning to find out its rules.

Q. Xu (✉) · M. Liu
School of Information Science and Engineering, University of Jinan,
No 106, JiWei Road, Jinan, China
e-mail: ujn_xuqig@163.com

With the linear relationship of output and weights, the training method is rapid and easy. There is no local optimal problem [1].

PSO (Particle Swarm Optimization) algorithm is put forward by Dr Eberhart and Dr Kennedy based on bird flock foraging behavior in 1995. The concept of this algorithm is simple. The algorithm is easy to realize, has fast convergence rate, less parameter setting. It is a kind of efficient search algorithm and can solve the parameters of neural network learning problems very well [2, 3].

The second section of the paper introduces the RBFNN structure and the parameter training method, the third part introduces the sample construction method, the forth part gives the experimental results and conclusion.

27.2 RBFNN Model and PSO Algorithm

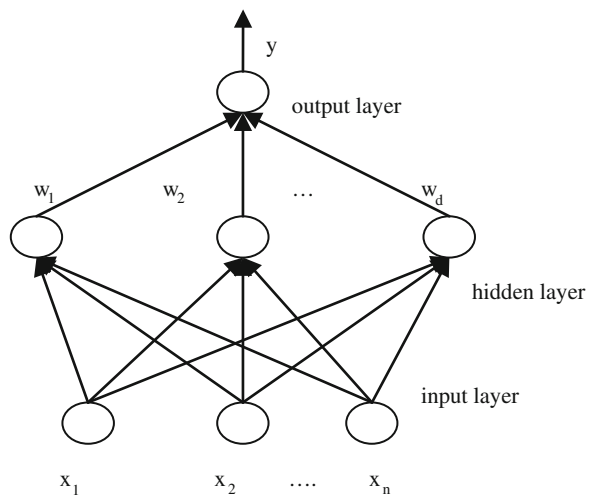
27.2.1 RBFNN Structure

RBFNN model is constituted by input layer, hidden layer and output layer of three layer neurons (Fig. 27.1). The input layer transfer input signal to the hidden layer, hidden layer nodes composition by the gaussian kernel function, and output layer node is linear function, the unit number are n , d and m . The basis function of hidden layer unit's center is μ_j and width is σ_j . Between the hidden layer and output layer is weight: w_k [4, 5].

Assume that the number of learn samples is P . The input mode for $X = (x_1, x_2, \dots, x_n)$. H_k represents the output of hidden layer, and y represents the output of output layer.

The output of hidden layer formula:

Fig. 27.1 Architecture of the radial basis function artificial neural net work



$$H_k(X) = \exp\left(-\frac{\|X - \mu_k\|}{\sigma_k^2}\right) \quad (27.1)$$

The output of output layer formula:

$$y = \sum_{k=1}^d w_k H_k(X) \quad (27.2)$$

Hidden neurons number general according to the complexity of the problem to determine, more neurons can improve the network accuracy, but the network training time will long and maybe produce the over-fitting problem. The paper after many training comparison, determine the number of hidden layer is 4.

27.2.2 PSO Algorithm Learn RBFNN Parameters

There are many ways to learn the RBFNN Parameters, this paper use the PSO Algorithm. Use the PSO algorithm, each solution of optimization problem is one “particle” of search space. All the particles have a fitness function (E) and a speed, decided the particle’s direction and distance. In each iteration process, particles update the velocity (V_i) and position (P_i) through tracking the two extreme (individual extreme P_{best} and global extreme G_{best}):

$$V_i = W \cdot V_i + C_1 \cdot rand() \cdot (P_{best} - P_i) + C_2 \cdot rand() \cdot (G_{best} - P_i) \quad (27.3)$$

$$P_i = P_i + V_i \quad (27.4)$$

$$W = \frac{k_{max} - k}{k_{max}} \quad (27.5)$$

The above formula, $C_1 = 0.05$, $C_2 = 0.07$, $rand()$ generation float numbers from 0 to 1. k_{max} is the biggest iterations and k id current iteration times. They are used to control the particle make it have better search ability. The fitness function is defined as follows:

$$E = \frac{1}{N} \sum_{i=1}^N (R_i - y_i)^2 \quad (27.6)$$

The above formula, N is the number of train samples, R is the observed and y is the actual output value. The parameters which PSO algorithm will optimized, namely each particle composition including the center of the hidden layer neurons μ , and width σ . Between the hidden layer and output layer is weight w and threshold t . The detailed algorithm process please Ref. [6].

27.3 Sample Construction Method

The price data of Chinese cabbage in Qingdao south village wholesale market at Shandong province is from the department of agriculture of Shandong province. There are a total of 888 data from 5 December 2009 to 10 May 2012. As follows Table 27.1:

Table 27.1 Date format of Chinese cabbage

Serial	Date	Price (kg/yuan)	Serial	Date	Price (kg/yuan)
1	5-12-2009	0.4	5	9-12-2009	0.24
2	6-12-2009	0.4
3	7-12-2009	0.22	887	9-05-2012	0.8
4	8-12-2009		888	10-05-2012	0.8

The date of Table 27.1 is too much and incomplete, which needed to data processing and normalized. Through the expert guidance, we complete all the data, like Serial 4, the Price is 0.22. Due to the large amount of data, and the recurrence rate is too high, so we take the average of every three days as a sample. About the normalization, we take the method divided by the maximum. The maximum value is 2. At last there are 296 values of training samples. As follows Table 27.2:

Table 27.2 The value if training samples

X(i)	Value	X(i)	Value	X(i)	Value	X(i)	Value	X(i)	Value	X(i)	Value
1	0.103	5	0.12	9	0.325	13	0.433	289	0.35	293	0.3
2	0.117	6	0.175	10	0.358	290	0.35	294	0.333
3	0.12	7	0.175	11	0.375	291	0.35	295	0.4
4	0.12	8	0.275	12	0.375	287	0.35	292	0.317	296	0.4

About Fig. 27.1, we set the number of input layer is 9, hidden layer is 4, and output layer is 1. Through the cycle operation, we can use the data of every first 27 days to predict future data. Because we need every 9 input sample values for prediction, and the total of sample values are 296, so the number of construction sample is 287 [7]. As follows Table 27.3:

Table 27.3 Sample construction method

Sam_id	Input	Output	Input value	Output value
1	[X (1), X (2),..., X (9)]	X(10)	[0.103, 0.117, ..., 0.325]	0.358
2	[X (2), X (3),..., X (10)]	X(11)	[0.117, 0.12, ..., 0.358]	0.375
...	[...]
t	[X (t), X (t + 1),..., X (t + 8)]	X(t + 9)
...	[...]
287	[X (287), X (288),..., X (295)]	X(296)	[0.35, 0.35, ... 0.4]	0.4

27.4 Experimental Results and Conclusion

27.4.1 Experimental Results

All the experimental results were realized in Java program. From the Table 27.3, we choose the Sam_id 1–220 as the training samples and 221–287 as the testing samples. Figure 27.2 is the diagram of observed value (blue solid line) and simulation value (red dotted line) of the model. Figure 27.3 is the diagram of observed value and predicted value (red dotted line) Abscissa representative the date, for example: 0 which in Fig. 27.2 is 5 December 2009, and 867 which in Fig. 27.3 is 20 April 2012, then later each day plus one. Ordinate represent a price, the unit is kg/yuan. All the curves are selected through special point and spline [8] results.

We set the particle’s size for 100, the largest iterations (k_{max}) for 1,000. We randomly chose five times the experimental results as follows Table 27.4.

Fig. 27.2 Curves of observed value and simulation value of the model

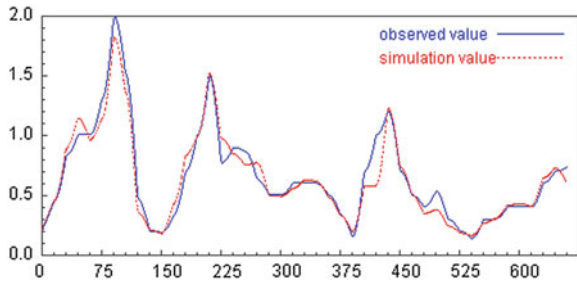


Fig. 27.3 Curves of observed value and predicted value of the model

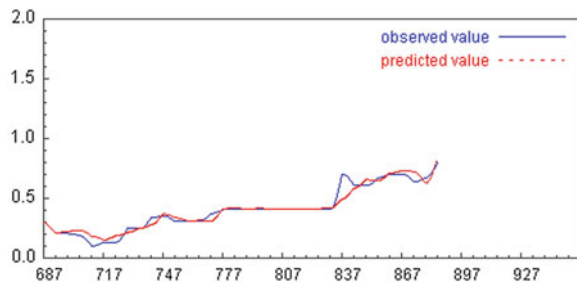


Table 27.4 Experimental error

	1	2	3	4	5	Average
Simulation error	0.014625	0.015851	0.015305	0.021541	0.019803	0.017425
Prediction error	0.032093	0.032768	0.032307	0.034461	0.032649	0.032856

27.4.2 Conclusion

The approximation ability and the learning speed of RBFNN model are improved, and PSO algorithm has a better speed than simple neural network model, so the PSO-RBFNN model has good application prospect. Calculation experimental results show that the model for the Chinese cabbage in Qingdao south village wholesale market at Shandong province has high simulation accuracy and prediction accuracy.

At present, the experiment only focus on Chinese cabbage's short-term prediction research. In future, the experiment will extend to other produce for their long-term application research.

Acknowledgments Project supported by Natural Science Foundation of Shandong Province, China (ZR2011FL016).

References

1. Lian GY, Huang KL, Chen JH et al (2010) Training algorithm for radial basis function basis function neural network based on quantum-behaved particle swarm optimization. *Int J Comput Math* 87(3):629–641
2. Ratnaweer A, Halgamuge SK (2004) Self organizing—hierarchical particle swarm optimizer with time varying acceleration coefficients. *IEEE Trans Evol Comput* 8(3):240–255
3. Hu D, Sarosh A, Dong Y-F (2011) An improved particle swarm optimizer for parametric optimization of flexible satellite controller. *Appl Math Comput* 217(21):8512–8521
4. Han JW, Kamber M, Pei J (2012) *Data mining concepts and techniques*, 3rd edn. China machine press, Beijing, pp 398–408
5. Rafiq MY, Bugmann G, Easterbrook DJ (2001) Neural network design for engineering applications. *Comput Struct* 79(17):1541–1552
6. Wang DS, Li SH, Zhou XP (2011) Assessment method of raw water quality based on PSO-RBF neural network model and its application. *J SE Univ (Nat Sci Ed)* 41(5):1019–1023 (in Chinese)
7. Peng T, Liang X, Yang A et al (2005) Short-term prediction of soft ground settlement based on RBF neural network. *Geol Sci Technol Inf* 24(4):99–102 (in Chinese)
8. Xu C, Sun S (2002) *Introduction to computational method*, 2nd edn. Higher education press, Beijing, pp 49–54. (in Chinese)

Chapter 28

A Belief-Rule-Based Inference Method for Carrier Battle Group Recognition

Lianmeng Jiao, Quan Pan, Xiaoxue Feng and Feng Yang

Abstract This paper proposes a method for carrier battle group recognition with over-the-horizon radar outputs. A newly developed belief-rule-based inference method is employed to deal with uncertainties in both radar outputs and domain knowledge. The recognition belief-rule base is constructed considering the constraints among sub-targets in the carrier battle group and subsequently the inference according to such hierarchical belief-rule base is implemented. Moreover, the parameters training method is designed to update the belief-rule base through accumulated historical data. The simulation results show that the belief-rule-based inference method is effective to address the uncertainties in carrier battle group recognition, and the method performs much better after parameters training.

Keywords Belief-rule base · Carrier battle group · Over-the-horizon radar · Target recognition

28.1 Introduction

The carrier battle group (CVBG) consists of an aircraft carrier and its escorts (carrier-borne aircrafts and other warships), together comprising the combat formation [1]. The CVBG includes capabilities sufficient to accomplish a variety of combat tasks in war, and so the detection and recognition of CVBG become quite urgent for early warning. Over-the-horizon radar (OTHR), as important equipment in early-warning system, can detect beyond-the-horizon targets at ranges of thousands of kilometers [2]. Generally, the outputs of OTHR are target tracks and very limited attribute information can be obtained. However, it's believed that the

L. Jiao (✉) · Q. Pan · X. Feng · F. Yang
School of Automation, Northwestern Polytechnical University, No 127 Youyi Road,
Xi'an 710072, China
e-mail: jiaolianmeng@mail.nwpu.edu.cn

sub-targets in CVBG usually satisfy some kinds of spacial and subordinate relationship and it's possible to recognize CVGB as a whole with higher reliability by mining the internal constraints among the sub-targets.

The CVGB recognition problem based on the outputs of OTHR faces many challenges as follows. Firstly, because of the vast sight scope, the clutters may be mistakenly detected as target and thus it makes the target tracks information with great probability uncertainty. Secondly, limited by radar's detecting accuracy, the target tracks information has great fuzzy uncertainty. Lastly, sometimes the experts' subjective information will be utilized when the target tracks information provided by radar is inadequate. As a result, an inference method that can address the information with both probability uncertainty and fuzzy uncertainty, as well as subjective information, is needed. Recently, a generic rule-based inference methodology using the evidential reasoning approach (RIMER) has been proposed [3], which provides a flexible and effective framework to represent not only precise data but also vagueness and ignorance in knowledge, as well as a rigorous inference procedure to deal with such hybrid uncertain information. It has been used for clinical guideline [4], nuclear safeguards evaluation [5], and new product development [6].

Motivated by above consideration, to support modelling and reasoning with radar outputs information and domain knowledge under uncertainties, we propose to employ RIMER for developing the CVGB recognition method. The belief-rule base (BRB) for CVGB recognition is constructed considering the constraints among sub-targets in CVGB and subsequently the inference based on such hierarchical BRB is implemented. Furthermore, the parameters training method is designed to update the BRB through accumulated historical cases in order to obtain higher recognition rate.

28.2 Outline of RIMER

In RIMER, BRB is used to model domain specific knowledge under uncertainty, and the evidential reasoning (ER) approach is employed for inference with BRB. In this section, we provide a brief introduction to BRB first, and then we outline the process of inference with BRB using the ER approach.

28.2.1 *Modelling Domain Knowledge Using BRB*

In order to model the uncertainty in domain knowledge, the belief rule extended from the traditional 'IF-THEN' rule with a belief structure can be described as

$$R_k : \text{ If } x_1 \text{ is } A_1^k \wedge x_2 \text{ is } A_2^k \wedge \cdots \wedge x_M \text{ is } A_M^k \\ \text{ then } \{(D_1, \beta_{1,k}), (D_2, \beta_{2,k}), \cdots, (D_N, \beta_{N,k})\} \quad (28.1)$$

with a rule weight θ_k and attribute weight $\bar{\delta}_1, \bar{\delta}_2, \cdots, \bar{\delta}_M$,

where $\beta_{j,k}$ ($j = 1, 2, \cdots, N$, $k = 1, 2, \cdots, L$) is the belief degree to which D_j is believed to be the consequent if, in the k th rule, the input $x = [x_1, x_2, \cdots, x_M]$ satisfies the antecedent referential value vector $A_k = [A_1^k, A_2^k, \cdots, A_M^k]$. θ_k is the relative weight of the k th rule and $\bar{\delta}_1, \bar{\delta}_2, \cdots, \bar{\delta}_M$ are the relative weights of the M antecedent attributes that are used in the k th rule.

BRB is a collection of belief rules as described by Eq. (28.1) [3]. Inference with BRB is implemented using the ER approach, and knowledge representation parameters including rule weights θ_k , antecedent attribute weights $\bar{\delta}_m$ and consequent belief degrees $\beta_{j,k}$ are usually given by domain experts.

28.2.2 Inference with BRB Using the ER Approach

The analytical format of the ER approach [7] used for inference with the BRB and the input data under uncertainties can be described as follows.

$$\beta_j = \frac{\mu \times \left[\prod_{k=1}^L \left(\omega_k \beta_{j,k} + 1 - \omega_k \sum_{j=1}^N \beta_{j,k} \right) - \prod_{k=1}^L \left(1 - \omega_k \sum_{j=1}^N \beta_{j,k} \right) \right]}{1 - \mu \times \left[\prod_{k=1}^L (1 - \omega_k) \right]}, \quad j = 1, \cdots, N \quad (28.2)$$

with

$$\mu = \left[\sum_{j=1}^N \prod_{k=1}^L \left(\omega_k \beta_{j,k} + 1 - \omega_k \sum_{j=1}^N \beta_{j,k} \right) - (N-1) \times \prod_{k=1}^L \left(1 - \omega_k \sum_{j=1}^N \beta_{j,k} \right) \right]^{-1} \quad (28.3)$$

where, β_j ($j = 1, \cdots, N$) is the final belief degree attached to the j th consequent D_j after combining all activated rules in BRB; $\beta_{j,k}$ ($j = 1, 2, \cdots, N$, $k = 1, 2, \cdots, L$) is the original belief degree assigned to D_j in the k th belief rule, and ω_k is the k th rule's activation weight which can be calculated by

$$\omega_k = \theta_k \prod_{m=1}^M (\alpha_m^k)^{\bar{\delta}_m} / \left[\sum_{l=1}^L \theta_l \prod_{m=1}^M (\alpha_m^l)^{\bar{\delta}_m} \right] \quad (28.4)$$

where, α_m^k ($m = 1, 2, \dots, M$) is the individual matching degree to which the input x_m belongs to A_m^k that is the referential value of the m th antecedent attribute used in the k th rule.

The final combined result generated by ER approach is represented by $\{(D_1, \beta_1), (D_2, \beta_2), \dots, (D_j, \beta_j), \dots, (D_N, \beta_N)\}$, where β_j ($j = 1, 2, \dots, N$) is the final belief degree attached to the j th consequent D_j after combining all activated rules in the BRB.

28.3 CVBG Recognition Based on RIMER

28.3.1 Overview

The outputs of OTHR are series of target tracks within the surveillance area, which are used as the inputs of the inference system for CVBG recognition. It's believed that the most significant indication of CVBG is that the carrier-borne aircrafts and warship formation usually operate together. So, if the OTHR can detect both the carrier-borne aircrafts and warship formation in the same area, it can make the judgement of CVBG with high confidence. Further, the warship formation can be distinguished from other targets according to its velocity and parallel tracks. On the other hand, the carrier-borne aircraft can be distinguished from other targets according to its velocity and track that initiates and terminates at sea. As a result, the inference logics can be formulated based on the above constraints using the outputs of OTHR.

Besides, some external information, for example, the prior-known operation regulations, can be used as another source of evidence for CVBG recognition independent with the outputs of OTHR.

Remark 1 This paper emphasize on the construction of BRB for CVBG recognition and the inference implementation based on BRB, and the track processing procedures (such as the judgment of parallel tracks) are not discussed in detail here.

28.3.2 Construction of BRB for CVBG Recognition

According to the above analysis of the constraints among sub-targets in CVBG, the structure of BRB for CVBG recognition can be constructed as Fig. 28.1, which is composed of four sub-BRBs. This BRB system uses five input variables (X_3, X_6, X_7, X_8, X_9) and three intermediate variables (X_2, X_4, X_5) to predict X_1 . For illustration purposes, each of these input variables and the output variable are

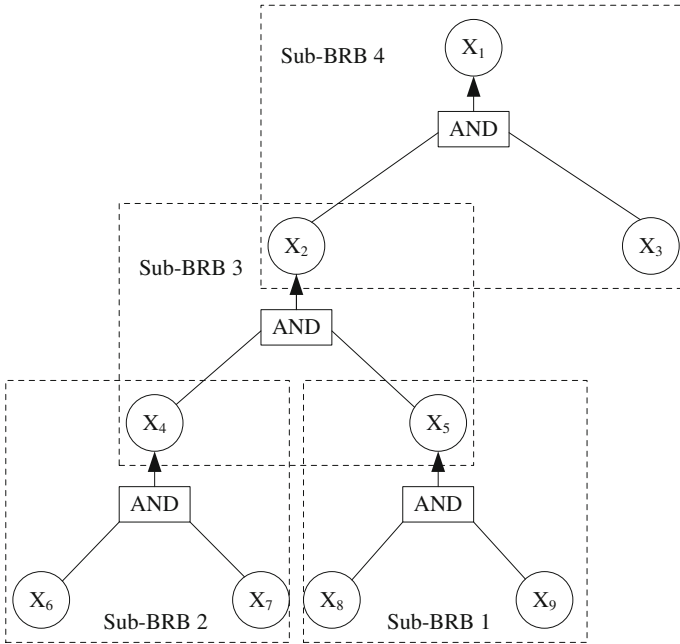


Fig. 28.1 The hierarchical BRB structure for CVBG recognition

defined in terms of qualitative linguistic values (high (H), medium (M), or low (L)).

In Fig. 28.1, the parameters are defined as follows.

- X_1 —CVBG recognition confidence.
- X_2 —CVBG recognition confidence based on OTHR outputs.
- X_3 —CVBG recognition confidence based on operation regulations.
- X_4 —Warship formation recognition confidence.
- X_5 —Carrier-borne aircraft recognition confidence.
- X_6 —Warship formation recognition confidence based on velocity.
- X_7 —Warship formation recognition confidence based on parallel tracks.
- X_8 —Carrier-borne aircraft recognition confidence based on velocity.
- X_9 —Carrier-borne aircraft recognition confidence based on track that initiates and terminates at sea.

Based on the above hierarchical BRB structure, the CVBG recognition BRB, composed of 36 belief rules, can be constructed as Table 28.1, in which, the initial BRB parameters including rule weights, attribute weights and consequent belief degrees are usually given by domain experts.

Table 28.1 BRB for CVBG recognition

Rule No.	Antecedent		Initial BRB		Trained BRB	
			W	Consequent	W	Consequent
1	X_8 is $H \wedge X_9$ is H		1	X_5 is $\{(H, 1)\}$	1	X_5 is $\{(H, 1)\}$
2	X_8 is $H \wedge X_9$ is M		1	X_5 is $\{(H, 0.5), (M, 0.5)\}$	1	X_5 is $\{(H, 0.2), (M, 0.8)\}$
3	X_8 is $H \wedge X_9$ is L		1	X_5 is $\{(M, 1)\}$	0.5	X_5 is $\{(M, 0.3), (L, 0.7)\}$
4	X_8 is $M \wedge X_9$ is H		1	X_5 is $\{(H, 0.5), (M, 0.5)\}$	0.8	X_5 is $\{(H, 0.5), (M, 0.5)\}$
5	X_8 is $M \wedge X_9$ is M		1	X_5 is $\{(M, 1)\}$	1	X_5 is $\{(M, 1)\}$
6	X_8 is $M \wedge X_9$ is L		1	X_5 is $\{(M, 0.5), (L, 0.5)\}$	0.8	X_5 is $\{(M, 0.1), (L, 0.9)\}$
7	X_8 is $L \wedge X_9$ is H		1	X_5 is $\{(M, 1)\}$	0.5	X_5 is $\{(H, 0.2), (M, 0.2), (L, 0.6)\}$
8	X_8 is $L \wedge X_9$ is M		1	X_5 is $\{(M, 0.5), (L, 0.5)\}$	0.8	X_5 is $\{(M, 0.4), (L, 0.6)\}$
9	X_8 is $L \wedge X_9$ is L		1	X_5 is $\{(L, 1)\}$	1	X_5 is $\{(L, 1)\}$
10	X_6 is $H \wedge X_7$ is H		1	X_4 is $\{(H, 1)\}$	1	X_4 is $\{(H, 1)\}$
11	X_6 is $H \wedge X_7$ is M		1	X_4 is $\{(H, 0.5), (M, 0.5)\}$	1	X_4 is $\{(H, 0.3), (M, 0.7)\}$
12	X_6 is $H \wedge X_7$ is L		1	X_4 is $\{(M, 1)\}$	1	X_4 is $\{(H, 0.3), (M, 0.7)\}$
13	X_6 is $M \wedge X_7$ is H		1	X_4 is $\{(H, 0.5), (M, 0.5)\}$	1	X_4 is $\{(H, 0.4), (M, 0.6)\}$
14	X_6 is $M \wedge X_7$ is M		1	X_4 is $\{(M, 1)\}$	0.4	X_4 is $\{(M, 1)\}$
15	X_6 is $M \wedge X_7$ is L		1	X_4 is $\{(M, 0.5), (L, 0.5)\}$	1	X_4 is $\{(M, 0.1), (L, 0.9)\}$
16	X_6 is $L \wedge X_7$ is H		1	X_4 is $\{(M, 1)\}$	0.2	X_4 is $\{(H, 0.1), (M, 0.3), (L, 0.6)\}$
17	X_6 is $L \wedge X_7$ is M		1	X_4 is $\{(M, 0.5), (L, 0.5)\}$	1	X_4 is $\{(M, 0.3), (L, 0.7)\}$
18	X_6 is $L \wedge X_7$ is L		1	X_4 is $\{(L, 1)\}$	1	X_4 is $\{(L, 1)\}$
19	X_4 is $H \wedge X_5$ is H		1	X_2 is $\{(H, 1)\}$	1	X_2 is $\{(H, 1)\}$
20	X_4 is $H \wedge X_5$ is M		1	X_2 is $\{(H, 0.5), (M, 0.5)\}$	0.6	X_2 is $\{(H, 0.4), (M, 0.6)\}$
21	X_4 is $H \wedge X_5$ is L		1	X_2 is $\{(M, 1)\}$	1	X_2 is $\{(H, 0.2), (M, 0.3), (L, 0.5)\}$
22	X_4 is $M \wedge X_5$ is H		1	X_2 is $\{(H, 0.5), (M, 0.5)\}$	0.6	X_2 is $\{(H, 0.2), (M, 0.8)\}$
23	X_4 is $M \wedge X_5$ is M		1	X_2 is $\{(M, 1)\}$	0.6	X_2 is $\{(M, 1)\}$
24	X_4 is $M \wedge X_5$ is L		1	X_2 is $\{(M, 0.5), (L, 0.5)\}$	1	X_2 is $\{(M, 0.2), (L, 0.8)\}$
25	X_4 is $L \wedge X_5$ is H		1	X_2 is $\{(M, 1)\}$	1	X_2 is $\{(H, 0.1), (M, 0.2), (L, 0.7)\}$

(continued)

Table 28.1 (continued)

Rule No.	Antecedent	Initial BRB		Trained BRB	
		W	Consequent	W	Consequent
26	$X_4 \text{ is } L \wedge X_5 \text{ is } M$	1	$X_2 \text{ is } \{(M, 0.5), (L, 0.5)\}$	1	$X_2 \text{ is } \{(M, 0.2), (L, 0.8)\}$
27	$X_4 \text{ is } L \wedge X_5 \text{ is } L$	1	$X_2 \text{ is } \{(L, 1)\}$	1	$X_2 \text{ is } \{(L, 1)\}$
28	$X_2 \text{ is } H \wedge X_3 \text{ is } H$	1	$X_1 \text{ is } \{(H, 1)\}$	1	$X_1 \text{ is } \{(H, 1)\}$
29	$X_2 \text{ is } H \wedge X_3 \text{ is } M$	1	$X_1 \text{ is } \{(H, 0.5), (M, 0.5)\}$	0.2	$X_1 \text{ is } \{(H, 0.3), (M, 0.7)\}$
30	$X_2 \text{ is } H \wedge X_3 \text{ is } L$	1	$X_1 \text{ is } \{(M, 1)\}$	0.8	$X_1 \text{ is } \{(H, 0.1), (M, 0.3), (L, 0.6)\}$
31	$X_2 \text{ is } M \wedge X_3 \text{ is } H$	1	$X_1 \text{ is } \{(H, 0.5), (M, 0.5)\}$	1	$X_1 \text{ is } \{(H, 0.2), (M, 0.8)\}$
32	$X_2 \text{ is } M \wedge X_3 \text{ is } M$	1	$X_1 \text{ is } \{(M, 1)\}$	0.4	$X_1 \text{ is } \{(M, 1)\}$
33	$X_2 \text{ is } M \wedge X_3 \text{ is } L$	1	$X_1 \text{ is } \{(M, 0.5), (L, 0.5)\}$	1	$X_1 \text{ is } \{(M, 0.3), (L, 0.7)\}$
34	$X_2 \text{ is } L \wedge X_3 \text{ is } H$	1	$X_1 \text{ is } \{(M, 1)\}$	1	$X_1 \text{ is } \{(H, 0.1), (M, 0.2), (L, 0.7)\}$
35	$X_2 \text{ is } L \wedge X_3 \text{ is } M$	1	$X_1 \text{ is } \{(M, 0.5), (L, 0.5)\}$	1	$X_1 \text{ is } \{(M, 0.2), (L, 0.8)\}$
36	$X_2 \text{ is } L \wedge X_3 \text{ is } L$	1	$X_1 \text{ is } \{(L, 1)\}$	1	$X_1 \text{ is } \{(L, 1)\}$

28.3.3 Inference with Hierarchical BRB

From previous subsection, it can be seen that the CVBG recognition BRB has hierarchical structure. The inference based on this hierarchical BRB can be implemented from bottom to up using the single-level inference method revisited in Sect. 28.2.2. Specifically, the output of sub-BRB 1 (X_5) and the output of sub-BRB 2 (X_4) are taken as the input states to sub-BRB 3; the output of sub-BRB 3 (X_2) together with the independent input state X_3 are taken as the input states to get the final result X_1 .

Noting that the input value are usually depicted as a single probability, before the inference can be started, input values need to be transformed and represented in terms of the referential values (low, medium, and high) with belief degrees. The rule-based transformation technique [8] is used for the quantitative data transformation. The equivalence rules are given as

1 is equivalently transformed to $\{(H, 1)\}$;
 0.5 is equivalently transformed to $\{(M, 1)\}$;
 0 is equivalently transformed to $\{(L, 1)\}$.

Hence,

0.95 is equivalently transformed to $\{(H, 0.9), (M, 0.1)\}$;
 0.6 is equivalently transformed to $\{(H, 0.2), (M, 0.8)\}$;
 0.4 is equivalently transformed to $\{(M, 0.8), (L, 0.2)\}$;
 0.1 is equivalently transformed to $\{(M, 0.2), (L, 0.8)\}$.

28.3.4 BRB Training

Practically, it is difficult to accurately determine the parameters of a BRB entirely subjectively, particularly, for a large-scale BRB with tens or even hundreds of rules. An initial BRB can be trained using historical data to improve its ability for representing domain knowledge.

The training process is implemented through minimizing the discrepancy between BRB results and sampled data. Assuming there are T cases in a training sample, and the input–output pairs of the T cases are (\hat{x}_t, \hat{y}_t) ($t = 1, \dots, T$), the process of learning from these T datasets can be depicted as in Fig. 28.2, where y_t is produced by the BRB system, the real output \hat{y}_t is observed by experts or acquired by instruments, and $\zeta(V)$ represents the difference between the real output and the system output with $V = [\theta_k^z, \bar{\delta}_i^z, \beta_{j,k}^z]^T$. In the BRB optimization model, the objective function is to minimize $\zeta(V)$, and the constraints define what the knowledge representation parameters of a BRB system should follow.

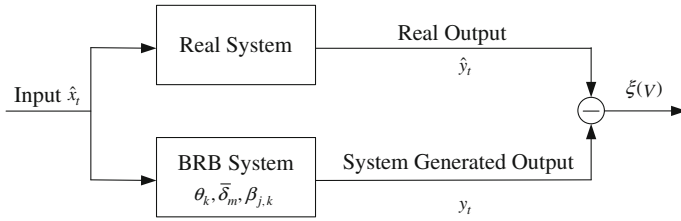


Fig. 28.2 The flow chart for BRB system parameters training

Table 28.2 Recognition results (X_{II}—Initial BRB based, X_{IT}—Trained BRB based, X_{IR}—Real)

Dataset	X ₃	X ₆	X ₇	X ₈	X ₉	X _{II}	X _{IT}	X _{IR}
1	0.6	0.9	0.8	0.9	0.8	0.9022/1	0.8098/1	1
2	0.8	0.3	0.2	0.3	0.2	0.5061/1	0.1501/0	0
3	0.3	0.5	0.3	0.5	0.2	0.0638/0	0.2852/0	0
4	0.5	0.8	0.8	0.2	0.2	0.4867/0	0.1438/0	0
5	0.5	0.9	0.3	0.9	0.3	0.5015/1	0.2767/0	0

Considering the initial BRB for CVBG recognition displayed as Table 28.1 (columns 1–4), the input $\hat{x}_t = [X_3^t, X_6^t, X_7^t, X_8^t, X_9^t]^T$, the output $\hat{y}_t = [X_1^t]$ and \hat{y}_t is a numerical value representing the target is CVBG ($y_t = 1$) or not ($y_t = 0$).

For certain input \hat{x}_t , the CVBG recognition BRB system can get the following output after inference

$$y_t = \{(D_j, \beta_j(t)), j = 1, 2, \dots, N\}. \tag{28.5}$$

For comparison, it’s necessary to transform the above belief-degree structure into average utility as follows.

$$y_t = \sum_{j=1}^N \mu(D_j) \beta_j(t) \tag{28.6}$$

where, $\mu(D_j)$ the utility (or score) of an individual consequent D_j and for this problem, the values of $\mu(D_j)$ can be set as

$$\mu(D_j) = \begin{cases} 1, & \text{if } D_j = H \\ 0.5, & \text{if } D_j = M \\ 0, & \text{if } D_j = L \end{cases} \tag{28.7}$$

So, the objective function in Fig. 28.2 can be developed as

$$\xi(V) = \frac{1}{T} \sum_{t=1}^T (y_t - \hat{y}_t)^2 \tag{28.8}$$

The constraints are constructed according to the requirements of the application and if there is no additional requirement, the basic constraints can be given as follows.

$$\begin{cases} 0 \leq \theta_k^z \leq 1, & k = 1, 2, \dots, L_z, z = 1, 2, \dots, Z \\ 0 \leq \bar{\delta}_i^z \leq 1, & i = 1, 2, \dots, M_z, z = 1, 2, \dots, Z \\ 0 \leq \beta_{j,k}^z \leq 1, & j = 1, 2, \dots, N_z, k = 1, 2, \dots, L_z, z = 1, 2, \dots, Z \\ \sum_{j=1}^{N_z} \beta_{j,k}^z = 1, & k = 1, 2, \dots, L_z, z = 1, 2, \dots, Z \end{cases} \quad (28.9)$$

where, Z is the number of sub-BRBs; L_z is the number of belief rules in z th sub-BRB; M_z is the number of antecedent attributes in z th sub-BRB; N_z is the number of possible consequents in z th sub-BRB. The BRB training is therefore a nonlinear optimization problem with $S_1 = \sum_{z=1}^Z (L_z + M_z + N_z \times L_z)$ variables and $S_2 = \sum_{z=1}^Z (2L_z + M_z + N_z \times L_z)$ constraints, and can be solved using existing optimization software packages.

28.4 Numerical Simulations

In this section, we would like to evaluate the proposed CVBG recognition method through some numerical simulations. To support BRB training and algorithm evaluation, a set of 50 scenarios of the over-the-horizon radar outputs is simulated with some scenarios having CVBG and other scenarios only containing false targets (airliners or freighters). The simulated dataset is randomly divided into two groups (45 scenarios and 5 scenarios) as the training dataset and test dataset, respectively.

First, the first group dataset is taken to train the BRB. Usually, the difference among weights of antecedent attributes is little, so for simplicity, it's assumed that $\bar{\delta}_i^z = 1$ ($i = 1, 2, \dots, M_z, z = 1, 2, \dots, Z$). After parameter training using Eqs. (28.8) and (28.9), we can get the trained CVBG recognition BRB as shown in Table 28.1 (columns 5–6).

Second, for comparison, the test dataset is used to conduct the inference based on the initial BRB and trained BRB respectively, and the results are shown in Table 28.2, in which, columns 2–6 are the inputs of BRB, columns 7–8 are the inference results (conference/decision result) based on the initial BRB and trained BRB respectively, and column 9 gives the real result.

From the simulation results in Table 28.2, it can be seen that

- Overall, the recognition rate can improve efficiently (from 60 to 100 %) through BRB training.
- As for the second dataset, actually the antecedent attribute X_3 is not reliable, but in the initial BRB, X_3 and X_2 are treated with same importance, while in the trained BRB, X_2 is more importance than X_3 . So, when the confidence input for

X_3 is high and the confidence input for X_2 is low, the wrong inference result will be obtained based on the initial BRB.

- As for the fifth dataset, the input confidence is high for X_6 and X_8 , and low for X_7 and X_9 , in which case, the targets are single airliner and single freighter for the real scenario. Noting that, after BRB training, the antecedent attributes X_7 and X_9 that reflect the track parallelity, initiation and termination constraints information, are much more important than X_6 and X_8 , inference based on trained BRB will not make mistake.

28.5 Conclusion

The recognition of CVBG is critical for early warning. This paper proposes a belief-rule-based inference method for CVBG recognition with over-the-horizon radar outputs under uncertainty. The BRB for CVBG recognition is constructed considering the constraints among sub-targets in CVBG and subsequently the inference according to such hierarchical BRB is implemented. Moreover, the parameters training method is designed to update the BRB through accumulated historical cases. The simulation results show efficiency of the proposed method to address the uncertainties in both radar outputs and domain knowledge, and the method performs much better after BRB training.

Acknowledgments This work was partially supported by the China National Science Foundation (No.61135001 and No.61075029) and the Doctorate Foundation of Northwestern Polytechnical University (No.CX201319).

References

1. Oxendine E, Nissen EM (2001) Knowledge process and system design for the carrier battle group. *Knowl Innov* 1(3):89–109
2. Krolik JL, Anderson RH (1997) Maximum likelihood coordinate registration for over-the-horizon radar. *IEEE Trans Signal Process* 45(4):945–959
3. Yang JB, Liu J, Wang J (2006) A belief rule base inference methodology using the evidential reasoning approach-RIMER. *IEEE Trans Syst Man Cybern Part A Syst Hum* 36(2):266–285
4. Kong GL, Xu DL, Richard B (2012) A belief rule-based decision support system for clinical risk assessment of cardiac chest pain. *Eur J Oper Res* 219(2):564–573
5. Liu J, Yang JB, Wang J (2005) Engineering system safety analysis and synthesis using the fuzzy rule-based evidential reasoning approach. *Qual Reliab Eng Int* 21(2):387–411
6. Tang D-W, Yang JB, Chin K-S (2011) A methodology to generate a belief rule base for customer perception risk analysis in new product development. *Expert Syst Appl* 38(12):5373–5383
7. Wang YM, Yang JB, Xu DL (2006) Environmental impact assessment using the evidential reasoning approach. *Eur J Oper Res* 174(3):1885–1913
8. Yang JB (2001) Rule and utility based evidential reasoning approach for multi-attribute decision analysis under uncertainties. *Eur J Oper Res* 131(1):31–61

Chapter 29

Multi-Robot Cooperation Handling Based on Immune Algorithm in the Known Environment

Mingxin Yuan, Zhaoli Ye, Shuai Cheng and Yafeng Jiang

Abstract In order to solve the multi-robot cooperation handling in the known environment, the affinity between any two antibodies as well as affinity between antibody and antigen are both defined firstly, and then a new immune network allocation algorithm with the feedback mechanism (IFAA) is proposed by adding the capability loss factor into the immune network. The simulation results show that, the proposed algorithm can not only reduce the robot's capacity loss and shorten the entire planning path, but also decrease the number of robots participating cooperation handling. Compared with other immune allocation algorithms, the proposed algorithm is characterized by higher efficiency.

Keywords Multi-robot cooperation · Idiotypic immune network · Capability loss · Task allocation

29.1 Introduction

Compared with single robot system, multi-robot system has higher performance and efficiency to fulfill the given task. As one of the key technology in robot cooperation handling, at present the allocation methods are mainly studied based on behaviour [1], market mechanism [2] and linear programming [3]. The stimulation results show that it is difficult for conventional methods to get optimal allocation results, and their robustness and flexibility are not good enough. In recent years, with the development of artificial intelligence, swarm intelligence allocation algorithms have caused extensive concern. An allocation algorithm based on ant colony algorithm is presented by Liu [4]. A kind of immune task

M. Yuan (✉) · Z. Ye · S. Cheng · Y. Jiang
School of Mechanical-Electronic and Automotive Engineering, Jiangsu University
of Science and Technology, Zhangjiagang, China
e-mail: mxyuan78@163.com

allocation algorithm is raised by Gao and Wu [5, 6]. The simulation results show that the intelligence allocation algorithms have higher efficiency and better robustness. To solve the multi-robot task allocation in the known environment, such as the handling of quay container, a new immune allocation algorithm based on known task weight is put forward, and it improves the allocation efficiency.

29.2 Multi-Robot Task Allocation on Immune Network Model

29.2.1 Immune Network Model

Biological immune system is a highly evolved, complicated adaptability system. Idiotypic network hypothesis proposed by Jerne is one of the important immune theories. The basic idea of this hypothesis is that: The invading antigen will break the balance of immune system. The stimulation and suppression among different antibodies will be carried out through the communication, and the antigen will be overcome again to maintain the stability of immune system [7]. On the basis of immune network theory, the dynamic equation for calculating stimulus level and concentration is put forward by Farmer [8], and it can be described as follows:

$$A_i(t) = A_i(t-1) + \left(\frac{\alpha}{n} \sum_{j=1}^n m_{ji} a_j(t-1) - \frac{\alpha}{n} \sum_{j=1}^n m_{ki} a_j(t-1) + \beta g_i - k_i \right) a_i(t-1) \quad (29.1)$$

where,

$$a_i(t) = \frac{1}{1 + \exp(0.5 - A_i(t))} \quad (29.2)$$

In Eq. (29.1), the first term and second term in the bracket represent the stimulation and suppression among antibodies respectively; the third item represents the antigen stimulation; the fourth term is the natural death of antibody. m_{ji} , m_{ki} and β are coefficients. Equation (29.2) is the normalization equation.

29.2.2 Basic Definitions

29.2.2.1 Affinity Between Antibody and Antigen

Let the affinity between the i th robot (R_i) and the k th box (T_k) be O_i ($i = 1, \dots, m$, $k = 1, \dots, n$. m and n are the number of robots and boxes respectively). Before the robots are allocated, the O_i is defined as follows:

$$O_i = \frac{f_i \cdot u}{(\lambda_1 d_{ik} + \lambda_2 d_{ko})} \quad (29.3)$$

where,

$$u = \begin{cases} 1 + r & (x_r - x_b)(x_b - x_o) \geq 0 \\ 1 - r & (x_r - x_b)(x_b - x_o) < 0 \end{cases} \quad (29.4)$$

In Eq. (29.3), f_i is the push force of robot R_i . d_{ik} is the distance of robot R_i and box T_k . d_{ko} is the distance between the box T_k and goal. λ_1 and λ_2 are adjustment coefficients, and $\lambda_1 + \lambda_2 = 1$.

In Eq. (29.4), u is the stimulating or suppression factor. x_r , x_b , and x_o represent the value of x axis coordinates of robot, box and goal respectively.

After the original allocation based on Eq. (29.4), some robots are allocated to the boxes. Judge whether they can carry the box to goal. If not, recount stimulus between the robot R_i and box T_k to find other free robots to help accomplish the handling. Let the stimulus be g_i , and it is defined as follows:

$$g_i = \frac{n \cdot f \cdot f_i \cdot u}{(\lambda_1 d_{ik} + \lambda_2 d_{ko})} \quad (29.5)$$

In Eq. (29.5), n is the number of robots which are waiting for free cooperative robots around the box, and f is the total push force of robots.

29.2.2.2 Affinity Between Antibodies

The affinity coefficient between any two antibodies is defined as follows:

$$m = \frac{f_i \cdot f_j \cdot u}{(\lambda_1 d_{ij} + \lambda_2 d_{jg})} \quad (29.6)$$

where, f_i and f_j are the push force of R_i and R_j respectively. The distance between R_i and R_j is d_{ij} . d_{jg} is the distance between R_j and goal.

29.2.2.3 Allocation Model Based on Capability Loss Factor

To play the superiority of Farmer's dynamic model, a new allocated model is defined as follows:

$$A_i(t) = A_i(t-1) + \left(\frac{\alpha}{n} \sum_{j=1}^n m a_j(t-1) + \beta m_i + error - k_i \right) a_i(t-1) \quad (29.7)$$

where,

$$error = \frac{1}{|m_{k-1} + f_j - m_k| + \delta} \quad (29.8)$$

To simulate uniqueness of antibody, a factor “error” is introduced in Eq. (29.7) by taking robots’ capability loss into consideration. $\delta = 0.001$ is an adjustment coefficient. m_{k-1} is the force that has already been applied to the waiting box T_k . m_k is the weight of box T_k . f_j is the force of collaboration robot. The stimulus level and concentration of antibody is regulated according to the value of “error”, and then the appropriate robots are selected to execute the given task.

29.2.3 Task Allocation Flow for Multi-Robot System

- Step 1: Initialize the information of antigen and antibody, and then calculate the affinity between box and robot according to Eq. (29.3) or (29.5).
- Step 2: Select the robots to handling boxes according to the stimulus value, and the selected robots move to corresponding boxes.
- Step 3: Judge whether the selected robots can push the box. If can, the box is pushed towards the goal, and other free robots are prevent from cooperation; Otherwise, the selected robots should wait for help from other free robots according to Eq. (29.6). Judge whether the box has arrived at the goal. If not, go to step 3; otherwise, output the allocation results.
- Step 4: Update information of all robots and boxes, repeat steps 2–4 until all the boxes have been pushed to goal.

29.3 Multi-Robot Cooperation Handling Experiment Based on Immune Network

29.3.1 Description of the Experiment

To verify the effectiveness of proposed algorithm (IFAA), six different environments are set with the number of robots and boxes as 3, 3; 4, 3; 3, 4; 4, 4; 4, 5; 6, 5, and the allocation experiments are carried out with MATLAB7.1 on an Intel Pentium IV 1.2 GHz computer with 1.96 GB RAM. The allocation results are compared with the Immune agent network algorithm (IANA) [5] and Immune network exploration algorithm (INEA) [6]. Partial algorithm parameters of IFAA are as follows: $\alpha = 0.5$; $\beta = 0.1$; $k = 0.002$; $A_i(0) = a_i(0) = 0.5$; $\lambda_1 = 0.8$; $\lambda_2 = 0.2$.

29.3.2 Results and Analysis of the Experiment

Definition The planning matrix X among robots and boxes are defined as follows: x_{ij} ($i = 1, \dots, m; j = 1, \dots, n$) is the element of X . $x_{ij} = 1$ means that robot R_i is selected to push box T_j . If R_i is not selected to push box T_j , $x_{ij} = 0$. X_1, X_2, X_3 are the planning matrices of IANA, INEA and IFAA respectively.

$$E1 \quad X_1 = \begin{pmatrix} 0 & 0 & 0 \\ 0 & 1 & 1 \\ 1 & 1 & 1 \end{pmatrix} X_2 = \begin{pmatrix} 0 & 0 & 0 \\ 0 & 1 & 1 \\ 1 & 1 & 1 \end{pmatrix} X_3 = \begin{pmatrix} 1 & 0 & 0 \\ 0 & 1 & 1 \\ 0 & 1 & 1 \end{pmatrix}$$

$$E2 \quad X_1 = \begin{pmatrix} 0 & 0 & 0 \\ 0 & 1 & 0 \\ 1 & 1 & 1 \\ 0 & 0 & 1 \end{pmatrix} X_2 = \begin{pmatrix} 0 & 0 & 0 \\ 0 & 1 & 0 \\ 1 & 1 & 1 \\ 0 & 0 & 1 \end{pmatrix} X_3 = \begin{pmatrix} 1 & 0 & 0 \\ 0 & 0 & 0 \\ 0 & 0 & 1 \\ 0 & 1 & 1 \end{pmatrix}$$

$$E3 \quad X_1 = \begin{pmatrix} 1 & 0 & 0 & 0 \\ 0 & 0 & 1 & 1 \\ 0 & 1 & 1 & 1 \end{pmatrix} X_2 = \begin{pmatrix} 1 & 0 & 0 & 0 \\ 0 & 0 & 1 & 1 \\ 0 & 1 & 1 & 1 \end{pmatrix} X_3 = \begin{pmatrix} 1 & 0 & 0 & 0 \\ 0 & 0 & 1 & 1 \\ 0 & 1 & 1 & 1 \end{pmatrix}$$

$$E4 \quad X_1 = \begin{pmatrix} 0 & 0 & 0 & 0 \\ 0 & 0 & 0 & 0 \\ 0 & 1 & 0 & 1 \\ 1 & 1 & 1 & 1 \end{pmatrix} X_2 = \begin{pmatrix} 0 & 0 & 0 & 0 \\ 0 & 0 & 0 & 1 \\ 0 & 1 & 0 & 0 \\ 1 & 1 & 1 & 1 \end{pmatrix} X_3 = \begin{pmatrix} 1 & 0 & 0 & 0 \\ 0 & 0 & 0 & 1 \\ 0 & 0 & 1 & 0 \\ 0 & 1 & 1 & 1 \end{pmatrix}$$

$$E5 \quad X_1 = \begin{pmatrix} 0 & 1 & 0 & 0 & 0 \\ 0 & 1 & 0 & 0 & 0 \\ 0 & 0 & 1 & 0 & 1 \\ 1 & 1 & 1 & 1 & 1 \end{pmatrix} X_2 = \begin{pmatrix} 0 & 1 & 0 & 0 & 0 \\ 0 & 1 & 0 & 0 & 0 \\ 0 & 0 & 1 & 0 & 1 \\ 1 & 1 & 1 & 1 & 1 \end{pmatrix} X_3 = \begin{pmatrix} 1 & 0 & 0 & 0 & 0 \\ 0 & 0 & 0 & 1 & 0 \\ 0 & 0 & 1 & 0 & 1 \\ 0 & 1 & 1 & 1 & 1 \end{pmatrix}$$

$$E6 \quad X_1 = \begin{pmatrix} 0 & 0 & 0 & 0 & 0 \\ 0 & 0 & 1 & 0 & 0 \\ 0 & 0 & 0 & 1 & 0 \\ 1 & 0 & 0 & 0 & 0 \\ 0 & 0 & 0 & 1 & 1 \\ 0 & 1 & 1 & 0 & 1 \end{pmatrix} X_2 = \begin{pmatrix} 0 & 0 & 0 & 0 & 0 \\ 0 & 0 & 1 & 0 & 0 \\ 0 & 0 & 0 & 1 & 0 \\ 1 & 0 & 0 & 0 & 0 \\ 0 & 0 & 0 & 1 & 1 \\ 0 & 1 & 1 & 0 & 1 \end{pmatrix} X_3 = \begin{pmatrix} 1 & 0 & 0 & 0 & 0 \\ 0 & 0 & 0 & 0 & 1 \\ 0 & 0 & 0 & 1 & 0 \\ 0 & 1 & 0 & 0 & 0 \\ 0 & 0 & 0 & 0 & 0 \\ 0 & 0 & 1 & 1 & 1 \end{pmatrix}$$

From the planning matrix, the choosing information among robots and boxes of three algorithms in each environment can be seen obviously.

The comparison of task allocation results among three algorithms are shown in Table 29.1. From the table, it can be seen that three allocation performances, namely total steps, capability loss and number of cooperation robots are all different among three algorithms under the same environment. As a whole, in the allocation results of proposed IFFA, the total handling distance of mobile robots is the shortest, the capability loss of robots is the smallest, and the number of collaboration robots is the least, which verifies the superiority of proposed task allocation algorithm.

Table 29.1 Comparison of results among three algorithms in multi-robot cooperation handling

Environments	Total steps of robots			Capability loss of robots (Unit: Kg)			Number of cooperation robots		
	IANA	INEA	IFAA	IANA	INEA	IFAA	IANA	INEA	IFAA
E1	148	141	132	2	2	2	5	5	5
E2	149	137	128	4	4	2	5	5	4
E3	234	222	222	1	1	1	6	6	6
E4	232	208	186	3	2	2	6	6	6
E5	299	285	273	4	4	2	9	9	8
E6	256	218	203	9	9	4	8	8	7

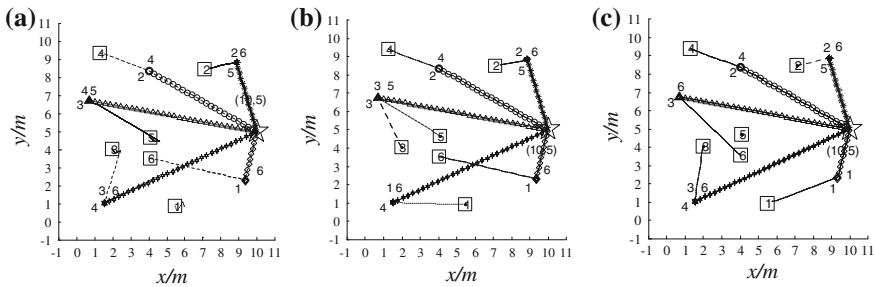


Fig. 29.1 Allocation results of three algorithms in environment 6. **a** IANA. **b** INEA. **c** IFAA

To further clearly see the allocation results of different algorithms, taking environment 6 as an example, the allocation results of each algorithm are shown in Fig. 29.1.

In Fig. 29.1, square is represented for six robots. Similarly, five different boxes are noted with diamond, circle, triangle, hexagon, and asterisk respectively. Pentagram stands for target. From the figures, it can be seen that the redefinition of affinity between two antibodies, affinity between antibody and antigen, as well as the capacity loss factor, makes the handling path more concise, which improves the handling efficiency and reduces the capacity loss.

29.4 Conclusions

Aiming at the multi-robot cooperation handling problems in the known environment, on the basis of Jerne’s idiotypic immune network hypothesis, a new immune allocation algorithm is presented through adding the capacity loss factor, redefining affinity among antibodies and antigen, and so on. The allocation experiments in different environments show that the proposed algorithm can fully present the rationality of task allocation strategy, and significantly reduce the moving steps as well as capacity loss of robots, which verifies the validity of propose allocation algorithms.

Acknowledgments This work was supported in part by the National Nature Science Foundation of China (NSFC) under Grant 61105071, Qing Lan Project of Jiangsu Province, industry-academia cooperation innovation fund projects of jiangsu province under Grant SBY201220397, Scientific Research Starting Foundation for Doctors from Jiangsu University of Science and Technology under Grant 35271004.

References

1. Tang F, Parker LE (2005) Asymtre: automated synthesis of multi-robot task solution through software reconfiguration. In: Proceedings of IEEE international conference on robotics and automation, Barcelona, Spain, pp 1501–1508
2. Li P, Yang YM, Lian JL (2009) Utility function based on task allocation for multi-robot system. *Appl Res Comput* 26(2):537–539
3. Gao PA, Cai ZX (2006) Multi-robot task allocation for exploration. *J Cent South Univ Technol* 13(5):548–551 (in Chinese)
4. Liu SH, Zhang Y, Wu HY (2010) Multi robot task allocation based on swarm intelligence. *J Jilin Univ Eng Technol Ed* 40(1):123–129 (in Chinese)
5. Gao YY, Wei W (2006) Multi-robot autonomous cooperation integrated with immune based dynamic task allocation. In: Proceedings of the 6th international conference on intelligence systems design and applications. Jinan, China, pp 586–591
6. Wu H, Tian GH, Huang B (2008) Research on the collaboration strategy of multi-robot for exploring unknown environment. *J Shandong Univ* 38(4):27–31 (in Chinese)
7. Yuan MX, Wang SA, Wu CY, Li KP (2010) Hybrid ant colony and immune network algorithm based on improved APF for optimal motion planning. *ROBOTICA* 28(6):833–846
8. Ishiguro A, Watanabe Y, Kondo T (1997) A robot with a decentralized consensus-making mechanism based on the immune system. In: Proceedings of the international symposium on autonomous decentralized systems, Nagoya, Japan, pp 231–237

Chapter 30

Global Exponential Synchronization Between Two Different Complex Networks with Time Vary Delays

Guoliang Cai, Yihong Du and Xianbin Wu

Abstract This paper deals with the global exponential synchronization between two different complex networks with time vary delays. Based on the Derivation method and the Halanay inequality technique, the global exponential synchronization of two complex networks is derived between some simple conditions and some delay-independent criteria, respectively. Furthermore, the advantages of both methods were compared, simply. Finally, an illustrative example is presented to verify the effectiveness of the synchronization scheme.

Keywords Complex networks · Global exponential synchronization · Derivation method · Halanay inequality

30.1 Introduction

Complex networks are made up of interconnected nodes and are used to describe various systems of real world. Synchronization of all dynamical nodes is an interesting phenomenon and has been intensively studied in the recent years since Pecora and Carroll [1] introduced a method for synchronization two identical chaotic systems with different initial conditions. Especially in recent decades, As the Internet and the World Wide Web are continuously expanding over our world, all things in our world are connected much more closely than before. As a result, some new types of synchronization have appeared in the literatures, such as

G. Cai (✉) · Y. Du

Nonlinear Scientific Research Center, Jiangsu University, Zhenjiang, Jiangsu 212013, China
e-mail: glcai@ujs.edu.cn

X. Wu

Junior College, Zhejiang Wanli University, Ningbo, Zhejiang 315100, China
e-mail: wxb3210@zwu.edu.cn

complete synchronization [2], projective synchronization [3, 4], impulsive synchronization [5], cluster synchronization [6, 7] and [8], mixed synchronization [9], and so on.

It has been noticed that some papers discussed the global synchronization based on the Lyapunov function approach, but the obtained conditions are either difficult to be verified or reformulated to be in a conservative form such as a linear matrix inequality (LMI) [10]. Furthermore, in general, the structure of a network is partially known or even completely unknown, which cause it is very difficult to achieve the expected network synchronization in terms of the centralized control method. Therefore, in this paper, by applying the Halanay inequality lemma and designing some unknown and decentralized controllers, some simple delay-independent criteria are derived to ensure the global exponential synchronization of different complex networks.

30.2 Networks Model and Preliminaries

Consider the driving networks:

$$\begin{cases} \dot{x}_i(t) = f(x_i(t)) + \sum_{j=1}^r c_{ij}\Gamma x_j(t - \tau), & i = 1, 2, \dots, r \\ \dot{x}_i(t) = k_i(\bar{x}_r(t)) + \sum_{j=r+1}^n d_{ij}x_j(t), & i = r + 1, r + 2, \dots, n \end{cases} \quad (30.1)$$

where $x_i(t) = (x_{i1}(t), x_{i2}(t), \dots, x_{in}(t))^T \in R^n$ denotes the state variables of the i th node, $\bar{x}_r(t) = (x_1(t), x_2(t), \dots, x_r(t))^T$, r is an integer and $1 \leq r \leq n$, $\tau > 0$. $f(\cdot): R \times R^r \rightarrow R^r$ is a smooth nonlinear vector valued function, and $f_i(0) = 0$. $k_i(\cdot) \in C[R^r, R]$ and $k_i(0) = 0$. We further assume that the inner connecting matrix $\Gamma = \text{diag}(\gamma_1, \gamma_2, \dots, \gamma_r)$ and assume $\|\Gamma\| = \gamma > 0$, $C = (c_{ij})_{r \times r} \in R^{r \times r}$ is the coupling configuration matrix. $D = (d_{ij})_{(n-r) \times (n-r)}$ is real matrixes, which denote the strength of inter connections. If there is a connection from node i to node j ($i \neq j$), then the coupling $d_{ij} = 1$ otherwise, $d_{ij} = 0$, and the diagonal elements of matrix D are defined by $d_{ii} = - \sum_{j=1, j \neq i}^r d_{ij}$, $i = 1, 2, \dots, r$, which denote the strength of neuron interconnections. The initial values with (30.1) are: $x_i(t) = \Phi_i(t) \in C([-\tau, 0], R)$, $i = 1, 2, \dots, n$.

The controlled response networks is:

$$\begin{cases} \dot{y}_i(t) = Ay_i(t) + Bg(y_j(t)) + \sum_{j=1}^r c_{ij}\Gamma y_j(t - \tau) + \mu_i(t), & i = 1, 2, \dots, r \\ \dot{y}_i(t) = k_i(\bar{y}_r(t)) + \sum_{j=r+1}^n d_{ij}y_j(t), & i = r + 1, r + 2, \dots, n \end{cases} \quad (30.2)$$

where $y_i(t) = (y_{i1}(t), y_{i2}(t), \dots, y_{in}(t))^T \in R^n$ denotes the state variables of the i th node, $\mu_i(t)$ indicates the external control input that will be appropriately designed for a control objective, and $\bar{y}_r(t) = (y_1(t), y_2(t), \dots, y_r(t))^T$. A and B are system matrices with proper dimensions satisfy $\|A\| \leq \alpha, \|B\| \leq \beta$, $g(\cdot)$ is continuous function. The initial values with (2) are: $y_i(t) = \varphi_i(t) \in C([-\tau, 0], R)$, $i = 1, 2, \dots, n$. And, at least, there exists a constant $i(1 \leq i \leq r)$ such that $\phi_i(t) \neq \varphi_i(t)$, for $t \in [-\tau, 0]$.

Assumption 1 For any different $\forall x, y \in R^r$ there exist nonnegative \tilde{L} such that

$$\|g(x) - g(y)\| \leq \tilde{L}\|x - y\|.$$

The norm $\|\cdot\|$ of a variable is defined as $\|x\| = (x^T x)^{1/2}$.

Definition 1 System (1) and (2) are said to be globally exponentially synchronized if there exist constants $M \geq 1$ and $\lambda > 0$ such that

$$\|x(t) - y(t)\| \leq M \sup_{-\tau \leq s \leq 0} \|\phi(s) - \varphi(s)\| e^{-\lambda t}, \quad t \geq 0,$$

where $\varphi(s) = (\varphi_1(s), \varphi_2(s), \dots, \varphi_n(s))^T$, $\phi(s) = (\phi_1(s), \phi_2(s), \dots, \phi_n(s))^T$.

Moreover, the constant λ is defined as the exponential synchronization rate.

Lemma 1 Cheng et al. [11]. For a $r \times r$ real symmetric matrix Ω , Ω is positive definite if and only if all its eigenvalues are positive. Moreover, the inequality holds:

$$\lambda_{\min}(\Omega)\|x\|^2 \leq x^T \Omega x \leq \lambda_{\max}(\Omega)\|x\|^2. \quad \forall x \in R^r$$

Lemma 2 Halanay inequality Lemma [12]. Let $\tau \geq 0$ be a constant, $V(t)$ be a non-negative continuous function defined for $[-\tau, \infty)$ which satisfies: $\dot{V}(t) \leq -pV(t) + q(\sup_{t-\tau \leq s \leq t} V(s))(t > 0)$, where p and q are constants. If $p > q > 0$, then

$$V(t) \leq (\sup_{-\tau \leq s \leq 0} V(s))e^{-\delta t}, \quad t > 0,$$

where δ is a unique positive root of the equation $\delta = p - q \exp(\delta\tau)$.

Lemma 3 Xiong et al. [12]. If system (1) is globally exponentially stable about its partial variables $\tilde{e}_r(t)$ with system (2), where $\tilde{e}_r(t) = (e_1(t), e_2(t), \dots, e_r(t))^T$, the constant matrix D is Hurwitz, and

$$\|K(\tilde{e}_r(t))\| \leq \zeta \|\tilde{e}_r(t)\|^\beta,$$

for some constants $\zeta > 0$ and $\beta > 0$, then system (1) is also globally exponentially stable about its partial variables $\tilde{e}_{n-r}(t)$ with system (2), where $\tilde{e}_{n-r}(t) = (e_{n+1}(t), e_{n+2}(t), \dots, e_n(t))^T$.

30.3 Global Exponential Synchronization for Two Complex Networks with Time Vary Delays

Let $e_i(t) = x_i(t) - y_i(t)$, considering the following control input vector:

$$\mu_i(t) = f(x_i(t)) - Bg(x_i(t)) - A(x_i(t)) + \xi_i(x_i(t) - y_i(t)), \quad i = 1, 2, \dots, r.$$

The error system of (1) and (2) are defined as:

$$\begin{cases} \dot{e}_i(t) = BG(e_i(t)) + Ae_i(t) + \sum_{j=1}^r c_{ij}\Gamma e_j(t - \tau) - \xi_i e_i(t), & i = 1, 2, \dots, r \\ \dot{e}_i(t) = K_i(\bar{e}_r(t)) + \sum_{j=r+1}^n d_{ij}e_j(t), & i = r + 1, r + 2, \dots, n \end{cases} \tag{30.3}$$

where $G(e_i(t)) = g(x_i(t)) - g(y_i(t))$.

Theorem 1 *Under assumption 1, system (3) is globally exponentially stable if the following conditions are satisfied:*

1. ξ_i of the control input vector $\mu_i(t)$ are constants such that

$$\xi_i - \tilde{L}|B| - |A| - \sum_{j=1}^r |c_{ij}|\Gamma > 0, \quad i = 1, 2 \dots, r \tag{30.4}$$

2. Matrix D is Hurwitz, and

$$\|K(\tilde{e}_r(t))\| \leq \zeta \|\tilde{e}_r(t)\|^\beta,$$

for some constants $\zeta > 0$ and $\beta > 0$.

Proof Choose the following Lyapunov function:

$$V(t) = \sum_{i=1}^r (e^{\mu t} |e_i(t)|) + \sum_{j=1}^r |c_{ij}|\Gamma e^{\mu \tau} \int_{t-\tau}^t e^{\mu s} |e_i(s)| ds \tag{30.5}$$

Obviously, 0 is the zero solution of system (3). With assumption 1, the following inequalities can be obtained from the first equation of system (3)

$$D^+ |e_i(t)| \leq \tilde{L}|B| |e_i(t)| + |A| |e_i(t)| + \sum_{j=1}^r |c_{ij}|\Gamma e_j(t - \tau) - \xi_i e_i(t) \tag{30.6}$$

for $i = 1, 2, \dots, r$. where D^+ denotes the upper right derivative.

It is easy to verify that $V(t)$ is a non-negative function over $[-\tau, \infty)$ and radically unbounded, i.e., $V(t) \rightarrow \infty$ as $|e_i(t)| \rightarrow \infty$ $i = 1, 2, \dots, r$. Calculating the upper right derivative of $V(t)$ along (30.6), we obtain

$$\begin{aligned}
 D^+V(t) &= \sum_{i=1}^r [\mu e^{\mu t} |e_i(t)| + e^{\mu t} D^+ |e_i(t)| + \sum_{j=1}^r |c_{ij}| \Gamma e^{\mu(\tau+t)} |e_i(t)| - \sum_{j=1}^r |c_{ij}| \Gamma e^{\mu t} |e_i(t-\tau)|] \\
 &\leq \sum_{i=1}^r [\mu e^{\mu t} |e_i(t)| + e^{\mu t} (\tilde{L}|B| |e_i(t)| + |A| |e_i(t)| + \sum_{j=1}^r |c_{ij}| \Gamma e_j(t-\tau) - \zeta_i |e_i(t)|)] \\
 &\quad + \sum_{j=1}^r |c_{ij}| \Gamma e^{\mu(\tau+t)} |e_i(t)| - \sum_{j=1}^r |c_{ij}| \Gamma e^{\mu t} |e_i(t-\tau)| \\
 &= \sum_{i=1}^r [\mu e^{\mu t} |e_i(t)| + e^{\mu t} \tilde{L}|B| |e_i(t)| + e^{\mu t} |A| |e_i(t)| + \sum_{j=1}^r |c_{ij}| \Gamma e^{\mu(\tau+t)} |e_i(t)| - \zeta_i e^{\mu t} |e_i(t)|] \\
 &= - \sum_{i=1}^r (\zeta_i - \mu - \tilde{L}|B| - |A| - \sum_{j=1}^r |c_{ij}| \Gamma e^{\mu \tau}) e^{\mu t} |e_i(t)|
 \end{aligned} \tag{30.7}$$

Define continuous functions $\Delta_i(\bar{\mu})$ are as follows

$$\Delta_i(\bar{\mu}) = \zeta_i - \bar{\mu} - \tilde{L}|B| - |A| - \sum_{j=1}^r |c_{ij}| \Gamma e^{\bar{\mu} \tau}, \quad i = 1, 2, \dots, r$$

Note that from condition (30.5)

$$\Delta_i(0) = \zeta_i - \tilde{L}|B| - |A| - \sum_{j=1}^r |c_{ij}| \Gamma > 0, \quad i = 1, 2, \dots, r$$

According to the continuity of $\Delta_i(\cdot)$ on $[0, \infty)$, there exist a constant $\mu > 0$ such that

$$\Delta_i(\mu) = \zeta_i - \mu - \tilde{L}|B| - |A| - \sum_{j=1}^r |c_{ij}| \Gamma e^{\mu \tau} \geq 0, \quad i = 1, 2, \dots, r \tag{30.8}$$

Combining (30.7) and (30.8), we have $D^+V(t) \leq 0, t > 0$ which implies that $V(t) \leq V(0), t > 0$. In terms of Eq. (30.5), we obtain

$$\begin{aligned}
 \sum_{i=1}^r e^{\mu t} |e_i(t)| &\leq \sum_{i=1}^r (|e_i(0)| + \sum_{j=1}^r |c_{ij}| \Gamma e^{\mu \tau} \int_{-\tau}^0 e^{\mu s} |e_i(s)| ds) \\
 &\leq \sum_{i=1}^r (1 + \sum_{j=1}^r |c_{ij}| \Gamma e^{\mu \tau} \cdot \tau) (\sup_{s \in [-\tau, 0]} e^{\mu s} |e_i(s)|), \quad t > 0 \\
 \sum_{i=1}^r |e_i(t)| &\leq e^{-\mu t} \cdot M \cdot \sum_{i=1}^r (\sup_{s \in [-\tau, 0]} |\phi_i(s) - \varphi_i(s)|),
 \end{aligned}$$

where $M = \max_{1 \leq i \leq r} \left\{ \sum_{i=1}^r (1 + \sum_{j=1}^r |c_{ij}| \Gamma e^{\mu \tau} \cdot \tau) \right\} > 0$.

Therefore, system (3) is globally exponentially stable about its partial variables $\tilde{e}_r(t)$. Combining condition 2 and Lemma 3, it is easy to conclude that the zero solution $\tilde{e}_n(t) = 0$ of system (3) is globally and exponentially stable.

Designing another different control input vector, we can establish different synchronous conditions.

Considering the following control input vector:

$$\begin{aligned} \mu_i(t) &= f(x_i(t)) - Bg(x_i(t)) - A(x_i(t)) \\ &\quad + \sum_{j=1}^r \omega_{ij}(x_j(t) - y_j(t)), \quad i = 1, 2, \dots, r, \text{ i.e.,} \\ \tilde{\mu}_r(t) &= f(\bar{x}_r(t)) - Bg(\bar{x}_r(t)) - A(\bar{x}_r(t)) + \sum_{j=1}^r \omega(\bar{x}_r(t) - \bar{y}_r(t)) \end{aligned} \tag{30.9}$$

where $\omega_{ij}(i, j = 1, 2, \dots, r)$ are constants, and $\omega = (\omega_{ij})_{r \times r}$. Then, (30.3) can be rewritten as

$$\begin{cases} \dot{\bar{e}}_r(t) = B\bar{G}(\bar{e}_r(t)) + A\bar{e}_r(t) + C\bar{\Gamma}\bar{e}_r(t - \tau) - \omega\bar{e}_r(t), & i = 1, 2, \dots, r \\ \dot{\bar{e}}_{n-r}(t) = K(\bar{e}_r(t)) + D\bar{e}_{n-r}(t), & i = r + 1, r + 2, \dots, n \end{cases} \tag{30.10}$$

Theorem 2 *Under assumption 1, system (10) is globally exponentially stable if the following conditions are satisfied:*

1. Matrix A and matrix ω are real symmetric and positive, and satisfy that

$$\lambda_{\min}(\omega) > \lambda_{\max}(A) + \tilde{L}\|B\| + \|C\| \cdot \|\Gamma\| \tag{30.11}$$

2. Matrix D is Hurwitz, and

$$\|K(\bar{e}_r(t))\| \leq \zeta \|\bar{e}_r(t)\|^\beta,$$

for some constants $\zeta > 0$ and $\beta > 0$.

Proof Choose the following Lyapunov function:

$$V(t) = \frac{1}{2} \bar{e}_r^T(t) \bar{e}_r(t) = \frac{1}{2} \|\bar{e}_r(t)\|^2, \quad t > 0.$$

It is easy to verify that $V(t)$ is a non-negative function over $[-\tau, \infty)$ and radically unbounded, i.e., $V(t) \rightarrow \infty$ as $|\bar{e}_r(t)| \rightarrow \infty$.

Under assumption 1, we gain

$$\|G(\bar{e}_r(t))\|^2 \leq \tilde{L}^2 \|\bar{e}_r(t)\|^2. \tag{30.12}$$

In terms of Lemma 1 and (30.12), the time derivative of $V(t)$ along the trajectory of (30.10) is

$$\begin{aligned}\dot{V}(t) &= \bar{e}_r^T(t)BG(\bar{e}_r(t)) + \bar{e}_r^T(t)A\bar{e}_r(t) + \bar{e}_r^T(t)C\Gamma\bar{e}_r(t - \tau) - \bar{e}_r^T(t)\omega\bar{e}_r(t) \\ &\leq \lambda_{\max}(A)\|\bar{e}_r(t)\|^2 - \lambda_{\min}(\omega)\|\bar{e}_r(t)\|^2 + \tilde{L}\|B\| \cdot \|\bar{e}_r(t)\|^2 \\ &\quad + \|C\| \cdot \|\Gamma\| \cdot \|\bar{e}_r(t)\| \cdot \|\bar{e}_r(t - \tau)\| \\ &\leq -(2\lambda_{\min}(\omega) - 2\lambda_{\max}(A) - 2\tilde{L}\|B\| - \|C\| \cdot \|\Gamma\|)V(t) \\ &\quad + \|C\| \cdot \|\Gamma\| \left(\sup_{t-\tau \leq s \leq t} V(s) \right).\end{aligned}$$

Condition (30.11) denotes that

$$2\lambda_{\min}(\omega) - 2\lambda_{\max}(A) - 2\tilde{L}\|B\| - \|C\| \cdot \|\Gamma\| > \|C\| \cdot \|\Gamma\| > 0.$$

According to Lemma 2, we have

$$\begin{aligned}V(t) &\leq \left(\sup_{-\tau \leq s \leq 0} V(s) \right) e^{-\delta t}, t > 0, \\ \|\bar{e}_r(t)\| &\leq \sup_{s \in [-\tau, 0]} \|\bar{\phi}_r(s) - \bar{\varphi}_r(s)\| \cdot \exp\left(-\frac{1}{2}\delta t\right), t > 0\end{aligned}$$

Therefore, system (10) is globally exponentially stable about its partial variables $\bar{e}_r(t)$. Combining condition 2 and Lemma 3, it is easy to conclude that the zero solution $\bar{e}_n(t) = 0$ of system (10) is globally and exponentially stable.

Remark 1 In Theorem 1, under certain conditions, it is easy to be verified the global exponential synchronization base on the Derivation method, but it is difficult to find $V(t)$.

Remark 2 In Theorem 2, by designing different controllers and applying the Halanay inequality Lemma, it is more economic and timesaving to obtain $V(t)$, but it is difficult to be verified.

30.4 Numerical Simulations

Let us consider the following Lü system:

$$\dot{x} = f(x) = \begin{pmatrix} a(x_2 - x_1) \\ cx_2 - x_1x_3 \\ -bx_3 + x_1x_2 \end{pmatrix} \quad (30.13)$$

where $a = 36$, $b = 3$, $c = 20$. The Rössler system is known as:

$$\dot{y} = Ay + Bg(y) = \begin{pmatrix} -y_2 - y_3 \\ y_1 + \omega y_2 \\ \lambda + y_3(y_1 - \theta) \end{pmatrix} \quad (30.14)$$

where $\omega = 0.2, \lambda = 3, \theta = 5.7$. Thus $a = \|A\| = 5.7, \beta = \|B\| = 1$.

Considering our driving system with 6-nodes:

$$\begin{cases} \dot{x}_i(t) = f(x_i(t)) + \sum_{j=1}^5 c_{ij}\Gamma x_j(t - \tau), & i = 1, 2, \dots, 5 \\ \dot{x}_6(t) = x_1(t) - x_6(t) \end{cases}$$

where $f(x_i)$ is shown in Eq. (30.14). The response system is:

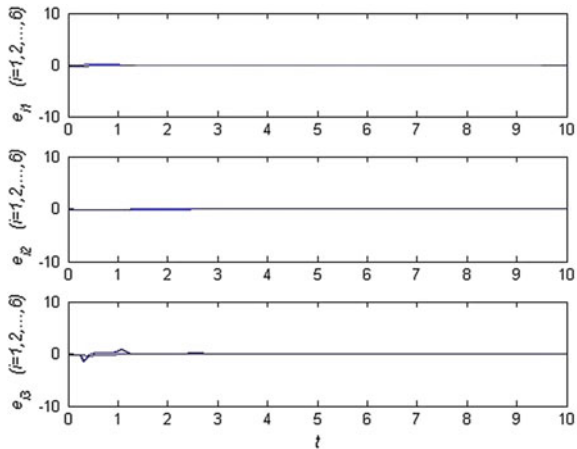
$$\begin{cases} \dot{y}_i(t) = Ay_i(t) + Bg(y_i(t)) + \sum_{j=1}^5 c_{ij}\Gamma y_j(t - \tau(t)) + \mu_i, & i = 1, 2, \dots, 5 \\ \dot{y}_6(t) = y_1(t) - y_6(t). \end{cases}$$

where $g(y_i), A$ and B are shown in Eq. (30.14), $\mu_i(t) = f(x_i(t)) - Bg(x_i(t)) - A(x_i(t)) - (x_i(t) - y_i(t))$. C is the configuration matrix as follows:

$$\begin{pmatrix} -0.4 & 0.3 & 0 & 0.1 & 0 \\ 0.2 & -0.3 & 0.1 & 0 & 0 \\ 0 & 0.1 & -0.2 & 0.1 & 0 \\ 0 & 0 & 0.4 & -0.4 & 0 \\ 0.1 & 0 & 0.1 & 0 & -0.2 \end{pmatrix}$$

In the numerical simulations, we select $\Gamma = \text{diag} (1,1,1), \|\Gamma\| = \gamma = 1, \tau(t) = \frac{e^t}{1+e^t}$. The initial values of the drive system and the response system are chosen as $x_i(0) = (0.3 + 0.01i, 0.3 + 0.01i, 0.3 + 0.01i)^T, y_i(0) = (0.4 + 0.01i, 0.4 + 0.01i, 0.4 + 0.01i)^T$. The numerical results show as follows (Fig. 30.1):

Fig. 30.1 The exponential synchronization errors of system (13) and system (14)



30.5 Conclusions

In this paper, the global exponential synchronization of the delayed chaotic network has been investigated effectively. Based on Derivation method and the Halanay inequality technique, it is successfully used to guarantee the global stability of the error system, which includes server delay-independent conditions. The method presented in this paper is much general and effectiveness compared with someone. Consequently, it is a more comprehensive way to apply to the practice.

Acknowledgments This work was supported by the National Nature Science foundation of China (Nos.51276081, 11171135), the Society Science Foundation from Ministry of Education of China (Nos. 12YJAZH002, 08JA790057), the Project Funded by the Priority Academic Program Development of Jiangsu Higher Education Institutions, the Advanced Talents' Foundation of Jiangsu University (Nos. 07JDG054, 10JDG140), and the Students' Research Foundation of Jiangsu University (Nos. 11A179, Y11A079).

References

1. Pecora LM, Carroll TL (1990) Synchronization in chaotic systems. *Phys Rev Lett* 64:821–824
2. Li CG, Chen GR (2004) Synchronization in general complex dynamical networks with coupling delays. *Phys A* 343:263–278
3. Hu MF, Xu ZY, Yang YQ (2008) Projective cluster synchronization in drive-response dynamical networks. *Phys A* 387:3759–3768
4. Zheng S, Bi QS, Cai GL (2009) Adaptive projective synchronization in complex networks with time-varying coupling delay. *Phys Lett A* 373:1553–1559
5. Zheng S, Dong G, Bi Q (2009) Impulsive synchronization of complex networks with non-delayed and delayed coupling. *Phys Lett A* 373:4255–4259
6. Wang KH, Fu XC, Li KZ (2009) Cluster synchronization in community networks with nonidentical nodes. *Chaos* 19:023106
7. Guirey E, Bees M, Martin A, Srokosz M (2010) Persistence of cluster synchronization under the influence of advection. *Phys Rev E* 81:051902
8. Lu WL, Liu B, Chen TP (2010) Cluster synchronization in networks of coupled nonidentical dynamical systems. *Chaos* 20:013120
9. Wang JW, Ma QH, Zeng L, Abd-Elouahab MS (2009) Mixed outer synchronization of coupled complex networks with time-varying coupling delay. *Chaos* 21:013121
10. Shao HJ, Cai GL, Wang HX (2010) An linear matrix inequality approach to global synchronisation of non-parameters perturbations of multi-delay Hopfield neural network. *Chin Phys B* 19(11):110512.1–110512.6
11. Cheng CJ, Liao TL, Hwang CC (2005) Exponential synchronization of a class of chaotic neural networks. *Chaos, Solitons Fract* 24:197–206
12. Xiong WJ, Xie W, Cao JD (2006) Adaptive exponential synchronization of delayed chaotic networks. *Phys A* 370:832–842

Chapter 31

Pattern Recognition of the Thigh Amputee Motion Based on Genetic Algorithm and BP

Lei Liu, Peng Yang, Zuojun Liu, Lingling Chen and Yanli Geng

Abstract In order to recognize the pattern of the powered type lower limb prosthesis movement accurately, a genetic algorithm and neural network algorithm was proposed in this paper. Gyroscope sensor which was installed in the prosthetic socket and pressure sensors which were installed in the Prosthetic foot were used for data acquisition in the experiment. The mean of the angle was calculated in different motion mode corresponding support phase and swing phase. They were input variables of the BP neural network model. Genetic algorithm was used to optimize the weights and bias of BP neural network. Optimized BP neural network was applied to establish recognition model. The results showed that the proposed method offered the advantages of high precision and fast convergence in contrast with BP neural network.

Keywords Prosthesis · Gyroscope · Genetic algorithm · BP pattern recognition

31.1 Introduction

It is shown that with the increment of the population and the process of the ageing. The number of the disabled people is getting larger and larger before 2020. The number of the lower limb amputation accounted for about 85 % of the total number of the amputation. It is convenient for them to live their lives and work, if the high performance intelligent lower limb prosthesis are installed. It is high time for us to do research in the technology of the intelligent lower limb prosthesis control.

L. Liu (✉) · P. Yang · Z. Liu · L. Chen · Y. Geng
Department of Automation Engineering, School of Control Science and Engineering, Hebei University of Technology, Guangrongdao, Hongqiao District, Tianjin, China
e-mail: liulei2006000@126.com

The research of the technology of the intelligent lower limb prosthesis was done almost 30 years in our country. Professor Jin De Wen of Tsinghua university have done a lot of groundbreaking research in this topic [1, 2]. The professor Tan Guan Zheng in Central south university developed a kind of the intelligent bionic artificial leg named CIP-I Leg based on the nonlinear PID control [3]. Professor Yang Peng in Hebei university of technology national rehabilitation covers research center and other units cooperation have done research and developed the variable damping passive lower limb prosthesis using the angle sensor in order to judge the person's walking pace They can regulate the pneumatic cylinder damping so as to coordinate the walking gait [4].

It is shown that powered prosthesis can make the artificial limb movement gait closer to the sound limb. They can provide the patients with the help force when the patients going up the stairs and they can achieve a variety of walking pattern conversion timely if the intelligent prosthesis can recognize the human movement pattern correctly.

The application of the BP neural network in the motion pattern recognition is hot in recent years. They have made some good scientific research results already. The most commonly used method contains three steps. First, extract the signal characteristic vector later, then, the vector as the input of the network, the corresponding action mode as the output, through the learning and training to realize, finally pattern classification is got. But the initial weights and threshold value of the BP neural network is selected at random, if the position of these parameters selected properly, it will lead to the network convergence speed slowly, fall into the local optimal value [5, 6]. Genetic algorithm is a kind of parallel random search optimization method. It has ability of the global search. So the GA algorithm was used to determine the BP neural network weights and threshold value. Then the momentum primers BP learning algorithm was introduced for local optimization in order to converge to the global optimal solution quickly. In this paper gyroscope sensor which was assembled in the prosthetic sockets and pressure sensors which was assembled in the artificial limb plantar were used to acquire data. We analyzed the angle of hip each motion segmentation mode corresponding to the mean as the characteristic value, then the GA-BP algorithm was used to recognize the motion walking pattern.

31.2 The Model of the Thigh Amputees Motion Pattern Recognition Based on Genetic BP Neural Network

Genetic algorithm was a kind of evolutionary algorithm. The basic principle was to imitate the biological material as natural selection, survival of the fittest "evolution law". It was put forward by John Holland in 1975 at first. Genetic algorithm was a calculation model which simulated Darwin's genetic selection and natural selection of biological evolution process. Genetic algorithm took a group of all

individual as the object. Randomized technical was used to guide a coded parameter space in order to search effectively until meeting the requirements [7]. The BP neural network and genetic algorithm were combined in order to search the optimal network initial weights and threshold value. It can make up defects of the initial weights and threshold value at random and make the network predict the output of the system more accurately. In this paper, the object was lower-limb amputee motion pattern recognition model and the output is the model of the lower-limb amputee motion. According to the theory of Kolmogorov, three layer BP neural network model was used in the experiment. Specific steps were as follows.

Step 1. The population was initialized at random. The way of individual coding was the mode of the real number coding. Each individual was a string of real number. It consisted of the input layer and hidden layer connection weights and the hidden layer threshold value; hidden layer and output layer connection weights and output layer threshold value. The form of the Individual was:

$$w_{11} \quad w_{21} \dots w_{n1} w_{12} w_{22} \dots w_{n2} \dots w_{1l} w_{2l} \dots w_{nl} a_1 \dots a_l$$

$$w'_{11} w'_{21} \dots w'_{l1} b_1$$

Step 2. The fitness function was determined In order to make the classification of residual value and expectations as small as possible of the BP neural network, so took the norm of the error matrix between the prediction data and the expectation data as the output of the objective function. The function of sort fitness distribution was used as the fitness function. $F = ranking(obj)$, obj was the output of the objective function.

Step 3. Selection operation. Several individual were chosen from population as parents who intended to reproduce. The method of the roulette wheel selection was used in the experiment. The probability of the individual of higher fitness genetic to the next generation was larger. The probability that individual of lower fitness genetic to the next generation was smaller. The probability that each individual such as i was chosen was

$$p_i = F_i / \sum_{i=1}^c F_i \tag{31.1}$$

c was the number of individual of the population, F_i was the value of the Individual fitness.

Step 4. Interlace operation. Two pairs of individual exchanged some of the gene according to some way. The probability of the crossover was p_c , so two new individuals were formed using the real bracketing method. The method of genes cross operation between k_1 and k_2 one in the j position of individual was as follows:

$$g_{k_1j} = g_{k_1j}r + g_{k_2j}(1 - r) \quad (31.2)$$

$$g_{k_2j} = g_{k_2j}r + g_{k_1j}(1 - r) \quad (31.3)$$

g_{k_1j} was the gene of the individual k_1 in the position j . g_{k_2j} was the gene of the individual k_2 in the position j . r was a random number between 0 and 1.

Step 5. Mutation operator. The gene g_{ij} of the j of the individual i was chosen to mutate with a relatively small mutation probability in order to increase the diversity of population. The method of the mutation operator was as follows:

$$g_{ij} = \begin{cases} g_{ij}r + (g_{ij} - g_{\max})r_1(1 - s/s_{\max}), & r_2 \geq 0.5; \\ g_{ij}r + (g_{\min} - g_{ij})r_1(1 - s/s_{\max}), & r_2 < 0.5. \end{cases} \quad (31.4)$$

In the formula, g_{\max} was the upper bounds of the gene, g_{\min} was the lower bounds of the gene. r_1 was a random number, s was the current iterations, s_{\max} was the largest number of evolution. r_2 was a random number between 0 and 1.

- Step 6. The value of the fitness function was calculated. If they met the condition of the end of the algorithm, optimization of the weights and threshold value were got. If they didn't meet the condition of the end of the algorithm, it would return to the third step.
- Step 7. The optimization of the weights and threshold which were output of the GA were the initial weights and threshold value of BP neural network. BP neural network were trained using the training samples in order to get the model of the lower-limb amputees motion pattern recognition.
- Step 8. The new samples were used so as to test the generalization ability of the classification model.

31.3 Simulation Example

It is important of Lower limb movement information collection for intelligent lower limb prosthesis movement pattern recognition. The change of the angle had obvious regularity when people were walking. It can be used as important information of gait recognition. Hip Angle and angular velocity were important information of gait recognition [8]. Gyroscope sensor which was installed in the prosthetic socket and pressure sensors which were installed in the Prosthetic foot were used for data acquisition in the experiment. MEMS gyroscope can be used to measure angular velocity. The unit was degrees/second. Angular velocity is integral in order to get the hip angle.

Through the study on the motion mode of the human body movement of the lower limbs, it was shown that the time of a single movement cycle was between

1.3 and 2.0. At the same time, in order to describe the different feature information of the hip angle more accurately. It can be divided into 4 parts of the single leg attitude in the motion mode. They were support falling phase, full supporting phase, supporting rising phase, and the swing phase. When doing the experiment of the feature extraction of the hip angle, the method of the mean angle was used to extract characterization of the above period of characteristic value in this paper. First of all, the mean of the angle was calculated in different motion mode corresponding support phase and swing phase. Then, the mean of the angle was calculated in each motion segmentation mode respectively.

The detailed statement was below:

$$\theta = \sum_{i=1}^{N_i} \theta_i / N_i, \theta_1 = \sum_{i=1}^{n_i} \theta_i / n_i \tag{31.5}$$

θ_i was the angle value of stretch hip in the interval of Sampling. N_i was the sampling points of the corresponding period. n_i was the sampling points of the Segmentation mode. The characteristic value of the segmentation mode according to the above method were calculated which were shown in Table 31.1.

In order to prevent the absolute value of the net input too big and cause the output of the neuron saturation. The adjustment of the weights got into error surface flat area. It was essential to normalize the characteristic value of the sample. The data of the input layer were mapped between 0 and 1. After training, the output of the model was reflected the range of the original data. The number of the output node depended on the number of the classification. (1, 0, 0) was the ground walking. (0, 1, 0) was the upstairs. (0, 0, 1) was the downstairs. (1, 0, 1) was the upslope. (1, 1, 0) was the downhill. There were five kinds of motion in all in the experiment. According to the Kolmogrov theory, the number of hidden layer nodes was $2n+1$ of the BP neural network. The function of the hidden layer was tansig function. The function of the output was pureline function. The goal error of neural network training was 0.01, η was 0.1, the biggest training-step was 1,000, β was 0.1. If the initial population of Genetic algorithm (GA) was too small, the performance of the algorithm was very poor. The solution of the problem was not feasible. If the population was larger, it would increase the optimization information. But it would increase the amount of calculation so as to make the

Table 31.1 Characteristic value of the lower limbs hip angle of the segmentation mode

	Support falling phase	Full supporting phase	Supporting rising phase	The swing phase
The ground walking	22.2575	6.4098	-1.4949	30.9110
Upstairs	54.1314	23.0392	5.2203	46.5572
Downstairs	25.0168	26.2200	38.1582	53.4834
Upslope	30.8788	24.4289	14.3133	52.6149
Downhill	101.4532	101.1638	94.9766	106.7536

convergence time too long. In the paper the time of the evolution was 100, the number of the population was 20. The probability of the crossover was used to control the frequency of the crossover operation. If the probability of the crossover was too large, the population of the individual updated soon, and individual of high fitness were broken soon. The probability of the crossover was 0.5 after doing experiment many times. If the probability of the mutation was too large, it would make search at random. If the probability of the mutation was too small, it would not produce new individual. The probability of the mutation was 0.05 in the paper after doing experiment. Genetic algorithm was used to optimize the BP network weights. The average error of each generation was calculated. It was an important index of the genetic algorithm which was used to optimize parameter. At the same time, in order to compare with the classical algorithm. This paper also used the same parameters to train and test the BP neural network. The results of the experiment were shown in Figs. 31.2, 31.3. The error of training Genetic BP neural network was shown Fig. 31.3 and the error of training BP network was shown in Fig. 31.2. BP network converge to a scheduled accuracy after 12-step, but the genetic BP network only need 2-step. The algorithm of GA-BP increased the speed of convergence. A conclusion was drawn that the algorithm of GA-BP was better than the improved BP (Fig. 31.1).

After training, 100-group of the test data was input to the net respectively using the trained network. 91-group movement model was identified correctly using Genetic BP network. But 70-group movement model were identified correctly using BP network in the experiment. It was shown that the performance of genetic BP network in motion pattern recognition was better. There were some errors of the identification of the results in the experiment. First: This experiment platform was 15-degree slope in the experiment which was made according to the building barrier-free channel. The gradient of the slope was low. The data of walking on the downhill was similar to the data of walking on the flat. It caused some errors of identification of some samples. Second: Because the data of the actual statistics

Fig. 31.1 Error evolution curve

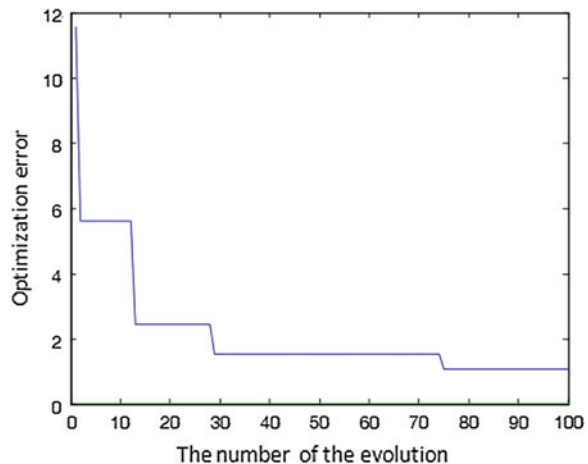


Fig. 31.2 The error curve of the improved BP network

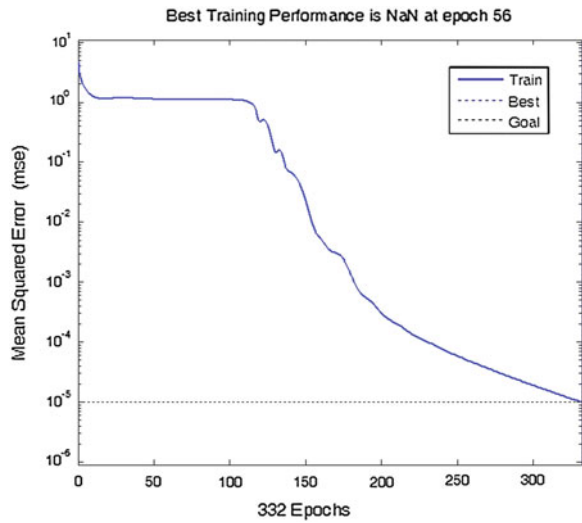
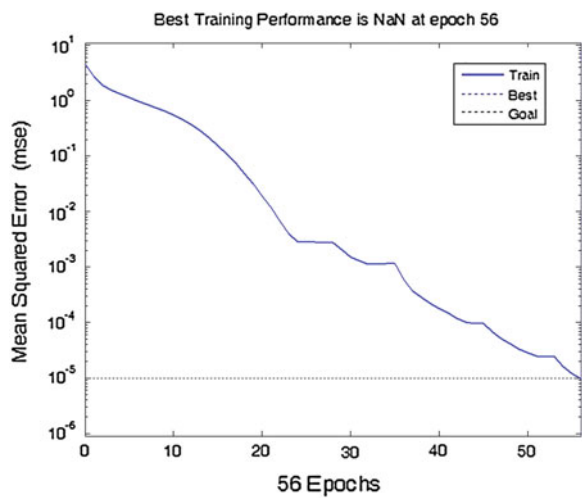


Fig. 31.3 The error curve of GA-BP network



was limited, the quantity of the sample was limited. In order to make the simulation results more close to the actual value, attention should be paid to the improvement of the model and enough samples should be provided.

31.4 Conclusion

A new method of pattern recognition of the leg amputee motion based on the BP neural network and genetic algorithm was proposed. Genetic algorithm was used to optimize the weights and bias of BP neural network. Optimized BP neural

network was trained. The result was better than BP algorithm. Training time was short, the speed of convergence was fast and the accuracy of the classification was high. It can realize recognition of the motion pattern.

Acknowledgments This work is supported by Natural Science Foundation of China (61174009) and Natural Science Foundation of Hebei Province, China (F2011202155).

References

1. Au S, Berniker M, Herr H (2008) Powered ankle-foot prosthesis to assist level-ground and stair-descent gaits. *Neural Netw* 21:654–659
2. Chen LL, Yang P, Xu XY (2008) Above-knee prosthesis control based on posture recognition by support vector machine. In: *IEEE International conference on robotics, automation and mechatronics*, pp 307–312
3. Shen L, Yu HL (2012) Development course of prosthetics at home and abroad. *Chin J Tissue Eng Res* 16(3):2451–2454 (in Chinese)
4. Gong SY, Yang P, Song L, Chen LL (2011) Simulation of swing phase dynamics in transfemoral prostheses based on MATLAB. *J Hebei Univ Technol* 40(2):6–9 (in Chinese)
5. Ma YL, Xu WL, Meng M, Luo ZZ, Yang JQ (2010) Adaptive control for intelligent lower limb prosthesis based on neural net work. *J Zhejiang Univ (Eng Sci)* 44(7):1373–1377 (in Chinese)
6. Yu HL, Guan SHY, Qian SHS, Zhao Zh (2008) The control method of the Knee prosthesis intelligent. *Chin J Rehab Med* 23(2):145–147 (in Chinese)
7. Li WG, Huang YY, Ye XJ (2011) Feature selection based on genetic neural network and its application in classification. *J Syst Simul* 23(10):2094–2097 (in Chinese)
8. Li SH, Luo ZHZ, Meng M (2009) Acquisition method for the lower limb motion information based on accelerometers. *Mech Electr Eng Mag* 26(1):5–7 (in Chinese)

Chapter 32

R -Fuzzy Subsemigroups

Xiao-ying Zhu, Zu-hua Liao and Cui-yun Hao

Abstract By combining R -implication operators and fuzzy subsemigroups, the concept of a new fuzzy algebra structure, such R -fuzzy subsemigroup, is introduced. Furthermore, some fundamental properties and equivalence conditions on eight concrete implication operations of such fuzzy subsemigroup are discussed.

Keywords R -fuzzy subsemigroup · Implication operator · Semigroup homomorphism

32.1 Introduction

Zadeh, a cybernetics expert of California University in America, first proposed the concepts of fuzzy sets and fuzzy convex sets [1] in 1965. Subsequently, Rosenfeld introduced the definition of fuzzy subgroup [2] in 1971, which had initiated new study fields of fuzzy algebra. In 1980, Kuroki began to study fuzzy semigroup, which is one of the most active research fields in fuzzy algebra. Then, In 1982 Wangjin Liu further introduced some new notions in [3–5], such as fuzzy invariant subgroups of group G , fuzzy ideals of a ring and so on, which made fuzzy algebra study further deep into all aspects of each algebraic branch, such as fuzzy subgroup, fuzzy subring, fuzzy sublattice, fuzzy subdomain and so on.

X. Zhu · Z. Liao (✉) · C. Hao
School of Science, Jiangnan University, Wuxi 214122, China
e-mail: liaozuhua57@yahoo.cn

X. Zhu
e-mail: zhuxy58087@sina.com

C. Hao
e-mail: haocuiyun0@gmail.com

Yanying Zhao and Xuehai Yuan defined fuzzy subgroups based on implication operators in [6] and Jizhong Shen introduced the definition of L -fuzzy subgroup and some results in [7]. Mordeson, Malik, Kuroki systematically and Xiangyun Xie, Mingfen Wu gave the definition, properties, basic operations and so on of fuzzy subsemigroup in [8, 9]. This paper is the continuation of those. By the combination between R -implication operators and fuzzy subsemigroups, R -fuzzy subsemigroup is defined and some relative properties are discussed. In general fuzzy algebras, the combination of two homomorphic fuzzy algebras is not always still the homomorphic one. However, in the paper, we prove that the combination or intersection of any R -fuzzy subsemigroup is still R -fuzzy subsemigroup in certain conditions. Based on the definition of semigroup homomorphism, we also deduce that the full homomorphic image or homomorphic preimage of a R -fuzzy subsemigroup is still a R -fuzzy subsemigroup. From those conclusions, which rich the study of fuzzy algebra, we have a deeper understanding on the nature of R -fuzzy subsemigroup. The final part of this paper makes a conclusion and prospects the further study of fuzzy prime ideal.

32.2 Preliminaries

In the paper, S is denoted as a semigroup. $F(S)$ is the collection of all the fuzzy subsets of S .

Definition 1 [9] Let $A \in F(S)$. If A satisfies the condition: $A(xy) \geq A(x) \wedge A(y)$, $\forall x, y \in S$, then A is said to be a fuzzy subsemigroup of S .

Definition 2 [9] Let L and M be two any semigroups. A mapping: $f : L \rightarrow M$ is called union homomorphism if it satisfies the condition: (1) $f(x \vee y) = f(x) \vee f(y)$, $\forall x, y \in L$. Dually, f is called intersection homomorphism if it satisfies the condition: (2) $f(x \wedge y) = f(x) \wedge f(y)$, $\forall x, y \in L$. When f satisfies (1) as well as (2), it is said to be semigroup homomorphism (called homomorphic for short).

Let $f : L \rightarrow M$ is semigroup homomorphism. If f is a single mapping, then it's called single homomorphism. If f is a full mapping, then it's called full homomorphism, when we also call L and M are homomorphic, denoted as $L \sim M$. If f is a one-to-one mapping, then it is said to be a semigroup isomorphism (called isomorphism for short), when we also call L and M are isomorphic, denoted as $L \cong M$. If $L = M$, then the corresponding homomorphism (isomorphism) is called self-homomorphism (self-isomorphism).

Definition 3 [6] In classical logic, 0 or 1 is true value. The implication operator based on $\{0, 1\}$ is denoted as: $R(a,b) = \begin{cases} 0, & a = 1, b = 0; \\ 1, & \text{otherwise.} \end{cases}$

By generalizing such operator into $[0, 1]$, we obtain the following concept:

Definition 4 [10] A mapping $R: [0, 1] \times [0, 1] \rightarrow [0, 1]$ is said to be an implication operator.

Many properties of implication operators are discussed in all kinds of additive conditions in [10–15]. In this paper, we take advantage of implication operators without any additive conditions to study fuzzy subsemigroup.

Now some frequently-used implication operators are mainly as follows:

- (1) Zadeh operator: $R_z(a, b) = (1 - a) \vee (a \wedge b)$,
- (2) Mamdam operator: $R_M(a, b) = a \wedge b$,
- (3) Lukasiewicz operator: $R_{Lu}(a, b) = (1 - a + b) \wedge 1$,
- (4) Gaines Rescher operator: $R_{GR}(a, b) = \begin{cases} 1, & a \leq b; \\ 0, & a > b. \end{cases}$
- (5) Godel operator: $R_G(a, b) = \begin{cases} 1, & a \leq b; \\ b, & a > b. \end{cases}$
- (6) Goguen operator: $R_{Go}(a, b) = \begin{cases} 1, & a = 0; \\ \frac{b}{a} \wedge 1, & a \neq 0. \end{cases}$
- (7) Kleene Dienes operator: $R_{KD}(a, b) = (1 - a) \vee b$,
- (8) R_o 算子: $R_o(a, b) = \begin{cases} 1, & a \leq b; \\ (1 - a) \vee b, & a > b. \end{cases}$

32.3 R-Fuzzy Subsemigroup

Firstly, a description of fuzzy subsemigroup is given by classical implication operator.

Theorem 1 Let H be a nonempty fuzzy subset of S and R be classical logic implication operator.

$$\text{Then } H \leq S \Leftrightarrow R(H(x) \wedge H(y), H(xy)) = 1, \forall x, y \in S.$$

Proof is omitted. Following, the definition of R -fuzzy subsemigroup is given according to implication operators on $[0, 1]$.

Definition 5 Let R be an implication operator on $[0, 1]$, $A \in F(S)$ and $\lambda \in (0, 1]$. If A satisfies the condition: $R(A(x) \wedge A(y), A(xy)) \geq \lambda, \forall x, y \in S$, then A is said to be a R -fuzzy subsemigroup of S .

Furthermore, some properties of R -fuzzy subsemigroup are discussed.

Theorem 2 Let R be an implication operator on $[0, 1]$ and R satisfies the condition: when $a \leq a^*$, $R(a, b) \geq R(a^*, b)$. If A or B is R -fuzzy semigroup ideal of S , then $A \cap B$ is also R -fuzzy semigroup of S .

Proof According to the known conditions, we have $R(A(x) \wedge A(y), A(xy)) \geq \lambda$, $R(B(x) \wedge B(y), B(xy)) \geq \lambda$. For any $x, y \in S$, assume $A(xy) \geq B(xy)$, then it

follows that $R((A \cap B)(x) \wedge (A \cap B)(y), (A \cap B)(xy)) = R(A(x) \wedge A(y) \wedge B(x) \wedge B(y), B(xy)) \geq R(B(x) \wedge B(y), B(xy)) \geq \lambda$. So $A \cap B$ is a R -fuzzy subsemigroup of S .

Inference 1 Let R be an implication operator on $[0, 1]$ and R satisfies the condition: when $a \leq a^*, R(a, b) \geq R(a^*, b)$. If $A_i (1 \leq i \leq n)$ is R -fuzzy subsemigroup of S , then $\cap_{i=1}^n A_i$ is also a R -fuzzy subsemigroup of S .

Theorem 3 Let R be an implication operator on $[0, 1]$ and R satisfies the condition: when $a \geq a^*, R(a, b) \geq R(a^*, b)$. If A or B is R -fuzzy semigroup ideal of S , then $A \cup B$ is also R -fuzzy semigroup of S .

Proof According to the known conditions, we have $R(A(x) \wedge A(y), A(xy)) \geq \lambda, R(B(x) \wedge B(y), B(xy)) \geq \lambda$ and $(A \cup B)(x) \wedge (A \cup B)(y) \geq A(x) \wedge A(y)$. For any $x, y \in S$, assume $A(xy) \geq B(xy)$, then it follows that $R((A \cup B)(x) \wedge (A \cup B)(y), (A \cup B)(xy)) \geq R(A(x) \wedge A(y), A(xy)) \geq \lambda$. So $A \cup B$ is a R -fuzzy subsemigroup of S .

Inference 2 Let R be an implication operator on $[0, 1]$ and R satisfies the condition: when $a \geq a^*, R(a, b) \geq R(a^*, b)$. If $A_i (1 \leq i \leq n)$ is R -fuzzy subsemigroup of S , then $\cup_{i=1}^n A_i$ is also a R -fuzzy subsemigroup of S .

Theorem 4 Let R be an implication operator on $[0, 1]$ and R satisfies conditions: (1) When $a \leq a^*, R(a, b) \geq R(a^*, b)$; (2) When $b \leq b^*, R(a, b) \leq R(a^*, b)$; (3) $R(x, y)$ is continuous about x . Let $f : S \rightarrow H$ be a full homomorphism of a semigroup. If A is R -fuzzy subsemigroup of S , then $f(A)$ is also R -fuzzy subsemigroup of H .

Proof For every $\varepsilon > 0, z_1, z_2 \in H$, there exists $x_1, x_2 \in S$ such that $f(x_1) = z_1, f(x_2) = z_2, A(x_1) > f(A)(z_1) - \varepsilon$ and $A(x_2) > f(A)(z_2) - \varepsilon$. It follows that $A(x_1) \wedge A(x_2) > (f(A)(z_1) \wedge f(A)(z_2)) - \varepsilon$. According to the known conditions, we have $R(f(A)(z_1) \wedge f(A)(z_2), f(A)(z_1 z_2)) = R(\lim_{\varepsilon \rightarrow 0} (f(A)(z_1) \wedge f(A)(z_2)) - \varepsilon, f(A)(z_1 z_2)) = \lim_{\varepsilon \rightarrow 0} R((f(A)(z_1) \wedge f(A)(z_2)) - \varepsilon, f(A)(z_1 z_2)) \geq \lim_{\varepsilon \rightarrow 0} R(A(x_1) \wedge A(x_2), f(A)(z_1 z_2)) = R(A(x_1) \wedge A(x_2), f(A)(z_1 z_2)) \geq R(A(x_1) \wedge A(x_2), A(x_1 x_2)) \geq \lambda$. So $f(A)$ is a R -fuzzy sub semigroup of H .

Theorem 5 Let R be an implication operator on $[0, 1]$ and $f : S \rightarrow H$ be a homomorphism of a semigroup. If B is R -fuzzy subsemigroup of H , then $f^{-1}(B)$ is also R -fuzzy subsemigroup of S .

Proof For all $x, y \in S, R(f^{-1}(B)(x) \wedge f^{-1}(B)(y), f^{-1}(B)(xy)) = R(B(f(x)) \wedge B(f(y)), B(f(xy))) = R(B(f(x)) \wedge B(f(y)), B(f(x)f(y))) \geq \lambda$. So $f^{-1}(B)$ is a R -fuzzy subsemigroup of S .

Theorem 6 Let R be an implication operator on $[0, 1]$ and R satisfies the condition: $R(a, b) = 1 \Leftrightarrow a \leq b$. If A is a fuzzy subsemigroup of S , then A is R -fuzzy subsemigroup of S .

Proof According to the known conditions, for all $x, y \in S$, we have $A(xy) \geq A(x) \wedge A(y)$. It follows that $R(A(x) \wedge A(y), A(xy)) = 1 \geq \lambda$. So A is a R -fuzzy subsemigroup of S .

Finally, the equivalence conditions on eight concrete implication operations of R -fuzzy subsemiare given.

Theorem 7 *Let $t \in (0, 1]$. Discussing the above listed eight implication operators, we obtain conclusions as follows (for all $x, y \in \mathfrak{R}$):*

- (1) A is R_{GR} -fuzzy subsemigroup of $S \Leftrightarrow A$ is a fuzzy subsemigroup of S ;
- (2) A is R_{GR} -fuzzy subsemigroup of $S \Leftrightarrow A(xy) \geq t(A(x) \wedge A(y))$;
- (3) A is R_{GR} -fuzzy subsemigroup of $S \Leftrightarrow A(x) \wedge A(y) - A(xy) \leq 1 - t$;
- (4) A is R_G -fuzzy subsemigroup of $S \Leftrightarrow A(xy) \geq A(x) \wedge A(y) \wedge t$;
- (5) A is R_M -fuzzy subsemigroup of $S \Leftrightarrow A(x) \geq t, \forall x \in G$;
- (6) A is R_Z -fuzzy subsemigroup of $S \Leftrightarrow A(x) \wedge A(y) \leq 1 - t$ or $A(x) \wedge A(y) \wedge A(xy) \geq t$;
- (7) A is R_{KD} -fuzzy subsemigroup of $S \Leftrightarrow A(x) \wedge A(y) \leq 1 - t$ or $A(xy) \geq t$;
- (8) A is R_o -fuzzy subsemigroup of $S \Leftrightarrow A(x) \wedge A(y) \leq A(xy)$ or $A(xy) < A(x) \wedge A(y) \leq 1 - t$ or $A(x) \wedge A(y) > A(xy) \geq t$.

Proof By Theorem 6, the proposition (1) is obvious. For the proof from (2) to (8), we just show Godel operator as examples. In other conditions, the proof is similar.

(2) If: According to the known condition, for all $x, y \in S$, we have $R_{Go}(A(x) \wedge A(y), A(xy)) \geq t$, that is $A(x) \wedge A(y) = 0$ or $(A(xy) / (A(x) \wedge A(y))) \wedge 1 \geq t(A(x) \wedge A(y) \neq 0)$. So it follows that $A(xy) \geq t(A(x) \wedge A(y))$.

Only if: From $A(xy) \geq t(A(x) \wedge A(y))$, we have $A(x) \wedge A(y) = 0$ or $(A(xy) / (A(x) \wedge A(y))) \geq t(A(x) \wedge A(y) \neq 0)$

Thus $(A(xy) / (A(x) \wedge A(y))) \wedge 1 \geq t$.

$$\text{Since } R_{Go}(A(x) \wedge A(y), A(xy)) = \begin{cases} 1, & A(x) \wedge A(y) = 0; \\ (A(xy) / (A(x) \wedge A(y))) \wedge 1, & A(x) \wedge A(y) \neq 0. \end{cases}$$

we have $R_{Go}(A(x) \wedge A(y), A(xy)) \geq t$. So A is R_{Go} -fuzzy subsemigroup of S .

32.4 Conclusion

At present, papers about R -fuzzy subsemigroup are few at home and abroad. And there is much work for us to study. For example, there are more than 400 kinds of implication operators. In this paper, we just discuss the common eight kinds of those. Besides, by the effective integration between fuzzy algebra and fuzzy logic,

we would obtain more richer results. In a word, there is much room for further study in this aspect, which is significant in riching the basis of fuzzy algebra.

Acknowledgments This work is supported by the National Natural Science Foundation of China (No: 11001109) and Program for Innovative Research Team of Jiangnan University (Applied Mathematics No: 200902).

References

1. Zadeh LA (1965) Fuzzy sets. *Inf Control* 8:338–353
2. Rosenfeld A (1971) Fuzzy groups. *J Math Anal Appl* 35:512–517
3. Liu WJ (1982) Fuzzy invariant subgroups and Fuzzy ideas. *Fuzzy Sets Syst* 8:133–139
4. Liu WJ (1981) Fuzzy ideas and characteristics of fields. *Fuzzy Math* 1:101
5. Liu WJ (1980) Basic concepts of fuzziness algebras. *J Sichuan Normal Coll (Nat Sci)* 3:25–33
6. Zhao YY, Yuan XH, Zhao Q (2002) Fuzzy subgroup based on implication operator. *J Beihua Univ (Nat Sci)* 3:378–380
7. Shen JZ (2002) Homomorphism of groups based on logic. *J Jiangxi Normal Univ (Nat Sci)* 26:4–9
8. Mordeson JN, Malik DS, Nobuaki K (2003) *Fuzzy semigroups*. Springer
9. Xie XY, Wu MF (2005) *Fuzzy theory of semigroups*. Science Press, Beijing
10. Wang GJ (2005) *Computational intelligence—computing with words and Fuzzy set*, vol 2. Higher Education Press, Beijing
11. Dubois D, Prade H (1991) Fuzzy sets in approximate reasoning, part 1: inference with possibility distributions. *Fuzzy Sets Syst* 40:143–202
12. Dubois D, Lang J, Prade H (1991) Fuzzy sets in approximate reasoning, part 2: logical approaches. *Fuzzy Sets Syst* 40:203–244
13. Wang GJ (2008) *Non-classical mathematical logic and approximate reasoning*, 2nd edn. Science Press, Beijing
14. Wu WM (1994) *The principle and method of fuzzy reasoning*. Technology Press of Guizhou, Guiyang
15. You F (2007) *Fuzzy implication operators and response performance of their fuzzy system*. Industry University Press of Xibei, Xi'an

Chapter 33

A New Constant Gain Kalman Filter Based on TP Model Transformation

Fan Yang, Zhen Chen, Xiangdong Liu and Bing Liu

Abstract A constant gain Kalman filter is proposed in this paper concerned with the problem of the complexity and large calculation in nonlinear system estimation. With the introduction of linear parameter varying (LPV) model and tensor product (TP) model transformation method, the nonlinear system is represented by a linear polytopic model. The transformation directly leads to the reduction of the conservativeness for the linear polytopic model gained by the parameter bounds method and avoids solving infinite number of linear matrix inequalities (LMIs). Moreover, a constant gain filter is developed based on the EKF and robust H₂ filtering, which greatly reduces the calculation number. Finally, an example is employed to illustrate the effectiveness of the proposed filter.

Keywords Nonlinear system · LPV · TP · Robust H₂ filter · Polytope

33.1 Introduction

Nonlinear filtering algorithms, such as the EKF, the Unscented Kalman filter (UKF) and particle filter, are commonly used to estimate the states of the nonlinear system from noisy measurements [1, 2]. The most popular nonlinear filtering is the EKF, which processes sensor measurements recursively to gain the state estimates under the sensing of the minimum mean squared error estimates. However, the method needs to evaluate the Jacobian matrices and update the filter gain on line, resulting in large amount of computation. Many efforts have been made in the direction of reducing the complexity and the computation cost of the algorithm, such as constant gain extended Kalman filter (CGEKF).

F. Yang · Z. Chen (✉) · X. Liu · B. Liu
School of Automational, Beijing Institute of Technology, 5 South Zhongguancun
Street, Haidian District, Beijing 100081, China
e-mail: chenchen76@bit.edu.cn

Compared with the EKF, CGEKF updates the constant gain offline without evaluating the covariance for the state estimation errors and greatly reduces the computation burden [3]. However, the filter is appropriate for the smooth estimation as it simply applies the steady gain as the filter gain.

More recently, linear parameter varying (LPV) systems have received a rapidly increasing attention [4, 5], due to the fact that they are excellent for representing certain classes of nonlinear systems. But in the most filtering problems, only the affine LPV system is considered, for it's easy to represent the affine LPV system via a polytopic model by the parameter bound method and design a robust filter for the system. However, it's conservative to obtain the polytopic model for the general system that is not affine.

This paper develops a new method for the design of the CGEKF suitable for the general nonlinear filtering problems. Firstly, the nonlinear filter design problem is converted into the linear filtering design problem based on Jacobian linearization, which reduces the algorithm complexity effectively. Then the tensor product (TP) model transformation theory is used to represent a general LPV model, given over a bounded domain, by a specific polytopic model without the restriction of the dependence of parameters. Finally, a constant gain filter is designed according to the step prediction equations of the EKF and robust H2 filtering, which avoids updating filter gain on line and decreases the calculation amount.

33.2 The New Filter for Nonlinear System

Consider the following nonlinear dynamical system

$$\begin{aligned}\dot{x} &= f(x) + w \\ z &= h(x) + v\end{aligned}\tag{33.1}$$

where, $x \in R^N$ is the state, $z \in R^M$ is the measurement, $w \in R^N$ and $v \in R^M$ are the process noise and measurement noise, which are assumed to be uncorrelated noises.

The state predicted estimate and the predicted observation for (33.1) satisfy: $\hat{x} = f(\hat{x})$, $\hat{z} = h(\hat{x})$. Define the state estimate error as $\Delta x = x - \hat{x}$, the estimation error system of (33.1) can be approximated via a LPV model by the Jacobian linearization as follows:

$$\begin{aligned}\Delta\dot{x} &= F(x)\Delta x + Bn_w \\ \Delta z &= H(x)\Delta x + Dn_w\end{aligned}\tag{33.2}$$

where, $F(x) = \frac{\partial f(x)}{\partial x}$, $H(x) = \frac{\partial h(x)}{\partial x}$, $F(x)$ and $H(x)$ are real Jacobian matrices that depend on the state vector x , $B = [I_{N \times N} \quad 0_{N \times M}]$ $D = [0_{M \times N} \quad I_{M \times M}]$, $n_w = [w^T \quad v^T]^T$.

The system matrix $s(x) = \begin{pmatrix} F(x) \\ H(x) \end{pmatrix}$ is a parametrically varying object depended on the time varying system state x . Assume that x is bounded by the N -dimensional space $x = [x_1 \ x_2 \ \dots \ x_N] \in \Omega : [a_1, b_1] \times [a_2, b_2] \times \dots \times [a_N, b_N]$.

33.2.1 Linear Polytopic Model

The affine system can be represented by a polytopic model directly with the parameter bounded method. However, it may be conservative to describe the general LPV system, for there is complex nonlinearity between parameters. In order to reduce the conservativeness of the polytopic model, we introduce the TP model transformation algorithm. The specific steps are as follows [6]:

1. Confirm the parameter space of $x = [x_1 \ x_2 \ \dots \ x_N]$ by the dynamic model.
2. Let the given function be sampled over the uniformly distributed $i_1 \times i_2 \times \dots \times i_N$ grid points in the bounded domain Ω and stores the sampled matrices into the tensor \mathbf{S} .
3. Execute higher order singular value decomposition (HOSVD) on every mode of tensor \mathbf{S} . Computation of the HOSVD can be done by executing SVD on each dimension of tensor \mathbf{S} . Namely, U_n is determined by executing SVD on the n -mode matrix $A_{(n)}$ of tensor \mathbf{S} as

$$A_{(n)} = (U_n \ U_n^d) \begin{pmatrix} D_n & 0 \\ 0 & D_n^d \end{pmatrix} (V_n \ V_n^d)^T \quad (33.3)$$

where, diagonal matrix D_n contains the retained n -mode singular values, matrix D_n^d contains the discarded n -mode singular values $\sigma_{i_n}^{(n)}$, the number of the discarded singular values is I_n , the number of all the singular values is R_n . Therefore

$$A_{(n)} = U_n D_n V_n^T \quad (33.4)$$

Then, let $S_{(n)} = D_n V_n^T$. Restoring $S_{(n)}$ into tensor \mathbf{S}_n , leads to

$$A = \mathbf{S}_n \times_n U_n \quad (33.5)$$

Determination of U_{n+1} is done in the same way. The SVD is executed on the $n + 1$ th dimension of tensor \mathbf{S}_n obtained in the previous step. Again let the SVD be executed on the $n + 1$ -mode matrix $(S_n)_{(n+1)}$ of tensor \mathbf{S}_n . This results in

$$\mathbf{A} = \mathbf{S}_{n+1} \times_n U_n \times_{n+1} U_{n+1} \quad (33.6)$$

Repeating the above step on all dimensions leads to

$$A = S \otimes_{n=1}^N U_n \quad (33.7)$$

As a result, the approximation error can be expressed as

$$\|S(x) - \mathbf{S} \otimes_{n=1}^N U_n\|^2 \leq \sum_{n=1}^N \left(\sum_{i_n=l_n+1}^{R_n} (\sigma_{i_n}^{(n)})^2 \right)$$

where, tensor \mathbf{S} contains polytopic vertices F_i, H_i .

The polytopic linear model for (33.2) can be expressed as follows by applying the TP model transformation algorithm:

$$\begin{aligned} \Delta \dot{x} &= F \Delta x + B n_w \\ \Delta z &= H \Delta x + D n_w \end{aligned} \quad (33.8)$$

where, $(F, H) = \left\{ \sum_{i=1}^l \lambda_i (F_i, H_i) \mid \sum_{i=1}^l \lambda_i = 1 \right\}$

33.2.2 The New Filter

The system (33.8) can be expressed in the discrete form

$$\begin{aligned} \Delta x_{k+1} &= A \Delta x_k + B n_{wk} \\ \Delta z_k &= C \Delta x_k + D n_{wk} \end{aligned} \quad (33.9)$$

where, $A = I + F \cdot \Delta T$, $n_{wk} = [w_k^T \ v_k^T]^T$, w_k and v_k are the discrete process noise and the measurement noise at the moment k respectively, ΔT is the sample time for the discretization. It's evident that the matrix A belongs to an uncertain polytope $A = \left\{ \sum_{i=1}^l \lambda_i A_i \mid A_i = I_{N \times N} + F_i \cdot \Delta T, 0 < \lambda_i < 1, \sum_{i=1}^l \lambda_i = 1 \right\}$, C belongs to

$$C = \left\{ \sum_{i=1}^l \lambda_i C_i \mid C_i = H_i, 0 < \lambda_i < 1, \sum_{i=1}^l \lambda_i = 1, \right\}$$

Lemma 33.1 [7] Consider the system (33.9), a filter of the following form

$$\begin{aligned} \hat{x}_{mk+1} &= A_F \hat{x}_{mk} + B_F \Delta z_k \\ \Delta \hat{x}_k &= C_F \hat{x}_{mk} + D_F \Delta z_k \end{aligned} \quad (33.10)$$

that gives a suboptimal guaranteed filtering error covariance bound can be derived from the following optimization.

$$\begin{aligned}
& \min_{(G_{11}, G_{21}, G_2, F_{11}, F_{21}, S_A, S_B, S_C, S_D, P_{11i}, P_{12i}, P_{22i}, i=1 \dots N, \delta_1, \delta_2)} \text{trace}(Z) \\
& s.t. \left[\begin{array}{ccc} G_{11} + G_{11}^T - P_{11i} & G_2 + G_{21}^T - P_{12i} & \psi_{1i} \\ * & G_2 + G_{21}^T - P_{22i} & \psi_{2i} \\ * & * & \psi_{3i} \\ * & * & * \\ * & * & * \\ S_A - F_{21}^T & G_{11}B_i + S_B D_i & \\ S_A - \lambda_2 G_2^T & G_{21}B_i + S_B D_i & \\ \psi_{4i} & -F_{11}B_i - \delta_1 S_B D_i & \\ P_{22i} - \delta_2 S_A - \delta_2 S_A^T & -F_{21}B_i - \delta_2 S_B D_i & \\ * & I & \end{array} \right] > 0, \\
& \left[\begin{array}{ccc} Z & I - S_D C_i & -S_C & -S_D D_i \\ * & P_{11i} & P_{12i} & 0 \\ * & * & P_{22i} & 0 \\ * & * & * & I \end{array} \right] > 0, \quad i = 1, 2, \dots, l
\end{aligned} \tag{33.11}$$

where, $\psi_{1i} = G_{11}A_i + S_B C_i - F_{11}^T$, $\psi_{2i} = G_{21}A_i + S_B C_i - \delta_1 G_2^T$

$$\psi_{3i} = P_{11i} - F_{11}A_i - \delta_1 S_B C_i - A_i^T F_{11}^T - \delta_1 C_i^T S_B^T$$

$$\psi_{4i} = P_{12i} - \delta_1 S_A - A_i^T F_{21}^T - \delta_2 C_i^T S_B^T$$

The suboptimal filter is given by

$$A_F = G_2^{-1} S_A, B_F = G_2^{-1} S_B, C_F = S_C, D_F = S_D \tag{33.12}$$

Obviously, the justified equations with constant filter gain of the predicted error for the system (33.2) can be obtained by the robust H2 filtering and the covariance of the error system is minimum. Combined with the predicted equations of the EKF, the new CGEKF can be derived as follows:

One-step prediction:

$$\hat{x}_{k,k-1} = \hat{x}_{k-1} + f(\hat{x}_{k-1}) \cdot \Delta T \tag{33.13}$$

State estimation:

$$\hat{x}_k = \hat{x}_{k,k-1} + \Delta x_k \tag{33.14}$$

where, the justified quantity Δx_k for the state predicted error is obtain by (33.10).

33.3 Example Application

To illustrate the effectiveness of the proposed filter, a numerical simulation is conducted and the results are compared with the EKF.

The example in [8] is chosen for it has significant nonlinear property, the dynamic model of the system is

$$\begin{aligned} \dot{x}_1 &= 2x_1 \cos 4x_1 + x_2^2 + w_1 \\ \dot{x}_2 &= 3x_1 + x_2^3 \sin x_1 + w_2 \end{aligned} \tag{33.15}$$

where, w_1 and w_2 are zero-mean, uncorrelated noise with covariance given by $Q = \begin{bmatrix} 0.01 & 0 \\ 0 & 0.01 \end{bmatrix}$. And the measurement model can be presented as

$$z = x + v \tag{33.16}$$

where, $v = [v_1, v_2]$, v_1 and v_2 are uncorrelated observation noise with covariance $R = \begin{bmatrix} 0.01 & 0 \\ 0 & 0.01 \end{bmatrix}$.

The system (33.15) is implemented using the new filter and the EKF. Figures 33.1 and 33.2 show the comparison of steady estimation errors for the state x_1 and the state x_2 respectively.

The estimation errors converge over the time, implying that the new filter works well for the attitude estimation.

According to the statistics on the steady estimation errors shown in Table 33.1, the orders of the magnitude for the steady estimation errors in the two filters are both 0.001, and the steady estimation errors are nearly equal in the two filters, indicating that both of the two filters can estimate the state effectively. As

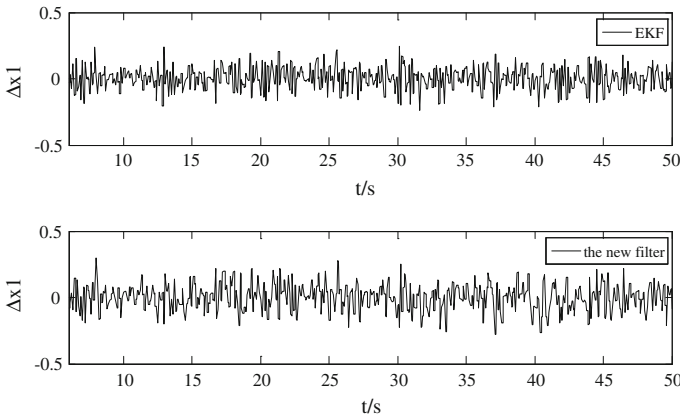


Fig. 33.1 Comparison of the steady estimate error in state x_1

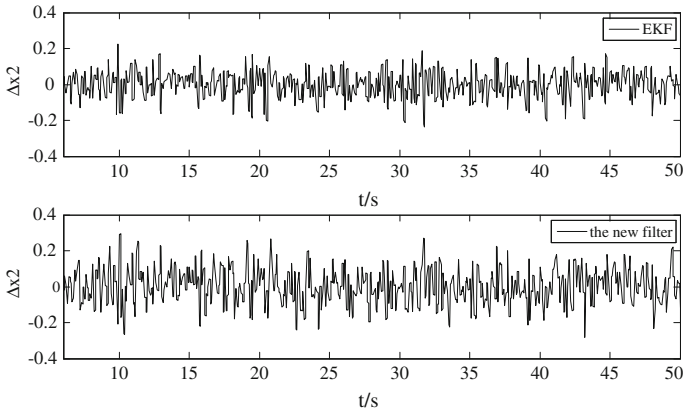


Fig. 33.2 Comparison of the steady estimate error in state x_2

Table 33.1 The steady error result of the two filters

	EKF		The new filter	
	Δx_1	Δx_2	Δx_1	Δx_2
Mean error value	0.0058	0.00056	0.0016	0.0013
Maximum absolute error	0.2452	0.2327	0.2985	0.2930

Table 33.2 Calculation comparison of the two filters

Calculation	EKF	The new filter
Addition	12	50
Multiplication	16	68

summarized in Table33.2, it s evident that the calculation number of the new filter is much less than that of the EKF.

We can conclude that the real-time performance of the new filter is much better than the EKF applied in nonlinear system estimation. In a word, the new filter should be preferred over the EKF in the virtually nonlinear filtering application with high real-time performance demand.

33.4 Conclusion

This paper develops a new CGEKF for the nonlinear system based on TP model transformation and the robust H2 filter algorithm. The complexity of the filter design is greatly reduced by transforming the nonlinear filtering design problem into linear filtering design problem. Moreover, the filter gain is constant without evaluating the Jacobian matrices on time and updating the filter gain on line, the

calculation number of the filter is decline much. Simulation results show that the proposed filter performs excellently in the nonlinear state estimations.

References

1. Crassidis JL, Markley FL, Cheng Y (2007) Survey of nonlinear attitude estimation methods. *J Guidance Control Dyn* 30(1):12–28
2. Bae J, Kim Y (2010) Satellite attitude determination and estimation using two star trackers. *Guidance, navigation, and control conference*, Toronto, Ontario, Canada
3. Qin Q (2006) The investigation of Kalman filter in radar target tracking arithmetic. PhD thesis, Dalian Maritime University. (in Chinese)
4. Li H, Wang TS, Zhang T et al (2009) H₂ gain scheduled filtering for polytopic discrete-time linear parameter-varying systems. *International conference on computer and automation engineering*, 31–35
5. Apkarian P, Gahinet P, Becker G (1994) Self-scheduled H_∞ control of linear parameter varying system. In: *Proceeding of the American control conference*, Baltimore, Maryland, 856–860
6. Baranyi P (2004) TP model transformation as a way to LMI-Based controller design. *IEEE Trans Ind Electron* 51(2):387–400
7. Duan ZHSH, Zhang JX (2006) Robust H₂ and H_∞ filtering for uncertain linear systems. *Automatia* 42:1919–1926
8. Li WQ (2009) Research and application of robust gain-scheduling based on LPV system. Doctor thesis, Graduate school of national university of defense technology, 39–41. (in Chinese)

Chapter 34

Spacecraft Attitude Control via New Non-Singular Fast Terminal Sliding Mode Control

Xin Lv, Zhen Chen, Xiangdong Liu, Binglong Cong and Liang Wang

Abstract In the final approach phase of rendezvous in space, the chaser attitude control system is expected to track the given attitude with high precision under the influences of disturbances. Furthermore, the attitude tracking mission is required to be completed in finite time. To satisfy those requirements, an attitude controller is presented by combining non-singular fast terminal sliding mode control (NFTSMC) with higher order sliding mode (HOSM) concept. The proposed controller contains two parts: one is used to achieve finite time stabilization of the higher order input–output dynamics without uncertainties; the other is made to reject the bounded uncertainties. By the virtue of HOSM, the chattering phenomenon can also be attuned. Numerical simulations are performed to verify the effectiveness of the proposed strategy.

Keywords Rendezvous · Attitude control · Finite time · Terminal sliding · Super-twisting

34.1 Introduction

In the final approach phase of RvD, the chase attitude control system is required to track the given attitude, such as the target's local vertical local horizontal (LVLH) frame in finite time in the presence of external disturbance and parameter variations with high accuracy.

X. Lv · Z. Chen (✉) · X. Liu · B. Cong · L. Wang
School of Automation, Beijing Institute of Technology, 5 South Zhongguancun Street,
Haidian District, Beijing 100081, China
e-mail: chenzhen76@bit.edu.cn

Sliding Mode Control (SMC) is well known for their robustness to system parameter variations and external disturbances. However, the proceeding SMC-based attitude control methods can only guarantee the attitude error converge to equilibrium points asymptotically. Due to the different time scales between orbit control system and attitude control system, the attitude control system for the chaser is expected to track to the given attitude as soon as possible. Fast terminal sliding mode control (FTSMC) has been widely used in controller designs [1, 2], which ensures fast transient convergence both at a distance from and at a close range of the equilibriums. However, it can suffer from singularity. According to the characteristic of FTSMC, [3] develops a new NFTSMC, which resolves the singularity problem of FTSMC completely.

The objective of this paper is to present a new methodology which can meet the requirements of finite time attitude tracking with high tracking precision for the final approach phase of autonomous rendezvous.

34.2 Mathematical Preliminaries

First, three coordinate frames used in this paper are introduced, where F_i , F_d and F_b stand for the inertial frame, the target LVLH frame, and the body-fixed frame of the chaser. No special instructions, all vector parameters are expressed in their corresponding coordinate systems.

The attitude dynamics of a thruster controlled rigid spacecraft is given by:

$$\widehat{J}_b \dot{\omega}_b + [\omega_b \times] \widehat{J}_b \omega_b = u + \Delta f \quad (34.1)$$

where $u \in R^3$ is control torque vector; $\omega_b = [\omega_{bx}, \omega_{by}, \omega_{bz}]^T \in R^3$ denotes the angular velocity vector F_b relative to F_i ; $\Delta f = f_d - \Delta J \dot{\omega}_b - [\omega_b \times] \Delta J \omega_b$ is the polymerization of inertial matrix uncertainties and external disturbances; ΔJ denotes the uncertainties of inertial matrix caused by the changes of the mass properties and \widehat{J}_b is the nominal inertial matrix; $[\omega \times]$ is skew-symmetric matrix [4].

The chief attitude kinematics in terms of Modified Rodrigues parameters (MRPs) is defined by:

$$\dot{\sigma}_b = M(\sigma_b) \omega_b \quad (34.2)$$

where the Jacobian matrix $M(\sigma_b)$ is

$$M(\sigma_b) = \frac{1}{4} [(1 - \sigma_b^T \sigma_b) I_3 + 2[\sigma_b \times] + 2\sigma_b \sigma_b^T] \quad (34.3)$$

Let σ_d and ω_d stand for the MRP of target's LVLH frame with respect to the inertial frame and the corresponding angular velocity expressed in F_d .

Supposing the target is in a free movement without any active control torque, the governing equations for its attitude motion is described by:

$$\begin{cases} J_d \dot{\omega}_d + [\omega_d \times] J_d \omega_d = 0 \\ \dot{\sigma}_d = M(\sigma_d) \omega_d \end{cases}$$

Then, attitude tracking error equation in the form of second order Euler-Lagrange equation [5]:

$$\ddot{\sigma}_e = \dot{M}(\sigma_e) \omega_e + M(\sigma_e) (-\dot{\omega}_d^b - \widehat{J}_b^{-1} [\omega_b \times] \widehat{J}_b \omega_b + \widehat{J}_b^{-1} u + \widehat{J}_b^{-1} \Delta f) \quad (34.4)$$

where $u = u_{eq} + u_1$.

Before moving on, some useful lemmas used in this paper are described as follows:

Lemma 34.1 [6] *Suppose $V(x)$ is a C^1 smooth positive-definite function (defined on $x \in \mathbb{R}^n$) and $\dot{V}(x) + \lambda V^o(x)$ is a negative semi-definite function on $U_0 \subset \mathbb{R}^n$ for $o \in (0, 1)$ and $\lambda \in \mathbb{R}^+$, then there exists an area such that any $V(x)$ which starts from $U_0 \subset \mathbb{R}^n$ can reach $V(x) \equiv 0$ in finite time:*

$$T_{reach} \leq \frac{V^{1-o}(x_0)}{\lambda(1-o)} \quad (34.5)$$

where $V(x_0)$ is the initial value of $V(x)$.

Lemma 34.2 [7] *Considering the following second-order system*

$$\begin{cases} \dot{\psi}_1 = -k_1 |\psi_1|^{1/2} \text{sgn}(\psi_1) + \psi_2 \\ \dot{\psi}_2 = -k_2 \text{sgn}(\psi_1) + \varepsilon(\psi, t) \end{cases} \quad (34.6)$$

where $|\varepsilon(\psi, t)| < L$, when the gains k_1, k_2 are appropriately selected, the states ψ_1, ψ_2 can converge to zero in finite time.

Remark 34.1 For clarity, define the following relationships

$$\begin{aligned} sig(\phi)^\kappa &= [|\phi_1|^{\kappa_1} \text{sgn}(\phi_1), |\phi_2|^{\kappa_2} \text{sgn}(\phi_2), |\phi_3|^{\kappa_3} \text{sgn}(\phi_3)]^T, \\ \phi^\kappa &= [\phi_1^{\kappa_1}, \phi_2^{\kappa_2}, \phi_3^{\kappa_3}]^T, \quad |\phi|^\kappa = [|\phi_1|^{\kappa_1}, |\phi_2|^{\kappa_2}, |\phi_3|^{\kappa_3}]^T \end{aligned}$$

Remark 34.2 In order to facility the analysis, it is assumed that the polymerization disturbances and its differential are bounded by the known constants, i.e., $|\Delta f| < f_{\max}$ and $|\dot{\Delta f}| < d_{\max}$.

34.3 Main Results

34.3.1 Nominal Controller Design

Non-singular fast terminal sliding function is [3].

$$s = \sigma_e + \alpha \text{sig}(\sigma_e)^v + \beta \text{sig}(\dot{\sigma}_e)^\gamma = 0 \quad (34.7)$$

where $\alpha = \text{diag}(\alpha_1, \alpha_2, \alpha_3)$ and $\beta = \text{diag}(\beta_1, \beta_2, \beta_3)$ with $\alpha_i, \beta_i > 0$, $v = [v_1, v_2, v_3]^T$ and $\gamma = [\gamma_1, \gamma_2, \gamma_3]^T$, $1 < \gamma_i < 2$, $v_i > \gamma_i (i = 1, 2, 3)$.

The time derivative of Eq. (34.7) is

$$\dot{s} = \dot{\sigma}_e + \alpha v |\sigma_e|^{v-1} \dot{\sigma}_e + \beta \gamma |\dot{\sigma}_e|^{\gamma-1} \ddot{\sigma}_e = 0 \quad (34.8)$$

Reference [3] has proved that the system states can converge to zeros in a finite time on NFTSM surface proposed in Eq. (34.7).

Firstly, considering the nominal system described by Eq. (34.9):

$$\ddot{\sigma}_e = \dot{M}(\sigma_e)\omega_e + M(\sigma_e)(-\dot{\omega}_d^b - \hat{J}_b^{-1}[\omega_b \times] \hat{J}_b \omega_b + \hat{J}_b^{-1} u_{eq}) \quad (34.9)$$

The nominal controller u_{eq} is designed as follows:

$$u_{eq} = [\omega_b \times] \hat{J}_b \omega_b + \hat{J}_b \dot{\omega}_d^b - \hat{J}_b M^{-1}(\sigma_e) \dot{M}(\sigma_e) \omega_e - \hat{J}_b M^{-1}(\sigma_e) \frac{1}{\beta \gamma_2} \text{sig}(\dot{\sigma}_e)^{2-\gamma_2} \left(1 + \alpha \gamma_1 |\sigma_e|^{\gamma_1-1} \right) - \hat{J}_b M^{-1}(\sigma_e) (k \text{sgn}(s)) \quad (34.10)$$

where $k > 0$. Then the following theorem can be obtained.

Theorem 34.1 *For the nominal attitude tracking system characterized by Eq. (34.9), the nominal control law with the form of Eq. (34.10) is designed, the attitude error can converge to zeros in finite time. Moreover, no occurring of singularity is ensured during the whole process.*

Proof Considering the Lyapunov function as

$$V_1 = \frac{1}{2} s^T s \quad (34.11)$$

Taking the time derivative of Eq. (34.11), combining with Eq. (34.8), Eq. (34.9) and Eq. (34.10) one can have:

$$\begin{aligned} \dot{V}_1 &= s^T \dot{s} = s^T \left(\dot{\sigma}_e + \alpha v |\sigma_e|^{v-1} \dot{\sigma}_e + \beta \gamma |\dot{\sigma}_e|^{\gamma-1} \ddot{\sigma}_e \right) \\ &= -K_1 \beta \gamma \dot{V}_1 < -\rho(\dot{\sigma}_e) V_1^{1/2} \end{aligned} \quad (34.12)$$

where $\rho(\dot{\sigma}_e) = \sqrt{2} K_1 \beta \gamma |\dot{\sigma}_e|^{\gamma-1}$. It can be derived that when $\dot{\sigma}_e \neq 0$, $\rho_1 > 0$, and thus from lemma 34.1, the system states will move fast to the sliding mode within

finite time. Then considering the case $\dot{\sigma}_e = 0$, and substituting Eq. (34.10) into Eq. (34.9), Eq. (34.9) turns to be

$$\ddot{\sigma}_e = -K_1 \text{sgn}(s) \quad (34.13)$$

Reference [8] proves that the form of Eq. (34.13) has the quality of fast convergence around zeros. Besides, as the use of NFTSM proposed in Eq. (34.7), So one can conclude that the nominal system Eq. (34.9), with the control of Eq. (34.10), the system states can converge to zero fast without any singularity occurring. The proof is complete.

34.3.2 Disturbance Resistant Control Law

Now considering the system determined by Eq. (34.4), the disturbances resistant control law is designed based on super-twisting [7] algorithm as follows:

$$\begin{aligned} u_1 &= -\lambda |s|^{1/2} \text{sgn}(s) + \vartheta \\ \dot{\vartheta} &= -W \text{sgn}(s) \end{aligned} \quad (34.14)$$

where $\lambda > d_{\max}$, $W > 0$.

Theorem 34.2 *Considering the system Eq. (34.4), via the control law determined by Eq. (34.14), the system states can reach the sliding mode surface in finite time and on which resist the disturbances effectively without chattering occurring.*

Proof Suppose $\tau_1 = s$, $\tau_2 = -W \int \text{sgn}(s) + \Delta f$, then Eq. (34.14) turns to:

$$\begin{cases} \dot{\tau}_1 = \tau_2 - \lambda |\tau_1|^{1/2} \text{sgn}(\tau_1) \\ \dot{\tau}_2 = -W \text{sgn}(\tau_1) + \Delta f \end{cases} \quad (34.15)$$

where $|\Delta \dot{f}| < d_{\max}$ is bounded.

According to lemma 34.2, when λ, W are suitable selected, the states τ_1, τ_2 can converge to zero in finite time. So we have:

$$\dot{\tau}_1 = \dot{s} = u_1 + \Delta f = 0 \quad (34.16)$$

Thus, the theorem 34.2 is proved.

So from the analysis presented above, we can conclude for the attitude tracking control system characterized by Eq. (34.4), by choosing sliding mode function with the form of Eq. (34.7), and attitude control law determined by Eq. (34.9) and Eq. (34.14), attitude tracking error can converge to 0 in finite time in the presence of unknown polymerization disturbances upper bounds without chattering phenomenon.

34.4 Numerical Simulation

To verify the effectiveness of the designed attitude controller in this paper, numerical simulation is conducted in this section. Simulation parameters are as follows:

Target spacecraft: the initial angle velocity $\omega_d(t_0) = [0.2, 0.2, 0.2]^T/s$; the initial MRPs attitude $\sigma_d(t_0) = [-0.01, 0.022, -0.01]^T$; the inertia matrix $J_d =$

$$\begin{bmatrix} 301.21.5 \\ 1.2341.7 \\ 1.51.738.5 \end{bmatrix} \text{kg} \cdot \text{m}^2$$

Chaser spacecraft: the initial angle velocity $\omega_b(t_0) =$

$[3, -3, 6]^T/s$, the initial MRPs attitude $\sigma_b(t_0) = [0.5, -0.8, 0.6]^T$; the nominal

inertia matrix $\hat{J}_b = \begin{bmatrix} 93.4 & 14.9 & -1.2 \\ 14.9 & 35.8 & -7.3 \\ -1 & -7.3 & 80.5 \end{bmatrix} \text{kg} \cdot \text{m}^2$, and uncertainty ΔJ is 10% of

nominal inertia matrix; external disturbance $f_d = [1 \ 2 \ 1]^T * \sin(t) (\text{N} \cdot \text{m})$. Controller parameters: $\alpha = \text{diag}(1, 1, 1)$, $\beta = \text{diag}(3, 3, 3)$, $v = [2.1, 2.1, 2.1]^T$, $\gamma = [1.2, 1.2, 1.2]^T$, $W = 0.1$, $\lambda = 1$, $K = 0.5$. The simulation results are illustrated as follows:

The simulation plots presented below demonstrate the good performance of fast and high-precision tracking with the proposed scheme which based on NFTSM and super-twisting. Figure 34.1 shows the sliding mode motion is established in finite time. From Fig. 34.4, it is noticed that neither singularity nor chattering

Fig. 34.1 Time history of sliding mode

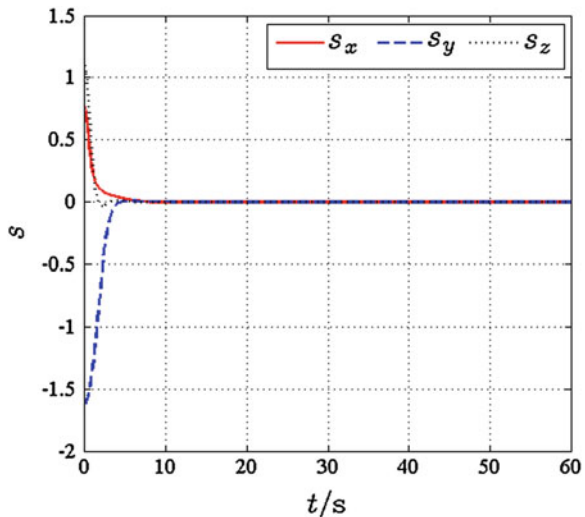


Fig. 34.2 Time history of MRPs attitude error

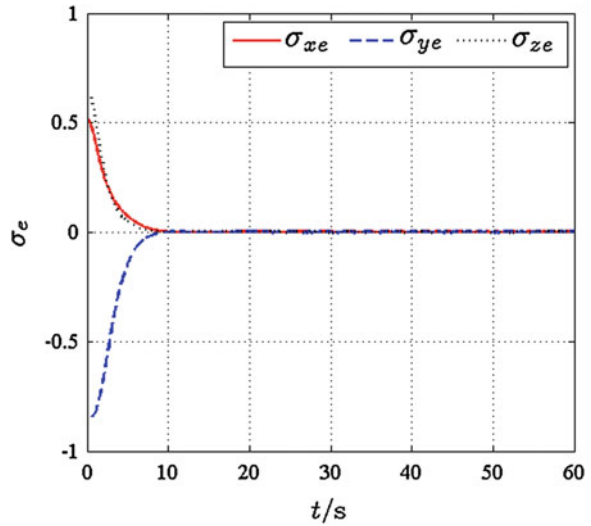
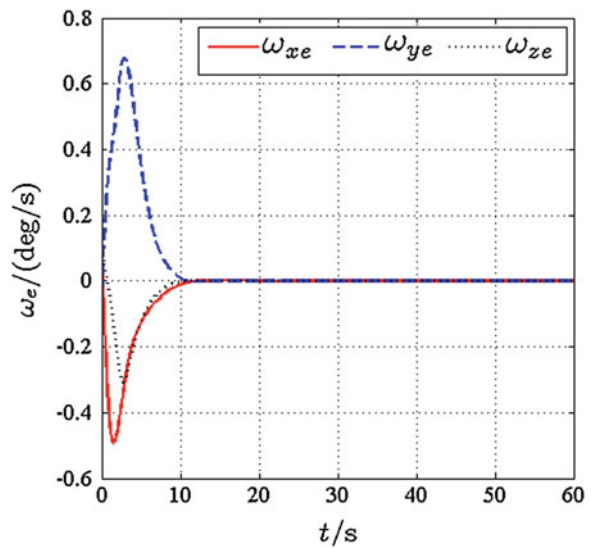
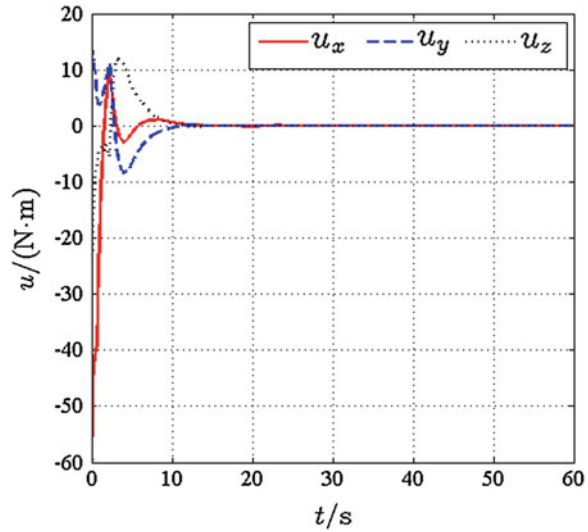


Fig. 34.3 Time history of attitude angle velocity error



occurs during the whole response. So it is more suitable for engineering application. From Figs. 34.2 and 34.3, one can see the MRPs attitude errors and attitude velocity errors converge to zero on the sliding manifold with limited time.

Fig. 34.4 Time history of control torque



34.5 Conclusion

A robust attitude tracking controller for rigid spacecraft is proposed in this article. To meet the requirement to fast response and high accuracy on the attitude control of final approach in rendezvous. The controller consists two parts: a nominal controller based on NFTSMC technology is used to drive the nominal system states to equilibrium points in finite time; and another part, with the utilizing of super-twisting strategy, is to resist disturbances and counteract chattering with high accuracy. Simulation results indicate the controller proposed in this paper is effective.

References

1. Yu XH, Man ZH (2002) Fast terminal sliding-mode control design for nonlinear dynamical systems. *IEEE Trans Circ Sys* 49:263–264
2. Yu X, Man Z (2000) Fast terminal sliding mode control for single input systems. In: *Proceedings of 2000 Asian control conference*, Shanghai, China
3. Yang L, Yang JY (2001) Nonsingular fast terminal sliding-mode control for nonlinear dynamical systems. *Int J Robust Nonlinear Control* 21:1865–1879
4. Cong BL, Liu XD, Chen Z (2010) Exponential time-varying sliding mode control for large angle attitude Eigenaxis maneuver of rigid spacecraft. *Chinese J Aero* 23:447–453
5. Du HD, Li SH, Qian CJ (2011) Finite-time attitude tracking control of spacecraft with application to attitude synchronization. *IEEE Trans Automat Contr* 56(11):2711–2717
6. Hardy GH, Littlewood JE, Polya G (1952) *Inequalities*. Cambridge University Press, Cambridge

7. Moreno JA, Osorio M (2012) Strict lyapunov functions for the super-twisting algorithm. *IEEE Trans Automat Contr* 57(4):1035–1040
8. Feng Y, Yu X, Man Z (2002) Non-singular adaptive terminal sliding mode control of rigid manipulators. *Automatica* 38(12):2159–2167

Chapter 35

Time-Variant Gait Planning for Under-Actuated Biped Robot via Optimization

Xiaowei OuYang, Gang Pan and Ling Yu

Abstract The objective of this paper is to obtain time-variant optimal gaits for under-actuated biped robot via optimization. A time-variant gait planning method based on genetic algorithm is proposed in this paper. The reference trajectories of the actuated joints are defined as polynomial functions of time t . The trajectory of the under-actuated joint can be deduced from the rotational dynamics of the biped. To get the coefficients of the polynomial functions, optimization method based on genetic algorithm is adopted and minimal torque cost is chosen as the optimize criteria. Various low torque cost gaits can be obtained by considering different constraints during optimization. Simulation results illustrate the efficiency of our method.

Keywords Under-actuated biped robot · Time-variant gait planning · Genetic algorithm optimization

35.1 Introduction

Much work has been devoted to the research of biped robot. Biped robot can be mainly divided into two classes [1]: fully actuated robot [2], limit cycle robot. Limit cycle robot includes passive robot [3], semi-passive robot [4] and under-actuated robot [5, 6]. Under-actuated robot takes advantage of the passive performance of its own, because of which it costs lower energy and is faster than fully actuated robot while has better stability and is easier to control than passive robot. As reference gait directly affects the stability, energy cost, speed of robot motion,

X. OuYang (✉) · G. Pan · L. Yu
Department of Control Science and Engineering, Zhejiang University,
New Industrial Control Building 417, Hangzhou, China
e-mail: ouyangxiaowei2009@163.com

gait planning is a crucial part of the study of biped robot. Therefore, we focus on gait planning for under-actuated biped robot in this paper.

Methods usually used for gait planning are: time-invariant gait planning via optimization [7, 8], gait planning via the imitation of human walking [9], gait planning based on neural network and learning algorithm [10, 11]. Among them, gait planning via the imitation of human walking produces subhuman gaits but needs the data of human walking and has constraints on robot model. Gait planning based on neural network and learning algorithm simulates the decision-making ability of human brain, because of which it has good adaptability to the environment. However, it is difficult to realize and the learning process costs quite a long time. Both gait planning based on neural network and time-invariant gait planning are combined with control, namely, only the control is realized can we get the specific gaits. To avoid this, we propose time-variant gait planning [12] via optimization in this paper. The trajectories of actuated joints are defined as polynomial functions of time t and the trajectory of under-actuated joint is deduced from the rotational dynamics of the robot. Coefficients of the polynomial functions are obtained by optimization. Optimization methods usually used include genetic algorithm, particle swarm optimization algorithm, simulated annealing algorithm and so on. Among them, genetic algorithm searches for optimal solution by imitating the process of natural evolution. It starts with a set of solutions, instead of a single solution, of the problem, which makes it more effective and easier to get the global best solution. Therefore, we choose genetic algorithm as our optimization method.

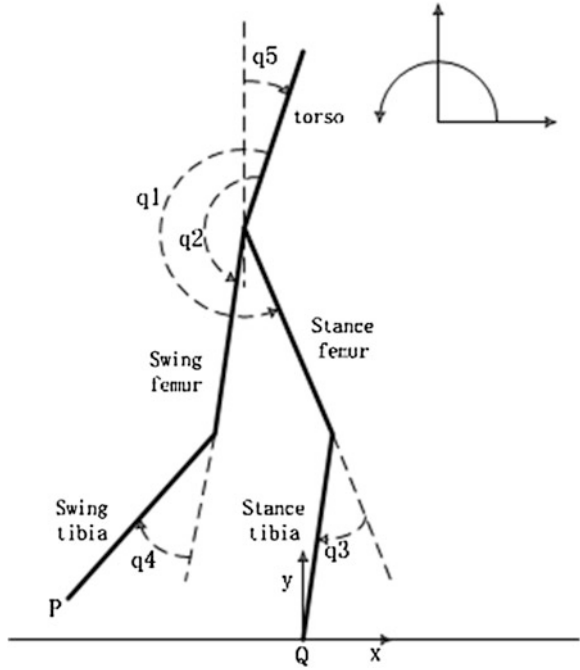
[Section 35.2](#) mainly introduces the dynamic model of the biped robot. [Section 35.3](#) presents gait designing and optimization based on genetic algorithm. [Section 35.4](#) shows simulation results. [Section 35.5](#) summaries this paper.

35.2 Dynamic Model of Biped Robot

Our biped robot consists of a torso, two identical femurs and two identical tibias. There are two actuators in hip joint and another two in knee joints but no actuator between stance tibia and the ground. It is a five-link, four-actuator under-actuated robot and has point-foot with the ground. The configuration of the robot can be determined by five angle variables, namely the absolute angle of the torso, q_5 , and four relative joint angles, q_1 , q_2 , q_3 , q_4 . As shown in [Fig. 35.1](#), where P, Q represent the tip of swing leg and stance leg respectively. A Cartesian coordinate frame is constructed and anticlockwise direction is chosen as the positive direction for angles.

The robot walks in xy plain and its motion is composed of successive single support phases and instantaneous double support phases. During single support phase, stance leg acts as a pivot and swing leg swings from behind to the front in the air. During double support phase, namely, the impact moment, both stance leg and swing leg are in contact with the ground.

Fig. 35.1 The robot model



According to the Lagrangian dynamics, the motion equation of the robot in single support phase can be written as:

$$D(q)\ddot{q} + C(q, \dot{q})\dot{q} + G(q) = Bu \tag{35.1}$$

where, D is the inertia matrix, C is the matrix of centripetal and Coriolis terms, G is the matrix of gravity terms, B describes the effects of actuators on the joint angles, $q = (q_1, q_2, q_3, q_4, q_5)'$ is the joint angles, $u = (u_1, u_2, u_3, u_4)'$ is the torques generated by servomotors. Let $x = (q, \dot{q})'$, we can transfer Eq. (35.1) to state space form:

$$\dot{x} = f(x) + g(x)u \tag{35.2}$$

where $f(x) = \begin{bmatrix} \dot{q} \\ D^{-1}(q)(-C(q, \dot{q})\dot{q} - G(q)) \end{bmatrix}, g(x) = \begin{bmatrix} 0 \\ D^{-1}(q)B \end{bmatrix}.$

Double support phase is the moment when swing leg collides with the ground. We assume that the impact is perfectly inelastic impact and results in no rebound and no slipping of the swing leg. After impact, the joint angles of the robot remain unchanged while velocities change instantaneously. The impact model can be written as [13]:

$$x^+ = \Delta(x^-) \tag{35.3}$$

where $x^- = (q^-, \dot{q}^-), x^+ = (q^+, \dot{q}^+)$ stand for the state just before and after impact respectively, Δ is the mapping matrix.

According to Eqs. (35.2) and (35.3), the overall dynamic model of the robot can be expressed as a nonlinear hybrid model:

$$\begin{cases} \dot{x} = f(x) + g(x)u, & x^- \notin S \\ x^+ = \Delta(x^-), & x^- \in S \end{cases} \quad (35.4)$$

where $S = \{(q, \dot{q}) | p_v = 0, p_h > 0\}$ is the switching set of impact.

35.3 Gait Planning and Optimization

35.3.1 Design of Active Joint Angles

Polynomial functions in terms of time t is used to express actuated joint angles q_1, q_2, q_3, q_4 . To guarantee the continuity and periodicity of the gait, the joint angles and angular velocities at the beginning and end of each phase must be taken into account. Therefore, third-order polynomial functions are needed at least. In some cases, this minimal order may lead to unexpected collision of the swing leg and the ground. To avoid this, we choose fourth-order polynomial functions:

$$q_j(t) = a_{j0} + a_{j1}t + a_{j2}t^2 + a_{j3}t^3 + a_{j4}t^4, j = 1, \dots, 4 \quad (35.5)$$

Let T denote the duration of half step. Then the coefficients of the polynomial functions can be uniquely determined by $q_{ai}, \dot{q}_{ai}, q_{al}, \dot{q}_{al}, q_{aint}, T$, where q_{ai}, \dot{q}_{ai} and q_{al}, \dot{q}_{al} represent actuated joint angles, joint angular velocities at the beginning ($t = 0$) and the end ($t = T$) of the single support phase, respectively. q_{aint} is the actuated joint angles at the middle ($t = T/2$) of single support phase.

35.3.2 Evolution of the Passive Joint Angle

Under-actuated joint angle can't be directly defined as polynomial functions of t , because once actuated joint angles are determined, under-actuated joint angle is determined in some way.

Let σ denote the total angular momentum of the robot around the stance leg tip Q , it can be written as:

$$\sigma = F_1(q_a(t), q_u(t))\dot{q}_u(t) + F_2(q_a(t), q_u(t))\dot{q}_a(t) \quad (35.6)$$

where $q_a(t), q_u(t)$ represent the actuated joint angles and the under-actuated joint angle respectively. For the robot, the external forces are the force of gravity and ground reaction force applied on Q . Torque around Q generated by ground reaction force is zero. Therefore, the total external torque τ_{ext} around Q can be written as:

$$\tau_{ext} = -Mgx_{mc}(q_a(t), q_u(t)) \quad (35.7)$$

where M is the mass of the robot, x_{mc} is the abscissa of the mass center.

According to rotational dynamics, the rate of angular momentum equals the total external torques, namely, $\dot{\sigma} = \tau_{ext}$. Then, from Eqs. (35.6) and (35.7), we obtain:

$$\ddot{q}_u = F(q_u, \dot{q}_u, q_a, \dot{q}_a) \quad (35.8)$$

If the initial state of the under-actuated joint angle q_{ui} and angular velocity \dot{q}_{ui} are known, we can get its trajectory $q_u(t), \dot{q}_u(t)$ by integrating Eq. (35.8).

35.3.3 Constraints Analysis

So far, we have got the definition of actuated joint angles and evolution of under-actuated joint angle and we need the following parameters: $q_{ai}, \dot{q}_{ai}, q_{al}, \dot{q}_{al}, q_{aint}, T, q_{ui}, \dot{q}_{ui}$. In fact, they are not independent. This section mainly analyses the constraints for the parameters. By this analysis we can diminish the number of the needed parameters and get the nonlinear constraints, which will be considered in optimization.

At both the beginning and the end of single support phase, the legs of the robot are in contact with ground, so:

$$\begin{cases} l_t \cos(q_{ai2} + q_{ai4} + q_{ui}) + l_f \cos(q_{ai2} + q_{ui}) = l_f \cos(q_{ai1} + q_{ai5}) \\ \quad + l_t \cos(q_{ai1} + q_{ai3} + q_{ui}) \\ l_t \cos(q_{al2} + q_{al4} + q_{ul}) + l_f \cos(q_{al2} + q_{ul}) = l_f \cos(q_{al1} + q_{al5}) \\ \quad + l_t \cos(q_{al1} + q_{al3} + q_{ul}) \end{cases} \quad (35.9)$$

where l_t, l_f represent the length of tibia and femur respectively.

In fact, $q_i = (q_{ai}, q_{ui})', q_l = (q_{al}, q_{ul})'$ are the joint angles at the beginning and end of single support phase respectively and $\dot{q}_i = (\dot{q}_{ai}, \dot{q}_{ui})', \dot{q}_l = (\dot{q}_{al}, \dot{q}_{ul})'$ are the joint angular velocities at the beginning and end of single support phase respectively. According to Eq. (35.3), we obtain:

$$x_i = \Delta(x_f) \quad (35.10)$$

where $x_i = (q_i, \dot{q}_i)', x_f = (q_f, \dot{q}_f)'$.

Through the analysis above, to get reference gait, we only need fourteen parameters: $q_{al1}, q_{al2}, q_{al3}, \dot{q}_{al}, q_{aint}, q_{ul}, \dot{q}_{ul}, T$. However, these parameters are still not independent. $q_u(t), \dot{q}_u(t)$ are obtained by integrating Eq. (35.12). Among the parameters, q_{ul}, \dot{q}_{ul} represents the state of the under-actuated joint angle and angular velocity at $t = T$ respectively. So two constraints for the parameters:

$$\begin{aligned} q_u(T) &= q_{ul} \\ \dot{q}_u(T) &= \dot{q}_{ul} \end{aligned} \quad (35.11)$$

In addition, to guarantee the validity of the gait, the following constraints must be satisfied:

1. The ground reaction force at impact moment must be directed upward, namely, $F^N > 0$.
2. The ratio between the horizontal component and vertical component of the ground reaction force must be less than the friction coefficient, namely, $F^T/F^N < \mu$, where μ is the friction coefficient of the ground.
3. The swing leg tip must be above ground before the impact, namely, $y_{swingleg}(q_a(t)) > 0, T > t > 0$.

To get diverse gaits, some constraints related to velocity or step length are set. For example, if gaits with velocity near 0.6 m/s are needed, constraint $0.58 < \frac{L}{T} < 0.62$ (where L represents the step length) is set. Thus, low energy gaits with different velocity or step length are obtained. As these constraints are inequality constraints or nonlinear equality constraints, the number of needed parameters can't be diminished any more. They will be considered in optimization.

35.3.4 Optimization Via Genetic Algorithm

The gait planning problem can be concluded as an optimization problem with constraints. We choose genetic algorithm as the optimization method because of its efficiency and low possibility to fall into local minimum value.

Torque cost, which is defined as the integral of the norm of the torque for one meter, namely,

$$C_{tc} = \frac{\int_0^T \Gamma' \cdot \Gamma dt}{L} \quad (35.12)$$

is considered as the optimize criteria.

Fitness function is quite important in genetic algorithm as it directly determines the selection of individuals in next generation. Taking the constraints into account, we define the fitness function as:

$$fitness = \frac{c}{C_{tc}} + \sum_{i=1}^n p_i \quad (35.13)$$

where c is a constant, n is the number of constraints and p_i represents the penalty related to constraint i . Thus, parameters which can't satisfy the constraints will die

out along with evolution and parameters which not only satisfy the constraints but also get low torque cost will be kept to the last generation.

35.4 Simulation

In this paper, the same model parameters with robot Rabbit [14] are adopted, as shown in Table 35.1 Simulation of gait planning is done on Matlab. Table 35.2 shows the parameters of genetic algorithm, where NP stands for population size, NG stands for times of generation, Pc represents the probability of cross, Pm represents the probability of variation and eps represents the precision of gait parameters. Table 35.3 shows the range of gait parameters.

Several gaits with different velocity are obtained by setting different velocity constraint. Velocity, step length, cycle of each gait is shown in Table 35.4. Figure 35.2 depicts the stick diagram of Gait3. Figure 35.3 shows the joint trajectories of Gait3. This result directly proves the efficiency of the proposed gait planning method.

Table 35.1 Parameters of the robot

Links	Torso	Femur	Tibia
Mass in kg	12	6.8	3.2
Length in m	0.625	0.4	0.4
Mass center in m	0.24	0.11	0.24
Inertia in $\text{kg} \cdot \text{m}^2$	1.33	0.47	0.20

Table 35.2 Parameters of genetic algorithm

NP	NG	Pc	Pm	eps
500	800	0.9	0.04	0.0001

Table 35.3 Range of optimization parameters

q_{al1}	q_{al2}	q_{al3}	\dot{q}_{al1}	\dot{q}_{al2}	\dot{q}_{al3}	\dot{q}_{al4}
[3, 3.6]	[3.6, 4.2]	[-0.6, 0.1]	[-10, 10]	[-10, 10]	[-10, 10]	[-10, 10]
q_{aint1}	q_{aint2}	q_{aint3}	q_{aint4}	q_{ul}	\dot{q}_{ul}	T
[3, 4.2]	[3, 4.2]	[-1, 1]	[-1, 1]	[-0.5, 0]	[-10, 10]	[0.4, 1]

Table 35.4 Properties of gaits with different velocity

Index	Gait1	Gait2	Gait3	Gait3
Velocity in m/s	0.6774	0.7601	0.9532	1.3729
Step length in m	0.5312	0.5450	0.6825	0.9224
Cycle in s	0.7843	0.7164	0.7160	0.6719

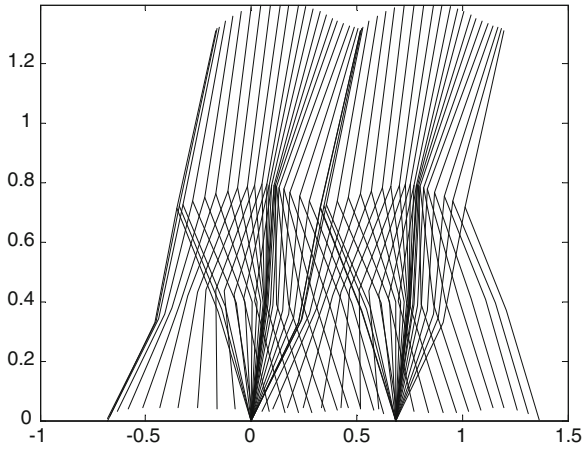


Fig. 35.2 Stick diagram of gait3

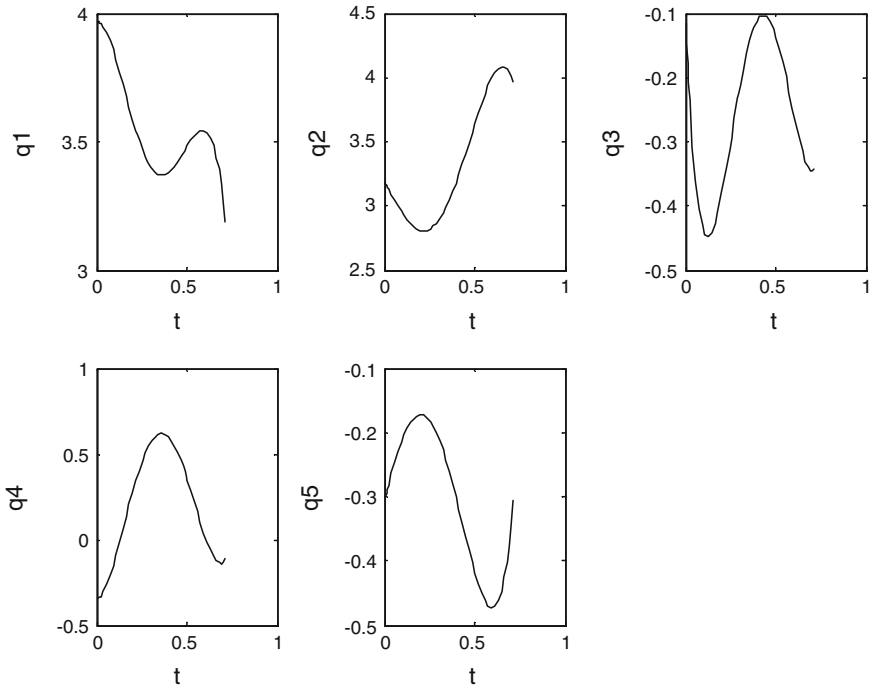


Fig. 35.3 Optimal reference trajectories

Table 35.5 Optimal parameters

q_{al1}	q_{al2}	q_{al3}	\dot{q}_{al1}	\dot{q}_{al2}	\dot{q}_{al3}	\dot{q}_{al4}
3.3690	3.7906	-0.5993	-3.8273	-5.5156	-1.4176	6.0827
q_{aint1}	q_{aint2}	q_{aint3}	q_{aint4}	q_{ul}	\dot{q}_{ul}	T
3.4303	3.4137	-0.3030	-0.3238	-0.2216	2.2520	0.7164

Table 35.6 Torque cost comparison

	Velocity in m/s	Torque cost in N ² ms
Reference [12]	0.750	871
This paper	0.761	653.7

To compare with Ref. [12], velocity is set near 0.75 m/s and the optimal parameters are shown in Table 35.5. A comparison about torque cost between this paper and Ref. [12] is conducted in Table 35.6. Obviously, with nearly the same velocity, gait in this paper has lower torque cost.

35.5 Conclusion

Optimal cyclic reference trajectories for walking of under-actuated biped robot are proposed in this paper. The reference trajectories of actuated joint angles are defined as polynomial functions of time. Reference trajectory of under-actuated joint angle is deduced from rotational dynamics. Several constraints to guarantee the validity of the gait are considered. Method based on genetic algorithm is adopted and low torque cost is chosen as optimize criteria to get optimal gait parameters. Velocity of the robot can be controlled by adding a constraint to the optimization process. Various optimal gaits can be got with different velocities. Simulation results show the efficiency of our method.

References

1. Xiong YY (2012) Research on walking control for under-actuated planar biped robot, (in Chinese)
2. Furuta T, Shimomura M, Tawara T, Endo K, Okumura Y, Shimizu M, et al (2003) In: Muscato G, Longo D (eds) Realtime ZMP compensation for humanoid robot ‘morph3’ using adaptive inertia force control. Professional Engineering Publishing Ltd, Westminster, pp 171–179
3. Spong MW, Holm JK, Lee D (2007) Passivity-based control of bipedal locomotion: regulating walking by exploiting passive gaits in 2-D and 3-D bipeds. IEEE Robot Autom Mag 14(2):30–40. PubMed PMID: WOS:000247833500007. English

4. Anderson SO, Wisse M, Atkeson CG, Hodgins JK, Zeglin GJ, Moyer B (eds) (2005) Powered bipeds based on passive dynamic principles. *Humanoid robots, 2005 5th IEEE-RAS international conference on*; 2005 5–5
5. Chevallereau C, Formal'sky A, Djoudi D (2004) Tracking a joint path for the walk of an underactuated biped. *Robotica*. 2004 Jan–Feb 22:15–28. English
6. Chemori A, Loria A (eds) (2004) Walking control strategy for a planar under-actuated biped robot based on optimal reference trajectories and partial feedback linearization. In: *Robot motion and control, 2004 RoMoCo'04 proceedings of the fourth international workshop, 17–20 June 2004*
7. Westervelt ER, Grizzle JW (eds) (2002) Design of asymptotically stable walking for a 5-link planar biped walker via optimization. In: *Robotics and automation, 2002 proceedings ICRA '02 IEEE international conference on 2002*
8. Fu CL, Chen K (2006) Gait planning and nonlinear control of dynamic walking for a five-link, four-actuator, planar biped robot. *Robot* 28:7 (in Chinese)
9. Zeyang X, Guodong C, Zhenzhong J, Jing X, Chen K (eds) (2009) Human walking capture and its inspiration to biped gait planning. *Mechatronics and Automation, 2009 ICMA 2009 International Conference 9–12 Aug 2009*
10. Kurcmatsu Y, Katayama O, Iwata M, Kitamura S (eds) (1991) Autonomous trajectory generation of a biped locomotive robot. In: *Neural networks, 1991 IEEE international joint conference 18–21 Nov 1991*
11. Sabourin C, Bruneau O, Buche G (2005) IEEE. Experimental validation of a robust control strategy for the robot RABBIT. In: *2005 IEEE international conference on robotics and automation. IEEE International conference on robotics and automation. IEEE, New York, pp 2393–2398*
12. Chevallereau C, Aoustin Y (2001) Optimal reference trajectories for walking and running of a biped robot. *Robotica*. 2001 Sep–Oct;19:557–69. PubMed PMID: WOS:000171492800009. English
13. Grizzle JW, Abba G, Plestan F (2001) Asymptotically stable walking for biped robots: Analysis via systems with impulse effects (vol 46, pg 51, 2001). *IEEE Trans Autom Control* 46(3):513. PubMed PMID: WOS:000167658000025. English
14. Chevallereau C, Abba G, Aoustin Y, Plestan F, Westervelt ER, Canudas-de-Wit C et al (2003) RABBIT: a testbed for advanced control theory. *IEEE Control Syst* 23(5):57–79

Chapter 36

Immune Network Risk Evaluation Model Based on the Spreading of Infectious Diseases

Jin Yang, Tang Liu and Lingxi Peng

Abstract From the mechanism of infectious epidemic spreading, the theory of network epidemic spreading was studied in this paper. The process of the developments and changes of the network intrusion behaviors were analyzed, and an improved network situation awareness model on the basis of the immunity was created, which is based on the SIR model. The concepts and formal definitions of immune cells are given, and dynamically evaluative equations for self, immune tolerance and immune memory are presented, distributed management framework of the proposed model are built. An improved epidemic spreading model was proposed to study the mechanisms of aggressive behaviors spreading, to predict the future course of an outbreak and to evaluate strategies to control a network epidemic. Experimental results show that the proposed model has the features of real-time processing for network situation awareness and can improve the ability of intrusion detection.

Keywords Network security · Artificial immune systems · SIR

J. Yang

School of Information Science and Technology, Southwest Jiaotong University,
Chengdu, China
e-mail: jinnyang@163.com

J. Yang

Department of Computer Science, LeShan Normal University, LeShan 614000, China

T. Liu (✉)

College of Computer Science, Sichuan University Chengdu, Chengdu 610065, China
e-mail: bigluckboy@163.com

L. Peng

Department of Computer and Education Software, Guangzhou University,
Guangzhou, China

36.1 Introduction

Network security issues have become increasingly prominent with the rapid development of Information technology. Network security technology is playing a crucial role of protecting of personal privacy, ensuring economic development, maintaining social stability, and safeguarding national security. The traditional network security approaches include virus detection, frangibility evaluation, and firewall etc., e.g., the Intrusion Detection System [1]. They rely upon collecting and analyzing the viruses' specimens or intrusion signatures with some traditional techniques. The problems in the field of computer security and Artificial Immune Systems have the astonishing similarity of keeping the system stable in a continuous changing environment [2, 3]. Artificial Immune System can use biological immune theoretic for references to search and design relevant models and algorithms to solve the various problems occurred in the field of computer security. Based on the correspondence between the artificial immune system antibody in the artificial immune systems and pathogen invasion intensity, this paper is to establish a network security evaluation model for network security situational awareness.

36.2 Network Epidemic Spreading Dynamics Model

The Susceptible, Infected and Recovered epidemic model (SIR) was proposed by Willam Kermack and McKendrick in 1927, which the infectivity of an individual depends on the time [4–6]. This model can effectively study these diseases which acquired immunity after have been treated, such as smallpox, influenza, hepatitis, measles and other infectious diseases. Here we introduce the model to create and study network security model, since between network intrusion and infectious disease have many similarities.

36.2.1 Network Epidemic Spreading Model Base on SIR

We introduced the infectious disease model to study the spread of network intrusion and need to make the following assumptions. And we assume that network intrusion behaviors spread through contact or close proximity between infected and healthy hosts [7].

Do not take these factors into account such as increasing, decreasing and changing in network intrusion surveillance area. We assume that the total number of hosts $N(t)$ is constant.

Let $s(t)$ be susceptible host which is the number of susceptible hosts. Initially, host is susceptible to infection: no pathogen is present; just a low-level nonspecific

immunity within the host. Let $i(t)$ be infective hosts, which is the number of infected hosts. Host encounters infectious host and becomes infected with a zombie computer.

Let λ represent the rate an infected individual gives rise to new infections. When normal information points effective contact with infected, normal information points become infected points, then

$$N \frac{di}{dt} = \lambda N s i \quad (36.1)$$

there holds

$$s(t) + i(t) = 1 \quad (36.2)$$

Let $i(0)$ be the initial rate of infected hosts. We have

$$\begin{cases} \frac{di}{dt} = \lambda i(1 - i) \\ i(0) = i_0 \end{cases} \quad (36.3)$$

Solving the Logistic equations, we obtain

$$i(t) = \left[1 + \left(\frac{1}{i_0} - 1 \right) e^{-\lambda t} \right]^{-1} \quad (36.4)$$

When $i = 1/2$, $\frac{di}{dt}$ reached the maximum value. It indicates that the spreading of infection is the strongest at this time. We can easily conclude that when $t \rightarrow +\infty$, $i \rightarrow 1$. It indicates that all of the nodes will eventually be infected and all of the hosts will become to Zombie computers. But this does not conform to the actual situation. Considering that some of hosts have self recovery abilities, called rehabilitation hosts, we introduce the Susceptible, Infective, and Recovered (SIR) model [8] to study the strong immune capability network security model.

Let $r(t)$ be recovered host: The host is either no longer infectious. Those in this category are not able to be invaded again or to transmit the virus to other hosts.

Let μ be recovery rate which is constant. $1/\mu$ is average infectious period. The contact number $\sigma = \lambda/\mu$ during infectious period.

The total number of hosts in this model is a constant in SIR model, where

$$s(t) + i(t) + r(t) = 1 \quad (36.5)$$

This model described above can be expressed by the following set of ordinary differential equations:

$$\left\{ \begin{array}{l} \frac{di}{dt} = \lambda si - \mu i \\ \frac{ds}{dt} = -\lambda si \\ \frac{dr}{dt} = \mu i \\ i(0) = i_0 \\ s(0) = s_0 \end{array} \right. \quad (36.6)$$

where $s(0)$ and $i(0)$ are the initial numbers of, respectively, susceptible and infected hosts. This model is a simple but good model for network intrusion which once infected with can not be intruded again. Let

$$r_0 = \sigma = \lambda/\mu \quad (36.7)$$

then we have, (36.1) If $r_0 < 1$, then there is no epidemic. (36.2) If $r_0 > 1$, then the infection will be established in the hosts.

36.2.2 An Improved Network Epidemic Spreading Model with Immunity

Many network intrusion behaviors have the latent and exposed phase, during which the host was infected but not infectious. In early stages, the host may or may not exhibit obvious signs of infection and abundance of network intrusion behaviors can be too low to allow further transmission. Let $e(t)$ be exposed hosts in the latent period, where $1/\omega$ is average latent period.

The λ is constant in the SIER model. Considering that the effective infection rate λ will change with the alteration of network intrusion in fact, we propose the following form of dynamic infection rates, as shown in the Fig. 36.1

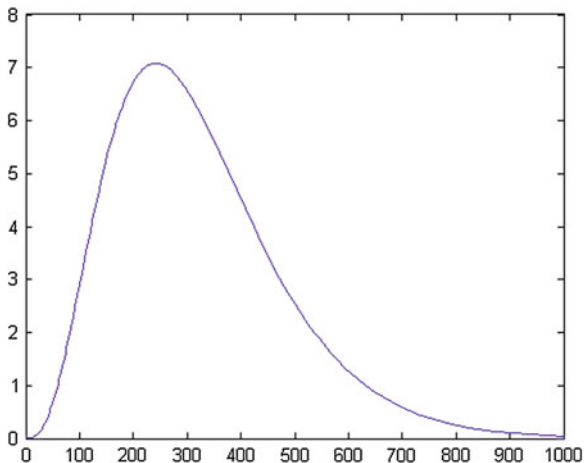
$$\lambda(t) = \zeta \cdot t^a e^{-bt}, \quad a, b, t > 0 \quad (36.8)$$

where ζ is the coefficient of infection rate.

When aggressive behaviors begin to spread and people have not taken any measures at initial stage, the harmful intrusion spread rapidly and the number of infected hosts rapid grow. As the time goes on, with preventing the aggressive behaviors, the number of infected hosts and infection rates are beginning to decline.

Thus, our model becomes,

Fig. 36.1 Infection rate



$$\begin{aligned}
 \frac{ds}{dt} &= -\lambda si \\
 \frac{de}{dt} &= \lambda si - \omega e \\
 \frac{di}{dt} &= \omega e - \mu i \\
 \frac{dr}{dt} &= \mu i
 \end{aligned}
 \tag{36.9}$$

for which it holds: $s + e + i + r = 1$

Definition Antigens $(Ag, Ag \subseteq U, D = \{0, 1\}^l)$ are fixed-length binary strings extracted from the Internet Protocol (IP) packets transferred in the network. The antigen consists of the source and destination IP addresses, port number, protocol type, IP flags, IP overall packet length, TCP/UDP/ICMP fields [9], etc. The structure of an antibody is the same as that of an antigen. For virus detection, the nonself set (*Nonself*) represents IP packets from a computer network attack, while the self set (*Self*) is normal sanctioned network service transactions and non-malicious background clutter. Set *Ag* contains two subsets, $Self \subseteq Ag$ and $Nonself \subseteq Ag$ such that $Self \cup Nonself = Ag$ $Self \cap Nonself = \Phi$

In this model the host is broken into four compartments: susceptible, exposed, infectious, and recovered respectively by $s(t)$, $e(t)$, $i(t)$, $r(t)$, that is $1 = s(t) + e(t) + i(t) + r(t)$. We use this model to study the mechanisms of aggressive behaviors spreading, to predict the future course of an outbreak and to evaluate strategies to control a network epidemic.

36.3 Experimental Results

The following experiments were carried out in the Laboratory of Computer Network Security. Let $\lambda = 12$, $\mu = 2.5$, $\omega = 1/2.45$, $s(0) = 0.95$, $i(0) = 0.05$, $e(0) = 0.01$. We get the periodogram of network epidemic spreading as the Fig. 36.2 shown.

In Eq. 36.9, when $t = 0$, if

$$\begin{aligned} \left[\frac{de}{dt}\right]_{t=0} + \left[\frac{di}{dt}\right]_{t=0} &= \lambda s_0 i - \omega e + \omega e - \mu i \\ &= \lambda s_0 i - \mu i < 0 \end{aligned} \tag{36.10}$$

we have $s_0 < \frac{\mu}{\lambda}$. The total number of groups $e(t)$ and $i(t)$ are on the decline under this condition. If let $P = \frac{s_0 \lambda}{\mu}$, we have, (36.1) when $P > 1$, the number of infected hosts will increase, which indicate the deteriorated network situation. (36.2) when $P < 1$, the number of infected hosts will decline, which indicate the improved network situation.

To avoid the deterioration of the network situation, we can reduce the P value by declining s_0 and λ , and increasing μ . Generally speaking, we can reduce the density of susceptible host s_0 , such as reducing the number of susceptible host in a network epidemic outbreak early stage. Isolating infected hosts can be used to reduce the daily infection rate λ value, which can cut down the infected host communication channels. To improve day cure rate μ value, we can strengthen correct defensive measures. In addition, we must pay more attention to the behavior re-infecting the system which can evolve into a more serious intrusion.

This task is aimed at showing the character of network epidemic spreading without latent infection host, where initial value $\lambda = 12$, $\mu = 2.5$, $\omega = 1/2.45$. When $i(0) = 0.025, 0.050, 0.075, 0.100, 0.125, 0.150, 0.200, 0.300$ and 0.400 respectively, we obtain the changes of network epidemic as shown in the Fig. 36.3. With the increasing of the initial infected hosts, it will lead to a climbing maximum numbers of infected hosts. In addition, the fewer the hosts are infected in

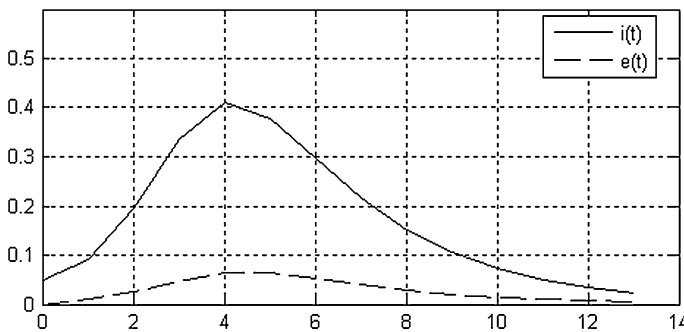


Fig. 36.2 Periodogram of network epidemic spreading

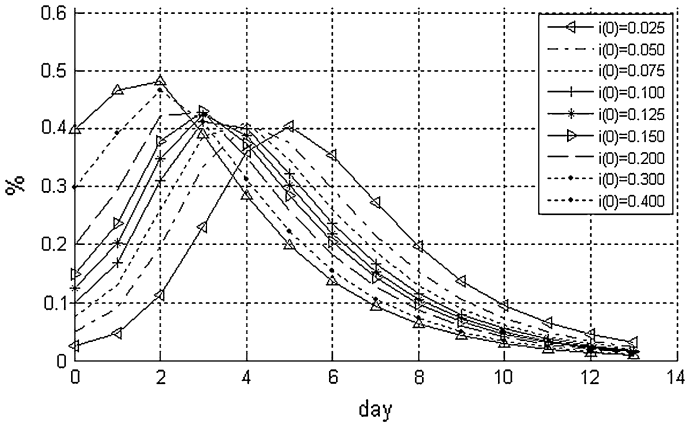


Fig. 36.3 Influence of initial value $i(0)$ making on the network epidemic spreading

initial period, the later the outbreak time of the network epidemic will be postponed, The energy is relatively lower.

The following task is aimed at showing the character of network epidemic spreading with immunity host, where initial value $\mu = 2.5$, $\omega = 1/2.45$. When $k = 2-6$ respectively, we obtain the changes of network epidemic as shown in the Fig. 36.4. With the increasing of k , it will lead to a postponed outbreak time of the network epidemic. In addition, the fewer the hosts are infected in initial period, the later the outbreak time of the network epidemic will be postponed. The energy is relatively lower too. In a real network environment, when an invasion happened again in a short time, the system with immunity can maintain a high degree of vigilance.

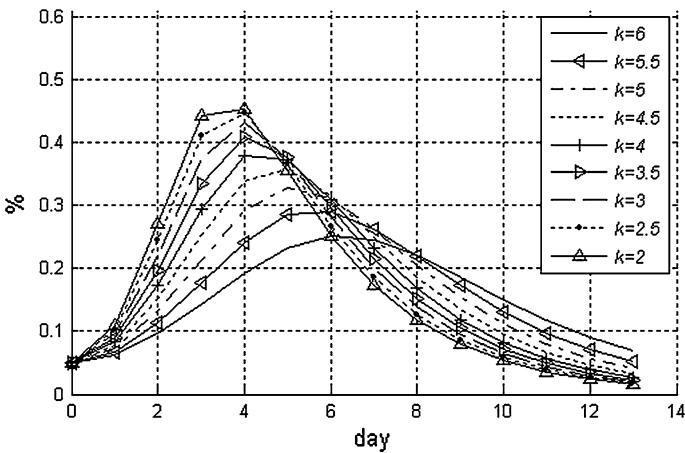


Fig. 36.4 Influence of immunity making on the network epidemic spreading

36.4 Conclusions

The self-adaptability, distributed character and quantization of antibody concentration that biological immune system bears are just the effective method to solve the technological problems of network security situation awareness. So we apply the characteristics of biological immune mechanism to the field of network situation awareness, and establish an immune network awareness system to make real-time and quantitative analysis. We propose an improved epidemic spreading model to study the mechanisms of aggressive behaviors spreading, to predict the future course of an outbreak and to evaluate strategies to control a network epidemic. The research area of this paper belongs to the interdisciplinary study of life science and computer science. The experimental results show that the proposed model has the features of real-time processing that provide a good solution for network surveillance.

Acknowledgments This work was supported by the National Natural Science Foundation of China (No.61003310, No.61100150) and Special Foundation of China Postdoctoral Science (No.2012T50783) and the China Postdoctoral Science Foundation (No.2011M501419) and Sichuan Province Philosophy and Social Key Research Base of “social development risk control research center” project (No. SR12B04) and LeShan Science and Technology project (No.12GZD014) and supported by the Scientific Research Fund of SiChuan Provincial Education Department (No.13TD0014).

References

1. Sangkatsanee P, Wattanapongsakorn N, Charnsripinyo C (2011) Practical real-time intrusion detection using machine learning approaches. *Comput Commun* 34(18):2227–2235
2. Hofmeyr SA, Forrest S (2000) Architecture for an artificial immune system. *Evol Comput* 8:443–473
3. Forrest S, Perelson AS, Allen L, Cherukuri R (1994) Self-nonsel self discrimination in a computer. In: *Proceedings of IEEE symposium on re-search in security and privacy*, Oakland
4. Kermack WO, McKendrick AG (1927) A contribution to the mathematical theory of epidemics. *Proc Roy Soc London* 115(772):700–721
5. Neal Peter (2012) The basic reproduction number and the probability of extinction for a dynamic epidemic model. *Math Biosci* 236(1):31–35
6. Elshoush HT (2011) Alert correlation in collaborative intelligent intrusion detection systems-A survey. *Appl Soft Comput* 11(7):4349–4365
7. Amiri F, Rezaei Yousefi MM (2011) Mutual information-based feature selection for intrusion detection systems. *J Netw Comput Appl* 34(4):1184–1199
8. Kermack WO, McKendrick AG (1932) A contribution to the mathematical theory of epidemics. *Probl Endemicity Proc Roy Soc London* 138(834):55–83
9. Li T (2005) An immunity based network security risk estimation. *Sci China Ser. F: Inf Sci* 48:557–578

Chapter 37

Recurrent Neural Network for Human Activity Recognition in Smart Home

Hongqing Fang, Hao Si and Long Chen

Abstract One of the most important functions of smart home is to monitor and assist individuals who are old or disabled. Recognizing the human activities is critical for the smart home application. In this paper, recurrent neural network (RNN) is applied to recognize the human activities. To evaluate the accuracy of the recognition algorithms, the results using real data collected from participants performing activities were assessed. With proper feature selections, the results of recurrent neural network show the significant ability to recognize human activities in smart home.

Keywords Smart home · Recurrent neural network · Human activity recognition · Feature selections

37.1 Introduction

The number of people who live with cognitive or physical impairments is rising because of the world's population ages. Many of old adults living in rural areas have no way to get health care [1]. Today, these old people without familiar surroundings who need special health care usually leave home to meet medical needs. Providing this health care at home will become an uncommon thing because

H. Fang (✉) · H. Si · L. Chen
College of Energy and Electrical Engineering, Hohai University, 8 Focheng West Road,
Jiangning, Nanjing, Jiangsu 211100, People's Republic of China
e-mail: fanghongqing@sohu.com

H. Si
e-mail: a758128298@163.com

L. Chen
e-mail: cдалong@hhu.edu.cn

of mounts of old adults can not afford to accept health care because of the high cost. Therefore, the need for smart home technologies is underscored by the aging of population, high cost of normal health care, etc. Individuals should be able to complete the Activities of Daily Living (ADLs) [2] who are independent in their own homes of the field of smart home. A range of intelligent systems built for providing health care [3] and wellness enable people to living in home with an improved overall quality of life.

The CASAS smart home project is a research project at Washington State University focused on the creation of an intelligent home environment. The CASAS smart home project consists of various sensor data collected by the smart environment such as motion sensors, light sensors, etc. Much of the theory and most of the algorithms are designed to handle one individual [4] in the space at a time. Passive tracking, activity recognition, event prediction, and behavior automation become significantly difficult. To achieve of the goal of monitoring and assistance, one of the most important step is to recognize the activity that an individual is performing in a smart environment. Over the past few years, there have been many approaches to model and recognize activities such as hidden Markov model (HMM) [5, 6], naïve Bayes classifier (NBC) [7, 8], support vector machine (SVM) [9, 10], etc.

Applying recurrent neural network to the field of human activity recognition in smart home is the main focus of this paper, which is compared with the others (HMM and NBC). In addition, the feature selections for human activity recognition is introduced simply. Finally, the experimental results are presented.

37.2 Data Collection

To validate the algorithms, we tested them in a smart apartment test bed located on the Washington State University which is maintained as part of the ongoing CASAS smart home project [11, 12]. For this studies, we used the lab space on the campus and many different kinds of activities took place throughout the room. The smart apartment is designed to equip with motion and temperature sensors as well as analog sensors. As shown in Fig. 37.1, there are three bedrooms, one bathroom, a kitchen, and a living/dining room. The motion sensors are located on the ceiling distributed approximately throughout the space. In addition sensors are equipped to provide ambient temperature readings and custom-built analog sensors to provide reading for hot water, cold water and stove burner use. Voice over IP captures phone usage using Asterisk software and contact switch sensors are used to monitor usage of a cooking pot, the phone book, and the medicine container. Sensor data [13] for activity recognition is captured using a customized sensor network and then stored in a SQL database. To maintain privacy, participant names and identifying information are removed and encrypt collected data before it is transmitted over the network.



Fig. 37.1 The smart apartment testbed

37.2.1 Data Representation

To provide physical training data for this algorithms, we recruited many volunteer participants to perform a series of activities in the smart apartment. The collected sensor events were manually labeled with the activity ID. Total of 10 activities is in the smart apartment. Those activities are as follows:

- Bed to toilet (activity 0): Transition between bed and toilet in the night;
- Breakfast (activity 1): The participants have breakfast;
- Bed (activity 2): The activity is sleeping in bed marked with defined end and begin;
- Computer work (activity 3): The activity is the participant who is working in the office space of the smart home;
- Dinner (activity 4): The participants have dinner;
- Laundry (activity 5): The participants clean clothes using laundry machine in the smart home;
- Leave home (activity 6): The activity of the participant who is leaving the smart home;
- Lunch (activity 7): The participants have lunch;
- Night wondering (activity 8): The activity of the participant who is wondering in the midnight;
- Take medicine (activity 9):The activity is the participant who is taking medicine marked with defined begin and end.

37.2.2 Feature Generation

Training data were gathered during several weeks in the test space. Relevant features are generated from the annotated data that is helpful in recognizing the activities. The data gathered by CASAS smart home project is presented by the following features:

- **Sensors ID**
This is an integer value from 0 to 9. Instead of using the original number of physical sensors, they are mapped to the labels in order to corresponding to the room in which the sensors installed.
- **Time of the day**
This is the input time of the sensor event in seconds. The feature is an integer value from 0 to 23.
- **The day of week**
The feature represent the day of the activity that occurred.
- **Previous of the activity**
This is the activity that occurred before the current activity. The feature is an integer value from 0 to 9.
- **Activity length**
The feature represents the length of the current activity. The feature is an integer value from 0 to 14.
- **Duration of activity**
The feature represents the duration of the activity. The feature is an integer value from 0 to 9.

The CASAS smart home project middleware generates the first four fields automatically. The annotated class field is the target feature for this learning problem and represents an aim for the activity for the activity to which the other fields can be mapped. Sample data collected in the smart work place is shown in Table 37.1. There are five fields represented as follows include Date, Time, Sensor ID, Message and Label.

Table 37.1 Data used for learning

Data	Time	Sensor ID	Sensor value	Label
09-06-10	03:20:59.08	M006	ON	Night wandering begin
09-06-10	03:25:19.05	M012	ON	
09-06-10	03:25:19.08	M011	ON	
09-06-10	03:25:24.05	M011	OFF	
09-06-10	03:20:59.08	M012	OFF	Night wandering end

37.3 Recurrent Neural Network for Human Activity Recognition

The proposed recurrent neural network [14, 15] consists of three layers as shown in Fig. 37.2. The employed recurrent neural network has typical dynamic networks and the dynamic mapping characteristics by storing states and better nonlinear mapping ability [16].

In the recurrent neural network, each hidden unit is connected with itself and fully connected with all input units and other output units. Therefore, the output value of the i th output unit at cycle k is obtained as follows:

$$O_i(k) = \sum_j w_{ji}^o X_j(k) \tag{37.1}$$

$$X_i(k) = f(S_j(k)) \tag{37.2}$$

$$S_j(k) = w_j^D X_j(k - 1) + \sum_m (w_{mj}^I I_m(k)) \tag{37.3}$$

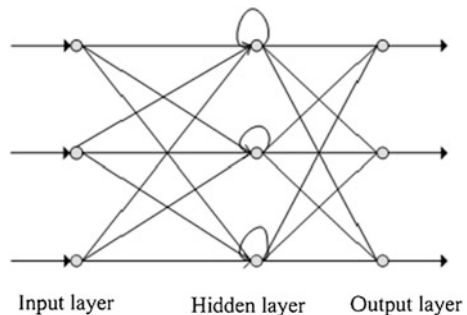
where $X_j(k)$ is the output value of the j th hidden unit at the cycle k , w_{ji}^o is the weight between the j th hidden unit and the i th output unit, $X_j(k - 1)$ is the output value of the j th hidden unit at cycle $k - 1$, w_j^D is the weight between the output value of the j th hidden unit and the input value of the j th hidden unit, $I_m(k)$ is the output value of the m th input unit at the cycle k , w_{mj}^I is the weight between the m th input unit and the j th hidden unit, $S_j(k)$ is the input value of the j th hidden unit at the cycle k , $O_i(k)$ is the output value of the i th output unit at the cycle k .

The weight correction of the recurrent neural network is in training phase. The weight of the proposed recurrent neural network in training phase is as follows:

$$w_j^D(k) = w_j^D(k - 1) + \eta_D \Delta w_j^D(k) + \alpha (w_j^D(k - 1) - w_j^D(k - 2)) \tag{37.4}$$

where η_D is the learning rate of the recurrent neural network, α is the momentum coefficient of the proposed recurrent neural network, $\Delta w_j^D(k)$ is the weight

Fig. 37.2 Three layers of recurrent neural network



correction of the proposed recurrent neural network. The correction of the other weights is as same as Eq. (37.4).

The essence of recurrent neural network algorithm is to obtain the minimum issue of the error function. This algorithm uses rapid decline method in nonlinear programming and modifies weight coefficient by the negative gradient direction of the error function.

$$E_p = \frac{1}{2} \sum_i (y_i(k) - O_i(k))^2 \quad (37.5)$$

where $y_i(k)$ is the target of the output value of the i th output unit, E_p is the performance error indicator of the error function.

Learning algorithm of the recurrent neural network is to modify the each layer weights of the output value of the output layer close to the process of target.

37.4 Test Result

In the recurrent neural network, the number of neurons of the input layer is 6, the number of neurons of the output layer is 10 and the number of neurons of the hidden layer is 10. In order to simplify the calculation, all of the layers of the learning rate and the momentum coefficient were set as same size. Therefore, α is 0.9 and η is 0.005. The samples have been collected in the CASAS smart apartment testbed for 55 days, resulting in total 600 instances of these ten activities and 647,485 collected motion sensor events.

In this paper, the 3-fold cross validation is applied. The results are shown in Table 37.2, which shows that recurrent neural network performs better on the 80 % of the activities than HMM and NBC. Recurrent neural network performs better on activity 0, activity 2, activity 3, activity 5, activity 6 and activity 9. While, recurrent neural network have a lower recognition accuracy on activity 8 than the other activities. It can be found that recurrent neural network can effectively identify these activities compared with HMM and NBC.

Table 37.2 Activity recognition rate

Activity	0	1	2	3	4
HMM	0.500	0.896	0.870	0.261	0.929
NBC	0.300	0.917	0.860	0.500	1.000
RNN	0.667	0.854	0.908	0.826	1.000
Activity	5	6	7	8	9
HMM	0.400	0.884	0.892	0.582	0.795
NBC	0.300	0.928	0.973	0.940	0.705
RNN	0.800	0.942	0.838	0.537	0.909

37.5 Conclusion

In this paper, recurrent neural network were applied to solving the activity recognition problem in smart home. In order to get a better observation about the recognition performance of recurrent neural network, it was compared with hidden Markov model and naïve Bayes classifier. By the experimental results, it is obvious that recurrent neural network is better than those two algorithms in the field of human activity recognition.

Acknowledgments This work was partially supported by Qing Lan Project, Jiangsu Province, China, and the data were collected from the smart home test-bed located on the Washington State University campus.

References

1. Rialle V, Ollivet C, Guigui C, Herve C (2008) What do family caregivers of Alzheimer's disease patients desire in smart home technologies? *Methods Inf Med* 47:63–69
2. Liao L, Fox D, Kautz H (2005) Location-based activity recognition using relational Markov networks. In: *Proceedings of the international joint conference on artificial intelligence*, 773–778
3. Singla G, Cook DJ, Schmitter-Edgecombe M (2010) Recognizing independent and joint activities among multiple residents in smart environments. *J Ambient Intell Hum Comput* 1:57–63
4. Yin J, Yang Q, Pan J (2008) Sensor-based abnormal human-activity detection. *IEEE Trans Knowl Data Eng* 20(8):1082–1090
5. Rabiner L (1989) A tutorial on hidden Markov models and selected applications in speech recognition. *Proc IEEE* 77(2):257–286
6. Ephraim Y, Merhav N (2003) Hidden markov processes. *IEEE Trans Inform Theory* 48:1518–1569
7. van Kasteren T, Krose B (2007) Bayesian activity recognition in residence for elders. In: *IET International Conference on Intelligent Environments*. IE. 209–212
8. Cook D, Schmitter-Edgecombe M (2009) Assessing the quality of activities in a smart environment. *Methods Inf Med* 48(5):480–485
9. Zhong L (2010) Network intrusion detection method by least squares support vector machine classifier. In: *The 3rd IEEE international conference on computer science and information technology*, vol 2, 295–297
10. Jakkula VR, Crandall AS, Cook DJ (2009). Enhancing anomaly detection using temporal pattern discovery. In: *Advanced intelligent environments*, 175–194
11. Cook D, Rashidi P (2009) Keeping the resident in the loop: adapting the smart home to the user. *IEEE Trans Syst, Man, Cybern, Part A* 39(5):949–959
12. Deleawe S, Kusznir J, Lamb B, Cook D (2010) Predicting air quality in smart environments. *J Ambient Intell Smart Environ* 2(2):145–154
13. Maurer U, Smailagic A, Siewiorek D, Deisher M (2006) Activity recognition and monitoring using multiple sensors on different body positions. In: *Proceedings of the international workshop on wearable and implantable body sensor networks*, 99–102
14. Kim T (2010) Sunspot series prediction using a multiscale recurrent neural network. *IEEE international symposium on signal processing and information technology*. 399–403

15. Lee T, Ching PC, Chang LW (1998) Isolated word recognition using modular recurrent neural networks. *Pattern Recognition* 31(6):751–760
16. Song HH, Kang SM, Lee SW (1996) A new recurrent neural network architecture for pattern recognition. *IEEE Trans Neural Netw* 8(2):331–340

Chapter 38

Optimization of an Advanced Guidance Scheme for Long-Range AAMs Based on SPSO

Xilian Li, Shutang Fu and Huitao Fan

Abstract Range is one of the main performances of air-to-air missiles (AAMs) to pursue, and one of the key measures is to optimize AAMs' guidance algorithm. An advanced engineering guidance scheme is proposed based on the idea of piecewise trajectory-shaping, and the optimization of design parameters is completed based on the standard particle swarm optimization algorithm (SPSO). Simulation and optimization results draw some beneficial conclusions, providing new ideas for AAMs' advanced navigation and guidance modes. Polynomial fitting or looking-up table and interpolation can be applied to realize the optimal guidance scheme in engineering. Simulations show that the trajectory obtained from polynomial fitting parameters is very close to that based on SPSO, which provides an effective way for applications in engineering.

Keywords Advanced guidance scheme · The optimal trajectory · Standard particle swarm optimization · Applications in engineering

38.1 Introduction

In recent years, the local war situation and the development trend of air combat indicate that airpower is one of the key factors to determine the outcome of a war. First view and first shot become one of the most important means to maintain the superiority of battlefield and airpower. Range is one of the main performances of AMMs to pursue, and the prerequisite to realize "first shot" [1].

Since the 1980s, one of the key measures taken by military developed countries is to optimize the air-to-air missile guidance algorithm, to increase tactical missiles' (especially AAMs') range. Energy consumption resulted from the resistance

X. Li (✉) · S. Fu · H. Fan
Luoyang Optoelectro Technology Development Center, No 166 Jiefang Road,
Xigong District, Luoyang City, China
e-mail: bluecc87@gmail.com

and control can be reduced by optimizing flight programs or guidance algorithms, so as to improve the trajectory performance and increase the range. The singular perturbation theory was firstly proposed by Gupta and Menon to attain the approximate analytic solution of the AAMs' Optimal midcourse Guidance, to minimize the energy consumption [2] or the attack time [3]. In China, Fu [4] put forward a fast climb and rapid decline midcourse guidance law based on the boundary layer theory proposed by Menon, which has been applied to the study on the medium and long range hypersonic air-ship missile guidance by Qiao [5]. However, complicated solutions are needed to obtain the guidance law based on the singular perturbation theory, and simplifications are to be applied to simulations, so it's difficult for engineering applications. Nonlinear numerical solutions and neural network methods [6] have been proposed to solve AAMs' trajectory-shaping problem, which is a two-point boundary value problem. Since the essence of the numerical solutions is to obtain the characteristic trajectory based on initial conditions, terminal constraints, and index functions, the geometry of optimal trajectories, still cannot be described by a clear control relationship [7] which is necessary for engineering realization at present. Besides, the numerical calculation sometimes has instability problems.

In summary, the control relationship or guidance scheme algorithms design is of great significance to obtain the characteristic trajectory. In this paper, an advanced engineering guidance scheme is proposed based on the idea of piecewise trajectory-shaping, and the SPSO algorithm is applied optimizing design parameters. Simulation and optimization results draw some beneficial conclusions, and provide new ideas for AAMs' advanced navigation and guidance modes.

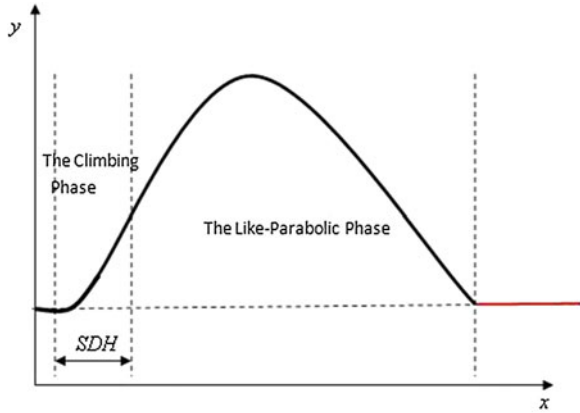
38.2 Design of the Guidance Scheme

Previous studies indicate that optimal trajectories have parabola-like geometry features in the vertical plane for AAMs with finite thrust. The demand overload is very small throughout the parabolic trajectory to save energy, in line with the requirements of the optimal trajectory-shaping design [8]. According to the geometric characteristics of optimal trajectories, and the launching means and guidance mode for AAMs, the following guidance scheme illustrated in Fig. 38.1 is selected.

38.2.1 Algorithms for the Climb

Considering the greater speed in the boost phase, and the greater resistance loss in the low altitude, the faster climbing rate is necessary to reduce the low-altitude residence time. And the given normal overload is to ensure that the structural failure won't occur. The horizontal displacement of missile during the climbing

Fig. 38.1 Design of the parabolic trajectory



phase is denoted by SDH, which is designed to ensure that the missile has enough distance to decline to the altitude of the target.

To ensure a smooth transition to the like-parabolic phase, while not missing the target during the climb, the integration guided system is to be applied with control relationships as follows:

$$n_y^*(t) = n_{y1} + n_{y2}(t), n_z^*(t) = n_{z2}(t) \tag{38.1}$$

Here, $n_{y2}(t)$ and $n_{z2}(t)$ are obtained by the guidance algorithm of the like-parabolic trajectory. Considering the influence of the launching distance and the carrier aircraft flight altitude, the given overload should be a function of the launching distance R and height H_0 . As for the altitude difference between the target and the carrier aircraft, the correction term $f_2(\Delta H)$ should be necessary. Then,

$$n_{y1} = f_1(R, H_0) + f_2(\Delta H), \Delta H = H_{target} - H_0 \tag{38.2}$$

As can be seen, if the carrier aircraft is below the target, a faster climbing rate is necessary to ensure the missile leaving the low-altitude air rapidly.

38.2.2 Guidance Algorithms for the Like-Parabolic Trajectory

LQG optimal guidance law (based on Linear-Quadratic-Gaussian theory) can minimize the control energy consumption and the miss distance, which has a much higher precision than PN (the Proportional Navigation guidance law) against big maneuvering targets [9]. And the demand overload is even lower than PN, in line with the characteristic of the parabolic trajectory. Therefore, LQG optimal guidance law is a better choice to realize the like-parabolic segment, and it can be expressed as follows:

$$u^*(t) = \frac{K}{t_{go}^2} [1, t_{go}, D(t_{go}, T_t), -D(t_{go}, T)] \hat{Y} \tag{38.3}$$

Here, t_{go} is the missile’s remaining flight time, $T = \omega_m t_{go}$ and $T_t = \lambda_t t_{go}$ are respectively the constant time of the missile and the target flight control system, K , $D(t_{go}, T_t)$ and $D(t_{go}, T)$ are functions of the remaining flight time and the constant time, which should be further simplified for simulation or engineering applications. The simplified solutions [10] are:

$$\begin{cases} u_y = \left(3 + \frac{6}{T+2}\right) \left(\frac{y_r + t_{go} y_r}{t_{go}^2} + \frac{1}{2} a_{ty} - \frac{1}{T+2} a_{my}\right) \\ u_z = \left(3 + \frac{6}{T+2}\right) \left(\frac{z_r + t_{go} z_r}{t_{go}^2} + \frac{1}{2} a_{tz} - \frac{1}{\omega_{az} t_{go} + 2} a_{mz}\right) \end{cases} \tag{38.4}$$

Here, a_{tz} and a_{ty} denote the target maneuvering accelerations, a_{mz} and a_{my} denote the missile maneuvering accelerations, ω_{az} denotes the autopilot bandwidth. Simulations show that the proposed guidance scheme can increase the flight distance effectively, reduce the attack time, and increase the terminal velocity. Besides, it’s easy to realize in engineering with the explicit control relationship.

38.3 Optimization of the Guidance Scheme

Parameters during the climb including n_y and SDH , determine the geometry of the whole flight trajectory, and affect the trajectory performance. Each of them is a function of the flight distance and the launching height. To achieve a certain best trajectory performance index, the parameters’ optimization under different launch height and distance should be necessary for the proposed guidance scheme. The function between parameters and launching conditions is completely unknown, and the optimization is a multi-parameter problem. Swarm intelligent algorithms need only the output value of the objective function, and don’t require any associated gradient information. Particle Swarm Optimization (PSO) is one of the main algorithms in the swarm intelligence research field, which is easy to realize and has a stronger global optimization capability, compared with other algorithms.

38.3.1 The Principle of SPSO

PSO is the simulation of the bird flock foraging process. Each candidate solution is called “a particle” and a number of candidate solutions form a group of birds. Each particle has no weight or volume and its fitness value is determined by the objective function. Moving in the solution space, the direction and distance of each particle depends on its speed. And the particles dynamically adjust their positions by following their own individual best positions and the global best position of the group.

In order to adjust the global detection and local development ability for the best, Shi [11] introduced the inertia weight ω into the velocity updating formula, which is called SPSO (the Standard Particle Swarm Algorithm). Better optimization results can be obtained for a dynamic ω than a fixed one. The linear decreasing weight strategy has been used widely, and the following formula is proposed by Shi [11]:

$$\omega = \frac{(\omega_{in} - \omega_{end})(iter - g)}{iter} + \omega_{end} \quad (38.5)$$

Here, $iter$ denotes the maximum iterations, ω_{in} is the initial inertia weight, and ω_{end} is the terminal inertia weight when the iteration ends. The typical values are $\omega_{in} = 0.9$ and $\omega_{end} = 0.4$ [12]. Assume that the searching space is N-dimensional and the size of the group of particles is M, then in the t-th iteration, the current updating formula of the speed and position can be expressed as following:

$$V_{i,j}(t+1) = \omega V_{i,j}(t) + c_1 \gamma_{1,i,j}(t)(P_{i,j}(t) - X_{i,j}(t)) + c_2 \gamma_{2,i,j}(t)(G_{i,j}(t) - X_{i,j}(t)) \quad (38.6)$$

$$X_{i,j}(t+1) = V_{i,j}(t) + X_{i,j}(t) \quad (38.7)$$

Here, $1 \leq i \leq M$, $1 \leq j \leq N$, t denotes the t-th iteration, c_1 and c_2 denote learning factors, and c_1 adjusts the step of flying to the individual best position while c_2 adjusts the step of flying to the global best position. $\gamma_{1,i,j}(t)$ and $\gamma_{2,i,j}(t)$ are independent random sequences uniformly distributed on $[0,1]$. In order to reduce the probability of particles exiting the search space, the range of particles' velocities and positions can be limited within a certain interval, such as $V_{i,j}(t) \in [-V_{\max}, V_{\max}]$, $X_{i,j}(t) \in [-X_{\max}, X_{\max}]$.

38.3.2 The Optimization Program

Under conditions of different launching heights and flight distances, parameters are to be optimized to achieve the maximum final velocity V_{ifmax} and the shortest time t_{fmin} using SPSO, with M particles in the N-dimensional space. As for the proposed guidance scheme, the control variable n_y and the ending sign of the climb SDH , which form a two-dimensional space $[x_1, x_2]$, are main factors to determine the trajectory performance. With the limitation of the missile structural strength, the normal overload x_1 is to be within the $[0, 10]$, while x_2 within $[0, R]$. To avoid the multi-peak problem, the interval $[0, R]$ is divided into subintervals with the length of 10 or 20 km. And optimizations are performed in each interval. The optimization program is as follows:

- Step 1: Determining operating parameters for SPSO.
- Step 2: Initialization Process.

- Step 3: Assigning individual fitness the value of the attack time or terminal velocity, such as $\text{fitness} = \max [V]$.
- Step 4: Comparing $\text{fitness}(i)$ with each particle's individual best position $\text{pbest}(i)$, and the superior is to be $\text{pbest}[i]$.
- Step 5: Comparing $\text{fitness}(i)$ with the global best position, and the superior is to be $\text{gbest}(i)$.
- Step 6: Updating the velocity and position of each particle.
- Step 7: Acquiring the current best trajectory and corresponding parameters.
- Step 8: Confirming whether to meet the terminal condition $\text{iter} = 2,500$. if not, go back to step 3. Otherwise, it is the end.

And the initialization includes:

1. Setting the group size, $M = 20$ for 10 km, while $M = 40$ for 20 km.
2. For any i , $X_{i,j}(0)$ is to be obtained randomly in the interval $[0,10]$.
3. For any j , $X_{i,j}(0)$ is to be obtained randomly in the interval $[0,R]$.
4. For any i and j , $P_{i,j}(0) = X_{i,j}(0)$.

The height of medium and long-range AAMs is generally no more than 30 km, while the carrier aircrafts are generally in the height of 0–15 km. Therefore, 8 km is selected as the typical launching height, while the dimensionless distance 1, 2, 3, 4, 5, 6, 7, 8 and 9 are selected as different simulation conditions. Then, 5 is selected as the typical dimensionless flight distance, and the launching altitude 5, 8, 10, 12 and 15 km are selected as different simulation conditions. The optimization includes the following two bullets:

- A. For the typical height of 8 km, optimizing under different flight distances, to obtain the shortest time trajectory and the maximum terminal velocity trajectory as well as corresponding parameters. If the flight distance is less than 100 km, the length of the optimization is 10 km, while the group size $M = 20$. If the flight distance is greater than 100 km, it's to be 20 km, while the group size $M = 40$.
- B. For the Dimensionless typical flight distance 5, optimizing under different heights to obtain the shortest time trajectory and the maximum terminal velocity trajectory as well as the corresponding parameters.

38.4 Optimization Results and Analysis

38.4.1 Optimization Under Different Flight Distances

Simulations show that with the increasing flight distance, limited to the minimum terminal speed and maximum flying height, the feasible region of parameters decreases. Optimization results for the mini-attack time are shown in Table 38.1.

As can be seen, with the increase of the flight distance, the optimization effect will be gradually reduced. However, if the flight distance is too small, the

Table 38.1 Results of the shortest attack aime

Flight distance	1	2	3	4	5	6	7	8	9
n_y	1.48	3.18	5.45	6.32	6.53	7.58	7.84	7.93	8.56
SDH	0.817	1.846	2.668	3.651	4.659	5.743	6.731	7.774	8.826
Shortest attack time	0.866	1.634	2.522	3.366	4.244	5.068	5.893	6.673	7.571
Longest attack time	0.905	3.211	4.166	5.152	6.403	7.797	8.706	9.145	9.491
Optimization effect/%	4.346	49.16	39.56	34.66	33.71	34.99	32.29	27.02	20.22

All the data is dimensionless except for n_y

Table 38.2 Results of the maximum terminal velocity

Flight distance	1.00	2.00	3.00	4.00	5.00	6.00	7.00	8.00	9.00
n_y	0.934	5.727	4.662	3.990	7.816	8.640	8.458	7.907	7.974
SDH	0	0.347	0.252	0.339	3.65	4.698	5.725	6.761	7.776
Maxi-terminal velocity	2.548	1.956	1.755	1.672	1.672	1.654	1.640	1.521	1.487
Mini-terminal velocity	2.415	1.001	1.000	1.000	1.000	1.000	1.000	1.000	1.000
Optimization effect/%	4.3460	49.166	39.567	34.665	33.711	34.994	32.298	27.024	20.223

optimization effect would be not obvious either. In fact, this guidance scheme is not proposed when the non-dimensional flight distance is less than 2.

Optimization results for the maximum terminal velocity are shown in Table 38.2.

As can be seen, the change of the optimization effect of the maximum terminal velocity is in line with that of the shortest attack time. As for the optimal parameters, it can be found that the optimization of the maximum terminal velocity is a bimodal problem, and when the dimensionless flight distance is 4, two peaks reach equilibrium. That is to say, the optimal parameters are smaller when the flight distance is less than 4 and greater when the flight distance is greater than 4.

38.4.2 Optimization Under Different Launching Heights

Simulations show that with the launching height decreasing, limited to the minimum terminal speed, the feasible region of parameters decreases, due to greater resistance. But at the height of 15 km, the feasible region accounts for only 50 % with the limit of the flight height. Optimization results for the shortest attack time are shown in Table 38.3.

As can be seen from the results, the optimization effect is not obvious when the launching height is too low or too high, and the effect is best near the altitude of

Table 38.3 Results of the shortest attack time

Launching height/km	5	8	10	12	15
n_y	9.163	7.850	6.529	5.578	2.999
SDH	0.943	0.943	0.932	0.924	0.715
Shortest attack time	5.399	4.605	4.244	3.963	3.628
Longest attack time	6.080	6.824	6.403	5.342	4.633
Optimization effect/%	11.200	32.518	33.711	25.809	21.707

Table 38.4 Results of the maximum terminal velocity

Launching height/km	5	8	10	12	15
n_y	9.031	9.300	8.640	7.763	6.300
SDH	0.930	0.947	0.940	0.940	0.933
Maxi-terminal velocity	1.108	1.453	1.654	1.852	2.127
Mini- terminal velocity	9.031	9.300	8.640	7.763	6.300
Optimization effect/%	0.930	0.947	0.940	0.940	0.933

10 km, which also indicates the best applicable range of the launching height for the proposed guidance scheme.

Optimization results for the maximum terminal velocity are shown in Table 38.4. Results show that the optimization effect gradually increases with the launching height increasing.

38.4.3 Analysis and Simulation for Applications

Optimal parameters have been obtained based on SPSO, under conditions of different launching heights and flight distances. Engineering applications can be achieved by real-time online interpolating, since the optimal parameters can be bound into a form related to the launching height and the flight distance. But an approximate function relationship can be obtained by polynomial fitting, which is to be applied during the following simulation. With the launching height of 8 km as an example, the approximate function between design parameters and the flight distance can be expressed as follows. And for the shortest attack time,

$$\begin{cases} n_y = A_3x^3 + A_2x^2 + A_1x + A_0 \\ SDH = B_1x + B_0 \end{cases} \quad (38.8)$$

For the maximum terminal velocity time,

$$\begin{cases} n_y = C_3x^3 + C_2x^2 + C_1x + C_0 \\ SDH = D_3x^3 + D_2x^2 + D_1x + D_0 \end{cases} \text{ if flight distance} \leq 4 \quad (38.9)$$

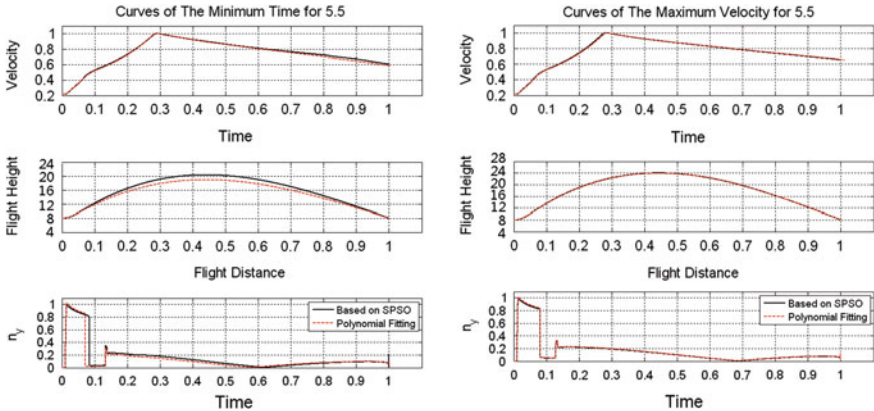


Fig. 38.2 Curves of the mini-attack time trajectory and the maxi-terminal velocity trajectory

Or

$$\begin{cases} n_y = C_3x^3 + C_2x^2 + C_1x + C_0 \\ SDH = D_1x + D_0 \end{cases} \text{ if flight distance} > 4 \quad (38.10)$$

Here, A_i , B_i , C_i , and D_i denote coefficients obtained by polynomial fitting, which are not suitable for open. Simulation results are shown in Fig. 38.2, when the launching height is 8 km, and the flight distance is 5.5. The trajectory obtained from polynomial fitting parameters is very close to that obtained by SPSO, and both of them have a very small normal overload. Besides, the maximum terminal velocity trajectory is much higher than the minimum attack time trajectory.

38.5 Conclusions

An advanced guidance scheme is proposed in this paper, which can be achieved easily in engineering, and SPSO is applied to complete the optimization of key parameters during the guidance scheme, under conditions of different launching heights and flight distances. Results show that the optimization is very effective, and beneficial conclusions have been obtained:

- With the increase of the flight distance, the optimization effect of the minimum attack time and the maximum terminal velocity will gradually decrease.
- With the increase of the launching height, the optimization effect of the maximum terminal velocity is gradually increased, while the optimization effect of the minimum attack time can reach the best near the height of 10 km.
- It is important to realize that if the flight distance is too small or the launching height is too low, the optimization effect is not obvious. In fact, it is not necessary to employ the proposed guidance scheme.

- The maximum terminal velocity trajectory is much higher than the minimum attack time trajectory.

The optimization based on SPSO cannot be achieved real-time online in engineering. The optimal parameters obtained from off-line optimizations can be bound into a form related with the launching height and flight distance. Then, the optimal guidance scheme can be realized by means of polynomial fitting or looking-up table. Simulation results show that the trajectory obtained by polynomial fitting parameters is very consistent with that based on SPSO. The proposed advanced guidance scheme has a broad application prospects.

References

1. Fan H, Wang Q (2006) Development and key technology of long-range air-to-air missiles. *Aero Weapon* 1:3–7 (in Chinese)
2. Cheng VHL, Gupta NK (1986) Advanced midcourse guidance for air-to-air missiles. *J Guidance Control Dyn* 8:103–107
3. Mennon PKA, Briggs MM (1990) Near-optimal midcourse guidance for air-to-air missiles. *J Guidance* 13(A):596–602
4. Fu L, Fan Y (1998) Singularly perturbed midcourse guidance law for quickly ascending air-to-ground missiles. *J Beijing Univ Aeronaut Astronaut* 24(6):707–710 (in Chinese)
5. Qiao Y, Chen G (2008) Design on a rapidly ascending and descending singular perturbation optimum guidance law. *J Solid Rocket Technol* 31(3):205–224 (in Chinese)
6. Chen G, Fu Y (2011) Survey of aircraft trajectory optimization methods. *Flight Dyn* 29(4):1–5 (in Chinese)
7. Chang C, Lin D (2009) Modeling and Simulation of kinetic optimal midcourse guidance law for air-to-air missiles. In: *Second international conference on information and computing science*, doi 10.1109, 452–456
8. Li X, Fan H (2012) Trajectory-shaping for long-range air-to-air missiles. The academic annual conference of society of aeronautics and aviation weapon system, Oct 1–10. (in Chinese)
9. Lei H, Liang Y (2002) An optimal guidance law based on linear quadratic gaussian theory. *J Air Force Eng Univ (Nat Sci Ed)* 3(2):27–31 (in Chinese)
10. Lei H, Tian C (2002) A kind of simplified engineering realization method for LQG optimal guidance. *Control Technol Tactical Missile* 1:5–8 (in Chinese)
11. Shi Y, Eberhart R (1998) A modified particle swarm optimizer. *Proceedings of the IEEE congress on evolutionary computation*, pp 69–73
12. Guo W, Chen G (2007) A new strategy of inertia weight adjustment for particle swarm optimization. *Comput Eng Sci* 29(1):70–72 (in Chinese)

Chapter 39

Research on High-Accuracy Data Association of Space-Borne SAR and AIS

Zhi Zhao, Kefeng Ji, Xiangwei Xing and Huanxin Zou

Abstract Many countries attach importance to maritime surveillance for its wide applications in exclusive economic zone surveillance, environmental monitoring and anti-piracy operations, etc. Space-borne Synthetic Aperture Radar (SAR) is optimal for its high resolution over wide swaths and all weather working capabilities for ship surveillance, but limited to the level of SAR imaging and image interpretation. Meanwhile, with rapid development of space-borne Automatic Identification System (AIS), almost real time and global coverage for ship surveillance has become possible, but not all ships operate or equip with AIS terminal transmitter. Space-borne SAR and AIS has cooperative nature, so ship surveillance by integration of them has attracted more attention. This paper focuses on the data association of space-borne SAR and AIS. State-of-the-art association methods have good performance except in the high-sea-state and high-density-shipping situations. To improve the flexibility and validity, we emphasis on analyzing two factors: AIS-projected position and Doppler displacement, which mainly affect the accuracy. Firstly, this paper presents the theory of data association in detail. Then state-of-the-art method for projecting AIS position based on Dead Reckoning is researched on further, and improved method based on Gray Prediction Model MGRM (1, N) is introduced. High-accuracy estimation of Doppler displacement is discussed later profoundly. The application of Point Pattern Matching using Shape Context in the association is also investigated, and the simulation results illustrate that it outperforms current state-of-the-art method both in the precision as well as robustness.

Keywords Ship surveillance · Synthetic aperture radar · Automatic identification system · Data association

Z. Zhao (✉) · K. Ji · X. Xing · H. Zou
School of Electronic Science and Engineering, National University of Defense Technology,
Sanyi Avenue, Kaifu District Changsha, Hunan, China
e-mail: zhaozhi_nudt@yahoo.com

39.1 Introduction

Ship surveillance is indispensable for maritime safety and security. It has attracted many countries' attentions. Space-borne SAR has advantages both in high resolution over wide swaths and all weather working capabilities, meanwhile, with rapid development of space-borne AIS almost real time and global coverage for ship surveillance has become possible. On consideration of cooperative nature for space-borne SAR and AIS, ship surveillance by integration of them is beneficial. The fundamental problem is data association. The characters of space-borne SAR and AIS data verify the feasibility of data association. Ship features, such as position, size, Course over Ground (CoG) and Speed over Ground (SoG), can be all derived or calculated from SAR image or acquired from AIS data directly. The flowchart of space-borne SAR and AIS data association is shown in Fig. 39.1. It illustrates that the data association consists of Time Matching and Position Matching [1, 2]. Both of them affect the ultimate accuracy. Position Projecting and Position Prediction play more important roles in the association, and contribute most to the accuracy. Position Prediction actually relies on the compensation for Doppler Displacement. So this paper firstly focuses on two main schemes: AIS-Projected Position and Doppler Displacement Estimation. Secondly, we research on the application of Point Pattern Matching using Shape Context in the association to improve adaptability.

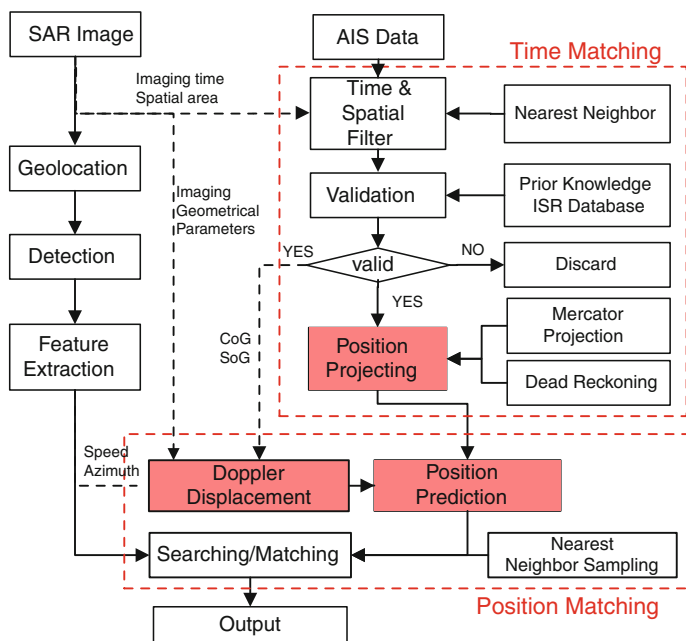


Fig. 39.1 Space-borne SAR and AIS data association

39.2 AIS-Projected Position Estimation

Affected by the sea wind and wave, ship has roll, pitch and yaw motion. On consideration of the difficulty to predict ship movement especially under high-sea-state conditions, this section investigates traditional DR-based method further and introduces the improved method based on Gray Prediction.

39.2.1 Dead Reckoning Based Estimation

Dead Reckoning [3], which consists of two parts: prediction and convergence, has proved to be suitable to predict position. The zero-order, first order and second order derivative polynomials are all limited to predict linear movements, but the real ships' movements are always non-linear. High-order (greater than three) prediction model could enhance the accuracy [3, 4], which uses Taylor Formula below:

$$f(x) = f(x_0) + f'(x_0)(x - x_0) + \frac{1}{2}f''(x_0)(x - x_0)^2 + \cdots + \frac{1}{n!}f^{(n)}(x_0)(x - x_0)^n + R_n \quad (39.1)$$

where

$$R_n = \frac{1}{(n+1)!}f^{(n+1)}(\xi)(x - x_0)^{n+1}, \xi \in (x_0, x).$$

But it only considers the vessel's own moving status, without considering the environmental factors. Meanwhile, higher derivatives increase the risk of inaccurate prediction caused by imprecise acceleration prediction and the computational burden, it might be safer to content with first-order or second-order prediction [3].

Using two AIS snapshots-the initial (ideally pre-image) and final (ideally post-image) snapshot to develop an interpolation method based on Dead Reckoning to project position has been proved to be practical [5]. Figure 39.2 shows the two cases for single manoeuvre. Point C is the position predicted by single snapshot (pre-image). Point D and Point E are the position predicted using pairwise snapshots. According to the continuity of ship's motion, D and E are more nearer to the real position and C is farther. The offset δ and the angular offset φ parameterize the remaining degree of freedom, the arc radii, and the total path length. To sum up, the estimation based on pair-wise AIS snapshots is better than on single AIS snapshot. Moreover, if rate of turn (ROT) from AIS data is available, it should be taken into account to improve accuracy.

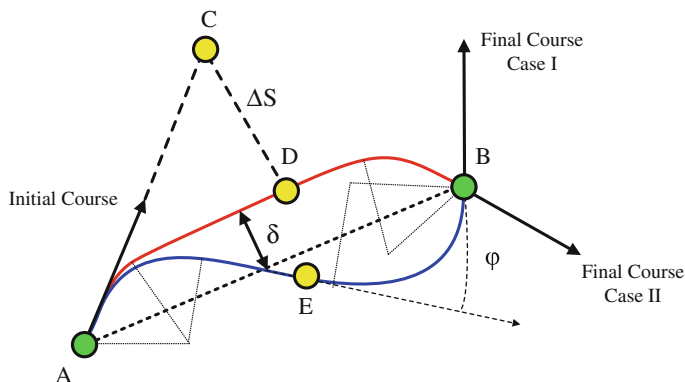


Fig. 39.2 Interpolation for the single manoeuvre condition

39.2.2 Gray Prediction Based Estimation

Gray Prediction has better prediction performance under the condition that there are small samples and poor information, and it's characterized by advantages of simplicity and practicability. Affected by the stochastic factors, ship's motion can be considered as a linear movement plus a random movement. Gray Prediction on the observation data sequence (AIS snapshots) could reduce the random influences caused by dynamic sea and enhance the intrinsic regularity of the sequence.

The grey model MGRM (1, N) based on multiple variables and reciprocal generating operation is established, which is made up of two models-MGM(1,N) and GRM(1,N). The ship position coordinate which consists of x-coordinate and y-coordinate, is also influenced by course and speed. Considering the above multiple variables are interactional, MGM(1,N) model is adopted. The GRM(1,N) model is also characterized by high accuracy and better practical values, and can be both used in non-equal interval and equal interval time series [6, 7]. AIS snapshots' intervals depended on SoG can either be equal or non-equal. The number of AIS snapshots used to predict should also be restricted properly.

Considering that the input of MGRM model should be the monotonic decreasing sequences, so firstly the satisfied sequences of ship position x-coordinates and y-coordinates should be selected. The sequences will be made up of both pre-image and post-image data to improve the accuracy. Ship's track always keeps monotonic within a short term, so certain number of AIS snapshots around SAR image acquisition time, which satisfy monotonic decreasing trend after self-adaptable translation and rotation of coordinate system, can be selected. Figure 39.3 shows how the monotonic decreasing sequences are selected. Ship moves from left down to right up. The selected sequential AIS snapshots in red box, which starts from the initial to the final shown in the figure, is monotonic decreasing in the coordinate system xoy.

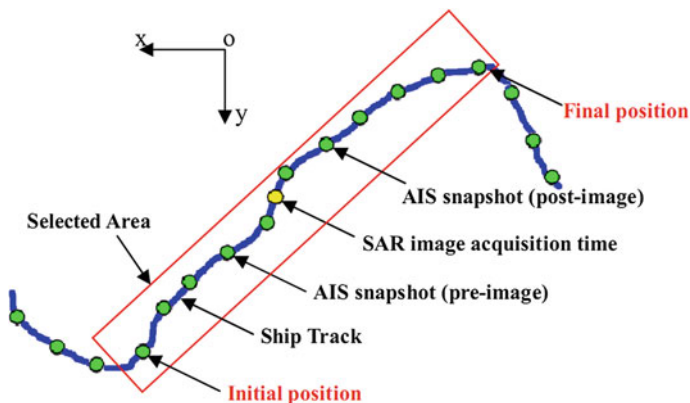


Fig. 39.3 Sketch map of sequence selection

39.3 Doppler Displacement Estimation

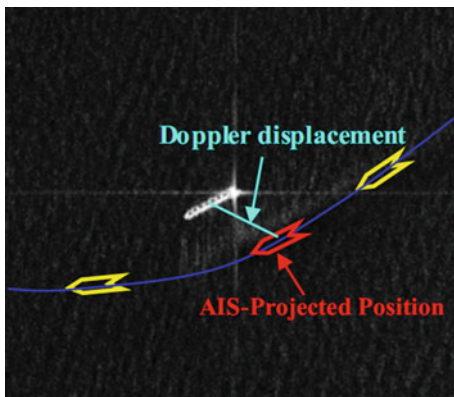
Doppler displacement exists for moving ship in SAR image, so there is azimuth shift between the AIS-projected position and ship position in SAR image (see Fig. 39.4). The effective shift in azimuth is defined as [5]:

$$\Delta_{AZ} = \frac{R_s v_r}{v_s} \tag{39.2}$$

where R_s is slant range from SAR to the ship, v_s is the velocity of SAR, v_r is radial velocity of the ship.

If we shift the SAR signature to the AIS-projected contact in azimuth, the radial velocity and range velocity of the ship should be derived from sequence of single-look images or ship wake, but not all ships appeared in SAR image have wakes. Ship’s aspect angle estimation could extract ship’s principle axis, leading edge or minimum circum-rectangle, all of which have disadvantages such as 180 degrees

Fig. 39.4 Doppler displacement compensation



blurring. The ship detected in high resolution SAR image has obvious structural features which could be used to identify the blurring aspect angle.

Considering the simplicity and accuracy, we traditionally shift the AIS-projected ship position to the position in SAR image in azimuth. SoG and CoG could be estimated more accurately. The Gray model based method above could be used to achieve better prediction performance. Also SoG and CoG in the image acquisition time could be estimated using pair-wise AIS snapshots (pre-image and post-image). Additionally, influenced by sea wind and waves, the AIS-predicted ship speed is a part of the real speed, so errors are unavoidable.

39.4 Searching and Matching Method

Traditional searching and matching method adopts Nearest Neighbor Sampling (NNS). Though AIS projected and prediction methods could be improved, unforeseen systematic errors would lead to worse performance especially when the ship's movement is extremely irregular and the sea is highly dynamic. So this section researches on the application of Point Pattern Matching Method based on Shape Context (SC-PPM) to improve the efficiency and accuracy.

39.4.1 SC-PPM Based Matching

Firstly the two point sets to be matched should be made up. After ship detection and extraction of centroids, we get the first point set made up of ship targets' centroids. Then ships' positions from AIS data could make up the second point set. These two point sets have similar shape with Doppler displacements differences theoretically. So it is possible to use point pattern matching methods.

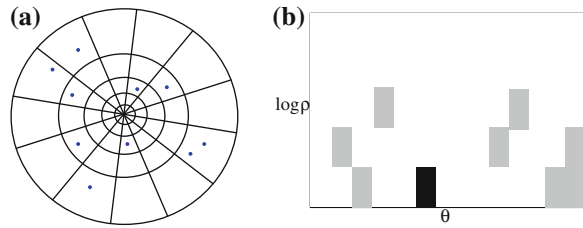
Belongie et al. [8] presented an invariant feature descriptor-Shape Context, which describes the shape of point set. The shape context of point $x_i(\rho, \theta)$ is defined as the histogram of other remaining points' relative coordinates:

$$h_i(m) = \#\{x \neq x_i : (x - x_i) \in \text{bin}(m)\} \quad (39.3)$$

Then it uses the diagram of log-polar histogram bins to compute the shape context. Figure 39.5 shows that there are five bins for $\log \rho$ and twelve bins for θ . The shade of bins represents the number of points falling into the bins. Consider a point x_i of the first point set and a point y_j of the second one. The cost of matching uses χ^2 test statistic:

$$C(x_i, y_j) = \frac{1}{2} \sum_{m=1}^M \frac{[h_i(m) - h_j(m)]^2}{h_i(m) + h_j(m)} \quad (39.4)$$

Fig. 39.5 Shape Context



39.4.2 Comparison of Matching Methods Based on SC-PPM and NNS

Because not all ships send AIS signals or equip with AIS terminal transmitters, so the ships detected in SAR image may not have corresponding AIS data. The quantities of points in two point sets have not to be equal, so outliers may exist. Meanwhile ship's Doppler displacement can either be positive or negative, which depends on the ship's movement relative to SAR platform. So three conditions are considered below:

1. All ships' displacements are positive or negative. Figure 39.6a shows the results of SC-PPM based method, and no errors. (b) shows the results of NNS based method with lower accuracy. AIS-Predicted positions 4 and 5 correspond with SAR ship position 4 wrongly. Similarly, AIS-Predicted positions 7, 10, 13 and 18 are matched in error.
2. Ships' displacements are not all positive or negative. In Fig. 39.7, compared with (a), errors also exist in (b). AIS-Predicted positions 1, 6, 10, 21 are matched in error.
3. Some ships do not have corresponding AIS data. Figure 39.8 shows the condition that there are outliers numbered from 17 to 22. The results based on SC-

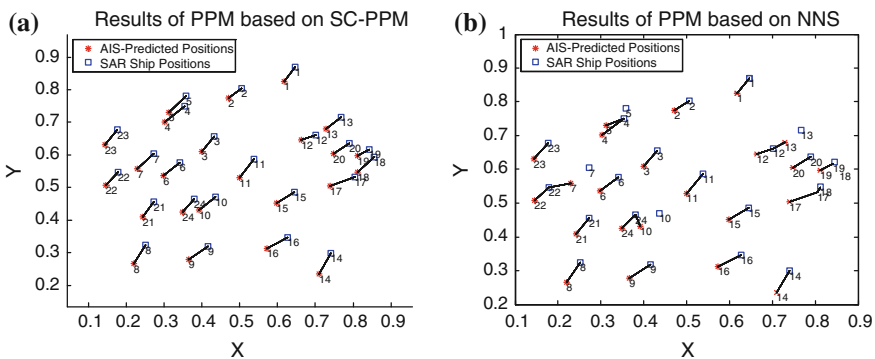


Fig. 39.6 Comparison for condition 1

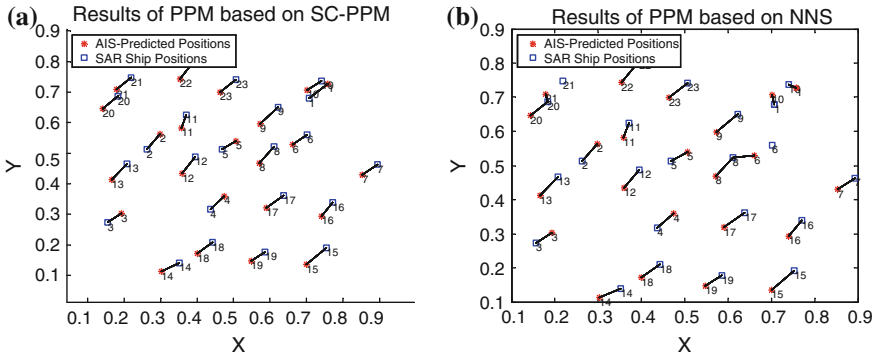


Fig. 39.7 Comparison for condition 2

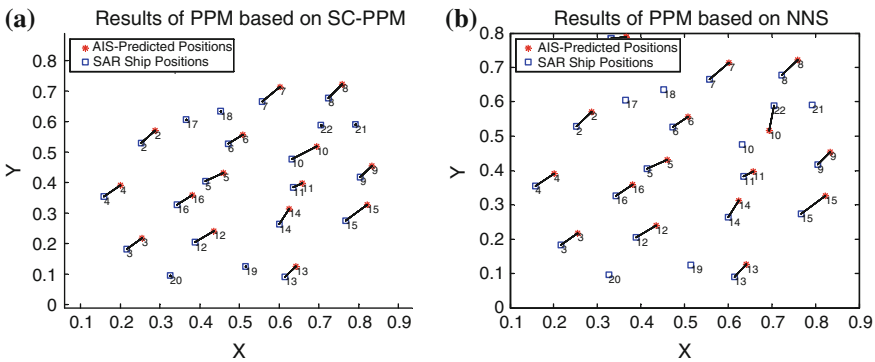


Fig. 39.8 Comparison for condition 3

PPM are accurate shown in (a). From (b) we can see AIS-Predicted position 10 is wrongly matched with the outlier 22.

39.5 Conclusion

This paper researches on high-accuracy data association of space-borne SAR and AIS, and emphasizes on the crucial techniques including AIS-Projected position estimation, Doppler displacement estimation and Matching method. On the further analysis of state-of-the-art methods, the model MGRM(1,N) is presented in the AIS-Projected position estimation, then Doppler displacement estimation is analyzed profoundly. Shape context is also attempted in the searching and matching

method, and the simulation results illustrate that improved method outperform current state-of-the-art method both in the adaptability as well as precision.

References

1. Yang C, Kim T (2012) Integration of SAR and AIS for ship detection and identification. Ocean Sensing and Monitoring. In: Proceedings of the SPIE, vol 8372(0), 1–6
2. Zhao Z, Ji KF, Xing XW, Zou HX (2012) Research on ship surveillance by integration of space-borne SAR and AIS. China high resolution observation to earth academic seminar—Satellite remote sensing and applications. Beijing. vol 4(62), pp 5–8. (in Chinese)
3. Jouni S, Timo K, Harri H (2002) A review on networking and multiplayer computer games. Game Developer Magazine, USA. p 33–45
4. Qu Z, Gao H, Zhu Y (2008) Research on high-accuracy position prediction algorithm in online game. In: IEEE international symposium on electronic commerce and security (ISECS), 79–80 2008
5. Paris WV, Ryan AE, John W (2007) Signatures in RADARSAT-1 ScanSAR Narrow B Imagery-Analysis with AISLive Data. TECHNICAL MEMORANDUM. DRDC Ottawa. TM 2007-052, p 7–11
6. Yang B, Zhang Z (2003) The Grey Model Has Been Accumulated Generating Operation in Reciprocal Number and Its Application. Math Pract Theory 33(10):21–25
7. Zou R, Mou X, Yi W (2012) The non-equidistant grey GRM (1, 1) model and its application. Int J Mod Nonlinear Theory Appl. 1:51–54
8. Belongie S, Malik J, Puzicha J (2002) Shape matching and object recognition using shape contexts. IEEE Trans Pattern Anal Mach Intell 24(4):509–522

Chapter 40

A Control Method of Inclined Inverted Pendulum on a Mobile Foundation with Disturbances

Cheng Guo, Xiaoyu Han and Yingmin Jia

Abstract In this paper, a mechanical and mathematical model is made for the inclined furuta pendulum, firstly. And for this model, the balance and switch controllers are designed, in order to stabilize the inclined furuta pendulum even with disturbances and moving. The results of simulation and experiment show that this control method can realize swing up, stabilize the inclined furuta pendulum, increase the system stability rate and improve the anti-interference performance even the inclined furuta pendulum is on a velocity-varying mobile foundation.

Keywords Furuta pendulum · Inclined plane · Balance and switch control · Mobile foundation

40.1 Introduction

There are almost three typical control strategies for the inverted pendulum. The first one is based on the classical control theory, such as the PID control. Another one employs the modern control theory and the balance of the inverted pendulum can be realized, such as the pole allocation and the LQR optimal regulators. And the last one is called the intelligent control theory, which including theories of fuzzy logic, artificial neural network and genetic algorithm and so on.

Based on those theories introduced above, this paper put forward a modelling method on Lagrange dynamical theory [1], where we made mechanical analysis of the inclined furuta pendulum and worked out a new dynamical model and the new balance point. As this system is controllable, we designed a controller for swing-up and balance, which can make the pendulum stabilize around the new balance

C. Guo (✉) · X. Han · Y. Jia
The Seventh Research Division and the Department of Systems and Control,
Beihang University (BUAA), Beijing 100191, China
e-mail: guo9363@163.com

point, and we realized the experiments both on simulation and real pendulum. At last, a mobile foundation, which can be seen as an interference are brought to the system to test its property of anti-interference.

40.2 The Model of the Inverted Furuta Pendulum

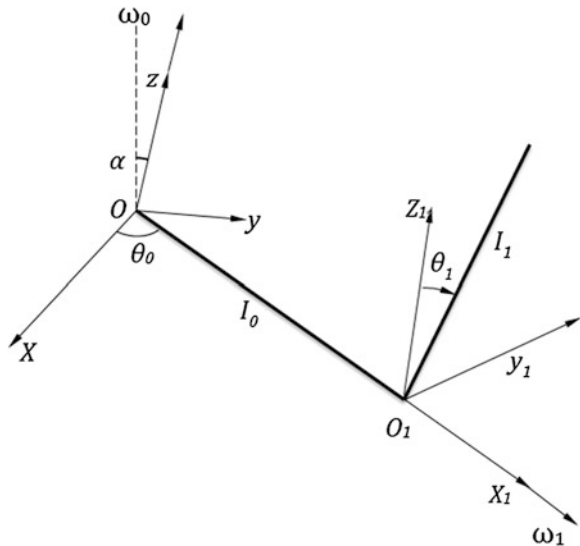
The experiment is based on the electromechanical integrated platform of furuta pendulum by Quancer Company and the structure diagram is shown in Fig. 40.1. By ignoring all kinds of resistance and friction, the arm and swinging rod can be abstracted into two homogeneous rods. Where arms length is l_0 , the angular is θ_0 related to its horizontal zero, the distance between swinging rod and hinge is l_1 , the angular is θ_1 related to its vertical direction zero. The angular velocity of arm and swinging rod is ω_0 and ω_1 . The rotary inertia of arm is J_0 , the rotary inertia around the centroid of swinging rod is J_1 , and the inclined angle is α .

The kinetic energy of the system is composed of the following three parts [2, 3]:

1. Rotational energy of arm T_1 : $T_1 = \frac{1}{2} J_0 \dot{\theta}_0^2$
2. Translational kinetic energy of swinging rod T_2
3. Rotational energy of swinging rod T_3 :

$$\begin{aligned}
 C_x &= l_1 \cos \theta_1 \\
 C_y &= l_0 \cos \theta_0 - l_1 \sin \theta_0 \sin \theta_1 \\
 C_z &= l_0 \sin \theta_0 + l_1 \cos \theta_0 \sin \theta_1
 \end{aligned}
 \tag{40.1}$$

Fig. 40.1 Model of inclined furuta pendulum



and

$$v_c^2 = C_x'^2 + C_y'^2 + C_z'^2 \quad (40.2)$$

So

$$\begin{aligned} T_2 &= \frac{1}{2} m_1 v_c^2 \\ &= \frac{1}{2} m_1 (l_0^2 \dot{\theta}_0^2 + l_1^2 \dot{\theta}_1^2 + l_1^2 \dot{\theta}_0^2 \sin^2 \theta_1 + 2l_0 l_1 \dot{\theta}_0 \dot{\theta}_1 \cos \theta_1) \\ T_3 &= \frac{1}{2} J_1 (\dot{\theta}_1^2 + \dot{\theta}_0^2 \sin^2 \theta_1) \end{aligned} \quad (40.3)$$

Here,

$$\begin{aligned} T &= T_1 + T_2 + T_3 \\ &= \frac{1}{2} J_0 \dot{\theta}_0^2 + \frac{1}{2} m_1 (l_0^2 \dot{\theta}_0^2 + l_1^2 \dot{\theta}_1^2 + l_1^2 \dot{\theta}_0^2 \sin^2 \theta_1 + 2l_0 l_1 \dot{\theta}_0 \dot{\theta}_1 \cos \theta_1) \\ &\quad + \frac{1}{2} J_1 (\dot{\theta}_1^2 + \dot{\theta}_0^2 \sin^2 \theta_1) \end{aligned} \quad (40.4)$$

System potential energy is:

$$V = m_1 l_1 \cos \theta_1 g \cos \alpha - \left[m_0 \frac{1}{2} l_0 \sin \theta_0 + m_1 (l_0 \sin \theta_0 + l_1 \sin \theta_1 \cos \theta_0) \right] g \sin \alpha \quad (40.5)$$

Putting in the second type Lagrange theorem we can get differential equations. More specifically, the matrix form is

$$M\ddot{\theta} + C\dot{\theta} + G = \tau, \quad \theta = (\theta, \dot{\theta})^T \quad (40.6)$$

and as [4], we set

$$x = (\theta, \dot{\theta})^T \in R^3 \quad (40.7)$$

The equation can be displayed as:

$$\begin{aligned} \dot{x} &= Ax + Bu \\ y &= [E \quad 0]x \end{aligned} \quad (40.8)$$

The new balance point of the system is $\theta^0 = (0, a)$ and the balance of torque is

$$u_0 = \left(\frac{1}{2} m_0 l_0 + m_1 l_0 \right) g \sin \alpha \quad (40.9)$$

We can determine that the α is controllable within the scope of $(-\frac{\pi}{2}, \frac{\pi}{2})$, and the greater the $|\alpha|$ is, the more decreases of the system stability will be [5, 6].

In practical calculation when $|\alpha| > \frac{\pi}{8}$, the system need a large reply torque. For real system can't provide such a big moment, that also causes the system does poorly in stability.

40.3 Designing Balance Controller and Switch Controller

The balance control algorithm is appropriate while $|\theta_0| \leq 1.5$ and $|\theta_1| \leq 0.3$ [7], and the rest of time swing up control algorithm is used to control the system.

According to the results of the analysis for the parameters of the system, by using the linear equations before, we can get the state equation near balance point on an inclined platform. Modifying the zero point of balance, output torques and applying the state feedback near to the balance [8].

The state feedback control volume in different angles on the inclined plane.

From the Table 40.1, we can see that in the control systems that the angles more than $\frac{\pi}{8}$ requires too much reply torque, that the real system cannot satisfy to, so the simulation and experiment is only for the angle less than $\frac{\pi}{8}$. And the value, which is bigger than $\frac{\pi}{8}$, is replaced by $\frac{\pi}{8}$ (Fig. 40.2).

Table 40.1 Title of the table

α	k_1	k_2	k_3	k_4
0	-7.7867	-76.3241	-2.8551	-10.3450
$\pi/16$	-9.3760	-86.6543	-3.4382	-12.4084
$\pi/8$	-15.7078	-124.214	-5.7606	-20.6178

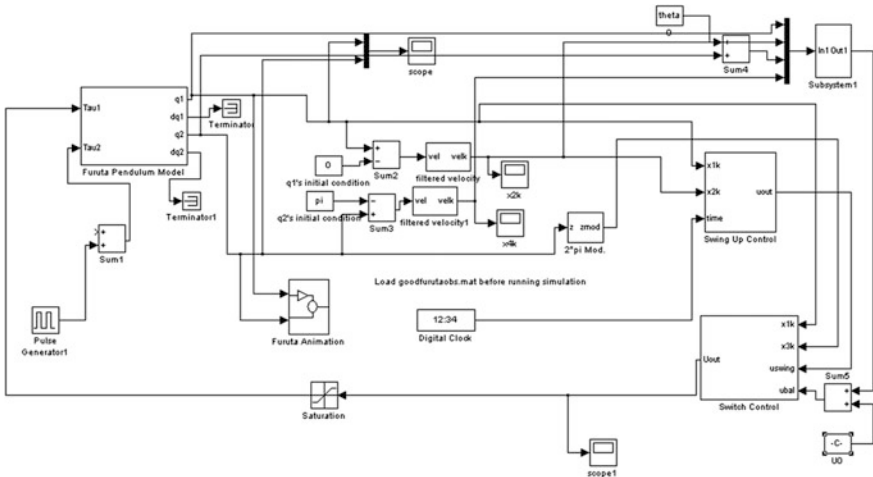
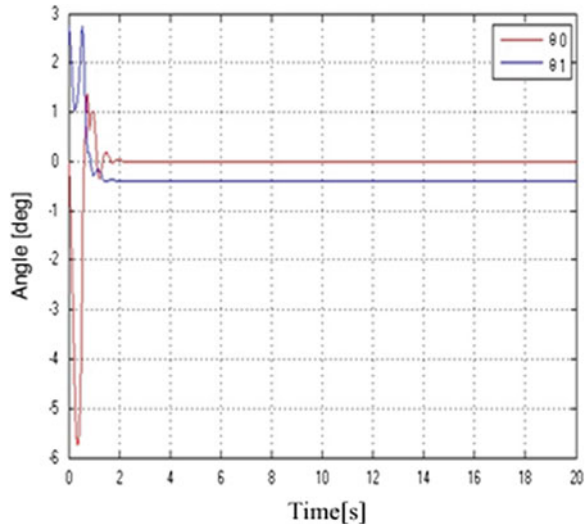


Fig. 40.2 Simulink of inclined invertedfuruta pendulum

Fig. 40.3 Simulation curve of arm and swing rod when $\alpha = \pi/8$



40.4 Simulation and Experiment

As seen from the Fig. 40.3, the swing rod is steady in the position of the new balance less than two seconds. Therefore, the designed controller can make inverted pendulum become quick and stable in zero position and the control effect is very well. From the Fig. 40.4, we can see the real control of furuta can still stable in system zero. Therefore, the control effect of the controller designed in physical experiment is also very well.

Fig. 40.4 Experimental curve of arm and swing rod when $\alpha = \pi/8$

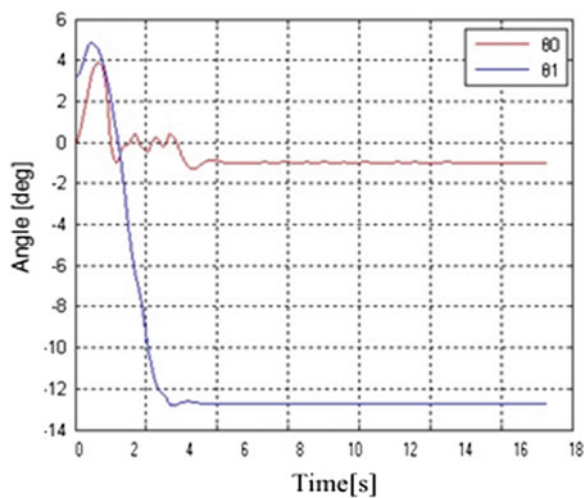
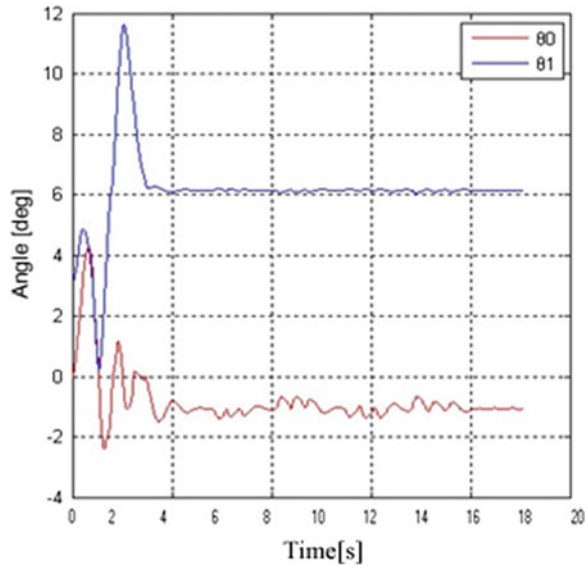


Fig. 40.5 Experimental curve of arm and swing rod when on a mobile robot



In this experiment, we put the pendulum in a mobile robot. When the system keeps stable around the zero point, we make the robot move forward and backward to increase interference. The result is showed in Fig. 40.5. We can see that within a certain range of external interference, furuta pendulum's swinging rod and arm can always became stable near new zero point.

40.5 Conclusion

This paper studied the model of inclined Furuta pendulum and established the mathematical model of the control system, where we linearize this system in the new balance point. Then this paper improved the swing up and balance controller based on the energy equation and achieved the stable control for Furuta. Simulation and experimental result showed that the controller can keep the system stable in new zero point and has certain properties of anti-jamming and robust.

References

1. Wu N (2010) The movement modeling and simulation of the scheme of angle movement controlling of the simple inverted pendulum. *J Syst Simul* (9)
2. Zeng MX, Fang C, Zhao Q (2010) Pole placement and quadratic optimal control for the signal arm-driven inverted pendulum. *J Mech Electr Eng* (3)

3. Wu A, Zhang X, Zhang Z (2005) Lagrange equation modeling based on the single stage rotating inverted pendulum control. *China Eng Sci* 7
4. Liu J (2004) *Advanced PID control matlab simulation* [M]. Electronic Industry Press, Beijing
5. Zhang M, Zhu S (2004) Single inverted pendulum swinging annular level control study. *J Jiangnan Univ* 3(5)
6. Zhang S, Zhu S (2003) Based on lagrange equation modeling rotation inverted pendulum analysis and control. *Ind Control Comput* (8):30–32
7. Duan X (2002) Single stage of rotating inverted pendulum modeling and control simulation. *Robot Technol Appl*
8. Astrom KJ, Furuta K (2000) Winging up a pendulum by energy control. *Automatica* 36:287–295

Chapter 41

TiltRotor Aircraft Flight Control Study Based on Fuzzy Logic Control via Genetic Algorithm

Heng Chen, Xu Wang and Tengfei Lei

Abstract Tiltrotor aircraft combines the vertical takeoff and Landing (VTOL) capability of helicopters with the high speed performance of turboprop airplanes. A longitudinal rigid body tiltrotor model is developed in this paper. Because it is very difficult to obtain the accuracy model, this paper investigates the theory about the fuzzy logic control and genetic algorithm. Then this theory is used to design the tiltrotor aircraft flight controller. Numerical methods are investigated and numerical simulation is conducted to account for the good flight controller designed based on Fuzzy Logic control via GA of the tiltrotor aircraft.

Keywords Tiltrotor aircraft · Fuzzy logic control · Genetic algorithm

41.1 Introduction

Tiltrotor aircraft combines the vertical takeoff and Landing (VTOL) capability of helicopters with the high speed performance of turboprop airplanes. Their versatile flight abilities come from the combination of two propellers with the body of an airplane [1]. To takeoff vertically, the propeller planes are parallel with the ground and the engines are vertical. Once in the air, the engines can be rotated forward to utilize the aerodynamic advantages of the airplane flight.

A longitudinal rigid body tiltrotor model is developed. It is not easy to obtain the accuracy model so that this paper investigates the theory about the fuzzy logic control and genetic algorithm. Then this theory is used to design the tiltrotor aircraft flight controller. Numerical methods are investigated and a direct approach

H. Chen (✉) · X. Wang · T. Lei
Department of Engineering, Xijing University, Xi'an ChangAn Qu,
Xijing Road No.1 710123 Xi'an, China
e-mail: chenhenrys@yahoo.com.cn

is implemented. Numerical simulation is conducted to account for the good performance of the flight control system designed.

41.2 Modeling for the TiltRotor Aircraft

To investigate optimal tiltrotor operations, a mathematical model must be used that both adequately describes tiltrotor dynamics and is simple enough to be used efficiently in designing the flight control. A general longitudinal tiltrotor model is introduced in this paper that is suitable for designing purposes.

The longitudinal rigid-body dynamics are introduced and the equations of motion are defined [2]. The model is then scaled and normalized for efficient numerical computation. It also helps validate the model by describing realistic flight. The model is studied as follow [3]:

The moment is written.

$$M = 2T \cdot [h_R \cos(i_n - \beta) + d \sin \beta] \quad (41.1)$$

The longitudinal state equations are

$$\dot{w} = \frac{A_z}{m} - 2 \frac{T}{m} \sin(i_n - \beta) + g \cos \theta + qu \quad (41.2)$$

$$\dot{u} = \frac{A_x}{m} + 2 \frac{T}{m} \cos(i_n - \beta) - g \sin \theta - qw \quad (41.3)$$

$$\dot{\theta} = q \quad (41.4)$$

$$\dot{q} = \frac{M_A}{I_y} - \frac{2}{I_y} T [h_R \cos(i_n - \beta) + d \sin \beta] \quad (41.5)$$

$$\dot{h} = u \sin \theta - w \cos \theta \quad (41.6)$$

$$\dot{x} = u \cos \theta + w \sin \theta \quad (41.7)$$

where g is the acceleration of gravity, A_z and A_x are vertical and horizontal components of aerodynamic forces (respectively) in the body frame, and M_z is the aerodynamic moment about the y axis. I_y is the moment of inertia about the y axis (Tables 41.1 and 41.2).

41.3 Fuzzy Logic Control via Genetic Algorithm

Modern tiltrotor aircraft that tends to trade stability for high maneuverability rely heavily on the high quality control. The tiltrotor aircraft control system has to be designed to ensure static and dynamic stability while providing satisfactory

Table 41.1 The variables of the above equations

Variable	Represents
w	Vertical component of velocity in the body frame
u	Horizontal component of velocity in the body frame
θ	Pitch angle (angle between the reference frames)
q	Pitch rate
h	Height in the inertial frame
x	Forward distance in the inertial frame

Table 41.2 The control variables of the model

Variable	Represents
T	Thrust produced by 1 proprotor
i_n	Nacelle angle

handling qualities. Further, increasing requirements on the tiltrotor aircraft for performing large maneuvers within an expanding flight envelope introduce uncertainties in the tiltrotor aircraft control. These include fuzzy logic (FL), genetic algorithm (GA) and neural network based techniques. This paper applies the fuzzy logic via genetic algorithm to design the flight controller for the tiltrotor aircraft.

41.3.1 Fuzzy Logic Control

Fuzzy systems theory applied to control of complex processes has emerged, as a major alternative to conventional control techniques. The distinguishing features of fuzzy logic, namely, redundancy of an appropriate mathematical model to describe a system [4] and ability to model system of arbitrary nonlinearity [5] to desired accuracy, have facilitated the implementation of fuzzy control over processes that are mathematically intractable or are imprecisely defined [6]. However, in case of processes those are complex but well modelled. That prevailing view in the control-theory community [7] is that fuzzy controllers are easier to establish but fall short of performance good conventional controllers.

Complex maneuvers of the tiltrotor aircraft involving large incidences induce significant nonlinearities in aircraft dynamics. These are mathematically difficult to model and complicate the task of developing conventional controllers. Fuzzy logic control, with its implicit encapsulation of nonlinearities and redundancy in need for mathematical models, appears naturally advantageous in these regions.

41.3.2 Genetic Algorithms

Genetic Algorithms (GA) is exploratory search and optimization procedures that are based on the principles of biological evolution. GA have been applied for

designing membership function and rule_bases in fuzzy systems [8], among others. GA is considered for controller parameter optimization primarily because of their robustness. This robustness stems from the fact that no special characteristics, like continuity or differentiability, are required of the function being optimized. Each point of the solution vector space is assigned a ‘fitness’ value based on this function; the algorithm follows natural evolutionary principles to arrive at that point in the total domain space that has the highest fitness. A typical genetic algorithm tends to slow down in convergence speed, and even stagnate, as it approaches close to the optimum point, and acceleration of the algorithm in this zone is an active research subject [9]. Certain acceleration techniques are investigated in this paper in the process of using GA for FLC optimization.

41.4 Design of Flight Controller for the TiltRotor Aircraft Based on Fuzzy Logic via GA

Genetic algorithm (GA) is exploratory search and optimization procedures that are based on the principles of biological evolution. The ‘survival of the fittest’ dictum is allowed to drive the parameters of a physical process to the state that produces optimal or ‘fittest’ value of a ‘fitness function’.

There are three well defined operations in a GA procedure—selection, crossover, and mutation. Starting with a population of strings representing codified solution space, selection creates a new generation of population by randomly selecting strings from the current generation, with weight given to the fitness value of each string strings with higher fitness are likely to get more copies in the new generation, and those with low fitness might be eliminated, the word ‘might’ signifying the probabilistic nature of the GA. Crossover takes up pairs of strings and switches the bits lying on one side of a particular common ‘crossover point’. Mutation flips individual bits of a string once in a while based on a probability of mutation. The operation of crossover leads to creation of new solutions, while mutation allows the solution to jump from one point of the solution space to another. Together, all three operations complementarily guide the GA process towards the optimal solution with highest fitness.

The flight control system of the tiltrotor aircraft is shown in Fig. 41.1. Inputs of the Fuzzy controller are the pitch error and pitch error rate and output of the controller is the engine nacelle angle.

41.4.1 Optimization Steps of Genetic Algorithm

The rule optimization procedure consists of the following steps.

- step 1 Select the population

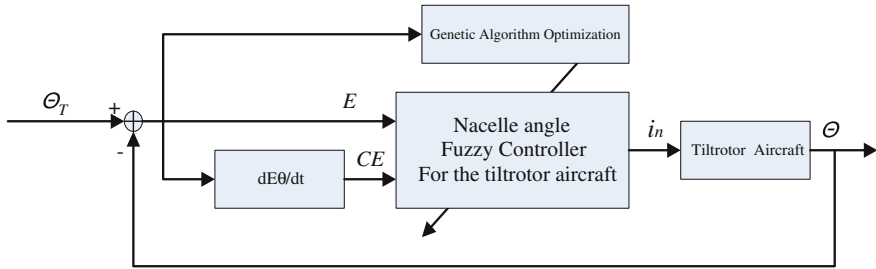


Fig. 41.1 The flight control system of the tiltrotor aircraft

- step 2 Generate the new generation by using operations crossover and mutation
- step 3 Domain of the fuzzy variables program into the string
- step 4 Calculate the fitness function
- step 5 Select the fittest body, then generate new generation population
- step 6 If find the best result, optimization is over
- step 7 Go to step 2.

41.4.2 To Create Coding String

The mix binary and decimal coding string is used in this paper. The optimizing parameters are the domains of two inputs and one output of the fuzzy logic controller and control value. The string is consisted of the first decimal control value (output of the FLC) part and second binary domain part. The decimal string represents the 49 control values. The binary string represents six binary 16 bits number as the total 96 bits string. In this case, the high optimization effect will be obtained (Tables 41.3 and 41.4).

41.4.3 To Select the Fitness Function

The fitness function is very important for the whole system. The fitness is selected on the requirements of the tiltrotor aircraft flight control.

Table 41.3 The decimal string

$u_{1,1}$	$u_{1,2}$...	$u_{2,1}$...	$u_{7,7}$
-----------	-----------	-----	-----------	-----	-----------

Table 41.4 The binary string

a_e	b_e	a_{ce}	b_{ce}	a_u	b_u
-------	-------	----------	----------	-------	-------

Table 41.5 Domain of the inputs and outputs

a_e	b_e	a_{ce}	b_{ce}
-0.099	8.599	-1.958	5.900

Table 41.6 The fuzzy function controller parameters

U	CE												
E	N6	N5	N4	N3	N2	N1	Z	P1	P2	P3	P4	P5	E
N6	4.5	7.9	-4.1	-6.8	-8.6	-5.2	6.5	11.2	1.7	-3.5	1.8	9.7	0.0
N5	5.1	10.6	-4.8	3.7	-8.9	-11.7	7.6	-4.2	5.6	-9.3	5.2	0.3	-1.7
N4	5.9	-6.9	-3.5	12.1	-8.0	5.0	10.9	4.0	0.2	1.7	12.0	6.0	1.6
N3	-0.5	-6.7	-2.7	4.2	-2.0	3.9	8.9	-2.8	7.1	8.3	6.5	-2.0	3.0
N2	1.4	-11.7	2.3	9.6	9.2	12.0	-3.4	3.3	-0.2	4.5	6.2	11.9	-10.0
N1	-9.8	-10.9	-9.8	-12.0	-0.2	1.3	3.1	5.1	-8.1	12.0	-1.7	-11.1	10.3
Z	-1.2	3.6	-12.0	-9.4	8.2	-2.5	6.0	-2.6	5.2	12.0	3.4	1.3	6.6
P1	5.6	-8.0	-1.0	8.2	-1.0	-7.8	-7.9	-2.2	12.0	-11.4	7.8	-5.4	7.5
P2	10.2	8.9	9.6	-1.8	-1.1	3.2	10.5	4.0	7.9	-3.6	-10.8	9.3	8.1
P3	-5.8	-8.4	11.2	10.1	-1.2	6.0	1.7	8.7	5.2	1.2	11.5	-4.2	4.4
P4	-6.3	-8.5	-6.1	6.1	-2.2	-3.2	3.4	-3.3	-0.3	-6.1	10.8	4.6	-7.7
P5	9.5	12.0	-8.8	4.8	10.4	-12.7	-6.9	-1.9	-10.0	2.5	2.6	-11.6	-5.8
P6	-6.9	-1.5	9.6	-4.0	-12.0	-2.0	1.2	2.4	4.2	-11.7	-6.4	-3.7	3.2

$$f = \alpha \cdot \left| \frac{\sigma_m - \sigma}{\sigma_m} \right| + \beta \cdot \left| \frac{t_{sm} - t_s}{t_{sm}} \right| + \gamma \cdot \left| \frac{e_m - e_s}{e_m} \right| \tag{41.7}$$

In the above formula, α is the overshoot, t_s is the settling time for the whole control system, e_s is the stable error, α , β , γ are the weight value for these characters volume. After adjusting the weight value, the performance of the system can be obtained.

Then the fitness function is designed. Meanwhile the mutation, and crossover and will be used to produce the new generation population.

41.4.4 Design of the Fuzzy Controller

When the tiltrotor aircraft takes off vertically, the nacelle is fixed 90° position. By controlling pitch angle, the aircraft pitch will be adjusted. After the vertical takeoff is over, the tiltrotor aircraft begins the conversion procedure. During the takeoff procedure the attitudes angle is very important for the tiltrotor aircraft. Controlling the attitudes angle is main task during the takeoff procedure.

Variables can be shown as follow:

$$T = T_{max}, i_n = 90^\circ, \theta = 10^\circ, h = 400 \text{ ft}$$

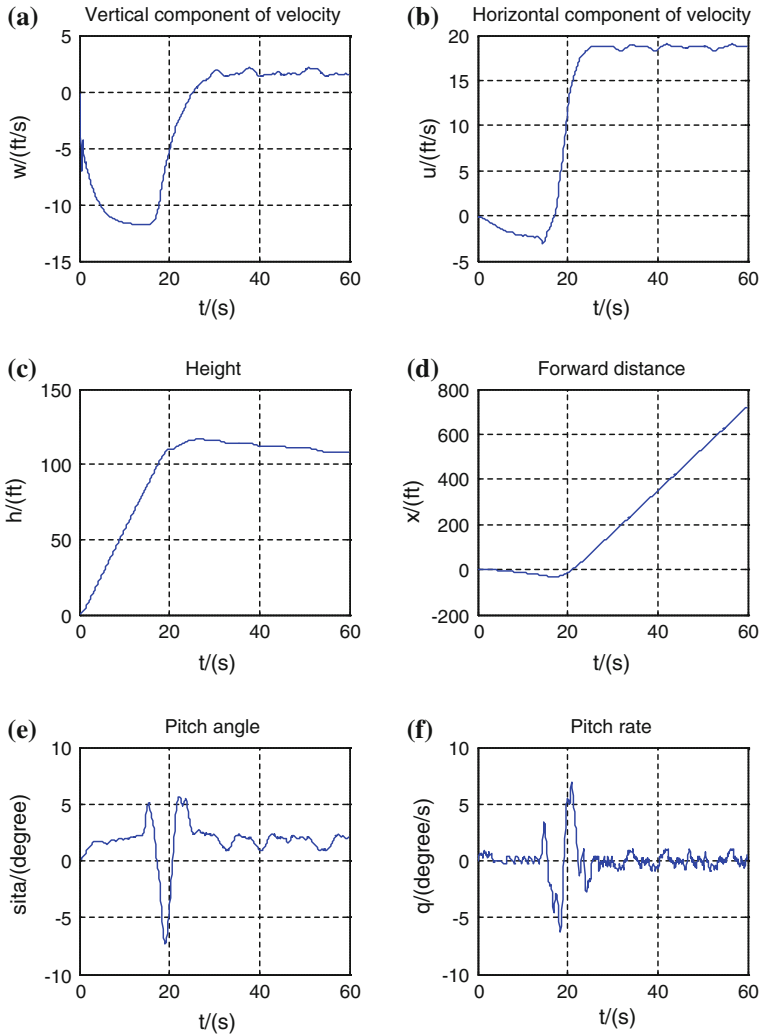


Fig. 41.2 Tiltrotor aircraft converse procedure performance

Control variable is prorotor pitch angle θ .

The population is selected 40. Firstly the variables are produced randomly such which are a_e, b_e, a_{ce}, b_{ce} . Then the function has to be selected in the domain of the inputs and outputs. After derived 300 generations, the following variables will be obtained. Weight variables can be obtained: $\alpha = 0.1, \beta = 0.45, \gamma = 0.45$, at this situation the optimization parameters as follow Tables 41.5 and 41.6.

41.5 Simulation and Conclusion

This paper has investigated designing the controller for the tiltrotor aircraft takeoff and conversion procedures. A longitudinal rigid body tiltrotor model was developed. Numerical methods were investigated and a direct approach using collocation and nonlinear programming was implemented. The figures (Fig. 41.2) for converse procedure performance show that the whole control system possess the perfect performance and demonstrate that the method of design the fuzzy logic controller via genetic algorithm is very useful for the tiltrotor aircraft.

References

1. Heng C, Xiaoyang Z, Yuzhuo Z (2007) Tiltrotor aircraft key technology developing research. *J Flight Dyn* 25(1):5–8
2. YongHua F, Jun Y, Shuiqing L (2007) Design of an optimal flight control system for tiltrotor conversion. *J Flight Dyn* 25(1):47–50
3. Carlson EB (1999) Optimal tiltRotor aircraft operations during power failure[D]. University of Minnesota, Minnesota
4. Chen CL, Hsieh CT (1996) User-friendly design method for fuzzy logic controller. *IEE Proc Control Theor Appl* 143(4):358–366
5. Krishnakumar K, Consalves P, Satyadas A, Zacharias G (1995) Hybrid fuzzy logic flight controller synthesis via pilot modeling. *J Guidance, Control Dyn* 18(5):1098–1105
6. Carlson EB, Zhao Y, Chen RTN (1999) Optimal tiltrotor runway operations in one engine inoperative. AIAA-99-3961
7. Lin CM, Maa JH (1997) Flight control system design by self-organizing fuzzy logic controller. *J Guidance, Control Dyn* 20(3):557–564
8. Rahmoun A, Benmohamed M (1998) Genetic algorithm based methodology to generate automatically optimal fuzzy systems. *IEE Proc Control Theor* 145(6):583–586
9. Herrera F, Lozano M, Verdegay JL (1998) A learning process for fuzzy control rules using genetic algorithm. *J Fuzzy Sets Syst* 100:143–158

Chapter 42

Hybrid Projective Synchronization of a New Hyperchaotic System

Jinchen Yu and Caiyan Zhang

Abstract The hybrid projective synchronization (HPS) of a new hyperchaotic system is studied using a nonlinear feedback control. The nonlinear controller is designed according to Lyapunov's direct method to guarantee HPS, which includes synchronization, anti-synchronization and projective synchronization. Numerical examples are presented in order to verify the effectiveness of the proposed scheme.

Keywords Chaos · Synchronization · Lyapunov theory

42.1 Introduction

In 1990, Pecora and Carroll proposed a successful method to synchronize two identical chaotic systems with different initial conditions [1]. Since then, synchronization has become a hot subject in the field of nonlinear science due to its wide-scope potential applications in various disciplines. The idea of synchronization is to use the output of a drive system to control a response system so that the response of the latter follows the output of the drive system asymptotically. There exist many types of synchronization such as complete synchronization [2, 3], phase synchronization [4, 5], anti-synchronization [6–8], and generalized

J. Yu (✉)

Department of Mathematics, Beijing Jiaotong University, Beijing, China
e-mail: 10118375@bjtu.edu.cn

J. Yu

School of Science, Shandong Jiaotong University, Jinan, China

C. Zhang

Department of Mathematics, Shandong College of Electronic Technology, Jinan, China
e-mail: weihua_yu@sohu.com

synchronization [9, 10]. A new form of chaos synchronization was reported by [11], termed as projective synchronization, that the drive and response systems could be synchronized up to a scaling factor α (a proportional relation), which is usually observable in a class of systems with partial linearity, such as chen system. Projective synchronization attracted lots of attention to study because of its proportionality between the synchronized dynamical states. In application to secure communications, this feature can be used to extend binary digital to M-nary digital communication [12] for achieving fast communication. Recently [13] presented a hybrid projective synchronization between two dynamical systems. Motivated by the above discussion, in this paper, we will investigate the HPS of a new hyperchaotic system [14] based on the Lyapunov stability theorem. A general controller is proposed. The chaos synchronization of the system is proved by the Lyapunov stability theory.

42.2 Analysis and Method

Suppose a chaotic system as

$$x' = f(t, x) \tag{42.1}$$

Choose system (42.1) as drive system, response system is as follows

$$y' = g(t, y) + u(t, x, y) \tag{42.2}$$

where $x, y \in R^n, f, g \in C^s[R_+ \times R^n, R^n], u \in C^s[R_+ \times R^n \times R^n, R^n]$ and $s \geq 1$.

R_+ is a set of non-negative real numbers. $u(t, x, y)$ is the nonlinear control vector. If $\forall x(t_0), y(t_0) \in R^n$, there exists a nonzero constant diagonal matrix $\alpha = \text{diag}(\alpha_1, \alpha_2, \dots, \alpha_n) \in R^{n \times n}$ such that $\lim_{t \rightarrow \infty} \|y(t) - \alpha x(t)\| = 0$ then the response and drive systems are said to be in hybrid projective synchronization. Where α is called scaling matrix, $\alpha_1, \alpha_2, \dots, \alpha_n$ are called scaling factors. In particular, the two systems achieve complete synchronization when all values of α_i are equal to 1. Further, if all values of α_i are equal to -1 , then the two systems are said to be in anti-synchronization.

In this section, our purpose is to achieve HPS of two hyperchaotic systems based on Lyapunov's direct method. For the new hyperchaotic system, the drive and response systems are defined as follows: the drive system is

$$\begin{cases} x'_1 = a(x_2 - x_1) \\ x'_2 = cx_2 - x_1x_3 + x_4 \\ x'_3 = -bx_3 + x_1x_2 \\ x'_4 = -k_1x_1 - k_2x_2 \end{cases} \tag{42.3}$$

and the response system with control has the following form

$$\begin{cases} y_1' = a(y_2 - y_1) + u_1 \\ y_2' = cy_2 - y_1y_3 + y_4 + u_2 \\ y_3' = -by_3 + y_1y_2 + u_3 \\ y_4' = -k_1y_1 - k_2y_2 + u_4 \end{cases} \quad (42.4)$$

where a, b, c, k_1, k_2 are known parameters, u_1, u_2, u_3, u_4 are the controllers which are to be designed such that the two hyperchaotic systems can achieve HPS.

Subtracting drive system (42.3) from response system (42.4) yields the following error dynamical system:

$$\begin{cases} e_1' = a(e_2 - e_1) + a(\alpha_2 - \alpha_1)x_2 + u_1 \\ e_2' = ce_2 + e_4 + (\alpha_4 - \alpha_2)x_4 - y_1y_3 + \alpha_2x_1x_3 + u_2 \\ e_3' = -be_3 + y_1y_2 - \alpha_3x_1x_2 + u_3 \\ e_4' = -k_1e_1 - k_2e_2 + (\alpha_4 - \alpha_1)k_1x_1 + (\alpha_4 - \alpha_2)k_2x_2 + u_4 \end{cases}$$

where $e_i = y_i - \alpha_i x_i$, $i = 1, 2, 3, 4$.

Choose the following Lyapunov function:

$$V = \frac{1}{2}(e_1^2 + e_2^2 + e_3^2 + e_4^2) \quad (42.5)$$

It is clear that the Lyapunov function, $V(t)$, is a positive function.

To guarantee the error dynamical system converges to the origin asymptotically, we choose the controller as

$$\begin{cases} u_1 = a(\alpha_1 - \alpha_2)x_2 - ae_2 \\ u_2 = -(c + l_1)e_2 - e_4 + (\alpha_2 - \alpha_4)x_4 + y_1y_3 - \alpha_2x_1x_3 \\ u_3 = \alpha_3x_1x_2 - y_1y_2 \\ u_4 = k_1e_1 + k_2e_2 + (\alpha_1 - \alpha_4)k_1x_1 + (\alpha_2 - \alpha_4)k_2x_2 - l_2e_4 \end{cases}$$

With this choice, the time derivative of the Lyapunov function is

$$V' = -ae_1^2 - l_1e_2^2 - be_3^2 - l_2e_4^2 = -e^T Q e \quad (42.6)$$

where $Q = \begin{bmatrix} a & 0 & 0 & 0 \\ 0 & l_1 & 0 & 0 \\ 0 & 0 & b & 0 \\ 0 & 0 & 0 & l_2 \end{bmatrix}$.

Obviously, ensuring that the origin of error system is asymptotically stable implies that V' is negative definite. The case is satisfied if and only if the following inequalities hold:

$$l_1 > 0 \text{ and } l_2 > 0$$

Based on Lyapunov’s direct method, this translates to: $\lim_{t \rightarrow \infty} \|e(t)\| = 0$. Thus the response and drive systems are globally asymptotically hybrid projective synchronized.

42.3 Numerical Results

Numerical simulations are displayed to demonstrate the effectiveness of the proposed control law for HPS. Let the system parameters be $a = 36, b = 3, c = 20, k_1 = 1, k_2 = 1$ so that the system (42.3) has a chaotic attractor. The initial states of

Fig. 42.1 Synchronization errors versus time t

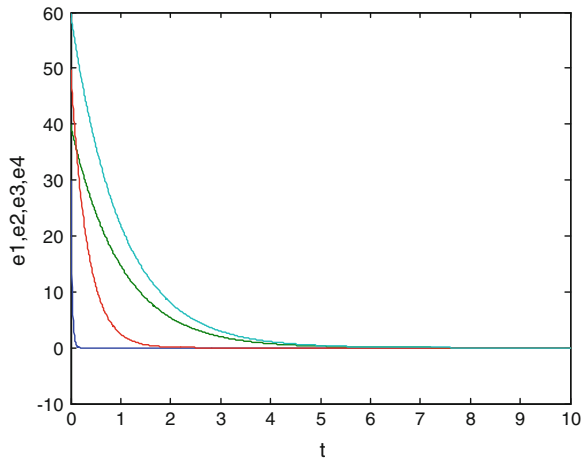


Fig. 42.2 Anti-Synchronization errors versus time t

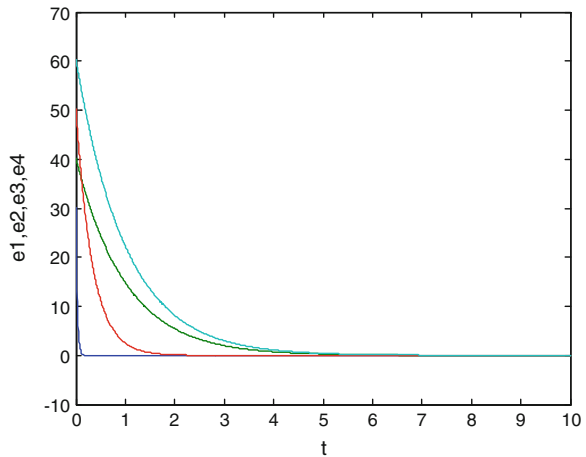
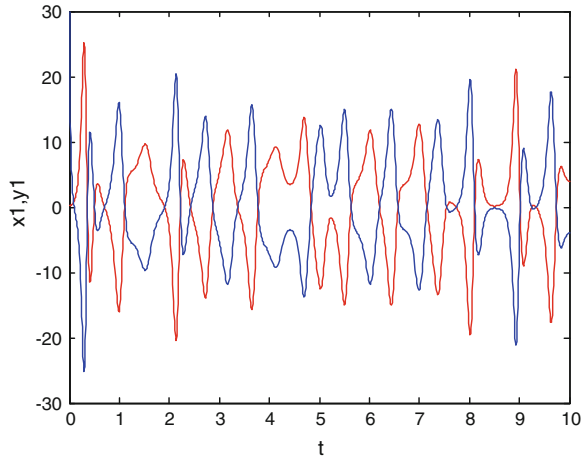


Fig. 42.3 The time series of two identical systems



the drive and response systems are chosen as $x_1(0) = 0.1, x_2(0) = 0.2, x_3(0) = 0.3, x_4(0) = 0.4, y_1(0) = 30, y_2(0) = 40, y_3(0) = 50, y_4(0) = 60$ and $l_1 = l_2 = 1$, respectively. Thus the initial states of the error system are $e_1(0) = 29.9, e_2(0) = 39.8, e_3(0) = 49.7, e_4(0) = 59.6$. Next, the error system is solved by adopting fourth-order Runge–Kutta method with time step size 0.001.

Example 1 The synchronization errors of systems (42.3) and (42.4) are displayed in Fig. 42.1 with $\alpha_1 = \alpha_2 = \alpha_3 = \alpha_4 = 1$. From the figure, it can be observed that each error converges to zero and the two identical systems achieve complete synchronization.

Example 2 Also, the synchronization errors of systems (42.3) and (42.4) are shown in Fig. 42.2 with $\alpha_1 = \alpha_2 = \alpha_3 = \alpha_4 = -1$. The time series of the drive and response systems are illustrated in Fig. 42.3. Obviously, the synchronization errors converge to 0, too. And the two systems do indeed achieve anti-synchronization.

Fig. 42.4 Hybrid projective errors versus time t

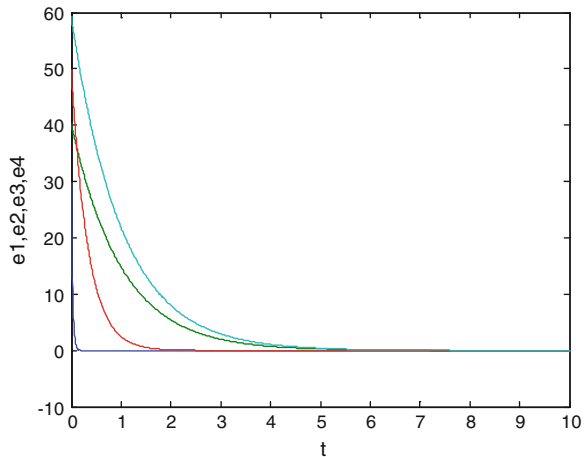
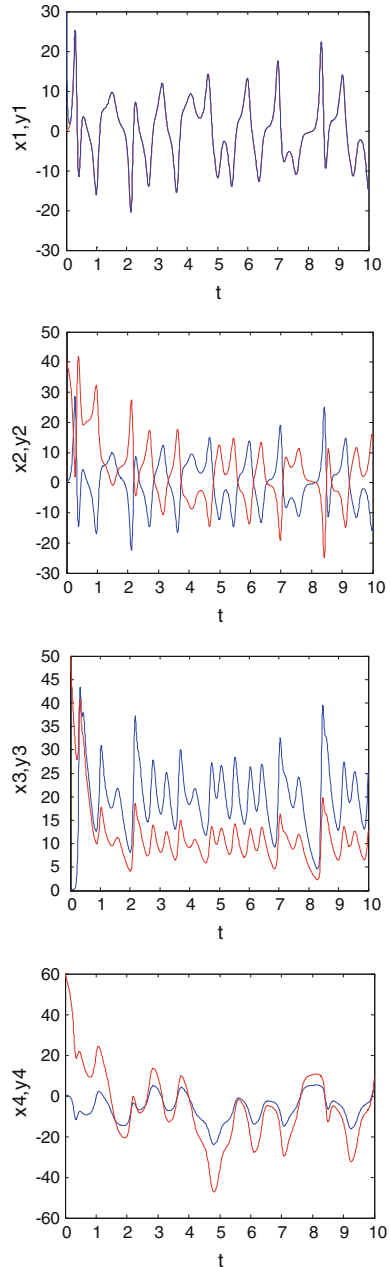


Fig. 42.5 The time series of two identical systems



Example 3 The same initial states of the drive and response systems are chosen as in Examples 1 and 2 with $\alpha_1 = 1, \alpha_2 = -1, \alpha_3 = 1/2, \alpha_4 = 2$. The hybrid projective errors are displayed in Fig. 42.4. We can see that all of the synchronization errors converge to 0. For further observations, the time series of the drive and

response systems are depicted in Fig. 42.5. As can be seen, variables x_1 versus y_1 display a complete synchronization behavior, variables x_2 versus y_2 show anti-synchronization phenomenon, variable y_3 converges to half of the value of x_3 and variable y_4 finally converges to two times the value of x_4 . It is clear that the two hyperchaotic systems (42.3) and (42.4) can achieve HPS.

42.4 Conclusion

Hybrid projective synchronization for a new hyperchaotic system is considered. Based on nonlinear feedback control theory and Lyapunov stable theory, the nonlinear controller is designed to guarantee HPS, which includes synchronization, anti-synchronization and projective synchronization. Numerical simulations are shown to verify and illustrate the effectiveness of this controller. Of course, it remains other problems such as HPS of them with uncertain structures undiscussed here which will be our future work.

Acknowledgments This research is supported by the Science Foundation of Shandong Jiaotong University (Nos: Z201030, Z201130, Z201203 and Z201204) and the Scientific Research Foundation of Shandong Education Office of China (No J12LI55).

References

1. Pecora LM, Carroll TL (1990) Synchronization in chaotic systems. *Phys Rev Lett* 64(8):821–824
2. Carroll TL, Pecora LM (1991) Synchronizing chaotic circuits. *IEEE Trans Circuits Syst* 38(4):453–456
3. Ma J, Li F, Huang L, Jin W-Y (2011) Complete synchronization, phase synchronization and parameters estimation in a realistic chaotic system. *Commun Nonlin Sci Numer Simul* 16(9):3770–3785
4. Taghvafard H, Erjaee DH (2011) Phase and anti-phase synchronization of fractional order chaotic systems via active control. *Commun Nonlin Sci Numer Simul* 16(10):4079–4088
5. Li D, Li XL, Cui D, Li ZH (2011) Phase synchronization with harmonic wavelet transform with application to neuronal populations. *Neurocomputing* 74(17):3389–3403
6. Chen Y, Li MY, Cheng ZF (2010) Global anti-synchronization of master–slave chaotic modified Chua’s circuits coupled by linear feedback control. *Math Comput Model* 52(3):567–573
7. Liu ST, Liu P (2011) Adaptive anti-synchronization of chaotic complex nonlinear systems with unknown parameters. *Nonlin Anal Real World Appl* 12(6):3046–3055
8. Zhao HY, Zhang Q (2011) Global impulsive exponential anti-synchronization of delayed chaotic neural networks. *Neurocomputing* 74(4):563–567
9. Zhang LP, Jiang HB (2011) Impulsive generalized synchronization for a class of nonlinear discrete chaotic systems. *Commun Nonlin Sci Numer Simul* 16(4):2027–2032
10. Wu YQ, Li CP, Wu YJ, Jürgen K (2012) Generalized synchronization between two different complex networks. *Commun Nonlin Sci Numer Simul* 17(1):349–355
11. Mainieri R, Rehacek J (1999) Projective synchronization in three-dimensional chaotic systems. *Phys Rev Lett* 82:3042–3045

12. Chen CY, Xu D (2005) Secure digital communication using controlled projective synchronization of chaos. *Chaos Solitons Fractals* 23:1063–1070
13. Wen GL, Xu D (2005) Nonlinear observer control for full-state projective synchronization in chaotic continuous-time systems. *Chaos Solitons Fractals* 26:71–77
14. Pang S, LiuY (2011) A new hyperchaotic system from the Lu system and its control. *J Comput Appl Math* 235:2775–2789

Chapter 43

Fuzzy Observer-Based Robust H_∞ Guaranteed Cost Fault-Tolerant Design for Nonlinear NCS

Jun Wang, Wei Li and Zhanming Li

Abstract A fault-tolerant control problem of robust H_∞ guaranteed is addressed for nonlinear networked control systems (NNCS) with network-induced delay and packet dropout based on T-S fuzzy model. The delay-dependent sufficient condition against actuator failures is given by employing state observer and state feedback control strategy. Observer-based controller gain and state feedback controller gain can be obtained and optimized. An example is used to illustrate the effectiveness and feasibility of proposed approach.

Keywords Networked control system · State observer · T-S fuzzy model · H_∞ guaranteed cost · Fault-tolerant control

43.1 Introduction

Due to widespread use of networked control systems (NCS) in aerospace, petrochemical, transportation, energy and other industries, more and more researchers have started to focus on the fault-tolerant control of NCS, hoping to get better performances and higher safety and reliability [1, 2]. However, because of the complexity of the nonlinear system, the fault-tolerant research is still very limited in nonlinear NCS (NNCS) [3, 4]. Especially when fail to direct measure all state variables of the system, it will cause difficulties in the physical implementation of the state feedback. In Ref. [5], dynamic output compensation controller is used to do preliminary researches on the fault-tolerant control of NNCS. But some difficulties are emerged in the solution to the controller. In [6], For a class of NNCS with network-induced delay and packet dropout, which is influenced by external

J. Wang (✉) · W. Li · Z. Li
College of Electrical and Information Engineering, Lanzhou University of Technology, No.
287, Langongping Road, Qilihe District, Lanzhou, Gansu, China
e-mail: wangj31901@163.com

disturbance with limited energy in transmission, the H_∞ integrality problem with actuator failures and immeasurable state is analyzed based on state observer. But the uncertainty and dynamic performance of the system is not considered.

Therefore, for a class of uncertain NNCS with time-delay and packet dropout, based on T-S fuzzy model, adopted state observer, this paper studies the fault-tolerant control problems of the robust H_∞ guaranteed cost under the condition of possible actuator failures.

43.2 System Description

Typical uncertain NNCS described by T-S fuzzy model is shown in Fig 43.1:

In Fig. 43.1, τ_{ca} and τ_{sc} are the time-varying network-induced delays from controller to actuator and from sensor to controller, respectively. According to analysis about network-induced delays and data packet dropouts in the literature [5, 7], we have

$$\tau_{sc1} \leq \tau_1(t) \leq (\delta_{1M} + 1)T + \tau_{sc2} \quad \tau_{ca1} \leq \tau_2(t) \leq (\delta_{2M} + 1)T + \tau_{ca2}$$

define $\tau_{s2} = (\delta_{1M} + 1)T + \tau_{sc2}$, $\tau_{s1} = \tau_{sc1}$, then $\tau_{s1} \leq \tau_1(t) \leq \tau_{s2}$, similarly have $\tau_{c1} \leq \tau_2(t) \leq \tau_{c2}$ where $\tau_1(t)$ and $\tau_2(t)$ are total time-varying delays respectively of controller-to-actuator and sensor-to-controller including network-induced delays and data packet dropouts. τ_{sc1} , τ_{sc2} and τ_{ca1} , τ_{ca2} are positive constant representing the lower and upper delay bound of corresponding transmission channel, respectively. δ_{1M} and δ_{2M} are maximum number of data packet dropouts of corresponding transmission channel, respectively.

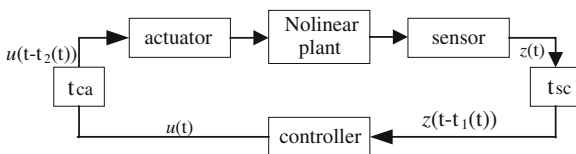
Fuzzy rule i : if $\theta_1(t)$ is F_{i1} and if $\theta_2(t)$ is F_{i2} and ... and $\theta_n(t)$ is F_{in} , then

$$\dot{x}(t) = \tilde{A}_i x(t) + \tilde{B}_i u(t - \tau_2(t)) + B_{1i} w(t) \tag{43.1}$$

$$z(t) = C_i x(t - \tau_1(t)) + D_i u(t - \tau_2(t)) \quad (i = 1, 2, \dots, N) \tag{43.2}$$

where $i(i = 1, 2, \dots, N)$ is the number of if-then rules; F_{ij} ($j = 1, 2, \dots, n$) and $\theta(t) = [\theta_1(t), \theta_2(t), \dots, \theta_n(t)]^T$ are fuzzy sets and premise variables, respectively; $x(t) \in R^n$, $u(t) \in R^m$ and $z(t) \in R^l$ are state vector, control input vector and output control vector, respectively; $\tilde{A}_i = A_i + \Delta A_i$, $\tilde{B}_i = B_i + \Delta B_i$, A_i , B_i , C_i and D_i are constant matrices with appropriate dimensions, respectively; ΔA_i and ΔB_i are time-varying unknown matrices with appropriate dimensions, respectively, which stand for uncertainty of structure in the system model.

Fig. 43.1 Framework of NNCS



Assume 1 the matrix with parameter uncertainty is norm-bounded, and can be described as $[\Delta A_i, \Delta B_i] = DF(t)[E_{ai}, E_{bi}]$, where D , E_{ai} and E_{bi} are known constant matrices with appropriate dimensions; $F(t)$ is an unknown matrix function with Lebesgue measurable elements satisfying the inequality $F^T(t)F(t) \leq I$.

By using a singleton fuzzifier, product inference and centre-average defuzzifier, the local models can be integrated into a global nonlinear model:

$$\dot{\mathbf{x}}(t) = \sum_{i=1}^N \mu_i(\theta(t)) [\tilde{A}_i \mathbf{x}(t) + \tilde{B}_i \mathbf{u}(t - \tau_2(t)) + \mathbf{B}_{1i} w(t)] \quad (43.3)$$

$$\mathbf{z}(t) = \sum_{i=1}^N \mu_i(\theta(t)) (\mathbf{C}_i \mathbf{x}(t - \tau_1(t)) + \mathbf{D}_i \mathbf{u}(t - \tau_2(t))) \quad (43.4)$$

where $\mu_i(\theta(t)) = \frac{a_i(\theta(t))}{\sum_{i=1}^N a_i(\theta(t))}$, and satisfying $\mu_i(\theta(t)) \geq 0$, $\sum_{i=1}^N \mu_i(\theta(t)) = 1$; $a_i(\theta(t)) = \prod_{j=1}^n F_{ij}(\theta_j(t))$, satisfying $a_i(\theta(t)) \geq 0$, $\sum_{i=1}^N a_i(\theta(t)) > 0$, and $F_{ij}(\theta_j(t))$ is grade of the membership of $\theta_j(t)$ in fuzzy set F_{ij} .

Assumed 2 all of the state variables are not easy to direct measurement in the uncertain NNCS, but they can completely be observed [6]. And define $\hat{\mathbf{x}}(t) \in R^n$ is the estimation of state vector $\mathbf{x}(t)$.

According to parallel distributed compensation (PDC) technique, the fuzzy dynamic output feedback controller based on state observer which shares the same premise parts as the fuzzy system has the following form

$$\begin{aligned} \dot{\hat{\mathbf{x}}}(t) = & \sum_{i=1}^N \mu_i(\theta(t)) [\tilde{A}_i \hat{\mathbf{x}}(t) + \tilde{B}_i \mathbf{u}(t) + \mathbf{B}_{1i} w(t) + \mathbf{I}_i [\mathbf{C}_i \mathbf{x}(t - \tau_1(t)) \\ & + \mathbf{D}_i \mathbf{u}(t - \tau_2(t) - \mathbf{C}_i \hat{\mathbf{x}}(t) - \mathbf{D}_i \mathbf{u}(t)]] \end{aligned} \quad (43.5)$$

$$\mathbf{u}(t) = \sum_{i=1}^N \mu_i(\theta(t)) \mathbf{K}_i \hat{\mathbf{x}}(t) \quad (43.6)$$

where, \mathbf{K}_j is the control gain matrix for the j th controller rule, \mathbf{I}_i is the observer gain matrix for the i th observer rule.

Substituting (43.6) into (43.3) and (43.5) yields the close-loop NNCS as follow

$$\begin{aligned} \dot{\hat{\mathbf{x}}}(t) = & \sum_{i=1}^N \sum_{j=1}^N \mu_i(\theta(t)) \mu_j(\theta(t)) [(\tilde{A}_i + \tilde{B}_i \mathbf{K}_j - \mathbf{I}_i \mathbf{C}_i - \mathbf{I}_i \mathbf{D}_i \mathbf{K}_j) \hat{\mathbf{x}}(t) + \mathbf{I}_i \mathbf{C}_i \mathbf{x}(t - \tau_1(t)) \\ & + \mathbf{I}_i \mathbf{D}_i \mathbf{K}_j \hat{\mathbf{x}}(t - \tau_2(t) + \mathbf{B}_{1i} w(t)] \end{aligned} \quad (43.7)$$

$$\dot{\mathbf{x}}(t) = \sum_{i=1}^N \sum_{j=1}^N \mu_i(\theta(t)) \mu_j(\theta(t)) [\tilde{A}_i \mathbf{x}(t) + \tilde{B}_i \mathbf{K}_j \hat{\mathbf{x}}(t - \tau_2(t)) + \mathbf{B}_{1i} w(t)] \quad (43.8)$$

Defining the estimation error $\mathbf{e}(t) = \hat{\mathbf{x}}(t) - \mathbf{x}(t)$, we get

$$\begin{aligned} \dot{\mathbf{e}}(t) = & \sum_{i=1}^N \sum_{j=1}^N \mu_i(\theta(t)) \mu_j(\theta(t)) [(\tilde{\mathbf{A}}_i + \tilde{\mathbf{B}}_i \mathbf{K}_j - \mathbf{I}_i \mathbf{C}_i - \mathbf{I}_i \mathbf{D}_i \mathbf{K}_j) \mathbf{e}(t) + (\tilde{\mathbf{B}}_i \mathbf{K}_j - \mathbf{I}_i \mathbf{C}_i \\ & - \mathbf{I}_i \mathbf{D}_i \mathbf{K}_j) \mathbf{x}(t) + \mathbf{I}_i \mathbf{C}_i \mathbf{x}(t - \tau_1(t)) + \mathbf{I}_i \mathbf{D}_i \mathbf{K}_j \mathbf{x}(t - \tau_2(t)) + \mathbf{I}_i \mathbf{D}_i \mathbf{K}_j \mathbf{e}(t - \tau_2(t)) \\ & - \tilde{\mathbf{B}}_i \mathbf{K}_j \mathbf{x}(t - \tau_2(t)) - \tilde{\mathbf{B}}_i \mathbf{K}_j \mathbf{e}(t - \tau_2(t))] \end{aligned} \quad (43.9)$$

43.3 Main Results

According to the Ref. [7], we can introduce a switching matrix L as follow:

$L = \text{diag} \{l_1, l_2, \dots, l_n\}$, where

$$l_i = \begin{cases} 1, & \text{the } i\text{th actuator normal} \\ 0, & \text{the } i\text{th actuator failure} \end{cases}$$

So we get the following uncertain nonlinear networked closed-loop fault system (NNCFS) based on fuzzy state observer.

$$\begin{aligned} \dot{\mathbf{x}}(t) = & \sum_{i=1}^N \sum_{j=1}^N \mu_i(\theta(t)) \mu_j(\theta(t)) [\tilde{\mathbf{A}}_i \mathbf{x}(t) + \tilde{\mathbf{B}}_i \mathbf{L} \mathbf{K}_j \mathbf{x}(t - \tau_2(t)) \\ & + \tilde{\mathbf{B}}_i \mathbf{L} \mathbf{K}_j \mathbf{e}(t - \tau_2(t)) + \mathbf{B}_{1i} w(t)] \end{aligned} \quad (43.10)$$

$$\begin{aligned} \dot{\mathbf{e}}(t) = & \sum_{i=1}^N \sum_{j=1}^N \mu_i(\theta(t)) \mu_j(\theta(t)) [(\tilde{\mathbf{A}}_i + \tilde{\mathbf{B}}_i \mathbf{L} \mathbf{K}_j - \mathbf{I}_i \mathbf{C}_i - \mathbf{I}_i \mathbf{D}_i \mathbf{K}_j) \mathbf{e}(t) \\ & + (\tilde{\mathbf{B}}_i \mathbf{L} \mathbf{K}_j - \mathbf{I}_i \mathbf{C}_i - \mathbf{I}_i \mathbf{D}_i \mathbf{K}_j) \mathbf{x}(t) + \mathbf{I}_i \mathbf{C}_i \mathbf{x}(t - \tau_1(t)) + \mathbf{I}_i \mathbf{D}_i \mathbf{K}_j \mathbf{x}(t - \tau_2(t)) \\ & + \mathbf{I}_i \mathbf{D}_i \mathbf{K}_j \mathbf{e}(t - \tau_2(t)) - \tilde{\mathbf{B}}_i \mathbf{L} \mathbf{K}_j \mathbf{x}(t - \tau_2(t)) - \tilde{\mathbf{B}}_i \mathbf{L} \mathbf{K}_j \mathbf{e}(t - \tau_2(t))] \end{aligned} \quad (43.11)$$

According to the uncertain NNCFS, we define the H_∞ guaranteed cost function, namely $J = \int_0^\infty [x^T(t) \mathbf{Q} x(t) + u^T(t) \mathbf{R} u(t)] dt$ where \mathbf{Q} and \mathbf{R} are given positive definite symmetric matrices.

In our study, considering the possible actuator failures, based on fuzzy state observer, the aim of robust H_∞ guaranteed cost fault-tolerant control is to seek the control gain matrix \mathbf{K}_j and the observer gain matrix \mathbf{I}_i such that the uncertain NNCFS meet the following conditions: 1) when $w(t) = 0$, the uncertain NNCFS is asymptotically stable; 2) when $w(t) = 0$, the H_∞ guaranteed cost function J satisfies $J \leq J^*$, and then J^* is said to upper boundary of H_∞ guaranteed cost function;

3) for all non-zero $w(t) \in L_2[0, \infty)$, $\|z(t)\|_2 < \gamma \|w(t)\|_2$ is satisfied under the zero-initial condition. Where $\gamma > 0$ denotes prescribed attenuation level, $\|\cdot\|_2$ denotes norm of $L_2[0, \infty)$.

Theorem 1 For the uncertain NNCFs described by (43.10–43.11) and the H_∞ guaranteed cost function J , given positive constants d , τ_{sc1} , τ_{sc2} , τ_{ca1} , τ_{ca2} , δ_{1M} and δ_{2M} , if there exist matrices $\mathbf{P}_1 = \mathbf{P}_1^T > 0$, $\mathbf{Z}_i = \mathbf{Z}_i^T > 0$ ($i = 1, 2, 3, 4$), $\bar{\mathbf{Q}} = \bar{\mathbf{Q}}^T > 0$, $\bar{\mathbf{Q}}_{ij} = \bar{\mathbf{Q}}_{ij}^T > 0$ ($i, j = 1, 2$) and \mathbf{X} , \mathbf{Y}_{1j} , \mathbf{Y}_{2i} ($i, j = 1, 2, \dots, N$) with appropriate dimensions, satisfying the following LMIs for all uncertain matrixes:

$$\begin{bmatrix} \bar{\Pi}_{ij}^1 & \bar{\mathbf{H}}_1 & \varepsilon_1^{-1} \bar{\mathbf{E}}_1^T & \bar{\mathbf{H}}_2 & \varepsilon_2^{-1} \bar{\mathbf{E}}_2^T \\ & -\varepsilon_1^{-1} \mathbf{I} & \mathbf{0} & \mathbf{0} & \mathbf{0} \\ & & -\varepsilon_1^{-1} \mathbf{I} & \mathbf{0} & \mathbf{0} \\ & * & & -\varepsilon_2^{-1} \mathbf{I} & \mathbf{0} \\ & & & & -\varepsilon_2^{-1} \mathbf{I} \end{bmatrix} < 0 \quad (43.12)$$

$$\bar{\Pi}_{ij}^2 = \begin{bmatrix} \bar{\Pi}_{1ij}^2 & \bar{\Pi}_{2ij}^2 \end{bmatrix} < 0 \quad (43.13)$$

where

$$\bar{\Pi}_{ij}^1 = \begin{bmatrix} \bar{\Pi}_{1ij}^1 & \bar{\Pi}_{2ij}^1 \\ * & \bar{\Pi}_{3ij}^1 \end{bmatrix} \quad \bar{\Pi}_{1ij}^1 = \begin{bmatrix} \bar{\Phi}_{11} & \mathbf{0} & \bar{\Phi}_{13} & \bar{\Phi}_{14} & \bar{\Phi}_{15} & \mathbf{B}_{1i} \\ & \mathbf{0} & \mathbf{0} & \mathbf{0} & \mathbf{0} & \mathbf{0} \\ & & \mathbf{0} & \bar{\Phi}_{34} & \mathbf{0} & \mathbf{0} \\ & & & \bar{\Phi}_{44} & \bar{\Phi}_{45} & \mathbf{0} \\ * & & & & \mathbf{0} & \mathbf{0} \\ & & & & & -\gamma^2 \mathbf{I} \end{bmatrix}$$

$$\bar{\Phi}_{11} = \mathbf{A}_i \mathbf{X}^T + \mathbf{X} \mathbf{A}_i^T + \bar{\mathbf{Q}}, \quad \bar{\Phi}_{13} = \mathbf{B}_i \mathbf{L} \mathbf{Y}_{1j}, \quad \bar{\Phi}_{14} = d \mathbf{Y}_{1j}^T \mathbf{L}^T \mathbf{B}_i^T$$

$$\bar{\Phi}_{15} = \mathbf{B}_i \mathbf{L} \mathbf{Y}_{1j}, \quad \bar{\Phi}_{34} = -d \mathbf{Y}_{1j}^T \mathbf{L}^T \mathbf{B}_i^T,$$

$$\bar{\Phi}_{44} = d \mathbf{A}_i \mathbf{X}^T + d \mathbf{B}_i \mathbf{L} \mathbf{Y}_{1j} + d \mathbf{X} \mathbf{A}_i^T + d \mathbf{Y}_{1j}^T \mathbf{L}^T \mathbf{B}_i^T, \quad \bar{\Phi}_{45} = -d \mathbf{B}_i \mathbf{L} \mathbf{Y}_{1j}$$

$$\bar{\Pi}_{2ij}^1 = \begin{bmatrix} \bar{\Phi}_{17} & \bar{\Phi}_{18} & \bar{\Phi}_{19} & \bar{\Phi}_{110} & \bar{\Phi}_{111} & \mathbf{Y}_{1j}^T & \mathbf{0} \\ \mathbf{0} & \mathbf{0} & \mathbf{0} & \mathbf{0} & \mathbf{0} & \mathbf{0} & \mathbf{C}_i^T \\ \bar{\Phi}_{37} & \bar{\Phi}_{38} & \bar{\Phi}_{39} & \bar{\Phi}_{310} & \bar{\Phi}_{311} & \mathbf{0} & \bar{\Phi}_{313} \\ \bar{\Phi}_{47} & \mathbf{0} & \mathbf{0} & \mathbf{0} & \mathbf{0} & \mathbf{Y}_{1j}^T & \mathbf{0} \\ \bar{\Phi}_{57} & \bar{\Phi}_{58} & \bar{\Phi}_{59} & \bar{\Phi}_{510} & \bar{\Phi}_{511} & \mathbf{0} & \bar{\Phi}_{513} \\ \mathbf{0} & \bar{\Phi}_{68} & \bar{\Phi}_{69} & \bar{\Phi}_{610} & \bar{\Phi}_{611} & \mathbf{0} & \mathbf{0} \end{bmatrix}$$

$$\begin{aligned}
 \bar{\Phi}_{17} &= -Y_{lj}^T D_i^T, \bar{\Phi}_{18} = XA_i^T \tau_{s2}, \bar{\Phi}_{19} = XA_i^T \tau_{c2}, \bar{\Phi}_{110} = XA_i^T (\alpha_1 - \tau_{s1}) \\
 \bar{\Phi}_{111} &= XA_i^T (\alpha_2 - \tau_{c1}), \bar{\Phi}_{37} = Y_{lj}^T D_i^T, \bar{\Phi}_{38} = (B_i LY_{lj})^T \tau_{s2}, \\
 \bar{\Phi}_{39} &= (B_i LY_{lj})^T \tau_{c2}, \bar{\Phi}_{310} = (B_i LY_{lj})^T (\alpha_1 - \tau_{s1}) \\
 \bar{\Phi}_{311} &= (B_i LY_{lj})^T (\alpha_2 - \tau_{c1}), \bar{\Phi}_{313} = Y_{lj}^T D_i^T, \bar{\Phi}_{47} = -Y_{lj}^T D_i^T, \bar{\Phi}_{57} = Y_{lj}^T D_i^T \\
 \bar{\Phi}_{58} &= (B_i LY_{lj})^T \tau_{s2}, \bar{\Phi}_{59} = (B_i LY_{lj})^T \tau_{c2}, \bar{\Phi}_{510} = (B_i LY_{lj})^T (\alpha_1 - \tau_{s1}) \\
 \bar{\Phi}_{511} &= (B_i LY_{lj})^T (\alpha_2 - \tau_{c1}), \bar{\Phi}_{513} = Y_{lj}^T D_i^T, \bar{\Phi}_{68} = B_{li}^T \tau_{s2}, \bar{\Phi}_{69} = B_{li}^T \tau_{c2} \\
 \bar{\Phi}_{610} &= B_{li}^T (\alpha_1 - \tau_{s1}), \bar{\Phi}_{611} = B_{li}^T (\alpha_2 - \tau_{c1})
 \end{aligned}$$

$$\begin{aligned}
 \bar{H}_1^T &= [D^T \quad 0 \quad 0 \quad 0 \quad 0 \quad 0 \quad 0 \quad D^T \tau_{s2} \quad D^T \tau_{c2} \quad D^T (\alpha_1 - \tau_{s1}) \quad D^T (\alpha_2 - \tau_{c1}) \quad 0 \quad 0] \\
 \bar{E}_1 &= [E_{ai} X^T \quad 0 \quad E_{bi} LY_{lj} \quad 0 \quad E_{bi} LY_{lj} \quad 0 \quad \cdots \quad 0]_{1 \times 13} \\
 \bar{H}_2^T &= [0 \quad 0 \quad 0 \quad dD^T \quad 0 \quad \cdots \quad 0]_{1 \times 13} \\
 \bar{E}_2 &= [E_{bi} LY_{lj} \quad 0 \quad -E_{bi} LY_{lj} \quad E_{ai} X^T + E_{bi} LY_{lj} \quad -E_{bi} LY_{lj} \quad 0 \quad \cdots \quad 0]_{1 \times 13} \\
 \bar{\Pi}_{3ij}^1 &= \text{zeros}(7)
 \end{aligned}$$

$$\bar{\Pi}_{2ij}^2 = \begin{bmatrix} 0 & -C_i^T Y_{2i}^T & 0 \\ 0 & C_i^T Y_{2i}^T & 0 \\ Z_4 & 0 & 0 \\ 0 & 0 & 0 \\ -Q_{21} - Z_4 & 0 & 0 \\ * & Q_{12} + Q_{22} - Y_{2i} C_i - C_i^T Y_{2i}^T & Y_{2i} \epsilon^{-1} \\ * & * & 0 \end{bmatrix}$$

then existing the dynamic output feedback control law of robust H_∞ guaranteed cost fault-tolerant such that uncertain NNCFS is asymptotically stable with $K_j = Y_{lj} X^{-T}$ and $I_i = d^{-1} X Y_{2i}$, disturbance attenuation level is γ , and the H_∞ guaranteed cost function satisfies the following boundary

$$\begin{aligned}
 J^* &= \begin{bmatrix} x^T(0) \\ e^T(0) \end{bmatrix}^T \begin{bmatrix} P_1 & 0 \\ 0 & P_2 \end{bmatrix} \begin{bmatrix} x(0) \\ e(0) \end{bmatrix} \\
 &+ \sum_{i=1}^2 \int_{-\alpha_i}^0 \begin{bmatrix} x^T(s) \\ e^T(s) \end{bmatrix}^T \begin{bmatrix} Q_{i1} & 0 \\ 0 & Q_{i2} \end{bmatrix} \begin{bmatrix} x(s) \\ e(s) \end{bmatrix} ds \\
 &+ \int_{-\tau_{s2}}^0 \int_s^0 \tau_{s2} \dot{x}^T(v) Z_1 \dot{x}(v) dv ds + \int_{-\tau_{c2}}^0 \int_s^0 \tau_{c2} \dot{x}^T(v) Z_2 \dot{x}(v) dv ds \\
 &+ \int_{-\alpha_1}^{-\tau_{s1}} \int_s^0 (\alpha_1 - \tau_{s1}) \dot{x}^T(v) Z_3 \dot{x}(v) dv ds \\
 &+ \int_{-\alpha_2}^{-\tau_{c1}} \int_s^0 (\alpha_2 - \tau_{c1}) \dot{x}^T(v) Z_4 \dot{x}(v) dv ds
 \end{aligned}$$

Proof the proof is cut off due to space limitation contact the authors for the detailed proof.

Remark 1 In theorem 1, without model transformation and free-weighting matrix, only Jensen inequality has been employed for cross terms. Especially, time delay is segmented into two sections, and introduced the intermediate variables α_1 and α_2 of delay information these reduce the conservatism to some extent [8, 9].

Remark 2 all relevant items including variables x and e are used to make the matrix dimension twice as large as that in the design of single-state feedback controller [6, 7]. This paper introduced the variables α_1 and α_2 , which reduced the complexity of the calculation by decreasing matrix dimension.

Remark 3 This paper did not introduce any free-weighting matrix, therefore the computational complexity caused by excessive decision variables has been significantly decreased.

43.4 Computer Simulation

In this section, we use an example to demonstrate the effectiveness of our main result, in which NNCS with parameter uncertainties is the same as [7].

In cases of actuator normal and possible failures, the switching matrices $L_0 = \text{diag}(1,1)$, $L_1 = \text{diag}(0,1)$ and $L_2 = \text{diag}(1,0)$ indicate actuator normal and actuator 1,2 failure, respectively.

Considering the actual NCS, we assume $T = 0.05$ s, and set $\gamma = 0.9$, $\delta_{im}(i = 1, 2) = 2$, $\tau_{sci}(i = 1, 2)$ are 0.01 s and 0.1 s, respectively. $\tau_{cai}(i = 1, 2)$ are 0.01 s and 0.1 s, respectively. Then we can solve convex problem (43.12, 43.13) by using LMI toolbox to obtain

$$\mathbf{K}_1 = \begin{bmatrix} -3.5235 & -0.3810 \\ 1.2765 & -1.8105 \end{bmatrix}, \mathbf{K}_2 = \begin{bmatrix} -4.2102 & -0.4680 \\ 1.4688 & -1.9980 \end{bmatrix}$$

$$\mathbf{I}_1 = \begin{bmatrix} -1.17450 & 0.1270 \\ 0.42550 & 0.6035 \end{bmatrix}, \mathbf{I}_2 = \begin{bmatrix} -1.16950 & 0.1300 \\ 0.40800 & 0.5550 \end{bmatrix}$$

and H_∞ guaranteed cost function $J \leq 36.148$.

Setting the initial conditions of the system $x(0) = [2]^T$, $e(0) = [0.2, 0.2]^T$, in the cases of L_0 , L_1 and L_2 , response curve of the error vector e_1 , e_2 are shown in Figs. 43.2, 43.3 response curve of the state vector x_1 , x_2 are shown in Figs. 43.4, 43.5.

It is seen from Fig. 43.2 that state estimation error quickly approximate to zero, which show that the states of closed-loop NNCS with possible actuator failures can't be direct measured, but can be estimated well via the observer. Figure 43.3 can be seen that uncertain NNCS is not only asymptotically stable, but also has good dynamic performance and disturbance-resistant performance. These indicate that the proposed method makes the uncertain NNCS which includes time-delay

Fig. 43.2 Response curve of the error vector e1

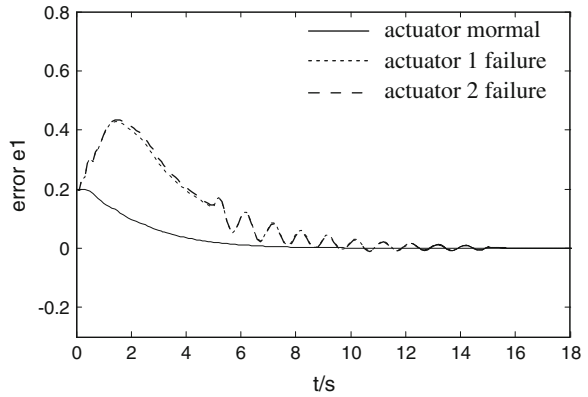


Fig. 43.3 Response curve of the error vector e2

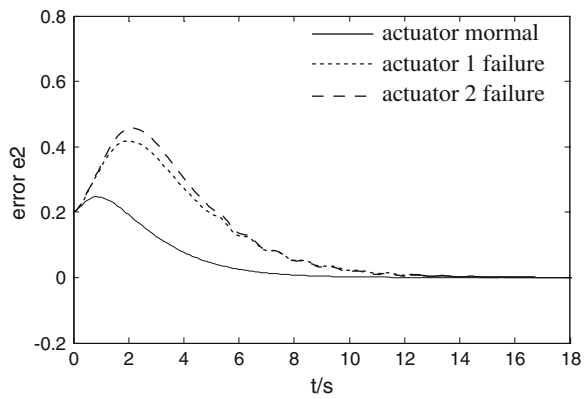
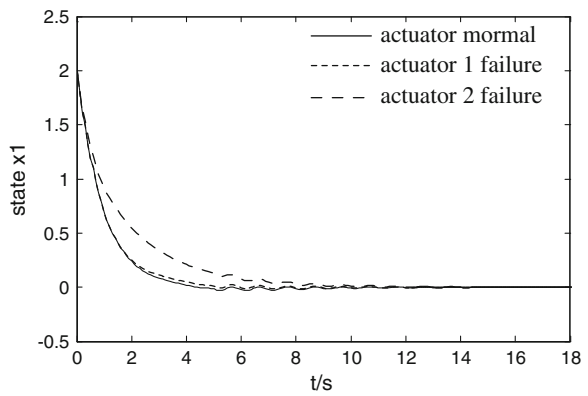
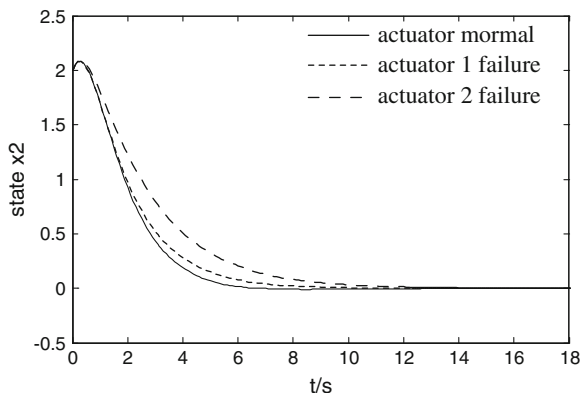


Fig. 43.4 Response curve of the state vector x1



and packet dropout against possible actuator failures have the ability of robust H_∞ guaranteed cost fault-tolerant.

Fig. 43.5 Response curve of the state vector x_2



Further, we can optimize minimum allowable γ for possible actuator failures via the mincx solver of LMI tools to obtain $\gamma_{\min} = 0.6325$. In addition, we also received the following optimal robust H_∞ guaranteed cost fault-tolerant controller gains:

$$\begin{aligned} \mathbf{K}_{\gamma-opt1} &= \begin{bmatrix} -1.7349 & -1.2540 \\ 1.8521 & 2.2074 \end{bmatrix} & \mathbf{I}_{\gamma-opt1} &= \begin{bmatrix} -1.2349 & 1.1254 \\ 1.1851 & 1.1207 \end{bmatrix} \\ \mathbf{K}_{\gamma-opt2} &= \begin{bmatrix} -1.8339 & -1.2650 \\ 1.8116 & 2.1210 \end{bmatrix} & \mathbf{I}_{\gamma-opt2} &= \begin{bmatrix} -1.2739 & 1.1260 \\ 1.3816 & 1.2110 \end{bmatrix} \end{aligned}$$

and upper boundary of H_∞ guaranteed cost function $J^* = 32.237$.

If set $\gamma = 0.9$, the minimum upper boundary of guaranteed cost J_a^* can be obtained using the optimized processing. That is $J_a^* = 29.64$, and optimal robust H_∞ guaranteed cost fault-tolerant controller gains are as follows:

$$\begin{aligned} \mathbf{K}_{J-opt2} &= \begin{bmatrix} -1.9580 & -1.4881 \\ 1.0862 & 2.4315 \end{bmatrix} & \mathbf{I}_{J-opt1} &= \begin{bmatrix} -1.5559 & 1.4464 \\ 1.4061 & 1.4417 \end{bmatrix} \\ \mathbf{K}_{J-opt1} &= \begin{bmatrix} -1.0670 & -1.4991 \\ 1.0457 & 2.4420 \end{bmatrix} & \mathbf{I}_{J-opt2} &= \begin{bmatrix} -1.5949 & 1.4470 \\ 1.6026 & 1.5320 \end{bmatrix} \end{aligned}$$

43.5 Conclusion

This paper, based on T-S fuzzy model, studies the fault-tolerant control problems of the robust H_∞ guaranteed cost on uncertain NNCS with time-delay and packet dropout under the condition of actuator failures. By constructing appropriate Lyapunov–Krasovskii function and adopting the Jensen inequality and matrix separation technologies, this paper deduces the delay-dependent sufficient condition of robust H_∞ guaranteed cost fault-tolerant against possible actuator failures. Further, we get the optimal robust fault-tolerant guaranteed cost controller gains

via ways of optimizing. Finally, a simulation example is given to shown the effectiveness and the feasibility of the obtained results.

Acknowledgments This work is partially supported by National Natural Science Foundation of China under Grant 60964003, Gansu Natural Science Foundation under Grant 096RJZA101.

References

1. Huo Z, Fang H (2007) Research on robust fault-tolerant control for networked control system with packet dropout. *J Syst Eng Electron* 18(1):76–82
2. Guo YN, Zhang QY, Gong DW, Zhang JH (2008) Robust fault-tolerant control of networked control systems with time-varying delays. *Control Decision*, 23(8):689–692 (in Chinese)
3. Yang F, Zhang H, Hui G, Wang S (2012) Mode-independent fuzzy fault-tolerant variable sampling stabilization of nonlinear networked systems with both time-varying and random delays. *Fuzzy Sets Syst* 10(2):1–19
4. Feng J, Wang SQ (2012) Reliable fuzzy control for a class of nonlinear networked control systems with time delay. *Acta Automatica Sinica* 38(7):1091–1099
5. Li W, Luo W, Jiang DN (2012) Fault-tolerant control for nonlinear networked control system based on dynamic output feedback. *J Lanzhou Univ Technol*, 38(1):63–70 (in Chinese)
6. Wang J, Li W, Li ZM (2012) Observer-based H_∞ integrity design for nonlinear NNCS. *J Jiangnan Univ (Natural Science edn)*, 6(11):442–452 (in Chinese)
7. Wang J, Li W, Li Z (2011) Design of robust H_∞ guaranteed cost and fault-tolerant for uncertain and nonlinear NCS. *J Huazhong Univ Sci Technol (Natural Science edn)*, 39(9):72–77 (in Chinese)
8. Peng C, Han QL (2011) Delay-range- dependent robust stabilization for uncertain for uncertain T-S fuzzy control systems with interval time-varying delays. *Inf Sci* 181:4287–4299
9. Chu H, Fei S, Yue D, Peng C, Sun J (2011) H_∞ quantized control for nonlinear networked control systems. *Fuzzy Sets Syst* 1174:99–113

Chapter 44

Study on Adaptive Parameters for GDFNN via Genetic Algorithms

Jin Chen, Shaojian Song and Xiaofeng Lin

Abstract In this paper, to solve the difficulty of artificial setting the parameters of generalized dynamic fuzzy neural network (GDFNN), an improved algorithm is proposed based on the genetic algorithm. The variable weighted-average is selected as fitness-function to transform the multi-objective optimization into single-objective optimization. The initial parameters of GDFNN can be set automatically by using genetic algorithm which optimizes the fitting and generalization effect. The efficiency of algorithm is tested by building MISO and MIMO set models. The results of experiments show that the improved algorithm has a better effect on fitting and generalization than artificial deciding parameters without over-fitting, and adapts to different objects, which solves the difficulty of initial parameters setting.

Keywords GDFNN · GA · Adaptive optimization of parameters · Modeling

44.1 Introduction

Generalized dynamic fuzzy neural network (GDFNN) is a kind of neural network, which is functional equivalent to fuzzy system. GDFNN is an improved type of Dynamic fuzzy neural network (D-FNN) based on the elliptical basis function (EBF) [1, 2]. By training the neural network, the difficulty of determining the membership degree functions and fuzzy rules is solved. In present research, using GDFNN in training of some kinds of objects, there have been some results [3]. But less research in determining of parameters of GDFNN has been achieved. The parameters are closely related to training effect. But there is not obvious

J. Chen (✉) · S. Song · X. Lin
School of Electrical Engineering, Guangxi University, Room 701, Nanning 530004, China
e-mail: chenjingxdx@163.com

mathematical relationships between parameters and training effect, artificial setting the parameters is difficultly. To solve the above problem, an improved algorithm is proposed based on the genetic algorithm, which can adapt to different training data and set the parameters of GDFNN automatically.

44.2 The GDFNN Algorithm and Existing Problems

GDFNN adopts four layer network structure, including the input layer, the membership function layer T-norm layer and output layer [1, 2]. T-norm layer actually is fuzzy rules of fuzzy algorithm. The network structure of GDFNN is shown in Fig. 44.1: where r is the number of variables, $x_i (i = 1, \dots, r)$ is the input variables, $A_{ij} (i = 1, \dots, r, j = 1, \dots, u)$ is the membership function, R_j is the j -th fuzzy rule, w_j is the connection weights of j -th fuzzy rule, y is the output of network.

According to the GDFNN training process described in the literature [1, 2], the parameter k decides the follow-up width of Gauss membership then the first membership function determining; parameter k_{mf} decides the similarity of adjacent membership function; parameter k_{error} decides the number of neurons of T-norm layer. In the process of GDFNN training, these three parameters have great influence on the network training effect. We consider an algorithm which can automatically adjust the initial parameters of GDFNN to adapting to different training data.

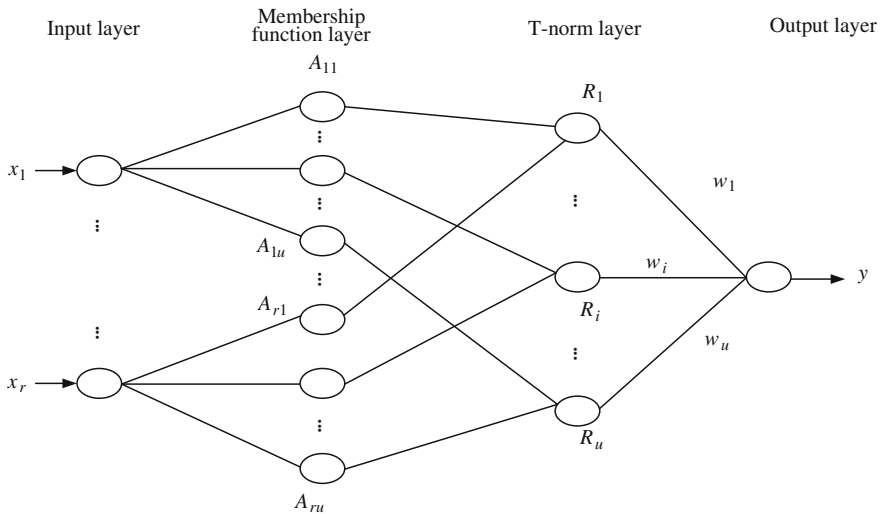


Fig. 44.1 Structure of GDFNN

44.3 Design of Adaptive Training Algorithm

The current researches which combine the optimization algorithm [4] with neural network training to optimize the parameters of network [5, 6], did not solve the problem of initial network parameters setting. In this paper, an improved algorithm is proposed which can set the initial parameters of GDFNN automatically by using genetic algorithm which optimizes the fitting and generalization effect.

44.3.1 Fitness Function of Genetic Algorithms

In order to shorten the operation time, by selecting the appropriate fitness function of genetic algorithm according to the characteristic of GDFNN, the multi-objective optimization problem is transformed into the single objective optimization problem. The fitness function is given in Eq. (44.1),

$$\begin{aligned}
 J &= k_f \cdot RMSE_f + k_g \cdot RMSE_g \\
 k_f &= \sin^2 \left(\frac{RMSE_f}{RMSE_f + RMSE_g} \cdot \frac{\pi}{2} \right) \\
 k_g &= \sin^2 \left(\frac{RMSE_g}{RMSE_f + RMSE_g} \cdot \frac{\pi}{2} \right)
 \end{aligned} \tag{44.1}$$

where, k_f is the weight of fitting root mean square error, k_g is the weight of generalization root mean square error, $RMSE_f$ is the fitting root mean square error, $RMSE_g$ is the generalization root mean square error.

Comparing with the constant weight fitness function, the variable weight function has the following advantages: 1. In the condition of same J , the difference of $RMSE_f$ and $RMSE_g$ can be reduced; 2. The fitness function is close to the larger one of $RMSE_f$ and $RMSE_g$. The fitness function can reflect the effect of objective better. The proving is given as following:

The constant weight fitness function is given as Eq. (44.2),

$$J = K_f \cdot RMSE_f + K_g \cdot RMSE_g \tag{44.2}$$

where, K_f and K_g are constants greater than 0, and $K_f + K_g = 1$. In a certain parameter range, $RMSE_f$ and $RMSE_g$ are negative correlation, and $RMSE_g - RMSE_f > 0$.

When $RMSE_f = 0$, $RMSE_g - RMSE_f$ gets the maximum value.

Let $J = a$, obtain that,

$$RMSE_g = \frac{a}{K_g} \tag{44.3}$$

then,

$$\max(RMSE_g - RMSE_f) = \frac{a}{K_g} \quad (44.4)$$

Similarly, take the fitness function as Eq. (44.1), then,

$$\max(RMSE_g - RMSE_f) = a \quad (44.5)$$

and $0 < K_g < 1$, then,

$$a < \frac{a}{K_g} \quad (44.6)$$

In conclusion, compared with fitness function as Eq. (44.2), the fitness function as Eq. (44.1) can reduce the difference of $RMSE_f$ and $RMSE_g$, by structure the weights as the function of $RMSE_f$ and $RMSE_g$.

Take the fitness function as Eq. (44.2), let $RMSE_f > RMSE_g$, because of $K_f + K_g = 1$, then,

$$RMSE_f - J = K_g(RMSE_f - RMSE_g) > 0 \quad (44.7)$$

$$RMSE_g - J = K_f(RMSE_g - RMSE_f) < 0 \quad (44.8)$$

when $RMSE_f > RMSE_g$, according to Eqs. (44.7) and (44.8),

$$RMSE_f > J > RMSE_g \quad (44.9)$$

let $K_f > K_g$, then,

$$K_g(RMSE_g - RMSE_f) > K_f(RMSE_g - RMSE_f) \quad (44.10)$$

substitute Eqs. (44.7) and (44.8) into Eq. (44.10), then,

$$|RMSE_f - J| < |RMSE_g - J| \quad (44.11)$$

Similarly, when $RMSE_f < RMSE_g$,

$$|RMSE_f - J| < |RMSE_g - J| \quad (44.12)$$

I.e. when take the constant weighted average function as Eq. (44.2) to be fitness function, the value of the fitness function will be closed to variable which weight is large.

Suppose the function as,

$$f(x_1, x_2) = \sin^2\left(\frac{x_1}{x_1 + x_2} \cdot \frac{\pi}{2}\right) \quad (44.13)$$

where, $x_1 > 0$ and $x_2 > 0$, then,

$$\frac{\partial f(x_1, x_2)}{\partial x_1} = 2 \cdot \sin\left(\frac{x_1}{x_1 + x_2} \cdot \frac{\pi}{2}\right) \cdot \cos\left(\frac{x_1}{x_1 + x_2} \cdot \frac{\pi}{2}\right) \cdot \frac{(x_1 + x_2) - x_1}{(x_1 + x_2)^2} \cdot \frac{\pi}{2} > 0 \quad (44.14)$$

because of Eq. (44.14), the function $f(x_1, x_2)$ in the average of $x_1 \in (0, \infty)$ and $x_2 \in (0, \infty)$ is monotonically increasing functions on x_1 ; The function $f(x_2, x_1)$ in the average of $x_2 \in (0, \infty)$ and $x_1 \in (0, \infty)$ is monotonically increasing functions on x_2 .

It can be proved, when $RMSE_f > RMSE_g$,

$$|RMSE_f - J| < |RMSE_g - J| \quad (44.15)$$

when $RMSE_f < RMSE_g$,

$$|RMSE_f - J| > |RMSE_g - J| \quad (44.16)$$

In conclusion, compared with fitness function as Eq. (44.2), the value of fitness function as Eq. (44.1) can be closed to the larger variable. The value of fitness function as Eq. (44.1) can reflect the objective of genetic algorithm better.

44.3.2 Genetic Algorithm Process

Commonly used genetic algorithm encoding includes binary encoding [3] and decimal encoding [4, 5]. There are following disadvantages when use binary encoding to solving the problems, such as the two bodies of small Euclid distance still may be large Hamming distance, that will reduce the efficiency of the genetic algorithm search. Accuracy which is determined by the binary encoded string length can't fine-tune (That the binary encoded string is too short will affect the accuracy. But that the binary encoding string is too long will reduce the efficiency of the algorithm). Decimal encoding which does not have encoding and decoding process can improve the accuracy and speed of operating [4]. Therefore, in this paper, decimal encoding is used in genetic algorithm.

The training algorithm proposed in this paper is as below,

1. Give the data for training, and the parameters of object, including the number of input and output, and whether the noise data is removed.
2. The data is divided into a plurality of multi-input single-output training data, according to the number of output.
3. The chromosome of genetic algorithm is be initialized (here is the three parameters of GDFNN k , k_{mf} , k_{error}), then the network is trained using the current chromosome and calculate the value of J . The complete chromosome is

$$[k \quad k_{mf} \quad k_{error} \quad J \quad RMSE_f \quad RMSE_g]$$

4. The current population is sorted from smallest to largest according to the 4th column of the individual. Then delete the individuals which number is larger than the number of population, i.e. natural selection.
5. Carry on the genetic operation, including crossover and mutation, then take the new individual into GDFNN for training, and calculate the value of J .
6. Repeat the steps from 4-th to 5-th, until the end of iteration or the value of J is meet the requirements.
7. The individuals in front of population are genetic algorithm solution sets. Take the first individual as the optimized parameters of GDFNN and get the training results.
8. Repeat the steps from 3-th to 7-th to each set of training data. Complete the mathematical model.

44.4 The Test of Algorithm Efficiency

The efficiency of algorithm is tested by building multi-input multi-output (MISO) and multi-input and single-output (MIMO) set models.

According to the meaning of the initial parameters of GDFNN, set the range of parameters: $k \in [1, 100]$, $k_{mf} \in [0.2, 0.8]$, $k_{error} \in [0.001, 0.1]$, set other parameters of network $e_{min} = 0.03$, $e_{max} = 0.08$, $\varepsilon_{min} = 0.5$, $\varepsilon_{max} = 0.8$, $k_s = 0.8$. Set the number of the genetic algorithm initial population to be 10, the size of population to be 400 and number of genetic times to be 10.

In order to test the algorithm efficiency to MISO set, the data of Coulombic Efficiency (EC) of single flow zinc-nickel battery [7] is used. This set is 3 input (the number of cycles, the charge–discharge current density and the voltage of cycle pump) and 1 output (EC) object with coupling. Through the training of the algorithm in this paper, the optimized initial parameters are as below: $k = 27.2247$, $k_{mf} = 0.4979$, $k_{error} = 0.0083$. The Structure of GDFNN is 3-15-5-1. Part training data of Single flow zinc-nickel battery is given as Table 44.1.

Compared with artificial setting the parameters of GDFNN, the training results of the algorithm using the data in Table 44.1 is as shown in Table 44.2.

Table 44.1 Part data of Single flow zinc-nickel battery

Number of simple	Cycle times	current density (mA/cm ²)	Pump voltage (V)	EC (%)
1	1	10.0	140	64.40
2	2	10.0	140	98.60
3	3	10.0	140	97.70
...
272	10	27.5	150	98.29

Table 44.2 Performance comparison of EC of single flow zinc-nickel battery between the proposed method and traditional artificial selecting parameters

Variables	Artificial setting parameters	Adaptive computing parameters
RMSE of EC fitting	3.7787	3.6971
RMSE of EC generalization	4.1487	4.0885
Value of Fitness function J	3.9772	3.9082

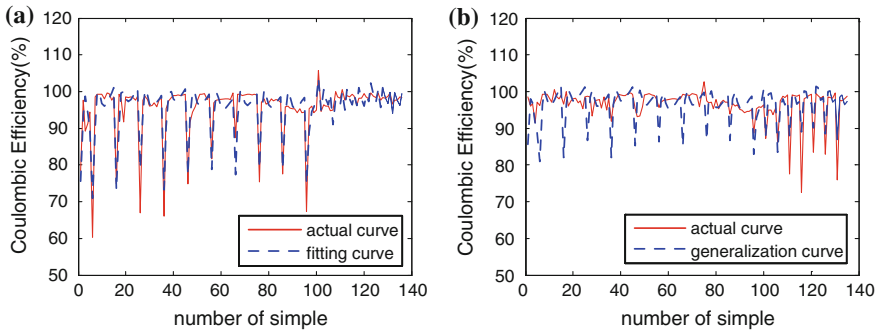


Fig. 44.2 The fitting and generalization curve of EC of single flow zinc-nickel battery. **a** fitting curve of EC. **b** generalization curve of EC

Table 44.3 Part data of filtered second carbonation section

Number of simple	pH of carbonation (pH)	Temperature (°C)	Sugarcane juice flow (t/h)	Color value (U.I.)	Alkalinity (CaO % °Bx)
1	8.22	76.60	320	60	0.25
2	8.17	75.20	320	67	0.28
3	8.27	75.20	320	65	0.25
...
109	8.25	75.20	335	64	0.26

After parameter optimization, the fitting and generalization curve of EC of single flow zinc-nickel battery by GDFNN is shown as Fig. 44.2.

In order to test the algorithm efficiency to MIMO set, the data of filtered second carbonation section [8] is used. This set is 3 input (pH of carbonation, Temperature and Sugarcane juice flow) and 2 output (the color value of second carbonation section and the alkalinity of second carbonation section) object with coupling and delay. The optimization parameters of GDFNN in training of color value model is as below, $k = 49.1916$, $k_{mf} = 0.7994$, $k_{error} = 0.0010$. The Structure of GDFNN is 3-18-6-1. The optimization parameters of GDFNN in training of alkalinity model is as below, $k = 88.6798$, $k_{mf} = 0.8000$, $k_{error} = 0.0097$. The Structure of GDFNN is 3-15-5-1. Part training data of filtered second carbonation section is given as Table 44.3.

Table 44.4 Performance comparison of color value and alkalinity of second carbonation section between the proposed method and traditional artificial selecting parameters

Variables	Artificial setting parameters	Adaptive computing parameters
RMSE of Color Value fitting	1.5067	1.5888
RMSE of Color Value generalization	3.7026	2.6244
Value of Fitness function J	3.2797	2.3016
RMSE of Alkalinity fitting	0.0085	0.0086
RMSE of Alkalinity generalization	0.0158	0.0134
Value of Fitness function J	0.0138	0.0118

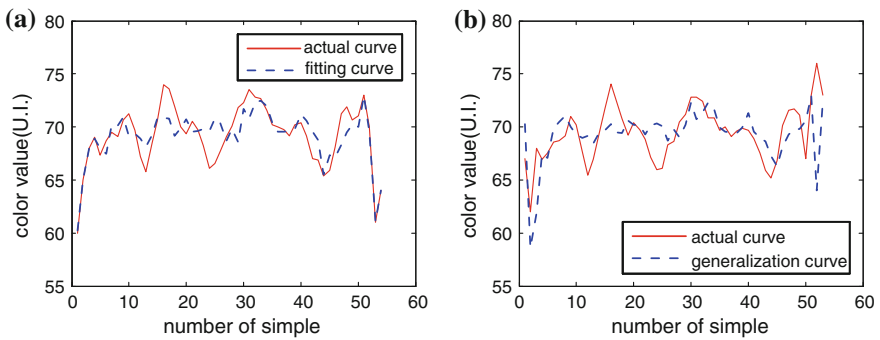


Fig. 44.3 The fitting and generalization curve of color value of second carbonation section. **a** fitting curve of color value. **b** generalization curve of color value

Compared with artificial setting the parameters of GDFNN, the training results of the algorithm using the data in Table 44.3 is as shown in Table 44.4.

After parameter optimization, the fitting and generalization curve of the color value and alkalinity of second carbonation section by GDFNN is shown as Figs. 44.3 and 44.4

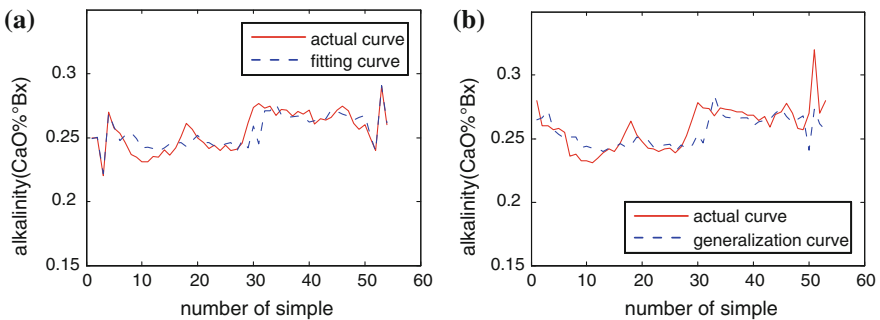


Fig. 44.4 The fitting and generalization curve of alkalinity of second carbonation section. **a** fitting curve of alkalinity. **b** generalization curve of alkalinity

44.5 Conclusion

In this paper, an improved algorithm is proposed based on the genetic algorithm. The variable weighted-average is selected as fitness-function to transform the multi-objective optimization into single-objective optimization, which raises the speed of calculation. The results which build the models of EC of single flow zinc-nickel battery and process of filtered second carbonation section using the algorithm in this paper shows that: 1. By optimize the initial parameters of GDFNN, the fitting and generalization effect of GDFNN training is improved, and the over-fitting which is leaded by unseasonable initial parameters is solved well. 2. The improved algorithm can get the initial parameters of GDFNN automatically. The user doesn't need to find the appropriate parameters by experiment. The difficult of artificial setting parameters is solved.

Acknowledgments This work was supported by the National Natural Science Foundation of China (61034002).

References

1. Shiqian W, Jun X (2008) Dynamic fuzzy neural network: design and Application. Tsinghua University Press, Beijing, pp 106–122 (in Chinese)
2. Shiqian W, Er MJ, Gao Y (2001) A fast approach for automatic generation of fuzzy rules by generalized dynamic fuzzy neural networks. *IEEE Trans Fuzzy Syst* 9(4):578–594
3. Li Y, Wang D, Han P (2006) Generalized dynamic fuzzy neural networks and application in thermal identification. *Electric Power Sci Eng*, 36(2):38–41 (in Chinese)
4. Guang-Nan X, Cheng R (2004) Genetic algorithms and engineering optimization. Tsinghua University Press, Beijing, p 76 (in Chinese)
5. Blanco A, Delgado M, Pegalajar MC (2001) A real-coded genetic algorithm for training recurrent neural networks. *Neural Networks* 14:93–105
6. Ferentinos KP (2005) Biological engineering applications of feed forward neural networks designed and parameterized by genetic algorithms. *Neural Networks* 18:934–950
7. Li Z, Cheng J, Yang YS et al (2008) Preliminary study of zinc electrodes performance for zinc/nickel battery. *Electrochemistry*, 14(3):248–252 (in Chinese)
8. Song S, Shi C, Lin X et al (2009) RBFNN modeling for neutralizing the pH value of the clarifying process in sulfitation sugar mill. *Tech Autom Appl*, 28(11):7–10 (in Chinese)

Chapter 45

A Decreased Extreme Learning Machine with Ridge Parameter for Online Identification of Nonlinear Systems

Mingtao Zhang, Yi Liu and Zengliang Gao

Abstract A recursive method of decreased extreme learning machine (DELM) is proposed for online identification of nonlinear systems. The output weights of ELM can be recursively updated by decreasing the hidden nodes one by one in an efficient manner. Furthermore, a ridge parameter is introduced into the transposed matrix to overcome the singular problem. The simulation results for several benchmark problems demonstrate that the proposed DELM method can reduce the computational complexity efficiently, and maintain the good prediction performance of the model, compared to the traditional ELM algorithm.

Keywords Extreme learning machine · Recursive method · Online identification

45.1 Introduction

Nonlinear system identification, which is to estimate models of nonlinear dynamic systems from observed input–output data, is still a difficult task in practice. Neural networks (NN), wavelet networks, as well as fuzzy systems and other data/rule-based empirical methods have been proposed and applied to many areas in past two decades [1]. However, the structure determination and generalization ability of these empirical models are still unsolved completely. Additionally, an amount of training examples are required to obtain reliable modeling performance, which is generally difficult to be satisfied in practice.

Generally, the slow learning speed of the traditional NN algorithms cannot satisfy the requirements for online identification of nonlinear systems.

M. Zhang · Y. Liu (✉) · Z. Gao
Engineering Research Center of Process Equipment and Remanufacturing, Ministry of Education, Institute of Process Equipment and Control Engineering, Zhejiang University of Technology, Hangzhou, China
e-mail: yliuzju@zjut.edu.cn

Alternatively, simple and fast nonlinear modeling methods with a low computational complexity are attractive. Recently, a new learning algorithm based on the single-hidden layer feed-forward neural networks (SLFNs), i.e. extreme learning machine (ELM), was first proposed by Huang et al. [2–6]. Unlike the conventional NN algorithms whose parameters are difficult to be adjusted, there is no connection in the hidden layers in ELM. The input weights and biases can be arbitrarily assigned and then quickly selected without resorting to the complex tuning algorithms. Due to this reason, the learning speed of ELM can be reduced greatly. Additionally, the output weights in ELM can be obtained by calculating the inverse matrix of output matrix of hidden-layer in a simple way [2–6].

As for online identification of nonlinear systems, only using the offline model is not suitable for process automation applications because the new information is difficult to be absorbed directly into the established model. Although the model can be retrained from the scratch when the training set is modified, it is cumbersome and computationally inefficient [7]. Therefore, it is desirable and necessary to develop recursive algorithms to update the model efficiently. Feng et al. [6] proposed a recursive method of ELM when the hidden nodes are growing. However, some hidden nodes should be deleted when they are trivial or the nodes are too many. Consequently, in this paper, a decremented ELM (DELM) method is proposed to prune arbitrary hidden nodes in a recursive manner. Whenever a node is deleted, the output weights can be updated efficiently.

The paper is organized as follows. The ELM algorithm is briefly introduced in Sect. 45.2. Section 45.3 gives the derivation of the DELM in details. Section 45.4 investigates several benchmark problems to demonstrate the advantages of the proposed algorithm, compared to ELM. Finally, some conclusions are drawn in Sect. 45.5.

45.2 Extreme Learning Machine (ELM)

In this section, the main algorithm of ELM is briefly introduced [2–6]. Given a training set of N samples $\{(\mathbf{x}_i, \mathbf{y}_i)\}_{i=1}^N$ with the input $\mathbf{x}_i = [x_{i1}, x_{i2}, \dots, x_{in}]^T \in \mathbf{R}^n$ and the output $\mathbf{y}_i = [y_{i1}, y_{i2}, \dots, y_{im}]^T \in \mathbf{R}^m$, the traditional SLFNs with L hidden nodes and the activation function $g(\cdot)$ can be formulated as [3]:

$$\sum_{i=1}^L \beta_i g(\langle \mathbf{a}_i, \mathbf{x}_j \rangle + \mathbf{b}_i) = \mathbf{y}_j, \quad j = 1, \dots, N \quad (45.1)$$

where \mathbf{a}_i is the input weight connecting the i th hidden node and input nodes; \mathbf{b}_i is the bias of the i th hidden node; and β_i is the output weight related the i th hidden node and output nodes, and $\langle \mathbf{a}_i, \mathbf{x}_j \rangle$ denotes the inner product.

Compactly, Eq. (45.1) can be rewritten as

$$\mathbf{H}\boldsymbol{\beta} = \mathbf{Y} \quad (45.2)$$

$$\mathbf{H} = [\mathbf{h}_1, \mathbf{h}_2, \dots, \mathbf{h}_L]_{N \times L} \text{ with } \mathbf{h}_i = \begin{bmatrix} (\langle \mathbf{a}_i, \mathbf{x}_1 \rangle + b_i) \\ \vdots \\ (\langle \mathbf{a}_i, \mathbf{x}_N \rangle + b_i) \end{bmatrix}_{N \times 1}, i = 1, \dots, L \quad (45.3)$$

In this case, \mathbf{H} is the output matrix of hidden-layer, \mathbf{h}_i is the output of the i th hidden node. The determination of the only unknown parameter $\boldsymbol{\beta}$ is equivalent to find the resolution of the linear system. It means that the solution can be obtained by calculating its minimum norm least squares [3]:

$$\hat{\boldsymbol{\beta}} = \mathbf{H}^+ \mathbf{Y} \quad (45.4)$$

where \mathbf{H}^+ is the Moore–Penrose generalized inverse of the matrix \mathbf{H} .

Because of the smaller output weights and training errors, ELM has better generalization performance than traditional SLFNs algorithms [4]. Meanwhile, ELM can be simply implemented by reaching the solution directly. Compared with the other classical NN algorithms which need long time to determination of the model structure, the computational load of ELM can be reduced greatly [2, 4].

45.3 The Proposed DELM Method

In this section, a recursive method with hidden nodes decreased one by one of ELM is proposed. Given a training set $\{(\mathbf{x}_i, \mathbf{y}_i)\}_{i=1}^N$ with L hidden nodes and the activation function $g(\cdot)$, the output matrix of hidden-layer can be described as

$$\mathbf{H}_L = [\mathbf{h}_1, \mathbf{h}_2, \dots, \mathbf{h}_L] \quad (45.5)$$

Once the i th hidden node is deleted, which means the output of the i th hidden node \mathbf{h}_i , $1 < i < L$, is removed from \mathbf{H}_L . Then, the new output matrix of hidden-layer can be obtained

$$\mathbf{H}_{L-1} = [\mathbf{h}_1, \dots, \mathbf{h}_{i-1}, \mathbf{h}_{i+1}, \dots, \mathbf{h}_L], 1 < i < L \quad (45.6)$$

Denote

$$\mathbf{H}_{11} = [\mathbf{h}_1, \dots, \mathbf{h}_{i-1}] \text{ and } \mathbf{H}_{12} = [\mathbf{h}_{i+1}, \dots, \mathbf{h}_L] \quad (45.7)$$

Eqs. (45.5–45.7) can be rewritten as

$$\mathbf{H}_{L-1} = [\mathbf{H}_{11}, \mathbf{H}_{12}] \quad (45.8)$$

$$\mathbf{H}_L = [\mathbf{H}_{11}, \mathbf{h}_i, \mathbf{H}_{12}] \quad (45.9)$$

Huang et al. [4] proposed that \mathbf{H}^+ can be expressed as $(\mathbf{H}^T\mathbf{H})^{-1}\mathbf{H}^T$ when $\mathbf{H}^T\mathbf{H}$ is nonsingular. However, if $\mathbf{H}^T\mathbf{H}$ tends to be singular and it becomes noninvertible. According to the idea of ridge regression, a ridge parameter k can be applied to overcome this problem [8–9]. That is, \mathbf{H}^+ can be simply substituted by $(\mathbf{H}^T\mathbf{H} + k\mathbf{I})^{-1}\mathbf{H}^T$, where the ridge parameter k is a small positive value and can be easily chosen [9]. The leave-one-out (LOO) criterion is applied to determine the suitable value of ridge parameter k . The average error of the N estimated residuals $r(N)$ can be written as [9]:

$$r(N) = \frac{1}{N} \sum_{i=1}^N r(N_i)^2 = \frac{1}{N} \sum_{i=1}^N (\mathbf{y}_i - f_i(\mathbf{x}_i))^2 \quad (45.10)$$

where $f_i(\mathbf{x}_i) = \mathbf{H}_{x_i}(\mathbf{H}_i^T\mathbf{H}_i + k\mathbf{I})^{-1}\mathbf{H}_i^T\mathbf{Y}_i$ is the estimated output of the i th sample; and $r(N_i)$ means the residual between $f_i(\mathbf{x}_i)$ and \mathbf{y}_i . \mathbf{Y}_i means the output set of the rest of the $N - 1$ samples. \mathbf{H}_{x_i} and \mathbf{H}_i are the hidden-layer output matrix of the i th sample and the rest of the $N - 1$ samples, respectively.

According to Eqs. (45.8–45.9)

$$\mathbf{H}_L^T\mathbf{H}_L + k\mathbf{I}_L = \begin{bmatrix} \mathbf{H}_{11}^T\mathbf{H}_{11} + k\mathbf{I}_{11} & \mathbf{H}_{11}^T\mathbf{h}_i & \mathbf{H}_{11}^T\mathbf{H}_{12} \\ \mathbf{h}_i^T\mathbf{H}_{11} & \mathbf{h}_i^T\mathbf{h}_i + k\mathbf{I}_i & \mathbf{h}_i^T\mathbf{H}_{12} \\ \mathbf{H}_{12}^T\mathbf{H}_{11} & \mathbf{H}_{12}^T\mathbf{h}_i & \mathbf{H}_{12}^T\mathbf{H}_{12} + k\mathbf{I}_{12} \end{bmatrix} \quad (45.11)$$

$$\mathbf{H}_{L-1}^T\mathbf{H}_{L-1} + k\mathbf{I}_{L-1} = \begin{bmatrix} \mathbf{H}_{11}^T\mathbf{H}_{11} + k\mathbf{I}_{11} & \mathbf{H}_{11}^T\mathbf{H}_{12} \\ \mathbf{H}_{12}^T\mathbf{H}_{11} & \mathbf{H}_{12}^T\mathbf{H}_{12} + k\mathbf{I}_{12} \end{bmatrix} \quad (45.12)$$

where $\mathbf{I}_L = \begin{bmatrix} \mathbf{I}_{11} & \mathbf{0} & \mathbf{0} \\ \mathbf{0} & \mathbf{I}_i & \mathbf{0} \\ \mathbf{0} & \mathbf{0} & \mathbf{I}_{12} \end{bmatrix}$ and $\mathbf{0}$ a corresponding null matrix, and \mathbf{I}_{11} , \mathbf{I}_i , \mathbf{I}_{12}

are unit matrices with the same dimensions as $\mathbf{H}_{11}^T\mathbf{H}_{11}$, $\mathbf{h}_i^T\mathbf{h}_i$, $\mathbf{H}_{12}^T\mathbf{H}_{12}$, respectively.

Denote

$$(\mathbf{H}_L^T\mathbf{H}_L + k\mathbf{I}_L)^{-1} = \mathbf{K}_L = \begin{bmatrix} \mathbf{K}_{11} & \mathbf{k}_{1i} & \mathbf{K}_{12} \\ \mathbf{k}_{1i}^T & k_L & \mathbf{k}_{2i}^T \\ \mathbf{K}_{12}^T & \mathbf{k}_{2i} & \mathbf{K}_{22} \end{bmatrix} \quad (45.13)$$

$$\bar{\mathbf{K}}_L = \begin{bmatrix} \mathbf{k}_{11} & \mathbf{k}_{12} \\ \mathbf{k}_{12}^T & \mathbf{k}_{22} \end{bmatrix} \quad (45.14)$$

$$\mathbf{k}_L = \begin{bmatrix} \mathbf{k}_{1i} \\ \mathbf{k}_{2i} \end{bmatrix} \quad (45.15)$$

$$(\mathbf{H}_{L-1}^T\mathbf{H}_{L-1} + k\mathbf{I}_{L-1})^{-1} = \mathbf{K}_{L-1} \quad (45.16)$$

Referring to the appendix of [7], the following formula can be obtained

$$\mathbf{K}_{L-1} = \bar{\mathbf{K}}_L - \mathbf{k}_L \mathbf{k}_L^T / k_L \quad (45.17)$$

Consequently, the output weights $\hat{\boldsymbol{\beta}}_{L-1}$ with the ridge parameter k can be recursively renewed in an efficient way as follows

$$\begin{aligned} \hat{\boldsymbol{\beta}}_{L-1} &= \mathbf{H}_{L-1}^+ \mathbf{Y} \\ &= (\mathbf{H}_{L-1}^T \mathbf{H}_{L-1} + k \mathbf{I}_{L-1})^{-1} \mathbf{H}_{L-1}^T \mathbf{Y} \\ &= (\bar{\mathbf{K}}_L - \mathbf{k}_L \mathbf{k}_L^T / k_L) \mathbf{H}_{L-1}^T \mathbf{Y} \end{aligned} \quad (45.18)$$

Briefly, the proposed DELM algorithm can be implemented as follows:

Algorithm: DELM

Step 1. Build the network structure based on the original ELM with the initial number of hidden nodes.

Step 2. The ridge parameter k is chosen by the LOO criterion.

Step 3. Once an arbitrary hidden node is deleted, the new output weights can be recursively obtained using $\hat{\boldsymbol{\beta}}_{L-1} = (\bar{\mathbf{K}}_L - \mathbf{k}_L \mathbf{k}_L^T / k_L) \mathbf{H}_{L-1}^T \mathbf{Y}$.

In the original ELM algorithm, when a hidden nodes is achieved, and its hidden-layer has to be totally rebuild accordingly. Consequently, the corresponding output weights $\hat{\boldsymbol{\beta}}$ need to be recounted in a cumbersome manner. The proposed DELM adopts the recursive method to reduce the computational complexity. Therefore, it is more suitable for online identification of nonlinear systems.

45.4 Simulation Results and Discussion

In this section, several benchmark problems for nonlinear systems identification are investigated to evaluate the performance of DELM, compared with ELM. All the simulations are carried out on the same PC (2.93 GHZ processor and 2 GB of memory) using Matlab R2010a. The sigmoid action function $g(\cdot) = 1/[1 + \exp(-\mathbf{x})]$ is utilized for ELM and DELM. The obtained results are the average of 20 Monte Carlo simulations.

First, a nonlinear continuous stirred tank reactor (CSTR) process [7] is chosen to demonstrate the performance of proposed DELM. Referring to <http://homes.esat.kuleuven.be/~smc/daisy/daisydata.html>, a data set including 7,500 samples of this process can be obtained. And q and C_A are chosen as the input variable and the output variable. 5,000 samples are assigned into the train set, and the rest are test samples. In this case, the initial number of the hidden nodes is set as 100, and decreased one by one until only one hidden node is left.

The computational complexity comparison of both DELM and ELM algorithms on the CSTR process is shown in Fig. 45.1. With the number of hidden nodes

decreasing, both algorithms spend less time on training. And with the help of recursive method, DELM improves the computational efficiency, compared to the traditional ELM algorithm. As shown in Fig. 45.1, when the number of the hidden nodes is larger, the more time can be reduced in training. Consequently, the proposed DELM is more suitable for fast pruning an ELM model with larger number of the hidden nodes. As for online identification of nonlinear systems, DELM can be implemented in an efficient manner despite of nodes changing.

The root mean square error ($\text{RMSE} = \sqrt{\sum_{i=1}^N (\hat{y}_i - y_i)^2 / N}$) and the average absolute relative error ($\text{AARE} = \frac{1}{N} \sum_{i=1}^N \left| \frac{\hat{y}_i - y_i}{y_i} \right| \times 100\%$) are provided to assess the performance of the model, y_i is the experimental value, \hat{y}_i the is the prediction value, and N is the sample number. The average test accuracy RMSE of DELM and ELM for CSTR is shown in Fig. 45.2. DELM and ELM can obtain almost the same prediction accuracy with the number of hidden nodes decreasing. Furthermore, the average test accuracy of DELM is more reliable than the original ELM. As mentioned previously, in the original ELM, its hidden-layer has to be rebuilt when a hidden node is achieved. To avoid the disadvantage, the proposed DELM method adopts the recursive method to keep the consistency of the model. Therefore, DELM is more suitable for online identification of nonlinear systems because it can not only reduce the computational complexity of the model, but also guarantee its generalization performance.

More simulations and comparisons for several benchmark problems, including pHdata and exchanger (<http://homes.esat.kuleuven.be/~smc/daisy/daisydata.html>), are investigated and listed in Table 45.1. All the cases are conducted in the same environment. And the initial hidden nodes are chosen as 100. Then, the number of the hidden nodes is decreased one by one until it reaches 30. The comparison of training time and average test accuracy (RMSE and AARE)

Fig. 45.1 Computational complexity comparison of DELM and ELM when pruning a node

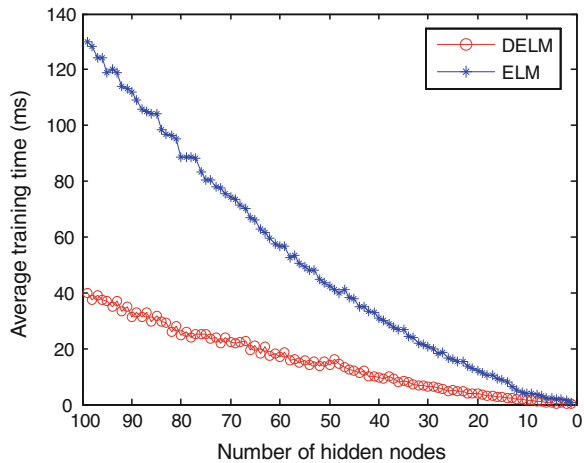


Fig. 45.2 Average test RMSE comparison of DELM and ELM algorithms when pruning a node

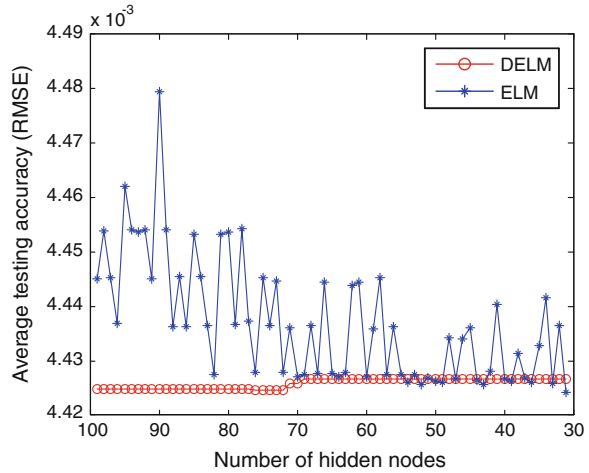


Table 45.1 Specification benchmarking applications

Identification problem	Types	Training data	Test data
pHdata	Regression	1500	501
Exchanger	Regression	3500	500

of the different applications is tabulated in Table 45.2. As can be seen from Table 45.2, when the number of the hidden nodes reaches 95, 75, 55, and 35, respectively in the pruning procedure, both algorithms need less time on training when the hidden nodes is decreasing. With the same number of hidden nodes, DELM is much faster than the original ELM algorithm, because of its recursive manner. Meanwhile, DELM can maintain its prediction accuracy and the

Table 45.2 Comparison of training time and average test accuracy (RMSE and AARE) by different algorithms when the hidden nodes decreased one by one

Number of the hidden nodes	Methods	pHdata			Exchanger		
		Training time (ms)	RMSE	AARE (%)	Training time (ms)	RMSE	AARE (%)
95	DELM	9.34	0.91	4.77	21.86	1.40	11.89
	ELM	36.80	0.88	4.76	82.31	1.39	11.89
75	DELM	6.80	0.94	5.09	16.05	1.40	11.88
	ELM	24.59	0.96	5.33	53.50	1.39	11.89
55	DELM	4.17	0.96	5.43	10.40	1.38	11.78
	ELM	15.35	1.04	6.14	32.11	1.39	11.89
35	DELM	1.88	0.99	5.34	5.17	1.38	11.75
	ELM	6.88	0.99	5.88	15.88	1.39	11.89

Note that the better results with less training time are in boldface.

reliability of the model. Consequently, all the obtained results suggest that the proposed DELM approach is more suitable and practical for online implementation of nonlinear systems identification.

45.5 Conclusion

In this paper, a simple and efficient recursive algorithm is proposed for online identification of nonlinear systems. The proposed DELM method can prune its nodes in a recursive manner. Thus, the output weights can be renewed efficiently. The simulation results show that the improved DELM method can significantly reduce the computational complexity and keep the reliability of the model. This makes DELM a practical algorithm for online identification of nonlinear systems.

Acknowledgments The authors would like to gratefully acknowledge National Natural Science Foundation of China (Grant Nos. 61004136 and 61273069) for the financial support.

References

1. Ljung L, Hjalmarsson H (2011) Four encounters with system identification. *Eur J Control* 17(5–6):449–471
2. Miche Y, Sorjamaa A, Lendasse A (2008) OP-ELM: theory, experiment and a toolbox. *Lect Notes Comput Sci* 5163:145–153
3. Huang GB, Wang DH, Lan Y (2011) Extreme learning machines: a survey. *Int J Machine Learn Cybernet* 2:107–122
4. Huang GB, Zhu Y, Siew CK (2006) Extreme learning machine: theory and applications. *Neurocomputing* 70:489–501
5. Huang GB, Li MB, Chen L (2008) Incremental extreme learning machine with fully complex hidden nodes. *Neurocomputing* 71:1–7
6. Feng G, Huang GB, Lin QP (2009) Error minimized extreme learning machine with growth of hidden nodes and incremental learning. *IEEE Trans Neural Networks* 20(8):1352–1356
7. Liu Y, Wang HQ, Yu J, Li P (2010) Selective recursive kernel learning for online identification of nonlinear systems with NARX form. *J Process Control* 20(2):181–194
8. Golub GH, Heath M, Wahha G (1979) Generalize cross-validation as a method for choosing a good ridge parameter. *Technometrics* 21(2):215–223
9. Yu Q, Miche Y, Eirola E, van Heeswijk M, Severin E, Lendasse A (2011) Regularized extreme learning machine for regression with missing data. In: *Proceedings of the international symposium on extreme learning machines*. Hangzhou, pp 1–17

Chapter 46

Security Region Estimation of the Peak of Track Irregularity Based on Dangerous Points Distribution Ratio and SVM

Yong Qin, Shan Yu, Yuan Zhang, Limin Jia and Zongyi Xing

Abstract The security regions of track irregularities' peak amplitudes for high-speed railways are estimated by the simulation data and based on the theory of data classification, and the security regions boundaries with different speeds are solved, and this method can provide reference for the management and developing standards of track geometry on high-speed railways. First, by establishing a high-speed passenger vehicle dynamics simulation model using SIMPACK, inputs including vertical profile irregularities and alignment irregularities and outputs including three safety indicators data (derailment coefficient, wheel load reduction rate and wheel-rail lateral force) were collected under two different level track regularity states, and the irregularity data were marked as 'safe' or 'dangerous' according to certain safety evaluation criteria. And then, considering the difficulty of directly using SVM for irregularity data classification, a new classification method based on dangerous points distribution ratio combined with SVM was proposed which can reduce the difficulty and improve the efficiency greatly. At last, the test results and the comparisons of the domestic and international management standards of track geometry indicated that the proposed approach is effective and practicable.

Keywords Track irregularities · Security region estimation · Data classification · Dangerous points distribution ratio · Support vector machines

Y. Qin · L. Jia

State Key Laboratory of Rail Traffic Control and Safety, Beijing Jiaotong University, Beijing 100044, China

S. Yu · Y. Zhang

School of Traffic and Transportation, Beijing Jiaotong University, Beijing 100044, China

Z. Xing (✉)

Department of Automation, Nanjing University of Science and Technology, Nanjing, 210094 Jiangsu, China

e-mail: zhangyuan111@gmail.com

46.1 Introduction

Track irregularity is the main course of violent vibration, and the track geometry directly affects the quality of the vehicle operation and the force between the wheels and rails. Therefore, good track condition is the main requirement of ensuring traffic safety and reducing the rail-wheel forces [1, 2]. The peak of the track irregularity amplitude influences the operation safety [3–6], and it is the basic indicator of the track geometry management standard to evaluation the track state [7]. Lian et al. [8] simulated the dynamic response of the rail vehicles and summarized the range of the track irregularity adverse wavelength of the communist rail. Wu [9] proposed the suggestion value of the track irregularity management of the test section of Qinhuangdao-Shenyang passenger railway. However, most of the conclusions ignored the influence of track irregularity peak value during operation. So they cannot present the system in real environment exactly, and reduce the reliability of using in engineering practice.

In term of region, we employ two kinds of level track spectrums as track excitation, including multi-wavelength and multi-amplitude random irregularities in two types of vertical profile and alignment. In order to get safety indicators, a high-speed vehicle dynamics model was built and the track irregularity amplitude based on several certain safety evaluation rules were marked. With the marked data, we propose a new kind of irregularity amplitude classification method based on SVM and the dangerous points distribution ratio to get the peaks' security region boundary of vertical profile irregularity and alignment irregularity in different speed.

46.2 Simulation Modeling and Data Acquiring

46.2.1 High-Speed Passenger Vehicle Dynamics Model

Based on the multi-body dynamics simulation software SIMPACK, a high-speed passenger vehicle dynamic model was established. The track was set to straight track and track size was based on UIC60, and the wheel-rail contact model chose single point elastic contact.

The model considers degrees of freedom of the body, frame, and the wheels in six directions. Forces considered in the modeling process include air spring force, damping force and stopping block force of vibration dampers in the secondary suspension interface. Axle spring force, axle positioning device force, damping force, the normal force and the creep force and creep torque of the wheel-rail interface in the primary suspension interface, and the wheel-rail force in the wheel-rail interface were generated by the software automatically [10].

46.2.2 Data Collection and Preprocessing

In order to simulate high-speed railway geometry condition more accurately, we set the German high-speed low-interference track spectrum and the United States sixth track spectrum as the track excitation inputs, and tested the simulation with two different levels of irregularities, and then combined the data together.

Considering the possibility of the risk of climbing rail or suspension, the Derailment Coefficient (DC), Wheel Load Reduction Rate (WLRR) and the Wheel-rail Lateral Force (WRLC) were selected as the safety indicators. Furthermore, considering the continuing role of the DC, smoothed it with 2 m moving average method in UIC518; since the substantial threat to wheel-rail is the WRLC in the low-frequency, a 4-order Butterfly IIR low-pass filter was employed for $0 \sim 40$ Hz filter processing.

We collected 4 groups which including two-dimension input and three-dimensional output data in speed of 200, 240, 280, 320 km/h. Figure 46.1 shows the input and output data in 200 km/h after pretreatment, Fig. 46.1a shows the track excitations (vertical profile irregularities and alignment irregularities), Fig. 46.1b shows the output signals of the DC, WLRR and WRLC.

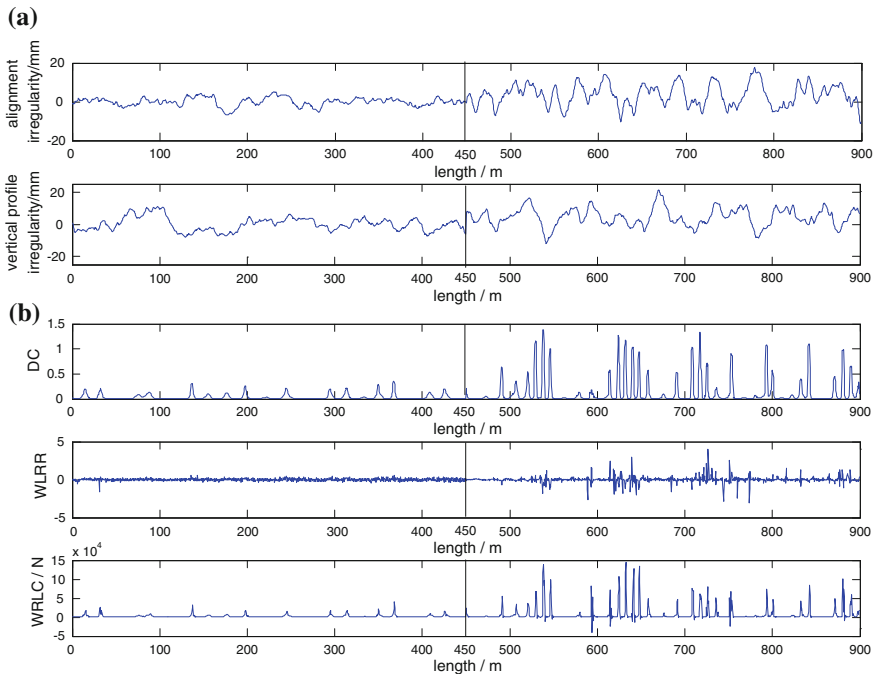


Fig. 46.1 Inputs and outputs data ($v = 200$ km/h)

46.3 Security Region Estimation Method Based on Dangerous Points Distribution Ratio and SVM

In order to get the best separation surface (that is, the security region boundary) of the track irregularity amplitude by training SVM classifier, the irregularity amplitude data should be marked into ‘safe’ or ‘dangerous’. The paper employs the following rules to mark the excitation points for improving the safety margin of high-speed operation and considering the comfortableness:

$$\begin{aligned} & \text{if } DC \geq 0.6 \text{ or } WLRR \geq 0.6 \text{ or } WRLC \geq 0.8 \times SWL \\ & \text{then } y = +1 \\ & \text{else } y = -1 \end{aligned} \quad (46.1)$$

where SWL is the static wheel load, $SWL = 48.690$ kN; y is the discriminate variable, $y = +1$ presents ‘safe’ and $y = -1$ presents ‘dangerous’.

Originally, SVM training could be started after the first marking. However, when the negative phase of the vertical profile and alignment irregularity composition, it would lead the irregularity amplitude small but influence the safety indicators a lot [2]. This may lead the classifier cannot get the optimal separate surface since SVM may treat all input data as support vectors to improve the accurate.

Therefore, the track irregularity data classification method based on the Dangerous Points Distribution Ratio (DPDR) is proposed, and is hereinafter referred to as DPDR-SVM. According to DPDR threshold to do the second mark, and then classify the grids with SVM to obtain the security region boundary of the irregularity amplitude.

As in Eq. (46.2), DPDR of the grid is the ratio of the number of the dangerous points and the sum of all points in the grid. The larger of its value indicates that the security of the irregularity amplitude of this grid is lower (that means it has a higher risk). The rule of the second mark is shown in Eq. (46.3).

$$DPDR = \frac{\text{num}(\text{danger points})}{\text{num}(\text{all sample points})} \in [0, 1] \quad (46.2)$$

$$\begin{aligned} & \text{if } DPDR \geq b_{DPDR} \\ & \text{then } y' = -1 \\ & \text{else } y' = +1 \end{aligned} \quad (46.3)$$

where b_{DPDR} is the threshold of DPDR; y' is the discriminate variable of the second mark, $y' = +1$ presents ‘safe’ and $y' = -1$ presents ‘dangerous’.

In order to classify data of irregularity amplitude presented by the grids, it is necessary to set the threshold of DPDR. The threshold of DPDR was determined as 0.5 and 1.0 for analyzing two representative situations of both half of the points in the grid is dangerous at least and all the points in the grid are dangerous.

Implementation steps of the DPDR-SVM as follow:

- Step 1. Based on the safety indicators and the judge rule Eq. (46.1), mark the vertical profile and alignment irregularities into ‘safe’ or ‘dangerous’ points.
- Step 2. Confirm the size of track irregularity amplitude area and the space of the grid, and be mashed.
- Step 3. Count number of the sample points and the dangerous points in each grid, and calculate the DPDR value of each grid with the Eq. (46.2).
- Step 4. Confirm the DPDR threshold to judge the security of the amplitude in each grid.
- Step 5. Compare the DPDR threshold with the DPDR value in each grid, mark the grids into ‘safe’ or ‘dangerous’ grids based on Eq. (46.3).
- Step 6. Train the SVM classifier based on the marked mesh data and get the optimal classification hyperplane.

Based on the present administrative standards of track irregularity amplitude [7], the irregularity amplitude range of the abscissa and ordinate were taken as 0–22 mm, and the intervals were set to 0.5 mm.

46.4 Experiment and Results

As noted in section ‘Security region of track irregularities’, we collect 4 groups of data at different speeds, and there are 1,800 pairs of data in each group. During the training of the SVM classifier, the data was separated into training data and testing data in a 6:4 proportion.

Table 46.1 shows the number of dangerous grids and classification accuracy at different speeds and different DPDR thresholds. Based on the DPDR-SVM method, Fig. 46.2 shows the boundaries of security regions of track irregularity amplitude at different speeds. The Eq. (46.2) proves that at the same speed, the number of dangerous grids is inversely proportional to the DPDR threshold, and the boundary is far from the zero point. It has been shown in Table 46.1 and Fig. 46.2, the number of dangerous grids is smaller at the DPDR threshold of 1

Table 46.1 The number of dangerous grids and classification accuracy under different speeds and different DPDR thresholds

Velocity (km/h)	Number of danger grids		Classification accuracy	
	DPDR threshold = 0.5	DPDR threshold = 1.0	DPDR threshold = 0.5	DPDR threshold = 1.0
200	43	21	0.8158	0.7832
240	98	54	0.8089	0.8101
280	117	75	0.8556	0.8022
320	240	143	0.8376	0.8001

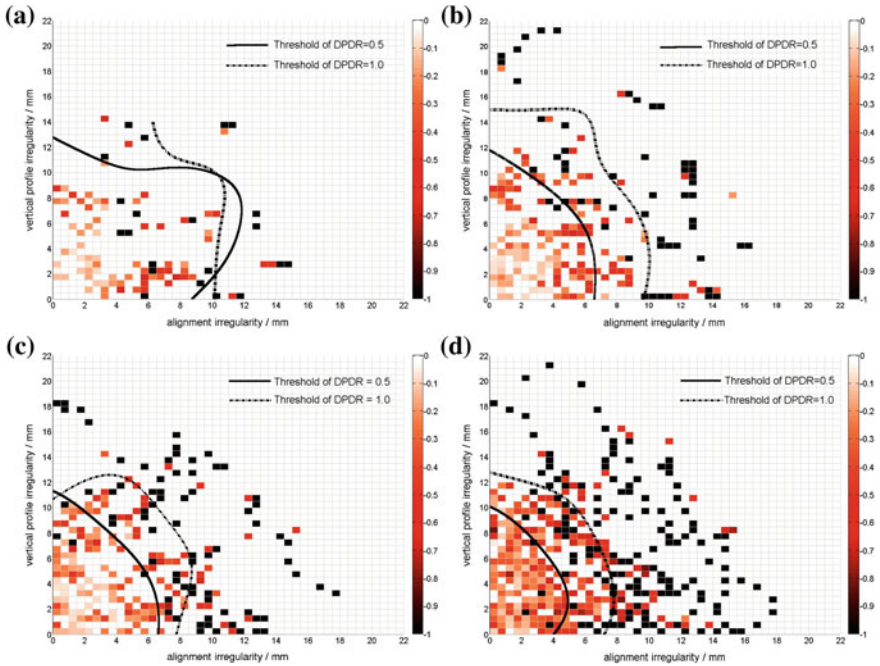


Fig. 46.2 The boundaries of security regions of track irregularity amplitude at different speeds. **a** The boundaries of security regions at 200km/h speed. **b** The boundaries of security regions at 240km/h speed. **c** The boundaries of security regions at 280km/h speed. **d** The boundaries of security regions at 320km/h speed

than which the DPDR threshold is 0.5 and the boundary of security region of the DPDR equals 0.5 contains the boundary of security region of the DPDR equals 1 which fits the subjective understand of the DPDR. Furthermore, the classification accuracy in each testing dataset is over 0.8, except when the DPDR threshold equals 1 at the speed of 200 km/h since the dangerous girds is too limited to classification. It proves the DPDR-SVM is effective and accuracy in high-speed railway security region estimates of track irregularity amplitude.

Figure 46.3 shows the boundaries of security regions of track irregularity amplitude at different DPDR thresholds and different speed respectively, outward from the zero point the boundary presents the security regions at the speed of 320, 280, 240 and 200 km/h. The figure shows the security region boundary at low speed surrounding the boundary at high speed, which means that with the speed increasing the security region lessen. It further proves the effective and accuracy of the method proposed in this paper.

Table 46.2 shows the peak amplitude of vertical profile and alignment irregularities at different speeds and different DPDR thresholds. Introduce the meaning of the table with the last line data: when the velocity is 320 km/h and the threshold of DPDR = 1, the operation safety can be ensured when the vertical profile and

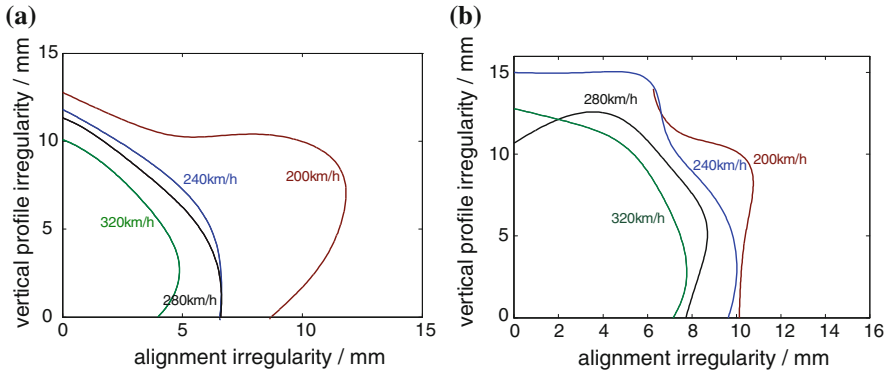


Fig. 46.3 The boundaries of security regions of track irregularity amplitude at different DPDR thresholds. **a** Threshold of DPDR = 0.5. **b**. Threshold of DPDR = 1.0

Table 46.2 The peak amplitude of vertical profile and alignment irregularities at different speeds and different DPDR thresholds

Velocity (km/h)	DPDR = 0.5		DPDR = 1	
	Irregularity peak (mm)		Irregularity peak (mm)	
	Vertical profile	Alignment	Vertical profile	Alignment
200	12.87	11.74	>15.10	10.70
240	11.80	6.62	15.10	9.99
280	11.27	6.67	12.62	8.73
320	9.96	4.95	12.59	7.76

alignment irregularities amplitude is less than 9.96 and 4.95 mm, respectively. And when the threshold of DPDR = 0.5, the operation safety can be ensured when the vertical profile and alignment irregularities amplitude is less than 12.59 and 7.76 mm, respectively. Comparing with the management standards provided in the Ref. [7], the result showed in Table 46.2 is reasonable which also proves the correctness and reliability of our approach.

46.5 Conclusions

This paper is in view of the high-speed railway track irregularity amplitude security region estimation, using data classification ideology and for optimizing the classification results, proposing a data classification method based on combination of dangerous point distribution radio and SVM, and gets the vertical profile and alignment irregularities peak of security reign boundaries under different circumstances. The experiment results show the proposed method is correct and feasible.

The subsequent studies includes joining cross-level and gauge irregularities excitation to get a more comprehensive track irregularity amplitude security region estimation, and evaluate safety of the track geometric state based on security region boundary. Since the DPDR threshold greatly affects the security region boundary, putting forward a method which can determine a reasonable DPDR threshold is also a future research direction.

Acknowledgments This research was sponsored by National High-tech R&D Program of China (863 Program, No. 2011AA110501) and Science Foundation & Purple Star Foundation and Research Funding (2010GJPY007) of NUST and the State Key Laboratory of Rail Traffic Control and Safety (No. RCS2010ZZ002, RCS2010ZZ005 and RCS2011K005), Beijing Jiaotong University. The supports are gratefully acknowledged.

References

1. Luo L, Zhang GM, Wu WQ, Chai XS (2006) Control of track irregularity in wheel-rail system. China Railway Publishing House, Beijing (in Chinese)
2. Zhai WM (2007) Vehicle-track coupling dynamics, 3rd edn. Science Press, Beijing (in Chinese)
3. Shafiullah GM, Ali ABMS, Thompson A, Wolfs PJ (2010) Predicting vertical acceleration of railway wagons using regression algorithms. *IEEE Trans Intell Transp Syst* 11(2):290–299
4. Gua G, Lilley DM, Franklin FJ (2010) A structural articulation method for assessing railway bridges subject to dynamic impact loading from track irregularities. *Veh Syst Dyn* 48(10):1077–1095
5. Furukawa A, Yoshimura A (2005) Identification of rolling stock lateral dynamic characteristics and their track irregularity maintenance applications. *Quart Rep RTRI* 46(1):7–12
6. Tanaka H, Furukawa A (2009) Management method for large wheel loads and lateral forces using Axle-box acceleration and track irregularity. *Quart Rep RTRI* 50(2):116–122
7. Xu YD, Li HF, Dai YH (2007) Track maintenance & management for urban mass transit. Tongji University Press, Shanghai (in Chinese)
8. Lian SL, Huang JF (2004) Study of the detrimental wavelengths of track irregularities for railways with passenger and freight traffic. *J China Railw Soc* 26(2):111–115 (in Chinese)
9. Wu WQ (2003) Research on recommended value of track irregularity management standards in Qinhuangdao-Shenyang dedicated passenger line. *J Railw Stan Des* 4:1–4 (in Chinese)
10. Ren ZS (2009) Fundamentals of vehicle dynamics. China Railway Publishing House, Beijing (in Chinese)

Chapter 47

On the Symmetry of Interval Type-2 Fuzzy Logic Controllers Using Different Type-Reduction Methods

Chengdong Li, Guiqing Zhang, Jianqiang Yi and Ming Wang

Abstract In order to deepen the theoretical understanding of the interval type-2 (IT2) fuzzy logic controllers (FLCs), it is meaningful to explore the fundamental properties of IT2FLCs, e.g. continuity, monotonicity, smoothness, adaptiveness, novelty, stability and robustness. This paper studies another fundamental property—the symmetry, which is always required in real-world control applications. Symmetric conditions are derived to ensure the symmetry of FLCs, including both IT2FLCs and type-1 FLCs (T1FLCs). For IT2FLCs, we consider three most commonly-used type-reduction and defuzzification methods—the Karnik–Mendel (KM) method, the uncertainty bound (UB) method and the Begian-Melek-Mendel (BMM) method. At last, an application is given to verify the correctness of the derived results.

Keywords Type-2 fuzzy · Odd symmetry · Fuzzy logic controller · Type-reduction and defuzzification method

47.1 Introduction

In recent years, a number of extensions to traditional (type-1) fuzzy logic systems (FLSs) are attracting interest. One of the most widely-used extensions is the type-2 FLS [1–4], especially interval type-2 (IT2) FLS. IT2 FLSs have been executed in various fields, especially in the control fields [5–8]. In control applications,

C. Li (✉) · G. Zhang · M. Wang
School of Information and Electrical Engineering, Shandong Jianzhu University,
Jinan 250101, China
e-mail: chengdong.li@ia.ac.cn

J. Yi
Institute of Automation, Chinese Academy of Sciences, Beijing 100090, China
e-mail: jianqiang.yi@ia.ac.cn

IT2FLSs become IT2 fuzzy logic controllers (IT2FLCs). IT2FLSs and IT2FLCs have obvious advantages for handling different sources of uncertainties, reducing the number of fuzzy rules, and achieving better performance, etc., as they utilize interval type-2 fuzzy sets (IT2FSs) which can provide additional degrees of freedom and have more parameters than type-1 fuzzy sets (T1FSs) in T1 FLSs [1–4].

There are several fundamental properties of IT2FLCs investigated by researchers recently, such as the continuity [9], monotonicity [10, 11], adaptiveness [12], novelty [12], stability [13, 14] and robustness [15, 16]. These fundamental studies on IT2FLCs have the following importance: (1) such studies can deepen our theoretical understanding of IT2FLCs; (2) related results can guide us to choose and design appropriate IT2FLCs for control applications more easily; (3) by constraining the parameters of the IT2FLCs in the optimization problems, the parameter searching spacer can be reduced, and better results may be obtained; (4) such studies can help us to choose suitable type-reduction and defuzzification methods, as some specific type-reduction methods may be not suitable for some applications.

In most of the real-world control applications, the controllers for them need to be odd symmetric. To achieve satisfactory performance, the FLCs designed for these applications should meet such requirement. Hence, the symmetry is another fundamental property of FLCs. Till now, to the best of the authors' knowledge, no paper has studied this issue. This paper will focus on the symmetry of FLCs, including both IT2FLCs and T1FLCs. As well known, for IT2FLCs, different type-reduction and defuzzification methods can result in different inference results. In this study, we take into account three most widely-used type-reduction and defuzzification methods, which are the Karnik–Mendel (KM) method [1], the uncertainty bound (UB) method [17, 18], and the Begian-Melek-Mendel (BMM) method [19, 20]. At last, we use one real-world application to show the correctness of the derived results.

47.2 Review of IT2FLC and Type-Reduction Methods

47.2.1 IT2FLC

An IT2FLC is shown in Fig. 47.1. The IT2FLC is also characterized by fuzzy IF–THEN rules, but the membership functions of the IT2FLCs are now IT2FSs. Assume that there are M rules in the rule base, each of which has the following form

$$\text{Rule } k : x_1 = \tilde{A}_1^k, \dots, x_p = \tilde{A}_p^k \rightarrow y = [\underline{\omega}^k, \bar{\omega}^k]$$

where $k = 1, 2, \dots, M$, p is the number of the input variables in the antecedent part, \tilde{A}_i^k s are IT2FSs of the IF-part, and $[\underline{\omega}^k, \bar{\omega}^k]$ s are consequent interval weights of the THEN-part.

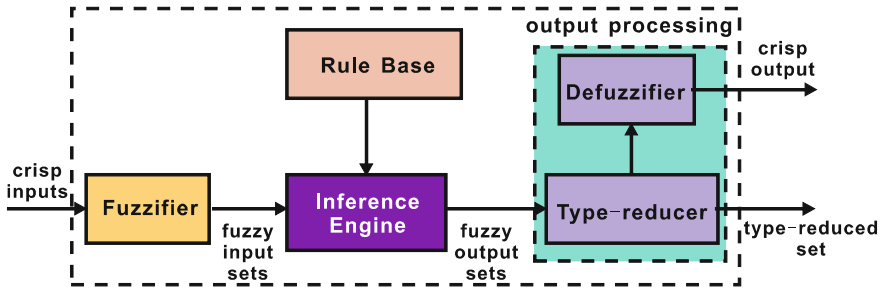


Fig. 47.1 The structure of an IT2FLC [1, 2, 4]

Once a crisp input $X = (x_1, x_2, \dots, x_p)$ is applied to the IT2FLC, through the singleton fuzzifier and the inference process, the firing strength of the k th rule which is an interval type-1 set can be obtained as

$$F^k(X) = [f_{\underline{}}^k(X), \bar{f}^k(X)]$$

where $f_{\underline{}}^k(X), \bar{f}^k(X)$ can be computed as

$$f_{\underline{}}^k(X) = \underline{\mu}_{\bar{A}_1^k}(x_1) * \underline{\mu}_{\bar{A}_2^k}(x_2) * \dots * \underline{\mu}_{\bar{A}_p^k}(x_p)$$

$$\bar{f}^k(X) = \bar{\mu}_{\bar{A}_1^k}(x_1) * \bar{\mu}_{\bar{A}_2^k}(x_2) * \dots * \bar{\mu}_{\bar{A}_p^k}(x_p)$$

in which $\underline{\mu}(), \bar{\mu}()$ denote the grades of the lower and upper membership functions of IT2FSs, and $*$ denotes minimum or product t -norm.

To generate a crisp output, the outputs of the inference engine should be type-reduced and then defuzzified. With different type-reduction methods, the expressions of the outputs of the IT2FLCs are different. In the following subsection, we will review three most widely-used type-reduction and defuzzification methods for IT2FLCs.

47.2.2 The Widely-Used Type-Reduction Methods

For an IT2FLC, the type-reduction block is needed to map an IT2FS into aT1FS in order to obtain a crisp output from the IT2FLC. There are several type-reduction methods. The most widely used ones are the KM type-reduction method [1], the UB type-reduction method [17, 18] and the BMM type-reduction method [19, 20].

47.2.2.1 The KM Type-Reduction Method

With the KM type-reduction method [1], the type-reduced type-1 output $[y_l(X), y_r(X)]$ can be obtained as

$$y_l(X) = \min \left\{ \frac{\sum_{k=1}^M f^k(X)\omega^k}{\sum_{k=1}^M f^k(X)} \mid f^k(X) \in [f^k(X), \bar{f}^k(X)], \omega^k \in [\underline{\omega}^k, \bar{\omega}^k] \right\}$$

$$y_r(X) = \max \left\{ \frac{\sum_{k=1}^M f^k(X)\omega^k}{\sum_{k=1}^M f^k(X)} \mid f^k(X) \in [f^k(X), \bar{f}^k(X)], \omega^k \in [\underline{\omega}^k, \bar{\omega}^k] \right\}$$

where the left end point $y_l(X)$ and the right end point $y_r(X)$ can be computed by the Karnik–Mendel algorithms which are iterative procedures [1].

The final output of the IT2FLC using the KM type-reduction method can be computed by

$$y_{KM}(X) = \frac{1}{2} [y_l(X) + y_r(X)].$$

47.2.2.2 The UB Type-Reduction Method

With the UB type-reduction method [17, 18], the type-reduced type-1 output $[y_l(X), y_r(X)]$ can be obtained as

$$y_l(X) = \frac{1}{2} (y_l(X) + \bar{y}_l(X)), \quad y_r(X) = \frac{1}{2} (y_r(X) + \bar{y}_r(X))$$

where

$$\bar{y}_l(X) = \min \{y_l^0(X), y_l^M(X)\}, \quad y_l(X) = \bar{y}_l(X) - \delta_l(X)$$

$$y_r(X) = \max \{y_r^0(X), y_r^M(X)\}, \quad \bar{y}_r(X) = y_r(X) + \delta_r(X)$$

in which

$$y_l^0(X) = \frac{\sum_{k=1}^M \underline{f}^k(X)\underline{\omega}^k}{\sum_{k=1}^M \underline{f}^k(X)}, \quad y_l^M(X) = \frac{\sum_{k=1}^M \bar{f}^k(X)\underline{\omega}^k}{\sum_{k=1}^M \bar{f}^k(X)}$$

$$y_r^0(X) = \frac{\sum_{k=1}^M \bar{f}^k(X)\bar{\omega}^k}{\sum_{k=1}^M \bar{f}^k(X)}, \quad y_r^M(X) = \frac{\sum_{k=1}^M \underline{f}^k(X)\bar{\omega}^k}{\sum_{k=1}^M \underline{f}^k(X)}$$

$$\delta_l(X) = \frac{\sum_{k=1}^M [\bar{f}^k(X) - \underline{f}^k(X)]}{\sum_{k=1}^M \bar{f}^k(X) \sum_{k=1}^M \underline{f}^k(X)} \frac{\sum_{k=1}^M \underline{f}^k(X)[\underline{\omega}^k - \underline{\omega}^1] \sum_{k=1}^M \bar{f}^k(X)[\underline{\omega}^M - \underline{\omega}^k]}{\sum_{k=1}^M \underline{f}^k(X)[\underline{\omega}^k - \underline{\omega}^1] + \sum_{k=1}^M \bar{f}^k(X)[\underline{\omega}^M - \underline{\omega}^k]}$$

$$\delta_r(X) = \frac{\sum_{k=1}^M [\bar{f}^k(X) - \underline{f}^k(X)]}{\sum_{k=1}^M \bar{f}^k(X) \sum_{k=1}^M \underline{f}^k(X)} \frac{\sum_{k=1}^M \bar{f}^k(X)[\bar{\omega}^k - \bar{\omega}^1] \sum_{k=1}^M \underline{f}^k(X)[\bar{\omega}^M - \bar{\omega}^k]}{\sum_{k=1}^M \bar{f}^k(X)[\bar{\omega}^k - \bar{\omega}^1] + \sum_{k=1}^M \underline{f}^k(X)[\bar{\omega}^M - \bar{\omega}^k]}$$

The final output of the IT2FLC using the KM type-reduction method can be computed by

$$y_{UB}(X) = \frac{1}{2}[y_l(X) + y_r(X)] = \frac{1}{4}(\underline{y}_l(X) + \bar{y}_l(X) + \underline{y}_r(X) + \bar{y}_r(X)).$$

47.2.2.3 The BMM Type-Reduction Method

With the BMM method [19, 20], the final output of the IT2FLC can be derived by

$$y_{BMM}(X) = \alpha y_l(X) + \beta y_r(X)$$

where $\alpha + \beta = 1$, and $y_l(X), y_r(X)$ are obtained by

$$y_l(X) = \frac{\sum_{k=1}^M \underline{f}^k(X) \omega^k}{\sum_{k=1}^M \underline{f}^k(X)}, \quad y_r(X) = \frac{\sum_{k=1}^M \bar{f}^k(X) \omega^k}{\sum_{k=1}^M \bar{f}^k(X)}$$

In this case, the consequent parts of the fuzzy rules need to be crisp values. We can realize this by setting $\omega^k = \frac{1}{2}(\underline{\omega}^k + \bar{\omega}^k)$.

47.3 Symmetry of Interval Type-2 Fuzzy Logic Controllers

For most of the control applications, the fuzzy rule bases designed for them should be symmetric and the FLCs with the symmetric fuzzy rule bases should be odd symmetric. In the following discussion, we will show that, using a symmetric fuzzy rule base, KM-IT2FLC, UB-IT2FLC and BMM-IT2FLC are all odd symmetric. To begin, two definitions are presented.

Definition 1 (*Symmetric Fuzzy Rule Base*): Consider a fuzzy rule base $\mathbf{R} = \{R^1, R^2, \dots, R^M\}$. Assume that the fuzzy rules $R^{k_1}, R^{k_2}, \dots, R^{k_t}$ can be fired when X is input to \mathbf{R} , while the fuzzy rules $R^{k_1^*}, R^{k_2^*}, \dots, R^{k_t^*}$ can be fired when $-X$ is input to \mathbf{R} . \mathbf{R} is said to be symmetric, if: (1) $\tilde{t} = t$; (2) the firing intervals satisfy that $[\underline{f}^{k_i}(X), \bar{f}^{k_i}(X)] = [\underline{f}^{k_i^*}(X), \bar{f}^{k_i^*}(X)]$; (3) the consequent interval weights satisfy that $\underline{\omega}^{k_i} = -\bar{\omega}^{k_i^*}, \bar{\omega}^{k_i} = -\underline{\omega}^{k_i^*}$.

Definition 2 (*Odd Symmetric FLC*): A FLC $y(X)$ is said to be odd symmetric, if $y(X) = -y(-X)$.

Theorem 1 *Using a symmetric fuzzy rule base \mathbf{R} , KM-IT2FLC, UB-IT2FLC and BMM-IT2FLC are all odd symmetric. In other words, $y_{KM}(X) = -y_{KM}(-X)$, $y_{UB}(X) = -y_{UB}(-X)$ and $y_{BMM}(X) = -y_{BMM}(-X)$.*

Proof Assume that the fuzzy rules $R^{k_1}, R^{k_2}, \dots, R^{k_t}$ can be fired when X is input to \mathbf{R} , while the fuzzy rules $R^{k_1^*}, R^{k_2^*}, \dots, R^{k_t^*}$ can be fired when $-X$ is input to \mathbf{R} . Then, we have $[\underline{f}^{k_i}(X), \bar{f}^{k_i}(X)] = [\underline{f}^{k_i^*}(X), \bar{f}^{k_i^*}(X)]$, and $\underline{\omega}^{k_i} = -\bar{\omega}^{k_i^*}, \bar{\omega}^{k_i} = -\underline{\omega}^{k_i^*}$. □

1. First, we prove that $y_{KM}(X) = -y_{KM}(-X)$.

Note that

$$\begin{aligned} y_l(X) &= \min \left\{ \frac{\sum_{s=1}^t f^{k_s}(X) \omega^{k_s}}{\sum_{s=1}^t f^{k_s}(X)} \mid f^{k_s}(X) \in [\underline{f}^{k_s}(X), \bar{f}^{k_s}(X)], \omega^{k_s} \in [\underline{\omega}^{k_s}, \bar{\omega}^{k_s}] \right\} \\ &= -\max \left\{ \frac{\sum_{s=1}^t f^{k_s}(X) (-\omega^{k_s})}{\sum_{s=1}^t f^{k_s}(X)} \mid f^{k_s}(X) \in [\underline{f}^{k_s}(X), \bar{f}^{k_s}(X)], -\omega^{k_s} \in [-\bar{\omega}^{k_s}, -\underline{\omega}^{k_s}] \right\} \\ &= -\max \left\{ \frac{\sum_{s=1}^t f^{k_s^*}(-X) (\omega^{k_s^*})}{\sum_{s=1}^t f^{k_s^*}(-X)} \mid f^{k_s^*}(-X) \in [\underline{f}^{k_s^*}(-X), \bar{f}^{k_s^*}(-X)], \omega^{k_s^*} \in [\underline{\omega}^{k_s^*}, \bar{\omega}^{k_s^*}] \right\} \\ &= -y_r(-X) \end{aligned}$$

Therefore,

$$y_{KM}(X) = \frac{1}{2} [y_l(X) + y_r(X)] = \frac{1}{2} [-y_r(-X) - y_l(-X)] = -y_{KM}(-X).$$

2. Now, let us prove that $y_{UB}(X) = -y_{UB}(-X)$.

Note that

$$\begin{aligned} y_l^0(X) &= \frac{\sum_{s=1}^t \underline{f}^{k_s}(X) \underline{\omega}^{k_s}}{\sum_{s=1}^t \underline{f}^{k_s}(X)} = -\frac{\sum_{s=1}^t \underline{f}^{k_s}(X) (-\underline{\omega}^{k_s})}{\sum_{s=1}^t \underline{f}^{k_s}(X)} = -\frac{\sum_{s=1}^t \underline{f}^{k_s^*}(-X) \bar{\omega}^{k_s^*}}{\sum_{s=1}^t \underline{f}^{k_s^*}(-X)} \\ &= -y_r^M(-X) \end{aligned}$$

In the similar way, $y_l^M(X) = -y_r^0(-X)$.

Hence,

$$\begin{aligned} \bar{y}_l(X) &= \min \{ y_l^0(X), y_l^M(X) \} = \min \{ -y_r^M(-X), -y_r^0(-X) \} \\ &= -\max \{ y_r^M(-X), y_r^0(-X) \} = -\underline{y}_r(-X) \end{aligned}$$

It is easy to show that $\delta_l(X) = \delta_r(-X)$, $\delta_r(X) = \delta_l(-X)$.

Therefore,

$$\begin{aligned} y_{UB}(X) &= \frac{1}{4} (y_l(X) + \bar{y}_l(X) + \underline{y}_r(X) + \bar{y}_r(X)) = \frac{1}{4} (2\bar{y}_l(X) - \delta_l(X) + 2\underline{y}_r(X) + \delta_r(X)) \\ &= \frac{1}{4} (-2\bar{y}_r(-X) - \delta_r(-X) - 2\bar{y}_l(-X) + \delta_l(-X)) = -y_{UB}(-X) \end{aligned}$$

3. For the BMM-IT2FLC, it is easy to show that the conclusion holds. □

As the special case of IT2FLCs, for the type-1 case, we have the following corollary:

Corollary 1 *Using a symmetric fuzzy rule base \mathbf{R} , T1FLC is odd symmetric. In other words, $y_{T1}(X) = -y_{T1}(-X)$.*

Theorem 1 shows that, using an symmetric fuzzy rule base, the control surfaces of KM-IT2FLC, UB-IT2FLC and BMM-IT2FLC are all odd symmetric. And it is

also easy to show that, if a symmetric fuzzy rule base is used and the input of KM-IT2FLC, UB-IT2FLC or BMM-IT2FLC is 0, then the output of KM-IT2FLC, UB-IT2FLC or BMM-IT2FLC is 0. In other words, $y_{KM}(0) = y_{UB}(0) = y_{BMM}(0) = 0$, if a symmetric fuzzy rule base is used.

47.4 Examples

This section will use one real-world application to show the symmetry property of the FLCs.

We take the inverted pendulum system for example. For details on this application, please see [21, 22]. From our control experience, we know that, to stabilize the pole, the output of the controllers should be odd symmetric. Generally, to keep the pole upright, we can adopt the fuzzy rule base shown in Table 47.1, the FSs in which are shown in Fig. 47.2. Obviously, this fuzzy rule base is symmetric. With this fuzzy rule base, the control surfaces of the T1FLC, KM-IT2FLC, UB-IT2FLC and BMM-IT2FLC are demonstrated in Fig. 47.3. From this figure, we can observe that with the symmetric fuzzy rule base, the control surfaces of the T1FLC, KM-IT2FLC, UB-IT2FLC and BMM-IT2FLC are all odd symmetric. This is consistent with Theorem 1 and Corollary 1.

Table 47.1 Symmetric rule base for the inverted pendulum system

u		θ				
		NB	NS	ZR	PS	PB
$\dot{\theta}$	NB	PB	PB	PB	PS	ZR
	NS	PB	PB	PS	ZR	NS
	ZR	PB	PS	ZR	NS	NB
	PS	PS	ZR	NS	NB	NB
	PB	ZR	NS	NB	NB	NB

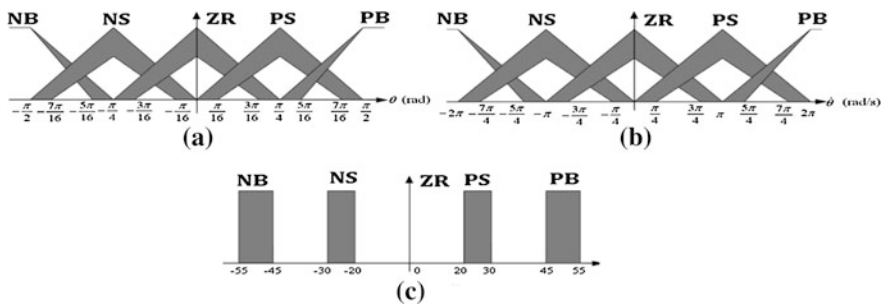


Fig. 47.2 Interval type-2 fuzzy partitions of the inputs and output

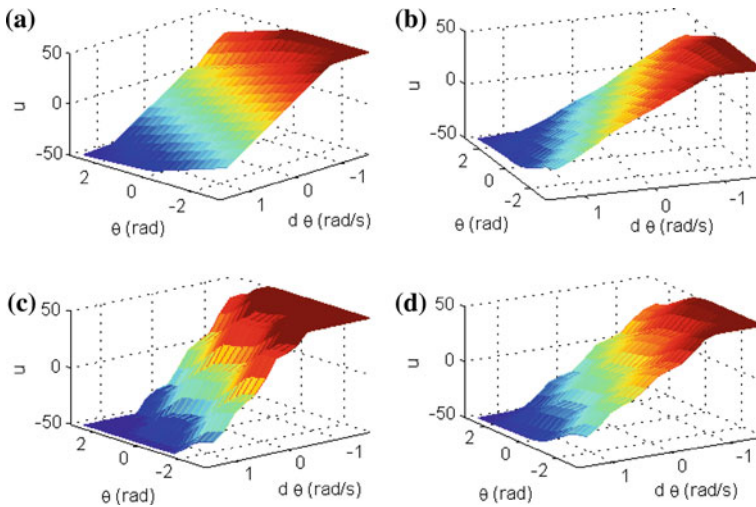


Fig. 47.3 Control surfaces of the **a** T1FLC, **b** KM-IT2FLC, **c** UB-IT2FLC and **d** BMM-IT2FLC

47.5 Conclusions

The fundamental properties have great importance on the analysis, design and optimization of IT2FLCs. This study explored one kind of such properties—the symmetry of IT2FLCs. Also, we derived the symmetric conditions for three widely-used type-reduction and defuzzification methods based IT2FLCs. Simulation results have verified the proposed results. Our results will be useful in applications when the controllers designed are required to be odd symmetric. In the future, we will use existing results on the fundamental properties of IT2FLCs to guide the design and optimizations.

Acknowledgments This work is supported by National Natural Science Foundation of China (61105077, 61273149, 61074149 and 61273326), and the Excellent Young and Middle-Aged Scientist Award Grant of Shandong Province of China (BS2012DX026).

References

1. Mendel JM (2001) Uncertain rule-based fuzzy logic systems: introduction and new directions. Prentice-Hall, Upper Saddle River, NJ
2. Castillo O, Melin P (2008) Type-2 fuzzy logic theory and applications. Springer, Berlin
3. Wagner C, Hagsras H (2010) Toward general type-2 fuzzy logic systems based on zSlices. *IEEE Trans Fuzzy Syst* 18(4):637–660
4. Hagsras H, Wagner C (2012) Towards the wide spread use of type-2 fuzzy logic systems in real world applications. *IEEE Comput Intell Mag* 7(3):14–24
5. Manceur M, Essounbouli N, Hamzaoui A (2012) Second-order sliding fuzzy interval type-2 control for an uncertain system with real application. *IEEE Trans Fuzzy Syst* 20(2):262–275

6. Barkat S, Tlemcani A, Nouri H (2011) Noninteracting adaptive control of PMSM using interval type-2 fuzzy logic systems. *IEEE Trans Fuzzy Syst* 19(5):925–936
7. Castillo O, Melin P (2012) A review on the design and optimization of interval type-2 fuzzy controllers. *Appl Soft Comput* 12(4):1267–1278
8. Castillo O, Martinez-Marroquin R, Melin P et al (2012) Comparative study of bio-inspired algorithms applied to the optimization of type-1 and type-2 fuzzy controllers for an autonomous mobile robot. *Inf Sci* 192:19–38
9. Wu D, Mendel JM (2011) On the continuity of type-1 and interval type-2 fuzzy logic systems. *IEEE Trans Fuzzy Syst* 19(1):179–192
10. Li C, Yi J, Wang M, Zhang G (2012) Monotonic type-2 fuzzy neural network and its application to thermal comfort prediction. *Neural Comput Appl*. doi:10.1007/s00521-012-1140-x
11. Li C, Yi J, Zhao D (2009) Analysis and design of monotonic type-2 fuzzy inference systems. *FUZZ-IEEE* 2009:1193–1198
12. Wu D (2012) On the fundamental differences between interval type-2 and type-1 fuzzy logic controllers. *IEEE Trans Fuzzy Syst* 20(5):832–848
13. Jafarzadeh S, Fadali S, Sonbol A (2011) Stability analysis and control of discrete type-1 and type-2 TSK fuzzy systems: Part I stability analysis. *IEEE Trans Fuzzy Syst* 19(6):989–1000
14. Jafarzadeh S, Fadali S, Sonbol A (2011) Stability analysis and control of discrete type-1 and type-2 TSK fuzzy systems: part II control design. *IEEE Trans Fuzzy Syst* 19(6):1001–1013
15. Biglarbegian M, Melek W, Mendel JM (2011) On the robustness of type-1 and interval type-2 fuzzy logic systems in modeling. *Inf Sci* 181(7):1325–1347
16. Wu D, Tan WW (2010) Interval type-2 fuzzy PI controllers: Why they are more robust. *FUZZ-IEEE* 2010:802–807
17. Wu H, Mendel JM (2002) Uncertainty bounds and their use in the design of interval type-2 fuzzy logic systems. *IEEE Trans Fuzzy Syst* 10(5):622–639
18. Lynch C, Hagrais H, Callaghan V (2005) Embedded type-2 FLC for real-time speed control of marine & traction diesel engines. *FUZZ-IEEE* 2005:347–352
19. Biglarbegian M, Melek W, Mendel JM (2010) On the stability of interval type-2 TSK fuzzy logic control systems. *IEEE Trans Syst Man Cybern: B Cybern* 41(5):798–818
20. Li C, Zhang G, Yi J, Wang T (2011) On the properties of SIRMs connected type-1 and type-2 fuzzy inference systems. *FUZZ-IEEE* 2011:1982–1988
21. Phan PA, Gale TJ (2008) Direct adaptive fuzzy control with a self-structuring algorithm. *Fuzzy Sets Syst* 159:871–899
22. Hsiao M-Y, Li T-HS, Lee J-Z et al (2008) Design of interval type-2 fuzzy sliding-mode controller. *Inf Sci* 178:1696–1716

Chapter 48

Development of Database System for Overhead Power Transmission Line Inspection Robot

Dezheng Zhao, En Li, Guodong Yang and Zize Liang

Abstract In order to store and manage the basic information and inspection task for overhead high voltage power transmission line inspection robots, a database system is built up. This database system can store and manage such information as sensor information, historical data, report, inspection task, and line fault detected. Moreover, there is a simple line fault expert database in the database system developed for automatic line fault detection of the robots. SQLite is adopted as the backend database in this system. According to the specific requirements of the actual inspection application, the E-R model of the database system is designed, which is composed of two parts: sensor data model and line inspection model. Application experiments reveal that this database system can accomplish the information storage and management work for inspection robots.

Keywords Inspection robot · Power transmission line · Database system · SQLite · Entity-relationship model

D. Zhao (✉) · E. Li · G. Yang · Z. Liang
State Key Laboratory of Management and Control for Complex Systems, Institute
of Automation, Chinese Academy of Sciences, No. 95, Zhongguancun East Road, Haidian,
Beijing, China
e-mail: Dezheng.zhao@ia.ac.cn

E. Li
e-mail: En.li@ia.ac.cn

G. Yang
e-mail: Guodong.yang@ia.ac.cn

Z. Liang
e-mail: Zize.liang@ia.ac.cn

48.1 Introduction

The main way of long-distance power transmission is high voltage and extra high voltage overhead power line. It must be reliably guaranteed for its operational safety. These critical components, such as transmission line, line fittings, and insulators, are prone to bring damage and fault resulting from long term exposure in the field environment. Without repairing them timely, it may expand and cause a serious accident, such as regional massive blackout and indeed results in huge economic losses. Therefore the power companies need to inspect the transmission lines regularly to obtain the operation status, detect and eliminate security risks in order to guarantee the normal operation of transmission lines.

There are two main transmission line inspection methods including ground visual method and aerial method at present. But they have their own inherent defects in terms of work efficiency, technical difficulty and operating costs [1, 2]. In recent years, high voltage power transmission line inspection robots [3, 4] gradually have become one of the research hotspots in high voltage line inspection field. This kind of robots can walk quickly on the transmission line with its self-navigation and can overcome such various obstacles as strain clamp, anti-vibration hammer, suspension clamp etc. [5, 6]. Meanwhile, the robots can carry all kinds of sensors, GPS positioning device and transmission line detection equipment used for real-time online detection of operation status of transmission line.

The historical data plays a vital role in operation and maintenance of the inspection robots. By analyzing the historical inspection data, the operator can make further planning of inspection task for robots. By analyzing the historical running data, the operator can improve the running algorithm and the path planning method of the robots. This brings great convenience for maintenance and upgrade of robots. Besides, it should be stored in a stable database for such information as sensor information, inspection task information, transmission line information, and line fault information. So the robots need a safe and stable database to store the historical data and the information related to robots and inspection task.

This paper introduces a database system for inspection based on SQLite [7, 8]. Firstly, the system architecture is described. Secondly, in view of the practical application of inspection robots, the E-R (Entity-Relationship) model of the database system is designed. Finally, running experiments on this system are conducted and the experimental results are analyzed.

48.2 System Architecture

Inspection robot control system is designed in hierarchical structure which includes management level, organization level, coordination level and execution level as shown in Fig. 48.1. As the top of the entire system, management level is

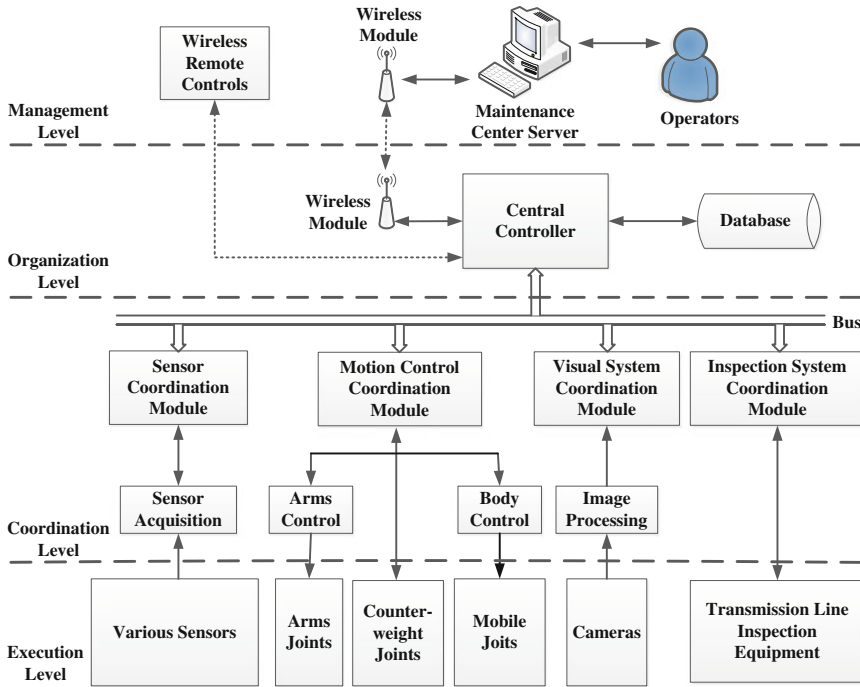


Fig. 48.1 Inspection robot control block diagram

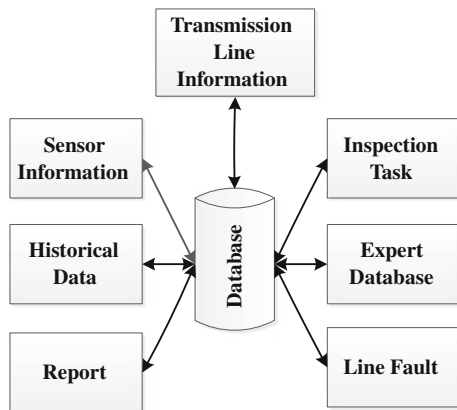
the interface for operator controlling and maintaining the robots, mainly including wireless remote control and remote maintenance center server. Wireless remote control connected via wireless RF transceiver module with robots is used for operator manually controlling the robots. Remote maintenance center server is the remote maintenance terminal through which operator can remotely maintain the robots running in the complex field environment. As the core of the entire system, organization level operates the entire system to organize, manage and interact with the outside world, mainly including master controller and database. Coordination level is the interface between the central controller and peripheral instruments. It is composed of various control module subsystems including sensor coordination module, motion control coordination module, vision system coordination module and line inspection system coordination module. The sensor coordination module is responsible for the acquisition and pre-processing of the sensor data; the motion control coordination module, for the motion planning parsing and joint movement control of the robot; the vision system coordination module, for such functions as image acquisition, image feature extraction, robot vision self-navigation and so on; the line inspection system coordination module, for controlling the transmission line detection equipment and obtaining the detection results. As the bottom of the entire system, the execution level is responsible for the actual implementation of a

variety of tasks. It is mainly composed of kinds of sensors, robot joints, cameras and transmission line detection equipment.

As shown in Fig. 48.2, the database system is composed of six modules including sensor information module, historical data module, report module, inspection task module, expert database module and line fault module. Sensor information module is used to store the basic sensor information, for example, sensor number, name, assembly time etc. Historical data module is used to store the running historical data of robots, while report module to store the report which is the subtotals for historical data. By analyzing the historical data and report, operator can improve the motion control method and inspection method. Transmission line information module is used to store the basic information of the transmission line such as the towers count, wire type, transmission power voltage, distance etc. Inspection task module is used to store the inspection task of the robots. There are many line fault types and their fault information stored in the expert database module, so the inspection robot can diagnose the line fault type through querying the expert database. Line fault module is used to store the line fault information the inspection robot has detected. According to the location and coordinates information from the line fault record, the line maintenance personnel can accurately arrive at the site of the line fault to repair.

The SQLite is used as the backend database of the inspection robots database system. As a Relational Database Management System (RDMS) abide by the Atomicity, Consistency, Isolation, Durability (ACID), the SQLite is an open source project created by D. Richard Hipp which is contained in a relatively small C programming library. Unlike common client/server database architecture, SQLite engine is not a separate process accessed by the client application but an integral part of the application. So all of the communication process is the direct API calls within the programming language, and it plays an important role in reducing the delay time. The entire database (definitions, tables, indexes, and data) are stored in a single file which makes it extremely simple and flexible. It occupies a very low resources and there are only hundreds kilobytes of memory needed in

Fig. 48.2 Database structure



embedded system. It makes SQLite a prevalent choice as embedded database. And it has been used in many embedded products at present. In conclusion, the advantages of SQLite lie in zero configuration, portability, compactness, simplicity, flexibility and reliability. Indeed these advantages make SQLite appropriate as the backend database of the inspection robot database system.

48.3 Database E-R Model

Database E-R model is composed of two parts, sensor data model and line inspection model. Sensor data model is used to store the sensor information and historical data of the robot, while line inspection model to store such information as inspection task planning, transmission line information, inspection results, fault expert diagnostic information etc.

Sensor data model contains four entities, sensor, data type, sensor data and report as shown in the Fig. 48.3. Sensor entity is used to store the basic information of sensors and mainly contains four field properties, sensor id, sensor name, category and assembly time. Sensor id field property is used to store the sensor serial name; name field property, to store the sensor name; category field property, to store the sensor category; assembly time field property, to store the assembly time of the sensors. Otherwise sensor entity also contains one extra field property used to store the sensor data type whose value comes from data type entity. Sensor data entity is used to store the historical data of the sensors and contains two field properties, data and acquisition time which are used to store sensor data and acquisition time respectively. Report entity is used to store the subtotals for the

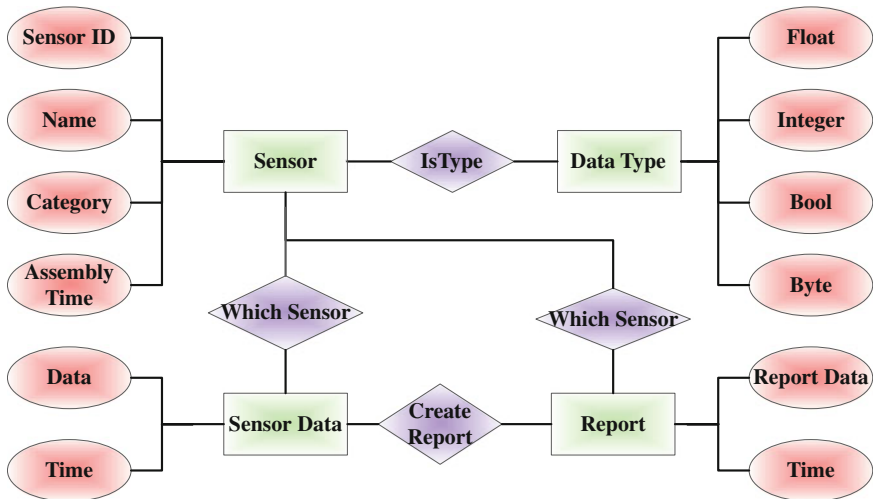


Fig. 48.3 Sensor data E-R model

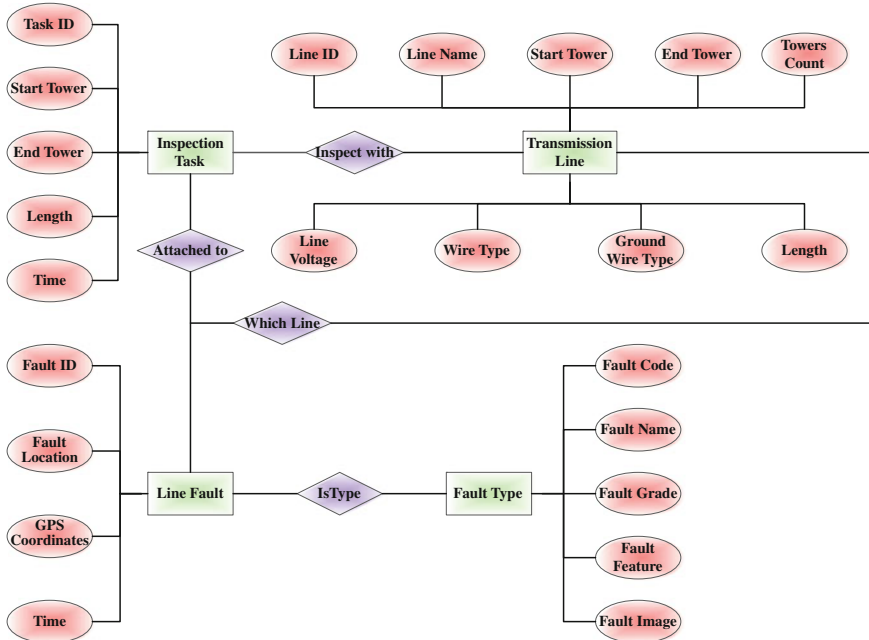


Fig. 48.4 Inspection E-R model

historical data of the sensors, which contains two field properties, report data and time.

As shown in the Fig. 48.4, line inspection model contains four entities, inspection task, transmission line, line fault and fault type. Inspection task entity is used to store the inspection task of the robot; transmission line entity, to store the basic information of the transmission line; line fault entity, to store the line fault detected by the robot; fault type entity, to store the basic information of the line fault. Inspection task entity contains five field properties, task id, start tower, end tower, length and Time. Task id field property is used to store the inspection task serial number; start tower field property, to store the start tower of the inspection task; end tower field property, to store the end tower of the inspection task; length field property, to store the length of the inspection task; time field property, to store the performing time of the inspection task. And the inspection task will be planned through configuring these field properties above. Furthermore, there is one extra field property used to store the information of the transmission line inspected whose value comes from transmission line entity. Transmission line entity contains nine field properties, line id, line name, start tower, end tower, towers count, line voltage, wire type, ground wire type and length. The basic information of the transmission line is stored in these field properties and the robots can perform specific inspection tasks according to this information. Line fault entity contains four field properties, fault id, fault location, GPS coordinates and time. Fault id

field property is used to store the line fault serial number; fault location and GPS coordinates field property, to store the geographical coordinates information of the line fault detected by the inspection robots, according to which the line maintenance personnel can accurately arrive at the site of the line fault to repair; time field property, to store the detecting time. Moreover, line fault entity contains three extra field properties used to store the inspection task, transmission line and fault type respectively. Fault type entity contains five field properties, fault code, fault name, fault grade, fault feature and fault image. This entity actually forms a simple transmission line fault expert database and the robots can diagnose the line fault type by comparing the fault features stored in it. According to the fault priorities, the faults are divided into different grades which will be stored in the fault grade field property. When transmission line fault detected, the robots will take the corresponding treatment method according to the fault grade.

48.4 Experiments and Analysis

The inspection robot database system is constructed based on the architecture above and several application experiments are carried out to test it. The storing response time is an important indicator of database system performance, so the delay time is tested through contiguously storing different number of records. The statistic result is shown in Table 48.1. In Table 48.1, records number is the continuous storing number of records; delay 1 is the delay time of continuous storage without SQLite transaction; delay 2 is the delay time of continuous storage time with SQLite transaction. It can be seen that, with the increasing of the number of continuous storage, the delay time of continuous storage without SQLite transaction is also obviously increasing, whereas with SQLite transaction the delay time is less increasing and keeps in a few milliseconds within certain limit of continuous storage number(In this experiment, the maximum number is 500). For SQLite, file IO operation is the bottleneck of writing/reading of the database, so the storing response time of database mainly depends on file I/O operation speed. But the file I/O operation speed depends on OS, so SQLite can't improve the storing response time through changing the speed. In this case, it is the only way to improve the storing response time that reducing the number of file I/O operation as much as possible in one storing operation. And SQLite transaction is introduced for this purpose. In SQLite transaction, all operations are suspended to the queue rather than directly synchronized to the database file, and operations in the queue will be sequentially synchronized to the database file when the user commits the transaction. Therefore it can perform many database operations and only needs just one file I/O operation by using SQLite transaction. Then it can greatly improve the storing response time with SQLite transaction which is proved by the statistic results in Table 48.1. Without SQLite transaction, one storing operation needs one database file I/O operation which results in that the delay time is obviously increasing with the increasing of the number of continuous storage as delay 1

Table 48.1 Delay time statistic result

Records number	5	10	15	20	25	...	100	200	300	400	500
Delay 1 (millisecond)	9	15	23	31	38	...	142	310	496	624	725
Delay 2 (millisecond)	3	1	2	3	1	...	2	2	2	4	3

shows in Table 48.1. In contrast, with SQLite transaction, many operations only need just one file I/O operation which results in that the delay time is less increasing with the increasing of the number of continuous storage as delay 2 shows in Table 48.1. Hence, the storing response time can fully meet the requirements of inspection robots in the database system above by using SQLite transaction mechanism.

48.5 Conclusion

According to the practical application of power transmission line inspection robots, a complete design scheme of database system is proposed, which is used for storing such information of the robots as historical data, inspection task, line fault data, etc. This system adopts SQLite as the backend database and the E-R model is designed according to the specific requirements of the inspection task. Furthermore, line fault diagnosis expert database is built for automatic line fault detection of the inspection robots. After several actual operating experiments of the database system, it proves that the system can accomplish well the basic information storing and management work for inspection robots.

Acknowledgments This work is supported by the National High Technology Research and Development Program of China (863 Program) (No. 2011AA04A104).

References

1. Jaensch G, Hoffmann H, Markees A (1998) Locating defects in high voltage transmission lines. In: Proceedings of IEEE 8th international conference on transmission & distribution construction, operation & live-line maintenance 1998, ESMO 1998, pp 179–186
2. Whitworth CC, Duller AWG, Jones DI, Earp GK (2001) Aerial video inspection of overhead power lines. *Power Eng J* 15:25–32
3. Sawada J, Kusumoto K, Maikawa Y, Munakata T, Ishikawa Y (1991) A mobile robot for inspection of power transmission lines. *IEEE Trans Power Delivery* 6:309–315
4. Peungsungwal S, Pungsiri B, Chamnongthai K, Okuda M (2001) Autonomous robot for a power transmission line inspection. In: Proceedings of the IEEE international symposium on circuits and systems 2001, ISCAS 2001 vol 2, pp 121–124
5. Debenest P, Guarnieri M, Takita K, Fukushima EF, Hirose S, Tamura K et al (2008) Expliner—robot for inspection of transmission lines. In: Proceedings of IEEE international conference on robotics and automation 2008, ICRA 2008, pp 3978–3984

6. N. Pouliot and S. Montambault (2008) Geometric design of the LineScout, a teleoperated robot for power line inspection and maintenance, in Robotics and Automation, 2008. ICRA 2008. IEEE International Conference on, pp. 3970-3977
7. Wikipedia SQLite Available: <http://en.wikipedia.org/wiki/SQLite>
8. Lv J, Xu S, Li Y (2009) Application research of embedded database SQLite. In: Proceedings of international forum on information technology and applications 2009, IFITA 2009, pp 539–543

Chapter 49

Two Methods for Solving the Parameters of Weibull Distribution of Wind Velocity

Baoqing Xu, Rui Tian and Guolin Yang

Abstract According to the distribution of wind velocity, the velocity of wind is analyzed as discrete variable and continuous variable. Weibull function can be got while the discrete distribution of wind velocity is fitted. As a continuous distribution function, Weibull function can be used in describe the wind velocity distribution correctly. In order to get the two parameters of scale parameter c and shape parameter k , the characteristic of this Weibull function is analyzed, and two ways of circulation test algorithm and gradient direction search method are presented for solving the two parameters of Weibull function. With the example of actual wind velocity data of Xinba'erhuqi in Inner Mongolian, these two methods are compared and analyzed. It shows that circulation test algorithm is easy to be understood, while the gradient direction search method is much more accurate. For different user, each of them has its own advantages and disadvantages, so they should be applied according to the actual cases.

Keywords Wind velocity · Weibull distribution · Circulation test algorithm · Gradient direction search method

B. Xu (✉) · G. Yang

School of Information and Engineering, Inner Mongolia University of Technology, No 49
Aimin Street, Hohhot, Inner Mongolia Autonomous Region 010051, China
e-mail: bqingxu@yahoo.com.cn

R. Tian

School of Energy and Power Engineering, Inner Mongolia University of Technology, No 49
Aimin Street, Hohhot city, Inner Mongolia Autonomous Region 010051, China
e-mail: tianri@imut.edu.cn

49.1 Introduction

Wind velocity distribution is an important indicator of the wind energy assessment and wind power development [1, 2]. In the National Standard of GBT 18451.2-2003 Wind turbine generator system- Power characteristic test, Raleigh function is recommended for calculating the annual energy production, however, Rayleigh function is just a special case of the Weibull function. Therefore, Weibull function with two parameters is usually adopted as the wind speed distribution function [3, 4]. Weibull distribution function is determined mainly by the two parameters of scale parameter c and the shape parameter k . So, the key problem is how to get the values of these two parameters. Regression method, standard deviation analysis and confidence interval method are the common methods used for the solution to these two parameters. Based on least square method, circulation test algorithm and the gradient direction search method have been introduced in this paper, and the two methods are analyzed and discussed.

49.2 Section Heading Distribution Characteristic of Wind Velocity

49.2.1 Discrete Characteristic of Wind Velocity

Because of the uncertainty and instability of the wind velocity distribution, it can be discussed as a random variable [5, 6]. Wind speed can be divided into n sections from 0–1, 1–2 m/s, to $(n - 1)$ – n m/s, where n is the largest integer value of the local wind speed. Then $v_1, v_2 \dots, v_n$ is marked, indicating that the wind speed of 1 m/s, 2 m/s, ... , n m/s. After the cumulative time of wind speed at each wind speed section is added up as h_{ij} h, which means the hours of wind speed v_j appears in i month ($i = 1, 2, \dots, 12; j = 1, 2, \dots, n$). So the occurrence probability p_j of wind speed v_j in the whole year can be calculated as follows:

$$p_j = p(v_j = j) = p(v = j) = \frac{1}{8760} \sum_{i=1}^{12} h_{ij}, j = 1, 2, \dots, n \tag{49.1}$$

Therefore, the discrete distribution of wind speed in the region is:

$$F_F(v) = \begin{cases} 0, & v_j < 0 \\ \sum_{j=1}^m p_j, & m \leq v_j < m + 1, 0 < m \leq n \\ 1, & v_j > n \end{cases} \tag{49.2}$$

49.2.2 Continuous Characteristic of Wind Velocity

When the wind velocity is discussed as a continuous variable, Weibull function can be a kind of probability density function of wind velocity [7]:

$$p(v) = \frac{k}{c} \left(\frac{v}{c}\right)^{k-1} e^{-\left(\frac{v}{c}\right)^k}, \quad v > 0 \tag{49.3}$$

And its distribution function is:

$$F_W(v) = 1 - e^{-\left(\frac{v}{c}\right)^k}, \quad v > 0 \tag{49.4}$$

where c is the scale parameter, the unit is m/s; k is the shape parameter, dimensionless; and v is the continuous wind velocity, the unit is m/s.

49.3 Fitting Function $W(c, k)$ of Wind Speed

Discrete distribution of wind speed usually can be used in analysis on data, and its empirical distribution can be got. But the actual speed of wind is continuous; it should be described as a continuous variable. Therefore, the Weibull distribution can be used to fit this empirical distribution, and define the two parameters of c and k according to the real characteristic of wind speed distribution. With the least squares method, the fitting function $W(c, k)$ can be obtained:

$$W(c, k) = \sum_v [F_F(v) - F_W(v)]^2 \tag{49.5}$$

So, when the function $W(c, k)$ reaches its minimum, the c and k corresponding to this minimum value is just the two parameter values we are looking for.

Let $phy_j = \sum_{pk=1}^j p_{pk}$; $j = 1, 2, \dots, n$, formula (49.6) can be got by (49.1), (49.2) and (49.4):

$$\begin{aligned} W(c, k) &= \sum_{j=1}^n [F_F(j) - F_W(j)]^2 = \sum_{j=1}^n \left[phy_j - 1 + e^{-\left(\frac{j}{c}\right)^k} \right]^2 \\ &= \sum_{j=1}^n \left[\sum_{pk=1}^j p_{pk} - 1 + e^{-\left(\frac{j}{c}\right)^k} \right]^2 \end{aligned} \tag{49.6}$$

phy_j is constant for the function $W_j(c, k)$; So each $W_j(c, k)$ is the continuous function in $D = \{(c, k)/c > 0, k > 0\}$. Consequently, $W(c, k)$ is a continuous function of c and k . Thus the first derivative of the continuous function $W(c, k)$ can be got by (49.6):

$$\frac{\partial W}{\partial c} = \frac{2k}{c} \sum_{j=1}^n \left[phy_j - 1 + e^{-\left(\frac{j}{c}\right)^k} \right] e^{-\left(\frac{j}{c}\right)^k} \cdot \left(\frac{j}{c}\right)^k \tag{49.7}$$

$$\frac{\partial W}{\partial c} = -2 \sum_{j=1}^n \left[phy_j - 1 + e^{-\left(\frac{j}{c}\right)^k} \right] e^{-\left(\frac{j}{c}\right)^k} \cdot \left(\frac{j}{c}\right)^k \cdot \ln\left(\frac{j}{c}\right) \tag{49.8}$$

Marked:

$$W^c(c, k) = \frac{\partial W}{\partial c}, \quad W^k(c, k) = \frac{\partial W}{\partial k} \tag{49.9}$$

$$\begin{aligned} W_j^c(c, k) &= \left[phy_j - 1 + e^{-\left(\frac{j}{c}\right)^k} \right] e^{-\left(\frac{j}{c}\right)^k} \cdot \left(\frac{j}{c}\right)^k \\ W_j^k(c, k) &= \left[phy_j - 1 + e^{-\left(\frac{j}{c}\right)^k} \right] e^{-\left(\frac{j}{c}\right)^k} \cdot \left(\frac{j}{c}\right)^k \cdot \ln\left(\frac{j}{c}\right) \end{aligned} \tag{49.10}$$

$$j = 1, 2, \dots, n$$

Then formula (49.11) can be got:

$$W^c(c, k) = \frac{2k}{c} \sum_{j=1}^n W_j^c(c, k); \quad W^k(c, k) = -2 \sum_{j=1}^n W_j^k(c, k) \tag{49.11}$$

Shown as (49.11), $W_j^c(c, k)$ and $W_j^k(c, k)$ is continuous functions of c and k for each j , so $W^c(c, k)$ and $W^k(c, k)$ are both continuous functions of c and k .

49.4 Determination of Parameters c and k

49.4.1 Circulation Test Algorithm

Based on the wind velocity characteristics in the given area, the maximum integer values of c and k can be given as c_{\max} and k_{\max} . According to different precision requirement, step-size d_{ck} can be given. Then in the region $D = \{(c, k) | c > 0, k > 0\}$, any point like $W_0 = W(c_0, k_0)$ can be specified as the initial point of $W(c, k)$. Proceeding from this point, and according to the following formula:

$$\begin{aligned} c_p &= c_0 + (p - 1)d_{ck}, \quad p = 1, 2, \dots, c_{\max} \\ k_q &= k_0 + (q - 1)d_{ck}, \quad q = 1, 2, \dots, k_{\max} \end{aligned} \tag{49.12}$$

Take the c_p and k_q into (49.5), you can get $[c_{\max}/d_{ck}] \times [k_{\max}/d_{ck}]$ values of $W(c_p, k_q)$, select its minimum value; record the c_p and k_q corresponding to this minimum value. This is right values of the two parameters c and k we needed.

49.4.2 Gradient Direction Search Method

For binary function $W = W(c, k)$, based on the above analysis and the definition of gradient, it has the first derivative of the continuous function in D . And for each point of $Q(c, k) \in D$, according to the gradient definition [8], the gradient of function $W = W(c, k)$ at this point can be defined:

$$\text{grad}W(c, k) = \frac{\partial W}{\partial c} \vec{i} + \frac{\partial W}{\partial k} \vec{j} = W^c(c, k) \vec{i} + W^k(c, k) \vec{j} \quad (49.13)$$

Take a point $Q_0(c_0, k_0)$ in D , the gradient at this point is:

$$\text{grad}W(c_0, k_0) = W^c(c_0, k_0) \vec{i} + W^k(c_0, k_0) \vec{j} \quad (49.14)$$

Along the gradient direction of $W^c(c, k) \vec{i} + W^k(c, k) \vec{j}$, the values of $W(c, k)$ increases fastest on the surface; on the contrary, along the opposite direction:

$$\vec{l} = -W^c(c, k) \vec{i} - W^k(c, k) \vec{j} \quad (49.15)$$

The values of $W(c, k)$ decreases fastest on the surface. So, the minimum of $W(c, k)$ can be certainly found along this direction of \vec{l} . Take a point $Q_0(c_0, k_0)$ in D corresponding to the surface value of $W_0 = W(c_0, k_0)$ as the beginning point, from this point, along the direction of \vec{l} , the point (c_t, k_t) can be expressed as:

$$\begin{aligned} c_t &= c_0 - tW^c(c_0, k_0) \\ k_t &= k_0 - tW^k(c_0, k_0) \end{aligned} \quad (49.16)$$

In this way, each t corresponds to a $W(c_t, k_t)$, denoted by $W(t)$. Take r as an arbitrary real constant, when $t = r$, the following two cases will be encountered:

1. If $W(r) < W_0$, then calculate $W(2r)$, $W(4r)$, ..., $W(2^m r)$ ($m \in \mathbb{N}$), until you find a point $W(2^m r)$, it makes

$$\begin{cases} W(2^m r) \geq W(2^{(m-1)} r) \\ W(2^{(m-1)} r) < W_0 \end{cases} \quad (49.17)$$

Take $W_1(2^m r)$, $W_2(2^{(m-1)} r)$ and $W_3(r)$, this three points can determine a parabola on the plane of t and $W(t)$:

$$w(t) = at^2 + bt + e \quad (49.18)$$

2. if $W(r) \geq W_0$, then calculate $W(\frac{1}{2}r)$, $W(\frac{1}{4}r)$, ..., $W(\frac{1}{2^m}r)$, until a point $W(\frac{1}{2^m}r)$ can be found, it makes:

$$\begin{cases} W\left(\frac{1}{2^m} r\right) \leq W\left(\frac{1}{2^{m-1}} r\right) \\ W\left(\frac{1}{2^m} r\right) < W_0 \end{cases} \tag{49.19}$$

In this case, the three points should be $W_1\left(\frac{1}{2^m} r\right)$, $W_2\left(\frac{1}{2^{m-1}} r\right)$ and $W_3(r)$. These three points can determine a parabola on the plane of t and $W(t)$ by (49.18).

When the three points determined in above cases are substituted into (49.18), a ternary quadratic equation group and their solutions can be got:

$$a = \frac{\frac{W_3-W_1}{t_3-t_1} - \frac{W_2-W_1}{t_2-t_1}}{t_3 - t_2}; b = \frac{W_2 - W_1}{t_2 - t_1} - a(t_2 + t_1); e = W_1 - at_1^2 - bt_1 \tag{49.20}$$

By the nature of the quadratic function, it can be known, When $t = -\frac{b}{2a}$, $W(t)$ reaches its minimum. While the corresponding c and k can be get by (49.16), and these two parameters are just what we want the two parameters of c and k in Weibull distribution.

49.5 Examples and Conclusions

49.5.1 Experiments and Results

Take an example of Xinba'erhuqi in Inner Mongolia Autonomous Region, with the relevant data given in Ref. [9], the discrete probability p_j and the distribution function $F_F(v)$ in this region can be obtained. The specific data is shown in Fig. 49.1.

Calculated respectively by circulation test algorithm and gradient direction search method, the minimum of the least squares fitting function $W(c, k)$ and its corresponding c and k are listed in Table 49.1.

Fig. 49.1 Discrete distribution values of wind velocity in Xinba'erhuqi in Inner Mongolia

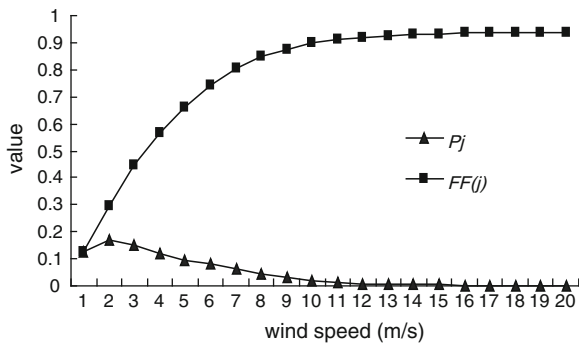


Table 49.1 The minimum values of $W(c, k)$ and the parameters of the Weibull distribution in Xinba'erhuqi

Method	$W(c, k)$	c	k
Circulation test algorithm	0.018231	4.83001	1.07
Gradient direction search	0.031047	4.85145	1.18

49.5.2 Analysis and conclusions

Table 49.1 shows the results of these two calculation methods are consistent and have the following characteristics:

- Circulation test algorithm depends on the initial and final values of the parameters, as well as on the step which determines the accuracy of the results. Therefore, the range of c and k , and accuracy requirements should be given according to the characteristics of the region. If the wind speed distribution is not easy to be obtained, then the gradient direction search method is the best choice.
- The step of c and k in circulation test algorithm both are d_{ck} are, the maximum distance value between of two adjacent test points in the plane domain D is $\sqrt{2d_{ck}}$, that is the accuracy determined by d_{ck} is fixed, it do not change with the number of tests. However, the step of t in gradient direction search method changes with its initial value and the number of calculation. For example, the step t is $2^m r$ or $\frac{1}{2^m} r$ of the m th computing. So d_{ck} and r should be set according to different accuracy demand and data.
- In circulation test algorithm, the function $W(c, k)$ will be called $[c_{max}/d_{ck}] * [k_{max}/d_{ck}]$ times. If c and k has a large range, and with a high accuracy, then the number of tests is a very large value. Table 49.2 shows the c, k and the times of $W(c, k)$ called in different range and accuracy.
- It can be seen, if only the range of k changes from $[1, 2]$ to $[1, 5]$, the number of loop will increase from 30,300 to 120,000 times, but c and k are the same. Therefore, the appropriate range and step is crucial for the efficiency and accuracy in circulation test algorithm.
- In gradient direction search method, the initial and step of the parameter also have effects on the call times of $W(c, k)$ and the results of c and k . As shown in Table 49.3, the number of loop in this method is much less than that in

Table 49.2 Effect of the ranges of c and k and accuracy on the results by circulation test algorithm

c_0	c_{max}	k_0	k_{max}	d_{ck}	c	k	Loop times
2	5	1	2	0.01	4.83001	1.07	30300
1	5	1	2	0.01	4.83001	1.07	40400
1	5	1	2	0.1	4.79999	1.10	410
2	5	1	5	0.01	4.83001	1.07	120000

Table 49.3 Effect of the initial values of c & k and accuracy on the results by gradient direction search method

c_0	k_0	r	c	k	Loop times
3	1	0.1	3.367051	0.754358	7
3	2	0.1	4.851457	1.186452	7
3	2	0.01	4.985549	1.248500	10
3	2	0.001	4.800591	1.318504	14
4	2	0.01	4.649706	1.284174	10
4	2	0.1	4.537368	1.407944	7

circulation test algorithm. Moreover, since the gradient can specify the value direction, therefore, the impact on the results of c and k , and the times of loop from the initial value and step is not so obvious like that in circulation test algorithm.

Acknowledgments This work was supported by the Inner Mongolia University of Technology as an important project (ZD201227), and by the Ministry of Education Key Laboratory on Wind and Solar Energy and the Inner Mongolia Autonomous Region Renewable Energy Key Laboratory. Thanks for their foundation support for my project.

References

- Xu B, Tian D, Li Q, Zhao D (2008) Solving the mathematical expectation of wind velocity with the methods of Gauss-Laguerre integral formula. *J Inner Mongolia Univ* 39(3):337–341
- Lubosny Z, Bialek JW (2007) Supervisory control of wind farm. *IEEE Trans Power Syst* 22(3):985–994
- Garrad Hassan & Partners. Offshorewind. <http://www.gi-garradhassan.com/en/Offshore.php>
- Luo CL, Far HG, Banakar H (2007) Estimation of wind penetration as limited by frequency deviation. *IEEE Trans Energy Convers* 22(3):783–791
- Xu B (2012) Wind turbine generator system design theory and method, 1st edn. Peking University Press, Beijing, pp 1–252 (in Chinese)
- Sheng J, Xie S, Pan C (2001) Probability theory and mathematical statistics, 3rd edn. Higher Education Press, Beijing, pp 109–137 (in Chinese)
- Chellali F, Khellaf A, Belouchrani A et al (2012) A comparison between wind speed distributions derived from the maximum entropy principle and Weibull distribution case of study: six regions of Algeria. *Renew Sustain Energy Rev* 16(1):379–385
- Ren B (2006) Vector analysis and field theory instruction, guidance, guide test. Northwestern Polytechnical University Press, Beijing, pp 62–69 (in Chinese)
- Xu B, Li Q, Shi X (2000) The optimum matching of wind/pv hybrid system. *J Inner Mongolia Univ* 30(1):107–111 (in Chinese)

Chapter 50

A Direct Robust Predictive Control Algorithm for Multi-Rate Systems

Xiaohua Liu and Rong Gao

Abstract In view of the existing interference of actual system, a direct robust predictive control algorithm is presented when the update rate of input and output is not the same as the sampling rate. Combined robust predictive control and system parameter estimation algorithm, the robust predictive control algorithm for multi-rate systems using min–max method is derived directly according to the input/output data of the system. The results are illustrated with examples.

Keywords Multi-rate systems · Robust predictive control · Least square method

50.1 Introduction

Single-rate system is relative to multi-rate system. With the increasing of industry process complexity, the measurement of controlled variables and the control variables cannot be completed in time. Control system adopting the same input/output frequency already cannot satisfy the industrial requirements. Therefore multi-rate systems have received little attention [1–4]. Such linear theory is not applicable when output measurements are available only periodically with the control law periodically time varying [5].

The complex multi-rate systems include some certain mismatched disturbance. And this condition exists in many actual systems, such as in chemical process and so on. Therefore, this paper focuses on those systems in which disturbance exist. Robust predictive control algorithm is extended to multi-rate systems and the robust stability of multi-rate generalized predictive control system is analyzed [6]. When plant and model are mismatch, the dual-rate predictive control system has

X. Liu (✉) · R. Gao
School of mathematics and Information, Ludong University, Yantai,
Shandong 264025, China
e-mail: xhliu_yt@sina.com

better performance than single-rate generalized predictive control [7]. The robust stability is analyzed when the sampling period changes. A dual-rate min–max robust generalized predictive control algorithm is put forward [8]. More information is obtained through increasing output time-domain and the robust stability of system is analyzes when there are plus uncertainties and multiplicative uncertainties.

In order to solve the disturbance in which system exist, we design a multi-rate robust predictive control. The aim of this paper is to reduce the effect of disturbance. In particular, the inter-sample output is lost so we need establish the unknown output during control design. This is very important for multi-rate system. In order to solve such problems, this paper introduces the polynomial transform technique and parameter estimation algorithm to deduce the unknown inter-sample output. For disturbance exist in system, we use the min–max thought to design the controller. We find a worst condition first, and then we design a controller under this worst condition. This paper is organized as follows. Section 50.2 deduces the inter-sample output. Polynomial transform is introduced. Section 50.3 use min–max thought to gives a directly robust predictive control algorithm for multi-rate systems. An example is given in Sect. 50.4.

50.2 Estimation of Unknown Sample Output

Throughout the paper, we assume that P_c in Fig. 50.1 is a linear time-invariant continuous time process with disturbance. The input–output data available are $\{u(k), k = 0, 1, \dots\}$ at the fast rate and $\{y(kh), k = 0, 1, \dots\}$ at the slow rate, where $y_0(k)$ is the system output without disturbance and $y(k)$ is the system real output. From Fig. 50.1 we have:

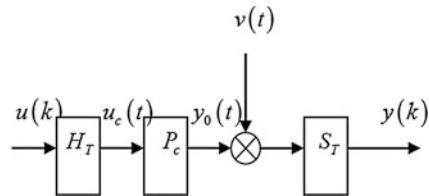
$$y_0(k) = \frac{B(z^{-1})}{A(z^{-1})}u(k) \tag{50.1}$$

$$y(k) = y_0(k) + v(k) \tag{50.2}$$

where $A(z^{-1}) = 1 + a_1z^{-1} + a_2z^{-2} + \dots + a_nz^{-n}$, $B(z^{-1}) = b_0 + b_1z^{-1} + b_2z^{-2} + \dots + b_nz^{-n}$.

We assume a_i and b_i are unknown parameters. From (50.1), we have:

Fig. 50.1 Multi-rate sampling system



$$A(z^{-1})y_0(k) = B(z^{-1})u(k),$$

or

$$y_0(k) = -a_1y_0(k-1) - \cdots - a_ny_0(k-n) + b_0u(k) + b_1u(k-1) + \cdots + b_nu(k-n) \quad (50.3)$$

Let $\varphi(k) = [-y_0(k-1) \ \cdots \ -y_0(k-n) \ u(k) \ \cdots \ u(k-n)]^T$ and $\theta_0 = [a_1 \ \cdots \ a_n \ b_0 \ \cdots \ b_n]^T$, then (50.3) could write as: $y_0(k) = \varphi^T(k)\theta_0$.

We assume the root of $A(z^{-1}) = 0$ is z_i , then $A(z^{-1})$ could express as follows:

$$A(z^{-1}) = \prod_{i=1}^n (1 - z_i z^{-1}).$$

Define $\phi_h(z^{-1}) = \prod_{i=1}^n (1 + z_i z^{-1} + z_i^2 z^{-2} + \cdots + z_i^{h-1} z^{-h+1}) = \prod_{i=1}^n \frac{1 - z_i^h z^{-h}}{1 - z_i z^{-1}}$, from (50.1), we have

$$\alpha(z^{-1})y_0(k) = \beta(z^{-1})u(k) \quad \text{or} \quad \alpha(z^{-1})y_0(kh) = \beta(z^{-1})u(kh) \quad (50.4)$$

where

$$\alpha(z^{-1}) = A(z^{-1})\phi_h(z^{-1}) \quad \text{and} \quad \beta(z^{-1}) = B(z^{-1})\phi_h(z^{-1}) \quad (50.5)$$

Using the formulation $1 - x^h = (1 - x)(1 + x + x^2 + \cdots + x^{h-1})$, we have:

$$\begin{aligned} \alpha(z^{-1}) &= A(z^{-1})\phi_h(z^{-1}) = \prod_{i=1}^n (1 - z_i z^{-1})(1 + z_i z^{-1} + \cdots + z_i^{h-1} z^{-h+1}) \\ &= \prod_{i=1}^n (1 - z_i^h z^{-h}) = 1 + \alpha_1 z^{-h} + \cdots + \alpha_n z^{-nh} \\ \beta(z^{-1}) &= B(z^{-1})\phi_h(z^{-1}) = \prod_{i=1}^n (b_0 + b_1 z^{-1} + \cdots + b_n z^{-n})(1 + z_i z^{-1} + \cdots + z_i^{h-1} z^{-h+1}) \\ &= \beta_0 + \beta_1 z^{-1} + \cdots + \beta_{nh} z^{-nh} \end{aligned}$$

Define the parameter vector θ and the information vector $\varphi(kh)$ as follows:

$$\begin{aligned} \theta &= [\alpha_1 \ \cdots \ \alpha_n \ \beta_0 \ \cdots \ \beta_{nh}]^T, \\ \varphi(kh) &= [-y_0(kh-h) \ \cdots \ -y_0(kh-nh) \ u(kh) \ u(kh-1) \ \cdots \ u(kh-nh)]^T. \end{aligned}$$

Then (50.4) can be written as:

$$y_0(kh) = \varphi^T(kh)\theta.$$

Therefore, from (50.2), we have: $y(kh) = \varphi^T(kh)\theta + v(kh)$.

Denote $\hat{\theta}(kh)$ to be the estimate θ at time kh . Because of the information vector $\varphi(kh)$ do not include unknown output $y(kh - j)$, $j = 1, 2, \dots, h - 1$, so we use least square algorithm to estimate unknown parameter vector θ :

$$\hat{\theta}(kh) = \hat{\theta}(kh - h) + L(kh) \left[y(kh) - \varphi^T(kh)\hat{\theta}(kh - h) \right], \quad \hat{\theta}(kh + i) = \hat{\theta}(kh),$$

$$i = 0, 1, \dots, h - 1,$$

$$L(kh) = P(kh - h)\varphi(kh) \left[1 + \varphi^T(kh)P(kh - h) \times \varphi(kh) \right]^{-1},$$

$$P(kh) = \left[I - L(kh)\varphi^T(kh) \right] P(kh - h),$$

$$\varphi(kh) = \left[-y(kh - h) \quad \dots \quad -y(kh - nh) \quad u(kh) \quad u(kh - 1) \quad \dots \quad u(kh - nh) \right]^T$$

$$\hat{\theta}(kh) = \left[\hat{\alpha}_1(kh) \quad \dots \quad \hat{\alpha}_n(kh) \quad \hat{\beta}_0(kh) \quad \hat{\beta}_1(kh) \quad \dots \quad \hat{\beta}_{nh}(kh) \right]^T$$

According to estimated value $\hat{\theta}(kh)$, we have the estimation of polynomial

$$\alpha(z^{-1}) \text{ and } \beta(z^{-1}) : \quad \hat{\alpha}(kh, z^{-1}) = 1 + \hat{\alpha}_1(kh)z^{-h} + \dots + \hat{\alpha}_n(kh)z^{-nh},$$

$$\hat{\beta}(kh, z^{-1}) = \hat{\beta}_0(kh) + \hat{\beta}_1(kh)z^{-1} \dots + \hat{\beta}_{nh}(kh)z^{-nh}.$$

Define the estimation of $A(z^{-1})$ and $\beta(z^{-1})$:

$$\hat{A}(kh, z^{-1}) = 1 + a_1(kh)z^{-1} + \dots + a_n(kh)z^{-n},$$

$$\hat{B}(kh, z^{-1}) = \hat{b}_0(kh) + \hat{b}_1(kh)z^{-1} \dots + \hat{b}_n(kh)z^{-n}.$$

From (50.5), we have:

$$\frac{\alpha(z^{-1})}{\beta(z^{-1})} = \frac{A(z^{-1})}{B(z^{-1})} \tag{50.6}$$

We replace $\alpha(z^{-1})$ and $\beta(z^{-1})$ in (50.6) by $\hat{\alpha}(kh, z^{-1})$ and $\hat{\beta}(kh, z^{-1})$ respectively, according to model equivalent thought, we know the estimation of $A(z^{-1})$ and $B(z^{-1})$ satisfy:

$$\frac{\hat{\alpha}(kh, z^{-1})}{\hat{\beta}(kh, z^{-1})} = \frac{\hat{A}(kh, z^{-1})}{\hat{B}(kh, z^{-1})},$$

or

$$\hat{\alpha}(kh, z^{-1})\hat{B}(kh, z^{-1}) = \hat{\beta}(kh, z^{-1})\hat{A}(kh, z^{-1}) \tag{50.7}$$

Substituting $\hat{\alpha}(kh, z^{-1})$, $\hat{\beta}(kh, z^{-1})$, $\hat{A}(kh, z^{-1})$ and $\hat{B}(kh, z^{-1})$ into (50.7), we have:

$$\left[1 + \hat{\alpha}_1(kh)z^{-h} + \dots + \hat{\alpha}_n(kh)z^{-nh} \right] \left[\hat{b}_0(kh) + \hat{b}_1(kh)z^{-1} \dots + \hat{b}_n(kh)z^{-n} \right]$$

$$= \left[\hat{\beta}_0(kh) + \hat{\beta}_1(kh)z^{-1} \dots + \hat{\beta}_{nh}(kh)z^{-nh} \right] \left[1 + \hat{a}_0(kh)z^{-1} + \dots + \hat{a}_n(kh)z^{-n} \right] \tag{50.8}$$

Unfold (50.8) and compare the same coefficient of z^{-1} both sides, we get:

$$\begin{aligned}
\hat{\beta}_0(kh) &= \hat{b}_0(kh) \\
\hat{\beta}_1(kh) &= -\hat{\beta}_0(kh)\hat{a}_1(kh) + \gamma_1(kh)\hat{b}_0(kh) + \hat{b}_1(kh) \\
\hat{\beta}_2(kh) &= -\hat{\beta}_1(kh)\hat{a}_1(kh) - \hat{\beta}_0(kh)\hat{a}_2(kh) + \gamma_2(kh)\hat{b}_0(kh) + \gamma_1(kh)\hat{b}_1(kh) + \hat{b}_2(kh) \\
&\vdots \\
0 &= -\hat{\beta}_{nh}(kh)\hat{a}_n(kh) + \gamma_{nh}(kh)\hat{b}_n(kh)
\end{aligned}$$

or

$$R(kh)\hat{\theta}_0(kh) = \rho(kh) \quad (50.9)$$

where

$$R(kh) = \begin{bmatrix} 0 & \cdots & 0 & 1 & \cdots & 0 \\ -\hat{\beta}_0(kh) & \cdots & 0 & \gamma_1(kh) & \cdots & \vdots \\ -\hat{\beta}_1(kh) & \cdots & \vdots & \gamma_2(kh) & \ddots & 0 \\ -\hat{\beta}_2(kh) & \ddots & 0 & \gamma_3(kh) & \ddots & 1 \\ \vdots & \ddots & -\hat{\beta}_0(kh) & \vdots & \ddots & \gamma_1(kh) \\ -\hat{\beta}_{nh}(kh) & & -\hat{\beta}_1(kh) & \gamma_{nh}(kh) & & \gamma_2(kh) \\ 0 & & 0 & 0 & \cdots & \gamma_3(kh) \\ \vdots & \ddots & & \vdots & \ddots & \vdots \\ 0 & 0 & -\hat{\beta}_{nh}(kh) & 0 & 0 & \gamma_{nh}(kh) \end{bmatrix}$$

$$\begin{aligned}
\hat{\theta}_0(kh) &= [\hat{a}_1(kh) \quad \hat{a}_2(kh) \quad \cdots \quad \hat{a}_n(kh) \quad \hat{b}_0(kh) \quad \hat{b}_1(kh) \quad \cdots \quad \hat{b}_n(kh)]^T \\
\rho(kh) &= [\hat{\beta}_0(kh) \quad \hat{\beta}_1(kh) \quad \cdots \quad \hat{\beta}_{nh}(kh) \quad 0 \quad \cdots \quad 0]^T.
\end{aligned}$$

From (50.9), we get the least square estimation of $\hat{\theta}_0(kh)$ as follows:

$$\bar{\theta}_0(kh) = [R^T(kh)R(kh)]^{-1}R^T(kh)\rho(kh).$$

Because of $\hat{\theta}_0(kh)$ is keep unchanged between the inter-sample, so $\bar{\theta}_0(kh)$ is unchanged, else, for example $\bar{\theta}_0(kh+j) = \bar{\theta}_0(kh)$, $j = 1, 2, \dots, h-1$. Using $u(kh+j)$ and the estimation model, we could compute inter-sample output $\tilde{y}(kh+j)$. From (50.2), we have:

$$\tilde{y}(kh+j) = \begin{cases} y(kh), j = 0, \\ \frac{\hat{B}(kh, z^{-1})}{\hat{A}(kh, z^{-1})}u(kh+j), j = 1, 2, \dots, h-1. \end{cases}$$

50.3 Directly Robust Predictive Control Algorithm

From (50.2), we replace $A(z^{-1})$ and $B(z^{-1})$ by $\hat{A}(kh, z^{-1})$ and $\hat{B}(kh, z^{-1})$, respectively. Then we get:

$$y(kh) = \frac{\hat{B}(kh, z^{-1})}{\hat{A}(kh, z^{-1})}u(kh) + w(kh) \quad (50.10)$$

where $w(kh)$ is a random noise in (50.10), include the error caused by the estimation of polynomial substitution and the system random disturbance $v(kh)$, it can be considered as white noise.

Let j is the predictive steps ($j = 1, 2, \dots, h$), and consider Diophantine equation:

$$1 = E_j(z^{-1})\hat{A}(kh, z^{-1}) + z^{-j}F_j(z^{-1}) \quad (50.11)$$

where $E_j(z^{-1})$ and $F_j(z^{-1})$ is the only polynomial determined by predictive steps j :

$$\begin{aligned} E_j(z^{-1}) &= 1 + e_{j,1}z^{-1} + \dots + e_{j,j-1}z^{-(j-1)}, \\ F_j(z^{-1}) &= f_{j,0} + f_{j,1}z^{-1} + \dots + f_{j,n}z^{-n}. \end{aligned}$$

Form (50.11), we get the following recursive equations:

$$E_{j+1}(z^{-1}) = E_j(z^{-1}) + e_{j+1,j}z^{-j}, F_{j+1}(z^{-1}) = z[F_j(z^{-1}) - e_{j+1,j}\hat{A}(kh, z^{-1})],$$

(50.10) multiply by $E_j(z^{-1})$ both sides, we get:

$$\begin{aligned} E_j(z^{-1})\hat{A}(kh, z^{-1})y(kh) &= E_j(z^{-1})\hat{B}(kh, z^{-1})u(kh) + E_j(z^{-1})\hat{A}(kh, z^{-1})w(kh) \\ &= G_j(z^{-1})u(kh) + H_j(z^{-1})w(kh) \end{aligned} \quad (50.12)$$

where $G_j(z^{-1}) = E_j(z^{-1})\hat{B}(kh, z^{-1}) = g_{j,1}z^{-1} + \dots + g_{j,n+j-1}z^{-(n+j-1)}$

$$H_j(z^{-1}) = E_j(z^{-1})\hat{A}(kh, z^{-1}) = 1 + h_{j,1}z^{-1} + \dots + h_{j,n+j-1}z^{-(n+j-1)}$$

Substituting (50.11) into (50.12), we have:

$$y(kh) = z^{-j}F_j(z^{-1})y(kh) + G_j(z^{-1})u(kh) + H_j(z^{-1})w(kh)$$

or

$$y(kh + j) = F_j(z^{-1})y(kh) + G_j(z^{-1})u(kh + j) + H_j(z^{-1})w(kh + j) \quad (50.13)$$

Define future output vector $Y(kh)$, past output vector $Y_P(kh)$, future input vector $U(kh)$, past input vector $U_P(kh)$ and disturbance vector $W(kh)$ as follows, respectively

$$\begin{aligned}
Y(kh) &= [y(kh+1) \quad y(kh+2) \quad \cdots \quad y(kh+h)]^T, \\
Y_P(kh) &= [y(kh) \quad y(kh-1) \quad \cdots \quad y(kh-n)]^T, \\
U(kh) &= [u(kh+1) \quad u(kh+2) \quad \cdots \quad u(kh+h)]^T, \\
U_P(kh) &= [u(kh) \quad u(kh-1) \quad \cdots \quad u(kh-n+1)]^T, \\
W(kh) &= [w(kh+1) \quad w(kh+2) \quad \cdots \quad w(kh+h)]^T.
\end{aligned}$$

From (50.13), when $j = 1, 2, \dots, h$, we get h equations, write them into matrix form:

$$Y(kh) = G_1 U_P(kh) + G_2 U(kh) + F Y_P(kh) + H W \quad (50.14)$$

where

$$\begin{aligned}
G_1 &= \begin{bmatrix} g_{1,1} & g_{1,2} & \cdots & g_{1,n} \\ g_{2,2} & g_{2,3} & \cdots & g_{2,n+1} \\ \vdots & \vdots & \ddots & \vdots \\ g_{h,h} & g_{h,h+1} & \cdots & g_{h,h+n-1} \end{bmatrix}, \quad G_2 = \begin{bmatrix} g_{1,0} & 0 & \cdots & 0 \\ g_{2,1} & g_{2,0} & \cdots & 0 \\ \vdots & \vdots & \ddots & \vdots \\ g_{h,h-1} & g_{h,h-2} & \cdots & g_{h,0} \end{bmatrix}, \\
H &= \begin{bmatrix} H_1(z^{-1}) & 0 & \cdots & 0 \\ 0 & H_2(z^{-1}) & \cdots & 0 \\ \vdots & \vdots & \ddots & \vdots \\ 0 & 0 & \cdots & H_h(z^{-1}) \end{bmatrix}, \quad F = \begin{bmatrix} f_{1,0} & f_{1,1} & \cdots & f_{1,n} \\ f_{2,0} & f_{2,1} & \cdots & f_{2,n} \\ \vdots & \vdots & \ddots & \vdots \\ f_{h,0} & f_{h,1} & \cdots & f_{h,n} \end{bmatrix},
\end{aligned}$$

Because of $Y_P(kh)$ contains unknown output $y(kh-j)$, so we replace $y(kh-j)$ by $\tilde{y}(kh-j)$.

Define $\hat{Y}_P(kh) = [\tilde{y}(kh+1) \quad \tilde{y}(kh+2) \quad \cdots \quad \tilde{y}(kh+h)]^T$, then (50.14) can transform as:

$$Y(kh) = G_1 U_P(kh) + G_2 U(kh) + F \hat{Y}_P(kh) + H W \quad (50.15)$$

Consider the following performance index:

$$\begin{aligned}
\min_u \max_w J &= \sum_{i=1}^h \left[\|y(kh+i) - y_r(kh+i)\|_l^2 + \|u(kh+i|kh)\|_r^2 \right] - \mu^2 w^T w \\
&= \|Y(kh) - Y_r(kh)\|_L^2 + \|U(kh)\|_R^2 - \mu^2 W^T W
\end{aligned} \quad (50.16)$$

Where $L = U, R = rI, l > 0, r > 0$. $y_r(kh+i)$ is expected output at time $kh+i$, then the optimal solution of (50.16) exists when the following conditions satisfied:

$$\left. \frac{\partial J}{\partial W} \right|_{W=W^*} = 0, \quad \left. \frac{\partial^2 J}{\partial W^2} \right|_{W=W^*} \leq 0 \quad (50.17)$$

$$\left. \frac{\partial J}{\partial U} \right|_{U=U^*} = 0, \left. \frac{\partial^2 J}{\partial U^2} \right|_{U=U^*} \geq 0 \tag{50.18}$$

Solving (50.17), we get the worst disturbance:

$$W^* = \psi^{-1} H^T L (G_1 U_P + G_2 U + F \hat{Y}_P - Y_r),$$

where $\psi = \mu^2 I - H^T L H$ and the full condition of that W^* is the biggest is $\psi > 0$.

Put W^* into J and solve (50.18), we get the optimal control as follows:

$$U = \xi_2^{-1} [K_3 U_P + K_4 \hat{Y}_P - K_5 Y_r],$$

where $K_1 = I + \psi^{-1} H^T L$, $K_2 = G_2 + H \psi^{-1} H^T G_2$, $\xi_1 = \psi^{-1} G_2^T L H \psi^{-1} H^T L$,

$$\begin{aligned} \xi_2 &= \mu^2 \psi G_2 - R - K_2^T L K_2, K_3 = K_2^T L K_1 G - \mu^2 \xi_1 G_1, K_5 = K_2^T L + \mu^2 \xi_1, K_4 \\ &= K_2^T L K_1 F - \mu^2 \xi_1 F. \end{aligned}$$

50.4 Numerical Simulations

Consider random system as follows:

$$(1 - 1.5z^{-1} + 0.09z^{-2})y(z) = (0.512z^{-1} + 0.209z^{-2})u(z) + v(k)$$

where $\{v(k)\}$ as a white noise sequence with zero mean and variance $\sigma_v^2 = 0.01^2$. Assume expect system output is $y^*(k) = 1$. When $h = 2$, we apply dual-rate directly robust predictive control algorithm, design a predictive controller. The results are shown in Figs. 50.2 and 50.3.

It is clearly, especially from the Figs. 50.2 and 50.3, when the system exist disturbance, we could see the system output can follow the tracks of the expect output. When we use this algorithm, the performance of this control is satisfying our requirement.

Fig. 50.2 System output $y(k)$ and expect output $y^*(k)$

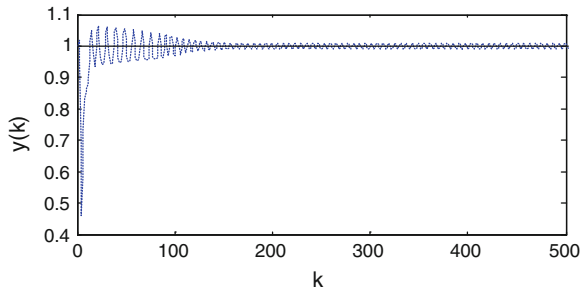
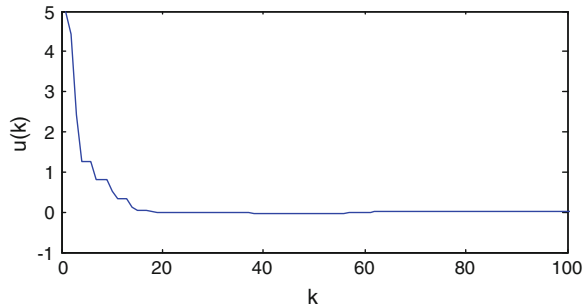


Fig. 50.3 Control input $u(k)$ 

50.5 Conclusions

For multi-rate system, a direct robust predictive control algorithm is presented based on dual-rate input–output data. Because disturbance is existed in real systems, we put disturbance into the process of predictive controller design. Use min–max thought to design predictive controller in the worst conditions. Although the controller in the paper is done for dual-rate system with an additive white noise disturbance, the methods developed can be easily extended to multi-rate systems. Finally, we present an illustrative example to show the effectiveness of the algorithm proposed in the paper.

Acknowledgments This work is supported by National Nature Science Foundation under Grant61174097.

References

1. Kalman RE, Bertram JE (1959) A unified approach to the theory of sampling systems. *J Franklin Inst* 267(5):405–436
2. Fukushima H, Bitmead RR (2005) Robust constrained predictive control using comparison model. *Automatica* 41:97–106
3. Zhou L, Dong H, Qian J (1999) Multirate dynamic matrix control for multivariable systems. In: *Proceedings of 14th World Congress of IFAC*, pp 241–246
4. Rossiter JA, Sheng J, Chen T, Shah SL (2005) Interpretations of and options in dual-rate predictive control. *J Process Control* 15:135–148
5. Sheng J, Chen T, Sirish SL (2002) Generalized predictive control for non-uniformly sampled systems. *J Process Control* 12(3):875–885
6. Sheng J, Chen T, Sirish LS (2001) On stability robustness of dual-rate generalized predictive control systems. *Proceedings of the American Control Conference*, Arlington, VA, 3415–3420
7. Rossiter JA, Sheng J, Chen T, Shah SL (2004) Robustness of dual-rate inferential MPC systems. In: *Proceeding of the American control conference*, Boston, pp 251–253
8. Liu J, Liu X (2006) Dual-rate min-max robust generalized predictive control. *The sixth world congress on intelligent control and automation*, Da Lian, pp 536–539

Chapter 51

Nonlinear Adaptive Control of Magnetic Levitation System with Uncertain Parameters and Unknown Disturbances

Baobin Liu

Abstract Due to the changes of viscous friction coefficients and the disturbance of control current, the suspended height of magnetic levitation ball is different from its reference location. The nonlinear adaptive backstepping is proposed to deal with this problem, which is the controller design of magnetic levitation system with uncertain parameters and unknown disturbances. The proposed method can estimate viscous friction coefficients online, and guarantee stability of controlled system with complex disturbances rapidly. The simulation results show that the dynamic performance of the magnetic levitation system can be significantly improved by using proposed nonlinear adaptive backstepping method. Furthermore, the global asymptotically stability of the control system and the robustness for complex disturbances can both be guaranteed by simulation results.

Keywords Magnetic levitation · Adaptive control · Nonlinear system · Backstepping

51.1 Introduction

Magnetic levitation technology applies a magnetic field to levitate a magnetic object. A magnetic ball can be levitated and stabilized in a magnetic system with a photoelectronic feedback. In a sense, the magnetic levitation technology can eliminate consumption caused by the friction. The technology is widely used in the field of the fast trains, vibration isolation tables and magnetic bearings for its high efficiency.

B. Liu (✉)

Jiangsu Institute of Economic and Trade Technology, No. 104 Guang Hua Road,
Bai Xia, Nan Jing 210007, Peoples Republic of China
e-mail: jsliubin@sina.com.cn

Magnetic levitation system has been receiving increasing attention recently owing to its practical importance and its unique advantages. The controller is an important unit of the magnetic levitation system, so it is widely concerned in the design of the system. Classic design methods of magnetic levitation system are proportional integral differential control [1], generalized proportional integral control [2] and quantitative feedback theory [3]. However, magnetic levitation system is a typical nonlinear system with uncertain parameters and unknown disturbances. It is defective for linear control method to reduce the control accuracy and cause system deterioration because of excessive linearization [4]. In recent years, the continuous improvement of robust control and adaptive control provides advanced theory for the research of magnetic levitation system [5–8].

We will apply adaptive control method to design the controller of magnetic levitation system. The target of global adaptive control is to find a continuous steady state control $u = \mu(x, \hat{\theta})$ and an update-rate $\dot{\hat{\theta}} = \gamma(x, \hat{\theta})$. Thus the closed-loop system given by the following

$$\begin{cases} \dot{x} = f(x, \theta) + g(x, \theta)\mu(x, \hat{\theta}) \\ \dot{\hat{\theta}} = \gamma(x, \hat{\theta}) \end{cases} \quad (51.1)$$

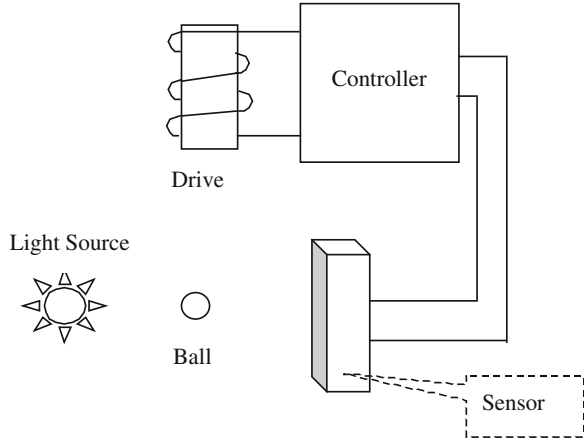
is a Lyapunov stability system. The control method with update-rate can accurately estimate the uncertain parameters even if we do not know its approximation value.

51.2 Model of Magnetic Levitation System

Figure 51.1 illustrates a schematic diagram of the magnetic levitation system. The drive in Fig. 51.1 is an electromagnet, and the ball is a magnetic ball. The current in the coils of the electromagnet generates an electromagnetic force. If electromagnetic force equals to the ball's gravity, the magnetic ball can be in equilibrium and it can be suspended in the air. Such a balanced state is unstable. Slightly disturbances, such as voltage pulsation or the change of viscous friction coefficient, would cause the height of the ball changed. Therefore, the closed-loop control of the system is very necessary. A measuring device composed by a light source and a sensor, is used to detect the change of the displacement between the ball and the electromagnet. Two parameters will change with the height of magnetic ball. The first change is the distance between the magnetic ball and electromagnet, and the second one is light intensity received by the photoelectric sensor. At last, the change of light intensity is converted into a feedback control signal. The designed controller needs to increase or decrease the current in the coils according to the feedback signal, so as to increase or decrease the electromagnetic force to make the ball go back to the original equilibrium position.

Through stress analysis, we obtain the equation of the ball motion as below:

Fig. 51.1 A schematic diagram of magnetic levitation system



$$m\ddot{h} = -k\dot{h} + mg - F(h, i) \tag{51.2}$$

where m is the mass of the ball, $h \geq 0$ is the vertical position, k is a viscous friction coefficient and i is a drive current [9]. In (51.2), the viscous friction coefficient is an uncertain parameter. And $F(h, i)$ is given by the following:

$$F(h, i) = 0.5aL_0(i + \Delta i)^2(a + h)^{-2} \tag{51.3}$$

where Δi is the disturbance current and a, L_0 are positive constants.

51.3 Design of Nonlinear Adaptive Controller

In this section, we have three tasks. First, we establish mathematical model of magnetic levitation system with parametric-strict-feedback form [10–12]. Then, use backstepping to design an adaptive controller. At last, we prove that the system is globally asymptotically stable.

51.3.1 Model Formulation

Ignoring the square of the disturbance current. Let $x_1 = h, x_2 = \dot{h}, u = i^2$ and $\Delta u = \Delta i$. The differential equations of the magnetic levitation system can be written as below:

$$\begin{cases} \dot{x}_1 = x_2 \\ \dot{x}_2 = -\frac{k}{m}x_2 + g - \frac{aL_0}{2m(a+x_1)^2}u + \eta(x_1, u, \Delta u), \\ y = x_1 \end{cases} \tag{51.4}$$

where u is a control variable and $\eta(x_1, u, \Delta u)$ is a disturbance. According to (51.3), $\eta(x_1, u, \Delta u)$ can be written as following:

$$\eta(x_1, u, \Delta u) = aL_0u^{0.5}\Delta u/(a + x_1)^2. \quad (51.5)$$

Obviously, $\eta(x_1, u, \Delta u)$ is a bounded disturbance.

51.3.2 Controller Design

We use backstepping method to design the controller. If ψ_r is the actual output of system, there must be an error between ideal output x_1 and actual output ψ_r . Define the error variable ξ_1 given by the following:

$$\xi_1 = x_1 - \psi_r. \quad (51.6)$$

Control target is that: $\xi_1 \rightarrow 0$ as $t \rightarrow \infty$. It can be known from (51.6) that

$$\dot{\xi}_1 = \dot{x}_1 - \dot{\psi}_r = x_2 - \dot{\psi}_r. \quad (51.7)$$

Define variable α as the virtual control of x_2 and α can be written as follow:

$$\alpha = -C_1\xi_1 + \dot{\psi}_r, \quad (51.8)$$

where C_1 is a positive undermined constant. The error variable ξ_2 between α and x_2 is given by the following:

$$\xi_2 = x_2 - \alpha = x_2 + C_1\xi_1 - \dot{\psi}_r. \quad (51.9)$$

The Lyapunov function of first-order system will be given as follow:

$$V_1 = 0.5\xi_1^2. \quad (51.10)$$

The time derivative of V_1 , computed with (51.7) is given as below:

$$\dot{V}_1 = \xi_1\dot{\xi}_1 = \xi_1(x_2 - \dot{\psi}_r) = -C_1\xi_1^2 + \xi_1\xi_2, \quad (51.11)$$

where $-C_1\xi_1^2$ is a semi-negative definite polynomial, while $\xi_1\xi_2$ is not uncertain. The first-order system is undesirable due to its lack of stability, and we need to eliminate $\xi_1\xi_2$ in later algorithms.

The time derivative of ξ_2 , compute with (51.4) and (51.7) is given in the following:

$$\begin{aligned} \dot{\xi}_2 = & -km^{-1}\xi_1 + g - 0.5aL_0m^{-1}(a + \xi_1)^{-2}u + \eta(\xi_1, u, \Delta u) + C_1(\xi_2 - C_1\xi_1) \\ & - \ddot{\psi}_r. \end{aligned} \quad (51.12)$$

Similarly, select Lyapunov function of second-order system as below:

$$V_2 = 0.5\xi_1^2 + 0.5\xi_2^2 + 0.5(k - \hat{k})^2, \quad (51.13)$$

where \hat{k} is the parameter estimation of k . Then we have the following equation:

$$\dot{V}_2 = \xi_1 \dot{\xi}_1 + \xi_2 \dot{\xi}_2 - (k - \hat{k}) \dot{\hat{k}}. \quad (51.14)$$

The actual control variable u appears in (51.12), so we can design the actual control. According to the Lyapunov stability theory, the design of the control variable should try to eliminate non-negative definite polynomial in (51.14). Define control variable as below:

$$u = -\frac{2m(a+x_1)^2}{aL_0} \left[\frac{\hat{k}}{m} x_1 - g - C_2 \xi_2 - \xi_1 - C_1(\xi_2 - C_1 \xi_1) + \ddot{y}_r - \eta^*(\xi_1, u, \Delta u) \right], \quad (51.15)$$

where C_2 is a positive undermined constant, $\eta^*(\xi_1, u, \Delta u)$ is an undetermined function which will be designed to deal with $\eta(\xi_1, u, \Delta u)$ and regulate system characteristics.

We can obtain from (51.7, 51.12) and (51.15) that

$$\dot{\xi}_2 = (\hat{k} - k)\xi_1 - C_2 \xi_2 - \xi_1 + \eta(\xi_1, u, \Delta u) - \eta^*(\xi_1, u, \Delta u), \quad (51.16)$$

$$\dot{V}_2 = -C_1 \xi_1^2 - C_2 \xi_2^2 + (k - \hat{k})(\dot{\hat{k}} + \xi_1 \xi_2) + \xi_2 \eta(\xi_1, u, \Delta u) - \xi_2 \eta^*(\xi_1, u, \Delta u). \quad (51.17)$$

From the Lyapunov function of second-order system we can know that $-C_1 \xi_1^2$ and $-C_2 \xi_2^2$ are both semi-negative definite polynomials. And the sign of $(k - \hat{k})$ is random. Define

$$\dot{\hat{k}} = -\xi_1 \xi_2. \quad (51.18)$$

As long as $\xi_2[\eta(\xi_1, u, \Delta u) - \eta^*(\xi_1, u, \Delta u)] \leq 0$, second-order system is stable in the Lyapunov sense. For $\eta(x_1, u, \Delta u)$ is a bounded disturbance, we have the following relationship as $\bar{b}(\xi_1, u, \Delta u) \geq \eta_{\max}(\xi_1, u, \Delta u) \geq \eta(\xi_1, u, \Delta u)$. Define

$$\eta^*(\xi_1, u, \Delta u) = \bar{b}(\xi_1, u, \Delta u) \text{ sign} \xi_2. \quad (51.19)$$

We can conclude that $\xi_2[\eta(\xi_1, u, \Delta u) - \eta^*(\xi_1, u, \Delta u)] \leq 0$.

For $V_2 = 0.5\xi_1^2 + 0.5\xi_2^2 + 0.5(k - \hat{k})^2 \geq 0$ and $\dot{V}_2 \leq 0$, and the whole system is stable in the Lyapunov sense.

51.3.3 The Stability of System

Furthermore, we analyze the stability of system. First, \dot{V}_2 is a semi-negative definite function. Then \ddot{V}_2 is a continuous function of ξ_1 and ξ_2 . And k is a

bounded unknown parameter. So \dot{V}_2 is consistently continuous. According to Barbalat lemma, $\xi_1 \rightarrow 0$ and $\xi_2 \rightarrow 0$ (equivalent $x_1 \rightarrow 0$ and $x_2 \rightarrow 0$), as $t \rightarrow \infty$ [13]. The system is global asymptotically stable.

51.4 Simulations and Analysis

Use the following numerical data: $m = 0.1$ kg, $a = 0.05$ m and $L_0 = 0.01$ H. Select the constants $C_1 = 1$ and $C_2 = 2$. The simulation results of error variable ξ_2 , which is also called state variable, and parameter estimation variable \hat{k} without disturbance are shown in Fig. 51.2a and b. However, adjustment time of the curves is 2–3 s, so it maybe a little longer.

We apply the simulation experiments to prove the rapidity and robustness of designed controller. For the stability of nonlinear system, Lyapunov’s second method is only sufficient but not necessary condition [14]. Assume that the disturbance is a single pulse, which appears in 0.3–0.4 s. If we do not add $\eta^*(\xi_1, u, \Delta u) = \bar{b}(\xi_1, u, \Delta u) \text{sign}\xi_2$ in (51.15) and (51.17), the profile of ξ_2 is shown in Fig. 51.2a. Then we add a function $\eta^*(\xi_1, u, \Delta u) = b(\xi_1, u, \Delta u) \text{sign}\xi_2$ in controller, where $0 < b(\xi_1, u, \Delta u) < \eta_{\max}(\xi_1, u, \Delta u)$. When the function $b(\xi_1, u, \Delta u)$ increases, the profiles of ξ_2 are shown in Fig. 51.3b, c and d. It can be seen that the adding $b(\xi_1, u, \Delta u)$ significantly shortens the adjustment time. And in Fig. 51.2d, adjustment time is reduced to less than about 0.03 s. Increasing function $b(\xi_1, u, \Delta u)$ can further shorten the oscillation amplitude and adjustment time caused by the disturbance. Next, we follow the design ideas of the paper, select $\eta^*(\xi_1, u, \Delta u) = \bar{b}(\xi_1, u, \Delta u) \text{sign}\xi_2$. The profile of state variable ξ_2 is shown Fig. 51.2e. It can be seen that single pulse disturbance does not cause the destruction of the system balance and designed controller has strong robustness if $\bar{b}(\xi_1, u, \Delta u) \geq \eta_{\max}(\xi_1, u, \Delta u)$.

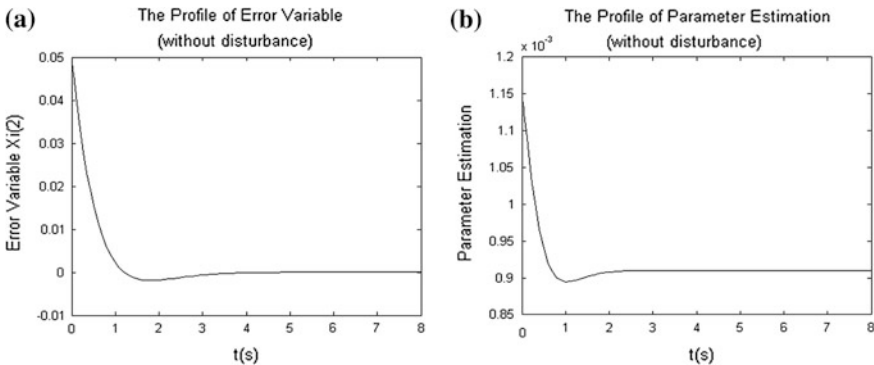


Fig. 51.2 The profiles of ξ_2 and \hat{k} without disturbance (a) state variable, (b) parameter estimation

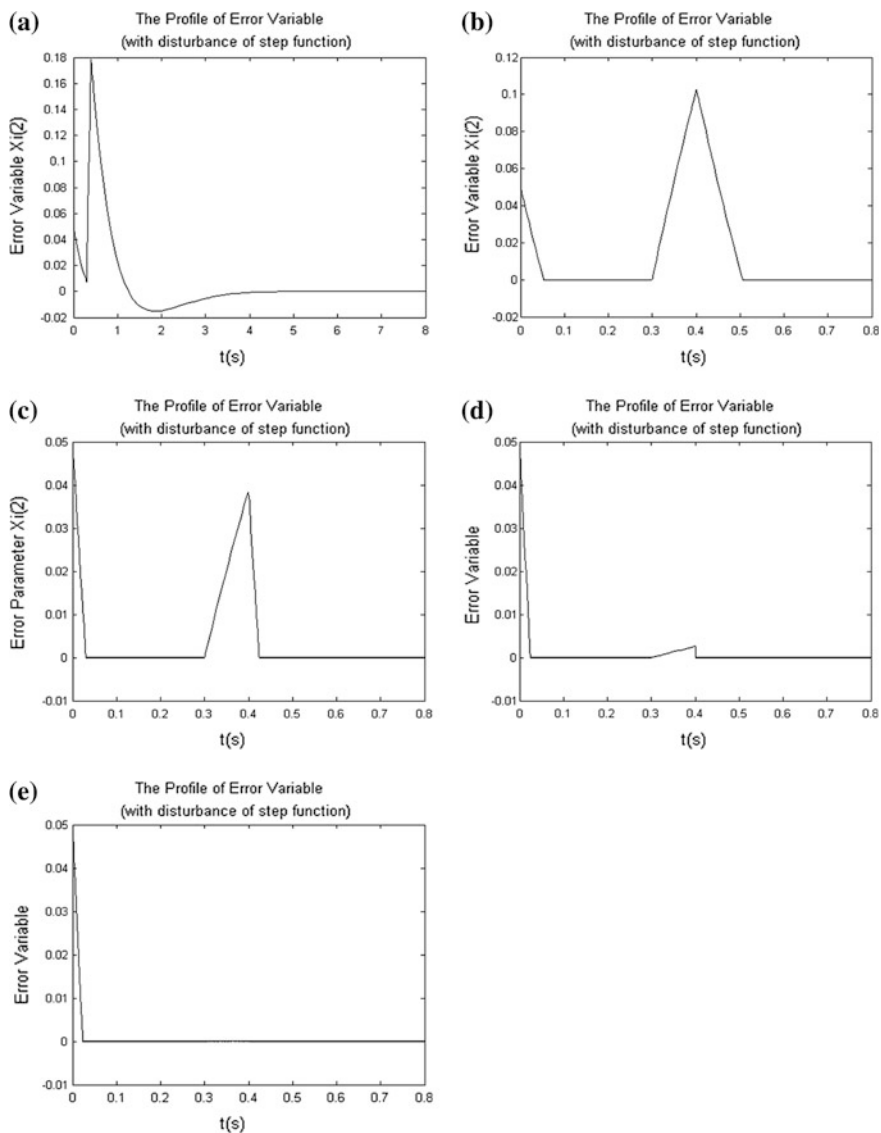


Fig. 51.3 The profiles of state (error) variable ξ_2 with single pulse disturbance

Furthermore, we assume that the disturbances are multiple harmonics. The profiles of state variable and parameter estimation are shown in Fig. 51.4. The parameter estimation is consistent with [10] but more accurate. In short, the system has strong robustness. The designed controller can also maintain system equilibrium.

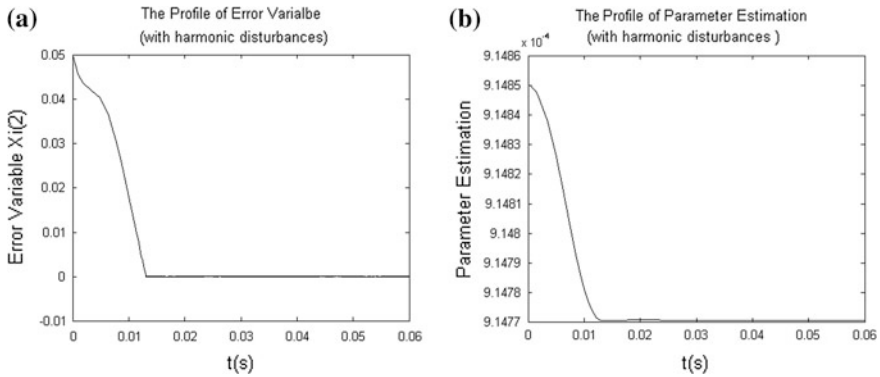


Fig. 51.4 The profiles of ξ_2 and \hat{k} with complex disturbances (a) z_2 , (b) \hat{k}

51.5 Conclusions

In this paper, we apply adaptive backstepping method to track magnetic ball location of magnetic levitation system and complete the following work:

1. Establish mathematical model of magnetic levitation system with parametric-strict-feedback form.
2. Apply adaptive backstepping method to design nonlinear adaptive controller of magnetic levitation system. Designed controller can estimate uncertain viscous friction online and ensure global asymptotical stability of the system.
3. The application of advanced algorithms significantly reduces the adjustment time and eliminates the oscillation caused by disturbances.
4. Using simulation experiments, we analyze the stability of the system and demonstrate rapidity and robustness of the system.

References

1. Wai RJ, Lee JD, Chuang KL (2011) Real-time PID control strategy for maglev transportation system via particle swarm optimization. *IEEE Trans Industr Electron* 58(2):629–646
2. Morales R, Sira-Ramirez H (2010) Trajectory tracking for the magnetic ball levitation system via exact feedforward linearisation and GPI control. *Int J Control* 83(6):1155–1166
3. Wang ZH, Chen ZQ, Sun QL et al (2006) Survey of the development for quantitative feedback theory. *Control Theory Appl* 23(3):403–410
4. Chen DZ (1988) *Geometric theory of nonlinear systems*, 1st edn. Science Press, Beijing
5. Jiang ZP (2000) Robust exponential regulation of nonholonomic system with uncertainties. *Automatica* 36(1):189–209
6. Kanellakopoulos I, Kokotovic PV, Morse AS (1991) Systematic design of adaptive controller for feedback linearizable systems. *IEEE Trans Autom Control* 36(11):1241–1253

7. Ye XD, Jiang JP (1998) Adaptive nonlinear design without a priori knowledge of control directions. *IEEE Trans Autom Control* 43(11):1617–1621
8. Ge Shuzi Sam, Wang J (2003) Robust adaptive tracking for time-varying uncertain nonlinear systems with unknown control coefficients. *IEEE Trans Autom Control* 48(8):1463–1469
9. Chiang HK, Chen CA, Li MY (2006) Integral variable-structure grey control for magnetic levitation system. *IEEE Proc—Electr Power App* 153(6):809–814
10. Khalil HK (2007) *Nonlinear systems*, 3rd edn. Publishing House of Electronics Industry, Beijing
11. Adriana González & Graciela (2003) Adaptive control for the discrete-time parametric-strict-feedback form. *Int J Control* 76(11):1095–1101
12. Sung JY, Jin BP, Yoon HC (2007) Adaptive dynamic surface control for stabilization of parametric strict-feedback nonlinear systems with unknown time delays. *IEEE Trans Autom Control* 52(12):2360–2365
13. Ye XD (2003) Global adaptive control of nonlinearly parameterized systems. *IEEE Trans Autom Control* 48(1):169–173
14. Liu B (2002) *Modern control theory*, 2nd edn. China Machine Press, Beijing in Chinese

Chapter 52

Mass Metrology Based on Robotic Mass Measurement System

Xiaoping Ren, Changqing Cai, Yi Li, Aibin Chen and Qingxiong Ren

Abstract Considering the requirements for the dissemination of mass and a large number of weights to be handled, traditional mass comparators are not sufficient for daily work. Automatic robot system can be able to perform the dissemination of the mass scale without any manual intervention as well as the fast speed calibration of weight samples against a reference weight. In the paper, a new robotic measurement system CCR10 is used to calibrate two weight sets (from 10 g down to 1 g) against one 10 g reference weight by subdivision method. The mean values of the weighing differences of 10 ABBA cycles are used for the adjustment calculation. A detailed description of the weighing design as well as the result of evaluation of the expanded uncertainty is given.

Keywords Mass metrology · Robotic mass measurement system · Automated mass measuring system

X. Ren (✉) · C. Cai

Division of Mechanics and Acoustics, National Institute of Metrology,
No.18, North San Huan Road, Beijing, Chaoyang 100013, People's Republic of China
e-mail: renxp@nim.ac.cn; xiaopingren@csu.edu.cn

C. Cai

e-mail: caichq@nim.ac.cn

Y. Li

Department of Intelligent Science and Technology, School of Information Science and Engineering, Central South University, No. 932, South Lushan Road, Changsha 410083 Hunan, People's Republic of China

A. Chen

College of Computer Science and Information Technology, Central South University of Forestry and Technology, No. 498, South Shaoshan Road, Changsha 410004 Hunan, People's Republic of China

Q. Ren

Shanxi Province Institute of Metrology, No. 29, Fuxi Street, Taiyuan 030002 Shanxi, People's Republic of China

52.1 Introduction

For a national metrology institute, there are huge quantities of weights to be calibrated. Automatic system can perform the dissemination of the mass scale without any manual intervention as well as the fast speed calibration of weights or weight sets [1], force measurement [2] or volume measurement (density determination) [3, 4]. Besides, the threat of confounding weights is also omnipresent [5].

To meet the requirements for calibration of weights, it is necessary to build up new equipment [6, 7]. This paper introduced research development of robotic measurement system. Then discussed a sub-multiple calibration scheme adopted on a fully-automatic CCR10 system.

52.2 Developments on the Robotic Mass Measurement System

In Table 52.1, it lists out the recently important research development of robotic mass measurement system and corresponding references.

At the year of 2001, Mettler-Toledo company developed a series of automatic comparator line consists of a5, a100 and a1000 comparator [5]. In 2007, Fröhlich used a fully automated mass comparator robot system to calibrate an entire 1 kg-1 mg weight set against one 1 kg reference by subdivision [8]. Zelenka in BEV of Austria introduced modified weighing design for automatic calibration of weights on high-precision mass comparators [9]. The whole system, which is based on computer control and linear drive trains, was first mentioned by Christian Buchner early at 2007 [6]. In the report by Christian Buchner [10], they gave out detailed design objectives and implementation method [11].

52.3 Mass Dissemination Using a Robotic Measurement System

CCR10 robot system from Sartorius AG/Germany was built up in National Institute of Metrology (NIM, China) in Oct 2012. The sub-multiple calibration scheme is shown in Table 52.2. Symbol “1”, “-1” and “0” represent the factors indicating the constituent weights at a given comparing mass. Equilibriums of 7 mass comparisons are given by Eqs. (52.1) and summary of all performed mass comparisons are concluded in Table 52.3.

Table 52.1 Development of automatic comparator in national metrology institutes

Years	Main designer	Range	Reference
2001	Mettler-Toledo Company, Switzerland	5 g, 100 g, 1 kg	[5]
2005	Technical University of Ilmenau(TUI), Germany	BIPM and Sartorius AG (Göttingen)	Up to 1 kg [13, 14]
2007	Sartorius AG (Göttingen)	Technical University of Ilmenau (TUI), Germany	1 mg ~ 1 kg [1, 8]
2007	Austrian federal office of metrology and surveying (BEV)	Sartorius AG (Göttingen) and Vienna University of Technology	1 mg ~ 10 g, 10 g ~ 1 kg, 1 kg ~ 20 (50) kg [6]
2009	Austrian federal office of metrology and surveying (BEV)	Sartorius AG (Göttingen) and Vienna University of Technology.	1 mg ~ 10 g [9]
2009	Austrian federal office of metrology and surveying (BEV)	Institute of production engineering (IFT) of the Vienna University of Technology	Force measurement 5 N–2 kN, 50 N–250 kN [2]
2009	Austrian federal office of metrology and surveying (BEV)	Institute of production engineering (IFT) of the Vienna University of Technology	Volume of 1 kg and up to 50 kg [3]
2012	Austrian federal office of metrology and surveying (BEV)	Sartorius AG (Göttingen)	10 g up to 1 kg [15]

$$\begin{aligned}
 W_1(10 \text{ g}) - W_R(10 \text{ g}) &= \Delta m_1 \\
 W_2(5 \text{ g}) + W_3(5 \text{ g}) - W_R(10 \text{ g}) &= \Delta m_2 \\
 W_3(5 \text{ g}) - W_2(5 \text{ g}) &= \Delta m_3 \\
 W_4(2 \text{ g}) + W_5(2 \text{ g}) + W_6(1 \text{ g}) - W_2(5 \text{ g}) &= \Delta m_4 \\
 W_6(1 \text{ g}) + W_7(1 \text{ g}) - W_4(2 \text{ g}) &= \Delta m_5 \\
 W_6(1 \text{ g}) + W_7(1 \text{ g}) - W_4(2 \text{ g}) &= \Delta m_6 \\
 W_7(1 \text{ g}) - W_6(1 \text{ g}) &= \Delta m_7
 \end{aligned} \tag{52.1}$$

The mass difference Δm_i is calculated from the indication differences of the balance in the above equations. The conventional masses of the W_R (10 g) reference weights are referred and from results of these mass difference measurements, the masses of the weights to be calibrated are then estimated by the least squares method [12]. The masses, m_1, m_2, \dots, m_7 are respectively given by Eq. (52.2) [16]:

Table 52.2 Weighing scheme for calibration of 10 g, 5 g, 2 g, 1 g weights

Weight Value (g)	W_1	W_2	W_3	W_4	W_5	W_6	W_7	W_R	Mass difference
Group task Id	0012#	cyc1#	0012#	cyc1#	0012#	cyc1#	0012#	Ref.	
1	1	0	0	0	0	0	0	-1	Δm_1
2	0	1	1	0	0	0	0	-1	Δm_2
3	0	-1	1	0	0	0	0	0	Δm_3
4	0	-1	0	1	1	1	0	0	Δm_4
5	0	0	0	-1	0	1	1	0	Δm_5
6	0	0	0	0	-1	1	1	0	Δm_6
7	0	0	0	0	0	-1	1	0	Δm_7

Table 52.3 Summary file from the robot system application software

Task Id	Date	Time	Pos. A	Pos. B	Nominal/g	Value/mg Δm_i	Std. Dev/ μg $S(\Delta m_i)$
000001	28-11-2012	12:09:09	I1	I5	10	-0.073195	0.290
000002	28-11-2012	13:16:47	I1	I2 I6	10	-0.040850	0.095
000003	28-11-2012	14:27:04	I2	I6	5	-0.042980	0.090
000004	28-11-2012	15:34:48	I2	I3 I7 I4	5	0.159105	0.095
000005	28-11-2012	16:48:09	I3	I4 I8	2	-0.034090	0.065
000006	28-11-2012	17:58:47	I7	I4 I8	2	0.079520	0.070
000007	28-11-2012	19:09:27	I4	I8	1	-0.072170	0.080

$$\begin{aligned}
 m_{W_1} &= m_{W_R} + \Delta m_1 \\
 m_{W_2} &= (m_{W_R} + \Delta m_2 - \Delta m_3)/2 \\
 m_{W_3} &= (m_{W_R} + \Delta m_2 + \Delta m_3)/2 \\
 m_{W_4} &= (2m_{W_2} + 2\Delta m_4 - 3\Delta m_5 + 2\Delta m_6 + \Delta m_7)/5 \\
 m_{W_5} &= (2m_{W_2} + 2\Delta m_4 + 2\Delta m_5 - 3\Delta m_6 + \Delta m_7)/5 \\
 m_{W_6} &= (m_{W_4} + \Delta m_5 - \Delta m_7)/2 \\
 m_{W_7} &= (m_{W_4} + \Delta m_5 + \Delta m_7)/2
 \end{aligned}
 \tag{52.2}$$

52.4 Uncertainty Calculations

Combined standard uncertainty u_c of the sub-multiple calibration of the weights by means of the calibration scheme shown in Table 52.2 is estimated by Eq. (52.3)

$$u_c = \sqrt{u^2(\overline{\Delta m_c}) + u^2(m_r) + u_b^2 + u_{ba}^2}.
 \tag{52.3}$$

52.4.1 Standard Uncertainty of the Weighting Process $u(\overline{\Delta m_c})$

The standard uncertainty of the weighting process $u(\overline{\Delta m_i})$ is the standard deviation of the mass difference (see the 8th column of Table 52.3). Here for 10 cycles of measurements, it can be computed by Eq. (52.4):

$$u(\overline{\Delta m_i}) = s(\Delta m_i) / \sqrt{10} \quad (52.4)$$

Standard uncertainty of the weighting process of 7 mass comparison measurements is shown in Table 52.4.

52.4.2 Uncertainty of the Reference Weight $u(m_r)$

The standard uncertainty $u(m_r)$ of the mass of the reference weight should be calculated from the calibration certificate by dividing the quoted expanded uncertainty U , by the coverage factor k , and should be combined with the uncertainty due to the instability of the mass of the reference weight, $u_{\text{inst}}(m_r)$.

From Eq. (52.2), it is inferred that the reference weight of W_1 , W_2 and W_3 is W_R (10 g) which expanded uncertainty U is 3.2 μg ($k = 2$). The instability of W_R can be estimated from observed mass changes after the reference weight has been calibrated several times (shown in Table 52.5).

Table 52.4 Standard uncertainty of the weighting process

Task Id	Standard deviation of mass difference $S(\Delta m_i)$	Standard uncertainty of weighting process $u(\overline{\Delta m_i})$
1	0.290	0.091706
2	0.095	0.030042
3	0.090	0.028460
4	0.095	0.030042
5	0.065	0.020555
6	0.070	0.022136
7	0.080	0.025298

Table 52.5 Corrected value of vacuum mass in different years

Year	Corrected value of vacuum mass (mg)
2011	$mc_{2011} = 0.0928$
2009	$mc_{2009} = 0.0899$
2005	$mc_{2005} = 0.0901$

Then $u_{\text{inst}}(m_{\text{cr}}) = s(\Delta m) = \sqrt{\frac{(\sum_{i=1}^n \Delta m - \bar{\Delta m})^2}{(n-1)}} = 0.001322 \text{ mg}$, where $\bar{\Delta m} = \frac{1}{n} \sum_{i=\text{year}}^n \Delta m_{\text{c-year}} = 0.090933 \text{ mg}$. So the uncertainty of the reference weight is:

$$u(m_r) = \sqrt{(U/k)^2 + u_{\text{inst}}(m_r)} = \sqrt{(1.6)^2 + 1.322} = 2.0755 \text{ } \mu\text{g} \tag{52.5}$$

52.4.3 Uncertainty of Air Buoyancy Correction u_b

The uncertainty of the air buoyancy correction can be calculated by Eq. (52.6), and the result of uncertainty of the air buoyancy correction is shown in Table 52.6

$$u_b^2 = (V_{\text{ref}} - V_{\text{test}})^2 u^2(\rho_a) + \rho_a^2 (u^2(V_{\text{test}}) + u^2(V_{\text{ref}})) + 2 \frac{\partial m_{\text{test}}}{\partial m_{\text{ref}}} \cdot \frac{\partial m_{\text{test}}}{\partial \rho_a} \cdot u(m_{\text{ref}}, \rho_a) + 2 \frac{\partial m_{\text{test}}}{\partial m_{\text{ref}}} \cdot \frac{\partial m_{\text{test}}}{\partial V_{\text{ref}}} \cdot u(m_{\text{ref}}, V_{\text{ref}}). \tag{52.6}$$

52.4.4 Uncertainty of the Mass Comparator u_{ba}

The uncertainty of the mass comparator itself can be divided into four components, which are sensitivity of the balance u_s , display resolution of a digital balance u_d , eccentric loading u_E and magnetism u_{ma} . Here we just consider u_s and u_E , which are listed in Table 52.7.

52.4.5 Combined Standard Uncertainty of the Conventional Mass of Test Weight

Table 52.8 gives out final result for standard uncertainty of each test weight.

Table 52.6 Result of uncertainty of the air buoyancy correction

TaskId	u_b (μg)	Task Id	u_b (μg)
1	0.506829985	5	0.130693728
2	0.279969415	6	0.198220399
3	0.146132088	7	9.70374E - 05
4	0.302920686	/	/

Table 52.7 Combined standard uncertainty of the balance

Task Id	$ \Delta I_1 - \Delta I_2 _{\max}$ (μg)	$u_E = \Delta I_1 - \Delta I_2 _{\max}/\sqrt{3}$ (μg)	$u_d = \left(\frac{d/2}{\sqrt{3}}\right) \times \sqrt{2}$	$u_{ba} = \sqrt{u_d^2 + u_E^2}$
1	0.22	0.1270	0.0408	0.133393
2	0.19	0.1097	0.0408	0.117042
3	0.17	0.0981	0.0408	0.106246
4	0.16	0.0923	0.0408	0.100915
5	0.15	0.0866	0.0408	0.09573
6	0.13	0.0751	0.0408	0.085467
7	0.14	0.0808	0.0408	0.090517

Table 52.8 Combined standard uncertainty of test weight

Standard uncertainty of test weight	Uncertainty of the reference weight $u(m_r)$	Combined standard uncertainty u_c	Expanded uncertainty $U(k = 2, \mu\text{g})$	Corrected value of vacuum mass (mg)
$u_{W_1} = \sqrt{u^2(m_r) + u_1^2}$ ^a	$u_{W_R} = 2.0755$	2.142611	4.3	0.017692
$u_{W_2} = \frac{1}{2} \sqrt{u^2(m_r) + u_2^2 + u_3^2 + 2u_2u_3}$	$u_{W_R} = 2.0755$	1.118956	2.2	0.003470
$u_{W_3} = \frac{1}{2} \sqrt{u^2(m_r) + u_2^2 + u_3^2 + 2u_2u_3}$	$u_{W_R} = 2.0755$	1.118956	2.2	0.006535
$u_{W_4} = \frac{2}{5} \sqrt{\frac{u_{W_2}^2 + u_4^2 + u_5^2 + u_6^2 + u_7^2 + 2u_4u_5 + 2u_4u_6}{+2u_4u_7 + 2u_5u_6 + 2u_5u_7 + 2u_6u_7}}$	$u_{W_2} = 1.118956$	0.549044	1.1	0.006823
$u_{W_5} = \frac{2}{5} \sqrt{\frac{u_{W_2}^2 + u_4^2 + u_5^2 + u_6^2 + u_7^2 + 2u_4u_5 + 2u_4u_6}{+2u_4u_7 + 2u_5u_6 + 2u_5u_7 + 2u_6u_7}}$	$u_{W_2} = 1.118956$	0.549044	1.1	0.047643
$u_{W_6} = \frac{1}{2} \sqrt{u_{W_4}^2 + u_5^2 + u_7^2 + 2u_5u_7}$	$u_{W_4} = 0.549044$	0.282315	0.56	0.120503
$u_{W_7} = \frac{1}{2} \sqrt{u_{W_4}^2 + u_5^2 + u_7^2 + 2u_5u_7}$	$u_{W_4} = 0.549044$	0.282315	0.56	0.079232

^a The reference weight of W_1, W_2 and W_3 is $W_R, u(m_r)$ is computed by Eq. (52.5)

52.5 Conclusion

Mass measurement system based on robot can automatically execute all steps including: disseminations, moving of the weights and the necessary comparisons. The experiment and analysis of CCR10 robotic measurement system shows that it has excellent repeatability.

Acknowledgments The author wish to thank for the grant of National Science and Technology Support Program (2011BAK15B06); Special-Funded Program on National Key Scientific Instruments and Equipment Development (2012YQ090208).

References

1. Fehling T, Fröhlich T, Heydenbluth D (2007) Design and performance of the new Sartorius robot-system. In: Proceedings of the 20th TC3, 3rd TC16 and 1st TC22 international conference cultivating metrological knowledge, IMEKO, 27–30, Merida, pp 1–8
2. Christian B, Zoltan Z, Thomas M (2012) Determination of forces from 10 N up to 250 kN using two full automatic dead weight machines developed by the BEV. In: Proceedings of IMEKO, 9–14, Busan, pp 1–5
3. Christian B (2009) Development and realization of a fully automatic testing facility for determining the volume of E1 weights up to 50 kg based on hydrostatic weighing. In: Proceedings of XIX IMEKO world congress fundamental and applied metrology, 6–11, Lisbon, pp 182–185
4. Wang J, Wang XL, Yao H et al (2012) Research on volume measurement system of weight below 100 g. In: Proceedings of 2012 international conference on intelligent systems design and engineering application, 6–7, Sanya, pp 1110–1112
5. Arthur R (2001) A new mass comparator generation for the automatic calibration of weight sets. In: Proceedings of the 17th international conference on force, mass, torque and pressure measurements, IMEKO, 17–21, Istanbul, pp 310–319
6. Christian B (2007) Fully automatic mass laboratory from 1 mg up to 50 kg—robots perform high precision mass determination. In: Proceedings of IMEKO 20th TC3, 3rd TC16 and 1st TC22 international conference cultivating metrological knowledge, 27–30, Merida, pp 1–18
7. Masaaki U (2007) Uncertainty evaluation on the fully-automated sub-multiple calibration in the milligram range. In: Proceedings of SICE annual conference, 17–20, Ibaraki, pp 24–28
8. Fröhlich T, Fehling T, Gatzemeier B et al (2007) Mass dissemination using a fully automated mass comparator robot system. Proceedings of IMEKO 20th TC3, 3rd TC16 and 1st TC22 international conference cultivating metrological knowledge, 27–30, Merida, pp 1–8
9. Zoltan Z (2009) Dissemination of the unit of mass in a fully automatic mass laboratory using subdivision. In: Proceedings of XIX IMEKO world congress fundamental and applied metrology, 6–11, Lisbon, pp 277–279
10. Christian B, Dietmar S (2012) Robot performs high-precision mass determination on weights of up to 20 kg. Available via DIALOG http://www.sartorius.com/fileadmin/fm-dam/sartorius_media/Mechanics/Success_Stories/English/APPL-Mass_Determination-BEV_Wien-2004-2e.pdf
11. Adriana V, Dumitru D (2009) Subdivision method applied for OIML weights using an automatic comparator. Proceedings of the XIX IMEKO world congress fundamental and applied metrology, IMEKO, 6–11, Lisbon, pp 280–284
12. Bich W (2003) From the SI mass unit to multiples and submultiples: an overview. *Metrologia* 2003(40):306–311
13. Fehling T, Fröhlich T, Heydenbluth D (2005) The new sartorius 1 kg-prototype balance for high precision mass determination and research applications. In: Proceedings of 50th Internationales Wissenschaftliches Kolloquium of Technische Universität Ilmenau, 19–23, Ilmenau, pp 1–10
14. Fröhlich T, Fehling T, Heydenbluth D et al (2010) Vacuum transfer system for loading the Sartorius prototype mass comparator CCL1007. In: Proceeding of IMEKO 2010 TC3, TC5 and TC22 conferences metrology in modern context, 22–25, Pattaya, pp 77–80
15. Zoltan Z (2012) New primary balance of BEV for high precision mass determination and realization of the mass scale in the range from 10 g up to 1 kg. In: Proceedings of XX IMEKO world congress metrology for green growth, 9–14, Busan, pp 1–4
16. Vălcu A (2012) Improvement of the calibration process for class E1 weights using an adaptive subdivision method. In: Proceedings of 2012 the fourth international conference on adaptive and self-adaptive systems and applications, 22–27, Nice, pp 51–56

Chapter 53

A Reconfigurable Intelligent Gateway for Heterogeneous Networks

Tiantian Guo, Ming'an Zhou and Qing Shen

Abstract Communication and interoperation among heterogeneous networks is studied. Firstly, on the basis of current situation and developing trend of industrial automatic control, the function, structure, pros and cons of existing protocol converting gateway and middleware are analyzed. Then a reconfigurable intelligent gateway is proposed, the functional block diagram, hardware architecture, software structure and protocol converting and communication model are presented. The proposed gateway can achieve communication and interoperation among multiple field bus networks and TCP/IP network, has a strong intelligent control ability, flexibility, reliability, fast conversion speed, consolidated device description and upper-level interface, can be updated online, used as protocol converter or stand-alone intelligent controller, and has great theoretical significance and practical value in the field of industrial automation.

Keywords Heterogeneous network · Communication and interoperation · Intelligent gateway · Online reconfiguration

53.1 Introduction

With the development of information and automation technology, the industrial control system is changing from Decentralized Control System (DCS) to Field-Bus Control System (FCS), and the complexity, scalability, accuracy, real-time requirement is increasing continuously. Some certain mechanism should be adopted to achieve communication, interoperations and remote control among multiple heterogeneous field-bus based distributed sub-networks and TCP/IP

T. Guo (✉) · M. Zhou · Q. Shen
School of Basic Education for Commanding Officers, National University of Defence
Technology, Changsha 410072, China
e-mail: ttguo_mail@126.com

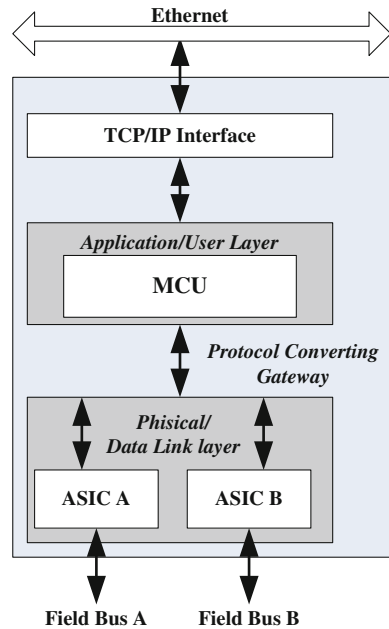
networks. Usually, there are several kinds of field-bus such as FF, CAN, Profibus, Modbus, Lonworks, DNP3 [1, 2] in a FCS. These fields buses varied from protocol, data format, structure, media, application field, etc. Gateway and middle-ware are used to perform protocol converting for the communication and interoperation among heterogeneous networks.

53.1.1 Protocol Converting Gateway

Field Bus protocol is based on ISO/OSI Open Systems Interconnection model. A typical field bus protocol contains physical layer, data link layer, the network layer, application layer and user layer. Each field bus has its own definition of the layers, so the protocol conversion is taken place mainly on data link layer, application layer and user layer by a MCU + ASIC (dedicated interface chip) architecture gateway [3], which is illustrated in Fig. 53.1.

The MCU + ASIC protocol converting gateway has simple structure and easy to be implemented. It can convert protocol among field bus A, field bus B and Ethernet. The ASIC contains the physical layer and data link layer, is the bottom-level data transceiver. The MCU is the application layer and user layer, complete the data mapping and format conversion [4]. This kind of gateway is widely used in the industrial automatic control. However, the following deficiencies are also exposed in practical applications.

Fig. 53.1 MCU + ASIC based protocol converting gateway



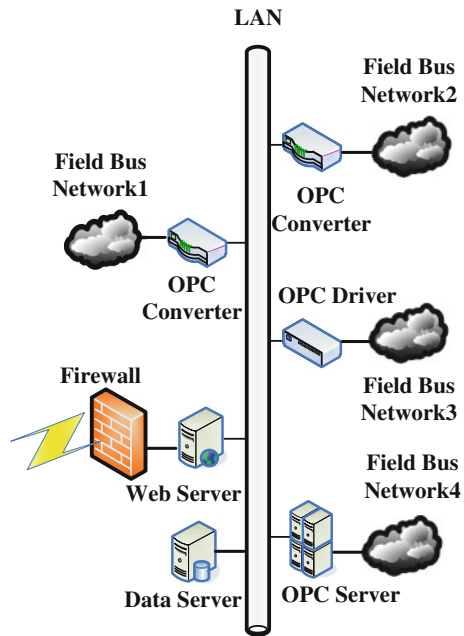
- Poor expansibility and upgrade ability. If the protocol was changed during the field equipment upgrade, or a new sensor and actuator with different protocol was added into the network, the gateway will lose its function.
- Limited processing capacity. In some kind of broadcast network, the irrelevant data should be filtered on the bottom layer, but the data was processed on the upper layer in existing gateway which impairs the system’s processing power and real-time performance.
- Lack of control ability. In order to reduce the communication and ensure the real-time performance of large distributed system, data preprocessing and some simple control function should be performed on the field, while the existing gateway is without this ability.

53.1.2 Interconnection Middleware

The middleware has standard communication interface and protocol, and is used in some heterogeneous network interconnection [5, 6]. Regardless of the change and update of bottom layer system software, as long as the middleware was updated and the interface remained unchanged, the upper software can remain unchanged.

The existing heterogeneous network interconnection middleware is mainly based on OPC, DDE and ODBC, etc., Fig. 53.2 is the middleware module based on OPC interface. The middleware can not satisfy the real-time performance and data security requirements, and lack of bottom layer hardware support [7].

Fig. 53.2 Middleware module based on OPC interface



With the constantly emerging of new technology and device, the off-shelf gateway and middleware are insufficient in the aspects of intelligence, flexibility, online update, real-time performance, control ability, etc. In order to solve these problems, a reconfigurable intelligent gateway is proposed on the basis of current heterogeneous networks protocol converting gateway and middleware, which combining the advantages of both, and has better intelligence, flexibility, scalability.

53.2 Reconfigurable Intelligent Gateway

According to the developing trends of heterogeneous network communication and interoperability [8, 9], and for the shortcomings of the existing gateway and middleware, a reconfigurable intelligent protocol converting gateway is proposed.

53.2.1 System Function Diagram and Hardware Architecture

The desired function of the reconfigurable intelligent gateway is as follows.

- Protocol conversion among different field-bus and TCP/IP network.
- Conversion at different levels.
- Online update.
- Data processing and control ability.
- Remote access and control.
- Unified device description and upper-level interface [10].

Powerful data processing unit, rapid online update, protocol conversion at different levels, remote access interface, unified description are needed for the gateway to fulfil the above functional requirements, and the corresponding designed hardware structure is illustrated in Fig. 53.3.

The gateway is based on a 32 bit ARM processor, a high capacity and density FPGA, with multiple interface chips, large volume SDRAM and NVRAM, convenient HMI, multi-I/O, A/D and D/A. Each network connects to FPGA through the specific interface chip. The FPGA is mapped to the memory space of ARM, and can be accessed either as I/O or memory.

53.2.2 System Software Structure

The system software is divided into two layers [11] as illustrated in Fig. 53.4. The bottom layer is system software including Linux operating system and BSPs, the

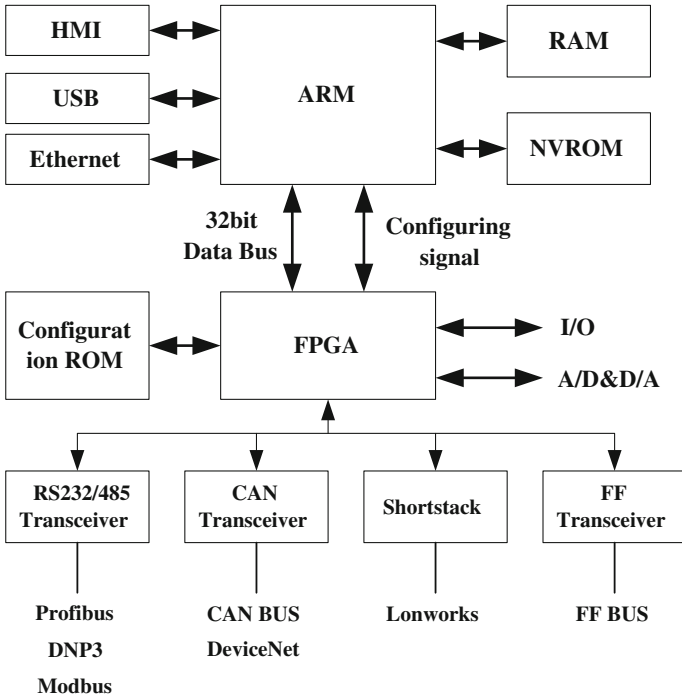


Fig. 53.3 Hardware architecture

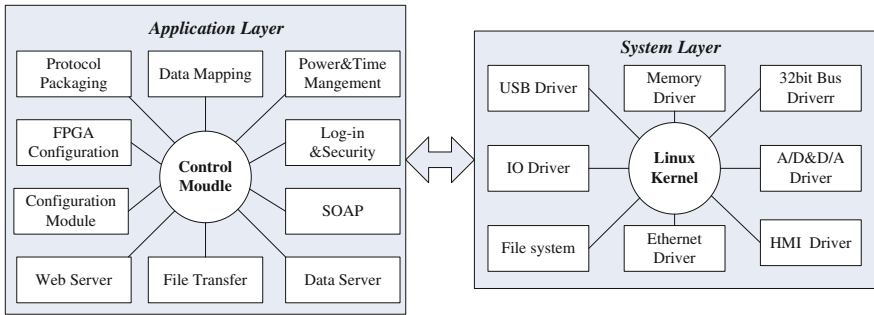


Fig. 53.4 Software architecture

top layer is application software including the modules of control, data mapping, protocol package, WEB server, FPGA configuration, file transfer, power and clock management, login and security, SOAP, etc.

53.2.3 Protocol Converting and Communication Model

The proposed protocol converting and communication model is illustrated in Fig. 53.5 which contains several virtual nodes, communication management module and TCP/IP stack.

The protocol stack, converting algorithm and user specific functions of each network are all packed into a virtual node. The virtual node acts and communicates in the same way as real node, for those real nodes in the network there is no difference between real and virtual nodes. The gateway can contain multiple virtual nodes with different protocol at the same time.

The communication management module will establish a virtual channel when communication among virtual nodes and TCP/IP network occurred as well as check the status of the whole link. If there is any fault in the link, messages will be sent to the upper-level. In order to ensure the real-time performance, several real-time event channels is reserved in the communication management module [12].

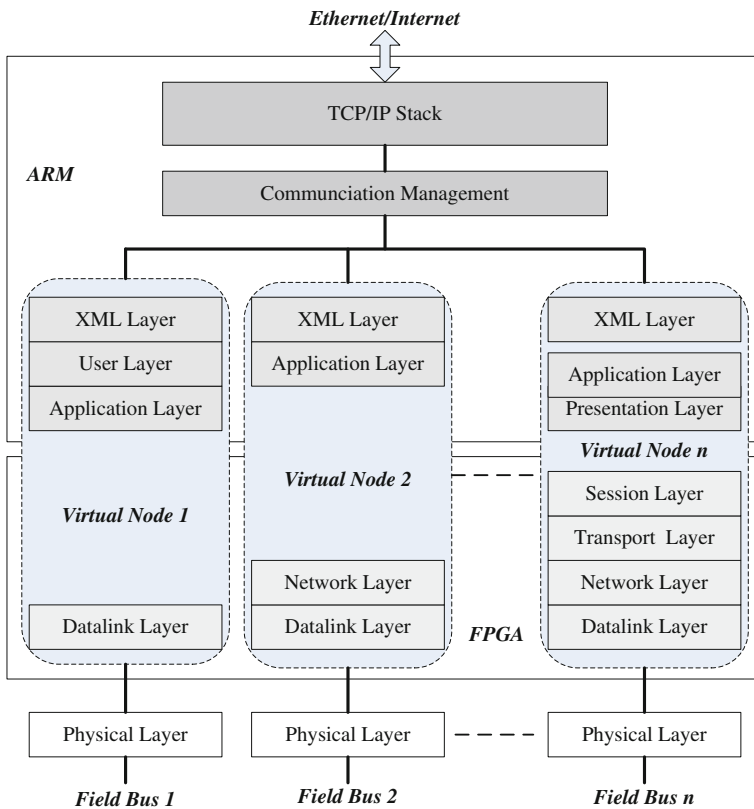


Fig. 53.5 Protocol converting and communication model

The protocol parsing and converting is shared by FPGA and ARM, the FPGA is in charge of the data link layer, network layer and transport layer, ARM is responsible for the other layers. The deployment of FPGA makes the gateway possess the ability of rapid online update, if a new protocol is added or an existing protocol is changed, just reconfiguring the FPGA [13]. The establishment and management of the virtual channel and real-time event channel, system resources managing, scheduling, data-mapping, FPGA reconfiguration are performed by ARM with embedded WEB server and real-time status database [14, 15].

The heterogeneous networks are integrated into one system in this way, data exchanging and interoperating are realized in real-time among different field buses and TCP/IP network with the ability of rapid online update, intelligent data processing, and being controlled through remote access interface and unified device description.

53.3 Application

There are three control systems in a railway station, the BAS is based on CAN 2.0, public-address system and LED guidance system are based on RS485 with self-defined protocol, the LED guidance system contains two kinds of data formats, and controlled by three computers separately. With the use of Internet based control software, the protocol conversion is needed for the systems to connect to the TCP/IP network.

According to the model presented above, we designed and implemented an embedded protocol converting gateway with SAMSUNG S3C2440 ARM9 processor, Xilinx XC6VHX255T FPGA, 256 MB NAND FLASH, 128 M SDRAM, 2 100 M Ethernet interface, one CAN bus interface, four RS485 interface, six inputs, six outputs, illustrated in Fig. 53.6.

Fig. 53.6 Embedded reconfigurable intelligent gateway



Table 53.1 Simulation test results

	Baud rate	Maximum transmission delay (us)	Packet loss rate (100 million frames)
BAS ¹	100 K	50	0
Public address system	9600	480	0
LED guidance system	9600	500	0

¹ Building Automation system

FPGA performs the parsing and packaging of data link layer, the application and user layer is performed by ARM. The operating system is based on Linux 2.8.30 kernel. XML description for the three systems, real-time status database and embedded WEB server are established, SOAP is used for the communication with upper-level software. The maximum transmission delay and packet loss rate are tested on a simulation testing environment, Table 53.1 is the result.

More than 5,000 h of fault-free operation showed that the gateway provided fast communication channels among the three sub-systems and TCP/IP network, integrated with the upper-level software seamlessly, simplified the system structure and improved the production efficiency.

53.4 Conclusion

A reconfigurable intelligent gateway is proposed for heterogeneous network communication and interoperation, the functional block diagram, hardware structure, software structure and protocol converting model are presented.

The proposed gateway contains rich logic control resources, multiple physical interfaces, strong intelligent data process and control ability, flexibility, reliability, consolidated device description and upper-level interface, can be updated online and accomplish communication and interoperation among various field buses and TCP/IP network. It inherits the advantages of existing gateway and middleware, but has better performance on intelligence, flexibility, Scalability and universality, and can be used as protocol converter or stand-alone intelligent controller.

Simulated test result and actual operation on a railway station showed that the proposed gateway has a fast converting speed, high reliability and flexibility. It has a great theoretical significance and practical value in the field of industrial automation.

References

1. Choi BW, Kim JS, Lee CH, Kim JB, Lim KY (2000) Implementation of the field bus system which used EIA-709.1 control network protocol. *J Control Autom Syst Eng* 10(2):594–601
2. Lee KC, Lee S, Lee HH (2004) Implementation and PID tuning of network-based control systems via Profibus polling network. *Comput Stan Interfaces* 26(3):229–240

3. Perkins CE, Royer EM (1999) Ad-hoc on-demand distance vector routing. Second IEEE Workshop Mob Comput Syst Appl, 90–100
4. Jeon II Moon, Kim JS, Kim JB, Lim KY, Choi BW (2005) A hardware implementation of distributed network protocol. *Comput Stan Interfaces* 27(3):221–232
5. Sun Y, Tang S-J, Luo H (2012) The QoS guarantee problem for multimedia sensor networks. *Acta Electronica Sinica* 40(4):625–631 (in Chinese)
6. Wang S, Xu Z, Cao J, Zhang J (2007) A middleware for web service-enabled integration and interoperation of intelligent building systems. *Autom Constr* 16(1):112–121
7. George A, Aphrodite T, Michael P (2006) Interoperability among heterogeneous services. In: SCC '06, IEEE international conference on services computing, pp 174–181
8. Brennan RW, Vrba P, Tichy P, Zoitl A, Sunder C, Strasser T, Marik V (2008) Developments in dynamic and intelligent reconfiguration of industrial automation. *Comput Ind* 59(6):533–547
9. Peres E, Fernandes MA, Morais R, Cunha CR (2011) An autonomous intelligent gateway infrastructure for in-field processing in precision viticulture. *Comput Electron Agric* 78(2):176–187
10. Zhun W-K, Wang W, He L-S (2004) Embedded industrial device gateway based on internet. *Instrum Tech Sens* (10):41–46 (in Chinese)
11. Capone A, Cesana M, De Donno D, Filippini I (2010) Deploying multiple interconnected gateways in heterogeneous wireless sensor networks: an optimization approach. *Comput Commun* 33(10):1151–1161
12. Kaiser J, Brudna C, Mitidieri C (2005) COSMIC: a real-time event-based middleware for the CAN-bus. *J Syst Softw* 77(1):27–36
13. Wang T, Wang L, Liu Q (2011) A three-ply reconfigurable CNC system based on FPGA and field-bus. *Int J Adv Manuf Technol* 57(5–8):671–682
14. Song KW, Choi GS (2010) Fieldbus based distributed servo control using LonWorks/IP gateway/web servers. *Mechatronics* 20(3):415–423
15. Zhou ZD, Liu Q, Qingsong A, Cheng X (2011) Intelligent monitoring and diagnosis for modern mechanical equipment based on the integration of embedded technology and FBGS technology. *Measurement* 44(9):1499–1511

Chapter 54

Robust Stability of a Class of Uncertain Discrete-Time Stochastic Systems

Fengwei Yang, Yali Dong and Yangang Wang

Abstract The problem of robust stochastic stability of a class of uncertain discrete-time stochastic systems is considered. The linear rate vector of a discrete-time system is perturbed by a nonlinear function that satisfies a quadratic constraint. In the concerned model, stochastic disturbance is described by a Brownian motion. By using a Lyapunov–Krasovskii functional, the sufficient condition in terms of linear matrix inequalities (LMIs) is presented, which guarantees the robust stochastic stability of the stochastic system. Finally, a numerical example is provided to demonstrate the effectiveness of the result obtained.

Keywords Discrete-time stochastic system • Robust stochastic stability • Linear matrix inequalities

54.1 Introduction

Stochastic systems arise in a wide area of applications in control engineering such as filtering, adaptive systems and identification, and learning and image recognition, etc. [1–3]. It is essential to determine the stability of a unique equilibrium point for a stochastic system and the stability analysis of both continuous and

F. Yang (✉) · Y. Dong
School of Science, Tianjin Polytechnic University, Tianjin 300387, China
e-mail: weilwalklife@sina.com

Y. Dong
e-mail: dongyl@vip.sina.com

Y. Wang
Information Technology Center, Tianjin Polytechnic University, Tianjin 300387, China
e-mail: dongyl11250228@sina.com

discrete-time stochastic systems has attracted many researchers in system science area for decades.

On the other hand, as an important class of systems, time-delay systems are ubiquitous in chemical process, aerodynamics, and communication networks [4, 5]. It is well known that the time-delays are inherent features of many physical processes, which are often the main cause for instability or undesirable system performance of a control system. Therefore, the research on time-delay systems has attracted many researchers [6–8].

The problem of robust quadratic stability of systems under nonlinear perturbation was studied for continuous systems [9] and for discrete-time systems [10]. The solutions provided are for quadratically bounded nonlinear perturbations and are available for only deterministic systems. Even though a larger foundation has been laid out for stability of discrete-time stochastic system, thus far the problem of robust quadratic stability of discrete-time stochastic systems under nonlinear perturbation has been given very little attention.

In this paper, we investigate the problem of stochastic stability for a class of uncertain discrete-time stochastic systems. Based on the Lyapunov–Krasovskii functional approach and the LMI technique, the sufficient condition of stochastic stability is provided.

Notations: Throughout this paper, R^n and $R^{n \times m}$ denote, respectively, the n -dimensional Euclidean space and the set of all $n \times m$ real matrices. The notation $X \geq Y$ (respectively, $X > Y$) means that X and Y are symmetric matrices, and that $X - Y$ is nonnegative definite (respectively, positive definite). I is the identity matrix with compatible dimension. $\lambda_{\max}(A)$ (respectively, $\lambda_{\min}(A)$) means the maximum (respectively, minimal) value of the real part of the eigenvalue of matrix A . The asterisk $*$ always denotes the symmetric block in a symmetric matrix. $(\Omega, F, (F_t)_{t \geq 0}, P)$ denotes a complete probability space and $E\{\cdot\}$ stands for the mathematical expectation operator with respect to the given probability measure.

54.1.1 Problem Formulation and Preliminaries

In the section, we start by introducing some definitions and basic results that will be used in this paper.

Consider the discrete-time stochastic system with time delay in the following form

$$\begin{aligned} x(k+1) = & (A_0 + \Delta A_0(k))x(k) + (A_1 + \Delta A_1(k))x(k - \tau(k)) \\ & + h(k, x(k), x(k - \tau(k))) + A_2x(k)\omega(k), \end{aligned} \quad (54.1)$$

where $x(k) \in R^n$ is the state of the stochastic system at step $k \in \{k_0, k_0 + 1, \dots\}$, A_0, A_1 and A_2 are known real constant matrices with appropriate dimensions, $\tau(k)$ denotes the time-varying delay satisfying $0 \leq \tau(k) \leq \tau_d$, where τ_d is a positive

integers, $h(k, x(k), x(k - \tau(k)))$ is the nonlinear function. $\omega(k)$ is scalar Wiener process on $(\Omega, F, (F_t)_{t \geq 0}, P)$ with

$$E[\omega(k)] = 0, \quad E[\omega^2(k)] = 1, \quad E[\omega(i)\omega(j)] = 0, i \neq j. \tag{54.2}$$

The parameter uncertainties $\Delta A_0(k)$ and $\Delta A_1(k)$ are defined as follows:

$$[\Delta A_0(k) \quad \Delta A_1(k)] = MF(k)[N_1 \quad N_2], \tag{54.3}$$

where N_1, N_2 and M are known constant matrices with appropriate dimensions and $F(k)$ is an unknown time-varying matrix bounded by $F^T(k)F(k) \leq I$.

For further discussion, we will introduce the following assumptions and definitions.

Assumption 1 The nonlinear function $h(k, x(k), x(k - \tau(k)))$ satisfies the following inequality

$$h^T(k, x(k), x(k - \tau(k)))h(k, x(k), x(k - \tau(k))) \leq \alpha_1^2 x^T(k)H_1^T H_1 x(k) + \alpha_2^2 x^T(k - \tau(k))H_2^T H_2 x(k - \tau(k)), \tag{54.4}$$

where $\alpha_1, \alpha_2 > 0$ are the bounding parameter on the perturbation function $h(k, x(k), x(k - \tau(k)))$, H_1, H_2 are known constant matrices.

Remark 1 The inequality (54.4) can be rewritten as

$$\xi^T(k)diag\{-\alpha_1^2 H_1^T H_1, -\alpha_2^2 H_2^T H_2, 0, I\}\xi(k) \leq 0, \tag{54.5}$$

where $\xi(k) = [x^T(k) \quad x^T(k - \tau(k)) \quad x^T(k - \tau_d) \quad h^T(k, x(k), x(k - \tau(k)))]$.

Definition 1 System (1) is said to be robustly stochastically stable with margin α_1, α_2 , if there exists a constant $T(x(k_0), \alpha_1, \alpha_2)$ such that the following inequality holds for all admissible uncertainties:

$$E\left[\sum_{k=k_0}^{\infty} x^T(k)x(k)|x(k_0)\right] \leq T(x(k_0), \alpha_1, \alpha_2).$$

Lemma 1 [11] Let A, D, E and F be real matrices of appropriate dimensions with $P = P^T > 0, F^T F \leq I$, there exists $\varepsilon > 0$ satisfying $P^{-1} - \varepsilon DD^T > 0$ such that

$$(A + DFE)^T P(A + DFE) \leq A^T (P^{-1} - \varepsilon DD^T)^{-1} A + \varepsilon^{-1} E^T E.$$

Lemma 2 [12] (Schur complements) For a given matrix $S = \begin{bmatrix} S_{11} & S_{12} \\ S_{12}^T & S_{22} \end{bmatrix}$ with $S_{11} = S_{11}^T, S_{22} = S_{22}^T$, then the following conditions are equivalent:

- (1) $S < 0$, (2) $S_{22} < 0, S_{11} - S_{12}S_{22}^{-1}S_{12}^T < 0$.

54.1.2 Main Results

In the section, we give the main result of the stochastic stability of the stochastic system (1).

Theorem 1 *Assume that Assumption 1 holds. The system (1) is robustly stochastically stable with margin α_1, α_2 , if there exist symmetric positive definite matrices $P > 0, Q > 0, R > 0$ and scalars $\varepsilon_1 > 0, \varepsilon_2 > 0$ such that the following linear matrix inequalities hold:*

$$\begin{aligned}
 &PMM^T < \varepsilon_1 I, \\
 \Psi = &\begin{bmatrix}
 \Psi_{11} & \varepsilon_1 N_1^T N_2 & 0 & 0 & A_0^T P & 0 & \varepsilon_2 H_1^T & 0 \\
 * & \Psi_{22} & 0 & 0 & A_1^T P & 0 & 0 & \varepsilon_2 H_2^T \\
 * & * & -Q & 0 & 0 & 0 & 0 & 0 \\
 * & * & * & -\varepsilon_2 I & P & 0 & 0 & 0 \\
 * & * & * & * & -P & PM & 0 & 0 \\
 * & * & * & * & * & -\varepsilon_1 I & 0 & 0 \\
 * & * & * & * & * & * & -\varepsilon_2 \alpha_1^{-2} I & 0 \\
 * & * & * & * & * & * & * & -\varepsilon_2 \alpha_1^{-2} I
 \end{bmatrix} < 0,
 \end{aligned}
 \tag{54.6}$$

where $\Psi_{11} = -P + Q + R + \varepsilon_1 N_1^T N_1 + A_2^T P A_2$, $\Psi_{22} = -R + \varepsilon_1 N_2^T N_2$.

Proof Consider the following Lyapunov–Krasovskii functional

$$V(k) = V_1(k) + V_2(k) + V_3(k),$$

where

$$V_1(k) = x^T(k) P x(k), \quad V_2(k) = \sum_{s=k-\tau_d}^{k-1} x^T(s) Q x(s), \quad V_3(k) = \sum_{s=k-\tau(k)}^{k-1} x^T(s) R x(s).$$

The difference generator of $V_1(k)$ is given by

$$\begin{aligned}
 \ell V_1(k) &= E[V_1(k+1) - V_1(k) | x(k_0)] \\
 &= E\{[A_0 x(k) + A_1 x(k - \tau(k)) + A_2 x(k) \omega(k) + h + MF(k)(N_1 x(k) \\
 &\quad + N_2 x(k - \tau(k)))]^T P [A_0 x(k) + A_1 x(k - \tau(k)) + A_2 x(k) \omega(k) + h \\
 &\quad + MF(k)(N_1 x(k) + N_2 x(k - \tau(k)))] - x^T(k) P x(k) | x(k_0)\} \\
 &= E\{[A_0 x(k) + A_1 x(k - \tau(k)) + h + MF(k)(N_1 x(k) + N_2 x(k - \tau(k)))]^T \\
 &\quad \times P [A_0 x(k) + A_1 x(k - \tau(k)) + h + MF(k)(N_1 x(k) + N_2 x(k - \tau(k)))] \\
 &\quad + x^T(k) A_2^T P A_2 x(k) - x^T(k) P x(k) | x(k_0)\}.
 \end{aligned}
 \tag{54.7}$$

From Lemma 1, we get

$$\begin{aligned} \ell V_1(k) \leq & E\{[A_0x(k) + A_1x(k - \tau(k)) + h]^T(P^{-1} - \varepsilon_1^{-1}MM^T)^{-1}[A_0x(k) \\ & + A_1x(k - \tau(k)) + h] + \varepsilon_1[N_1x(k) + N_2x(k - \tau(k))]^T[N_1x(k) \\ & + N_2x(k - \tau(k))] + x^T(k)A_2^TPA_2x(k) - x^T(k)Px(k)|x(k_0)\}, \end{aligned}$$

For $V_2(k), V_3(k)$, we have

$$\begin{aligned} \ell V_2(k) &= E[V_2(k+1) - V_2(k)|x(k_0)] \\ &= E\left\{\sum_{s=k-\tau_d+1}^k x^T(s)Qx(s) - \sum_{s=k-\tau_d}^{k-1} x^T(s)Qx(s)|x(k_0)\right\} \quad (54.8) \\ &= E\{x^T(k)Qx(k) - x^T(k - \tau_d)Qx(k - \tau_d)|x(k_0)\}, \end{aligned}$$

$$\begin{aligned} \ell V_3(k) &= E[V_3(k+1) - V_3(k)|x(k_0)] \\ &= E\left\{\sum_{s=k-\tau(k)+1}^k x^T(s)Rx(s) - \sum_{s=k-\tau(k)}^{k-1} x^T(s)Rx(s)|x(k_0)\right\} \quad (54.9) \\ &= E\{x^T(k)Rx(k) - x^T(k - \tau(k))Rx(k - \tau(k))|x(k_0)\}, \end{aligned}$$

Combine (54.4, 54.7–54.9), we get

$$\ell V(k) \leq E\{\xi^T(k)\Xi\xi(k)|x(k_0)\}, \quad (54.10)$$

where $\Xi = \Xi^T = (\Xi_{ij})_{4 \times 4}$,

$$\begin{aligned} \Xi_{11} &= A_0^T(P^{-1} - \varepsilon_1^{-1}MM^T)^{-1}A_0 + A_2^TPA_2 + \varepsilon_1N_1^TN_1 - P + Q + R + \varepsilon_2\alpha_1^2H_1^TH_1, \\ \Xi_{12} &= A_0^T(P^{-1} - \varepsilon_1^{-1}MM^T)^{-1}A_1 + \varepsilon_1N_1^TN_2, \quad \Xi_{13} = 0, \quad \Xi_{14} = A_0^T(P^{-1} - \varepsilon_1^{-1}MM^T)^{-1}, \\ \Xi_{22} &= A_1^T(P^{-1} - \varepsilon_1^{-1}MM^T)^{-1}A_1 + \varepsilon_1N_2^TN_2 - R + \varepsilon_2\alpha_2^2H_2^TH_2, \quad \Xi_{23} = 0, \\ \Xi_{24} &= A_1^T(P^{-1} - \varepsilon_1^{-1}MM^T)^{-1}, \quad \Xi_{33} = -Q, \quad \Xi_{34} = 0, \quad \Xi_{44} = (P^{-1} - \varepsilon_1^{-1}MM^T)^{-1} - \varepsilon_2I. \end{aligned}$$

From Lemma 54.2 and (6), we have

$$\Xi < 0. \quad (54.11)$$

Hence, we obtain

$$\ell V(k) \leq -\lambda_{\min}(-\Xi)E\{\xi^T(k)\xi(k)|x(k_0)\}. \quad (54.12)$$

Summing up both side of (54.12) for $T \geq k_0$, we have

$$\begin{aligned}
 E[V(T)|x(k_0)] - E[V(k_0)] &= E\left[\sum_{k=k_0}^T \ell V(k)|x(k_0)\right] \\
 &\leq -\lambda_{\min}(-\Xi)E\left[\sum_{k=k_0}^T \zeta^T(k)\zeta(k)|x(k_0)\right].
 \end{aligned} \tag{54.13}$$

Thus,

$$\lambda_{\min}(-\Xi)E\left[\sum_{k=k_0}^T \zeta^T(k)\zeta(k)|x(k_0)\right] \leq E[V(k_0)] - E[V(T)|x(k_0)] \leq E[V(k_0)]. \tag{54.14}$$

We get

$$E\left[\sum_{k=k_0}^T \zeta^T(k)\zeta(k)|x(k_0)\right] \leq \frac{E[V(k_0)]}{\lambda_{\min}(-\Xi)}. \tag{54.15}$$

Obviously, $\|x\| \leq \|\zeta\|$ and this leads to

$$E\left[\sum_{k=k_0}^T x^T(k)x(k)|x(k_0)\right] \leq \frac{E[V(k_0)]}{\lambda_{\min}(-\Xi)}, \tag{54.16}$$

which leads to the robust stochastic stability of (1).

54.1.3 Numerical Example

In this section, we present a numerical example to illustrate our main result.

Example 1 Consider the system (1) with the following parameters

$$\begin{aligned}
 A_0 &= \begin{bmatrix} 0.02 & 0.01 \\ 0.03 & 0.04 \end{bmatrix}, A_1 = \begin{bmatrix} -0.2 & 0 \\ 0.1 & -0.4 \end{bmatrix}, A_2 = \begin{bmatrix} 0.01 & 0.1 \\ 0.06 & 0.14 \end{bmatrix}, \\
 M &= \begin{bmatrix} 0.5 & 0 \\ 0 & 0.5 \end{bmatrix}, N_1 = N_2 = \begin{bmatrix} 0.1 & 0 \\ 0 & 0.1 \end{bmatrix}.
 \end{aligned}$$

Set $H_1 = H_2 = \begin{bmatrix} 1.3 & 0 \\ 0 & 1.3 \end{bmatrix}$, $\alpha_1 = 0.2$, $\alpha_2 = 0.1$, $\tau_d = 5$. One can check that LMIs (54.6) in Theorem 1 is feasible. By using Matlab LMI toolbox, a feasible solution to the LMIs is obtained as follows:

$$P = \begin{bmatrix} 1.1951 & 0.0166 \\ 0.0166 & 0.8985 \end{bmatrix}, \quad Q = \begin{bmatrix} 0.3016 & 0.0368 \\ 0.0368 & 0.1248 \end{bmatrix},$$

$$R = \begin{bmatrix} 0.5474 & -0.0435 \\ -0.0435 & 0.4932 \end{bmatrix}, \quad \varepsilon_1 = 5.6833, \quad \varepsilon_2 = 1.6166.$$

Therefore, according to Theorem 1, the stochastic system (1) is robustly stochastically stable.

54.2 Conclusions

This paper has investigated the problem of robust stochastic stability for a class of uncertain discrete-time stochastic systems. By constructing a novel Lyapunov–Krasovskii functional, the sufficient condition is provided in terms of LMI, which guarantees the robust stochastic stability of a class of uncertain discrete-time stochastic systems. Finally, a numerical example has been given to demonstrate the effectiveness of the proposed method.

Acknowledgments This work was supported by the Natural Science Foundation of Tianjin under Grant 11JCYBJC06800.

References

1. Davis MHA (1977) Linear estimation and control. Wiley, New York
2. Kumar PR, Vairaiya P (1986) Stochastic system: estimation. Identification and adaptive control. Prentice Hall, New Jersey
3. Chen G, Chen G, Hsu S (1995) Linear stochastic control systems. CRC Press, Boca Raton
4. Dugard L, Verrist EL (1998) Stability and control of time-delay systems. Springer, London, New York
5. Hale JK (1977) Theory of functional differential equations. Springer, Berlin
6. Dong Y, Liu J, Mei S, Li M (2011) Stabilization for switched nonlinear time-delay systems. Nonlinear analysis: hybrid systems 5:78–88
7. Dong Y, Wang X, Mei S, Li W (2012) Exponential stabilization of nonlinear uncertain systems with time-varying delay. J Eng Math 77:225–237
8. Liu Y, Hu LS, Shi P (2012) A novel approach on stabilization for linear systems with time-varying input delay. Appl Math Comput 218(10):5937–5947
9. Siljak DD, Stipanovic DM (2000) Robust stabilization of nonlinear systems: the LMI approach. Math Probl Eng 6:461–493
10. Stipanovic DM, Siljak DD (2001) Robust stability and stabilization of discrete-time nonlinear systems: the LMI approach. Int J Control 74(9):873–879
11. Luo M, Zhong S, Wang R, Kang W (2009) Robust stability analysis for discrete-time stochastic neural networks systems with time-varying delays. Appl Math Comput 209:305–313
12. Boyd L, El Ghaoui, Feron E, Balakrishnan V (1994) Linear matrix inequalities in system and control theory. SIAM, Philadelphia

Chapter 55

H_2 Controller Design for Markov Jump Systems with Polytopic-Type Uncertainty and Partly Known Transition Probabilities

Quanyong Fan, Dan Ye and Xinglei Gao

Abstract This paper considers the problem of robust H_2 control for a class of continuous-time Markov jump systems with polytopic-type parameter uncertainty and partly known transition probabilities. The considered transition probabilities are more general, which include completely known case, partly unknown with known lower and upper bounds case and completely unknown case. By making use of novel techniques, new stability condition for this kind of uncertain Markov jump systems is derived. And then the corresponding robust H_2 controller design method is proposed in the framework of linear matrix inequalities. Finally, numerical examples are presented to demonstrate the effectiveness of the proposed method.

Keywords Markov jump system · Partly known transition probabilities · Polytopic-type uncertainty · H_2 control · Parameter-dependent Lyapunov function

55.1 Introduction

Markov jump system (MJS) is a good mathematical model to represent a class of dynamic systems with randomly jumping parameters, where the jumps among different subsystems are governed by a Markov chain. In recent years, much attention has been devoted to MJSs [1–3], which have been widely used to model many practical systems, such as power systems, manufacturing systems and economic systems in which they may experience failure or repairs, abrupt environmental disturbances, abrupt changes in the operating point of a nonlinear plant. On the other hand, the robust control problem for MJSs with parameter uncertainties

Q. Fan · D. Ye (✉) · X. Gao

College of Information Science and Engineering, Northeastern University, No. 11, No. 3 Lane, Wenhua Road, Shenyang, Heping, China
e-mail: yedan@ise.neu.edu.cn

has been one of the most challenging problems and received considerable attention [4, 5]. In this paper, the MJS with polytopic-type uncertainties is considered.

For MJSs, the transition probabilities of the jumping process are important, but most of the previous issues usually assumed that the elements of the transition probability matrix are completely known. However, some elements can not be obtained directly or might be time-variable in many practical engineering applications. Therefore, the study of Markov jump systems with partly known transition probability becomes a necessary and some well known results have been published [6–8]. In some cases, the exact value of some elements of the transition probability matrix can not be obtained, but their lower and upper bounds can be determined. The case has been addressed by [9], but its method cannot be used to deal with the case where there is no information available for transition probabilities. In [10], the more general partly known transition probabilities are investigated, which covers the cases that the transition probabilities are exactly known, unknown, and unknown but with known bounds. However, a conservative condition to relax inequality is used to deal with this kind of transition probabilities.

In this paper, the more general cases about transition probabilities are considered, which means the information of the transition probabilities can be fully utilized. Using the parameter-dependent Lyapunov function method and some new techniques, which are motivated by [7], to deal with the partly known transition probabilities, less conservative performance can be obtained.

55.2 Problem Statement

A continuous-time MJS with polytopic-type parameter uncertainty is described by the following state-space equations:

$$\mathbf{S} \begin{cases} \dot{x}(t) = \mathcal{A}(r(t))x(t) + \mathcal{B}_1(r(t))\omega(t) + \mathcal{B}_2(r(t))u(t) \\ z(t) = \mathcal{C}(r(t))x(t) + \mathcal{D}(r(t))u(t) \end{cases} \quad (55.1)$$

where $x(t) \in R^n$ is the state vector, $u(t) \in R^p$ is the control input, $\omega(t) \in R^m$ is the disturbance, $z(t) \in R^q$ is the controlled output. $\{r(t), t \geq 0\}$ is a homogeneous Markov chain on a finite state space $\mathcal{R} = \{1, 2, \dots, r\}$. The transition probability is defined as:

$$\Pr\{r(t+h) = j | r(t) = i\} = \begin{cases} \pi_{ij}h + o(h), & j \neq i \\ 1 + \pi_{ii}h + o(h), & j = i \end{cases} \quad (55.2)$$

where $h > 0$, $\lim_{h \rightarrow 0} (o(h)/h) = 0$, $\pi_{ij} \geq 0$ ($i, j \in \tau, j \neq i$) and $\pi_{ii} = -\sum_{j=1, j \neq i}^r \pi_{ij}$, $i = 1, 2, \dots, r$. In addition, the transition matrix is defined as $\Lambda = (\pi_{ij})_{rr}$.

$$\Lambda = \begin{bmatrix} \pi_{11} & ? & \pi_{13} & \cdots & \pi_{1r} \\ ? & ? & \alpha & \cdots & \pi_{2r} \\ \beta & ? & ? & \cdots & \pi_{3r} \\ \vdots & \cdots & \cdots & \ddots & \vdots \\ \pi_{r1} & \pi_{r2} & ? & \cdots & \pi_{rr} \end{bmatrix} \quad (55.3)$$

where “?” denote the unknown elements, α and β have known lower and upper bounds ($\underline{\alpha} < \alpha < \bar{\alpha}$, $\underline{\beta} < \beta < \bar{\beta}$), π_{ij} is exactly known. For notation clarity, we further define the following symbols: $\mathbf{L}_k^i = \{j : \underline{\pi}_{ij} \leq \pi_{ij} \leq \bar{\pi}_{ij}\}$, $\mathbf{L}_{uk}^i = \{j : j \notin L_k^i\}$, $\mathcal{L}_k^i = \{m | m \in L_k^i, m \neq i\}$, $\mathcal{L}_{uk}^i = \{m | m \in L_{uk}^i, m \neq i\}$, $\lambda_k^i = \sum_{j \in \mathcal{L}_k^i} \pi_{ij}$, $\underline{\lambda}_k^i = \sum_{j \in \mathcal{L}_k^i} \underline{\pi}_{ij}$, $P_k^i = \sum_{j \in \mathcal{L}_k^i} \pi_{ij} \bar{P}_j$, $\bar{P}_k^i = \sum_{j \in \mathcal{L}_k^i} \bar{\pi}_{ij} \bar{P}_j$, $\delta_i = \pi_{ii} + \lambda_k^i$, $\underline{\delta}_i = \underline{\pi}_{ii} + \underline{\lambda}_k^i$, $He(X) = X + X^T$.

Remark 1 When π_{ij} is exactly known. It also can be regarded as bounded one, namely, $\underline{\pi}_{ij} = \pi_{ij} = \bar{\pi}_{ij}$ \square .

When $r(t) = i$, $\mathcal{A}(r(t))$, $\mathcal{B}_1(r(t))$, $\mathcal{B}_2(r(t))$, $\mathcal{C}(r(t))$ and $\mathcal{D}(r(t))$ are denoted as A_i , B_{1i} , B_{2i} , C_i and D_i , which belong to the following polytopic-type uncertainty:

$$(\mathcal{A}_i, \mathcal{B}_{1i}, \mathcal{B}_{2i}, \mathcal{C}_i, \mathcal{D}_i) = \sum_{l=1}^N \alpha_l (A_i^l, B_{1i}^l, B_{2i}^l, C_i^l, D_i^l), \alpha_l \geq 0, \sum_{l=1}^N \alpha_l = 1.$$

Moreover, $P(r(0) = i) = \mu_i$, $i \in \mathcal{R}$ is the initial distribution of Markov chain. Some notions are given as follow.

Definition 1 ([5]) The system (55.1) with $\omega(t) = 0$ is mean square stable (MSS) if $E(x^T(t)x(t)) \rightarrow 0$, when $t \rightarrow \infty$ for any initial condition $x(0)$ and initial distribution $r(0)$.

Definition 2 ([5]) The H_2 norm for MSS system (55.1) is defined as

$$\|S\|_2^2 = \sum_{j=1}^q \sum_{i=1}^r \mu_i \|z_{j,i}\|_2^2. z_{j,i} \text{ is output } \{z(t) : t \geq 0\}, \text{ and } \|z_{j,i}\|_2^2 = \int_0^\infty E(|z(t)|) dt, \text{ and}$$

1. the input is given by $\omega = \{\omega(t) : t \geq 0\}$, $\omega(t) = e_s \eta(t)$, $\eta(t)$ is the unitary impulse, and e_s is the m-dimensional unitary vector formed by 1 at the s th position and zero elsewhere;
2. $x(0) = 0, r(0) = i$.

A state-feedback control law $u(t) = K(r(t))x(t)$ is to be designed to make the closed-loop system (55.4) be MSS and have required H_2 performance.

$$\begin{cases} \dot{x}(t) = (\mathcal{A}(r(t)) + \mathcal{B}_2(r(t))K(r(t)))x(t) + \mathcal{B}_1(r(t))\omega(t) \\ z(t) = (\mathcal{C}(r(t)) + \mathcal{D}(r(t))K(r(t)))x(t) \end{cases} \quad (55.4)$$

Lemma 1 ([5]) *If there exist symmetric matrices $\bar{P}_i > 0, 1 \leq i \leq r$ such that*

$$\mathcal{A}_i^T \bar{P}_i + \bar{P}_i \mathcal{A}_i + \sum_{j=1}^r \pi_{ij} \bar{P}_j + \mathcal{C}_i^T \mathcal{C}_i < 0 \tag{55.5}$$

$$\sum_{i=1}^r \mu_i \text{Tr}(\mathcal{B}_{1i}^T \bar{P}_i \mathcal{B}_{1i}) < \gamma \tag{55.6}$$

where \bar{P}_i ($1 \leq i \leq r$) is the function of $\alpha = (\alpha_1, \dots, \alpha_N)$, then the continuous-time MJS (55.1) is MSS and its H_2 norm is less than $\sqrt{\gamma}$.

55.3 Robust H_2 Controller Design

This section will present the robust H_2 controller design method for MJSs with partly known probabilities and polytopic-type parameter uncertainty. Firstly, new robust MSS conditions will be given based on the Lemma 1.

Theorem 1 Consider the system (55.1) with the partly known transition probabilities (55.3). If there exist symmetric matrices $W_i, \bar{P}_i > 0$, ($1 \leq i \leq r$), such that

$$i \in L_k^i \{ \text{He}(\bar{P}_i \mathcal{A}_i) + \bar{P}_k^i + \bar{\pi}_{ii} \bar{P}_i - \underline{\delta}_i \bar{P}_h + \mathcal{C}_i^T \mathcal{C}_i < 0, h \in L_{uk}^i \} \tag{55.7}$$

$$i \in L_{uk}^i \left\{ \begin{array}{l} \text{He}(\bar{P}_i \mathcal{A}_i) + \bar{P}_k^i - \underline{\lambda}_k^i \bar{P}_i + \mathcal{C}_i^T \mathcal{C}_i < 0 \\ \bar{P}_j \leq \bar{P}_i, j \in L_{uk}^i \end{array} \right. \tag{55.8}$$

$$\sum_{i=1}^r \mu_i \text{Tr}(\mathcal{B}_{1i}^T \bar{P}_i \mathcal{B}_{1i}) < \gamma \tag{55.9}$$

then the system (55.1) is MSS and with H_2 performance less than $\sqrt{\gamma}$.

Proof The proof is separated into two cases, $i \in L_k^i$ and $i \in L_{uk}^i$ \square

Case 1 $i \in L_k^i$. In this case, π_{ii} is bounded or exactly known. Using $-\sum_{h \in L_{uk}^i} \pi_{ih} / \delta_i = 1$, it is easy to obtain that

$$\begin{aligned} \mathcal{A}_i^T \bar{P}_i + \bar{P}_i \mathcal{A}_i + \sum_{j=1}^r \pi_{ij} \bar{P}_j + \mathcal{C}_i^T \mathcal{C}_i &= \text{He}(\bar{P}_i \mathcal{A}_i) + \mathcal{C}_i^T \mathcal{C}_i + \sum_{j \in L_k^i} \pi_{ij} \bar{P}_j + \pi_{ii} \bar{P}_i + \sum_{h \in L_{uk}^i} \pi_{ij} \bar{P}_h \\ &= -\frac{\sum_{h \in L_{uk}^i} \pi_{ih}}{\delta_i} (\text{He}(\bar{P}_i \mathcal{A}_i) + \mathcal{C}_i^T \mathcal{C}_i + \sum_{j \in L_k^i} \pi_{ij} \bar{P}_j + \pi_{ii} \bar{P}_i - \delta_i \bar{P}_h) \end{aligned} \tag{55.10}$$

Considering the fact that $0 \leq -\pi_{ih}/\delta_i \leq 1$, it is easy to obtain that $He(\bar{P}_i \mathcal{A}_i) + \mathcal{C}_i^T \mathcal{C}_i + P_k^i + \pi_{ii} \bar{P}_i - \delta_i \bar{P}_h < 0$, $h \in L_{uk}^i$ can guarantee (55.5) is established.

Since $\underline{\pi}_{ij} \leq \pi_{ij} \leq \bar{\pi}_{ij}$, the following inequality can be obtained.

$$He(\bar{P}_i \mathcal{A}_i) + \mathcal{C}_i^T \mathcal{C}_i + P_k^i + \pi_{ii} \bar{P}_i - \delta_i \bar{P}_h \leq He(\bar{P}_i \mathcal{A}_i) + \mathcal{C}_i^T \mathcal{C}_i + \bar{P}_k^i + \bar{\pi}_{ii} \bar{P}_i - \underline{\delta}_i \bar{P}_h \quad (55.11)$$

So in this case, if (55.7) holds, (55.5) can be achieved.

Case 2 $i \in L_{uk}^i$. By using $\sum_{j=1}^r \pi_{ij} \bar{P}_i = \sum_{j \in \mathcal{L}_k^i} \pi_{ij} \bar{P}_i + \pi_{ii} \bar{P}_i + \sum_{j \in \mathcal{L}_{uk}^i} \pi_{ij} \bar{P}_i = 0$, it follows

$$\begin{aligned} & \mathcal{A}_i^T \bar{P}_i + \bar{P}_i \mathcal{A}_i + \sum_{j=1}^r \pi_{ij} \bar{P}_j + \mathcal{C}_i^T \mathcal{C}_i \\ & = He(\mathcal{A}_i^T \bar{P}_i) + \sum_{j \in \mathcal{L}_k^i} \pi_{ij} (\bar{P}_j - \bar{P}_i) + \sum_{j \in \mathcal{L}_{uk}^i} \pi_{ij} (\bar{P}_j - \bar{P}_i) + \mathcal{C}_i^T \mathcal{C}_i \end{aligned} \quad (55.12)$$

Considering $\underline{\pi}_{ij} \leq \pi_{ij} \leq \bar{\pi}_{ij}$, it's easy to get that if (55.8) hold, (55.5) can be achieved in this case.

Moreover, (55.9) is the equivalent to (55.6). Therefore, the proof is completed.

Then, the following theorem gives the controller design method.

Theorem 2 *If there exist symmetric matrices $Q_i^l > 0$, T_i^l , Z_i^l ($1 \leq i \leq r, 1 \leq l \leq N$) and matrices V_i , R_i ($1 \leq i \leq r$) such that*

$$i \in L_k^i \left\{ \begin{bmatrix} He(-V_i) & * & * & * & * & * \\ A_i^l V_i + B_{2i}^l R_i + Q_i^l & \bar{\pi}_{ii} Q_i^l + T_i^l - 2Q_i^l & * & * & * & * \\ C_i^l V_i + D_i^l R_i & 0 & -I & * & * & * \\ V_i & 0 & 0 & -T_i^l & * & * \\ \Psi_i & 0 & 0 & 0 & -\Phi_i^l & * \\ \sqrt{-\underline{\delta}_i} V_i & 0 & 0 & 0 & 0 & -Q_i^l \end{bmatrix} < 0, h \in L_{uk}^i \right. \quad (55.13)$$

$$i \in L_{uk}^i \left\{ \begin{bmatrix} He(-V_i) & * & * & * & * \\ A_i^l V_i + B_{2i}^l R_i + Q_i^l & -\underline{\lambda}_k^i Q_i^l + T_i^l - 2Q_i^l & * & * & * \\ C_i^l V_i + D_i^l R_i & 0 & -I & * & * \\ V_i & 0 & 0 & -T_i^l & * \\ \Psi_i & 0 & 0 & 0 & -\Phi_i^l \\ & Q_i^l \leq Q_j^l, j \in L_{uk}^i & & & \end{bmatrix} < 0 \right. \quad (55.14)$$

$$\begin{bmatrix} -Z_i^l & * \\ B_{1i}^l & -Q_i^l \end{bmatrix} < 0, \quad \sum_{i=1}^r \mu_i \text{Tr}(Z_i^l) < \gamma \tag{55.15}$$

where $\Psi_i = \underbrace{[\sqrt{\pi_{ij_1}}V_i^T \cdots \sqrt{\pi_{ij_\sigma}}V_i^T]^T}_{j_\sigma \in \mathcal{L}_k^i}, \Phi_i = \text{diag} \left\{ \underbrace{Q_{j_1}^l \cdots Q_{j_\sigma}^l}_{j_\sigma \in \mathcal{L}_k^i} \right\}$

then the control law $u_i(t) = K_i x(t), K_i = R_i V_i^{-1}$ makes the system (55.1) MSS and with H_2 performance less than $\sqrt{\gamma}$.

Proof Firstly, based on the Theorem 1 and using the same method as the proof of Lemma 6 in [4], the following proposition can be proved. \square

Proposition *If there exist symmetric matrices $Q_i > 0, T_i, Z_i (1 \leq i \leq r, 1 \leq l \leq N)$ and matrices $V_i, R_i (1 \leq i \leq r)$ such that*

$$i \in L_k^i \left\{ \begin{bmatrix} He(-V_i) & * & * & * & * & * \\ \mathcal{A}_i V_i + Q_i & \bar{\pi}_{ii} Q_i + T_i - 2Q_i & * & * & * & * \\ C_i V_i & 0 & -I & * & * & * \\ V_i & 0 & 0 & -T_i & * & * \\ \Psi_i & 0 & 0 & 0 & -\Phi_i & * \\ \sqrt{-\delta_i} V_i & 0 & 0 & 0 & 0 & -Q_h \end{bmatrix} < 0, h \in L_{uk}^i \right. \tag{55.16}$$

$$i \in L_{uk}^i \left\{ \begin{bmatrix} He(-V_i) & * & * & * & * \\ \mathcal{A}_i V_i + Q_i & -\underline{\lambda}_k^i Q_i + T_i - 2Q_i & * & * & * \\ C_i V_i & 0 & -I & * & * \\ V_i & 0 & 0 & -T_i & * \\ \Psi_i & 0 & 0 & 0 & -\Phi_i \end{bmatrix} < 0 \right. \tag{55.17}$$

$Q_i \leq Q_j, j \in \mathcal{L}_{uk}^i$

$$\sum_{i=1}^r \mu_i \text{Tr}(B_{1i}^T Q_i^{-1} B_{1i}) < \gamma \tag{55.18}$$

where $\Phi_i = \text{diag} \left\{ \underbrace{Q_{j_1} \cdots Q_{j_\sigma}}_{j_\sigma \in \mathcal{L}_k^i} \right\}$ then the system (55.1) is MSS and with H_2 performance less than $\sqrt{\gamma}$.

Then, choose $Q_i = \sum_{l=1}^N \alpha_l Q_i^l, T_i = \sum_{l=1}^N \alpha_l T_i^l, Z_i = \sum_{l=1}^N \alpha_l Z_i^l$ and $R_i = K_i V_i$, the proof can be completed by applying the above proposition.

55.4 Example

In this section, one numerical example is presented to illustrate the effectiveness and less conservativeness of the proposed method.

Example Consider a continuous-time Markov jump system (1) with

$$\begin{aligned}
 A_1^1 = A_1^2 &= \begin{bmatrix} 1 & 0.7 \\ 0.5 & -1.3 \end{bmatrix}, A_2^1 = A_2^2 = \begin{bmatrix} 1.4 & -1.6 \\ 1.8 & 0.6 \end{bmatrix}, A_3^1 = A_3^2 = \begin{bmatrix} -2.1 & 2 \\ -0.8 & 1.4 \end{bmatrix}, \\
 A_4^1 = A_4^2 &= \begin{bmatrix} -1.9 & 2.3 \\ -1.2 & -2.4 \end{bmatrix}, B_{11}^1 = B_{11}^2 = \begin{bmatrix} 0.1 \\ 0.3 \end{bmatrix}, B_{12}^1 = B_{12}^2 = \begin{bmatrix} -0.2 \\ 0.3 \end{bmatrix}, B_{13}^1 = B_{13}^2 = \begin{bmatrix} 0.2 \\ 0.4 \end{bmatrix}, \\
 B_{14}^1 = B_{14}^2 &= \begin{bmatrix} 0.3 \\ 0.2 \end{bmatrix}, B_{21}^1 = B_{21}^2 = \begin{bmatrix} 0.1 \\ 0.2 \end{bmatrix}, B_{22}^1 = B_{22}^2 = \begin{bmatrix} 0.1 \\ 0.3 \end{bmatrix}, B_{23}^1 = B_{23}^2 = \begin{bmatrix} 0.3 \\ 0.3 \end{bmatrix}, \\
 B_{24}^1 &= \begin{bmatrix} 0.6+e \\ 0.2 \end{bmatrix}, B_{24}^2 = \begin{bmatrix} 0.6-e \\ 0.2 \end{bmatrix}, C_1^1 = C_1^2 = [0.2 \quad 0.3], C_2^1 = C_2^2 = [0.5 \quad 0.6], \\
 C_3^1 = C_3^2 &= [0.5 \quad 0.1], C_4^1 = C_4^2 = [0.2 \quad 0.2], D_1^1 = D_1^2 = -0.4, \\
 D_2^1 = D_2^2 &= 0.5, D_3^1 = D_3^2 = 0.3, D_4^1 = D_4^2 = 0.7.
 \end{aligned}$$

The transition matrix is $\begin{bmatrix} -1.2 & ? & ? & 0.2 \\ ? & -1.5 & 0.4 & ? \\ \beta & ? & -1 & ? \\ ? & 0.3 & ? & -1.3 \end{bmatrix}$ and $0.4 \leq \beta \leq 0.5$. The

initial distribution is given as $(0.25, 0.25, 0.25, 0.25)$. Applying the Theorem 2, the H_2 norm for different scalar e is presented in Table 55.1.

From the Table 55.1, it is shown that the method proposed above can be applied to H_2 controller design for the class of uncertain MJSs in this paper.

Choose $e = 0$, there is no uncertainty. Table 55.2 can be obtained.

From Table 55.2, it is easy to see that for different ranges of β , the proposed method in this paper always has better performance. Moreover, the more precise transition probabilities knowledge the system has, the better the performance may be achieved.

Table 55.1 The H_2 norm for different scalar e

e	0.3	0.4	0.5	0.6
$\sqrt{\gamma}$	1.3740	1.3804	1.3981	1.4269

Table 55.2 The comparison of H_2 norm for different rang of β

β	$0.2 \leq \beta \leq 0.7$	$0.3 \leq \beta \leq 0.6$	$0.4 \leq \beta \leq 0.5$
$\sqrt{\gamma}$ by this paper	1.3507	1.3396	1.3281
$\sqrt{\gamma}$ by [5]	1.6986	1.6697	1.6401

55.5 Conclusion

In this paper, the robust H_2 controller design for a class of uncertain MJSs with partly known transition probabilities has been studied. The polytopic-type uncertainty is considered in the system model. A new method is introduced to deal with the more general transition probabilities. Less conservative conditions for the H_2 performance of the considered system are obtained. Numerical example has also demonstrated the effectiveness of the results.

Acknowledgments This work is supported by National Natural Science Foundation of China (No. 61273155), New Century Excellent Talents in University (No. NCET-11-0083), A Foundation for the Author of National Excellent Doctoral Dissertation of P.R. China (No. 201157), the Foundation of State Key Laboratory of Robotics (No. 2012-001), the Fundamental Research Funds for the Central Universities (Grant No. N120504003).

References

1. Boukas EK (2005) Stochastic switching systems: analysis and design. Birkhauser, Basel
2. Costa E, Val DJ (2002) On the observability and detectability of continuous-time Markov jump linear systems. *SIAM J Control Optim* 41(4):1295–1314
3. Li W, Su H, Wang K (2012) Global stability of coupled nonlinear systems with Markovian switching. *Commun Nonlinear Sci Numer Simulat* 17(6):2609–2616
4. Dong J, Yang G (2008) Robust H_2 control of continuous-time Markov jump linear systems. *Automatica* 44:1431–1436
5. de Farias DP, Geromel JC, do Val JBR, Costa OLV (2000) Output feedback control of Markov jump linear systems in continuous-time. *IEEE Trans Autom Control* 45(5):944–949
6. Zhang LX, Boukas EK (2009) Stability and stabilization of Markovian jump linear systems with partly unknown transition probabilities. *Automatica* 45(2):436–468
7. Zhang L, James L (2010) Necessary and sufficient conditions for analysis and synthesis of markov jump linear systems with incomplete transition descriptions. *IEEE Trans Autom Control* 55:1695–1701
8. Zhang Y, He Y, Zhang J (2011) Stabilization for Markovian jump systems with partial information on transition probability based on free-connection weighting matrices. *Automatica* 47:79–84
9. Boukas EK (2009) H_∞ control of discrete-time Markov jump systems with bounded transition probabilities. *Optimal Control Appl Methods* 30:477–494
10. Shen M, Yang GH (2010) H_2 state feedback controller design for continuous Markov jump linear systems with partly known information. *Int J Syst Sci* 43(4):786–796

Chapter 56

A New Control Method in pH Neutralization Process

Juan Chen, Zhanfu Liu, Yawei Peng and Qing Guo

Abstract PH neutralization process is composed of a complex and multivariable nonlinear coupling. This paper combines the fuzzy control and sliding mode control, and studying on the control of pH value and liquid level of pH neutralization process. On one hand, this approach simplifies the fuzzy control, on the other hand, it adjusts the universe of fuzzy control system by quantification scale factor changing adaptively and makes system control signals soften and reduces the chattering of sliding mode control. Here, quantification scale factor improves control accuracy of systems. The simulation results show that even a major change in operating point, the systems still have good anti-disturbance and strong robustness.

Keywords Fuzzy sliding mode control · Nonlinear and multivariable system · PH neutralization process

56.1 Introduction

At present the control method of pH neutralization process is mainly PID control [1] and almost all the control is based on single variable system [1–4]. This method has not only less robustness but also poor control accuracy. Especially, the pH neutralization process contains complex nonlinear at neutralization point.

J. Chen (✉)

Beijing University of Chemical Technology, 15 BeiSanhuan East Road, P.O.BOX 94,
Beijing 100029 Chaoyang, China
e-mail: jchen@mail.buct.edu.cn

Z. Liu · Y. Peng · Q. Guo

School Information Science & Technology, Beijing University of Chemical Technology,
Beijing 100029, China
e-mail: lzf0610@gmail.com

Therefore, this paper adopts fuzzy sliding mode control for SISO and MIMO pH neutralization process. Sliding mode control (SMC) has good robustness on nonlinear systems but this depends on the mathematic model of process. Fuzzy control do not rely on the mathematic model, but it needs more input dimension and control rules, which makes the control method rather complex. The combination of fuzzy control and slide control can reduce the input number of fuzzy controller and fully utilize the information of system state, this method is of ease to create fuzzy rule table.

56.2 PH Model

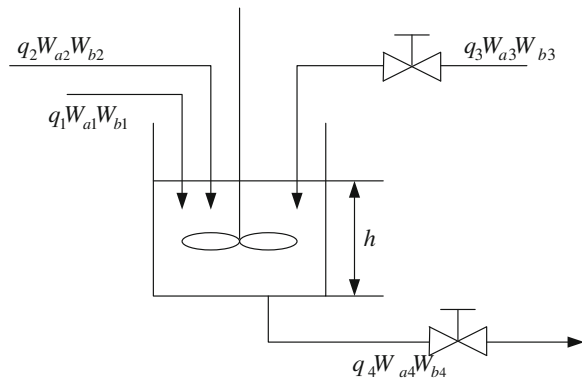
pH control has been used in several practical papers (Boling, Seborg & Hespanha 2007 etc.). A simplified schematic diagram of the system is shown in Fig. 56.1. The neutralization process essentially involves a strong acid stream (q_1), a buffer stream (q_2) and an alkali stream (q_3) and the three are mixed together. q_4 is output stream; W_{a1} , W_{a2} , W_{a3} and W_{a4} is respectively the charge balance factor of acid stream, buffers stream, alkali stream and output stream. W_{b1} , W_{b2} , W_{b3} and W_{b4} is respectively the material balance factor of acid stream, buffers stream, alkali stream and output stream. The model of multivariable pH neutralization process is described as follows four equations [5]:

$$\dot{W}_{a4} = \frac{1}{Ah} [(W_{a1} - W_{a4}) * q_1 + (W_{a2} - W_{a4}) * q_2 + (W_{a3} - W_{a4}) * q_3] \quad (56.1)$$

$$\dot{W}_{b4} = \frac{1}{Ah} [(W_{b1} - W_{b4}) * q_1 + (W_{b2} - W_{b4}) * q_2 + (W_{b3} - W_{b4}) * q_3] \quad (56.2)$$

$$\dot{h} = \frac{1}{A} (q_1 + q_2 + q_3 - C_v h^{0.5}) \quad (56.3)$$

Fig. 56.1 A diagram of the pH neutralization process



$$W_{a4} + 10^{pH-14} + W_{b4} \frac{1 + 2 \times 10^{pH-pk_2}}{1 + 10^{pk_1-pH} + 10^{pH-pk_2}} - 10^{-pH} = 0 \quad (56.4)$$

where, $W_a = [H^+] - [OH^-] - [HCO_3^-] - 2[CO_3^{2-}]$, $W_b = [H_2CO_3] + [HCO_3^-] + [CO_3^{2-}]$. Defined the system state as following: $x = [W_{a4} \ W_{b4} \ h]$. Then pH neutralization processes can be written as:

$$\dot{x} = f(x) + g(x)u \quad (56.5)$$

56.3 Controller Design

The sliding surface of sliding mode control is defined as:

$$s(\tilde{x}, t) = \left(\frac{d}{dt} + c\right)^{n+1} \tilde{x} = \sum_{i=1}^{n-1} c_i \tilde{x}_i + \tilde{x}_n \quad (56.6)$$

where, $c_i > 0$, $\tilde{x} = x_i - x_{di}$, ($i = 1, 2, \dots, n$). \tilde{x} is state error and x_{di} is set value during this time. Upon reaching sliding surface, the control law of system is equivalent control. System is less sensitive to model uncertainty, bounded disturbance and model parameter's change. Equivalent control can make the state vector x_i of the system tracking the state vector x_{di} . Control law is always meeting the conditions as follows:

$$\frac{1}{2} \frac{d}{dt} s^2 \leq -\eta |\tilde{x}| \leq 0 \quad (56.7)$$

Here, η is positive constant. The controller output u is called equivalent control u_{eq} . Because the system contains uncertainty and disturbance, the control law must add a discontinuous condition, that is selecting a switching function, it must meet the sliding surface sliding condition and stability.

$$\mathbf{u} = u_{eq} + u_s = u_{eq} + k \cdot \text{sign}(s) \quad (56.8)$$

Here, k is a constant and $\text{sign}(s)$ is a switch function. The controller design is based on formula (56.8). We adopt $V(t) = (1/2)s^2$ as Lyapunov function of fuzzy control system. We define s and \dot{s} are two inputs of the fuzzy controller and u is the controller output. Through the analysis for input and output, it can be shown that the input and output follow rules: If $s > 0$, decreasing u causes $s\dot{s} < 0$ and if $s < 0$, increasing u causes $s\dot{s} < 0$, and meets the controller stability. In this paper, we use seven fuzzy sets assigned to each control variable: NB, NM, NS, Z, PS, PM, PB, and respectively represent: negative big, negative medium, negative small, zero, positive small, positive medium, positive big. The rule table shows at Table (56.1).

In the actual industrial process, general control rules of fuzzy controller are the summary of experience that its adaptive ability is bad and can't reach the expected

Table 56.1 Fuzzy rule table of MIMO system

u		\dot{s}						
		NB	NM	NS	ZE	PS	PM	PB
s	PB	ZE	NS	NM	NB	NB	NB	NB
	PM	PS	ZE	NS	NM	NB	NB	NB
	PS	PM	PS	ZE	NS	NM	NB	NB
	ZE	PB	PM	PS	ZE	NS	NM	NB
	NS	PB	PB	PM	PS	ZE	NS	NM
	NM	PB	PB	PB	PM	PS	ZE	NS
	NB	PB	PB	PB	PB	PM	PS	ZE

effect of control. Consider a fuzzy controller: $X = [-X_{\max}, X_{\max}]$ is the domain of input variable. A so-called variable domain means that the domain will change along with changing of input variable s and \dot{s} , denoted by: $X(s) = [-\alpha_1(s)X_{\max}, \alpha_1(s)X_{\max}]$ and $X(\dot{s}) = [-\alpha_2(\dot{s})X_{\max}, \alpha_2(\dot{s})X_{\max}]$, where $\alpha_1(s)$ and $\alpha_2(\dot{s})$ are called contraction–expansion factor. Being relative to variable domain, the original domain is naturally called initial domain. Hong-xing Li [6] gave the expression of contraction–expansion factor: In practical applications, the fuzzy control rules look-up table is always adopted for real-time control, which can simplify the complicated fuzzy logic reasoning and improve the efficiency of control. The domain becomes $X(s) = [-\alpha(s)X_{\max}, \alpha(s)X_{\max}]$ after introducing contraction expansion factor. The method gives rise to a number of arbitrary rules. However, in practical application, every time the domain changes, a new fuzzy control rules look-up table needs to be established. Thereby, it will take much more time on data-reading, and response will became slow. To solve this problem, this paper presents a modified variable universe fuzzy control method based on quantitative factors.

Consider a fuzzy controller with input variables s and \dot{s} . The domains are $[-X_{\max}, X_{\max}]$ and $[-\Delta X_{\max}, \Delta X_{\max}]$, and the quantified stages are $2n + 1$ and $2m + 1$ respectively. Then the quantitative factors can be defined as:

$$k(s) = \frac{n}{X_{\max}}, k(\dot{s}) = \frac{m}{\Delta X_{\max}} \tag{56.9}$$

According to Eq. (56.8), the domain can change along with the change of quantitative factor. When quantitative factor k_e increases, the initial domain $[-X_{\max}, X_{\max}]$ will contract. Thus, the control accuracy will enhance. On the contrary, the accuracy will decline. Consequently, the change of quantitative factor is equivalent to the change of domain. Based on this theory, the quantitative factors are designed as functions of s and \dot{s} in this paper. They can be attained that:

$$k(s) = \frac{n}{\alpha_1(s) \cdot X_{\max}}, k(\dot{s}) = \frac{m}{\alpha_2(\dot{s}) \cdot \Delta e_{\max}} \tag{56.10}$$

This method is equal to the one uses $\alpha_1(s)$ and $\alpha_2(\dot{s})$ as contraction–expansion factor. However, in application, only one fuzzy control rules look-up table needs to

be established, which can improve the efficiency and be suitable to apply on real-time on-line control. According to the pH model [7], we choose contraction-expansion as follows: $k(s) = 1 - \lambda_1 e^{\beta_1 \cdot s^2}$, $k(\dot{s}) = 1 - \lambda_2 e^{\beta_2 \cdot s^2}$ where $\lambda_1 = 0.7$, $\beta_1 = -0.1$, $\lambda_2 = 0.9$, $\beta_2 = -0.1$. The stability analysis of variable universe FSMC controller, fuzzy basis function is defined as follows:

$$p_j(x) = \prod_{i=1}^n A_{ij} \frac{x_i(t)}{\alpha(x_i(t))} \quad (56.11)$$

Then the output of the fuzzy controller is:

$$u_f = \mu(y) \sum_{j=1}^M p_j(x) y_j = \sum_{j=1}^M p_j(x) \mu(y) \cdot y_j = \sum_{j=1}^M p_j(x) \theta_j = \mu \eta \quad (56.12)$$

Fuzzy control variables are defined in a bounded domain of the fuzzy variables such as $Sup|u^* - u_f| < \zeta$. When the system state variables are in the bounded area, fuzzy control output u_f approximate sliding mode control law u_f^* . As we know, there is a best approximation of fuzzy control parameters: $\theta^* = [\theta_1^* \theta_2^* \dots \theta_m^*]^T$. So the optimal output of the fuzzy controller is:

$$u_f^* = \sum_{j=1}^M p_j(x) \theta_j^* \quad (56.13)$$

$$u_f - u_f^* = \sum_{j=1}^M p_j(x) (\theta_j - \theta_j^*) = \sum_{j=1}^M p_j(x) \tilde{\theta}_j \quad (56.14)$$

where, $\tilde{\theta}_j = \theta_j - \theta_j^*$ from (56.6), we have

$$u_{eq} = \frac{1}{g} \left[-f(x) - d(x) - \sum_{i=1}^{n-1} c_i \tilde{x}(i) + x_d^n \right] \quad (56.15)$$

$$\dot{s} = c_1 \dot{\tilde{x}}_1 + c_2 \dot{\tilde{x}}_2 + \dots + \dot{\tilde{x}}_n = \sum_{i=1}^{n-1} c_i \dot{\tilde{x}}_i + \dot{\tilde{x}}_n = \sum_{i=1}^{n-1} c_i \dot{\tilde{x}}_i + x^{(n)} - x_d^{(n)} \quad (56.16)$$

And also, from (56.1), (56.15) and (56.16), we have $\dot{s} = g(x)(u_{eq} - u_f)$

$$\dot{s} = g(x)(u - u_s - u_f) \quad (56.17)$$

Then (56.17) can be reduce to $s\dot{s} = g(x)(u_{eq} - u_f)$. For nonlinear system, we choose Lyapunov function as follows:

$$V = \frac{1}{2g(x)} s^2 + \frac{1}{2} \tilde{\theta}^T \tilde{\theta} \quad (56.18)$$

From (56.18), we obtain

$$\dot{V} = \frac{1}{g(\tilde{x})} s(\tilde{x}) g(x) (u - u_s - u_f) + \sum_{j=1}^M \dot{\tilde{\theta}}_j \tilde{\theta}_j \quad (56.19)$$

We choose $u_s = k \text{sign}(s)$ and $k > 0$, so from (56.19) we have

$$\dot{V} \leq s(\tilde{x}) (\varepsilon - \sum_{j=1}^M p_j(x) \tilde{\theta}_j - k \text{sign}(s(\tilde{x}))) + \sum_{j=1}^M \dot{\tilde{\theta}}_j \tilde{\theta}_j \quad (56.20)$$

When using variable universe function as follows:

$$\dot{\tilde{\theta}}_j = \tilde{\theta} = |s(\tilde{x})| \beta p_j(x) \quad (56.21)$$

From (56.21), we have $\dot{V} \leq \beta |s\tilde{x}| \varepsilon - \beta |s\tilde{x}| k = \beta |s\tilde{x}| (\varepsilon - k) \leq 0$. So the controller is stable.

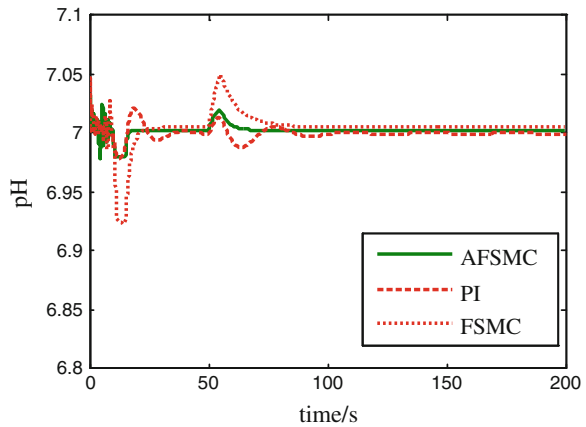
56.4 Simulation Results

In this paper, we study on pH Neutralization process. There are three liquid streams: an acid flow (q_1), a bluffer flow (q_2), and a base flow (q_3). It is desired to control the pH of the effluent stream and the level height h at a specified set point in the presence of disturbances in buffer flow rate. The parameters [8] of the model and operating conditions are summarized in Table 56.2.

Table 56.2 The parameters of the pH neutralization reactor

Variable	Value
pk_1	6.35
pk_2	10.25
W_{a1}	$0.003 \text{ mol} \cdot \text{L}^{-1}$
W_{a2}	$-0.003 \text{ mol} \cdot \text{L}^{-1}$
W_{a3}	$-0.00305 \text{ mol} \cdot \text{L}^{-1}$
W_{b1}	$0.0 \text{ mol} \cdot \text{L}^{-1}$
W_{b2}	$0.00005 \text{ mol} \cdot \text{L}^{-1}$
W_{b3}	$0.00005 \text{ mol} \cdot \text{L}^{-1}$
q_1	$16.6 \text{ ml} \cdot \text{s}^{-1}$
q_2	$0.55 \text{ ml} \cdot \text{s}^{-1}$
q_3	$15.6 \text{ ml} \cdot \text{s}^{-1}$
A	207 cm^2
θ	30 s
h	14 cm

Fig. 56.2 The compare result of q_1 rate changes



PH sensor delays in the real process, it is important to note a delay of 30 s is used in the single variable pH control system. The acid flow rate (q_1) increase by 5 % at $t = 10$ s for a 5 s interval, after which it returned to its original value and was followed by a 10 % decrease at $t = 50$ s for 5 s. The simulation shows in Fig. 56.2. Compared with PI controller, it can be quickly stable and have less reduction. The pH value is quickly reaches back to 7. In the multi-variable system, when the disturbance of buffer flow changes as a square wave alternating between 0.55 and 0 at time points $t = 900$ s and 1,800 s each for 300 s duration, The simulation results are shown in Figs. 56.3 and 56.4. According to Figs. 56.3 and 56.4, the controller has a good result with flow disturbance of buffer flow.

Fig. 56.3 PH value response of q_2 changes

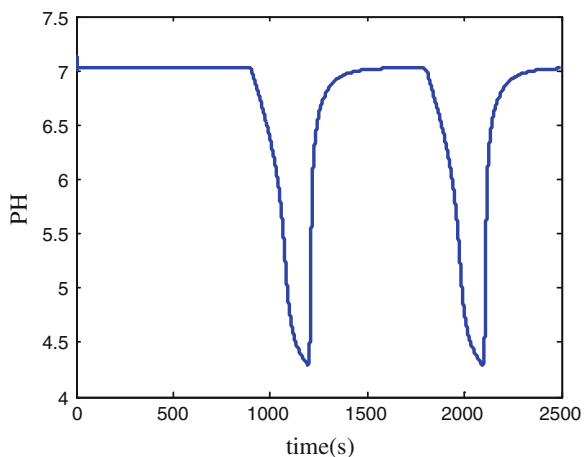
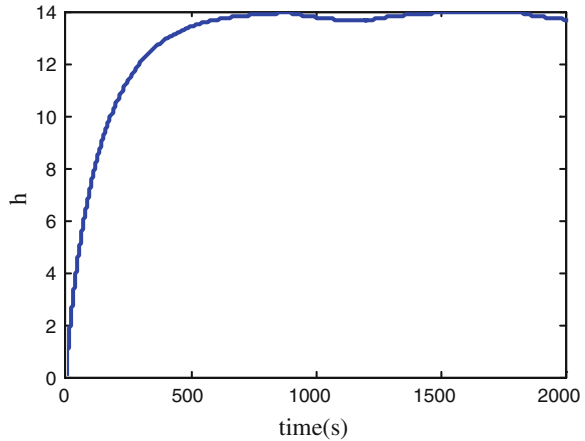


Fig. 56.4 The liquid level response of q_2 rate changes



56.5 Conclusions

FSMC as an intelligent control method of nonlinear can be applied to nonlinear complex systems. The combination of fuzzy control and slide control contains more information of systems than two divisional fuzzy controllers and the fuzzy table is not complex. This method reduces the chattering of SMC by introducing fuzzy control. This paper presents a new control method of PH value and liquid level in pH neutralization process and analysis the stability of FSMC controller. This method improves control accuracy of systems by changing quantification scale factors. Simulation results show that FSMC controller has good performance in pH value and liquid level control, even a major changes in operating point or suffer greater interference, the systems still have good anti-disturbance and strong robustness.

Acknowledgments This work is supported by National Natural Science Foundation of China (21146009).

References

1. Hu Q, Saha P, Rangaiah GP (2000) Experimental evaluation of an augmented IMC for nonlinear systems. *Control Eng Pract* 8:1167–1176
2. Wright RA, Kravaris C (2001) On-line identification and nonlinear control of an industrial pH process. *J Process Control* 11:361–374
3. Bling JM, Seborg DE, Hespaha JP (2007) Multi-model adaptive control of a simulated pH neutralization process. *Control Eng Pract* 15:663–672
4. Hahraz A, Bozorgmehry Boozarjomehry R (2009) A fuzzy sliding mode control approach for nonlinear chemical processes. *Control Eng Pract* 17:541–550
5. Zhang Z, Wang S (2002) Predictive control of pH nonlinear process based on multiple model. *J Zhejiang Univ(Eng Sci)* 36(1):29–31,55 (in Chinese)

6. Li H, Miao Z, Wang J (2002) Variable universe stable adaptive fuzzy control of nonlinear system. *Sci Chin, Ser.E* 32:211–223
7. Dai W, Wang X (2010) Self-tuning fuzzy predictive functional control strategy for cascade time-delay system. *J Chem Ind Eng* 61(8):2132–2137
8. Yang J, Zhao J, Qian J, Niu J (2008) Adaptive nonlinear model predictive control for a class of multivariable chemical processes. *J Chem Ind Eng* 59:934–940

Chapter 57

Control Technology Research of the Underground Hydraulic Support Motion Simulation

Guoying Zhang, Jiangwei You, Liang Xu and Yiyu Cheng

Abstract Motion simulation of hydraulic support (HS) is the key issue of the coalface scene simulation. These collaborative movement relationships among the components of HS are difficult to be described for its complex structure. A movement simulation method by generating key frames is proposed in this paper, which extracts these relationships between HS's space position and movement time, and describes the complex cyclical movement. A collaborative control algorithm mused in controlling HS movement is proposed according to the geometric structure and motion relations among these components, which includes the movement model of the steady among adjacent frames and cooperative movement models of the other parts. The movement simulation of HS is implemented by the above two algorithms on OSG graphics platform, the experimental result is real-time and accuracy.

Keywords Movement simulation · Hydraulic support · Collaborative control · Key frame

57.1 Introduction

Virtual reality (VR) is used for the coalface three-dimensional scene simulation, visualization and simulation the entire mining process, hidden danger warning service in the face to improve the security of the coal mining, and also for coal mine staff technical training.

G. Zhang (✉) · J. You · L. Xu · Y. Cheng
School of Electromechanical and Information Engineering, China University of Mining and Technology (Beijing), 705b Room, Keji Building, Xueyuan Road, Haidian District 100083 Beijing, People's Republic of China
e-mail: zhangguoying1101@163.com

Coalface equipment including scraper-conveyors, shearers and HS, and structures of HS is complex. HS is constituted by a plurality of parts which include many types, the movement pattern of the member varies, and includes a vertical direction of the lifting movement, the horizontal direction of the translational movement, rotational movement dependent lifting and so on. Relationship of movement between the components is difficult to accurately describe. To accurately simulate HS movement is based on design HS motion control technology, which is the key technology of simulation coalface.

In the coal mining areas VR technology is used for virtual design of coal mining equipment, mine fire simulation and gas explosion simulation and so on [1], but there are the equipment simulation model rough, scene control technology is simple and real-time defects. Few the scene of the coalface simulation studies due to the diversity of coal mining equipment, coal mining process and the complexity of the scene, Motion simulation of hydraulic support and motion control studies have not been reported [2, 3].

Because interconnected between the components of the HS, and the movement of components is interdependent, movement relationships is complex, the real-time function path of the movement is hard to extract. Complex movement path function to implement of movement simulation has some problems, such as computationally intensive, real-time poor, rendering low efficiency [4], need to design a new efficient method to control the implementation of the HS motion simulation. HS movement has periodically characteristics, this paper mainly proposed to extract spatial geometry of the HS method based on time parameters, in the period of the campaign generated a number of key frames. Components motion model are the core work of this article.

57.2 The Basis Movement Theory of the HS

The HS's movement is controlled by the world and local coordinate system at the same time, the world coordinate system to express the whole HS sports scenes, the expression of each component of the HS by the respective local coordinate system. The world coordinate system indicates the relative position of the components in the scene, the local coordinate system for expressing the motion relationship of the different components of the model itself.

The HS is constituted by the rigid components, we could take the rigid body as a particle. If rigid parts are translated, each particle should have the same trajectory and speed; if the rigid parts are rotated, the entire rigid body should have around a shaft or a point of rotation, the trajectory of each particle, the speed associated with the rotation angle.

57.2.1 Movement of Particle

HS rigid body parts' translational can be expressed as a particle motion, rotation of a rigid body parts need to be described the motion of the particle collection, Any rigid particle P by homogeneous coordinates is expressed as $P(x, y, z, 1)$, through the transformation matrix from the initial position transformation to the subsequent position $P'(x', y', z', 1)$. Matrix transformation is the core of the rigid body transformation operations, according to the transformation matrix T to translation, rotation, scaling, etc., transformation matrix T expressed as:

$$T = \begin{bmatrix} a & b & c & p \\ d & e & f & q \\ j & h & i & r \\ l & m & n & s \end{bmatrix}$$

Among a, b, c, d, e, f, j, h, I set the scaling, rotation and symmetry transformation of rigid body; l, m, n set the translation of rigid body transformation; p, q, r setting perspective projection transformation; s whole scale transform [5].

According to the relationships of translation and rotation, as in x, y, z three directions of displacement respectively s_x, s_y, s_z , around the z axis rotation angle for θ , the transformation matrix for motion and rotation is:

$$T_{z\theta}(s_x, s_y, s_z) = \begin{bmatrix} \cos \theta & \sin \theta & 0 & 0 \\ -\sin \theta & \cos \theta & 0 & 0 \\ 0 & 0 & 1 & 0 \\ s_x & s_y & s_z & 1 \end{bmatrix}$$

Any particle $P(x, y, z, 1)$ in the 3d coordinate space, through the matrix transformation to $P'(x', y', z', 1)$

57.3 Key Frames Generation Technique Independent of the Path Based on Time

57.3.1 The Structure and Movement of the HS

57.3.1.1 Components of HS

HS is composed of six parts altogether: front beam, roof beam, column, base, cover beam and connecting rod, as shown in Fig. 57.1. HS structure can be simplified as the Fig. 57.2, which A is roof beam, B is the column, C is the base, D cover beam, E is the connecting rod, and F is front beam.

Fig. 57.1 Original HS

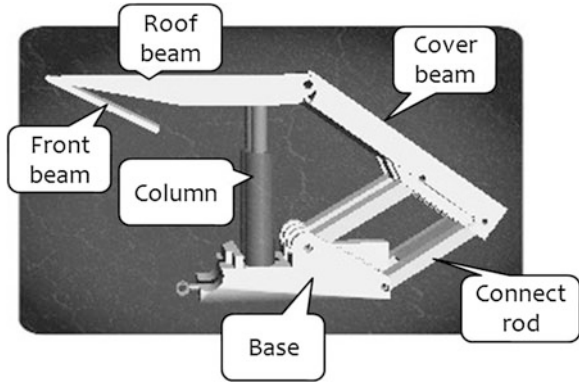
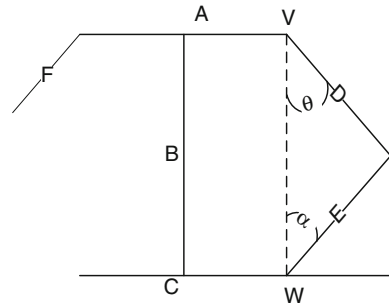


Fig. 57.2 HS simplified diagram



57.3.1.2 The Movement Relationships of HS

The rise and fall of the column is the leading factor for the movement of the HS, with the rise and fall of B, roof beam A follow, the base C remain unchanged, connecting rod E around the W point, cover beam D motion is one of the most complex, not only have lift but also rotation, the motion control of D is the top priority of the work. HS components described in Table 57.1 as follows.

Table 57.1 HS components description table

Components of HS	Roof beam	Column	Base	Cover beam	Connect rod	Front beam
Representative symbols	A	B	C	D	E	F
Motion properties	Negative	Active	Negative	Negative	Negative	Negative
Motion mode	Translate	Translate	Translate	Translate and rotation	Translate and rotation	Translate and rotation

57.4 HS Collaborative Movement Control Model

Hydraulic support is divided into the four stages of the movement, the periodic motion begin with decline stage. In simulation process, the period T is decomposed into several key frames are controlled by the time parameters. The control of movement mode of the first, third and fourth of the three stages each are not identical, respectively established motion model of the HS's components. State diagram of HS decline stage between adjacent frames is shown in Fig. 57.3.

Between two frames, column B decline is active movement, through V_{A-B} , drive roof beam A drop, A through V_{A-D} and V_{A-F} respectively affects shield beam D and front beam F fall, cover beam D through V_{D-E} interlocking connect rod E. When bottomed out, front beam F around V_{A-F} counterclockwise rotation.

57.4.1 Compound Motion Between Two Frames

Between two frames both translational and rotational parts is cover beam D, should do in the world coordinate system of its translation, and also do in the local coordinate system of its rotation, so the description the movement of cover beam D is the key in this paper. Beam A through point V_{A-D} rive cover beam D translation and rotation, from the i frame move to the $i + 1$ frame, cover beam D fall under the world coordinate system can be expressed in the formula is:

$$h_D(t_{i+1}) = h_D(t_i) - v \cdot \Delta t \tag{57.3}$$

Also cover beam D around the point V'_{A-D} rotate $\Delta\theta$, connect rod E around point V'_{C-E} rotate $\Delta\alpha$, because we don't know the speed of rotation, $\Delta\theta$ and $\Delta\alpha$ depends on the geometrical relationship to calculated:

$$l_D \cdot \cos \theta + l_E \cdot \cos \alpha = h_B(t_i) \tag{57.4}$$

$$l_E \cdot \sin \alpha = l_D \cdot \sin \theta \tag{57.5}$$

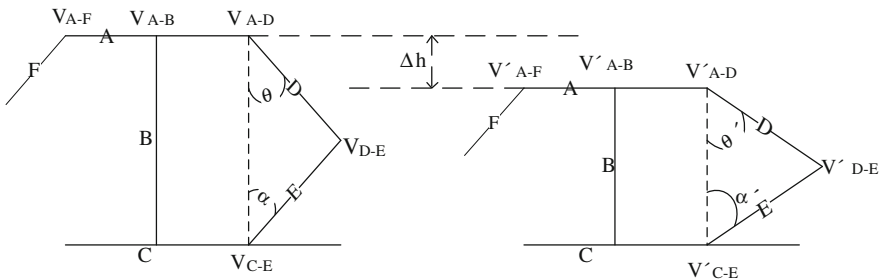


Fig. 57.3 The state of HS's frame i and $i + 1$

$$l_D \cdot \cos \theta' + l_E \cdot \cos \alpha' = h_B(t_{i+1}) \quad (57.6)$$

$$l_E \cdot \sin \alpha' = l_D \cdot \sin \theta' \quad (57.7)$$

Calculated the result of θ and θ' , α and α' .

$$\Delta\theta = \theta' - \theta \quad (57.8)$$

$$\Delta\alpha = \alpha' - \alpha \quad (57.9)$$

From the i frame to $i + 1$ frame, the rotation process of cover beam D around point V'_{A-D} and connect rod E around point V'_{C-E} can be expressed as:

$$\theta_D(t_{i+1}) = \theta_D(t_i) - \Delta\theta \quad (57.10)$$

$$\theta_E(t_{i+1}) = \theta_E(t_i) - \Delta\alpha \quad (57.11)$$

This is the motion relationship of the HS's components, clear movement relationship after, you can write animation callback function realization animation process, only pay attention to the point that, movement of all parts is started at the same time, so those are not out of the collaboration.

57.5 To Realize the HS Movement Simulation

57.5.1 Introduction for Realizing Platform of OSG

This system is developed based on OpenSceneGraph (OSG) graphics library, OSG contains a series of open source graphics library, mainly to provide the development of the image application scene management and graphics rendering the function of optimization. It uses portable ANSI c++, and use has become the industry standard bottom OpenGL rendering API. Therefore, OSG have cross-platform, can run on Windows, Mac OS X and most types of UNIX, Linux operating system [12].

OSG provides a tree structure model to build scene, and effectively organization the scene. 3DSMAX created six equipment component model files at first, and organization, and then deduced by OSGExp plugin for.osg format files.

57.5.2 Load and Control Model

HS is the key equipment model of the coal face simulation, through the function `osgDB::readNodeFile()` of OSG to read model from file. And then corresponding motion control of the scene model.

When load the model of HS, first of all, according to the rang of placement and moving time for HS, segment out several key point for control, Control variables including: double-precision time variable, for the starting time and duration of the animation; Vector type variable `osg::Vec`, used to control the position of nodes at the key point; express movement way of quaternions variable `osg::Quat`, vector part of its axis, scalar part express the rotation angle between two key points.

57.5.2.1 Set the Initial State of HS Model

In OSG, a lot of functions and methods are packaged to control the movement and set up attribute of model in the scene, function `osg::MatrixTransform::setMatrix()` setting model scaling, the initial position and rotation angle, function `osg::Matrix::scale()` control scale, the parameters of `osg::Vec` on behalf of the local coordinate system x, y, z three directions of scale; Function `osg::Matrix::translate()` set the HS's local coordinate system origin position its parameters `osg::Vec` says the world coordinate system origin position; Function `osg::Matrix::rotate()` setting model rotation, parameter `osg::Quat` is quaternions variable, the parameters of `osg::Matrixd::value_type` said rotation angle, and the other parameters `osg::Vec` said the axis of rotation.

57.5.2.2 Motion Control of HS

Due to the HS components different function, its movement form is also different. And it for periodic motion, we analyzed the motion of the components in different stages of the cycle above, according to different stages of different motions to write different animation function for parts.

First set the duration of the animation, for the entire period T within a period of time, starting time `time_start`, as well as the animation process consists of n key frames.

Rotation and translation set shield beam D as an example, the first set rotation angle, translation displacement. Between Key points the rotation angle is angle/n , translation distance is $\text{displacement}/n$, used time is time/n , by function `osg::Quat rotation()` update the rotation angle, by function `osg::Vec position()` update the translation. Finally still call `insert()` function to insert the time and the current state, return the animation path. The last node shield beam D call callback `osg::Node::setUpdateCallback()` finish the motion path (Figs. 57.4 and 57.5).

Fig. 57.4 The beginning state of the HS

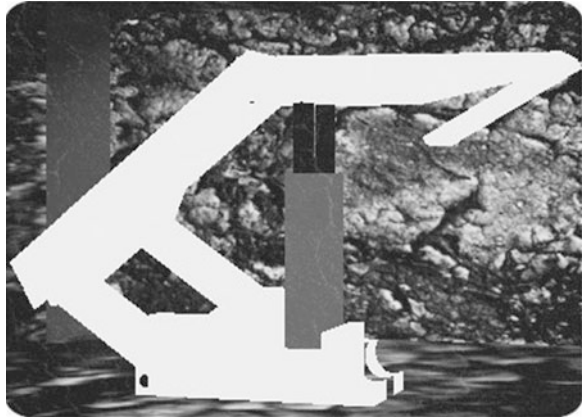
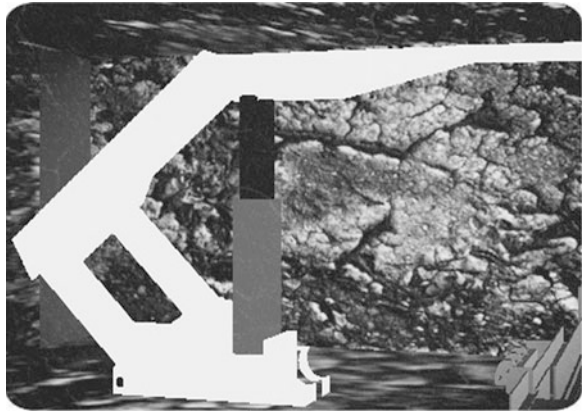


Fig. 57.5 The support state of the HS



57.6 Conclusion

This thesis mainly studied the theory and method which the model of movement in the virtual scene required based on OSG, especially in motion control technology of HS in detail design, put forward a new method of motion control equipment, can be solved under complex animation path relationship of rigid body movement to do precise motion control, very good to solve the complex motion of the relationship in coal face. And can be applied in other more complex scene simulation, can through the extraction of the space geometric relation mathematical model to replace the movement path, and achieve the same simulation effect [12].

Along with the development of digital mine, virtual reality technology will be more and more widely used in mining industry, the future can combine with 3d simulation of virtual reality technology and dynamics theory, reach the authenticity of the scene, and can combine with sensor and network equipment, to achieve real-time performance of the scene [13].

Acknowledgments The authors deeply appreciate the financial supports provided by National Science and Technology Support Program of China (No. 2009BAB48B02).

References

1. Yu L (2008) Investigation of coalface simulation system. Shandong University of Science and Technology (in Chinese)
2. Luo S, Li X (2005) A high performance object-oriented scene-graph system. *J Syst Simul* 2:424–424 (in Chinese)
3. Wang S, Tan J, Zhang S (2003) Research on Scene presentation for assembly design in virtual environment. *J Comput Aided Comput Graph* 15(1):76–80 (in Chinese)
4. Du J (2010) Research on motion control and interactive technology in virtual scene based on OSG. Wuhan University of Technology, Wuhan (in Chinese)
5. Sun J (1996) *Computer Graphics*, 3rd edn. Tsinghua University Press, Beijing (in Chinese)
6. Zheng J, Zhang W, Wu H, Sun F (2004) 3-D animational simulation of a flexible dual-manipulator space robot based on Vega. *Comput Eng Sci* 2004(10):72–74 (in Chinese)
7. Song Z, Kang F (2004) Key techniques in scene simulation. *Comput Appl* (5):67–68 (in Chinese)
8. Choi SH, Samavedam S (2002) Modelling and optimization of rapid prototyping. *Comput Ind* 1:39–53
9. Guo M, Hou K (2009) Virtual reality simulation system for underground mining process. In: *Proceedings of 2009 4th international conference on computer science & education*
10. Li M, Sun J (2005) Key techniques and generation in virtual battlefield environment. *J Syst Simul* (5):1153–1156 (in Chinese)
11. Zhou Y, Yan Q (2006) Collision detection algorithms analysis in virtual environment. *J Syst Simul* (S1):103–107 (in Chinese)
12. Yang H *OpenSceneGraph3.0 Three dimension visual simulation technology development detailed analysis*. Guo Fang Gong Yan Press, Beijing (in Chinese)
13. Squelch AP (2001) Virtual reality on mine safety in South Africa. *South Africa Inst Min Metall* 101(4):209–216

Chapter 58

Research on Chilled Water Pressure Difference of the Model Reference Adaptive Control

Hongmei Jiang, Dongdong Cai, Yugui Nian and Qingchang Ren

Abstract Air-conditioning system chilled water pressure difference is a time-varying complicated nonlinear system, using the conventional PID control loop is difficult to achieve good control quality. According to the actual control requirements, puts forward the RBF neural network model reference adaptive control strategy, design the chilled water pressure difference control system. It use the RBF neural network controller and DRNN network model identification parameter learning algorithm. The simulation results show that this control strategy has good effect, it can achieve control requirements better.

Keywords Pressure difference control · Neural network · Model reference · Adaptive · Model identification

58.1 Introduction

Air-conditioning water system provides cold water or hot water for air-conditioning terminals to eliminate waste heat or compensate for the heat loss. Because most of the time the air-conditioning system is under load, so making water system

H. Jiang (✉)
College of Electrical and Information Engineering, Lanzhou University of Technology,
Lanzhou, China
e-mail: jhmxmsh@sina.com

D. Cai · Y. Nian
Luoyang Power Supply Company, Luoyang, China
e-mail: lysc12@126.com

Q. Ren
School of Civil Engineering, Xi'an University of Architecture and Technology, Xi'an,
China
e-mail: renqch@163.com

variable flow and save energy consumption appears especially important [1]. Air-conditioning chilled water pressure difference control system is not only related secondary pump frequency, but also related the freezing water valve opening. It is a complexity system and has strong nonlinear. So the conventional PID control loop is difficult to achieve good control quality. Sometime it can cause the system unstable. In view of the above features, this paper proposes a method based on RBF neural network model reference adaptive control strategy. It is independent the accurate mathematical model of controlled object. And it can adjust controller according to the change of the controlled object parameters. These characteristics on the one hand can overcome the difficulties to establish accurate mathematical model of the air-conditioning chilled water pressure difference system, and on the other hand, it can adapt to the need of load variation, can achieve better control effect.

58.2 Air-Conditioning System Chilled Water Pressure Difference Control System Design

58.2.1 Description of the Chilled Water Pressure Difference

The control principle of Air-conditioning system chilled water pressure difference diagram is shown in Fig. 58.1. Due to load changes, the cold quantity also changed. Chilled water valve make chilled water volume change to meet the cold quantity by changing the valve opening. But the change of chilled water volume caused the change of the chilled water differential pressure. The pressure difference sensors detect the actual pressure difference. Compared with the setpoint value, the controller change the output using the deviation. Then the secondary pump frequency changed until the error between set value and actual value is zero. So in air-conditioning system, chilled water pressure difference can be expressed as:

$$P_{sw} = f(u_{wp}, u_{sw}) \quad (58.1)$$

where P_{sw} is chilled water pressure difference, u_{wp} is secondary pump speed and u_{sw} is chilled water valve opening on average. So we hypothesis the system in place $(P_{sw0}, u_{wp0}, u_{sw0})$ is get balance, the balance on the near for Taylor's series and ignore the secondary and above term of higher order to:

$$P_{sw} = f(u_{wp0}, u_{sw0}) + \left. \frac{\partial f}{\partial u_{wp}} \right|_{(u_{wp0}, u_{sw0})} (u_{wp} - u_{wp0}) + \left. \frac{\partial f}{\partial u_{sw}} \right|_{(u_{wp0}, u_{sw0})} (u_{sw} - u_{sw0}) \quad (58.2)$$

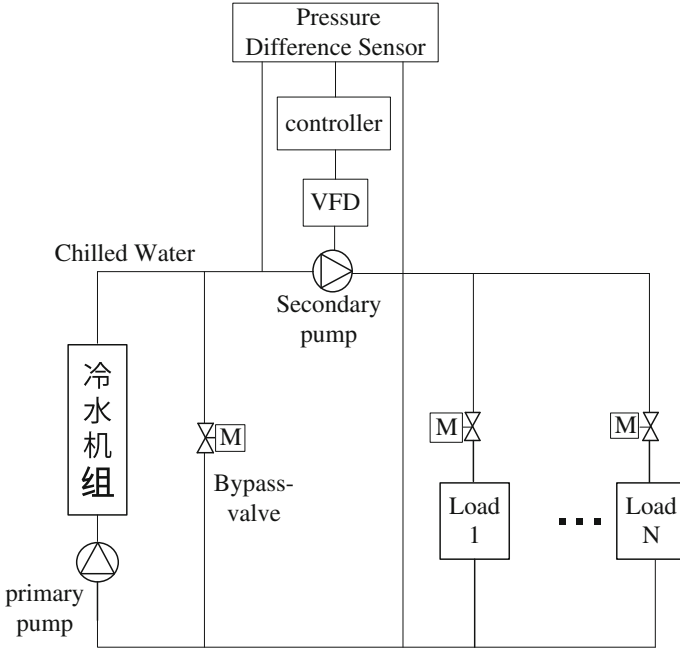


Fig. 58.1 Air-conditioning system chilled water pressure difference diagram

Definition:

$$\delta P_{sw} = P_{sw} - P_{sw0}; \delta u_{wp} = u_{wp} - u_{wp0}; \delta u_{sw} = u_{sw} - u_{sw0};$$

$$K_{wp} = \left. \frac{\partial f}{\partial u_{wp}} \right|_{(u_{wp0}, u_{sw0})}; K_{sw} = \left. \frac{\partial f}{\partial u_{sw}} \right|_{(u_{wp0}, u_{sw0})}$$

Then $\delta P_{sw} = K_{wp}\delta u_{wp} + K_{sw}\delta u_{sw}$

Getting rid of the δ , Considering the dynamic characteristic of the process, formula (58.2) can be changed to:

$$P_{sw}(s) = \frac{K_1}{T_1s + 1} e^{-\tau_1s} u_{wp}(s) + \frac{K_2}{T_2s + 1} e^{-\tau_2s} u_{sw}(s)$$

From this we can see air-conditioning chilled water pressure difference system is a nonlinear system. For this system, using the conventional PID controller is difficult to meet the required control performance, and even cause the system unstable. So, to air conditioning system chilled water for back pressure difference control system, we need to take a effective control method to carry on the control requirements.

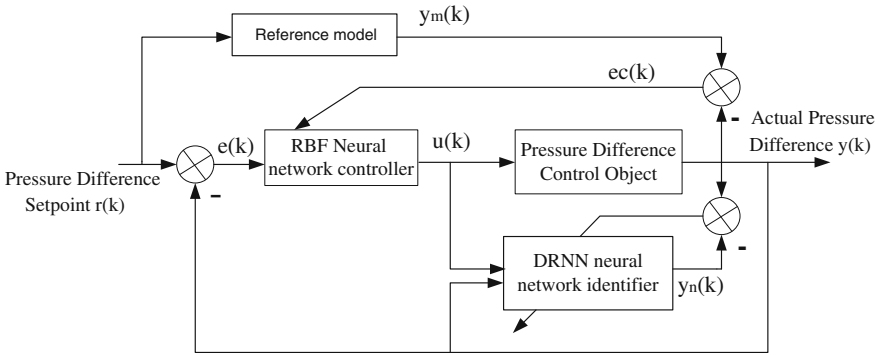


Fig. 58.2 Chilled water pressure difference model reference adaptive control structure chart

58.2.2 Air-Conditioning System Chilled Water Pressure Difference of the Model Reference Adaptive Control

Due to the air-conditioning system frozen water pressure differential system is nonlinear, we can use a model reference adaptive method to carry on the control requirements. The model reference adaptive control structure is shown in Fig. 58.2.

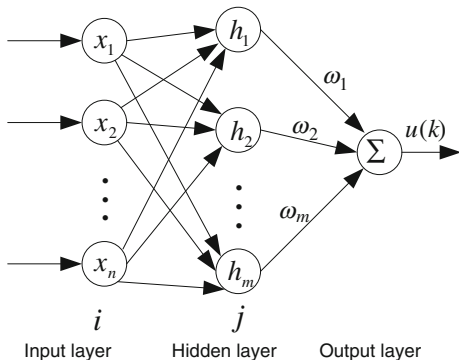
In Fig. 58.2, $r(k)$ is a given value of frozen water pressure difference, $e(k)$ is the error between actual pressure difference and the given value. $u(k)$ is the output of RBF neural network, also it is the control value of the controller. $ec(k)$ is the error between actual output and the reference model output. $y_m(k)$ is output of the reference model, $y(k)$ is actual pressure difference, $y_n(k)$ is output of DRNN neural network identifier. Neural network model reference adaptive control is divided into two kinds, direct model reference adaptive control and indirect model reference adaptive control. This paper is indirect model reference adaptive control, shown as Fig. 58.2. DRNN neural network is identifier, provide Jacobian information of controlled object to RBF neural network controller. The RBF neural network controller used it for learning [2-4].

58.2.3 RBF Neural Network Controller

The Radial Basis Function (RBF) neural network used radial basis function for hidden unit activation function. It is a three layer feed forward network which has single hidden layer. RBF network is a kind of local approximation network, which can approximate any continuous function with arbitrary precision [5-8].

RBF neural network structure is shown in Fig. 58.3. In the RBF network structure, $X = [x_1, x_2, \dots, x_n]^T$ is the neural network's input vector. $H = [h_1, h_2, \dots, h_m]^T$ is radial base vector. h_j is gaussian basis function.

Fig. 58.3 RBF neural network structure chart



$$h_j = \exp\left(-\frac{\|X - C_j\|^2}{2b_j^2}\right), j = 1, 2, \dots, m \tag{58.3}$$

where C_j is the center vector of the j th node, b_j is the base width parameter of the j th node. $C_j = [c_{j1}, c_{j2}, \dots, c_{jn}]^T, i = 1, 2, \dots, n$.

The network base width vector: $B = [b_1, b_2, \dots, b_m]^T$

The network weight vector: $W = [\omega_1, \omega_2, \dots, \omega_m]^T$

In Fig. 58.2, $y_m(k)$ is output of the reference model, the control system request the actual output $y(k)$ can follow the output of the reference model $y_m(k)$. So, the tracking error is: $ec(k) = y(k) - y_m(k)$.

Take $r(k), e(k), u(k - 1)$ as the input of RBF neural network, $u(k)$ as the output of RBF neural network. The output of the RBF neural network controller is: $u(k) = \omega_1 h_1 + \omega_2 h_2 + \dots + \omega_m h_m$

The performance index function is:

$$J = \frac{1}{2}(y(k) - y_m(k))^2 \tag{58.4}$$

The gradient descent method and the chain rule for the weight of network output, the node center vector and base width parameter use the iterative algorithm is as follows:

$$\Delta\omega_j(k) = -\beta \frac{\partial J(k)}{\partial \omega} = \beta ec(k) \frac{\partial y(k)}{\partial u(k)} h_j \tag{58.5}$$

$$\omega_j(k) = \omega_j(k - 1) + \Delta\omega_j(k) + \alpha\Delta\omega_j(k) \tag{58.6}$$

$$\Delta b_j(k) = -\beta \frac{\partial J(k)}{\partial b_j} = \beta ec(k) \frac{\partial y(k)}{\partial u(k)} \frac{\partial u(k)}{\partial b_j} = \beta ec(k) \frac{\partial y(k)}{\partial u(k)} \omega_j h_j \frac{\|X - C_j\|^2}{b_j^3} \tag{58.7}$$

$$b_j(k) = b_j(k - 1) + \beta\Delta b_j + \alpha(b_j(k - 1) - b_j(k - 2)) \tag{58.8}$$

$$\Delta c_{ij} = -\beta \frac{\partial J(k)}{\partial c_{ij}} = \beta ec(k) \frac{\partial y(k)}{\partial u(k)} \frac{\partial u(k)}{\partial c_{ij}} = \beta ec(k) \frac{\partial y(k)}{\partial u(k)} \omega_{jh} \frac{x_j - c_{ij}}{b_j^2} \quad (58.9)$$

$$c_{ij}(k) = c_{ij}(k - 1) + \beta \Delta c_{ij} + \alpha (c_{ij}(k - 1) - c_{ij}(k - 2)) \quad (58.10)$$

where β is the learning rate, α is momentum factor.

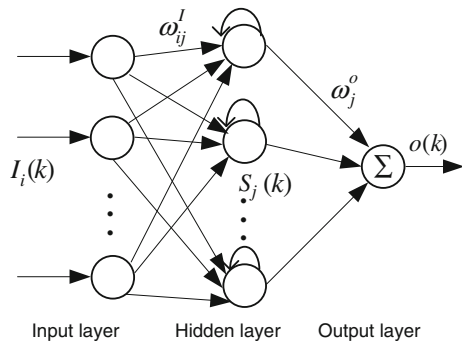
In the learning algorithm, $\frac{\partial y(k)}{\partial u(k)}$ called the Jacobian information. It means the sensitivity of output to input of the control system, its value can be made of the neural network identification. In the neural network algorithm, the value $\frac{\partial y(k)}{\partial u(k)}$ of the accuracy is not high. The part that is not accurate can be adjusted through the network parameters. The symbol is important, so it can be positive and negative number instead of $\frac{\partial y(k)}{\partial u(k)}$. This can make the algorithm more simple.

58.2.4 DRNN Model Distinguished Network and its Learning Algorithm

Diagonal Recurrent Neural Network (DRNN) Neural Network is a kind of regression neural Network. The network structure has three layer. The hidden layer is regression layer. DRNN neural network has the function of dynamic characteristics of mapping, so using DRNN network can online identification of the control system model. DRNN network structure is shown in Fig. 58.4.

In this network, $I = [I_1, I_2, \dots, I_n]$ is input vector, $I_i(k)$ is input of the i th neuron in input layer. $X_j(k)$ is output of the j th neuron in regression layer, $S_j(k)$ is the input sum of the j th regression neural. $o(k)$ is output of the DRNN network. W^D and W^o are respectively the weight vector for the network regression layer and output layer. W^I is weight vector for the network input layer. k is network iteration steps.

Fig. 58.4 DRNN neural network structure chart



In Fig. 58.2, DRNN is a network identifier. $y(k)$ is the actual system output, $y_n(k)$ is the output of the DRNN. The input for the identifier is $u(k)$ and $y(k)$. The error between system output and network output is the adjustment signal for identifier.

The output of the output layer is: $y_n(k) = o(k) = \sum_j w_j^o X_j(k)$

The output of the regression layer is: $X_j(k) = f(S_j(k))$

The input of the regression layer is: $S_j(k) = W_j^D X_j(k-1) + \sum_j W_{ij}^I I_i(k)$

Identification error is: $en(k) = y(k) - y_n(k)$

Identification index is: $E(k) = \frac{1}{2} en(k)^2$

Learning algorithm using gradient descent method:

$$\Delta w_j^o(k) = \frac{\partial E(k)}{\partial w_j^o} = en(k) \frac{\partial y_n}{\partial w_j^o} = en(k) X_j(k)$$

$$w_j^o(k) = w_j^o(k-1) + \eta_o \Delta w_j^o(k) + a(w_j^o(k-1) - w_j^o(k-2))$$

$$\Delta w_{ij}^I(k) = \frac{\partial E(k)}{\partial w_{ij}^I} = en(k) \frac{\partial y_n}{\partial w_{ij}^I} = en(k) \frac{\partial y_n}{\partial X_j} \frac{\partial X_j}{\partial w_{ij}^I} = en(k) w_j^o Q_{ij}(k)$$

$$w_{ij}^I(k) = w_{ij}^I(k-1) + \eta_I \Delta w_{ij}^I(k) + a(w_{ij}^I(k-1) - w_{ij}^I(k-2))$$

$$\Delta w_j^D(k) = \frac{\partial E(k)}{\partial w_j^D} = en(k) \frac{\partial y_n}{\partial w_j^D} = en(k) \frac{\partial y_n}{\partial X_j} \frac{\partial X_j}{\partial w_j^D} = en(k) w_j^D P_j(k)$$

$$w_j^D(k) = w_j^D(k-1) + \eta_D \Delta w_j^D(k) + a(w_j^D(k-1) - w_j^D(k-2))$$

Among them, the regression layer neuron take sfunction is: $f(x) = \frac{1 - e^{-x}}{1 + e^{-x}}$;

$$P_j(k) = \frac{\partial X_j}{\partial w_j^D} = f'(S_j) X_j(k-1); Q_{ij}(k) = \frac{\partial X_j}{\partial w_{ij}^I} = f'(S_j) I_i(k)$$

where η_I , η_D , η_o is learning rat of the input layer, regression layer and output layer. a is the inertia coefficient.

The Jacobian information of the object is $\frac{\partial y}{\partial u} \approx \frac{\partial y_n}{\partial u} = \sum_j w_j^o f'(S_j) w_{ij}^I$.

58.3 Control Algorithm Simulation and Experiment

Due to the actual air-conditioning system, chilled water pressure difference control system mathematical model is unknown, this paper using the actual measured data to training DRNN neural network structure. According to the above formula of RBF neural network controller and model recognition network learning algorithm, we can use MATLAB simulation. In RBF neural network controller, learning rate β choose 0.36, momentum factor α choose 0.06. In DRNN neural network model identification, learning rate η all choose 0.35, inertia coefficient a choose 0.05.

Experimental research on the frozen water pressure difference, in summer conditions, it is assumed that the set value of 0.063 MPa, in the experimental

Fig. 58.5 Pressure difference control chart

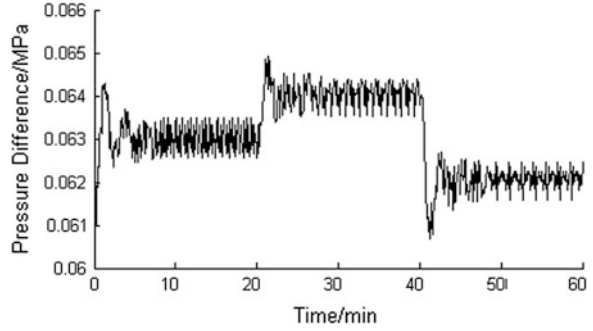
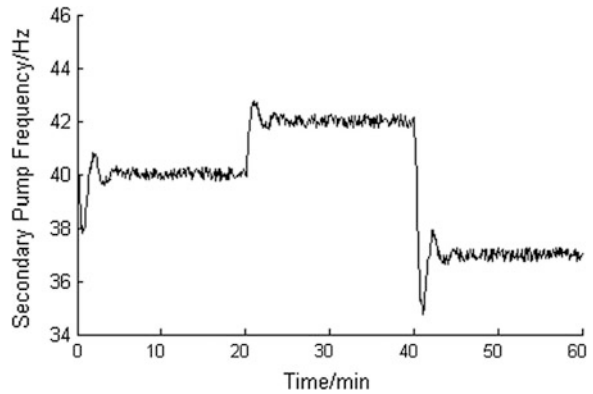


Fig. 58.6 Change of secondary pump frequency chart



process, we change the chilled water valve opening to simulate the load change. The frozen water valve opened from 30 to 60 %, it used to produce interference. And we change the set value artificially; the control effect is shown in Fig. 58.5. Control variable is secondary pump frequency; its change is shown in Fig. 58.6.

From Figs. 58.5 and 58.6, we can see, the system control effect is good, the system only has a slight oscillation in a seconds, then the operation is very stable. The error between system output and reference model output is small, fully meet the control requirements. The model reference adaptive method can also overcome the influence of interference, effective tracking the set value. We can see the control effect is good.

58.4 Conclusion

Air-conditioning chilled water pressure difference control system is nonlinear. It is a complex system that affected by many kinds of factors. The conventional PID control loop can't achieve satisfactory control effect. Based on the analysis of air-conditioning chilled water pressure difference control system. We adopt the neural

network model reference adaptive control. From the simulation and experimental result, we can see that the control effect of neural network model reference adaptive control is good. It is of great significance in the actual air-conditioning system for chilled water pressure difference control.

Acknowledgments The work is supported by ministry of construction of housing of urban and rural science technology project (N0.2012-K1-35).

References

1. Zlatanovi'c I, Gligorevi'c K, Ivanovi'c S (2011) Energy-saving estimation model for hypermarket HVAC systems applications. *Energy Buildings* 43:3353–3359
2. Lim Y, Venugopal R (2012) Auto-tuning and adaptive control of sheet metal forming. *Control Eng Practice* 20:156–164
3. Zhang Y, Hu X, Fang-rui G (2008) Simulating research on RBF neural network model reference adaptive control strategy in temperature control. *J Syst Simul* 20(2):429–432(in Chinese)
4. Liua YT, Chang KM, Li WZ (2010) Model reference adaptive control for a piezo-positioning system. *Precision Eng* 34:62–69
5. Nestorovic Trajkov T, Koppe H, Gabbert U (2008) Direct model reference adaptive control (MRAC) design and simulation for the vibration suppression of piezoelectric smart structures. *Commun Nonlinear Sci Numer Simul* 13:1896–1909
6. Han HG, Chen Q, Qiao JF (2011) An efficient self-organizing RBF neural network for water quality prediction. *Neural Netw* 24:717–725
7. Bayona V, Moscoso M, Kindelan M (2012) Gaussian RBF-FD weights and its corresponding local truncation errors. *Eng Anal Boundary Elem* 36:1361–1369
8. Han HG, Chen Q, Qiao JF (2011) An efficient self-organizing RBF neural network for water quality prediction. *Neural Netw* 24:717–725

Chapter 59

Research on Greenhouse Climate Control Based on RBF Neural Networks

Baicheng Liu, Yifei Chen, Kai Qi and Shangfeng Du

Abstract Greenhouse climate control is the most effective approach to increase the crop yields and reduce the energy consumption. In this paper, a satisfactory greenhouse climate control system model has been set up by analysing the greenhouse climate control rules and using the hybrid learning algorithm for RBF networks. In order to validate the practicability of this system, paper has worked on the simulations and compared the performances between BP networks and RBF networks. By comparing the training processes and mean square deviations, the superiorities of RBF networks have been embodied in the convergence rate and control precision. This new control strategy can meet the demands of greenhouse climate control and has a certain application prospect.

Keywords Greenhouse climate · Control · RBF · Neural networks

59.1 Introduction

Greenhouse is the most important constitution of the modern agriculture and remains to be researched emphatically, especially in China. Greenhouse climate control system is complicated, reflecting in its nonlinearity, time-variation, time delay, distributed parameters and multivariable coupling, therefore no accurate mathematical model has been derived. The most difficult problem was that the greenhouse environmental factors can't be controlled exactly [1]. To solve this problem, there have been many control strategies proposed based on fuzzy control or BP neural networks [2, 3]. However, the fuzzy rules can't be adjusted and require many experiences [4]; and the slow convergence, multiple parameters and

B. Liu · Y. Chen (✉) · K. Qi · S. Du
College of Information and Electrical Engineering of China Agricultural University,
Beijing 100083, China
e-mail: glhfei@126.com

local minimum of BP neural networks (Back Propagation Neural Networks, BP NN) lead to the unsatisfactory applications of the greenhouse climate control [5].

This paper designs an application of the RBF neural networks (Radial Basis Function Neural Networks, RBF NN) in the field of greenhouse climate control, and it overcomes the problem of that greenhouse climate system hard to be controlled exactly. Compared with the BP NN, the RBF NN has more powerful ability in function approximation, and it also has many advantages such as simple structure, fast convergence, high-precision and strong generalization ability. In addition, the RBF NN has the qualities of global optimality and best approximation [6]. The results of experiments explain that the system of greenhouse climate control based on RBF neural networks has high adaptability, high precision and great robustness.

59.2 Greenhouse Climate Control System Design Based on Neural Networks

59.2.1 The Analysis of Greenhouse Environmental Factors and Control Rules

Both the crop yields and the energy consumptions of greenhouse are chained down to many factors, such as temperature, relative humidity, solar radiation, CO₂ concentration, soil humidity, soil nutrient, etc. and the couplings between the factors make the control rules complicated. The aims of greenhouse climate control system are to increase the crop yields and to save the energy by regulating those environmental factors.

There are many kinds of control devices in modern greenhouse system, such as sunshade, ventilation window, heating pipe, wet curtain air cooling machine, CO₂ device, drip irrigation system, etc. and the duty of greenhouse climate control system is to make the control rules on the basis of environmental factors.

59.2.2 The Architecture of Greenhouse Climate Control System Based on RBF Neural Networks

According to the expert experiences, the primary greenhouse environmental factors of northerly summer tomato plants are temperature, relative humidity, solar radiation and soil humidity. The main control devices are sunshade, wet curtain air cooling machine and drip irrigation system. Because the coupling between the temperature and relative humidity exists simultaneously, the climate control is very difficult in traditional way. This paper studies the algorithms of RBF and proposes a new greenhouse climate control strategy. The architecture of greenhouse climate control system based on RBF neural networks is shown in Fig. 59.1.

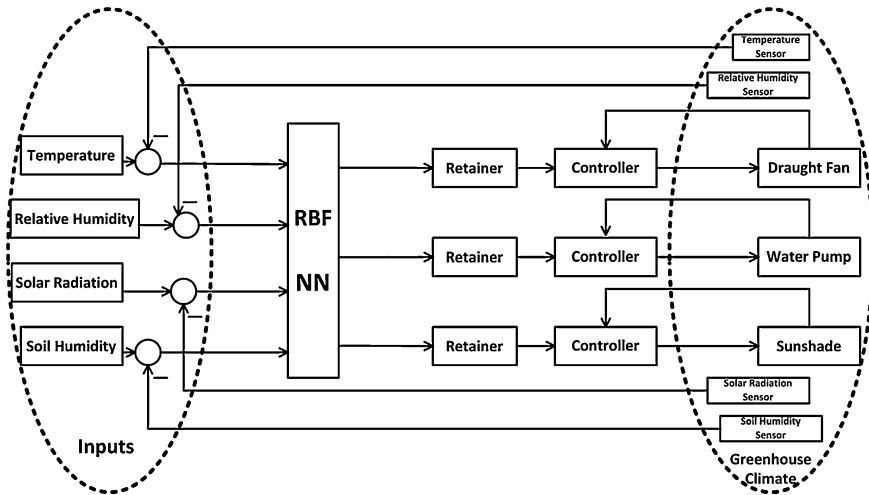


Fig. 59.1 The architecture of greenhouse climate control system based on RBF neural networks

There are four input factors of neural networks: temperature, relative humidity, solar radiation and soil humidity, and the data of inputs are obtained from sensors. Because of the great inertia of greenhouse climate system, the four input factors should enter the neural networks through timer switches, and it can accelerate the training process. There are three output factors of neural networks: sunshade, draught fan and water pump. The real-time requirement of greenhouse climate system is not so high that the three outputs need to enter the neural networks through time switches and retainers, and it can save the energy. This system is controlled by two-stage feedbacks, the first is to make the target outputs and the actual outputs equal, and the second is to update the inputs accurately.

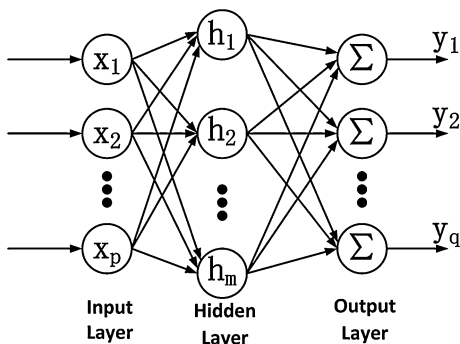
59.3 The Research of RBF Algorithm

59.3.1 The Architecture of RBF NN

As a popular three-layer feed-forward neural networks paradigm, the RBF NN has been applied in many fields, and it can be shown that any continuous function on a compact interval can in principle be interpolated with arbitrary accuracy, if a sufficiently large number of nodes are used [7]. Every neuron of hidden layer has two important parameters: the center and width. Owing to the feature of local approach, the RBF can accelerate the convergence and avoid plunging into local optimal value [8].

The RBF NN consists of three layers: an input layer, a hidden layer and an output layer. The architecture of a typical RBF NN is presented in Fig. 59.2. X , a

Fig. 59.2 The architecture of RBF NN



p -dimensional vector, is the input of RBF NN, and $\mathbf{X} = [x_1, x_2, \dots, x_p]^T$; \mathbf{Y} , a q -dimensional vector, is the output of RBF NN, and $\mathbf{Y} = [y_1, y_2, \dots, y_q]^T$. where, \mathbf{H} is a m -dimensional vector, and it represents the radial basis vector of RBF NN, $\mathbf{H} = [h_1, h_2, \dots, h_m]^T$, and the h_j represents Gaussian basis function, that is described by:

$$h_j = \exp\left(-\frac{\|X - C_j\|^2}{2b_j^2}\right), j = 1, 2, \dots, m \tag{59.1}$$

Here, $\|\cdot\|$ represents Euclid norm and $\exp(\cdot)$ represents Gaussian basis function. Owing to the local receptive field of Gaussian basis function, the outputs will strengthen when approaching the center, and decay when being far away from the center [9].

The task of RBF NN is to select the centers and widths of the hidden-layer neurons, and then to calculate the weights, in the condition of being given N groups of learning samples, and finally to approximate the actual outputs [10].

59.3.2 The Learning Algorithm of RBF

The algorithm of RBF needs three important vectors (the centers, widths and weights), as shown below:

$$\begin{aligned} C &= [c_{j1}, c_{j2}, \dots, c_{ji}, \dots, c_{jp}]^T, j = 1, 2, \dots, m; i = 1, 2, \dots, p \\ B &= [b_1, b_2, \dots, b_j, \dots, b_m]^T, j = 1, 2, \dots, m \\ W &= [w_{1j}, w_{2j}, \dots, w_{sj}, \dots, w_{qj}]^T, j = 1, 2, \dots, m; s = 1, 2, \dots, q \end{aligned} \tag{59.2}$$

And then the output function and error function can be defined.

$$\begin{aligned} Y_s(k) &= w_{s1}h_1 + w_{s2}h_2 + \dots + w_{sm}h_m, s = 1, 2, \dots, q \\ E(k) &= \frac{1}{2}e(k)^2 = \frac{1}{2}(Y_R(k) - Y(k))^2 \end{aligned} \tag{59.3}$$

$Y_R(k)$, as shown in Eq. (59.3), represents the actual output of RBF NN. There are many methods of training RBF NN, such as k-means clustering, trial method, least-square method, gradient descent algorithm and genetic algorithm, etc. but all of them can hardly ascertain the best topology of RBF NN. In this paper, we designed a rational RBF NN, which could be applied to greenhouse climate control system, by using the hybrid learning algorithm based on the nearest neighbor clustering and gradient descent algorithm, described as following:

- Step 1: Initializing the significant parameters of RBF, include the learning rate β ($\beta \in [0,1]$), the momentum factor α ($\alpha \in [0,1]$), the target deviation E_{\max} and the width of Gaussian basis function r .
- Step 2: Training the RBF NN by the first set of data, and the number of hidden-layer neurons is only 1 at present. $C_i = X_i$ ($i = 1, 2, \dots, p$), $b_1 = r$, $w_s = Y_s$ ($s = 1, 2, \dots, q$).
- Step 3: Training the RBF NN by the n -th set of data ($n \geq 2$), and deciding whether it is necessary to create a new hidden-layer neuron, according to the nearest neighbor clustering.

$$\|X - C_{nearest}\| > r \quad (59.4)$$

- Step 4: Calculating the centers, widths and weights, according to the gradient descent algorithm [11].

$$\begin{aligned} w_{sj}(k) &= w_{sj}(k-1) - \beta \frac{\partial E(k-1)}{\partial w_{sj}(k-1)} + \alpha(w_{sj}(k-1) - w_{sj}(k-2)) \\ b_j(k) &= b_j(k-1) - \beta \frac{\partial E(k-1)}{\partial b_j(k-1)} + \alpha(b_j(k-1) - b_j(k-2)) \\ c_{ji}(k) &= c_{ji}(k-1) - \beta \frac{\partial E(k-1)}{\partial c_{ji}(k-1)} + \alpha(c_{ji}(k-1) - c_{ji}(k-2)) \end{aligned} \quad (59.5)$$

This hybrid learning algorithm solves the center-determination problem of the RBF, and it is efficient in improving the accuracy and the training speed of the RBF NN.

59.4 Experiments and Results

59.4.1 The Obtaining of Learning Samples

All of the learning samples are obtained from the greenhouse of intelligent agricultural base in Zhuozhou, and the crops are tomatoes. The area of this greenhouse is 325.3 m², and the electrical control system is provided by GLH. From April

30th to June 7th in 2012, we experimented and obtained 268 groups of data, and finally selected 113 groups as training samples for the RBF NN, according to the effectiveness and representativeness of the data. Every training sample contains seven values which are temperature, relative humidity, solar radiation, soil humidity, sunshade, draught fan and water pump, and all of the data need to be normalized, as shown below:

$$y_i = \frac{1}{2} \frac{x_i - \bar{x}}{x_{max} - x_{min}} \tag{59.6}$$

The meanings of these parameters are: measured value (x_i), average value (\bar{x}), maximum value (x_{max}) and minimum value (x_{min}). The range of normalized result (y_i) is from -0.5 to $+0.5$.

59.4.2 Results and Discussion

In order to prove the practicability of greenhouse climate control based on RBF NN, we constructed the BP NN and RBF NN with the same parameters, and contrasted the performances of them through a series of simulations. The number of the training samples is 80, the target deviation is less than 0.001 ($E_{max} < 0.001$), the learning rate is 0.6 ($\beta = 0.6$) and the momentum factor is 0.012 ($\alpha = 0.012$). The training processes of the BP NN and RBF NN are depicted in Fig. 59.3.

By inspection of Fig. 59.3, it can be easily seen that BP NN needs 62 hidden-layer neurons and RBF NN needs only 41. So the computing time of RBF NN is shorter and the convergence speed is faster than the BP NN's.

Another 33 groups of samples are used to test the control accuracy and stability of the neural networks. By curve fitting analysis, as shown in Fig. 59.4, the three output values of RBF NN can meet the standard of greenhouse climate control.

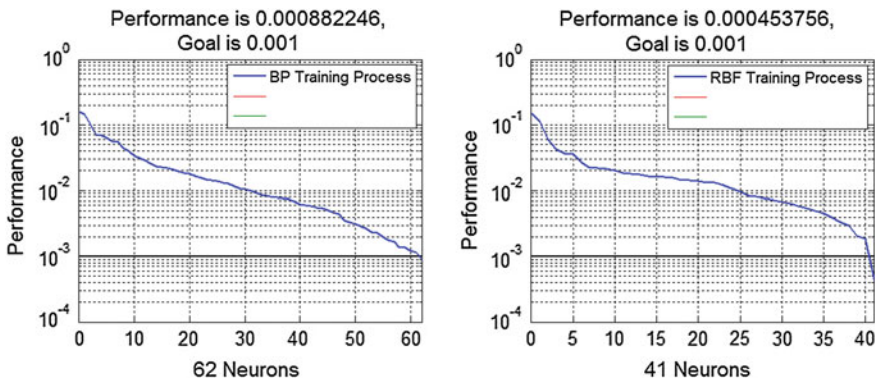


Fig. 59.3 The training process of BP NN and RBF NN

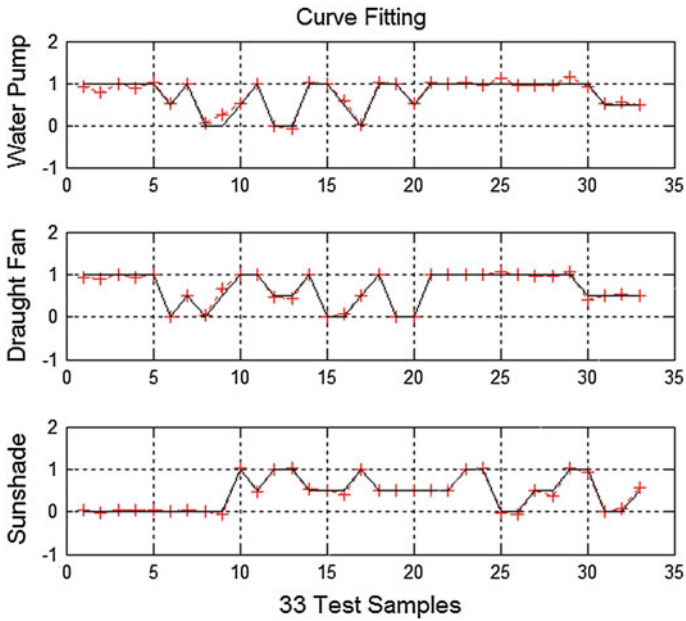
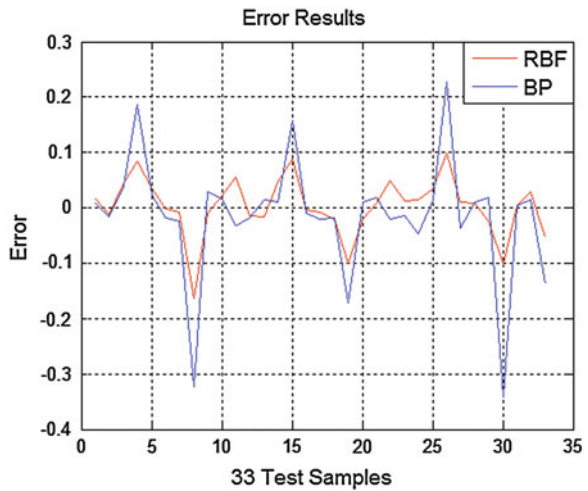


Fig. 59.4 Curve fitting of the three output values gained from RBF NN

Fig. 59.5 The comparison of error results



Compared with the BP NN, the control accuracy and the stability of RBF NN have been improved a lot, as shown in Fig. 59.5. The mean square deviation of BP NN is 0.0436 and the RBF NN's is 0.0112.

59.5 Conclusions and Future Work

This paper proposes a new research based on RBF neural networks for the greenhouse climate control, in which the control rules of greenhouse climate have been analysed and the algorithms of RBF networks have been studied. According to the expert experiences, the primary greenhouse environmental factors of northerly summer tomato plants are temperature, relative humidity, solar radiation and soil humidity, and the control rules can basically meet the needs of tomato plants. In order to prove the practicability of this system, paper has worked on the simulations and compared the performances between BP NN and RBF NN. By the comparison of training processes, it can be easily seen that the computing time of RBF NN is shorter and the convergence speed is faster than the BP NN's. By curve fitting analysis, the 3output values of RBF NN can meet the standard of greenhouse climate control, and the mean square deviations shows that the control accuracy and the stability of RBF NN, compared with the BP NN, have been improved a lot. This system has a great application prospect owing to its fast convergence speed, high control accuracy and great stability.

As all of the present algorithms can hardly ascertain the best topology of RBF NN, future work will focus on the study of more effective algorithm. At the same time, owing to the greenhouse climate control results can hardly be evaluated, some of training samples are unreasonable, so we will also focus on the studies of greenhouse environmental factors and control rules.

Acknowledgments This work was supported by the National Natural Science Foundation of China (Grant No. 61174088).

References

1. Medagam PV (2009) Optimal control of nonlinear systems using RBF neural network and adaptive extended Kalman. American Control Conference
2. Fathi M (2009) Evaluation of intelligent greenhouse climate control system, based fuzzy logic in relation to conventional systems. In: International conference on artificial intelligence and computational intelligence
3. Chen L, Du S (2005) Predicting and controlling the greenhouse environment with artificial neural networks. 79–84 (in Chinese)
4. Markarain NR, Igneault C, Frennie GY (2012) Computerized monitoring and control for a research controlled atmosphere storage facility. 40(7):4437–4438
5. Ma W, Ma W (2011) The current situation and trend of intelligent environment control technology in greenhouse. (23):179–180 (in Chinese)
6. Xia C, Qi W, Rong Y, Shi T (2004) Identification and model reference adaptive networks. In: Proceedings of the CSEE, vol 24 no 7, pp 117–124
7. Chai J, Jiang Q, Cao Z (2002) Function approximation capability and algorithms of RBF neural networks. 15(3):310–321 (in Chinese)
8. Wang H, Wang M, Wang L, Li Q (2008) Forecast on weak electrical signals by analysis of RBF neural networks. J Zhejiang Univ (Engineering Science) 42(12):2127–2134

9. Yang P, Liu P, Zhang Y (2009) Improved multivariable predictive control based on RBF networks. *Control Eng China* 6(1):39–44 (in Chinese)
10. Gomm JB, Yu DL (2003) Selecting radial basis function network centers with recursive orthogonal least squares training. 18(5):637–642
11. Sigrimis N et al (2002) An intelligent nonlinear acting technique for climate control of greenhouses. IFAC 15th Triennial World Congress, Barcelona, Spain

Chapter 60

Research on Neural Network Model for Greenhouse Temperature Predictive Control

Kai Qi, Yifei Chen, Baicheng Liu and Shangfeng Du

Abstract In this article, we present the application of a neural-network-based model predictive control (NNPC) scheme to control temperature in a greenhouse. We use a neural network model as the nonlinear prediction model to predict the future behavior of the controlled process. Predictive control strategy is used to optimize future behavior of the greenhouse environment by computed the controller's optimal inputs. The effect of the algorithm is verified by simulation and an air heat exchanger is chosen as a controlled process.

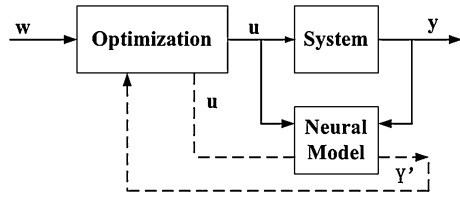
Keywords NN model · Predictive control · Greenhouse

60.1 Introduction

Temperature is the most important factor of greenhouse environment. As we all know, the environment of greenhouse is a combination of great inertia, pure time-delay, nonlinear and model uncertainty which make it difficult for us to get a precise mathematical model of the greenhouse environment. So there are some difficulties for some traditional algorithms which are based on accurate mathematical model, such as PID control, to perform well in greenhouse temperature control [1]. To solve this problem, this article combines Model Predictive Control and Neural Network. A potential drawback of the MPC methodology is that the optimization problem might be computationally quite demanding, especially for nonlinear system [2]. The powerful approximation feature of Neural Network Control (NNC) makes it appropriate for solving that problem. Specifically, the method is that training the Neural Network off line to get an approximate predictive model.

K. Qi (✉) · Y. Chen · B. Liu · S. Du
China Agricultural University East Campus, No. 17 Tsinghua East Road, Postbox 65,
HaiDian District Beijing, People's Republic of China
e-mail: boyqikai@gmail.com

Fig. 60.1 The scheme of predictive neural control



60.2 Construction of Algorithm

Model Predictive Control (MPC) refers to a class of algorithms that compute a sequence of manipulated variable adjustments in order to optimize the future behaviour of a plant [3]. According to the target function, the optimizer will get the optimal control law after collecting the predictive outputs and set point.

Connection of this control structure is show in Fig. 60.1. It uses direct NN model to predict future outputs of process and u' refers the control variable. This control variable is optimized in each step of control process, so that predicted value of output step reaches reference value w .

The whole construction also contains four main parts, namely, prediction model, feedback, reference, and optimization. In the article, algorithm adapts greenhouse temperature's discrete model given by Fig. 60.1.

In this model, y and u correspondingly represent the temperature of greenhouse and controlling quantity imposed in heater. n represent order of prediction. "d" is system's delay. System's destitution is to get system's output y more consistent with set point u by imposing proper control values on the heater.

60.2.1 Model Prediction

One of the most important parts in this algorithm is prediction model [4]. It is necessary to get a model of a plant, which can predict the plant's output in the future according to the plant's past outputs and inputs. This paper takes BP neural network model as the predictive model that is shown in Fig. 60.2.

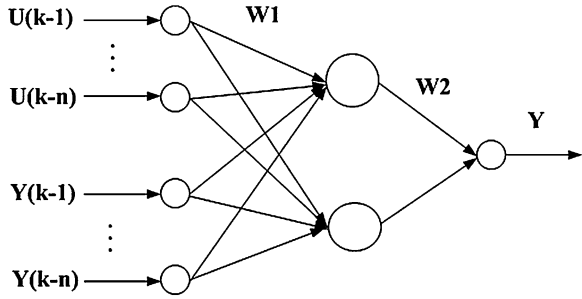
In this model, the hidden layer function is Hyperbolic Tangent Function (HTF). The output layer adapts the linear summation function. It is described in Fig 60.2.

$$\hat{y}(k) = W_2[\tanh(W_1P + WB_1)] + B_2 \tag{60.1}$$

where, w_1 and w_2 represent the weight matrix between layers; B_1 and B_2 represent the threshold of the neuron. Besides, before application, the NN should be trained off- line to get approximate outputs and inputs characters of the greenhouse temperature [5].

According to greenhouse temperature's discrete model, the controller can get system's predictive output for several steps in given conditions. In the calculation

Fig. 60.2 The structure of neural network



of $Y_m(k + d)$, the weight of BP neural network is constant, what should be regulated is the value of u . Once we know the value of u , we need to keep u constant for several steps and replace the $y(k + p - 1)$, $y(k + p - 2)$, ..., $y(k + p - m)$ with predictive value of NN. P is the predictive horizon and m is control horizon.

60.2.2 Receding Optimization

Generally, optimization problem in nonlinear system usually can be solved by Dynamic Programming (DP) [6]. Target of Receding optimization is given by

$$J = \sum_{j=i}^m e^2(t + j) + \beta \sum_{i=1}^N [\Delta u(t + k - 1)]^2 e(t + j) = y_r(t + i) - \hat{y}(t + j|t). \tag{60.2}$$

In this formula, $e(t + j)$ is the error between predictive output and the actual output; k represents the minimum output prediction interval and m represents the maximum. B is the weight coefficient which indicates the importance of control quantity's change.

Neural network predictive model gives the predictive value, $\hat{y}(k + j|t)$, ($j = k, k + 1, \dots, m$), according to the historical input/output. If they are precise enough, the system will get proper control quantity. Referring to control horizon, the control quantities calculated in each sampling point have some time span. What we need is the first control quantity. Next sampling time, we do the process again, namely rolling optimization. Feedback correction is to guarantee the accuracy of prediction.

Process of algorithm is represented as follows:

1. Get the expectation output sequences (after filtering).

$$y_r(t + j) \quad (j = k, k + 1, \dots, m) \tag{60.3}$$

2. Generate the predictive output by neural network predictive model.

$$\hat{y}(t+j) \quad (j = k, k+1, \dots, m) \quad (60.4)$$

$$y(t+j|t) = \hat{y}(k+j|t) + h_j[y_r(t+j) - y(t+j|t-1)] \quad (j = k, k+1, \dots, m)$$

3. Compute the error between the input and actual output.

$$e(t+j) = y_r(t+i) - y(t+j|t) \quad (j = k, k+1, \dots, m) \quad (60.5)$$

4. Minimize the index J to get the optimal control sequence.

$$u(t+j) \quad (j = 0, 1, 2, \dots, n) \quad (60.6)$$

5. Impose the first control quantity on heater then go back to step 1.

60.3 Greenhouse Temperature Control System

Model predictive control is an algorithm that has been widely applied to industrial field [7]. However, there are only few examples about the algorithm applied to agriculture. The greenhouse temperature model predictive control system based on neural network model is shown in Fig. 60.3.

There are total four parts in this system, which are NNP controller, heater, greenhouse and temperature sensor. Considering the large amounts of calculation, the platform should be built on ARM. The heater is warm air condition. The controller gets the greenhouse's temperature from sensor, then calculates the control quantity and imposes on heater.

60.4 Simulations

The approximate nonlinear model of the greenhouse temperature is described by:

$$y(t) = \frac{0.9y(t-1) + u(t-5)}{1 + u(t-6)} + \frac{e(t)}{\Delta u} \quad (60.7)$$

The first step is to train the Neural Network to get the predictive model. Among the coefficient of BP neural network, layer weight w lie between 1 and -1 . Learning rate η take the value of 0.5 and momentum parameters α take the value of 0.05. Target function for training is Minimum Squared-Error (MSE). The result of training is shown in Fig. 60.4.

After get the neural network trained, the next step is simulation. The simulation structure of the system in MATLAB is shown in Fig. 60.5.

The reference block generates random signals. The plant block represents the heater and greenhouse. In this simulation, sampling period T equals 1 s. Control horizon equals 3 and predictive horizon takes 20; control and error weight

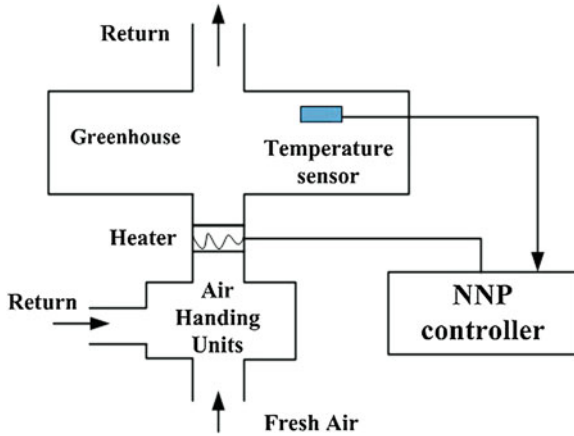


Fig. 60.3 The structure of control system

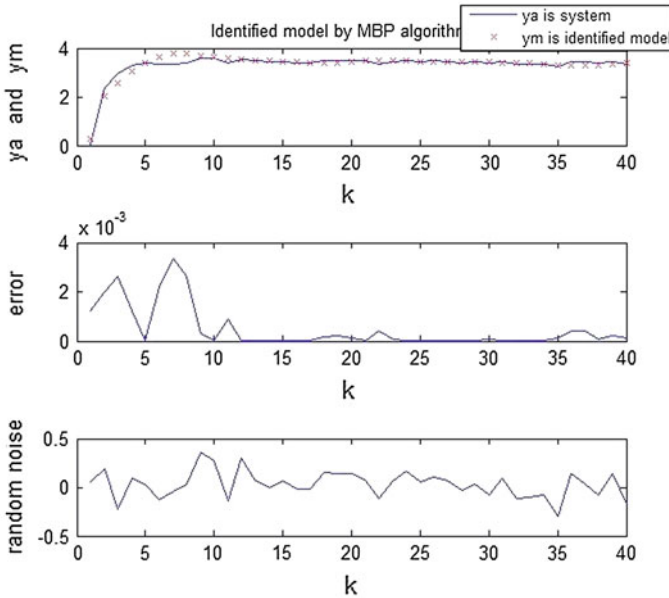


Fig. 60.4 The result of training NN model

parameter respectively take 0.3 and 0.4. We also compare the performance of NNP with PID in this simulation. Results are as shown in Figs. 60.6 and 60.7.

We can see from the result of simulation that compared with PID, the NNP algorithm has a perfect performance, that is, fast response, strong ability of depress the overshoot, high accuracy and so on. What's more, we also can get the result that the NNP system has nice ability of track performance from the Fig. 60.7.

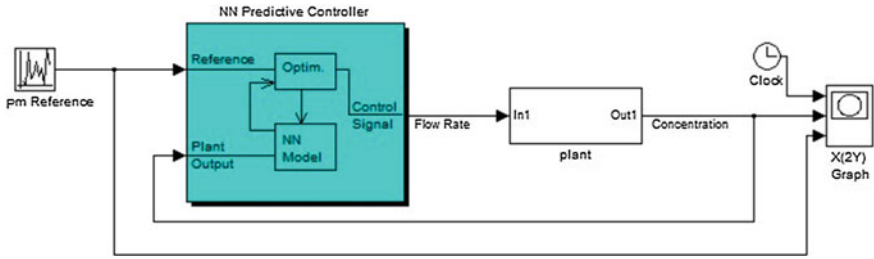


Fig. 60.5 The structure of system simulation in MATLAB

Fig. 60.6 The output with random reference

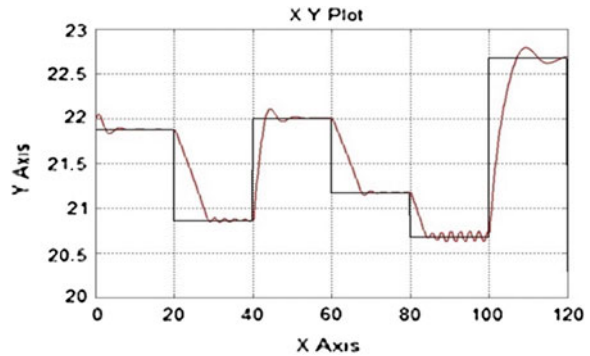
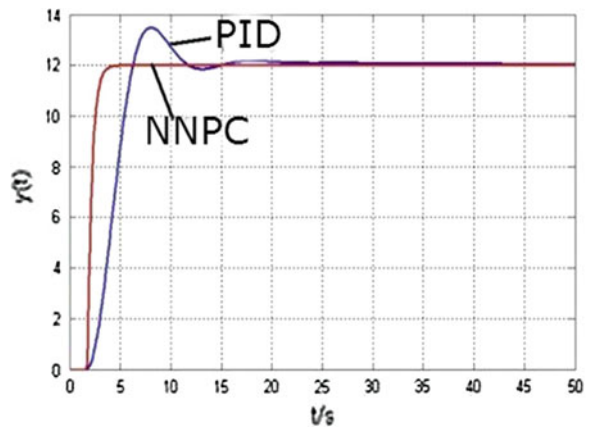


Fig. 60.7 Comparison with PID control



60.5 Conclusion

This paper demonstrates the reliability of neural network predictive algorithm in greenhouse temperature control. The simulation results affirm that neural network model predictive control as a nonlinear-model-based algorithm is an effective

solution to the control of greenhouse temperature control with constrained, non-linear processes.

The advantage of this strategy is that by solving an optimization problem over a future time horizon using a nonlinear model [8], the greenhouse temperature control can be optimally controlled. That result can lead to lower energy consumption of electricity used for air heat exchanger compared with normal PID control and it is also confirmed by the simulation results above. Application of NNPC into agriculture has some advantages: (1) the NN model is parsimonious, allowing for fast execution in a prediction algorithm; (2) it can save large amount of energy if it is widespread.

Acknowledgments This work was supported by the National Natural Science Foundation of China (Grant No. 61174088).

References

1. Qin SJ, Badgwell TA (2003) A survey of industrial model predictive control technology. *Control Eng Pract* 11(2003):733–764
2. Akesson BM, Toivonen HT (2006) A neural network model predictive controller. *J Process Control* 16(9):937–946
3. Vasičkaninová A, Bakošová M (2009) Neural network predictive control of a chemical reactor. *Acta Chimica Slovaca* 2(2):21–36
4. Vasičkaninová A, Bakosová M (2009) Neural network predictive control of a chemical reactor. *Acta Chimica Slovaca* 2(2):21–36
5. Lawrynczuk M (2007) A family of model predictive control algorithms with artificial neural networks. *Comput Sci* 17(2):217–232
6. Wang SW, Yu DL, Gomm JB, Page GR, Douglas SS (2006) Adaptive neural network model based predictive control for air–fuel ratio of SI engines. *Eng Appl Artif Intell* 19(2):189–200
7. Na J, Ren X, Shang C, Guo Y (2012) Adaptive neural network predictive control for nonlinear pure feedback systems with input delay. *J Process Control* 22(1):194–206
8. Piche S, Sayyar-Rodsari B, Johnson D, Gerules M (2012) Nonlinear model predictive control using neural networks. *Control Syst* 20(3):53–62

Chapter 61

The Research on Fault Diagnosis Method of the Coal Mill Based on Information Fusion

Zheng Zhao and Xueyan Lu

Abstract The coal mills are key equipments in the power plant, so it is important for unit's security and stable operation that condition monitoring and fault diagnosis should be applied in the coal mills. A precise fault diagnosis model is hard to handle the faults of complex system with fuzzy and uncertain. A diagnosis method of coal mill fault based on fuzzy clustering analysis and evidence theory is proposed in this paper. This method can solve the fuzzy problem of fault diagnosis, so as to resolve the uncertain problem of fault diagnosis. The results of faults diagnosis show that the method is feasible and effective.

Keywords Coal mill · Fault diagnosis · Fuzzy clustering analysis · Evidence theory · Information fusion

61.1 Introduction

The coal mills are key equipments in the power plant [1]. Faults often happen because they work in the complex operating environment. Through analyzing faults, we find that faults of the coal mills present characteristics of fuzzy and uncertain, which a kind of fault may exhibit a variety of different fault symptoms, and for different fault types may also produce the same fault symptom. So a precise fault diagnosis model is hard to handle the faults of complex system with fuzzy and uncertain. Dempster-Shafer evidence theory is an efficient method to process uncertain, incomplete and vague information in data fusion [2, 3]. In the D-S evidence theory, one of the main difficulties is how to initialize the mass function of basic probability assignment as well as possible [4].

Z. Zhao (✉) · X. Lu
Department of Automation, North China Electric Power University,
Hebei 071003 Baoding, China
e-mail: zhaozheng_hd@163.com

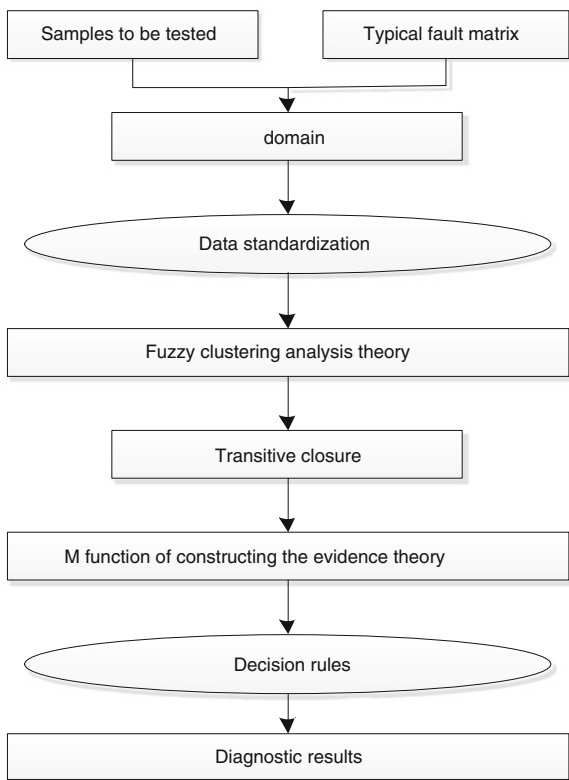
In this paper, we proposed a fault diagnosis method based on fuzzy clustering analysis and D-S evidence theory to solve the problem of the faults of complex system with fuzzy and uncertain. This method is applied in the fault diagnosis of MPS mills in a coal-fired unit. The results of faults diagnosis show that the method is feasible and effective.

61.2 Fault Diagnosis Method Based on Fuzzy Clustering Analysis and D-S Evidence Theory

61.2.1 Introduction

Using the equivalent matrices of fuzzy clustering analysis structure the trust distribution function of D-S evidence theory, which combine the two methods together to solve not only the coal mill fault diagnosis fuzzy problem, but also the structure subjectivity problem of basic probability assignment function of the D-S evidence theory. Specific diagnostic process is shown in Fig. 61.1.

Fig. 61.1 Algorithm flow chart



61.2.2 Fault Diagnosis Steps

61.2.2.1 Constructing Domains X of Fault Diagnosis

Let a set of standard fault samples are a_1, a_2, \dots, a_n , which respectively represent the n kinds of standard fault occurs frequently, and the fault sample to be detected is b , the two sets of samples together constitute a new one $x_1, x_2, \dots, x_n, x_{n+1}$, where $x_1 = b$, $x_2 = a_1$, $x_3 = a_2, \dots, x_{n+1} = a_n$, each sample has m feature parameters, so that $x_i = (x_{i1}, x_{i2}, \dots, x_{im})$.

61.2.2.2 Data Standardization

Because the dimensions of each feature vector which related to classification are different, so elimination the affection of dimensions before calculating the corresponding coefficients, that standardize the datum and prepare for the subsequent analysis. There are lots of data standardization processing methods, which commonly used methods are the standard deviation method, maximum method, extreme value method, mean method, center method and logarithm method [5]. The extreme value method is correct and an easy way which can reach the purpose after only one step of calculating in all these methods. Utilizing extreme value method can achieve the purpose that the data after standardization can fall into the closed interval $[0, 1]$.

Using range value method to compute the matrices X , then get the data matrices U after standardized.

$$u_{ij} = \frac{x_{ij} - \min_j x_{ij}}{\max_j x_{ij} - \min_j x_{ij}} \quad (i = 1, 2, \dots, n, j = 1, 2, \dots, m) \quad (61.1)$$

where $\max_j x_{ij} = \max\{x_{1j}, x_{2j}, \dots, x_{nj}\}$

$$\min_j x_{ij} = \min\{x_{1j}, x_{2j}, \dots, x_{nj}\}$$

61.2.2.3 Constructing Fuzzy Initial Similarity Matrices R

Calculating the similarity r_{ij} of the sample set of each two samples to be classified in order to determine the affinities of the individual classification sample. There are many ways to calculate the degree of similarity r_{ij} , such as hamming distance, Chebyshev distance, index similarity factor method, subtrahend of absolute value, reciprocal of absolute value. After analysis and comparing we find out reciprocal of absolute value is the best method to construct fuzzy similar matrices. Therefore, select this method, and get the fuzzy initial similarity matrices R .

Reciprocal of absolute value

$$r_{ij} = \begin{cases} 1 & i = j \\ \frac{c}{\sum_{k=1}^m |x_{ik} - x_{jk}|} & i \neq j \end{cases} \tag{61.2}$$

61.2.2.4 Finding the Transitive Closure $t(R)$

Matrices R are the fuzzy relation in the domain U , so that the transitive closure of matrices R is the minimum relation which includes matrices R and has transitivity. If R is the general fuzzy relations without reflexive, and use the conventional methods to get the transitive closure, when n is large, calculation will be very tedious [6]. This paper adapts a short-cut calculation method introduced in the paper [7] to find the transitive closure $t(R)$.

Theorem: Note that $R = (r_{ij})_{m \times n}$, $t(R) = (r_{ij}^*)_{m \times n}$, so that,

- Let r_{ij} as the representative element of R , then $r_{ij}^* = r_{ij}$;
- Let r_{ij} as the same output element of r_{kl} , then $r_{ij}^* = r_{kl}$;

By the basis theory above, a short-cut calculation method has been proposed for finding the transitive closure:

- Step 1: find the representative element of R ;
- Step 2: some of the representative elements have same output element in the matrices R , find those same output elements;
- Step 3: write out the relation $t(R) = (r_{ij}^*)_{m \times n}$.

61.2.2.5 Using Transitive Closure $t(R)$ to Establish Basic Belief Assignment Function of D-S Evidence Theory

Transitive closure $t(R) = (r_{ij}^*)_{m \times n}$, its' element r_{ij}^* represent the similar relationship size of sample i and j , fault diagnosis only need to consider the relationship closeness between the tested samples and the standard fault. So only the elements $r_{12}^*, r_{13}^*, \dots, r_{1n}^*, r_{1n+1}^*$ of $t(R)$ were necessary to the fault diagnosis, they each represents the sample's degree of supporting towards standard fault model, that is to say diagnosis sample as fault i under the level of trust r_{1i}^* . Using elements $r_{12}^*, r_{13}^*, \dots, r_{1n}^*, r_{1n+1}^*$ to form a vector $r^* = (r_{12}^*, r_{13}^*, \dots, r_{1n}^*, r_{1n+1}^*)$. Do a two-step treatment towards vector r^* as follows:

- Weighted handle the level of trust, aims to highlight the impact of a greater level of trust in the calculation, smaller trust levels while reducing the impact on the

results. Let $r_{\max}^* = \max(r_{12}^*, r_{13}^*, \dots, r_{1n}^*, r_{1n+1}^*)$, the calculate formulas are as follows:

$$d_i = \frac{r_{1i+1}^* * r_{1i+1}^*}{r_{\max}^*} (i = 1, 2, \dots, n) \quad (61.3)$$

then we can get vector d .

- Construct basic belief assignment value function.

Construct the conditions of basic belief assignment value function $\sum_{A \subset U} m(A) = 1$, request that the summation of all assumptions basic belief assignment to be 1 towards all the power set 2^U in U , ensure the normalization of all assumptions of belief assignment. Obviously, the vector d is not satisfied with this condition, should do further treatment towards vector d to satisfy the normalization, establish the basic belief assignment function as follows:

$$m(i) = \frac{d_i}{\sum d_i} \quad (61.4)$$

61.2.2.6 Diagnosis and Predictive Failure According to the Value of Basic Probability Assignment Function

The following two rules are to judge the target fault mode:

- The value of basic probability assignment function of target fault mode is the maximum in all values;
- The difference between the value of basic probability assignment function of target fault mode and other failure modes basic probability assignment function should be larger than a set value. This value is relating to the number of the target fault and evidence selected in diagnosing procedure, different numbers correspond to different set values. The choice of setting is very important, to set the value too large will cause the missing, while too small will lead to misjudge. The set value can be selected according to Table 61.1, the datum in Table 61.1 are the ideal condition. One third of the datum in Table 61.1 should be chosen as the set value should in actual use [8].

61.3 Specific Example

To demonstrate the validity of the method, an example is given in this section. This method is applied in the fault diagnosis of MPS mills in a coal-fired power plant. In this unit, the boiler with 500 MW capacity uses positive-pressure direct-fired pulverizing system The mediu speed coal mill type is MPS-245.

Table 61.1 Difference value of confidence function distribution

Evidence number	The target mode number				
	3	4	5	6	7
2	0.5000	0.2381	0.1346	0.0857	0.0591
3	0.7000	0.3725	0.2151	0.1371	0.0942
4	0.8333	0.5039	0.3017	0.1937	0.1330
5	0.9118	0.6224	0.3913	0.2548	0.1753
6	0.9545	0.7220	0.4802	0.3193	0.2210
7	0.9769	0.9008	0.5649	0.3858	0.2696
8	0.9884	0.8603	0.6426	0.4526	0.3204
9	0.9942	0.9035	0.7113	0.5181	0.3727

61.3.1 Typical Faults and Feature Parameters

Supposing that $\Theta = \{A_1, A_2, A_3, A_4\}$ is a frame of discernment, where four singleton hypotheses A_1, A_2, A_3 and A_4 are used to describe the coal spontaneous combustion fault, the coal overflow fault, the coal interruption fault and the normal condition.

From eight different sensors, the system has constructed five feature parameter fault symptoms of coal mill. Supposing that $X = \{x_1, x_2, x_3, x_4, x_5\}$ is a frame of feature parameters, where five singleton parameters x_1, x_2, x_3, x_4 and x_5 are used to describe the ratio of primary air flow and coal flow, the temperature difference of mill outlet and mill inlet, the change rate of combustion chamber draft, the ratio of mill's electric current and coal flow and the ratio of generated power of unit and coal flow.

61.3.2 Typical Fault Samples and Detected Fault Samples

In Table 61.2 the data of typical faults is given [7]. They are obtained based on the operating data and the failure analysis reports in a power plant from 1996 to 2003 combined with experience of expert.

In Table 61.3 the detected fault samples are given. The data of sample 1 is obtained from the operating data when the coal spontaneous combustion fault (A_1) occurs. The data of sample 2 and 3 is obtained from the operating data at five minutes and two minutes before the coal interruption fault (A_3) occurs, respectively. The data of sample 4 is randomly-selected from the normal operating data (A_4).

61.3.3 The Corresponding Belief Function $m(A)$

The belief function value can be calculated by the method introduced in Sect. 61.2. The results are shown in Table 61.4. The faults of the coal mills can be diagnosed and forecasted based on the mass value $m(A)$.

Table 61.2 The data of typical fault samples

Feature parameters	A_1	A_2	A_3	A_4
$x_1/(m^3 s^{-1})(kg s^{-1})^{-1}$	1.50	0.63	3.25	1.69
$x_2/^\circ C$	17	176	107	135
$x_3/(% s^{-1})$	10	3	3	0
$x_4/(kg s^{-1})^{-1}$	1.31	2.22	0.95	1.15
$x_5/MW (kg s^{-1})^{-1}$	2.43	1.87	1.92	2.50

Table 61.3 Detected fault samples of coal mills

Samples	x_1	x_2	x_3	x_4	x_5
1	1.55	15	11	1.22	2.48
2	2.45	117	4	1.01	2.38
3	2.93	103	2	0.95	2.23
4	1.59	134	0.05	1.18	2.65

61.3.4 Fault Diagnosis and Analysis

From Table 61.1, the limited ideal value can be selected as 0.6224 for five bodies of evidence and four target modes. Threshold value is 1/3 of ideal value,so threshold value is 0.2075.

From Table 61.4, the decision-making process can be easily completed, which is the maximum belief of the combination mass function. That is,

$$m(A) = \max\{m(A_i), A_i \in \Theta\} \tag{61.5}$$

And

$$m(A) - m(A_j) \geq 0.2075, \{m(A_j) \neq m(A), A_j \in \Theta\} \tag{61.6}$$

For example, from Table 61.4 for sample 1, the mass function values as follows:

$$m_1 : m_1(\{A_1\}) = 0.9530, m_1(\{A_2\}) = 0.0112, m_1(\{A_3\}) = 0.0158, m_1(\{A_4\}) = 0.02$$

The real fault is A_1 (the coal spontaneous combustion fault) can be diagnosed according to decision-making rules (Eqs. (61.5) and (61.6)).

Table 61.4 Fault diagnosis results

	A_1	A_2	A_3	A_4
$m_1(A_i)$	0.9530	0.0112	0.01580	0.0200
$m_2(A_i)$	0.1149	0.0834	0.3395	0.4322
$m_3(A_i)$	0.0883	0.0587	0.6790	0.1740
$m_4(A_i)$	0.0164	0.0108	0.0172	0.9556

In the same way, the real faults can be diagnosed for sample 3 and 4. For sample 3, the real condition is A_3 (the coal interruption fault). For sample 4, the real condition is A_4 (the normal condition). Our proposed method can provide the correct conclusion according to decision-making rules.

For a special case, from Table 61.4 for sample 2, the mass function values as follows:

$$m_2 : m_2(\{A_1\}) = 0.1149, m_2(\{A_2\}) = 0.0834, m_2(\{A_3\}) = 0.3395, \\ m_2(\{A_4\}) = 0.4322$$

According to decision-making rules, the maximum belief of the combination mass function is

$$m_2(A_4) = \max\{m_2(A_i), A_i \in \Theta\}$$

And

$$m_2(A_4) - m_2(A_1) \geq 0.2075 \text{ and } m_2(A_4) - m_2(A_2) \geq 0.2075$$

But

$$m_2(A_4) - m_2(A_3) < 0.2075$$

So, the final condition can't be decided according to decision-making rules. But we can draw a conclusion that the system is going wrong and has a tendency to occur the A_3 (the coal interruption fault) at present. With the development of time, the fault tendency becomes marked and confirms the state through comparing $m_2(A_3)$ with $m_3(A_3)$. This fault diagnosis method can forecast the fault.

As can be seen from Table 61.4, the results of fault diagnosis are consistent with the actual situation on the basis of the fusion result and decision-making rule.

61.4 Conclusion

In this study fault diagnosis of the coal mills with fuzzy and uncertain was discussed. A diagnosis method of coal mill fault based on fuzzy clustering analysis and evidence theory is proposed in this paper. This method can solve the fuzzy problem of fault diagnosis, so as to resolve the uncertain problem of fault diagnosis. Finally, this method is applied in the fault diagnosis of MPS mills in a coal-fired unit. The results of fault diagnosis are consistent with the actual situation. This validates our approach.

Acknowledgments This research was partially supported by “the Fundamental Research Funds for the Central Universities(12MS120)” and “the Natural Science Foundation of Hebei Province (F2012202032)”.

References

1. Dingping L, Xiangrong Y (2009) Fault diagnosis of medium speed mill based on KPCA and LSSVM. *J Power Eng* 29(2):155–158 (in Chinese)
2. Tzuchao L (2007) Improving D-S evidenc theory for data fusion system. *J Wufeng* 15:263–276
3. Jiyong Li, Honghua W (2008) A study on fault diagnosis of hydroelectric generator based on D-S evidence theory. *Electr Mach Syst* 10:17–20
4. Deliang Z, Zepeng C (2007) Fault analysis of coal mills by using gray correlation and D-S combination rules. *J Power Eng* 27(2):207–210 (in Chinese)
5. Liqing L, Qiaolin D (2011) Data pretreatment method of fuzzy c-means clustering effects. *Electr Power Sci Eng* 27(8):24–27 (in Chinese)
6. Zhengming G, Bin H (2008) Application study of fault diagnosis of liquid rochet engine based on fuzzy clustering analysis theory. *J Vib Shock* 27(S):12–14 (in Chinese)
7. Qingh Z, Feng Z (2010) An algorithm for transitive closure of fuzzy relation. *Fujian Comput* 7:87–88 (in Chinese)
8. Liang T, Taihua C (2005) Fault diagnosis of a boiler milling system on the basis of a typical-swath data fusion method. *J Power Eng* 20(2):163–166 (in Chinese)

Chapter 62

Higher Sliding Mode Tracking Control for Underactuated Surface Vessel

Zhuang Lin, Benjie Dong and Zhiqun Guo

Abstract A higher order sliding mode control algorithm is proposed for an underactuated surface vessel in presence of parameter variations and external disturbances. With the second order sliding mode control scheme, a new design methodology is proposed to tackle both the stabilization and tracking problems by Lyapunov direct method and hierarchal strategy. Theoretical analysis and simulation results demonstrates the advantages of the strategy and show that the method can achieve the tracking maneuver precision positioning and get global stability and robustness at the same time.

Keywords Underactuated surface vessel · Higher-order · Sliding mode · Tracking control

62.1 Introduction

Stabilization and tracking control of position (sway and surge) and orientation (yaw) of underactuated surface ships have recently received considerable attention from the control community. The challenge of these problems is due to the fact that the motion of the underactuated ship in question possesses three degrees of freedom (yaw, sway and surge neglecting the motion in roll, pitch and heave) whereas there are only two available controls (surge force and yaw moment) under a non-integrable second-order nonholonomic constraint. (See [1–3] and references therein). That means the surface vessels under consideration are a class of underactuated systems with non-integrable dynamics and are not transformed into a driftless system [4].

Z. Lin (✉) · B. Dong · Z. Guo
College of Shipbuilding Engineering, Harbin Engineering University,
No. 145 Nantong Street, Nangang Dist, Harbin, China
e-mail: drlinzhuang@163.com

Control of nonlinear underactuated systems has proved to be a challenging problem because the techniques developed for fully actuated systems cannot be used directly. Therefore, the study of underactuated systems focused mainly on a certain aspect. In [5], the authors attempted to solve the tracking control problem of an underactuated ship under a relaxed condition. They proposed a global asymptotical tracking controller was proposed to force a ship to track a reference trajectory generated by a suitable virtual ship in a frame attached to the ship body. Based on Lyapunov's direct method and backstepping technique, a universal controller was proposed in [6] to achieve stabilization and tracking simultaneously. In [7], the Lipschitz projection algorithm proposed in [8] was used to estimate the unknown disturbances components and a robust tracking control law was proposed. But all the unknown mean environmental force was assumed to be constant (or at least slowly varying).

In [9–11], robust adaptive controllers were proposed to force an underactuated surface ship to follow a predefined path at a desired speed, and in [12] the mass and damping matrices are not assumed to be diagonal, as often required in the literature. However they are rather complex, and the online adaptive laws for uncertainty hydrodynamic damping coefficients make the tracking control laws difficult to realize in engineering application.

Sliding mode control [13] has been shown to be a robust and effective control approach for underactuated nonlinear systems. Ghommam and others utilized unified backstepping design methodology to achieve global tracking control target and get a good performance, but the design procedure was complex and the system stabilization time was longer than other articles' results [30]. For this issue, lots of sliding mode control method with sliding mode higher order dynamic characteristics was consider to insert into the controller [14–16].

In [17, 18], The authors presented a range of design method about quasi-continuous higher order sliding mode controller, which achieved any relatively higher order sliding mode discretionarily, therefore the method was greatly simplified compared with other higher order sliding mode control above, and could provide higher control accuracy in the maintain of sliding mode robustness in conventional sense. In this paper, with the higher order sliding mode control method [19, 20], we address the trajectory tracking control problem of an underactuated ship in the presence of uncertainty associated with the hydrodynamic damping coefficients. And based on the model characteristics and integral sliding mode method we design an asymptotic stability higher order sliding mode control law and give the proof of global stability in Lyapunov's sense. The simulation results show that the method can effectively achieve underactuated surface vessel control target, get global stability and robustness.

62.2 Underactuated Surface Vessel Model

The 3-DOF planar model of a surface vessel shown in Fig. 62.1 is considered in this work. we consider the trajectory tracking control problem of a surface vessel that has no side thruster, but two independent main thrusters located at a distance from the center line in order to provide both surge force and yaw moment. Neglecting the motions in heave, roll and pitch, the simplified kinematic model, which describes the geometrical relationship between the earth-fixed (E-frame) and the body fixed (B-frame) motion, is given as

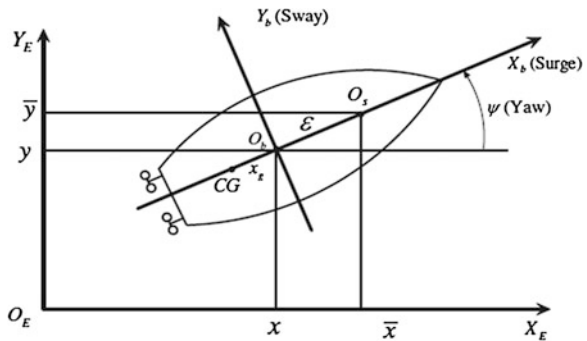
$$\begin{bmatrix} \dot{x} \\ \dot{y} \\ \dot{\psi} \end{bmatrix} = \begin{bmatrix} \cos \psi & -\sin \psi & 0 \\ \sin \psi & \cos \psi & 0 \\ 0 & 0 & 1 \end{bmatrix} \begin{bmatrix} u \\ v \\ r \end{bmatrix}$$

where (x, y) denote the position of the ship given in an inertial frame and ψ denotes the heading angle of the ship. (u, v) are the surges and sway velocities, respectively, and r is the angular velocity of the vessel in the body-fixed frame. For simplicity, we assume that the environment forces because of wind, currents and waves can be neglected. Also assume that the inertia, added mass and damping matrices are diagonal. Then the dynamic equations of motion of the vehicle can be expressed in the B-frame as (see for details [15])

$$\begin{cases} m_{11}\dot{u} - m_{22}vr + d_{11}u = f_1 \\ m_{22}\dot{v} - m_{11}ur + d_{22}v + \Delta v = 0 \\ m_{33}\dot{r} - (m_{22} - m_{11})ur + d_{33}r = f_2 \end{cases}$$

where $m_{11}, m_{22}, m_{33}, d_{11}, d_{22}, d_{33}$ denote the hydrodynamic damping and ship inertia including added mass in surge, sway and yaw. Δv is the external perturbation force. The available controls are the surge force f_1 and the yaw control moment f_2 . For there is no available control in the sway direction, the problem of controlling the ship in three degrees of freedom is therefore an underactuated control problem.

Fig. 62.1 Model of Underactuated Surface vessel



62.3 Sliding Mode Controller Design

For future uses, we introduce the following tracking errors:

$$\begin{aligned}x_e &= x - x_d, y_e = y - y_d, \psi_e = \psi - \psi_d. \\u_e &= u - u_d, v_e = v - v_d, r_e = r - r_d\end{aligned}$$

where x_d, y_d, ψ_d are the desired trajectories and $u_e = u - u_d, v_e = v - v_d, r_e = r - r_d$ are the desired velocities.

With the integral sliding surface method, we define the function of sliding mode surface as:

$$\begin{cases} s_1 = u_e + \int_0^t k_1 u_e(\xi) d\xi \\ s_2 = v_e + \int_0^t k_2 v_e(\xi) d\xi \\ s_3 = r_e + \int_0^t k_3 r_e(\xi) d\xi \end{cases} \quad (62.1)$$

where $k_i > 0, i = 1, 2, 3$. We take the derivative of the first and third formula. According to the equivalent control theory and combining the model (62.8)–(62.17), we will have equivalent control below:

$$f_{eq1} = -m_{22}vr + d_{11}u - m_{11}k_1u_e + m_{11}\dot{u}_d \quad (62.2)$$

$$f_{eq2} = -(m_{22} - m_{11})ur + d_{33}r - m_{33}k_3r_e + m_{33}\dot{r}_d \quad (62.3)$$

Apparently the control input of two formulas above cannot realize the requirement of tracking control of underactuated surface vessel and the conventional sliding mode control method is unable to be applied directly. Then we reform the sliding mode function as following:

$$s = h_1s_1 + h_2s_2 + h_3s_3 \quad (62.4)$$

In which, $h_i > 0, i = 1, 2, 3$. According to the high order sliding mode control theory and Lyapunov stability principle, we have the control law as:

$$f_1 = f_{eq1} + \hat{f} \quad (62.5)$$

$$f_2 = f_{eq2} + \hat{f} \quad (62.6)$$

$$\hat{f} = -\frac{1}{(h_1 + h_3)} \left(f_b + \alpha \cdot \frac{\ddot{s} + 2 \left(|\dot{s}| + |s|^{\frac{2}{3}} \right)^{-\frac{1}{2}} \left(\dot{s} + |s|^{\frac{2}{3}} \text{sgn}(s) \right)}{|\ddot{s}| + 2 \left(|\dot{s}| + |s|^{\frac{2}{3}} \right)^{\frac{1}{2}} + \varepsilon} \right) \quad (62.7)$$

In which, ε is positive constant which is as small as possible to avoid dividing by zero.

$$f_b = \frac{m_{11}}{m_{22}}ur - \frac{d_{22}}{m_{22}}v + k_2v \quad (62.8)$$

f_b is the feedback control compensation. The control law meets the sliding mode reaching condition and ensures the system reaches sliding surface manifold. For $\lim_{t \rightarrow \infty} (x_e, y_e, r_e) = (0, 0, 0)$, it's certainly guarantee system stability and global convergence.

Proof: define Lyapunov function

$$V = \frac{1}{2}s^2 \quad (62.9)$$

We take the derivative of the formula above, and substitute the formulas (62.1–62.3).Then we will have:

$$\begin{aligned} \dot{V} = s\dot{s} &= s \left[h_1\hat{\tau} + h_3\hat{\tau} + h_2 \left(\frac{m_{11}}{m_{22}}ur - \frac{d_{22}}{m_{22}}v + k_2v - \dot{v}_d + k_2v_d \right) \right] \\ &= \alpha|s| \left[\frac{\gamma \text{sgn}(s)}{\alpha} - \frac{\ddot{s} \cdot \text{sgn}(s) + 2 \frac{(\dot{s} \cdot \text{sgn}(s) + |\dot{s}|^{\frac{2}{3}})}{(|\dot{s}| + |\dot{s}|^{2/3})^{1/2}}}{|\dot{s}| + 2(|\dot{s}| + |\dot{s}|^{2/3})^{1/2} + \varepsilon} \right] \end{aligned} \quad (62.10)$$

where $\gamma = h_2(-\dot{v}_d + k_2v_d)$; In order to ensure that the formula equals zero, that the system could reach the sliding surface, the following formula has to be satisfied.

$$\frac{\gamma \text{sgn}(s)}{\alpha} \leq \frac{\ddot{s} \cdot \text{sgn}(s) + 2 \frac{(\dot{s} \cdot \text{sgn}(s) + |\dot{s}|^{2/3})}{(|\dot{s}| + |\dot{s}|^{2/3})^{1/2}}}{|\dot{s}| + 2(|\dot{s}| + |\dot{s}|^{2/3})^{1/2} + \varepsilon} \quad (62.11)$$

As the following inequality holds:

$$\dot{s} \text{sgn}(s) \leq |\dot{s}| \quad (62.12)$$

$$\ddot{s} \text{sgn}(s) \leq |\ddot{s}| \quad (62.13)$$

$$2 \frac{(\dot{s} \cdot \text{sgn}(s) + |\dot{s}|^{2/3})}{(|\dot{s}| + |\dot{s}|^{2/3})^{1/2}} \leq 2(|\dot{s}| + |\dot{s}|^{2/3})^{1/2} \quad (62.14)$$

In addition, due to $\varepsilon > 0$, we will have

$$\frac{\ddot{s} \text{sgn}(s) + 2 \frac{(\dot{s} \cdot \text{sgn}(s) + |\dot{s}|^{2/3})}{(|\dot{s}| + |\dot{s}|^{2/3})^{1/2}}}{|\dot{s}| + 2(|\dot{s}| + |\dot{s}|^{2/3})^{1/2} + \varepsilon} \leq 1 \quad (62.15)$$

Then we get

$$1 \geq \frac{\ddot{s} \cdot \text{sgn}(s) + 2 \frac{(\dot{s} \text{sgn}(s) + |s|^{2/3})}{(|\dot{s}| + |s|^{2/3})^{1/2}}}{|\dot{s}| + 2(|\dot{s}| + |s|^{2/3})^{1/2} + \varepsilon} \geq \frac{\gamma \text{sgn}(s)}{\alpha} \quad (62.16)$$

where, the utilization of ε is avoid the singularity when $\dot{s} = s = 0$. While the formula above is equated with

$$\alpha \geq \gamma \text{sgn}(s) \quad (62.17)$$

Due to that the upper bound of γ could be obtained by estimation of the underactuated system; this means that when the following formula is satisfied

$$|\gamma| < \gamma^{\max}(v_d, \dot{v}_d) \leq \alpha \quad (62.18)$$

There must be $\dot{V} < 0$ and it is illustrated that the total sliding surface s is stabilized in Lyapunov sense.

62.4 System Stability Analysis

For the convenience of proof, we take a stricter condition as

$$\alpha \geq 2\gamma \text{sgn}(s) \quad (62.19)$$

Then, we will get

$$\dot{V} = s\dot{s} \leq -\alpha|s| \leq 0 \quad (62.20)$$

By taking the integral of both sides, we get,

$$\int_0^t \dot{V} d\sigma = \int_0^t (-\alpha|s|) d\sigma \quad (62.21)$$

$$V(t) = V(0) - \int_0^t \alpha|s| d\sigma \leq V(0) - \int_0^\infty \alpha|s| d\sigma < V(0) \quad (62.22)$$

According to the lyapunov function and the definition of sliding mode surface,

$$V(0) = \frac{1}{2} s^2(0) < \infty \quad (62.23)$$

Then,

$$V(t) = \frac{1}{2} s^2 < \infty \quad (62.24)$$

$$\sup_{t \geq 0} |s| = \|s\|_{\infty} < \infty \quad (62.25)$$

It is easily get (62.26) from (62.20).

$$\sup_{t \geq 0} |\dot{s}| = \|\dot{s}\|_{\infty} < \infty \quad (62.26)$$

It means $s \in L_{\infty}$ and $\dot{s} \in L_{\infty}$. The two formulas above indicate s, \dot{s} are bounded functions.

Next, according to formula (62.22)

$$0 < V(0) - \int_0^{\infty} \alpha |s| d\sigma \quad (62.27)$$

$$\int_0^{\infty} \alpha |s| d\sigma < V(0) < \infty \quad (62.28)$$

In the above formula, it is apparently that s could be absolute integral, and $s \in L_1$. And because,

$$\int_0^{\infty} s^2 d\sigma = \int_0^{\infty} |s| \cdot |s| d\sigma \leq \|s\|_{\infty} \int_0^{\infty} |s| d\sigma < \infty \quad (62.29)$$

This indicates that s is square integral as well, so there is $s \in L_2$. Then, according to the formulas (62.24) (62.25) and $\int_0^{\infty} s^2 d\sigma < \infty, \int_0^{\infty} |s| d\sigma < \infty$, we will have $\lim_{t \rightarrow \infty} \dot{s} = 0$ based on the correlated condition of Babarlat's Lemma. And obviously we can prove that s is global asymptotic stable for the square integrability.

And with the same method we can easily get that $s_i, i = 1, 3$ are not only stable under the Lyapunov functions, but also global asymptotic stable. Then we have $\lim_{t \rightarrow \infty} (x_e, u_e) = 0$ and $\lim_{t \rightarrow \infty} (\psi_e, r_e) = 0$.

62.5 Control Simulation

In this section, we carry out some computer simulations to demonstrate the performance of our controller for an underactuated ship model. Consider an underactuated surface vessel with model parameter $m_{11} = 1.956 \pm 0.019$, $m_{22} = 2.405 \pm 0.117$, $m_{33} = 0.043 \pm 0.0068$, $d_{11} = 2.436 \pm 0.023$, $d_{22} = 12.992 \pm 0.297$, $d_{33} = 0.0564 \pm 0.00085$. The desired trajectory is presented as $x_d = 10 \cos(\frac{\pi}{6}t)$, $y_d = 10 \sin(\frac{\pi}{6}t)$, $\psi_d = t + \frac{\pi}{2}$; the external disturbance is $\Delta v = 0.15 \sin(10x) + 0.2 \cos(10x)$. The simulation results as follows (Figs 62.2, 62.3, 62.4),

Fig. 62.2 x and y errors

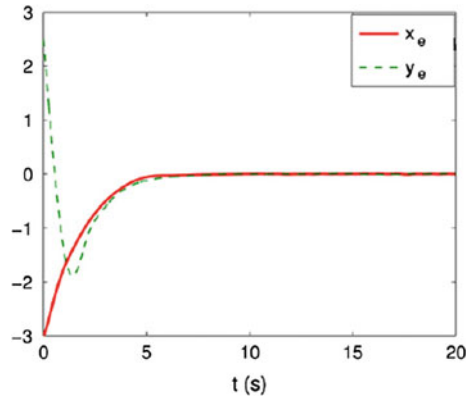


Fig. 62.3 Ship motion Trajectory

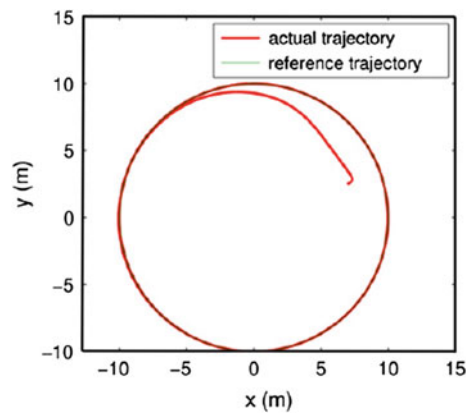
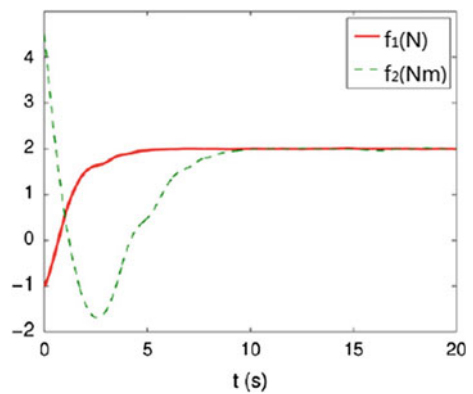


Fig. 62.4 Control input



As we can see that the simulations show that the system can realize attitude stabilization system into steady state in 10 s, and to achieve effective control in 20 s. System response speed has obvious improvement than the similar results in

relevant papers. In conclusion, the higher order sliding mode attitude controller can efficiently achieve motion control of underactuated surface vessel, reduce the stabilization time of system, and improve the control effect as well as improve the robustness of the system.

62.6 Conclusion

Considering the motion control problem for underactuated surface vessel, this paper proposed a higher order sliding mode trajectory tracking control system for underactuated surface vessel, by mean of higher order sliding mode variable structure control theory. Firstly, according to the characteristics of motion control of underactuated surface vessel, a higher order sliding mode tracking controller has been designed. Then, system globally stability was proven in Lyapunov sense. Finally, the simulation results demonstrated that higher order sliding mode controller was able to reduce the stabilization time of the control system of underactuated surface vessel and possessed better stronger robustness and applicability.

Acknowledgments This work is supported by the Fundamental Research Funds for the Central Universities under Grant HEUCFR1001 and the National Natural Science Foundation under Grant 61004008 and LBH-10138 Higher Sliding Mode Control for Underactuated Surface Ship.

References

1. Spong MW (1998) Underactuated mechanical systems. In: Siciliano B, Valavanis KP (eds) Control Problems Robotics and Automation. LNCIS, vol 230, Springer Verlag, London, pp 135–150
2. OrioloG, Nakamura Y (1991) Control of mechanical systems with second-order nonholonomic constraints: underactuated manipulators. In: 30th IEEE Conference on Decision and Control, pp 2398–2403, 1991
3. Rathinam M, Murray RM (1996) Configuration flatness of Lagrangian systems underactuated by one control. In: 35th IEEE Conference on Decision and Control, pp 1688–1693, 1996
4. Wichlund KY, Sordalen OJ, Egeland O (1995) Control properties of underactuated vehicles. In: Proceedings, IEEE international conference on robotics and automation, Nagoya, Japan, pp 2009–2014, 1995
5. Do KD, Jiang ZP, Pan J (2002) Underactuated ship global tracking under relaxed conditions. *IEEE Trans Autom Control* 47(9):1529–1536
6. Do KD, Jiang ZP, Pan J (2002) Universal controllers for stabilization and tracking of underactuated ships. *Syst Control Lett* 47:299–317
7. Do KD, Pan J (2006) Robust path-following of underactuated ships: theory and experiments on a model ship. *Ocean Eng* 33:1354–1372
8. Pomet JB, Praly L (1992) Adaptive nonlinear regulation: estimation from the Lyapunov equation. *IEEE Trans Autom Control* 37:729–740
9. Do KD, Jiang ZP, Pan J (2004) Robust adaptive path following of underactuated ships. *Automatica* 40:929–944

10. Do KD, Pan J (2006) Global robust adaptive path following of underactuated ships. *Automatica* 42:1713–1722
11. Do KD, Pan J (2005) Global tracking control of underactuated ships with nonzero off-diagonal terms in their system matrices. *Automatica* 41:87–95
12. Ghommam J, Mnif F (2009) Coordinated path-following control for a group of underactuated surface vessels. *IEEE Trans Ind Electron* 56(10):3951–3963
13. Fan JS, Zhang HX et al (2012) Quasi-continuous higher-order sliding mode control for attitudes of re-entry vehicle. *Control Theory Appl* 29(7):841–846
14. Evangelista C, Puleston P, Valenciaga F, Fridman LM (2013) Lyapunov-Designed Super-Twisting Sliding Mode Control for Wind Energy Conversion Optimization. *IEEE Trans Ind Electr* 60(2):538–545
15. McNinch LC, Ashrafiuon H (2011) Predictive and sliding mode cascade control for unmanned surface vessels. In: 2011 American control conference on O'Farrell Street, San Francisco, CA, USA, 184–189, June 29–July 01, 2011
16. Levant A (2005) Quasi-continuous high-order sliding-mode controllers. *IEEE Trans Autom Control* 50(11):1812–1816
17. Levant A (2005) Homogeneity approach to high-order sliding mode design. *Automatica* 41(4):823–830
18. Levant A (2007) Finite differences in homogeneous discontinuous control. *IEEE Trans Autom Control* 52(7):1208–1217
19. Xiaoming H (2008) High-order sliding control of nonlinear affine control systems. *J Acta Autom Sinica* 28(2):284–289
20. Lin Z, Duan G (2010) Research on sliding mode control for underactuated rigid spacecraft attitude maneuver. *J Control Decis* 25(3):389–393

Chapter 63

Modeling and Simulation of Biomimetic Motion Dynamics for Dexterous Hand

Mingkun Zhang, Yizhi Shi, Jun Shen and Yao Li

Abstract Analysis of kinematics and dynamics of the BarrettHand BH8 is implemented. Forward kinematic, inverse kinematic and differential kinematic model of one finger are established. Workspace of the fingertip and inverse kinematic examples are simulated and the analytical solution of inverse kinematics is obtained. The dynamic modeling and motion simulation of the dexterous hand finger are performed by SimMechanics toolbox in Matlab/Simulink environment. The results indicate that the proposed simulation method is effective in analyzing designing complex biomimetic motion dynamics for dextrous hand.

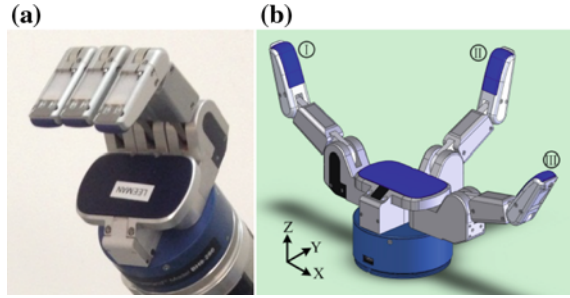
Keywords Dexterous hand · Biomimetic motion dynamics · Lagrangian method · SimMechanics

63.1 Introduction

Biomimetic robot today is a key research area in robotics, while the design of end effector largely determines the flexibility and sophistication of a robot when performing tasks. So far, many dexterous hands have been developed where mechanics, electronics and intelligent control are integrated, such as Gifu II hand [1], Shadow five fingers humanoid hand [2], HIT/DLR II hand [3]. These dexterous hands not only have multi-fingers with multi-degrees of freedom, but also have various sensors, such as position, force and torque. These features greatly enhance the intelligence of dexterous hand.

M. Zhang · Y. Shi · J. Shen · Y. Li (✉)
Intelligent Neural Mechatronics Center, Chongqing Institute of Green and Intelligent Technology of Chinese Academy Sciences, 10th floor, block B of Hon Kwok Centre in Jin Yu Road No. 85, Yubei District, Chongqing 401122, China
e-mail: yaoli@cigit.ac.cn

Fig. 63.1 BarrettHand BH8-280. **a** Physical picture. **b** SolidWorks model



BarrettHand series from Barrett technology [4] are mainly for teaching and scientific research and medical applications. As shown in Fig. 63.1, BarrettHand BH8-280 has three fingers, two of which (I and III) are 3-DOF fingers that can realize side swing and flexion movements, the other one (II) is a 2-DOF finger which can only realize flexion movement. The fingers of this hand have force and torque sensors, which assist research in tactile feedback control and humanoid postural regulator [5, 6]. Before this research, we need to establish the mathematical and computer simulation model of this dexterous hand to test and observe the motion behavior in different conditions.

CAD and CAE technologies have been widely used in robot design and test nowadays. Computer modeling and simulation can resolve the complex mechanical structure and verify the mechanical structure design and motion planning accurately and quickly [7].

In this article, BarrettHand model is built by SolidWorks. Finger I and III are set along the direction of X-axis while finger II is along Y-axis (Fig. 63.1b). Then, forward kinematics, inverse kinematics, differential kinematics and dynamics are established, workspace and kinematic examples of single finger are simulated. Finally, SimMechanics model for dynamic analysis is built, and the torque of each joint is calculated when fingertip doing dexterous spiral movement.

63.2 Mathematical Modeling

63.2.1 Forward Kinematics

Coordinate system of this dexterous hand is generated in D–H method [8], so homogeneous transformation matrix of adjacent joints can be written as

$$\begin{aligned}
 A_i^{i-1} &= Trans_z(d_i)Rot_z(\theta_i)Trans_x(a_i)Rot_x(\alpha_i) \\
 &= \begin{pmatrix} c\theta_i & -c\alpha_i s\theta_i & s\alpha_i s\theta_i & a_i c\theta_i \\ s\theta_i & c\alpha_i c\theta_i & -s\alpha_i c\theta_i & a_i s\theta_i \\ 0 & s\alpha_i & c\alpha_i & d_i \\ 0 & 0 & 0 & 1 \end{pmatrix} \quad (63.1)
 \end{aligned}$$

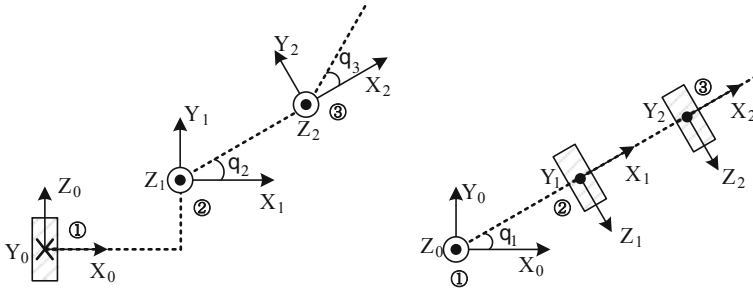


Fig. 63.2 Front view (left) and top view (right) of finger III D–H coordinate

Table 63.1 D–H values of finger III

Joint No.	a_i (mm)	d_i (mm)	α_{i-1} (°)	θ_i (°)
1	$a_1 = 50$	$d_1 = 33.5$	$\alpha_0 = 0$	$\theta_1 \in [-90, 90]$
2	$a_2 = 70$	$d_2 = 0$	$\alpha_1 = 90$	$\theta_2 \in [0, 140]$
3	$a_3 = 56$	$d_3 = 0$	$\alpha_2 = 0$	$\theta_3 \in [45, 90]$

in which i represents joint number, c and s represent cosine and sine separately.

Figure 63.2 shows joint rotations of finger III in view of Y-axis and Z-axis. \times or \bullet represents the forward direction of an axis perpendicular to the page inward or outward respectively. Joint number from bottom to top is ①, ② and ③, the D–H parameters are shown in Table 63.1. The forward kinematics of each finger is the product of three transformation matrices of adjacent joints, take finger III for example

$$A_3^0 = A_1^0 \cdot A_2^1 \cdot A_3^2 = \begin{pmatrix} c_1c_{2+3} & -c_1s_{2+3} & s_1 & c_1(a_1 + a_2c_2 + a_3c_{2+3}) \\ s_1c_{2+3} & -s_1s_{2+3} & -c_1 & s_1(a_1 + a_2c_2 + a_3c_{2+3}) \\ s_{2+3} & c_{2+3} & 0 & a_3s_{2+3} + a_2s_2 + d_1 \\ 0 & 0 & 0 & 1 \end{pmatrix} \tag{63.2}$$

In which $s_i = \sin\theta_i$, $c_i = \cos\theta_i$, $s_{i+j} = \sin(\theta_i + \theta_j)$, $c_{i+j} = \cos(\theta_i + \theta_j)$. The forward kinematic equations of the finger are

$$x = \cos\theta_1[a_1 + a_2\cos\theta_2 + a_3\cos(\theta_2 + \theta_3)] \tag{63.3}$$

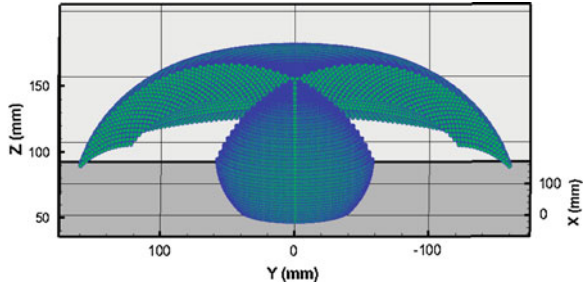
$$y = \sin\theta_1[a_1 + a_2\cos\theta_2 + a_3\cos(\theta_2 + \theta_3)] \tag{63.4}$$

$$z = a_3\sin(\theta_2 + \theta_3) + a_2\sin\theta_2 + d_1 \tag{63.5}$$

Similarly, the forward kinematics of finger I and II are available.

Substitute the parameters of Table 63.1 into Eqs. (63.3)–(63.5), we can calculate the workspace of finger III with Matlab, as shown in Fig. 63.3.

Fig. 63.3 Workspace of finger III



63.2.2 Inverse Kinematics

In order to achieve the desired hand posture, we need to derive the inverse kinematic solution to determine the joint angles. With the analytic method, from Eqs. (63.3) and (63.4) we obtain

$$\theta_1 = \tan^{-1} \frac{y}{x} \tag{63.6}$$

θ_2 can be expressed as

$$\theta_2 = \pm \tan^{-1} \left(\frac{C}{\sqrt{A^2 + B^2 - C^2}} \right) - \tan^{-1} \frac{B}{A} \tag{63.7}$$

in which $A = 2(z - d_1)a_2$, $B = 2(x/\cos\theta_1 - a_1)a_2$, $C = (x/\cos\theta_1)^2 + a_2^2 + (z - d_1)^2 - a_3^2$.

While θ_3 is:

$$\theta_3 = \sin^{-1} \left(\frac{z - a_2 \sin\theta_2 - d_1}{a_3} \right) - \theta_2$$

or $\theta_3 = - \sin^{-1} \left(\frac{z - a_2 \sin\theta_2 - d_1}{a_3} \right) - \theta_2 + \pi$ (63.8)

Motions of finger III along the three axes with a speed of 20 mm/s are simulated using the results of Eqs. (63.6)–(63.8). Firstly, uniform motion of the fingertip from $x = 100$ to $x = 0$ is simulated in $y = 0$, $z = 130$ plane (Fig. 63.4); then uniform motion from $y = -50$ to $y = 50$ is simulated in $x = 100$, $z = 110$ plane (Fig. 63.5); finally, fingertip motion from $z = 130$ to $z = 110$ is simulated in $x = 100$, $y = 0$ plane (Fig. 63.6). The results accurately show the angle changes of each joint according to the predetermined motion of the fingertip.

63.2.3 Differential Kinematics

Jacobian matrix $J(\theta)$ is the relationship between joint space velocity and task space velocity which can be expressed as follows:

Fig. 63.4 Fingertip motion along X-axis

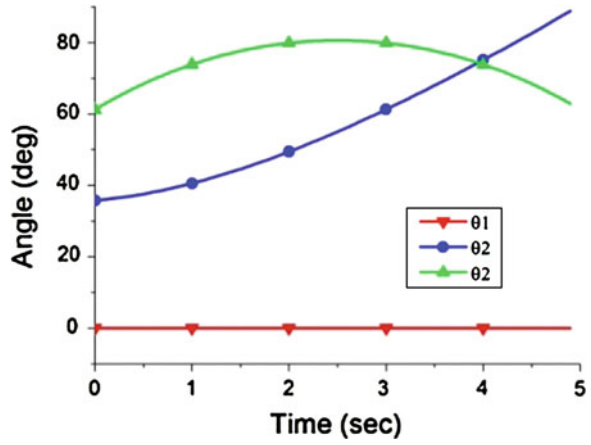


Fig. 63.5 Fingertip motion along Y-axis

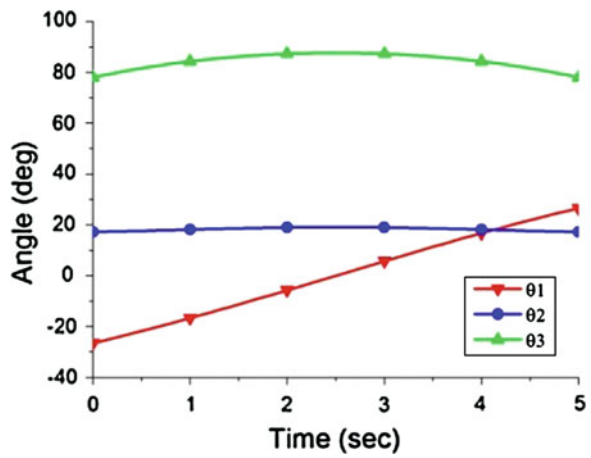
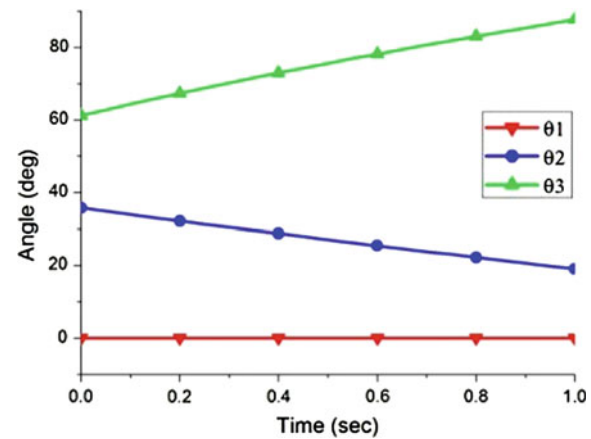


Fig. 63.6 Fingertip motion along Z-axis



$$[\dot{x} \quad \dot{y} \quad \dot{z}]^T = J(\theta) \cdot [\dot{\theta}_1 \quad \dot{\theta}_2 \quad \dot{\theta}_3]^T \quad (63.9)$$

From Eqs. (63.3) to (63.5) we obtain

$$J(\theta) = \begin{pmatrix} -s_1(a_1 + a_2c_2 + a_3c_{2+3}) & -c_1(a_2s_2 + a_3s_{2+3}) & -a_3c_1s_{2+3} \\ c_1(a_1 + a_2c_2 + a_3c_{2+3}) & -s_1(a_2s_2 + a_3s_{2+3}) & -a_3s_1s_{2+3} \\ 0 & a_2c_2 + a_3c_{2+3} & a_3c_{2+3} \end{pmatrix} \quad (63.10)$$

In which $s_i = \sin\theta_i$, $c_i = \cos\theta_i$, $s_{i+j} = \sin(\theta_i + \theta_j)$, $c_{i+j} = \cos(\theta_i + \theta_j)$.

63.2.4 Dynamics

From joint angular, angular velocity and angular acceleration corresponding to a motion trajectory, joint torque can be obtained through dynamic equations. Generally, Lagrange method and Euler method are used to study robot dynamics. Here, we select Lagrange method [9]. For any mechanical system, Lagrange equation can be written as

$$\tau = \frac{d}{dt} \left(\frac{\partial L}{\partial \dot{\theta}} \right) - \frac{\partial L}{\partial \theta} \quad (63.11)$$

in which τ is joint torque; t is time; θ is joint angle; Lagrange function L is the difference of total kinetic energy E_k and total potential energy E_p , $L = E_k - E_p$. For this model, total kinetic energy E_k of a finger is the sum of the kinetic energy of three fingers' segments. The kinetic energy of each finger segment is the sum of the energy produced by line velocity of the centroid and the angular velocity around the centroid, which can be expressed as

$$E_k = \sum_{i=1}^3 E_{ki} = \sum_{i=1}^3 \left(\frac{1}{2} m_i v_{ci}^T v_{ci} + \frac{1}{2} J_{ci} \omega_{ci}^T \omega_{ci} \right) \quad (63.12)$$

in which m_i is the mass of each finger segment; J_{ci} is the moment of inertia to the centroid of each finger segment; ω_{ci} is the angular velocity around the centroid of each finger segment, $\omega_{ci} = [\omega_{ci,X} \quad \omega_{ci,Y} \quad \omega_{ci,Z}]^T$; v_{ci} is the line velocity of each finger segment, $v_{ci} = [v_{ci,X} \quad v_{ci,Y} \quad v_{ci,Z}]^T$, each coordinate component can be obtained through the time derivative of the centroid coordinates

$$v_{ci} = [v_{ci,X} \quad v_{ci,Y} \quad v_{ci,Z}]^T = [\dot{x}_c \quad \dot{y}_c \quad \dot{z}_c]^T \quad (63.13)$$

Total potential energy of the model is

$$E_p = \sum_{i=1}^3 E_{pi} = m_i g h_{ci} \quad (63.14)$$

in which h_{ci} is the distance between centroid of each finger segment and zero potential energy surface. According to Eq. (63.11), joint torque can be calculated as

$$\tau = M(\theta) \cdot \ddot{\theta} + C(\theta, \dot{\theta}) + G(\theta) \quad (63.15)$$

In which $M(\theta)$ is the $n \times n$ positive definite symmetric matrix, known as the inertia matrix of finger segment; $C(\theta, \dot{\theta})$ is the $n \times 1$ centrifugal force and Coriolis force vector; $G(\theta)$ is the gravity vector.

Take finger III as an example, let l_i be the length between the left and right side axes of each finger segment; l_{ci} be the length between the left side axis and the centroid of each finger segment; τ_i is the torque of each axis marked ①, ② and ③ in Fig. 63.2. Take the X–Y plane which crosses the centroid of segment ① as the zero potential energy plane, the dynamic equations can be written as

$$\begin{pmatrix} \tau_1 \\ \tau_2 \\ \tau_3 \end{pmatrix} = \begin{pmatrix} M_{11} & 0 & 0 \\ 0 & M_{22} & M_{23} \\ 0 & M_{32} & M_{33} \end{pmatrix} \begin{pmatrix} \ddot{\theta}_1 \\ \ddot{\theta}_2 \\ \ddot{\theta}_3 \end{pmatrix} + \begin{pmatrix} C_1 \\ C_2 \\ C_3 \end{pmatrix} + \begin{pmatrix} 0 \\ G_2 \\ G_3 \end{pmatrix} \quad (63.16)$$

in which

$$M_{11} = m_1 l_{c1}^2 + m_2 (l_1^2 + 2l_1 l_{c2} \cos \theta_2 + l_{c2}^2 \cos^2 \theta_2) + m_3 \{ l_1^2 + 2l_1 l_2 \cos \theta_2 + l_2^2 \cos^2 \theta_2 + l_{c3} \cos(\theta_2 + \theta_3) [2l_1 + 2l_2 \cos \theta_2 + l_{c3} \cos(\theta_2 + \theta_3)] \} + J_{c1} + J_{c2} + J_{c3}$$

$$M_{22} = m_2 l_{c2}^2 + m_3 (l_2^2 + l_{c3}^2 + 2l_2 l_{c3} \cos \theta_3) + J_{c2} + J_{c3}$$

$$M_{23} = m_3 l_{c3} (l_2 \cos \theta_3 + l_{c3}) + J_{c3}$$

$$M_{32} = M_{23}$$

$$M_{33} = m_3 l_{c3}^2 + J_{c3}$$

$$C_1 = - \{ 2m_2 l_{c2} \sin \theta_2 (l_1 + l_{c2} \cos \theta_2) + 2m_3 \{ l_1 l_2 \sin \theta_2 + l_2^2 \sin \theta_2 \cos \theta_2 + l_2 l_{c3} \sin(2\theta_2 + \theta_3) + l_{c3} \sin(\theta_2 + \theta_3) [l_1 + l_{c3} \cos(\theta_2 + \theta_3)] \} \} \cdot \dot{\theta}_1 \dot{\theta}_2$$

$$C_2 = \{ m_2 l_{c2} \sin \theta_2 (l_1 + l_{c2} \cos \theta_2) + m_3 \{ l_1 l_2 \sin \theta_2 + l_2^2 \sin \theta_2 \cos \theta_2 + l_2 l_{c3} \sin(2\theta_2 + \theta_3) + l_{c3} \sin(\theta_2 + \theta_3) [l_1 + l_{c3} \cos(\theta_2 + \theta_3)] \} \} \cdot \dot{\theta}_1^2 - m_3 l_2 l_{c3} \sin \theta_3 \cdot \dot{\theta}_3^2$$

$$- 2m_3 l_2 l_{c3} \sin \theta_3 \cdot \dot{\theta}_2 \dot{\theta}_3$$

$$C_3 = m_3 l_{c3} \sin(\theta_2 + \theta_3) [l_1 + l_2 \cos \theta_2 + l_{c3} \cos(\theta_2 + \theta_3)] \cdot \dot{\theta}_1^2 + m_3 l_2 l_{c3} \sin \theta_3 \cdot \dot{\theta}_2^2$$

$$G_2 = m_2 g l_{c2} \cos \theta_2 + m_3 g [l_2 \cos \theta_2 + l_{c3} \cos(\theta_2 + \theta_3)]$$

$$G_3 = m_3 g l_{c3} \cos(\theta_2 + \theta_3).$$

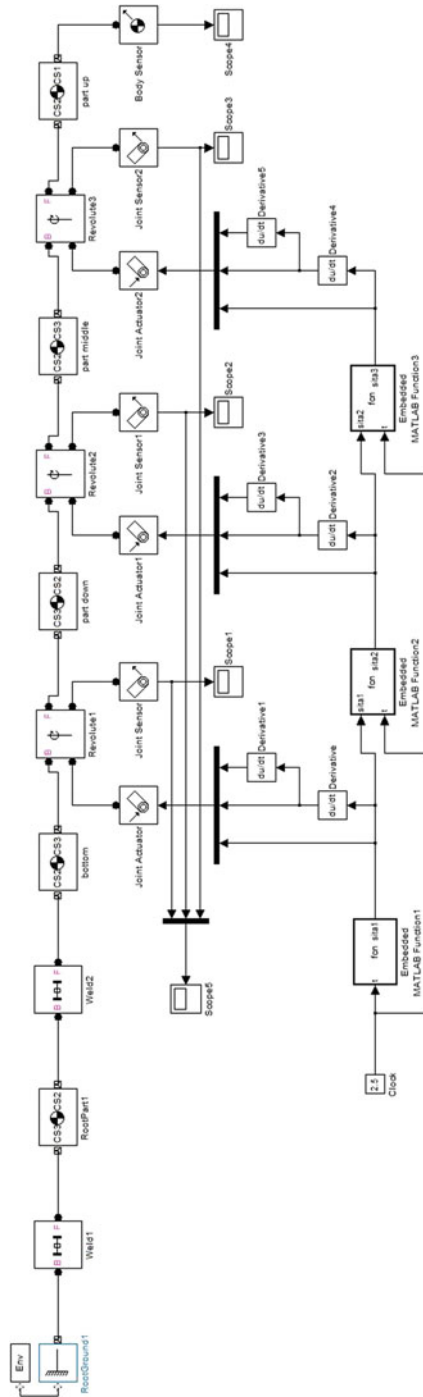
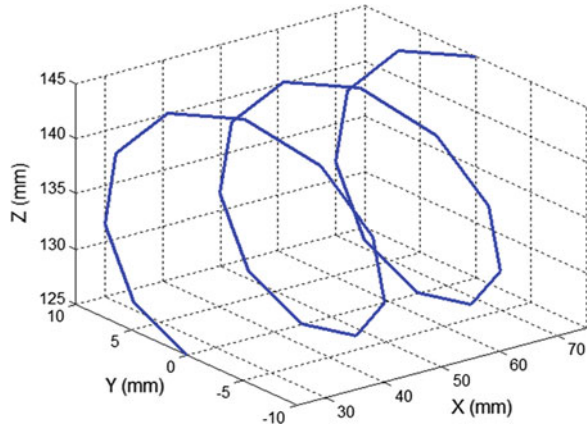


Fig. 63.7 SimMechanics model

Fig. 63.8 Spiral motion of the fingertip



63.2.5 SimMechanics Model and Dynamics Simulation

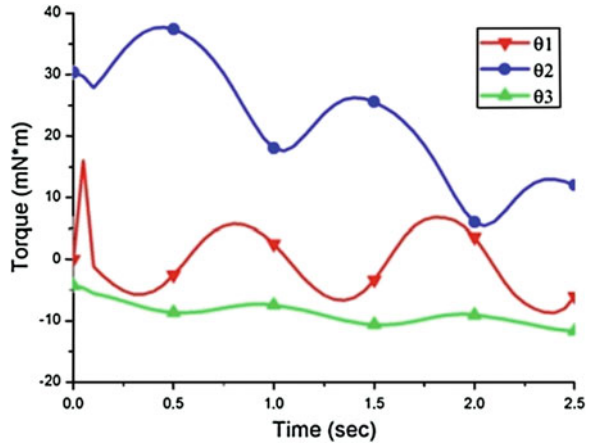
SimMechanics [10] is a module of Simulink in Matlab, which is mainly used for mechanical system modeling and simulation. Connecting rods, joints and other mechanical parts are expressed as abstract module in SimMechanics. We only need to connect these modules with lines and set the quality, inertia and coordinate system etc., of each module, then we can get a complete model of the mechanical system, which clearly expresses the geometric and kinematic relations of all parts. SoildWorks and SimMechanics can build interface, save a SoildWorks model as an XML file and open it in Matlab, we will generate the SimMechanics model which inherits all the physical parameters of the mechanism, such as size, mass, inertia etc. [11]. In addition, actuator and sensor modules need to be added to complete the SimMechanics dynamic model of finger III as shown in Fig. 63.7 [12]. The control mode is to apply motion signal to each rotary joint.

Spiral motion of the fingertip is simulated by SimMechanics model (see Fig. 63.7). The spiral expression is

$$\begin{cases} x = 75 - 20 \cdot t \\ y = 10 \sin(2\pi \cdot t) \\ z = 135 + 10 \cos(2\pi \cdot t) \end{cases} \quad (63.17)$$

in which t is the time. The corresponding angle change is obtained through the inverse kinematic Eqs. (63.6)–(63.8), and the result is set to SimMechanics model to run a simulation of 2.5 s. Figure 63.8 is the trajectory of the fingertip which is in full accordance with the predetermined trajectory. Figure 63.9 shows the variation of each joint torque with simulation time.

Fig. 63.9 Variation of each joint torque with time



63.3 Conclusion

The dynamic and kinematic modeling and simulation of the BarrettHand BH8 were carried out. Firstly, forward kinematic model was established and the workspace of a finger was simulated. Secondly, analytical solution of inverse kinematics was derived, and three typical motions were simulated, which proves the algorithm. Thirdly, dynamics was established by using Lagrange method. Finally, SimMechanics model was established in Matlab/Simulink environment, and spiral motion of a finger was simulated. The result shows that the fingertip is able to exercise completely according to a predetermined trajectory; each joint torque in motion was obtained at the same time.

Acknowledgments This work was supported by the foundation of Chongqing Key Technologies R&D Project (No.cstc2012ggC10001) of the Chongqing Municipal Science and Technology Commission.

References

1. Kawasaki H, Komatsu T, Uchiyama K (2002) Dexterous anthropomorphic robot hand with distributed tactile sensor: Gifu hand II. *IEEE/ASME Trans Mechatron* 7(3):296–303
2. Walkler R (2004) Developments in dextrous hands for advanced robotic applications. In: *Robotics: trends, principles, and applications. Proceedings of the sixth biannual world automation congress*, pp 123–128
3. Liu H, Meusel P, Hirzinger G, Jin MH, Liu YW, Xie ZW (2008) The modular multisensory DLR-HIT-Hand: hardware and software architecture. *IEEE/ASME Trans Mechatron* 13(4):461–469
4. William T (2000) The BarrettHand grasper—programmably flexible part handling and assembly. *Ind Rob: Int J* 27(3):181–188

5. Li Y, Levine WS (2009) An optimal control model for human postural regulation. Am Control Conf 4705–4710
6. Li Y, Levine WS, Yang YH, He CQ (2011) A nonlinear optimal human postural regulator. Am Control Conf 5420–5425
7. Qiu SY, Wu HT, Liu HB (2011) The modeling design and simulation of pastry slicer based on SolidWorks. Mechatronics 17(4):89–93 (in Chinese)
8. Denavit J, Hartenberg RS (1955) A kinematic notation for lower- pair mechanism based on matrices. ASME J Appl Mech 6:215–221
9. Huo W(2005) Robot dynamics and control. Higher Education Press, Beijing (in Chinese)
10. The MathWorks Inc (2011) SimMechanics User's Guide
11. Ge T, Wang HM, Yf Lu (2011) Research on the interface of CAD software and Matlab/SimMechanics. Mech Electr Inf 24:201–202 (in Chinese)
12. Yuan SQ, Liu Z, Li XS (2008) Modeling and simulation of robot based on Matlab/SimMechanics. Chin Control Conf 161–165

Chapter 64

Nonlinear Integrator Sliding Mode Control for Brushless Double-Fed Wind Power Generation System

Zongkai Shao, Jichen Hu and Guoyong Huang

Abstract To deal with the problem of variable-speed constant-frequency brushless-fed wind power generation system suffering from the uncertainties of wind energy, the maximum wind energy tracking problem is transformed into the speed control concept of the generator based on analysis of the wind turbine operation characteristics. A nonlinear integrator sliding mode control strategy is proposed to realize the maximum wind energy tracking. To promote the performance of the traditional integral sliding mode control, this approach uses a nonlinear saturation function which enhances small errors and will be saturated with large errors. The approach enables the system to be better in robustness against parameters uncertainties. Finally, simulation studies are provided to confirm the performance and the effectiveness of the proposed control approach.

Keywords Brushless doubly-fed machine · Sliding mode control · Nonlinear integrator · Variable speed constant frequency

64.1 Introduction

Wind power is a clean and reusable energy. Many researchers have paid very close attention to this area. Wind power generation technologies have gotten notable improvement since 1980 [1–3]. When wind power generation works connected with power grid, the output frequency of generation must be accordant with the frequency of grid. Using the generated method of variable speed constant frequency (VSCF) technology can improve the use ratio of wind power [4–6]. When use VSCF technology in wind power generation field, brushless double-fed

Z. Shao (✉) · J. Hu · G. Huang
Faculty of Information Engineering and Automation, Kunming University of Science and Technology, No 727 JingMing South Road, Cheng Gong, Kunming City, China
e-mail: hgmy@sina.com

machine(BDFM) has broader application prospects than double-fed induction generator(DFIG). The reason is that BDFM has no brush and slip ring and is simple in construction and reliable.

One of the core technologies of wind power generation field is maximum power-point tracking (MPPT) problem nowadays. The MPPT technology can improve the converted efficiency of wind power. The BDFM using VSCF technology can realize MPPT. It is necessary to use modern control method to BDFM for BDFM is uncertain and has unmolded dynamics. Many researchers focus on the control strategy to MPPT. Fuzzy control, vector control, adaptive control has been used to this field. Sliding mode control is one of the most effective methods in BDFM control scheme. The traditional sliding mode control has the shortcomings of convergence slowly, weak robustness. A nonlinear integrator sliding mode control is proposed to MPPT. This scheme promises fast tracking speed and strong robustness against traditional integrator sliding mode control.

The paper is organized as follows. The analysis of wind power generation and its control model are given in Sect. 64.2. A nonlinear integral sliding mode control is designed in Sect. 64.3. As comparison, the example from [3] is given to illustrate the results of the proposed controller in Sect. 64.4. Finally, the paper is concluded in Sect. 64.5.

64.2 Analysis of Wind Power Generation

From the aerodynamics of wind power machine, the input power is

$$p_m = 1/2\rho S_w v^3 \tag{64.1}$$

where ρ is air density, S_w is the area of sweeping of wind power machine against the wind, v is the wind velocity.

The output power is

$$p_0 = C_p p_m \tag{64.2}$$

where C_p is the power coefficient of wind power machine, and the function of tip velocity ratio λ and blade pitch Angle β

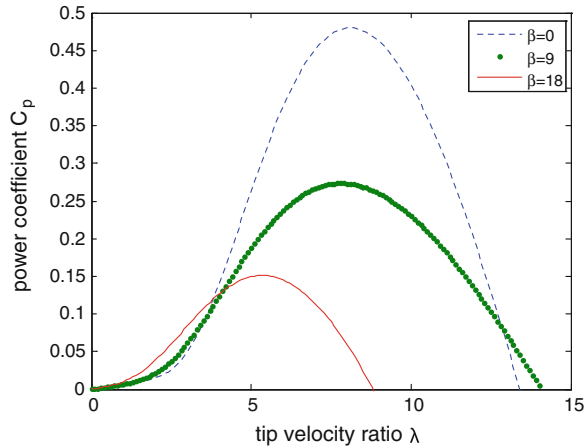
$$C_p(\lambda, \beta) = 0.5176\left(\frac{116}{\lambda_i} - 0.4\beta - 5\right)e^{-\frac{21}{\lambda_i}} + 0.0068\lambda$$

$$\frac{1}{\lambda_i} = \frac{1}{\lambda + 0.08\beta} - \frac{0.035}{\beta^3 + 1}, \lambda = \frac{\omega_n R}{v} \tag{64.3}$$

↑where ω_n is the angular velocity of wind power machine, R is the paddle radius of wind power machine.

From Eq. (64.3), the curves of $C_p-\lambda$ under the variation of β can be plotted as Fig. 64.1 is given.

Fig. 64.1 Curves of $C_p-\lambda$



From Eqs. (64.1)–(64.3), it can be summarized that the output power of wind power machine is only related to its angular velocity when the blade pitch Angle and the wind velocity are constants. The wind power machine is connected with BDFM through gear box whose speed increasing ratio N , then $\omega_r = N\omega_m$. The optimal rotate speed of generation is given by

$$n_{ropt} = \frac{60}{2\pi} \omega_{ropt} = \frac{60}{2\pi} N \frac{v\lambda_{opt}}{R} \tag{64.4}$$

where n_{ropt} is the optimal rotate speed of generation, ω_r is the angular velocity of generation, ω_m is the angular velocity of wind power machine. From Eqs (64.3)–(64.4), the MPPT is achieved when the rotate speed of generation tracks the wind velocity. It is said that the generation run on the optimum rotate speed.

64.3 Sliding Model Control Design

The BDFM model is shown as Eq. (64.5) when the power winding uses d-q coordinate.

$$T_e = \frac{3}{2}(p_p + p_c)\Psi_{dp}i_{qc} = J \frac{d\omega_r}{dt} + K_d\omega_r + T_l \tag{64.5}$$

where p_p, p_c are the numbers of electric pole of power winding and control winding, Ψ_{dp} is the d-axis flux linkage of power winding, i_{qc} is the q-axis current of control winding, J is the mechanical inertia of rotor, K_d is rolling damping ratio, T_e is total magnetic torque, T_l is load torque.

From (64.5), when the control is considered, the dynamics of BDFM is

$$\dot{\omega}_r = -a\omega_r + bu \tag{64.6}$$

where u is the control, $a = K_d/J, b = 1/J$.

The task of this section is to develop a sliding mode controller. To realize MPPT, the controller should be robust to the wind disturbances. The nonlinear integral sliding mode surface is proposed as [7]

$$\begin{cases} s = e + k_p \int_0^t e d\tau + k_I \sigma = 0 \\ \dot{\sigma} = g(e) \end{cases} \tag{64.7}$$

where s denotes the switch function, e is the error, k_p, k_I are positive design parameters, $g(e)$ is a nonlinear function with the property of amplifying little error and saturating big error. For analysis $g(e)$ simply, $G(e)$ is given as

$$G(e) = \begin{cases} \frac{2\beta^2}{\pi} (1 - \cos \frac{\pi e}{2\beta}), |e| < \beta \\ \beta e - \frac{\pi-2}{\pi} \beta^2, e \geq \beta \\ -\beta e - \frac{\pi-2}{\pi} \beta^2, e \leq -\beta \end{cases} \tag{64.8}$$

where β is a positive design parameter. Differentiating (64.8) with respect to e ,

$$g(e) = \begin{cases} \beta \sin \frac{\pi e}{2\beta}, |e| < \beta \\ \beta, e \geq \beta \\ -\beta, e \leq -\beta \end{cases} \tag{64.9}$$

From (64.8) and (64.9), lemma 1 is formulated as follow.

Lemma 1:

1. if $e \neq 0$, then $G(e) > 0$; if $e = 0$, then $G(e) = 0$ and $g(e) = 0$.
2. $g(e)$ is a strictly increase monotonically function when $|e| < \beta$; $g(e)$ saturates when $|e| \geq \beta$.

From lemma 1, it can be concluded that $|g(e)| \geq |e|$ when $|e| \leq \beta$; $|g(e)| < |e|$ when $|e| > \beta$. This property is called ‘amplifying little error and saturating big error’. By selecting β , the expect performance is gotten with respect to above property. For system (64.6), the nonlinear integrator sliding mode surface is designed as

$$\begin{cases} s_\omega = e_\omega + k_p \int_0^t e_\omega d\tau + k_I \sigma = 0 \\ \dot{\sigma} = g(e_\omega) \end{cases} \tag{64.10}$$

where $e_\omega = \omega_r - \omega_r^*$ denotes the angular velocity error, ω_r^* is the expect angular velocity. Considering uncertainties, Eq. (64.8) can be rewritten as

$$\dot{\omega}_r = -(a + \Delta a)\omega_r + bu + d(t) \tag{64.11}$$

where Δa is parameter uncertainties, $d(t)$ denotes the disturbance, and satisfied

$$|\Delta a| \leq C, |d(t)| \leq D(t) \tag{64.12}$$

Theorem 1 For system (64.11), the sliding mode surface is designed as (64.10) and the controller is (64.13), then the sliding mode surface (64.10) is reachable and $\lim_{t \rightarrow \infty} e_\omega = 0$.

Proof: Let the Lyapunov function candidate of the closed-system (64.11) be given by

$$V = \frac{1}{2} s^2 \quad (64.13)$$

Differentiating (64.14) yields

$$\begin{aligned} \dot{V} &= s\dot{s} \\ &= s(\dot{e}_\omega + k_P e_\omega + k_I g(e_\omega)) \\ &= s(\dot{\omega}_r - \dot{\omega}_r^* + k_P e_\omega + k_I g(e_\omega)) \end{aligned} \quad (64.14)$$

Substituting (64.11) and (64.13) into (64.15), yields

$$\begin{aligned} \dot{V} &= s(\dot{\omega}_r - \dot{\omega}_r^* + k_P e_\omega + k_I g(e_\omega)) \\ &= s(-\Delta a \omega_r + d(t) - (C|\omega_r| + D(t) + k)\text{sign}(s)) \\ &= -\Delta a \omega_r s + d(t)s - D(t)|s| - k|s| - C|\omega_r||s| \\ &\leq -k|s| \end{aligned} \quad (64.15)$$

Therefore,

$$s\dot{s} \leq -k|s| \quad (64.16)$$

Let t_r be the time when the sliding mode surface is reach. Then

$$t_r \leq \frac{|s(0)|}{k} \quad (64.17)$$

From (64.18), the sliding mode surface is reachable in finite time. The next step is to prove $\lim_{t \rightarrow \infty} e_\omega = 0$. If $t > t_r$, then $s=0$. That means

$$e_\omega + k_P \int_0^t e_\omega d\tau + k_I \sigma = 0 \quad (64.18)$$

Differentiating (64.19) yields

$$\dot{e}_\omega + k_P e_\omega + k_I \dot{\sigma} = 0 \quad (64.19)$$

The Lyapunov function candidate of (64.20) is given by

$$V = \frac{1}{2} e_\omega^2 + k_I G(e_\omega) \quad (64.20)$$

Differentiating (64.20) yields

$$\dot{V} = e_\omega \dot{e}_\omega + k_I g(e_\omega) \dot{e}_\omega \quad (64.21)$$

Substituting (64.20) into (64.22), yields

$$\begin{aligned} \dot{V} &= e_\omega (-k_P e_\omega - k_I \dot{\sigma}) + k_I g(e_\omega) \\ &= -k_P e_\omega^2 < 0 \text{ (when } e_\omega \neq 0) \end{aligned} \quad (64.22)$$

According to Lyapunov theorem

$$\lim_{t \rightarrow \infty} e_\omega = 0 \quad (64.23)$$

The proof is completed.

To eliminate the chattering, the term $|s|^{1/3} \text{sign}(s)$ is used to substitute for $\text{sign}(s)$ [8].

64.4 Simulation and Results

To demonstrate the validity of the suggested control scheme, a 6/2 poles BDFM is considered. Simulation parameters are given below. The synchronization rotate speed is 750 r/min, and the nominal power is 5 kw, and the nominal frequency is 50 Hz, and the nominal voltage is 380 V, $J_0 = 0.03 \text{kg} \cdot \text{m}^2$, $p_p = 3$, $p_c = 1$. The parameters of wind power machine are $R = 3 \text{m}$, $\beta = 0$. Then the optimal tip velocity ratio $\lambda_{opt} = 8.1$, the maximum power coefficient $C_{popt} = 0.48$. $N = 4.125$, $\rho = 1.29 \text{kg/m}^3$, the nominal wind velocity $v = 12 \text{m/s}$.

The initial wind velocity is 7m/s, then changes to 10m/s when $t = 5 \text{s}$. From (4), the optimal rotate speed of wind power machine changes from 750 r/min to 1064 r/min. Figure 64.2 is the curves of rotate speed of wind power machine tracking the changes of wind power when $d(t) = 0$. From Fig. 64.2, the response of rotate speed of wind power machine is fast and the settling time is short. Compare to the results in [3], the results using the proposed controller have no chattering when the wind velocity changes. Figure 64.3 is the response of BDFM rotate speed in the case that the mechanical inertia of rotor increase 100 % when $t = 10 \text{s}$. The curve is nearly invariant and has no overshoot which appears in [3]. Figure 64.4 is the response of BDFM rotate speed in the case that the wind velocity varies randomly and $d(t) = \sin(t)$. The closed system recovers stability rapidly when the model is varying and the disturbance exists. From the results, it can be concluded that the closed system is robust. The character given above is the foundation of MPPT.

Fig. 64.2 Curve of BDFM rotate speed tracking wind velocity. **a** Wind velocity, **b** Rotate speed of generation

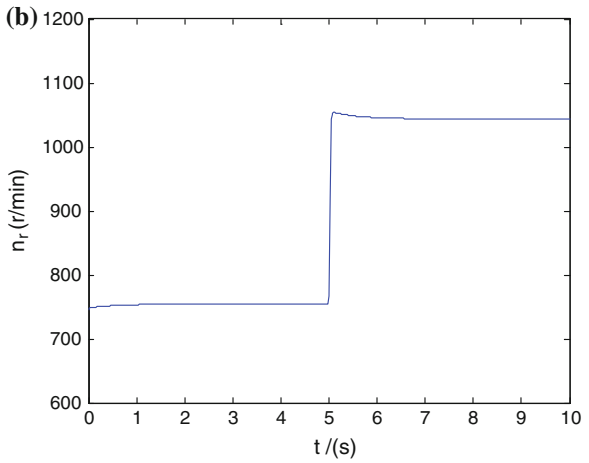
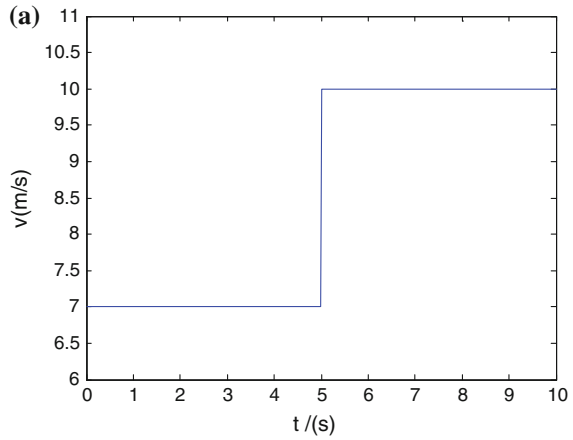


Fig. 64.3 Curve of BDFM rotate speed when exists disturbance

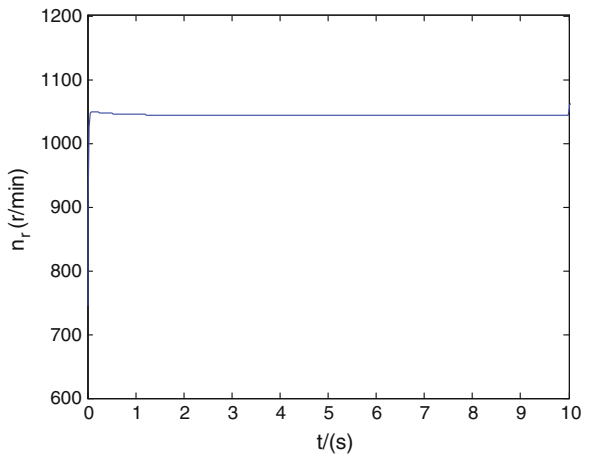
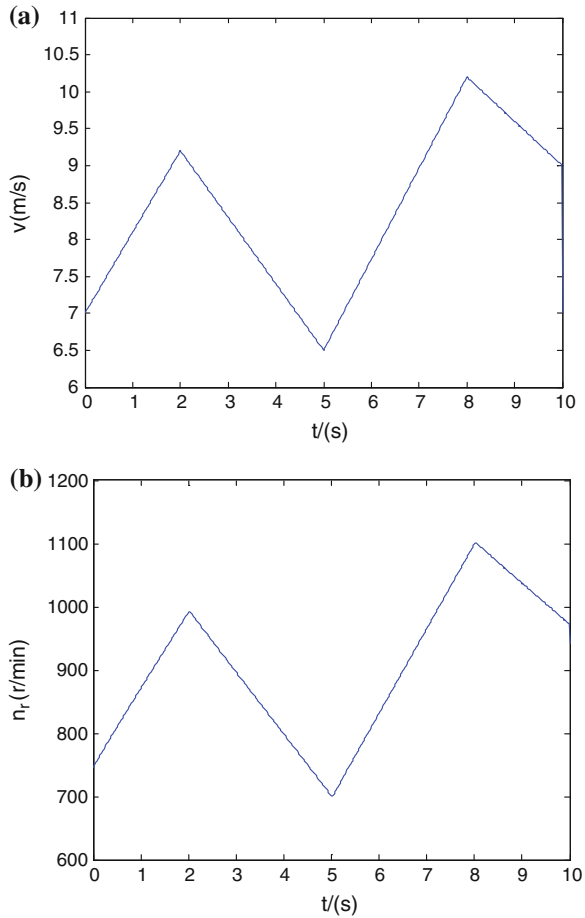


Fig. 64.4 Curve of BDFM rotate speed tracking random wind velocity. **a** Wind velocity, **b** Rotate speed of generation



64.5 Conclusions

The BDFM rotate speed tracks the wind velocity rapidly is the foundation of MPPT. The BDFM parameters are varying and uncertain because of the random and instability of wind speed. The nonlinear integrator sliding mode control is proposed. The nonlinear integrator sliding surface is design to eliminate the tracking error. The control law provides the design sliding surface is reachable. All performances are proved using Lyapunov theorem strictly. The simulation results have demonstrated that the designed scheme is robust to the variations of wind velocity and system parameters. At the same time, the BDFM rotate speed can track the wind velocity rapidly which provides the basis for MPPT.

Acknowledgments This paper is supported by Application Foundation Project of Yunnan Province of China (Grant No. 2011FZ036) and Foundation of Yunnan Educational Committee (Grant No. 2011Y386).

References

1. Wu GX, Huang JM et al (2008) A synthetic control strategy for DFIG wind power generation. *Electr Mach Control* 25(8):435–441 (in Chinese)
2. Yang YH, Hui J (2008) Control strategy realization of variable speed wind turbine with a brushless doubly-fed reluctance machine. *Electr Mach Control* 11(4):364–368 (in Chinese)
3. Zhang FQ, Jin S (2010) L_2 robust control for brushless double –fed wind doubly-fed power generation. *Electr Mach Control* 14(8):70–74 (in Chinese)
4. Frenandez LM, Garcia CA (2008) Comparative study on the performance of control systems for double fed induction generation wind turbines operating with power regulation. *Energy* 33(2):1438–1452
5. Miao ZX, Fan LL (2008) The art modeling and simulation of induction generator in wind generation applications using high-order model. *Simul Model Pract Theory* 16(5):1239–1253
6. Zheng XM, Li L et al (2010) Sliding-mode control of maximum power-point tracking in wind-power system for doubly-fed induction generator. *Control Theory Appl* 21(1):11–16 (in Chinese)
7. Li P, Zheng ZQ (2011) Sliding mode control approach with nonlinear integrator. *Control Theory Appl* 28(3):421–425 (in Chinese)
8. Huang GY (2011) Terminal sliding mode control based on neural network disturbance observer. *J Jilin Univ (Eng Ed)* 41(6):1726–1730 (in Chinese)

Chapter 65

Time-Varying Constant Identification Based on PSO and Dynamic Compensation of Temperature Sensors

Chao Wang, Yakun Zhao and Hongbing Ding

Abstract In this paper, a time-varying double-thermal-resistance model for discharge from a gas tank through solenoid valves was presented. Then a new intelligent identification method based on Particle Swarm Optimization (PSO) was proposed to identify the time constant of thermal resistance. Lastly, the sensor was dynamically compensated by Extended Kalman Filtering (EKF) reconstruction. Both simulation and experimental results confirmed that PSO is of the ability to track the variation of time constants accurately and efficiently.

Keywords PSO identification · Time-varying system · Time constant · Thermal resistance · Dynamic compensation

65.1 Introduction

Discharge method is one of most common methods to measure the flow-rate characteristics of pneumatic components. However, during the process of discharge, the tank is a complex and dynamic system, especially, the temperature in the tank changes rapidly [1]. The accuracy of temperature measurement influences the discharge method greatly. Generally, there exist two devices for industrial temperature measurement, namely thermocouple and thermal resistance. Thermocouple is of preferable dynamic performance but low accuracy while the dynamic performance of thermal resistance is poor due to large time constant but the accuracy is satisfying. In this paper, thermal resistance is applied for the temperature measurement. In order to improve the dynamic performance of

C. Wang (✉) · Y. Zhao · H. Ding
Tianjin Key Laboratory of Process Measurement and Control, School of Electrical Engineering and Automation, Tianjin University, No. 92, Weijin Road,
Tianjin 300072, China
e-mail: wangchao@tju.edu.cn

thermal resistance, a double-thermal-resistance system was established [2] and the corresponding model was presented. A new intelligent identification method based on PSO is proposed to estimate the time constant of thermal resistance.

In discrete time domain, the thermal resistance is generally described by a nonlinear difference equation [3]

$$T_m(k) = aT_m(k-1) + bT_g(k-1) \quad (65.1)$$

where T_g and T_m are the real temperature of gas and the temperature measured by sensor respectively namely input and output of the thermal resistance, τ is the time constant of sensor. $a = e^{-\tau_0/\tau}$, $b = 1 - a$, τ_0 is the sampling time. The time constant τ is influenced by numerous parameters. However, τ is mainly affected by the sensor wire diameter d , the gas velocity u and the gas density ρ_g . Thus, the time constant is approximately given by Eq. (65.2) [2]

$$\tau = \kappa d^{2-m} (u_g \rho_g)^{-m} \quad (65.2)$$

where, other parameters are lumped in the parameters κ and m ($0.3 \leq m \leq 0.7$) which almost stay unchanged for the thermal resistance system.

There exist numerous methods to identify the time constant for temperature sensors based on the first-order model. The most common method which was originally proposed by Pfriem [4] is to use two temperature sensors with different diameters installed as close as possible. The identified parameters are used to reconstruct the temperature sensor input and compensate for the high inertia and delay due to large sensor diameter. Methods for time constant identification and input reconstruction are available in both time domain [2, 3] and frequency domain [5]. In this paper, the research is in discrete time domain.

Since the noise interference cannot be neglected during the measurement, least square method (LS) is usually applied for parameter identification. When the noise is sufficiently high, total least squares method (TLS) is used instead of LS [3]. In order to realize online estimation, the recursive least squares (RLS) algorithm has been proposed and studied for several decades. In this paper, a new intelligent identification method based PSO, which is more easily implemented and requires less computational resources, is proposed. Both experimental and simulation results demonstrated that PSO is of the ability to track the time-varying parameters efficiently.

65.2 Time Constant Identification

Experimental data is firstly pre-processed using a sliding window method for smoothing before the identification is conducted. Then, time-varying model of double-thermal-resistance is presented and PSO is carried out to identify the time constant. Compared with the system identification using the genetic algorithm, the proposed method is easy to be implemented and requires less computational resources.

Based on the double-thermal-resistance method proposed by Pfriem, two thermal resistances with different diameters are used in the experiment [2]. According to Eq. (65.1), a double thermal resistance identification method using the Auto-regressive exogenous (ARX) model can be developed as follows.

$$\begin{cases} T_{m1}(k) = a_1 T_{m1}(k-1) + (1-a_1)T_g(k-1) \\ T_{m2}(k) = a_2 T_{m2}(k-1) + (1-a_2)T_g(k-1) \end{cases} \quad (65.3)$$

where, the subscripts 1, 2 represent the first and second sensor respectively. The real gas temperature T_g is assumed to be identical for both sensors.

Hung presented the Gamma method as Eq. (65.4) shows. But the three parameters γ_i lead to the problem of an over-determined system for the two unknown parameters a_1 and a_2 [6].

$$T_{m2}(k) = \gamma_1 T_{m2}(k-1) + \gamma_2 T_{m1}(k) + \gamma_3 T_{m1}(k-1) \quad (65.4)$$

where $\gamma_1, \gamma_2, \gamma_3$ are parameters as follows.

$$\gamma_1 = a_2, \quad \gamma_2 = (1-a_2)/(1-a_1), \quad \gamma_3 = a_1(1-a_2)/(1-a_1) \quad (65.5)$$

$T_{m1}(k)$ is regarded as the input variable and $T_{m2}(k)$ is chosen as the output variable. To overcome the over-determined problem, a new model called Beta model which has only two unknown parameters β, b_2 is carried out. Define β as below

$$\beta = b_2/b_1 = (1-a_2)/(1-a_1) \quad (65.6)$$

Equation (65.4) can be written as

$$Y = X\theta, \quad \begin{cases} Y = [T_{m2}(k) - T_{m2}(k-1)]^T \\ X = [T_{m1}(k) - T_{m2}(k-1) \quad T_{m1}(k-1) - T_{m2}(k-1)]^T \\ \theta = [\beta \quad b_2]^T \end{cases} \quad (65.7)$$

Thus, θ is the parameter which will be identified based on PSO. To ensure the validity of identification results, it is necessary to perform signal pre-conditioning before the time constant is identified. Data could be filtered using a low-pass filtering to minimize the effect of the noise on the signal in the reconstruction process. Nevertheless, it can cause a new lag into the online identification process meanwhile. Thus, a data smoothing method using a sliding window on data and fitting a curve to the data in this window by LS is applied.

PSO is a kind of evolutionary computation which was firstly proposed by Eberhart and Kennedy in 1995 [7]. From sharing the information of each particle of swarm which makes the motion of the total swarm well-organized in the search space, the optimal solution is obtained. Each particle represents a single potential solution. The particles evaluate their positions relative to the fitness at iteration, and companion particles share memories of their best positions, and then use these memories to adjust their own velocities and positions. Parameters including $x_i = (x_{i1}, x_{i2}, \dots, x_{in})^T$, $v_i = (v_{i1}, v_{i2}, \dots, v_{in})^T$, $f(x_i)$ and $P_i = (p_{i1}, p_{i2}, \dots, p_{in})^T$ are

the current position, current velocity, the current fitness of particle i respectively, and the optimal position where particle i reaches the maximum fitness respectively, where $i = 1, 2, \dots, s$ and s is the number of particles. To the minimization problem, the lower the value of the objective function is, the better the corresponding fitness is. $f(X)$ is defined as the minimized objective function. $P_g(t)$ is the optional position where all particles reach the maximum fitness.

$$P_g(t) = \min\{f[P_0(t)], f[P_1(t)], \dots, f[P_s(t)]\} \quad (65.8)$$

The particles interact and move according to the following equations

$$\begin{cases} v_{ij}(t+1) = w \cdot v_{ij}(t) + c_1 r_1(t) [p_{ij}(t) - x_{ij}(t)] + c_2 r_2(t) [p_{gj}(t) - x_{ij}(t)] \\ x_{ij}(t+1) = x_{ij}(t) + v_{ij}(t+1) \end{cases} \quad (65.9)$$

where, c_1 and c_2 are called the cognitive and social learning rates respectively which are both set as 2. r_1 and r_2 are two independent random functions which range from 0 to 1. To reduce the possibility which particles may fly out of the searching region during the iteration, v_{ij} is generally constrained to a certain scope and in this paper, v_{ij} is among $[-2, 2]$. The searching region is $[-2, 2; -2, 2]$ which is sufficiently large for the optimal solution.

Similar to the system identification based on genetic algorithm, the identification based on PSO is to convert the identification problem into optimization problem. Without loss of generality, the following ARX model is considered [8]

$$\left(1 + \sum_{i=1}^n a_i(t) z^{-i}\right) y(t) = \left(1 + \sum_{i=1}^n b_i(t) z^{-i}\right) u(t) + \eta(t) \quad (65.10)$$

where, t is discrete-time variable, $y(t)$ is the output of system, $u(t)$ is the input signal, $\eta(t)$ is white noise, $\eta(t)$ and $u(t)$ are independent with one another, z^{-1} is called "Delay Factor", namely $z^{-1}y(t) = y(t-1)$. Define parameter vector $\theta(t)$ as below.

$$\theta(t) = [a_1(t) \quad a_2(t) \quad \dots \quad a_n(t) \quad b_1(t) \quad b_2(t) \quad \dots \quad b_n(t)]^T \quad (65.11)$$

The target of on-line identification is to estimate the time-varying $\theta(t)$ with the input and output of the system. In this paper, the identified error is judged by the formula below.

$$J(\theta_h(t)) = \frac{1}{h} \sum_0^h \lambda^i [y(t-i) - \hat{y}(t-i)]^2 \quad (65.12)$$

where the forgetting factor λ is set as 0.9 invariantly, the sliding window width h is 20, the maximum identified error is set as 10^{-10} , the maximum iteration number is 2,000. In order to reduce the time of searching for optimal solution, the start of searching point is intelligently set as the value of the optimal solution for last searching.

When the time constant is identified, the sensor output can be compensated dynamically by input reconstruction. EKF is applied for input reconstruction [9]

$$x(k) = Ax(k-1) + v(k), \quad y(k) = Cx(k) + w(k) \quad (65.13)$$

where, $x(k) = Ax(k-1) + v(k)$, $y(k) = Cx(k) + w(k)$, $v(k)$ and $w(k)$ are the process and measurement noise respectively and assumed to be independent Gaussian noise, with the following prior statistics.

$$A = \begin{bmatrix} a_1 & 0 & b_1 \\ 0 & a_2 & b_2 \\ 0 & 0 & 1 \end{bmatrix}, \quad C = \begin{bmatrix} 1 & 0 & 0 \\ 0 & 1 & 0 \end{bmatrix} \quad (65.14)$$

The covariance matrices for the process noise and measurement noise Q, R can be calculated by

$$\begin{aligned} Ew &= 0, & Ev &= 0, & E[ww^T] &= 0 \\ E[ww^T] &= Q, & E[vv^T] &= R \\ Q &= \text{diag}([\sigma_{n1,model}^2 & \sigma_{n2,model}^2 & \sigma_{ng}^2]) & R &= \text{diag}([\sigma_{n1}^2 & \sigma_{n2}^2]) \end{aligned} \quad (65.15)$$

where, the system noise $\sigma_{n,model}^2$ is close to zero since the model (65.1) can characterize accurately the output of temperature sensors.

65.3 Numerical Simulation

Simulation is conducted to verify the validity of PSO identification. Firstly Simulink is carried out to generate the response of step signal with different time constants τ which simulates two thermal resistances with different wire diameters. As is evidently shown in Fig. 65.1, time constant τ changes abruptly (a) in the 50th second and τ changes gradually with time during the middle 100 s (b).

To simulate the real circumstances, white noise with standard deviation $\sigma = 0.01$ is added to T_m . PSO is carried out to identify those time constant of thermal resistance. The identified data are smoothed firstly to remove the big fluctuations due to noise disturbance. As is shown in Fig. 65.2, PSO can rapidly identify the right value of τ . When τ changes suddenly in Fig. 65.2a, PSO is of the ability to track the variation of τ swiftly, while in Fig. 65.2b, PSO also can well track the tendency of τ when two time constants change gradually.

After the time constant is obtained, EKF is applied for the input reconstruction. As is indicated in Fig. 65.3a, b, the reconstructed temperatures T_{g1}, T_{g2} can rapidly almost reach the exact value of simulated temperature T_g . In Fig. 65.4a, when time constant changes abruptly, small fluctuations appears, but T_{g1}, T_{g2} soon reach the exact T_g . When time constant changes gradually, the reconstructed temperature can still track T_g accurately.

As can be seen from the simulation above, PSO is of the ability to identify the accurate time constant rapidly and the reconstructed temperature can track the real temperature. Thus, the validity of identification based on PSO is confirmed.

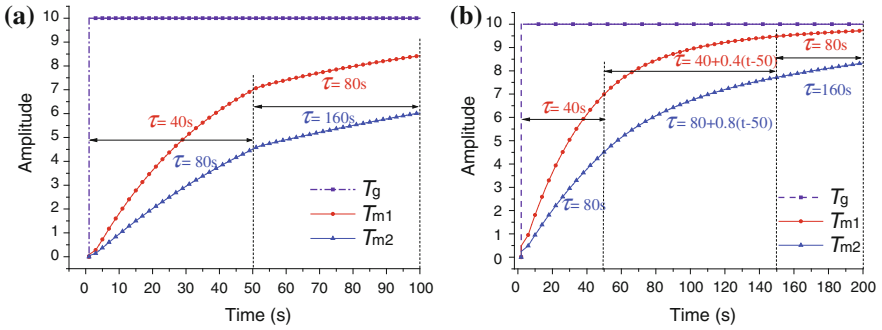


Fig. 65.1 Simulated temperature T_g with step change, response temperature T_{m1} , T_{m2} of τ . **a** τ with abrupt change. **b** τ with gradual change

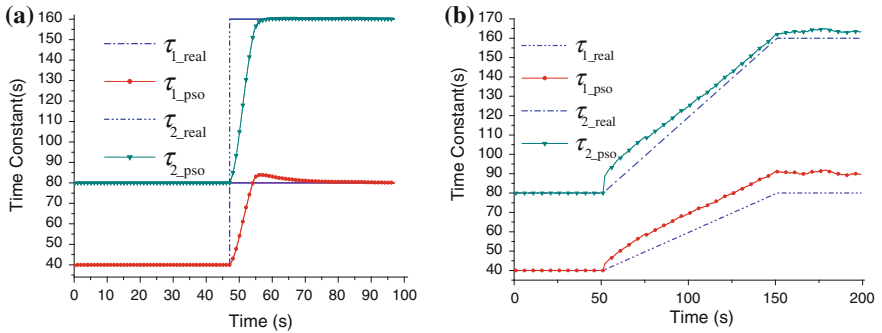


Fig. 65.2 PSO identification of τ . **a** τ with abrupt change. **b** τ with gradual change

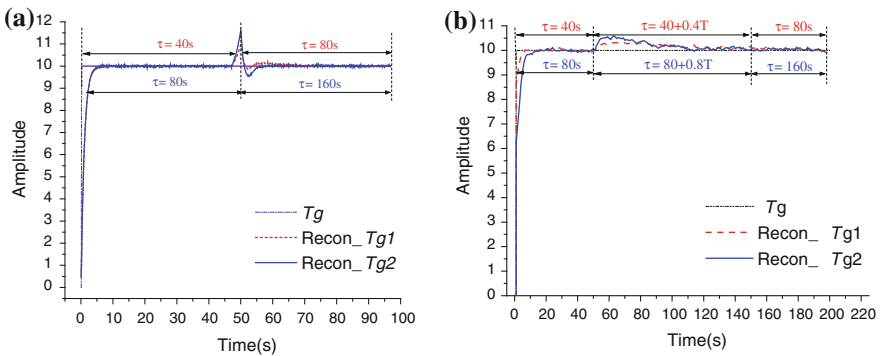
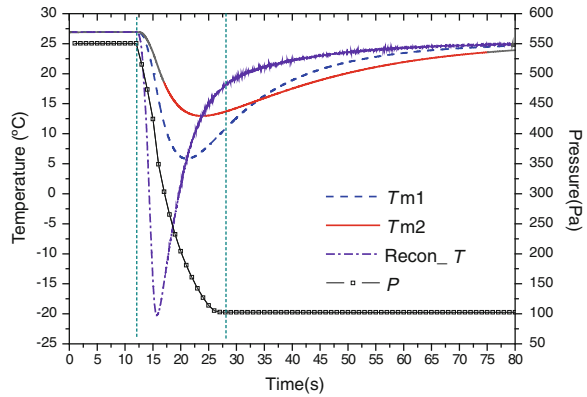


Fig. 65.3 Simulation of gas temperature and reconstructed temperature. **a** τ with abrupt change. **b** τ with gradual change

Fig. 65.4 Measured temperatures and reconstructed temperature varying with pressure

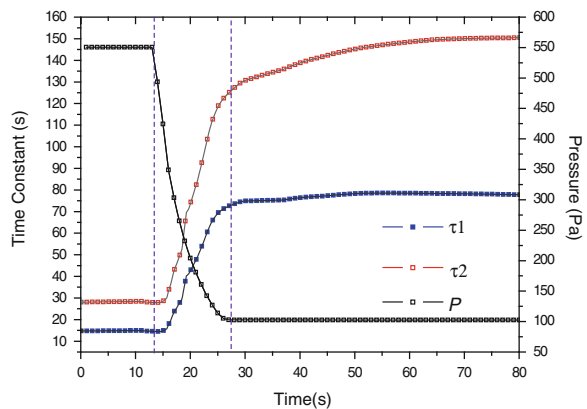


65.4 Experiment

Experiments with two different thermal resistances installed closely to each other in a gas-pressurized tank are conducted. The diameter of the first thermal resistance is 3 mm, and the other is 6 mm. The initial pressure and temperature of tank stabilize at approximately 550 kPa and 27 °C respectively, and then tank starts to deflate until the condition reaches balance again. τ_1 and τ_2 are the time constant of two thermal resistances identified by PSO respectively. T_{m1} and T_{m2} are the temperature measured by the first and second sensor respectively. $Recon_T_g$ are the temperature reconstructed by EKF.

According to ideal gas law, when the tank starts to discharge, the pressure decreases rapidly and the temperature drops correspondingly. In this experiment, the time of deflation is relatively short and the temperature changes quite fast. As is shown in Fig. 65.4, both thermal resistances cannot track the rapid change of temperature.

Fig. 65.5 PSO identification of two varying time-constant thermal resistances



As is well-known, the gas density ρ_g is reverse with the gas pressure P . Thus, according to Eq. (65.2), the time constant τ varies inversely with P which can be demonstrated evidently in Fig. 65.5. The reconstructed temperature Recon- T_g changes inversely with pressure which satisfies the regulations mentioned above, which is apparently shown in Fig. 65.4. Additionally, when the process of discharge is finished, there still exist fluctuations of the gas velocity in the tank. From Eq. (65.2), τ is also influenced by the gas velocity in the tank. Thus, as can be seen from the figure, after the tank pressure reaches balance, it still takes a while for the time constant τ to get balance.

65.5 Conclusion

A new intelligent identification method based on PSO was presented. Through simulation and experiments, it is confirmed that PSO could be used to track time-varying variables accurately and efficiently. Due to the high efficiency of PSO identification, this method could also be applied for the online dynamic sensor compensation.

Acknowledgments This work is supported by National Natural Science Foundation of China under Grant 61072101 and Program for New Century Excellent Talents in University under Grant NCET-10-0621.

References

1. Yang LH (2007) Study on the numerical simulation and the thermodynamic model of the tank discharge process. Doctor Dissertation, Shanghai Jiaotong University (in Chinese)
2. O'Reilly PG, Kee RJ, Fleck R, McEntee PT (2001) Two-wire thermocouples: a nonlinear state estimation approach to temperature reconstruction. *Rev Sci Instrum* 72(8):3449–3457
3. Ralf Z, Rolf I (2010) Nonlinear time constant estimation and dynamic compensation of temperature sensors. *Control Eng Pract* 18(3):300–310
4. Pfiem H (1936) On the measurement of fluctuating temperatures of gases and fluids. *Forschung auf dem Gebiete des Ingenieurwesens* 7(2):85–92
5. Forney LJ, Fralick GC (1994) Two wire thermocouple: frequency response in constant flow. *Rev Sci Instrum* 65(10):3252–3257
6. Hung PC, Irwin G, Kee R, McLoone S (2005) Difference equation approach to two-thermocouple sensor characterization in constant velocity flow environments. *Rev Sci Instrum* 76(2):024902–024910
7. Eberhart RC, Kennedy J (1995) A new optimizer using particle swarm theory. In: Proceedings of the 1995 6th international symposium on micro machine and human science, IEEE Service Center, Piscataway, NJ, pp 39–43
8. Ke J, Li WW, Qian JX (2003) Identification of time varying-system based on particle swarm optimization. *Syst Eng Electron* 25(10):1256–1259
9. Welch G, Bishop G (2001) An introduction to the Kalman filter. In: SIGGRAPH 2001, annual conference on computer graphics and interactive techniques, ACM Press, Addison-Wesley, Los Angeles

Chapter 66

Path Tracking Control of Underactuated AUVs Based on ADRC

Yushan Sun, Yinghao Zhang, Guocheng Zhang and Yueming Li

Abstract To weaken the influence of the disturbance caused by the current, signal transportation and other situations which are likely to occur when the underactuated autonomous underwater vehicles (AUVs) are working under water, this paper addresses a path tracking control method based on the active disturbance rejection control (ADRC) which can eliminate error according to its situation and has the capacity to establish and compensate the real time disturbance. In this paper, one underactuated AUV is simulated to track the same path in different disturbance which is separately instantaneous and random. The results of the simulation indicate that compared with the traditional PID controller, the controller based on ADRC has a better control capability to restrain the shock, overshoot and other phenomena caused by the disturbance.

Keywords Underactuated AUV · Path tracking control · Active disturbance rejection control (ADRC)

66.1 Introduction

The underactuated AUV is the autonomous underwater vehicle whose independent dimensions of input are less than the degrees of freedom [1]. The path tracking control, one of the most significant technologies for an AUV, is to make sure the AUV follows one certain path which can satisfy the course demands and the performance limitation, and which has no relationship with time. This motion control is mainly aimed at the static targets such as the pipelines, cables and topography under water [2].

Y. Sun · Y. Zhang (✉) · G. Zhang · Y. Li
State Key Laboratory of AUV, Harbin Engineering University, Harbin 150001, China
e-mail: zhangyinghao555@126.com

According to the publications about the underactuated AUV's path tracking control [3–6], most of the solutions are based on the path tracking error equations, combined with one or multiple control theories and finally turn the path tracking into the error stabilization. To investigate the underactuated AUV's path tracking problem, in this paper, we build the path tracking error equations in Serret-Frenet coordinate system, establish the path tracking controller according to the ADRC and make some simulations.

66.2 Problem Formulation

66.2.1 Coordinate Systems

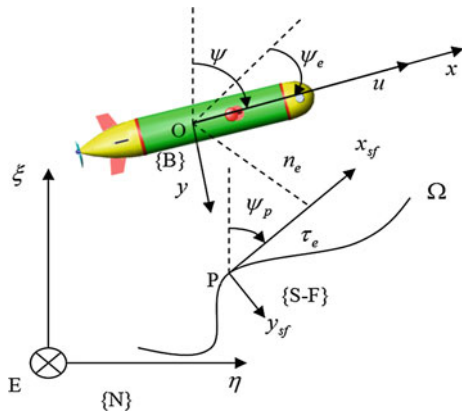
To make it convenient in investigating the path tracking problem, we make three coordinate systems in horizontal plane, as is shown in Fig. 66.1, the earth coordinate system $E - \xi\eta(\{N\})$, the body coordinate system $O - xy(\{B\})$ [7] and the Serret-Frenet coordinate system $P - x_{sf}y_{sf}(\{S - F\})$. P is a free reference point on the path Ω . x_{sf} points to P 's tangential direction and y_{sf} points to P 's normal direction.

66.2.2 Underactuated AUV's Kinematic and Dynamic Model

In this paper, ignoring the effect of the vertical motion, the horizontal kinematic and dynamic model can be expressed as Eqs. (66.1) and (66.2):

$$\dot{\eta} = TV \tag{66.1}$$

Fig. 66.1 AUV's coordinate systems



$$M\dot{V} + C(V)V + D(V)V + f = \tau \quad (66.2)$$

The detailed information of Eqs. (66.1) and (66.2) can be found in [7]. As the simulation carrier's shape has vertical, horizontal, and front and rear symmetry, we can make some simplification of the former two equations and considering the underactuated situation, the $O - y$ input of τ is 0.

66.2.3 Underactuated AUV's Path Tracking Error Equation

As is shown in Fig. 66.1, U_p is P 's velocity in the certain path and ψ_p is the angle between $P - x_{sf}$ and $E - \xi$. O 's position in $\{S - F\}$ is $(\tau_e, n_e, 0)$. τ_e and n_e are the path tracking errors. Being similar to T , R is defined as the switch matrix from $\{S - F\}$ to $\{N\}$:

$$R = \begin{bmatrix} \cos \psi_p & -\sin \psi_p & 0 \\ \sin \psi_p & \cos \psi_p & 0 \\ 0 & 0 & 1 \end{bmatrix} \quad (66.3)$$

Using R , we can switch the AUV's velocity from $\{N\}$ to $\{S - F\}$ and combining with Eq. (2.1), we can get the path tracking error equations:

$$\begin{aligned} \dot{\tau}_e &= -U_p + r_p n_e + u \cos \psi_e - v \sin \psi_e \\ \dot{n}_e &= -r_p \tau_e + u \sin \psi_e + v \cos \psi_e \\ \dot{\psi}_e &= r - r_p \end{aligned} \quad (66.4)$$

where $\psi_e = \psi - \psi_p$, U_p is P 's velocity in $\{S - F\}$.

u_E is longitudinal velocity tracking error and $u_E = u - u_d$. ψ_E is heading angle tracking error:

$$\psi_E = \Psi_e - \Psi_{ed} \quad (66.5)$$

where $\Psi_e = \psi_e + \beta_d$, $\Psi_{ed} = -\arctan(0.1n_e)$ and $\Psi_e, \Psi_{ed} \in (-\frac{\pi}{2}, \frac{\pi}{2})$. β_d is the drift angle and $\beta_d = \arctan(\frac{v}{u_d})$.

66.3 Path Tracking Controller

66.3.1 ADRC

Active disturbance rejection controller (ADRC), put forward by researcher Jingqing Han from Chinese Academy of Sciences [8], is a control theory based on the Error Feedback, which has the same engineering practicability of the

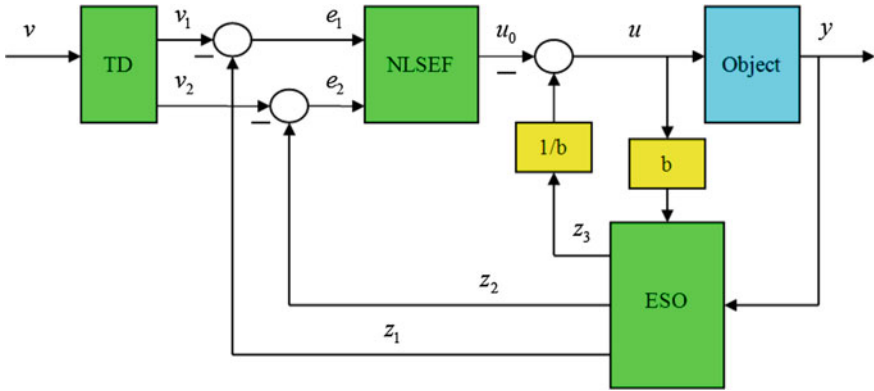


Fig. 66.2 The basic structure of ADRC

traditional PID and overcomes some disadvantages of PID’s. ADRC mainly contains four parts—tracking differential controller (TD), extended state observer (ESO), nonlinear states error feed-back (NLSEF) and the disturbance compensation. TD is used to arrange the transition process. Figure 66.2 is the basic structure block diagrams of the second-order ADRC.

TD, ESO, NLSEF and the disturbance compensation have several laws of arithmetic separately [9]. In this paper, we choose the following laws according to the needs of the path tracking control:

TD:

$$\begin{cases} fh = fhan(x_1(k) - v(t), x_2(k), r, h_0) \\ x_1(k + 1) = x_1(k) + hx_2(k) \\ x_2(k + 1) = x_2(k) + hfh \end{cases} \quad (66.6)$$

ESO:

$$\begin{cases} e = z_1 - y, fe = fal(e, 0.5, \delta), fe_1 = fal(e, 0.25, \delta) \\ z_1 = z_1 + h(z_2 - \beta_{01}e) \\ z_2 = z_2 + h(z_3 - \beta_{02}fe + bu) \\ z_3 = z_3 + h(-\beta_{03}fe_1) \end{cases} \quad (66.7)$$

NLSEF:

$$\begin{aligned} u &= \beta_0 fal(e_0, \alpha_0, \delta) + \beta_1 fal(e_1, \alpha_1, \delta) + \beta_2 fal(e_2, \alpha_2, \delta), \\ &\alpha_0 < 0 < \alpha_1 < 1 < \alpha_2 \text{ or } 0 < \alpha_0 < \alpha_1 < 1 < \alpha_2 \end{aligned} \quad (66.8)$$

Disturbance compensation:

$$u = u_0 - \frac{z_3}{b} \quad (66.9)$$

The detailed information of Eq. (66.6–66.9) can be found in [9].

66.3.2 Underactuated AUV's Path Tracking Controller

According to the ADRC theory, we use second-order ADRC to design velocity and heading controllers respectively. Figure 66.3 shows the basic information frame of the underactuated AUV's path tracking controller in horizontal plane.

In the longitudinal velocity ADRC controller, we make some adjustments by removing TD and preserving ESO, NLSEF and disturbance compensation. TD is used to follow the expected velocity. The basic information frame of the heading ADRC controller is similar to the one of the longitudinal velocity ADRC controller.

66.4 Simulation

In the simulation, our carrier is based on MAUV-2 which is operated jointly by the rudder, propeller and wing. Its appearance and some major parameters are shown in Fig. 66.4 and Table 66.1 respectively. This AUV can not head back.

We make the path tracking control simulations by ADRC and traditional PID in MATLAB/Simulink separately. In the simulations, we expect the AUV can track a circle path whose radius is 50 m with the center at the origin of $\{N\}$, at the speed of 2 kn in horizontal plane. AUV's initial position in $\{N\}$ is $(0, 10)$. Initial heading angle is 0. Initial velocity is 0 and we set the P 's velocity in $\{S-F\}$ as $U_p = \sqrt{u^2 + v^2} + 0.1 \times \tau_e$.

Before the simulations start, we find the proper parameters under no disturbance and set the longitudinal velocity controller and the heading controller in the same

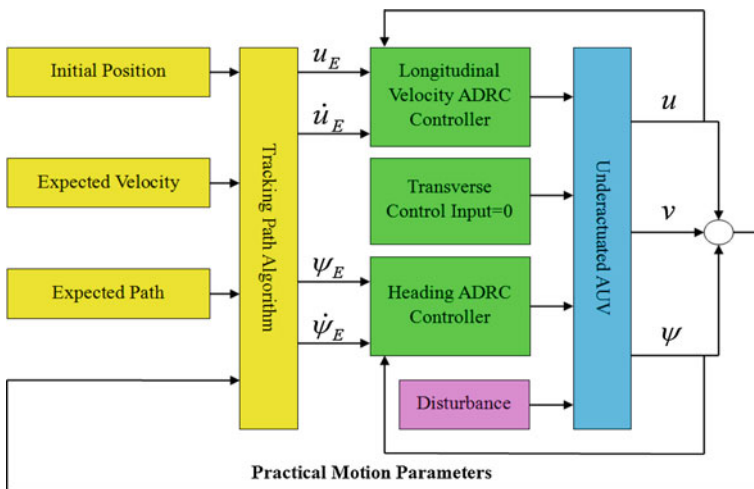


Fig. 66.3 The information frame of the path tracking controller

Fig. 66.4 The MAUV-2

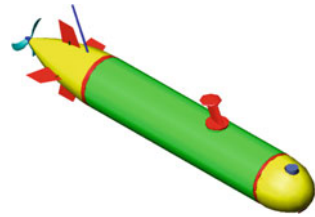


Table 66.1 Some parameters of MAUV-2

Item	Length L	Mass m	Moment of inertia I_z	Cruising speed
Amount	1.5 m	45 Kg	8.067 Kgm^2	2 kn

Fig. 66.5 u and the tracking path in the instantaneous disturbance

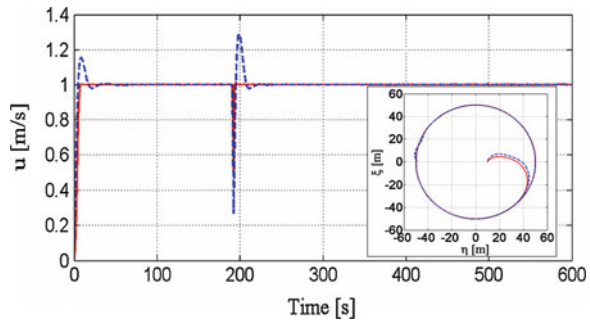
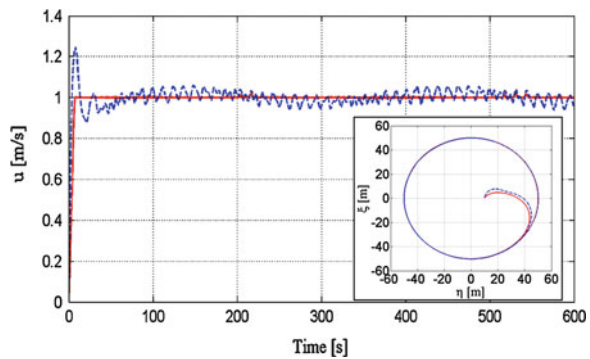


Fig. 66.6 u and the tracking path in the random disturbance



corresponding parameters. After that, we make the simulations under instantaneous and random disturbance respectively. The results of ADRC path tracking controller and PID controller are represented by a red continuous line and a blue dashed line respectively.

In the instantaneous disturbance, we add disturbance of 100 N when $t = 190$ s. Figure 66.5 shows the simulation results.

In the random disturbance, the disturbance is combined by Step, Sine Wave and Band-Limited White Noise. We add the random disturbance to the direction of $E - \eta$ and $E - \xi$ respectively. Figure 66.6 shows the simulation results.

66.5 Conclusion

From the simulation results, the ADRC path tracking controller has a better transition process, less overshoot, can get to the steady-state faster and has greater restrain capacity to disturbance. The ADRC controller, which eliminates error according to its situation, can achieve the goal to make the underactuated AUV track a certain path at certain velocity.

Acknowledgments This research was part of the project (20100480964, 2012T50331) supported by Postdoctoral Science Foundation of China. It has also been partially supported by the National High-tech Research and Development Program of China (2008AA092301). Great thanks are addressed to them by the research team.

References

1. Fang W, Lei W, Ye L, Yu-min S, Yu-ru X (2010) A survey on development of motion control for underactuated AUV. *Shipbuilding China* 51(2):227–241.2009 (in Chinese)
2. Nakamura M, Hyakudome T, Yoshida H, Aoki T (2009) Path control of AUV “MR-X1” using thrusters. In: *Proceedings of the international offshore and polar engineering conference* pp 657–664
3. Raimondi FM (2010) Hierarchical fuzzy/lyapunov control for horizontal plane trajectory tracking of underactuated AUV. *IEEE international symposium on industrial electronics*, pp 1875–1882
4. Shu-Wei S, Wei-Sheng Y, Gao J, Li W (2010) Path-following control of an AUV in the horizontal plane with constant ocean currents. *Binggong Xuebao* 31(3):375–379 in Chinese
5. He B, Zhou X (2010) Path planning and tracking for AUV in large-scale environment. *CAR 2010—2010 2nd international Asia conference on informatics in control vol 1. Automation and Robotics*, pp 318–321
6. Wang L, Zhang LJ, Jia HM, Wang HB (2012) Horizontal tracking control for AUV based on nonlinear sliding mode. *2012 IEEE international conference on information and automation, ICIA 2012*, pp 460–463
7. Sheng-Da S (1995) *Submarine maneuverability*. National Defence Industry Press, China (in Chinese)
8. Han J (2008) *Active disturbance rejection control technique: the technique for estimating and compensating the uncertainties*. National Defence Industry Press, China (in Chinese)
9. Han J (1998) *Auto-disturbances-rejection controller and its applications*. *Control Decision* 13(1):19–23 in Chinese

Chapter 67

Fuzzy Method for Sub-Communities Identification in Complex Networks

Danling Wang and Yanfei Wang

Abstract Detection of sub-communities in complex networks, such as social networks and protein–protein interaction networks, can enhance our understanding of structures and functions of different communities. In this paper, we introduced a novel method combined fuzzy clustering and IP values to identify community structures in complex networks. We evaluated our method on two real-world social networks with known communities. The experiment results show that our method works well for detecting sub-communities and give a reasonable understanding of these communities.

Keywords Complex networks · Fuzzy clustering · Sub-communities

67.1 Introduction

Community structure or module, which consists of groups of vertices with dense connections, is a significant feature in complex networks. It plays an important role in analysis of complex networks. Different communities often correspond to different functional organizations. For instance, in protein–protein interaction networks, sub-communities are topological expression of protein complexes [1]; in social networks, we can snoop the groupuscule according to the sub-structure of networks [2]. Therefore, detecting sub-communities can enhance our

D. Wang

School of Mathematics and Physics/School of Automation, University of Science and Technology Beijing, 30 Xueyuan Road, Haidian District, Beijing 100083, China
e-mail: wang_dan_ling@sina.com

Y. Wang (✉)

Department of Applied Mathematics, School of Sciences, China Agriculture University, 17 Tsinghuadonglu Road, Haidian District, Beijing 100083, China
e-mail: yfmu@sina.com

understanding of the whole networks and its functional modules. In the past several decades, Amount of methods for sub-communities detection was proposed. However, most of methods usually focus on design of the algorithms themselves and ignore the original structure of the network [3]. Meanwhile, the complex networks contain amount of uncertain information. The traditional “Hard” clustering method is not suitable for analysis [4]. How to gain a efficient and accurate sub-communities detecting algorithm is still a key step in analysis of complex networks.

Since the fuzzy set theory was proposed by Zadeh in 1965, fuzzy clustering has been applied in many fields. Fuzzy relation can effectively describe the uncertainty information between two objectives, like the concepts “similar” and “different” [6]. Sun et al. establish a fuzzy relation model between every pair of nodes in complex networks. However, in this method original topological structure of the network which contains important information for clustering analysis is ignored. That’s why in this paper we consider the sub-networks obtained from fuzzy relation model as the skeleton and compute the interaction probability (IP) of each node to identify the non-overlapping sub-communities.

67.2 Theoretical Background

The topology of a network concerns the relative connectivity of its nodes. Different topologies affect specific network properties. In this work, we consider a network as a graph. The definition of a graph is as followed:

67.2.1 Definition of Graph

A graph (or network) is a ordered pair $G = (V, E)$, where

1. $V = \{v_1, v_2, \dots, v_n\}$, $V \neq \emptyset$, is called the vertex or node set of G ;
2. $E = \{e_1, e_2, \dots, e_m\}$ is the edge set of G in which $e_i = \{v_j, v_l\}$ or $\langle v_j, v_l \rangle$ is the edge linking two nodes v_j and v_l .

If every edge in a graph G is undirected, the graph G is called an undirected graph; if every edge in a graph G is directed, the graph G is called a directed graph. The two nodes linked by one edge are called adjacent nodes; the edges linking the same node are called adjacent edges. Networks are naturally represented in matrix form. A graph of N nodes is described by an $N \times N$ adjacency matrix A whose non-zero elements a_{ij} indicate connections between nodes. For undirected networks, a non-diagonal element a_{ij} of an adjacency matrix is equal to the number of edges between nodes i and j , and so the matrix is symmetric. In our method, adjacency matrix is used to calculate the similarity between two different nodes.

67.2.2 Fuzzy Clustering

Fuzzy clustering is based on the description of fuzzy relation which is also proposed by Zadeh [5]. In this section we will give some introduction on fuzzy relation theory. The letter 'R' can denote not only a fuzzy relation, but also a fuzzy matrix based on the fuzzy relation [7].

67.2.2.1 Definition of Fuzzy relation

Let U and V be nonempty sets. A fuzzy relation $R \in F(U \times V)$ is a fuzzy set of the Cartesian product $U \times V$, $F(U \times V)$ is the set of all the fuzzy relations of $U \times V$. $\forall (u, v) \in U \times V$, $R(u, v)$ can be interpreted as the grade of membership of the ordered pair (u, v) in R . If $U = V$, then we can say that R is a binary fuzzy relation in U . Here, we apply the binary fuzzy relation for identification of sub-communities [7].

The steps of fuzzy clustering are as followed:

1. Data normalization.
2. Establishing fuzzy similarity matrix.

After normalization of observation values, we can establish fuzzy similarity matrix via computing the similarity relation between any two samples. For different node i and j , we compute the similarity value between them, which should satisfy $0 \leq r_{ij} \leq 1$, $i, j = 1, 2, \dots, n$. Then we obtain a fuzzy similarity matrix R which shows the similarity between every pair sample:

$$R = \begin{pmatrix} r_{11} & r_{12} & \dots & r_{1n} \\ r_{21} & r_{22} & \dots & r_{2n} \\ \dots & \dots & \dots & \dots \\ r_{n1} & r_{n2} & \dots & r_{nn} \end{pmatrix}$$

3. Computing the transitive closure [7] of the fuzzy similarity matrix via the method of squares.
4. Transforming the transitive closure to a Boolean matrix via computing the λ -cut matrix. The Boolean matrix is the skeleton of clustering result.

67.2.3 Similarity Value Between Different Nodes

In practice, we need to choose a proper method to compute the similarity value. We can also define a new method which is suitable for the clustering analysis in the problem. Here we apply the clustering coefficient defined by Sun et al. [8] based on the interaction matrix of a network:

$$r_{ij} = \begin{cases} \frac{|N_i \cap N_j| + 1}{\sqrt{N_i \cdot N_j}} & (i, j) \in E, i \neq j \\ 0 & (i, j) \notin E \\ 1 & i = j \end{cases},$$

where N_i and N_j are sets of neighbours of vertices i and j respectively. $|N_i \cap N_j|$ represents the number of joint neighbours of vertices i and j . Note that vertices i and j are also connected by an edge. Sun et al. prove that the clustering coefficient is in $[0, 1]$.

67.3 Method

In this part we introduce our method on identification of sub-communities. We combine fuzzy relation clustering analysis with IP value and hub structure in sub-networks, which we call the FRIPH method. We can obtain the cluster skeleton of a network via the Boolean matrix transformed from the transitive closure of a fuzzy similarity matrix. However, some nodes are separated and they don't belong to any clusters. Thus, how to deal with them is a critical problem. Li et al. [9] proposed a new concept, Interaction Probability IP_{vi} to measure how strongly an outside vertex v connects to another sub-network which doesn't contain v . Interaction probability IP_{vi} of any vertex v with respect to any sub-network i of size $|V_i|$ is defined as

$$IP_{vi} = \frac{|E_{vi}|}{|V_i|},$$

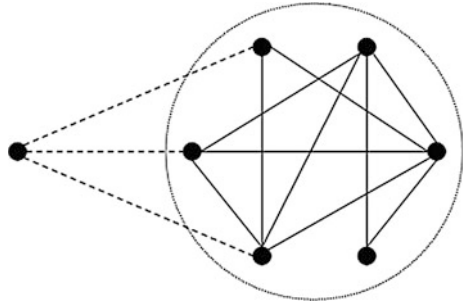
where $|E_{vi}|$ is the number of edges between the vertex v and the sub-network i . As shown in Fig. 67.1, the IP_{vi} of the vertex v to the sub-network i is 0.5.

For every vertex v in the original PPI network, we calculate its IP_{vi} in all sub-communities, $i = 1, 2, 3, \dots, m$. Suppose vertex v is in sub-community j . If sub-community i has the greatest IP_{vi} with vertex v , then v can be "added" to sub-community i . To summarize,

If $IP_{vi} = \max_k (IP_{vk}), k = 1, 2, \dots, m$, then v is also in sub-community i .

However, sometimes vertex v has the same greatest IP value with several sub-networks. In this situation, we need to compare the nodes connected to vertex v in these sub-networks. If vertex v is connected with a hub in sub-network i , then v can be also in sub-network i . The algorithm FRIPH can be divided into the following steps: (1) Generate an adjacency matrix from complex networks. (2) Choose a suitable method to compute similarity between each node in the network. (3) Compute transitive closure of the fuzzy matrix. (4) Transform the transitive closure to Boolean matrix via λ -cut matrix. (5) Compute IP values and compare hub structure in the original network.

Fig. 67.1 The interaction probability IP_{vi} of a vertex v with respect to the sub-network i is 0.5



67.4 Result and Discussion

Firstly, we apply our method to two social networks. The first one is Zachary's karate club network. The second one is Network of American college football teams. We aim to identify the non-overlapping sub-communities in the two networks.

67.4.1 Zachary's Karate Club Network

This is a widely used data as a test example for methods of identifying sub-networks in complex networks. In this data, there are 34 nodes representing 34 people [10]. Zachary observed them for more than 2 years. During this study, a disagreement developed between the administrator (node 34) of the club and the club's instructor (node 1), which ultimately resulted in the instructor's leaving and starting a new club, taking about a half of original club members with him. Zachary constructed the network between these members in the original club based on their friendship with each other and using a variety of measures to estimate the strength of ties between individuals. Figure 67.2 shows the graph of the network. There are 78 edges and two non-overlapping sub-networks in the graph, representing two groups of people with the administrator (circle label) and the instructor (square label). We apply our FRIPH to try to identify the two groups.

Following the step of FRIPH, we separated the original networks into two sub-networks and two single nodes when we choose the value of λ as 0.75. Figure 67.3 shows the result we obtain.

Comparing Fig. 67.3 with the original network in Fig. 67.2, the instructor group is perfectly separated from the original network. For the administrator group, node 10 and node 28 are not in the group but as two single points. The remaining nodes are all in administrator's group. Then we calculate the IP values of node 10 and node 28. For node 28 in Fig. 67.3, it is connected with nodes 34, 24 and 25, which all belong to administrator's group; only node 3 belongs to instructor's group, thus the IP value of node 28 in administrator's group is greater than that of node 28 in

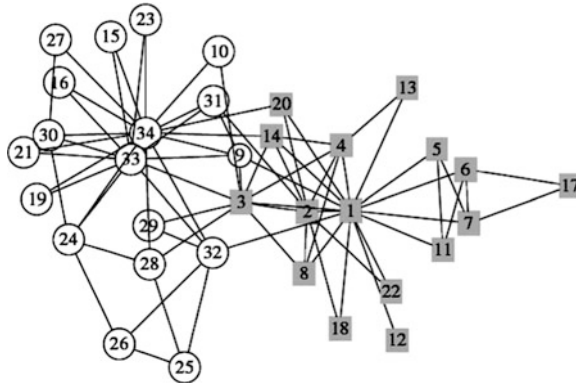


Fig. 67.2 Zachary's karate club network. Square nodes and circle nodes represent the instructor's faction and the administrator's faction, respectively [10]

instructor's group. Node 28 should belong to administrator's group. For node 10, it is just connected with nodes 34 and 3. However, node 34 is the administrator which is the hub of that group. Therefore, node 10 also belongs to administrator's group. From the result of karate club data, the FRIPH method detects the two sub-networks correctly. However, the edges in the sub-networks are totally changed; these new edges have no meaning in the sub-network. But they have no effect on the correctness of groups of sub-networks.

The second social network we test is the network of American college football teams which represents the game schedule of the 2,000 season of Division I of the US college football league. In this data set, there are 115 nodes representing the teams and 613 edges presenting games played in the course of the year. The teams

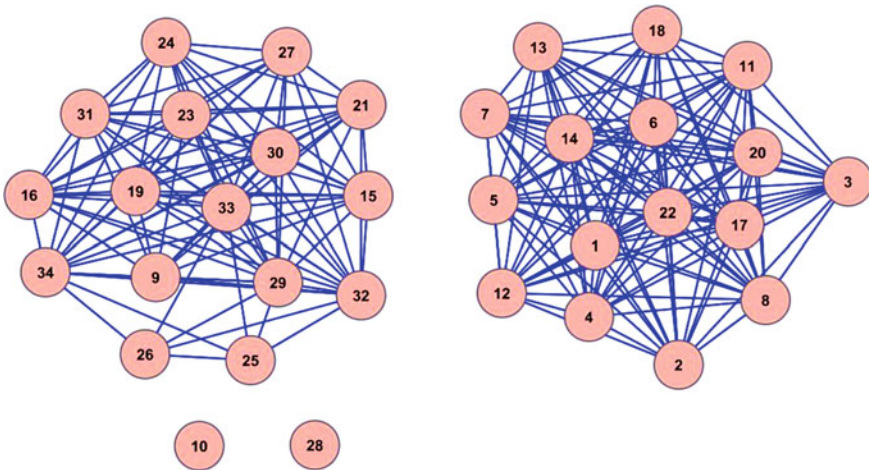


Fig. 67.3 Sub-networks of Zachary's karate club network, obtained by FRIPH

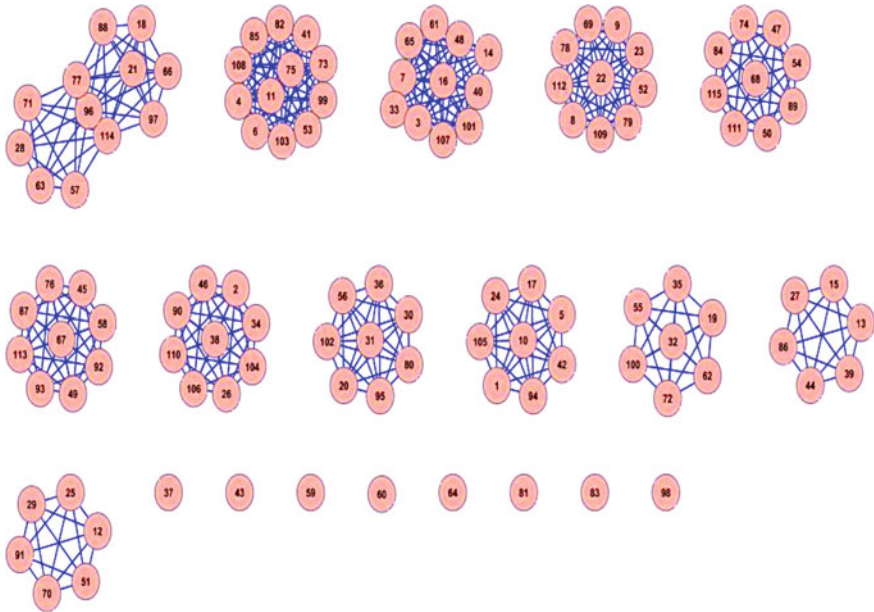


Fig. 67.4 Sub-networks of American college football team network, obtained by FRIPH

are divided into 12 conferences containing around 8–12 teams each. We apply our method on this data set and obtain the result showed in Fig. 67.4. However, the result is not satisfactory. For our result most nodes in the last three sub-communities belong to the Sunbelt conference and should be in the same group, but they divide into three sub-communities and group with members of the Western Athletic conference. This happens because the Sunbelt teams played nearly as many games against Western Athletic teams as they did against teams in their own conference [10]. Meanwhile, there are 8 points which cannot be grouped in any sub-communities. That’s because these nodes generally connect evenly with more than one community, thus our method cannot group them into one specific sub-network correctly. These nodes are the “fuzzy” nodes which cannot be classified correctly by the current edge information. Generally, these points play a “bridge” role in two or more sub-communities of the original network [11].

67.5 Conclusion

In this paper, we proposed a novel method which combines the fuzzy clustering method and interaction probability to identify the non-overlapping community structures in complex networks. Our method is based on both the fuzzy relation model and the graph model. Fuzzy theory is suitable to describe the uncertainty information between two objects, such as ‘similarity’ and ‘differences’. On the

other hand the original graph model contains significant clustering information, thus we do not ignore the original structure of the network, but combine it with the fuzzy relation model. We applied the method on two social networks. The results showed that our method works well for detecting sub-networks and gives a reasonable understanding of these communities.

Acknowledgments This work is supported by Chinese Universities Scientific Fund No. 2013XJ010 and the Fundamental Research Funds for the Central Universities No. FRF-TP-13-020A.

References

1. Adamcsek B, Palla G, Farkas I, Derenvi I et al (2006) Cfinder locating cliques and overlapping modules in biological networks. *Bioinformatics* 22(8):1021–1023
2. Newman MEJ (2004) Fast algorithm for detecting community structure in networks. *Phys Rev E* 69(6):66–133
3. Gao L, Sun PG, Song J (2009) Clustering algorithms for detecting functional modules in protein interaction networks. *J Bioinf Comput Biol* 7:217–242
4. Baraldi A, Blonda P (1999) A survey of fuzzy clustering algorithms for pattern recognition. *IEEE Trans Syst Man Cybern* 29:778–785
5. Zimmermann HJ (2010) Fuzzy set theory, wires. *Comp Stat* 2:317–332
6. Zadeh LA (2005) Fuzzy sets. *Inf Control* 8:338–353
7. Zimmermann HJ (2001) Fuzzy set theory—and its applications. Kluwer Academic Publisher, Dordrecht
8. Sun PG, Gao L, Han S (2011) Identification of overlapping and non-overlapping community structure by fuzzy clustering in complex networks. *Inf Sci* 181:1060–1071
9. Li M, Wang JX, Zhao C et al (2010) Identifying the overlapping complexes in protein interaction networks. *Int J Data Min Bioinf* 4(1):56–71
10. Girvan E, Newman MEJ (2002) Community structure in Social and Biological networks, *PNAS* 99 12:7821–7826
11. Zhang SH, Wang RS, Zahng XS (2007) Identification of overlapping community structure in complex networks using fuzzy c-means clustering. *Phys A* 374:483–490

Chapter 68

Modeling for the Clarifying Process of Sugar Mills with ESN

Xiao-feng Lin and Yun-peng Liu

Abstract Sugar industry is one of the pillar industries in Guangxi of China. The control of sugar clarifying processing directly related to the quality of the sugar. An accurate and effective model is the premise. Due to the characteristics of strong coupling and larger time-delay, it is difficult to model this process based on the mechanism. In this paper, Echo State Network (ESN) based on data is introduced to model this process. The simulation results show that the model based on ESN can reflect the clarification process of sugar mill well.

Keywords Echo state network · Neural network · Modeling

68.1 Introduction

As one of the pillar industries in Guangxi of China, the production of sugar was 6.8 million tons during 2010/2011, accounting for the national sugar production is about 70 %, ranking the first in our country, so the sugar industry has become a very influential industry in our country [1]. On the other hand, sugar is not only an indispensable flavoring material in our lives, but also a very important raw material of food industry, and the quality of sugar directly related to our lives. Considering the key factor that affect the quality of sugar is the clarifying process in sugar mill, so the controlling of the clarifying process is very important.

Due to the characteristics of complexity, strongly nonlinear, large time delay and time-varying of the clarifying process, it is too difficult to model based on mechanism. So the neural network modeling method, which is based on the data, is usually used. In [2], RBFNN was used to model this process, but the accuracy of

X. Lin · Y. Liu (✉)

School of Electrical Engineering, Guangxi University, Room 703, Nanning 530004, China
e-mail: lyptrey@qq.com

the model needs to be improved. In this paper, a novel recurrent neural network called Echo State Network (ESN) is introduced.

Echo State Network is proposed in 2004 on science by Herbert Jaeger [3]. This network has strong nonlinear approximation ability, and will not fall into the local minimum point unlike other networks such as BP neural network. In this paper, ESN is used to build the clarifying process model.

68.2 The Clarifying Process of Cane Manufacture

In cane manufacture, the cane juice from the press workshop, due to it mixed with a large number of non-sugar and impurities, is called mixed juice. The process that remove non-sugar and impurities is called clarifying process. The mixed juice that removed non-sugar and impurities is called purified juice. The purified juice color value means the absorption rate of the juice on the specific wavelength lightwave, and it shows the content of non-sugar and impurities in purified juice. The clarifying process includes pre-liming, first heating, sulfitation, second heating, etc.

Pre-liming means that adding lime into mixed juice, and its mainly intention is to neutralize the free acid, precipitate certain anions and preserve. Sulfitation means that adding sulfur dioxide and lime into cane juice, and its mainly intention is to generate the large particles precipitated material, adsorb most colloidal suspension and non-sugar in cane juice [4]. Figure 68.1 is a clarifying process flow diagram of a sugar factory.

68.3 Echo State Network

68.3.1 The Structure of ESN

Figure 68.2 is the schematic diagram of Echo State Network (ESN). Consider of such a network with L input units $u = (u_1, u_2, \dots, u_L)$, M internal units $x = (x_1, x_2, \dots, x_M)$, N output units $y = (y_1, y_2, \dots, y_N)$. The state equation and output equation are [5, 6]:

$$x(n+1) = f(Wx(n) + W_{in}u(n) + W_{back}y(n)) \quad (68.1)$$

$$y(n+1) = f_{out}(W_{out}[x(n+1), u(n)]) \quad (68.2)$$

where W is the internal connection weight matrix, W_{in} is the input connection weight matrix, W_{back} is the backprojection weight matrix, W_{out} is the output connection weight matrix. $f(\cdot)$, $f_{out}(\cdot)$ are activation function.

Dynamic reservoir (DR) is the most important part of ESN. Its parameters directly determine the effect of the network [7]. The DR parameters include that:

Fig. 68.1 The clarifying process flow diagram of a sugar factory

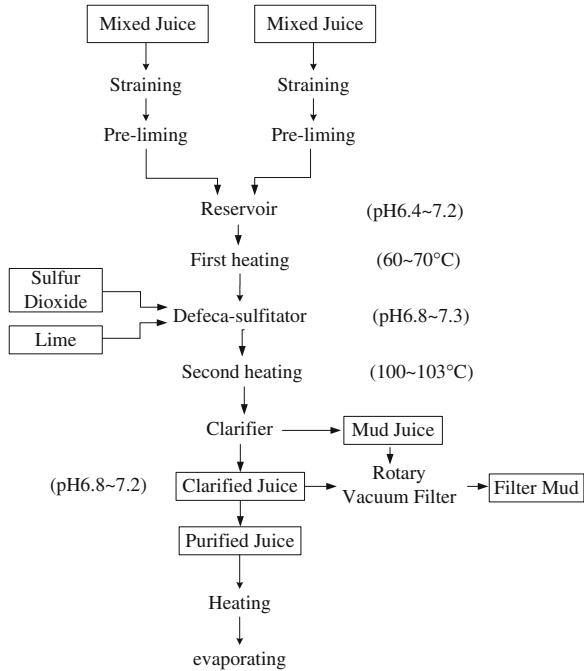
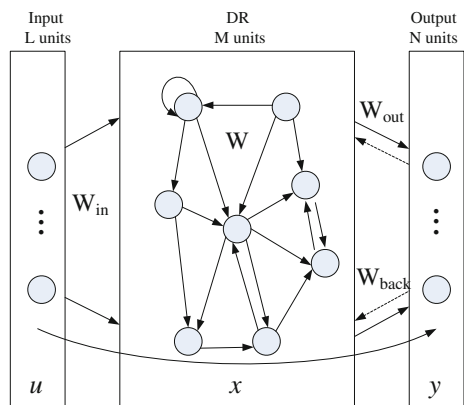


Fig. 68.2 The schematic diagram of echo state network



- **Sparsity Degree (SD)** is the ratio of the number of interconnected neurons and the number of total neurons in DR. SD is usually taken from the interval 5 ~ 10 %.
- **Spectral Radius (SR)** is the maximum absolute value of the eigenvalues of the internal neuron connection weight matrix W . SR must be less than 1 [8, 9].

68.3.2 Training Echo State Network

During the training of Echo State Network, the internal connection weights matrix W , the input connection weights matrix W_{in} and the backprojection connection weights matrix W_{back} are randomly generated and once generated never change. The purpose of training ESN is to seek the output connection weights matrix W_{out} . The goal of training ESN is to make network output equal to the desired output, which is to minimize that:

$$\frac{1}{n - m + 1} \sum_{j=m}^n \left(y(j) - \sum_{i=1}^N w_{out}^i [x_i(j), u_i(j)] \right)^2 \quad (68.3)$$

Commonly used pseudo-inverse method, that is:

$$W_{out} = M^{-1}T \quad (68.4)$$

where M is a collected matrix that makes the internal state and input variables as row vector. T is the corresponding matrix that makes the desired output as column vector.

68.4 Data Processing

The prediction model of sugar mills clarifying process is a MIMO system. Because purified juice color value and purified juice pH value are important indicators to evaluate the clarifying process, so purified juice color value and purified juice pH value are chosen as the output variables of the clarifying process prediction model. And the most important factors that affect purified juice color value and purified juice pH are the cane juice flow, pre-liming pH value, sulfitation strength, lime milk flow, purified juice pH value of the previous time and purified juice color value of the previous time. Because the object of this paper takes a double-line pre-liming, so the input variables are first line cane juice flow, first line pre-liming pH value, second line cane juice flow, second line pre-liming pH value, sulfitation strength, the value position of lime milk, neutral juice pH value, purified juice pH value of the previous time and purified juice color value of the previous time.

After the input and output variables determined, the abnormal data is excluded according to the process requirements, and then process the remaining data normalization. 75 % of the total sample is selected as the training data set, 25 % of the total sample is selected as the test data set. Table 68.1 is the online and offline data table of a sugar mill.

Table 68.1 The online and offline data table of a sugar mill

First line cane juice flow (m ³ /h)	Second line cane juice flow (m ³ /h)	First line pre-liming pH value	Second line pre-liming pH value	Sulfitation strength (mL)	The valve position of lime milk (%)	Neutral juice pH value	Purified juice pH value	Purified juice color value (°St)
182.929	125.781	6.87	6.82	19.01	20.26	6.95	7.35	1,934
92.968	142.968	6.90	7.19	8.59	70.43	6.90	7.33	1,583
117.468	143.046	6.93	7.50	19.48	55.73	7.22	7.34	1,293
...
118.070	153.984	6.95	7.28	20.27	36.93	7.08	7.40	1,288

68.5 Modeling for Clarifying Process with ESN

After determined the input and output variables of the prediction model, then set dynamic reservoir structure for that:

- The number of DR neurons is 500.
- SD is 5 %.
- SR is 0.8.
- The internal activation function $f = \tanh$.
- The output activation function $f_{out} = 1$.

Programming in MATLAB 7.0, the process is as follows:

- Step 1. Set parameters of the dynamic reservoir.
- Step 2. Initialize the network connection weight matrix: W , W_{in} , W_{back} and the internal state of reservoir.
- Step 3. Input training samples in turn, calculate reservoir state according to the ESN state Eq. (68.1) and then collect these states into matrix M .
- Step 4. Calculate output connection weights matrix with pseudo-inverse method, that is Eq. (68.4).
- Step 5. Save the parameters of the dynamic reservoir and connection weights matrix W , W_{in} , W_{back} , W_{out} .

Figure 68.3 is the fitting curve of the purified juice color value. Figure 68.4 is the fitting curve of the purified juice pH value. The root mean square error of the purified juice color value fitting is 1.67 and its maximum relative error is 0.42 %. The root mean square error of the purified juice pH value fitting is 0.00085 and its maximum relative error is 0.04 %.

Fig. 68.3 The fitting curve of the purified juice color value

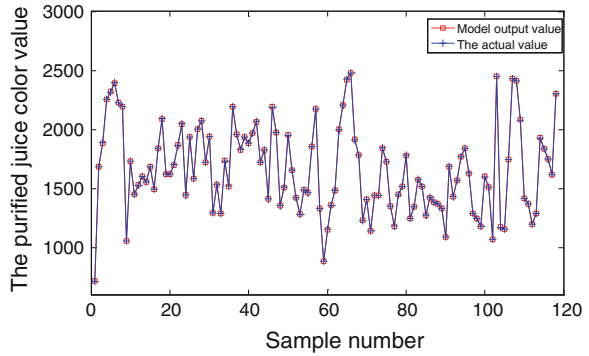
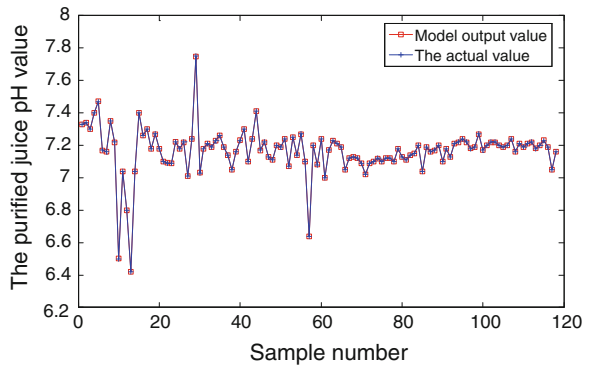


Fig. 68.4 The fitting curve of the purified juice pH value



68.6 Simulation of the Clarifying Process Model

Programming in MATLAB 7.0, the predictive simulation process is as follows:

- Step 1. Load the trained ESN model, initialize the internal state of reservoir.
- Step 2. Input a group of test data, calculate reservoir state according to the ESN state Eq. (68.1).
- Step 3. Calculate network predictive value according to the ESN output Eq. (68.2) and save it.
- Step 4. Update the internal state of reservoir, go to step 2 until finish the prediction.

Figure 68.5 is the predictive curve of the purified juice color value. Figure 68.6 is the predictive curve of the purified juice pH value. The root mean square error of the purified juice color value production is 37.48 and its maximum relative error is 5.34 %. The root mean square error of the purified juice pH value production is 0.021 and its maximum relative error is 0.91 %.

Fig. 68.5 The predictive curve of the purified juice color value

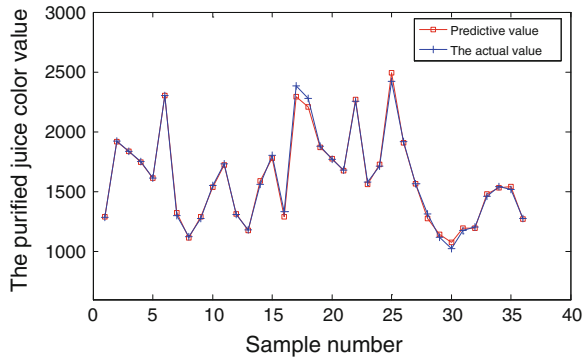
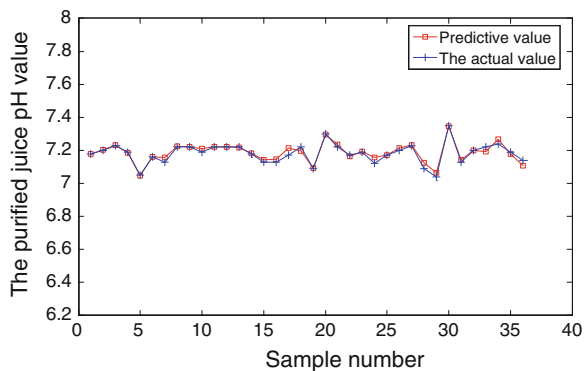


Fig. 68.6 The predictive curve of the purified juice pH value



68.7 Conclusion

In this paper, ESN is used to model the clarifying process in MATLAB using the historical data, and then predict the model output using the test data set to verify the accuracy of the model. The results show that the clarifying process model based on ESN is very accurate. This model is the foundation of the subsequent optimization control.

Acknowledgments This work was supported by the National Natural Science Foundation of China (61034002); by the Natural Science Foundation of Guangxi, China (2011GXNSFC018017); by the Key Project of Guangxi Science and Technology Lab Center (LGZX201106).

References

1. Zhao R, Wang W, Liu H (2011) Analysis of Guangxi sugar industry. Chin Mark 2011(49):171–173 (in Chinese)
2. Song S, Shi C, Lin X, Song C (2009) Study on modeling for clarification process of sugar mills with RBFNN. Control Theor Appl 2009(28):7–10 (in Chinese)

3. Jaeger H, Haas H (2004) Harnessing nonlinearity: predicting chaotic systems and saving energy in wireless communication. *Science* 304(5667):78–80
4. Chen W, Xu S (2001) Principles and techniques of sugar cane. China Light Industry Press, Beijing (in Chinese)
5. Jaeger H (2001) The echo state approach to analysing and training recurrent neural networks. German Nat Res Center Inf Technol
6. Xia Y, Principe JC (2011) An augmented echo state network for nonlinear adaptive filtering of complex noncircular signals. *IEEE Trans Neural Netw* 22(1)
7. Li B, Li Y, Rong X (2011) Comparison of echo state network and extreme learning machine on nonlinear prediction. *J Comput Inf Syst* 7(6):1863–1870
8. Jaeger H (2002) A tutorial on training recurrent neural network, covering BPPT, RTRL, EKF, and the “echo state network” approach. German National Research Center for Information Technology, Germany
9. Jaeger H (2003) Adaptive nonlinear system identification with echo state networks. *Adv Neural Inf Process Syst*

Chapter 69

A Method of Metro Vehicle Auxiliary Inverter Fault Diagnosis Based on Weighted Fuzzy Clustering Algorithm

Zengtao Ma, Junwei Gao, Bin Zhang, Dechen Yao and Yong Qin

Abstract In this paper, the principle of weighted fuzzy C-means clustering algorithm is introduced, and the application of the algorithm in the fault diagnosis of auxiliary inverter is studied. MATLAB software is used and several fault types are set during the simulation, such as voltage frequency variation, power supply interruption, pulse transient and so on. Fault feature vectors are obtained by the method of decomposition of wavelet packet, express the relative degree of importance of various data by weights, and then calculating the similarity degree of the samples to be diagnosed and the standard samples to realize the recognition of fault pattern. The experiment results show that the faults can be identified accurately.

Keywords Auxiliary inverter · Wavelet packet · Weighted fuzzy C-means clustering algorithm · Fault diagnosis

Auxiliary inverter is one of the most important parts of the metro vehicle, the main role of which is to invert DC high voltage to 380 V AC so as to power to the passenger compartment air conditioning system, lighting system and control system equipment. At the same time, straight transform can produce 110 V DC to charge the battery and to supply power for other DC load. In order to solve the problems of auxiliary inverter causing by its complicated structure, the inverter operation monitoring and fault diagnosis for the subway auxiliary are of important practical value to subway safely.

The fuzzy clustering theory is evolved on the basis of the fuzzy mathematics. The classified multivariate statistical analysis techniques are conducted according

Z. Ma · J. Gao (✉) · B. Zhang
College of Automation Engineering, Qingdao University, No 308 Ningxia Road,
Qingdao 266071, China
e-mail: qdgao163@163.com

J. Gao · D. Yao · Y. Qin
State Key Laboratory of Rail Traffic Control and Safety, Beijing Jiaotong University,
Beijing 100044, China

to the similarity between the object and the object. Bezdek [1] proposes the fuzzy C-means clustering (FCM) algorithm on the basis of the hard C-means clustering (HCM) algorithm. Reference [2] puts the gear pump as the study object and proposes a kind of fault classification which uses the fuzzy C-means clustering algorithm to get the gear pump. Reference [3] improves the FCM algorithm and proposes a weighted fuzzy C-means clustering (WFCM) algorithm which is used for airborne weapon systems fault diagnosis with the weight of sample distribution density size. WFCM algorithm is used in fault diagnosis of metro vehicle auxiliary inverter based on [2–6] in this paper.

69.1 Weighted Fuzzy C-means Clustering Algorithm

69.1.1 The Problem Description

The input sample sets $X = \{x_1, x_2, \dots, x_n\}$, each sample x_i attribute vector is $x_i = \{x_{i1}, x_{i2}, \dots, x_{is}\}$. The clustering process is to calculate the optimal solution of the objective function under the constraints. The objective function and the constraints of FCM algorithm are shown by Eqs. (69.1) and (69.2).

$$\min J(U, V) = \sum_{i=1}^C \sum_{j=1}^n u_{ij}^m d_{ij}^2 \quad (69.1)$$

$$\begin{cases} \sum_{i=1}^C u_{ij}^m = 1 \\ 0 \leq u_{ij} \leq 1 \\ 0 < \sum_{j=1}^n u_{ij} < n \end{cases} \quad (1 \leq i \leq C, 1 \leq j \leq n) \quad (69.2)$$

where C is the number of classifications, m is weight coefficient, n is the number of input samples, $U = [u_{ij}]_{C \times n}$ is membership degree matrix, $V = [v_1, v_2, \dots, v_C]$ is clustering center matrix, d_{ij} shows the distance between j th sample to i th clustering center.

The weighted fuzzy C-means clustering algorithm is improved on the basis of FCM algorithm [5]. All the attributes of samples have the same effect on fault classification in FCM algorithm. However, the influences of each attributes of sample maybe differ to others, even there is difference among them [6]. Weights of sample attributes show that different sample attributes have different influence on fault classification, and makes fault classification more accurately. In response to these issues above, WFCM also can be described into multi-constraint optimization problem, the objective function and the constraints are shown by Eqs. (69.3) and (69.4).

$$\min J(U, V, W) = \sum_{i=1}^C \sum_{j=1}^n \sum_{k=1}^s u_{ij}^m w_k^\beta d(v_{ik}, x_{jk}) \tag{69.3}$$

$$\begin{cases} 0 < \sum_{j=1}^n u_{ij} < n, \sum_{i=1}^C u_{ij} = 1 \\ 0 \leq u_{ij} \leq 1 \\ \sum_{k=1}^s w_k = 1, 0 \leq w_k \leq 1 \end{cases} \quad (1 \leq i \leq C, 1 \leq j \leq n, 1 \leq k \leq s) \tag{69.4}$$

where $W = [w_1, w_2, \dots, w_s]$ is attribute weight matrix, s is the dimension of the sample characteristics, β is attribute weight index.

69.1.2 General Steps of WFCM

In this paper, the method [6] is used to obtain the membership degree matrix U , the clustering center matrix V and the attribute weight matrix W with the partial optimization method to solve the problem above. General steps of WFCM algorithm used in fault diagnosis are shown as follows:

1. Calculate the initial classification with the equivalent fuzzy matrix method [7], and determine the appropriate number of initial classification C .
2. Set the initial clustering center $V_i^{(0)}$ ($i = 1, 2, \dots, C$), initialize the attribute weight matrix $W^{(0)} = \{1/s, 1/s, \dots, 1/s\}$.
3. Calculate the initial membership degree matrix $U^{(0)}$.

$$\mu_{ij}^{(0)} = r_{ij} / \sum_{i=1}^C r_{ij}, (i = 1, 2, \dots, C; j = 1, 2, \dots, n) \tag{69.5}$$

where

$$r_{ij} = \sum_{k=1}^C \min(x_{ik}, v_{jk}) / \sum_{k=1}^C \max(x_{ik}, v_{jk}), (i, j = 1, 2, \dots, n; k = 1, 2, \dots, m)$$

shows the approximation degree between i th sample and j th clustering center. v_{jk} is the element of clustering center.

4. Set the maximum number of loop, calculate the membership degree matrix $U^{(l)}$ and clustering center matrix $V^{(l)}$ after l th loop.

$$U^{(l)} = \frac{1}{\sum_{s=1}^C (d_{ij}/d_{sj})^{\frac{2}{m-1}}}, (i, s = 1, 2, \dots, C; j = 1, 2, \dots, n) \tag{69.6}$$

$$V^{(l)} = \frac{\sum_{j=1}^n (u_{ij})^m S_j}{\sum_{j=1}^n (u_{ij})^m}, (i = 1, 2, \dots, C; j = 1, 2, \dots, n) \tag{69.7}$$

where $d_{ij} = \sum_{k=1}^s w_k^\beta (v_{ik} - x_{jk})^2$ is the weighted distance formula, S_j is the j -th sample.

5. Update weight attribute matrix W .

$$w_k^{(l)} = \begin{cases} 0 & \delta_k = 0 \\ \left[\sum_{r=1}^s \left(\frac{\delta_k}{\delta_r} \right)^{\frac{1}{\beta-1}} \right]^{-1} & \delta_k \neq 0 \end{cases} \tag{69.8}$$

where $\delta_k = \sum_{i=1}^c \sum_{j=1}^n u_{ij}^m (v_{ik} - x_{jk})^2$.

6. Set a small positive number ε as the maximum permissible error, judge $\|U^{(l+1)} - U^{(l)}\| < \varepsilon$ whether it is true, if true, end the loop. Otherwise, return to step 2 until the inequality is true or reach the maximum loop. Obtain the ultimate membership degree matrix U , the ultimate clustering center matrix V and the ultimate attribute weight matrix W .

7. Found the standard sample. Each row of the ultimate clustering center matrix V regards as a standard sample, and then calculates the similarity degree between the samples to be diagnosed and the standard samples based on Eq. (69.9). Choose the maximum similarity degree as the basis for classification of test sample.

$$\sigma(X, V) = \frac{\sum_{k=1}^m \min(x_{ik}, v_{jk})}{\sum_{k=1}^m \max(x_{ik}, v_{jk})}, (i = 1, 2, \dots, n; j = 1, 2, \dots, C) \tag{69.9}$$

69.2 Fault Feature Extraction Algorithm

In this paper, the authors extract fault feature with the method of wavelet packet decomposition. Wavelet packet transform theory is evolved from wavelet transform theory. Both low frequency part and high frequency part of the fault signals

are decomposed in wavelet packet theory [8, 9]. The fault feature vector extraction steps are shown as follows.

1. Decompose the fault signals with 3-level wavelet packet; extract the fault signals feature from low-frequency parts to high-frequency parts.
2. Reconstruct the wavelet packet decomposition coefficients, extract each frequency band signal feature. S_{3j} is the reconstructed signal of 3rd level j -th node.

The original signal S can be shown as $S = \sum_{j=0}^7 S_{3j}$.

3. Calculate every frequency band energy of the fault signals and normalized. Here the reconstructed signals energy are represented by E_{3j} ($j = 0, 1, \dots, 7$). Each frequency band energy can be calculated by the equation

$$E_{3j} = \int |S_{3j}(t)|^2 dt = \sum_{k=1}^n |x_{jk}|^2, \text{ where } x_{jk} \text{ is the amplitude of discrete points of}$$

reconstructed signal S_{3j} . The proportion of each band energy in the total energy after normalization can be expressed by $p_{3j} = E_{3j}/E$, and total energy is

$$E = \sum_{j=0}^7 E_{3j}.$$

4. Found the fault signals feature vectors $T = [p_{30}, p_{31}, \dots, p_{37}]$.

69.3 Fault Diagnosis Examples

In this paper, the authors set three types fault signals in the metro vehicle auxiliary inverter simulation, such as voltage frequency variation, power supply interruption and pulse transient. Voltage frequency variation signal is shown in Fig. 69.1, in which fault occurs between 0.5 and 0.6 s. The sampling frequency of fault signal is 4,096 Hz.

Based on the wavelet packet decomposition method, the authors extract three samples from fault types of voltage frequency variation, power supply interruption

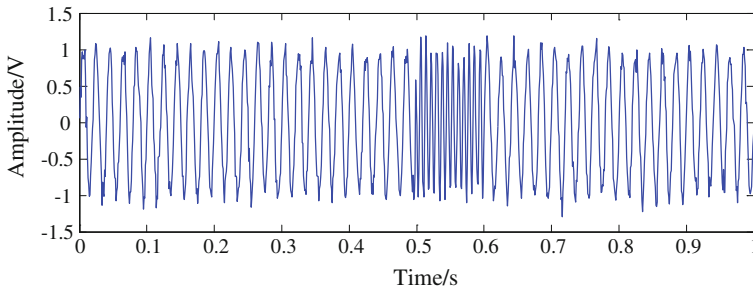


Fig. 69.1 Voltage frequency variation waveform in time domain

Table 69.1 Fault samples and the corresponding fault types

Samples characteristics data								Fault type
0.9160	0.0342	0.0025	0.0024	0.0351	0.0040	0.0028	0.0029	Voltage frequency variation
0.8567	0.0301	0.0030	0.0027	0.0976	0.0048	0.0025	0.0025	
0.9115	0.0338	0.0027	0.0043	0.0373	0.0041	0.0033	0.0030	Pulse transient
0.4274	0.3801	0.0390	0.1063	0.0051	0.0068	0.0291	0.0062	
0.4385	0.4197	0.0370	0.0617	0.0111	0.0150	0.0083	0.0087	Power supply interruption
0.4797	0.3779	0.0309	0.0838	0.0061	0.0072	0.0093	0.0050	
0.5950	0.1232	0.0533	0.0974	0.0018	0.0119	0.0858	0.0317	Power supply interruption
0.5929	0.1188	0.0505	0.1072	0.0020	0.0118	0.0836	0.0332	
0.6019	0.1284	0.0510	0.0916	0.0019	0.0122	0.0833	0.0297	

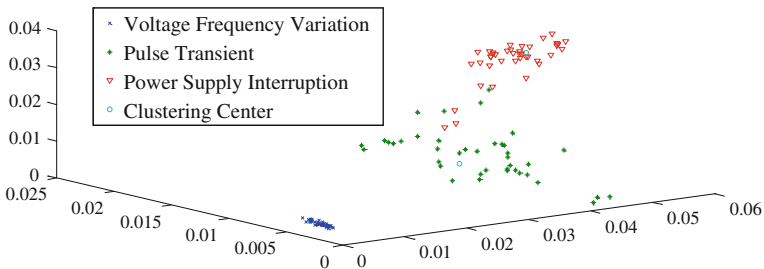


Fig. 69.2 Distribution of the samples of different fault types in the three-dimensional graph

Table 69.2 Comparison of fault diagnosis results

Fault type	Total number of samples	FCM			WFCM		
		Accurate number	Wrong number	Accurate ratio (%)	Accurate number	Wrong number	Accurate ratio (%)
Power supply interruption	40	40	0	100.00	40	0	100.00
Pulse transient	40	36	4	90.00	37	3	92.50
Voltage frequency variation	40	36	4	90.00	38	2	95.00
Sum/accurate ratio	120	93.33			95.83		

and pulse transient respectively. These samples which used for initial clustering are shown in Table 69.1.

There are 120 fault samples as the test samples which include three types of fault. Set weight coefficient $m = 3$, attribute weight index $\beta = 5$, maximum permissible error $\varepsilon = 1.0 \times 10^{-4}$. Final attribute weight matrix is:

$$W = [0.0579 \quad 0.0801 \quad 0.1833 \quad 0.0803 \quad 0.0628 \quad 0.1828 \quad 0.1136 \quad 0.2391]$$

Concluded from attribute weight matrix W , the 3rd, 6th, 8th band of wavelet packet energy have greater influence on fault sample classification. Figure 69.2 is

shown as 3-dimensional map of fault samples distribution which the 3rd, 6th, 8th band of wavelet packet energy as the coordinates. All the test samples are divided into three classes approximately in Fig. 69.2. Fault diagnosis results by FCM and WFCM are shown in Table 69.2.

69.4 Conclusion

In this paper, WFCM algorithm is used in the field of metro vehicle auxiliary inverter fault diagnosis on the basis of FCM algorithm. In the following study, the time domain indexes and the frequency domain indexes of metro vehicle auxiliary inverter fault signals can be extracted and then combine with the energy of wavelet packet to form the united feature. By evaluating the fault feature indexes and founding the evaluation model in the research, Fault diagnosis can be realized by analyzing the optimum indexes in WFCM method.

Acknowledgments This work is partially supported by the National Key Technology R&D Program (2011BAG01B05), the Foundation of Shandong Province (BS2011DX008, ZR2011FQ012, ZR2011FM008), 863 Program (2011AA110501) and the State Key Laboratory of Rail Traffic Control and Safety Foundation (RCS2011K005, RCS2012K006) Beijing Jiaotong University.

References

1. Bezdek JC (1974) Cluster validity with fuzzy sets. *J Cybern* 3(3):58–72
2. Wang XP, Wang HG, Chen XH (2009) Diagnosis technics of gear pump fault based on the fuzzy C-means clustering algorithm. *Mach Tool Hydraul* 37(10):269–272 (in Chinese)
3. Lu Q, Feng JF, Hu JH et al (2007) Fault diagnosis based on WFCM. *J Vib Meas Diagn* 27(4):308–311 (in Chinese)
4. Chen D, Cui DW, Li X et al (2008) A weighted fuzzy clustering algorithm and its application to fault diagnosis of power transformer. *J Xi'an Univ Technol* 24(2):182–186 (in Chinese)
5. Sui WT, Lu CH, Zhang D (2010) Bearings fault diagnosis based on feature weighted FCM algorithm. *J Wuhan Univ Technol (Transportation Science and Engineering)* 34(1):72–75 (in Chinese)
6. Li JX, Gao XB, Gao YE (2007) A feature weighted fuzzy clustering algorithm. *J Beijing Electron Sci Technol Inst* 15(2):74–76 (in Chinese)
7. Yin AD, Zhao H, Yang ZM (2006) Research on the fault diagnosis of vehicle transmission gear based on wavelet transform—Fuzzy cluster. *China Mech Eng* 17(20):2121–2125 (in Chinese)
8. Gao JW, Yu JP, Leng ZW et al (2013) The application of PSO-LSSVM in fault diagnosis of subway auxiliary inverter. *ICIC Express Letters, Part B: Applications* 4(3):777–784
9. Sun JD, Jin SJ (2010) Feature extraction method based on wavelet packet energy and high-order spectrum. *J Tianjin Univ* 43(6):563–566 (in Chinese)

Chapter 70

The Inverted Pendulum Control System Based on Two Degree of Freedom Model Driven PID

Lixiang Zhang and Haiyan Zhang

Abstract PID control systems are the most commonly used control technology in industries. However, there are issues on control performances for some controlled processes, such as large time-delay processes and unstable processes. The inverted pendulum is a kind of system with instinct instability, studying the efficient control strategies are needed to keep it's stable at the position of dynamic balance. In this paper, a new two degree of freedom model driven PID control system is introduced and it is used to the inverted pendulum. Simulation results show that the model driven PID control is capable of stabilizing with unstable processes by using PD feedback, regulating quickly for disturbance and tracking quickly to the change of set point.

Keywords Inverted pendulum control · Two-degree-of-freedom · Model driven PID · Instinct instability

70.1 Introduction

PID control systems are still widely used as a basic control technology in today's industries due to its well-known simple PID control structure and its ability of correcting error in control systems, stabilizing process. However, the tuning of the PID control systems is not always easy, because of its simple control structure for wide class of process characteristics, such as lager time-delay processes, oscillatory processes and unstable processes. What is a widely applicable and simple process controller with an easy tuning and good control performance? Recently, the concept of "From Model-based Control to Model Driven Control" was

L. Zhang (✉) · H. Zhang
Department of Automation, Engineering College of Shanxi University, Taiyuan,
Shanxi, China
e-mail: lxz_8177757@sina.com

lectured by Kimura [1] at the International Conference on Decision and Control (CDC 2000) in Sydney. He defined a Model-Driven Control (MDC) concept as “a control system architecture which uses a model of the plant as a principal component of controller”. Features of MDC are simple structure, easy tuning approach and proven stability and robustness. Model algorithmic control (MAC) by Rouhani [2] and Predictive PI (PPI) control systems by Astrom and Hagglund [3] and Self-tuning Internal Model Controller (IMC) by Shu [4] can be considered to belong to the same class of MDC. However, it is difficult to realize the Model Driven control system for unstable processes. In order to improve these issues, a Model-Driven PID control system, which is combined with PD feedback block, IMC block and a set point filter block was proposed by Shigemasa et al. [5]. Yukitomo et al. [6] suggested using a Two Degree of Freedom Model Driven PID (TDF MD PID) to replace the IMC which has One Degree of Freedom, with an IMC Q filter which has Two Degrees of Freedom. The reason is that a TDF MD PID control system owns better disturbance rejection properties by adding one more tuning parameter to MD PID control system. In this paper, a design method based the TDF MD PID control system for The inverted pendulum processes is described. The TDF MD PID control is capable of stabilizing with unstable processes by using PD feedback, regulating quickly for disturbance and tracking quickly to the change of set point. With TDF MD PID inverted pendulum control system study comparing with conventional PID control systems was done.

70.2 TDF MD PID Control System

TDF MD PID control system configuration can be expressed as shown in Fig. 70.1. In this figure, r , u , d , y and v are set point variable, manipulated variable, disturbance signal, process variable and output signal of Main Controller. The control system consists of the overall control process, main controller and set point filter, each of which plays a different role in the control system. The main controller can be further decomposed into a gain block K_c , a second order Q filter $Q(s)$ with tuning parameter λ , α and a first order model with time delay.

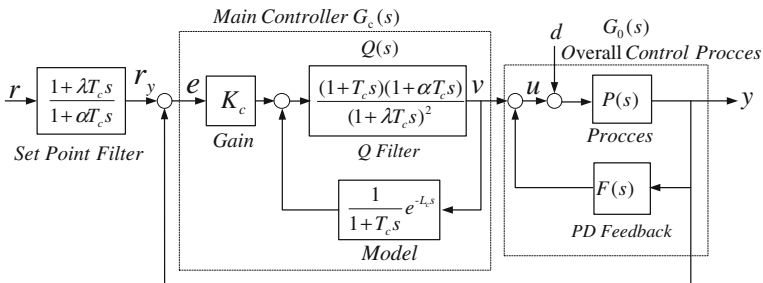


Fig. 70.1 TDF MD PID control system

70.2.1 Overall Controlled Process $G_0(s)$

The overall controlled process $G_0(s)$ should be designed as the controlled plant $P(s)$ with PD feedback. By using PD feedback compensator $F(s)$, the process $P(s)$ can be compensated and to make it into a first order system with time delay. A well designed PD feedback compensator $F(s)$ will treat the integral oscillatory processes or unstable processes to achieve the control objective. Obviously, the transfer function of the overall controlled process, that is, from v to y is expressed by:

$$G_0(s) = \frac{P(s)}{1 + P(s)F(s)} = \frac{K}{1 + Ts} e^{-Ls} \quad (70.1)$$

where K , T and L are gain, time constant and dead time of the overall controlled process respectively. If gain K and time constant T can be smaller than those of the originally controlled process $P(s)$, the integral error of TDF MD PID control system will be smaller than that of the originally controlled process $P(s)$, good control performance can be obtained. The control parameters, gain K , time constant T and dead time L should be chosen properly and then the required compensator $F(s)$ is designed. The PD feedback compensator is designed as:

$$F(s) = \frac{K_f(T_f s + 1)}{1 + kT_f s} \quad (70.2)$$

where K_f , T_f and K are constants.

70.2.2 Main Controller $G_c(s)$

The main controller $G_c(s)$ consists of gain block, Q filter block $Q(s)$ and model block. The model block is the Overall controlled process $G_0(s)$. After $G_0(s)$ is identified in the form of Eq. (70.1), the main controller is designed by adjusting the parameters λ and α in $Q(s)$ to meet the design performances. The main controller transfer function is derived as follows.

$$G_c(s) = K_c \frac{\frac{(1+T_c s)(1+\alpha T_c s)}{(1+\lambda T_c s)^2}}{1 - \frac{(1+T_c s)(1+\alpha T_c s)}{(1+\lambda T_c s)^2} \times \frac{1}{1+T_c s} e^{-L_c s}} = \frac{1}{K} \frac{(1 + Ts)(1 + \alpha Ts)}{(1 + \lambda Ts)^2 - (1 + \alpha Ts)e^{-Ls}} \quad (70.3)$$

where the parameters are set as, $K_c = 1/K$, $T_c = T$, $L_c = L$.

We can get the open-loop transfer function of system (from e to y) and the closed-loop transfer function of system (from r_y to y) and the interference transfer function of system (from d to y) by a similar approach as shown above.

Obviously, K_c and $(1 + T_c s)$ in $G_c(s)$ are used to cancel K and $(1 + Ts)$ in $G_0(s)$, thus the steady state position error is zero, i.e. $e = 0$, there are $y/r_y = 1$ and $y/d = 0$ for step input signal. The main controller improves the speed response ability of the system, and helps in rejecting the noise d from entering system. Hence, the main controller can allow almost all reference signals enter into system while the noise is rejected.

70.2.3 Set Point Filter

The set point filter is used to cancel one zero and one pole in the closed-loop transfer function of system and thus to reduce the order of the system from second order to first one. The transfer function of system (from r to y) is

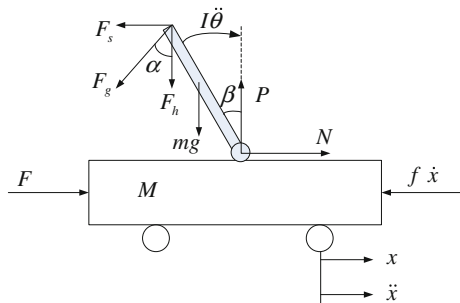
$$G_{r \rightarrow y}(s) = \frac{y(s)}{r(s)} = \frac{1 + \lambda Ts}{1 + \alpha Ts} \times \frac{1 + \alpha Ts}{(1 + \lambda Ts)^2} e^{-Ls} = \frac{e^{-Ls}}{1 + \lambda Ts} \quad (70.4)$$

70.3 Inverted Pendulum Mathematical Model

Our study addresses the inverted pendulum of Googol Technology GLIP series which is a typical experimental equipment, constituted by a pendulum bar and a movement cart. As is shown in the Fig. 70.2, the detailed parameters are as follows [7, 8].

M is the mass of cart, 1.096 kg; m is the mass of pendulum, 0.109 kg; f is the friction factor of cart, 0.1 N/m/sec; l is the distance between axis of rotation and the centroid of pendulum, 0.25 m; I is the moment of inertia, 0.00223 kg*m*m; θ is the angle between pendulum and pure vertical, $\theta = \pi + \beta$; F is the force on the cart; g is the acceleration of gravity, 9.8 m/s²; F_s is a horizontal disturbance force; F_h is a vertical disturbance force; F_g is the joint forces of F_s and F_h ; N and P are the

Fig. 70.2 Force analysis of inverted pendulum system



horizontal and vertical components of the interaction force of the cart and pendulum.

The horizontal force of the pendulum bar is expressed by:

$$N - F_S = m \frac{d^2}{dt^2} (x + l \sin \theta) \quad (70.5)$$

where $F_S = F_g \sin \alpha$, α is the angle between F_g and F_h .

The vertical force of the pendulum bar is expressed by:

$$-P + mg + F_h = m \frac{d^2}{dt^2} (l - l \cos \theta) \quad (70.6)$$

where $F_h = F_g \cos \alpha$.

Torque balance equation is

$$F_g l \sin \alpha \cos \theta + F_g \cos \alpha \sin \theta + P l \sin \theta + N l \cos \theta + I \ddot{\theta} = 0 \quad (70.7)$$

where $I = \frac{1}{3} m l^2$, the moment of inertia of the pendulum bar.

Because $\theta = \pi + \beta$ and $\beta \ll 1$, then $\sin \theta = -\sin \beta$ and $\cos \theta = -\cos \beta$. According to Eqs. 70.5, 70.6 and 70.7, and F_g is ignored, we can derived as

$$\ddot{\beta} - 29.4\beta = 3\ddot{x} \quad (70.8)$$

70.4 Simulation Experiment

The transfer function of acceleration input and angle output is $P(s) = \frac{3}{s^2 - 29.4}$, the PD feedback was designed to $F(s) = \frac{16.266(0.184s+1)}{(0.02s+1)}$. The overall controlled process is approximated as $G_0(s) = \frac{0.1547}{(0.291s+1)} e^{-0.125s}$ by using the PD compensator. So the parameters of the TDF MD PID control system are set as: $K_c = 1/K = 6.464$, $T_c = T = 0.291$, $L_c = 0.125$, $\gamma = 0.92$, $\alpha = 0.28$. The parameters of the PID control system are set as: $K_p = 50$, $K_I = 25$, $K_D = 20$. When the reference input is unit-square wave with period 20 s, the simulation results are shown in Figs. 70.3 and 70.4. The TDF MD PID control system shows quick response for set point tracking and has no overshoot when the model parameters changes of increasing 0.005 s time delay. The TDF MD PID control system has better performance than the PID control system.

Fig. 70.3 Comparison of response curves of the control system in model parameters not change

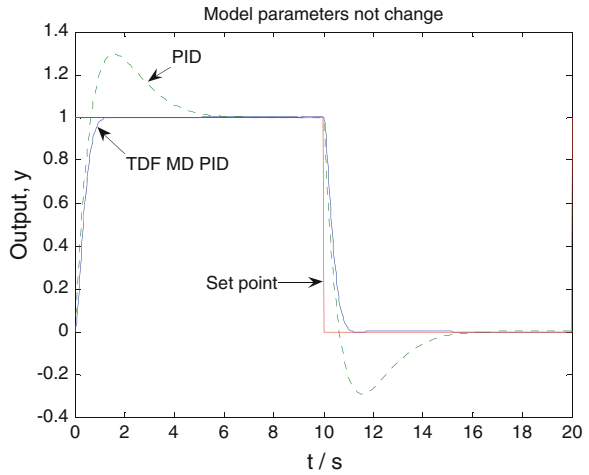
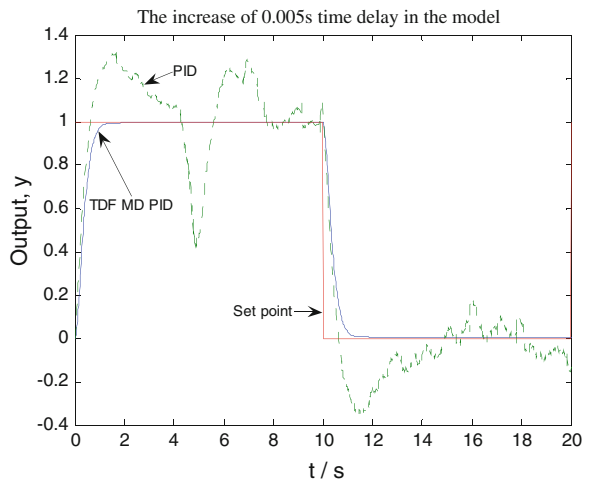


Fig. 70.4 Comparison of response curves of the control system in model parameters changes



70.5 Conclusions

In this paper, the TDF MD PID control system was introduced, it is combined with PD feedback block, Q filter and Set point filter. It is understood that the TDF MD PID control system has strong capability to stabilize by using the PD feedback, to regulate quickly against disturbance and to track quickly to the change of set point without overshoot or has a bit overshoot by studied cases. The TDF MD PID control system is suitable to be applied widely to improve the control performance of processes in industries.

Acknowledgments This work was financially supported by project funded of key subjects construction in colleges and universities in Shanxi Province (No: 20111048), titled with the Inverted Pendulum Control Strategy Research and Development Based on Embedded System.

References

1. Kimura H (2000) Is the model a good controller? Perspectives on brain motor control. In: 39 the IEEE conference on decision and control, Sydney
2. Rouhani R (1982) Model algorithmic control (MAC), basic theoretical properties. *Automatic* 18(4):401–414
3. Astrom KJ, Hagglund T (1995) PID controllers: theory, design and tuning, second edition. Instrument Society of America, Research Triangle Park, NC
4. Shu DQ (1933) Self-tuning internal model controller. *J Univ Sci Technol Beijing* 15(4):400–407
5. Masanori Y, Takashi S, Baba Y (2002) A model driven PID control system and its application to chemical processes. *Proceeding of SICE annual conference*. vol. 4. pp 2656–660
6. Yukioto M, Shigemasa T, Baba Y, Kojima F (2004) A two degrees of freedom PID control system, its features and applications. In: 5th Asian control conference, vol. 1. pp 456–59
7. Jing Z, Lixiang Z, Jing X (2011) Application of Memetic Algorithm in Control of Linear Inverted Pendulum. In : *Proceedings of IEEE CCIS 2011*. pp 103–107
8. Googoltech. Linear inverted pendulum. http://www.googoltech.com.cn/webtech_cn/dispro.php?findid=161&flord=prol53154

Chapter 71

Delay-Dependent Robust Stabilization for Singular Nonlinear System with Markovian Jumping Parameters

Chunmei Duan and Hongqian Lu

Abstract This paper considers the problem of delay-dependent robust stabilization for singular nonlinear system with Markovian jumping parameters. The considered systems are not necessarily assumed to be regular and impulse free. A state feedback controller is designed in terms of a set of linear coupled matrix inequalities.

Keywords: Singular system · Linear matrix inequality (LMI) · Nonlinear

71.1 Introduction

In recent years, more attention has been devoted to the study of singular system. A great number of fundamental notions and results based on the theory of regular systems have been extended to the area of singular system [1, 2].

Markovian jump systems can model stochastic systems with abrupt structural variation resulting from the occurrence of some inner discrete events in the system such as failures and repairs of machine in manufacturing systems, modifications of the operating point of a linearized model of a nonlinear system [3, 4]. Therefore, For Markovian jump systems, there have been many nice results [5–9]. However, most of the results reported in the literature are few even nonexistent. Therefore, an alternate to solve the stochastic stabilizability problems for the class of nonlinear systems is needed.

C. Duan

School of Management Science and Engineering, Shandong Normal University,
East Wenhua Road, Jinan, Shandong Province 250014, People's Republic of China
e-mail: chunmeiduan@mail.sdu.edu.cn

H. Lu (✉)

School of Electrical Engineering and Automation, Shandong Polytechnic University,
Shandong Province 250353, People's Republic of China
e-mail: hqlu@163.com

In this paper, we study the problem of the stochastic stabilizability for singular nonlinear systems. Attention will be focused on the design of state feedback controllers such that the closed-loop system is stochastically admissible. A sufficient condition for the solvability of the control problem is derived.

71.2 Problem Formulation and Preliminaries

Let $\{r(t), t \geq 0\}$ be a continuous-time discrete-state Markov process with right continuous trajectories taking value in a finite set $\mathcal{S} = \{1, 2, \dots, N\}$ with transition probability matrix $\Pi = (\pi_{ij})(i, j \in \mathcal{S})$ given by

$$P\{r(t+h) = j | r(t) = i\} = \begin{cases} \pi_{ij}h + o(h), & i \neq j, \\ 1 + \pi_{ii}h + o(h), & i = j, \end{cases}$$

where $h > 0$ and $\lim_{h \rightarrow \infty} \frac{o(h)}{h} = 0$, $\pi_{ij} > 0$ is the transition rate from i to j if $i \neq j$ and $\pi_{ii} = -\sum_{j=1, j \neq i}^N \pi_{ij}$.

In this note, we consider uncertain singular systems with time-delay and Markovian jump parameters described by

$$\begin{cases} E(r(t))\dot{x}(t) = A(r(t))x(t) + A_d(r(t))x(t-d) + B(r(t))u(t) \\ \quad + f(r(t), x(t), x(t-d)) \\ x(t) = \phi(t), t \in [-\bar{d}, 0], \end{cases} \tag{71.1}$$

where $x(t) \in R^n$ is the state vector, $u(t) \in R^m$ is the control input. d is the time-delay with known constant scalars \bar{d} satisfying

$$0 \leq d \leq \bar{d}, \quad \forall t \geq 0, \tag{71.2}$$

$\phi(t) \in C_{n,d}$ is a compatible vector valued initial function. For fixed system mode, the matrix $E(r(t)) \in R^{n \times n}$ may be singular and we assume that $0 < \text{rank} E(r(t)) = r$, $E(r(t)) \leq n$, $A(r(t))$, $B(r(t))$ and $A_d(r(t))$ are known real constant matrices with appropriate dimensions. $f(r(t), x(t), x(t-d)) \in R^n$ is a given disturbance function.

Assumption 1 Let the following holds for every $i \in \mathcal{S}$:

$$\|f(r(t), x(t), x(t-d))\|^2 \leq \alpha(r(t))\|x(t)\|^2 + \beta(r(t))\|x(t-d)\|^2, \tag{71.3}$$

The nominal Markovian jump singular nonlinear system and time-delay system of system (71.1) are as follows:

$$E(r(t))\dot{x}(t) = A(r(t))x(t). \tag{71.4}$$

$$E(r(t))\dot{x}(t) = A(r(t))x(t) + A_d(r(t))x(t - d). \tag{71.5}$$

Recall that the Markov process $\{r(t), t \geq 0\}$ takes values in the finite set $S = \{1, 2, \dots, N\}$. For the sake of simplicity, we write $E(i) = E_i$, $A(i) = A_i$, $A_d = A_{di}$, $B(i) = B_i$, $f(i) = f_i$.

This paper deals with the class of singular nonlinear systems with Markovian jumping parameters under study and provides some sufficient conditions on the stochastic stability and the stochastic stabilizability.

71.3 Main Results

In this section, we first introduce a sufficient condition of stochastic admissible for system (71.1) with $u(t) = 0$.

Theorem 1: *For a prescribed scalar $\bar{d} > 0$ and any time delay d satisfying $0 \leq d \leq \bar{d}$, the system (71.1) is stochastically admissible with $u(t) = 0$, if there exist symmetric positive-definite matrices Q, Z and matrices $P_{1i}, P_{2i}, P_{3i}, Y_{1i}, Y_{2i}$, and T_{1i} with appropriate dimensions such that*

$$E_i^T P_{1i} = P_{1i}^T E_i \geq 0, \tag{71.6a}$$

$$\begin{bmatrix} \Phi_i + \Gamma_{1i} & \Gamma_{2i} \\ * & \Gamma_{3i} \end{bmatrix} < 0 \tag{71.6b}$$

Where

$$\Gamma_{1i} = \begin{bmatrix} (\varepsilon_{1i} + \varepsilon_{2i})\alpha_i & 0 & 0 & 0 \\ 0 & (\varepsilon_{1i} + \varepsilon_{2i})\beta_i & 0 & 0 \\ 0 & 0 & 0 & 0 \\ 0 & 0 & 0 & 0 \end{bmatrix}, \Gamma_{2i} = \begin{bmatrix} P_{2i} & 0 & 0 & 0 \\ 0 & 0 & P_{3i} & 0 \end{bmatrix}^T,$$

$$\Gamma_{3i} = \begin{bmatrix} -\varepsilon_{1i}I & 0 \\ 0 & -\varepsilon_{2i}I \end{bmatrix}.$$

Proof First, we propose the following Lyapunov function:

$$\begin{aligned} V(x(t), r(t)) = & x^T(t)E^T(r(t))P_1(r(t))x(t) + \int_{t-d}^t x^T(\alpha)Qx(\alpha)d\alpha \\ & + \int_{-d}^0 \int_{t+\beta}^t \dot{x}^T(\alpha)E^T(r(t))ZE(r(t))\dot{x}(\alpha)d\alpha d\beta, \end{aligned} \tag{71.7}$$

From (71.6b) we can get

$$\Phi_i + \Gamma_i < 0 \tag{71.8}$$

Where

$$\Gamma_i = \begin{bmatrix} \varepsilon_{1i}^{-1} P_{2i}^T P_{2i} + (\varepsilon_{1i} + \varepsilon_{2i}) \alpha_i & 0 & 0 & 0 \\ 0 & (\varepsilon_{1i} + \varepsilon_{2i}) \beta_i & 0 & 0 \\ 0 & 0 & \varepsilon_{1i}^{-1} P_{3i}^T P_{3i} & 0 \\ 0 & 0 & 0 & 0 \end{bmatrix}$$

Consider the Lyapunov function (71.7), we have

$$\begin{aligned} & AV(x(t), r(t) = i) \\ &= \lim_{\Delta \rightarrow 0} \frac{1}{\Delta} [\mathcal{E}\{V(x(t + \Delta), r(t + \Delta)) | x(t), r(t) = i\} - V(x(t), r(t) = i)] \\ &\leq 2x^T(t) P_{1i}^T E_i \dot{x}(t) + x^T(t) \left(\sum_{j=1}^N \pi_{ij} E_j^T P_{1j} \right) x(t) + x^T(t) Qx(t) - x^T(t-d) Qx(t-d) \\ &\quad + \bar{d} \dot{x}^T(t) E_i^T Z E_i \dot{x}(t) - \int_{t-d}^t \dot{x}^T(\alpha) E_i^T Z E_i \dot{x}(\alpha) d\alpha \\ &\leq 2x^T(t) P_{1i}^T E_i \dot{x}(t) + x^T(t) \left(\sum_{j=1}^N \pi_{ij} E_j^T P_{1j} \right) x(t) + x^T(t) Qx(t) - x^T(t-d) Qx(t-d) \\ &\quad + \bar{d} \dot{x}^T(t) E_i^T Z E_i \dot{x}(t) - \zeta_i^T(\alpha) (\bar{d} Z) \zeta_i(\alpha), \end{aligned}$$

Where

$$\zeta_i(\alpha) = \int_{t-d}^t \frac{E_i \dot{x}(\alpha)}{d} d\alpha.$$

Notice that for each $i \in \mathcal{S}$,

$$\begin{aligned} & 2[x^T(t) Y_{1i} + (E_i \dot{x}(t))^T Y_{2i} + x^T(t-d) T_{1i}] \\ & \times [E_i x(t) - E_i x(t-d) - \int_{t-d}^t E_i \dot{x}(\alpha) d\alpha] = 0, \end{aligned} \tag{71.9}$$

$$\begin{aligned} & 2[x^T(t) P_{2i}^T + (E_i \dot{x}(t))^T P_{3i}^T] \\ & \times [-E_i \dot{x}(t) + A_i x(t) + A_{di} x(t-d) + f_i(x(t), x(t-d))] = 0. \end{aligned} \tag{71.10}$$

Where

$$\zeta^T(t) = [x^T(t) \quad (E_i \dot{x}(t))^T \quad x^T(t-d) \quad \zeta_i^T(t)]^T.$$

Then, according to the result of the theorem 1 in [9], we can deduce that the system (71.1) with $u(t) = 0$ is stochastically admissible. This completes the proof.

Consider the following linear state feedback controller

$$u(t) = K(r(t))x(t), K(r(t)) \in R^{m \times n} \tag{71.11}$$

for $r(t) \in \mathcal{S}$, where $K(r(t))$ is to be determined. Substituting (71.11) into (71.1) yields the following closed-loop system:

$$\begin{cases} E(r(t))\dot{x}(t) = A_K(r(t))x(t) + A_d(r(t))x(t-d) + f(r(t), x(t), x(t-d)), \\ x(t) = \phi(t), t \in [-\bar{d}, 0], \end{cases} \quad (71.12)$$

where $A_K(r(t)) = A(r(t)) + B(r(t))K(r(t))$.

Theorem 2: For a prescribed scalar $\bar{d} > 0$ and the singular delay closed-loop system (71.12) is stochastically admissible if there exist scalars $\mu_i > 0$, $\lambda_{ij} > 0 (i \neq j)$, δ_{1i} and δ_{2i} , symmetric positive-definite matrices W_i, X and matrices L_{1i}, L_{2i}, L_{3i} and V_i , with appropriate dimensions such that for $i = 1, 2, \dots, N$,

$$E_i L_{1i} = L_{1i}^T E_i^T \geq 0, \quad (71.13a)$$

$$E_i^T P_{1j} \leq \lambda_{ij}^{-1} I, \quad (71.13b)$$

$$\left[\begin{array}{cccccccccc} \Phi_{11i} & \Phi_{12i} & \Phi_{13i} & 0 & \bar{d}L_{2i}^T & (\varepsilon_{1i} + \varepsilon_{2i})L_{1i}^T & (\varepsilon_{1i} + \varepsilon_{2i})L_{2i}^T & W_{3i} & 0 & \Psi_i \\ * & \Phi_{22i} & \Phi_{23i} & \bar{d}\delta_{1i}X & \bar{d}L_{3i}^T & 0 & (\varepsilon_{1i} + \varepsilon_{2i})L_{3i}^T & 0 & 0 & 0 \\ * & * & \Phi_{33i} & \bar{d}\delta_{2i}X & 0 & 0 & 0 & 0 & W_{4i} & 0 \\ * & * & * & -\bar{d}X & 0 & 0 & 0 & 0 & 0 & 0 \\ * & * & * & * & -\bar{d}X & 0 & 0 & 0 & 0 & 0 \\ * & * & * & * & * & -(\varepsilon_{1i} + \varepsilon_{2i})W_{2i} & 0 & 0 & 0 & 0 \\ * & * & * & * & * & * & -(\varepsilon_{1i} + \varepsilon_{2i})W_{5i} & 0 & 0 & 0 \\ * & * & * & * & * & * & * & -\varepsilon_{1i}I & 0 & 0 \\ * & * & * & * & * & * & * & 0 & -\varepsilon_{2i}I & 0 \\ * & * & * & * & * & * & * & * & * & -J_i \end{array} \right] < 0 \quad (71.13c)$$

Where

$$\begin{aligned} \Theta_{11i} &= L_{2i} + L_{2i}^T + W_{1i} + \pi_{ii}L_{1i}^T E_i^T, \\ \Theta_{12i} &= L_{3i} - L_{2i}^T + L_{1i}^T A_i^T + V_i^T B_i^T + \delta_{1i}L_{1i}^T E_i^T, \\ \Theta_{13i} &= \delta_{2i}L_{1i}^T E_i^T, \Theta_{22i} = -L_{3i} - L_{3i}^T, \\ \Theta_{23i} &= A_{di}L_{1i} + \delta_{1i}E_i L_{1i}, \Theta_{33i} = -W_i - \delta_{2i}E_i L_{1i} - \delta_{2i}L_{1i}^T E_i^T, \\ \Psi_i &= [\sqrt{\pi_{1i}}L_{1i}^T \cdots \sqrt{\pi_{ii-1}}L_{1i}^T \sqrt{\pi_{ii+1}}L_{1i}^T \cdots \sqrt{\pi_{iN}}L_{1i}^T], \\ J_i &= \text{diag}\{\lambda_{i1}I, \dots, \lambda_{ii-1}I, \lambda_{ii+1}I, \dots, \lambda_{iN}I\}. \end{aligned}$$

In this case, a desired state feedback controller is given by

$$u(t) = V_i L_{1i}^{-1} x(t). \quad (71.14)$$

Proof: Condition (71.19) with A_i replaced by $A_{Ki} = A_i + B_i K_i$, can be written as

$$\begin{bmatrix} \Omega_i & P_i^T \begin{bmatrix} 0 \\ A_{di} \end{bmatrix} - \begin{bmatrix} Y_{1i} \\ Y_{2i} \end{bmatrix} E_i + \begin{bmatrix} E_i^T \\ 0 \end{bmatrix} T_{1i}^T & \bar{d} \begin{bmatrix} Y_{1i} \\ Y_{2i} \end{bmatrix} & \begin{bmatrix} P_{2i}^T & 0 \\ 0 & 0 \end{bmatrix} \\ * & -Q - T_{1i} E_i - E_i^T T_{1i}^T & dT_{1i} & \begin{bmatrix} 0 & P_{3i}^T \\ 0 & 0 \end{bmatrix} \\ * & * & -\bar{d}Z & \\ * & * & * & \begin{bmatrix} -\varepsilon_1 I \\ -\varepsilon_2 I \end{bmatrix} \end{bmatrix} < 0 \tag{71.15}$$

where

$$\begin{aligned} P_i &= \begin{bmatrix} P_{1i} & 0 \\ P_{2i} & P_{3i} \end{bmatrix}, \\ \Omega_i &= P_i^T \begin{bmatrix} 0 & I \\ A_{Ki} & -I \end{bmatrix} + \begin{bmatrix} 0 & I \\ A_{Ki} & -I \end{bmatrix}^T P_i + \begin{bmatrix} Q + (\varepsilon_{1i} + \varepsilon_{2i})\alpha_i & 0 \\ 0 & \bar{d}Z + (\varepsilon_{1i} + \varepsilon_{2i})\beta_i \end{bmatrix} \\ &+ \begin{bmatrix} Y_{1i} \\ Y_{2i} \end{bmatrix} [E_i \ 0] + \left(\begin{bmatrix} Y_{1i} \\ Y_{2i} \end{bmatrix} [E_i \ 0] \right)^T + \sum_{j=1}^N \pi_{ij} \begin{bmatrix} E_i^T & 0 \\ 0 & 0 \end{bmatrix} P_i. \end{aligned}$$

From Theorem 1, the close-loop system (71.12) is stochastically admissible under zero-initial conditions, if there exist symmetric positive-definite matrices Q , Z and matrices $P_{1i}, P_{2i}, P_{3i}, Y_{1i}, Y_{2i}$ and T_{1i} with appropriate dimensions such that (71.6a) and (71.15) hold.

In the follows, we want to change (71.6a) and (71.15) into (71.13a) and (71.13c).

From the proof of Lemma4, P_i is invertible and Y_{1i}, Y_{2i} and T_{1i} are arbitrary. Define.

$$P_i^{-1} = L_i = \begin{bmatrix} L_{1i} & 0 \\ L_{2i} & L_{3i} \end{bmatrix}, \begin{bmatrix} Y_{1i} \\ Y_{2i} \end{bmatrix} = \delta_{1i} \begin{bmatrix} P_{2i}^T \\ P_{3i}^T \end{bmatrix}, T_{1i} = \delta_{2i} P_{1i}^T.$$

From (71.13b), we have

$$E_j^T P_{1j} \leq \lambda_j P_{1j}^T P_{1j} = \lambda_j (L_{1j} L_{1j}^T)^{-1}. \tag{71.16}$$

Note that for $j = 1, \dots, i - 1, i + 1, \dots, N$,

$$\lambda_j^{-1} L_{1j} L_{1j}^T \geq L_{1j}^T + L_{1j} - \lambda_j I. \tag{71.17}$$

Pre-and post-multiply (71.6a) by L_{1i}^T and L_{1i} , respectively. Similarly, pre- and post-multiply (71.15) by $diag\{L_{1i}^T, L_{1i}^T, Z^{-T}, I\}$ and $diag\{L_{1i}, L_{1i}, Z^{-1}, I\}$ respectively. Introduce change of variables such that $W_{1i} = L_{1i}^T Q L_{1i}$, $W_{2i} = \alpha_i^{-1}$, $W_{3i} = L_{1i}^T P_{2i}^T$, $W_{4i} = L_{1i}^T P_{3i}^T$, $W_{5i} = \beta_i^{-1} X = Z^{-1}$, $V_i = K_i L_{1i}$. After some manipulation including Schur complement we obtain (71.13c). This completes the proof.

71.4 Conclusion

This paper has studied the problems of robust control for singular time-delay nonlinear systems with Markovian jumping parameters. The considered systems are not necessarily assumed to be regular and impulse free and the time-delay is time-variable. A state feedback controller has been designed such that the closed-loop system is stochastically admissible.

Acknowledgments This research was supported by the National Nature Science Foundation of China (61170038), a Project of Shandong Province Higher Educational Science and Technology Program (J13LN14) and the Open Project Program of the Shandong Provincial Key Lab of Software Engineering (2011SE003), China.

References

1. Dai L (1989) Singular control systems. Springer-Verlag, Berlin
2. Mao X (2002) Exponential stability of stochastic delay internal systems with Markovian switching. *IEEE Trans Autom Control* 47:1604–1612
3. Wang Z, Ho D (2003) Filtering on nonlinear time-delay stochastic systems. *Automatica* 39:101–109
4. Xiong J, Lam J, Gao H (2005) On robust stabilization of Markovian jump systems with uncertain switching probabilities. *Automatica* 41:897–903
5. Mao X, Lam J, Xu S, Gao H (2006) Razumikhin method and exponential stability of hybrid stochastic delay interval systems. *J Math Anal Appl* 314:45–66
6. Xu S, Lam J (2006) Robust control and filtering of singular systems. Springer-Verlag, Berlin
7. Fu M, Duan G (2005) Robust guaranteed cost observer for uncertain descriptor time-delay systems with Markovian jumping parameters. *Acta Automatica Sinica* 31:479–483
8. Xie L, Souza C (1992) Robust H_∞ control for linear systems with norm-bounded time-varying uncertainties. *IEEE Trans Autom Control* 14:1188–1191
9. Lu H, Zhou W, Xu Y, Fang J (2011) Time-delay dependent H_∞ model simplification for singular systems with Markovian jumping parameters. *Optimal Control Appl Methods* 32:379–395

Chapter 72

A Free-Weighting Matrices Technique for Stochastic Stability Analysis of Uncertain Singular Hybrid System

Hongqian Lu, Wuneng Zhou and Xingping Liu

Abstract In this paper, the problems of stochastic stability for a class of uncertain singular hybrid systems with time-varying delay are investigated. The parameter uncertainties are assumed to be time-varying norm-bounded appearing in both the state and input matrices. In terms of a linear matrix inequality, some less conservative delay-dependent stochastic stability criteria for uncertain singular hybrid systems with state delay are proposed.

Keywords Singular system · Uncertainty · Nonlinear

72.1 Introduction

The free-weighting matrices to estimate the upper bound of the derivative of Lyapunov functional has been proposed [1, 2]. In recent years, more attention has been devoted to the study of Markovian jump systems. Therefore, much attention has been addressed to investigate such a class of stochastic systems and control issues related to Markovian jump systems have been studied [3–5].

On the other hand, many control and filtering problems, based on singular systems, have been studied for many years [6–8]. The stochastic stability problem for nonlinear singular stochastic hybrid systems were studied [9]. The problem of delay-dependent H_∞ filtering is addressed for singular Markovian jump systems with time-varying delay in a range [10].

H. Lu (✉) · W. Zhou
College of Information Science and Technology, Donghua University, Shanghai 201620,
People's Republic of China
e-mail: hqlu@163.com

H. Lu · X. Liu
School of Electrical Engineering and Automation, Shandong Polytechnic University,
Shandong 250353, People's Republic of China

In this paper, we investigate the problem of delay-dependent stochastic stability analysis for uncertain singular hybrid systems. In terms of a set of linear matrix inequalities, some less conservative delay-dependent stochastic stability criteria for uncertain singular hybrid systems with state delay are proposed. Up to date, the problems of stochastic stability analysis of uncertain singular hybrid systems with time-varying delay have not yet been fully investigated.

72.2 Problem Statement

Consider the following singular stochastic system with time-varying delay:

$$\begin{cases} E(r_t)d\dot{x}(t) = [(A(r_t) + \Delta A(t, r_t))x(t) + (A_d(r_t) + \Delta A_d(t, r_t))x(t - d(t))]dt \\ \quad + [W(r_t) + \Delta W(t, r_t)]x(t)d\omega(t), t > 0 \\ x(t) = \phi(t), t \in [-\bar{d}, 0], \end{cases} \tag{72.1}$$

where $x(t) \in R^n$ is the state vector, $\omega(t) \in R$ is a standard Wiener process. $d(t)$ is a time-varying differentiable function that satisfies

$$0 \leq d(t) \leq \bar{d}, \quad \forall t \geq 0, \tag{72.2}$$

and

$$|\dot{d}(t)| \leq \mu \tag{72.3}$$

where $\bar{d} > 0$ and μ are constants. The initial condition, $\phi(t)$, is a continuous and differentiable vector-valued function of $t \in [-h, 0]$. $\{r_t\}$ is a continuous-time Markovian process with right continuous trajectories taking values in a finite set $\mathcal{S} = \{1, 2, \dots, s\}$ with transition probability matrix $\Pi = (\pi_{ij})(i, j \in \mathcal{S})$ given by

$$P\{r(t+h) = j | r(t) = i\} = \begin{cases} \pi_{ij}h + o(h), i \neq j, \\ 1 + \pi_{ii}h + o(h), i = j, \end{cases}$$

where $h > 0$ and $\lim_{h \rightarrow \infty} \frac{o(h)}{h} = 0$, $\pi_{ij} > 0$ is the transition rate from i to j if $i \neq j$ and $\pi_{ii} = - \sum_{j=1, j \neq i}^N \pi_{ij}$.

For notational simplicity, in the sequel, for each possible $r_t = i, i \in \mathcal{S}$, for example, the matrix $A(r_t)$ will be denoted by A_i . The matrix $E_i \in R^{n \times n}$ may be singular and we assume that $0 < rank E_i = r \leq n$. It is assumed that the uncertainties are norm-bounded and, for each $i \in \mathcal{S}$, can be described as

$$[\Delta A_i(t) \quad \Delta A_{di}(t) \quad \Delta W_i(t)] = D_i F_i(t) [E_{ai} \quad E_{adi} \quad E_{Wi}] \tag{72.4}$$

where D_i, E_{ai}, E_{adi} are known constant matrices with compatible dimensions for each $i \in \mathcal{S}$, and $F_i(t)$ are unknown matrix functions satisfying

$$F_i^T(t)F_i(t) \leq I, \forall t, \forall i \in \mathcal{S}. \tag{72.5}$$

when $F_i(t) \equiv 0$, the system is referred to as a nominal system

$$E_i d\dot{x}(t)\dot{x}(t) = [A_i x(t) + A_{di} x(t-d)]dt + W_i x(t)d\omega(t). \tag{72.6}$$

For the system (6), we introduce the following definitions and lemmas, which will be used in the proof of our main results.

Definition 1 (Boukas [9]) System (6) is said to be stochastically stable if there exists a finite positive constant $T(x_0, r_0)$ such that the following holds for any initial conditions (x_0, r_0) :

$$\mathcal{E} \left\{ \int_0^\infty \|x(t)\|^2 dt | x_0, r_0 \right\} \leq T(x_0, r_0)$$

Lemma 1 [11]: Given matrices Ω, Γ and Ξ with appropriate dimensions and with Ω symmetrical, then $\Omega + \Gamma F \Xi + \Xi^T F^T \Gamma^T < 0$ for any F satisfying $F^T F \leq I$. If and only if there exists a scalar $\varepsilon > 0$ such that $\Omega + \varepsilon \Gamma \Gamma^T + \varepsilon^{-1} \Xi^T \Xi < 0$.

Lemma 2 [11]: For symmetric positive-definite matrix Q and matrices P, R with appropriate dimensions, the following inequality holds,

$$PR^T + RP^T \leq RQR^T + PQ^{-1}P^T.$$

72.3 Main Results

In this section, we shall give a delay dependent sufficient condition under which system (6) is stochastically stable by LMI approach. The result in this section will play a key role in solving the aforementioned problem.

Theorem 1 Given scalars $\bar{d} > 0, \varepsilon < 1$ and μ , the system (6) with a time varying delay $d(t)$ satisfying (2) and (3) is stochastically stable if there exist matrices $P_i = P_i^T > 0, Q = Q^T \geq 0, R = R^T \geq 0, Z_1 = Z_1^T > 0, Z_2 = Z_2^T > 0, N_{1i}, N_{2i}, N_{3i}, S_{1i}, S_{2i}, S_{3i}, M_{1i}, M_{2i}, M_{3i}, i = 1, 2, \dots, s$ such that the following LMI holds:

$$E_i^T P_i = P_i^T E_i \geq 0, \tag{72.7a}$$

$$\Gamma_i = \begin{bmatrix} \Phi_i & \bar{d}N_i & \bar{d}S_i & \bar{d}M_i & \bar{d}T_i(Z_1 + Z_2) & \tilde{W}_i P_i & \tilde{W}_i P_i^T \\ * & -\bar{d}Z_1 & 0 & 0 & 0 & 0 & 0 \\ * & * & -\bar{d}Z_1 & 0 & 0 & 0 & 0 \\ * & * & * & -\bar{d}Z_2 & 0 & 0 & 0 \\ * & * & * & * & -\bar{d}(Z_1 + Z_2) & 0 & 0 \\ * & * & * & * & * & -\varepsilon P_i & 0 \\ * & * & * & * & * & * & -\varepsilon P_i^T \end{bmatrix} < 0 \quad (72.7b)$$

where

$$\Phi_i = \begin{bmatrix} \Phi_{11i} & P_i A_{di} & 0 \\ * & -(1 - \mu)Q & 0 \\ * & * & -R \end{bmatrix} + \Omega_i \text{diag}(E_i, E_i, E_i) + \text{diag}(E_i^T, E_i^T, E_i^T)\Omega_i^T,$$

with

$$\begin{aligned} \Phi_{11i} &= P_i A_i + A_i^T P_i + Q + R + \sum_{j=1}^s \pi_{ij} E_j^T P_j, \\ \Omega_i &= \begin{bmatrix} N_{1i} + M_{1i} & -N_{1i} + S_{1i} & -M_{1i} - S_{1i} \\ N_{2i} + M_{2i} & -N_{2i} + S_{2i} & -M_{2i} - S_{2i} \\ N_{3i} + M_{3i} & -N_{3i} + S_{3i} & -M_{3i} - S_{3i} \end{bmatrix}, \quad N_i = [N_{1i}^T \quad N_{2i}^T \quad N_{3i}^T]^T, \\ S_i &= [S_{1i}^T \quad S_{2i}^T \quad S_{3i}^T]^T, \quad M_i = [M_{1i}^T \quad M_{2i}^T \quad M_{3i}^T]^T, \\ T_i &= [A_i \quad A_{di} \quad 0]^T, \quad \tilde{W}_i = [W_i \quad 0 \quad 0]^T. \end{aligned}$$

Proof We prove the stochastic stability of system (6). To this end, we propose the following function for each $r_t = i, i \in \mathcal{S}$:

$$\begin{aligned} V(x(t), r_t = i) &= x^T(t) E_i^T P_i x(t) + \int_{-\bar{d}}^0 \int_{t+\beta}^t \dot{x}^T(\alpha) E_i^T (Z_1 + Z_2) E_i \dot{x}(\alpha) d\alpha d\beta \\ &+ \int_{t-d(t)}^t x^T(\alpha) Q x(\alpha) d\alpha + \int_{t-\bar{d}}^t x^T(\alpha) R x(\alpha) d\alpha. \end{aligned} \quad (72.8)$$

From the Leibniz-Newton formula, the following equations are true

$$2\zeta^T(t) N_i [E_i x(t) - E_i x(t - d(t))] - \int_{t-d(t)}^t E_i \dot{x}(\alpha) d\alpha = 0, \quad (72.9)$$

$$2\zeta^T(t) S_i [E_i x(t - d(t)) - E_i x(t - \bar{d})] - \int_{t-\bar{d}}^{t-d(t)} E_i \dot{x}(\alpha) d\alpha = 0, \quad (72.10)$$

$$2\zeta^T(t)M_i[E_i\dot{x}(t) - E_i\dot{x}(t - \bar{d}) - \int_{t-\bar{d}}^t E_i\dot{x}(\alpha)d\alpha] = 0, \quad (72.11)$$

where $\zeta(t) = [x^T(t) \quad x^T(t - d(t)) \quad x^T(t - \bar{d})]^T$.

By ito's formula, we obtain the stochastic differential of the random process $\{x(t), r_i\}$. Then, for each $r_i = i$, $i \in \mathcal{S}$, we have

$$dVx(t) = \mathcal{L}Vx(t)dt + 2x(t)^T P_i^T E_i W_i d\omega(t),$$

where

$$\begin{aligned} \mathcal{L}Vx(t) &= 2x^T(t)P_i^T E_i f(x) + x^T(t) \left(\sum_{j=1}^N \pi_{ij} E_j^T P_j \right) x(t) \\ &\quad + x^T(t) Q x(t) - (1 - \dot{d}(t)) x^T(t - d(t)) Q x(t - d(t)) \\ &\quad + x^T(t) R x(t) - x^T(t - \bar{d}) R x(t - \bar{d}) + \bar{d} f(x)^T E_i^T x(t) (Z_1 + Z_2) E_i^T f(x) \\ &\quad - \int_{t-\bar{d}}^t \dot{x}^T(\alpha) E_i^T (Z_1 + Z_2) E_i \dot{x}(\alpha) d\alpha + x^T(t) W_i^T E_j^T P_i W_i x(t) \\ &\leq 2x(t)^T P_i E_i \dot{x}(t) + x^T(t) \left(\sum_{j=1}^N \pi_{ij} E_j^T P_j \right) x(t) + x^T(t) (Q + R) x(t) \\ &\quad - (1 - \mu) x^T(t - d(t)) Q x(t - d(t)) \\ &\quad - x^T(t - \bar{d}) R x(t - \bar{d}) + \bar{d} \dot{x}^T x(t) E_i (Z_1 + Z_2) E_i \dot{x}(t) \\ &\quad - \int_{t-d(t)}^t \dot{x}^T(\alpha) E_i^T Z_1 E_i \dot{x}(\alpha) d\alpha - \int_{t-\bar{d}}^{t-d(t)} \dot{x}^T(\alpha) E_i^T Z_1 E_i \dot{x}(\alpha) \\ &\quad - \int_{t-\bar{d}}^t \dot{x}^T(\alpha) E_i^T Z_2 E_i \dot{x}(\alpha) d\alpha + x^T(t) W_i^T E_j^T P_i W_i x(t) \\ &\quad + 2\zeta^T(t) N_i [E_i x(t) - E_i x(t - d(t)) - \int_{t-d(t)}^t E_i \dot{x}(\alpha) d\alpha] \\ &\quad + 2\zeta^T(t) S_i [E_i x(t - d(t)) - E_i x(t - \bar{d}) - \int_{t-\bar{d}}^{t-d(t)} E_i \dot{x}(\alpha) d\alpha] \\ &\quad + 2\zeta^T(t) M_i [E_i x(t) - E_i x(t - \bar{d}) - \int_{t-\bar{d}}^t E_i \dot{x}(\alpha) d\alpha] \\ &\leq \zeta^T(t) [\Phi_i + \bar{d} T_i (Z_1 + Z_2) T_i^T + \bar{d} N_i Z_1^{-1} N_i^T + \bar{d} S_i Z_1^{-1} S_i^T \\ &\quad + [W_i \ 0 \ 0]^T E_j^T P_i [W_i \ 0 \ 0] + \bar{d} M_i Z_2^{-1} M_i^T] \zeta(t) + \Xi_i, \end{aligned} \quad (72.12)$$

where

$$\begin{aligned}
 f(x) &= A_i x(t) + A_{di} x(t-d), \\
 \Xi_i &= - \int_{t-d(t)}^t [\zeta^T(t) N_i + \dot{x}^T(\alpha) E_i^T Z_1] Z_1^{-1} [N_i^T \zeta^T(t) + Z_1 E_i \dot{x}(\alpha)] d\alpha \\
 &\quad - \int_{t-\bar{d}}^{t-d(t)} [\zeta^T(t) S_i + \dot{x}^T(\alpha) E_i^T Z_1] Z_1^{-1} [S_i^T \zeta^T(t) + Z_1 E_i \dot{x}(\alpha)] d\alpha \\
 &\quad - \int_{t-\bar{d}}^t [\zeta^T(t) M_i + \dot{x}^T(\alpha) E_i^T Z_2] Z_2^{-1} [M_i^T \zeta^T(t) + Z_1 E_i \dot{x}(\alpha)] d\alpha.
 \end{aligned}$$

Since $Z_1 > 0, Z_2 > 0$, then, we have $\Xi_i < 0$. From (72.7b), by Schur complements we can deduce

$$\begin{aligned}
 &\Phi_i + \bar{d} T_i (Z_1 + Z_2) T_i^T + \bar{d} N_i Z_1^{-1} N_i^T + \bar{d} S_i Z_1^{-1} S_i^T \\
 &\quad + \bar{d} M_i Z_2^{-1} M_i^T + [W_i \quad 0 \quad 0]^T E_i^T P_i [W_i \quad 0 \quad 0] < 0.
 \end{aligned}$$

From 72.7a, and assuming that $E_i^T P_i \leq \varepsilon^{-1} [P_i + P_i^T]$ with $\varepsilon < 1$ (known) holds for each $r_t = i, i \in \mathcal{S}$.

Therefore, we have

$$\begin{aligned}
 LV(x(t), r_t = i) &\leq \zeta^T(t) [\Phi_i + \bar{d} T_i (Z_1 + Z_2) T_i^T + \bar{d} N_i Z_1^{-1} N_i^T \\
 &\quad + \bar{d} S_i Z_1^{-1} S_i^T + \bar{d} M_i Z_2^{-1} M_i^T] \zeta(t) < 0,
 \end{aligned} \tag{72.13}$$

which, with (72.7b) implies that there exists a scalar $\varepsilon > 0$, such that

$$LV(x(t), r_t = i) \leq -\varepsilon x^T(t)x(t). \tag{72.14}$$

Now, based on the Definition 1 and the method of proof in Boukas [8, 9], We can get that the Markovian jump singular system in (6) is stochastically stable. This completes the proof.

Now, we generalize Theorem 1 to the uncertain case, and give the following sufficient condition on stochastically stable.

Theorem 2 *Given scalars $\bar{d} > 0, \varepsilon < 1$ and μ , the system (1) with a time varying delay $d(t)$ satisfying (2) and (3) is stochastically stable if there exist matrices $P_i = P_i^T > 0, Q = Q^T \geq 0, R = R^T \geq 0, Z_1 = Z_1^T > 0, Z_2 = Z_2^T > 0, N_{1i}, N_{2i}, N_{3i}, S_{1i}, S_{2i}, S_{3i}, M_{1i}, M_{2i}, M_{3i}, i = 1, 2, \dots, s$ and scalars $\lambda_{1i} > 0, \lambda_{2i} > 0$ such that the following LMI holds:*

$$E_i^T P_i = P_i^T E_i \geq 0, \tag{72.15a}$$

$$\begin{bmatrix}
 \Phi_i & \bar{d}N_i & \bar{d}S_i & \bar{d}M_i & \bar{d}T_i(Z_1 + Z_2) & Y_i D_i & \tilde{W}_i P_i & \tilde{W}_i P_i^T & X_i \\
 * & -\bar{d}Z_1 & 0 & 0 & 0 & 0 & 0 & 0 & 0 \\
 * & * & -\bar{d}Z_1 & 0 & 0 & 0 & 0 & 0 & 0 \\
 * & * & * & -\bar{d}Z_2 & 0 & 0 & 0 & 0 & 0 \\
 * & * & * & * & -\bar{d}(Z_1 + Z_2) & \bar{d}(Z_1 + Z_2)D_i & 0 & 0 & 0 \\
 * & * & * & * & * & -\lambda_{1i}I & 0 & 0 & 0 \\
 * & * & * & * & * & * & -\varepsilon P_i & 0 & 0 \\
 * & * & * & * & * & * & * & -\varepsilon P_i^T & 0 \\
 * & * & * & * & * & * & * & * & -\lambda_{2i}I
 \end{bmatrix} < 0 \tag{72.15b}$$

where

$$\begin{aligned}
 \Phi_i = & \begin{bmatrix} \Phi_{11i} & P_i A_{di} & 0 \\ * & -(1-u)Q & 0 \\ * & * & -R \end{bmatrix} + \Omega_i \text{diag}(E_i, E_i, E_i) + \text{diag}(E_i^T, E_i^T, E_i^T)\Omega_i^T \\
 & + \begin{bmatrix} \lambda_i E_{ai}^T E_{ai} & \lambda_i E_{ai}^T E_{adi} & 0 \\ * & \lambda_i E_{ai} E_{adi} & 0 \\ * & * & 0 \end{bmatrix} + \begin{bmatrix} \lambda_{2i} E_{Wi}^T E_{Wi} & 0 & 0 \\ * & 0 & 0 \\ * & * & 0 \end{bmatrix},
 \end{aligned}$$

$Y_i = [P_i \ 0 \ 0]^T$, $X_i = [D_i^T P_i \ D_i^T P_i^T \ 0]^T$ and $\Phi_i, T_i, M_i, N_i, S_i, \Omega_i, \tilde{W}_i$ are defined in Theorem 1,

Proof Replacing A_i, A_{di}, W_i in (7b) with $A_i + D_i F_i(t) E_{ai}, A_{di} + D_i F_i(t) E_{adi}$ and $W_i + D_i F_i(t) E_{Wi}$, respectively, we have

$$\begin{aligned}
 & \Gamma_i + [[D_i^T P_i \ 0 \ 0] \ 0 \ 0 \ 0 \ [\bar{d}D_i^T(Z_1 + Z_2)^T \ 0 \ 0] \ 0 \ 0]^T \\
 & \quad F_i(t)[[E_{ai} \ 0 \ 0] \ [E_{adi} \ 0 \ 0] \ 0 \ 0 \ 0 \ 0 \ 0] \\
 & + [[E_{ai} \ 0 \ 0] \ [E_{adi} \ 0 \ 0] \ 0 \ 0 \ 0 \ 0 \ 0]^T F_i(t) \\
 & \quad [[D_i^T P_i \ 0 \ 0] \ 0 \ 0 \ 0 \ [\bar{d}D_i^T(Z_1 + Z_2)^T \ 0 \ 0] \ 0 \ 0] \\
 & + [[D_i^T P_i \ D_i^T P_i^T \ 0] \ 0 \ 0 \ 0 \ 0 \ 0 \ 0]^T \\
 & \quad F_i(t)[[E_{Wi} \ 0 \ 0] \ 0 \ 0 \ 0 \ 0 \ 0 \ 0] \\
 & + [[E_{Wi} \ 0 \ 0] \ 0 \ 0 \ 0 \ 0 \ 0 \ 0]^T F_i(t) \\
 & \quad [[D_i^T P_i \ D_i^T P_i^T \ 0] \ 0 \ 0 \ 0 \ 0 \ 0 \ 0] < 0
 \end{aligned} \tag{72.16}$$

where Γ_i is defined in Theorem 1. From Theorem 1, the system (1) is stochastically stable, if (72.16) and (72.15a) hold for all $F_i(k)$ satisfying (5). By Lemma 1, it follows that (72.16) holds for all $F_i(k)$ satisfying (5), if and only if there exists a scalar $\lambda_{1i} > 0, \lambda_{2i} > 0$ such that

$$\begin{aligned}
& \Gamma_i + \lambda_{1i}^{-1} [[D_i^T P_i \ 0 \ 0] \ 0 \ 0 \ 0 \ [\bar{d}D_i^T (Z_1 + Z_2)^T \ 0 \ 0] \ 0 \ 0]^T \\
& [[D_i^T P_i \ 0 \ 0] \ 0 \ 0 \ 0 \ [\bar{d}D_i^T (Z_1 + Z_2)^T \ 0 \ 0] \ 0 \ 0] \\
& + \lambda_{1i} [[E_{ai} \ 0 \ 0] \ [E_{adi} \ 0 \ 0] \ 0 \ 0 \ 0 \ 0 \ 0]^T \\
& [[E_{ai} \ 0 \ 0] \ [E_{adi} \ 0 \ 0] \ 0 \ 0 \ 0 \ 0 \ 0] \\
& + \lambda_{2i}^{-1} [[D_i^T P_i \ D_i^T P_i^T \ 0] \ 0 \ 0 \ 0 \ 0 \ 0 \ 0]^T \\
& [[D_i^T P_i \ D_i^T P_i^T \ 0] \ 0 \ 0 \ 0 \ 0 \ 0 \ 0] \\
& + \lambda_{2i} [[E_{wi} \ 0 \ 0] \ 0 \ 0 \ 0 \ 0 \ 0 \ 0]^T \\
& [[E_{wi} \ 0 \ 0] \ 0 \ 0 \ 0 \ 0 \ 0 \ 0] < 0
\end{aligned} \tag{72.17}$$

By Schur complement, it can be easily shown that (72.17) is equivalent to (72.15b). This completes the proof.

72.4 Conclusion

In this paper we has studied the problem of stochastic stability analysis of uncertain singular hybrid system with time-varying delay. Some new sufficient conditions for stochastic stability of a singular hybrid system with time-varying delay are proposed. The results we developed here can easily be solved using any LMI toolbox.

Acknowledgments This research was supported by the National Nature Science Foundation of China (61170038), and the Open Project Program of the Shandong Provincial Key Lab of Software Engineering (2011SE003), China. This work is supported by the National Natural Science Foundation of China (61075060), the Innovation Program of Shanghai Municipal Education Commission (12zz064), the Open Project of State Key Laboratory of Industrial Control Technology.

References

1. Wu M, He Y, She JH, Liu GP (2004) Delay-dependent criteria for robust stability of time-varying delay systems. *Automatica* 40(8):1435–1439
2. He Y, Wang Q, Xie L, Lin C (2007) Further improvement of free-weighting matrices technique for systems with time-varying delay. *IEEE Trans Autom Control* 52:293–299
3. Wang Z, Ho DWC (2003) Filtering on nonlinear time-delay stochastic systems. *Automatica* 39:101–109
4. Xiong J, Lam J, Gao H, Ho DWC (2005) On robust stabilization of Markovian jump systems with uncertain switching probabilities. *Automatica* 41:897–903
5. Mao X, Lam J, Xu S, Gao H (2006) Razumikhin method and exponential stability of hybrid stochastic delay interval systems. *J Math Anal Appl* 314:45–66
6. Dai L (1989) *Singular control systems*. Springer, Berlin

7. Xu S, Yang C, Boukas E-K (2000) State feedback control for discrete singular systems. *IEEE Trans Autom Control* 45:1405–1409
8. Wu Z, Zhou W (2007) Delay-dependent robust H_∞ control for uncertain singular time-delay systems, *IET Control Theory Appl* 1234–1241
9. Boukas E-K (2005) On robust stability of singular systems with random abrupt changes. *Nonlinear Anal* 63:301–310
10. Wu Z, Su H, Chu J (2010) Delay-dependent H_∞ filtering for singular Markovian jump time-delay systems, *signal processing*, vol 90, 1815–1824
11. L. Xie, C. E. Souza, Robust H (1992) H_∞ Control for linear systems with norm-bounded time-varying uncertainties. *IEEE Trans Autom Control* 14:1188–1191
12. Boukas E-K (2006) Stabilization of stochastic singular nonlinear hybrid systems. *Nonlinear Anal* 64:217–228

Chapter 73

Application of EKF Training RBFNN in Fault Diagnosis of Subway Auxiliary Inverter

Junwei Gao, Ziwen Leng, Yong Qin, Xiaofeng Li and Dechen Yao

Abstract Fault signals usually have the characteristics of nonlinearity and instability, and RBF neural network (RBFNN) has the defect of lacking of generalization capability when it is used for fault diagnosis. To improve the precision of fault identification and network convergence, the paper introduces the extended Kalman filter (EKF) as the learning algorithm of RBFNN to estimate the center vector of hidden layer and the network connection weight, extracts the feature vectors of fault signals in subway auxiliary inverter by wavelet package, which will be taken as the input samples of the optimized network. Simulation results show that, compared with traditional gradient descent algorithm, RBFNN trained by extended Kalman filter has better effect in improving the diagnostic precision and speeding up the network convergence, and the proposed method can be applied in fault diagnosis of auxiliary inverter.

Keywords RBF neural network · Extended Kalman filter · Subway auxiliary inverter · Fault diagnosis

73.1 Introduction

Subway auxiliary inverter is the core component of auxiliary system, while it takes the responsibility for supplying continuous and stable power to the AC loads, such as ventilator, air conditioner and so on. As a consequence, fast and accurate fault

J. Gao (✉) · Z. Leng
College of Automation Engineering, Qingdao University, No 308 Ningxia Road,
Qingdao 266071, China
e-mail: qdgao163@163.com

J. Gao · Y. Qin · X. Li · D. Yao
State Key Laboratory of Rail Traffic Control and Safety, Beijing Jiaotong University,
Beijing 100044, China

diagnosis is the necessary condition to ensure the safety and high efficiency of auxiliary inverter.

RBF neural network has the characteristics of simple network structure, strong nonlinear approximation and fault tolerance, and self-learning ability [1], which is widely applied in the fields of function approximation [2], pattern recognition [3]. When the hidden layer neurons and the width of basis function in RBFNN are determined, the center vector of hidden layer and the network connection weight will have a great influence on the network performance. Therefore, corresponding algorithms are proposed to optimize the network. K-means clustering was brought forward as the network learning algorithm in [4], but it is sensitive to initial clustering center and cannot take full advantage of information in training samples. Gradient descent algorithm was put forward to train the network in [5]. However, its calculation process is more complicated, and the network is prone to gradient disappear or running into local extremum [1, 6]. As a state optimal estimate filtering algorithm, Kalman filter has been applied in the training process of neural network and has achieved better results, which have been testified with faster convergence rate and forecasting precision than gradient descent algorithm in [6, 7].

Wavelet packet inherits the advantages of good time–frequency localization of wavelet transform [8], which will be able to conduct multi-scale and refined analysis of fault signals. Therefore, the paper adopts the fault feature vector extracted by wavelet packet transform as the input of neural network, which will greatly simplify the network structure and improve the diagnostic efficiency. On the basis of RBF neural network with multi-input and multi-output, the paper introduces the extended Kalman filter to establish the diagnostic model of auxiliary inverter, which will be concretely described and tested in the following sections.

73.2 Basic Theory of RBFNN

Typical RBF neural network includes input layer, hidden layer and output layer. Suppose that input layer has n neurons with input vector $x = [x_1, x_2, \dots, x_n]^T$; hidden layer selects basis function as the activation function with h neurons, while basis function is a non-negative and nonlinear function with radial symmetry and attenuation in center; output layer has m neurons with linear function as the activation function, and the network output is $Y = [y_1, y_2, \dots, y_m]^T$.

Basis function in hidden layer usually selects the Gaussian function, which is shown as follows.

$$\varphi_i = \exp\left(-\frac{\|x - c_i\|^2}{2\sigma_i^2}\right), \quad i = 1, 2, \dots, h \quad (73.1)$$

where φ_i is Gaussian function, $c_i = [c_{i1}, c_{i2}, \dots, c_{in}]^T$ is the center vector of the i th basis function, σ_i is the width of basis function, $\|\cdot\|$ is Euclidean norm.

Output of RBF neural network is:

$$y_k = \sum_{j=1}^h w_{jk} \varphi_j \quad k = 1, 2, \dots, m \quad (73.2)$$

where y_k is the output of the k th neuron in output layer, w_{jk} is weight between the j th neuron of hidden layer and the k th neuron in output layer.

When the hidden layer neurons and the width are determined, the center vector and network connection weight can be estimated by extended Kalman filter.

73.3 Application of Extended Kalman Filter in RBFNN

Kalman filter is the optimal estimate theory in linear system, while extended Kalman filter is applied in nonlinear system. Taken the nonlinear mapping of RBF neural network into consideration, the paper takes extended Kalman filter to conduct linear approximation processing of the state equation and observation equation in nonlinear system.

For nonlinear discrete-time system, the state space expression is as follows [9].

$$\begin{cases} \theta_{k+1} = f(\theta_k) + w_k \\ y_k = h(\theta_k) + v_k \end{cases} \quad (73.3)$$

where θ_k is stable vector, $f(\cdot)$ is a nonlinear state transition matrix, $w(k)$ is process noise, $y(k)$ is observation vector, $h(\cdot)$ is a nonlinear observation matrix, $v(k)$ is observation noise.

Both process noise $w(k)$ and observation noise $v(k)$ are independent Gaussian white noise sequences with average value zero, the following expressions show the statistical characteristics.

$$\begin{cases} E\{w(k)\} = 0; E\{v(k)\} = 0 \\ E\{w(k)v^T(j)\} = 0 \\ E\{w(k)w^T(j)\} = Q(k)\delta_{k,j} \\ E\{v(k)v^T(j)\} = R(k)\delta_{k,j} \end{cases} \quad (73.4)$$

where E represents the mathematical expectation, $Q(k)$ is the covariance matrix of process noise $w(k)$, $R(k)$ is the covariance matrix of observation noise $v(k)$, $\delta_{k,j}$ is Kronecker δ function.

Initial conditions satisfy: $E\{x(0)\} = x_0$; $E\{[x(0) - x_0][x(0) - x_0]^T\} = P_0$.

If nonlinear state space in Eq. (73.3) is sufficiently smooth, $f(\theta_k)$ and $h(\theta_k)$ can be expanded to Taylor series around the estimate $\bar{\theta}_k$.

$$\begin{cases} f(\theta_k) = f(\bar{\theta}_k) + F_k \times (\theta_k - \bar{\theta}_k) + \Delta \\ h(\theta_k) = h(\bar{\theta}_k) + H_k^T \times (\theta_k - \bar{\theta}_k) + \Delta \end{cases} \quad (73.5)$$

where $F_k = \frac{\partial f(\theta)}{\partial \theta} \Big|_{\theta=\bar{\theta}_k}$, $H_k^T = \frac{\partial h(\theta)}{\partial \theta} \Big|_{\theta=\bar{\theta}_k}$, Δ is higher-order term.

Neglect the higher-order term in Eq. (73.5) and combine Eq. (73.3), the following equation is obtained:

$$\begin{cases} \theta_{k+1} = F_k \theta_k + f(\bar{\theta}_k) - F_k \bar{\theta}_k + w_k \\ y_k = H_k^T \theta_k + h(\bar{\theta}_k) - H_k^T \bar{\theta}_k + v_k \end{cases} \quad (73.6)$$

Select the center vector c_i and network weight w_{ij} to make up the state vector θ of extended Kalman filter, while the network output is taken as the observation of extended Kalman filter. The training criterion is to minimize the network error.

$$\theta = [w_1^T w_2^T \cdots w_n^T c_1^T c_2^T \cdots c_h^T]^T \quad (73.7)$$

$$Error = \sum_{k=1}^m (y_k - \bar{y}_k)^2 \quad (73.8)$$

where y_k is the actual network output, \bar{y}_k is the desired output.

For RBF neural network, the processed state space in which Kalman filter can be used is shown as follows [7].

$$\begin{cases} \theta_{k+1} = \theta_k + w_k \\ y_k = h(\theta_k) + v_k \end{cases} \quad (73.9)$$

Based on the recursive equations of Kalman filter, the state estimate $\bar{\theta}$ can be calculated.

$$\begin{cases} \bar{\theta}_k = \bar{\theta}_{k-1} + G_k [y_k - h(\bar{\theta}_{k-1})] \\ G_k = P_k H_k (R + H_k^T P_k H_k)^{-1} \\ P_{k+1} = F_k (P_k - G_k H_k^T P_k) F_k^T + Q \end{cases} \quad (73.10)$$

where $\bar{\theta}_k$ is the state estimate at the time k , $h(\bar{\theta}_{k-1})$ is the network output at the time $k - 1$, G_k is Kalman gain, P_k is state estimate error variance.

73.4 Extraction of Fault Feature by Wavelet Package Transform

Based on multi-resolution analysis of wavelet transform, wavelet package can make further decomposition of high-frequency parts. When faults appear in auxiliary inverter, frequency band energy in signal will be greatly changed. This paper extracts the energy feature of signal by wavelet package transform, so as to give a specific description of different faults. Extraction steps are shown as follows.

- Select appropriate wavelet basis and scale to decompose the fault signal.
- Reconstruct the extracted coefficients of frequency bands. S_{ij} represents the reconstructed signal at the i th layer of the j th node.
- Extract the energy feature of the reconstructed signal S_{3k} .

$$E_{3k} = \int |S_{3k}(t)|^2 dt = \sum_{i=0}^{N-1} |d_{ki}|^2, \quad k = 0, 1, \dots, 7 \tag{73.11}$$

where i is sample point, d_{ki} is the amplitude of discrete point in the reconstructed signal S_{3k} , N is the total number of sample point.

- Compose the feature vector T of fault signal. Calculate the whole energy E , execute the normalized processing to the feature vector.

$$T = [E_{30}/E, E_{31}/E, \dots, E_{37}/E]; \quad E = \sum_{j=0}^7 E_{3j} \tag{73.12}$$

73.5 Simulation Experiments

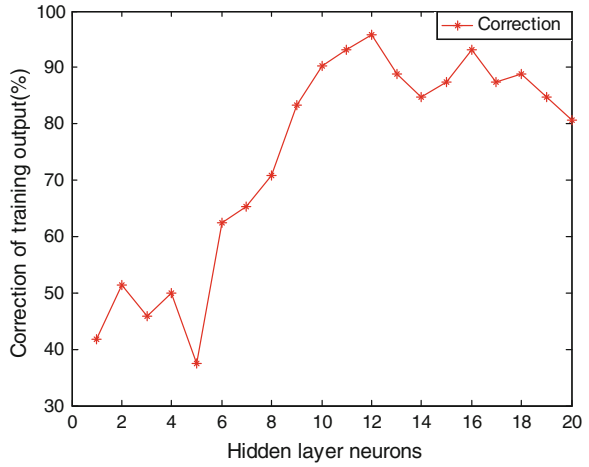
Common faults in auxiliary inverter include frequency variation, pulse transient, transient oscillation and voltage fluctuation. 30 groups of data of each fault are collected, with a total of 120 groups and sample frequency 4096 Hz. The paper randomly selects 18 groups of each fault to constitute the training samples, while the remaining 48 groups are taken as the testing samples. The diagnostic labels of the four faults are defined as (1 0 0 0), (0 1 0 0), (0 0 1 0) and (0 0 0 1).

For the fault signals, the paper extracts fault feature vectors with the dimension 8 by wavelet package transform. Parts of feature samples are shown in Table 73.1.

Table 73.1 Parts of fault feature samples

Fault type	E_0	E_1	E_2	E_3	E_4	E_5	E_6	E_7
Frequency variation	0.2719	0.2198	0.1445	0.1986	0.0085	0.0236	0.0901	0.0428
	0.3408	0.1785	0.1481	0.1750	0.0089	0.0211	0.0891	0.0385
Pulse transient	0.4849	0.2889	0.0194	0.0853	0.0050	0.0389	0.0662	0.0113
	0.5195	0.2799	0.0182	0.0840	0.0026	0.0328	0.0551	0.0080
Transient oscillation	0.4464	0.1297	0.1086	0.1080	0.0305	0.0334	0.0833	0.0601
	0.4870	0.1277	0.0999	0.0962	0.0258	0.0330	0.0807	0.0497
Voltage fluctuation	0.8427	0.0434	0.0294	0.0382	0.0015	0.0046	0.0270	0.0132
	0.8394	0.0414	0.0299	0.0417	0.0017	0.0049	0.0274	0.0135

Fig. 73.1 Curve of hidden layer neurons and the training accuracy

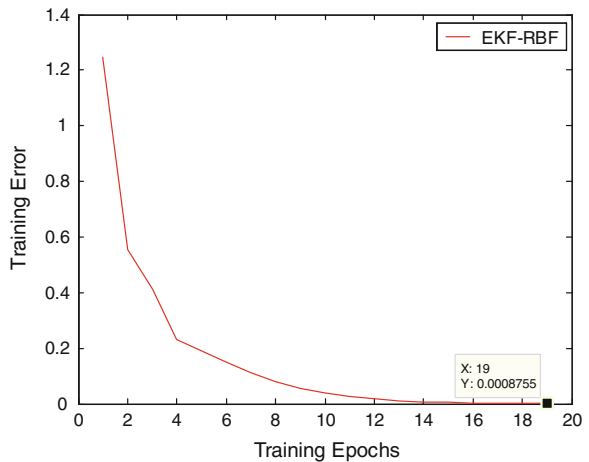


73.5.1 Experiment Results

Based on the fault feature samples, the neurons of input layer and output layer in EKF-RBFNN are determined 8 and 4. The width of basis function in hidden layer is 0.2, and the training target error is 0.001. The hidden layer neurons can be determined based on the accuracy of network training output. Figure 73.1 shows the relationship between hidden layer neurons and the training accuracy. As is seen in Fig. 73.1, the range of hidden layer neurons is from 1 to 20, the network training accuracy reaches the maximum 95.83 % when hidden layer neurons are 12. As a consequence, the network structure is ascertained at 8-12-4.

This paper also establishes the RBFNN based on gradient descent algorithm, with gradient descent step 0.01. Other parameters are the same as the EKF-

Fig. 73.2 Training error curve of EKF-RBF



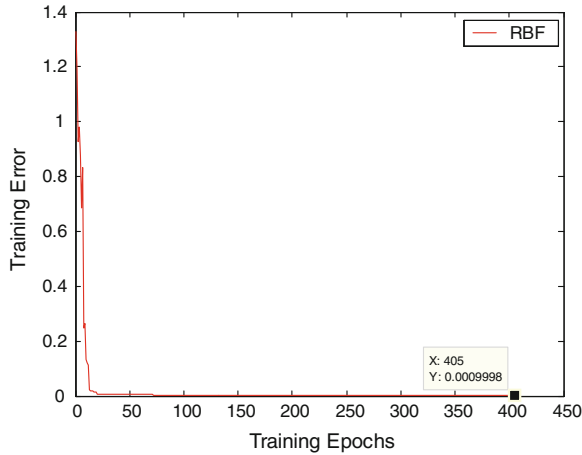


Fig. 73.3 Training error curve of RBFNN

Table 73.2 Parts of network outputs of EKF-RBF

Fault type	Network outputs				Desired outputs
Frequency variation	1.0114	-0.0452	-0.0223	0.0237	1 0 0 0
	0.9874	0.0676	-0.0929	0.0176	1 0 0 0
Pulse transient	0.0165	0.9680	0.1202	0.0734	0 1 0 0
	-0.0126	0.9684	0.0827	0.0691	0 1 0 0
Transient oscillation	0.0738	-0.0256	0.9718	0.0720	0 0 1 0
	0.0695	-0.0240	0.9845	0.0981	0 0 1 0
Voltage fluctuation	-0.0796	0.0608	-0.0378	0.9762	0 0 0 1
	-0.0385	0.1077	-0.0399	1.0667	0 0 0 1

RBFNN. The training error curves of EKF-RBFNN and RBFNN are shown in Figs. 73.2 and 73.3. After the center vector of hidden layer and network connection weight are trained by EKF, read the testing samples and obtain the network outputs. Parts of network outputs of EKF-RBFNN are shown in Table 73.2. Comparisons of diagnostic results of EKF-RBFNN and RBFNN are shown in Table 73.3.

Table 73.3 Comparisons of fault diagnosis

Model	Frequency variation	Pulse transient	Transient oscillation	Voltage fluctuation	Diagnostic accuracy
EKF-RBFNN	12/12	11/12	10/12	12/12	93.75 % (45/48)
RBFNN	10/12	12/12	10/12	11/12	89.58 % (43/48)

Concluded from simulation results, when the target error is 0.001, the EKF-RBFNN only needs 19 steps to converge to 0.001, while traditional RBF neural network takes 405 steps. For 48 groups of testing data, the wrong diagnosis of EKF-RBFNN is 3 groups with the diagnostic accuracy 93.75 %, while the diagnostic accuracy of RBFNN is 89.58 %. As a consequence, the proposed EKF-RBFNN has better superiority to RBFNN in convergence rate and diagnostic precision.

73.6 Conclusion

Considering that RBFNN with gradient descent algorithm has the shortcomings of slower convergence rate and lacking of generalization capability, the paper introduces extended Kalman filter to train the center vector and network connection weight of RBF neural network, establishes the multi-input and multi-output network model and applies it to the fault diagnosis of auxiliary inverter. Simulation results have testified the feasibility and validity of the proposed method. Further research will contain how to optimize the width of basis function of hidden layer.

Acknowledgments This work is partially supported by the National Key Technology R&D Program (2011BAG01B05), the Foundation of Shandong Province (BS2011DX008, ZR2011FQ012, ZR2011FM008), 863 Program (2011AA110501) and the State Key Laboratory of Rail Traffic Control and Safety Foundation (RCS2011K005, RCS2012K006) Beijing Jiaotong University.

References

1. Chen J, Ren Z, San Y (2008) A two-level learning hierarchy for the radial basis function networks. *Control Theor Appl* 25(4):655–660 (in Chinese)
2. Wang J, Zhu L, Cai ZH (2006) A novel learning algorithm for RBF network based on Kalman filter and fuzzy control. *Comput Appl* 26(7):1700–1705 (in Chinese)
3. Fu Q, Chen TF, Zhu JJ (2012) Transformer fault diagnosis using self-adaptive RBF neural network algorithm. *High Volt Eng* 38(6):1368–1375 (in Chinese)
4. Yuan F, Zhou ZY, Song X (2007) K-means clustering algorithm with meliorated initial center. *Comput Eng* 33(3):65–66 (in Chinese)
5. Karayiannis N (1999) Reformulated radial basis neural networks trained by gradient descent. *IEEE Trans Neural Networks* 3:657–671
6. Wang L, Pan ZW, Ye JJ (2008) Training radial basis function neural networks with extended Kalman filter and their application to mechanical faults diagnosis. *J Vibr Meas Diagn* 28(4):358–361 (in Chinese)
7. Simon D (2002) Training radial basis neural networks with the extended Kalman filter. *Neurocomputing* 48:255–475
8. Gao JW, Yu JP, Leng ZW et al (2013) The application of PSO-LSSVM in fault diagnosis of subway auxiliary inverter. *ICIC Express Lett Part B Appl* 4(3):777–784
9. Simon H (2001) *Kalman filtering and neural networks*. Wiley, New York

Chapter 74

Fuzzy Combination Rule of Multiple Classifiers System Based on Yager Triangular Norm

Pengtao Jia, Shuhui Liang and Jun Deng

Abstract This article focuses on the fuzzy combination rule of multiple classification system. As one of the fuzzy triangular norm operation model, Yager triangular norm can improve the generalization capability of pattern classification systems. We extend the Yager t-norm from binary form to multivariate weighted form. Based on it, we put forward a new fuzzy combination rule. The new rule is a set of continuously changing operator clusters that can make better use of the classified information of sub-classifiers. It generates different computing models by the different characteristics of datasets to combine sub-classifiers. We use genetic algorithm to evaluate the parameters of the new rule and use UCI standard datasets to test it. The experimental results show that our rule leads to less error and better performance than product rule, mean rule, median rule, and majority vote rule.

Keywords Yager triangular norm · Multiple classifiers system · Combination rule · Genetic algorithm

74.1 Introduction

One of the paradigms emerged recently in machine learning is the Multiple Classifiers System (MCS) [1]. A MCS is a pattern classification system made up of an ensemble of individual classifiers, whose outputs or decisions on an input sample are combined in some way to get a final decision on its classification. MCS can overcome some known limitations of the traditional approaches to classifier

P. Jia (✉) · S. Liang · J. Deng
School of Computer Science, Xi'an University of Science and Technology, No 58 Yanta Road, Xi'an City, China
e-mail: pengtao.jia@gmail.com

design (namely, using a monolithic classifier chosen as the best one for the application at hand, among a given set of available classification algorithms) [2].

A MCS should estimate and then select the most appropriate component classifiers from an ensemble of classifiers. By using integration of multiple classifiers, we can reduce the recognition error rate and improve the robustness of classification [3]. At present, recognition based on MCS has been applied in many fields, such as handwritten and text recognition [4, 5], face recognition [6], language recognition [7], time-series prediction [8], etc.

The structure of MCS has serial structure and parallel structure. Most of MCS work has been focused on parallel structure, especially the combination rule of parallel structure.

Several effective methods have been proposed to combine the results of the component classifiers. In the simple voting method (also called majority voting and select all majority) [9], the prediction of each component classifier is an equally weighted vote in the result favor produced by the component classifier. The result which receives most votes is selected. There are also more sophisticated methods to combine the results of the classifiers. These include the stacking (stacked generalization) architecture [8], and combining the nearest neighbor classifiers through multiple feature subsets [10]. In many papers, different versions of resampling (boosting, bagging, cross-validated resampling, etc.) have also been suggested as examples, these resampling train the base classifiers by using a learning algorithm and the sub samples of the training set, then simply voting to combine their results. But these integration methods always have not good capability in different datasets. The challenge of the combination rule problem is to decide which classifiers to rely on or how to combine results of several classifiers. In the recent researches, the classification system based on fuzzy rule is one of the most popular fuzzy modeling systems used in pattern classification problems. Triangular norms are important family operations in fuzzy logic. We try to introduce it in MCS to improve the performance of MCS.

In mathematics, a t-norm is a special kind of binary operation on the real unit interval $[0, 1]$ used in the framework of probabilistic metric spaces and in multi-valued logic, specifically in fuzzy logic. And triangular norm can improve the generalization capability of pattern classification problems [11]. In addition, Yager t-norm is one of the best known parameterized families of t-norms, so we put forward a new fuzzy Combination Rule of MCS based on Yager T-norm (CRYT).

The new rule is the set of continuously changing operator cluster that can make better use of the classified information of sub-classifiers. It generates different computing models in combination classifier by the different characteristics of datasets. We use different datasets to train and test our rule. After comparing our rule with others, the result shows that the performance of classification is improved. Then, we arrive at a conclusion that our rule has better classification ability than others.

74.2 Fuzzy Combination Rule Based on Yager Triangular Norm

74.2.1 The Definition of Triangular Norm

A t-norm generalizes intersection in a lattice and conjunction in logic. The definition of t-norm is shown as follows.

Definition 1 [12] A t-norm is a function $T : [0, 1] \times [0, 1] \rightarrow [0, 1]$ which satisfies the following properties:

- Commutativity: $T(x, y) = T(y, x)$.
- Monotonicity: $T(x_1, y_1) \leq T(x_2, y_2)$ if $x_1 \leq x_2$ and $y_1 \leq y_2$.
- Associativity: $T(x, T(y, z)) = T(T(x, y), z)$.
- Boundary conditions: $T(0, y) = 0$, $T(1, y) = y$.

The construction of t-norms by additive generators is based on the following theorem:

Theorem 1 Let $f : [0, 1] \rightarrow [0, +\infty]$ be a strictly decreasing function such that $f(1) = 0$ and $f(x) + f(y)$ is in the range of f or equal to $f(0^+)$ or $+\infty$ for all x, y in $[0, 1]$. Then the function $T : [0, 1] \times [0, 1] \rightarrow [0, 1]$ defined as $T(x, y) = f^{-1}(f(x) + f(y))$ is a t-norm.

Proof Omitted.

Definition 3 The function $f(x)$ in Theorem 1 is called additive generators of $T(x, y)$.

Examples:

- The function f defined as $f(x) = 1 - x$ for x in $[0, 1]$ generates the Łukasiewicz t-norm $T(x, y) = \max(0, x + y - 1)$.
- The function f defined as $f(x) = -\log(x)$ for $0 \leq x < 1$ and $f(1) = 0$ generates the product t-norm $T(x, y) = xy$.
- The function f defined as $f(x) = 1 - 1/x$ for x in $[0, 1]$ generates the Hamacher t-norm $T(x, y) = xy/(x + y - xy)$.

74.2.2 Yager T-norm

Many families of related t-norms can be defined by an explicit formula depending on a parameter p . The family of Yager t-norms [13], introduced in the early 1980s by Ronald R. Yager, is given for $0 < p < +\infty$ by

$$T^Y(x, y) = \max(0, 1 - \sqrt[p]{(1-x)^p + (1-y)^p}) \tag{74.1}$$

The Yager t-norm T^Y is

- Nilpotent if and only if $0 < p < +\infty$ (for $p = 1$ it is the Łukasiewicz t-norm).
- Strictly increasing and continuous with respect to p .
- Arises from the Łukasiewicz t-norm by raising its additive generator to the power of p .

74.2.3 Multivariate Yager t-norm

The t-norm is a binary operator knowing from its definition. But in practical applications, t-norm needs to be extended from the binary function to multivariate function. Because t-norms meet the associativity, so they are likely to be extended to the multivariate function.

Theorem 2 *t-norms can be extended to multivariate operations.*

Proof Provable by associativity.

So the multivariate Yager t-norm is

$$T_p^Y(x_1, x_2, \dots, x_n) = \max(0, 1 - \sqrt[p]{(1-x_1)^p + (1-x_2)^p + \dots + (1-x_n)^p}) \tag{74.2}$$

In complex practical system, every factor generally has unequal weight. So we put forward a multivariate weighted Yager t-norm as follows:

$$T_{pz}^Y(x_1, x_2, \dots, x_n) = \max(0, 1 - \sqrt[p]{\alpha_1(1-x_1)^p + \alpha_2(1-x_2)^p + \dots + \alpha_n(1-x_n)^p}) \tag{74.3}$$

where

$$\alpha_i \in [0, 1], \sum_{i=0}^n \alpha_i = 1 (i = 1, 2, \dots, n), 0 < p < +\infty.$$

74.2.4 Algorithm of MCS with CRYT

The algorithm of MCS with CRYT can be described as follows:

- We use GENDAT function of Pattern Recognition toolbox (PRtool) in matlab for random generation of datasets for training and testing. If a dataset with

d features, we divide it into three subsets: U_1 , U_2 and U_3 randomly. U_1 is used to train the single classifiers, and U_2 is used to train the ensemble rules and U_3 is used to test the MCS.

- We can gain n classifiers in training dataset U_1 using n algorithms. After that U_2 is used to test the n classifiers, and the results being normalized of n classifiers are input variables in formula 74.3. Because output values being anti-normalized are continuous, we assign them to class labels by simple rounding rule.
- Using genetic algorithm to evaluate parameters in formula (74.3) in U_2 .
- Using U_3 to test the performance of our model.

74.2.5 Parameter Estimation

The Genetic Algorithm (GA) is a search heuristic that mimics the process of natural evolution. This heuristic is routinely used to generate useful solutions to optimization and search problems. Thus we use genetic algorithm to estimate the parameters $\alpha_1, \alpha_2, \dots, \alpha_n$ and p of CRYT.

The genetic algorithm uses three main types of rules at each step to create the next generation from the current population:

- Selection rules: select the individuals, called parents that contribute to the population at the next generation.
- Crossover rules: combine two parents to form children for the next generation.
- Mutation rules: apply random changes to individual parents to form children.

Parameters in GA should be set as follows:

- The initial population is an entirely random population, including 20 individuals.
- Binary code of eight bits is used.
- Random uniform distribution model is used to select the highest fitness value chromosome to get into the next generation in selection operation.
- The separated crossover is used for forming children for the next generation.

74.3 Experiments and Discussion

74.3.1 Datasets

In order to validate our model, we select four datasets from the UCI repository of machine learning database [14]. We divide every dataset into three subsets: U_1 , U_2 and U_3 randomly. Table 74.1 shows these datasets and their descriptions.

Table 74.1 Brief descriptions of datasets

ID	Name	Attributes	Dataset size	Classes	U_1	U_2	U_3
1	Gunx	150	200	2	100	52	48
2	Iris	4	150	3	75	39	36
3	Synthetic_control	60	600	2	300	150	150
4	Trace	275	200	4	100	50	50

There are differences among the results of every experiment, because records of U_1 , U_2 and U_3 are selected randomly. Repeat the experiment for ten times, and consider the mean-value of the ten experimental results as the final result.

74.3.2 Experimental Procedure

The experimental procedure is as follows:

Step 1: there is discrepancy in the sequential values of the dataset. Thus we first normalize the values of time series in interval $[0, 1]$ for comparison. The formula of normalization is given as follow

$$norm(x_i) = \frac{x_i - \min(X)}{\max(X) - \min(X)} \quad (74.4)$$

Step 2: we choose three classifiers as component classifiers, namely, KNN, NB and BDT, where KNN is k-Nearest Neighbor classifier, and we set k with three; NB is Naive Bayes classifier; BDT is Binary Decision Tree classifier. Of course, there is no limit to select the number of component classifiers and the methods of component classifiers.

Step 3: U_1 is used to train the single classifiers and U_2 is used to test the single classifiers and to train the MCS with CRYT.

Step 4: U_3 is used to test the single classifiers, the MCS with CRYT and the MCS with other combination rules. In order to validate our rule, we select product rule, mean rule, median rule, and majority vote rule as comparison rules [15].

74.3.3 Results Analysis and Discussion

Table 74.2 shows the error rate of single classifiers, MCS with comparison rule and MCS with CRYT in U_3 .

According to the comparative error rates in Table 74.2, we draw a conclusion that not all combination rules can lead to less error than individual classifier in the same dataset, such as Gunx and Synthetic Control. For Gunx dataset, 3-NN

Table 74.2 Error rates of single classifier, comparison rules and CRYT in U_3

Name	BDT	NB	3- NN	Product Rule	Mean rule	Median rule	Majority vote rule	CRYT
Gunx	0.123	0.096	0.066	0.094	0.096	0.112	0.074	0.040
Iris	0.095	0.039	0.039	0.042	0.039	0.083	0.036	0.028
Synthetic control	0.107	0.118	0.003	0.098	0.118	0.090	0.034	0.003
Trace	0.227	0.241	0.340	0.229	0.241	0.225	0.227	0.083

classifier obtains the best classification result, and the error rate is 0.066 in Table 74.2. Only CRYT rule is better than it, the error rate is 0.040. For Synthetic Control dataset, 3-NN classifier also obtains the best classification result, and the error rate is 0.003. Only CRYT is equal to 3-NN classifier. Knowing from Table 74.2, only CRYT has the lowest error rate in all datasets. So we can conclude that CRYT can keep lower error rate and better performance than comparison rules.

Comparing with other rules, the time complexity of CRYT algorithm is higher than that of other comparison rules on training dataset, because using genetic algorithm to estimate the parameters $\alpha_1, \alpha_2, \dots, \alpha_n$ and p of CRYT needs more time than other rules.

74.4 Conclusion

It is well know that combining multiple classifiers can lead to less error than individual classifier. But sometimes the result is dissatisfactory, because uncomfortable combination rule may lead to bad performance. So selecting appropriate combination rule is important to MCS. The combination rule with generalized ability is also needed. Due to Yager t-norm has better generalization, thus we introduce a new combination rule algorithm CRYT. The experimental results on datasets show that the classification performance of UCI is better than that of the fixed combination rules, which are product rule, mean rule, median rule, and majority vote rule.

Acknowledgments Pengtao Jia thanks National Natural Science Foundation (NNSF) of Shaanxi under Grant(2012JQ8035) and innovation team of the Ministry of Education-funded project(IRT0856) for facilitating this research.

References

1. Farahbod F, Eftekhari M (2012) Comparison of different t-norm operators in classification problems. *Int J Fuzzy Logic Sys* 2(3):33–39
2. Kuncheva LI (2004) *Combining pattern classifiers: methods and algorithms*. Hoboken (N.J.), Wiley, New York

3. Duin RPW, Tax DMJ (2000) Experiments with classifier combining rules. In: Proceeding of 1st international workshop on multiple classifier system, MC, June 21–23 2000, Cagliari, Italy, pp 16–29
4. Ebrahimipour R, Hamed S (2009) Hand written digit recognition by multiple classifier fusion based on decision templates approach. *World Acad Sci Eng Tech* 57(9):560–565
5. Bell DA, Guan JW, Yaxin B (2005) On combining classifier mass functions for text categorization. *IEEE Trans Knowl Data Eng* 17(10):1307–1319
6. Diego IM, Serrano A, Conde C, Cabello E (2010) Face verification with a kernel fusion method. *Pattern Recogn Lett* 31(9):837–844
7. Krajewski J, Batliner A, Kesse LS (2010) Comparing multiple classifiers for speech-based detection of self-confidence—a pilot study. *International Conference on pattern recognition, ICPR 2010, Aug. 23–26, Istanbul, Turkey*, pp 3717–3719
8. Chitra A, Uma S (2010) An ensemble model of multiple classifiers for time series prediction. *Int J Comput Theor Eng* 2(3):1793–8201
9. Duda RO, Hart PE, Stork DG (2001) *Pattern classification*, 2nd edn. Wiley, New York
10. Bay SD (1998) Combining nearest neighbor classifiers through multiple feature subsets. In: *Proceeding of 15th International Conference on Machine Learning, Morgan Kaufmann, San Francisco* pp 37–45
11. Kou ZB, Zhang CS (2003) Multi-agent based classifier combination. *Chin J Comput* 26(2) 174–179(in Chinese)
12. Mizumoto M (1989) Pictorial representation of fuzzy connectives, part 1: cases of t-norms, t-conorms and averaging operators. *Fuzzy Sets Syst* 31:217–242
13. Hauke W (1997) Using Yager's t-norms for aggregation of fuzzy intervals. *Fuzzy Sets Syst* 101(1):59–65
14. Blake CL, Newman DJ, Merz CJ (1998) UCI repository of machine learning databases. <http://www.ics.uci.edu/~mllearn/MLRepository.html>. University of California, Department of Information and Computer Science, Irvine, CA
15. Jia PT, He HC, Lin W (2005) Decision by maximum of posterior probability average with weights: a method of multiple classifiers combination. *IEEE Proceeding international conference on machine learning and cybernetics, Guangzhou, In*, pp 1949–1954

Chapter 75

Application of Swarm Intelligence Optimization in EEG Analysis

Lu Huang and Hong Wang

Abstract In order to improve time efficiency of brain-computer interface (BCI), swarm intelligence optimization (SIO) based algorithms were used to analyze electroencephalogram (EEG). Artificial fish swarm algorithm (AFSA), a SIO algorithm, initiated several points in feasible domain of de-mixing matrix w , and parallel searched. These mechanism made the algorithm iterate fasterly. Ulteriorly, the introduction of chaos searching enhanced convergence precision. The experiments ran on real EEG data for ocular artifacts removal and P300 extraction respectively. PIs were all less than 0.08 and iteration numbers were superior than classic algorithm. These results show SIO based algorithms can effectively reduce computation time for EEG based BCI with the operation precision remaining unimpaired.

Keywords Brain-computer interface (BCI) · Electroencephalogram (EEG) · Swarm intelligence optimization (SIO) · PI

75.1 Introduction

An electroencephalogram (EEG) based brain-computer interface (BCI) is a communication system in which messages that users send to the computer or other electronic equipments do not go through the peripheral nerve pathways but are

L. Huang
Sino-Dutch Biomedical and Information Engineering School, Northeastern University,
Shenyang 110819, China
e-mail: hanglu@dlo.u.edu.cn

L. Huang
College of Information Engineering, Dalian Ocean University, Dalian 116023, China

H. Wang (✉)
Northeastern University, POB 319, Shenyang 110004, China
e-mail: hongwang@mail.neu.edu.cn

detected through EEG activity [1]. Some characteristic potentials embodied in EEG help us to judge how those users think. But the measured scalp EEG can not be used for pattern classification directly. It contains many spontaneous EEG, ocular artifacts and power line interference except those helpful characteristic potentials [2]. So EEG analysis, such as preprocessing and feature extraction, etc., is even more important for EEG based BCI.

Because of the mutual independence between every different EEG constituent, independent component analysis (ICA) is a suitable technique for EEG analysis [3]. FastICA algorithm is a more popular ICA algorithm [4]. It can separate some characteristic potentials from EEG successfully. But because of the second order convergence, FastICA algorithm itself needs a long time computation. Furthermore, the EEG data size is very huge because of the numerous electrodes and repeated measurement. So, facing such a large volume of EEG data, FastICA runs slow and can not satisfy the real-time BCI system.

Aiming at above-mentioned situation, the application of swarm intelligence optimization (SIO) in EEG analysis was proposed. We combined artificial fish swarm algorithm (AFSA), a kind of SIO algorithm, with ICA technique and used this AFSA based ICA (AFSA_ICA) to analyze people's EEG activities. According to the idea of SIO, we made ICA iteration from several randomly generated points and parallel search in the feasible domain so as to converge rapidly, and led ourselves to reduce computation time for EEG analysis. Ulteriorly, in view of convergence precision, AFSA_ICA algorithm was improved with chaos searching, called CAFSA_ICA. The ergodicity and global searching ability of chaos searching made artificial fishes (AFs) jump out local optimization efficiently and enhance convergence precision further so as to improve the performance of the separation of the mixed signals in EEG.

75.2 Swarm Intelligence Optimization

SI is the intelligence of the swarm which is composed of some unintelligent and autonomous elements. SIO accomplish the best value calculation for objective function by imitating the actions of social animals in nature [5]. This kind of algorithms are easy to realize and requirements of them for CPU and memory are also tolerant. There exist several SIO algorithms. We use AFSA in this paper.

AFSA is a newly emerging method for SIO [6]. Every AF in whole swarm has abilities to achieve four basic actions: preying, following, swarming and moving. AFSA algorithm begins with several initial points, having the capability of parallel searching and information sharing. Moving action is defined as follow:

$$u_j = u_i + visual \cdot rand \quad (75.1)$$

where u_i is the current position of AF, u_j is the position AF randomly moves to,

$visual$ is AF's vision scope, $rand$ is a random function. If the food concentration of \mathbf{u}_j is higher than that of \mathbf{u}_i , preying action impels AF update by:

$$\mathbf{u}_i = \mathbf{u}_i + \frac{(\mathbf{u}_j - \mathbf{u}_i) + (\mathbf{u}_{best} - \mathbf{u}_i)}{\|(\mathbf{u}_j - \mathbf{u}_i) + (\mathbf{u}_{best} - \mathbf{u}_i)\|} \cdot step \cdot rand \quad (75.2)$$

where \mathbf{u}_{best} is the best position of all AFs, and $step$ means the moving step length. The best position of all AFs in the swarm is defined as \mathbf{u}_b . Following action impels AF update as follow if the food concentration of \mathbf{u}_b is higher than that of \mathbf{u}_i :

$$\mathbf{u}_i = \mathbf{u}_i + \frac{(\mathbf{u}_b - \mathbf{u}_i) + (\mathbf{u}_{best} - \mathbf{u}_i)}{\|(\mathbf{u}_b - \mathbf{u}_i) + (\mathbf{u}_{best} - \mathbf{u}_i)\|} \cdot step \cdot rand \quad (75.3)$$

The center position of all AFs in the swarm is defined as \mathbf{u}_c . If the food concentration of \mathbf{u}_c is higher than that of \mathbf{u}_i , swarming action impels AF update by:

$$\mathbf{u}_i = \mathbf{u}_i + \frac{(\mathbf{u}_c - \mathbf{u}_i) + (\mathbf{u}_{best} - \mathbf{u}_i)}{\|(\mathbf{u}_c - \mathbf{u}_i) + (\mathbf{u}_{best} - \mathbf{u}_i)\|} \cdot step \cdot rand \quad (75.4)$$

75.3 Iterating ICA Using AFSA

ICA is one of blind source separation (BSS) techniques. It can work well without any prior knowledge about the mixing matrix [7]. We denote the mixed signals by $\mathbf{x}(t)$ and the source signals consisting of ICs by $\mathbf{s}(t)$, the object of ICA is to find de-mixing matrix $\bar{\mathbf{w}}$ and $\mathbf{y}(t) = \bar{\mathbf{w}}\mathbf{x}(t)$ is the approximation for the source signals $\mathbf{s}(t)$. According to negentropy maximum criterion, objective function of ICA is:

$$C(\mathbf{y}) = \sum_{i=1}^m J(y_i) \quad (75.5)$$

where $y_i = w_i\mathbf{x}(t)$, $J(y_i) \approx \rho(E\{G_i(y_i)\} - E\{G_i(v)\})^2$, ρ is a positive constant, $G_i(\cdot)$ is a non-quadratic function, $E\{\cdot\}$ is a mean function and v is a Gaussian variable having zero mean and unit variance.

When negentropy of ICA is to be objective function of AFSA, AFSA_ICA algorithm is built up. The steps of AFSA_ICA algorithm are as follows:

1. Transform the $m \times n$ dimensional de-mixing matrix \mathbf{w} to the $1 \times (m \times n)$ dimensional AF position matrix \mathbf{uw} ;
2. Initialize all the AF positions $\mathbf{uw}(0)$ and all dependent parameters, where $\mathbf{uw} = \{uw_i \mid i = 1, 2, \dots, total\}$;
3. Use Eq. (75.5) to calculate the objective function values of all AFs, specially $\mathbf{y}(t) = \mathbf{uw}_i * \mathbf{x}(t)$;
4. Evaluate every AF, and then select one of the four basic actions to execute, updating its position;

5. Record every global optimum, if maximum iterations or minimum error is attained, stop the evolutions, otherwise go back to the step 3.
6. Transform the $1 \times (m \times n)$ dimensional AF position matrix \mathbf{uw} to the $m \times n$ dimensional de-mixing matrix $\bar{\mathbf{w}}$, so $y(t) = \bar{\mathbf{w}}x(t)$ is the approximation for the source signals $s(t)$.

75.4 Iterating ICA Using CAFSA

Chaos is defined as a random and non-uniform phenomenon in the deterministic nonlinear system and the hidden discipline in a complex system can be revealed by chaos theory [8]. It can traverse all status in a certain range without repeatability. These characters of chaos searching make it a good mechanism that can avoid getting into local extreme point efficiently and reach global extreme point fasterly. Logistic mapping can generate chaos variables by iteration as follow:

$$z(k+1) = \mu z(k)[1 - z(k)] \quad (75.6)$$

where k is the iteration number, $\mu = 4$ is the control parameter, $z(k) \in [0, 1]$ is the k th iteration value of the chaos variable z .

Chaos based AFSA algorithm (CAFSA) combines basic AFSA algorithm with chaos searching. The current AF position is defined as u_i and its position after changing is u'_i . Every component of u'_i is mapped to chaos variable by:

$$cu'_{i,j} = \frac{u'_{i,j} - u_{i,j}^{\min}}{u_{i,j}^{\max} - u_{i,j}^{\min}} \quad (75.7)$$

where j is the dimension index of AF definition domain, $u_{i,j}^{\max}$ and $u_{i,j}^{\min}$ are respectively the maximum and the minimum of u'_i in the j th dimension. Then using logistic mapping on the basis of $cu'_{i,j}$, a new chaos variable $cu''_{i,j}$ can be generated. At last, $cu''_{i,j}$ is mapped back to the AF feasible domain:

$$u''_{i,j} = u_{i,j}^{\min} + cu''_{i,j} \cdot (u_{i,j}^{\max} - u_{i,j}^{\min}) \quad (75.8)$$

We called AFSA_ICA improved with chaos searching as CAFSA_ICA.

75.5 Experiments and Results Analysis

75.5.1 Ocular Artifacts Removal

Experiment data came from Neuro dynamics Laboratory at the State University of New York Health Center [9]. The 64 electrode positions were located at standard

Fig. 75.1 The 18 channel \times 10 s EEG signals

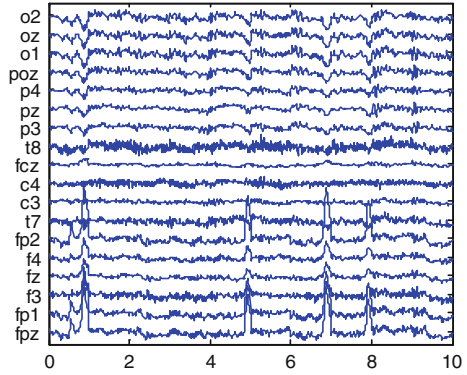
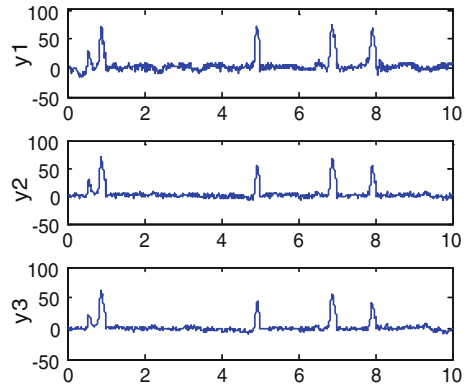


Fig. 75.2 The separated ocular artifacts by using three algorithms respectively



sites and sampled at 256 Hz. We selected 18 channels \times 10 s EEG signals as our research object, shown in Fig. 75.1. Our task was to extract the obvious ocular artifacts occurring at about 1, 5, 7 and 8 s in EEG.

For comparison, we used FastICA, AFSA_ICA and CAFSA_ICA in turn to separate the ocular artifacts, with the results exhibited in Fig. 75.2. The performance of separation is measured by PI [10]:

$$PI = \frac{1}{2M} \sum_{i=1}^M \left\{ \left(\sum_{j=1}^M \frac{|c_{ij}|^2}{\max_k |c_{ik}|^2} - 1 \right) + \left(\sum_{j=1}^M \frac{|c_{ji}|^2}{\max_k |c_{ki}|^2} - 1 \right) \right\} \quad (75.9)$$

where $c = wA = (c_{ij})$, and M is the number of variables. PI is zero when the desired subset of ICs is perfectly separated. The low PI of AFSA_ICA and CAFSA_ICA listed in Table 75.1 indicated their superior performances over FastICA. Among them, CAFSA_ICA achieved the lowest PI because chaos searching provided a better convergence precision. Meanwhile, the fewer iteration number and time reflected that AFSA_ICA and CAFSA_ICA were more advantageous than FastICA as for time efficiency. Furthermore, CAFSA_ICA, which

Table 75.1 Iteration performances for ocular artifacts removal using three algorithms

	FastICA	AFSA_ICA	CAFSA_ICA
PI	0.10	0.07	0.06
Iteration number	172	103	48
Iteration time (s)	18.9	12.7	12.6

introduced chaos searching reached global extreme point fasterly, leading to lesser iteration number. But because of adding the chaos computation in the iteration, the iteration time of it was not cut down greatly.

75.5.2 P300 Extraction

Experiment data came from the BCI research group of Ecole Polytechnic Federale de Lausanne [11]. It contained EEG data from 4 disabled subjects and 4 healthy subjects, with measurements from 32 electrodes placed at standard sites. In the experiment, every subject needed to finish 4 recording processes, with every process including 6 flashing sequence and aiming at one target stimulation.

For this EEG data, the obtained ICs using FastICA, AFSA_ICA and CAFSA_ICA were respectively averaged between 0 and 600 ms according to the same stimulus row/column. The ICs, which got their maximum amplitude at 250–400 ms after the onset of stimulus and got their top two maxima amplitudes on channel C_z , C_1 or C_2 , were kept, with the others abandoned. The kept ICs were inverse operated to the scalp electrode and then 0–10 Hz filtered. Figures 75.3, 75.4 and 75.5 gave the obtained P300 of subject 6 on channel Cz with 16 times averaged using three algorithms respectively.

The averaged iteration performances for all eight subjects using three algorithms were listed in Table 75.2. Iteration number and time were for one stimulus. Obviously, AFSA_ICA and CAFSA_ICA showed their superior separation performances and superior time efficiency. These favorable properties could help the following classification more accurate and more timesaving.

Fig. 75.3 P300 derived by FastICA

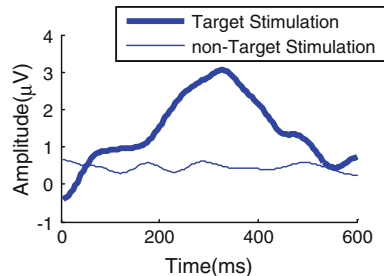


Fig. 75.4 P300 derived by AFSA_ICA

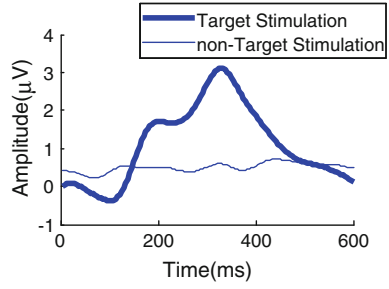


Fig. 75.5 P300 derived by CAFSA_ICA

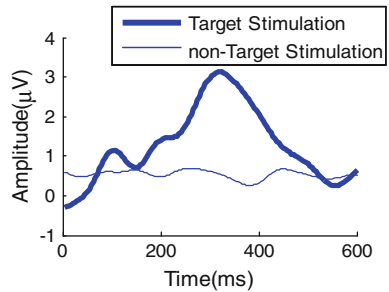
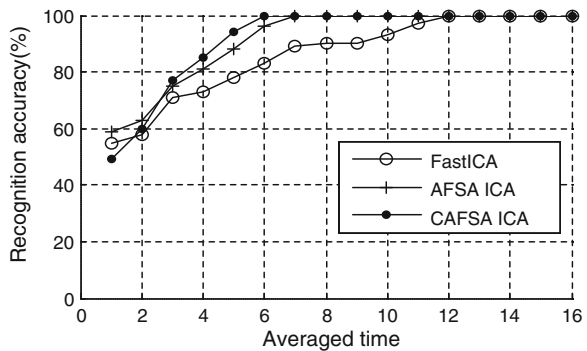


Table 75.2 Iteration performances for P300 extraction using three algorithms

	FastICA	AFSA_ICA	CAFSA_ICA
PI	0.11	0.08	0.06
Iteration number	351	127	69
Iteration time (s)	45.3	31.2	33.7

Fig. 75.6 The averaged recognition accuracies using three algorithms with different averaged times



On the former basis, we defined a time window which began at 250 ms after the stimulus and finished at 400 ms. In this window, peak amplitude and wave area were extracted to build a 2-dimensional feature vector, sent to a simple liner classifier. The averaged recognition accuracies for all eight subjects employing

three algorithms with different averaged times were described in Fig. 75.6. As we saw, three algorithms all achieved 100 % recognition accuracy with 16 times averaged. While in the condition of less times, AFSA_ICA and CAFSA_ICA performed better. This phenomenon indicated that SIO based algorithms could extract our interesting components from the low-SNR EEG, owning a good robustness. It was worth further researching in the weak signal process area.

75.6 Conclusion

EEG analysis in EEG based BCI computes slow and can not satisfy the real-time BCI system. We proposed the application of SIO in EEG analysis. The advantages of SIO, such as beginning with several initial points, having the capability of parallel searching and information sharing, etc., were combined with ICA technique so as to reduce the iteration number with PI not increased. Furthermore, chaos searching was introduced to our algorithm to enhance the convergence precision further. Using real EEG data, we validated our algorithm as for ocular artifacts removal and P300 extraction. The results show that SIO based algorithms can effectively reduce computation time for EEG based BCI and own a good robustness, fitting to be developed in real-time BCI research area.

Acknowledgments This work was supported by National Natural Science Foundation of China(No. 61071057).

References

1. Suk H-I, Lee S-W (2013) A novel bayesian framework for discriminative feature extraction in brain-computer interfaces. *IEEE Trans Pattern Anal Mach Intell* 35(2):286–299
2. Mammone N, La Foresta F, Morabito FC (2012) Automatic artifact rejection from multichannel scalp EEG by wavelet ICA. *IEEE Sens J* 12(3):533–542
3. Selvam VS, Shenbagadevi S (2011) Brain tumor detection using scalp eeg with modified wavelet-ICA and multi layer feed forward neural network. In: Annual international conference of the IEEE engineering in medicine and biology society, EMBC, Boston, Massachusetts, USA, pp 6104–6109
4. Hyvärinen A (1999) Fast and robust fixed-point algorithms for independent component analysis. *IEEE Trans Neural Netw* 10:626–634
5. Bala Krishna M, Doja MN (2011) Swarm intelligence-based topology maintenance protocol for wireless sensor networks. *IET Wireless Sens Syst* 1(4):181–190
6. Li XL, Shao ZJ, Qian JX (2002) An optimizing method based on autonomous animats: fish-swarm algorithm. *Syst Eng Theory Pract* 22:32–38 (in chinese)
7. Hyvärinen A, Oja E (2000) Independent component analysis: algorithms and applications. *Neural Networks* 13:411–430
8. Zhao H, Shi Y-Q, Chen Z (2013) Detecting covert channels in computer networks based on chaos theory. *IEEE Trans Inf Forensics Secur* 8(2):273–282
9. Ingber L (1998) Statistical mechanics of neocortical interactions: training and testing canonical momenta indicators of EEG. *Math Comput Model* 27(3):33–64

10. Ji C, Hu XN, Zhu LC et al (2011) Improved higher order convergent FastICA algorithm. J Northeast Univ (Nat Sci) 32(10):1390–1393 (in chinese)
11. Hoffmann U, Vesin JM, Ebrahimi T et al (2008) An efficient P300-based brain-computer interface for disabled subjects. J Neurosci Meth 167:115–125

Chapter 76

Blind Detection of BPSK Signals Using Hysteretic Hopfield Neural Network

Shu-Juan Yu, Di Feng and Yun Zhang

Abstract A new algorithm based on Hysteretic Hopfield neural network (HHNN) is proposed to detect BPSK signals blindly. Considering the characteristic of hysteretic activation function, the new algorithm has a tendency to overcome local minima. The new energy functions for HHNN are constructed, and the stability of the network is also analyzed. Simulation results show that the algorithm proposed show satisfactory performance in detecting BPSK with shorter received signals.

Keywords Hysteretic Hopfield neural network (HHNN) · Blind detection · BPSK signals

76.1 Introduction

In many communication systems, digital signals suffer from inter-symbol interference (ISI) caused by multi-path effects. Blind channel estimation and equalization may be used to mitigate multipath propagation and to improve both bandwidth and energy efficiency. This is especially important for wideband sensor networks such as those for acoustic location or video surveillance.

Although blind detection algorithm based on SOS has the merit of fast convergence rate, all of which are easy to fall into local minima. Considering the characteristic of hysteretic activation function, a new algorithm based on Hysteretic Hopfield neural network has a tendency to overcome local minima.

Models of hysteresis appear and hysteretic neuron models using signum functions have been proposed for associative memory [1, 2]. They demonstrated

S.-J. Yu (✉) · D. Feng · Y. Zhang
School of Electronic Science and Engineering, Nanjing University of Posts and Telecommunications, No 66 XingMoFan Road, NanJing City, China
e-mail: yusj@njupt.edu.cn

that their hysteretic models performed better than nonhysteretic neuron models, in terms of capacity, signal-to-noise ratio, recall ability, etc.

Bharitkar and Meni introduced a neuron which is multivalued, has memory, and is adaptive. They have also introduced the HHNN and its associated circuit model, proved Lyapunov stability for the HHNN [2]. Liu and Xiu proposed a appropriate parameters, the neuron can possess hysteresis property and chaos property simultaneously. However, these network are also confined to binary neurons and real region, may not be appropriate for complex signals such as BPSK. Hysteretic Hopfield Network use for blind BPSK signals detection has never been mentioned in this lecture.

76.2 Hysteretic Hopfield Neural Network

Hysteretic Hopfield neural network differs from other neural networks in that its nonlinear gain (activation) function is the hysteresis function depicted in Fig. 76.1. Observe that hysteresis activation function is composed of two offset sigmoid functions and this neuron’s output not only depends on its input, but also on derivative information. The Hysteretic Hopfield neural network is designed as Fig. 76.2.

A general state space equation of a HHNN is given by

$$\mathbf{s}(k + 1) = f(\mathbf{W}\mathbf{s}(k)) = f(\mathbf{y}(k)) \tag{76.1}$$

Where $\mathbf{W}^T = \mathbf{W}$.

$$\mathbf{s}(k) = [s_1(k), s_2(k), \dots, s_N(k)]^T \tag{76.2}$$

$$y_i(k) = \sum_{j=1}^N w_{ij}s_j(k), i = 1, \dots, N \tag{76.3}$$

Fig. 76.1 Hysteretic activation function

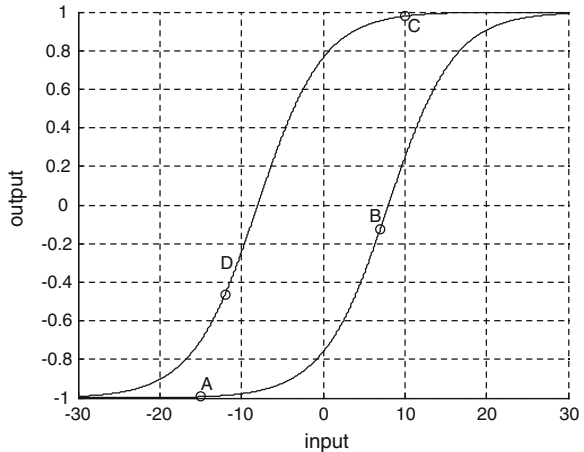
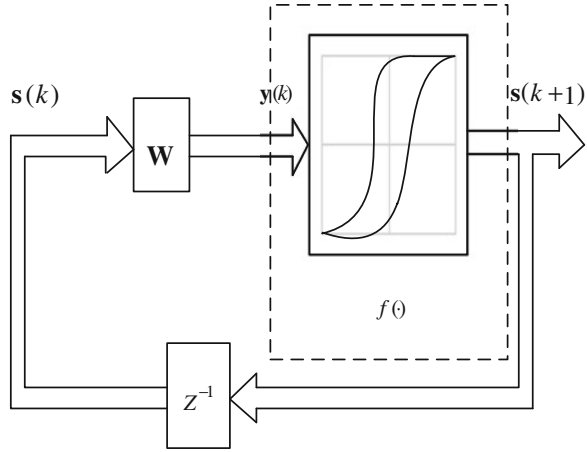


Fig. 76.2 Hysteretic Hopfield neural network



The Hysteretic activation function is defined as:

If $\dot{s}(t - \Delta t) \geq 0$

$$f(y(t)|\dot{s}(t - \Delta t)) = \tanh[\lambda(\dot{s}(t - \Delta t))(y(t) + \mu(\dot{s}(t - \Delta t)))] \tag{76.4}$$

if $\dot{s}(t - \Delta t) < 0$

$$f(y(t)|\dot{s}(t - \Delta t)) = \tanh[\lambda(\dot{s}(t - \Delta t))(y(t) - \mu(\dot{s}(t - \Delta t)))] \tag{76.5}$$

where

$$\lambda(\dot{s}(t - \Delta t)) = \begin{cases} \lambda_\alpha & \dot{s}(t - \Delta t) \geq 0 \\ \lambda_\beta & \dot{s}(t - \Delta t) < 0 \end{cases} \tag{76.6}$$

$$\mu(\dot{s}(t - \Delta t)) = \begin{cases} -\alpha & \dot{s}(t - \Delta t) \geq 0 \\ \beta & \dot{s}(t - \Delta t) < 0 \end{cases} \tag{76.7}$$

$\dot{s}(t - \Delta t) = \lim_{\Delta t \rightarrow 0} \frac{s(t) - s(t - \Delta t)}{\Delta t}$ $\beta > -\alpha, (\lambda_\alpha, \lambda_\beta) > 0$, Note that the hysteretic neuron's activation function has four parameters associated with it, namely, $\lambda_\alpha, \lambda_\beta, \alpha, \beta$. Usually, one does not tune a neuron's activation function because, for the most part, there are no parameters to tune. The hysteretic neuron is different in this sense, and we can think about tuning all of its parameters in order to maximize its performance. So, it seems that the hysteretic neuron provides us with much more flexibility than the usual neuron.

The qualitative properties of the proposed network can be investigated by introducing an energy function defined on the state-space in terms of the weight coefficients:

$$E(x_1, x_2 \cdots x_N) = -\frac{1}{2} \sum_{i=1}^N \sum_{j=1}^N w_{ij} x_i x_j + \sum_{i=1}^N \int_0^{x_i} f_i^{-1}[x_i(s_i|\dot{s}(t - \Delta t))] dx_i \tag{76.8}$$

Fellow the associated circuit model of HHNN, applying Kirchhoff's current law to node j , we obtain the following circuit equation:

$$\frac{ds_j(t)}{dt} + s_j(t) = \sum_{i=1}^N w_{ji}x_i + \mu_j(\dot{s}(t - \Delta t)) \quad (76.9)$$

The stability of the HHNN can be demonstrated as follow:

$$\begin{aligned} \frac{dE}{dt} &= \sum_{j=1}^N \frac{\partial E}{\partial x_j} \frac{\partial x_j}{\partial s_j} \frac{\partial s_j}{\partial t} \\ &= \sum_{j=1}^N \left(s_j - \mu_j(\dot{s}(t - \Delta t)) - \sum_{i=1}^N w_{ji}x_i \right) \frac{\partial x_j}{\partial s_j} \frac{\partial s_j}{\partial t} \\ &= - \sum_{j=1}^N \left(\frac{ds_j}{dt} \right)^2 \frac{\Delta x_j}{\Delta s_j} \end{aligned} \quad (76.10)$$

Obviously, if $\frac{\Delta x_j}{\Delta s_j} > 0$, then $\frac{dE}{dt} < 0$

According to Eq. (76.4)–(76.7), and Fig. 76.1, we analyze Eq. (76.8) by considering the following transitions:

- 1) Transition 1 for which input of the neuron is positive, and $\Delta s_j > 0$, then activation function get A-B: We can obtain $\Delta x_j > 0$, $\frac{\Delta x_j}{\Delta s_j} > 0$.
- 2) Transition 1 for which input of the neuron is positive, and $\Delta s_j < 0$, then activation function get C-D: We can obtain $\Delta x_j < 0$, $\frac{\Delta x_j}{\Delta s_j} > 0$.

For which input of the neuron is negative, the proof is similar. To summarize, we can get $\frac{\Delta x_j}{\Delta s_j} > 0$, Implies that $\frac{dE}{dt} < 0$. Because $\frac{dE}{dt} < 0$ for all possible transitions, we have shown that the equilibrium point for the HHNN is stable in the sense of Lyapunov.

76.3 The Synaptic Weight Matrix of HHNN for Blind BPSK Signal Detection

Without loss of generality, the following discussion is based on the Single-Input Multi-output (SIMO) system. The discrete time model of SIMO channels output vector is usually given by [3–5]

$$\begin{aligned} (\mathbf{x}(k))_{q \times 1} &= [\mathbf{h}_0, \dots, \mathbf{h}_M](s(k))_{(M+1) \times 1} \\ &= \sum_{j=0}^M (\mathbf{h}_j)_{q \times 1} s(k-j) \end{aligned} \quad (76.11)$$

$$\mathbf{X}_N = \mathbf{S}\Gamma^T \quad (76.12)$$

where $(\mathbf{\Gamma})_{(L+1)q \times (L+M+1)}$ is an block Toeplitz matrix form of $\mathbf{h}_j (j = 0, 1, 2, \dots, M)$, $[\mathbf{h}_0, \dots, \mathbf{h}_M]$ is the channel impulse response matrix, $(\mathbf{X}_N)_{N \times (L+1)q}$ is the received signal vector. Equation (76.11) implies that there exists an $\mathbf{Q} = \mathbf{U}\mathbf{U}_c^T$, such that $\mathbf{Q}\mathbf{s}_N(k-d) = \mathbf{0}$, if $\mathbf{\Gamma}$ is full rank. Where $\mathbf{U}_c \in R^{N \times (N-(L+M+1))}$ is an unitary matrix of the Singular Value Decomposition (SVD) of $\mathbf{X}_N = [\mathbf{U}, \mathbf{U}_c] \begin{bmatrix} \mathbf{D} \\ \mathbf{0} \end{bmatrix} \mathbf{V}^T$ then we can write the cost function [6, 7]

$$J_0 = \mathbf{S}_N^T(k-d)\mathbf{Q}\mathbf{s}_N(k-d) = \mathbf{S}^T\mathbf{Q}\mathbf{S} \quad (76.13)$$

$$\hat{\mathbf{s}} = \arg \min\{J_0\} \quad (76.14)$$

By using CHNN to solve the Eq. (76.12), The synaptic weight matrix is defined as

$$\mathbf{W} = \mathbf{I} - \mathbf{Q} \quad (76.15)$$

Where \mathbf{I} is a identity matrix.

While $\mathbf{s}(k)$ is stable equilibrium point of the energy function, we get

$$\mathbf{S}(k) = \mathbf{S}(k+1) \quad (76.16)$$

$$\mathbf{S}(k) = f(\mathbf{S}(k) - \mathbf{Q}\mathbf{S}(k)) \quad (76.17)$$

Where $\mathbf{Q}\mathbf{S}(k) = \mathbf{0}$, satisfied Eq. (76.11). While the weight matrix of HHNN is constructed by the complementary projection operator of received signals, the problem of quadratic optimization with integer constraints can successfully solved with the HHNN, and the BPSK signals are blindly detected.

76.4 Simulation Result

In this section, simulation results are presented to illustrate the quantitative performance of the algorithm. For convenience's sake of draw picture, while bit error rate (BER) equals 0, we set the BER = 10^{-5} . We also set $\gamma_{ij}^{\alpha}(0) = 0, \gamma_{ij}^{\beta}(0) = 0,$

$$\alpha_{ij}(0) = 0, \beta_{ij}(0) = 0, \eta_1 = 0.02, \eta_2 = 0.02, \eta_3 = 0.08, \eta_4 = 0.01.$$

Experiment 1—performance comparison of HHNN and HNN under fixed data number.

Figures 76.3 and 76.4 illustrates BER comparison of HHNN and HNN with synchronous and asynchronous operating mode. The results are averaged over 100

Fig. 76.3 BER under synchronous operating mode

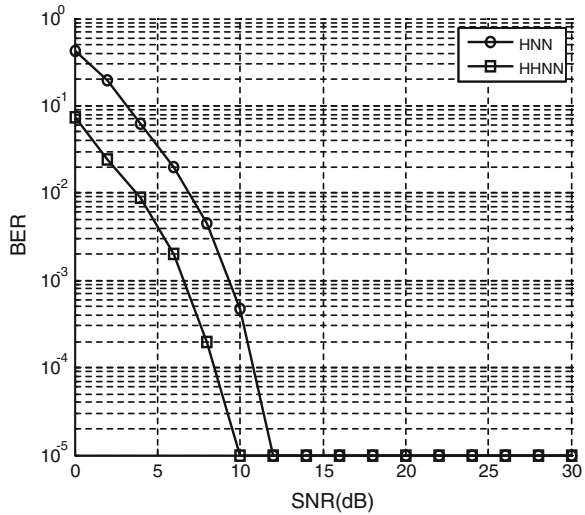
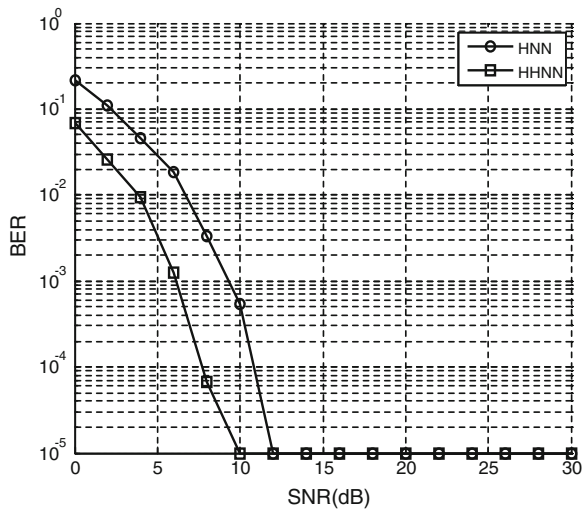


Fig. 76.4 BER under asynchronous operating mode



Monte Carlo simulations which show that the proposed new algorithm can blindly detect the transmitted signals effectively. The transmitted signals number is 300.

Simulation results show that the HHNN has better performance than traditional HNN under both synchronous and asynchronous operating mode.

Experiment 2—performance comparison of HHNN under different data number.

Figures 76.5 and 76.6 illustrates BER comparison of HHNN with synchronous and asynchronous operating mode under different data number.

Fig. 76.5 BER under different data with synchronous operating mode

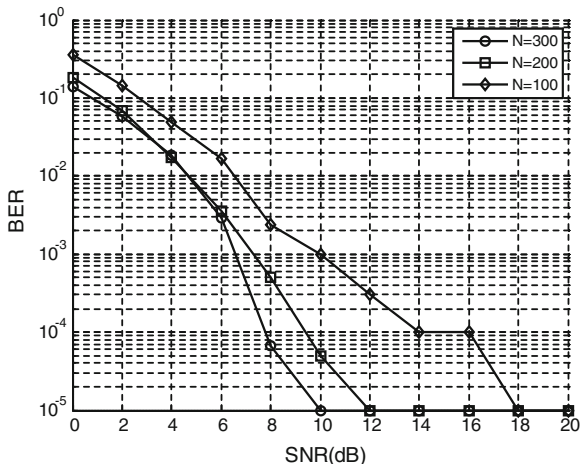
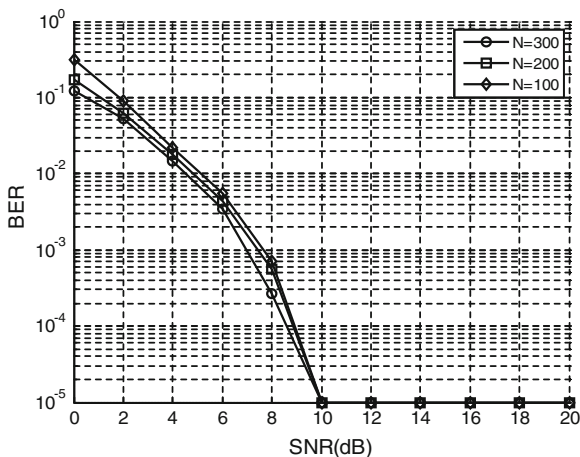


Fig. 76.6 BER under different data with asynchronous operating mode



Results show that the proposed HHNN can be used to blindly detect BPSK constellation signals with shorter received signals under both synchronous and asynchronous operating mode.

Experiment 3—performance comparison of HHNN under different channels

Figures 76.7 and 76.8 illustrates the performance comparison of HHNN under different channels. The channel 1 is random channel as experiment 1 and experiment 2; channel 2 is random channel with a common zeros; channel 3 is from literature [8].

Simulation results show that the HHNN is appropriate for both channel with common zeros or not.

Fig. 76.7 BER under different channel with synchronous operating mode

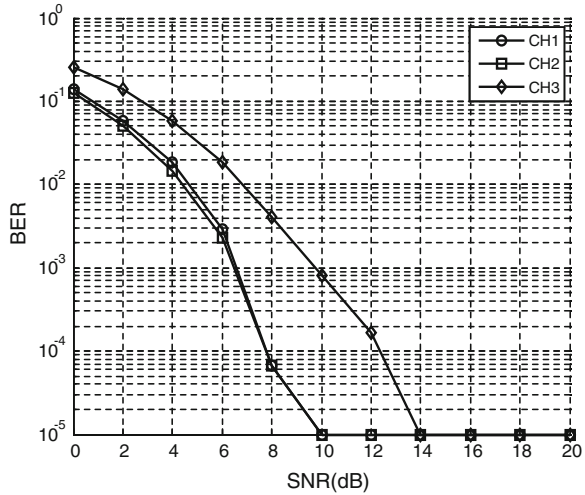
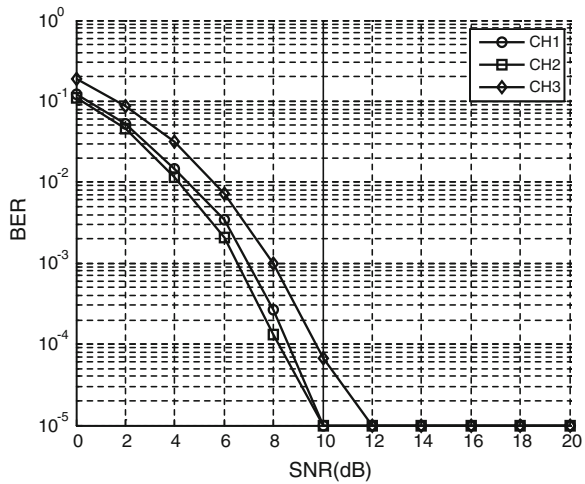


Fig. 76.8 BER under different channel with asynchronous operating mode



76.5 Conclusion

Blind Hopfield neural network algorithms in literatures are mostly easy to fall into local minima, which are not suitable for quadratic optimization problems. This paper focuses on the blind detection of the BPSK signals based on HHNN. Besides some straightforward generalizations of the conventional Hopfield model, HHNN can also be an efficient tool to blind detect BPSK signals. The simulation results indicate that the HHNN have satisfactory performance.

Acknowledgments The research work is supported by Youth Science Foundation of Nanjing University of Posts and Telecommunications (NY212022).

References

1. Liu X, Xiu C (2007) A novel hysteretic chaotic neural networks and its applications. *Neuro Comput* 70:2561–2565
2. Bharitkar S, Mendel JM (2000) The hysteretic hopfield neural network. *IEEE Trans Neural Netw* 11(4):879–888
3. Zhang Y, Yu S, Zhang Z et al (2013) Blind detection of QAM signals with a complex Hopfield neural network with real-imaginary-type soft-multistate-activation-function. *Acta Electronic Sinica* 41(2):255–259 (in Chinese)
4. Zhang Y, Zhang Z (2011) Blind detection algorithm of complex multi-valued discrete Hopfield network. *Acta Phys. Sin* 60(9):090703 (in Chinese)
5. Zhang ZY, Bai EW (2005) Direct blind sequence detection of SIMO channels with common zeros. *Dianzi Xuebao (Acta Electronica Sinica)* 33(4):671–675
6. Yun Z, Zhi-Yong Z, Shu-Juan Y (2012) Blind detection of M-ary quaternary phase shift keying signals by a complex Hopfield neural network with amplitude-phase-type hard-multistate-activation-function. *Acta Phys Sin* 61(14):140701 (in Chinese)
7. Zhang Y, Zhang ZY (2011) Blind detection of 64QAM signals with a complex discrete hopfield network. *Acta Phys Sin* V33(2):315–320 (in Chinese)
8. Ding Z, Li Y (2002) Blind equalization and identification. Marcel Dekker, New York, Chapter 5

Chapter 77

Design of Sewage Treatment Using Iron Nanoparticles Based on Fuzzy Logic Control

Miaomiao Tan, Yinan Li and Hui Jiao

Abstract Good microbial destroy can be obtained by using iron nanoparticles in sewage microbial treatment, because iron nanoparticles have a large specific surface area and strong reducibility. In this paper, an automatic control system of sewage treatment using iron nanoparticles was designed. The adding amount of iron nanoparticles were important parameter affecting sewage treatment. Controlling the adding amount of iron nanoparticles precisely can effectively improve the sewage treatment efficiency and saving energy or reducing consumption. According to the lag system and nonlinear of sewage treatment, a control algorithm for accurate adding amount of iron nanoparticles combining fuzzy logic control and expert system was provided, which realize the automatic control of sewage treatment using iron nanoparticles.

KeyWords Iron nanoparticle · Sewage treatment · Fuzzy logic control

77.1 Introduction

The influence of microbial pollution in water environment on human health and survival environment has caused high attention. A microbial pretreatment technology of water needs desperately to be provided to reduce the related biological health risk.

M. Tan (✉) · Y. Li

College of Mechanical and Electrical Engineering, Beijing Union University, Baijiazhuang Xili No12, Chaoyang, Beijing, People's Republic of China
e-mail: jdtmiaomiao@buu.edu.cn

H. Jiao

Patent Examination Cooperation Center of The Patent Office, SIPO, Beijing, People's Republic of China
e-mail: jiaohui@sipo.gov.cn

A large number of researches on the treatment of heavy metal wastewater using zero-valent iron are completed. It indicates that zero-valent iron on treating heavy metal wastewater have high removal efficiency, simple technology and outstanding advantages. The increased amount of iron and acidic conditions can enhance treatment effect. Additionally, the size of iron particle is more significant [1, 2].

Iron nanoparticle refers to the grain size in the 1-100 nm range of zero-valent iron particle, which has large ratio surface area and strong reducibility. Because the contact area between iron particle and microorganism greatly increases, the adsorption capacity of iron nanoparticle is stronger than ordinary zero-valent iron particles. Not only the effect of sewage treatment exceeds activated carbon or iron oxide, but also the problem of secondary pollution using Cl₂ or O₃ is overcome. The iron nanoparticles in water treatment shows superior performance, low cost and high efficiency, which has a broad application prospect [3].

With the function and stability of online testing instrument is obtained further consummation, the industrial bus gets development and the control theory achieves increasingly perfect. The automatic control system based on online detection and analysis is widely used in sewage treatment. In system of sewage treatment using iron nanoparticles, the control of adding amount of iron nanoparticles is an important factor influencing microbial inactivation effect. The quality of sewage is randomness and degeneration, so each variable are highly nonlinear. As a branch of intelligent control, the fuzzy control has been successful application in sewage treatment field, especially in activated sludge sewage treatment system. In this paper, referring to experiences of sewage treatment control system, and based on sewage treatment system using iron nanoparticles, fuzzy control combined with expert system is provided to solve the problem of controlling adding amount of iron nanoparticles precisely.

77.2 Sewage Treatment System Using Iron Nanoparticles

The structure design of sewage treatment system using iron nanoparticles is shown as Fig. 77.1. The system is composed of flow control unit, adding iron nanoparticles unit, removal iron nanoparticles unit, detecting water quality unit, mixer and liquid level sensors. The working principles of system are described as follows: when opening the electromagnetic valve, pump will run and the sewage be pumped into the microbial treatment pool from sewage pool; then the liquid level sensors detect whether the sewage is up to the fixed value. The device of adding iron nanoparticles will be operated when the liquid level is right. The iron nanoparticles are added into microbial treatment pool, at the same time, the mixer runs to mix iron nanoparticles in sewage evenly, which can make the sufficient contact between iron nanoparticles with microbial in sewage. After a period of time reaction, the mixer is closed, and the electromagnet is powered on to remove the iron nanoparticles for their magnetism. Finally, the water quality is detected,

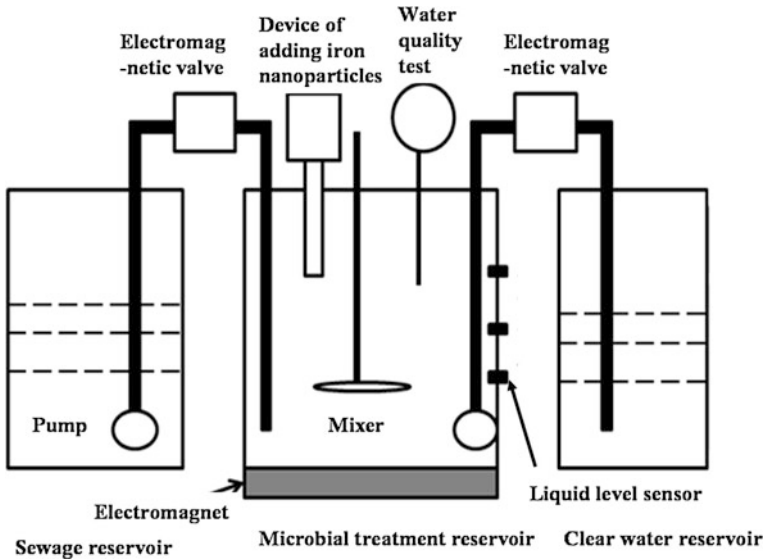


Fig. 77.1 Schematic of sewage treatment using iron nanoparticles

the water after treatment will be pumped into the clear water reservoirs when water quality is up to standard, or will in second circle of sewage treatment.

Because the microbial content in sewage changes every time and the required amount of iron nanoparticles varies correspondingly, controlling effectively the adding amount of iron nanoparticles can not only ensure the water quality requirements, but also can save consumption of iron nanoparticles and operation cost.

Online water quality testing is an important condition of effectively controlling sewage treatment. In this paper, the conductivity technology is used to detect the concentration of microbial in sewage. Microbial conductivity measurement is based on the theory of biological impedance technology research. Biological impedance refers to an organism, tissue, organ and cell shows the conductive characteristics and dielectric property when the weak current circulation below excitation threshold value is applied [4–6]. When microbial growing, some of the medium macromolecular nutrients such as protein, carbohydrates and decomposition into smaller or more active molecules. When microbial plate has occurrence of the above chemical change for microbial metabolic activity, the particle concentration produced by microbial is a bit lower than initial concentration of plate. The impedance change and then can be measured the faint variations using impedance instrument. This method can be used to monitoring the presence of microorganisms quickly and quantitative analysis [7, 8].

77.3 Control Algorithm

In this control system, fuzzy control combined with expert system is used. First of all, the water quality of sewage was forecasted by fuzzy control. The data was accumulated in the prediction process, and the fuzzy database was continuously optimized to improve by expert system, which reached the purpose of perfect their own fuzzy control parameters. The system block diagram of control strategy system was shown in Fig. 77.2.

The meaning is depicted in the picture:

r is given value of microbial content l ,

Deviation $e = r - ky$, k for proportional coefficient,

Deviation rate $ec = \frac{dr}{dt} - k \frac{dy}{dt}$,

X for microbial concentration testing before adding iron nanoparticles,

A is fuzzy set of x domain of discourse after fuzzification treatment,

B is the fuzzy set of Y domain of discourse after fuzzification treatment,

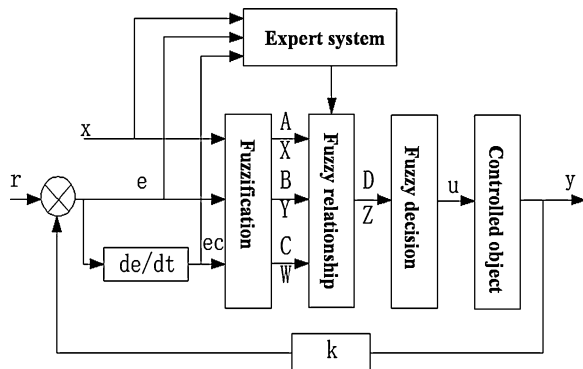
C is the fuzzy set of W domain of discourse after fuzzification treatment of ec ,

D is control value, the fuzzy set of Z domain of discourse.

The microbial quantity x before adding iron nanoparticles, deviation e , deviation rate ec and control value u were fuzzificated. According to the characteristics, the sewage was divided into grades and deviation of m, n, p, l , and the domain of discourse was obtained. Confirming membership and variable parameters, the fuzzification of input parameters were completed. Fuzzy control rule is correct or not will directly decide the success or failure of the control. Because of large number of variables in this system, the design of fuzzy control rules determined by the expert experience and statistical analysis data. Finally, after solution fuzzification of fuzzy control, the corresponding control value was obtained to control the adding amount of iron nanoparticles.

The database of expert system were improved through the input parameter, and the relationship among microbial quantity x before adding iron nanoparticles, deviation e , deviation rate ec and control value u were compared. Through certain reasoning machine set, the control value of fuzzy control was adjusted to improve

Fig. 77.2 Diagram of control strategy



the accuracy of fuzzy control. By doing experiments, three types of data including characteristic parameters, compensation parameters and online data were determined.

The control flow charts of sewage treatment are shown in Figs. 77.3 and 77.4. Firstly, testing equipments is normal or not, and then the microbial content in sewage before and after adding iron nanoparticles is detected. Testing sewage flow is in a small flow state or not. If the flow is small, the strategy of reducing iron nanoparticles will be applied. When the sewage flow is tested to be in normal stable state, several parameters such as microbial content are be in fuzzification processing, and then the adding amount of iron nanoparticles is determined by the results obtained from fuzzy algorithm. Finally, after analyzing historical testing data using expert system, the control effect is evaluated. If the effect is not well, the parameters optimization is implemented.

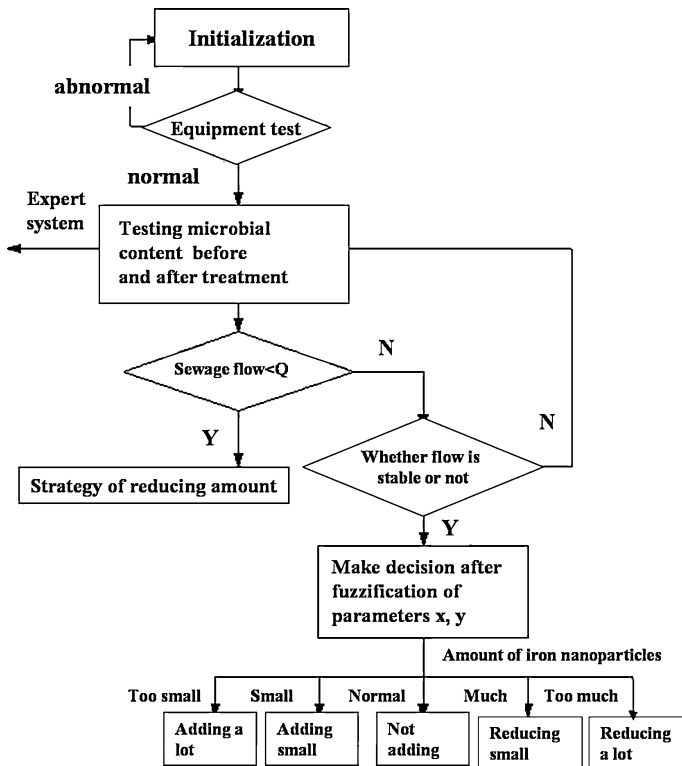
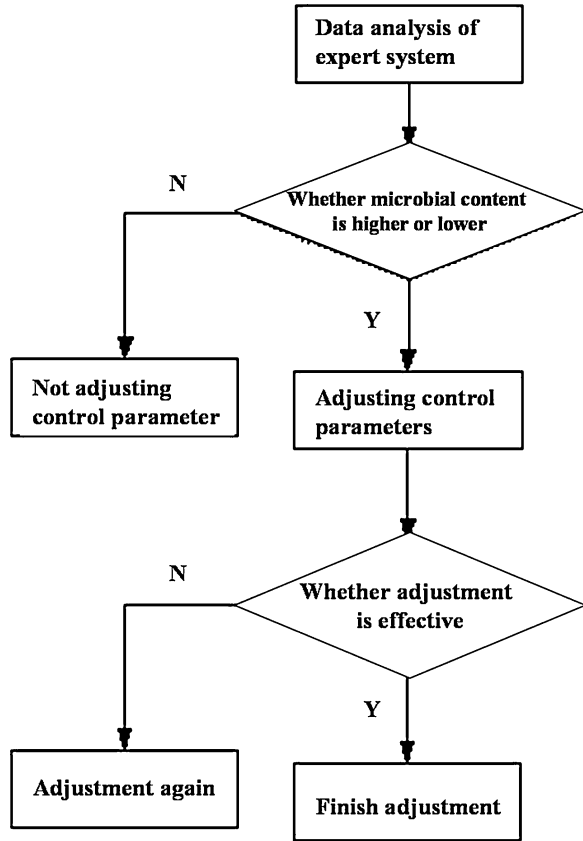


Fig. 77.3 Fuzzy control flow chart of precise iron nanoparticles adding amount

Fig. 77.4 Flow chart of expert system



77.4 Conclusion

Iron nanoparticles have perfect effect of inactivating microbial. In this paper, a sewage treatment system using iron nanoparticles and a control system of accurately controlling adding amount are provided. Because the variation of water quality is random and non-stationary, this system has features of big inertia and pure lag. Using control algorithm of combining fuzzy control with expert system, the precise control of iron nanoparticles adding amount will be realized.

Acknowledgments This study was supported by the New Starting Point Project of Beijing Union University (ZK201217).

References

1. Diao M, Yao M (2009) Use of zero-valent iron nanoparticles in inactivating microbes. *Water Res* 43:5243–5251
2. Barnes RJ, van der Gast CJ et al (2010) The impact of zero-valent iron nanoparticles on a river water bacterial community. *J Hazard Mater* 184:73–80
3. Kim HS, Ahn JY et al (2010) Atmospherically stable nanoscale zero-valent iron particles formed under controlled air contact: characteristics and reactivity. *Environ Sci Technol* 44:1750–1766
4. JT Peterson, Repovich WES, Parascand CR (2011) Accuracy of consumer grade bioelectrical impedance analysis devices compared to air displacement plethysmography. *Int J Exerc Sci* 4(3):176–184
5. Pliquett UF (2009) Changes in electrical impedance of biological matter due to the application of ultrashort high voltage pulses. *IEEE Trans Dielectr Electr Insul* 16(5):1273–1279
6. Pliquett U, Joshi RP, Sridhara V, Schoenbach K (2007) High electrical field effects on cell membranes. *Bioelectrochemistry* 70:275–282
7. Maki WC, Mishra NN, Cameron EG, Filanoski B, Rastogi SK, Maki GK (2008) Nanowire-transistor based ultra-sensitive DNA methylation detection. *Biosens Bioelectron* 23:780–787
8. Mainelis G, Willeke K, Baron P, Reponen T, Grinshpun SA, Górny RL, Trakumas S (2001) Electrical charges on airborne microorganisms. *J Aerosol Sci* 32:1087–1110

Chapter 78

The Application of Fuzzy PI and RBF Neural Network Tuning PID in Servo System

Guozhi Li, Xiaohong Ren, Bing Ren and Ling Qiu

Abstract Fuzzy logic and neural network control strategies are studied. Based on the servo system of PMSM, fuzzy logic and RBF neural network are used to tune the PID controller's parameters, and put forward a kind of auxiliary scheme about RBF neural network tuning PID controller. The simulation results show that, for difficult to establish the precise mathematical model of the time-varying, nonlinear systems and linear controller and traditional PID controller cannot obtain satisfactory control effect, combining fuzzy logic and neural network with the conventional PID can make the servo system has strong robustness, preferable control precision and faster dynamic response.

Keywords PID·Fuzzy · RBF neural network · Servo system

78.1 Introduction

It is a classic application that many servo systems of automatic control system use PID controller. But along with society progress and the development of industry, there are a lot of difficulty to establish precise mathematical model of actual industrial production process and time-varying, nonlinear system. During this case, conventional PID controller cannot obtain satisfactory control result [1]. Intelligent system natural language and human reasoning can be mathematized by fuzzy logic and enable machine to obtain the ability of simulating human perception, reasoning and intelligent behavior [2]. Artificial neural network is the mathematical human brain thinking mode, which can reflect the basic brain characteristics and self learning characteristics. This can enable the machine to learn, to think and gives them the ability to process information. Therefore, a system combined with neural networks or fuzzy logic can reflects intelligence and obtains a more ideal control

G. Li (✉) · X. Ren · B. Ren · L. Qiu
College of Automation and Electronic Information, Sichuan University of Science and Engineering, NO.180 Huixinglu Road, Ziliujing, Zigong, Sichuan Province, China
e-mail: liptw1333@126.com

result [3]. This study based on the traditional servo control system, uses fuzzy logic and RBF neural network to combine with conventional PID.

78.2 The Principle and Structure of Fuzzy Controller

The basis of fuzzy control is the fuzzy controller. Its control law is programmed by microcomputer. The basic principle is put the input which is digital signals through fuzzy processing and then transform them into fuzzy quantities. This procedure called fuzzification. Then build a fuzzy reasoning module which includes fuzzy rules. After the approximate reasoning, a conclusion would be draw by fuzzy sets. And then a well defined procedure called defuzzification will generate a crisp output, the output is transformed to the next level and adjusting the object in order to achieve satisfactory results [4].

In the PMSM vector control system, use traditional PI controller is difficult to establish a precise mathematical model because of it is time-varying, nonlinear system and cannot get a satisfactory control result. In this paper, a two-dimensional fuzzy controller is combined with the conventional PI controller to construct a Fuzzy-PI compound controller. The control strategy is: set a universe of error regard the object. When there is a small deviation, use conventional PI control. Otherwise switch to Fuzzy control. The similar smooth switching fuzzy PI controller is set up a transitional area among fuzzy control and PI control switching universe, so that it can avoid switching jumping during the process and the control algorithm can switch smoothly.

From Fig. 78.1, smooth switching fuzzy PI controller is composed of single variable fuzzy controller and conventional PI controller. U_{PI} is the output of PI controller, U_F is the output of fuzzy controller, U is the output of compound controller, $\alpha(e)$ is smooth switching function.

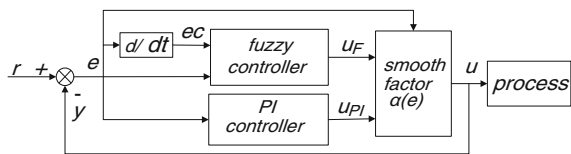
Compound controller output is given by the following [5]:

$$u = \alpha(e)u_F + [1 - \alpha(e)]u_{PI} \tag{78.1}$$

The greater $\alpha(e)$ is the stronger fuzzy control action is compared with the PI control action. The $\alpha(e)$ is given by:

$$\begin{cases} \alpha(e) = 0 & |e| \leq x_1 \\ \alpha(e) = \frac{\exp(|e|\rho) - \exp(x_1\rho)}{\exp(x_2\rho) - \exp(x_1\rho)} & x_1 < |e| \leq x_2 \\ \alpha(e) = 1 & |e| \leq x_2 \end{cases} \tag{78.2}$$

Fig. 78.1 The structure of smooth-switch fuzzy PI control



The value of ρ can influence smooth switching function $\alpha(e)$, which can choose the value regard Ref. [5] during a specific system.

Two-dimensional fuzzy controller usually uses system error e and error rate ec as input variables, and its output is single control quantity u . As fuzzy controller design needs to summarized engineering designer and expert’s personnel technical knowledge and practical experience, this paper uses the reference data, such as fuzzy sets and universe of e , ec and u [6]. Each universe is $[-6, -5, -4, -3, -2, -1, 0, 1, 2, 3, 4, 5, 6]$. Fuzzy subset: NB, NM, NS, ZO, PS, PM, PB. Membership of fuzzy subset of NB and PB is Gauss function, other fuzzy subset’s membership are triangular function. Fuzzy rules is shown in Table 78.1 [6].

78.3 RBF Neural Network Tuning PID

Radial Basis Function (RBF) neural networks were originally introduced into the literature for the purpose of interpolation of data points on a finite training set [7]. These kinds of artificial neural network which has three layers includes a single hidden layer [8]. The basis function uses the distances between the given input point and function training points as variables. As this kind of distances is radial, it is called radial basis function. Radial basis function simulate the structure of neural network which constructs human brain in the partial adjustment and receptive fields which covered each other, and it is the neural network which can approach every continuous function with arbitrary precision.

In the architecture, neural network input vector is $X = [x_1, x_2, \dots, x_n]^T$, radical basis vector is $H = [h_1, h_2, \dots, h_m]^T$, and h_j is the Gaussian basis function which is given by

$$h_j = \exp\left\{-\frac{\|X - C_j\|^2}{2b_j^2}\right\} \quad (j = 1, 2, \dots, m) \tag{78.3}$$

Table 78.1 Fuzzy control rules

$u \begin{matrix} / \\ ec \\ e \end{matrix}$	NB	NM	NS	ZO	PS	PM	PB
NB	PB	PB	PM	PM	PS	PS	NM
NM	PB	PM	PS	PS	PS	ZO	NM
NS	PB	PM	PS	PS	ZO	NS	NB
ZO	PB	PS	PS	ZO	NS	NS	NS
PS	PB	PS	ZO	NS	NS	NM	NB
PM	PM	ZO	NS	NS	NS	NM	NB
PB	PM	NS	NS	NM	NM	NB	NB

where $C_j = [x_{j1}, x_{j2}, \dots, x_{jn}]^T$ is the centre vector of the point of node j in the network. Network basis width vector is assumed as,

$$B = [b_1, b_2, \dots, b_m]^T \quad (78.4)$$

The parameter of basis width vector is b_j and it is positive. The weight vector is defined as following:

$$W = [w_1, w_2, \dots, w_j \dots w_m]^T \quad (78.5)$$

The performance function of identifier is:

$$J_1 = \frac{1}{2} (yout(k) - y_m(k))^2 \quad (78.6)$$

Based on gradient descent algorithm, we can use iterative algorithm to yield output weight, centre point and basis width parameter, the iterative algorithm is given by:

$$w_j(k)x = w_j(k-1) + \eta(yout(k) - y_m(k))h_j + \alpha(w_j(k-1) - w_j(k-2)) \quad (78.7)$$

$$\Delta b_j = (yout(k) - y_m(k))w_j h_j \frac{\|X - C_j\|^2}{b_j^3} \quad (78.8)$$

$$b_j(k) = b_j(k-1) + \eta \Delta b_j + \alpha(b_j(k-1) - b_j(k-2)) \quad (78.9)$$

$$\Delta c_{ij} = (yout(k) - y_m(k))w_j \frac{x_j - c_{ji}}{b_j^2} \quad (78.10)$$

$$c_{ji}(k) = c_{ji}(k-1) + \eta \Delta c_{ji} + \alpha(c_{ji}(k-1) - c_{ji}(k-2)) \quad (78.11)$$

where η is learning rate and α is a momentum factor.

In order to study the application of RBF neural network combined with conventional PID, I have designed a RBF neural network tuning PID controller as shown in Fig. 78.2.

It is a kind of auxiliary scheme about RBF neural network tuning PID controller and this control scheme can switch automatically based on system state. The basic principle of switching is: use RBF neural network tuning PID control when the present error is big, otherwise switch to PID control. The switching is performed by the computer program automatically during the given error universe.

The principle of RBF neural network tuning PID is shown as follows [4]:

$$error(k) = rin(k) - yout(k) \quad (78.12)$$

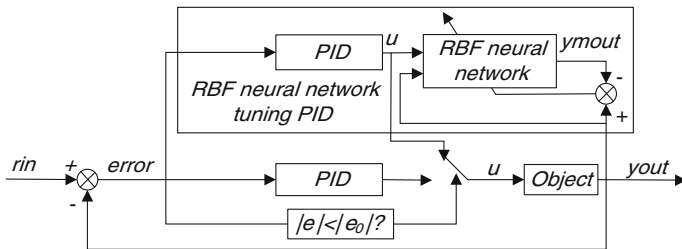


Fig. 78.2 The structure of smooth-switch RBF neural network tuning PID control system

The parameters of PID is given as following:

$$\begin{cases} xc(1) = error(k) - error(k - 1) \\ xc(2) = error(k) \\ xc(3) = error(k) - 2error(k - 1) + error(k - 2) \end{cases} \tag{78.13}$$

Incremental control algorithm is given as following:

$$u(k) = u(k - 1) + \Delta u(k) \tag{78.14}$$

$$\begin{aligned} \Delta u(k) = & k_p(error(k) - error(k - 1)) + k_i error(k) \\ & + k_d(error(k) - 2error(k - 1) + error(k - 2)) \end{aligned} \tag{78.15}$$

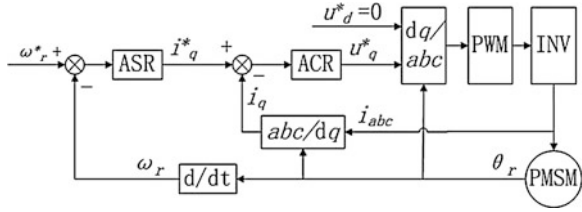
Neural network tuning indicator is defined as follows:

$$E(k) = \frac{1}{2} error(k)^2 \tag{78.16}$$

Use gradient descent algorithm to tune k_p, k_i, k_d :

$$\begin{cases} \Delta k_p = -\eta \frac{\partial E}{\partial k_p} = -\eta \frac{\partial E}{\partial y} \frac{\partial y}{\partial \Delta u} \frac{\partial \Delta u}{\partial \Delta k_p} = \eta error(k) \frac{\partial y}{\partial \Delta u} xc(1) \\ \Delta k_i = -\eta \frac{\partial E}{\partial k_i} = -\eta \frac{\partial E}{\partial y} \frac{\partial y}{\partial \Delta u} \frac{\partial \Delta u}{\partial \Delta k_i} = \eta error(k) \frac{\partial y}{\partial \Delta u} xc(2) \\ \Delta k_d = -\eta \frac{\partial E}{\partial k_d} = -\eta \frac{\partial E}{\partial y} \frac{\partial y}{\partial \Delta u} \frac{\partial \Delta u}{\partial \Delta k_d} = \eta error(k) \frac{\partial y}{\partial \Delta u} xc(3) \end{cases} \tag{78.17}$$

Fig. 78.3 The permanent magnet synchronous motor vector control system



78.4 Numerical Simulation

78.4.1 The Smooth-Switch Fuzzy-PI Controller

Build permanent magnet synchronous motor vector control system as shown in Fig. 78.3.

The simulation parameters of permanent magnet synchronous motor are shown below and neglect friction resistance:

$$R_s = 2.875(\Omega), L_d = 0.085(\text{H}), L_q = 0.0085(\text{H}), \Psi_r = 0.175(\text{Wb}),$$

$$T_n = 0.2625(\text{N} \cdot \text{m}), p = 1, J = 0.0008(\text{kg} \cdot \text{m}^2),$$

Use smooth-switch fuzzy-PI controller in the current loop and speed loop. During the process of simulation, at first, motor start without loading. Then loading $5.2\text{N} \cdot \text{m}$ at 0.08 s . The simulation results are shown in Figs. 78.4 and 78.5.

Fig. 78.4 The speed simulation diagram of the conventional PI control

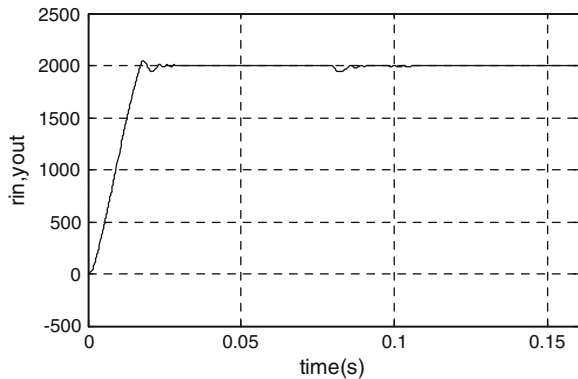
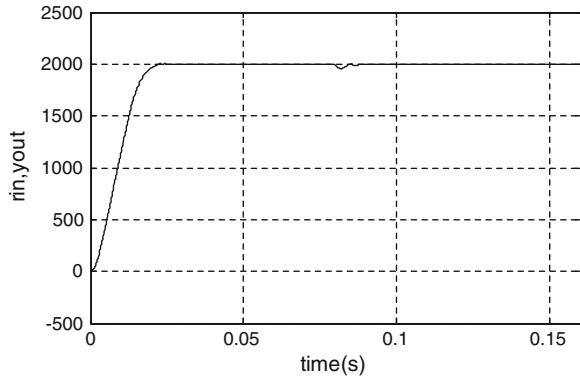
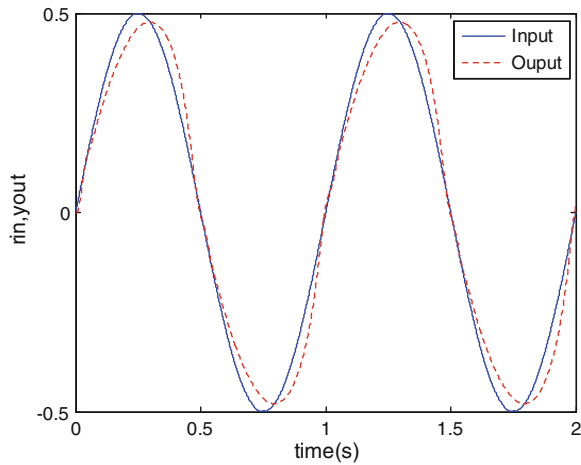


Fig. 78.5 The speed simulation diagram of smooth-switch F-PI control



78.4.2 RBF Neural Network Tuning PID Controller

Fig. 78.6 Sine wave response curve under RBF neural network tuning PID control

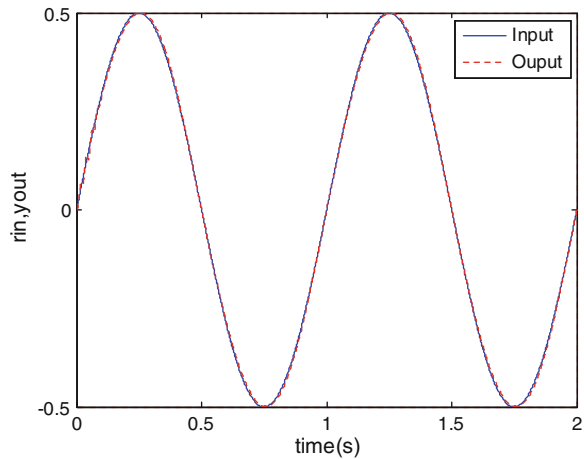


In this simulation, the control object is built as following:

$$yout(k) = \frac{yout(k - 1) + u(k - 1)}{1 + yout(k - 1)^2} \tag{78.18}$$

The input signal is $rin(t) = 0.5\sin(2\pi t)$, and the architecture of RBF neural network in the RBF neural network tuning PID is using 3 input nodes, 6 hidden nodes and 1 output node. The simulation results are shown in Figs. 78.6 and 78.7.

Fig. 78.7 Sine wave response curve under smooth-switch RBF neural network tuning PID control



78.5 Conclusion

In this study fuzzy PI and RBF neural network tuning PID are discussed. Figures 78.4 and 78.5 show the smooth-switch fuzzy PI controller has better ability to reduce the system response overshoot and decreases load shock than conventional PI controller dose in the PMSM vector control system. Figures 78.6 and 78.7 show that the RBF neural network tuning PID has a higher accuracy and quicker response than the conventional PID controller. When PID combined with fuzzy logic or neural network, the controller has better characteristics and nice adaptability while controlling time changeable and nonlinear system.

Acknowledgments Supported by:

Key Project of Artificial Intelligence Key Laboratory of Sichuan Province (2010RZ002); Key Project of Science and Technology Department of Sichuan Province (2011JY0051); 2011 Graduate Innovation Fund Project of Sichuan University of Science and Engineering (y2011010)

References

1. Yangliu X, La-wu Z, Shou-dao H, Rui Z (2010) The optimum current vector control of permanent magnet synchronous motor based on self-adaptive fuzzy PI. *Power Electron* 44(4):45–47 (In Chinese)
2. Gao J (2004) The research on system of permanent magnet synchronous motor variable frequency speed adjusting. Hunan University Master Degree Thesis. (In Chinese)
3. Ouyang L, Huang Y, Huang Y (2008) PID controller based on fuzzy RBF neural network and its application. *Comput Eng* 34(22):231–233 (In Chinese)
4. Liu J (2004) MATLAB simulation of advanced PID control, 2nd edn. Publishing House of Electronics Industry, Beijing, (In Chinese)

5. Xia J, Miao J, Yuan H (2008) Fuzzy PID compound control algorithm of rotary table servo system. *J Shenyang Univ Technol* 30(2):134–138 (In Chinese)
6. Ross TJ (2001) *Fuzzy logic with engineering application*, Publishing House of Electronics Industry, Beijing. (In Chinese)
7. Kumar S (2005) *Neural networks*. Tsinghua University Press, Beijing
8. Xu L (2009) *Neural network control*. 3rd edn. Publishing House of Electronics Industry, Beijing (In Chinese)

Chapter 79

Navigation Control of Humanoid Robot Based on Motor Imaginary

Fei Wang, Chucheng Zhou, Guangda Yang, Xiang Hao and Song Wang

Abstract As a research focus in bio-rehabilitation field, Brain-Computer Interface that can efficiently improve or recover self-care ability of disabled people has obtained fast development in recent years. In this paper, the phenomenon of event-related de-synchronization in EEG was pre-processed and features were extracted by using common space pattern filtering algorithm. Higher classification accuracy was then obtained by employing C-SVM for left, right hand and leg movement discrimination. Then the algorithms were applied in the design of brain computer interface for the control of humanoid robot. The operations by EEG and manual device were compared to illustrate the effectiveness of the BCI system.

Keywords BCI · Humanoid robot · Navigation · Common space pattern filtering · SVM

79.1 Introduction

Brain Computer Interface (BCI) is a new way of communication which based on the brain activity to communicate to the outside world, it avoid the usual information channels such as human nerve endings and muscles, by analysis of the EEG signal, we can convert user's intentions, such as motor imagery, to the language, device control input and so on. With users communicate with the outside environment for real-time interaction by EEG signal directly. To a certain extent,

F. Wang (✉) · C. Zhou · G. Yang · X. Hao · S. Wang
College of Information Science and Engineering, Northeastern University,
3-11 Wenhua Road, Heping Distric, Shenyang, Liaoning 110819, China
e-mail: wangfei@ise.neu.edu.cn

F. Wang
State Key Laboratory of Robotics and Systems, Harbin Institute of Technology,
92 West Dazhi Street, Nangang Distric, Harbin, Heilongjiang 150001, China

BCI system has sorted out patients' communication problem to the outside world with nerve endings damaged, muscle damaged, etc. It brings the gospel to people with disabilities.

In recent decades, with the development of electronic technology, computer technology, brain nerves and other disciplines, it also greatly promoted development of BCI swiftly [1–9]. Gradually, BCI system has shifted from the laboratory to people's real life. Sutter et al. [10] use visual induced potential signal to identify user's intention to choose some kind of symbol. This method offers a new way of communication to the patients that without normal ability to communicate. Using this system, the average patients can speak 10–12 words in one minute. Although the speed of speak has a great difference with normal people, it has a definite effect to improve the lives of these patients. Richard et al. [11] use cortex signals to manipulate the robotic hand to grasp an object successfully. Hochberg et al. [12] developed a BCI system, after nine months of learning, a quadriplegia patient can use this system do some actions, such as move the cursor of two-dimensional space of computer screen, seize the specified object and then move to other places, etc. In the study of BCI, we often use event-related de-synchronization (ERD), event related synchronization (ERS), movement related potentials (MRPs), slow cortical potential (SCPs) and P300, etc.

By means of filtering the original EEG, which collected when left, right hand and leg movement, we can obtain ERD. In this paper, we use Common Spatial Mode filtering algorithm pre-processing the ERD. Finally, by the means of experimental method, we can determine the dimension of feature vectors. Using the linear support vector machine, we can obtain a higher classification by classifying the two types of signals. The calculation of entire algorithm process is so simple that be able to be used as an online discrimination algorithm of BCI technology to control a humanoid robot for navigation.

79.2 Acquisition and Analysis of EEG Signal

The whole experiment process of EEG acquisition is as follows: one healthy subjects sitting in the chair, relax, and his fingers put on the keyboard in the standard way of typewriting. Experimental subjects use his left or right hand to press any key on the keyboard freely at any time. The experiments were divided into three groups, every group performed 6 min, all experiment were to be done in one day, each experimental time interval a few minutes. The locations of electrode of experiment are placed in accordance with the international 10–20 standard system, a total of 28 guided.

Experiment collected a total of 416 samples, in which, 316 samples as training samples, 100 samples as test samples. Data sampling frequency is set to 1 kHz, the length of time of sample data is set to 500 ms. We must be sure that the keyboard had been pressed in the last 130 ms, and all the data were filtered by the band-pass filter of 0.05–200 HZ.

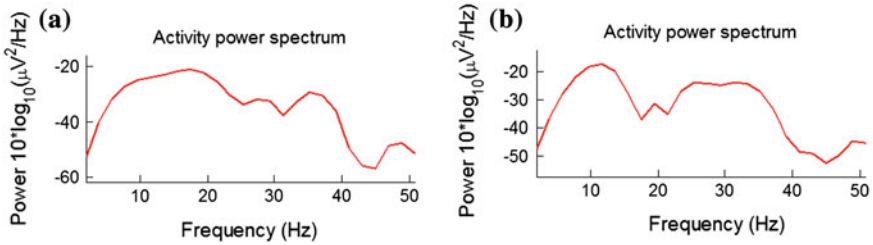


Fig. 79.1 Power spectrum of electrode C3, **a** *Left* hand movement, **b** *Right* hand movement

Healthy people's EEG is a rhythmic activity, whose waveform is very irregular. The amplitude of EEG's waveform range in the hundreds of micro-volts, whose frequency mainly concentrated in the low frequency, and the distribution of wave in approximate the range between 0.2 and 50 Hz. The EEG's rhythmic activities are influenced by the ideology and behavior, etc. Usually, by the location of the frequency, EEG can be divided into δ wave (0.2–3.99 Hz), θ wave (4–7.99 Hz), μ wave (8–12 Hz), α wave (8–12.99 Hz), β wave (13–29.99 Hz) and γ wave (30–50 Hz), etc. On the eve of movement (about 2 s ago), the rhythmic activity of some specific frequency behave low energy, the phenomenon be known as event-related de-synchronization; After exercise, specific frequency energy increases, this phenomenon is called event-related synchronization. These frequencies are mainly concentrated in the μ frequency and β frequency band. In addition, the EEG signal of γ frequency band are also has the phenomenon of the ERS.

As the data used in this article is mainly before the incident, ERD phenomenon would be more obvious, and ERS phenomenon may be did not reflect. So, the ERS phenomenon is not be studied in this experiment. Figure 79.1 is the power spectrum of electrode C3 when subjects doing left-hand movement (above) and right-hand movement (below). From the figure we can see that the right-hand movement is decayed more than the left-hand in the μ frequency and β frequency band. Obviously this phenomenon is in line with the principle of contra lateral advantage.

79.3 Common Space Pattern Filtering Based EEG Preprocessing

Because we use the signal of ERD frequency band in this paper. Firstly, we can obtain the signal of ERD frequency with band pass filter (10–33 Hz), we take the six-order Butterworth filter in here. In order to achieve better classification results before feature extraction, we can pre-process the signal with common spatial mode (CSP) filtering algorithm. CSP filtering algorithm is a brain signal pre-processing method which based on multi-channel potentials covariance, and a method of supervised spatial filtering, whose idea is to the spatial component of the two types

of signal filtering the biggest difference in the energy. That is, find one of the biggest variance, while the other smallest variance in the direction of projection.

The calculation of the basic steps is as follows:

- Calculating regularization covariance matrix R_a , R_b of each sample, reference Eq. (79.1), among them $X_a^{(1)}$, $X_b^{(1)}$, stand for the second brain potential sample matrixes of class a and class b , order number is $N \times T$, N stands for channel number, T stands for sampling number:

$$\begin{cases} R_a = \frac{1}{n_1} \sum_{i=1}^{n_1} \frac{X_a^{(i)} X_a^{(i)T}}{\text{trace}(X_a^{(i)} X_a^{(i)T})} \\ R_b = \frac{1}{n_2} \sum_{i=1}^{n_2} \frac{X_b^{(i)} X_b^{(i)T}}{\text{trace}(X_b^{(i)} X_b^{(i)T})} \end{cases} \quad (79.1)$$

- Calculating the composite covariance matrix $R = R_a + R_b$ and decompose R like Eq. (79.2) with the singular value, so we can get albino transform P like Eq. (79.3).

$$R = U_0 \Lambda_C U_0^T \quad (79.2)$$

$$P = \Lambda_C^{-1/2} U_0^T \quad (79.3)$$

- Get P calculated with R_a and R_b

$$\begin{cases} S_a = P R_a P^T \\ S_b = P R_b P^T \end{cases} \quad (79.4)$$

- Decomposing S_a and S_b with singular value, So U stands for characteristic vector of S_a and S_b , and ϕ_1 , ϕ_2 stand for characteristic value of S_a and S_b respectively, ϕ_1 here should be ranked in descending order.

$$\begin{cases} S_a = U \phi_1 U^T \\ S_b = U \phi_2 U^T \end{cases} \quad (79.5)$$

- Finally we get projection Eq. (79.6)

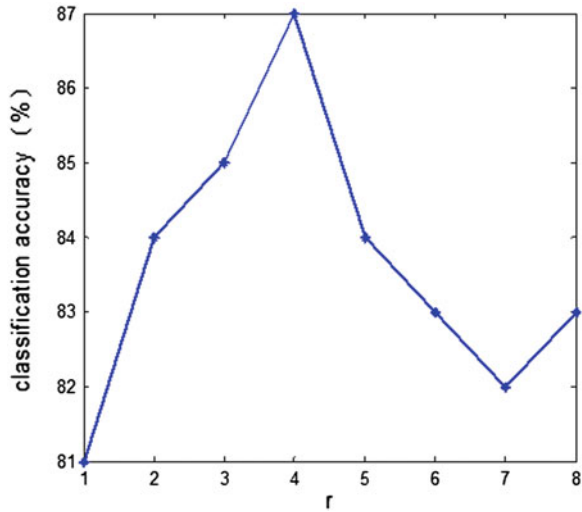
$$W = U^T P \quad (79.6)$$

79.4 Feature Extraction and Movement Classification

After the CSP filtering processing and mapping, we obtain the data:

$$Z = WX \quad (79.7)$$

Fig. 79.2 Classification accuracy for different parameter r



According to the following equation, we take the first r rows and last r rows as feature vector of Z .

$$feature(i) = var(Z^i) \quad i = 1, \dots, 2r \tag{79.8}$$

Support vector machine (SVM), is a new machine learning method based on VC dimension theory and the principle of structure minimum risk, to a great extent, it solves the model selection and a learning problems, nonlinear and dimension disasters, the local minimum points and so on, as the specific implementation of structural risk minimization rule, support vector machine has the global optimal and good generalization ability. In this paper, RBF kernel function is selected as nuclear function, the specific form of RBF kernel function is the following type:

$$K(x, x') = \exp\left(\frac{-0.5 * \|x - x'\|^2}{\gamma^2}\right) \tag{79.9}$$

Using C-support vector machine classifier, when r takes different value classification accuracy is shown in Fig. 79.2, we get the highest classification accuracy when r is 4, and classification accuracy rate is 87 %.

79.5 The Composition of Control System and Design of Experiment

79.5.1 The Composition of Control System

The designed humanoid robot operation control system that is controlled by motor imagination signal EEG is shown in Fig. 79.3. The system consists of three-

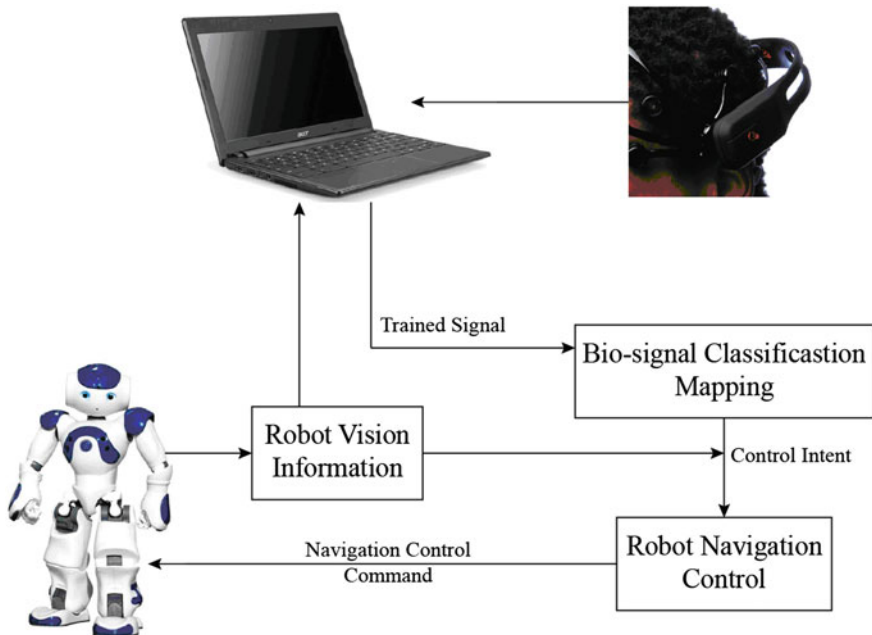


Fig. 79.3 Humanoid robot control system structure

subsystem composition: electrical perception system, the interface system and the robot control system.

Electrical perception system analyze collected brain electric signal. After the participants completed the training of EEG signals, system will do classifying map, decoding into control command and transfer to the movement control module. After the control module receives the control command, combination of the robot motion state, coordinate position and environment perception information that collected by forward vision sensor. The system generates robot motion control instruction, transfer them to the robot in wireless means, and realize the robot motion control based on EEG signals.

79.5.2 The Experiment Design of Control System

The experiment is mainly divided into two parts of brain—machine interface offline training and robot online control, each part being compared with manual keyboard operation. Offline training experiment is to train and adapt to the pre-define EEG signals, making the accuracy of signal control meets online control standards. Online control experimental uses trained brain electrical signals to complete robot navigation control tasks.

79.6 Experimental Results

For the experiments for designed EEG-control humanoid robot navigation system, the final results analysis should include the following aspects: (1) time: the time of finishing the task; (2) path length: walking distance of humanoid robot; (3) inflection point: the designed number of inflection points; 4) collisions: the number of collision.

Eight experiments were conducted to verify the reliability and stability of the proposed system. The experimental setup is as shown in Fig. 79.4. Figure 79.5 shows the experimental results for keyboard controlling and BCI controlling. It was clear that compared with manual operation, BCI operating takes more time, the ratio of it to manual operation is 1.15, The average number of inflection points passed in BCI operation are 4, but in manual operation almost pass all inflection points and without collision, in contrast, during BCI operation there are two collision. It can be obvious seen from Fig. 79.5 that walking trajectory of humanoid robot with manual operation is relatively more stable, the ratio is 1.12.

Although BCI operation is relatively inferior to manual operation performance, it still has high feasibility, and the results are very similar to that of manual operation.



Fig. 79.4 Motor imaginary based humanoid robot navigation control in experiment

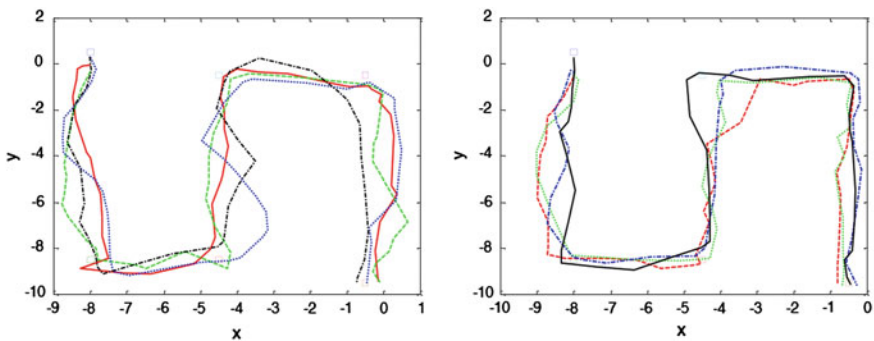


Fig. 79.5 Humanoid robot trajectories under operation of keyboard and BCI control

79.7 Conclusions

This paper describes the motor imagery based EEG control for humanoid robot navigation. Empirical mode decomposition combining with autoregressive model were used to extract the features of EEG signals, SVM was employed to discriminate the motion patterns. After offline training for five different motions, imagination training with NAO robot under simulation environments was conducted. Finally, real-time experiments for humanoid robot navigations were done to validate the effectiveness of the BCI control. Though control effectiveness is inferior compared with manual operation, BCI based navigation control propose an alternative way to operate humanoid robot with instinct seamless human-machine interface, and the proposed scheme has a great potential in the applications of home-care robotics.

Acknowledgments This work is partially supported by State Key Laboratory of Robotics and System (HIT) Grant #SKLRS-2010-ZD-03 and Research Funds for the Central Universities Grant #N110804005, #N120204002.

References

1. Mak JN, Wolpaw JR (2009) Clinical applications of brain-computer interfaces: current state and future prospects. *IEEE Rev Biomed Eng* 2:187–199
2. Birbaumer S (2006) Breaking the silence: brain-computer interfaces for communication and motor control. *Psychophysiology* 43(6):1517–1532
3. Lopes AC, Pires G, Is Vaz L, Nunes U (2011) Wheelchair navigation assisted by human-machine shared-control and a P300-based brain computer interface. 2011 IEEE/RSJ international conference on intelligent robots and systems. San Francisco, pp 2438–2444
4. Van Gerven M, Farquhar J, Schaefer R (2009) The brain-computer interface cycle. *J Neural Eng* 6(4):1–10
5. Vaughan TM, Wolpaw JR (2006) The third international meeting on brain-computer interface technology: making a difference. *IEEE Trans Neural Syst Rehabil Eng* 14(2):126–127
6. Dornhege G (2004) Boosting bit rates in noninvasive EEG single-trial classifications by feature combination and multiclass paradigms. *IEEE Trans Biomed Eng* 51(6):993–1002
7. Hinterberger T et al (2008) An EEG-driven brain-computer interface combined with functional magnetic resonance imaging (fMRI). *IEEE Trans Biomed Eng* 51(6):971–974
8. Liao X, Yin Y, Yao DZH (2006) Classification of imaginary hand movements by means of continuous wavelet transform and support vector machines. *Chin J Med Phys* 23(2):129–132
9. Blankertz B, Dornhege G, Krauledat M (2007) The non-invasive Berlin brain-computer interface: fast acquisition of effective performance in untrained subjects. *Neuro Image* 37:539–550
10. Sutter EE (1992) The brain response interface: communication through visually guided electrical brain responses. *J Microcomput Appl* 15(1):31–45
11. Richard TL, Peckham PH, Kilgore KL, Heetderks WJ (2000) Applications of cortical signals to neuroprosthetic control: A critical review. *IEEE Trans Rehabil Eng* 8(2):205–208
12. Hochberg LR, Mijail D et al (2006) Neuronal ensemble control of prosthetic devices by a human with tetraplegia. *Nature* 442(13):164–171

Chapter 80

Stabilizability of a Class of Singularly Perturbed Systems via Switched Output Feedback

Hongwang Yu and Baoshan Zhang

Abstract In this article, stability of a class of two-dimensional linear singularly perturbed systems via switched output feedback is investigated. It is shown that the whole closed-loop systems are either exponentially stable as the perturbed parameter goes to zero or are not stabilizable by any controller. Moreover, when stabilization is possible, in order to expand the upper range of the perturbation parameter, it is shown that the whole closed-loop singularly perturbed systems are exponentially stable as the feedback gain can be chosen to take on no more than two values throughout the entire state-space.

Keywords Singularly perturbed systems · Output feedback · Stability

80.1 Introduction

The study of stabilization of continuous time systems via hybrid feedback is an area that has pervaded research for more than a decade [1–5]. In particular, stability analysis of switched linear systems in the singular perturbation form has received much attention in the recent literature. In practice, many systems that involve dynamics operating in different time scales may be found in electric power systems, aerospace systems, robotics, chemical, biological systems and many other applications. In this case, standard control techniques lead to ill-conditioning problems. It is a well known topic for control scientists that singular perturbation theory has been used to model these systems characterized by the presence of both slow and fast transients in the system response to external stimuli. As far as a linear time invariant model is considered, a solution is obtained using time scale

H. Yu (✉) · B. Zhang

School of Mathematics and Statistics, Nanjing Audit University, Nanjing city,
Jiangsu province 211815, China
e-mail: yuhongwang@nau.edu.cn

separation which simplifies the analysis and avoids ill-conditioning by decomposing the problem into two independent well conditioned problems, one for the slow subsystem and another one for the fast subsystem. The controllers are designed for both the slow subsystem and the fast subsystem respectively. The combination controller is used to stabilize the whole original singularly perturbed systems as the perturbed parameter is goes to zero. How to get the upper range of the perturbation parameter is an important topic for singularly perturbed control systems.

The stability of continuous-time switched linear systems in the singular perturbation form is investigated in [6], and the discrete time case is also studied in [7]. They show that, under an arbitrary switching rule, stability of the slow and fast switched subsystems is not sufficient to assess stability of the original two time scale switched system, even if the singular perturbation parameter tends to zero. To guarantee the asymptotic stability of the singularly perturbed switched systems, an LMI based conditions to design a state feedback control law are proposed by means of using switched quadratic Lyapunov functions. Stability of two time scale switched discrete-time linear systems in the singular perturbed form are addressed in [8]. They show that the asymptotic stability of the slow and fast switched subsystems under arbitrary switching rules does not imply asymptotic stability of the corresponding two time scale switched system in the singular perturbation form even if the singular perturbation parameter tends to zero. Using switched quadratic Lyapunov functions, a coupling constrain expressed in term of LMI based conditions must be satisfied for stability analysis of discrete time singular perturbed switched systems.

This paper addressed the stability and the controller design for a class of planar linear singularly perturbed control systems. The designed controller strategies employed here just require the output of the system state. We will show that the whole closed-loop singularly perturbed systems are either exponentially stabilizable as the perturbed parameter goes to zero or are not stabilizable by any controller and arbitrary sufficiently small. In order to expand the upper range of the perturbation parameter, the switched output feedback controller is designed when stabilization is possible. The whole closed-loop singularly perturbed systems are shown to be exponentially stable when the feedback gain can be chosen to take on no more than two values throughout the entire state-space for any given perturbation parameter.

The paper is organized as follows. The stability and the controller design problem for singularly perturbed control systems are discussed in [Sect. 80.2](#). In [Sect. 80.3](#), stability analysis and the switched output feedback control design of a class of singularly perturbed systems are studied. Finally, the paper closes by stating the conclusion.

80.2 Preliminaries

In this section, we consider the continuous-time linear singularly perturbed control systems of the form

$$\begin{cases} \dot{x}(t) = A_{11}x(t) + A_{12}z(t) + B_1u(t) \\ \varepsilon \dot{z}(t) = A_{21}x(t) + A_{22}z(t) + B_2u(t) \\ y = C_1x(t) + C_2z(t) \end{cases} \quad (80.1)$$

where $x \in R^n$ and $z \in R^m$ are state of the slow and fast systems, respectively, $u \in R^p$ is the control input, $y \in R^l$ is the control output, $A_{ij}, B_i, C_i, i = 1, 2; j = 1, 2$ are constant matrices with appropriate dimensions, the positive scalar ε is a singular perturbation parameter.

The dynamic output feedback control problem of singularly perturbed systems has been addressed in many works. To the author's knowledge, there is few literature for the hybrid output feedback controller designed by means of a finite number of states instead. Here, we want to find the conditions on $A_{ij}, B_i, C_i, i = 1, 2; j = 1, 2$ and the singular perturbation parameter ε such that the resulting closed-loop singularly perturbed control systems are globally asymptotically stable for the switched output feedback control law of the form $u(x, z) = k(x, z)y$. When stability is achievable, we will give the control gain $k(x, z)$ which is implemented as a switch between the different static gains. Here, we first write the systems (80.1) as a continuous-time linear system in the singular perturbation form.

Denoting $\xi(t) = (x^T(t), z^T(t))^T$, one can get

$$\begin{cases} \dot{\xi}(t) = A\xi(t) + Bu(t) \\ y = C\xi(t) \end{cases} \quad (80.2)$$

where $A = \begin{bmatrix} A_{11} & A_{12} \\ \frac{A_{21}}{\varepsilon} & \frac{A_{22}}{\varepsilon} \end{bmatrix}$, $B = \begin{bmatrix} B_1 \\ \frac{B_2}{\varepsilon} \end{bmatrix}$, $C = [C_1 \ C_2]$. Taking the switched output feedback control law of the form $u = k(\xi)y$, one may get the whole closed-loop singularly perturbed systems in the following form

$$\dot{\xi}(t) = \Omega\xi(t), \quad (80.3)$$

where $\Omega = A + k(\xi)BC$. This is a continuous time linear system. It is well known that the stability of continuous time linear system completely depended on the matrix Ω . Thus we focus on discussing the eigenvalues of Ω by studying its characteristic polynomial.

The following lemma is key to our work.

Lemma 1 Consider the linear system $\dot{\eta}(t) = A\eta(t)$ where $A \in R^{2 \times 2}$ has two complex conjugate eigenvalues. Then for any $Q \in R^{2 \times 2}$ and any $Z(0)$, there exists $t_0 \in R$ such that $Q^T\eta(t_0) = 0$.

80.3 Stability Analysis

In this section, we will firstly discuss the stability of the system by the switched output feedback control in the form $u = k(\xi)y$. In order to highlight the purpose of this article and simplify computation, it is concerned with the stability of a class of planar linear singularly perturbed control systems of the form (80.3) with $B_1 = C_1 = 0, B_2 = C_2 = 1$, and we use a_{ij} instead of A_{ij} ($i = 1, 2; j = 1, 2$) in the remaining part.

Under the output feedback control $u = k(\xi)y$, the characteristic polynomial of matrix Ω is given in the following form

$$\Pi_{\Omega}(\lambda) = \lambda^2 - (a_{11} + \frac{a_{22} + k(\xi)}{\varepsilon})\lambda + \frac{a_{11}a_{22} - a_{12}a_{21} + a_{11}k(\xi)}{\varepsilon} \tag{80.4}$$

Theorem 1 *Suppose $a_{12}a_{21} \geq 0$, then system (80.3) is exponentially stabilizable via static output feedback if and only if $a_{11} < 0$ for given perturbation parameter ε . Otherwise, system (80.3) is not stabilizable for any choice of $k(\xi)$ even if the perturbation parameter ε is sufficiently small.*

Proof Considering the characteristic polynomial (80.4) and the condition $a_{12}a_{21} \geq 0$, one may get the discriminant of (80.4)

$$\Delta = \frac{(a_{11}\varepsilon - a_{22} - k(\xi))^2 + 4a_{12}a_{21}\varepsilon}{\varepsilon^2} \geq 0$$

Then the two eigenvalues of matrix Ω are real numbers. If $a_{12}a_{21} = 0$, it is easy to get two eigenvalues of matrix Ω

$$\lambda_1 = a_{11}, \lambda_2 = \frac{a_{22} + k(\xi)}{\varepsilon}$$

It is obvious that λ_2 can be a negative real number if $k(\xi)$ is chosen to be less than $-a_{22}$. But λ_1 is independent on the control gain $k(\xi)$. So system (80.3) is exponentially stabilizable via static output feedback if only if $a_{11} < 0$. Otherwise, system (80.3) is not stabilizable for any choice of $k(\xi)$ even if the perturbation parameter ε is sufficiently small.

If $a_{12}a_{21} > 0$, then the discriminant of (80.4) satisfies $\Delta > 0$. The two eigenvalues of matrix Ω are negative real number if and only if the following inequalities hold

$$\begin{cases} \lambda_1 + \lambda_2 = a_{11} + \frac{a_{22} + k(\xi)}{\varepsilon} < 0 \\ \lambda_1 \lambda_2 = \frac{a_{11}a_{22} - a_{12}a_{21} + a_{11}k(\xi)}{\varepsilon} > 0 \end{cases} \tag{80.5}$$

If $a_{11} < 0$, one can choose $k(\xi) = k < \min\{-a_{11}\varepsilon, \frac{-a_{12}a_{21}}{a_{11}}\}$ such that system (80.3) is exponentially stabilizable.

If $a_{11} = 0$, we can get $\lambda_1 + \lambda_2 = \frac{a_{22} + k(\xi)}{\varepsilon}$ and $\lambda_1 \lambda_2 = \frac{-a_{12}a_{21}}{\varepsilon}$. It is obvious that system (80.3) is not stabilizable for any choice of $k(\xi)$ if $a_{12}a_{21} > 0$.

If $a_{11} > 0$, it can be obtain $k(\xi) < -a_{22} - \varepsilon a_{11}$ from the first inequality of (80.5) and $k(\xi) > -a_{22} + \frac{a_{12}a_{21}}{a_{11}}$ from the second inequality of (80.5). They are contradictory since that $a_{12}a_{21} > 0$.

Theorem 2 Suppose $a_{12}a_{21} < 0$,

1. If $\varepsilon a_{11}^2 + a_{12}a_{21} < 0$, there exist $\varepsilon_0 \in R$, system (80.3) is exponentially stabilizable via static output feedback $k(\xi) = k$ for all $\varepsilon \in (0, \varepsilon_0)$.
2. If $\varepsilon a_{11}^2 + a_{12}a_{21} \geq 0$ for some ε , there exist $\varepsilon^* \in R$, system (80.3) is exponentially stabilizable by switched output feedback of the following form

$$k(\xi) = \begin{cases} k_1 & \text{if } w^T q = 0 \\ k_2 & \text{if } w^T q \neq 0 \end{cases}$$

for all $\varepsilon \in (0, \varepsilon_0)$, where k_1 is chosen such that the matrix Ω with $k(\xi) = k_1$ has a negative eigenvalue λ_0 and q is the corresponding stable eigenvector, k_2 is chosen such that the matrix Ω with $k(\xi) = k_2$ has two complex-conjugate eigenvalues and the matrix w satisfies $w^T q = 0$.

Proof Since the discriminant of (80.4) $\Delta = \frac{(a_{11}\varepsilon - a_{22} - k(\xi))^2 + 4a_{12}a_{21}\varepsilon}{\varepsilon^2}$, there exist $\varepsilon_0 \in R$ such that $\Delta > 0$ for all $\varepsilon \in (0, \varepsilon_0)$. Then system (80.3) is exponentially stabilizable via static output feedback if and only if the inequality (80.5) hold. If $a_{11} > 0$, one can choose $k < \frac{a_{12}a_{21} - a_{11}a_{22}}{a_{11}}$ such that system (80.3) is exponentially stabilizable. If $a_{11} = 0$, it is easy to get system (80.3) is exponentially stabilizable while $k < -a_{22}$. If $a_{11} < 0$ and $\varepsilon a_{11}^2 + a_{12}a_{21} < 0$, system (80.3) is exponentially stabilizable for all $\varepsilon \in (0, \varepsilon_0)$.

If $\varepsilon a_{11}^2 + a_{12}a_{21} \geq 0$ for some ε , we can choose $k(\xi) = k_1$ such that the matrix Ω has a negative eigenvalue and q is the corresponding stable eigenvector, and $k(\xi) = k_2$ such that the matrix Ω has two complex-conjugate eigenvalues. If $\xi(0) = aq$ for $a \in R$, then $\xi(t) = e^{\lambda_0 t} \xi(0)$ and the statement holds. Otherwise, $w^T \xi(0) \neq 0$, and there exists some values of $t_0 \in R$ such that $w^T \xi(t_0) = 0$. So $\xi(t) = e^{\lambda_0(t-t_0)} \xi(t_0)$ for all $t > t_0$.

80.4 Conclusion

In this article, we discussed the stability of a class of planar linear singularly perturbed systems via switched output feedback. It is shown that the whole closed-loop systems are either exponentially stable as the perturbed parameter goes to zero or are not stabilizable by any controller even if the perturbed parameter goes to zero. When stabilization is possible, the whole closed-loop singularly perturbed systems are exponentially stable as the feedback gain can be chosen to take on no

more than two values. The results in this paper are concerned on two-dimensional systems, which can be weakly extended to a sufficient condition for stabilizability in higher dimensions.

References

1. Cheng D (2005) Controllability of switched bilinear systems. *IEEE Trans Autom Control* 50(4):511–515
2. Balde M, Boscain U (2008) Stability of planar switched systems: the nondiagonalizable case. *Commun Pure Appl Anal* 7(1):1–21
3. Balde M, Boscain U, Mason P (2009) A note on Stability conditions for planar switched systems. *Int J Control* 82(10):1882–1888
4. Shorten R, Wirth F, Mason O, Wuff K, King C (2007) Stability criteria for switched and hybrid systems. *SIAM Rev* 49(4):545–592
5. Santarelli KR, Megretski A, Dahleh MA (2008) Stabilizability of two-dimensional linear systems via switched output feedback. *Syst Control Lett* 57(3):228–235
6. Mallocci I, Daafouz J, Iung C (2009) Stabilization of continuous-time singularly perturbed switched system. In: *Proceedings of the 48th IEEE conference on decision and control and 28th Chinese control conference, Shanghai, Peoples Republic of China*, pp 6371–6376
7. Mallocci I, Daafouz J, Iung C (2010) Stability and stabilization of two time scale switched systems in discrete time. *IEEE Trans Autom Control* 55(6):1434–1438
8. El Hachemi F, Sigalotti M, Daafouz J (2012) Stability analysis of singularly perturbed switched linear systems. *IEEE Trans Autom Control* 57(8):2116–2121

Chapter 81

Design and Stability Analysis of the RRD Fuzzy Controller with D-Stability Constraint

Wenying Zhang, Xiuyan Peng, Zhonghui Hu and Yan Chang

Abstract In this paper, a new design of the T-S fuzzy controller for the RRD systems has been addressed. The stability analysis of the system was derived by Lyapunov functional method. Based on the conditions of D-Stability, the controller which we designed guarantees not only the globally asymptotical stability but also the expected dynamic performance. The results of simulation demonstrate the effectiveness of the proposed design method.

Keywords Fuzzy control · Stability · Lyapunov functions · Linear matrix inequality · Rudder

81.1 Introduction

The main motivation for using rudder-roll damping (RRD) systems on ships are to prevent cargo damage and to increase the effectiveness of the crew by avoiding or reducing seasickness. This is also important from a safety point of view. People have explored and developed various of stabilizers to reduce the roll since the early twentieth century, such as fin stabilizer, anti-rolling tank, rudder stabilizer, bilge keel and so on. Cowley and Lambert firstly published the version of their RRD theory, which was subsequently applied to a merchant ship successfully in

W. Zhang (✉)

School of Science, School of Automation, Harbin Engineering University,
Harbin, Heilongjiang, China
e-mail: shuxue_2005@163.com

X. Peng (✉) · Z. Hu

School of Automation, Harbin Engineering University, Harbin City, China
e-mail: pengxiuyan@hrbeu.edu.cn

Y. Chang

School of Nuclear, Harbin Engineering University, Harbin, China

1972 [1]. Numbers of scholars researched the rudder stabilizer. A lot of research results of sea trials were achieved since then.

More recently different control methods and technologies have been applied to RRD. Chengen et al. [2] proposed a RRD controller which was designed by the theory of μ analysis. The design of autopilot based on the idea of sliding mode-predictive were achieved by Song et al. [3]. Lately, Alarcin and Gulez [4] proposed a RRD controller based on the neural network algorithm. In 2009, O'Brien [5] projected a RRD controller in which the algorithm of multipath and nonlinear dynamic compensation were used. Lijun and Xianku [6] raised the RRD fuzzy controller based on the adaptive neural fuzzy inference system. In 2012, a fuzzy autopilot algorithm for maneuvering of surface ships were proposed by Bhattacharyya et al. [7].

A new design of RRD controller was presented in this paper. The T-S fuzzy model of the equations of the ship's nonlinear rolling motion was presented firstly. Then the parallel distributed compensation (PDC) principle was introduced to design the fuzzy controller. The stability analysis of the T-S fuzzy system was derived by Lyapunov functional method. Because the poles of closed-loop system in a suitable area can assure the stability and dynamic performance, the conditions that satisfy D-Stability were given subsequently. Finally, we design a T-S fuzzy controller of RRD control systems with D-Stability constraint, which not only guarantee the globally asymptotical stability of the system, but also have the expected dynamic performance.

81.2 The Model of the System

81.2.1 Roll Moment of Rudder

According to the hydromechanics, when the rudder rotates the angle δ , the roll moment of the rudder is

$$K_{\delta} = (1 + a_H)z_R F_N \cos \delta \quad (81.1)$$

where

δ is the rudder angle,

F_N is the force of rudder,

a_H is the additional coefficient of F_N ,

z_R is the vertical distance between the point of action of F_N and the center of gravity of ship,

$$F_N = \frac{6.13a \sin \delta}{a + 2.25} \cdot \frac{1}{2} \rho A_R V^2 \quad (81.2)$$

where

- a is aspect ratio of rudder
- A_R is the area of rudder
- ρ is the water density
- V is the speed of ship.

81.2.2 The Nonlinear Model of Roll

The nonlinear model of ship roll [8] can be represented by

$$\begin{cases} \dot{\phi} = p \\ (I_x + \Delta I_x)\dot{p} + B_1p + B_2|p|p + C_1\phi + C_3\phi^3 + C_5\phi^5 = K_\delta\delta \end{cases} \quad (81.3)$$

where

- ϕ is roll angle,
- p is roll angle speed,
- I_x and ΔI_x are the ship's moment of inertia and the additional inertia about the x , respectively,
- B_1 is the ship's damping moment of each unit roll angle speed,
- B_2, C_1, C_3, C_5 are the constants,
- δ represents the rudder angle,
- K_δ represents the moment of RRD.

When the ϕ is small, we can set $B_2 = C_3 = C_5 = 0$, which is the linear model of ship roll. With the increasing of ϕ , the nonlinear model of roll becomes more reasonable. In practice, there are two nonlinear instances. One is the equations with nonlinear damping moment and linear restoring moment, i.e. $C_3 = C_5 = 0$. The other is the equations with linear damping moment and nonlinear restoring moment, i.e. $B_2 = C_5 = 0$. In this paper, the second case is considered. The nonlinear equations of the roll motion are shown as follows:

$$\begin{cases} \dot{\phi} = p \\ (I_x + \Delta I_x)\dot{p} + B_1p + C_1\phi + C_3\phi^3 = K_\delta\delta \end{cases} \quad (81.4)$$

The motion of the direct sailing of a container ship is considered only. The rated speed of the container ship is $V = 7.8$ m/s. The principal parameters are represented by the follows: (Table 81.1)

Table 81.1 Principal parameters of the container ship

	ITEMS	SHIP
Length	L (m)	175
Breadth	B (m)	25
Displacement volume	(m ³)	21,222
Draught mean	(m)	8.5
Rudder Area	(m ²)	33.0376
Rudder Aspect ratio		1.8219
	K_δ	1.4288×10^7
	I_x	1.4805×10^9
	ΔI_x	2.86×10^8

81.3 Design and Stability Analysis of the T-S Fuzzy Controller

The fuzzy model proposed by Takagi and Sugeno is described by fuzzy IF–THEN rules which represent local linear input–output relations of a nonlinear system. The main feature of a T-S fuzzy model is to express the local dynamics of each fuzzy rule by a linear system model. The overall fuzzy model of the system is achieved by fuzzy “blending” of the linear system models.

81.3.1 The T-S Fuzzy Model of the Equations of the Ship’s Nonlinear Rolling Motion

The *i*th rules of the T-S fuzzy models of the continuous system are of the following forms

Model Rule *i* : IF $z_1(t)$ is M_{i1} and $z_p(t)$ is M_{ip} , THEN

$$\dot{x}(t) = A_i x(t) + B_i u(t), \quad i = 1, 2, \dots, r. \tag{81.5}$$

Here, M_{ij} is the fuzzy set and r is the number of model rules; $x(t) \in R^n$ is the state vector, $u(t) \in R^m$ is the input vector, $A_i \in R^{n \times n}$, $B_i \in R^{n \times m}$, $z(t) = [z_1(t), \dots, z_p(t)]^T$ is the vector containing all the individual elements $z_1(t), \dots, z_p(t)$, which are known premise variables that may be functions of the state variables, external disturbances, and/or time. Given a pair of $(x(t), u(t))$, the final outputs of the fuzzy systems are inferred as follows:

$$\dot{x}(t) = \sum_{i=1}^r \mu_i(z(t))(A_i x(t) + B_i u(t)) \tag{81.6}$$

where

$$\mu_i(z(t)) = \frac{\sum_{j=1}^p M_{ij}(z_j(t))}{\sum_{i=1}^r \sum_{j=1}^p M_{ij}(z_j(t))}$$

$$\mu_i(z(t)) \geq 0, \sum_{i=1}^r \mu_i(z(t)) = 1, \quad i = 1, 2, \dots, r,$$

for all t . The term $M_{ij}(z_j(t))$ is the grade of membership of $z_j(t)$ in M_{ij} .

The nonlinear Eq. (81.4) of the roll motion can be approximated using the T-S fuzzy system.

Model Rule:

R1: IF x_1 is about 0, THEN $\dot{x}(t) = A_1x(t) + B_1u(t)$;

R2: IF x_1 is about $\pm \frac{\pi}{12}$, THEN $\dot{x}(t) = A_2x(t) + B_2u(t)$;

The state vector of the fuzzy system is $x = [x_1, x_2]'$, $x_1 = \phi$, $x_2 = p$, $u = \delta$. Figure 81.1 shows the triangular membership functions of the roll angle “Negative,” “Zero,” and “Positive,” respectively.

The parameters of each subsystem are presented in the following:

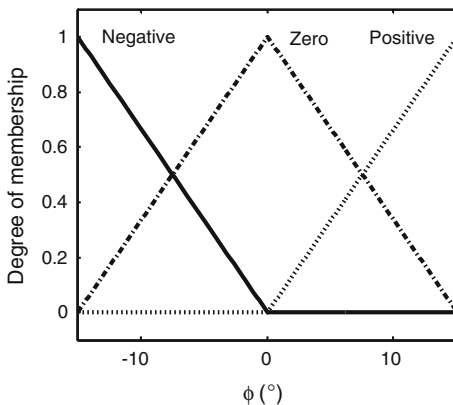
$$A_1 = \begin{bmatrix} 0 & 1 \\ -3.82 \times 10^{-2} & -1.59 \times 10^{-2} \end{bmatrix};$$

$$A_2 = \begin{bmatrix} 0 & 1 \\ -3.79 \times 10^{-2} & -1.59 \times 10^{-2} \end{bmatrix};$$

$$B_1 = B_2 = [0 \quad 8.1 \times 10^{-3}]^T;$$

$$\mu_1(z(t)) = \text{trimf}(x(1), [-0.2618, 0, 0.2618]); \mu_2(z(t)) = 1 - \mu_1(z(t)).$$

Fig. 81.1 Triangular membership functions of the roll angle



81.3.2 Parallel Distributed Compensation and the Stability Analysis

In the PDC design, each control rule is designed from the corresponding rule of a T-S fuzzy model. The designed fuzzy controller shares the same fuzzy sets with the fuzzy model in the premise parts. For the fuzzy model (81.5), we construct the following fuzzy controller via the PDC.

Control Rule i : IF $z_1(t)$ is M_{i1} and $z_p(t)$ is M_{ip} , THEN

$$u(t) = -K_i x(t), i = 1, 2, \dots, r.$$

The overall fuzzy controller is represented by

$$u(t) = - \sum_{i=1}^r \mu_i(z(t)) K_i x(t). \tag{81.7}$$

By substituting (81.7) into (81.6), we obtain the following closed-loop system

$$\dot{x}(t) = \sum_{i=1}^r \sum_{j=1}^r \mu_i(z(t)) \mu_j(z(t)) (A_i - B_i K_j) x(t). \tag{81.8}$$

Theorem 1 The equilibrium of the continuous fuzzy control system described by (81.8) is globally asymptotically stable if there exists a common positive definite matrix P such that

$$G_{ii}^T P + P G_{ii} < 0, \quad i = 1, 2, \dots, r, \tag{81.9}$$

$$\left(\frac{G_{ij} + G_{ji}}{2} \right)^T P + P \left(\frac{G_{ij} + G_{ji}}{2} \right) < 0, \quad i < j \leq r \tag{81.10}$$

where $G_{ij} = A_i - B_i K_j$.

Proof Consider a candidate of Lyapunov function $V(x(t)) = x^T(t) P x(t)$, where $P > 0$. Then,

$$\begin{aligned} \dot{V}(x(t)) &= \dot{x}^T(t) P x(t) + x^T(t) P \dot{x}(t) \\ &= \sum_{i=1}^r \sum_{j=1}^r \mu_i(z(t)) \mu_j(z(t)) \left[x^T(t) (A_i^T - K_j^T B_i^T) P x(t) + x^T(t) P (A_i - B_i K_j) x(t) \right] \\ &= \sum_{i=1}^r \sum_{j=1}^r \mu_i(z(t)) \mu_j(z(t)) x^T(t) \left[(A_i^T - K_j^T B_i^T) P + P (A_i - B_i K_j) \right] x(t) \\ &= \sum_{i=1}^r \mu_i^2(z(t)) x^T(t) (G_{ii}^T P + P G_{ii}) x(t) + \sum_{i < j}^r 2 \mu_i(z(t)) \mu_j(z(t)) x^T(t) \left[\left(\frac{G_{ij} + G_{ji}}{2} \right)^T P + P \left(\frac{G_{ij} + G_{ji}}{2} \right) \right] x(t) \end{aligned}$$

If condition (81.9) and (81.10) hold, $\dot{V}(x(t)) < 0$ at $x(t) \neq 0$. Theorem 1 can be obtained via Lyapunov stability theory.

For $r = 2$, multiply the inequality (81.9) and (81.10) on the left and right by P^{-1} , respectively. Define new variables $X = P^{-1}$, $Y_1 = -K_1X$ and $Y_2 = -K_2X$ so that for $X > 0$, we can rewrite the conditions as

$$\left\{ \begin{array}{l} XA_1^T + A_1X + Y_1^T B_1^T + B_1 Y_1 < 0 \\ XA_2^T + A_2X + Y_2^T B_2^T + B_2 Y_2 < 0 \\ XA_1^T + A_1X + XA_2^T + A_2X + Y_2^T B_1^T + B_1 Y_2 + Y_1^T B_2^T + B_2 Y_1 < 0 \end{array} \right. \quad (81.11)$$

81.3.3 LMI Area and D-Stability

If D is a disk with center at $(-q, 0)$ and radius r , we set $\zeta = \sqrt{q^2 - r^2} / q$. For the linear system the desired transient specification can be characterized by the damping ratio and the undamped natural frequency. The desired poles are of the form $s = -\xi\omega_n \pm \omega_n\sqrt{1 - \xi^2}i$ where ξ is the damping ratio and ω_n is the undamped natural frequency. For the nonlinear system, the desired transient specification is characterized by the decay rate and the ζ . It is known that the decay rate in the nonlinear system plays the same roles as $-\xi\omega_n$ in the linear system and ζ plays the same roles as the damping ratio in the linear system.

Definition 1 [9] For complex plane D , if there exists a symmetric matrix $L \in R^{m \times m}$ and a matrix $M \in R^{m \times m}$, satisfy

$$D = \{s \in C : L + sM + \bar{s}M^T < 0\} \quad (81.12)$$

Then we call D the Linear Matrix Inequality area, i.e. LMI area.

Definition 2 [9] (Quadratic D-stability) Given an LMI stability region D -stable defined by (81.12), the nonlinear system $\dot{x}(t) = f(x(t))x(t)$ is said to be quadratically D -stable if there exists a positive definite symmetric matrix $X \in R^{m \times m}$ such that

$$L \otimes X + M \otimes (Xf(x(t))) + M^T \otimes (Xf(x(t)))^T < 0 \quad (81.13)$$

where \otimes denotes the kronecker product of the matrices.

Theorem 1 [10] The system (81.6) is D -stable for some state feedback $K_j, j = 1, 2, \dots, r$, in an LMI region if there exist a positive definite symmetric matrix X and the matrices $Y_j, j = 1, 2, \dots, r$, such that

$$L \otimes X + M \otimes A_i X + M \otimes B_i Y_j + M^T \otimes X A_i^T + M^T \otimes Y_j^T B_i^T < 0, \quad (81.14)$$

$\forall i, j = 1, 2, \dots, r$. Where $K_j = -Y_j X^{-1}$.

81.3.4 Design of T-S Fuzzy Controller

Design the T-S fuzzy controller of the closed-loop system (81.8) as follows:

- Step 1. Check the controllability of each subsystem;
- Step 2. Set the parameters L and M of LMI stability region;
- Step 3. Using LMI optimization method, calculate the positive definite matrix X and $K_i (i = 1, 2)$ that satisfy (81.11) and (81.14). If there are X and $K_i (i = 1, 2)$ goto Step 4, else goto Step 2;
- Step 4. Using (81.7), get the overall fuzzy controller through the controller of the subsystems;
- Step 5. If we obtain the expected simulation results, goto the end, else goto Step 2.

81.4 Simulation

Consider the above container ship. IF D is a disk with center at $(-10, 0)$ and radius 9.9, this corresponds to $L = \begin{bmatrix} -9.9 & 10 \\ 10 & -9.9 \end{bmatrix}$ and $M = \begin{bmatrix} 0 & 0 \\ 1 & 0 \end{bmatrix}$. Let $V(x(t)) = x^T(t)Xx(t)$. From (81.13) we know that

$$\begin{bmatrix} -9.9 & 10 + \frac{1}{2} \frac{\dot{V}(x(t))}{V(x(t))} \\ 10 + \frac{1}{2} \frac{\dot{V}(x(t))}{V(x(t))} & -9.9 \end{bmatrix} < 0$$

Using the Schur complement, we obtain

$$-9.9^2 + \left(10 + \frac{1}{2} \frac{\dot{V}(x(t))}{V(x(t))} \right)^2 < 0.$$

We can see that the system's decay rates are constrained to lie within -39.8 and -0.2 .

Simulation results show that there exists symmetric positive definite matrix $X = [0.0499 - 0.0129; -0.0129 0.0734]$ that satisfies the conditions of theorem 3.2.1 and theorem 3.3.1. The closed-loop system of roll (81.8) were globally asymptotical stability, and every closed-loop subsystem is D-Stability. The state feedback gains of subsystems are $K_1 = [287.7177 \ 882.8735]$ and $K_2 = [287.7322 \ 882.8738]$.

The limitations of the rudder are $\dot{\delta}_{\max} = 15^\circ/s$ and $\delta_{\max} = 35^\circ$. For RRD, only high-frequency roll motion can be reduced. Consequently, only 1st-order wave disturbances are included in the simulation. These disturbances can be simulated using a 2nd-order linear approximation of the Pierson-Moskowitz spectral density function. Then, the disturbances $\omega_\phi = h(s)\omega(s)$, where $\omega(s)$ are Gaussian white

Fig. 81.2 Roll angle with the controller is turned off

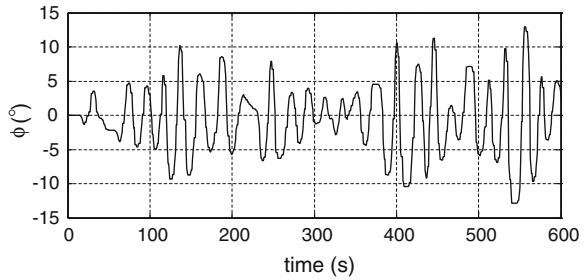
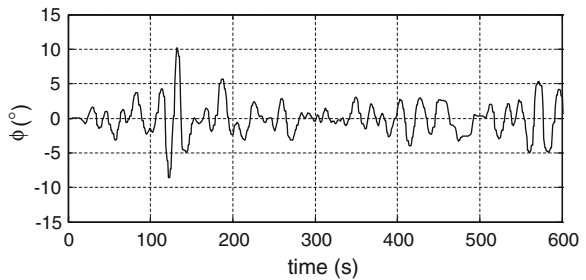


Fig. 81.3 Roll angle with the controller is active



noise. A damping ratio of approximately 42 % is the result of the RRD controller. It is seen that considerable roll damping is obtained (Figs. 81.2, 81.3).

In this paper, the new design of controller for the RRD systems have been presented. The stability conditions guarantee not only the stability of the system but also the expected dynamic performance. Simulation results show that the fuzzy controller not only can reduce roll effectively but also have good robustness.

Acknowledgments This work was supported by the Natural science foundation of Heilongjiang province (42400621-1-11209; LC2012C36), the Fundamental Research Funds for the Central Universities.

References

1. Cowley WE, Lambert TH (1972) The use of rudder as roll stabilizer. In: Proceeding of SCSS'72, vol 2, Bath, UK, (VII):C-1
2. Chengen Y, Xinle J, Yingjun B (1999) A robust RRD controller design with μ synthesis. Shipbuilding Chin 4:28–34 (in Chinese)
3. Song L, Li H, Chen S (2003) Sliding mode prediction-based discrete variable structure control and its application to ship autopilot. In: Proceedings of the CSEE 23(11):160–163 (in Chinese)
4. Alarcin F, Gulez K (2007) Rudder roll stabilization for fishing vessel using neural network approach. Ocean Eng 34:1811–1817
5. O'Brien JF (2009) Multi-path nonlinear dynamic compensation for rudder roll stabilization. Control Eng Practice 17(2009):1405–1414

6. Lijun W, Xianku Z (2011) Ship course-changing and course-keeping based on robust fuzzy control (in Chinese). *Navig Chin* 34(2):1–4
7. Bhattacharyya SK, Rajesh G, Deepak Kumar G (2011) Fuzzy autopilot for ship maneuvering. *Int Ship Build Prog* 58:191–218
8. Jin H, Yao X (2001) Control theory of ship (in Chinese). Harbin Engineering University Press, pp 133–140
9. Yuli (2002) Robust control-a linear matrix inequality approach (in Chinese). Tsinghua University Press, p 104
10. Feiyan C, Xiping C, Meifang C (2006) Design of fuzzy controller based on LMI. *J Sys Simul* 8:872–879 (in Chinese)

Chapter 82

Short-Term Forecasting of Traffic Flow Based on Genetic Algorithm and BP Neural Network

Junwei Gao, Ziwen Leng, Bin Zhang, Guoqiang Cai and Xin Liu

Abstract This paper focuses on the short-term traffic flow forecasting which plays an important role in traffic control and guidance system. To improve the efficiency and precision of short-term forecasting, the method of BP neural network optimized by genetic algorithm (GA) is put forward. Considering the shortcomings of traditional BP neural network, genetic algorithm is used to optimize the weight and threshold of BP neural network by training sample, then the optimized network is tested by testing sample and the network conducts short-term forecasting for 30 min by means of the rolling forecasting. The validity and accuracy of GA-BP forecasting model is tested on the basis of traffic flow. The simulation results demonstrate that the proposed model has higher superiority in convergence rate and forecasting precision.

Keywords Short-term forecasting · Traffic flow · BP neural network · Genetic algorithm

82.1 Introduction

With the rapid development and daily maturity of information technology, a variety of new methods and techniques are widely applied in traffic flow forecasting. Real-time, fast and accurate short-term forecasting has been an essential

J. Gao (✉) · Z. Leng · B. Zhang
College of Automation Engineering, Qingdao University, No 308 Ningxia Road,
Qingdao 266071, China
e-mail: qdgao163@163.com

J. Gao · G. Cai
State Key Laboratory of Rail Traffic Control and Safety, Beijing Jiaotong University,
Beijing 100044, China

X. Liu
Qingdao Hisense TransTech Co.,Ltd, Qingdao 266071, China

component of intelligent traffic system (ITS). As a consequence, the corresponding research is more concerned and many forecasting models are introduced and tested effectively in practical engineering application, such as Kalman filter [1], artificial neural network [2], genetic algorithm [3] and so on.

For high complexity, uncertainty and nonlinearity existing in traffic flow, traditional methods cannot achieve higher forecasting precision practically. Artificial neural network has the excellent capability of self-learning, self-organization and parallel processing [4], and can avoid the complicated model building process to research the state of system directly. Focusing on the characteristics of traffic flow, the typical BP neural network is appropriately used in short-term forecasting because of its high adaptability to the traffic flow regularity. However, drawbacks also exist in BP neural network, which includes easily running into local minimum point, slow convergence speed [5] and sensitivity of initial network weight. Genetic algorithm (GA) is a new type of optimized method [6] with better global search ability and extensive adaptability. After generations of evolution, the algorithm converges to the most adaptive individual and obtains the best solution.

Taking the weaknesses of BP neural network and the advantages of genetic algorithm into consideration, the paper proposes the combination of both to improve the forecasting precision of traffic flow. The new algorithm uses GA to make up for the random defects of connection weight and threshold in BP neural network. The process of optimizing BP neural network based on GA consists of the determination of BP structure, network optimization by GA and the forecasting output of network. The optimized BP neural network will show mapping ability, fast convergence and stronger learning capability.

82.2 Basic Theory of BP Neural Network

BP neural network is a single-way propagating, most maturely studied and most widely used feed forward network. The structure consists input layer, hidden layer and output layer. The whole learning process of network includes the positive propagation of signal and the back propagation of error. The main learning algorithm of BP is gradient descent method, which continuously adjusts the connection weights of network to search for the minimum mean square error of forecasting output and desired output.

Assume that input layer has m neurons with the input vector $X = \{x_1, x_2, \dots, x_m\}$, hidden layer has n neurons with the vector $Z = \{z_1, z_2, \dots, z_n\}$, and output layer has l neurons with output vector $Y = \{y_1, y_2, \dots, y_l\}$.

The output of hidden layer neuron i is:

$$Z_i = f\left(\sum_{j=1}^m w_{ij}X_j - \theta_i\right) \quad (82.1)$$

where w_{ij} is the connection weight between input layer neuron j and hidden layer neuron i , θ_i is the threshold of hidden layer neuron i , f is the activation function of hidden layer.

The output of output layer neuron k is:

$$Y_k = g \left(\sum_{i=1}^n w_{ki} Z_i - \theta_k \right) \quad (82.2)$$

where w_{ki} is the connection weight between hidden layer neuron i and output layer neuron k , θ_k is the threshold of output layer, g is the activation function of output layer.

82.3 Optimization of BP Neural Network Based on GA

Genetic algorithm is a type of computation model which imitates the process of biological evolution. As a new search algorithm of global optimization, GA executes simple and random operations similar to biological evolution and selects the optimal individual. Compared with BP neural network, GA can effectively avoid running into local minimum and optimize the structure of complex system.

82.3.1 Genetic Algorithm Optimizes BP Neural Network

In this paper, we adopt GA to optimize the initial weight and threshold of BP neural network, by conducting selection, crossover and mutation to search for the best individual, assigning the optimal individual to the weight and threshold of BP. Then the network takes the short-term forecasting model for local optimization and finally obtains the forecasting output which is the global optimal solution.

The algorithm is to search for the best desired parameters by which the network can obtain the global optimal solution, change the reliance on gradient information of BP neural network, and achieve the global minimum error, so as to improve the precision and speed of the network.

82.3.2 Process of GA Optimize BP Neural Network

The optimized process includes initialization of population, determination of fitness function, selection, crossover and mutation operations, and initialization of BP neural network.

1. Initialization of population

Set the population scale and generate initial population including individuals with the number N . Set the range of data, select linear interpolation function to generate real vectors as the individuals of GA. Each individual adopts real code and becomes a real string, which consists of the connection weight between input layer and hidden layer, threshold of hidden layer, connection weight between hidden layer and output layer, and threshold of output layer. When the BP neural network is established, the structure, weight and threshold will be ascertained according to each individual.

2. Determination of fitness function

The initial weight and threshold of BP neural network are assigned on the basis of individual. The network obtains forecasting output by training sample, calculates the training error between forecasting output and desired output, and adopts the sum of square training error as the fitness.

3. Selection

The paper uses roulette wheel selection [7] to determine the probability by which the individual will be selected. The roulette wheel selection is a kind of selecting strategy for individual based on the fitness proportion. The formula of selection probability is show as follows:

$$p_i = f_i / \sum_{i=1}^N f_i, \quad i = 1, 2, \dots, N \quad (82.3)$$

where N is the population scale, f_i is the reciprocal of individual fitness.

4. Crossover and Mutation

To generate new population, GA takes the operations of crossover and mutation to deal with current population. As a consequence, probabilities of crossover and mutation are two important parameters which will have a great effect on the performance and property of convergence of GA. Different from traditional algorithm, this paper proposes the adaptive genetic algorithm, in which probabilities of crossover and mutation can change adaptively according to individual fitness. The adaptive change will maintain the diversity of population, improve the capability of global search and avoid individual being earlier mature.

$$P_c = \begin{cases} P_{c1} - \frac{(P_{c1} - P_{c2})(f' - f_{avg})}{f_{max} - f_{avg}}, & f' > f_{avg} \\ P_{c1}, & f' < f_{avg} \end{cases} \quad (82.4)$$

$$P_m = \begin{cases} P_{m1} - \frac{(P_{m1} - P_{m2})(f - f_{avg})}{f_{max} - f_{avg}}, & f \geq f_{avg} \\ P_{m1}, & f < f_{avg} \end{cases} \quad (82.5)$$

where P_c is the crossover probability, P_m is the mutation probability, f_{\max} is the maximum fitness of population, f_{avg} is the average fitness, f' is the larger fitness of two individuals in crossover, f is the fitness of individual in mutation. Based on repeated experiments and former experience, the paper chooses $P_{c1} = 0.9$, $P_{c2} = 0.7$, $P_{m1} = 0.1$, $P_{m2} = 0.002$.

5. Initialization of BP neural network

After obtaining the optimal individual, decompose the individual into initial connection weight and threshold of BP neural network and train the new network to get desired forecasting output of time series.

82.4 Data Processing

Considering the unique characteristics of traffic flow and forecasting precision, it is necessary for the network to normalize input data to the acceptable range [0, 1]. Normalization formula is presented as follows:

$$\bar{x}_i = (x_i - \min(x)) / (\max(x) - \min(x)) \quad (82.6)$$

where x_i is the original input of the network, \bar{x}_i is the normalized value.

For the effective approximation and mapping ability of neural network, BP neural network plays an important way in the nonlinear forecasting of time series. When approximating the time series, the short-term forecasting model selects rolling forecasting to conduct one step of forecasting [8]. Firstly, select the former m values $(x(t - (m - 1)), x(t - (m - 2)), \dots, x(t))$ to forecast the next value $x(t + 1)$, then the forecasting value $x(t + 1)$ is feedback to compose the new input of the network $(x(t - (m - 2)), \dots, x(t), x(t + 1))$ for next value $x(t + 2)$, and the process will go on.

82.5 Simulation Results

On the programming platform of MATLAB, the paper establishes the short-term forecasting model and takes measured traffic flow of 6 days in Qingdao City from 6:00 AM to 21:00 PM with the sampling period of 5 min to verify the effectiveness of the combination of BP neural network and GA.

82.5.1 Sample Analysis and Choice of Network Parameters

In simulation experiment, the paper selects 5 days' data as the training sample and the former 120 groups of data of the sixth day as the testing sample. Then the model executes the rolling forecasting to get the short-term forecasting in 30 min (6 sampling periods).

According to the experience concluded from large amounts of experiments, future values should have certain connection with the former observations in the same road section, so the paper selects the values $x(t-3), x(t-2), x(t-1), x(t)$ to forecast the next value $x(t+1)$. Therefore, BP neural network consists of three layers with the input layer neurons 4 and output layer neuron 1. After many times of experiments, the hidden layer adopts 9 neurons with faster speed and better learning effect, so the structure of BP neural network is 4-9-1.

Transfer functions of hidden layer and output layer are *tansig* and *purelin*, while training function is *trainlm*. Population scale of GA is 10 with evolution times 100, training epochs are 1,000, training goal is 0.0001 and learning rate is 0.1.

82.5.2 Forecasting Results

After the establishment of short-term traffic flow forecasting model, the optimized BP neural network based on GA trains the sample, and the fitting curve of training output and measured traffic flow is shown in Fig. 82.1. Concluded from the training output, the optimized model is valid and the setting of parameters in the network is reasonable. As a consequence, the model can be applied for more accurate forecasting of traffic flow.

The normalized former 120 groups of traffic data are used as the input of the network to test the accuracy of the forecasting model. To compare the simulation

Fig. 82.1 Fitting curve of training output

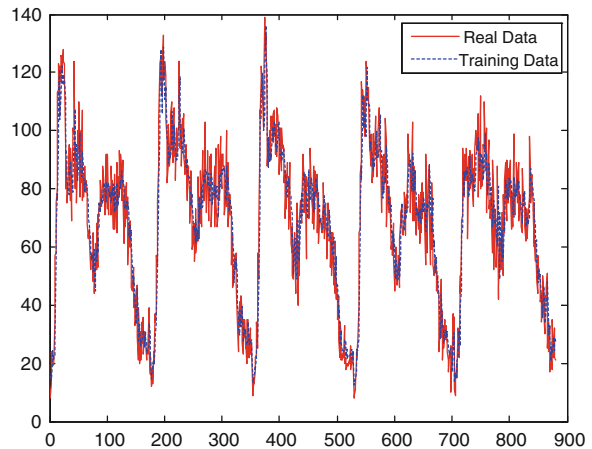
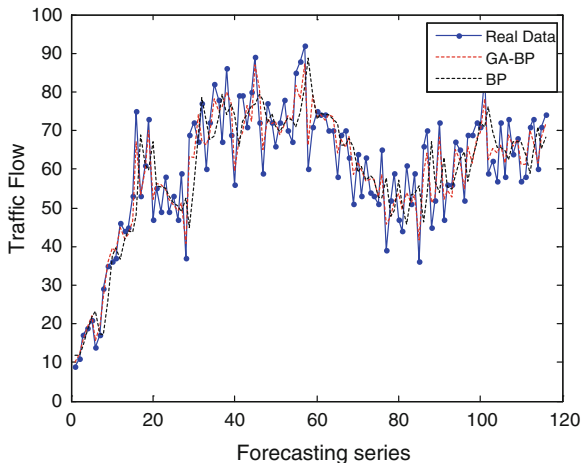


Fig. 82.2 Forecasting curves of GA-BP and BP



results and show the superiority of the optimized model, the paper also establishes forecasting model based on traditional BP neural network which has the same parameters with the optimized network. The forecasting curves of two models are shown in Fig. 82.2. From the figure we can see that the optimized network is more approximating the real data and has higher precision than the traditional network.

The relative error curve of the optimized BP neural network is shown in Fig. 82.3. Analyzing the curve, the errors are nearly in the acceptable range $[-0.15, 0.15]$ and the error is to decrease with the increase of input data. As a result, it is feasible for the optimized network to conduct short-term forecasting of traffic flow. In the following way, the paper conducts short-term forecasting for 30 min based on the rolling forecasting, which is given in Table 82.1.

Concluded from the table, the short-term traffic flow forecasting model can achieve better forecasting effect with average relative error 0.061, which is within

Fig. 82.3 Relative error curve of GA-BP

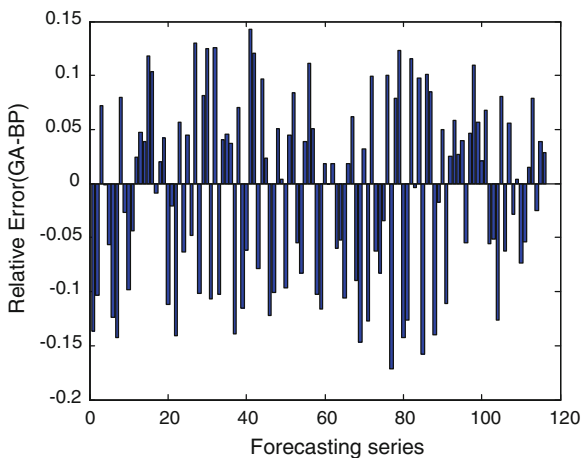


Table 82.1 Short-term forecasting of traffic flow

Time (min)	5	10	15	20	25	30
Actual flow (vehicle)	72	69	75	71	76	81
Forecasting flow (vehicle)	67.42	73.78	78.23	74.69	70.47	86.43
Relative error	0.064	0.069	0.043	0.052	0.073	0.066
Average error	0.061					

the allowable range. Thus, the model is valid and feasible to be applied in the short-term traffic flow forecasting.

82.6 Conclusion

Focusing on the characteristics of traffic flow, the paper proposes the combination of BP neural network and genetic algorithm, which uses the genetic algorithm to optimize the initial weight and threshold of BP neural network. The new proposed algorithm can take advantage of the global search ability of genetic algorithm and avoid the network to run into local minimum point. The simulation results indicate that the optimized BP neural network is highly superior to traditional neural network in forecasting precision for short-term traffic flow forecasting.

Acknowledgments This work is supported by the National Science & Technology Pillar Program (2011BAG01B05), Foundation of Shandong Province (BS2011DX008, ZR2011FM008), 863 Program (2012AA112309), and State Key Laboratory of Rail Traffic Control and Safety Foundation (RCS2011K005, RCS2012K006) Beijing Jiaotong University.

References

1. Gao JW, Leng ZW, Zhang B et al (2013) The application of adaptive Kalman filter in traffic flow forecasting. *Advanced Materials*. 680:495–500
2. Ma J, Li XD, Meng Y (2009) Research of urban traffic flow forecasting based on neural network. *Acta Electronica Sinica* 37(5):1092–1094 (in Chinese)
3. Liu MZ, Wang RL, Wu JS et al (2005) A genetic-algorithm-based neural network approach for short-term traffic flow forecasting. *Lect Notes Comput Sci* 3498(3):965–970
4. Gao JW, Cai GC, Li QC et al (2011) Short-term urban road traffic flow forecasting based on ANFIS. *ICIC Exp Lett* 5(10):3671–3675
5. Li S, Liu LJ, Jie YL (2011) Chaotic prediction for short-term traffic flow of optimized BP neural network based on genetic algorithm. *Control Decis* 26(10):1581–1585 (in Chinese)
6. Chen W, Pang LN (2009) The research of the application of GABP neural network in traffic flow prediction. *Microcomp Inf* 25(5–2):245–247 (in Chinese)
7. Zou YP, Liu HL (2008) New dynamic load balancing method based on roulette wheel selection and its implementation. *J Commun* 29(9):18–23
8. Du CH, Huang XY, Yang ZY et al (2008) Real-time rolling traffic flow forecasting based on neural networks and Markov chains. *J Sys Simul* 20(9):2464–2468 (in Chinese)

Chapter 83

Joint State and Parameter Estimation for a Robot Hydraulic Actuator

Guangbin Sun and Hong Wang

Abstract This paper presents a method for estimating the internal state and unknown parameters of hydraulic actuator simultaneously. A sequential Extended Kalman Filter is used to estimate the unknown parameters asynchronously: a nonlinear state space model is derived with transmission dynamics included, then parameters and states to be estimated are paired as an augmented state in form of state elements plus one unknown parameter during each iteration, finally sequential extended Kalman filter is applied to estimating the resultant augmented states. The validity is verified by ground-truth data sampled from a hydraulic humanoid robot. The results show sequential extended Kalman filter can jointly estimate the internal state and unknown parameters with very small RMS residual error.

Keywords Estimation · Sequential extended Kalman filter · Hydraulics · Augmented state

83.1 Introduction

Hydraulic systems are popular in industrial fields, especially in heavy-duty machinery such as off-highway excavators, and aircraft [1]. For the wide range of stiffness and compliance, hydraulic actuator is adopted in mobile robots in recent years [2–4].

G. Sun · H. Wang (✉)

School of Mechanical and Automation, Northeastern University, Lane 3,
Wenhua Road, Shenyang, Liaoning, China
e-mail: hongwang@mail.neu.edu.cn

G. Sun

e-mail: sunguangbin@yahoo.cn

Friction is one of the most important obstacles for getting an accurate control, especially under low velocity. It is tough to predict the friction accurately because of mechanical wear of seal and temperature-dependency of fluid viscous property as well as no access to the cylinders pressures in real time. Another important parameter is effective modulus, which determines the dynamic performance of hydraulic system as a measure of liquid resistance to compression. Furthermore, it is hard to get an accurate prediction of effective modulus for the temperature and pressure dependency. So it is desirable to fuse the available measurements at hand to estimate the internal state of the system and the unknown parameters.

An et al. [1] applies extended Kalman filter to estimating the valve spool displacement, the chamber pressures of the actuator and the velocity of the ram, responding reliably to pump pressure changes as little as 10 % of normal operating pressure. Chinniah et al. [5] makes use of extended Kalman filter technique to estimate viscous friction and effective bulk modulus for failure monitoring. Cui et al. [6] apply a robust Kalman filter to indirectly measuring the external leakage of the hydraulic servo-motor. For tackling the problem of unobservable augmented state-space model, this paper presents a method for jointly estimate the state and parameters based on sequential extended Kalman filter.

83.2 System Dynamics

The hydraulic system is shown in Fig. 83.1a. The transmission is a four bar mechanism as shown in Fig. 83.1b.

Choose the state vector x as:

$$x = [x_1, x_2, x_3, x_4]^T = [\theta, \dot{\theta}, p_1, p_2]^T \tag{83.1}$$

where, θ is the joint angle. $p_{1,2}$ are the pressures in the opposing chambers of the cylinder. Then the nonlinear state space model is shown below:

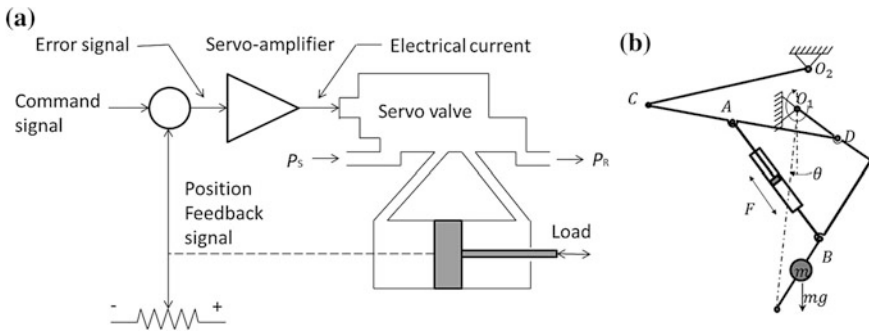


Fig. 83.1 The schematic diagram of the hydraulic servo system. **a** Valve-piston system. **b** Transmission mechanism

$$\left. \begin{aligned} \dot{x}_1 &= x_2 \\ \dot{x}_2 &= \frac{L_\tau}{J} [(x_3 - \alpha x_4) A_p - F_f] - \frac{mgl \sin(x_1)}{J} \\ \dot{x}_3 &= \frac{E'(x_3)}{V_1(x_1)} [Q_1(x_3, \frac{Ku}{\omega_n^2}) - A_p L_\tau x_2 + K_{Li}(x_4 - x_3)] \\ \dot{x}_4 &= \frac{E'(x_4)}{V_2(x_1)} [Q_2(x_4, \frac{Ku}{\omega_n^2}) + \alpha A_p L_\tau x_2 - K_{Li}(x_4 - x_3)] \end{aligned} \right\} \quad (83.2)$$

where, g is gravity constant. l is the length between the center of mass of the load and joint axis. J is moment of inertia of the load with respect to joint axis. L_τ is the moment arm. A_p is piston area. α is annulus ratio. $V_{1,2}$ are volumes of the cylinder chambers. E is effective modulus. u is valve input signal. K_{Li} is leakage coefficient of cylinder. $Q_{1,2}$ are the flows from the servo-valve to the piston chamber and ring chamber respectively. u is the valve input. ω_n is the valve natural frequency. K is the DC gain.

$$\left. \begin{aligned} Q_1 &= C_v \text{sg}(x_s) \text{sign}(P_S - p_1) \sqrt{|P_S - p_1|} - C_v \text{sg}(-x_s) \text{sign}(p_1 - P_R) \sqrt{|p_1 - P_R|} \\ Q_2 &= C_v \text{sg}(-x_s) \text{sign}(P_S - p_2) \sqrt{|P_S - p_2|} - C_v \text{sg}(x_s) \text{sign}(p_2 - P_R) \sqrt{|p_2 - P_R|} \end{aligned} \right\} \quad (83.3)$$

where P_S and P_R are the pump pressure and return pressure respectively. The pressures at chamber 1 and 2 of the cylinder are given as $p_{1,2}$. x_s is the spool displacement of the servo-valve. C_v is the valve coefficient.

The function sg is defined as:

$$\text{sg}(x) = \begin{cases} x & x \geq 0 \\ 0 & x < 0 \end{cases} \quad (83.4)$$

Cylinder friction is described as [7, 8]:

$$\frac{dF_f}{dt} = a|\dot{\theta}|F_f + b\dot{\theta} \quad (83.5)$$

where F_f is friction of cylinder, $\dot{\theta}$ is joint angular velocity, and a , b are two coefficients. The state space representation is further discretized using the forward difference method to apply the discrete sequential EKF algorithm.

83.3 Sequential EKF Based State and Parameter Estimation

Having established the system model, the associated parameters are required to be experimentally identified or estimated. The parameters that are hardly measurable but observable can be estimated using state-parameter estimation method.

To implement the joint state-parameter EKF, the original state vector (x) is augmented with the unknown parameter (θ) to form a new state vector (χ). The augmented state is assumed to be of random walk subject to zero-mean white noise (ζ). ζ is presumed to be uncorrelated with system noise (v) with a positive definite variance.

Forward difference method is then employed to discretize the state-space model of the system given in the previous section and the augmentative model. The resultant representation is:

$$\begin{cases} x^{k+1} = F(x^k, \theta^k) + \omega^k \\ \theta^{k+1} = \theta^k + \zeta^k \\ y^k = H(x^k, \theta^k) + v^k \end{cases} \quad (83.6)$$

where $\theta_{m \times 1}$ is the vector of model parameters. $\omega_{m \times 1}$ and $\zeta_{m \times 1}$ are process noises, while $v_{n \times 1}$ is the measurement noise. Thus, the stochastic dynamics of the system transforms into

$$\begin{cases} \chi^{k+1} = F(\chi^k) + \eta^k \\ y^k = H(\chi^k) + v^k \end{cases} \quad (83.7)$$

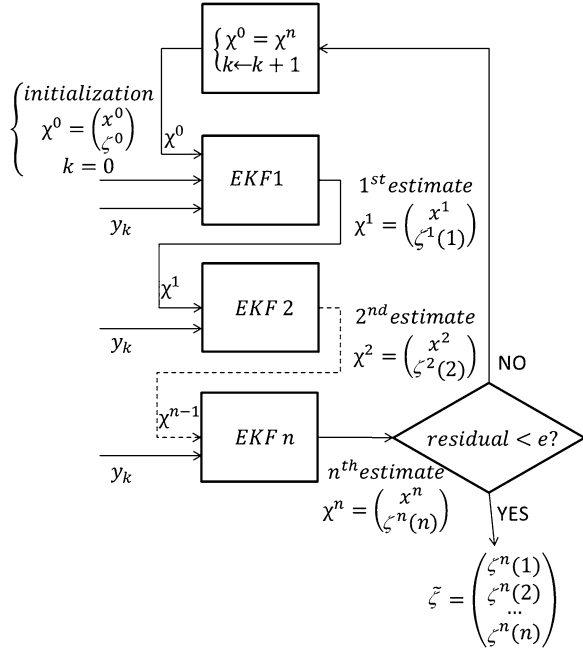
In which $\eta_{(m+1) \times 1}$ is the process noise of the new state vector (χ) written as:

$$\chi_{(m+1) \times 1}^k = \begin{pmatrix} x_{m \times 1}^k \\ \theta_{1 \times 1}^k \end{pmatrix} \quad (83.8)$$

The multiple EKF is then applied asynchronously to a subset of the states and the rest of them are treated as known values. The observability is considered when the number of states is chosen.

Each single EKF estimates the state of the system at current iteration plus one of the unknown parameters. The model is updated when the current iteration of estimation is completed. Then the next filter is triggered to estimate another parameter. The procedure is terminated once a narrow error bound is achieved. Figure 83.2 shows the procedure. x^i and θ^i denote state and parameter estimate respectively at i th iteration of time point k . Finally $\tilde{\theta}$ represents the estimated parameters values.

Fig. 83.2 The diagram of sequential EKF procedure



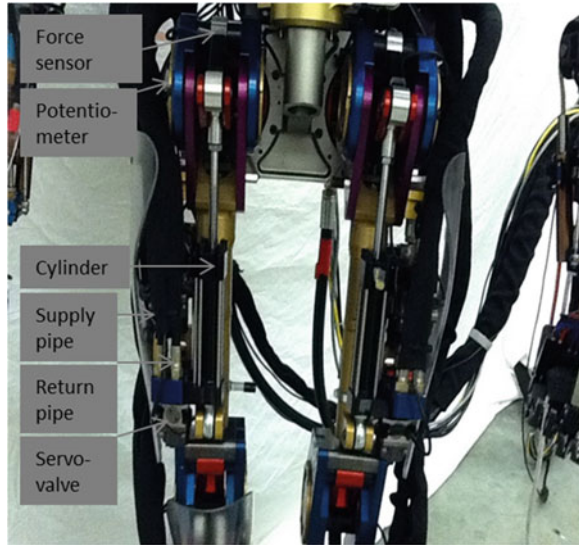
83.4 Implementation and Experiments

83.4.1 Instrumentation

The hydraulic test rig is the Left Hip Flex Extension (LHFE) joint actuator of SARCOS robot. A Moog servo valve (0-400AC03547-002) is mounted to regulate the hydraulic flow. A high speed PC equipped with a data acquisition board to collect data at 5 kHz. The main controller board (SDC) mounted onto the robot has a sampling frequency of 20,000 Hz. A rotating potentiometer is used to measure the joint angle and a force sensor used to measure the torque exerted by the actuator on the load. A LVDT sensor is used to measure the linear velocity of the piston. The cylinder used is asymmetric with 9.525 mm of piston diameter and annulus ratio of 0.635. The normal operating supply pressure is 3,000 psi. The Moog valve is controlled by current and a current other than 0 will cause a differential oil flow applied to the opposing sides of the piston. The flow accumulation will result in pressure changes in pressures of cylinder chamber and in reverse the chambers pressures will affect the flow, which perplexes the hydraulic dynamics. In the case of no load, the linear velocity of the actuator is approximately proportional to the current. The data from potentiometer and force sensor are subsampled and transmitted to the upper PC at 1 kHz (Fig. 83.3).

A sinusoidal signal of 0.3319 Hz is used as valve input. The sampled data is filtered by median filter and Butterworth filter. Because for the time being the

Fig. 83.3 Experimental instrument



estimator is applied to offline data, the Butterworth filter is used in way of zero-phase forward and reverse IIR filtering to cancel the lag incurred. The parameters except the to-be-estimated ones are predetermined by calibration or from product catalogue. The estimated parameters are compared with their baseline values to prove the validity of the method proposed.

83.4.2 *Experimental Results*

The data used as measurement reference is sampled. The next problem is how to apply the estimator. If the state variable is augmented with too many parameters, it is often the case that the system becomes unobservable. So only one parameter is paired with the state vector and the system model is dexterously reformed to keep the system observable. Then a sequence of EKFs is implemented to estimate the state and parameters asynchronously.

Each individual EKF is tuned. The initial error covariance matrices are chosen to be large in order to ensure rapid convergence. The measurement noise variance R is set to be 0.01 in each filter. The noise is assumed to be time invariant. For the high nonlinearity, assuming a random initial state may results in divergence. Furthermore local minima are also an important consideration.

As shown in Fig. 84.4a and b, the estimated pressures in piston and ring chambers are close to baseline values with a RMS error of 1.8×10^6 Pa and 0.8×10^6 Pa respectively. In Fig. 84.4c and d, the friction coefficients a and b are estimated and the estimating process is asymptotically stable, and the quasi-static state is reached after around 5,000 ms to be about 3.2×10^{-5} and 7.0×10^{-6}

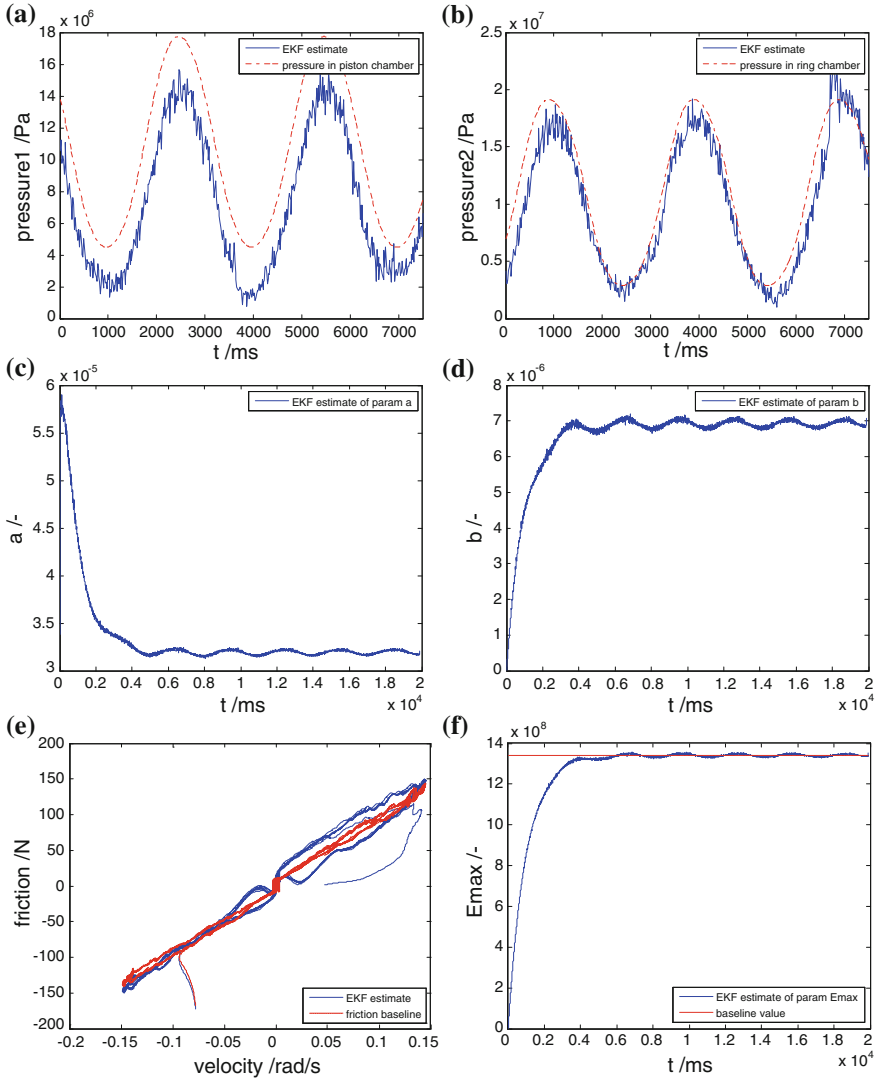


Fig. 83.4 a–f (from left to right): **a** Pressure estimate in piston chamber, **b** pressure estimate in ring chamber, **c** estimate of friction parameter *a*, **d** estimate of friction parameter *b*, **e** estimate of friction (plotted vs. velocity), **f** estimate of max effective bulk modulus

respectively. The prediction friction using estimated parameters *a* and *b* is shown in Fig. 84.4e, and the feature when the velocity crosses zero is well captured. On the other side, the friction estimate has a different performance in two directions and the estimate at negative velocity is obviously better than that at positive velocity. In Fig. 84.4f, the estimate of max effective modulus is close to baseline value with RMS error of 2×10^7 Pa corresponding relative error of 1.49 %.

83.5 Conclusion

In this paper, the sequential EKF is used to estimate the state and unknown parameters of a hydraulic actuator asynchronously. A 4-state nonlinear model is derived with friction included. The unknown parameters, i.e. friction coefficients and maximum effective modulus, are augmented to the state vector to form a new state vector. Then a sequence of EKFs is applied asynchronously with state plus one parameter estimated in each iteration. The method proposed is applied to ground-truth data from the hydraulic actuator and the experimental results proved the proposed method can estimate the state and parameter with good performance.

References

1. An L (2003) Hydraulic actuator circuit fault detection using extended Kalman filter. In: Proceedings of the American control conference, vol 5, pp 4261–4266
2. Raibert M, Buehler MG, Playter RR (2007) Boston dynamics. “BigDog”, SPIE defense and security symposium, Florida, USA, Apr 9–13
3. Bentivegna DC, Atkeson CG, Kim JY (2007) Compliant control of a hydraulic humanoid joint. 7th IEEE-RAS international conference on humanoid robots, pp 483–489
4. Semini C et al (2008) HyQ-Hydraulically actuated quadruped robot: Hopping leg prototype. 2nd IEEE RAS and EMBS international conference on biomedical robotics and biomechatronics, pp 593–599
5. Chinniah Y, Burton R, Habibi S (2006) Failure monitoring in a high performance hydrostatic actuation system using the extended Kalman filter. *Mechatronics* 16(10):643–653
6. Cui X, Dong Y, Zhao K (2009) Measurement of external leakage of hydraulic servo-motor based on robust extended kalman filter. ICEMI'09, 9th international conference on electronic measurement and instruments, vol 2, pp 680–684
7. Ray LR, Ramasubramanian A, Townsend J (2001) Adaptive friction compensation using extended Kalman–Bucy filter friction estimation. *Contr Eng Pract* 9(2):169–179
8. Walrath CD (1984) Adaptive bearing friction compensation based on recent knowledge of dynamic friction. *Automatica* 20(6):717–727

Chapter 84

Delay-Dependent Robust Control for Output PDFs of Discrete-Time Non-Gaussian Stochastic Processes

Yao An, Yang Yi, Weixing Zheng and Tianping Zhang

Abstract In this paper, the shaping tracking problem based on output probability density functions (PDFs) is studied for a class of discrete-time non-Gaussian stochastic processes. Following B-spline approximation for the output PDFs, the discrete-time PI control input is constructed to solve the tracking control problem for complex nonlinear weight dynamics with multiple unknown uncertainties and state delays. Moreover, by designing the new convex linear matrix inequalities (LMIs) based on delay-dependent, the satisfactory delay-dependent stability, robustness, dynamic tracking performance as well as state constraint can be achieved simultaneously. Finally, a simulation example is presented to illustrate the effectiveness of the proposed approach.

Keywords Non-Gaussian stochastic processes · Probability density functions (PDFs) · Delay dependent · Discrete-time PI controller

84.1 Introduction

Recently, a group of new control strategies on control the shape of output PDFs for non-Gaussian stochastic processes have received considerable attention [1–7]. The new control framework is an effective solution to the increased demand from those

Y. An · Y. Yi (✉) · T. Zhang

College of Information Engineering, Yangzhou University, Yangzhou 225127, China

e-mail: yiyangcontrol@163.com

T. Zhang

e-mail: tpzhang@yzu.edu.cn

W. Zheng

School of Computing, Engineering and Mathematics, University of Western Sydney,
Sydney 2751, Australia

e-mail: w.zheng@uws.edu.cn

non-Gaussian systems and can be seen in many processing industries (see [1, 2] for details). Following the B-spline expansion as the approximator to the output PDFs, a series of optimization and control approaches can be found to solve the non-Gaussian stochastic control and modeling problems (see [4–7]). For example, PI structure control algorithm [4], iterative learning algorithm [5], dynamic neural network modeling [6] and entropy minimization algorithm [7].

It is well known that the stability analysis of time-delay systems has always been a hot point in the field of control theory during the past few years [8]. Based on Lyapunov–Krasovskii theory and LMI optimization algorithms, the delay-dependent stabilization and robust control for uncertain nonlinear systems has gotten a large number of meaningful results (see [9–11]). However, there are few results about the delay-dependent control for non-Gaussian stochastic processes.

In this paper, we will discuss the delay-dependent robust control problem for a class of complex discrete-time non-Gaussian stochastic processes. The main contents include: (1) By combining the B-spline expansion with the discrete-time PI control input, the shape control of the output PDFs can be transformed into the multi-objective control problem for the complex weight dynamics with exogenous disturbances, uncertainties, nonlinear term and state delays, which extends the scope of model application compared with [2, 4]. (2) By solving a series of convex LMIs, the maximum time-delay d^* and the control gain can be obtained such that the delay-dependent stability and the satisfactory state constrained tracking can be guaranteed. Meanwhile, improved robustness can also be achieved based on $L1$ performance index.

84.2 Problem Formulation

For the dynamic stochastic processes, denote $u(k) \in R^m$ as the control input, $\eta(k) \in [a, b]$ as the stochastic output and the probability of output $\eta(k)$ lying inside $[a, \sigma]$ can be described as

$$P(a \leq \eta(k) < \sigma, u(k)) = \int_a^\sigma \gamma(y, u(k)) dy \quad (84.1)$$

where $\gamma(y, u(k))$ is the output PDF of the stochastic variable $\eta(k)$ under control input $u(k)$. Similar to [4–6], the square root B-spline expansion is used to approximate the out PDFs

$$\sqrt{\gamma(y, u(k))} = \sum_{i=1}^n v_i(u(k)) B_i(y) \quad (84.2)$$

where $B_i(y)$ ($i = 1, 2, \dots, n$) are pre-specified basis functions, $v_i(k) := v_i(u(k))$ are the corresponding weight dynamics. It is noted the probability distribution should satisfy the condition $\int_a^b \gamma(y, u(k)) dy = 1$, which shows only $n - 1$ weights are independent. So (84.2) can be rewritten as follows

$$\gamma(y, u(k)) = (C_0(y)V(k) + v_n(k)B_n(y))^2 \quad (84.3)$$

where $C_0(y) = [B_1(y) B_2(y) \dots B_{n-1}(y)]$, $V(k) = [v_1(k) v_2(k) \dots v_{n-1}(k)]^T$. In order to guarantee $\int_a^b \gamma(y, u(k)) dy = 1$, the following inequality

$$V^T(k)\Pi_0 V(k) \leq 1, \quad \Pi_0 = \Lambda_1 - \Lambda_3^{-1}\Lambda_2^T\Lambda_2 > 0 \quad (84.4)$$

should to be satisfied. It is noted that inequality (84.4) can be considered as a constraint on $V(k)$ (see [4] for details).

The next step is to model the dynamic relation between control input and weight dynamics. The nonlinear uncertain model will be considered as

$$V(k+1) = (A_0 + \Delta A_0)V(k) + (B_{01} + \Delta B_{01})u(k) + (B_{02} + \Delta B_{02})V(k-d) + F_0 f_0(V(k)) + B_{03}w(k) \quad (84.5)$$

where $V(k) \in R^{n-1}$ is the independent weight vector, $u(k)$ and $w(k)$ represent the control input and the exogenous disturbances respectively, and $w(k)$ is supposed to be norm bounded. d is the time delay. $A_0, B_{01}, B_{02}, B_{03}, F_0$ are known matrices with compatible dimension. In fact, these matrices can be obtained by either physical principles or an online estimation using the input and the output PDFs (see [1, 2]). $f_0(V(k))$ is a nonlinear function satisfying the globally Lipschitz condition

$$\|f_0(V_1(k)) - f_0(V_2(k))\| \leq \|U_0(V_1(k) - V_2(k))\| \quad (84.6)$$

for any $V_1(k), V_2(k)$, where U_0 is a known matrix. $\Delta A_0, \Delta B_{01}, \Delta B_{02}$ represent the parameter uncertainties and satisfy the following equation

$$[\Delta A_0 \quad \Delta B_{01} \quad \Delta B_{02}] = D_1 F_1(k) [E_1 \quad E_2 \quad E_3] \quad (84.7)$$

where D_1, E_1, E_2, E_3 are known coefficient matrices, $F_1(k)$ is time-varying perturbation matrix and is supposed to satisfy $F_1^T(k)F_1(k) \leq I$.

84.3 Discrete-Time PI Controller Design

Corresponding to (84.3), a desired PDF $g(y)$ can be given by

$$g(y) = (C_0(y)V_g + h(V_g)B_n(y))^2 \quad (84.8)$$

where V_g is the desired weight vector. The tracking objective is to find $u(k)$ such that $\gamma(y, u(k))$ can follow $g(y)$. Denoting the error between the output PDFs and the target PDFs is $\Delta_e(y, k) = \sqrt{\gamma(y, u(k))} - \sqrt{g(y)}$, we can get

$$\Delta_e(y, k) = C_0 e(k) + [h(V(k)) - h(V_g)]B_n(y) \quad (84.9)$$

where $e(k) = V(k) - V_g$. Due to the continuity of $h(V(k))$, $\Delta_e(y, k) \rightarrow 0$ holds as long as $e(k) \rightarrow 0$ (see [4] for details). Thus, the concerned problem will be transformed into a tracking control problem for weight vector $V(k)$.

The discrete-time PI controller is designed as follows:

$$\begin{cases} u(k) = K_P V(k) + K_I \zeta(k) \\ \zeta(k) = \zeta(k-1) + T_0 e(k-1) \end{cases} \tag{84.10}$$

where $T_0 > 0$ is the designed matrix, K_P, K_I represent the control gain to be decided later, $\zeta(k)$ can be seen a designed middle variable. Based on the system (84.5), we introduce a new variable $x(k) = [V^T(k), \zeta^T(k)]^T$. Then the augmented model can be expressed as:

$$\begin{cases} x(k+1) = (A + \Delta A)x(k) + (B_1 + \Delta B)u(k) + (B_2 + \Delta B_d)x(k-d) \\ \quad + Ff(x(k)) + B_3 w(k) + HV_g \\ z(k) = Cx(k) + Dw(k) \\ x(k) = \varphi(k), k \in [-d, 0] \end{cases} \tag{84.11}$$

where $z(k)$ is the measured output, and

$$\begin{aligned} A &= \begin{bmatrix} A_0 & 0 \\ T_0 & I \end{bmatrix}, \Delta A = \begin{bmatrix} \Delta A_0 & 0 \\ 0 & 0 \end{bmatrix}, B_1 = \begin{bmatrix} B_{01} \\ 0 \end{bmatrix}, \Delta B = \begin{bmatrix} \Delta B_{01} \\ 0 \end{bmatrix}, \\ B_2 &= \begin{bmatrix} B_{02} & 0 \\ 0 & 0 \end{bmatrix} \\ \Delta B_d &= \begin{bmatrix} \Delta B_{02} & 0 \\ 0 & 0 \end{bmatrix}, B_3 = \begin{bmatrix} B_{03} \\ 0 \end{bmatrix}, F = \begin{bmatrix} F_0 \\ 0 \end{bmatrix}, H = \begin{bmatrix} 0 \\ -T_0 \end{bmatrix}, \\ f(x(t)) &= [f_0^T(V(t)), 0]^T \end{aligned}$$

It can be seen that the PDF tracking problem can be further reduced to find the following control input

$$u(k) = Kx(k), \quad K = (K_P, K_I) \tag{84.12}$$

to ensure $e(k) \rightarrow 0$ and further obtain satisfactory robustness and state constrained control.

84.4 Main Results

In this section, we will resolve the delay-dependent stability problem, the dynamic tracking control problem, the L_1 robust control problem and the state constrained condition based on the following theorem.

Theorem For the known parameters $\lambda, u_i (i = 1, 2, 3), d^* > 0, a > 0, \varepsilon$ and matrix U , suppose that there exist matrices $N = P^{-1} > 0, \bar{Q} = NQN^T > 0, M = T^{-1} > 0, R$ and parameter $\gamma > 0$, such that the following LMIs

$$\begin{bmatrix} -N + \bar{Q} & 0 & 0 & 0 & 0 & NA^T + R^T B_1^T & N(A - I)^T + R^T B_1^T & NU^T & N\bar{E}_1^T + R^T \bar{E}_2^T & 0 & N \\ * & -\bar{Q} & 0 & 0 & 0 & NB_2^T & NB_2^T & 0 & N\bar{E}_3^T & 0 & 0 \\ * & * & -\lambda^2 I & 0 & 0 & F^T & F^T & 0 & 0 & 0 & 0 \\ * & * & * & -u_1^2 I & 0 & B_3^T & B_3^T & 0 & 0 & 0 & 0 \\ * & * & * & * & -u_2^2 I & H^T & H^T & 0 & 0 & 0 & 0 \\ * & * & * & * & * & -N & 0 & 0 & 0 & \bar{D}_1 & 0 \\ * & * & * & * & * & * & -d^{* - 1} N & 0 & 0 & \bar{D}_1 & 0 \\ * & * & * & * & * & * & * & -\lambda^{-2} I & 0 & 0 & 0 \\ * & * & * & * & * & * & * & * & -\varepsilon^{-2} I & 0 & 0 \\ * & * & * & * & * & * & * & * & * & -\varepsilon^2 I & 0 \\ * & * & * & * & * & * & * & * & * & * & -u_3^2 M \end{bmatrix} < 0 \tag{84.13}$$

$$\begin{bmatrix} M & 0 & MC^T \\ 0 & (\gamma - \alpha x_m^T x_m) I & D^T \\ CM & D & \gamma I \end{bmatrix} > 0 \quad \begin{bmatrix} u_3^2 M & 0 & MC^T \\ 0 & (\gamma - u_2^2 - u_1^2 r) I & D^T \\ CM & D & \gamma I \end{bmatrix} > 0 \quad \begin{bmatrix} \alpha I & I \\ I & M \end{bmatrix} > 0 \tag{84.14}$$

$$\begin{bmatrix} M & MG \\ GM & u_3^2 (u_2^2 + u_1^2 r)^{-1} I \end{bmatrix} \geq 0 \quad \begin{bmatrix} M & MG \\ GM & I \end{bmatrix} \geq 0 \quad \begin{bmatrix} 1 & x_m^T \\ x_m & M \end{bmatrix} \geq 0 \tag{84.15}$$

are solvable, then the system (84.11) under control input (84.12) is the stable and the tracking error convergent to zero. Meanwhile, the system satisfies the disturbance attenuation performance index $\sup_{0 \leq \|w\|_\infty \leq 1} \|z(k)\|_\infty < \gamma$ and the state constrained condition $V^T(k)\Pi_0 V(k) \leq 1$. The PI control gain can be computed via $R = KN^T$ and the time-delay d satisfying $0 \leq d \leq d^*$.

Proof Select a Lyapunov–Krasovskii functions as follows

$$\begin{aligned} V(x(k), k) &= x^T(k)Px(k) + \sum_{i=1}^d x^T(k - i)Qx(k - i) + \sum_{i=-d+1}^0 \sum_{j=k-1+i}^{k-1} y^T(j)Zy(j) \\ &\quad + \sum_{i=1}^{k-1} \left[\|\lambda Ux(i)\|^2 - \|\lambda f(x(i))\|^2 \right] \end{aligned} \tag{84.16}$$

where $y(k) = x(k + 1) - x(k)$. Furthermore, it can be seen that

$$\begin{aligned} \Delta V(x(k), k) &= V(x(k + 1), k + 1) - V(x(k), k) \\ &= \xi^T(k)\Upsilon_1 \xi(k) + u_1^2 \|w(k)\|^2 + u_2^2 \|V_g\|^2 - \sum_{i=1}^d y^T(k - i)Zy(k - i) \end{aligned} \tag{84.17}$$

where $\xi(k) = \begin{bmatrix} x^T(k) & x^T(k - d) & f^T(x(k)) & w^T(k) & V_g^T \end{bmatrix}^T$ and

$$\Upsilon_1 = \begin{bmatrix} \Upsilon_{11} & \bar{A}^T P \bar{B}_2 + d(\bar{A} - I)^T Z \bar{B}_2 & \bar{A}^T P F + d(\bar{A} - I)^T Z F & \bar{A}^T P B_3 + d(\bar{A} - I)^T Z B_3 & \bar{A}^T P H + d(\bar{A} - I)^T Z H \\ * & \bar{B}_2^T P \bar{B}_2 - Q + d\bar{B}_2^T Z \bar{B}_2 & \bar{B}_2^T P F + d\bar{B}_2^T Z F & \bar{B}_2^T P B_3 + d\bar{B}_2^T Z B_3 & \bar{B}_2^T P H + d\bar{B}_2^T Z H \\ * & * & F^T P F - \lambda^2 I + dF^T Z F & F^T P B_3 + dF^T Z B_3 & F^T P H + dF^T Z H \\ * & * & * & B_3^T P B_3 - u_1^2 I + dB_3^T Z B_3 & B_3^T P H + dB_3^T Z H \\ * & * & * & * & H^T P H - u_2^2 I + dH^T Z H \end{bmatrix}$$

$$\begin{aligned} \Upsilon_{11} &= \bar{A}^T P \bar{A} - P + Q + \lambda^2 U^T U + d(\bar{A} - I)^T Z (\bar{A} - I) \\ \bar{A} &= A + \Delta A + B_1 K + \Delta B K, \quad \bar{B}_2 = B_2 + \Delta B_d \end{aligned}$$

From (84.7), we have

$$\begin{aligned} \Delta A &= \begin{bmatrix} \Delta A_0 & 0 \\ 0 & 0 \end{bmatrix} = \begin{bmatrix} D_1 F_1(k) E_1 & 0 \\ 0 & 0 \end{bmatrix} = \begin{bmatrix} D_1 & 0 \\ 0 & 0 \end{bmatrix} \begin{bmatrix} F_1(k) & 0 \\ 0 & 0 \end{bmatrix} \begin{bmatrix} E_1 & 0 \\ 0 & 0 \end{bmatrix} = \bar{D}_1 \bar{F}_1(k) \bar{E}_1 \\ \Delta B &= \begin{bmatrix} \Delta B_{02} \\ 0 \end{bmatrix} = \begin{bmatrix} D_1 F_1(k) E_2 \\ 0 \end{bmatrix} = \begin{bmatrix} D_1 & 0 \\ 0 & 0 \end{bmatrix} \begin{bmatrix} F_1(k) & 0 \\ 0 & 0 \end{bmatrix} \begin{bmatrix} E_2 \\ 0 \end{bmatrix} = \bar{D}_1 \bar{F}_1(k) \bar{E}_2 \\ \Delta B_d &= \begin{bmatrix} \Delta B_{02} & 0 \\ 0 & 0 \end{bmatrix} = \begin{bmatrix} D_1 F_1(k) E_3 & 0 \\ 0 & 0 \end{bmatrix} = \begin{bmatrix} D_1 & 0 \\ 0 & 0 \end{bmatrix} \begin{bmatrix} F_1(k) & 0 \\ 0 & 0 \end{bmatrix} \begin{bmatrix} E_3 & 0 \\ 0 & 0 \end{bmatrix} = \bar{D}_1 \bar{F}_1(k) \bar{E}_3 \end{aligned}$$

Furthermore, invoking Schur complement formula, we can get

$$\Upsilon_1 < 0 \Leftrightarrow \Upsilon_2 + \Delta_1^T F_1^T \Delta_2 + \Delta_2^T F_1 \Delta_1 < 0 \tag{84.18}$$

$$\Upsilon_2 = \begin{bmatrix} -P + Q & 0 & 0 & 0 & 0 & A^T P + K^T B_1^T P & (A - I)^T Z + K^T B_1^T Z & U^T \\ * & -Q & 0 & 0 & 0 & B_2^T P & B_2^T Z & 0 \\ * & * & -\lambda^2 I & 0 & 0 & F^T P & F^T Z & 0 \\ * & * & * & -u_1^2 I & 0 & B_3^T P & B_3^T Z & 0 \\ * & * & * & * & -u_2^2 I & H^T P & H^T Z & 0 \\ * & * & * & * & * & -P & 0 & 0 \\ * & * & * & * & * & * & -d^{-1} Z & 0 \\ * & * & * & * & * & * & * & -\lambda^{-2} I \end{bmatrix}$$

$$\begin{aligned} \Delta_1 &= [\bar{E}_1 + \bar{E}_2 K \quad \bar{E}_3 \quad 0 \quad 0 \quad 0 \quad 0 \quad 0 \quad 0], \\ \Delta_2 &= [0 \quad 0 \quad 0 \quad 0 \quad 0 \quad \bar{D}_1^T P \quad \bar{D}_1^T Z \quad 0] \end{aligned}$$

Supposed that $Z = P$, and based on the inequality $E^T F^T D^T + D F E \leq \varepsilon^2 E^T E + \varepsilon^{-2} D^T D$ and $F_1^T F_1 \leq I$, we can get $\Upsilon_2 + \varepsilon^2 \Delta_1^T \Delta_1 + \varepsilon^{-2} \Delta_2^T \Delta_2 < 0 \Rightarrow \Upsilon_1 < 0$. By multiplying and post-multiplying $diag[P, P, I, I, P, P, I, I, I, I]$ to both side of (84.13), it can be seen the inequality $\Upsilon_1 < diag[-u_3^2 T, 0, 0, 0, 0, 0, 0]$ holds. Based on (84.17), for any $w(k)$ satisfying $\|w(k)\|_\infty \leq 1$, we can get

$$\Delta V(x(k), k) \leq -u_3^2 x^T(k) T x(k) + u_1^2 + u_2^2 r \tag{84.19}$$

where $r = \|V_g\|^2$. Thus, $\Delta V(x(k), k) < 0$ if $x^T(k) T x(k) > u_3^{-2}(u_1^2 r + u_2^2)$ holds. So for any $x(k)$, it can be verified that

$$\begin{aligned} x^T(k)Tx(k) &\leq \max\{x_m^T(k)Tx_m(k), u_3^{-2}(u_1^2r + u_2^2)\} \\ \|x_m\| &= \sup_{-d^* \leq k \leq 0} \|x(k)\| \end{aligned} \quad (84.20)$$

which also implies that the system (84.11) under PI control input is stable.

Similarly with the proof in [4], based on LMIs (84.14), the L_1 norm of the closed-loop system is less than γ . It also means the $\sup_{0 \leq \|w\|_\infty \leq 1} \|z(k)\|_\infty < \gamma$ can be guaranteed. Meanwhile, based on LMIs (84.15), the state constrained condition $V^T(k)\Pi_0V(k) \leq 1$ can be guaranteed (see [2, 4] for details).

In the following, we will consider the dynamic tracking problem. For a couple of $w(k)$ and V_g , suppose that $\theta_1(k)$, $\theta_2(k)$ are two trajectories of the system (84.11). Defining $\sigma(k) = \theta_1(k) - \theta_2(k)$, the dynamics for $\sigma(k)$ can be described as:

$$\begin{aligned} \sigma(k+1) &= [(A + \Delta A) + (B_1 + \Delta B)K]\sigma(k) + (B_2 + \Delta B_d)\sigma(k - \tau) + F(f(\theta_1(k)) \\ &\quad - f(\theta_2(k))) \end{aligned} \quad (84.21)$$

Similarly with (84.16), the Lyapunov–Krasovskii function can be constructed as:

$$\begin{aligned} V(\sigma(k), k) &= \sigma^T(k)P\sigma(k) + \sum_{i=1}^d \sigma^T(k-i)Q\sigma(k-i) + \sum_{i=1}^{k-1} \left[\|\sigma(i)\|^2 - \|\lambda f(\sigma(i))\|^2 \right] \\ &\quad + \sum_{i=-d+1}^0 \sum_{j=k-1+i}^{k-1} [\sigma(j+1) - \sigma(j)]^T(j)Z[\sigma(j+1) - \sigma(j)] \end{aligned} \quad (84.22)$$

Hence, it is easy to see that:

$$\dot{V}(\sigma(k), k) \leq -u_3^2 \sigma^T(k)T\sigma(k) \leq -u_3^2 \lambda_{\min}(T) \|\sigma(k)\|^2 < 0 \quad (84.23)$$

It can be verified that the system (84.21) is asymptotically stable and the state vectors satisfy $\sigma \rightarrow 0$. It means that the system (84.11) under control input also has a unique stable equilibrium point $x^* = [V^{*T}, \zeta^{*T}]^T$. Thus, it can be verified that $\lim_{k \rightarrow \infty} e(k) = \lim_{k \rightarrow \infty} T_0^{-1}[\zeta(k+1) - \zeta(k)] = T_0^{-1}[\zeta^* - \zeta^*] = 0$, which shows that the good tracking performance can be achieved.

84.5 A Simulation Example

Supposing that the output PDFs can be approximated using the following B-spline models described by (84.2) with $n = 3$, $y \in [0, 1.5]$, $i = 1, 2, 3$

$$B_i(y) = \begin{cases} |\sin 2\pi y| & y \in [0.5(i-1); 0.5i] \\ 0 & y \in [0.5(j-1); 0.5j] \quad i \neq j \end{cases}$$

It can be computed that the state constraint matrix satisfies

$$\Pi_0 = \int_0^{1.5} C_0^T(y)C_0(y)dy = \begin{bmatrix} \int_0^{1.5} B_1^2(y)dy & 0 \\ 0 & \int_0^{1.5} B_2^2(y)dy \end{bmatrix} = \begin{bmatrix} 0.25 & 0 \\ 0 & 0.25 \end{bmatrix}$$

The desired PDF $g(y)$ is supposed with $V_g = [1.1, 0.8]^T$, and the dynamic relations between $V(t)$ and $u(t)$ is described by (84.5) with the following selections

$$A_0 = \begin{bmatrix} 0.2 & -0.1 \\ -0.1 & 0.1 \end{bmatrix} \quad B_{01} = \begin{bmatrix} 0 & 0.1 \\ 0.1 & 0 \end{bmatrix} \quad B_{02} = \begin{bmatrix} -0.1 & 0 \\ 0 & -0.1 \end{bmatrix}$$

$$B_{03} = \begin{bmatrix} 0.1 & 0 \\ 0 & 0.1 \end{bmatrix} \quad F_0 = \begin{bmatrix} -0.3 & 0 \\ 0 & -0.3 \end{bmatrix} \quad f(V(t)) = \begin{bmatrix} v_2 - \cos v_1 \\ \sin v_2 \end{bmatrix}$$

By defining $\lambda^2 = 2 \varepsilon^2 = u_1^2 = u_2^2 = u_3^2 = 2$, $\gamma = 6$ and solving the LMIs (84.13–84.15), we can obtain

Fig. 84.1 Reponses of weight vectors

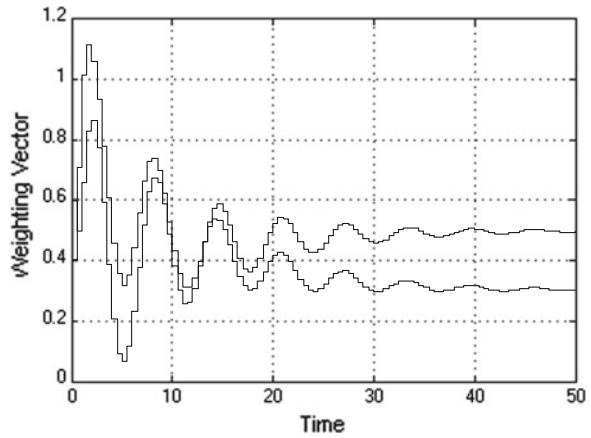
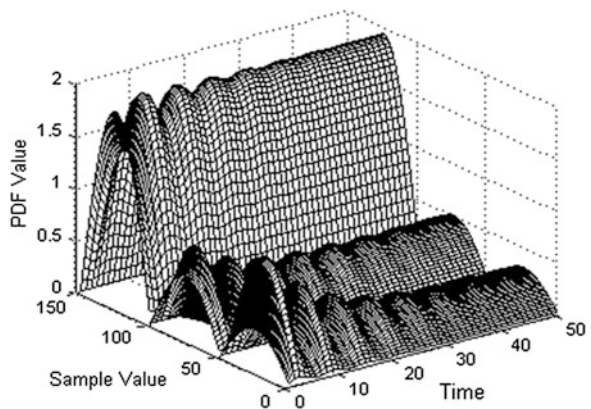


Fig. 84.2 3-D mesh of the PDFs



$$K_p = \begin{bmatrix} 0.4966 & 2.1165 \\ 1.6199 & 0.4966 \end{bmatrix}, K_I = \begin{bmatrix} -0.2691 & -2.2448 \\ -1.9757 & -0.2691 \end{bmatrix}, d^* = 3.84s$$

When the robust PI control law is applied, the responses of the dynamic weight vector are shown in Fig. 84.1. Under the proposed discrete-time PI controller, the 3D mesh plot of the PDFs is showed in Fig. 84.2.

84.6 Conclusion

This paper explores the multi-objective control problem for a class of discrete-time non-Gaussian stochastic processes. By computing the time delay upper bound and the PI control gains, the closed-loop dynamic weight system can be proved as delay-dependent stability and the tracking error can be guaranteed to convergent to zero. Meanwhile, the closed-loop system can also satisfy the disturbance attenuation performance and the state constrained condition.

Acknowledgments This paper is supported by the National Nature Science Foundation of China under Grants (60904030, 61174046, 61203195), China Postdoctoral Science Foundation under Grants (201000470067, 201104541), and a research grant from the Australian Research Council.

References

1. Wang H (2000) Bounded dynamic stochastic systems: modelling and control. Springer, London
2. Guo L, Wang H (2010) Stochastic distribution control system design: a convex optimization approach. Springer, UK
3. Forbes MG, Guay M, Forbes JF (2004) Control design for first-order processes: shaping the probability density of the process state. *J Proc Contr* 14:399–410
4. Yi Y, Guo L, Wang H (2009) Constrained PI tracking control for output probability distributions based on two-step neural networks. *IEEE Trans Circuits Syst I*(56):1416–1426
5. Wang H, Afshar P (2009) ILC-based fixed-structure controller design for output PDF shaping in stochastic systems using LMI techniques. *IEEE Trans Automat Contr* 54:760–773
6. Yi Y, Guo L, Wang H (2009) Adaptive statistic tracking control based on two steps neural networks with time delays. *IEEE Trans Neural Netw* 20:420–429
7. Ding JL, Chai TY, Wang H (2011) Offline modeling for product quality prediction of mineral processing using modeling error PDF shaping and entropy minimization. *IEEE Trans Neural Netw* 22:408–419
8. Gu K, Kharitonov VL, Chen J (2003) Stability of time-delay systems. Birkhauser, Boston
9. Xu S, James L (2007) On equivalence and efficiency of certain stability criteria for time-delay systems. *IEEE Trans Automat Contr* 52:95–101
10. Fang M (2010) Delay-dependent stability analysis for discrete singular systems with time-varying delays. *ACTA Automatic Sinica* 36:751–755
11. Huang H, Feng G (2009) Improved approach to delay-dependent stability analysis of discrete-time systems with time-varying delay. *IET Contr Theor Appl* 4:2152–2159

Chapter 85

Review and Perspective of Theories and Methods About Emergency Evacuation Plans for UMT Station

Yashu Kang, Jie Xu, Limin Jia, Jianyuan Guo and Xin Zhang

Abstract The current situation is that metro system is getting more and more crowded and that passenger distribution and train operation plan are closely related. It is important to study urban rail transit station passenger distribution law, emergency evacuation capacity and emergency plans optimization to generate theories and methods. To ensure that if unexpected accidents happened, emergency plans applicable to the actual situation can be worked out, this research that focused on metro system is meaningful. This work firstly brings up the current situation and existing problems in emergency planning, especially for urban mass transit system. Related researches domestic and overseas are also analyzed. Several important specific factors in urban mass transit system like passenger distribution, evacuation capacity and suitability are taken into consideration. In the end, the thoughts about emergency evacuation planning and theoretic methods are proposed.

Keywords Emergency evacuation · Urban rail transit · Passenger distribution

85.1 Introduction

Urban mass transit (UMT) system is rapidly expanding in recent years, which also brings up the importance of emergency plans. Since metro has been becoming a dense region of passenger flow, abnormal events will easily cause a huge negative social impact. A series of accidents called up the subject of how to deal with

Y. Kang · J. Xu (✉)

State Key Laboratory of Rail Traffic Control and Safety, School of Traffic and Transportation, Beijing Jiaotong University, Beijing, People's Republic of China
e-mail: delkys@foxmail.com

L. Jia · J. Guo · X. Zhang

School of Traffic and Transportation, Beijing Jiaotong University, Beijing, People's Republic of China

unexpected events, such as Tokyo subway gas attack, people crushed to death in Belarus subway, train explosion in Russia subway etc. [1]. However, most urban mass transit stations have features like closeness, high operating efficiency and a big passenger flow volume.

To deal with possible kinds of accidents during daily operation, efficient emergency and rescue plans are essential as well as disaster prevention alarm and disaster relief device [2].

This paper has summarized the domestic and foreign research current situation and development trends and proposed a theory and strategy on handling emergency evacuation in metro stations.

85.2 Existing Problems About Emergency Plans and UMT System

85.2.1 Diversity and Low Execution Rate

There are various contents of urban mass transit system emergency plans, including comprehensive plan, special plan and emergency plan [3]. These three levels mainly contain two kinds of processing strategy: establish the emergency organization and policy and allot responsibility to corresponding function departments; or use the “1 + 4” plan basic structure based on task or function, which is “Emergency plan = basic plan + (emergency function accessories + special risk plan + standard operating procedures + support accessories)” [4]. Yet this current running process is in absence of unified description format. In this way, the structure differences limit the complementary plan-sharing between units and departments [5].

85.2.2 Optimization of Content and Structure

Nowadays many emergency plans are developed by different agencies from various levels in China, the use of resources and responsibilities often have overlap. Human and material resources could be wasted during disposal process, and duties of each department are not clear. In addition there are differences in the format and contents between the format and contents for the same things, lacking plan support of different levels. To provide strong support for emergency decision-making and disposal under uncertain complex conditions, plans should be simple constructed and rigorous.

85.2.3 Passenger Distribution in Subway Station

Urban mass transit (UMT) has been becoming a prior choice for public transportation in recent years in China. It is getting more and more crowded in UMT system. The passenger volume has outnumbered 5 million in Beijing, Shanghai and Guangzhou [6].

In order to reduce the potential risk, usually the station operation management personnel set obstacles to make passengers detour. However, this does not control passenger volume. The big passenger volume and insufficient capacity are the main reasons causing the saturation for subway stations. There have been some researches focused on passengers' behavior or passenger flow assignment in metro system. But studies on passengers' gathering and distribution considering train operation plan are still not enough.

85.2.4 Passenger Evacuation

Urban mass transit stations are in several forms and also have diversified facilities and equipment, and the connections between them are very important [7]. The evacuation capacity of one subway station is determined by the forms, amount, layout of facilities and the connections between them. Some researchers have paid their attentions to design optimization [8], passenger flow organization and simulation [9]. Yet the regularity about different types of stations is not incisive.

85.2.5 Specialized Emergency Plan for UMT System

Relatively speaking, emergencies do not happen much in UMT system, but it could easily develop into public safety incidents with a big influence once it happened. The established plans might not cover all kinds of emergencies, which means the decision-making tends to be made based on intuition and experience. Therefore it is necessary to propose a more specific and scientific emergency plan and disposal theory.

85.3 Overseas and Domestic Research Statuses

At the moment, related researches for the emergency plans with special background are more mature [10–15], which covered relevant fields like emergency plan compilation modeling, drilling simulation, emergency plan evaluation and evacuation simulation etc. Since OASIS designed and developed Common

Alerting Protocol (CAP) in 2005 and Emergency Data Exchange Language (EDXL) in 2008, there have been some achievements on emergency plan compilation for different platforms [16–18]. Also some formalized description and modeling methods based on this standard and time series language [19–21]. The study that brought computational intelligence theory methods into plan management has acquired some achievements in dealing with some typical incidents such as fire [22–24]. Some researchers improved multiple attribute group decision making method [25, 26], based on decision-making process of digital plans [27]. The authors of [28] proposed the emergency plan semantic similarity calculation method based on case similarity and semantic similarity research. Simulation tools were developed based on Agent for design personnel, using complex adaptive system modeling method. The multi-agent based technology in [29] was employed to simulate the crowd behaviors with autonomously acting individuals and used a visualization component to provide 3D free observations for the simulation process.

These researches have given valuable achievement for us. Yet for a closed system like UMT and with its own rules, other factors should be considered. At present the plan formulation and management researches are mainly about fire disaster scenes [24, 30]. In [31] the authors set up evacuation and crowded evacuation model and simulation research. The reporting, processing procedure and methods about traffic accidents were introduced [32]. Also there are researches analyzing about fire prevention, monitoring, early warning, personnel rescue, general disaster fighting and post-treatment disaster [33, 34]. Others have focused on other aspects. In [35] a Cellular Automaton Model was built based on vehicle environmental constraints and passenger flow behavior characteristics.

On the other hand, some researchers focused on urban mass transit operation reliability evaluation technology, emergency mechanism and measures, the classification of plan and framework. A semi-quantitative evaluation was applied to assess UMT safety risk [36]. The authors of [37, 38] designed a preliminary hazard analysis table and established indexes for operation reliability, operational maintainability, and operational availability degrees. They also built object-oriented Petri net model and information framework for UMT network [39]. These works are mainly aimed at hidden danger or risk evaluation and analysis. Relevant results and conclusion could be used for reference in the plan generation theory method. In [40, 41] the authors put forward some existing problems about mechanism in the emergency rescue system.

However, subway station is a relatively closed space with big passenger volume and frequently running trains. In order to study emergency evacuation plan model and theory suitable for urban mass transit system, more research about analyzing the law of passengers' gathering and distribution and station evacuation capacity calculation is still necessary. There have been few papers about passenger distribution analysis based on train operation plan. So far most works are about operation organization or from the point of passenger flow organization.

85.4 Research Trend and Proposed Theory

To improve the effectiveness and efficiency of emergency decision-making and provide theory support, researches on the UMT station incident scene emergency disposal have urgent practical significance and academic significance. Given the current research status, this work proposed several issues and theoretic solution.

85.4.1 Research on Regulation of Station Passenger Distribution

Since it is a specific scene with its own rules, train operation plan should be regarded as an important factor. Firstly the analysis about subway trains' phases (headway phase, dwell phase, separation phase) in both peak and off-peak period is necessary; then establish the train behavior description model in both full load and non-full load state. After summarizing literatures about station passenger flow characteristics and survey, the regulation of station passenger distribution can be concluded.

85.4.2 Research on Dynamic Station Evacuation Capacity

Formalized description about facilities and equipment is basic for presenting the layout of different stations. Based on that evacuation path in a certain kind of station can be calculated. Afterwards it is fluent to consider each facility's evacuation capacity and establish dynamic capacity calculation model, combined with the emergency influence mechanism. This procedure might need computer simulation to implement and prepare for further work.

85.4.3 Research on Emergency Plan Structure for UMT System

Based on existing achievements, it is primary to accomplish emergency plan logical structure division and its relationship quantitative description. In this way, the service function framework, logic framework and physical framework of UMT station emergency plan can be determined. Also analysis on Evacuation emergency plan objects, performance and economic cost of emergency disposal should be carried out before structure optimization. Plans in text form could be considered to transform into optimized model and method.

85.4.4 Research on Passenger Guidance Plan

When emergency occurs, many kinds of uncertain factors like passenger flow, evacuation equipment and environment can lead to or worsen the situation. It is useful to grasp the information of dynamic passenger flow characteristics. Therefore station evacuation capacity and passenger flow characteristic information should be collected to construct a set of events and scene transformation model. Also, Emergency evacuation plan rules should be established to normalize the evacuation and guidance process.

85.4.5 Research on Emergency Plan Suitability Evaluation

The suitability of emergency plan is usually analyzed and evaluated by simulation, examining the effect of emergency disposal. Through the simulations and drills, we can analyze different types of participants, behavior, including operation managers, emergency response team, public security, fire department and so on. Using structured ways to express the solving process, the property for UMT station should be presented more directly.

85.5 Conclusion

This paper aimed at providing programmatic support for salutatory problems like emergency, through in-depth research about related theory method of station passenger flow distribution law and emergency planning suitable for urban rail transit and optimization. Similar researches are not enough in this field. Emergency plan system and management may be quite developed in other fields. However, theories and methods about emergency evacuation plans for Urban Mass Transit system still need to be perfected in further study.

Acknowledgments This work has been supported by National Key Technology Research and Development Programs (2011BAG01B02), Research Funds of State Key Laboratory of Rail Traffic Control and Safety (RCS2009ZT002, RCS2010ZZ002) and the Fundamental Research Funds for the Central Universities (I11JB00070).

References

1. Tsukahara M, Koshiba Y, Ohtani H (2011) Effectiveness of downward evacuation in a large-scale subway fire using fire dynamics simulator. *Tunn Undergr Space Technol* 26:573–581
2. Xu J, Liu CH, Li P (2005) On information sharing platform for urban transit system. *Urban Mass Transit* 8:35–39

3. Wang S, Wang Y (2005) The subway emergency rescue plan research. *Safety* 3:31–33
4. Xie Q (2005) Building emergency rescue system for urban transit systems. *Mod Urban Trans* 2:41–43
5. Gu JH, Xu RH (2006) Design of failure plan management information system for urban rail transit. *Urban Mass Trans* 2:57–59
6. Shi C et al (2012) Modeling and safety strategy of passenger evacuation in a metro station in China. *Saf Sci* 50:1319–1332
7. The fourth railway survey and design of urban construction court, The subway station structure design guidelines, 2005
8. Yao GW (2008) Study on structure and installation design optimizing of metro station based on simulation of the passenger evacuating. Beijing Jiaotong University, Beijing
9. Chow W, Candy M (2008) Waiting time in emergency evacuation of crowded public transport terminals. *Saf Sci* 46:844–857
10. Crichton M, Flin R (2001) Training for emergency management: tactical decision games. *J Hazard Mater* 88:255–266
11. Chiu Y, Zheng H (2007) Real-time mobilization decisions for multi-priority emergency response resources and evacuation groups: model formulation and solution. *Trans Res Part E* 43:710–736
12. Nikos Z, Nicolas M (2007) Design of formative evacuation plans using agent-based simulation. *Saf Sci* 45:920–940
13. Yoon S et al (2008) Transportation security decision support system for emergency response: a training prototype. *Decis Support Syst* 46:139–148
14. Yuan J, Fang Z, Wang Y (2009) Integrated network approach of evacuation simulation for large complex buildings. *Fire Saf J* 44:266–275
15. Han F, Qin L, Ma XY (2010) Development of emergency response plan complexity evaluation system. *Comput Syst Appl* 19:12–16
16. Xu W (2008) Modelling emergency response processes: comparative study on OWL and UML. In: Proceedings of the joint ISCRAM-CHINA and GI4DM conference Harbin. August 2008
17. Wang WJ, Yang P, Dong CX (2009) Study and application of emergency case ontology model. *J Comput Appl* 29:1437–1445
18. Onorati T, Malizia A, Diaz P et al. (2010) Interaction design for web emergency management information systems. In: Proceedings of the 7th international ISCRAM conference Seattle, vol 5, pp 1–10
19. Hernandez JZ, Serrano JM (2001) Knowledge-based models for emergency management systems. *Expert Syst Appl* 20:173–186
20. Li X, Liu G, Ling A, et al. (2008) Building a practical ontology for emergency response systems. In: 2008 international conference on computer science and software engineering, pp 222–225
21. Jiang XY, Chen WP, Ma LH (2010) Design and realization of emergency plan optimization structure based on arena. *Comput Eng Des* 29:2116–2119
22. Podofillini L, Zio E, Vatn J (2006) Risk-informed optimisation of railway tracks inspection and maintenance procedures. *Reliab Eng Syst Saf* 91:20–35
23. Kaakai F, Hayat S, Moudni A (2007) A hybrid Petri nets-based simulation model for evaluating the design of railway transit stations. *Simul Model Pract Theor* 15:935–969
24. Zarboutis N, Marmaras N (2007) Design of formative evacuation plans using agent-based simulation. *Saf Sci* 45:920–940
25. Sell C, Braun I (2009) Using a workflow management system to manage emergency plans. In: Proceedings of the 6th international ISCRAM conference, Gothenburg. May 2009
26. Dong CX, Wang WJ, Yang P (2010) Emergency plan system ontology and its application. *Comput Eng Appl* 46:235–238
27. Rosmullera N, Beroggib G (2004) Group decision making in infrastructure safety planning. *Saf Sci* 42:325–349

28. Jiang P (2009) Research on arithmetic of similarity of emergency case base-on Ontology. *J Nanchang Col* 3:159–161
29. Tang F, Zhang X (2008) A GIS-based 3D simulation for occupant evacuation in a building. *Tsinghua Sci Technol* 13:58–64
30. Manca D, Brambilla S (2011) A methodology based on the analytic hierarchy process for the quantitative assessment of emergency preparedness and response in road tunnels. *Transp Policy* 18(5):657–664
31. Fang WF (2003) The fire evacuation of cellular automata model research. University of science and technology of China, China
32. Xu ZX (2006) Urban mass transit security guarantee system design. Chang'an University
33. Raman M, Ryan T, Olfman L (2006) Knowledge management system for emergency preparedness: an action research study. In: *Proceedings of the 39th Hawaii international conference on system sciences*
34. Jiang YJ, Yang QX (2003) Primary study on disaster prevention and rescue system for subway. *Underground Space* 23:427–430
35. Victor J, Jeffrey L, Adler (2001) Cellular automata micro simulation for modeling bi-directional pedestrian walkways. *Transp Res Part B* 35:293–312
36. Jacinto C, Silva C (2010) A semi-quantitative assessment of occupational risks using bow-tie representation. *Saf Sci* 48:973–979
37. Zhao HX (2006) Reliability index and its calculation for UMT safety. *Urban Mass Transit* 3:44–46
38. Zhao HX (2006) Method for constructing reliability model of urban mass transit based on petri net. *J Tongji Univ (Nat Sci)* 34:355–358
39. Zhao HX, Yu SC (2006) Safety and reliability of urban mass transit system. *Urban Mass Transit* 1:7–10
40. Qin Y, Wang Z, Jia LM (2007) Research on the system framework and application of railway transportation emergency management. *J Chin Saf Sci* 17:57–65
41. Zhang DY, Jin J, Yang JS (2004) The safety research system of urban rail transit. *Urban Rapid Rail Transit* 4:1–3

Chapter 86

The Allocation of Berth and Quay Crane by Using a Particle Swarm Optimization Technique

Chutian Yang, Su Wang and Jun Zheng

Abstract This paper discusses the problem of berths and quay crane allocation in container terminal, while establishes a mixed integer linear programming model. A heuristic algorithm based on particle swarm optimization is proposed, which effectively reduces dimension of particle swarm optimization. Simulation experiments show that the algorithm converges fast and performs efficiently.

Keywords Container terminal · Berth allocation · Quay crane allocation · Particle swarm optimization

86.1 Introduction

Container transportation system has been an important issue of modern logistics. A container terminal system requires effective decision making processes to manage and allocate space resources as well as utilize transshipment equipments. A well-arranged solution on berth and quay crane allocation could obviously shorten the overall shipping service time while reduce operating costs and improve the efficiency of cargo-handling, which leads to higher customers' satisfaction and profitability.

Generally, berth allocation is to determine the berthing time and location of arriving vessel, while quay crane assignment has great impact on the service time of a vessel. As both scheduling process can be influenced by each other during plan making, these two resources should be considered simultaneously.

In terms of the berth allocation, many researchers have put great effort on the study. Lim [1] proved that berth allocation problem in container terminal is an

C. Yang (✉) · S. Wang · J. Zheng
Computer Center, School of Science and Engineering, East China Normal University,
3663 N. Zhongshan Rd, Shanghai, China
e-mail: yct21tok@gmail.com

NP-Hard problem. Wang and Lim [2] established a model where the docks were divided into discrete berth, and ships can't across multiple berth. Kim and Moon [3] find a solution to manage berth scheduling in continuous wharf. Kim and Park [4] developed a distributed optimization model using branch and bound and greedy randomized adaptive search procedure method to solve the problem. Bierwirth and Meisel [5] adopted a pruning method to optimize the algorithm.

Park and Kim [3] firstly gave an allocation method taking berth and quay crane scheduling as a whole process. Lokuge and Alahakoon [6] established a model where both issues were functionally integrated. Lee et al. [7] presented a feedback integration to solve the problem.

Currently, most studies consider berth and quay crane allocation as two independent processes, and few approaches the allocation problem in continuous berth. Hence, an algorithm is proposed to solve the problem of continuous berth and quay crane allocation in this paper.

This paper is organized as follows: The next section provides the problem formulation, followed by an algorithm based on particle swarm optimization of Sect. 86.3. The computational results are given in Sect. 86.4. The final section concludes the paper.

86.2 Problem Formulations

The goal of studying berth and quay crane allocation is to determine the berth position and amount of quay crane to be assigned when a vessel arrives. The assumptions of the model are presented as follows:

1. All berth and quay cranes are available at the beginning of time horizon. The arrival time of all vessels is known in advance.
2. The planning coordinate axis is divided into several equal time segments, which should be well determined to balance accuracy against speed.
3. The handling time of each vessel depends on the number of quay crane engaged in handling time.
4. All vessels can be served only once, which means service will not be disrupted before it is completed.
5. When a new vessel berths, quay cranes in service can be reassigned among ships if necessary. Quay cranes can move along the guide rail to start or resume service for another vessel, and the transferring time is ignored in order to bring more flexibility into the system.
6. As too few quay crane allocated delays the leaving time and too many may overpass the length of the vessel, a minimum and a maximum number of quay cranes are imposed for each vessel.
7. Each ship has a due time and a least-cost berthing position. When it delays or berths in other position, a penalty is cost.

The notations used of this model are summarized as follows:

Parameters:

L_w	The wharf length.
N	The number of vessels.
Q	The number of quay cranes.
T	The number of time periods.
$V = \{1,2,\dots,N\}$	The set of vessels.
$T = \{1,2,\dots,H\}$	The set of time periods.
A_i	The arrival time of vessel i .
L_i	The length of vessel i , including safety distance.
R_i^{\max}	The maximum number of quay cranes that can be assigned to vessel i .
R_i^{\min}	The minimum number of quay cranes that can be assigned to vessel i .
D_i	The due time for the departure of vessel i .
C_i	The penalty cost of vessel i per unit of time of delay beyond the due time.
B_i	The least-cost berthing position of vessel i .
F_i	The penalty cost of vessel i per unit distance between its position and its least-cost berthing position.
W_i	The task handling time of vessel i by single quay crane.
J_i	The priority of vessel i .
M	A sufficiently large positive value.

Decision variables:

p_i	The berth position of vessel i .
q_i	The amount of quay crane assigned to vessel i .
s_i	The processing start time of vessel i .
e_i	The processing end time of vessel i .
u_{it}	=1, if vessel i is processed in time period t ; = 0 otherwise.
$x_{ii'}$	=1, if the right side of vessel i is on the left of left side of vessel i' .
$y_{ii'}$	=1, if vessel i starts processing after vessel i' ends processing.

The berth and quay crane of problem is subject to the following constraints:

$$Minimize \left\{ \sum_{i \in V} B_i |p_i - b_i|^+ + \sum_{i \in V} C_i |e_i - D_i|^+ \right\} \tag{86.1}$$

$$\sum_{i \in V} q_i \cdot u_{it} = Q \quad \forall t \in T \tag{86.2}$$

$$q_{it} \cdot (e_i - s_i + 1) \geq W_i \quad \forall i \in V \tag{86.3}$$

$$q_i \leq R_i^{\max} \quad \forall i \in V \quad (86.4)$$

$$q_i \geq R_i^{\min} \quad \forall i \in V \quad (86.5)$$

$$t \bullet u_{it} \leq s_i \quad \forall i \in V, \forall t \in T \quad (86.6)$$

$$t \bullet u_{it} \leq e_i \quad \forall i \in V, \forall t \in T \quad (86.7)$$

$$p_i + l_i \leq p_{i'} + (1 - x_{i'i'}) \cdot M \quad \forall i \in V, \forall t \in T \quad (86.8)$$

$$e_i \leq s_{i'} + (1 - y_{i'i'}) \cdot M \quad \forall i, i' \in V \quad (86.9)$$

$$x_{i'i'} + y_{i'i'} + x_{i'i} + y_{i'i} \geq 1 \quad \forall i, i' \in V \quad (86.10)$$

$$0 \leq p_i \leq L_w - L_i \quad \forall i \in V \quad (86.11)$$

$$A_i \leq s_i \quad \forall i \in V \quad (86.12)$$

$$x_{i'i'}, y_{i'i'} \in \{0, 1\} \quad \forall i, i' \in V, \forall t \in T \quad (86.13)$$

$$q_i \in \text{Integer} \quad \forall i \in V \quad (86.14)$$

The objective function (86.1) is to minimize the sum of cost that results from non-optimal berthing location and penalty cost resulting from the delay in the departure of vessels. Constraint (86.2) implies that at any time the total number of quay crane in service will not exceed amount of quay crane at container terminal. Constraint (86.3) ensures vessel i will not depart until service is over. Constraints (86.4 and 86.5) require that number of quay crane assigned to vessel i should meet vessel's limit of quay crane. Constraints (86.6 and 86.7) is the definition of u_{it} . Constrains (86.8–86.10) guarantee that each pair of vessels would not overlap in space or time horizon. Constraint (86.11) ensures the berthing position of each vessel is in the port. Constraint (86.12) states that a vessel should begin its service after it arrives.

86.3 Simulation Based PSO Search

Particle swarm optimization is a computational method that optimizes a problem by iteratively trying to improve a candidate solution with regard to a given measure of quality. It was originally intended for simulating social behavior as a stylized representation of the movement of organisms in a bird flock or fish school. PSO optimizes a problem by having a population of candidate solutions, here dubbed particles, and moving these particles around in the search-space according to simple mathematical formulae over the particle's position and velocity. Each particle's movement is influenced by its local best known position called p_{best} and is also guided toward the best known positions in the search-space called g_{best} ,

which are updated as better positions are found by other particles. This is expected to move the swarm toward the best solutions. The Eqs. (86.15 and 86.16) shown below is particle fitness update and calculate function:

$$v_{i+1} = \omega * v_i + C_1 * \text{rand}() * (p_{\text{best}} - x_i) + C_2 * \text{rand}() * (g_{\text{best}} - x_i) \quad (86.15)$$

$$x_{i+1} = x_i + v_{i+1} \quad (86.16)$$

The acceleration constants C1 and C2 in Eq. (86.15) represent the weighting of the acceleration terms that pull each particle towards p_{best} and g_{best} positions, while ω represents the inertial weight factor that keeps particles move smoothly.

The problem of berth and quay crane allocation is formulated as a mixed-integer linear program according to constraints (86.1)–(86.14). We adopted a simulation based particle swarm optimization procedure to search for robust solutions.

86.3.1 Particle Representation

The particle representation in our problem consists of two kinds of dimensions: the discrete dimensions including vessel positions, and continuous dimensions including assigned quay crane amount. Figure 86.1 is a chromosome example with 4 ships.

In the iteration of algorithm, the discrete dimensions and continuous dimensions in a particle are computed and updated separately. Equations (86.15 and 86.16) can be used directly when calculate and update particle positions in continuous dimension, while the discrete dimensions of particle should be put from real space R^N to integer space I^N , which can be implemented by directly fetch the integer part of particle position or use round function.

As the vehicle of a particle is calculated, the fit value can be computed by simulating service of this vessel based on the position of particles calculated above. Then g_{best} and p_{best} can be updated and thus an iteration of particle swarm optimization is done.

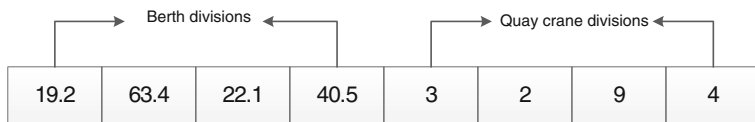


Fig. 86.1 Dimensions of particle

86.3.2 Generation of Service Sequence

After the position of a particle is calculated, the service sequence of vessels can be computed by topological sort.

A directive graph G can be built with each vertical represents a vessel. When there is relationship between vessel i and vessel j that guarantees that:

1. The position of vessel i overlaps with vessel j , or
2. Vessel i arrives early than vessel j ; or they both arrives at exactly same time, and the priority of vessel i is higher than vessel j .
3. Then an edge from vertical i points to vertical j is added to the graph G .

After topological sorted in graph G , the final sequence of vertical can be used as the service sequence of vessels. Figure 86.2 shows a graph G build with rules shown above.

The result of topologic sort is given in Fig. 86.3, that the final service sequence is vessel 1, vessel 5, vessel 4, vessel 6, vessel 2 and then vessel 3.

86.3.3 Simulation of Serve Process

According to the service sequence calculated above, the serving process of each vessel can be simulated. When vessel i reached the port, a beginning time segment is searched to ensure:

1. All vessels berths earlier that is overlapped with vessel i in space horizon should end its service before this time segment.
2. There should be a continuous time period after this time segment that enough quay crane can be assigned to vessel until service ends.

Fig. 86.2 Generated directive graph G

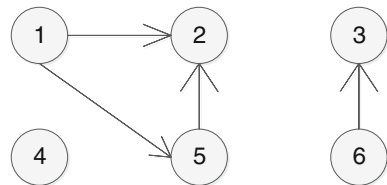


Fig. 86.3 Topologic sorted sequence of graph G

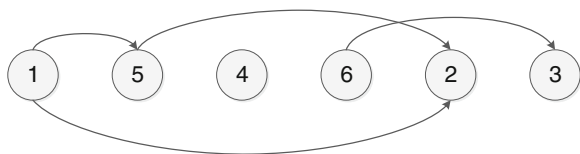
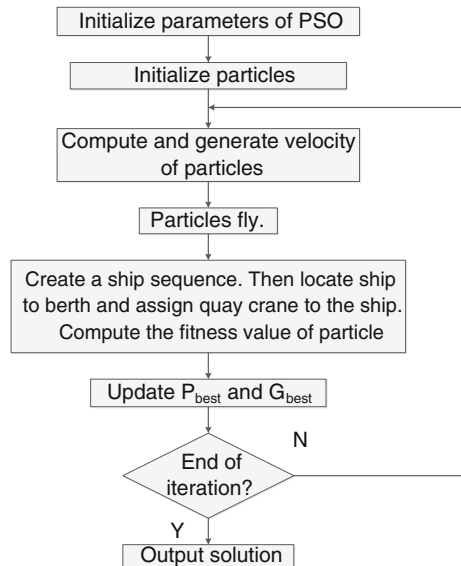


Fig. 86.4 Procedure of simulation based particle swarm optimization



86.3.4 Simulation Based Particle Swarm Optimization

As summarized in Fig. 86.4, a simulation based particle swarm optimization can be applied to berths and quay cranes allocation problem as follow steps:

1. Choose parameters appropriately and read data of the problem, including arrive time, length, maximum and minimum assign amount, workload, priority, favorite berth position of each vessel.
2. Initialize particle positions. Randomly choose real numbers that satisfy constrains (86.1–86.14) as initial value of each particle dimension.
3. Calculate the velocity of continuous and discrete dimensions separately according to Eq. (86.15), and then move particle using Eq. (86.16).
4. Create the service sequence according to particle positions generated above and compute the fitness value of each particle.
5. Update p_{best} and g_{best} as fitness value. End the process if a certain condition is satisfied, or else the iterations of algorithm should be continued.

86.4 Simulated Experiments

In order to verify the particle swarm optimization, we used a data set for 8 ships from a port, as shown in Table 86.1. The initial population size of particles is 50 and the maximum iteration amount is 100. The program is built using gnu compiler collection and run on Intel Core i3 2.13 GHZ CPU, GB RAM.

The result of search is shown in Table 86.2 and Fig. 86.5 shows a detailed solution of berth and quay crane assignment. The total completion time is about 6 s.

Table 86.1 Experimental data

Vessel ID	Arrive time	Task handling time	Least-cost berthing position	Due time for departure
1	2	16	300	7
2	5	18	280	13
3	4	14	0	6
4	0	17	60	5
5	6	11	0	8
6	16	13	370	20
7	6	9	200	10
8	19	27	50	23

Table 86.2 The assignment of each vessel

Vessel ID	Berth assignment	Quay crane assignment
1	309.2	4
2	296.8	3
3	0.1	4
4	53.2	6
5	0	5
6	370.4	6
7	198.7	2
8	63.2	7

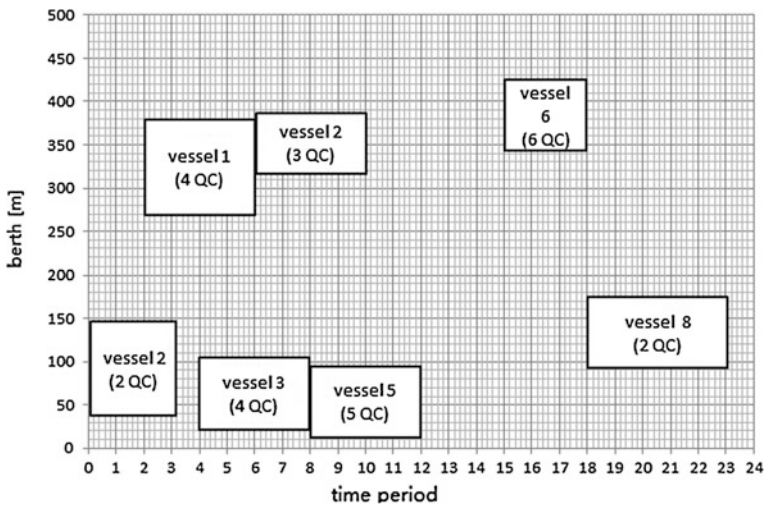


Fig. 86.5 A detailed solution of berth and quay crane assignment

Table 86.3 Convergence of algorithm

Vessel amount	Total completion time(s) of algorithm
32	17.581
17	6.894
46	24.727
37	18.342

Table 86.3 shows the convergence curve of the completion time with number of vessels changes. It is clear that the completion time of particle swarm optimization grows linearly as vessel amount increases, which suggests strong stability.

86.5 Conclusions

In this paper, a particle swarm optimization algorithm is proposed to solve the berth and quay crane allocation problem. As there is inherent interrelation-ship between the allocation and utilization of berth and quay cranes when performing quay side operations, the operational berth and QC schedules are simultaneously considered in decision making process. A mixed integer linear programming model is developed to formulate the problem. To solve the model, an effective search technique is proposed to obtain berth and quay crane allocation solution.

Experiment shows that the method could make best decisions in most cases, which improving efficiency in container terminals. Due to short computational time and stable convergence, this algorithm has been found a promising approach in the integration of berth planning with quay crane scheduling.

References

1. Lim A (1998) The berth planning problem. *Oper Res Lett* 22(2):105–110
2. Wang F, Lim A (2007) A stochastic beam search for the berth allocation problem. *Decis Support Syst* 42(4):2186–2196
3. Kim KH, Moon KC (2003) Berth scheduling by simulated annealing. *Transp Res Part B: Methodol* 37(6):541–560
4. Kim KH, Park YM (2004) A crane scheduling method for port container terminals. *Eur J Oper Res* 156(3):752–768
5. Bierwirth C, Meisel F (2009) A fast heuristic for quay crane scheduling with interference constraints. *J Sched.* doi:[10.1007/s10951-009-0105-0](https://doi.org/10.1007/s10951-009-0105-0)
6. Lokuge P, Alahakoon D (2007) Improving the adaptability in automated vessel scheduling in container ports using intelligent software agents. *Eur J Oper Res* 177(3):1985–2015
7. Lee D-H, Song L, Wang H (2006) Bilevel programming model and solutions of berth allocation and quay crane scheduling. In: Proceedings of 85th annual meeting of transportation research board (CD-ROM). Annual meeting of transportation research board. Washington

Chapter 87

Optimal Trajectory Planning of Gaze Shifts Based on Modified Simulated Annealing Algorithm

Ming Zeng, Zhanxie Wu, Haiyan Jia, Qinghao Meng and Hao Yang

Abstract Optimal trajectory planning of gaze shifts plays an important role in modeling visual attention mechanisms. In this paper, a new and simple technique based on the graph theory for imitating attention shifts of the human vision system is proposed. Firstly, the focuses of attention in a scene are achieved using an integrated technique which combines the SIFT algorithm with the JSEP segmentation algorithm. Then, we propose a modified simulated annealing algorithm in which the optimizing index is not distance but the connection loss cost which can be used to mediate two conflicted rules (i.e. the rule of proximity preference and the rule of descending order) of gaze shifts. Finally, the modified simulated annealing algorithm is adopted to obtain the optimal shift trajectory. Experimental results show that the proposed method agrees well with the basic rules of gaze shifts compared with the traditional “Winner-Take-All” method.

Keywords Trajectory planning · Gaze shifts · Focus of attention · Connection loss cost · Simulated annealing

87.1 Introduction

The human vision system has a specialized ability of selective visual attention to rapidly detect potentially relevant parts in a scene. From an evolutionary viewpoint, this rapid orienting capability is critical in allowing living systems to quickly become aware of possible preys, mates or predators in their cluttered visual world. Like in human vision, visual attention can play an important role in computer vision, given the high computational complexity of typical tasks. Thus, the paradigm of computational visual attention has been widely investigated

M. Zeng (✉) · Z. Wu · H. Jia · Q. Meng · H. Yang
Institute of Robotics and Autonomous Systems (IRAS), School of Electrical Engineering and Automation, Tianjin University, No.92 Weijin Avenue, Nankai District, Tianjin, China
e-mail: zengming@tju.edu.cn

during the last two decades, and numerous computational models of visual attention have been suggested [1].

In order to model visual attention mechanisms, at least two problems must be solved here. The one is how to evaluate the saliency of different regions, i.e., detecting regions of interest (ROI). The second problem is the gaze shift problem, i.e., how does the processing focus shift to another location. The previous researches are mainly focused on the former problem. Here, we introduce some state-of-art works on this topic. In most cases, a likely ROI candidate generally has visually and structurally distinctive features compared with its neighboring region. Therefore, some structural characteristics, such as contrast, color, region size and shape, distribution of contours or texture pattern, can be used to detect the ROIs. Most of the developed algorithms are based on this assumption. A selective visual attention model proposed by Aziz and Mertsching computes five properties for each region: color, size, symmetry, orientation and eccentricity. The rarity or contrast of these values determines the feature saliency values, which are then combined into a single salience map [2]. Inspired by the behavior and neuronal architecture of the early primate visual system, Itti and Koch used the strategy of multiscale centre-surround contrast in terms of intensity, color and orientation to find several salient locations in a scene [3]. Kootstra and Schomaker [4] used local symmetry operators to measure saliency, which they found to be a better match to experimental human data than Itti and Koch's contrast-based saliency measure. The integration of bottom-up, image-driven cues and perceptual properties of the human visual system (HVS) is crucial for the selection of salient locations. Therefore, Zeng et al. [5] propose a new model that takes both two factors into consideration. Zeng et al. [6] also proposed a new optimal feature gain modulation strategy to maximize the relative salience of the target, in which the top-down weight on a feature map depends on its stimulation intensity ratio (SIR) between the target and the distractors. Although a considerable amount of research has been done on ROI detection, there still does not exist an "off-the-shelf" solution applicable to all types of images. Here, in this paper, the focuses of attention in a scene are detected using an integrated technique which combines the SIFT algorithm with the JSEP segmentation algorithm.

There are some psychophysical and physiological theories that attempt to explain why and how attention is shifted as well as how attention is moved through space [7–9]. Here, we list four basic rules of gaze shifts.

- **Single focus:** Physical properties of the retina imply a single fixation point at a time, and FOA is therefore assumed to be at a single location.
- **Inhibition of return:** Psychophysical evidence shows that there is a tendency of delaying the return of FOA to a position recently attended to.
- **Descending order:** The selection process shifts preferentially to the next most conspicuous location.
- **Proximity preference:** The selection process shifts preferentially to conspicuous locations in the neighborhood of the presently selected location, rather than to the global maximum independent of any locality considerations.

Although different rules of gaze shifts have been found from numerous psychophysical and physiological experiments, how to integrate these different rules into a computational visual attention model is still challenging. Few researches are focused on this topic. The most widely used method is the “Winner-Take-All” (WTA) technique in the Itti’s visual attention model. However, The testing results show that the WTA method does not abide by some basic rules, i.e., descending order and proximity preference. Here, we propose a modified simulated annealing algorithm in which the optimizing index is not distance but the connection loss cost which can be used to mediate two conflicted rules (i.e. The rule of proximity preference and the rule of descending order) of gaze shifts.

The remainder of this paper is organized as follows. [Section 87.2](#) will describe the proposed trajectory planning scheme. Experimental results are reported in [Sect. 87.3](#). Finally, the conclusions are drawn in [Sect. 87.4](#).

87.2 Optimal Trajectory Planning of Gaze Shifts

87.2.1 *Extract the Focus of Attention*

As abovementioned, there are two basic issues to simulate the visual attention mechanisms of the human vision system, i.e., detecting the ROI and planning the trajectory of gaze shifts. Here, we propose a simple model for detecting regions of interest (ROI) inspired from keypoint analysis [10]. We adopted the idea that the appearance of an interest region can be well characterized by the distribution of its local features (e.g., keypoints). ROI detection involves several steps as follows: the input image is first decomposed into a set of low-level vision feature maps (e.g., intensity map, and two double-opponent color maps). Extreme in difference of Gaussian (DoG) scale space are then calculated for detecting the keypoints within each feature maps. The location and scale information of keypoints are integrated to create three conspicuity maps. These conspicuity maps are normalized and summed into an overall saliency map. Unlike other works, our method adds a step of image segmentation using the JSEG method. The benefit of this process is that our method can effectively determine the number of attention focus, and maintain a certain distance between the focuses of attention, and avoid refocusing the same object or region several times. Finally, the focuses of attention in a scene are achieved using an integrated technique which combines the SIFT algorithm with the JSEP segmentation algorithm.

87.2.2 *The Connection Loss Cost Based on F-Measure*

As abovementioned, there are four basic rules of gaze shifts, i.e., single focus, inhibition of return, descending order and proximity preference. Next, we attempt

to integrate the four rules to plan the trajectory. If not considering the rule of descending order, the gaze shift problem can be solved using the algorithm of Traveling Salesman Problem (TSP). Unfortunately, the rule of descending order and the rule of proximity preference are usually conflicted. Therefore, we introduce a new concept, i.e., connection loss cost based on the F-measure to balance two conflicted rules. The goal of the traditional Traveling Salesman Problem (TSP) is to minimize the total distance. Similarly, the goal of the modified TSP is to minimize connection loss cost. The benefit of this process is that the algorithms of TSP can be modified to solve the gaze shift problem. Among the numerous algorithms of TSP, we choose the simple, robust method called the simulated annealing algorithm.

The F-measure is a comprehensive evaluation index according to the precision (P) and recall rate (R). The specific definition is as follows:

$$F = \frac{2PR}{P + R} \quad (87.1)$$

In order to reflect the differences of importance between P and R, Chinchor gave a complete definition of F-measure in 1992. The formula is as follows:

$$F_{\beta} = \frac{(\beta^2 + 1)PR}{\beta^2 P + R} \quad (\beta \geq 0) \quad (87.2)$$

We use the formula (87.2) to reconcile the rules of “descending order” and “proximity preference” as follows:

$$P(i, j) = \frac{d(i, j)}{\max_dist} = \frac{\sqrt{(x_i - x_j)^2 + (y_i - y_j)^2}}{\max_dist} \quad (87.3)$$

where $P(i, j)$ represents the distance factor, the $d(i, j)$ represents the Euclidean distance between the FOA and the \max_dist represents the maximum of the distance. It is obvious that the parameter $P(i, j)$ considers the rule of proximity preference.

$$R(i, j) = \frac{|S_i - S_j|}{num - 1} \quad (87.4)$$

where $R(i, j)$ is the saliency difference of two FOAs. The parameter num is the number of FOAs. It is obvious that the parameter $R(i, j)$ considers the rule of descending order. Note that S_i and S_j are ranking values of saliency amplitude rather than the original values of saliency. The ranking value of a FOA with maximum saliency is set as num . Correspondingly, the ranking value of a FOA with smallest saliency is set as 1.

The value of β adjusts the degree of importance between the distance factor and the saliency factor. When the value of β is 1, the two factors play the same role; when the value of β is greater than 1, the saliency factor plays a more important role than the distance factor; when the value of β is less than 1, the distance factor

plays a more important role than the saliency. Particularly, when the value of β is 0, it only considers the distance factor, which is the same with the TSP. It should be pointed out that the standard TSP is a special case of our new technique.

87.2.3 Optimal Trajectory Planning of Gaze Shifts Based on Modified Simulated Annealing Algorithm

The principle of simulated annealing algorithm (SA) is very simple. Furthermore, it not only has the asymptotic convergence property, but also can get the optimal solution which is nothing to do with the selection of the initial solution. Therefore, this paper selects the SA to solve the problem of optimal trajectory planning of gaze shifts.

Because of the differences between the planning of optimal trajectory and the TSP, the functions of the SA need making some adjustments in the following three parts. Firstly, since the FOA with the strongest saliency is the first viewpoint to be noticed, so the starting point of the trajectory of gaze shifts should be fixed. Then, in order to reconcile the two conflicted rules, i.e., descending order and proximity preference, the optimal index should be changed from the distance to the connection loss cost. Correspondingly, the new objective function value of the SA is the sum of connection loss cost rather than the total distance. Finally, the trajectory of gaze shifts starts from the initial focus of attention and then through all different FOAs, without going back to the starting point. So the objective function of the SA should be removed the connection loss cost between the finally noticed focus and the starting point. In this way, we can obtain the optimal trajectory of gaze shifts.

87.3 Experimental Results

This section will compare the experimental results in two aspects. The first is the trajectories of gaze shifts when we adjust the parameter β with different values, and the next is the trajectories obtained by our proposed method and WTA method. In order to better explain the experimental results, a number of measured parameters are compared. These parameters are described as follows:

- Total connection loss cost: F

F represents the sum of the connection loss cost between the focuses in the trajectory of gaze shifts. Usually, the trajectory with the smallest F is more consistent with the human visual features.

- Total distance: D

D is the sum of the Euclidean distances between the focuses in the trajectory of gaze shifts. And the greater value of the D , the longer distance this trajectory passes by.

- Total loss of saliency: S

S is the accumulation of the different value of saliency between two adjacent focuses of attention in the trajectory of gaze shifts. The trajectory with the smaller S indicates that it is likely abide by the rule of descending.

- The trajectory of saliency: *Route*

Route is the order of scanning every FOA on the trajectory of gaze shifts according to its saliency.

87.3.1 Compare the Trajectories of Gaze Shifts with Different Values of β

As abovementioned, the parameter β can be used to balance the influence of two conflicted factors. Here, we provide some comparing results with different values of β , as shown in Fig. 87.1 in which the values of β are set as 0, 0.5 and 100

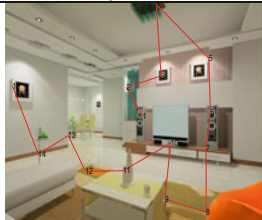
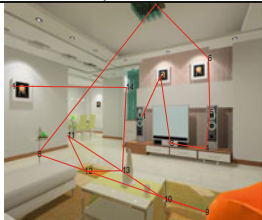
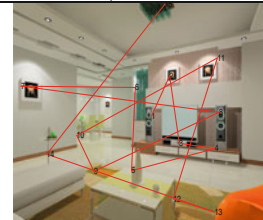
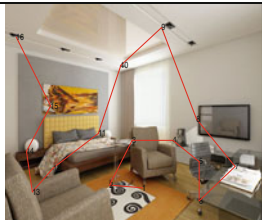
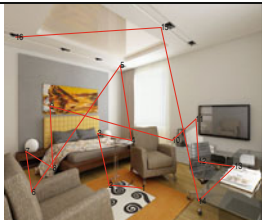
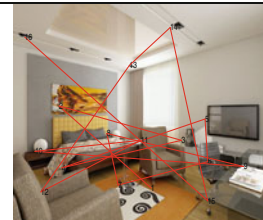
$\beta=0$	$\beta=0.5$	$\beta=100$
		
F=2.91 D=1134 S=70 Route:15-10-14-1-5-8-12-3-4-13-11-7-6-2-9	F=2.8 D=1872 S=26 Route:15-14-13-12-8-5-1-2-3-4-6-7-11-10-9	F=2.84 D=2626 S=14 Route:15-14-13-12-11-10-9-8-7-6-5-4-3-2-1
		
F=3.03 D=1270 S=91 Route:16-10-6-14-11-2-8-12-3-4-9-13-5-7-15-1	F=2.73 D=1799 S=39 Route:16-10-9-6-4-5-7-13-15-14-12-11-8-2-3-1	F=3.08 D=3320 S=15 Route:16-15-14-13-12-11-10-9-8-7-6-5-4-3-2-1

Fig. 87.1 The different trajectories with different values of β

respectively. Note that when the value of β is 0, it only considers the distance factor. When the value of β is 0.5, the distance factor plays a more important role than the saliency factor. When the value of β is 100 ($\beta \gg 1$), it almost only considers the saliency factor.

From the Fig. 87.1, it can be seen that when the adjustment parameter β is set as 0, the trajectory is very simple, more importantly, the corresponding evaluation parameter D is the smallest. Note that the evaluation parameter S is very high, which means that its trajectory does not abide by the rule of “descending order”. When the β is set as 100, the trajectory is messy and the corresponding evaluation parameter D is largest, at the same time, the evaluation parameter S is very small, which means that the trajectory abides by the rule of “descending order” but not the rule of proximity preference. If the adjustment parameter β is set as 0.5, both “proximity preference” and “descending order” are taken into account. Therefore, its prediction result is in line with that of human visual perception and the corresponding F is smallest. How to choose the proper value of β ? It should consider different practical tasks or applications.

87.3.2 Compare the Trajectories of Gaze Shifts Using Our Proposed Method and WTA Method

In the aspect of planning trajectory of gaze shifts, the most widely used method is the WTA technique. In order to evaluate the competitiveness of our planning strategy against existing strategies, we report our model’s predictions with comparison to the results of WTA method, as shown in Fig. 87.2.

From the comparison results ($\beta = 0.5$) of our method and the WTA method, it can be seen that the values of S in two cases are almost equal, evaluation parameter D of our method is much smaller than that of the WTA method. From the comparison results ($\beta = 100$) of our method and the WTA method, it can be seen that the values of D in two cases are almost equal, evaluation parameter S of our method is much smaller than that of the WTA method. From the above analysis, we can draw a conclusion that our proposed method outperforms the traditional WTA method and the WTA method does not abide by two important rules, i.e., descending order and proximity preference because its evaluation parameter S and D are all very high.

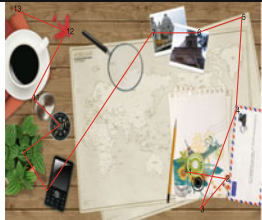
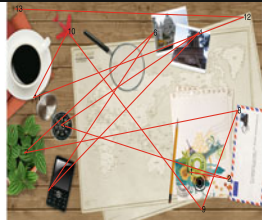



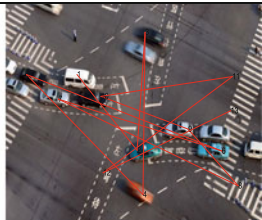
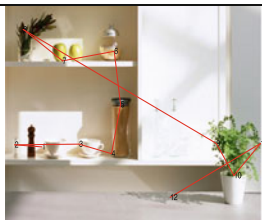
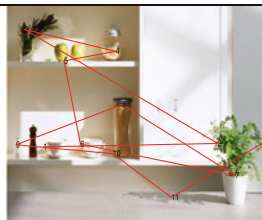
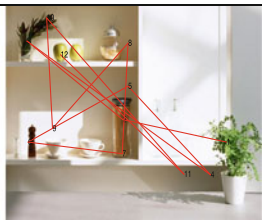
$\beta=0.5$		$\beta=100$		WTA method	
					
D=1347	S=42	D=3536	S=12	D=3156	S=43
Route: 13-12-5-6-2-10-8-9-7-11-3-4-1		Route: 13-12-11-10-9-8-7-6-5-4-3-2-1		Route: 13-12-10-11-7-1-8-2-9-3-4-5-6	
					
D=1420	S=45	D=2708	S=12	D=2994	S=54
Route: 13-10-9-3-4-11-1-2-6-5-7-12-8		Route: 13-12-11-10-9-8-7-6-5-4-3-2-1		Route: 13-8-9-10-1-11-2-3-4-12-5-6-7	
					
D=1285	S=36	D=2361	S=11	D=2543	S=38
Route: 12-4-7-3-5-9-8-10-11-6-1-2		Route: 12-11-10-9-8-7-6-5-4-3-2-1		Route: 12-11-5-6-7-8-9-1-10-2-3-4	

Fig. 87.2 Comparison results of the WTA algorithm and our proposed method

87.4 Conclusion

Two problems for modeling visual attention mechanisms must be solved. The one is how to detect regions of interest (ROI). The second problem is the gaze shift problem. The previous researches are mainly focused on the former problem. This paper is focused on the latter problem. Our technique integrate four basic rules of gaze shifts into a computational model. Considering the optimal objective of planning the trajectory of gaze shifts is similar to that of Traveling Salesman Problem (TSP), we modified some components of TSP and then we propose a modified simulated annealing algorithm to solve the gaze shift problem. Experimental results show that our method is superior to the WTA method.

Acknowledgments This work was supported in part by the National Natural Science Foundation of China under Grant Nos.61271321, 60802051, 60875053, in part by Tianjin Natural Science Foundation under Grant No. 09JCYBJC02100, in part by Youth Foundation of Tianjin University.

References

1. Ouerhani N, Wartburg RV (2004) Empirical validation of the saliency-based model of visual attention. *Electron Lett Comput Vision Image Anal* 3(1):13–24
2. Aziz MZ, Mertsching B (2008) Fast and robust generation of feature maps for region based visual attention. *IEEE Trans Image Process* 17(5):633–644
3. Itti L, Koch C, Niebur E (1998) A model of saliency-based visual attention for rapid scene analysis. *IEEE Trans Pattern Anal Mach Intell* 20(11):1254–1259
4. Kootstra G, Nederveen A, Boer B (2008) Paying attention to symmetry. In: proceedings of the British machine vision conference, pp 1115–1125
5. Zeng M, Li YF, Meng QH (2009) Integrating perceptual properties of the HVS into the computational model of visual attention. *IEEE international conference on image and signal processing*, pp 2402–2405
6. Zeng M, Li YF, Meng QH, Qiu XJ, Yang T (2010) Determination of optimal top-down gains for specific searching tasks. *IEEE international conference on image and signal processing*, pp 1629–1633
7. Zabrodsky H, Peleg S (1990) Attentive transmission. *J Vis Commun Image Represent* 1(2):189–198
8. Klein R (1988) Inhibitory tagging system facilitates visual search. *Nature* 334(4):430–431
9. Sagi D, Julesz B (1988) Enhanced detection in the aperture of focal attention during simple discrimination tasks. *Nature* 321:693–695
10. Zeng M, Yang T, Li YF, Meng QH, Liu J, Han TM (2011) Finding regions of interest based on scale-space keypoint detection. *International conference on computer science and education*, pp 428–435

Chapter 88

Robust Dissipative Filter for Time-Varying and Time-Delay T-S Fuzzy Descriptor Systems with Parameter Uncertainties

Yuechao Ma and Huijie Yan

Abstract This paper deals with the robust dissipative filter for a class of time-varying and time-delay T-S fuzzy descriptor systems with parameter uncertainties. The uncertainties in the system are time-varying and bounded. By simplifying the T-S fuzzy descriptor system to the time-delay system, and base on Lyapunov stability theory in stochastic differential equations, a sufficient condition on the existence of robust dissipative filters is derived. The designing problem of robust dissipative filters is turned into the solution problem of a set of coupled linear matrix inequalities. And then, the robust dissipative filtering problem of time-varying and time-delay T-S fuzzy descriptor systems can be solved in terms of a scaled dissipative filtering problem without uncertainties.

Keywords Time-delay T-S fuzzy descriptor systems · T-S fuzzy systems · Robust · Dissipative filter · Fuzzy system models

88.1 Introduction

In the past decades, there has been an increasing interest in the study of T-S fuzzy descriptor systems since T-S fuzzy descriptor systems provide an effective way in representing complex nonlinear descriptor system and time-varying system. Afterwards, on the base of this model, there have been significant results in the study of T-S fuzzy descriptor systems [1–7].

Descriptor systems are often encountered in the network, economy, robotics and other fields, and thus attracted more and more concern of scholars, so the filtering of descriptor system is especially important and has been extensively

Y. Ma (✉) · H. Yan
College of Science, Yanshan University, 438 Hebeidajie Road, Haigang, Qinhuangdao
Hebei 066004, People's Republic China
e-mail: 18716023220@163.com

studied (see, e.g., [8–12]). In addition, since 1970s, the dissipative system theory plays an important role in the process of stability of the system, the passivity control for a kind of T-S fuzzy descriptor system is studied in [13]. Recently, the robust dissipative filter attracted a lot of interest in academics, a dissipative filter for discrete fuzzy systems is studied in [14]. A dissipative filter for linear discrete time systems via LMI is studied in [15]. A robust dissipative filter for continuous-time polytopic uncertain neutral systems is studied in [16]. But at present, the problem of robust dissipative filter for time-varying and time-delay T-S fuzzy descriptor systems with parameter uncertainties has not been reported.

This paper for time-varying and time-delay T-S fuzzy descriptor systems with parameter uncertainties, summarizes up the ideology of H_∞ filter and passive filter, and discusses the design of robust dissipative filter. At first, given criterion of asymptotic stability for the parameters determine time-varying delay systems, and discussed the conditions and design methods of robust dissipative filter for time-varying and time-delay T-S fuzzy descriptor systems with parameter uncertainties. On this base, considering system with parameter uncertainty, transformed robust dissipative filter for parameter uncertainties systems into a system with parameter determine, and studied robust dissipative filter for time-varying and time delay T-S fuzzy descriptor systems with parameter uncertainties based on LMI. The result of designed filter is asymptotically stable for all the augmented system with uncertainty and satisfies the dissipation index required.

88.2 Problem Description

Consider the following uncertain time-varying and time-delay T-S fuzzy descriptor model, and assume the i -th fuzzy rule as the following form

$$\begin{aligned}
 &R_i: \text{ if } \varepsilon_1(t) \text{ is } M_{1i} \text{ and } \varepsilon_2(t) \text{ is } M_{2i} \dots \varepsilon_p(t) \text{ is } M_{pi} \\
 &\text{then } E\dot{x}(t) = (A_{1i} + \Delta A_{1i})x(t) + (A_{2i} + \Delta A_{2i})x(t - d) + (B_i + \Delta B_i)\omega(t) \\
 &y(t) = (C_{1i} + \Delta C_{1i})x(t) + (C_{2i} + \Delta C_{2i})x(t - d_i(t)) + (D_i + \Delta D_i)\omega(t) \\
 &z(t) = (L_i + \Delta L_i)x(t) \quad i = 1, 2, \dots, r
 \end{aligned} \tag{88.1}$$

where r is the number of model rules; $x(t) \in R^n$ is the input vector; $\omega(t) \in R^m$ is the disturbance vector of the system which belongs $L_2[0, +\infty)$; $y(t) \in R^q$ is the measurable output vector; $z(t) \in R^p$ is the signal vector to be estimated; E is singular matrix and we shall assume that $rankE = r \leq n$; $A_{1i}, A_{2i}, B_i, C_{1i}, C_{2i}, D_i, L_i$ are constant matrices with appropriate dimensions; $\varepsilon_j(t)$ and $M_{ij}(j = 1, 2, \dots, p)$ are the premise variable and the fuzzy sets; $d_i(t)$ is a time-varying continuous function that satisfies $\dot{d}_i(t) \leq u, 0 \leq d_1 \leq d_i(t) \leq d_2; \Delta A_{1i}, \Delta A_{2i}, \Delta B_i, \Delta C_{1i}, \Delta C_{2i},$

ΔD_i , ΔL_i are unknown matrices representing parametric uncertainties and are assumed to be of the form:

$$\begin{bmatrix} \Delta A_{1i} & \Delta A_{2i} & \Delta B_i \\ \Delta C_{1i} & \Delta C_{2i} & \Delta D_i \end{bmatrix} = \begin{bmatrix} H_{1i} \\ H_{2i} \end{bmatrix} F_i [E_{1i} \quad E_{2i} \quad E_{3i}], \quad \Delta L_i = H_{3i} F_i E_{4i} \quad (88.2)$$

where H_{1i} , H_{2i} , H_{3i} , E_{1i} , E_{2i} , E_{3i} , E_{4i} are known real constant matrices with appropriate dimensions, and is an unknown real time-varying matrix satisfying

$$F_i^T F_i \leq I \quad (88.3)$$

I is a unit matrix with appropriate dimensions.

Let $\varepsilon(t) = [\varepsilon_1(t) \quad \varepsilon_2(t) \quad \dots \quad \varepsilon_p(t)]^T$, through the use of ‘‘fuzzy blending’’, the fuzzy system (88.1) can be inferred as follows:

$$\begin{aligned} E\dot{x}(t) &= \sum_{i=1}^r h_i(\varepsilon(t)) [(A_{1i} + \Delta A_{1i})x(t) + (A_{2i} + \Delta A_{2i})x(t - d_i(t)) + (B_i + \Delta B_i)\omega(t)] \\ y(t) &= \sum_{i=1}^r h_i(\varepsilon(t)) [(C_{1i} + \Delta C_{1i})x(t) + (C_{2i} + \Delta C_{2i})x(t - d_i(t)) + (D_i + \Delta D_i)\omega(t)] \\ z(t) &= \sum_{i=1}^r h_i(\varepsilon(t)) [(L_i + \Delta L_i)x(t)] \end{aligned} \quad (88.4)$$

$$\beta_i(\varepsilon(t)) = \prod_{j=1}^p M_{ij}(\varepsilon_j(t)) \geq 0,$$

$$h_i(\varepsilon(t)) = \frac{\beta_i(\varepsilon(t))}{\sum_{i=1}^r \beta_i(\varepsilon(t))} \geq 0, \quad \sum_{i=1}^r h_i(\varepsilon(t)) = 1.$$

where $h_i(\varepsilon(t))$ is the normalized membership function, and assume that it is a continuous real function with time piecewise.

In this paper, we consider the following fuzzy filter:

$$\begin{aligned} E\hat{x}(t) &= \sum_{i=1}^r h_i(\varepsilon(t)) [A_{fi}\hat{x}(t) + B_{fi}y(t) + C_{fi}\hat{x}(t - d_i(t))] \\ \hat{z}(t) &= \sum_{i=1}^r h_i(\varepsilon(t)) [L_{fi}\hat{x}(t)] \quad i = 1, 2, \dots, r \end{aligned} \quad (88.5)$$

where $\hat{x}(t) \in R^k$ is the filter state vector, $\hat{z}(t) \in R^p$ is the estimated vector, A_{fi} , B_{fi} , C_{fi} , L_{fi} with compatible dimensions are the piecewise matrices functions to be determined.

We rewrite (88.1) and (88.5) in the following compact form:

$$\begin{aligned} \bar{E}\dot{\tilde{x}}(t) &= \sum_{i=1}^r \sum_{j=1}^r h_i(\varepsilon(t))h_j(\varepsilon(t))[A_{ij}\tilde{x}(t) + A_{dij}\tilde{x}(t - d_i(t)) + B_{ij}\omega(t)] \\ e(t) &= \sum_{i=1}^r \sum_{j=1}^r h_i(\varepsilon(t))h_j(\varepsilon(t))[L_{ij}\tilde{x}(t)] \end{aligned} \tag{88.6}$$

where $e(t) = z(t) - \hat{z}(t)$, $\tilde{x}(t) = [x^T(t) \quad \hat{x}^T(t)]^T$,

$$\begin{aligned} A_{ij} &= \begin{bmatrix} A_{1i} + \Delta A_{1i} & 0 \\ B_{fi}(C_{1i} + \Delta C_{1i}) & A_{fi} \end{bmatrix}, A_{dij} = \begin{bmatrix} A_{2i} + \Delta A_{2i} & 0 \\ B_{fi}(C_{2i} + \Delta C_{2i}) & C_{fi} \end{bmatrix}, \\ B_{ij} &= \begin{bmatrix} B_i + \Delta B_i \\ B_{fi}(D_i + \Delta D_i) \end{bmatrix}, \bar{E} = \begin{bmatrix} E & 0 \\ 0 & E \end{bmatrix}, L_{ij} = [L_i + \Delta L_i \quad -L_{fi}]. \end{aligned}$$

Denote $\langle x, Hy \rangle_T = \int_0^T x^T(t)Hy(t)dt$, in this article, we focus attention on the quadratic supply rate $E(\omega, e, T) = \langle e, Qe \rangle_T + 2\langle e, S\omega \rangle_T + \langle \omega, R\omega \rangle_T$

Where Q, S, R are appropriately dimensioned and Q, R are symmetric matrices.

Definition 1 [16] If filtering error system (88.6) is asymptotically stable and for all $T > 0$ and $0 \neq \omega(t) \in L_2[0, +\infty)$, there exist $\alpha > 0$ such that

$$E(\omega, e, T) > \alpha \langle \omega, \omega \rangle_T$$

Definition 2 Given a set of suited dimension real matrices Q, S, R , where Q, S, R are symmetric matrices, system (88.5) is called a robust dissipative filter of uncertain system(88.4). If there exist $A_{fi}, B_{fi}, C_{fi}, L_{fi}$, such that

- (a) the augmented system (88.6) with $\omega(t) = 0$ is robust asymptotically stable for all uncertainties;
- (b) the filtering error system (88.6) is strict robust (Q, S, R) dissipative.

Our aim is to determine parameters $A_{fi}, B_{fi}, C_{fi}, L_{fi}$ such that system (88.4) is a robust dissipative filter for uncertain system (88.1).

System (88.6) is simply denoted by the following form:

$$\begin{aligned} \bar{E}\dot{\tilde{x}}(t) &= \tilde{A}\tilde{x}(t) + \tilde{A}_d\tilde{x}(t - d_i(t)) + \tilde{B}\omega(t) \\ e(t) &= \tilde{L}\tilde{x}(t) \end{aligned} \tag{88.7}$$

where

$$\begin{aligned} \tilde{A} &= \sum_{i=1}^r \sum_{j=1}^r h_i(\varepsilon(t))h_j(\varepsilon(t))A_{ij}, \tilde{A}_d = \sum_{i=1}^r \sum_{j=1}^r h_i(\varepsilon(t))h_j(\varepsilon(t))A_{dij}, \\ \tilde{B} &= \sum_{i=1}^r \sum_{j=1}^r h_i(\varepsilon(t))h_j(\varepsilon(t))B_{ij}, \tilde{L} = \sum_{i=1}^r \sum_{j=1}^r h_i(\varepsilon(t))h_j(\varepsilon(t))L_{ij}. \end{aligned}$$

The following systems are regular consistent and with no pulse.

88.3 Main Results

Lemma 1 [11] *Given a set of suited dimension real matrices Q , H , E and Q is symmetric matrix, such that $Q + HFE + E^T F^T H^T < 0$, For all F satisfies $F^T F \leq I$; If and only if there exist $\varepsilon > 0$ such that*

$$Q + \varepsilon H H^T + \varepsilon^{-1} E^T E < 0$$

Theorem 1 *Given symmetric matrices Q , S , R , where Q is negative definite and with all uncertainties, the robust dissipative filtering problem is solved for system (7); if there exist symmetric positive definite matrix W and invertible matrix P , such that*

$$\bar{E}^T P = P^T \bar{E} \geq 0 \quad (88.8a)$$

$$\Sigma = \begin{bmatrix} \Sigma_{11} & P^T \tilde{A}_d & P^T \tilde{B} - \tilde{L}^T S \\ * & \Sigma_{22} & 0 \\ * & * & -R \end{bmatrix} < 0 \quad (88.8b)$$

where $\Sigma_{11} = P^T \tilde{A} + \tilde{A}^T P + \bar{E}^T W \bar{E} - \tilde{L}^T Q \tilde{L}$, $\Sigma_{22} = -(1 - u) \bar{E}^T W \bar{E}$.

Through the choice of a Lyapunov function, this theorem is easy to demonstrate.

Based on the sufficient conditions above, the design problem of robust dissipative filter can be transformed into a problem of linear matrix inequality.

Theorem 2 *Given symmetric matrices Q , S , R , where Q is negative definite and with all uncertainties, the robust dissipative filtering problem is solved for system (6); if there exist constant $\varepsilon > 0$, $\varepsilon_{ij} > 0$, symmetric positive definite matrix W and invertible matrix $P = \text{diag}(P_1, P_2)$, such that*

$$E^T P_1 = P_1^T E \geq 0, E^T P_2 = P_2^T E \geq 0$$

$$\begin{bmatrix} \Gamma_1 & \Gamma_2 \\ * & -\varepsilon^{-1} I \end{bmatrix} < 0, \begin{bmatrix} \bar{\Gamma}_1 & \bar{\Gamma}_2 \\ * & -\varepsilon_{ij}^{-1} I \end{bmatrix} < 0$$

where

$$\Gamma_1 = \begin{bmatrix} \varphi_{11} & \varphi_{12} & \varphi_{13} & 0 & \varphi_{15} & L_i^T \\ * & \varphi_{22} & M_{2i} C_{2i} & M_{3i} & \varphi_{25} & -L_{fi}^T \\ * & * & \varphi_{33} & \varphi_{34} & \varepsilon^{-1} E_{2i}^T E_{3i} & 0 \\ * & * & * & \varphi_{44} & 0 & 0 \\ * & * & * & * & \varphi_{55} & 0 \\ * & * & * & * & * & Q^{-1} \end{bmatrix},$$

$$\Gamma_2 = \begin{bmatrix} P_1^T H_{1i} & 0 & 0 & 0 & 0 & 0 \\ M_{2i} H_{2i} & 0 & 0 & 0 & 0 & 0 \\ 0 & 0 & 0 & 0 & 0 & 0 \\ 0 & 0 & 0 & 0 & 0 & 0 \\ 0 & -S^T H_{3i} & 0 & 0 & 0 & 0 \\ 0 & H_{3i} & 0 & 0 & 0 & 0 \end{bmatrix},$$

$$\bar{\Gamma}_1 = \begin{bmatrix} \bar{\varphi}_{11} & \bar{\varphi}_{12} & \bar{\varphi}_{13} & 0 & \bar{\varphi}_{15} & L_i^T + L_j^T \\ * & \bar{\varphi}_{22} & \bar{\varphi}_{23} & M_{3i} + M_{3j} & \bar{\varphi}_{25} & -L_{fi}^T + -L_{fj}^T \\ * & * & \bar{\varphi}_{33} & \bar{\varphi}_{34} & \bar{\varphi}_{35} & 0 \\ * & * & * & \bar{\varphi}_{44} & 0 & 0 \\ * & * & * & * & \bar{\varphi}_{55} & 0 \\ * & * & * & * & * & 2Q^{-1} \end{bmatrix},$$

$$\bar{\Gamma}_2 = \begin{bmatrix} P_1^T H_{1i} & P_1^T H_{1j} & 0 & 0 & 0 & 0 & 0 & 0 \\ M_{2j} H_{2i} & M_{2i} H_{2j} & 0 & 0 & 0 & 0 & 0 & 0 \\ 0 & 0 & 0 & 0 & 0 & 0 & 0 & 0 \\ 0 & 0 & 0 & 0 & 0 & 0 & 0 & 0 \\ 0 & 0 & -S^T H_{3i} & -S^T H_{3j} & 0 & 0 & 0 & 0 \\ 0 & 0 & H_{3i} & H_{3j} & 0 & 0 & 0 & 0 \end{bmatrix},$$

$$\begin{aligned} \varphi_{11} &= P_1^T A_{1i} + A_{1i}^T P_1 + E^T W_1 E + \varepsilon^{-1} (E_{1i}^T E_{1i} + E_{4i}^T E_{4i}), \\ \varphi_{13} &= P_1^T A_{2i} + \varepsilon^{-1} E_{1i}^T E_{2i}, \quad \varphi_{15} = P_1^T B_i - L_i^T S + \varepsilon^{-1} E_{1i}^T E_{3i} \\ \varphi_{22} &= M_{1i} + M_{1i}^T + E^T W_3 E, \quad \bar{\varphi}_{25} = M_{2i} D_j + M_{2j} D_i + L_{fi}^T S + L_{fj}^T S, \\ \bar{\varphi}_{33} &= -2E^T W_1 E + \varepsilon_{ij}^{-1} (E_{2i}^T E_{2i} + E_{2j}^T E_{2j}), \quad \bar{\varphi}_{34} = -2E^T W_2 E, \\ \bar{\varphi}_{35} &= \varepsilon_{ij}^{-1} (E_{2i}^T E_{3i} + E_{2j}^T E_{3j}), \\ \bar{\varphi}_{44} &= -2E^T W_3 E, \quad \bar{\varphi}_{55} = -2R + \varepsilon_{ij}^{-1} (E_{3i}^T E_{3i} + E_{3j}^T E_{3j}), \\ \bar{\varphi}_{11} &= P_1^T A_{1i} + A_{1i}^T P_1 + P_1^T A_{1j} + A_{1j}^T P_1 + 2E^T W_1 E + \varepsilon_{ij}^{-1} (E_{1i}^T E_{1i} + E_{1j}^T E_{1j} + \\ &\quad E_{4i}^T E_{4i} + E_{4j}^T E_{4j}), \quad \varphi_{12} = C_{1i}^T M_{2i}^T + E^T W_2 E, \\ \bar{\varphi}_{13} &= P_1^T A_{2i} + P_1^T A_{2j} + \varepsilon_{ij}^{-1} (E_{1i}^T E_{2i} + E_{1j}^T E_{2j}), \\ \bar{\varphi}_{15} &= P_1^T B_i + P_1^T B_j - L_i^T S - L_j^T S + \varepsilon_{ij}^{-1} (E_{1i}^T E_{3i} + E_{1j}^T E_{3j}), \\ \bar{\varphi}_{22} &= M_{1i} + M_{1j} + M_{1i}^T + M_{1j}^T + 2E^T W_3 E, \quad \bar{\varphi}_{23} = M_{2j} C_{2i} + M_{2i} C_{2j}. \end{aligned}$$

Let $M_{1i} = P_2^T A_{fi}$, $M_{2i} = P_2^T B_{fi}$, $M_{3i} = P_2^T C_{fi}$. The parameters of the robust dissipative filter are $A_{fi} = P_2^{-T} M_{1i}$, $B_{fi} = P_2^{-T} M_{2i}$, $C_{fi} = P_2^{-T} M_{3i}$, L_{fi} .

88.4 Conclusion

This paper based on linear matrix inequality, studied a design problem of robust dissipative filter for a class of discrete time-varying time-delay T-S fuzzy descriptor systems with parameter uncertainties. At first, the design of robust dissipative filter for a class of discrete time-varying time-delay T-S fuzzy descriptor systems with parameter uncertainties is simplified to a general delay systems with parameter determined. And the problem of robust dissipative filter for parameter determines can be solved by linear matrix inequalities. The results can be easily extended to systems with multiple delays, and the filtering is asymptotically stable for all the augmented system with uncertainty and satisfied the dissipation index required.

Acknowledgments This work is supported by National Natural Science Foundation of China, under Grant number 61273004. The authors also gratefully acknowledge the helpful comments and suggestions of the reviewers, which have improved the presentation.

References

1. Yoneyama J, Ichikawa A (1999) H_∞ control for Takagi-Sugeno fuzzy descriptor systems. IEEE conference on systems, man and cybernetics, Tokyo, pp 28–33
2. Zhu BY, Zhang QL (2004) Optimal guaranteed cost control for T-S fuzzy descriptor system with uncertain parameters. Sys Eng Theor Pract 12:49–57 (In Chinese)
3. Xu S, Lam J, Chen B (2004) Robust H_∞ control for uncertain fuzzy neutral delay systems. European J Contr 10(4):365–380
4. Yuan YH, Zhang QL, Chen B (2009) Hinfinitiy control for discrete T-S fuzzy descriptor systems. Contr Theor Appl 26(3):332–336 (In Chinese)
5. Bouarar T, Guelton K, Manamanni N (2010) Robust fuzzy Lyapunov stabilization for uncertain and disturbed Takagi-Sugeno descriptors. ISA Trans 49(4):447–461
6. Zhang HB, Shen YY, Feng G (2009) Delay dependent stability and H_∞ control for a class of fuzzy descriptor systems with time-delay. Fuzzy Sets Sys 12(16):1689–1707
7. Gong CZ, Zeng XW (2009) A descriptor system approach to uncertain fuzzy control system design via fuzzy Lyapunov functions. In: IEEE proceedings of the eighth international conference on machine learning and cybernetics, Baoding, 12–15 July, pp 498–503
8. Xu SY, Lam J (2007) Reduced-order H_∞ filtering for singular systems. Sci Dir Syst Contr Lett 56(1):48–57
9. Wu ZG, Su HY, Chu J (2010) Delay-dependent H_∞ filtering for singular Markovian jump time-delay systems. Sig Process 90(6):1815–1824
10. Kim JH (2010) Delay-dependent robust H_∞ filtering for uncertain discrete-time singular systems with interval time-varying delay. Automatica 46(3):591–597
11. Lu RQ, Xu Y, Xue AK (2010) H_∞ filtering for singular systems with communication delays. Sig Process 90(4):1240–1248
12. Lu RQ, Wang JH, Xue AK, Ye SH, Chu J (2007) Robust H_∞ filtering for a class of uncertain lurie time-delay singular systems. Acta Automatica Sinica 3(33):292–296

13. Zhu BY, Zhang QL, Tong SC (2006) The passivity control for a kind of T-S fuzzy descriptor system. *Sys Eng Theor Pract* 6(6):81–87 (in Chinese)
14. Lo JC, Wu DL (2008) Dissipative filtering for discrete fuzzy systems. *IEEE international conference on fuzzy systems, HongKong*, pp 361–365
15. Li CJ, An HY, Feng YF (2009) Dissipative filtering for linear discrete-time systems via LMI, *Chinese control and decision conference*, pp 3866–3870
16. Duan GR, Lv LL, Wu AG (2009) Robust dissipative filtering for continuous-time polytopic uncertain neutral systems. *Sys Eng Electr* 20(3):598–606

Chapter 89

The Realization of Fuzzy Control in Fire-Proof Material Batching System

Xue Jun He and Jun Zhang

Abstract Fire-proof material batching system is a multi-variable nonlinear system, so it is difficult to achieve the ideal control effect to use the conventional PID control. This paper puts forward a kind of fuzzy control algorithm of fire-proof material batching system, it is applied to fire-proof material batching control production line of Masami Benxi fire-proof material limited company, and has successfully run more than a year, The practice proved that this control algorithm has the advantage of mature technology, stable operation and strong robustness, its control effect is satisfactory.

Keywords Fuzzy control · Robustness · Batching control · Membership function

89.1 Introduction

Fire-proof material batching system is a multivariable nonlinear system, in which variables are mutually coupled, required to achieve higher control accuracy in a very short time and some of them are very difficult to measure so it is difficult to achieve the ideal control effect to use the conventional PID control. Fuzzy control is easy to realize rapid control because of its simple design, small calculated quantity, high operation speed, strong robustness. The influence on control effect by disturbance and parameter variation is strongly weakened.

X. J. He (✉) · J. Zhang (✉)

Electric and Information Engineering College, Liaoning Institute of Science and Technology, Benxi 117004, China
e-mail: asarah0624@163.com

J. Zhang

e-mail: benxi99129@163.com

89.2 Controlled Plant Analysis

The main process equipment in Masami Benxi fire-proof material batching system is consist of forty-four storage bins, nine hoppers, eleven electronic scales, two motor wagons and two blender mixer. There is powdered material in first twenty-four storage bins, the materials in every six storage bins flow down to one hopper in turn, that is controlled by screw feeder which is driven by frequency converter; There is granular material in the other twenty storage bins, the materials in every four storage bins flow down to one hopper in turn, that is controlled by shock feeder driven by voltage regulator. There a total of nine hoppers in the system, nine electronic scales under each hopper to measure material in them respectively. The other two electronic scales are fixed on the motor wagons. The batching system is shown in Fig. 89.1.

The traditional PID control is difficult to achieve the ideal control effect, because of realizing as much as 6 kinds of materials weighing in one electronic scale in a few seconds, according to the batching system process characteristics, so fuzzy control is an ideal control method.

89.3 Control System Composition and Working Principle

Control function block diagram of PLC controlled fire-proof material batching system is plotted in Fig. 89.2. The controller block in Fig. 89.2 is realized by S7-300 PLC, and monitoring function block by configuration software WinCC. This system can realize fire-proof material batching control by nine hoppers and electronic scales under them; realize the control of motor wagon moving,

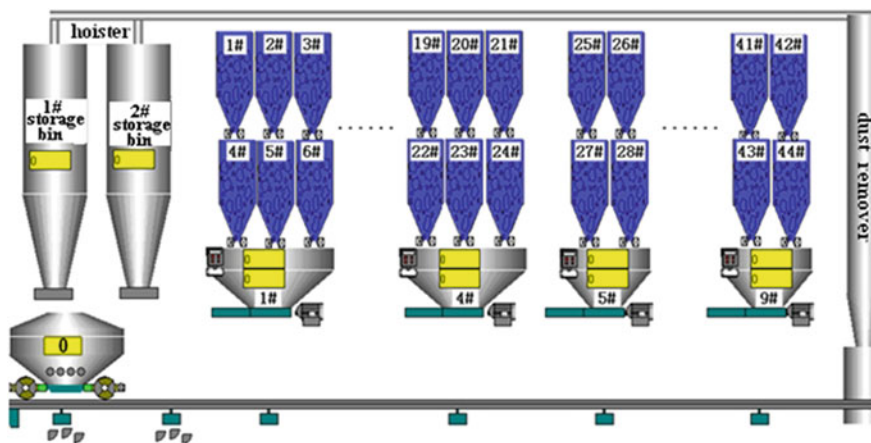


Fig. 89.1 System structure diagram

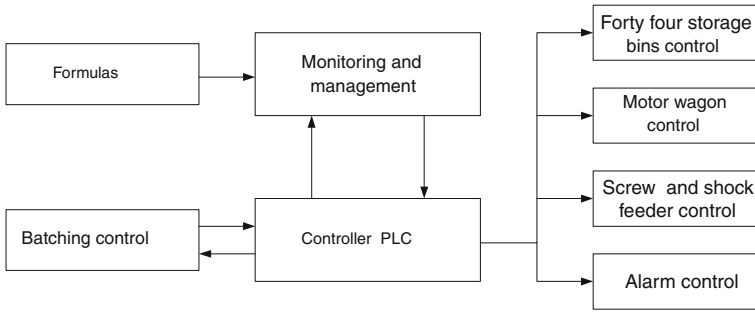


Fig. 89.2 Control function block diagram

orientation and charging; realize the frequency conversion control of screw feeder and the voltage control of shock feeder, The system also has the function of generating formula, auto alarm, fault diagnosis, display, print etc.

The host computer generates fire-proof material formulas according to the technological requirements and then calculates control values based on fuzzy algorithm, so as to realize the accurate batching control.

89.4 Control System Description

The controlled objects are the screw feeder driven by the frequency converter and the shock feeder driven by voltage regulator, the electronic scale (sensor) weighs the refractory. The output fire-proof material weight of screw feeder is controlled by the output frequency of frequency converter and that of shock feeder controlled by the output voltage of the voltage regulator. The schematic diagram of feeder fuzzy control system is shown in Fig. 89.3.

It is not difficult to see that this is a single input and single output system, control value is frequency (screw feeder) or voltage (shock feeder).

89.5 The Design of Fuzzy Controller

The structure of fuzzy controller. Fuzzy controller using following three fuzzy variables:

1. WE—weight error.
2. CWE—change in weight error.
3. CV—control value.

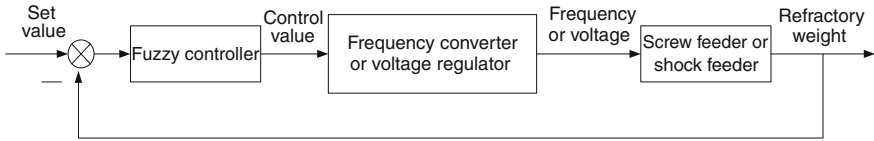


Fig. 89.3 Feeder fuzzy control system

Where WE and CWE are input fuzzy variables, CV is output fuzzy variable. Fuzzy controller is written in C language, input variables are WE and CWE, output variable is CV.

Domain and membership function of fuzzy variable. Take the domain of error (WE) and change in weight error (CWE) to be into seven quantization levels, that is

$$\{+0, +1, +2, \dots, +6\}$$

The subset of WE variable and CWE variable are selected as follow:

$$\{PB, PM, PS, PO\}$$

The membership function of WE subset is determined by Table 89.1, and that of CWE subset by Table 89.2.

Take the domain of CV to be into four blocks, that is

$$\{+0, +1, +2, 3\}$$

The subset of CV variable is selected as follow:

$$\{PB, PM, PS, PO\}$$

The membership function of WE subset is determined by Table 89.3

Control rules: The control rules of fuzzy controller are as follows:

if WE = PB then if CWE = (PB or PM or PS or PO) then CV = PB
or

if WE = PM then if CWE = (PS or PO) then CV = PB

or

if WE = PM then if CWE = (PB or PM) then CV = PM

or

if WE = PS then if CWE = (PS or PO) then CV = PM

or

if WE = PS then if CWE = (PB or PM) then CV = PS

or

if WE = PO then if CWE = (PS or PO) then CV = PS

or

if WE = PO then if CWE = (PB or PM) then CV = PO

Table 89.1 The membership function of WE fuzzy subset

Quantization level	$\mu(x)\backslash$ WE Quantization domain	PO	PS	PM	PB
0	$0.5 > WE$	1.0	0	0	0
1	$1.5 > WE \geq 0.5$	0.5	0.9	0	0
2	$2.5 > WE \geq 1.5$	0	1.0	0.2	0
3	$3.5 > WE \geq 2.5$	0	0.7	0.7	0.1
4	$4.5 > WE \geq 3.5$	0	0.2	1.0	0.4
5	$5.5 > WE \geq 4.5$	0	0	0.7	0.8
6	$WE \geq 5.5$	0	0	0.2	1.0

Table 89.2 The membership function of CWE fuzzy subset

Quantization level	$\mu(x)\backslash$ CWE Quantization domain	PO	PS	PM	PB
0	$0.5 > CWE$	1.0	0	0	0
1	$2.5 > CWE \geq 0.5$	0.5	0.9	0	0
2	$4.5 > CWE \geq 2.5$	0	1.0	0.2	0
3	$6.5 > CWE \geq 4.5$	0	0.7	0.7	0.1
4	$8.5 > CWE \geq 6.5$	0	0.2	1.0	0.4
5	$9.5 > CWE \geq 8.5$	0	0	0.7	0.8
6	$CWE \geq 9.5$	0	0	0.2	1.0

Table 89.3 The membership function of CV fuzzy subset

Quantization level	$\mu(x)\backslash$ CV Quantization domain	PO	PS	PM	PB
0	$0.3 > CV$	1.0	0.5	0	0
1	$0.6 > CV \geq 0.3$	0.5	1.0	0.5	0
2	$0.8 > CV \geq 0.6$	0	0.5	1.0	0.5
3	$1.0 > CV \geq 0.8$	0	0	0.5	1.0

The output of the fuzzy controller is sent to the variable area of the functional block FC7 after to be changed into precise value, then this block control the frequency of screw feeder and the voltage of shock feeder.

89.6 Conclusion

This system is applied to fire-proof material batching control production line of Masami Benxi fire-proof material limited company, and has successfully run more than a year., It shows that the system has the advantage of mature technology, high stability and strong anti-interference ability etc., The control effect is satisfactory.

Chapter 90

An Intuitionistic Fuzzy Neural Network with Triangular Membership Function

Xiaoguang Zhou, Renhou Zhao and Lili Zhang

Abstract In this paper, an intuitionistic fuzzy neural network model with a triangular membership and 1 minus triangular form non-membership functions is proposed. The network structure has six layers, and adopts Mandani's fuzzy reasoning. A new fuzzy inference system is applied in the model, which contains hesitation margin as a part. The two steps dynamic optimal training algorithms for the IFNN is development, the first step is membership function parameters training, the second step is membership function parameters training, which can promise the summing of the trained membership and non-membership functions on finite universal set less than 1. An example is given to demonstrate the intuitionistic fuzzy neural network has a higher degree of accuracy and higher learning efficiency than fuzzy neural network.

Keywords Intuitionistic fuzzy neural networks · Fuzzy inference system · Training algorithm

90.1 Introduction

Intuitionistic fuzzy sets (IFSs) are introduced by Atanassov [1, 2], which are generalization of the concept of fuzzy sets by adding an additional attribute parameter called non-membership [3]. IFSs are successful applied in many areas,

X. Zhou (✉) · R. Zhao

Flight Simulation and Training Center Navy Aviation Academy,
Hu Ludao, LiaoNing 125001, China
e-mail: zhanglili2117@163.com

L. Zhang

College of Opto-electronic Engineering, Changchun University of
Science and Technology, ChangChun 130022, China
e-mail: zhangliligf@163.com

multi-criteria fuzzy decision-making [4, 5], pattern recognition [6], air quality modelling [7], time series prediction [8], etc.

During the past decade, a fuzzy neural network has been found to solve many problems which cannot be solved before [9]. For instance, the fuzzy neural network has been successfully applied in system identification [10], intelligent control [11], etc. Since IFSs have proved to be more powerful to deal with vagueness and uncertainty than fuzzy sets, combination of IFSs and artificial neural networks is investigated by many experts. In [12], a max–min intuitionistic fuzzy Hopfield neural network (IFHNN) is proposed. In [13], an intuitionistic fuzzy neural model is present based on an simple intuitionistic inference system. There are some problems in this model, the inference mechanism is too simple, and the summing of the trained membership and non-membership will be greater than 1. In this paper, a intuitionistic fuzzy neural network is proposed by combining IFSs with neural network (IFNN) with triangular membership function and 1-triangular form non-membership function based on the new fuzzy inference present in [14]. The two steps dynamic optimal training algorithms for the IFNN is development, which can promise the summing of the trained membership and non-membership less than 1. An example is given to show the IFNN yield more improved performance than using fuzzy neural network.

This paper is organized as follows. In Sect. 90.2 the new intuitionistic fuzzy inference system will be introduced. In Sect. 90.3, a intuitionistic fuzzy neural network model with triangular membership function 1 minus triangular form non-membership function will be defined. In Sect. 90.4, the training algorithm will be given. In Sect. 90.5, An example is given to show the IFNN yield more improved performance than using fuzzy neural network. The conclusion and topics for future research are drawn in Sect. 90.6.

90.2 Intuitionistic Fuzzy Inference System

90.2.1 Intuitionistic Fuzzy Set

In [1] Atanassov defines an intuitionistic fuzzy set (IFS) A over a finite universal set E as an object having the following form:

$$A = \{(x, \mu_A(x), \nu_A(x)) | x \in X\}$$

where, $\mu_A : X \rightarrow [0, 1]$ and $\nu_A : X \rightarrow [0, 1]$: are such that $0 \leq \mu_A + \nu_A \leq 1$, $\mu_A(x)$ denote a degree of membership of $x \in A$, $\nu_A(x)$ denote a degree of non-membership of $x \in A$. For each intuitionistic fuzzy set in X , we call $\pi_A(x) = 1 - \mu_A(x) - \nu_A(x)$ a “hesitation margin” of $x \in A$, it expresses a hesitation degree of whether x belongs to A or not. It is obvious that $0 \leq \pi_A \leq 1$, for each $x \in X$.

90.2.2 Intuitionistic Fuzzy Inference System (IFIS)

A new IFIS is defined in [14]. Then it is possible to define its output y_η as

$$y_\eta = (1 - \pi(X))y_\mu + \pi_A(X)y_\nu$$

where y_η is output of the FIS using the membership function $\mu_A(x)$, y_ν is the output of the FIS using the non-membership function $\nu_A(x)$. For $\pi = 0$, output y_η will reduce to the output of a traditional fuzzy system.

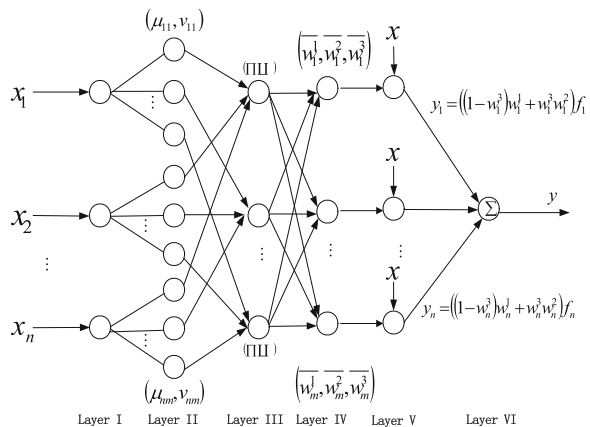
90.3 Intuitionistic Fuzzy Neural Networks with Triangular Membership Function

An intuitionistic fuzzy neural network system with six layers structure is shown in Fig. 90.1. The first layer is input layer. The second layer is membership and non-membership function creating layer. The third layer is inference layer. The fourth layer is normalized layer. The fifth layer is computation layer. The sixth layer is output layer.

- Layer 1: no computation is done in this layer, it just pass inputs into next layer.
- Layer 2: the membership and non-membership are determined for the neurons generation criteria:

$$\mu_{ij}(x_j) = \begin{cases} 1 - \frac{|x_j - a_{ij}|}{b_{ij}/2}, & \text{if } |x_j - a_{ij}| \leq \frac{b_{ij}}{2} \\ 0, & \text{otherwise} \end{cases} \tag{90.1}$$

Fig. 90.1 IFNN architecture



$$v_{ij}(x_j) = \begin{cases} \frac{|x_j - a_{ij}|}{c_{ij}/2}, & \text{if } |x_j - a_{ij}| \leq \frac{c_{ij}}{2} \\ 0, & \text{otherwise} \end{cases} \tag{90.2}$$

The membership and non-membership have the same peak parameter.

Layer 3: It is fuzzy inference layer. Each node represents a fuzzy rule. The degree of fulfillment and non-fulfillment of the i th rule is represented by the following equations:

$$w_i^1 = \prod_{j=1}^m \mu_{A_{ji}}(x_j), w_i^2 = \prod_{j=1}^m v_{A_{ji}}(x_j) \tag{90.3}$$

Layer 4: It normalized the degree of fulfillment and non-fulfillment of the fuzzy and calculated the hesitation margin index.

$$\overline{w}_i^1 = \frac{w_i^1}{\sum_{i=1}^n w_i^1}, \overline{w}_i^2 = \frac{w_i^2}{\sum_{i=1}^n w_i^2}, \overline{w}_i^3 = 1 - \overline{w}_i^1 - \overline{w}_i^2 \tag{90.4}$$

Layer 5: In this layer, the weight vector f_i and inference output τ_i is calculated as

$$f_i = k_1^i x_1 + k_2^i x_2 + \dots + k_m^i x_m \tag{90.5}$$

$$\tau_i = \left(1 - \overline{w}_i^3\right) \overline{w}_i^1 + \overline{w}_i^3 \overline{w}_i^2 = \left(\overline{w}_i^1\right)^2 - \left(\overline{w}_i^2\right)^2 + \overline{w}_i^2 \tag{90.6}$$

Layer 6: The output of the intuitionistic neural network with n rules can be calculated as

$$y = \sum_{i=1}^n \tau_i f_i = \sum_{i=1}^n y_i \tag{90.7}$$

where $y_i = \tau_i f_i$.

90.4 IFNN Training Algorithm

The IFNN architecture consists of two trainable parameter sets:

- (1) The polynomial parameters $[k_1, k_2, \dots, k_n]$.
- (2) The membership and non-membership function parameter $[a, b, c]$.

The polynomial parameters $[k_1, k_2, \dots, k_n]$ can be solved by least square regression techniques [14]. So in this part, only a gradient descent algorithm how to optimize the membership and non-membership function parameter is introduced. An improve two steps gradient descent algorithm is present to train membership and non-membership function parameter. In the step 1 of the algorithm, the

membership function parameters are trained. In the step 2 of the algorithm, based on the step 1 learning results, the non-membership function parameters are trained. The key of the improve two steps gradient descent algorithm is that when in optimizing the non-membership parameter, a feasible field is constructed based on the membership parameters, which can promise that the summing of the degree of membership and the degree of non-membership less than 1.

The objective error function E is chosen:

$$E = \frac{1}{2}(y - y^t)^2 \quad (90.8)$$

Step 1: membership function parameters training

According to the gradient descent algorithm, the peak parameter of membership and non-membership update rule is

$$a_{ij}(t + 1) = a_{ij}(t) - \frac{\eta_a}{p} \frac{\partial E}{\partial a_{ij}} \quad (90.9)$$

where, η_a is learning rate for a_{ij} , and p is the number of input patters. The chain rule can be used to calculate the derivatives used to update the parameter:

$$\begin{aligned} \frac{\partial E}{\partial a_{ij}} &= \frac{\partial E}{\partial y} \cdot \frac{\partial y}{\partial y_i} \cdot \frac{\partial y_i}{\partial \tau_i} \cdot \left(\frac{\partial \tau_i}{\partial w_i^1} \frac{\partial \overline{w}_i^1}{\partial w_i^1} \frac{\partial w_i^1}{\partial \mu_{ij}} \frac{\partial \mu_{ij}}{\partial a_{ij}} + \frac{\partial \tau_i}{\partial w_i^2} \frac{\partial \overline{w}_i^2}{\partial w_i^2} \frac{\partial w_i^2}{\partial v_{ij}} \frac{\partial v_{ij}}{\partial a_{ij}} \right) \\ &= 4(y - y^t) \cdot \frac{\sum_{j=1, j \neq i}^n w_j^1}{(\sum_{i=1}^n w_i^1)^3} \cdot \frac{(w_i^1)^2}{\mu_{ij}(x_j)} \cdot \frac{\text{sign}(x_j - a_{ij})}{b_{ij}} + (y - y^t) \cdot f_i \\ &\quad \cdot \left(1 - 2 \frac{w_i^2}{\sum_{i=1}^n w_i^2} \right) \cdot \frac{\sum_{j=1, j \neq i}^n w_j^2}{(\sum_{i=1}^n w_i^2)^2} \cdot \frac{w_i^2}{v_{ij}(x_j)} \\ &\quad + (y - y^t) \cdot f_i \cdot \left(1 - 2 \frac{w_i^2}{\sum_{i=1}^n w_i^2} \right) \cdot \frac{\sum_{j=1, j \neq i}^n w_j^2}{(\sum_{i=1}^n w_i^2)^2} \cdot \frac{w_i^2}{v_{ij}(x_j)} \cdot - \frac{2 * \text{sign}(x_j - a_{ij})}{d_{ij}} \end{aligned} \quad (90.10)$$

Similarly:

$$\frac{\partial E}{\partial b_{ij}} = 4(y - y^t) \cdot \frac{\sum_{j=1, j \neq i}^n w_j^1}{(\sum_{i=1}^n w_i^1)^3} \cdot \frac{(w_i^1)^2}{\mu_{ij}(x_j)} \cdot \frac{1 - \mu_{ij}(x_j)}{b_{ij}} \quad (90.11)$$

Step 2: non-membership function parameters training

According to the triangular membership and non-membership characteristic, only the parameters meet the condition $c_{ij} \geq b_{ij}$, the summing of membership and non-membership can less then 1, so the parameter c_{ij} of non-membership update rule is:

$$c_{ij}(t + 1) = \begin{cases} c_{ij}(t) - \frac{\eta_a}{p} \frac{\partial E}{\partial c_{ij}}, & \text{if } c_{ij}(t + 1)_{ij}(t + 1) \\ b_{ij}(t + 1), & \text{elseif} \end{cases} \quad (90.12)$$

where,

$$\frac{\partial E}{\partial c_{ij}} = (y - y^t) \cdot r_i \cdot \left(1 - 2 \frac{w_i^2}{\sum_{i=1}^n w_i^2} \right) \cdot \frac{\sum_{j=1, j \neq i}^n w_j^2}{(\sum_{i=1}^n w_i^2)^2} \cdot \frac{w_i^2}{v_{ij}(x_j)} \cdot \frac{-v_{ij}(x_{ij})}{c_{ij}} \quad (90.13)$$

Using the same method, we can give the training algorithm for non-symmetric triangular membership and 1 minus non-symmetric form non-membership. Because of the space limitation, this part of is omitted.

90.5 Specific Example

An example is given in [15], demonstrates the fuzzy neural with non-symmetric triangular membership after training using gradient descent algorithm and least squares regression techniques can approximate the function.

$$f(x) = 0.05 * x^3 - 0.02 * x^2 - 0.3 * x + 20$$

Using the same function, we can prove that, the intuitionistic neural network with non-symmetric triangular membership and 1 minus non-symmetric form non-membership can approximate the function more accurate than fuzzy neural network.

Three membership and non-membership functions of intuitionistic neural network are defined as the Fig. 90.2.

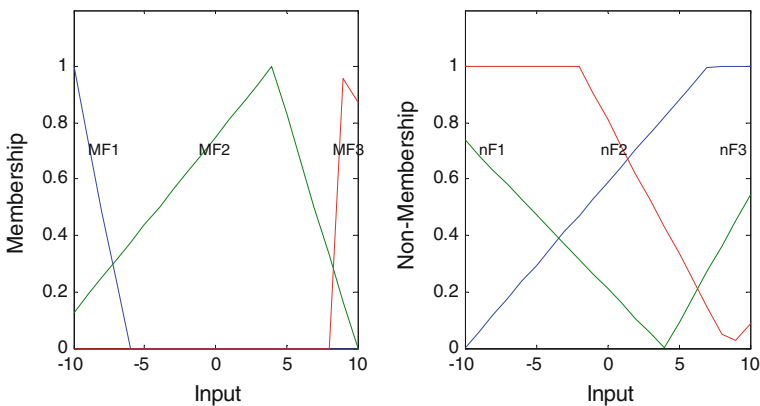


Fig. 90.2 Membership and non-membership function

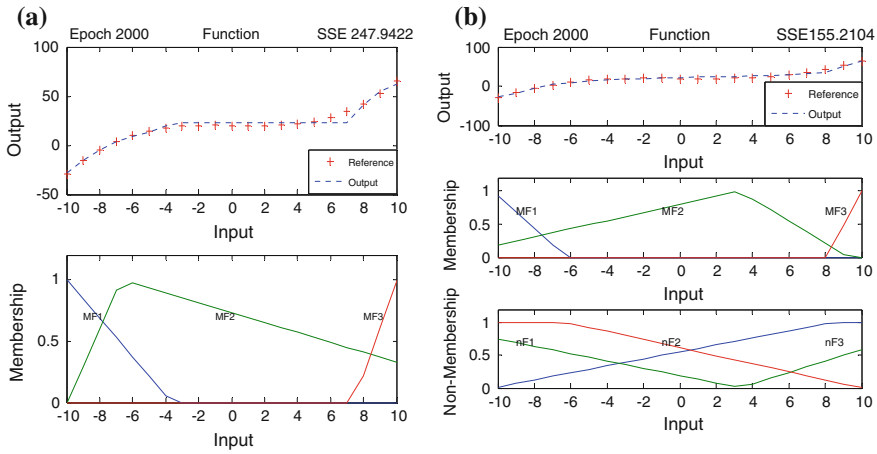


Fig. 90.3 Function approximation performance and membership and non-membership function. **a** FNN **b** IFNN

Learning rate of membership function parameters a, b, c are defined as 0.01, 0.01, 0.005, learning rate of non-membership function parameters d and e are defined as 0.01, 0.005.

After 2,000 epochs, the final membership functions and function approximation of FNN and the final membership and non-membership functions and function approximation of IFNN is shown in the below two graphs. From the two graphs, we can see that, after 2,000 epochs, the SSE of FNN is 247.9, and IFNN is 155.2, the IFNN has a higher degree of accuracy (Fig. 90.3).

The trajectory of total squared errors is plotted in Fig. 90.4. The Fig. 90.4 shows that difference between varying curve of error in FNN and IFNN. It shows that learning efficiency of IFF is higher than that of FNN, and IFF has faster convergence speed.

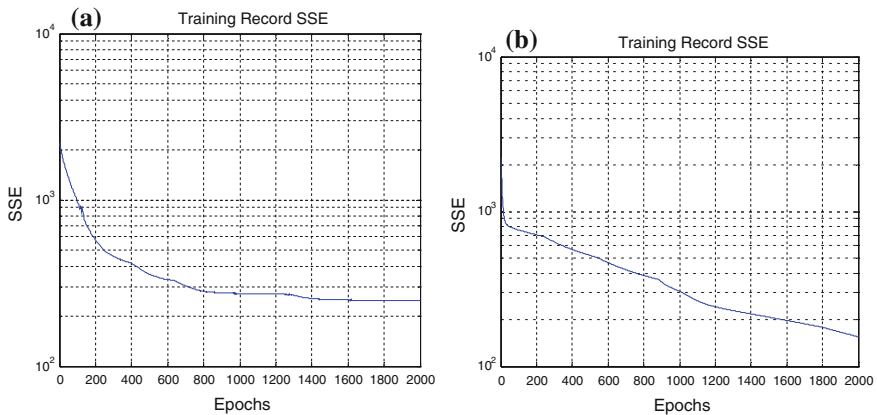


Fig. 90.4 SSE training performance **a** FNN **b** IFNN

90.6 Conclusion

An intuitionistic fuzzy neural network with triangular membership function and 1 minus triangular form non-membership function is proposed. The structure of the intuitionistic fuzzy neural is six layers. The two steps dynamic optimal training algorithms for the IFNN is development, the first step is membership function parameters training, the second step is membership function parameters training, which can promise the summing of the trained membership and non-membership functions on finite universal set less than 1. The simulation results demonstrated the IFNN has a higher degree of accuracy than FNN, and shows that learning efficiency of IFNN is higher than that of FNN.

References

1. Atanassov K (1986) Intuitionistic fuzzy sets. *Fuzzy Sets Syst* 20(11):87–96
2. Atanassov K (1989) More on Intuitionistic fuzzy sets. *Fuzzy Sets Syst* 33(3):37–46
3. Atanassov K (1999) Intuitionistic fuzzy sets: theory and applications. Physica Verlag, Wyrzburg 1999
4. Wei G, Yi W (2008) Method for intuitionistic fuzzy multiple attribute decision making without weight information but with preference information on alternatives. In: Chinese control and decision conference, pp 1974–1974
5. Xu AS (2007) Multi-person multi-attribute decision making models under intuitionistic fuzzy environment. *Fuzzy Opt Decis Making* 11(6):221–236
6. Li DF, Cheng CT (2002) New similarity measures of intuitionistic fuzzy sets and application to pattern recognitions. *Pattern Recogn Lett* 23(10):221–225
7. Olej V, Hajek P (2008) Air quality classification by intuitionistic fuzzy relations and Kohonen's self organizing feature maps. *Sci Papers Univ Pardubice* 8(11):146–152
8. Olej V (2010) IF-inference systems design for prediction of ozone time series. In: Proceedings of the 20th international conference on artificial neural networks, Thessaloniki, Greece
9. Liang YC, Feng DP, Liu GR, Yang XW, Han X (2003) Neural identification of rock parameters using fuzzy adaptive learning parameters. *Comput Struct* 81(1):2373–2382
10. Baruch IS, Lopez QB, Flores JM (2008) A fuzzy-neural multi-model for nonlinear systems identification and control. *Fuzzy Sets Syst* 159(1):2650–2667
11. Hsua CF, Linb PZ (1996) Adaptive asymmetric fuzzy. *Fuzzy Sets Syst* 79(4):403–405
12. Li L, Yang J, Wu W (2005) Intuitionistic fuzzy hopfield neural network and its stability. *Expert Syst Appl* 129(1):589–597
13. Lei Y, Lu Y, Li Z (2007) Function approximation capabilities of intuitionistic fuzzy reasoning neural networks. *Control Decis* 5(4):596–600 (in chinese)
14. Castillo O, Melin P (2003) A new method for fuzzy inference in intuitionistic fuzzy systems. In: Proceedings of the international conference NAFIPS 2003, IEEE Press, Chicago, pp 20–25
15. Wu SQ, Er MJ, Gao Y (2001) A fast approach for automatic generation of fuzzy rules by generalized dynamic fuzzy neural networks. *IEEE Trans Fuzzy Syst* 9(10):578–594

Chapter 91

Covariance Intersection Fusion Robust Steady-State Kalman Predictor for Two-Sensor Systems with Unknown Noise Variances

Wenjuan Qi, Peng Zhang and Zili Deng

Abstract For two-sensor systems with uncertainties of noise variances, a local robust steady-state Kalman one-step and multi-step predictors with the minimum upper bounds variances are presented respectively. Their robustness is proved based on the Lyapunov equation. Further, the covariance intersection (CI) fusion robust steady-state Kalman predictors are also presented by the convex combination of the local robust Kalman predictors. It is proved that its robust accuracy is higher than that of each local robust Kalman predictor. A Monte-Carlo simulation example shows its correctness and effectiveness.

Keywords Multisensor system · Uncertain noise variances · Covariance intersection fusion · Robust Kalman predictor

91.1 Introduction

The Kalman filtering is the basic tool to handle the state estimate problems, but it needs to know the exact system model parameters and noise variances. In many application problems, the systems have the uncertainties of model parameters or noise variances, in order to solve the filtering problems for uncertain systems, several results have been derived on the design of robust Kalman filters by the Riccati equation method [1, 2] or the linear matrix inequality (LMI) method [3]. These methods give the minimum upper bound of the filtering error variances for all admissible uncertainties of model parameters [4, 5], but have the limitation that the noise variances are assumed to be exactly known. Based on the Riccati equations, recently, the covariance intersection fusion method has been presented

W. Qi · P. Zhang · Z. Deng (✉)

Department of Automation, Heilongjiang University, XueFu Road 74, Heilongjiang University Electronic and Engineering College130, Harbin 150080, China
e-mail: dzl@hlju.edu.cn

by [6], which can handle the systems with unknown variances and cross-covariances.

In this paper, the two-sensor systems with uncertainties of noise variances are considered. First, the local robust steady-state Kalman one-step and multi-step predictors are presented. Their robustness is proved based on the Lyapunov equation. Then, the covariance intersection fusion robust Kalman predictor is proposed by the convex combination of the local robust Kalman predictors, whose robust accuracy is higher than that of each local robust Kalman predictor [8].

The geometric interpretation is given based on the covariance ellipses [8]. In order to verify the correctness of theoretical accuracy relations, a Monte-Carlo simulation example is given for a two-sensor tracking system.

91.2 Local Robust Steady-State One-Step Kalman Predictor

Consider the two-sensor system with uncertainty of noise variances

$$x(t + 1) = \Phi x(t) + \Gamma w(t) \tag{91.1}$$

$$y_i(t) = H_i x(t) + v_i(t), \quad i = 1, 2 \tag{91.2}$$

where t is the discrete time, $x(t) \in R^n$ is the state, $y_i(t) \in R^{m_i}$ is the measurement of the i th subsystem, $w(t) \in R^r$, $v_i(t) \in R^{m_i}$ are uncorrelated white noises with zeros mean and unknown actual variances \bar{Q}_w and \bar{Q}_{vi} , respectively. Φ , Γ and H_i are known constant matrices. Assume that Q_w and Q_{vi} are conservative upper bounds of \bar{Q}_w and \bar{Q}_{vi} , respectively, i.e.

$$\bar{Q}_w \leq Q_w, \bar{Q}_{vi} \leq Q_{vi}, \quad i = 1, 2 \tag{91.3}$$

And assume that each subsystem is completely observable and controllable.

Based on the i th sensor, the local steady-state Kalman one-step predictor with conservative upper bounds Q_w and Q_{vi} are given by [4, 5]

$$\hat{x}_i(t + 1|t) = \Psi_{pi} \hat{x}_i(t|t - 1) + K_{pi} y_i(t) \tag{91.4}$$

$$\Psi_{pi} = \Phi - K_{pi} H_i, K_{pi} = \Phi \Sigma_i H_i^T (H_i \Sigma_i H_i^T + Q_{vi})^{-1} \tag{91.5}$$

where the symbol T denotes the transpose, and Σ_i satisfies the Riccati equation

$$\Sigma_i = \Phi \left[\Sigma_i - \Sigma_i H_i^T (H_i \Sigma_i H_i^T + Q_{vi})^{-1} H_i \Sigma_i \right] \Phi^T + \Gamma Q_w \Gamma^T \tag{91.6}$$

From (91.5, 91.6) can be rewritten as the Layapunov equation

$$\Sigma_i = \Psi_{pi} \Sigma_i \Psi_{pi}^T + \Gamma Q_w \Gamma^T + K_{pi} Q_{vi} K_{pi}^T \tag{91.7}$$

Defining the actual steady-state one-step predictor error variance as

$$\bar{\Sigma}_i = E[\tilde{x}_i(t+1|t)\tilde{x}_i^T(t+1|t)], \tilde{x}_i(t+1|t) = x(t+1) - \hat{x}_i(t+1|t) \quad (91.8)$$

where E denotes the mathematical expectation, we have the following Theorem 1.

Theorem 1 *The Kalman one-step predictor (91.4–91.6) is robust for all admissible actual variances \bar{Q}_w and \bar{Q}_{vi} satisfying $\bar{Q}_w \leq Q_w, \bar{Q}_{vi} \leq Q_{vi}$, in the sense that*

$$\bar{\Sigma}_i \leq \Sigma_i \quad (91.9)$$

Proof Applying (91.1) and (91.8) yields $\tilde{x}_i(t+1|t) = \Phi\tilde{x}_i(t|t) + \Gamma w(t)$
 $\hat{x}_i(t+1|t) = \Phi\hat{x}_i(t|t)$, where
 $\tilde{x}_i(t|t) = [I_n - K_{fi}H]\tilde{x}_i(t|t-1) - K_{fi}v_i(t), K_{fi} = \Sigma_i H_i^T (H_i \Sigma_i H_i^T + Q_{vi})^{-1}$. Hence we have

$$\tilde{x}_i(t+1|t) = \Psi_{pi}\tilde{x}_i(t|t-1) + \Gamma w(t) - K_{pi}v_i(t) \quad (91.10)$$

Substituting (91.10) into (91.8) yields the actual one-step predictor error variance as

$$\bar{\Sigma}_i = \Psi_{pi}\bar{\Sigma}_i\Psi_{pi}^T + \Gamma\bar{Q}_w\Gamma^T + K_{pi}\bar{Q}_{vi}K_{pi}^T \quad (91.11)$$

Defining $\Delta\Sigma_i = \Sigma_i - \bar{\Sigma}_i$, and subtracting (91.11) from (91.6) yield the Lyapunov equation

$$\Delta\Sigma_i = \Psi_{pi}\Delta\Sigma_i\Psi_{pi}^T + \Gamma(Q_w - \bar{Q}_w)\Gamma^T + K_{pi}(Q_{vi} - \bar{Q}_{vi})K_{pi}^T \quad (91.12)$$

Applying (91.3), noting that Ψ_{pi} is a stable matrix, and applying the property of the Lyapunov equation [7] yield that $\Delta\Sigma_i \geq 0$, i.e. $\bar{\Sigma}_i \leq \Sigma_i$. The proof is completed.

91.3 Local Robust Steady-State Multi-Step Kalman Predictor

The local steady-state Kalman multi-step predictors are given by [4, 5]

$$\hat{x}_i(t+N|t) = \Phi^{N-1}\hat{x}_i(t+1|t), \quad N \geq 2, i = 1, 2 \quad (91.13)$$

The computed local steady-state multi-step predictor error variances are given as

$$P_i(N) = \Phi^{N-1}\Sigma_i(\Phi^{N-1})^T + \sum_{j=0}^{N-2} \Phi^j\Gamma Q_w\Gamma^T(\Phi^j)^T, \quad N \geq 2, i = 1, 2 \quad (91.14)$$

Defining the actual steady-state multi-step predictor error variance as

$$\bar{P}_i(N) = E[\tilde{x}_i(t+N|t)\tilde{x}_i^T(t+N|t)], \tilde{x}_i(t+N|t) = x(t+N) - \hat{x}_i(t+N|t) \quad (91.15)$$

Theorem 2 *The Kalman multi-step predictors (91.13–91.14) are robust for all admissible actual variances \bar{Q}_w and \bar{Q}_{vi} satisfying $\bar{Q}_w \leq Q_w$, $\bar{Q}_{vi} \leq Q_{vi}$, in the sense that*

$$\bar{P}_i(N) \leq P_i(N) \quad (91.16)$$

Proof Iterating $N - 1$ times for (91.1), we obtain the non-recursive formula as

$$x(t+N) = \Phi^{N-1}x(t+1) + \sum_{j=0}^{N-2} \Phi^j \Gamma w(t-1) \quad (91.17)$$

From (91.13) and (91.17), we obtain

$$\tilde{x}_i(t+N|t) = \Phi^{N-1}\tilde{x}_i(t+1|t) + \sum_{j=0}^{N-2} \Phi^j \Gamma w(t-1) \quad (91.18)$$

Substituting (91.18) into (91.15) yields the actual steady-state prediction error variance as

$$\bar{P}_i(N) = \Phi^{N-1}\bar{\Sigma}_i(\Phi^{N-1})^T + \sum_{j=0}^{N-2} \Phi^j \Gamma \bar{Q}_w \Gamma^T (\Phi^j)^T, N \geq 2 \quad (91.19)$$

Defining $\Delta P_i(N) = P_i(N) - \bar{P}_i(N)$, subtracting (91.19) from (91.14) yields

$$\Delta P_i(N) = \Phi^{N-1}(\Sigma_i - \bar{\Sigma}_i)(\Phi^{N-1})^T + \sum_{j=0}^{N-2} \Phi^j \Gamma (Q_w - \bar{Q}_w) \Gamma^T (\Phi^j)^T \quad (91.20)$$

Applying (91.3) and (91.9) yields that $\Sigma_i - \bar{\Sigma}_i \geq 0$ and $Q_w - \bar{Q}_w \geq 0$, so $\Delta P_i(N) \geq 0$, i.e. (91.16) holds. The proof is completed.

91.4 CI Fusion Robust Steady-State Kalman Predictor

Applying the CI fused algorithm [6], the CI fusion robust steady-state one-step and multi-step predictors are presented as following

$$\begin{aligned} \hat{x}_{CI}(t+N|t) &= P_{CI}(N)(\omega(N)P_1^{-1}(N)\hat{x}_1(t+N|t) \\ &\quad + (1-\omega(N))P_2^{-1}(N)\hat{x}_2(t+N|t)), N \geq 1 \end{aligned} \quad (91.21)$$

$$P_{CI}(N) = [\omega(N)P_1^{-1}(N) + (1-\omega(N))P_2^{-1}(N)]^{-1}, N \geq 1 \quad (91.22)$$

with the constraint $\omega(N) \geq 0$, when $N = 1$, defining $P_1(1) = \Sigma_1$, $P_2(1) = \Sigma_2$.

The weighting coefficient $\omega(N)$ is obtained by minimizing the performance index

$$\min_{\omega(N)} \text{tr} P_{CI}(N) = \min_{\omega(N) \in [0,1]} \text{tr} \left\{ [\omega(N)P_1^{-1}(N) + (1-\omega(N))P_2^{-1}(N)]^{-1} \right\} \quad (91.23)$$

where the symbol tr denotes the trace of matrix. For the optimization problem (91.23), the optimal weights $\omega(N)$ can be quickly obtained by the 0.618 method.

Theorem 3 *The covariance intersection fusion robust Kalman predictors (91.21) and (91.22) has the actual fused error variance $\bar{P}_{CI}(N)$ as*

$$\begin{aligned} \bar{P}_{CI}(N) &= \mathbb{E}[\tilde{x}_{CI}(t+N|t)\tilde{x}_{CI}^T(t+N|t)] \\ &= P_{CI}(N) [\omega^2(N)P_1^{-1}(N)\bar{P}_1(N)P_1^{-1}(N) \\ &\quad + \omega(N)(1-\omega(N))P_1^{-1}(N)\bar{P}_{12}(N)P_2^{-1}(N) \\ &\quad + \omega(N)(1-\omega(N))P_2^{-1}(N)\bar{P}_{21}(N)P_1^{-1}(N) \\ &\quad + (1-\omega(N))^2P_2^{-1}(N)\bar{P}_2(N)P_2^{-1}(N)] P_{CI}(N) \end{aligned} \tag{91.24}$$

where we define the actual fused prediction error and the actual cross-covariance between the local prediction errors as $\tilde{x}_{CI}(t+N|t) = x(t+N) - \hat{x}_{CI}(t+N|t)$, $\bar{P}_{12}(N) = \mathbb{E}[\tilde{x}_1(t+N|t)\tilde{x}_2^T(t+N|t)]$, $\bar{P}_{21}(N) = \bar{P}_{12}^T(N)$. When $N = 1$, we define $\bar{P}_1(1) = \bar{\Sigma}_1$, $\bar{P}_2(1) = \bar{\Sigma}_2$, $\bar{P}_{12}(1) = \bar{\Sigma}_{12}$, $\bar{P}_{21}(1) = \bar{\Sigma}_{21}$, $\bar{\Sigma}_{21} = \bar{\Sigma}_{12}^T$. Then we have

$$\bar{\Sigma}_{12} = \Psi_{p1}\bar{\Sigma}_{12}\Psi_{p2}^T + \Gamma\bar{Q}_w\Gamma^T, N = 1 \tag{91.25}$$

$$\bar{P}_{12}(N) = \Phi^{N-1}\bar{\Sigma}_{12}(\Phi^{N-1})^T + \sum_{j=0}^{N-2} \Phi^j\Gamma\bar{Q}_w\Gamma^T(\Phi^j)^T, N \geq 2 \tag{91.26}$$

Proof From (91.22), we have

$$x(t+N) = P_{CI}(N) [\omega(N)P_1^{-1}(N) + (1-\omega(N))P_2^{-1}(N)]x(t+N) \tag{91.27}$$

Subtracting (91.21) from (91.27), we obtain the CI fused actual predictor error

$$\begin{aligned} \tilde{x}_{CI}(t+N|t) &= P_{CI}(N) [\omega(N)P_1^{-1}(N)\tilde{x}_1(t+N|t) \\ &\quad + (1-\omega(N))P_2^{-1}(N)\tilde{x}_2(t+N|t)] \end{aligned} \tag{91.28}$$

which yields (91.24). From (91.10), we can easily obtain the actual one-step predictor error cross-covariance (91.25), and applying (91.18) yields (91.26). The proof is completed.

Theorem 4 *The two-sensor CI fuser (91.21–91.23) is robust with respect to uncertainty of noise variances, i.e. for all admissible \bar{Q}_w and \bar{Q}_{vi} satisfying (91.3)*

$$\bar{P}_{CI}(N) \leq P_{CI}(N) \tag{91.29}$$

Proof For $\bar{Q}_w \leq Q_w$, $\bar{Q}_{vi} \leq Q_{vi}$, from (91.16) we have $\bar{P}_i(N) \leq P_i(N)$. According to the consistency of the CI fuser [6], we have (91.29). The proof is completed.

Remark 1 From (91.9, 91.16) and (91.29), we see that for $\bar{Q}_w \leq Q_w, \bar{Q}_{vi} \leq Q_{vi}, \Sigma_i, P_i(N)$ and $P_{CI}(N)$ are the minimum upper bounds of the unknown actual variances $\bar{\Sigma}_i, \bar{P}_i(N)$ and $\bar{P}_{CI}(N)$, respectively. They control the global accuracies of the corresponding robust local and fused predictors. Therefore $\text{tr} \Sigma_i, \text{tr} P_i(N)$ and $\text{tr} P_{CI}(N)$ are called the robust accuracies of the corresponding robust predictors. The robustness means the minimum upper bound variances $\Sigma_i, P_i(N)$ and $P_{CI}(N)$ are ensured for uncertainty of noise variances satisfying (91.3).

91.5 Accuracy Analysis

Theorem 5 For the two-sensor uncertain system (91.1–91.3), the local and CI fused robust Kalman predictors have the following accuracy relations

$$\text{tr} \bar{P}_i(N) \leq \text{tr} P_i(N), i = 1, 2 \tag{91.30}$$

$$\text{tr} \bar{P}_{CI}(N) \leq \text{tr} P_{CI}(N) \leq \text{tr} P_i(N), i = 1, 2 \tag{91.31}$$

Proof From (91.16, 91.30) holds. From (91.29), the first inequality of (91.31) holds. Applying (91.23), taking $\omega = 1$ yields $\text{tr} P_{CI}(N) = \text{tr} P_1(N)$, and taking $\omega = 0$ yields $\text{tr} P_{CI}(N) = \text{tr} P_2(N)$, Hence when $\omega \in [0, 1]$, we have the accuracy relations $\text{tr} P_{CI}(N) \leq \text{tr} P_i(N), i = 1, 2$. The proof is completed.

Remark 2 The inequality (91.31) yields that the robust accuracy of the CI fusion predictor is higher than that of each local predictor.

91.6 Simulation Example

Consider the two-sensor tracking system (91.1–91.2) with uncertain noise variances, where $\Phi = \begin{bmatrix} 1 & T_0 \\ 0 & 1 \end{bmatrix}, \Gamma = \begin{bmatrix} 0.5T_0^2 \\ T_0 \end{bmatrix}, H_1 = [1 \ 0], H_2 = I_2, T_0 = 0.25$ is the sampled period, $x(t) = [x_1(t), x_2(t)]^T$ is the state, $x_1(t)$ and $x_2(t)$ are the position and velocity of target at time tT_0 . $w(t)$ and $v_i(t)$ are independent Gaussian white noises with zero mean and unknown actual variances \bar{Q}_w and \bar{Q}_{vi} respectively.

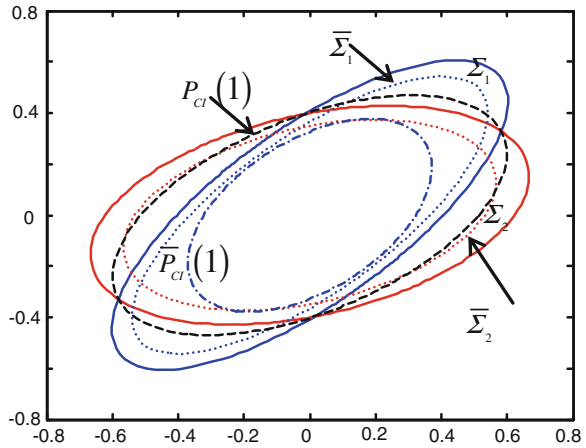
In the simulation, we take $Q_w = 1, Q_{v1} = 0.8, Q_{v2} = \text{diag}(8, 0.36), \bar{Q}_w = 0.8, \bar{Q}_{v1} = 0.65, \bar{Q}_{v2} = \text{diag}(6, 0.25), N = 1$.

The traces of the error variance of the local and CI fused one-step Kalman predictors are compared in Table 91.1. From Table 91.1, we see that the accuracy relations (91.30) and (91.31) hold.

Table 91.1 The robust accuracy comparison of local and fused Kalman predictors

	$\text{tr} \Sigma_1$	$\text{tr} \Sigma_2$	$\text{tr} \bar{\Sigma}_1$	$\text{tr} \bar{\Sigma}_2$	$\text{tr} P_{CI}$	$\text{tr} \bar{P}_{CI}$
$N = 1$	0.7291	0.6278	0.5875	0.4603	0.5788	0.2801

Fig. 91.1 The covariance ellipses of one-step robust Kalman predictors



The accuracy comparison based on the covariance ellipses is shown in Fig. 91.1. From Fig. 91.1, we see that the ellipses of the actual variances $\bar{\Sigma}_1$ are enclosed in that of the upper bound variances Σ_1 , which verify the robustness (91.9) [8]. The ellipse of actual CI fused variance $\bar{P}_{CI}(1)$ is enclosed in that of $P_{CI}(1)$, which verifies the robustness of (91.29) [8].

In order to verify the above theoretical accuracy relations, taking $\rho = 200$ runs, the curves of the mean square error (MSE) of local and fused Kalman one-step predictors are shown in Fig. 91.2. From Fig. 91.2, we see that the MSE values of

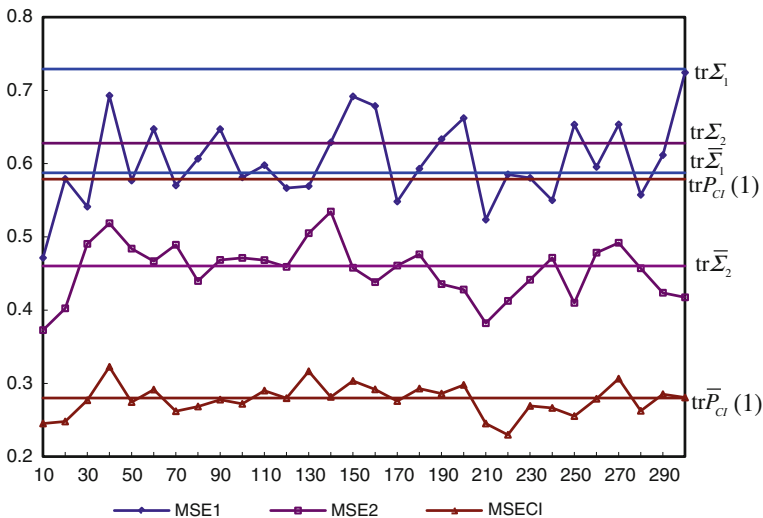


Fig. 91.2 The MSE curves of local and fused one-step predictors

local and CI fused predictors are close to the corresponding theoretical trace values, which also verifies the accuracy relations (91.30, 91.31) and the accuracy relations in Table 91.1.

91.7 Conclusion

The main distributions of this paper are as follows:

1. For the two-sensor systems with uncertainties of noise variances, the local one-step and multi-step robust steady-state Kalman predictors and the CI fusion robust Kalman predictor have been presented. The corresponding upper bound variances are given which are insensitive to the uncertainty of noise variances.
2. A new robustness analysis approach was presented, where the robustness of the proposed local Kalman predictors is proved based on the Lyapunov equation.
3. It was proved that the robust accuracy of the CI fusion predictor is higher than that of each local Kalman predictor.

Acknowledgments This work is supported by the Natural Science Foundation of China under grant NSFC-60874063, the 2012 Innovation and Scientific Research Foundation of graduate student of Heilongjiang Province under grant YJSCX2012-263HLJ, and the Support Program for Young Professionals in Regular Higher Education Institutions of Heilongjiang Province under grant 1251G012.

References

1. Lu X, Zhang H, Wang W (2007) Robust Kalman filtering for discrete-time systems with measurement delay. *IEEE Trans Circuits Syst II Express Briefs* 54(6):522–626
2. Zhu X, Soh YC, Xie L (2002) Design and analysis of discrete-time robust Kalman filters. *Automatica* 38:1069–1077
3. Wang F, Balakrishnan V (2003) Robust steady-state filtering for systems with deterministic and stochastic uncertainties. *IEEE Trans Signal Process* 51(10):2550–2668
4. Zhu X, Soh YC, Xie L (2002) Design and analysis of discrete-time robust Kalman filters. *Automatica* 38:1069–1077
5. Theodor Y, Shaked U (1996) Robust discrete-time minimum-variance filtering. *IEEE Trans Signal Process* 44(2):181–189
6. Julier SJ, Uhlman JK (2009) General decentralized data fusion with covariance intersection. In: Liggins ME, Hall DL, Linas JL (eds) *Handbook of multisensor data fusion, theory and practice*. CRC Press, New York, pp 319–342
7. Kailath T, Sayed AH, Hassibi B (2000) *Linear estimation*. Prentice Hall, New York
8. Deng Z, Zhang P, Qi W, Liu J, Gao Y (2012) Sequential covariance intersection fusion Kalman filter. *Inf Sci* 189:293–309

Chapter 92

Weighted Measurement Fusion

Steady-State Robust Kalman Filter

Peng Zhang, Wenjuan Qi and Zili Deng

Abstract For multisensor systems with uncertain noise variances, two kinds of weighted measurement fusion steady-state robust Kalman filters with the conservative upper bound of noise variances are presented. Based on Lyapunov equation, it is proved that the weighted measurement fusion, the centralized fusion and local steady-state Kalman filters are robust. Further, it is proved that the robust accuracy of weighted measurement fusion robust Kalman filter is equal to that of centralized robust Kalman filter, which are higher than that of local steady-state Kalman filter. A Monte-Carlo Simulation example shows its effectiveness.

Keywords Multisensor data fusion · Weighted measurement fusion · Uncertain noise variance · Robust · Kalman filter

92.1 Introduction

The multisensor data fusion Kalman filtering has been widely applied to many fields including defence, tracking, GPS positioning [1, 2]. The fundamental requirement of a fuser is that it is able to combine the local data or local estimators obtained from each sensor of multisensor to improve the estimator accuracy of the state or signal.

For Kalman filter-based data fusion, there exists two methodologies [3, 4], the state and measurement fusion methods. The state fusion methods combine the

P. Zhang

Department of Computer and Information Engineering,
Harbin Deqiang College of Commerce, Harbin 150025, China
e-mail: zp52218@sina.com.cn

W. Qi · Z. Deng (✉)

Department of Automation, Electronic and Engineering College,
Heilongjiang University, XueFu Road 74, Harbin 150080, China
e-mail: dzl@hlju.edu.cn

local state estimators to obtain an improved fusion state estimators, whereas measurement fusion methods directly fuse the sensor measurements to a weighted fused measurement, and then use a single Kalman filter to obtain the final fused state estimators [3, 4]. However, since the system model is usually an approximation to a physical situation in many applications, the model parameters and noise statistics are seldom exact. To solve the filtering problems for the systems with parameters uncertainties, based on Riccati equation, several results have been derived on the design of robust Kalman filter which give an upper bound on the filtering error variances for all admissible uncertainty of model parameters [5, 6].

In this paper, for multisensor systems with uncertain noise variances, the local, centralized fusion, weighted measurement fusion steady-state robust filters are presented, which give upper bounds of actual filtering error variances. And, based on the Lyapunov equations, their robustness and accuracy relations are proved.

92.2 Weighted Measurement, Centralized Fusion and Local Steady-State Robust Kalman Filter

Consider multisensor system with unknown noise variances

$$x(t + 1) = \Phi x(t) + \Gamma w(t) \tag{92.1}$$

$$y_i(t) = H_i x(t) + v_i(t), \quad i = 1, \dots, L \tag{92.2}$$

where t is the discrete time, $x(t) \in R^n$ is the state, $y_i(t) \in R^{m_i}$ is the measurement of the i th subsystem, $w(t) \in R^r$, $v_i(t) \in R^{m_i}$ are white noises with zero mean and unknown actual variances \bar{Q} and \bar{R}_i , respectively. $\Phi\Gamma$ and H_i are known constant matrices. Assume [7] that Q and R_i are conservative upper bounds of \bar{Q} and \bar{R}_i , respectively, i.e.

$$\bar{Q} \leq Q, \bar{R}_i \leq R_i, i = 1, \dots, L \tag{92.3}$$

and each subsystem is completely observable and completely controllable.

Assume that each subsystem measurement matrix H_i has a common $m \times n$ right factor H , i.e.

$$H_i = M_i H, i = 1, \dots, L \tag{92.4}$$

where M_i is $m_i \times n$ matrix, and there exists the inverse matrix $[H^{(0)T} R^{(0)-1} H^{(0)}]^{-1}$ or $[M^{(0)T} R^{(0)-1} M^{(0)}]^{-1}$, where define

$$M^{(0)} = [M_1^T, \dots, M_L^T]^T \tag{92.5}$$

Combining all the subsystems to a fused measurement equation as

$$y^{(l)}(t) = H^{(l)} x(t) + v^{(l)}(t), \quad l = 0, 1, 2 \tag{92.6}$$

When $I = 0$, (92.6) is called the centralized fusion measurement equation [9], where

$$\begin{aligned} y^{(0)}(t) &= [y_1^T(t), \dots, y_L^T(t)]^T, H^{(0)} = [H_1^T, \dots, H_L^T]^T, \\ v^{(0)}(t) &= [v_1^T(t), \dots, v_L^T(t)]^T, R^{(0)} = \text{block - diag}[R_1, \dots, R_L] \end{aligned} \quad (92.7)$$

When $I = 1$, (92.6) is called the measurement equation of weighted measurement fusion algorithm 1 [8], where

$$\begin{aligned} y^{(1)}(t) &= [M^{(0)T}R^{(0)-1}M^{(0)}]^{-1}M^{(0)T}R^{(0)-1}y^{(0)}(t), H^{(1)} = H, \\ v^{(1)}(t) &= \sum_{i=1}^L [M_i^T R_i^{-1} M_i]^{-1} \sum_{i=1}^L M_i^T R_i^{-1} v_i(t), R^{(1)} = [M^{(0)T}R^{(0)-1}M^{(0)}]^{-1} \end{aligned} \quad (92.8)$$

When $I = 2$, (92.6) is called the measurement equation of weighted measurement fusion algorithm 2 [8], where

$$\begin{aligned} y^{(2)}(t) &= [H^{(0)T}R^{(0)-1}H^{(0)}]^{-1}H^{(0)T}R^{(0)-1}y^{(0)}(t), H^{(2)} = I_n, \\ v^{(2)}(t) &= \sum_{i=1}^L [H_i^T R_i^{-1} H_i]^{-1} \sum_{i=1}^L H_i^T R_i^{-1} v_i(t), R^{(2)} = [H^{(0)T}R^{(0)-1}H^{(0)}]^{-1} \end{aligned} \quad (92.9)$$

The weighted measurement fusion, centralized fusion steady-state robust Kalman filters are given by [8]

$$\hat{x}^{(I)}(t|t) = \Psi^{(I)}\hat{x}^{(I)}(t-1|t-1) + K^{(I)}y^{(I)}(t), \quad I = 0, 1, 2 \quad (92.10)$$

where

$$\Psi^{(I)} = [I_n - K^{(I)}H^{(I)}]\Phi, K^{(I)} = \Sigma^{(I)}H^{(I)T}(H^{(I)}\Sigma^{(I)}H^{(I)T} + R^{(I)})^{-1} \quad (92.11)$$

the steady-state predicting error variance $\Sigma^{(I)}$ satisfies the Riccati equation

$$\Sigma^{(I)} = \Phi[\Sigma^{(I)} - \Sigma^{(I)}H^{(I)T}(H^{(I)}\Sigma^{(I)}H^{(I)T} + R^{(I)})^{-1}H^{(I)}\Sigma^{(I)}]\Phi^T + \Gamma Q \Gamma^T \quad (92.12)$$

The conservative upper bound fused filtering error variance $P^{(I)}$ with conservative upper bound Q and R is obtained by

$$P^{(I)} = (I_n - K^{(I)}H^{(I)})\Sigma^{(I)} \quad (92.13)$$

and from [7], it can be written as

$$P^{(I)} = \Psi^{(I)}P^{(I)}\Psi^{(I)T} + (I_n - K^{(I)}H^{(I)})\Gamma Q \Gamma^T (I_n - K^{(I)}H^{(I)})^T + K^{(I)}R^{(I)}K^{(I)T} \quad (92.14)$$

Defining the actual steady-state fusion error variance $\bar{P}^{(I)} = E[\tilde{x}^{(I)}(t|t)\tilde{x}^{(I)T}(t|t)]$, substituting (92.1, 92.6, 92.10) and (92.11) to $\tilde{x}^{(I)}(t|t) = x(t) - \hat{x}^{(I)}(t|t)$, we can obtain

$$\tilde{x}^{(l)}(t|t) = \Psi^{(l)}\tilde{x}^{(l)}(t-1|t-1) + (I_n - K^{(l)}H^{(l)})\Gamma w(t-1) - K^{(l)}v^{(l)}(t) \quad (92.15)$$

Therefore, we can obtain the actual fusion error variance $\bar{P}^{(l)}$ as

$$\bar{P}^{(l)} = \Psi^{(l)}\bar{P}^{(l)}\Psi^{(l)T} + (I_n - K^{(l)}H^{(l)})\Gamma\bar{Q}\Gamma^T(I_n - K^{(l)}H^{(l)})^T + K^{(l)}\bar{R}^{(l)}K^{(l)T} \quad (92.16)$$

Remark 1 For uncertain multisensor system (92.1) and (92.2), similar to weighted measurement fusion and centralized fusion steady-state Kalman filters, the local robust steady-state Kalman filter with conservative upper variances \bar{Q} and \bar{R}_i given by (92.3) is given by [9]

$$\begin{aligned} \hat{x}_i(t|t) &= \Psi_i\hat{x}_i(t-1|t-1) + K_i y_i(t) \\ \Psi_i &= [I_n - K_i H_i]\Phi, K_i = \Sigma_i H_i^T (H_i \Sigma_i H_i^T + R_i)^{-1} \\ \Sigma_i &= \Phi[\Sigma_i - \Sigma_i H_i^T (H_i \Sigma_i H_i^T + R_i)^{-1} H_i \Sigma_i]\Phi^T + \Gamma Q \Gamma^T \\ P_i &= (I_n - K_i H_i)\Sigma_i \end{aligned} \quad (92.17)$$

$$P_i = \Psi_i P_i \Psi_i^T + (I_n - K_i H_i)\Gamma Q \Gamma^T (I_n - K_i H_i)^T + K_i R_i K_i^T \quad (92.18)$$

and the actual local filtering error variance is given by

$$\bar{P}_i = \Psi_i \bar{P}_i \Psi_i^T + (I_n - K_i H_i)\Gamma \bar{Q} \Gamma^T (I_n - K_i H_i)^T + K_i \bar{R}_i K_i^T \quad (92.19)$$

Theorem 1 For uncertain multisensor system (92.1) and (92.2), the weighted measurement fusion, the centralized fusion and local steady-state robust Kalman filters are robust, i.e. for all admissible $\bar{Q} \leq Q, \bar{R}_i \leq R_i$, we have

$$\bar{P}^{(l)} \leq P^{(l)}, \bar{P}_i \leq P_i, I = 0, 1, 2, \quad i = 1, \dots, L \quad (92.20)$$

where the upper bound variances $P^{(l)}$ and P_i are independent of \bar{Q} and \bar{R}_i .

Proof Defining $\Delta P^{(l)} = P^{(l)} - \bar{P}^{(l)}$, and subtracting (92.16) from (92.14) yields the Lyapunov equation

$$\Delta P^{(l)} = \Psi^{(l)} \Delta P^{(l)} \Psi^{(l)T} + \Lambda^{(l)} \quad (92.21)$$

$$\Lambda^{(l)} = (I_n - K^{(l)}H^{(l)})\Gamma(Q - \bar{Q})\Gamma^T(I_n - K^{(l)}H^{(l)})^T + K^{(l)}(R^{(l)} - \bar{R}^{(l)})K^{(l)T} \quad (92.22)$$

From (92.3), we can obtain that $\bar{Q} \leq Q, \bar{R}^{(l)} \leq R^{(l)}$, therefore $\Lambda^{(l)} \geq 0$, noting that $\Psi^{(l)}$ is stable, applying the property of Lyapunov equation [9], we have $\Delta P^{(l)} \geq 0$, i.e., $\bar{P}^{(l)} \leq P^{(l)}$. Similarly, it is easily proved that $\bar{P}_i \leq P_i (i = 1, \dots, L)$, the proof is completed.

92.3 The Accuracy Comparison

Theorem 2 For the uncertain multisensor systems (92.1) and (92.2), the accuracy relations among the weighted measurement fusion, centralized fusion and local steady-state robust Kalman filters are given as

$$P^{(0)} = P^{(1)} = P^{(2)} \quad (92.23)$$

and taking the initial values $\hat{x}^{(0)}(0|0) = \hat{x}^{(1)}(0|0) = \hat{x}^{(II)}(0|0)$, we have

$$\hat{x}^{(0)}(t|t) = \hat{x}^{(1)}(t|t) = \hat{x}^{(II)}(t|t), \forall t \quad (92.24)$$

$$\bar{P}^{(0)} = \bar{P}^{(1)} = \bar{P}^{(2)} \quad (92.25)$$

$$\bar{P}^{(I)} \leq P^{(I)} \leq P_i, \quad I = 0, 1, 2, \quad i = 1, \dots, L \quad (92.26)$$

$$\text{tr}\bar{P}^{(I)} \leq \text{tr}P^{(I)} \leq \text{tr}P_i, \quad I = 0, 1, 2, \quad i = 1, \dots, L \quad (92.27)$$

Proof (92.23) and (92.24) have been proved in [8], which yield (92.25). The first inequality of (92.26) has been proved in (92.20). The local, weighted measurement and centralized optimal robust Kalman filters are time-varying and have the form in information filter [9]

$$P^{(I)-1}(t|t) = P^{(I)-1}(t|t-1) + H^{(I)T}R^{(I)-1}H^{(I)}, I = 0, 1, 2 \quad (92.28)$$

$$P_i^{-1}(t|t) = P_i^{-1}(t|t-1) + H_i^T R_i^{-1} H_i \quad (92.29)$$

$$P^{(I)}(t|t-1) = \Phi P^{(I)}(t-1|t-1) \Phi^T + \Gamma Q \Gamma^T \quad (92.30)$$

$$P_i(t|t-1) = \Phi P_i(t-1|t-1) \Phi^T + \Gamma Q \Gamma^T \quad (92.31)$$

Taking the same initial value $P^{(I)}(0|0) = P_i(0|0)$, from (92.28–92.31), by mathematical induction method, it is easily proved that

$$P^{(I)}(t|t) \leq P_i(t|t), \quad I = 0, 1, 2, \quad i = 1, \dots, L \quad (92.32)$$

Taking limitation to (92.32), we have $P^{(I)} \leq P_i$. Taking the trace operation for (92.26) yields (92.27). The proof is completed.

92.4 Simulation Example

Consider 3-sensor tracking system

$$x(t + 1) = \begin{bmatrix} 1 & T_0 \\ 0 & 1 \end{bmatrix}x(t) + \begin{bmatrix} 0.5T_0^2 \\ T_0 \end{bmatrix}w(t) \tag{92.33}$$

$$y_i(t) = H_i x(t) + v_i(t), \quad i = 1, 2, 3 \tag{92.34}$$

where T_0 is the sample period, $H_1 = [1 \ 0]$, $H_2 = I_2$, $H_3 = [1 \ 0]$, $x(t) \in \mathbb{R}^2$ is the state, $x(t) = [x_1(t), x_2(t)]^T$, $x_1(t)$ and $x_2(t)$ are the position and velocity of target at time tT_0 , $y_i(t)$ is the measurement for sensor i , $w(t)$ and $v_i(t)$ are white noise with zero mean and unknown variances \bar{Q} and \bar{R}_i , respectively. Assume that Q and R_i are conservative estimates of \bar{Q} and \bar{R}_i , respectively. In the simulation, we take $T_0 = 0.4$, $Q = 2.3$, $R_1 = 1$, $R_2 = \text{diag}(5.5, 0.36)$, $R_3 = \text{diag}(5, 1.8)$, $\bar{Q} = 2$, $\bar{R}_1 = 0.8$, $\bar{R}_2 = \text{diag}(4.9, 0.25)$, $\bar{R}_3 = \text{diag}(4.2, 1.5)$.

The comparisons of the filtering error variance matrices between the local and centralized fused Kalman filters are shown in Tables 92.1, 92.2 and 92.3. From Tables 92.1 and 92.2, we can obtain that $P_i - \bar{P}_i \geq 0$, $P^{(I)} - \bar{P}^{(I)} \geq 0$, $P_i - P^{(I)} \geq 0$ ($I = 0, 1, 2$, $i = 1, 2, 3$), i.e., these matrices are positive definite, and also shows that the relations (92.20, 92.23) and (92.24) hold.

In the simulation, taking the initial values $\hat{x}^{(0)}(0|0) = \hat{x}^{(I)}(0|0) = \hat{x}^{(II)}(0|0) = [0, 0]^T$, we have $\hat{x}^{(0)}(t|t) = \hat{x}^{(I)}(t|t) = \hat{x}^{(II)}(t|t) = [-105.6, -4.9]^T$, ($t = 100$), which demonstrates that (92.24) holds numerically.

In order to verify the above theoretical results for the accuracy relation, the 200 Monte-Carlo runs are performed. The mean-square error (MSE) curves of the local

Table 92.1 The accuracy comparison of $P_i, P^{(I)}, i = 1, 2, 3, I = 0, 1, 2$

P_1	P_2	P_3	$P^{(0)} = P^{(1)} = P^{(2)}$
$\begin{bmatrix} 0.5 & 0.4289 \\ 0.4289 & 0.8884 \end{bmatrix}$	$\begin{bmatrix} 0.5177 & 0.0849 \\ 0.0849 & 0.2222 \end{bmatrix}$	$\begin{bmatrix} 0.9644 & 0.3463 \\ 0.3463 & 0.5996 \end{bmatrix}$	$\begin{bmatrix} 0.1529 & 0.0569 \\ 0.0569 & 0.1893 \end{bmatrix}$

Table 92.2 The accuracy comparison of $\bar{P}_i, \bar{P}^{(I)}, i = 1, 2, 3, I = 0, 1, 2$

\bar{P}_1	\bar{P}_2	\bar{P}_3	$\bar{P}^{(0)} = \bar{P}^{(1)} = \bar{P}^{(2)}$
$\begin{bmatrix} 0.406 & 0.3555 \\ 0.3555 & 0.7544 \end{bmatrix}$	$\begin{bmatrix} 0.4149 & 0.0589 \\ 0.0589 & 0.1654 \end{bmatrix}$	$\begin{bmatrix} 0.8086 & 0.2901 \\ 0.2901 & 0.5094 \end{bmatrix}$	$\begin{bmatrix} 0.119 & 0.041 \\ 0.041 & 0.144 \end{bmatrix}$

Table 92.3 The accuracy comparison of $\text{tr}P_i, \text{tr}\bar{P}_i, i = 1, 2, 3, \text{tr}P^{(I)}$ and $\text{tr}\bar{P}^{(I)}, I = 0, 1, 2$

$\text{tr}P_1(\text{tr}\bar{P}_1)$	$\text{tr}P_2(\text{tr}\bar{P}_2)$	$\text{tr}P_3(\text{tr}\bar{P}_3)$	$\text{tr}P^{(I)}(\text{tr}\bar{P}^{(I)})$
1.3884 (1.1604)	0.73983 (0.58033)	1.5639 (1.3179)	0.34221 (0.263)

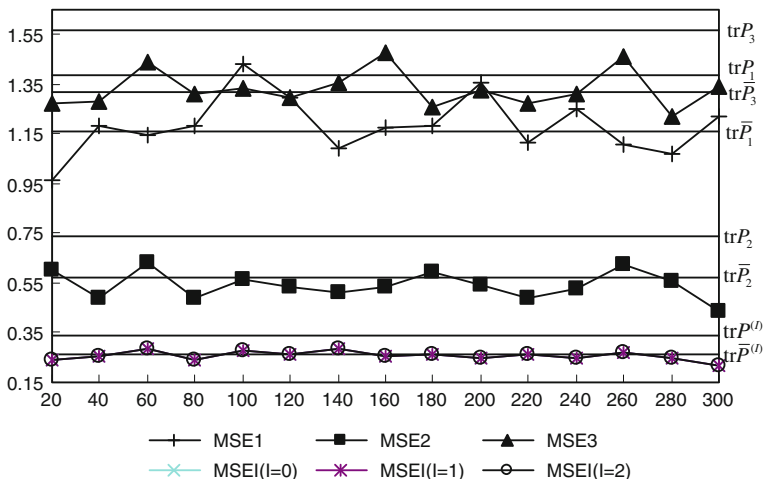


Fig. 92.1 The comparison of $MSE_i(t)$ and $MSE^{(l)}(t)$ $i = 1, 2, 3, l = 0, 1, 2$

and centralized fused Kalman filters are shown in Fig. 92.1, where the straight lines denote trP_i and $tr\bar{P}_i, i = 1, 2, 3, trP^{(l)}$ and $tr\bar{P}^{(l)}, l = 0, 1, 2$, the curves denote $MSE_i(t)$ and $MSE^{(l)}(t)$ values at time t which are defined as the sampled average for trP_i and $trP^{(l)}$.

$$tr\bar{P}^{(l)} \quad trP^{(l)} \quad trP_2 \quad tr\bar{P}_2 \quad tr\bar{P}_1 \quad trP_1 \quad tr\bar{P}_3 \quad trP_3$$

From Fig. 92.1, we see that the values of the $MSE_i(t)$ and $MSE^{(l)}(t)$ are close to the corresponding $tr\bar{P}_i$ and $tr\bar{P}^{(l)}$, and the robust accuracy relation (92.27) holds.

92.5 Conclusion

For multisensor systems with uncertain noises variances, the weighted measurement fusion, centralized fusion and local steady-state robust Kalman filters are presented. It is proved that they are robust, and we have proved that the robust accuracies of weighted measurement fusion and centralized fusion steady-state Kalman filters are same, and are higher than that of the local robust Kalman filter. Their actual accuracies are also same.

Acknowledgments This work is supported by the Natural Science Foundation of China under grant NSFC-60874063, the 2012 Innovation and Scientific Research Foundation of graduate student of Heilongjiang Province under grant YJSCX2012-263HLJ, and the Support Program for Young Professionals in Regular Higher Education Institutions of Heilongjiang Province under grant 1251G012.

References

1. Shalom YB, Li XR, Kirubarajan T (2001) Estimation with applications to tracking and navigation. Wiley, London
2. Sun SL, Deng ZL (2004) Multisensor optimal information Kalman filter. *Automatica* 40:1017–1023
3. Gan Q, Harris CJ (2001) Comparison of two measurement fusion methods for Kalman-filter-based multisensor data fusion. *IEEE Trans Aerospace Electron Syst* 37(1):273–280
4. Rocker JA, Mcgille CD (1988) Comparison of two-sensor tracking method based on state vector fusion and measurement fusion. *IEEE Trans Aerospace Electron Syst* 24(4):447–449
5. Zhu X, Yeng CS, Xie LH (2002) Design and analysis of discrete-time robust Kalman filters. *Automatica* 38:1069–1077
6. Xie LH, Yeng CS, de Souza Carlos E (1994) Robust Kalman filtering for uncertain discrete-time systems. *IEEE Trans. Autom Control* 39:1310–1314
7. Jazwinski AH (1970) Stochastic processed and filtering theory. Academic Press, New York
8. Ran CJ, Hu YS, Gu L, Deng ZL (2008) Correlated measurement fusion steady-state Kalman filtering algorithms and their optimality. *Acta Automatica Sinica* 34:233–239
9. Kailath T, Sayed AH, Hassibi B (2000) Linear estimation. Prentice Hall, New York

Chapter 93

Research on Evaluation of Cabin Design in Naval Ship Based on the Method of Intuitionistic Fuzzy Multiple Attribute Group Decision-Making

Xiaowen Li, P. Li, Z. Lin, Z. Guo and D. Yang

Abstract Crews have more and more requirements for the quality of work and life, cabin design has become an important factor affecting the compact capability of modern naval vessels. Based on naval rules and designer's subjective feeling and experience, traditional cabin design holds that weapons and equipments are more important than habitability. So crew's satisfaction is not high to the ship designed by traditional methods. In order to solve this problem, the method of intuitionistic fuzzy multiple attribute group decision-making was proposed to evaluate the cabin design projects. This method considered many factors affecting cabin design, established the target system, quantified fuzzy factors in cabin design, analyzed the need of crew and gave a reasonable evaluation on cabin design projects. Finally, an illustrative example analysis shows effectiveness and reliability of this method.

Keywords Cabin design · Intuitionistic fuzzy multiple attribute · Target system · Group decision-making

93.1 Introduction

Naval ship system is more complex than before and more and more ship space is occupied by high-tech weapons in new century. A proper cabin design project is necessary in the limited space, in order to meet the requirements of crews' and equipments'. Naval ship as a complex system of man-machine environment has a lot of fuzzy factors. In order to enhance the design quality of ships, an effective evaluation method is necessary in the beginning of the cabin design [1].

X. Li (✉) · P. Li · Z. Lin · Z. Guo · D. Yang
Harbin Engineering University, 8th Floor, Ship Building, No 145 Nantong Street,
Harbin, China
e-mail: lxwaza@163.com

Analytic hierarchy process (AHP) [2] and multi-objective fuzzy decision-making [2], the two evaluation methods are commonly used. The AHP only takes into account the views of experts and ignores the need of the terminal user. The multi-objective fuzzy decision only considers the membership information and ignores uncertain information. Although the later method is more objective, the two of them are not rational and scientific enough for lacking consistency between designers and users. Intuitionistic fuzzy multi-attribute group decision making [3] points out membership and non-membership information, has more expressive than traditional fuzzy sets in dealing with uncertain problems. This method is more flexible and rational than other methods and is more suitable to deal with practical problems [4, 5].

Ship cabin design involves the hull, air, vibration, noise, and other professions and disciplines. There are great differences among the judgments of experts in different fields. If using these judgments directly, the science and rationality of the evaluation will be lowered. So the method of intuitionistic fuzzy multi-attribute group decision making is suitable for this problem.

93.2 Establish Evaluation Target System of Cabin Design

Ship cabin design is actually the division of space and environment. The aim is to provide proper space for crews and equipments, ensure a good environment of working and life, achieve correspond of human-machine environment and enhance the combat effectiveness of the naval ship.

There are a lot of different cabins in naval ship to serve for crews and equipments. To realize the function of cabins, the factors, such as furniture, facility, route environment and so on should be considered as shown in Fig. 93.1.

93.3 Research Methods

93.3.1 Definition of Intuitionistic Fuzzy

In 1965, Professor Zadeh [6] proposed the theory of fuzzy sets which can describe ambiguous concepts and is an effective extension of the classical set. In 1986, Atanassov [7] proposed intuitionistic fuzzy set which is the most effective extension of fuzzy sets. There is a new attribute parameter to describe the fuzzy concepts, which is non-membership function. The intuitionistic fuzzy sets of Atanassov are defined as follows:

Definition 1 [7] Let X be a nonempty fixed set. An intuitionistic fuzzy set A is given by:

$$A = \{ \langle x, \mu_A(x), \nu_A(x) \rangle \mid x \in X \} \quad (93.1)$$

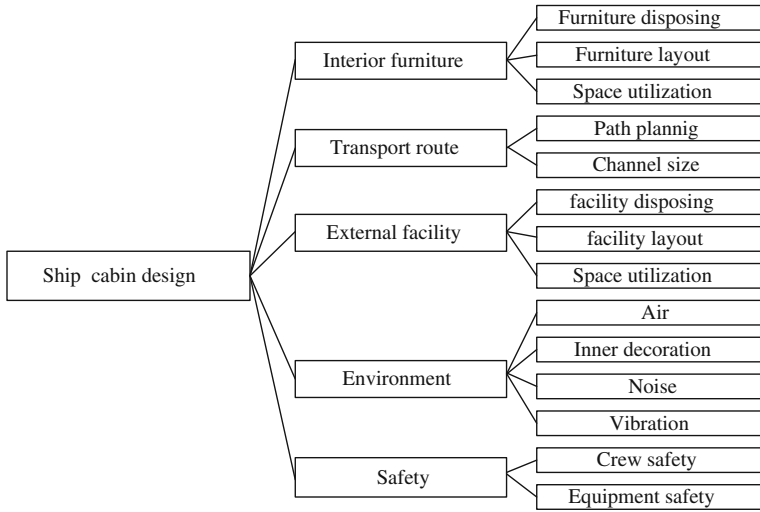


Fig. 93.1 Evaluation target system of Naval ship cabin design

where $\mu_A(x) : X \rightarrow [0, 1]$ and $\nu_A(x) : X \rightarrow [0, 1]$ are such that: $0 \leq \mu_A(x) + \nu_A(x) \leq 1$. And $\mu_A(x), \nu_A(x) \in [0, 1]$ denote degrees of membership and non-membership of $x \in A$, respectively. For each intuitionistic fuzzy set A in X , “hesitation margin” (or “intuitionistic fuzzy index”) of $x \in A$ is given by $\pi_A(x) = 1 - \mu_A(x) - \nu_A(x)$, which expresses a hesitation degree of whether x belongs to A or not. It is obvious that $0 \leq \pi_A(x) \leq 1$, for each $x \in X$.

For any intuitionistic fuzzy number $\alpha = (\mu_\alpha, \nu_\alpha)$, it can be evaluated by the score function [6] which is given by:

$$S(\alpha) = \mu(\alpha) - \nu(\alpha) \tag{93.2}$$

where $S(\alpha) \in [-1, 1]$.

Definition 2 [6–8] Intuitionistic fuzzy logic operations. For any two intuitionistic fuzzy numbers $\bar{\alpha}_1 = (\mu_{\alpha_1}, \nu_{\alpha_1})$ and $\bar{\alpha}_2 = (\mu_{\alpha_2}, \nu_{\alpha_2})$, then:

- (1) Conjunction (logical “and”), $P \wedge Q, x$ belongs A and B,

$$\bar{\alpha}_1 \wedge \bar{\alpha}_2 = (\min(\mu_{\alpha_1}, \mu_{\alpha_2}), \max(\nu_{\alpha_1}, \nu_{\alpha_2}));$$

- (2) Disjunction (logical “or”), $P \vee Q, x$ belongs A and B,

$$\bar{\alpha}_1 \vee \bar{\alpha}_2 = (\max(\mu_{\alpha_1}, \mu_{\alpha_2}), \min(\nu_{\alpha_1}, \nu_{\alpha_2}));$$

(3) Negation (logical “not”), $\neg\bar{\alpha}_1 = (v_{x1}, \mu_{x1})$;

(4) Implication, if x belongs A, then y belongs to B, $P \rightarrow Q = \neg P \vee Q$.

Definition 3 [2] The law of intuitionistic fuzzy logic operations. For any two intuitionistic fuzzy numbers $\bar{\alpha}_1 = (\mu_{x1}, v_{x1})$ and $\bar{\alpha}_2 = (\mu_{x2}, v_{x2})$, then:

$$\bar{\alpha}_1 + \bar{\alpha}_2 = (\mu_{x1} + \mu_{x2} - \mu_{x1} \bullet \mu_{x2}, v_{x1} \bullet v_{x2}) \tag{93.3}$$

$$\bar{\alpha}_1 \bullet \bar{\alpha}_2 = (\mu_{x1} \bullet \mu_{x2}, v_{x1} + v_{x2} - v_{x1} \bullet v_{x2}) \tag{93.4}$$

$$\lambda \bar{\alpha}_1 = (1 - (1 - \mu_{x1})^\lambda, v_{x1}^\lambda), \lambda > 0 \tag{93.5}$$

$$(\bar{\alpha}_1)^\lambda = (\mu_{x1}^\lambda, 1 - (1 - v_{x1})^\lambda), \lambda > 0 \tag{93.6}$$

93.3.2 Decision Rules and Models

First, establish rules of experts’ evaluation then consider the practical needs of crews, finally combine experts’ evaluations and crews’ needs. Rules and model as follows:

Rule 1 If there exist (G_1, t_1, τ_1) , considering the weight of G_1 is ω_1 , then $(G_1, \omega_1 \bullet t_1, \tau'_1)$;

Rule 2 If there exist (G_2, t_2, τ_2) , considering the weight of G_2 is ω_2 , then $(G_2, \omega_2 \bullet t_2, \tau'_2)$;

Rules q If there exist (G_q, t_q, τ_q) , considering the weight of G_q is ω_q , then $(G_q, \omega_q \bullet t_q, \tau'_q)$.

Considering the needs of the crews, the new result of evaluation is

$$\{(a_1, b_1), (a_2, b_2), \dots, (a_q, b_q)\}.$$

For matrix $r = (r_1, r_2, \dots, r_q)$, where $r_i = (a_i, b_i) \otimes (t_i \rightarrow \omega_i \bullet t_i)$, which follows the operation law of intuitionistic fuzzy sets and meets the law of commutation, increasing and association. And $t_i = (\mu_i, v_i)$ is the evaluation given by the experts on different attributes; τ_i is the hesitation margin of t_i and $\tau_i = 1 - \mu_i - v_i$, $\omega_i \in [0, 1]$.

To get the final evaluation results, it is necessary to ensure the logical relationship among the rules of (G_q, t_q, τ_q) and integrate them together. There are three models as following:

Model 1 If the logical relationship among the rules is disjunctive, then $r = \bigvee_{i=1}^q r_i$

Model 2 If the logical relationship among the rules is conjunctive, then $r = \bigwedge_{i=1}^q r_i$

Model 3 If the logical relationship among the rules is the combination of disjunctive and conjunctive, then r can be described with \wedge and \vee

93.3.3 Method of Intuitionistic Fuzzy Multiple Attribute Group Decision

(1) Establish Collections:

The set of projects, attributes, experts and users as follows:

$$A = \{A_1, A_2, \dots, A_m\}, (m \geq 2); G = \{G_1, G_2, \dots, G_n\}, (n \geq 2);$$

$$E = \{e_1, e_2, \dots, e_t\}, (t \geq 2); F = \{F_1, F_2, \dots, F_l\}, (l \geq 2);$$

The weight of attributes $w = \{w_1, w_2, \dots, w_n\}, (n \geq 2), w_i \in [0, 1], \sum_{w=1}^n w_i = 1;$

The weight of experts $\lambda = \{\lambda_1, \lambda_2, \dots, \lambda_t\}, (t \geq 2), \lambda_k \in [0, 1], \sum_{k=1}^t \lambda_k = 1.$

(2) Ensure the weight vector of experts and users by AHP [9].

(3) Evaluate the different attributes of each project then give the result $\tilde{a}_{ij}^k,$

$i = 1, 2, \dots, n, j = 1, 2, \dots, m, k = 1, 2, \dots, l,$ and then form decision making matrix $\tilde{R}^{(k)} = (\tilde{a}_{ij}^k)_{m \times n},$ finally calculate the membership and non-membership.

(4) Establish rules of experts' evaluation, then ensure the relationship among the rules, and conclude $r^{ij},$ where expert's evaluation to project A_i is $r^{ij}.$ Calculate the final results of A_i by the function $r^i = \lambda_1 \bullet r^{i1} \vee \lambda_2 \bullet r^{i2} \vee \dots \vee \lambda_t \bullet r^{it},$ where $\lambda_i (i = 1, 2, \dots, m)$ is the weight of expert.

(5) Choose the optimal project by attribute values.

93.4 Practical Applications

The method of intuitionistic fuzzy multiple attribute group decision making is applied to evaluate the projects of ship cabin design. For our purposes, take a relatively independent life area in ship for example. There are three projects $A = \{A_1, A_2, A_3\}$ (as shown in Fig. 93.2), five attributes {Transport route $G_1,$ Interior furniture $G_2,$ External facility $G_3,$ Environment $G_4,$ Safety G_5 }, three experts $e = \{e_1, e_2, e_3\}$ and one user $p_1.$

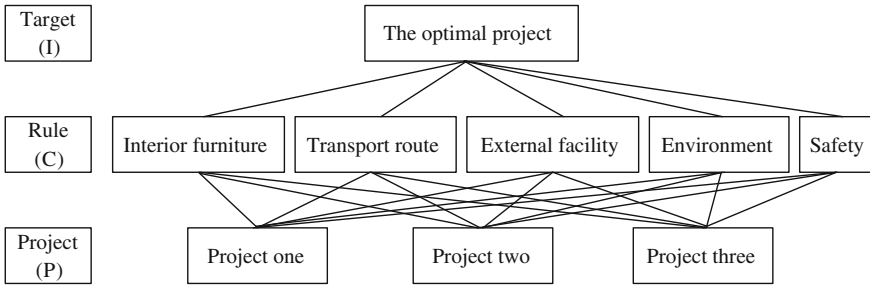


Fig. 93.2 Hierarchical structure model of ship cabin design

Three experts' evaluation as follows:

$$R_1 = (r_{mn}^{11}) = \begin{pmatrix} (0.3, 0.2) & (0.3, 0.1) & (0.5, 0.4) & (0.7, 0.1) & (0.8, 0.1) \\ (0.6, 0.1) & (0.4, 0.3) & (0.6, 0.2) & (0.3, 0.4) & (0.3, 0.2) \\ (0.5, 0.3) & (0.6, 0.1) & (0.9, 0.02) & (0.4, 0.5) & (0.3, 0.6) \end{pmatrix}$$

$$R_2 = (r_{mn}^{12}) = \begin{pmatrix} (0.2, 0.5) & (0.2, 0.2) & (0.3, 0.5) & (0.4, 0.5) & (0.5, 0.3) \\ (0.7, 0.1) & (0.8, 0.1) & (0.6, 0.2) & (0.7, 0.3) & (0.7, 0.2) \\ (0.6, 0.3) & (0.7, 0.2) & (0.4, 0.4) & (0.4, 0.1) & (0.7, 0.2) \end{pmatrix}$$

$$R_3 = (r_{mn}^{13}) = \begin{pmatrix} (0.6, 0.3) & (0.7, 0.2) & (0.5, 0.3) & (0.5, 0.2) & (0.7, 0.2) \\ (0.3, 0.4) & (0.3, 0.2) & (0.4, 0.1) & (0.8, 0.1) & (0.4, 0.5) \\ (0.7, 0.1) & (0.6, 0.2) & (0.5, 0.4) & (0.9, 0.001) & (0.8, 0.1) \end{pmatrix}$$

Where $m = \{1, 2, 3\}$, $n = \{1, 2, 3, 4, 5\}$, $t = \{1, 2, 3\}$, the weight of experts is given by $w = (0.7, 0.5, 0.4)$. The weight of attribute is given by $\omega = (0.2, 0.5, 0.3, 0.4, 0.6)$. The user's evaluation as follows:

$$P_1 = (p_{mn}^{11}) = \begin{pmatrix} (0.3, 0.2) & (0.3, 0.1) & (0.5, 0.4) & (0.7, 0.1) & (0.8, 0.1) \\ (0.6, 0.1) & (0.4, 0.3) & (0.6, 0.2) & (0.3, 0.4) & (0.3, 0.2) \\ (0.5, 0.3) & (0.6, 0.1) & (0.9, 0.02) & (0.4, 0.5) & (0.3, 0.6) \end{pmatrix}$$

where $m = \{1, 2, 3\}$, $n = \{1, 2, 3, 4, 5\}$, $l = 1$.

Based on decision model in Sect. 93.3.2, the results of comprehensive evaluation can be calculated by the function $r_n^{ij} = p_{mn}^{ij} \otimes (r_{mn}^{ij} \rightarrow \omega_n \bullet r_{mn}^{ij})$. Where, ω_n is the weight of G_n and the operation \otimes is equals to \vee .

The evaluation process of project A_1 as follows:

$$R_j^{i1} = \begin{pmatrix} (0.2, 0.5) & (0.1, 0.4) & (0.4, 0.2) & (0.1, 0.1) & (0.4, 0.4) \\ (0.1, 0.5) & (0.3, 0.4) & (0.2, 0.2) & (0.4, 0.1) & (0.2, 0.4) \\ (0.3, 0.5) & (0.1, 0.4) & (0.2, 0.2) & (0.5, 0.1) & (0.6, 0.4) \end{pmatrix}, i = 1, 2, 3; j = 1, 2, \dots, 5$$

Based on this problem, select the decision-making model 1 in Sect. 93.3.2, then the result of r^{ij} and R^m can be given by:

Table 93.1 Attribute values of projects

	A_1	A_2	A_3
$\mu(A_i)$	0.31	0.38	0.19
$\nu(A_i)$	0.20	0.01	0.01
$S(A_i)$	0.11	0.37	0.18

Table 93.2 Value of hierarchical ranking

Rule		C_1	C_2	C_3	C_4	C_5	Value	Index
		0.10	0.26	0.56	0.06	0.30		
Project	P_1	0.07	0.54	0.25	0.24	0.19	0.14	RI = 0.9
	P_2	0.52	0.08	0.10	0.13	0.12	0.31	CI = 0.03
	P_3	0.29	0.13	0.07	0.57	0.49	0.15	CR = 0.04

$$r^{11} = r_1^{11} \vee r_2^{11} \vee r_3^{11} \vee r_4^{11} \vee r_5^{11} = (0.4, 0.1); r^{21} = (0.4, 0.1); r^{31} = (0.4, 0.5).$$

$$R^1 = w_1 \bullet r_1^{11} \vee w_2 \bullet r_2^{11} \vee w_3 \bullet r_3^{11} = (0.31, 0.20). R^2 = (0.38, 0.01);$$

$$R^3 = (0.19, 0.01).$$

Using the formula $S(A_i) = \mu(A_i) - \nu(A_i)$ to calculate the score function, the attribute values can be concluded as shown in Table 93.1:

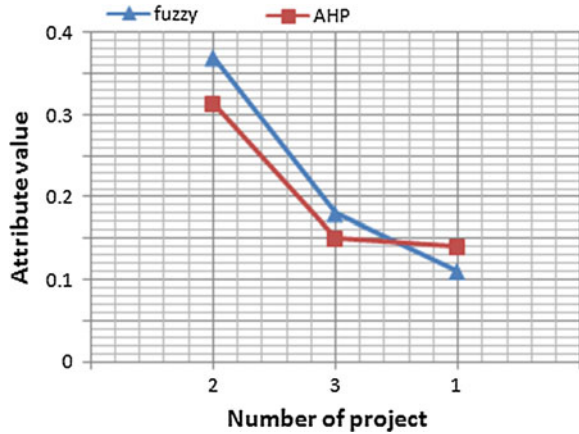
From Table 93.1, the result is obvious $A_2 > A_3 > A_1$ and A_2 is the optimal project. In fact, the project A_2 makes full use of space, considers the actual needs of the crews and is better at furniture disposing and layout as shown. The evaluation result was consistent with the reality, so the accuracy of this method was verified.

To further verify the effectiveness and reliability of intuitionistic fuzzy multiple attribute group decision making, AHP was applied to evaluate the same projects again. Establish the Hierarchical structure model as shown in Fig. 93.2.

In order to ensure the consistency of the judgments, use the same expert's evaluation to build judgment matrix. The optimal project was concluded after hierarchical ranking and consistency check [2], as shown in Table 93.2.

Table 93.2 illustrates the optimal project is P_2 and $P_2 > P_3 > P_1$. The two methods have the same result. Figure 93.3 shows the trend of the two curves is roughly the same, but the slope is different. The curve of intuitionistic fuzzy multi-attribute group decision has obvious advantage. So the reliability and effectiveness of intuitionistic fuzzy multi-attribute group decision was verified.

Fig. 93.3 Comparison of evaluation curves



93.5 Conclusions

The method of intuitionistic fuzzy multiple attribute group decision making synthesized rational and intuitive decision-making, added actual needs of terminal users, changed the traditional evaluation method which only considered the views of experts and enhance the efficiency of decision-making. Finally, the reliability, effectiveness and rationality of this method in ship cabin design were verified by example analysis and this method can also be used in other complex industrial design evaluation.

Acknowledgments This project was supported by National Natural Science Foundation of China (Grant No 61004008), the Central Universities under Grant HEUCFR1001 and LBH-10138 Higher Sliding Mode Control for Underactuated Surface Ship.

References

1. Wang J, Chen L (2010) Comprehensive assessment model and its application to general arrangement of ships. *Chin J Ship Res* 5(1):19–23, 38 (in Chinese)
2. Saaty TL (1980) *The analytic hierarchy process*. Mc Graw Hill Inc, New York
3. Xu Z (2008) *Theory and application of intuitionistic fuzzy information integration*. Science Press, Beijing (in Chinese)
4. Wan S (2010) Survey on intuitionistic fuzzy multi-attribute decision making approach. *Control Decis* 25(11):1601–1606 (in Chinese)
5. Xiaobing L, Yang X (2012) Method of multiple attribute group decision making based on intuitionistic reasoning. *Appl Res Comput* 29(2):533–536 (in Chinese)
6. Zadeh LA (1965) Fuzzy sets. *Inf Control* 8:338–353
7. Atanassov K (1986) Intuitionistic fuzzy sets. *Fuzzy Sets Syst* 20:87–96
8. Chen SM, Tan JM (2000) Handling multicriteria fuzzy decision-making problems based on vague set theory. *Fuzzy Sets Syst* 114:103–113
9. Hu Y, Ling L (2006) *Development and application of the decision supporting system*. China Machine Press, Beijing (in Chinese)

Chapter 94

Studying the Effect of the Group-Size on the Search Computing Cost of MEC for Function Optimization

Liai Wang and Chengyi Sun

Abstract Mind evolutionary computation (MEC) is an approach of evolution computation that was proposed in 1998 by Chengyi Sun. The search computing cost which is affected obviously by the group size is an important measurement to assess performance of the MEC for the desired precision. For using MEC to optimize functions better, the effect of the group size in peak radius MEC on the search computing cost should be studied. In this paper, a two-level MEC algorithm is used, in which the high-level MEC is adopted to optimize the parameters of the low-level MEC for multimodal optimization. In the study, two different dimensional and multimodal tested functions are used. The effect of different value of the group size on the search computing cost is discussed, and a reasonable range of the group size is gotten when optimize the global optimum and the local optimums respectively of the each function.

Keywords Evolutionary computation · Mind evolutionary computation · Multimodal optimization · Search computing cost

94.1 Introduction

Evolutionary Computation (EC) is a major research area for adaptation and optimization. It originates from the Darwin's principle of natural selection, also called survival of the fittest [1]. EC has its obvious characteristics of "population" and "evolution". EC is ubiquitous nowadays, having been successfully applied to

L. Wang (✉)

Information Engineering College, Yangzhou University, Yangzhou, China
e-mail: wla001@163.com

C. Sun

Artificial Intelligence Institute, Beijing City University, Beijing, China

numerous problems from different domains, including optimization, automatic programming, signal processing, bioinformatics, social systems, and so on [2].

Mind Evolution Computation (MEC) is an approach of EC presented by Chengyi Sun in 1998 [3]. MEC has three important mechanisms, and they are evolutionary directionality mechanism, memory mechanism and exploration. Due to the MEC's operations and three mechanisms, the excellent performances are accomplished in the numerical optimization, in which the computing efficiency and the convergence rate of MEC are generally higher than those of GAs by more than 50 % [4], and MEC can solve the non-numerical problem successfully [5, 6], such as TSP, Job-shop and dynamic modeling of system, etc. Now the MEC is studied in proving the MEC's convergence [7] and discussing the performance of MEC in high dimensional solution space [8]. The procedure of MEC is described in detail in the 2nd part of this paper.

The *search computing cost* called *computing cost* for short is an important measurement to assess performance of an algorithm for the desired precision. According to the past experiments, when use MEC to optimize the multimodal functions, the value of the group size S_G affects the MEC's *computing cost*. For improving the performance of MEC for optimizing functions, in this paper, use the two-level MEC [8] to study the effects of different sizes of groups S_G on the *computing cost*. In the studying, two well-known EC multimodal functions are taken as tested functions. Firstly, study the effect of different value of the S_G on the *search computing cost* when find the global maximum, and then discuss the effect when optimize the local optimums. A reasonable range of the S_G is gotten when ensures the *search computing cost* is lower and each solution is precise enough. According to the results, we can combine the actual need to select values for S_G exactly.

94.2 Algorithm Description of MEC

MEC is an evolutionary computation approach through iteration.

Population and group A population is the collection of all individuals in each evolutionary generation. The whole population is divided into some groups.

Billboard Billboard provides opportunities for the information to be exchanged between individuals and between groups. A billboard includes three kinds of basic information which are the order number in a population or in a group, action and score. It can also include other information if needed, such as information of previous several generations. The description of action is subjected to field. A local billboard provides information of the environment for the groups while a global billboard is used to exchange information for groups.

Similartaxis and dissimilation Similartaxis and dissimilation are two important operations in MEC.

Similartaxis is the process in which individuals compete against each other in a local area to search for the local optimum. The operation *similartaxis* serves as local exploitation.

In the process of *similartaxis*, if no more new winner appears in a group, the group is matured. Maturity of a group symbolizes the end of the group's *similartaxis*. The period from birth to maturity of a group is called its *life period*.

Dissimilation is the process in which groups compete with each other in a global area and to search new solutions in the whole solution space. The operation *dissimilation* does as global exploration in MEC.

There is no independent operation selection in MEC, different from GAs, but there is operation selection in procedures both for *similartaxis* and *dissimilation*.

MEC algorithm

The following pseudo codes are the description of the MEC algorithm.

```

/* Parameters in MEC: */
int S, SGi; /* sizes of population and ith group */
int NG; /* numbers of groups */
int NR, SR; /* numbers of groups and individuals released */
int t; /* numbers of generations */
float d; /* peak radius */
float cit; /* the center of group i */

/* Procedure of MEC: */

1. t ← 0
2. Scatter S individuals in the whole solution space randomly
3. Calculate scores of the individuals
4. Select NG best individuals as centers ci0 of groups
5. While (the number of solution in the billboard is not meet)
6. t ← t + 1
7. For the center cit-1 of each group
8. Scatter SGi individuals around the center cit-1 according to a distribution function
9. Calculate scores of the individuals
10. Select the best individual as new center of the group cit (elitist reserved)
11. End for
12. For each group i
13. If (the group i is mature)
14. If (the local optimization is better than a solution in the billboard)
15. Record local optimization in the billboard
16. End If
17. Release individuals of the group i
18. End If
19. End For
20. Note NR, SR as the numbers of groups and individuals released respectively

```

21. If ($N_R > 0$)

Scatter S_R individuals in the whole solution space randomly, and the distance between the each individual and all solutions in the billboard is bigger than d

22. Select N_R best individuals as centers of N_R superior groups respectively

23. End If

24. End While

Operation of similartaxis is defined as local search, and is made up of steps 7–11. The similartaxis exploits a local optimization from an initial solution. Operation of dissimilation is defined as global search, steps 2–4, steps 12–19 and steps 20–24 belong to the dissimilation operation. Both steps 2–4 and steps 20–24 search better initial solutions for groups by their competing with each other in a global area. Steps 12–19 select the global optimizations from the local optimizations found in the similartaxis operation.

94.3 Search Computing Cost

For comparing different algorithms' performance fairly, parameters of each algorithm should be adjusted to make the algorithm have its optimal state. As to different algorithm and tested function, when the algorithm reaches the global optimum with pre-given precision, record how many times that individuals have been evaluated. Run an algorithm repeatedly and independently and compute its average number of evaluation of multi-running. This average number is called its *search computing cost* of the algorithm, and is called *computing cost* for short.

The *search computing cost* is an important measurement to assess performance of an algorithm for the desired precision. Since all evolutionary algorithms are stochastic, each running of an algorithm has different number of evaluation. So we should run an algorithm repeatedly and independently and compute its average number of evaluation of multi-running, namely its *search computing cost* of the algorithm.

94.4 Effects of the Group Size on the Computing Cost

The group size S_G is very important, because it has an effect on whether an algorithm can find the global optimum. Too small group cannot search the solution space effectively, while too large group makes a time wasting to deal with some unnecessary individuals. So we use the two-level MEC to study the relation between S_G and the *search computing cost*.

94.4.1 Two-Level MEC

The two-level MEC is built firstly in [8] to research performance of MEC in high dimensional space. Every evolutionary algorithm has its particular parameters to control its search for a given problem. However, there are no hard and fast rules for choosing appropriate values for these parameters [8]. In 1986, Grefenstette used a meta-level GA to search through a six-dimensional parameter space of another GA [9]. It is clear that in this situation there are two optimization problems: the problem itself and the setting of parameters in an algorithm.

Based on this idea, we use a two-level MEC to optimize functions, in which the high-level MEC is used to deal with parameters optimization problem, while the low-level MEC optimizes tested functions. Accordingly the experiment efficiency is improved.

In high-level MEC, a set of parameters is regarded as an individual, and each individual will be evaluated by low-level MEC. After that, the number of evaluation in low-level MEC is returned as fitness of the individual.

Because of evaluation to be an important measurement to assess performance of an algorithm, and thinking about the precision of solutions optimized, in low-level MEC, add the number of evaluation of test function to the weighted absolute error between test function's real solutions and optimized solutions, and the sum is high-level MEC's fitness.

In two-level MEC, the peak radius dissimilation [10] is used in the low-level MEC. After a group is mature in the operation of similartaxis, when scatter individuals again by dissimilation, the distance between the new group's initial center and the mature groups' centers should be bigger than pre-given d (*peak radius*), and this strategy is called *peak radius dissimilation*. Because the local areas around the mature groups' centers have been searched carefully by the similartaxis, the new groups' centers should not be scattered in these areas to avoid being searched repeatedly.

94.4.2 Tested Functions

F1 consists of equally spaced peaks of non-uniform height. Maxima are located at x values of 0.1, 0.3, 0.5, 0.7 and 0.9. Maxima are of rounded height 1.000, 0.917, 0.707, 0.459, and 0.250 respectively. F1 is defined as follows.

$$F1 = e^{-2(\ln 2)\left(\frac{x-0.1}{0.8}\right)^2} \sin^6(5) \quad x \in [0, 1] \tag{94.1}$$

F2 consists of 25 peaks. The maximal six heights will be found. The six maxima are located at x and y values of (0.1, 0.1), (0.1, 0.3), (0.3, 0.1), (0.3, 0.3), (0.1, 0.5) and (0.5, 0.1). Maxima are of rounded height 2.000, 1.917, 1.917, 1.834, 1.707 and 1.707 respectively. F2 is defined as follows.

$$F2 = e^{-2(\ln 2)(\frac{x-0.1}{0.8})^2} \sin^6(5\pi x) + e^{-2(\ln 2)(\frac{y-0.1}{0.8})^2} \sin^6(5\pi y) \tag{94.2}$$

$x, y \in [0, 1]$.

94.4.3 Optimizing the Global Optimum

In this part, optimize the global maximum of the function F1 and F2, that is, F1's solution is 1.0 and F2's solution is 2.0. In the low-level MEC, three parameters are determined by the high-level MEC, and then are fixed. Once the value of S_G is given, and then run the low-level MEC 30 times independently, meanwhile the 30 times' average absolute error between test function's real solution and optimized solution is less than 5×10^{-6} . The data are showed in Figs. 94.1 and 94.2 respectively. The horizontal ordinate is S_G and the vertical ordinate is the *search computing cost*.

According to the figures, know that the too greater or too less value of S_G can result in the increasing of the *search computing cost*. Figure 94.1 shows that the value of S_G is fit for 3–11 for optimizing one-dimension function, when *computing cost* is less than 1,000. Know from Fig. 94.2: when *computing cost* is less than 20,000, the value of S_G is fit for 6–18 for optimizing two-dimension function.

94.4.4 Optimizing the Local Optimums

Test functions are still F1 and F2. In this part, we use two-level MEC to study how the group size S_G affects the *search computing cost* when optimize the functions' local optimums, that is, F1's five local optimums and F2's first six maximum respectively.

In the low-level MEC, three parameters are determined by the high-level MEC, and then are fixed. Once the value of S_G is given, and then run the low-level MEC 30 times independently, meanwhile the 30 times' average absolute error between test function's real solution and optimized solution is less than 3×10^{-6} . The

Fig. 94.1 Optimizing F1

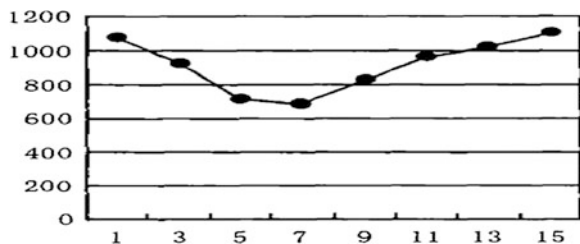


Fig. 94.2 Optimizing F2

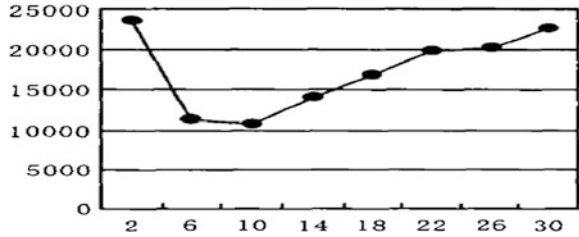


Fig. 94.3 Optimizing F1

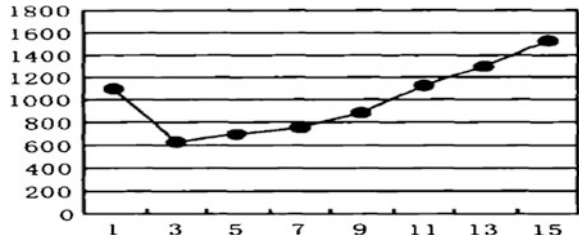
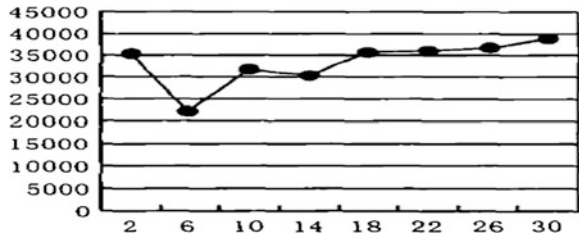


Fig. 94.4 Optimizing F2



experimental data are showed in Figs. 94.3 and 94.4 respectively. The horizontal ordinate is S_G and the vertical ordinate is the *search computing cost*.

The results still show that the too greater or too less value of S_G can result in the increasing of the *search computing cost*. Figure 94.3 reveals that when *computing cost* is less than 1,000, the value of S_G is fit for 3–11 for optimizing one-dimension function. From Fig. 94.4, we can see that a reasonable range of the S_G is 6–18 for optimizing two-dimension function, when *computing cost* is less than 35,000.

94.5 Conclusion

It has been more than a decade since MEC was proposed in 1998 and a preliminary integrated system has already been established. In this paper, build a two-level MEC algorithm and use it to study the effect of the group size S_G on the *search computing cost* of MEC used to function optimization. During the studying, take different dimensional functions F1 and F2 as tested functions, and they are well-known in EC optimization. In the experiments, firstly study how the different value

of the S_G affect the *search computing cost* when optimize the global maximum of F1 and F2, and then discuss the effects when optimize all the maxima of F1 and the six global solutions of F2, finally analyse the results.

The results show that: on the condition that the solutions found are precise enough, the too greater or too less value of S_G can lead to the increasing of the *search computing cost*, thus reduces the MEC's computation efficiency. From the results, can see that compared with optimizing one-dimension functions, greater *search computing cost* are needed when two-dimension functions are optimized, and can also see that optimizing the local optimums need greater *search computing cost* than that only optimizing the global optimum. In our future work, we will study other parameters in MEC for multimodal optimization further.

Acknowledgments This work is supported by the National Natural Science Foundation of China under grant No. 61003180, Natural Science Foundation of Jiangsu Province under contract BK2010318 and Natural Science Foundation of Education Department of Jiangsu Province under contract 12KJB520018. The authors express great acknowledgement for those.

References

1. Zhang BB, Wu Y, Lu JB, Du K-L (2011) Evolutionary computation and its applications in neural and fuzzy systems. *Appl Comput Intell Soft Comput* 2011:1–20
2. Abraham A (2005) Evolutionary computation. *Handbook of measuring system design*
3. Sun CY, Sun YS (1998) Mind-evolution-based machine learning: framework and the implementation of optimization. In: INES'98, Vienna, Austria, pp 355–359
4. Wang JL, Sun Y, Sun CY (2002) Comparison of performance of basic MEC and DC niching gas. In: *Proceedings 4th world congress on intelligent control and automation (WCICA2002)*, ShangHai, China, pp 2297–2303
5. Wang JW, Wang XW, Huang M (2008) A QoS multicast routing algorithm based on mind evolutionary computation and game theory. *J Northeastern Univ (Nat Sci Edn)* 29(2):201 (in Chinese)
6. Xue ZH, Liu WZ, Dong XS, Wu WG (2008) Research on mind evolutionary computation based job scheduling for server clusters. *J XIAN Jiao Tong Univ (Nat Sci Edn)* 42(6):651 (in Chinese)
7. Zhou XL, Sun CY (2007) Pareto-MEC and its convergence analysis. *Comput Eng* 33(10):233 (in Chinese)
8. Sun CY, Wang JL (2002) Performance of MEC in high dimensional space. In: *First international conference on control and automation, ICCA'02*, Xiamen, China, pp 976–980
9. Grefenstette JJ (1986) Optimization of control parameters for genetic algorithms. *IEEE Trans Syst, Man Cybern SMC-16(1)*:122–128
10. Zhang JQ, Sun CY, Wang JL (2001) MEC for solving multi-modal problems. In: *Progress of artificial intelligence in China 2001—proceedings of 9th conference of chinese association on artificial intelligence (CAAI-9)*, Beijing, China, pp 162–167, 1–3, (in Chinese)

Chapter 95

Covariance Intersection Fusion Robust Steady-State Kalman Filter for Multi-Sensor Systems with Unknown Noise Variances

Wenjuan Qi, Peng Zhang, Wenqing Feng and Zili Deng

Abstract For multi-sensor systems with uncertainties of noise variances, a local robust steady-state Kalman filter with conservative upper bounds of unknown noise variances is presented. Based on the Lyapunov equation, its robustness is proved. Further, the covariance intersection (CI) fusion robust steady-state Kalman filter is presented. It is proved that its robust accuracy is higher than that of each local robust Kalman filter. A Monte-Carlo simulation example shows its correctness and effectiveness.

Keywords Multi-sensor data fusion · Covariance intersection fusion · Robust Kalman filter · Uncertain noise variances

95.1 Introduction

The multi-sensor information fusion has received great attentions and has been widely applied in many high-technology fields, such as tracking, signal proceeding, GPS position, robotics and so on. There are three optimal distributed weighted state fusers [1] which have the limitation to compute the optimal weights, the computation of the variances and cross-covariances of the local estimators are required. However, in many application problems, the systems have the uncertainty of model parameters or noise variances, so that the local filtering error variances and cross-covariances are unknown. To solve the filtering problems for

W. Qi · P. Zhang · W. Feng · Z. Deng (✉)

Department of Automation, Heilongjiang University, XueFu Road 74, Harbin 150080, China

e-mail: dzl@hlju.edu.cn

W. Qi · P. Zhang · W. Feng · Z. Deng

Electronic and Engineering College, Heilongjiang University, 130 Harbin 150080, China

uncertain systems, in recent years, several results have been derived on the design of robust Kalman filters that give an upper bound of the filtering error variances for any admissible uncertainty of model parameters [2–4], based on the Riccati equations. Recently, the covariance intersection (CI) fusion method has been presented by Julier and Uhlman [5, 6], which can avoid the computation of cross-covariances, but which requires the consistency of the local Kalman filters.

In this paper, the multi-sensor uncertain systems with uncertainties of noise variances are considered. First, we construct the local robust Kalman filters which give the upper-bounds of actual filtering error variances, their robustness is proved based on the Lyapunov equation. Secondly, the covariance intersection fusion robust Kalman filter is proposed by the convex combination of the local robust Kalman filters, whose robust accuracy is higher than that of each local robust Kalman filter. The geometric interpretation of these accuracy relations is given based on the variance ellipses.

95.2 Local Robust Steady-State Kalman Filter

Consider the multi-sensor uncertain system with unknown noise variances

$$x(t + 1) = \Phi x(t) + \Gamma w(t) \tag{95.1}$$

$$y_i(t) = H_i x(t) + v_i(t), \quad i = 1, \dots, L \tag{95.2}$$

where t is the discrete time, $x(t) \in R^n$ is the state, $y_i(t) \in R^{m_i}$ is the measurement of the i th subsystem, $w(t) \in R^r$, $v_i(t) \in R^{m_i}$ are uncorrelated white noises with zeros mean and unknown actual variances \bar{Q} and \bar{R}_i , respectively. Φ , Γ and H_i are known constant matrices. Assume that Q and R_i have conservative upper bounds \bar{Q} and \bar{R}_i , respectively, i.e.

$$\bar{Q} \leq Q, \bar{R}_i \leq R_i, \quad i = 1, \dots, L \tag{95.3}$$

in the sense that $A \leq B$ means that $B - A \geq 0$ is a semi-positive definite matrix. And assume that each subsystem is completely observable and completely controllable.

Based on the i th sensor, the local steady-state suboptimal Kalman filters with upper bound variances Q and R_i are given by Kailath et al. [7] and Jazwinski [8]

$$\hat{x}_i(t|t) = \Psi_i \hat{x}_i(t - 1|t - 1) + K_i y_i(t) \tag{95.4}$$

$$\Psi_i = [I_n - K_i H_i] \Phi, \quad K_i = \Sigma_i H_i^T (H_i \Sigma_i H_i^T + R_i)^{-1} \tag{95.5}$$

where Ψ_i is a stable matrix and Σ_i satisfies the steady-state Riccati equation

$$\Sigma_i = \Phi \left[\Sigma_i - \Sigma_i H_i^T (H_i \Sigma_i H_i^T + R_i)^{-1} H_i \Sigma_i \right] \Phi^T + \Gamma Q \Gamma^T \tag{95.6}$$

where the symbol T denotes the transpose. The local steady-state conservative filtering error variances satisfy the Lyapunov equation

$$P_i = \Psi_i P_i \Psi_i^T + [I_n - K_i H_i] \Gamma Q \Gamma^T [I_n - K_i H_i]^T + K_i R_i K_i^T \tag{95.7}$$

Defining the actual steady-state filtering error variance as

$$\bar{P}_i = E[\tilde{x}_i(t|t)\tilde{x}_i^T(t|t)], \tilde{x}_i(t|t) = x(t) - \hat{x}_i(t|t) \tag{95.8}$$

Theorem 95.1 *The suboptimal conservative Kalman filters (95.4–95.7) is robust for all admissible actual variances \bar{Q} and \bar{R}_i , such that $\bar{Q} \leq Q$, $\bar{R}_i \leq R_i$ in the sense that $\bar{P}_i \leq P_i$. i.e. P_i is the upper bound variance.*

Proof Substituting (95.1) and (95.4) into $\tilde{x}_i(t|t) = x(t) - \hat{x}_i(t|t)$, we obtain that

$$\tilde{x}_i(t|t) = \Phi x(t-1) + \Gamma w(t-1) - \Psi_i \hat{x}(t-1|t-1) - K_i v_i(t) \tag{95.9}$$

Substituting (95.2) into the above equation yields

$$\tilde{x}_i(t|t) = \Psi_i \tilde{x}(t-1|t-1) + (I_n - K_i H_i) \Gamma w(t-1) - K_i v_i(t) \tag{95.10}$$

Substituting (95.10) into (95.8) yields the actual steady-state filtering error variances as

$$\bar{P}_i = \Psi_i \bar{P}_i \Psi_i^T + [I_n - K_i H_i] \Gamma \bar{Q} \Gamma^T [I_n - K_i H_i]^T + K_i \bar{R}_i K_i^T \tag{95.11}$$

Defining $\Delta P_i = P_i - \bar{P}_i$, subtracting (95.11) from (95.7) yields the Lyapunov equation

$$\Delta P_i = \Psi_i \Delta P_i \Psi_i^T + U_i \tag{95.12}$$

$$U_i = [I_n - K_i H_i] \Gamma (Q - \bar{Q}) \Gamma^T [I_n - K_i H_i]^T + K_i (R_i - \bar{R}_i) K_i^T \tag{95.13}$$

Applying (95.3) and (95.13) yields that $U_i \geq 0$, noting that Ψ_i is a stable matrix, applying the property of the Lyapunov equation [7], we have $\Delta P_i \geq 0$, i.e.

$$\bar{P}_i \leq P_i \tag{95.14}$$

The proof is completed.

Remark 95.1 The robustness (95.14) is also called the consistency or non-divergent estimation [5, 6]. If P_i^* is another upper bound variance for all admissible $\bar{Q} \leq Q$ and $\bar{R}_i \leq R_i$. Taking $\bar{Q} = Q$, $\bar{R}_i = R_i$ yields $P_i \leq P_i^*$. This shows that P_i is also the minimum upper bound variance.

3 CI Fusion Robust Steady-State Kalman Filter

Applying the CI fused algorithm [5, 6], the CI fusion robust steady-state filter is presented as following

$$\hat{x}_{CI}(t|t) = P_{CI} \sum_{i=1}^L \omega_i P_i^{-1} \hat{x}_i(t|t) \tag{95.15}$$

$$P_{CI} = \left[\sum_{i=1}^L \omega_i P_i^{-1} \right]^{-1}, \sum_{i=1}^L \omega_i = 1, \omega_i \geq 0 \tag{95.16}$$

The weighting coefficients ω_i is obtained by minimizing the performance index

$$\min_{\omega_i} \text{tr} P_{CI} = \min_{\substack{\omega_i \in [0,1] \\ \omega_1 + \dots + \omega_L = 1}} \text{tr} \left\{ \left[\sum_{i=1}^L \omega_i P_i^{-1} \right]^{-1} \right\} \tag{95.17}$$

where the symbol tr denotes the trace of matrix. For Eq. (95.17), the optimal weights ω_i can be obtained by “fmincon” function in Matlab.

Theorem 95.2 *The covariance intersection fused filter (95.15) and (95.16) has the actual error variance \bar{P}_{CI} as*

$$\bar{P}_{CI} = E[\tilde{x}_{CI}(t|t)\tilde{x}_{CI}^T(t|t)] = P_{CI} \left[\sum_{i=1}^L \sum_{j=1}^L \omega_i P_i^{-1} \bar{P}_{ij} P_j^{-1} \omega_j \right] P_{CI} \tag{95.18}$$

where $\tilde{x}_{CI}(t|t) = x(t) - \hat{x}_{CI}(t|t)$, $\bar{P}_{ij} = E[\tilde{x}_i(t|t)\tilde{x}_j^T(t|t)]$ are unknown actual cross-covariances among the local filtering errors, and it can be computed by the following Lyapunov equation

$$\bar{P}_{ij} = \Psi_i \bar{P}_{ij} \Psi_j^T + [I_n - K_i H_i] \Gamma \bar{Q} \Gamma^T [I_n - K_j H_j]^T, i, j = 1, \dots, L, i \neq j \tag{95.19}$$

$$\bar{P}_{ii} = \bar{P}_i \tag{95.20}$$

Proof From Eq. (95.16), we have

$$x(t) = P_{CI} \left[\sum_{i=1}^L \omega_i P_i^{-1} \right] x(t) \tag{95.21}$$

Subtracting (95.15) from (95.21), we easily obtain the CI fused actual filtering error

$$\tilde{x}_{CI}(t|t) = P_{CI} \sum_{i=1}^L \omega_i P_i^{-1} \tilde{x}_i(t|t) \tag{95.22}$$

Applying (95.10) and (95.11) yields (95.19) and substituting (95.22) into (95.18) yields the actual fused error variance (95.18). The proof is completed.

Remark 95.2 References [5, 6, 9] proved that when the local filter is robust or consistent, then the CI fusion filter is also robust or consistent, i.e.

$$\bar{P}_{CI} \leq P_{CI} \tag{95.23}$$

Remark 95.3 From (95.23), we can see that P_{CI} is a common upper bound of the unknown actual fused variances \bar{P}_{CI} for all possible \bar{P}_i satisfying the relation $\bar{P}_i \leq P_i$, ($i = 1, \dots, L$) and all possible unknown \bar{P}_{ij} . From 95.16, we see that P_{CI} is independent of actual variances P_i and cross-covariances P_{ij} . So that the accuracy of the CI fuser has the robustness with respect to unknown \bar{P}_i and \bar{P}_{ij} , or equivalently, the CI fuser is robust with respect to uncertainty of \bar{Q} and \bar{R}_i satisfying (95.3).

95.4 Accuracy Analysis

Theorem 95.3 *The accuracy comparison of the local and the CI fusion robust filter is given by*

$$\text{tr}\bar{P}_i \leq \text{tr}P_i, \quad i = 1, \dots, L \tag{95.24}$$

$$\text{tr}\bar{P}_{CI} \leq \text{tr}P_{CI} \leq \text{tr}P_i, \quad i = 1, \dots, L \tag{95.25}$$

Proof From the robustness (95.14), (95.24) holds. From (95.23), the first inequality of (95.25) holds. From (95.17), taking $\omega_i = 1$ and $\omega_j = 0$ ($j \neq i$) yield $\text{tr}P_{CI} = \text{tr}P_i$, hence we have the accuracy relations $\text{tr}P_{CI} \leq \text{tr}P_i$, $i = 1, \dots, L$. The proof is completed.

Remark 95.4 Equation (95.24) means that the actual accuracy of the local filter for all admissible \bar{Q} and \bar{R}_i satisfying (95.3) is globally controlled by $\text{tr}P_i$, therefore $\text{tr}P_i$ is called the robust accuracy of the local filter. From (95.25) we see that the actual accuracy of CI fuser is globally controlled by $\text{tr}P_{CI}$, hence $\text{tr}P_{CI}$ is also called the robust accuracy of the CI fuser. The second inequality of (95.25) means the robust accuracy of the CI fuser is higher than that of each local filter. The robustness of the local and CI fused filters means that the robust accuracies $\text{tr}P_i$ and $\text{tr}P_{CI}$ are independent of arbitrarily variances satisfying $\bar{Q} \leq Q$ and $\bar{R}_i \leq R_i$, i.e., $\text{tr}P_i$ and $\text{tr}P_{CI}$ are insensitive to uncertain \bar{Q} and \bar{R}_i .

95.5 Simulation Example

Consider the two-sensor tracking system with uncertain variances

$$x(t + 1) = \Phi x(t) + \Gamma w(t) \tag{95.26}$$

$$y_i(t) = H_i x(t) + v_i(t), i = 1, 2 \tag{95.27}$$

$$\Phi = \begin{bmatrix} 1 & T_0 \\ 0 & 1 \end{bmatrix}, \Gamma = \begin{bmatrix} 0.5T_0^2 \\ T_0 \end{bmatrix}, H_1 = [1 \quad 0], H_2 = I_2 \tag{95.28}$$

where $T_0 = 0.25$ is the sampled period, $x(t) = [x_1(t), x_2(t)]^T$ is the state, $x_1(t)$ and $x_2(t)$ are the position and velocity of target at time tT_0 . $w(t)$ and $v_i(t)$ are independent Gaussian white noises with zero mean and unknown variances Q and R_i respectively. In the simulation, we take $Q = 1, R_1 = 0.8, R_2 = \text{diag}(8, 0.36), \bar{Q} = 0.8, \bar{R}_1 = 0.65, \bar{R}_2 = \text{diag}(6, 0.25)$.

According to the Kalman filtering, the variances of the local and CI fused filter are obtained as

$$P_1 = \begin{bmatrix} 0.2492 & 0.1855 \\ 0.1855 & 0.3046 \end{bmatrix}, P_2 = \begin{bmatrix} 0.4035 & 0.0645 \\ 0.0645 & 0.121 \end{bmatrix}, \bar{P}_1 = \begin{bmatrix} 0.2019 & 0.1497 \\ 0.1497 & 0.2447 \end{bmatrix}, \\ \bar{P}_2 = \begin{bmatrix} 0.2922 & 0.0448 \\ 0.0448 & 0.0892 \end{bmatrix}, P_{CI} = \begin{bmatrix} 0.2645 & 0.0977 \\ 0.0977 & 0.1668 \end{bmatrix}, \bar{P}_{CI} = \begin{bmatrix} 0.0986 & 0.0386 \\ 0.0386 & 0.0944 \end{bmatrix}.$$

The accuracy of the local and CI fuser is defined as the trace of their error variance matrix, the smaller trace means the higher accuracy and the larger trace means the lower accuracy. The traces of the error variance of the local and CI fused Kalman filters are compared in Table 95.1. From Table 95.1, we see that the accuracy relations (95.24) and (95.25) hold.

In order to give a geometric interpretation of the accuracy relations, the covariance ellipse is defined as the locus of points $\{x : x^T P^{-1} x = c\}$, where P is the variance matrix and c is a constant. Generally, we select $c = 1$. It has been proved in [9] that $P_1 \leq P_2$ is equivalent to that the covariance ellipse of P_1 is enclosed in that of P_2 .

The accuracy comparison of the covariance ellipses is shown in Fig 95.1. From Fig 95.1, we see that the ellipse of the actual variance \bar{P}_1 or \bar{P}_2 is enclosed in that of the upper bound variance P_1 or P_2 , respectively, which verify the consistent Eq. (95.14). The ellipse of actual CI fused variance \bar{P}_{CI} is enclosed in that of P_{CI} , which verifies the robustness of the Eq. (95.23), and the ellipse of P_{CI} encloses the intersection of the variance ellipses formed by P_1 and P_2 , and passes through the four points of intersection of the local ellipses for P_1 and P_2 [9].

In order to verify the above theoretical accuracy relations, taking $N = 200$ runs, the curves of the mean square error (MSE) of local and fused Kalman filters are shown in Fig. 95.2.

Table 95.1 The accuracy comparison of local and fused filters

$\text{tr}P_1$	$\text{tr}P_2$	$\text{tr}\bar{P}_1$	$\text{tr}\bar{P}_2$	$\text{tr}P_{CI}$	$\text{tr}\bar{P}_{CI}$
0.5538	0.5245	0.4466	0.3814	0.4313	0.1930

Fig. 95.1 The covariance ellipses of Kalman filters

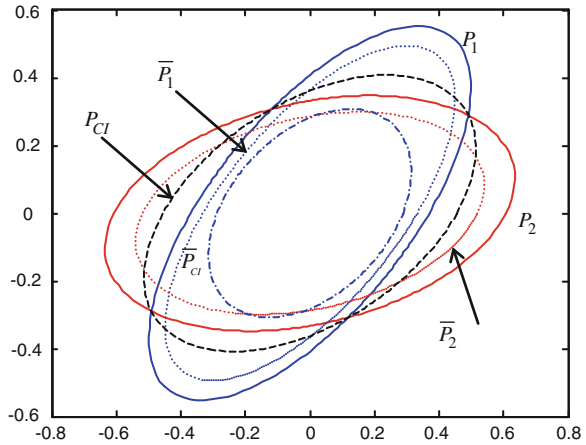
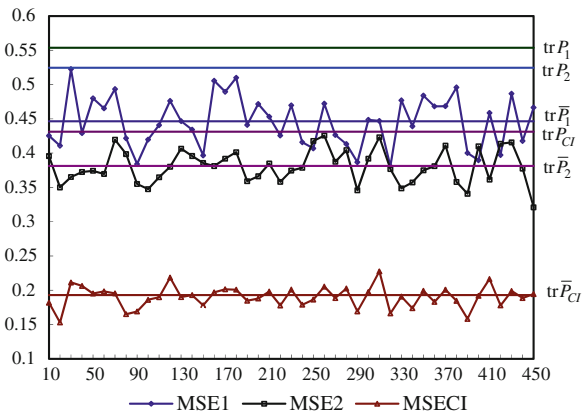


Fig. 95.2 The MSE curves of local and fused filters



From Fig. 95.2, we see that the $MSE_i(t)$ values of the local and CI fused filters are close to the corresponding theoretical trace values, which also verifies the accuracy relations (95.24), (95.25) and the accuracy relations in Table 95.1.

95.6 Conclusion

For the multi-sensor systems with uncertainties of noise variances, using the Kalman filtering the local steady-state robust Kalman filter and the CI robust fuser have been presented, and the robustness of the local filtering estimates is proved based on the Lyapunov equation. The corresponding CI fuser is also robust, and its robust accuracy is higher than that of each local robust filter.

Acknowledgments This work is supported by the Natural Science Foundation of China under grant NSFC-60874063, the 2012 Innovation and Scientific Research Foundation of graduate student of Heilongjiang Province under grant YJSCX2012-263HLJ, and the Support Program for Young Professionals in Regular Higher Education Institutions of Heilongjiang Province under grant 1251G012.

References

1. Deng ZL, Zhang P, Qi WJ, Gao Y, Liu JF (2013) The accuracy comparison of multisensor covariance intersection fuser and three weighting fusers. *Inf Fusion* 14:177–185
2. Zhu X, Soh YC, Xie L (2002) Design and analysis of discrete-time robust Kalman filters. *Automatica* 38:1069–1077
3. Xie L, Soh YC, de Souza CE (1994) Roust Kalman filtering for uncertain discrete-time systems. *IEEE Trans Autom Control* 39(6):1310–1314
4. Theodor Y, Shaked U (1996) Robust discrete-time minimum-variance filtering. *IEEE Trans Signal Process* 44(2):181–189
5. Julier SJ, Uhlman JK (1997) Non-divergent estimation algorithm in the presence of unknown correlations. *Proc Am Control Conf* 4:2369–2373
6. Julier SJ, Uhlman JK (2009) General decentralized data fusion with covariance intersection. in: Liggins ME, Hall DL, Llinas J (eds) *Handbook of multisensor data fusion theory and practice*. CRC Press, pp 319–342
7. Kailath T, Sayed AH, Hassibi B (2000) *Linear estimation*. Prentice Hall, New York
8. Jazwinski AH (1970) *Stochastic processed and filtering theory*. Academic Press, New York
9. Deng Z, Zhang P, Qi W, Liu J, Gao Y (2012) Sequential covariance intersection fusion Kalman filter. *Inf Sci* 189:293–309

Chapter 96

Study on Online ϵ NN Q-Learning for Multi-Robot System Based on Community Perception Network

Lu Jin, Yuequan Yang, Chunbo Ni, Yifei Kong and Zhiqiang Cao

Abstract Considering the curse of dimensionality and inadequate learning of the historical information provided by the other robots, an online ϵ -radius Nearest Neighbors (ϵ NN) classification method is employed in the community perception network environment. In order to increase learning efficiency, a new multi-robot reinforcement learning strategy is proposed by employing classification of historical states and information sharing mechanism. Finally, the analysis of convergence of Q values matrix is done, and simulations are shown the effectiveness and efficiency of the proposed scheme.

Keywords Multi-robot system · Q-learning · ϵ NN · Community perception network

96.1 Introduction

With the development of the multi-robot system [1], more useful information is needed to complete certain assignments for robots, which may lead to waste more time to complete such assignments due to limited perception scope of the sensors. It is inevitable for robots to improve perception intelligence of environment. Static intelligent perception nodes are laid in the working environment to provide more useful information for robots, which is expended to improve the efficiency of cooperation among robots. Furthermore, study on community network-based

L. Jin · Y. Yang (✉) · C. Ni · Y. Kong
College of Information Engineering, Yangzhou University, Yangzhou 225009, China
e-mail: yangyq@yzu.edu.cn

Z. Cao (✉)
State Key Laboratory of Management and Control for Complex Systems, Institute of
Automation Chinese Academy of Sciences, Beijing 100190, China
e-mail: zqcao@compsys.ia.ac.cn

multi-robot system [2–6] has attracted wide attention nowadays. With an increasing number of the robots, dimensions are increased exponentially because of the combination of the states and decision space which will cause the learning problem more complex. Much attention has been paid to research achievement of full information sharing and acceleration of convergence as well as improvement of the efficiency in cooperation and tasks completion [7]. However, the convergence performance becomes much worse and the learning efficiency decline greatly when state space and decision space increase. To enhance multi-robot learning efficiency, a kind of Neural Networks method [8] is used in traditional Q-learning, but which could not get a global optimal solution because of slower learning convergence and easier fall into a local minimum point. In addition, the complicacy of learning and the use of the algorithm range will both become more intricate and restricted. Another idea of Metropolis criterion of simulated annealing algorithm [9] is used to balance the relationship between the exploration and exploitation of fuzzy Q learning, which can significantly improve convergence rate faster than fuzzy Q-learning and traditional Q-learning, but it has a drawback of complexity in establishment of the rule base. The nearest neighbors' classification method combining with Q-learning algorithm [10, 11] is presented to resolve the combinatorial explosion problem [12–16]. A kind of local weighted KNN classification method [16] is proposed to firstly classify all states, which may bring inadequate learning of classified states during the learning procedure. ϵ NN [17] is used as a kind of non-parametric classification method, which is straightforward and easy to implement to reduce the number of the states. Based on this, we proposed an improved algorithm of Q-learning based on online ϵ NN method to classify all historical states. Because of the historical state corresponding to an updated Q values, it can bring about advantages of abundant and accumulative learning.

Owing to the increasing number of the state-action combination of the robots, it may cause a problem of inefficient of learning in the community perception network environment. The proposed algorithm based on Ref. [2] only share historical information of other robots when they are under the same state-action, which may bring inefficient information sharing and complicated calculation ultimately. The improved algorithm is to resolve the problem of combinatorial explosion of dimensionality and inefficient information sharing. It is more reasonable to classify all historical states to find the sets of nearest neighbors of their own states and their existing communities, which will make comprehensive use of robots' historical Q values and states provided by community perception networks. The motivation of this scheme is to optimize the Q-learning process and improve the learning efficiency. Finally, the convergence analysis of the robot s' Q values matrix is done by employing its 2-norm, and simulations are given to further show the effectiveness and efficiency of the proposed scheme.

96.2 Detection Framework

The sonar array with six sensors distributed evenly is used for each robot, where detection area is a fan-shaped region with a central angle of $3/\pi$. According to the detection information returned by the sensors, the current state of a robot is defined as $s_d = [\alpha_1, \dots, \alpha_6]$, where $\alpha_i (i = 1, \dots, 6)$ is detection information in its detection range. $\alpha_i = 1$ if an obstacle is detected, otherwise $\alpha_i = 0$. Correlative description about target position perception s_g of the robot is same with that in [16].

$$\rho_k = \begin{cases} \frac{\pi}{3}(k - \frac{5}{2}), & k = 1, \dots, 5 \\ -\frac{7}{6}\pi, & k = 6 \end{cases} \quad (96.1)$$

where ρ_k is the k th sensor's direction.

The description of the community perception network environment can be defined in [2].

96.3 Online ϵ NN Q-Learning

Taking into account of the similarity between the large amounts of states of the robots in the dynamic environment, the improved algorithm is used to reduce the dimensionalities. A local weighted Q-learning algorithm based on four part of perception environment information is proposed by employing the online ϵ NN classification method, which may accelerates the learning speed of Q-learning algorithm and reduce the misclassified probability in online ϵ NN classification method. A state of a robot can be divided into front, rear, right and left parts, denoted as $s_{df} = [\alpha_3, \alpha_2]$, $s_{db} = [\alpha_5, \alpha_6]$, $s_{dr} = [\alpha_1]$ and $s_{dl} = [\alpha_4]$ respectively. Because the role-playing of parts of a state is different in working circumstances, weighted value is arranged to corresponding part by experience.

In the multi-robot system based on community perception networks, the nearest neighbors of the current state s for robot R_k with two kinds of situations are determined as follows. Suppose that R_k enters the community C_m , and the Euclidian distance from current state s_i to each historical state s_j according to formula (96.2) is denoted as $d_{i,j}$. If the Euclidian distance is less than the threshold ϵ , correlative historical states satisfying (96.3) belong to the set of its own nearest neighbors of current state s_i denoted as $\epsilon NN(s_i)$, where ϵ is the radius of the sphere threshold. In accordance with (96.4), the weight $\omega_{i,j}$ and probability $p_{i,j}$ of each nearest neighbor can be calculated.

$$d_{i,j} = \sqrt{\sum_{l=1}^6 (\omega \times \rho_l^i - \omega \times \rho_l^j)^2} \quad (96.2)$$

$$\begin{cases} s_j \in \varepsilon NN(s_i), & \forall d_{i,j} < \varepsilon \\ s_j \notin \varepsilon NN(s_i), & \forall d_{i,j} \geq \varepsilon \end{cases} \quad (96.3)$$

$$\begin{cases} \omega_{i,j} = 1/1 + (d_{i,j})^2 \\ p_{i,j} = \omega_{i,j} / \sum_{k=1}^{\varepsilon NN(s_i)} \omega_{i,k}, \forall s_j \in \varepsilon NN(s_i) \end{cases} \quad (96.4)$$

In the community perception network environment, the historical decision-making information of other robots can be provided by static intelligent perception nodes. For better use of useful historical information, it is necessary to take into consideration not only of the impact of historical Q values of robot R_k under the same state-action but also of other robots under different state-action. Considering the impact of other robots' historical decision-making information, the Euclidian distance from current state s_i to each historical state s_j of other robots can be calculated according to formula (96.5).

$$d_{i,j}^{k,n} = \sqrt{\sum_{l=1}^6 (\omega \times \rho_l^{m,i} - \omega \times \rho_l^{n,j})^2}, \forall R_k, R_n \in C_m \quad (96.5)$$

where $\rho_l^{k,i}$ indicates the l th values of current state s_i of robot R_k ; $\rho_l^{n,j}$ indicates the l th values of historical state s_j of robot R_n . The historical state s_j of robot R_n will be the nearest neighbor of the current state s_i of robot R_k if the Euclidian distance is less than the threshold ε , which is defined as the set of community nearest neighbors and denoted as $\varepsilon NN_{C_m}(s_i)$. According to formula (96.6), the weight $\omega_{i,j}^{k,n}$ and probability $p_{i,j}^{k,n}$ of each nearest neighbors can be calculated.

$$\begin{cases} \omega_{i,j}^{k,n} = 1/1 + (d_{i,j}^{k,n})^2 \\ p_{i,j}^{k,n} = \omega_{i,j}^{k,n} / \sum_{l=1}^{\varepsilon NN_{C_m}(s_i)} \omega_{i,l}^{m,n}, \forall s_j \in \varepsilon NN_{C_m}(s_i) \end{cases} \quad (96.6)$$

While the robot R_k is at the Blind Area, the proposed classification method is similar to the current state s_i .

In the community perception network environment, it is more effective to communicate with each other by providing useful historical decision-making information of other robots. However, as the number of the robots increasing, combinatorial explosion of dimensionality may lead to generalization. The proposed algorithm has two advantages of linear function estimation characteristics and being easy to operate, which can be used to classify the historical states online to accelerate the convergence as well as enhance learning efficiency.

In the multi-robot system based on community perception networks, the learning rules of the proposed scheme are determined as follows.

Suppose that the robot R_k enters into the community C_m , its own Q values updating rule is

$$\begin{aligned} Q^k(s, a)_t \leftarrow & Q_{\varepsilon NN(s_i)}^k(s, a)_t + \alpha(r + \gamma_1 \max_{u \in A} Q^k(s, u)_{t+1} + \gamma_2 \max_{R_j \in C_m, u \in A} Q_{\varepsilon NN_{C_m}(s_i)}^n(s, u)_{t+1} \\ & - Q_{\varepsilon NN(s_i)}^k(s, a)_t), \exists R_k, R_n \in C_m, s_j \in \varepsilon NN_{C_m}(s_i) \end{aligned} \quad (96.7)$$

whereas the updating rule for state s_j belonging to the set of community nearest neighbors is

$$\begin{aligned} Q_{\varepsilon NN(s_i)}^k(s, a)_t \leftarrow & Q_{\varepsilon NN(s_i)}^k(s, a)_t + \alpha(r + \gamma_1 \max_{u \in A} Q_{\varepsilon NN(s_i)}^k(s, u)_{t+1} \\ & + \gamma_2 \max_{R_n \in C_m, u \in A} Q_{\varepsilon NN_{C_m}(s_i)}^n(s, u)_{t+1} - Q_{\varepsilon NN(s_i)}^k(s, a)_t), \quad (96.8) \\ & \exists R_k, R_n \in C_m, s_j \in \varepsilon NN_{C_m}(s_i) \end{aligned}$$

While the robot R_k is at the Blind Area, its updating rule is converted to

$$\begin{aligned} Q^k(s, a)_t \leftarrow & Q_{\varepsilon NN(s_i)}^k(s, a)_t + \alpha(r + \gamma \max_{u \in A} Q^k(s, u)_{t+1} \\ & - Q_{\varepsilon NN(s_i)}^k(s, a)_t), \exists R_i \in \bigcup_{m=1}^{N_c} C_m, s_j \in \varepsilon NN(s_i) \end{aligned} \quad (96.9)$$

whereas the updating rule for state s_j belonging to the set of the community nearest neighbors is

$$\begin{aligned} Q_{\varepsilon NN(s_i)}^k(s, a)_t \leftarrow & Q_{\varepsilon NN(s_i)}^k(s, a)_t + \alpha(r + \gamma \max_{u \in A} Q_{\varepsilon NN(s_i)}^k(s, u)_{t+1} \\ & - Q_{\varepsilon NN(s_i)}^k(s, a)_t), \forall R_i \in \bigcup_{m=1}^{N_c} C_m, s_j \in \varepsilon NN(s_i) \end{aligned} \quad (96.10)$$

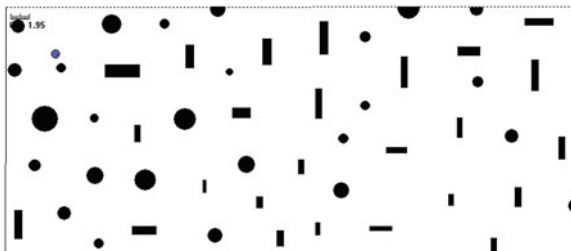
where $Q_{\varepsilon NN(s_i)}^k$ is the anticipant Q values of the set of the community nearest neighbors, which can be calculated according to formula (96.10); $s, s_i, s_j \in S$, S is the finite state set of the robot; $a, u \in A$, A is the finite action set of the robot; α is the learning rate; r means the reward values function; $\gamma, \gamma_1, \gamma_2$ refer to discount factor respectively.

96.4 Simulations

To verify the convergence of the proposed algorithm, the random strategy based on Simulated Annealing [18, 19] is applied to train the robots in the experimental scenarios shown in Fig. 96.1. Suppose that the number of robot $n = 4$, the number of robot sonar $m = 6$, the speed of the robot $v = 0.3$, the sensor radius $r = 2$, $\alpha = 0.4$, $\gamma = 0.5$, $\gamma_1 = 0.2$, $\gamma_2 = 0.8$ and $\varepsilon = 2$, respectively.

Q-value matrix is saved every 20 steps, and then the saved Q values matrix is processed to strike 2-norm by Matlab. Finally a diagram of steps and 2-norm of the

Fig. 96.1 The training situation



Q-value matrix is drawn shown in Fig. 96.2. From Fig. 96.2, it is through about 18,000 steps that the proposed algorithm begins to converge, while the Q-Learning based on community perception network and basic Q-learning are through about 23,000 steps and 35,000 steps respectively.

After learning phases, the test experiment is done, shown as in Fig. 96.3, which demonstrates that robots can reach their destinations efficiently and effectively.

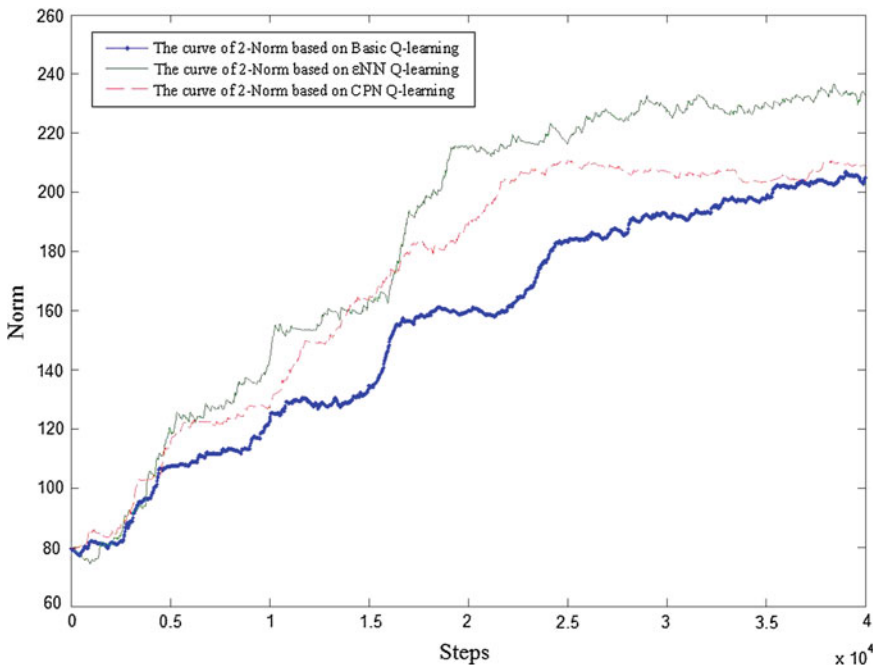


Fig. 96.2 Analysis of norm of the Q values

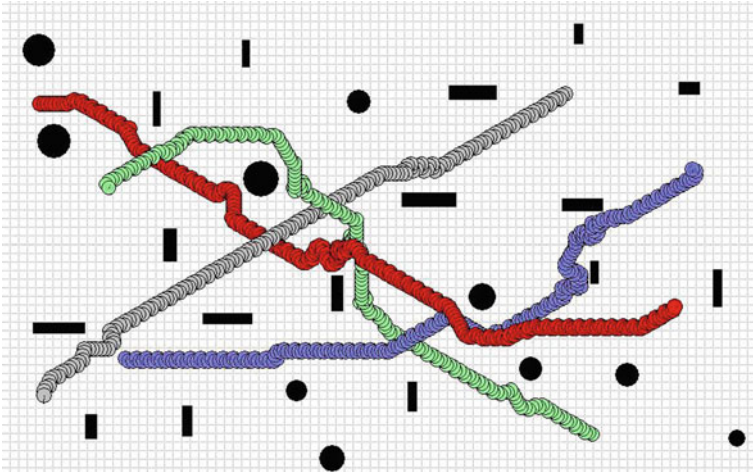


Fig. 96.3 The test experiment of training learning

96.5 Conclusions and Future Work

The proposed scheme can not only reduce the dimensions of the states but also share useful historical decision-making information of other robots in the community perception networks, which can avoid the duplication of learning procedure of robots and accelerate the learning convergence of robots in multi-robot system. The experiments show that the proposed strategy is effective and efficient. Learning capability is one of the effective ways to improve robotic intelligence. Community perception network play an important and efficient role of information channel to provide historical decision-making information for multi-robot systems. There is much critical work to be done in the future.

Acknowledgments This work is partially supported by the National Natural Science Foundation of China under Grant No. 61175111, 61174046, and 61273352, and the Natural Science Foundation of the Jiangsu Higher Education Institutions of China under Grant No. 10KJB510027.

References

1. Tan M, Wang S, Cao ZQ (2005) Multi-robot system. Tsinghua University Press, Beijing (in Chinese)
2. Jin L, Ni CB, Yang YQ, Cao ZQ (2012) Study on Q-learning of multi-robot systems based on community perception networks. In: International conference on mechanic automation and control engineering, ICMACE 2012, Baotou, pp 511–515
3. Alberto S, Norihiro H, Alessandro S (2008) Network robot systems. Robot Auton Syst 56(10):793–797
4. <http://urus.upc.es/index.html>

5. Kanda T, Shiomi M, Miyashita Z, Ishiguro H, Hagita N (2010) A Communication robot in a shopping mall. *IEEE Trans Rob* 26(5):897–913
6. Chao S, Kanda T, Shimada M, Yamaoka F, Ishiguro H, Hagita N (2010) Easy development of communicative behaviors in social robots. In: *IEEE/RSJ international conference on intelligent robots and systems, IROS 2010*, pp 5302–5309
7. Wu J, Xu X, Wang J, He HG (2011) Recent advances of reinforcement learning in multi-robot systems: a survey. *Control Decis* 26(11):1601–1610 (in Chinese)
8. Geng XL, Chang CJ (2011) Application of parallel reinforcement learning based on artificial neural network to adaptive planning. *Sci Technol Eng* 11(4):756–759 (in Chinese)
9. Liu ZY, Song ZD (2012) Chaotic fuzzy Q-learning control for urban area traffic signals. *Comput Eng Appl* 48(4):207–210 (in Chinese)
10. Su ZP, Jiang JG, Liang CY, Zhang GF (2011) Selection in disaster response management based on Q-learning. *Int J Autom Comput* 8(1):100–106 (in Chinese)
11. Ke WD, Pu SH, Peng ZP, Cai ZS, Yuan QD (2012) Cooperative Q-learning method based on π calculus in robot soccer. *Comput Appl* 48(4):207–210 (in Chinese)
12. Martin HJ, Lope J (2007) A k-NN based perception scheme for reinforcement learning. *EUROCAST* pp 138–145
13. Martin HJ, Lope J (2009) An effective algorithm for continuous actions reinforcement learning problems. In: *Proceedings of the 35th IEEE annual conference on industrial electronics society, IECON 2009, Oporto*, pp 2063–2068
14. Martin HJ, Lope J, Maravall D (2009) The kNN-TD reinforcement learning algorithm. *Lect Notes Comput Sci* 5901:305–314
15. Martin HJ, Lope J, Maravall D (2011) Robust high performance reinforcement learning through weighted k-nearest neighbors. *Neurocomputing* 74:1251–1259
16. Han F, Jin L, Yang YQ, Cao ZQ (2012) Research on robot motion control based on local weighted KNN-TD reinforcement learning. In: *Proceedings of the 10th world congress on intelligent control and automation, WCICA 2012, Beijing*, pp 3648–3651 (in Chinese)
17. Wu DG, Huang YW, Li J (2011) Research on the improved geodesic distance algorithm of LSSVM kernel function. *Process Autom Instrum* 32(12):5–8 (in Chinese)
18. Gao Y, Cheng SF, Lu X (2004) Research on reinforcement learning technology: a review. *Acta Automatic Sinica* 30(1):86–100 (in Chinese)
19. Kirkpatrick S, Gelatt CD, Vecchi MP (1983) Optimization by simulated annealing. *Sci New Ser* 220:671–680